



---

DEVELOPMENT AND STUDY OF NOVEL THERMALLY  
REARRANGED POLYMER MEMBRANES AND THEIR  
THERMOKINETIC AND REACTION MECHANISM  
AN EXPERIMENTAL AND MODELLING STUDY

---



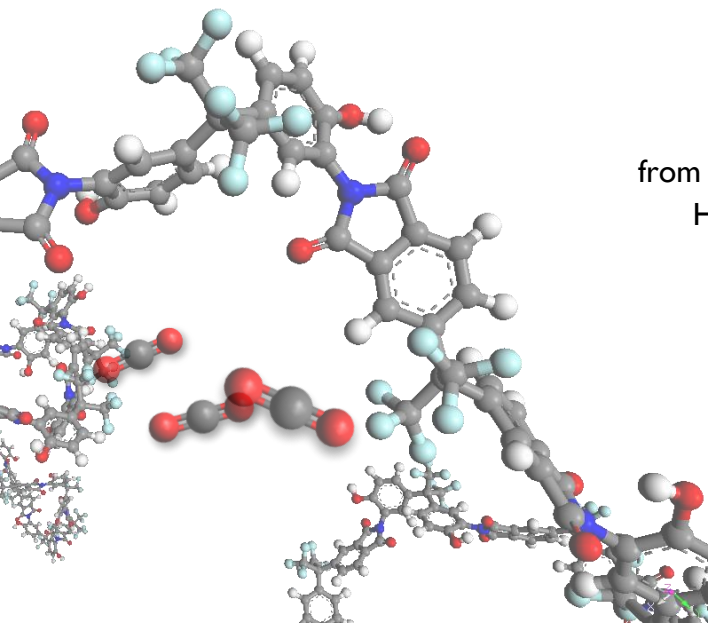
DISSERTATION

with the aim of achieving a doctoral degree (Dr. rer. nat.)

at the Faculty of Mathematics, Informatics and Natural Sciences  
Department of Chemistry, Institute of Physical Chemistry  
University of Hamburg

David Meis

from Frankfurt am Main  
Hamburg, 2021







1. Supervisor: Prof. Dr. Volker Abetz

2. Supervisor: Prof. Dr. Andrew Torda

Date of thesis defense: 04 June 2021

This work has been done between March 2015 and March 2021 at the Helmholtz-Centre Geesthacht for Materials and Coastal Research, Institute of Polymer Research under the supervision of Prof. Dr. Volker Abetz.

# LIST OF PUBLICATIONS

## Articles

- 1) A. Tena, S. Shishatskiy, D. Meis, J. Wind, V. Filiz, and V. Abetz *Macromolecules* 2017 50 (15), 5839-5849.
- 2) D. Meis, A. Tena, S. Neumann, P. Georgopoulos, T. Emmler, S. Shishatskiy, S. Rangou, V. Filiz and V. Abetz *Polym. Chem.*, 2018,9, 3987-3999.  
**Coverpage:** *Polym. Chem.*, 2018,9, 3964-3964
- 3) S. Neumann, G. Bengtson, D. Meis, V. Filiz, *Polymers* 2019, 11, 1241.

## Poster

- 1) D. Meis, A. Tena, S. Neumann, P. Georgopoulos, T. Emmler, S. Shishatskiy, S. Rangou, V. Filiz and V. Abetz, Improvement of the Gas Separation Performance in Claisen Thermally Rearranged (CTR) Polymers, Euromembrane in Valencia, Spain, 09.07.2018 – 13.07.2018.
- 2) D. Meis, A. Tena, S. Neumann, P. Georgopoulos, T. Emmler, S. Shishatskiy, S. Rangou, V. Filiz and V. Abetz, Improvement of the Gas Separation Performance in Claisen Thermally Rearranged (CTR) Polymers, Biennial Meeting of the division of macromolecular chemistry of GDCh, Karlsruhe, 24.09.2018 – 27.09.2018.



# TABLE OF CONTENTS

List of Publications .....	I
List of Abbreviations.....	IX
Abbreviations.....	IX
Chemicals.....	XV
Symbols.....	XVI
Preamble .....	XXII
PART I: <i>Summary</i> .....	XXV
1.1 Abstract.....	XXVII
1.2 Zusammenfassung .....	XXIX
PART II: <i>Introduction &amp; Theory</i> .....	1
Membranes .....	3
Gas Separation Membranes .....	4
Permeation theory .....	6
Solution-Diffusion Mechanism.....	7
Diffusion and Fractional Free Volume .....	9
Solubility .....	12
Polymeric Membranes .....	13
Trade-off Relationship .....	14
Polyimides.....	16
Synthesis .....	18
Imidization .....	21
Polyimide Structures and their features.....	22
Physical properties .....	24
PI in Gas Separation .....	25
Polymer of Intrinsic Microporosity (PIM)-PI .....	30
Thermally Rearranged Polyimides .....	35
Effect of the backbone .....	43
Effect of imidization.....	45
Crosslinking .....	47
Introduction of microporous backbones .....	51
Molecular Modelling.....	53

Thermochemistry .....	62
Pericyclic reactions .....	62
Cycloaddition.....	63
Sigmatropic Rearrangements.....	65
Cheletropic reactions.....	74
Cascade reactions .....	74
<b>PART III: <i>Scope of the Work</i></b> .....	<b>79</b>
Scope of the work .....	81
Critical Discussion of the Literature .....	83
<b>PART IV: <i>Results</i></b> .....	<b>87</b>
Thermally Rearranged Polymers (TRP) .....	89
Molecular Modelling of the Reaction Mechanism.....	89
<b>Thermally initiated Cascade Reaction Polymers (TCRP) .....</b>	<b>97</b>
<b><i>Polyimides with ortho-Allyloxy Groups</i> .....</b>	<b>97</b>
Effect of Allylation and the Degree of Allylation .....	97
Thermoanalysis.....	103
Investigation of Degree of Functionalization. ....	109
Effect of Allyl Group Distribution along the Polymer. ....	118
Film Properties.....	122
Key Messages .....	128
Effect of Allyl Derivatives in Thermal Cascade Reactions .....	131
Thermokinetic and -dynamic analysis. ....	133
Transfer to other backbones.....	148
Key Messages .....	150
Molecular Modelling Studies of <i>ortho</i> -Allyloxy Polyimides .....	152
Cyclization and Isomerization.....	159
Crosslinking .....	160
Thermal Rearrangement.....	169
Full Cascade Reaction Comparison with the Literature .....	174
Key Messages .....	180
Film Properties.....	181
Molecular Modelling Studies.....	183
Gas performance.....	195

Key messages .....	203
<i>Polyimides with ortho-Propargyloxy groups .....</i>	<i>204</i>
Thermokinetic- and dynamic analysis .....	206
Effect of the degree of propargylation.....	215
Effect of the Backbone.....	221
Effect of the Derivative .....	225
Key Messages .....	230
Molecular Modelling Studies.....	232
Claisen Rearrangement.....	233
Cyclization.....	238
Thermal Rearrangement.....	242
Crosslinking .....	244
Ring opening .....	257
Thermal Rearrangement.....	264
Diels-Alder Cycloaddition .....	268
Key Messages .....	271
Gas Separation .....	274
<i>Thermally initiated Cascade Decomposition Polymers (TCDP) .....</i>	<i>280</i>
<i>Polyimides with ortho-Alkyloxy and Acyloxy Groups .....</i>	<i>280</i>
Thermochemistry of <i>ortho</i> -alkyloxy and acyloxy polyimides.....	280
Methylated <i>ortho</i> -Hydroxy Polyimides.....	283
Thermoanalytics .....	283
Acetylated <i>ortho</i> -Hydroxy polyimides .....	294
Backbone effect .....	299
Ethylated <i>ortho</i> -Hydroxy Polyimides .....	306
Alkyloxy modifications .....	314
Acyloxy modifications.....	320
<i>Thermoreactive decomposition cascade reactions of ortho-carbonate Polyimides .....</i>	<i>331</i>
<i>PART V: Discussion .....</i>	<i>339</i>
Thermal Cascade Reaction Polymers .....	341
Thermal Cascade Decomposition Polymers.....	363
<i>PART VI: Outlook .....</i>	<i>371</i>
General.....	373

For synthetic chemists.....	374
For Membrane-Engineers.....	379
For Application-Scientists and Industry .....	380
<b>PART VII: <i>Experimental</i></b> .....	<b>383</b>
Synthesis .....	385
Chemicals.....	385
Polyimide synthesis .....	385
Polyamide synthesis.....	387
Allylation and Propargylation.....	388
Monomer modification.....	391
Alkylation .....	396
Esterification.....	397
Carbonate synthesis .....	399
Film Preparation.....	400
Thermal annealing.....	401
<b>Characterization</b> .....	<b>401</b>
Computational methodology.....	407
Molecular Dynamics .....	407
DFT simulations.....	411
<b>PART VIII: <i>Bibliography</i></b> .....	<b>413</b>
<b>PART IX: <i>Appendix</i></b> .....	<b>439</b>
Chemicals.....	441
Thermally Rearranged Polymers (TRP) .....	447
Thermally initiated Cascade Reaction Polymers (TCRP) .....	452
<b>Analytical methods</b> .....	<b>559</b>
Nuclear Magnetic Resonance Spectroscopy (NMR).....	559
Fourier-Transform Infrared Spectroscopy (FT IR).....	562
Gel Permeation Chromatography (GPC).....	564
Differential Scanning Calorimetry (DSC) .....	566
Thermogravimetical Analysis (TGA).....	571
Non-isothermal Isoconversional methods.....	574
X-Ray Diffraction (XRD) Spectroscopy .....	577
Density .....	578



Constant Volume/Variable Pressure Method („Time-Lag “Experiments).....	580
Tensile Testing .....	583
Broadband Dielectric Spectroscopy (BDS).....	584
Computational Chemistry.....	586
The potential energy surfaces .....	588
Geometry Optimization.....	590
QM Theory .....	594
The Hartree-Fock self-consistent field (SCF) method .....	596
Basis sets .....	597
Density Functional Theory.....	600
Molecular Mechanics .....	603
Force fields.....	608
Molecular Dynamics .....	611
Acknowledgement .....	614
Eidesstattliche Erklärung .....	617
Statement in Lieu of an Oath .....	617



# LIST of ABBREVIATIONS

## Abbreviations

Table 1. List of abbreviations, which were used in this PhD thesis.

6FBAHPP	2,2-bis(4-(4-amino-3-hydroxyphenoxy)phenyl)hexafluoropropane
6FpDA	2,2-bis(4-aminophenyl) hexafluoropropane
aHPI	Azeotropically imidized <i>ortho</i> -Hydroxy Polyimide
Allyl-PI	<i>ortho</i> -Allyloxy Polyimide
aPBO	Azeotropically Rearranged Polybenzoxazole
ASA	Accessible Solvent Area
ASTM	American Society for Testing and Materials
ATR	Attenuated Total Reflection
B3LYP	DFT Functional Becke , 3-parameter, Lee-Yang-Parr
BDO	Butane diol
BDS	Broadband Dielectric Spectroscopy
BET	Brunnau-Emmett-Teller Surface
BET	Brunnauer-Emmett-Teller
BHMAA	Bis( <i>o</i> -hydroxyl) maleic acid
BisATAF	2,2-Bis(3-amino-4-methylphenyl)-hexafluoropropane
BMI	Bismaleimides
BTDA	3,3',4,4'-Benzophenone tetracarboxylic dianhydride
CED	Cohesive Energy Density
CHCl <sub>3</sub>	Chloroform

cHPI	Chemically imidized <i>ortho</i> -Hydroxy Polyimide
CMS	Carbon Molecular Sieve
COMPASS	Condensed-Phase Optimized Molecular Potentials for Atomistic Simulation Studies
CoR	Cope Rearrangement
COSY	Correlated Spectroscopy
CP	Cross-Polarization
cPBO	Chemically Rearranged Polybenzoxazole
CR	Claisen Rearrangement
CTB	Carbocyclic pseudo Tröger's base
CTBDA	Carbocyclic pseudo Tröger's base diamine
CTC	Charge-Transfer Complex
CTMS	Chlorotrimethylsilane
CVVP	Constant Volume Variable Pressure Method
Cx	Crosslinking
Cy	Cyclization
dA	Degree of Allylation
DA	Diels-Alder
DAB	Diamino benzidine
DABA	Diamino benzoic acid
DACA	Diels-Alder [4+2] Cycloaddition
DAP	Diamino pyridine
DAR	Diamino Resorcinol

DFT	Density Functional Theory
DMAc	<i>N,N</i> -Dimethylacetamide
DMF	<i>N,N</i> -Dimethylformamide
DMN	3,3'-Dimethylnaphthidine
DMSO	Dimethyl sulfoxide
DSC	Differential Scanning Calorimetry
DTG	First Derivative of the TGA curve
DZ	Double <i>Zeta</i>
E	Educt
Eq	Equivalent
ESP	Electrostatic Potential
Et <sub>2</sub> O	Diethylether
EWG	Electron-withdrawing group
FFV	Fractional Free Volume
FID	Free induction decay
FT-IR	Fourier Transformation Infrared Spectroscopy
GPC	Gel Permeation Chromatography
GS	Gram-Schmid
HF	Hartree-Fock
HMBC	Heteronuclear Multiple Bond Correlation
HN	Havriliak-Negami
HOMO	Highest Occupied Molecular Orbital
HPA	<i>ortho</i> -Hydroxy Polyamide

HPAA	<i>ortho</i> -Hydroxy Polyamic acid
HPI	<i>ortho</i> -Hydroxy Polyimide
HR	High Rotation
HSQC	Heteronuclear Single Quantum Coherence
Int	Intermediate
iPBI	<i>ortho</i> -Carboxyl Polybenzimidazole
IR	Infrared Spectroscopy
IRC	Intrinsic Reaction Coordinate
IUPAC	International Union
K <sub>2</sub> CO <sub>3</sub>	Potassium carbonate
KAS	Kissinger-Akahira-Sunose
KS	Kohn-Sham
LJ	Lennard-Jones Potential
LST	Linear synchronous transit
LUMO	Lowest Unoccupied Molecular Orbital
MALLS	Multi angle laser light scattering
MAS	Magic Angle Spinning
MC	Monte-Carlo
MD	Molecular Dynamics
MeOH	Methanol
MM	Molecular Modelling
MM	Molecular Mechanics
MO	Molecular Orbital

MOCA	4,4'-Methylenebis(2-chloroaniline)
MOF	Metal Organic Framework
MOF	Metal-organic framework
MPDA	<i>meta</i> -phenylene diamine
MS	Mass Spectrometry
MSD	Mean-Square Displacement
NaOH	Sodium Hydroxide
NMP	<i>N</i> -Methylpyrrolidinone
NMR	Nuclear Magnetic Resonance Spectroscopy
NpT	Isotherm-isobar ensemble
NVT	Canonical Ensemble
P	Product
PAG	Phenyl allyl ether group
PALS	Positron-Annihilation Lifetime Spectroscopy
PBE	Perdew-Burke-Ernzerhof (gradient corrected correlation functional)
PW91	Perdew-Wang (gradient corrected correlation functional)
PBI	Polybenzimidazole
PBO	Polybenzoxazole
PDI	Polydispersity Index
PDMS	Polydimethylsiloxane
PES	Electron Surface
PG	Propargyl

PGPI	<i>ortho</i> -Propargyloxy Polyimide
PIM	Polymer of Intrinsic Microporosity
ppm	Parts per million
PSF	Polysulfone
Py	Pyridine
QM	Quantum Mechanics
QST	Quadratic Synchronous Transit
RT	Room Temperature
SAXS	Small-angle X-ray Spectroscopy
SCF	Self-consistent Field
SD	Steepest Descent
SEC	Size-exclusion Chromatography
SPE	Single Point Energy
SS	Solvent Surface
STO	Slater-type Orbital
STQN	Synchronous Transit-Guided Quasi-Newton
TB	Tröger Base
TBAHPB	1,4-bis(4-amino-3-hydroxyphenoxy)2,5-di- <i>tert</i> -butylbenzene
TBAP	1,4-bis(4-aminophenoxy)2,5-di- <i>tert</i> -butylbenzene
TCR	Thermally induced Cascade Reaction
T <sub>g</sub>	Glass-transition temperature
TGA	Thermogravimetical Analysis



TGA-EGA	Thermogravimetical Analysis coupled Evolution Gas Analysis
THF	Tetrahydrofuran
tHPI	Thermally imidized <i>ortho</i> -Hydroxy Polyimide
tPBO	Thermally Rearranged Polybenzoxazole
TR	Thermal Rearrangement
TR <sub>off</sub>	TR Offset temperature
TR <sub>on</sub>	TR Onset temperature
TR <sub>peak</sub>	TR Peak temperature
TS	Transition-State
UV	Ultraviolet
VVdW	Van-der-Waals Volume
WAXS	Wide-angle X-ray Spectroscopy
XRD	X-Ray Diffraction
ZIF-8	Zeolitic imidazolate framework 8

## Chemicals

BPDA	3,3',4,4'-Biphenyltetracarboxylic dianhydride
BPADA	4,4'-(4,4'-Isopropylidenediphenoxy)bi(phthalic anhydride)
HAB	3,3'-Dihydroxy benzidine
BisAPAF	2,2-Bis(3-amino-4-hydroxyphenyl) hexafluoropropane
6FDA	4,4'-(Hexafluoroisopropylidene) diphtalic anhydride
6FDC	4,4'-(Hexafluoroisopropylidene) dicarboxylic acid

PMDA	Pyromellitic dianhydride
EDA	4,4'-(Ethyne-1,2-diyl) diphthalic anhydride
ODPA	4,4'-Oxydiphthalic anhydride
BCODA	Bicyclo[2.2.2] oct-7-ene-2,3:5,6-tetracarboxylic dianhydride
DMSO-d <sub>6</sub>	Deuterated dimethylsulfoxide

## Symbols

A	Membrane area (m <sup>2</sup> )
A	Absorption (%)
B <sub>0</sub>	External magnetic field (Tesla)
C	Concentration (g m <sup>-3</sup> )
C' <sub>p</sub>	Maximum Capacity (Langmuir) (mg g <sup>-1</sup> )
C <sub>feed</sub>	Concentration on the feed side
C <sub>p</sub>	Heat capacity (J K <sup>-1</sup> )
d	Distance (m)
d	d-spacing (nm)
D	Diffusion Coefficient (m <sup>2</sup> s <sup>-1</sup> )
D <sub>eff</sub>	Efficient Diameter (nm)
D <sub>kin</sub>	Kinetic diameter (nm)
E	Young modulus (kg m <sup>-1</sup> s <sup>-2</sup> )
E	Eigen value
E <sub>D</sub>	Activation Energy for diffusion (J)
E <sub>kin</sub>	Kinetic Energy (J)

$E_{\alpha}$	conversion specific activation energy (J)
$F_n$	Tensile force (N)
$h$	Planck constant ( $6.62607015 \cdot 10^{-34}$ J Hz <sup>-1</sup> )
$H$	Enthalpy (J)
$\hat{H}$	Hamilton operator
$I$	Intensity (%)
$I$	Spin quantum number
$I_0$	Initial light intensity (%)
$J_D$	Diffusional Flux (mol m <sup>-2</sup> s <sup>-1</sup> )
$J_v$	viscous flow $J_v$ (m <sup>3</sup> s <sup>-1</sup> )
$k_B$	Boltzman constant ( $1.380\ 649 \cdot 10^{-23}$ J K <sup>-1</sup> )
$k_D$	Henry coefficient (mol m <sup>-3</sup> Pa <sup>-1</sup> )
$l$	Membrane thickness (m)
$L$	Length (m)
$L_0$	Initial Length (m)
$\lambda$	Jump length (nm)
$L_p$	hydrodynamic permeability $L_p$ (cm <sup>3</sup> s <sup>-1</sup> )
$m$	Mass (g)
$m_a$	Mass in air (g)
$m_l$	Mass in liquid (g)
$M_n$	Number-average molecular weight (g mol <sup>-1</sup> )
$M_w$	Weight-average molecular weight (g mol <sup>-1</sup> )
$n$	Amount of substance (mol)

$N_A$	Avogadro constant ( $6.02214076 \cdot 10^{23} \text{ mol}^{-1}$ )
$N_t$	Steady-state gas flux ( $\text{m}^3 \text{ s}^{-1}$ )
$\tilde{\nu}$	Wavenumber ( $\text{cm}^{-1}$ )
$P$	Permeability (Barrer)
$p$	Pressure (Pa)
$P_d$	Downstream pressure (Pa)
$P_u$	Upstream pressure (Pa)
$Q$	Heat (J)
$R$	Ideal gas constant ( $8.31446261815325 \text{ J K}^{-1} \text{ mol}^{-1}$ )
$S$	Solubility Coefficient ( $\text{mol m}^3 \text{ Pa}^{-1}$ )
$t$	Time (s)
$T$	Temperature (K)
$T$	Transmission (%)
$T_\alpha$	Temperature at conversion $\alpha$ (%)
$u_{th}$	Mean thermal velocity ( $\text{m s}^{-1}$ )
$V$	Volume (mL)
$V_R$	partial molar gas volume ( $\text{m}^3 \text{ mol}^{-1}$ )
$V_S$	ideal gas volume (22.710947 L)
$V_{SP}$	Specific volume (reciprocal density) $\text{m}^3 \text{ g}^{-1}$
$V_w$	Van der Waals Volume ( $\text{cm}^3 \text{ mol}^{-1}$ )
$W_1$	Weight before drying (g)
$W_2$	Swollen weight (g)
$W_3$	Weight after drying (g)

$w_{\text{air}}$	Weight dry in air (g)
$w_{\text{liq}}$	Weight in liquid (g)
$\alpha$	Ideal selectivity
$\alpha$	Conversion (%)
$\beta_0$	Heat rate ( $\text{K min}^{-1}$ )
$\gamma$	magnetogyric constant ( $\text{C Kg}^{-1}$ )
$\delta$	Chemical Shift (ppm)
$\Delta G$	Relative Gibbs Free Energy
$\Delta G_{\text{rel}}$	Relative Gibbs Free Energy
$\Delta H_s$	heat of solubility ( $\text{J mol}^{-1}$ )
$\varepsilon$	Elongation at break (%)
$\varepsilon'$	Dielectric permittivity ( $\text{A s V}^{-1} \text{m}^{-1}$ )
$\varepsilon^*$	Complex permittivity ( $\text{A s V}^{-1} \text{m}^{-1}$ )
$\varepsilon''$	Loss modulus ( $\text{A s V}^{-1} \text{m}^{-1}$ )
$\theta$	Angle ( $^\circ$ )
$\theta_{\text{TL}}$	Timelag (s)
$\lambda$	Wavelength (nm)
$\nu_0$	Initial frequency (Hz)
$P$	Pressure (Pa)
$\rho_{\text{liq}}$	Density of the liquid ( $\text{g m}^{-3}$ )
$\sigma$	Engineering stress ( $\text{Kg m}^{-1} \text{s}^{-2}$ )
$\sigma$	Spin part of the wave function
$\tau_{\text{HN}}$	Relaxation Time ( $\text{s}^{-1}$ )

$\nu$	Frequency (Hz)
$\varphi_p$	volume fraction of the amorphous polymer
$\chi$	Flory-Huggins interaction parameter
$\chi$	Spin orbital
$\Psi$	Wavefunction
$\psi$	Spatial part of the wave function
$\omega$	Angular modulation frequency (Hz)
$\omega_0$	Larmor frequency (Hz)

*“In the race for quality,  
there is no finish line.”*

David T. Kearns

## PREAMBLE

The present PhD thesis was written with the wish to shine some light on many still open questions with respect to the process of the Thermal Rearrangement of *ortho*-hydroxy polyimides and amides. For that purpose, numerous analytical methods in connection with molecular simulation were employed to target these questions. New methods and design strategies were used and developed, to improve the Thermal Rearrangement membrane material and highlight the impact of such an innovative and high-performance polymer. To make it as convenient as possible for the reader, each chapter ends with important take-home messages, the *key messages*. The single chapters are also containing separate *key messages* of the experimental and simulation part, to connect experimental and simulation results quickly while reading. Further support is given in the appendix part, which contains all important information that are not shown in the main text to keep the focus on the main aspects. Results, such as structure determination and simulation structures are shown and listed there as well as tables with corresponding results. The PhD work is divided as follows. Part I summary in English and German with main aspects of the whole PhD study. Subsequently, a literature review follows with Part II Introduction and Theory. Following is Part III, which deals with the scope of the PhD thesis work. Part IV contains the results. These are divided into 1) Investigation of the TR mechanism 2) Thermally initiated Cascade Reaction Polymers (allylated and propargylated TR polyimides), 3) Thermally initiated Cascade Decomposition Polymers (Alkyloxy-, Acyloxy and Carbonate modifications).

Part V is the discussion, which compares the results. Part VI is an outlook with future ideas and suggestions for scientists, who consider to go on the work, based on the herein presented results. In Part VII the experimental methodology and details to all used analytical and



simulation methods is described. Finally, Part VIII covers the bibliography, and Part IX encompasses the appendix with additional data. At the end you will find the acknowledgement, which is probably the most important part and finishing with the sworn declaration.

It was a lot of work, but also a lot of fun, and I hope you will learn as much as I did. The best of luck and a good time.

A handwritten signature in blue ink that reads "David Gies". The signature is written in a cursive style with a long, sweeping underline.



PART I

Summary



ABSTRACT

---

*Innovation is seeing**What everybody has seen**And thinking what nobody has thought*

Dr. Albert Szent-Györgyi

## 1.1 Abstract

Polymeric gas separation membranes are in use for about 5 decades, but there are still less than 10 polymers that are commercially used [1]. While many scientists put a lot of effort in finding new ways to overcome issues like plasticization, aging, fouling and the permeability-selectivity trade-off, promising strategies came up during the last two decades. One was the discovery of a thermal cyclization reaction forming rigid benzoxazole from *ortho*-hydroxy containing polyimide. Two decades of studies later, the mechanism has not been described and investigated in detail, a strong evidence for benzoxazole as the final structure is still missing, and despite attempts to simulate such systems via molecular dynamics (MD), no comprehensive study of the rearrangement towards structure changes were performed. Still they require temperatures of 450 °C to reach conversions above 90%. In this thesis, the mechanism was assumed to be less reasonable because of a heterolytic cleavage of a hydroxy group. Different mechanisms were proposed and simulated. The final mechanism was used in large-scale MD simulations and described the Thermal Rearrangement (TR) process and mechanism in a simulation to full extent for the first time, explaining the effect why thermally imidized films show better gas separation properties for instance. The impact of the amine and anhydride was simulated and in agreement with experiments based on a large set of *ortho*-hydroxy containing polyimides (HPI), with many non-reported materials. In a next step attempt, the use of hydroxy modified polyimides that recover their hydroxy group under thermal conditions based on the so-called Claisen Rearrangement were prepared. Effects such as the degree of modification, substitutions along the allyl and propargyl group, as well as the effect with different backbones was investigated. Therefore, thermoanalysis including modulated DSC, evolved gas analysis and model-free isothermal thermokinetics were used in combination with solid-state NMR and FT-IR. Low degrees of crosslinking have been

identified as a suitable method to disrupt the polymer chain packing to induce a higher degree of freedom for the polymer chain to undergo a mobility-dependent reaction such as the TR process. Low degrees of crosslinking are requiring to not overcompensate the spacer effect. Therefore, allyl derivatives were found to show lower degrees of crosslinking at full conversion of the hydroxy groups. The result were systems with hindered double bonds or a high tendency to form furan cyclization that improve the mobility without undergoing crosslinking reactions. Therefore, the modification with the lowest ever reported  $TR_{onset}$  in a widely used 6FDA-APAF backbone was prepared and showed 100% conversion at 350 °C, and a partial conversion at only 300 °C, which has not been reported before. All materials showed upper-bound performance, while most low-TR temperature TRPs show lower permselective. In addition, the use of propargyl was investigated in detail, which underwent Claisen-Rearrangement, crosslinking and cyclization as well. However, the formation of chromene cycles, which undergo crosslinking and initiate another cascade of up to 6 steps, was proposed and corroborated via DFT and MD simulations and was supported by comprehensive thermoanalysis. These steps were identified as ring opening, cycloaddition, and Thermal Rearrangement, which, however, requires higher temperatures as the degree of crosslinking appeared to be very high. These thermally stimulated cascade reaction polymers of extrinsically induced microporosity open a new toolbox of tailoring materials with specific porosities and thermal and mechanical stabilities depending on the separation task asked in an innovative way. The propargylated polyimide showed the highest permeability among all reported TR polymers so far, with a strong upper bound performance for several gas pairs, including only rarely described hydrocarbon separation, such as ethylene and ethane, and its performance seems to improve by physical aging in direction of the industrially more interesting target zone of higher selectivities. The amount of TR and crosslinking was controlled by the degree of modification and the used derivative. Additionally, the hydroxy group was converted in other systems to ether, ester or carbonates and their thermochemical behavior and gas separation performance was investigated and decomposition and TR initiation reactions of these systems were simulated. Among all materials methoxy, ethoxy and acetic ester were investigated in detail. Reports assumed a radical decomposition, while the evolved gas analysis and DSC measurements propose a radical and methyl transfer mechanism, which has been corroborated by DFT simulations. The effect of the amine as the stronger influencer on the TR initiation reaction, compared to the anhydride unit, holds true,

despite the lower degree of rotation of the amine unit, due to the larger methoxy group. Therefore methyl ether undergo different reactions than other ether groups, and show higher TR conversions leading to high gas performances, if the more flexible APAF diamine is used, with a gas separation performance that overcame the 2008 upper bound and approached the 2015 trade-off line, whereas ethoxy modified 6FDA-APAF showed an extraordinarily performance, due to small void formation as shown in a MD simulation study, leading to a perm selectivity of 2000 Barrer ( $\alpha$  CO<sub>2</sub>/CH<sub>4</sub>), which competes with other state-of-the-art TR polymers, while 100°C lower annealing temperatures were required.

## 1.2 Zusammenfassung

Polymerbasierte Membranen zur Gastrennung sind bereits seit der Entwicklung asymmetrischer Kompositmembranen im Jahre 1969 auch industriell im Einsatz, jedoch trotz 5 Dekaden an Entwicklung werden bisher nur bis zu 10 Polymere kommerziell genutzt[1]. Während intensive Bemühungen zur Überwindung inhärenter Probleme, wie dem Weichmacher-Effekt, *Aging*, *Fouling* und Permeabilität-Selektivität *Trade-off* zu finden, angestrebt wurden, konnten in den vergangenen 20 Jahren neue vielversprechende Designstrategien entwickelt werden. Neben intrinsisch mikroporösen Systemen wurden sogenannte Thermal Rearrangement Polymers (TRP) entdeckt. Hierbei handelt es sich um eine thermisch induzierte Zyklisierungsreaktion, die von einer Decarboxylierungsreaktion begleitet wird und starre, teils vernetzte Strukturen bildet. Aber auch 20 Jahre nach der ersten wissenschaftlichen Untersuchung, wurde der Mechanismus nicht vollständig beschrieben und auch die Bestätigung des Benzoxazols als finale Struktur konnte nie eindeutig nachgewiesen werden. Außerdem wurden bislang, trotz Bemühungen, keine moleküldynamischen Untersuchungen zum TR Prozess in einer Zelle selbst unternommen. Im Rahmen der vorliegenden Doktorarbeit wurde der literaturbekannte Mechanismus kritisch betrachtet und eine Reihe potentieller Reaktionsverläufe simuliert und ein passender Mechanismus in Einklang mit theoretisch-chemischen Überlegungen formuliert. Basierend auf dem Mechanismus wurden moleküldynamische Simulationen zum TR Prozess erstmals beschrieben um bislang ungeklärte Fragen, wie beispielsweise der erhöhten Porosität von

thermisch imidisierten TRPs, zu klären. In Übereinstimmung mit dem Experiment konnten Simulationen den größeren Einfluss der Aminkomponente auf die TR Temperatur gegenüber der Anhydrid Komponente bestätigen. Die Erkenntnis, dass die Kettenbeweglichkeit um das Amin von hoher Relevanz sind, hat zu der Entwicklung von modifizierten TRPs geführt, welche unter thermischer Behandlung die Hydroxygruppe regenerieren und gleichzeitig die Polymerketten weiterhin effizient separieren. Dazu wurde das Claisen Rearrangement genutzt. Effekte wie der Grad der Modifizierung, das Substitutionsmuster, sowie der Einfluss unterschiedlicher Polymerrückgräter wurden mittels umfangreicher Thermoanalyse untersucht. Dazu wurde sich der Temperatur-modulierten DSC, gekoppelten TGA-IR und Modellfreien isothermen thermokinetischen Methode in Kombination mit hochauflösender Festkörper-NMR und FT-IR Analyse bedient. Der Einsatz von *Spacern* und niedrige Vernetzungsgrade dienen der Polymerketten Separierung um den von der Kettenbeweglichkeit abhängenden TR Prozess zu unterstützen. Hohe Vernetzungsgrade würden die Freiheitsgrade wiederum enorm durch neue kovalente Bindungen überkompensieren und die TR Temperatur heraufsetzen. Allylierte TRP Präkursoren mit niedrigen Vernetzungstendenzen wurden entwickelt durch den gezielten Einsatz von Gruppen, die sterisch gehinderte Doppelbindungen und eine erhöhte Tendenz zur alternativen Zyklisierungsreaktion zum Furan aufweisen, entwickelt. Dies führte dazu, dass die niedrigste jemals berichtete TR Temperatur bekannter konventioneller TR Systeme durch Modifizierung beobachtet wurde. Damit konnte erstmals ein vollständiger Umsatz bei einer Behandlung unter 400 °C und Teilumsatz bei lediglich 300 °C beschrieben werden. Alle Materialien zeigten neben einer TR-Temperatur Reduktion auch eine *Upper-Bound Performance*. Weiterhin wurde neben der Allylgruppe auch die Propargylgruppe untersucht. Diese zeigte prinzipiell ähnliche Reaktionen wie dem Claisen Rearrangement, Vernetzung und des TR. Wie die eingehende Thermoanalyse in Kombination mit DFT und MD Simulationen zeigen konnte, sind Kaskadenreaktionen mit bis zu 6 Schritten möglich. Solch eine Kaskade besteht neben dem CR Prozess aus der Chromen Bildung und deren Vernetzung, Ring-Öffnung, Cycloaddition und der PBO Bildung. Aufgrund der daraus folgenden hohen Vernetzungsdichte und den resultierenden starren Strukturen sind hohe Temperaturen für die Umsetzung der letzten beiden Schritte nötig. Die Entwicklung dieser thermisch stimulierten Kaskadenreaktionspolymeren extrinsisch induzierter Mikroporosität eröffnen dem Synthetiker neue Möglichkeiten. Je nach gefragter Anwendung, können spezifische



Polymersysteme maßgeschneidert und sich aus einem Pool and Rückgraten, Derivatenund Vernetzungsgraden zu bedient werden. Das propargylierte Polyimid zeigte die höchste Permeabilität unter allen jemals berichteten TR Polymeren, mit einer hohen Permeabilität von über 9000 Barrer und deutlicher Upper-Bound *Performance*, welche durch *Aging* sogar noch in Richtung höherer Selektivität, und damit deutlich in den industriell attraktiveren Bereich der Permselectivität wandert. Ebenfalls für die kaum beschriebene Kohlenwasserstoffabtrennung, speziell der C2 Kohlenstoffverbindungen, wurden hervorragende Ergebnisse erzielt. Eine weitere Modifizierungsstrategie wurde verfolgt und neben Ethermodifizierungen wurden auch Ester und Carbonate untersucht. Die thermochemischen Prozesse und deren Einfluss auf den TR Prozess wurden experimentell untersucht, und zusätzlich simuliert und deren Mechanismus beschrieben. Im Speziellen wurden Methoxy Modifizierungen eingehend untersucht und auch hier der enorme Einfluss der Aminkomponente bestätigt. Darüber hinaus wurden zwei Reaktionsverläufe beschrieben, je nachdem ob ein flexibles oder starres Amin eingesetzt wird. Bislang wurde ausschließlich von einer radikalischen Zersetzung und anschließendem radikalischen TR Prozess ausgegangen. Dieser wurde nun genauer definiert und ein Methyl Transfer Mechanismus analog zum TR Mechanismus unmodifizierter TRPs beschrieben. So konnten reduzierte TRonsets, hohe Umsetzungsgrade zum PBO und hervorragende Gastrennungseigenschaften, die teils Richtung 2015er Upper-Bound gingen, erreicht werden. Auch die hier synthetisierten Filme zeigten ein entsprechen kompetitives Verhalten zu den besten bislang berichteten TRPs. Durch die Ethoxy Modifizierung konnte in weiteres Material hergestellt werden, welches unter 400 °C zu den *State-of-the-art* TRPs aufschließt.



## PART II

# Introduction & Theory



*The more you know,  
The more you know  
You don't know*  
Aristotle, 384 – 322 BC

## Membranes

First, what does the term “membrane” include and what does it basically describe? Membranes are available in different types of geometries. There are flat sheet membranes or hollow fiber membranes for instance[2, 3]. In addition, they can be made from different categories of materials in different ways. Therefore, it is better to describe a membrane more by its function. Principally a membrane is a functional material, which restricts the passage of certain penetrants, such as gas molecules, ions, or solvent molecules to name a few. Accordingly, even protective coatings, such as in clothes, work as membranes[2][4, 5]. In sport clothes for instance, the transport of liquid to the outside but not to the inside are required, while oxygen passes easily [5].

When membranes are considered, the type of membrane is of main interest, which in turn depends on the separation task. There are various types of membranes based on their building units and synthetic procedure. Therefore, membranes can be classified in many ways. One way is to distinguish between different porosities, which encompasses ultra-, micro-, nanofiltration and dense membranes for instance.

Another widely used classification is into inorganic and organic membranes on the first level. Many inorganic membranes exist, which encompasses ceramics, zeolites or carbon for example, as well as metallic membranes[6]. These systems show commonly high selectivities and good application adaptation potentials. However, they are very expensive and therefore less considered for the application at large-scale[7]. Organic membrane materials on the other hand are cheaper to produce and offer a large variety of materials so far [8-10]. However, in

many cases they have trouble to withstand the harsh conditions of some separation tasks, which includes high pressures, high temperatures or aggressive gases. Nevertheless, their large potential lies in the possibility to tailor materials specifically for the industrial needs and scale-up of these materials is usually not a problem[7]. They are well studied among many applications such as gas separation, pervaporation, fuel cell applications, hemolysis, and desalination [11, 12].

## **Gas Separation Membranes**

Despite its long history, membranes were not used for large-scale industrial applications before the 1980s [13]. The concept of semi-permeable polymer membranes for the separation of gas molecules dates to the works by Nollet in the 18<sup>th</sup> century who discovered the preferred transport of ethanol in an ethanol-water mixture through a pig's bladder. However, the first publication related to the diffusion of gas molecules through polymeric membranes were described in 1833 by Mitchell and later in 1866 by Graham[14]. Both observed the time dependent gas flux of hydrogen through a natural rubber balloon and concluded a diffusion of the gas through the polymeric material. Nevertheless, it took another nearly 100 years until a breakthrough was made by Loeb and Sourirajan in 1962 with the development of a preparation method of asymmetric membranes consisting of a highly porous support layer and a dense selective layer [15]. The large pores of the support layer have no significant resistance to the gas flux, and selectivity occurs via a thin, usually less than 100 nm thin layer [2, 7]. This layer is also called skin layer. Loeb and Sourirajan prepared the asymmetric membrane based on cellulose acetate for reverse-osmosis applications. Such a preparation consists of four steps. (1) Preparation of a dope solution, (2) molding, cast or spinning, (3) coagulation of the dope by a non-solvent and (4) drying [15]. An example is shown in Figure 1. The preparation of asymmetric membranes allowed to prepare mechanically stable but still selective polymer membranes, which can be easily up scaled.

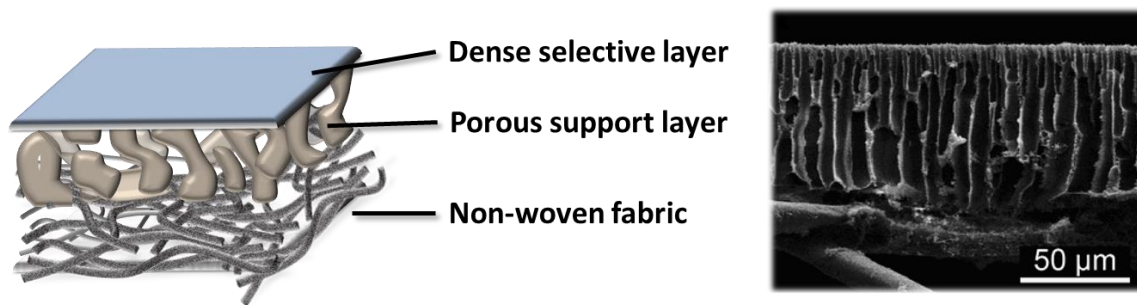


Figure 1. Schematic representation of a thin film composite membrane, with a non-woven fabric, porous support and thin selective layer (left side). Electron-microscopic measurement of a thin-film composite film (right, Reprinted with permission from Yin Yip, N., Tiraferri, A., Phillip, W.A., Schiffman, J.D. and Elimelech, M., *Environmental Science & Technology* 2010 44 (10), 3812-3818. Copyright {1969} American Chemical Society).

This milestone caused a strong increase of the number of publications with respect to the investigation of polymeric membrane systems and their preparation methods. The next big step towards commercialization of polymeric membranes was then made by the first large-scale gas separation facility for the ammonia purification, which was installed by Permea in 1980 [12, 16]. Since then, the number of industrial applications increased. This was the result of the many advantages of membranes for separation processes in industrial scale. These are easy operation, construction of small units, low energy cost, portability, reliability, and space efficiency. Different fabrications, depending on the operating facility, can be used. For instance flat sheet membranes or hollow fiber membranes (see Figure 2), despite other fabrications, such as a pocket system [2].

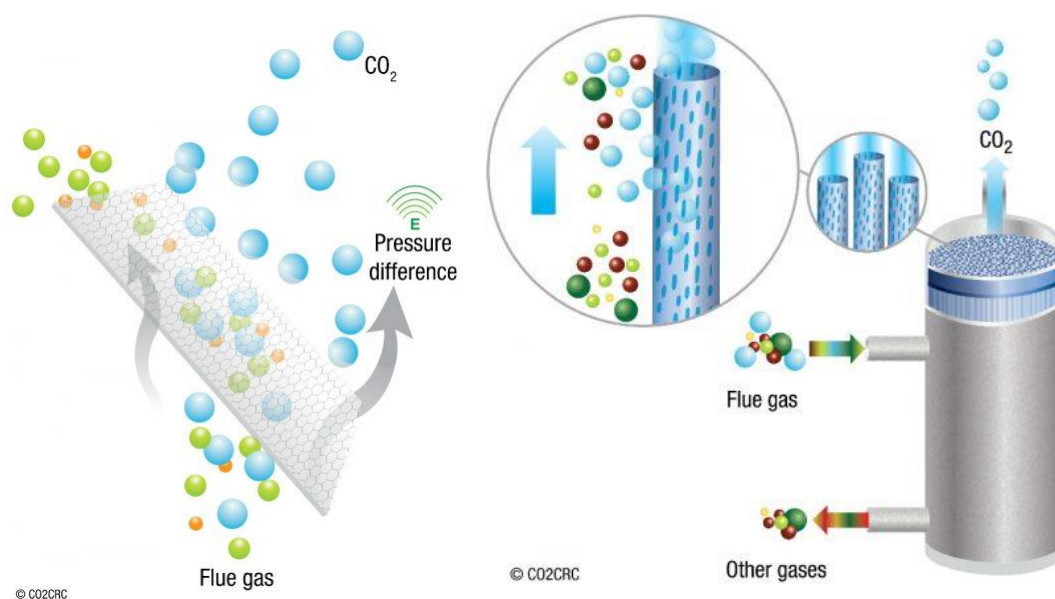


Figure 2. Structure of a flatsheet membrane (left) and a hollow-fiber membrane module (right). The images were made by courtesy of CO2CRC Ltd and used with permission.

## Permeation theory

To improve gas separation membranes, their diffusion processes need to be understood. To describe the mass transport through a polymeric membrane, different categories of gas separation transport have to be distinguished depending on the porosity and morphology of the membrane (Figure 3). The transport might occur either by absorption and diffusion through a dense polymeric membrane according to the so-called solution-diffusion mechanism[17-19], or with increasing pore sizes via molecular sieving or Knudsen diffusion once the pore sizes approach the mean-free path length of the separating gas molecules. Once the pores increase even more, the transport is better described by viscous flow. The viscous flow is described according to Darcy's law based on a hydrodynamic pressure gradient driving force

$$J_v = -L_p \cdot \frac{dp}{dz} \quad (1)$$

With the viscous flow  $J_v$ , the hydrodynamic permeability  $L_p$  and the pressure gradient  $dp/dz$ . The predominant separation mechanism depends mainly on the pore size in relation to the penetrant. The transfer from one mechanism to another is usually an overlapping relationship. However, Knudsen diffusion for example is usually the common mechanism if pores are smaller than 0.1  $\mu\text{m}$ , while surface diffusion occurs, if pores are significantly smaller, in the range from 1 to 2 nm. However, this can occur simultaneously to Knudsen[17], for instance if adsorbing molecules are passing them. Smaller pores lead to capillary condensation or micropore filling, whereas molecular sieving becomes the predominant transport mechanism if the pores reach micropore level with pore sizes of less than 0.5 nm[20].

In dense membrane materials, which are of main interest for the most polymeric membranes, molecules of similar sizes, even nitrogen and oxygen, can be separated based on the difference of their chemical potential and Fickian-diffusion [21] becomes the dominating mechanism. The transport is then concentration gradient  $dc/dz$  driven and described according to Fick's first



law of diffusion. With the diffusion coefficient  $D$ , and the concentration gradient  $dc/dz$ , the diffusional flux  $J_D$  is described as

$$J_D = -D \cdot \frac{dc}{dz} \quad (2)$$

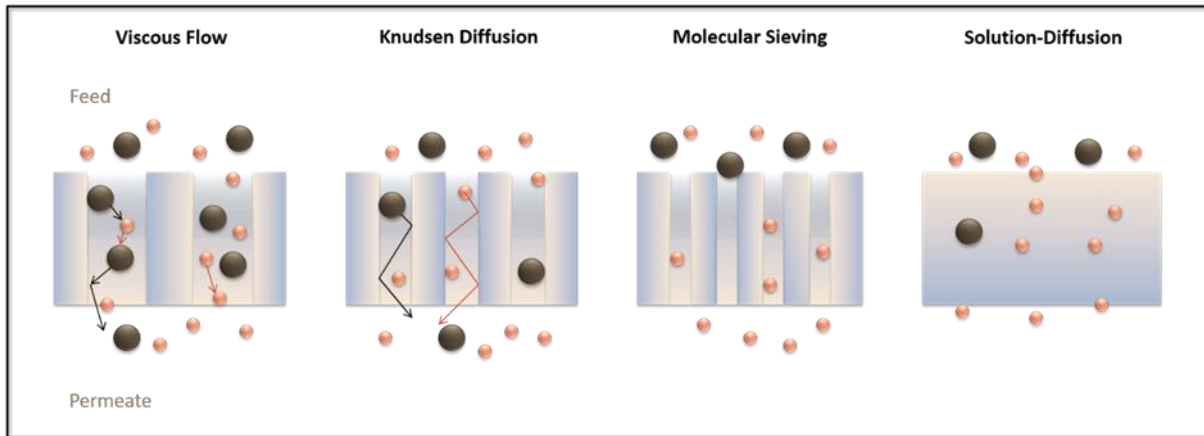


Figure 3. Different transport mechanism of penetrants through membranes in dependence of the porosity of the membrane.

### Solution-Diffusion Mechanism

As mentioned earlier, the first descriptions of the penetrant transport through non-porous polymeric membranes were described by Mitchell and Graham. Graham proposed in 1829 that the gas molecule transport through a non-porous polymer via permeation proceeds via three steps, namely adsorption, diffusion, and desorption [14]. Accordingly, the phenomenological observation was described in five steps according to Crank and Park[19] (Figure 4), that the penetrant first diffuses through the boundary layer at the interphase gas-solid of the high-pressure side (1) and dissolves in the polymer matrix (2). After the penetrant is dissolved, it diffuses through the polymer matrix (3). Under assumption that the sorption of the penetrant is high, the steps 1 and 3 are fast processes compared to step 2, for which reason the diffusion is assumed to be the rate-determining step. Which is also reasonable from a different point of view, since the penetrant cannot readily diffuse through fixed pathways. It rather diffuses through a series of jumps from one gap to another. This depends on the polymer chain mobility, as the gaps are opened if the specific activation energy is sufficient. Once it arrives at the low-pressure side it desorbs (4) and enters the gas phase out of the boundary layer and

diffuses through it (5). The dashed line shows the concentrations gradient of the penetrant from the feed to the permeate side.

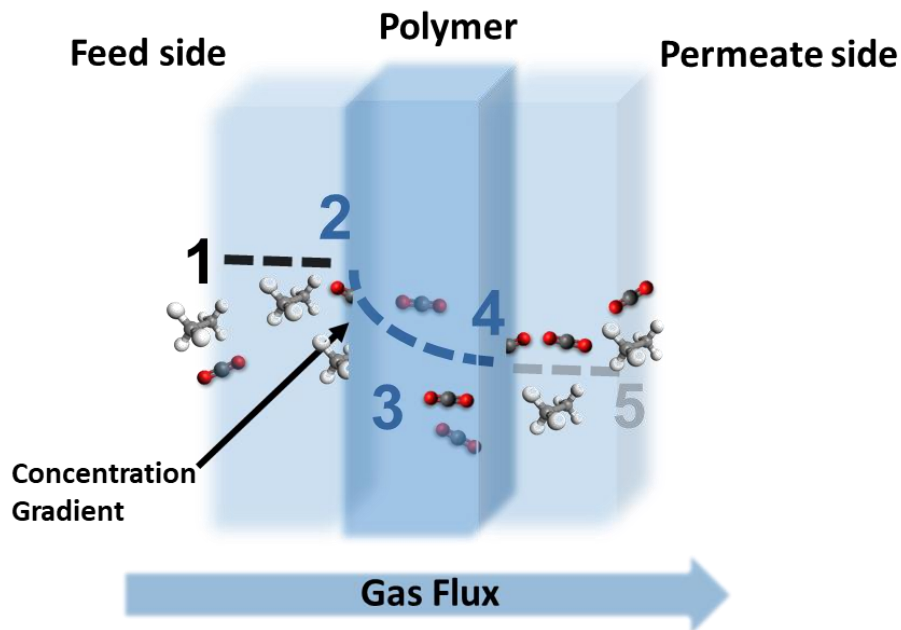


Figure 4. Representation of the five-step gas permeation across a polymer membrane in agreement with the solution-diffusion mechanism. Figure is based on a Figure from [22].

This phenomenological description is mathematically described by the product of the diffusion and solubility coefficient according to (3)

$$P = D \cdot S \quad (3)$$

This equation is derived if Fick's first law is rearranged and simplified by the assumption, that the upstream pressure is usually significantly larger. With the diffusion coefficient  $D$  and solubility  $S$ . The transport rate is defined as

$$1 \text{ Barrer} = 10^{-10} \text{ cm}^3(\text{STP})\text{cm}/(\text{cm}^2\text{scmHg})$$

The ratio of the permeability of two penetrants is commonly described as the ideal selectivity,

$$\alpha_{i/j} = \frac{P_i}{P_j} = \left( \frac{D_i}{D_j} \right) \left( \frac{S_i}{S_j} \right) \quad (4)$$

With the diffusion coefficients  $D$  and solubility coefficients  $S$  for the species  $i$  and  $j$ , respectively.

## Diffusion and Fractional Free Volume

Polymers above their glass transition temperature are in a state of equilibrium like liquids and are called to be in their rubbery state[23-25]. Their energy is sufficient enough to undergo changes in their conformations and can rotate along their torsional and bend angles and consequently can pack efficiently, which forms dense polymer materials, such as dense membranes. Polymers, which are already above their  $T_g$  at room temperature are accordingly called rubbery polymers[26]. Examples are polyethylene or polybutadienes. However, as they are cooled down below their glass transition temperature, they exhibit an excess enthalpy or free volume regarding to their equilibrium state[26]. If the enthalpy or volume is plotted against the temperature [23], see Figure 5. Above the glass transition temperature, the enthalpy or volume increases linearly with the temperature. Down to lower temperatures this line can be extrapolated for equilibrium liquids[26]. However, in polymers, they do not follow this line below their  $T_g$ . The volume decreases more slowly with decreasing temperatures. At this point it is called an out-of-equilibrium glass. One reason for the discrepancy to the equilibrium liquid line, is that below their  $T_g$ , the cooperative mobility of the polymer chains is too low to enter an equilibrium state.

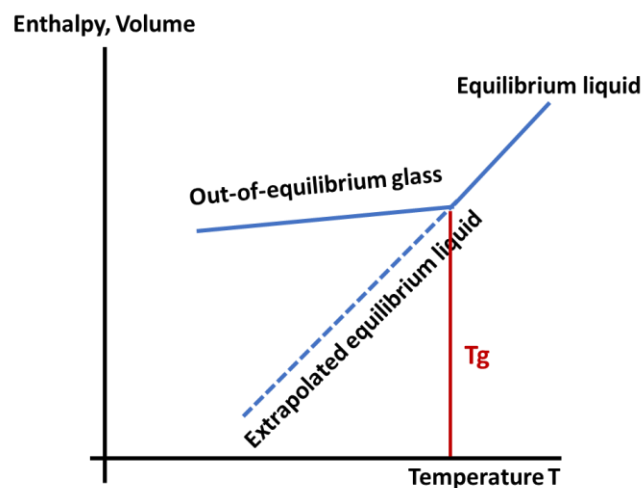


Figure 5. Enthalpy and volume versus temperature plot, describing the glass transition theory of out-of-equilibrium liquids.

In the glassy state, the excess free volume, which is the additional free volume due to the unrelaxed state, are locations of straight forward diffusion of the penetrants[27].

The concept of the free volume plays therefore a crucial role for the gas separation based on diffusional transport of penetrants[3, 23, 28].

While the diffusion coefficient in liquids can be described by the Stokes-Einstein relationship, it fails for dense and solid materials[2]. In those systems the diffusion depends on creation of empty space in which the penetrants can jump[18, 19], see Figure 6. A mathematical description which correlates such diffusional jumps with the diffusion coefficient is given by the following expression (5)

$$D = \frac{\lambda u_{th}}{2} \cdot e^{-E_D/RT} \quad (5)$$

With the diffusion coefficient  $D$ , excess activation energy for diffusion  $E_D$ , the jump length  $\lambda$  and the means thermal velocity  $u_{th}$ .

According to this description, the diffusion is dependent on the activation energy for the diffusion and the intersegmental and cooperative motion of the polymer chains as they must create new gaps, whose distance affects the diffusional jump length. The diffusional jump mechanism can be categorized into two categories[3] of models, the free-volume, and the molecular models.

The free volume models assume, that the diffusion occurs by the re-distribution of free volume elements due to random fluctuations, rather than by thermal activation energy. In such models, the diffusion only proceeds if the formed voids exceed a critical volume.

In contrast, molecular models assume, that microcavities in the polymer matrix fluctuate by time with respect to their size distribution [29]. According to such a mechanism, the dissolved penetrant jumps from cavity to cavity, if the activation energy for those jumps is provided. The transport by this model is driven by a concentration gradient in a certain direction, and the activation energy for the jump follows an Arrhenius relationship.

Such a model was independently described by Meares, Brandt[30] and by DiBenedetto[31] and Paul [32, 33]. Among these models, the Meares model correlated the activation energy for the jump with the square of the molecule's diameter. Such a model is correlated to the cohesive energy density of the polymer, which describes the required energy for the separation of polymer chains, which would be required to create voids for the diffusional jump, see Figure 7. Brandt[30] corroborated, that the activation energy depends more on the molecular structure itself. According to his explanation, two chains must bend symmetrically in order to

provide a sufficient passage for the gas transport. DiBenedetto breaks down a polymer in a homogenous continuum of segments, which undergo coordinated cooperative motions to create the void [31].

Such an intersegmental mobility in turn depends strongly on the flexibility of the polymer chains. PDMS and PSF are classical representants of rubbery and glassy polymers. The diffusion in rubbery materials is significantly larger. Since rubbery materials are in their

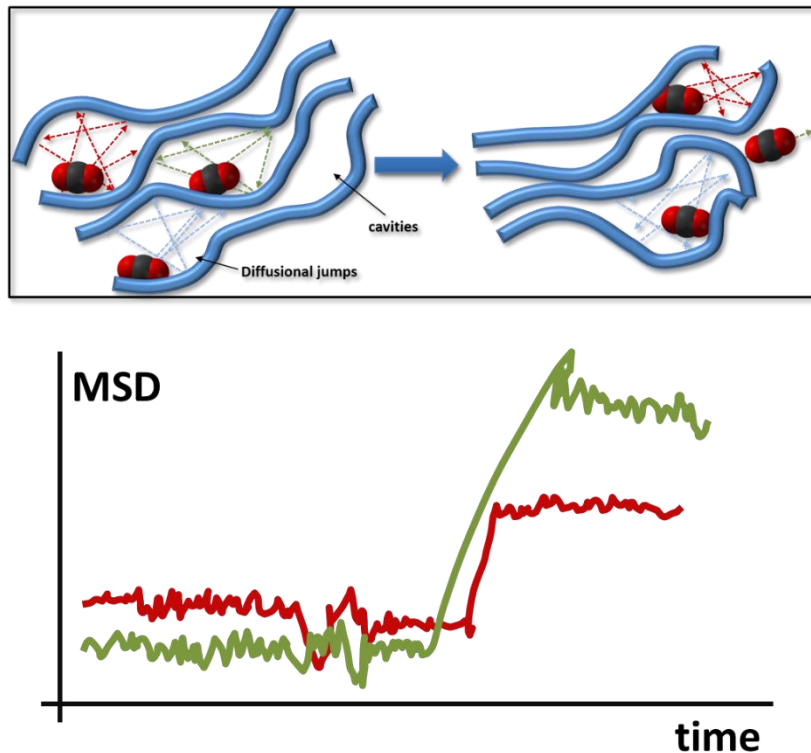


Figure 6. Diffusional jump model. Gas molecules are trapped in cavities until a pathway opens to reach another cavity by a diffusional jump. The trajectory is plotted as the mean-squared displacement versus time.

rubbery state, their mobility is significantly larger compared to glassy polymers. Accordingly, a cooperative motion of the polymer chains proceeds more easily than in glassy polymers [34]. Therefore, the void formation occurs significantly faster on a time-average basis. However, since the polymer chains in the rubbery state enlarge voids that can be penetrated by each individual component, the size selectivity by diffusional differences for different penetrants is rather low.

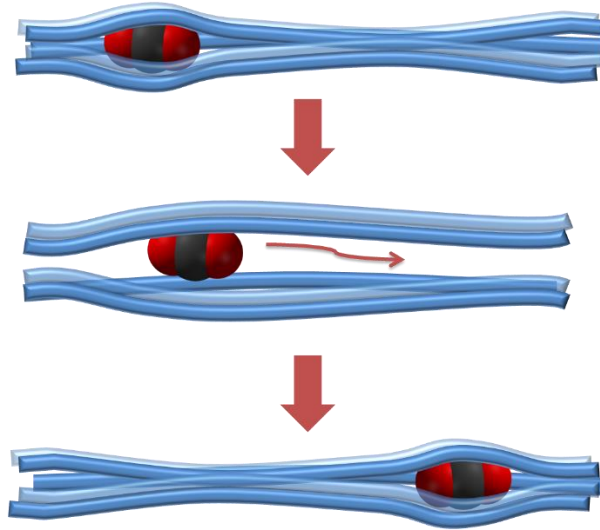


Figure 7. Gas molecule diffusion through densely packed polymer chains. Polymer chains have to open gaps by cooperative motions [35].

## Solubility

The second parameter of the solution-diffusion mechanism is the solubility. The solubility is a physical property that depends on how easily a solid, gas or liquid dissolves in another solid, liquid or gas. In terms of the solution-diffusion mechanism it is the description on how easily gas molecules dissolve. It is characterized by the solubility coefficient. The solubility in general depends on the pressure, temperature as well as the presence of other components, which can undergo repulsive or attractive interactions.

Correlations of the boiling and critical temperature of gas molecules with the solubility coefficients have been proven to be good parameters, even though the critical temperature is preferred due to a better overall correlation [18].

The sorption of gas molecules in rubbery polymers can be described by Henry's law, according to equation (6),

$$k_D = \frac{c}{p} \quad (6)$$

with concentration  $c$  of the solute in the polymer matrix, partial pressure  $p$  of the penetrant in the gas phase and Henry's coefficient  $k_D$ . In those systems the solubility corresponds to Henry's law. A more fundamental description for Henry's law constant is given in equation (6). It includes the volume fraction of the amorphous polymer ( $\varphi_p$ ), the partial molar gas volume  $V_R$ ,

the ideal gas volume  $V_S$ , which is  $22.410 \text{ cm}^3 \text{ mol}^{-1}$  and the Flory-Huggins interaction parameter  $\chi$ ,

$$k_D = \frac{\phi_p V_S}{V_R p_0} e^{-(1+\chi)} \quad (7)$$

The description for glassy polymers requires an additional sorption expression due to the presence of the sorption in the excess free volume parts according to the dual-sorption theory[36]. This is best described by the Langmuir isotherm with the maximum capacity  $C'_p$  of the free volume elements and the Langmuir affinity constant  $b$ . Including the Langmuir description, an expression for the solubility is given according to equation (8)

$$S = k_D + \frac{C'_p b}{1 + b} \quad (8)$$

The description of more condensable gases, such as higher hydrocarbons and also  $\text{CO}_2$ , which can interact with the polymer matrix, can be quantified by taking the heat of solubility  $\Delta H_S$  into account. The solubility is therefore described by equation (9)

$$S = S_0 \cdot e^{-\Delta H_S/RT} \quad (9)$$

## Polymeric Membranes

Polymeric membranes attained great interest since Loeb and Sourirajan developed asymmetric membranes, as seen by the increased number of publications (Figure 8). Since then, research groups worked hard to improve the polymer membrane properties to make them interesting for the industry. However, polymeric membranes still suffer from drawbacks, such as plasticization, physical aging, fouling or they are simply not strong enough to withstand the harsh conditions in pipelines. One aspect which motivates scientist to synthesize new materials with high permeabilities and selectivities. For that purpose, many classes of polymers were explored, such as polycarbonates, polyurethanes, polyamides, polyimides, polysulfones, polybutadienes, polynorbornenes and polyacetylenes to name a few. However, one big issue of polymeric membranes is their trade-off relationship between their permeability and selectivity.

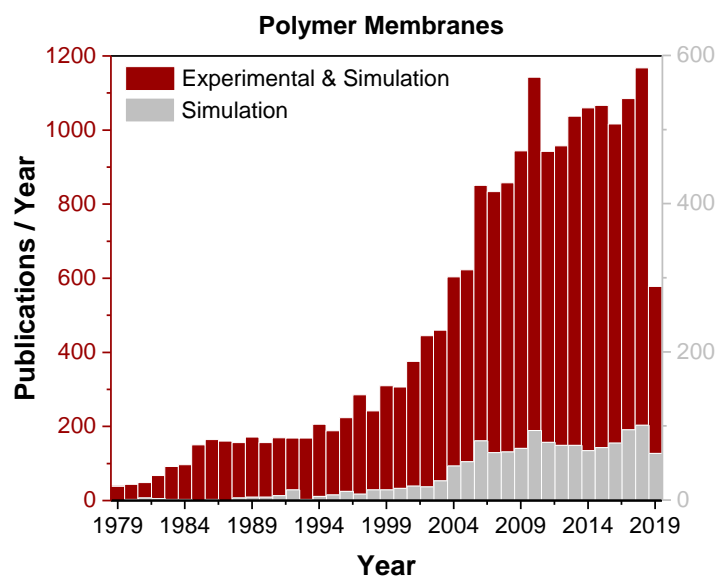


Figure 8. Number of publications based on bibliographic survey using the key word "polymeric membranes". The literature review was done by using SciFinder<sup>n</sup>.

## Trade-off Relationship

In 1991, Robeson collected and analyzed the data of various published polymeric membrane materials and reported a so-called upper bound [37], which is an empirical limit of the performance of polymeric membranes. When plotting the selectivity of a certain gas pair *versus* the permeability of the higher permeable gas species, these upper-bound lines seem to be the limit of polymeric membranes (Figure 9). Therefore, the investigated materials form clouds of permselective materials below this upper-bound. However, new methods lead to improvements of membrane materials, for which reason the upper bound had to be revisited in 2008[38, 39], since many materials emerged since 1991. Among these, the Thermal Rearrangement Polymers and Polymers of Intrinsic Microporosity caused a shift of this trade-off relationship[40]. Phenomenologically the data can be explained, by the fact, that membranes, which tend to have high permeabilities, usually have large free volume elements. Therefore, their size-selectivity decreases. If pores decrease in size to a level, that only specific gas molecules can pass them, the selectivity increases on the cost of permeability.



The trade-off lines are mathematically described by Freeman [41] as

$$\alpha_{i/j} = \frac{\beta_{i/j}}{P_i^{\lambda_{ij}}} \quad (10)$$

$$\lambda_{i/j} = \left(\frac{d_j}{d_i}\right)^2 - 1 \quad (11)$$

$$\beta_{i/j} = \frac{S_i^{1+\lambda_{i/j}}}{S_j} \exp\left\{-\lambda_{i/j} \left[b - f \left(\frac{1-a}{RT}\right)\right]\right\} \quad (12)$$

With  $a$  and  $b$  as fixed parameters of 0.64 and 11.5, the factor  $f$  as a description of the product of the energy barrier to open a gap and the equilibrium interchain spacing, with  $f=12600$  cal mol<sup>-1</sup>. [3] The different kinetic diameter in nm of the compared penetrants are  $d_j$  and  $d_i$ , whereas  $i$  corresponds to the more permeable penetrant.  $S_i$  and  $S_j$ , however, represent the solubility coefficient of the compared penetrants, respectively.  $R$  is the ideal gas constant in kJ mol<sup>-1</sup> and  $T$  is the measurement temperature in K.

Equation (10) describes the correlation of the selectivity of a gas pair and the permeability of the more permeable gas molecule and demonstrates its reciprocal relationship, as shown in Figure 9. The selectivity is accordingly described as the reciprocal of the permeability of penetrant  $i$  and a factor  $\beta_{i/j}$ , which includes a solubility term  $S$  and a term for describing the diffusivity difference by means of molecular size differences  $\lambda_{i/j}$ . The term for the difference of molecular kinetic diameters  $\lambda_{i/j}$  is part of  $\beta_{i/j}$  and serves as exponent of  $P_i$ . This exponent by Freeman is considered as reduced kinetic diameter [41].

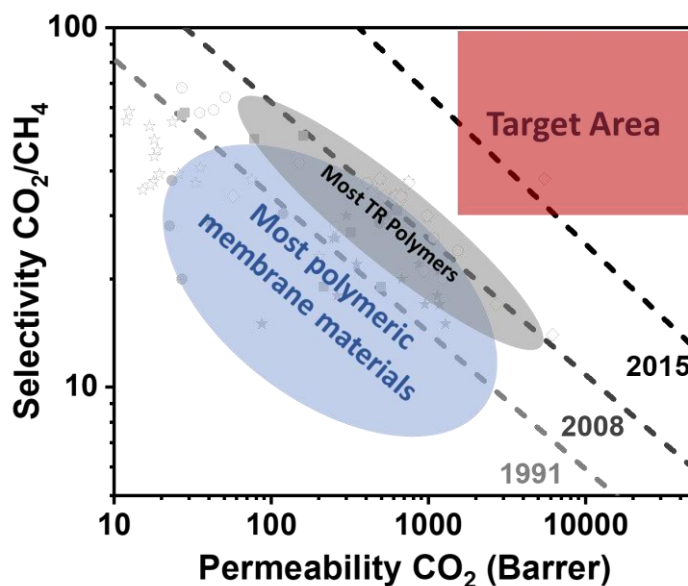


Figure 9. Robeson upper-bound plot for the gas pair  $\text{CO}_2/\text{CH}_4$ .

## Polyimides

In 1908 the first aromatic polyimide was synthesized by Marston Bogert [42]. It took 47 years until 1955 [43], that a high molecular weight aromatic polyimide was synthesized by a two-step polycondensation, as it is principally still done [43, 44]. In the 1960s DuPont presented the Kapton H film [43]. Since then, polyimides have attracted great interest due to their thermooxidative stability, strong mechanical properties, high chemical resistance, and unique electrical properties[45-47]. The large number of commercially available monomers and synthetic methods allow the design and preparation of polyimides with tuned properties for the required application[48, 49]. As a consequence, polyimides are widely used in various applications, such as photoresists, gas separation membranes, polyelectrolytes, fiber reinforced composites, active-matrix organic light-emitting diodes, solar cells[44].

Polyimides contain a  $\text{sp}^3$  hybridized nitrogen atom with two adjacent carbonyl groups, which usually exists as five- or six-membered rings, as shown in Figure 10.

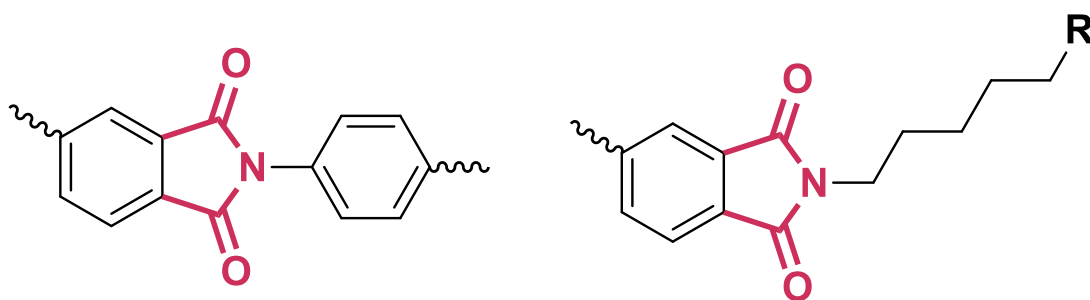


Figure 10. Basic unit of a polyimide. It can be aromatic or also contain aliphatic segments, as shown on the right side.

A special characteristic of polyimides is their self-interaction by formation of charge transfer complexes in aromatic polyimides[43, 44, 50-52]. The electron deficient anhydride component of a polymer chain interacts with the electron rich diamine component of a repetition unit of another polymer chain (Figure 11, Figure 12). The charge transfer complex is more pronounced in symmetric linear polyimides which can approach each other easily. The effect is increased if diamines with an improved electron donating ability are used as well as anhydrides with electrodeficiency[44]. Addition of electron withdrawing groups might support the CTC formation. As a consequence, polyimide films become dark orange to brown. The CTC formation was proven by Dinan *et al.*[53] by means of  $^{13}\text{C}$ -NMR spectroscopic analysis and by Kawakami *et al.*, using fluorescence spectroscopic investigations.

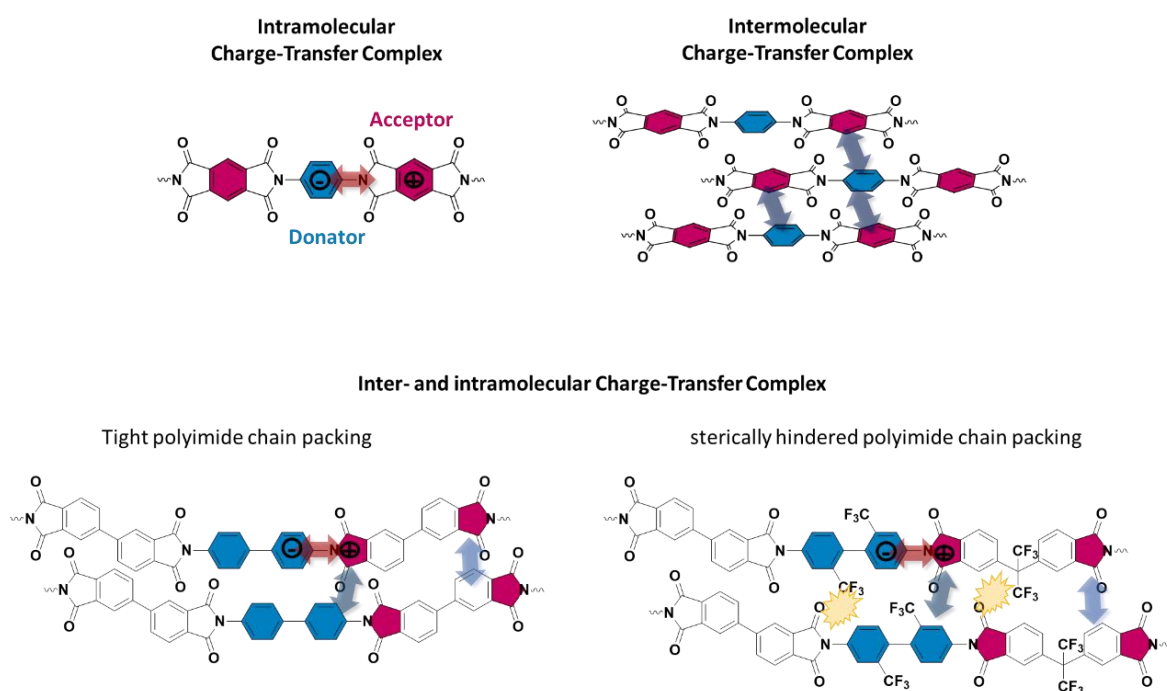


Figure 11. Intra- and intermolecular charge-transfer complex formation of a phenylene diamine and pyromellitic anhydride based polyimide (top). Effect of the backbone by incorporation of sterically hindered groups, such as  $\text{CF}_3$  (bottom).

Kawakami *et al.*[54] studied thermally annealed hexafluoroisopropylidene containing 6FDA-based polyimides for that purpose. Hasegawa has shown that polyimides with longer annealing times form stronger CTCs[55].

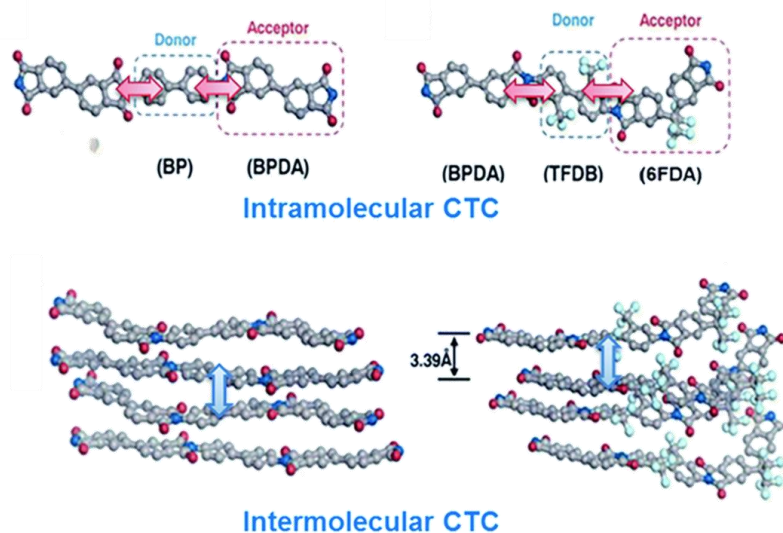


Figure 12. Simulated CTC of efficient and inefficient packing polyimides. Reprint with permission [50].

## Synthesis

Various methods to synthesize polyimides exist, while most are limited by the number of monomers and molecular weights are not high in many of these methods. Among these methods, the two-step polycondensation, the so-called amic acid route is the most common synthesis method [43, 44]. In the first step a diamine is dissolved in a dipolar aprotic high-boiling solvent, such as NMP, DMF, DMAc. Then the anhydride is added and stirred at low temperatures. Due to the exothermal of the reaction, the reactors are commonly cooled in an ice bath[43]. Instead of dianhydrides, it is also possible to use tetracarboxylic acids, diester acids or diester di acid chlorides[44, 48, 49]. However, dianhydrides usually result in the highest molecular weight polyimides. The reaction is a polycondensation reaction with the untypical behavior, that the condensate remains in the polymer (carboxylic acid) and produces a poly (amic acid). In principle an *ortho*-carboxyl containing polyamide. Therefore, the reaction is better considered as a polyaddition reaction with consecutive cyclodehydration reaction. The reaction is initiated by charge transfer formation between the anhydride and amine and follows the propagation step. The propagation occurs via nucleophilic attack of the amine on

the carbonyl carbon atom, as demonstrated in Figure 13. The reaction is a reversible reaction. The second step of the reaction is a condensation reaction. By means of thermal or chemical dehydration, the amic acid nitrogen atom attacks the carboxylic carbonyl group under cyclization to the corresponding cyclic imide ring accompanied by release of a condensate product. In case of using dianhydrides, the condensate is water.

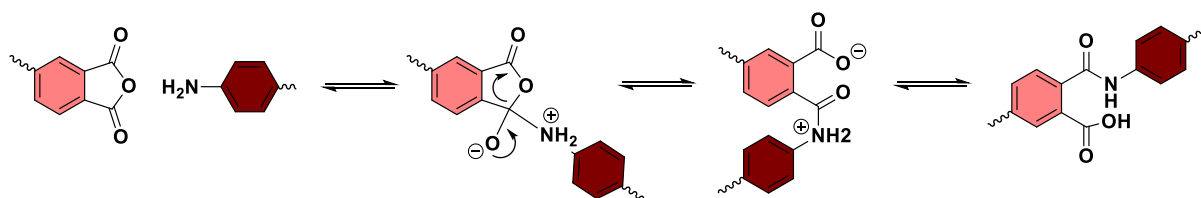


Figure 13. Reaction mechanism for the reaction of an amine and cyclic anhydride with the formation of an amic acid.

In order to reduce the back reaction, it is important to avoid the proton transfer from the carboxyl group to the amic acid amide unit. This can be done by using polar aprotic solvents which form strong hydrogen bonds with the carboxyl group. Accordingly, the equilibrium constant is reasonably high in favor of the propagation step ( $10^5 \text{ mol L}^{-1}$ )[44]. As a consequence, the stability of poly (amic acid)s in unpolar solvents decreases as an autocatalytic depolymerization via protonation of the amide group occurs. The polymerization rate increases if the used solvents are more polar and basic. The reaction rate increases in the order THF<acetonitrile<DMAc<NMP<*m*-cresol.

The reaction kinetics are also strongly dependent on the used monomers. Studies have shown that the reaction rate increases if the anhydrides electrophilicity is increased[44]. Correlations have shown that the electron affinity can be used as an indicator for the electron acceptance properties of the dianhydride [56-58]. In PMDA for instance, the electron withdrawing character of the opposite anhydride group in meta and para position activates the anhydride for the polymerization strongly. In anhydrides, which contain bridge groups, the electron affinity and therefore the reaction rate depend strongly on the nature of the corresponding group. In the case of the used diamine, an increased reaction rate results from electron donating character [56]. A correlation has been drawn between the  $pK_a$  value and the reaction rate. Diamines with higher  $pK_a$  values show higher polymerization rates. Nevertheless, changes in the diamine result in stronger effects towards polymerization rate, than changes in the dianhydride[44].

Apart from the used reactants and solvents, the synthetic procedure plays a crucial role. Higher molecular weights were obtained if the dianhydride was added to the diamine and not the other way around. The reaction of the dianhydride with the diamine is very fast and faster than other reactions. Therefore, the addition of the anhydride as a solid is beneficial in order to avoid side reactions by impurities or the solvent, such as transamidation. The anhydride hydrolysis for instance has a reaction constant of 0.1 to 0.41 mol<sup>-1</sup> sec<sup>-1</sup>, while the propagation ranges from 0.5 to 6.01 mol<sup>-1</sup> sec<sup>-1</sup> [43, 59, 60]. As a consequence of the slow dissolution of the dianhydride, the polymerization rate might overtake the dissolution rate. Accordingly, the process becomes diffusion controlled and interfacial polymerization at the particle-solvent interphase occurs[44]. The diffusion limitation can be enhanced by lower temperatures. Therefore, the molecular weights are usually higher compared to reaction limited step-growth polymerizations. Once the poly (amic acid) is formed, the following reactions might occur.

Studies have shown that the molecular weights strongly increase in the first 10 to 20 min, in a homogeneous polymerization, and tend to decrease after 10 to 12 h, due to the back reaction  $k_2$  and hydrolysis  $k_5$  [43, 44, 59, 60].

Table 3. Common rate constants of various reactions in poly(amic acid) synthesis[44, 59, 60].

<b>Reaction</b>	<b>Rate constant (mol<sup>-1</sup> s<sup>-1</sup>)</b>
<b>Propagation (<math>k_1</math>)</b>	0.5 – 6.01
<b>Depolymerisation (<math>k_2</math>)</b>	10 <sup>-5</sup> – 10 <sup>-6</sup>
<b>Imidization (<math>k_3</math>)</b>	10 <sup>-8</sup> – 10 <sup>-9</sup>
<b>Anhydride hydrolysis (<math>k_4</math>)</b>	0.1 . 0.41
<b>Amide hydrolysis (<math>k_5</math>)</b>	0 – 10 <sup>-6</sup>

## Imidization

### *Thermal imidization*

Studies have shown that annealing of polyimide films at 300 °C for 30 min could be sufficient to promote full conversion to the corresponding imide structure [61-65]. However, in fibers and even powder, the conversion decreases [44]. It was reported, that the anhydride peak can be observed above 100 °C and increases further until a temperature range from 175 to 225 °C was reached [66]. Above 250 °C the anhydride tends to decrease until it vanishes at 300 °C [62-65]. It is also noteworthy, that no crosslinking has been observed below 300 °C, since the imidization proceeds faster.

The thermal imidization proceeds via two stages. The first stage is very fast following a reaction of first order, while the second step is significantly slower [67]. The explanation for the observation is as follows. Amide solvents form strong hydrogen bonds, accordingly to the interplay between solvent and amic acid decrease as the number of solvent decreases[61]. The solvent carboxyl group complexation is an activation at the same time. Therefore, poly (amic acid) salts imidize significantly faster than uncharged poly (amic acids). As further heating leads to more solvent-COOH decomplexation, which is faster than the imidization reaction itself, the kinetic of the imidization drops. Possibilities to increase the imidization conversion are the use of thicker films to prevent solvent release and higher heating rates.

Furthermore, the glass transition temperature of the polymer increases as the number of the more rigid imide rings increases. Accordingly, the polymer mobility decreases, which is required for the imidization reaction.

### *Chemical imidization*

The chemical imidization is usually executed by addition of an aliphatic carboxyl anhydride and a tertiary amine base. The conversion depends strongly on the solubility of the polymer. From a mechanistic point of view, the tertiary amine deprotonates the carboxylic acid and converts the anhydride to the cationic amide intermediate. The imidization then occurs by two different pathways. The attack either occurs via the nitrogen atom and an isoimide is formed, or by the oxygen atom and an imide is formed. The isoimide however transfers readily to the imide.

## Polyimide Structures and their features

A short overview of generally available monomers is given. Monomers can be divided in different sub-categories. First of all, there are noncoplanar structures with specific key elements such as a kinked, spiro or cardo structures.

Kinked structures are based on methylene or isopropylidene groups in many cases. Liaw *et al.*[68] synthesized biphenyl methylene containing dianhydrides and diamines which exhibited good solubilities (Figure 14 b). They synthesized a diol and prepared the diamine or dianhydride by nitro displacement reaction afterwards. They also synthesized a dianhydride with a methylene hydroxy bridge (Figure 14 e).

Spiro structures were synthesized in order to prevent efficient chain packing and CTC formation. Spiro groups consist of two orthogonally fused rings, whose connecting atom, the spiro center, is a tetrahedral carbon atom. A famous example is the spirobifluorene group [69, 70]. Anhydride or amine groups can be distributed at the same fluorene unit or one per fluorene unit in order to increase the contortion of the polymer chain (Figure 14 c). The major structural aspect is the nearly 90° twisted angle at the spirocenter. Hsiao *et al.*[71, 72] synthesized spiro-diamines and dianhydrides with oxygen atoms in the corresponding fused rings. This special type of spiro compound is known as spirobischroman (Figure 14 d). These materials showed good solubility properties and transparent and mechanically stable films. A highly interesting dianhydride was prepared by Han *et al.*, who investigated a spirodilactone dianhydride with a high  $T_g$  above 400 °C (Figure 14 a) [73].



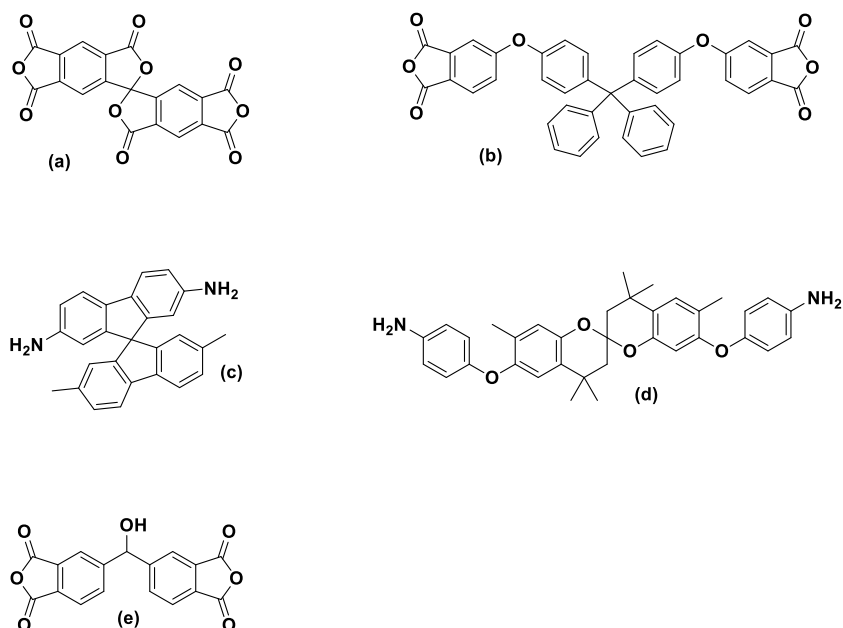


Figure 14. Polyimide monomer precursor with spiro units. (a) spirolactone- (b) methylenetetra-phenyl containing dianhydride, (c) bifluorene- and (d) bischromane containing diamines, (e) methylene hydroxy bridged dianhydride.

In addition, other noncoplanar structures were synthesized and investigated. Harris *et al.* studied polyimides with 2,2'-disubstituted biphenylene units. The forced twist reduced efficient chain packing such as in previously described contorted monomers. Liaw *et al.* [74] incorporated these units in an ether bridge containing diamines in order to improve the solubility of such polyimides (Figure 15).

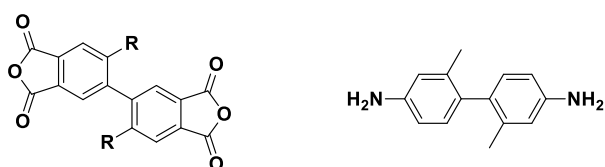


Figure 15. Monomers with 2,2'-disubstituted biphenylene units [68].

Another strategy to avoid close chain packing and strong intermolecular interactions, is the use of unsymmetrical monomers. Hergenrother *et al.* [75] for instance investigated symmetrical and unsymmetrical biphenylene dianhydrides, aBPDA and sBPDA. They reported that the unsymmetrical aBPDA had a higher  $T_g$  and higher optical transparency but lower tensile properties compared to sBPDA.

Alicyclic monomers have been synthesized in recent years to improve optoelectronic properties. Due to their low dielectric constant and lower chance of intermolecular interactions compared to aromatic polyimides, alicyclic polyimides were prepared and showed excellent transparency and processing properties [52, 76] (Figure 16).

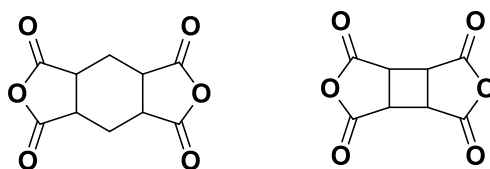


Figure 16. Examples of alicyclic dianhydrides. Cyclohexamethylene- (left) and cyclobutene (right) containing dianhydride [52, 76].

## Physical properties

### *Solubility*

In order to target higher solubilities, polyimides have to fulfill usually certain criteria: Reduced rigidity and regularity of the backbone and minimized density of imide groups along the polymer chain. Promising attempts were the introduction of hexafluoroisopropylidene or ether groups and aliphatic side chains [203]. Calle *et al.* prepared diamines with a pendant *tert*butyl group, which improved the solubility [77]. The use of noncoplanar kinked, spiro- or cardo containing structures improved the solubility without sacrificing other important physical properties. Apart from the backbone, the imidization route plays a crucial role. Thermally imidized polyimides for instance show lower solubilities, probably due to small amounts of crosslinking compared to chemically imidized polyimides [117].

### *Mechanical properties*

The influence of mechanical properties is highly complex as many parameters affect the final mechanical properties. Apart from the chemical structure, those are the viscosity, synthetic method, molecular weight, thermal history and purity. However, flexible polyimide backbones, with ether or isopropylidene bridges oftentimes show larger elongation at break values. In most cases, materials with higher elongations at break, show lower mechanical modulus [49].

### *Optical and electronical properties*

If polyimides are capable of forming charge transfer complexes, their color goes brown. If aliphatic dianhydrides or diamines are used, the CT interactions are lowered, and films become more colorless. This can also be achieved in aromatic polyimides, if the electron

acceptor properties of dianhydrides are reduced by electron withdrawing groups or by lowering the electron donating nature of the diamine, which weakens the CTC formation in total. Chain disruptors also help to prepare colorless polyimide films.

#### *Thermal properties*

Aromatic polyimides often have decomposition temperatures above 450 °C in air and 500 °C in inert atmosphere. Glass transition temperatures of aromatic polyimides are likely to range between 280 and 400°C.

## **PI in Gas Separation**

PI materials have attracted great interest in many industrial applications, so in gas separation due to their high permeability and selectivity as well. DuPont was the first company to use polyimide membranes in industrial gas separation processes [78]. They used PI membranes to purify helium from natural gas sources and for CO<sub>2</sub> purification tasks. In 1970 polyimides were suggested as solvent-resistant nanofiltration membranes by Strathmann due to their chemical resistance at elevated temperatures [79]. Hollow fiber (HF) PI membranes specifically for gas separations (N<sub>2</sub>, H<sub>2</sub>, CO<sub>2</sub> and dehydration) are commercially available from UBE America Inc. (USA)[80]. Specifically for SRNF, the Lenzing P84® based Starmem® membranes from W.R. Grace-Davison (Columbia, MD, USA), recently acquired by UOP, and distributed by Membrane Extraction Technology (MET), were the only commercially available PI based SRNF membranes on the market for a long time [78]. Recently, Evonik (UK), after acquiring MET, has commercialized a new line of PI membranes called Puramem™ as well as a line of crosslinked PI membranes called Duramem™ [80]. In addition, their high thermal, mechanical, and chemical resistance is beneficial for the application in gas separation. Their superior performance is the result of a strong imide bond and aromatic backbones. However, they suffer from strong intermolecular interactions which hinders their easy processability and their rigidity. Moreover, plasticization and physical aging are serious problems of many polyimide membrane systems[80].

PI's form CTCs which are based on the electronic interaction between an aromatic dianhydride in the function of an electron acceptor, while a diamine component acts as electron donor.

Their consequence is the inhibition of molecular mobility of the chain and their chain packing which narrows any interstitial space. This can improve the selectivity on the cost of the permeability. CTC can be reduced by adding bulky pendant groups, this can also enhance the solubility. Bos *et al.*[81] investigated the effect of thermal annealing at 350 °C of Matrimid polyimide membranes. They reported, that C2 plasticization and CO<sub>2</sub>/CH<sub>4</sub> selectivity were improved. Studies by Krol *et al.* in 2001 revealed the same effect towards selectivity and explained it by the CTC formation [82]. However, they also reported a drop in permeance. The CTC induced densification was also studied by means of SEM investigations. Mild temperatures of 200 °C were already sufficient enough to avoid plasticization. Zhou and Koros reported the avoidance of plasticization in HF membranes for the separation of acetic acid/water mixtures after annealing at 220°C [83, 84].

## Monomers

The molecular properties can be strongly altered by variation of the monomers. One advantage of PI is therefore the large number of aromatic and aliphatic available dianhydrides, diamines and synthesis methods which extends the number of monomers for PI synthesis, for instance by isocyanates. Also, a large number of new monomers with specific design characteristics were developed to tailor the PI properties. In gas separation kinked monomers, containing cardo or spiro units were synthesized.

### *Non-coplanar structures (kink, cardo, spiro)*

Most widely known examples are the 2,2'-substituted biphenylene diamines[49]. The substitution in 2,2' position leads to restricted rotations and causes increased chain stiffness. This also lowers the individual polymer chain interactions. Most prominent examples are binaphthyl and CH<sub>3</sub> or CF<sub>3</sub> groups in 2,2' position of biphenylene diamine. Among non-coplanar structures, the kinked structures interestingly decrease the chain stiffness but decrease molecular interactions at the same time. These monomers reduce chain packing and CTC formation. Examples are 4,4' functionalized biphenyl ethers or hexafluoroisopropylidene or simply isopropylidene unit containing diamines, such as BisAPAF, BisATAF or 6FPDA. Extreme substitution patterns such as diphenyl methylene linkages lead to higher solubility and thermal stability of the backbones compared to smaller isopropylidene versions. Ether

containing units are BAPP, a Bisphenol-based diamine. Dianhydrides such as 6FDA, ODPDA, BPADA are also commercially available.

In gas separation, spiro units are mainly known by PIMs [85-87]. However, spiro units were also synthesized and reported in PI monomers. Principally, it encompasses a sequence of rings, which are connected via one tetrahedral atom, usually a carbon atom, leading to a 90 ° angle twisted geometry. The synthesis is usually performed by diketones and aliphatic tetrahydroxy components, such as pentaerythritol. Such an oxy spiro compound is then the product of a full acetal formation. Like kinked structures, the chain packing is reduced and the thermal properties, such as stability and glass transition temperature are enhanced. An interesting unit for that class, is the spirobifluorene.

Cardo units are similar to previously described spiro units. While spiro units have two connected rings, in cardo, there is only one ring structure connected via one atom to two additional groups. The structure looks like a loop, which is the reason for the name (cardo is Latin for loop or hinge). They are readily synthesized from cyclic carbonyl group containing molecules via Friedel-Crafts catalysis with phenols or anilines for example. Fluorene containing diamines are commercially available with -F, Cl, CH<sub>3</sub> or -OH groups *ortho* to the amino group. Various fluorene monomers were synthesized for gas separation. The bulky groups interrupt efficient chain packing. Garcia *et al.*[88] synthesized a set of fluorenes containing monomers with and without hydroxy groups. While hydroxy groups improved the selectivity, their absence was beneficial for the permeability. Apart from fluorene, also adamantyl, norbornene and phthalide containing units were reported.

#### *Symmetrical and asymmetrical monomers*

Numerous asymmetrical monomers are known to be beneficial for the penetrant diffusion, as they do not form tight polymer packings. Asymmetric structures are for instance some hetero group containing diamines, or simply *meta* connected diamines. A famous example is DAT, DAP, MPDA. Moreover, symmetric diamines can prohibit efficient chain packing and induce free volume generation. Usually symmetrically substituted diamines, that have hindered degree of rotation lead to stiff PI. Examples are TBAPB, Durene DMN, MOCA [89].

## Molecular design

Conventional aromatic polyimides have issues, which hinder their commercialization for large-scale industrial use. Among these issues, the poor solubility in a few organic solvents due to their stiffness, high polarity and strong intermolecular  $\pi$ - $\pi$ - and CTC interactions follows. As a consequence of their high  $T_g$  and melting temperature, further processing of these materials is very difficult. Therefore, scientists have been trying to improve and commercialize PIs since the 1990s [89]. The main attempts to improve PIs for gas separation were the investigation and tuning of

- a) Spatial linkage configurations
- b) Type of bridging group
- c) Bulky and polar group incorporation

In order to tailor membranes more specific, two types of molecular design strategies have been used in the past. The design of new monomers, and the copolymerization with other polymer classes.

In many cases bulky pendant groups were introduced in order to lower the  $T_g$ , improve solubility and decrease polymer chain packing due to enhanced steric interactions. The substitution of hydrogen atoms *versus* polar groups or halogens increased the free volume and therefore the permeability and solubility as well. Studies have shown that using *meta*- instead of *para* linkages increases the selectivity due to the rotation inhibition. The free volume and gas permeability is decreased. For example, if the substitution in *para* to *meta* is changed in 6FDA, then the O<sub>2</sub>/N<sub>2</sub> selectivity increases by 47%. BTDA-6F*p*DA in *para* linkage for instance shows higher permeabilities than the *meta*-version BTDA-6F*m*DA. The same was observed for 6FDA-*m*HAB and 6FDA-*p*HAB with higher permeabilities but lower selectivities for the *para*-linked structure [90, 91].

### *Halogenated groups*

A widely used method to improve polyimides is the incorporation of polar, especially halogen containing, groups. Oftentimes fluorine groups were introduced. The small dipole due to the large electronegativity of fluorine and therefore low polarizability of the C-F bond as well as the larger volume of fluorine atoms with respect to hydrogen reduces the inter-chain

interactions, such as CTC formation, and disrupts the polymer chain packing in favor of higher free volume [92, 93]. It is noteworthy, that according to Bondi's group contribution method the van der Waals volume for -H is 3.44, -F is 5.7, -CH<sub>3</sub> is 13.67 and 21.3 for a bulky CF<sub>3</sub> group [94, 95]. The addition of CF<sub>3</sub> groups also demonstrated to increase the gas solubility, especially of CO<sub>2</sub> [96, 97]. It also increases the free volume and from a processing point of view the solubility is increased, despite the higher glass transition temperature [92, 93].

Bromination is another widely used method. The introduction of bromine groups improves the polymer solubility, since crystallinity and polymer chain interactions are reduced. However, it also reduces the degradation temperature, because of the formation of HBr and Br<sub>2</sub>, which makes it interesting for CMS membranes [98, 99]. However, another reason for the use in gas separation is the high reactivity towards numerous functional groups. Especially in fuel-cell membranes the bromination of benzylic groups is used to substitute the bromine group by tertiary amines to form charged cationic quaternary ammonium ions [100]. In addition, bromo methylene groups are often used for thermal crosslinking or chemical crosslinking by addition bifunctional nucleophilic groups [101].

#### *Bridging and substituent groups*

Large bridging groups are used to decrease the segmental mobility, which increases the  $T_g$ , but also the selectivity is improved due to the hindered rotation. The most common groups in commercially available monomers and also synthesized ones, are -O-; -SO<sub>2</sub>-, -C(CH<sub>3</sub>)-, C=O, -CH<sub>2</sub>- and -C(CF<sub>3</sub>)<sub>2</sub>-. Interestingly, the gas separation performance can be easily manipulated by combinations of substituents and bridging groups, as substituents effects are strongly dependent on the polymer backbone. Maier *et al.* synthesized diamines with an ether ketone backbone and an indane group such as in Matrimid [102]. The indane group contained either cyclohexyl or methyl groups. The amine was polymerized with various anhydrides. It is noteworthy, that the higher flexibility of the cyclohexyl group led to a lower CO<sub>2</sub>/N selectivity of 20.3 to 22.8 in comparison to the methyl substituent. This was achieved without a bridging group. With SO<sub>2</sub> as bridging group the selectivity of the methyl substituent was also higher with 22.5 vs 20.6 for the cyclohexyl group. However, introduction of a bridged group with more freedom of torsion like -O- increased the selectivity of the cyclohexyl substituent more. The selectivity was 47 for the cyclohexyl compound vs. 33.9 for the methyl derivative. In case

of  $-\text{C}(\text{CF}_3)_2-$ , the selectivity for the cyclohexyl group was larger as well with 29.2 vs. 17.4. Guzmán-Lucero investigated the same relationship with another diamine and drew the same conclusions [103]. Hence, bridge groups affect the performance strongly, and interact with other structural properties in different ways.

Another interesting study was done by Zhang *et al.*[104]. They synthesized Spirochroman-based polyimides with  $-\text{H}$ ,  $-\text{CH}_3$  or  $-\text{CF}_3$  groups in the diamine component. While the  $\text{CF}_3$  group showed the highest free volume and gas permeability due to the bulkiness of the group, the free volume and d-spacing for the methyl-derivative was also larger compared to the  $-\text{H}$  derivative. Nevertheless, the  $-\text{H}$  derivative showed a higher permeability despite its lower free volume and d-spacing. The conclusion of the investigation was that not only bulkiness but also the fluctuations and orientation of the groups play a crucial role. The perpendicular orientation of the methyl group increased the chain separation, but also blocked the penetrants pathways. Since this effect affects the permeation of larger gas molecules such as  $\text{CH}_4$  more than the linear  $\text{CO}_2$ , the selectivity is for  $\text{CO}_2/\text{CH}_4$  is increased by the pathway blocking.

### **Polymer of Intrinsic Microporosity (PIM)-PI**

#### *Iptycene*

Iptycenes are bicyclic systems, which imply a bulky backbone structure (Figure 17). These materials were usually accessed by cycloaddition of anthracene units in case of pentyptycene and anthracene with benzyne in case of triptycene. These so-called bridgehead systems are highly rigid and do not readily twist or rotate. Triptycene forms a roof-like group with a  $120^\circ$  angle between all three aromatic rings. Due to the stiff and bulky nature, triptycene and pentyptycene elements increase the free volume. Luo *et al.*[105] investigated the effect of additional methyl substituents, and figured out, that the free volume increase by further polymer chain disruption was very small. They concluded, that methyl groups were able to fill the voids between both bridgeheads of pentyptycene and called it the “partial filling mechanism”.

#### *Tröger Base*

In 1887 Julius Tröger synthesized and investigated the Tröger Base, which is a bicyclic amine 2,8-dimethyl-6H,12H-5,11-methanodibenzo [1,5] diazocine by reaction of p-toluidine and



formaldehyde [106]. The Tröger Base has a roof-type structure with two bridgehead stereogenic nitrogen atoms and a diazocine bridge (see Figure 17). Therefore, TB was previously discussed as a PIM structure. However, since the use of diamines allows the preparation of diamino Tröger Base, they can be used as monomers for the polyimide synthesis. The incorporation of a TB unit leads to a nitrogen-containing kinked heterocyclic rigid and roof- or V-shaped bicyclic backbone structure which leads to intrinsic microporosity and is therefore highly attractive for the preparation of gas separation polyimide membranes.

Zhuang *et al.*[107] prepared two TB based polyimides, PI-TB-1, and PI-TB-2. They were synthesized from 2,5-Dimethyl-1,4-phenylenediamine and either 6FDA or BTDA. Two diamines and an anhydride formed the precursor which was then polymerized by Tröger base formation in trifluoroacetic acid. The gas separation was significantly higher in case of 6FDA with 457 Barrer for CO<sub>2</sub> *versus* 55 Barrer in the case of BTDA due to the bulky kinked hexafluoroisopropylidene group.

Another attempt was the preparation of carbocyclic bicyclic dianhydrides similar to Tröger Base structures. Ma *et al.* synthesized two dianhydrides, CTB1 and CTB2 [108]. They prepared membranes by polymerization of these dianhydrides with 3,3'-dimethylnaphthidine (DMN) with BET surfaces of 580 and 469 m<sup>2</sup> g<sup>-1</sup> and a permeability of 1661 Barrer (60-day aging: 546 Barrer) for CTB1-DMN and a high CO<sub>2</sub>/CH<sub>4</sub> selectivity of 17.4 (60-day aging: 28.9), H<sub>2</sub>/CH<sub>4</sub> selectivity of 13.4 (39.1) and O<sub>2</sub>/N<sub>2</sub> of 4.2 (5.4). Abdulhamid *et al.* prepared such pseudo-TB containing polyimides by synthesis of carbocyclic diamines and polymerization with 6FDA. Both diamines CTBDA and *i*CTBDA varied in the position of the amino groups [109]. Both materials showed high BET surfaces with 587 and 562 m<sup>2</sup> g<sup>-1</sup>. They showed a gas permeability trend in accordance with other PIM-PIs with H<sub>2</sub>>CO<sub>2</sub>>O<sub>2</sub>>N<sub>2</sub>>CH<sub>4</sub> and typically for molecular sieves. 6FDA-CTBDA demonstrated a CO<sub>2</sub> permeability of 291 Barrer at a selectivity of 25 for the natural gas purification relevant gas pair CO<sub>2</sub>/CH<sub>4</sub>.

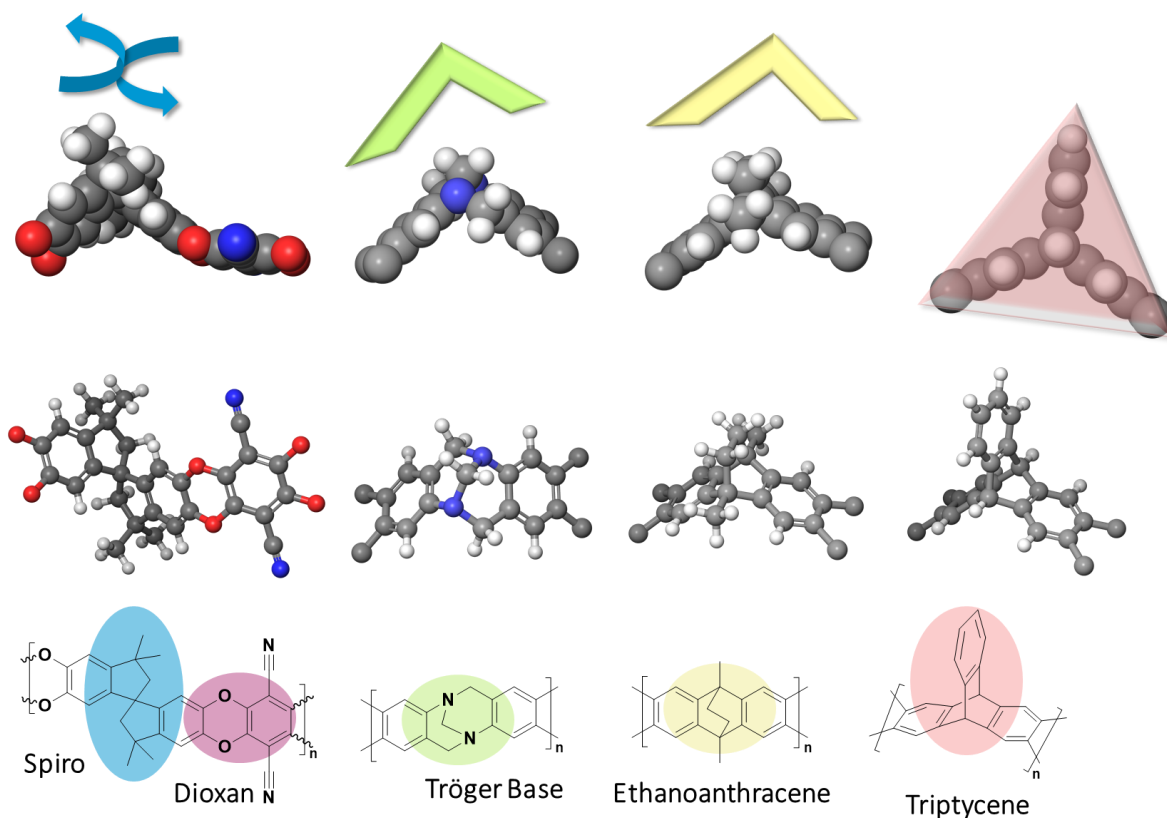


Figure 17. Simulated structures of the repetition units containing spiro-, dioxan-, Tröger base-, ethanoanthracene-, and triptycene units.

## Crosslinking

Crosslinking [110] defines the linkage of two and more polymer chains by physical and/or chemical connections. Linear polymer chains can result in highly branched complex networks by that way, which strongly alters the materials properties [111]. Usually, tight crosslinking leads to reduced polymer chain mobility and therefore increases the glass transition temperature, lowers the fractional free volume, and oftentimes increases the thermal, mechanical, and chemical resistance. However, after crosslinking, materials are not soluble and difficult to process, especially if non-reversible chemical crosslinks were introduced. The formation of crosslinks can be by physical interactions, such as hydrogen bonds, polar interactions such as anion-cation interactions, dipole interactions or complexation such as metal-ion coordination (aluminum acetylacetonate by Wind *et al.* [112]), solvent molecule coordination or complexes such as charge transfer complexes in polyimides. The techniques most often used, are chemical crosslinking. Chemical crosslinking means to covalently bind two molecules of two separate polymer chains or more by chemical reaction. The crosslinking does not necessarily need to be irreversible. For instance, in shape-memory materials reactions

such as Diels-Alder reactions between furan and maleimide groups, were introduced which can be specifically opened and closed, depending on the temperature. By use of UV light crosslinks [110] can be opened and closed, depending on the excitation wavelength, similar to the function of molecular switches [113]. Nevertheless, in most applications crosslinks were permanently introduced after membrane formation. Two types of crosslinking are considered. Possibility one is to use monomers or modify polymers after polymerization with functional groups which can crosslink after heating or irradiation. For instance, the presence of vinyl groups has been used to crosslink [114]. The second category is the addition of small multifunctional molecules, the crosslinker. These crosslinker can be diamines, diols for instance, which react with other present functional groups in the polymer chain. Both categories will be discussed in the following section [110].

#### *Stimuli-induced crosslinking*

The crosslinking without any additional crosslinker is carried out by different functional groups. An *et al.* reported a debromination-induced crosslinking [101]. They used bromomethyl groups and annealed them. At higher temperatures radical debromination occurred under formation of bromine and ethylene crosslinks. An *et al.* used 6FDA-durene which was post-polymerization modified by radical bromination. The CO<sub>2</sub> permeability of the durene system, since rigid crosslinks were formed, which favored the diffusion, increased compared to the brominated non-crosslinked polymer by 36 times [110].

Zhang *et al.*[115] reported a system of a phthalide containing polyimide. Phthalide is a known structure due to phenolphthalein, which contains a phthalide group under neutral conditions. Under basic conditions the lactone ring opens, and a carboxylic acid group is present [116]. However, the lactone ring opening can also be forced by heating [116, 117]. Accordingly, Zhang *et al.* synthesized a ring-opened diamine and polymerized it with various anhydrides. Upon heating the carboxyl groups react via condensation reaction under formation of an anhydride, which then decarboxylates into two phenyl radicals and releases CO<sub>2</sub> and carbon monoxide. Both phenyl radicals react by forming a biphenyl linkage, which is a very tight and rigid type of crosslink. The CO<sub>2</sub> permeability increased after annealing at 450 °C by 100 times from 18 to 1858 Barrer. However, the selectivity dropped from 31.3 to 18.9 for the gas pair

CO<sub>2</sub>/CH<sub>4</sub>. The materials were still flexible and showed excellent plasticization resistance. A major challenge remains however due to the high temperatures for the crosslinking reaction.

In addition, thermal oxidative crosslinking was reported for similar systems by Zhang *et al.* [117]. They used the same polymers from their previous study and annealed them, while the lactone ring was closed this time. Importantly, the annealing took place at 25 °C lower than the decarboxylation induced crosslinking and oxygen was present. As a consequence, the lactone ring opens by heating due to oxidative ring opening. Oxygen, which is a diradical, is then capable of attacking at four different sites. Full conversion was achieved upon heating to 400 °C and increased the permeability to 193.8 Barrer, which is significantly lower to their non-oxidative method. However, lower temperatures are required and higher selectivities were obtained (39.2 for CO<sub>2</sub>/CH<sub>4</sub>).

Another type of carboxylic acid crosslinking is the use of diamino benzoic acid (DABA). It is a common diamine for polyimide synthesis which introduces a carboxylic acid. Upon heating above 400 °C in most cases, the carboxylic acid groups crosslink under anhydride and biphenyl formation. Kratochvil and Koros introduced it in 2008 [118, 119].

### *Chemical Crosslinking*

Chemical crosslinking has the great advantage, that the final properties can be easily tuned and adapted by choosing from a large number of crosslinkers. Diols, diamines, dicarboxylic acids, dihalogenides, diazides diepoxy- or diethynyl containing alkanes were used. In addition, di, tri or tetra-functional crosslinkers were used. Pentaerythritol for instance contains four hydroxy groups. Moreover, even larger aromatic crosslinkers were used, such as tri- or tetraphenylene amines were used to synthesize large networks.

In 1997 Rezac *et al.* studied diacetylene group containing blends under thermal annealing procedures [120].

Diol crosslinking is executed by a reaction between diol hydroxy groups and pendant carboxylic acid groups on the polymer backbone. Two esterification reactions occur and crosslink both polymer chains. The diol crosslinking was reported by Koros *et al.* Eguchi *et al.* used glycidol to crosslink by reacting with DABA containing polymer chains [121]. For a similar system Staudt-Bickel *et al.* reported a plasticization resistance of DABA containing

6FDA-based polyimides up to a CO<sub>2</sub> feed pressure of 14 atm due to the hydrogen bonding between carboxyl groups [122]. The addition of ethylene glycol and hence the formation of covalent crosslinks suppressed plasticization up to a feed pressure of 35 atm.

Wind *et al.* reported in 2004 a beneficial effect towards permeability and selectivity upon crosslinking and annealing [119]. They annealed diol crosslinked and non-crosslinked DABA containing polyimides at 295 °C. While non-crosslinked polyimides showed a drop of the CO<sub>2</sub> permeability with a constant selectivity, the 1,4-butylene glycol crosslinked polyimides showed an increase of the permeability by a factor of 4.1 without sacrificing the selectivity. They concluded that crosslinking caused a polymer chain packing disruption with increased number of micro voids which enhanced the CO<sub>2</sub> sorption and accordingly the solubility selectivity.

Diamine crosslinking was investigated by Shao *et al.* [123]. They crosslinked Matrimid 5218 and 6FDA-durene based polyimides with various diamines. The crosslinking reaction rates increased from ethylene diamine to 1,3-propane diamine to 1,4-butane diamine in the order of increasing nucleophilicity of the amine group. They also drew as a conclusion that polymers with large inter chain spacing are reaction limited with respect to the crosslinking rate, while polymers with more efficient chain packing are diffusion limited by the diffusion rate of the diamine.

## **Thermally Rearranged Polyimides**

Polyimides have been a very important interesting polymer class for the use as gas separation membranes. Many approaches have been used to improve the gas separation performances and target specific problems, such as aging, plasticization and fouling resistance, while maintaining and improving the gas separation performance, as described before. Methods like crosslinking or the introduction of bulky and contorted monomers were successfully implemented in order to improve the microporosity. Ever since their discovery in 1999 and use as gas separation membrane precursor in 2007, the number of publications increased (Figure 18) up to more than 300, and various groups started focusing on TR polymer membranes.

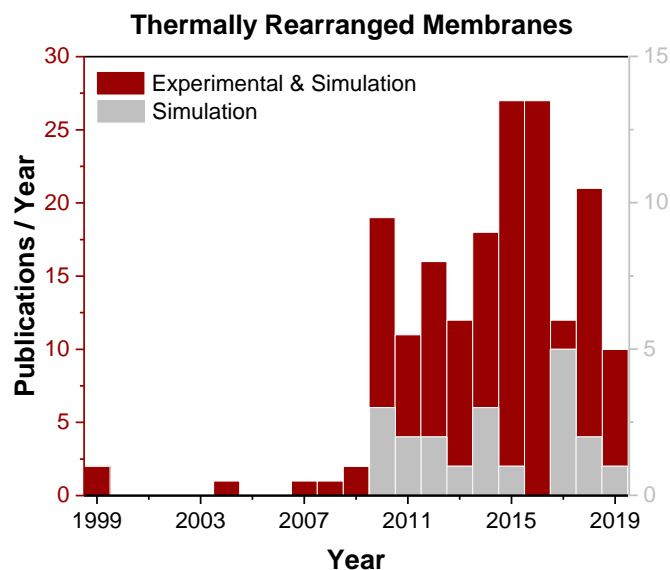


Figure 18. Number of publications based on bibliographic survey using the key word "Thermally Rearranged Membrane". The literature review was done by using SciFinder<sup>®</sup> [search performed on 25/08/2019].

Nevertheless, in 1999 Tullos *et al.*[124, 125] found by routine TGA measurements of *ortho*-hydroxy containing polyimides (HPI) that an "unexpected"[124] weight loss, caused by the release of two molecules of CO<sub>2</sub> per repetition unit at temperatures above 300 °C. The highly rigid BPDA-HAB polyimide was thermogravimetrically analyzed when a weight loss step of 18.6% was determined. Annealing at 500 °C caused a disappearance of the mass loss step upon heating up for a second time. Accordingly, an irreversible reaction occurred. FT-IR and <sup>13</sup>C-CP-MAS experiments revealed the formation of benzoxazole rings. Accordingly, a cyclization reaction was proposed, which was triggered by the high heat energy input at those high temperatures (Figure 19). Further investigations using different *ortho*-hydroxy containing diamines, such as BisAPAF and APA, and the dianhydrides BPDA, ODPA, 6FDA and BTDA as well as BPADA-DAPP, were conducted to investigate the potential of the cyclization reaction. While flexible BPADA containing precursor achieved high to complete conversions at treatments of approximately 350 °C, the very rigid BPDA-HAB required 500 °C for 1 h in order to complete the benzoxazole cyclization reaction. Hence, a backbone-mobility dependence to promote the TR process was concluded.

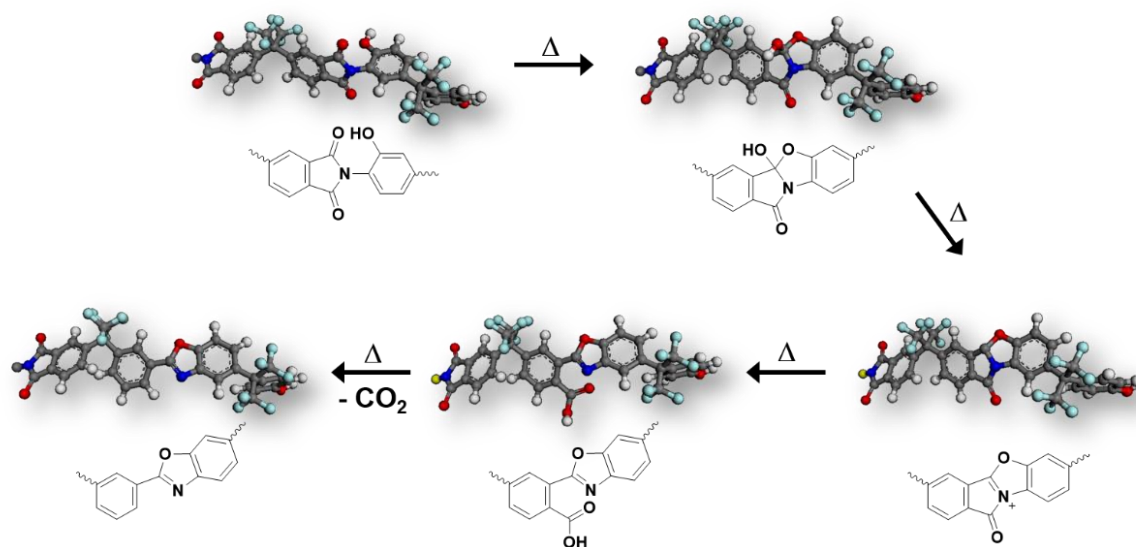


Figure 19. Proposed Thermal Rearrangement mechanism of *ortho*-hydroxy polyimides by Tullos et al. in 1999 [124, 125].

In an effort to evaluate and corroborate the proposed mechanism, a model compound study with *N*-(2-hydroxy phenyl) phthalimide was done [125]. Annealing at 400 °C under nitrogen for 30 min caused a conversion to the corresponding benzoxazole structure of 83%. To verify the proposed *ortho*-carboxyl benzoxazole structure as an intermediate of the reaction path, it was synthesized and investigated by means of thermoanalytical and spectroscopic experiments. Interestingly, above 350 °C a decarboxylation reaction occurred, leading to the suggested benzoxazole. However, annealing below 350 °C caused the *ortho*-carboxyl benzoxazole to undergo the “reverse” reaction to the *ortho*-hydroxy polyimide (HPI) as well as the formation of a di-benzoxazole, presumably due to the reaction with an already formed HPI.

About 8 years later in 2007 [126, 127] Ho Bum Park and Young Moo-Lee reported the use of *ortho*-hydroxy polyimides as precursors for the preparation of highly promising microporous polybenzoxazole (PBO) membranes by annealing at higher temperatures. The isothermal treatment of such polyimide films caused the formation of a microporous polymer film with heavily altered film properties and enhanced gas separation properties. They prepared polymers based on the diamine bisAPAF and various anhydrides, 6FDA, ODPA, BTDA, BPDA, PMDA and NTDA, and prepared thick films from them. Upon annealing to 450 °C at a heating rate of 5 °C min<sup>-1</sup> the films became dark, due to the formation of charge-transfer complexes as reported for polyimides and partial polymer degradation [56, 127]. The resulting

polymer membrane changed its pore size distribution from a monomodal distribution to a bimodal pore size distribution with pores of 0.3 nm and 0.8 nm. Furthermore, a high BET surface area above 500 m<sup>2</sup> g<sup>-1</sup> was determined. Moreover, the BET experiments have shown that a hysteresis was found during the desorption cycle. This was justified by the penetration of the nitrogen molecules into small interconnectivities between small cavities. The formation of such a bottleneck type pore characteristic was explained by the coalescence of small cavities with specific shapes, most likely due to the role of the released CO<sub>2</sub> caused by the decarboxylation step. The synthesis of a carboxyl group containing polymer, however, did not yield a comparable performance upon decarboxylation. Accordingly, the improved performance of TRPs is not solely attributed to the decarboxylation reaction. It is rather the combination of an intramolecular rearrangement, accompanied by a decarboxylation induced void formation, which is preserved due to the rigid polybenzoxazole units (see Figure 20). Furthermore, films of *para*-polybenzoxazoles, which were directly obtained by synthetic methods, did not show such a beneficial microporous structure as well. This was explained by the possibility to form *para* or *meta* linkages. Hence, the presence of *meta*- and *para* linkages are statistically distributed and cause a presence of different bond angles and torsional angles, which lead to inefficient chain packing and therefore a high degree of microporosity [127]. Molecular simulations of the initial polyimide and formed PBO have shown, that the responsible torsional angle for the TR process is also limited to a range of 45±15 ° and 135±15 ° [127]. At higher temperatures, the rotational barrier diminishes, as the polymer rotates more freely. The formed PBO consists of coplanar benzoxazole groups, which are resonance stabilized with the connected phenyl ring. This only allows a rotation of 0±10 °. The verification of the suggested geometrical assumptions was justified by the similarity of the physical properties of the simulated amorphous polymer cell and the experimentally determined density. The simulated cell with *para* and *meta* linkages had a density of 1.287 g cm<sup>-3</sup>, while the experimentally determined density after annealing at 450 °C changed to a density of 1.293 g cm<sup>-3</sup>.



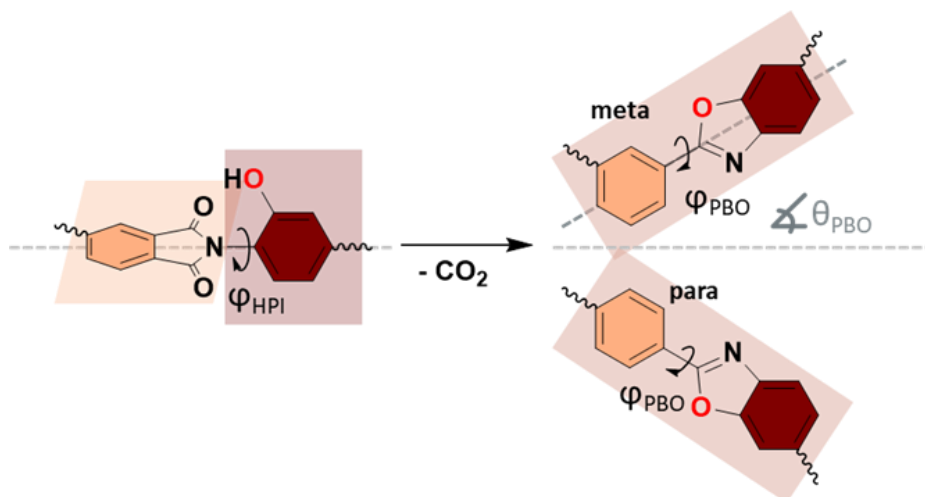


Figure 20. Geometric and steric changes, due to the Thermal Rearrangement induced cyclization, decarboxylation and respective rearrangement. The torsion  $\varphi$  along the main axis as well as the angle change of the polymer backbone main axis  $\theta$ .

### Benzoxazole reaction mechanism

Nowadays scientist do not agree on a common reaction mechanism. There is still a discussion about the real mechanism and the formed product going on. In 2011 Rusakova, Kostina *et al.*[128] performed a quantum mechanical study in combination with FT-IR spectroscopic investigations. They used DFT simulations on a B3LYP/6-31+G (d, p) level of theory to propose a reaction mechanism. They synthesized two polymers based on aromatic ether backbones and investigated the FT-IR spectrum after annealing at 450 °C. The presence of absorption bands at 1560 and 1670  $\text{cm}^{-1}$ , as well as the broad band from 3300 to 3620  $\text{cm}^{-1}$ , despite the consumption of all phenol groups by the thermally initiated TR reaction, were attributed to the presence of primary and secondary amides. This was assumed to be corroborated by a HCl treatment, which caused the vibration bands at 1560 and 1670  $\text{cm}^{-1}$  to disappear due to amide hydrolysis. Hence, they proposed a reaction mechanism, which formed a lactam as final product. This was supported by DFT simulations of the PBO mechanism and their proposed lactam path (see Figure 21). Both reaction coordinates showed activation energies in the same range. The PBO path had a maximum energy barrier of 403  $\text{kJ mol}^{-1}$ , while the lactam path required 414  $\text{kJ mol}^{-1}$ . However, the lactam path was still prioritized, since the formed lactam has a lower energy and is therefore the thermodynamically favored product.

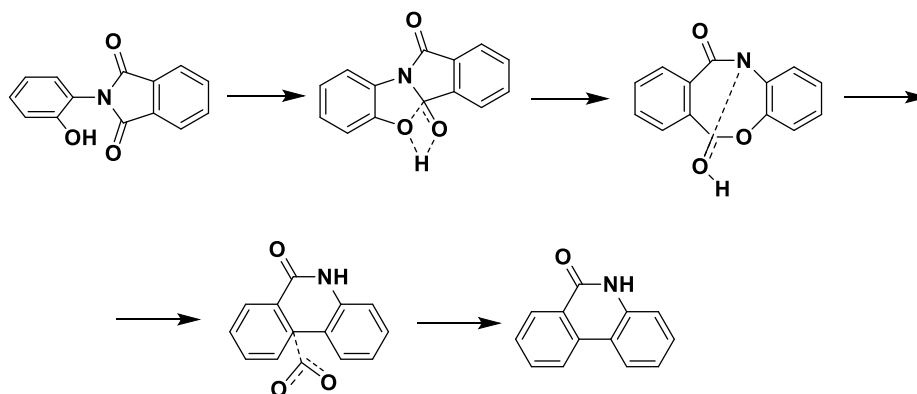


Figure 21. Proposed Thermal Rearrangement reaction mechanism by Kostina *et al* [128].

In 2009 Hodgkin *et al.* [129, 130] reported a publication, doubting that the proposed mechanism is really occurring. They published their thoughts and suggestions with the title “Thermal conversion of hydroxy-containing polyimides to polybenzoxazoles. Does this reaction really occur?” They criticized the inconsistency of the experimental data among various reports and the identification of the benzoxazole group by using different vibrations of the FT-IR spectrum at 1560 [124], 1480 [131], 1060 [127] or 1620  $\text{cm}^{-1}$ . They also claimed that the insolubility of the product is a problem, since other methods exist, that are capable to form soluble polybenzoxazoles. However, the main aspect of the discussion is the fact that, according to their opinion the widely described methods of polyimide synthesis by a two-step approach in dipolar aprotic solvents cause the formation of amic acid bonds, but also ester as defects. The reaction of the phenol group with the anhydride cannot be ruled out. These groups remain as polymer defects. Hence, a thermolabile ester bond and a more stable amide bond would be present and randomly distributed. Accordingly, upon annealing the ester groups would decompose, releasing  $\text{CO}_2$ , while the amide would remain intact. Accordingly, the mass loss step in the TGA is explained. The  $\text{CO}_2$  release, as detected via on-line FT-IR or MS measurements, is the consequence of the ester decomposition. Consequently, they suggest to investigate clean polyimides without ester defects, which is possible by using a water-based microwave synthesis [130]. Under these conditions, according to Hodgkin *et al.*, the formation of ester groups “normally” [130] does not occur. The experimental evidence for the defect free polyimides is shown by comparison of the imide carbonyl peak around 1720  $\text{cm}^{-1}$ . In the case of non-ideal synthetic conditions, defects, such as ester and carboxylic acids are formed and lead to a shoulder on the right (1706  $\text{cm}^{-1}$ ) and left (1728  $\text{cm}^{-1}$ ) side. Clean products do not show such a peak shape. They further used the prepared fine powder and annealed the sample in the DSC. According to their FT-IR measurements at different annealing temperatures, the

imide carbonyl peak does not decrease, it rather remains large and sharp and furthermore shifts to higher frequencies. However, since the carbonyl group remains present, while the hydroxy peak disappears completely, no polybenzoxazole formation occurred. However, a phenolic hydroxy group removal took place. This is expected by means of a water formation, which caused the formation of a benzyne intermediate, which immediately dimerizes (see Figure 22).

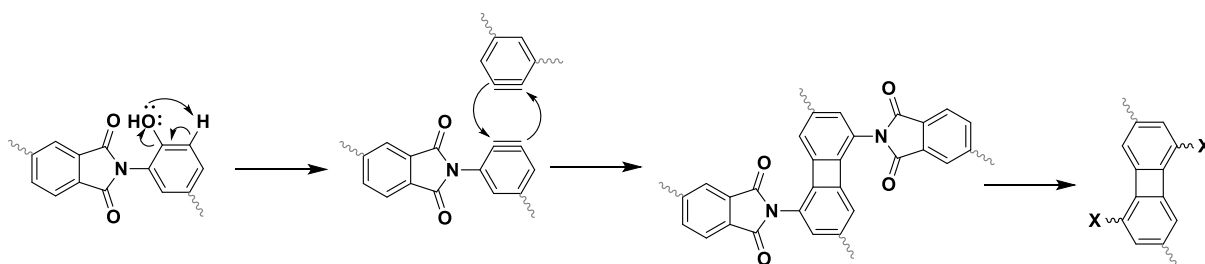


Figure 22. Proposed Thermal Rearrangement reaction mechanism according to Hodgkin *et al.* [130].

In 2015 another mechanism was proposed by Comesana *et al.* [132] She prepared 6FDA-HAB based polymers without any modification and an acetylated and methylated polymer. Analysis of the mass loss and evolved gas composition were used to analyze the possible underlying reaction mechanism in combination with FT-IR measurements. The results for the modified precursor will be discussed later. For the pristine material, a hydrogen transfer step to the imide nitrogen atom was suggested. The resulting protonation of the positively charged nitrogen atom causes a change of geometry from a trigonal planar structure to a tetrahedral-like conformation (Figure 23). As a consequence, the formed phenolate and carbonyl group come closer to each other with a distance below 0.2 nm (Figure 23). The lowered distance is expected to be beneficial for the reaction. As a conclusion of the simulation, which was based on a transition state geometry optimization by means of semi-empirical AM1 level of theory and subsequent single-point energy calculation via DFT at the B3LYP/6-31G level of theory, the reaction results in the formation of a cyclic ester-amide ring intermediate, which decarboxylates and forms the lactam (Figure 24), as suggested by Kostina and Rusakova [128]. However, no reaction coordinate and transition state geometry optimization at a higher level of theory was presented.

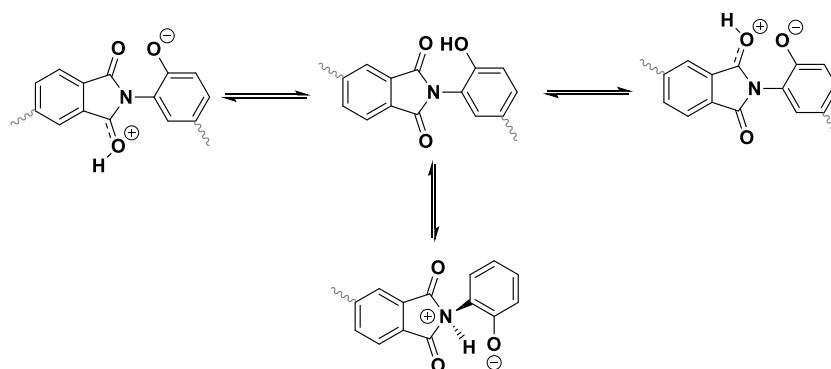


Figure 23. Initial step for the Thermal Rearrangement proposed by Comesana et al. based on semi-empirical simulations [132].

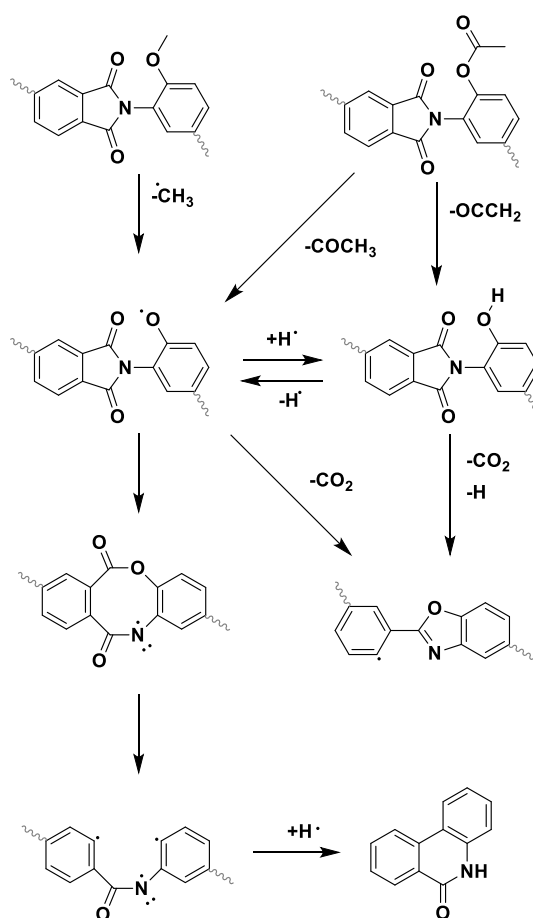


Figure 24. Mechanism of demethylation, deacetylation and subsequent Thermal Rearrangement for acetylated and methylated ortho-hydroxy polyimides [132].

A study by Smith *et al.* [133] in 2014 targeted the proof of the polybenzoxazole formation by means of  $^{13}\text{C}$ -CP MAS experiments of *ortho*-hydroxy polyamides and imides. They synthesized 6FDA-APAF and 6FCI-APAF, which are supposed to both form a polybenzoxazole structure. While the HPI yielded a gel content of 100% after annealing at 450 °C, the polyamide was annealed at 350 °C in agreement to the most widely used annealing procedure and had a gel fraction of only 74.9%. Accordingly, the soluble part was used for NMR studies. They used

2D-NMR techniques, such as COSY, HSQC and HMBC to analyze the product and their couplings. In addition, the integration of the aromatic peak has shown to consist of 14 protons, which contradicts the mechanism by Hodgkin, which would result in only 12 aromatic protons. The experiments revealed furthermore that protons were only coupled to carbon atoms and not nitrogen atoms, therefore the presence of lactam can be ruled out as well. Finally, the liquid NMR was compared to  $^{13}\text{C}$ -CP-MAS solid-state NMR spectra of the HPI and HPA, respectively. The solid-state NMR were in agreement to the solution NMR and both CP-MAS spectra from HPI and HPA were nearly identical. Only the peak at 136.5 ppm was not available in annealed HPI. This peak is assigned to the aromatic carbon atom, which is connected to the hexafluoroisopropylidene group in the anhydride moiety. Since in HPI the phenol group can attack one out of two carbonyl groups, both products are present. Depending on the attacking side, either a *para* or *meta* linkage is formed. Therefore, the peak is not as strong. Based on these investigations, the polybenzoxazole product was proposed. Despite the uncertainty of the final product and reaction mechanism, various parameters, which affect the TR process were analyzed. The major drawback of TR polymer membranes nowadays still is the high annealing temperatures in order to promote the HPI-to-PBO formation and convert the polymer to sufficient levels. Therefore, no reasonable support material was suggested, as commonly used support materials, based of polyacrylonitrile or polysulfones, degrade at the required high temperatures [134-137]. Accordingly, scientists are interested in finding a way to lower the Thermal Rearrangement temperature to a certain level, which allows the use of commercially available support materials. Since most TR polymers require annealing procedures of 450 °C for 1 h, side reactions such as crosslinking and polymer degradation already occurs [127]. One side reaction for instance is the degradation of the hexafluoroisopropylidene group in case of 6FDA or BisAPAF based polyimides. The decomposition then offers new locations for a crosslinking reaction [51].

### **Effect of the backbone**

For the purpose of getting better ideas, how the TR reaction is affected, Guo *et al.*[138] as well as Calle *et al.*[139] have executed studies with different TR precursor backbones. Calle *et al.* used four diamines and three dianhydrides and investigated the effect of the diamine and dianhydride flexibility towards glass transition temperature and their correlation with the TR

temperature. Three specific TR related temperatures were defined, TR1, TR2 and TR3 which are the onset, peak and offset temperature of the Thermal Rearrangement. The temperatures were based on the first derivative DTG of the mass loss curve and the onset temperature TR1 is defined as the first increment of the DTG. Calle observed that the order of the glass transition temperature always shows the same order based on the used diamine. The glass transition temperature increased in the order 6FBAHPP < TBAHPB < BisAPAF < HAB. While BisAPAF and HAB are commercially available diamines, both other diamines were synthesized and are basically aromatic ether. Apart from the glass transition temperature she also correlated the integrated heat under the exothermic heat flow curve at high temperatures for several polyimides. The determined enthalpy, by means of DSC experiments, ranged from 3 to 13.3 J g<sup>-1</sup>. The lowest enthalpy was determined for the lowest T<sub>g</sub> polyimide, namely 6FBAHPP-BPADA, while the highest enthalpy of 13.3 J g<sup>-1</sup> was obtained for the highest T<sub>g</sub> material 6FDA-HAB with a T<sub>g</sub> of 347 °C. A comparison of the used anhydrides with the described diamines shows that with each diamine the TR<sub>onset</sub> increases in the order BPADA < 6FDA < BPDA. Furthermore, the distance from the glass transition temperature to the Thermal Rearrangement reaction peak temperature increases as the rigidity of the anhydride decreases.

Guo *et al.* have investigated the correlation of the glass transition temperature and TR temperatures as well in a set of BisAPAF and HAB based polyimides [138]. Annealing at 400 °C revealed a full conversion of the material with the lowest T<sub>g</sub>, namely BPADA-APAF. In addition, a conversion of 91% was obtained for the ether containing flexible ODP (T<sub>g</sub> of 266 °C). PMDA-APAF converted only to 64% and had a higher T<sub>g</sub> of 288 °C. BTDA-APAF has a similar T<sub>g</sub> compared to PMDA-APAF. BTDA-APAF has a T<sub>g</sub> of 280 °C, however, a conversion of 84% was found. The lowest conversion of only 50% of the imide groups was detected for 6FDA-HAB with the highest T<sub>g</sub> among all tested materials. Interestingly, 6FDA-BisAPAF has a higher glass transition temperature than PMDA-APAF, but a 11% higher conversion of in total 75% was determined.

Guo *et al.* further compared the reaction progress of 6FDA-HAB and BPADA-APAF. A treatment at 320 °C was sufficient to promote full conversion within 2h. A rapid TR rate increase was reported, while a slowing down of the TR rate, even for BPADA-BisAPAF, was determined. This observation is rationalized by the fact, that the TR progress increases the number of rigid benzoxazole units, which continuously increase the T<sub>g</sub> of the polymer and are

accompanied by crosslinking which restricts the mobility even more (Figure 25). Therefore, gel fraction experiments were done. A gel content after an annealing at 350 °C of 100% was obtained for the BPADA-based and more flexible precursors. 6FDA-HAB and 6FDA-APAF had only 3 and 4% gel contents, respectively. 6FDA-BisAPAF did not achieve 100%, even after an annealing at 450 °C. At 400 °C a gel fraction of only 75% was detected.

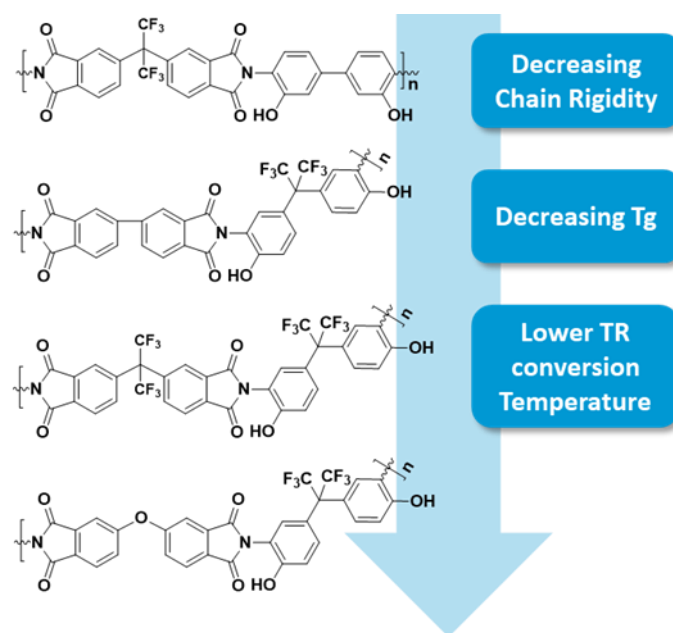


Figure 25. Correlation of the measured glass transition temperature, concluded mobility and measured Thermal Rearrangement conversion temperature of various HPI backbones according to Guo et al. [138].

## Effect of imidization

In 2010 Han *et al.*[140] studied the effect of the imidization route towards gas separation and thermoanalytical properties. Four different imidization routes were executed. The azeotropic imidization at high temperatures above 180 °C in solution with an azeotropic agent, such as *p*-xylene, can be used. Reaction times of at least six hours are required in order to promote a full imidization. Another method is the thermal imidization in solid-state. The polyimide solution is cast and the film is then thermally imidized at 300 °C for at least 1 h. Another imidization route is the chemical imidization by using acetic anhydride as decondensation agent. However, since *ortho*-hydroxy containing polyimides are used, they usually undergo an additional acetylation reaction. Han *et al.* compared the film properties with respect to the chosen method. The azeotropically imidized material had a density of 1.49 g cm<sup>-3</sup>. The

thermally imidized sample had a slightly lower density, which is attributed to the low tendency of crosslinking. In accordance the d-spacing as a measure of the free volume elements is with 0.57 nm larger for tHPI compared to 0.54 nm for the aHPI film. The density dropped in the case of the acetylated chemically imidized product to 1.45 g cm<sup>-3</sup>. The lower density and higher d-spacing are the consequence of the polymer chain disruption of the larger acetyl group, which acts as a spacer. Different imidization routes are shown in Figure 26.

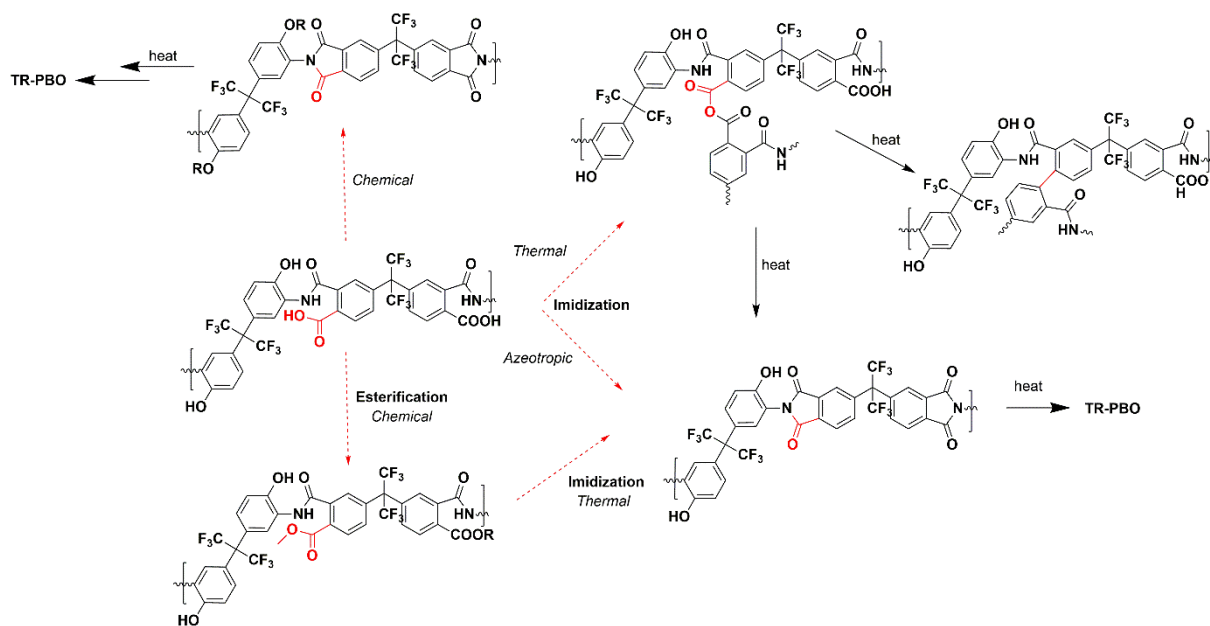


Figure 26. Imidization routes of ortho-hydroxy polyimides and thermally induced side- or consecutive reactions.

After annealing at 450 °C in order to thermally rearrange the structures to PBO, a shrinkage of the film due to the rearrangement and CO<sub>2</sub> loss was determined. The acetylated precursor shrunk by 10 to 11% due to the lower T<sub>g</sub> and loss of large acetic acid groups upon deacetylation. As a consequence, the fractional free volume (FFV) increased by 48% from 19 to 28% for tPBO. The conversion from aHPI to aPBO caused a FFV increase by 29% from 17 to 22%. The strongest increase was determined for the chemically imidized product. The increase of FFV was about 96% from 18 to 35%. Large BET surfaces and a still bimodal pore size distribution were determined as well. Permeabilities of 398 Barrer (aPBO), 4201 Barrer (tPBO) and 5568 Barrer for the cPBO [140] were reported.

The high permeability of the acetylated polymer was motivating many researchers to work with acetylated TRPs. Sanders *et al.* synthesized acetylated 6FDA-HAB and changed the acetyl group to a propionic and pivalic group and studied the effect of the modification size on the



decomposition and Thermal Rearrangement [141]. The effect was less pronounced in 6FDA-HAB. While permeabilities of 80 Barrer were measured for AcPI2 at 450 °C and 150 for n while samples treated at 350 °C only had 17 H<sub>2</sub> and 56 at conversion of 45%, the acetylated polymers had a Permeability of CO<sub>2</sub> of 320 and 170 at 400°C. Conversions were 60% and 68%, respectively. For the larger propionic group the conversion was 56% and 78% at 400 and 450°C, respectively, while permeabilities correspondingly increased to 118 and 530 Barrer and for H<sub>2</sub> to 215 and 690. The largest group, pivalic, had conversion of 58% and 81% and permeabilities of CO<sub>2</sub> of 61 and 500 and 230, and 600 for H<sub>2</sub>. The permeability increased with increasing acyloxy group size.

Smith *et al.* [133] described that the thermoanalytical measurement by means of TGA revealed that only 9.5%, 14.6% and 18.5% mass loss after, 350, 400 and 450 °C were determined, respectively. However, theoretically the full deacetylation and TR conversion would cause a mass loss of 18.4%. The lower conversion is very likely the result of the progressive stiffening of the polymer chain, which decreases the mobility.

A similar observation was made by Comesana *et al.* in 2015 [142]. She synthesized TRP from 2,4-diaminophenol (DAP) and 4,6-diamino resorcinol (DAR). Accordingly, DAR can undergo a TR reaction with both linked imide groups, since two phenol groups are present, while DAP undergoes only one benzoxazole formation, while one imide group remains. Therefore, a maximum conversion of 50% of the imide groups can be achieved. While the theoretical mass loss was almost hit, the 6FDA-DAR only showed a mass loss of 11% instead of 16%. Furthermore, while DAP shows a clear mass loss step, the mass loss step for DAR broadens continuously. This is presumably due to the larger amount of benzoxazole formation which increases the T<sub>g</sub> and lowers the overall chain mobility and therefore reactivity.

## **Crosslinking**

Thermally Rearranged Polymers undergo thermally induced crosslinking as gel fraction measurements by Guo *et al.* have shown [138]. This occurs as well for the thermally imidized tHPI, as demonstrated by Han *et al.* [140]. However, these crosslinking events are difficult to control, and as they are caused by the high temperatures of the annealing step at up to 450 °C. At these high temperatures partial degradation occurs, which offers new crosslinking sites [51, 143]. For instance, the thermal degradation leads to recovery of amine and anhydrides which

can react with non-converted phenol groups for instance [44]. In order to tailor the film properties and improve properties such as the plasticization resistance, physical aging and mechanical, chemical stability as well as selectivity of certain gas pairs, a controlled crosslinking strategy might help. So far, only a few publications dealt with synthetic crosslinking. Two studies by Calle *et al.* discussed the use of a non-TR monomer unit as crosslinking side [144, 145]. The use of diamino benzoic acid was already published and reported as a promising sub- $T_g$  crosslinking possibility by Koros *et al.*[118]

Hence, Calle *et al.*[144, 145] used this method of controlling the degree of crosslinking by adding different amounts of DABA. They varied the amount of DABA between 0 and 25 mol% in 5% steps. However, it is important to notice, that with each BisAPAF monomer which is replaced by a DABA molecule, two TR sites are removed. Accordingly, due to the crosslinking only one CO<sub>2</sub> molecule is released instead of two as evidenced by the TR process. The glass transition temperature changed only slightly and increased from 300 °C for the 6FDA-BisAPAF homopolymer to 305 °C upon adding 5 mol% of DABA, or by replacing 5% of BisAPAF by DABA. Furthermore, the  $T_g$  increases to 314 °C with 20 mol% of DABA in the polymer backbone. The crosslinking affected the TR temperature as well and the TR peak temperatures increased from 407 °C for the homopolymer to 417 °C with 5% DABA up to 429 °C with 25 mol% DABA. Hence, the TR temperature is more affected than the glass transition temperature. The CO<sub>2</sub> release due to the crosslinking of two DABA units occurs in a similar temperature range [118]. Therefore, it is not possible to distinguish between the conversion of the DABA and TR units with common techniques. However, the DABA caused weight loss is only responsible for about 2% of the weight loss. An increasing discrepancy between the theoretical weight loss if all TR and DABA units reacted, compared to the experimentally determined weight loss after annealing at 450 °C with increasing DABA amounts, was found. This difference is explained by the potential anhydride formation as reported by Koros *et al.* [118]. This stiffens the chains and hinders the mobility of the polymer chains furthermore. This reaction was reported to occur above 400 °C via condensation of two carboxylic acid groups. This was highly interesting as the incorporation of DABA obviously not only replaced TR units and reduced the overall number of polybenzoxazole units in the final polymer, but it also lowered the conversion. When butanediol is added to the DABA containing polyimide as a chain spacer and crosslinker, a more flexible crosslinking chain is

available. This was done by Calle *et al.* as well, by adding a large excess of 1,4-butanediol (BDO) and annealing at 250 °C for 24 h under vacuum in order to remove residual BDO [144, 146]. The crosslinking occurred very efficiently and gel fractions of 95.5 to 99.1% between 10 and 20 mol% of DABA were determined. However, the reaction does not necessarily lead to crosslinked sites, but esterification might also occur at only one site of BDO. Accordingly, crosslinked chains and spacer group containing sites are present. The glass transition temperatures were affected in a similar manner to the non-esterified DABA containing TR precursor by Calle *et al.* A  $T_g$  increase from 300 to 320 °C was obtained. However, the effect on the TR temperature was less pronounced, most likely due to the chain disrupting effect of free BDO groups, which counterbalances the mobility restrictions due to crosslinked sites. The density was affected by the crosslinking as well. Both classes showed a density increase from 1.5 to 1.52 g cm<sup>-3</sup> by the incorporation of DABA which increases the intermolecular physical crosslinking between carboxyl moieties. It is worth to notice that the dimerization of two carboxylic acid groups tends to have the strongest non-covalent intermolecular forces among functional group interactions [147]. Upon annealing at 450 °C the TR process causes a density drop as expected due to the pore formation by the CO<sub>2</sub> loss and rearrangement. Accordingly, the density dropped to 1.42 g cm<sup>-3</sup> for 5 mol% containing DABA polymers and 1.38 g cm<sup>-3</sup> for 20 mol% DABA. In accordance with that, the d-spacing increased from 0.54 to 0.57 nm before TR and to 0.62 after TR for the 5 mol% containing polyimides. It increases even more if 20 mol% were introduced, up to 0.66 nm. The same range of d-spacing values was covered if BDO was used as an additional crosslinker. The density dropped even more, to 1.36 g cm<sup>-3</sup> in case of 5 mol% DABA + BDO. PALS data showed the presence of a bimodal pore size distribution after the crosslinking. However, the difference between the pore sizes of the smallest and largest cavities tends to decrease and the pores come slightly closer to each other. This is most likely due to the crosslinking induced tightening. Even though new micro and ultra-micropores may be formed by the crosslinking, smaller pores might fuse to slightly larger ones, while large cavities are separated in smaller ones by the crosslinks. From PALS data it appeared that low number of crosslinks affected the smaller pores more than the larger ones, while increased numbers of DABA units appeared to affect the larger pores more. The crosslinking also strongly affects the gas separation. However, while BDO crosslinked polymers showed a permeability maximum for CO<sub>2</sub> at a DABA content of 10 mol%, with a slight decrease of the selectivity, the variations in the crosslinked polymers without an

additional crosslinker varied without a clear trend with respect to the amount of DABA. A high, the 2008 upper bound surpassing, performance was determined for the polymers. BDO containing systems showed an increase of the permeability of CO<sub>2</sub> from 261 Barrer to 980 Barrer. Selectivities between 29.7 and 37.5 for CO<sub>2</sub>/CH<sub>4</sub> were determined.

Another very interesting approach to prepare highly microporous tight networks, is the thermal polymerization of bismaleimides based on *ortho*-hydroxy diamines. This was reported by Do *et al.*[148], as shown in Figure 27. They prepared bis(*o*-hydroxyl) maleic acid (BHMAA) precursors and crosslinked and imidized them at about 250 °C, while further heating to 450 °C caused the units to undergo the Thermal Rearrangement reaction. The precursors were prepared from HAB or BisAPAF and maleic anhydride. Bismaleimides are reported to form tight and highly thermally stable networks. The obtained membranes from APAF based BMI networks showed excellent film properties with respect to gas separation. The BMI membrane exhibited a BET surface area of 1130 m<sup>2</sup> g<sup>-1</sup> after the Thermal Rearrangement. The CO<sub>2</sub> permeability was very high with 5440 Barrer, as well as a permeability of 1171 Barrer for O<sub>2</sub>. Accordingly, this material is one of the most permeable microporous polymer membranes and surpasses the Robeson Plot from 2008 by a lot [38, 39]. The prepared BMI rank among the most permeable TR polymers. This results in a high selectivity of 37 for the CO<sub>2</sub>/CH<sub>4</sub> gas pair and a permeability of H<sub>2</sub> of 5122 Barrer at a selectivity *versus* CH<sub>4</sub> of 35. Interestingly, the TR-BMI's based on HAB showed significantly lower gas separation performances. TR-BMI's based on HAB showed only a CO<sub>2</sub> permeability of 57 Barrer after annealing at 450 °C, while the selectivity towards CH<sub>4</sub> was also lower with 33. Blends with DAM and APAF containing polyimides were made by adding 5 wt% of the BHMI-6F precursor which caused a strong increase of the gas separation performance as well.

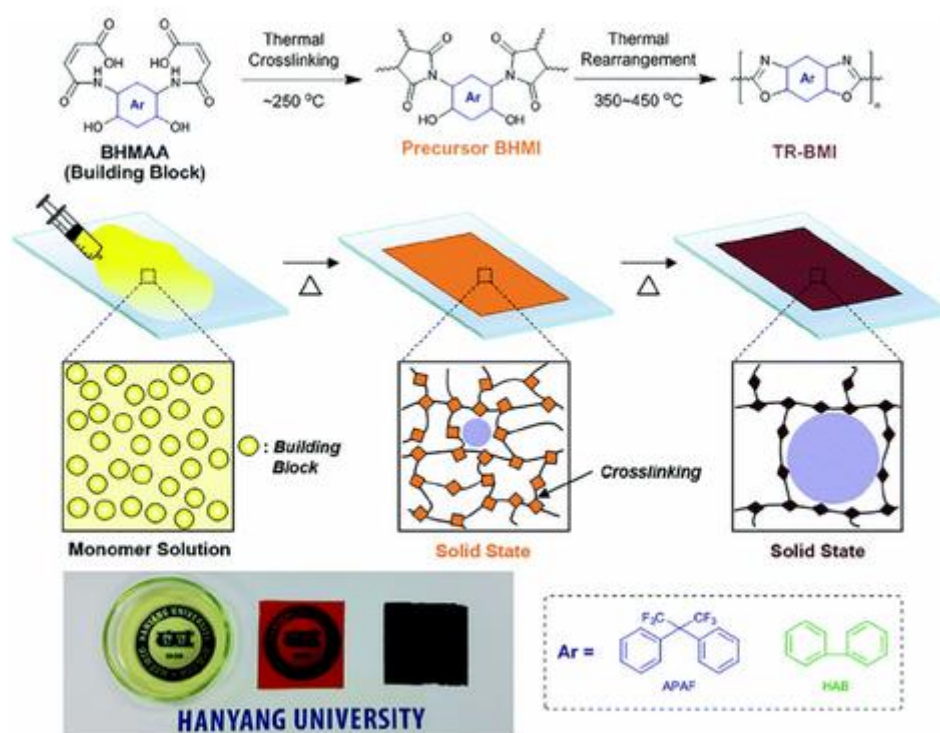


Figure 27. Synthetic route and chemical structures the used bismaleimides BHMI and TR-BMI. Reprint with permission from RSC. Reprinted from Do et al. from [148].

## Introduction of microporous backbones

In addition to the variation of the backbones, based on commercially available monomers, different approaches have been presented to tailor monomers that target the idea of lowering the Thermal Rearrangement temperature by incorporating ether and other flexible groups, such as isopropylidene units. Furthermore, these backbones should increase or at least maintain the gas separation performance with respect to the selectivity and permeability. However, since both effects are often oppositional, as more flexible backbones lower the TR temperature but also the presence of rigid-rod-like structures that preserve the formed voids after Thermal Rearrangement. Therefore, many groups started their efforts to apply their experience from Polymers of Intrinsic Microporosity and the derived PIM-PIs [106, 149-152], and the next step was to combine the Intrinsic microporosity of using contorted bulky and sterically demanding monomers and incorporate them into the TR backbone. This can be, and was, either done by using the contorted species within the dianhydride unit and polymerize it with commercially available *ortho*-hydroxy diamines, such as HAB or BisAPAF, or

alternatively, inherent microporous units were modified to yield *ortho*-hydroxy diamines from them and polymerize these monomers with commercially available dianhydrides.

One of these inherent microporous structures is iptycene, which has been successfully used as effective polymer chain disruptors [153]. Among iptycenes, the investigation of triptycenes is widely studied. Guo *et al.* prepared triptycene containing TR precursor with enhanced gas selectivities for the H<sub>2</sub> and CO<sub>2</sub> purification [154-157]. The polymer backbone can be polymerized either along the roof-top benzene ring (THPI-TR) or along the anthracene unit (TR TDA1-APAF) of the triptycene group. The latter was developed in Pinnau's group [155, 158]. While the polymers designed by Guo *et al.* contained a flexible ether backbone, the triptycene based TRPs by co-workers of Ingo Pinnau prepared ether-free highly rigid triptycene backbones [155, 158]. They synthesized triptycene containing dianhydrides as well as diamines. These materials showed an excellent air purification performance with oxygen permeabilities of 311 Barrer [155]. This was attributed to the improved pore formation. While the small-scale ultra-micropores did not change in number and size, the number of micropores above 7 Å increased. In addition, these triptycene monomers were co-polymerized. The d-spacing increased with increasing fractions of triptycene based monomers, as they efficiently disrupt the polymer chain packing [155].

The incorporation of fluorene groups into the polymer main chain was studied by Yeong *et al.* [159]. A ratio of only 10% of fluorene containing monomers caused an increase of the fractional free volume by 31% and an improvement with respect to the CO<sub>2</sub> permeability up to 1539 Barrer.

The most widely known contorted structure for the preparation of Polymers of Intrinsic Microporosity are spiro-center containing units, as described for PIM1 and PIM7 [85, 86, 160]. A set of spiro- and fluorene-based diamines were prepared and thermally rearranged to the corresponding PBO structure [152, 161, 162]. The highest FFV was obtained for the polymerization with the hexafluorinated 6FDA dianhydride. A fractional free volume of 27% and a CO<sub>2</sub> permeability of 675 Barrer were obtained [162]. In comparison the non-spiro containing TR precursor 6FDA-BisAPAF revealed a permeability of 398 Barrer and a FFV of 22% under the same thermal conditions. The introduction into dianhydride units was executed by Ma *et al.* They introduced the spiro-based units into diamines as well as dianhydrides and

expanded the number of available spiro-based TR precursors. The combination of spiro based dianhydride SPDA and spiro based diamine SBF led to a material with a high CO<sub>2</sub> permeability of 1280 Barrer [152].

Another microporosity inducing unit is the Tröger Base (TB) group. The TB unit was used to prepare TR precursor by Meckler *et al.*[163]. They combined the preparation of a Tröger Base containing diamine with various anhydrides and imidized them chemically to introduce additional acetate groups. An extraordinarily O<sub>2</sub>/N<sub>2</sub> performance was obtained with a permeability of 108 Barrer and a selectivity of 9.

In 2010 another approach for the modification of TR polymers was done by Han *et al.*[164]. He used tetraamino biphenylene (DAB) as a precursor for the polymer synthesis. The preparation of such *ortho*-amino rather than *ortho*-hydroxy containing polyimides caused a thermal cyclodehydration to the corresponding poly(pyrrolone) in the first step. Since the polypyrrolone can be isolated, as done by Scholes *et al.* as well, the reaction cascade stops at that point. Since the amino group contains two protons, the attacked carbonyl group is double protonated which causes a dehydration reaction in analogy to the TR mechanism of *ortho*-hydroxy polyamides at 300 to 450 °C. In order to promote the reaction to the polybenzimidazole (PBI), which is the nitrogen analog of polybenzoxazole, a base treatment with 1 M NaOH at 100 °C was performed. The corresponding *ortho*-carboxyl polybenzimidazole (iPBI) was then annealed at 450 °C to yield the PBI. A high gas permeability of 1624 Barrer for CO<sub>2</sub> and a selectivity towards CH<sub>4</sub> of 46.1 was determined. The iPBI had a selectivity of 93.1, but a low permeability of only 11 Barrer. The low permeability and high selectivity were explained by the large number of dimerized carboxyl groups, which form strong and very tight networks.

## **Molecular Modelling**

### Modelling of Polymer Membranes

Molecular Modelling provides the connection between theoretical chemistry approaches to describe molecules and their properties with application related empirical methods. It encompasses any type of methodology to model the behaviour of molecules on various length

and time scales. Commonly the term molecular modelling describes the computational methods to simulate the molecular properties.

Molecular Modelling tools offer a large variety of methods with the intention of simulating the molecule of interest. For very small molecules, especially small model units, this can be done by quantum mechanical (QM) simulations, which solve approximate solutions to the Schrödinger equation or use approximations with the purpose of determining the electron density, as it is done by means of DFT simulations. These highly accurate simulations, however, require large computational resources and cannot be used for the calculations of large systems, such as polymers. For such large models, molecular mechanics are commonly used, which use a set of empirical equations in the form of force fields in order to calculate molecular properties. In this chapter you will find an overview of the thesis relevant molecular modelling approaches and studies of gas separating polymer membrane systems. The computational, mathematical and physical theory is described with focus on the quantum mechanical description of the Hartree-Fock (HF) Theory and Density Functional Theory (DFT) (*Computational Chemistry* on page 586.), followed by the discussion of the execution of molecular modelling of larger systems by means of molecular mechanics (MM) from forcefields to molecular dynamics (MD) simulations. The chapter herein, starts with the development of the methodology to model larger polymeric systems based on molecular mechanics.

In order to estimate the properties of interest, it is not possible to use a single configuration of the system to predict the properties. For the determination of properties, such as the glass transition temperature or the diffusion gas molecules, it is required to simulate an ensemble of configurations, which is usually done via Monte-Carlo (MC) or molecular dynamics methods.

**Construction of amorphous polymers.** Since exact coordinates of atoms in a polymer chain configuration at a specific configurational “snapshot” are neither known nor experimentally available, of course, the initial configuration for a polymer chain has to be generated as realistic as possible as a starting configuration. Two different approaches for the model configuration are available, the reconstruction method and mimetic method [165]. The rarely described reconstruction method [166, 167] for polymeric systems, is based on a reverse Monte Carlo



simulation, which iteratively optimizes a structure towards experimental data, which is then the bottleneck of it at the same time. In most cases the mimetic approach is used, which is based on mimicking a polymeric configuration that is based on mimicking a synthesis, which is referred to the best chemical and physical understanding of the user.

The construction method by Theodorou and Suter [168, 169] was one of the first approaches to construct amorphous models and its algorithm is still used by most modelling software packages, even though it is adapted. The Theodorou-Suter (TS) method constructs an initial estimate of a polymer structure within a periodic box, the amorphous cell, according to probabilities of the chain configuration and chain conformation within a Monte Carlo simulation based on Flory's rotational isomeric state theory [170]. Initially the TS method was first used for the simulation of simple rubbery polymers, such as polypropylene. Nowadays it is widely used to model glassy polymers as well [171-173]. Other methods, which are based on Monte Carlo approaches are the random walk polymerization [174], recoil growth [175] or configurational-biased MC [176]. The model building can be extended by use of energy minimization and molecular dynamic calculations in order to ensure that thermodynamically favored models are constructed. Artifacts, such as ring catenation and spearing can be avoided by starting at low densities or introducing spacer molecules, such as solvent or gas molecules, as suggested by Hoffman and Heuchel [177-179]. However, problems are arising, once complicated ladder-type structures, such as in PIM-1, or crosslinked models are required. The used algorithm cannot polymerize two head- or tail atoms at the same time. Accordingly, a manual by hand ring closure is required [180]. This is reasonable for a few simulation boxes with low numbers of repetition units. However, if large screenings are done, this becomes a time-consuming and inefficient way to generate these models. Another approach to construct polymer models, is by inserting monomers in a periodic box and bonds are formed, once two monomers approached each other within a specific pre-defined cut-off distance [181].

After a model is constructed, it is of utmost importance to equilibrate it to become as representative and realistic as possible with respect to experimental data [182]. Since the models are usually constructed at very low densities or with residual solvent molecules inserted, sequences of MD simulations in the  $NVT$  or  $NpT$  ensemble are usually performed until certain properties or criteria are met, and physical properties are stable [177]. Commonly used techniques are cycles of stepwise compression-decompression, annealing, variable time

steps, scaling conformational energy and geometry optimization procedures [182], as demonstrated in Figure 28. Sometimes a pressure of 50k bar is used or temperatures of several thousand Kelvin. However, these simulations are only used to force the system to come into other states and leave local minima configurations for instance.

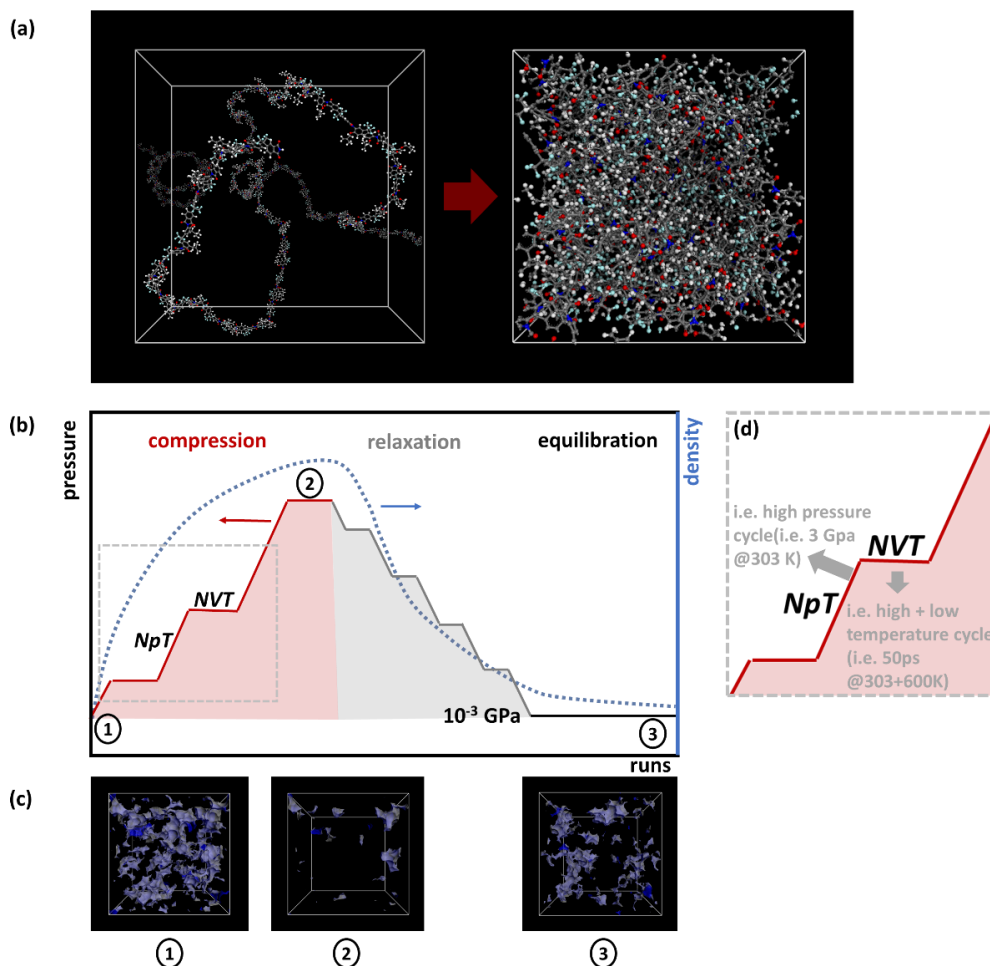


Figure 28. (a) Initial and final amorphous cell packing of a polymer chain after the compression-relaxation-equilibration (CRE) procedure. (b) Pressure and density progress within an exemplified CRE procedure. (c) Changes of the accessible solvent surface within a CRE procedure and (d) example of a NpT+NVT step within a compression process of the CRE method.

One method which has been developed is the 21-step compression/decompression equilibration procedure [182]. This method involves several NVT and Knot steps at higher pressures and temperatures. One advantage, especially when screening for new materials is on interest, is the fact that no target density has to be defined. This method was widely used in various glassy polymer systems[182-186]. The high temperatures, ideally above the systems glass transition temperature are used with the purpose of relaxing the polymers from metastable conformations. Furthermore, high pressures are used to force the rigid glassy

polymers to overcome the high activation barriers with the intention of achieving realistic densities in a reasonable time [187]. Other than earlier approaches, the stepwise compression and slow decompression is important, to prevent the residual stress to be transferred to the system, which was reported by Karayiannis *et al* [188].

**Characterization and validation.** Densities are widely discussed as validation methods for finding a reasonable model. However, since the experimental determination of the density itself varies strongly, for instance between 1.061 and 1.092 g cm<sup>-3</sup> for PIM-1[189], there is no accurate data for a model validation by using the density.

Surface areas are widely described properties of polymer films via experimental determination, for instance via BET measurements, but also very popular by modeling. The surface area is a good indicator, whether a polymeric material has large free volume elements or not. Additionally, the simulation of the geometric surface areas, such as the Connolly surface area or accessible solvent surface area are fast and can be used to compare different models (Figure 29). Park *et al.* described the determination of the accessible solvent area and divided it by the accessible volume [190]. This is an indicator of the surface to volume ratio. High surface to volume ratios could mean, that many small pores are available, since many small pores have larger surface areas than a few large pores with the same accessible volume in total. Determining this ratio for probe radii between 1 and 2 Å, shows that defects are generated during model building, which is the case if unreasonably high jumps are observed.

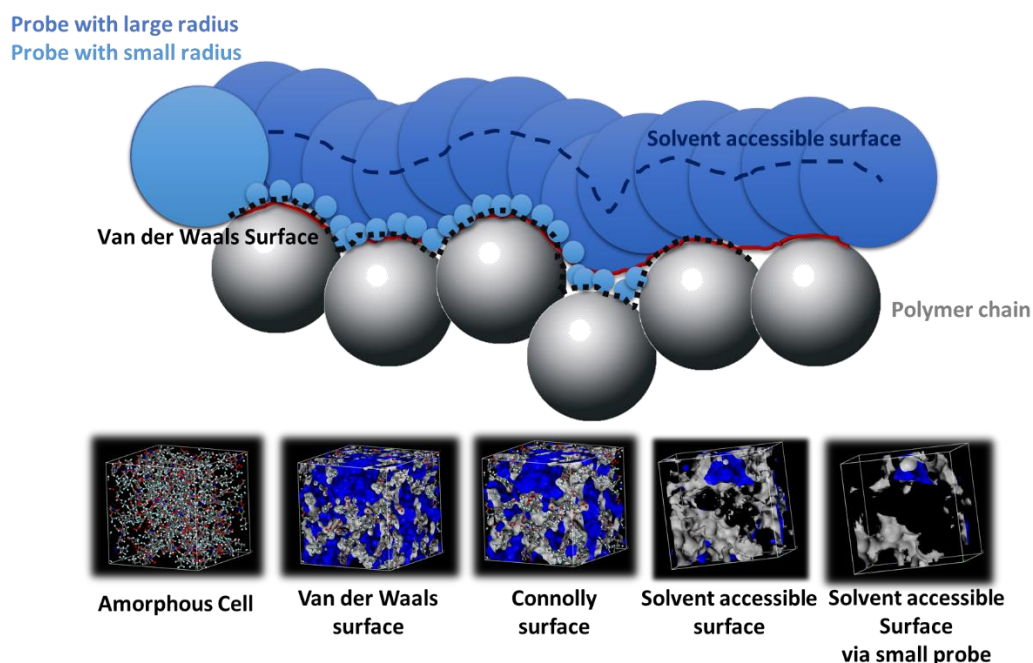


Figure 29. Method of determination of the occupied and accessible surface of a molecule via grid-search tool using a probe of different radii. Visualization of the different accessible surfaces by the grid search.

Another property, which is simulated for amorphous cells, is the diffusivity. The diffusion coefficient can be derived from molecular dynamic simulations, which are based on Einstein's equation. The diffusion coefficient is determined by simulating the mean-square displacement (MSD) of a molecule, such as a gas molecule within a polymer box. The simulated diffusivity is basically the self-diffusion [187]. However, such calculations require MSD analysis of very long MD runs in order to obtain a representative trajectory.

#### *Modelling of Polymers used in carbon dioxide applications*

The first group, which investigated PIMs by means of molecular simulations were Heuchel *et al.* in 2008 [189]. They constructed a model with five chains and 15 repetition units each. With the intention of avoiding ring catenations and other defects, they randomly inserted CH<sub>4</sub> molecules. Afterwards they used five stages of stepwise removal of the CH<sub>4</sub> molecules by using *NVT* and *NpT* MD runs at temperatures of 600 K and compression pressures of 10 bar. A final run of 1 ns via the isobaric ensemble at 1 bar and 308 K was used to equilibrate the cell. The determined densities were in the range of the experimentally established ones.

Since that, other groups became active and used other PIM polymers to evaluate the molecular properties. Fang *et al.* [191] modeled PIMs, like PIM-7 and PIM-1 with variable functionalities. Within their study they calculated diffusion coefficients after 20 ns MD runs and investigated the fractional free volume (FFV), pore structures, pore distributions as well as the CO<sub>2</sub> interactions with several atoms in the backbone by employing radial distribution functions.

Carta *et al.* simulated PIMs with ethanoanthracene as well as Tröger base units [192]. Additionally, MD simulations were used to investigate sulfur-containing PIMs, which haven't been synthesized yet. Since no experimental density was available, they used the 21-step compression-decompression method for their model relaxation.

Park *et al.* used molecular dynamics simulation to describe the thermal behavior of *ortho*-hydroxy polyimides, the TR precursor in order to get a better understanding of the TR reaction process and the parameters which affect the feasibility of the reaction [190, 193]. They published two studies. In their first one [193], they focused on the determination of torsional angles and investigated the formation of hydrogen bonds and the motions of the TR reaction centers at different temperatures. They described the randomly distributed torsional angles prior to the TR reaction and a very narrow range of torsional distributions of the corresponding polybenzoxazole (Figure 30).

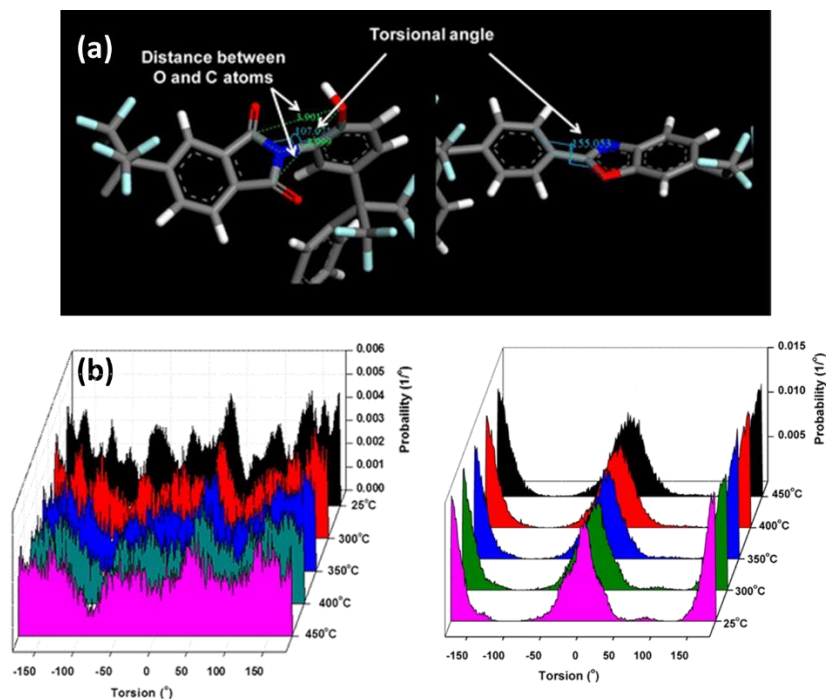


Figure 30. (a) Geometry of a simulated ortho-hydroxy imide and benzoxazole unit. (b) Simulated dihedral angle of the imide and benzoxazole dihedral at different temperatures based on molecular dynamics simulations. Reprint with permission from ACS. Images reprinted from Park et al. [193].

However, since no Thermal Rearrangement itself was modeled, they only compared starting materials and final PBOs, which were obtained by constructing cells based on benzoxazole monomers. Models with *para-para* linkages, *meta-meta*, and *para-meta* linkages were simulated. Since TRPs have randomly distributed linkages, it is impossible to mimic the average distribution. In the second study [190], the focus was on the investigation of the pore shapes (Figure 31). Since TRPs are reported to have specific bottleneck type of pores, which are responsible for the improvements of the permeability and selectivity of CO<sub>2</sub> at the same time, it is very interesting to understand the pore formation and type of pores, in order to get an idea, how these pore formations can be tailored and improved further in real experiments.

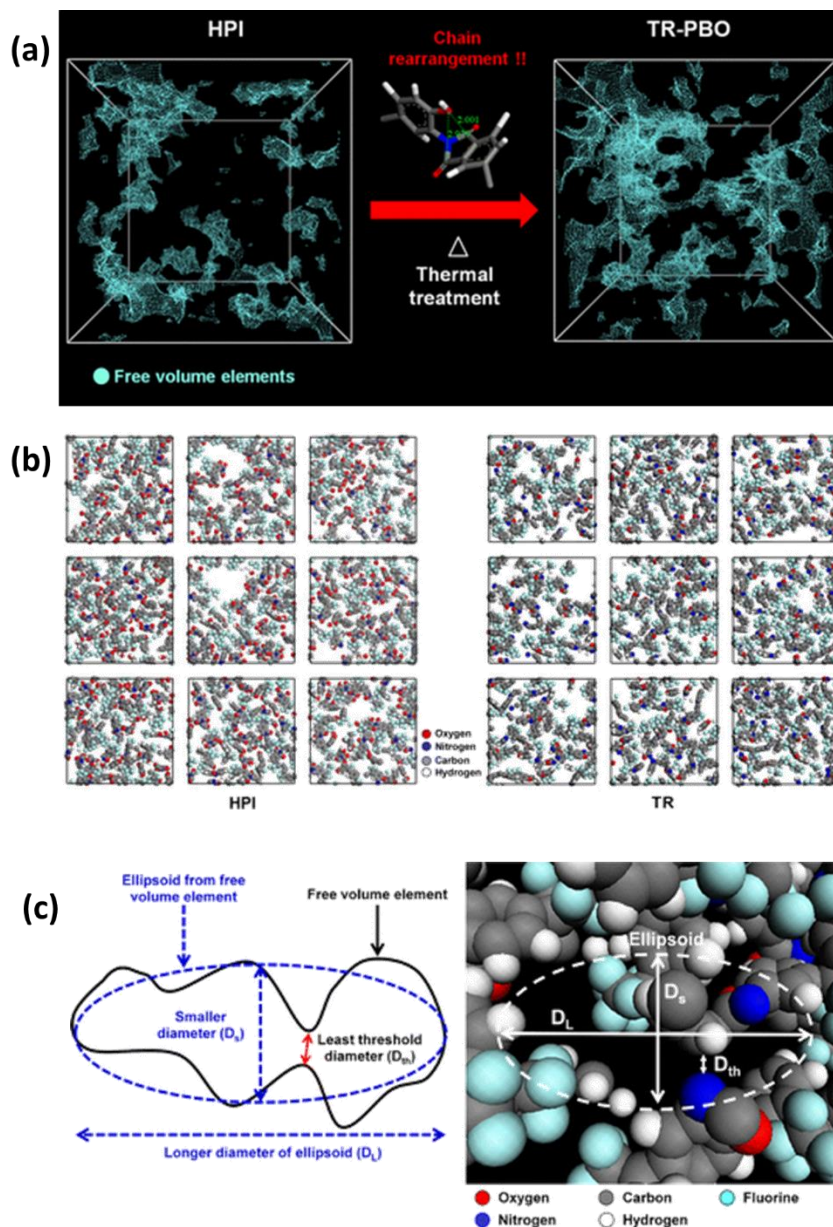


Figure 31. (a) Change of the free volume elements based on a grid-search analysis of the occupied and free volume in an amorphous cell constructed from an HPI (left) and PBO (right). (b) Slices of the constructed cells, demonstrating the pores. (c) Schematic representation (left) and image capture of a bottleneck-type pore in a simulated PBO amorphous cell. Reprint with permission from ACS. Images reprinted from Park et al. [190].

Since TRPs suffer from insolubility of high temperature induced crosslinking reactions, the number of experimental analysis methods is decreased. Therefore, modelling studies help to get further insights. Nevertheless, the cells, which were presented so far, were based on the cell formation of polybenzoxazole. Therefore, the TR process was not mimicked yet, as well as the effect of the  $\text{CO}_2$  release. Furthermore, the thermally induced crosslinking was not taken into account, yet. Accordingly, these simulations lack a more accurate representation of the real system. In addition, no analysis of TR polymers based on *ortho*-hydroxy polyamides was done yet.



## Thermochemistry

### Pericyclic reactions

Organic chemical reactions can be categorized in two characteristic types. In most cases reactions belong in group one and are described as reactions involving reactive intermediates, such as radicals, carbenes or ion pairs. Such reactions show electron flows from negative to positive charges, such as in ionic polymerization reactions of olefines. These reactions can be accelerated by an appropriate choice of solvents and catalysts. Apart from that group of organic reactions, any reaction which involves no reactive intermediate and proceeds by bond formation and breakage at a close timescale. Examples are nucleophilic substitutions and elimination reactions SN2 and E2, and one large group, the so-called pericyclic reactions [194, 195].

According to the IUPAC gold book, a pericyclic reaction is defined as “A chemical reaction in which concerted reorganization of bonding takes place throughout a cyclic array of continuously bonded atoms. It may be viewed as a reaction proceeding through a fully conjugated cyclic transition state. The number of atoms in the cyclic array is usually six, but other numbers are also possible. The term embraces a variety of processes, including cycloadditions, cheletropic reactions, electrocyclic reactions, sigmatropic rearrangements, etc. (provided they are concerted).” [196, 197]

The transition state (TS) involves the break and formation of a bond, even though it is not necessary that both processes happen to the same extent [198]. The transition state as well as the course of such a reaction type can be predicted in a very accurate manner, based on the determination of involved orbitals. According to Woodward and Hoffmann, orbital symmetry has to be conserved [199, 200]. These Woodward-Hofmann rules allow to predict energetically favored (“allowed”) transition states that proceed via cyclic geometries, while others are forbidden. In most cases 6 electron transition states are involved, forming six-membered rings, while larger and smaller transition state structure are known as well [194].

Pericyclic reactions are divided into mostly 3 to 4 categories: 1) Cycloaddition, 2) Electrocyclization, 3) Sigmatropic Rearrangement and 4) Cheletropic Reactions. The most widely known reactions are the Diels-Alder [4+2] cycloaddition, Huisgen 1,3-dipolar



cycloaddition, Wagner-Meerwein as well as the Cope- and Claisen-Rearrangement, Alder-ene reaction or the sulfoxide elimination [194, 195, 198, 201].

In the following section emphasis is put on the most relevant reactions, which are also relevant for the results and discussion. These reactions encompass 4+2, 3+2 cycloadditions, sigmatropic rearrangements such as Cope, Claisen and Hydride and alkyl shifts.

## Cycloaddition

The most widely studied and known pericyclic reactions are cycloadditions. According to the IUPAC definition a cycloaddition describes "A reaction in which two or more unsaturated molecules (or parts of the same molecule) combine with the formation of a cyclic adduct in which there is a net reduction of the bond multiplicity." [196, 197] Simply spoken two or more separate molecules or molecule fragments form a cyclic product without any molecule loss. This latter addition of the fragment is very important, when it comes to tandem reactions as described later in detail. From the notation, the number of involved atoms or electrons is known. For instance, if a fragment with four atoms and a fragment with 2 atoms form a six-membered cycle, it is a (4+2) Cycloaddition. If two  $\pi$ -bonds of fragment 1 interact with a  $\pi$ -bond in fragment 2, each with 2 electrons, then it is a [2+4] cycloaddition in that sense. Among various possible cycloaddition types, the most famous ones are the Diels-Alder (4+2) Cycloaddition, the Huisgen (1,3) dipolar cycloaddition and ketene and allene (2+2) cycloadditions.

Mechanistically, there is a cyclic electron flow, which would principally let anyone assume, that there are no restrictions in possible combinations. However, not every combination leads to cycloaddition reactions. Based on mechanistic works by Woodward and Hoffmann, applying orbital symmetry principles of the involved frontier orbitals, provide mechanistic insights and make it easy to understand whether a reaction is "allowed" or "forbidden" [194]. What would be expected, if  $\pi$ -bonds react with each other, as a consequence of their plane bond type, is a face-to-face approach of reacting molecules. Based on the frontier orbital symmetry rules, in order to have an allowed reaction, orbitals with same phases have to overlap with each other. If that is given, a so-called suprafacial mode of addition occurs. From

this system it becomes clear why only [2+4] additions are allowed, and not [2+2] or [4+4]. The general rule is, that suprafacial reactions are only allowed if  $[4n+2]$   $\pi$ -electrons are involved. According to Hückels rule for aromatic systems,  $[4n+2]\pi$ -electron systems proceed via an aromatic transition state. This makes it very stable and is a reason for its feasibility. A convenient synthesis condition is then given, if no strain, steric, and entropic restrictions might lead to very low kinetics. This mode is then a thermally allowed reaction.

**Diels-Alder Cycloaddition.** In this work, the Diels-Alder reaction is the most important cycloaddition reaction, why it is now emphasized. The Diels-Alder reaction is a [2+4] cycloaddition reaction of a conjugated diene and an alkene (dienophile) and was described in 1928 by Otto Diels and Kurt Alder for the first time, for which they got a noble prize in 1950 [195, 202]. The formed product is a cyclic cyclohexene if no substituents are present (Figure 32). The Diels-Alder reaction can occur with two free and separated molecules, for instance butadiene and ethene or intramolecularly between two fragments. It is also possible to involve heteroatoms, for example in a dienone. The full mechanism is controversially discussed in the literature between a two-step mechanism, by the addition of one terminus per molecule leading to a diradical or by a synchronous concerted one-step mechanism. However, simulations have shown, that the process is more of a one-step mechanism but asynchronous, leading to one sigma bond formed prior to the second (Figure 32). However, in a very short timescale, so that no intermediate results from that asynchronous mechanism. The tendency depends strongly on the steric and electronic properties of the substrate molecules. From an electronic point of view, electron withdrawing groups on the dienophile accelerate the reaction, while electron donating groups are favored on the diene [194]. Therefore, anhydrides and hydroquinone's are useful dienophiles. For the diene, it is important to be in cis-form in order to fulfil the Woodward-Hofmann rules [194, 195, 198, 200]. This can be achieved by simple rotation around the diene  $\sigma$ -bond, which is usually of lower energy and occurs rapid, but might become complicated in sterically hindered systems. In addition, it is important to notice, that bridged products are formed if cyclic diene or dienophiles are used. The frontier orbital symmetry rules are fulfilled in each case if the substituents on the dienophile are pointing to or away from the diene. If it points towards the diene it is called the endo-form, which is the kinetically favored product in most cases (Alder endo rule)(Figure 32) [194, 195,

198]. At high temperatures the Diels-Alder reaction can be reverse and is therefore called a reverse-Diels-Alder reaction.

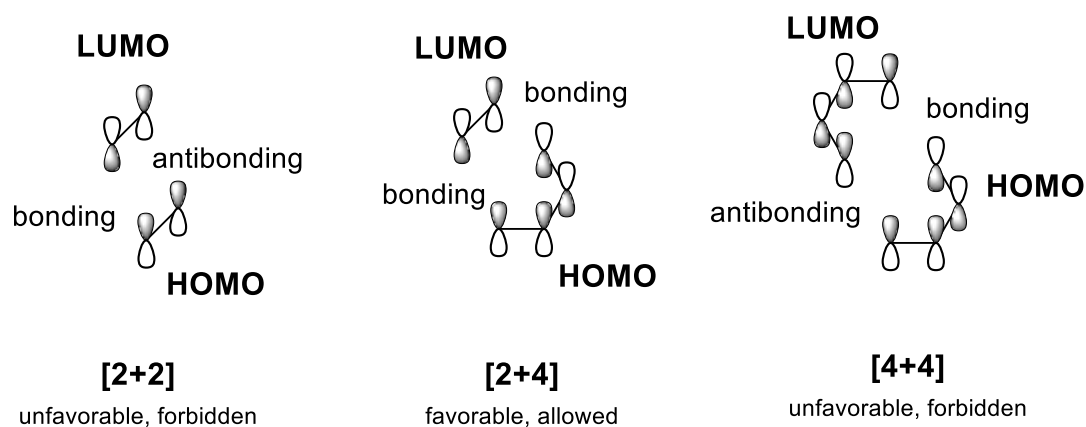
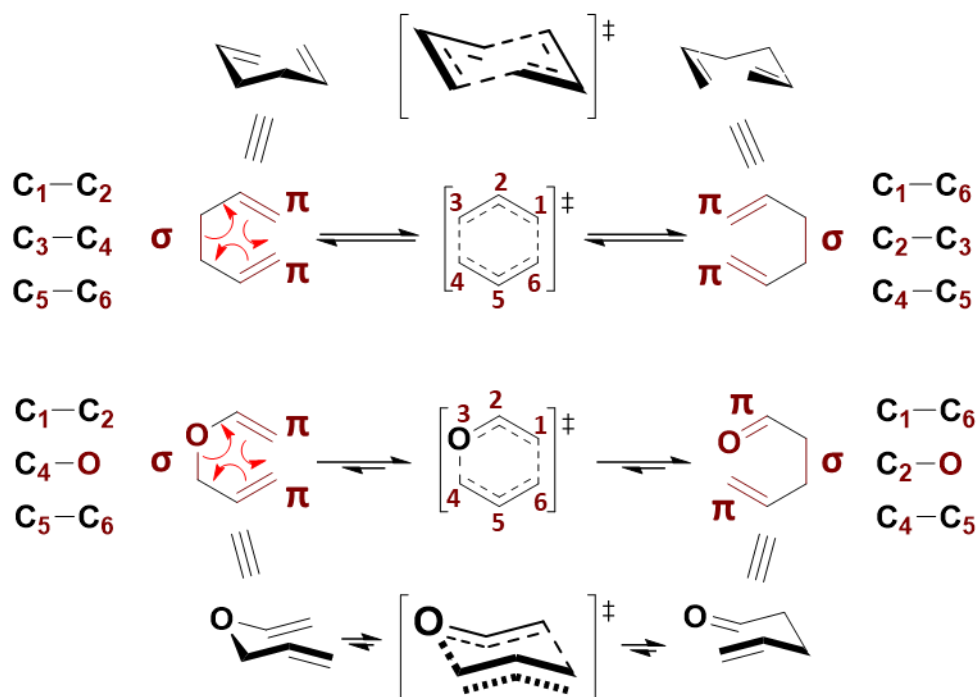


Figure 32. Frontier orbitals in exemplified cycloadditions, that are thermally allowed and forbidden according to the Woodward-Hoffman rules.

## Sigmatropic Rearrangements

Sigmatropic rearrangements are at best described as molecular in which an existing  $\sigma$ -bond breaks, while a new  $\sigma$ -bond is formed at the molecule terminus, connecting both ends, which were previously not connected. This often involves a relocation of  $\pi$ -bonds as well, whereas the total number of electrons,  $\sigma$ - and  $\pi$ -bonds remains the same. Sigmatropic rearrangements are designated as  $[i, j]$ , with  $i < j$ , with  $i$  and  $j$  being the labeled atoms, between which, the new bond is formed from the origin of the bond breaking atoms. The labeling is based on the structure of the transition state, which can be depicted as two fragments, connected at their termini by two partial  $\sigma$ -bonds, whereas one is formed and one broken. The Cope and Claisen-Rearrangement are one of the most famous rearrangements [196, 197, 201, 203], and shown in Figure 33.

## Cope Rearrangement



## Claisen Rearrangement

Figure 33. Mechanism of the Cope- and aliphatic Claisen Rearrangement. Representation of the broken and formed bonds, as well as the chair-type arrangement.

### Cope Rearrangement

The Cope Rearrangement is a [3,3] sigmatropic rearrangement. The easiest example is a 1,5-diene such as 1,5-hexadiene. In that case the  $\sigma$ -bond between atoms 3 and 4 moves to 1 and 6. In that case an identical molecule is formed (Figure 33). As unsymmetric substitutions are added, new molecules are accessible upon heating. Bond breaking and formation appear to occur nearly at the same time and occur via a cyclic aromatic transition state[201, 203].

### Claisen Rearrangement

If the previously investigated hexadiene incorporates an oxygen forming an allyl-vinyl ether, the rearranged product forms a  $\gamma, \delta$  unsaturated aldehyde. This process is called the Claisen Rearrangement of allyl-vinyl ethers (Figure 33).

The Claisen Rearrangement (CR) was reported for the first time in 1912 by Rainer Ludwig Claisen and the first ever reported [3,3] sigmatropic reaction [204]. The Cope Rearrangement

was reported in 1940 [201, 203]. The CR was described in allyl-phenyl ether, which upon annealing, form *ortho*-allyl phenols. Later the rearrangement was also described in aliphatic allyl-vinyl ether.

In aromatic allyl ether, the first step is considered the formation of a new C-C  $\sigma$ -bond between the terminal carbon of the allyl group (C9) and the *ortho*-positioned carbon atom (C2) to a cyclic *ortho*-dienone. A consecutive enolization of the dienone to its phenolic form, leading to the *ortho*-allylphenol and re-establishing the aromaticity (Figure 34).

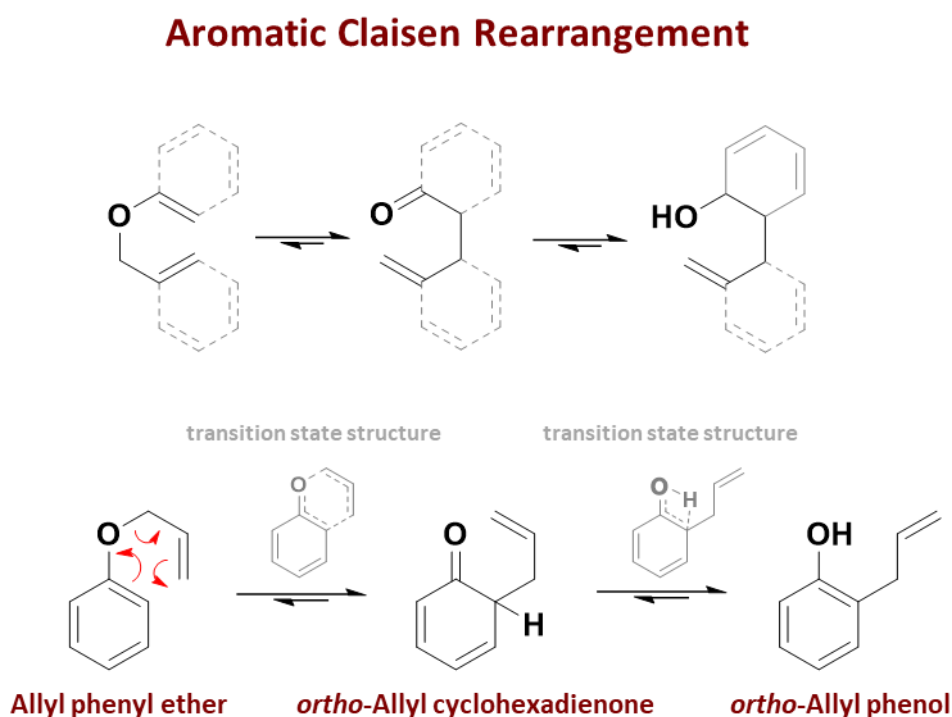


Figure 34. Mechanism of the aromatic Claisen Rearrangement.

Normally, the aromatic CR requires high temperatures of 180 – 220 °C, which can favor side reactions depending on the chemical surrounding. These side reactions can be strategically used to design reaction cascades. CR is highly interesting for designing tandem-reaction systems. Hence, aliphatic allyl-vinyl ether is reported to undergo CR followed by ene-reactions and are accordingly Claisen-ene tandem reactions [205]. In addition, CR/Conia-type oxa-ene reactions are reported [206]. In that case, the CR is followed by Conia oxa-ene reaction rearrangement. In that case the vinylic and allylic double bond react forming a keto-*ortho*-spirocyclopropane unit, which is opened due to the protonation of the keto group by one of a surrounding methyl or methylene group. This product is called the abnormal product. It can be reversed to the normal product via retro-Conia[201, 203].

In cases of *ortho* substituted aromatic allyl phenyl ether, the first isomerization is followed by a second [3,3] rearrangement, forming the corresponding *para*-dienone and after enolization the *para*-allyl phenol. The C $\alpha$  reacts with the *para*-C atom. The second step is called Cope rearrangement. The overall process accordingly as *para*-Claisen-Rearrangement.

If the allyl moiety contains alkyl substituents in  $\alpha$  or  $\gamma$ -position, the so-called abnormal-CR is possible. It was first reported by Lauer and Filbert in 1936 and via thermal conditions by Hund *et al.*[207]

However, apart from these types of reactions, the *ortho*-allyl phenol group can also undergo a subsequent cyclization reaction, forming coumarin (tetrahydro benzofuran) cycles[208-210], shown in Figure 35.

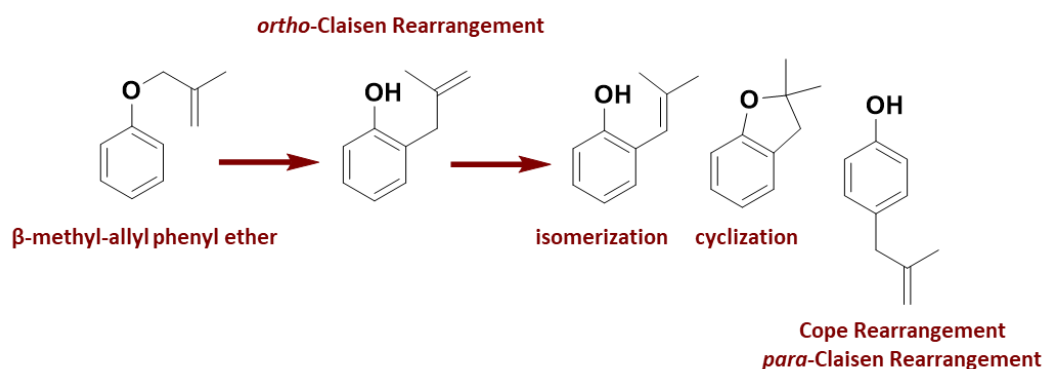


Figure 35. Possible consecutive reactions following an aromatic Claisen Rearrangement based on a phenyl- $\beta$ Mallyl ether.

#### Mechanistic and kinetic aspects

Allyl vinyl or allyl phenyl ether rearrange through aromatic transition states via  $\pi$ - and  $\sigma$ -bond orbital overlap. A C-C bond is formed and broken, and a weak C-C  $\pi$ -bond is exchanged with a strong carbonyl bond in the first step, which leads accordingly to a thermodynamically favored product.

As shown by thermal annealing of *ortho*-methyl *O*-allyl- and substituted allyl-phenyl ethers, have shown that no cross-allylation occurred. Which means no *ortho*-methyl allyl product and no 2-allylphenol product was formed. This led to the conclusion, that the CR occurs via an intramolecular cyclic concerted process. Also, the *ortho* product undergoes inversion of the substitution pattern, while *para* only undergoes migration of the allyl group reversing the

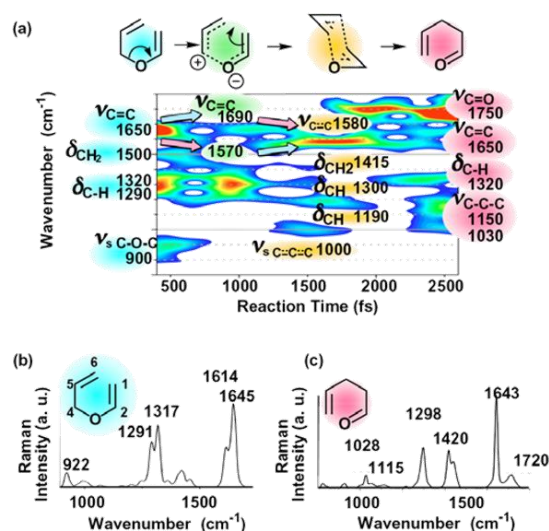
inversion of the first step, corroborating its intramolecular course of the reaction. These experiments have been done using  $^{14}\text{C}$ -labeled experiments at the  $\gamma$ -position (crotyl) [211]. However, the exact transition state geometry determination is still an ongoing task, despite the widely accepted nature of the intramolecular chair like TST.

Kinetic isotope effect accounting experiments were added by Singleton *et al.* to corroborate the chair like transition state [212]. Studies of substituted allyl-vinyl ether were performed by Carpenter *et al.* [213] and also Gajewski *et al.* [203], involving electron-donating and -withdrawing groups in different positions in order to investigate the polar nature of the transition state to distinguish between a radical and ionic transition state. Despite these structural influences, the effect of the solvent polarity can improve ionic-like transition states and corroborate their nature. White and Goering reported the rate increase by a factor of 103 in phenol and an increase in any polar solvent. This corroborates a more polar TS structure as well as an autocatalytic effect [208-210, 214].

Based on all of these studies, the transition state geometry ranges from diyl di-radical, to bis-allyl radicals, as well as ionic a fully aromatic [203]. This is assumed to depend strongly on the stabilizing- and destabilizing effects and varies from substrate to substrate as studies with phenyl substitutions have shown.

More clarification was gained by the development of time-resolved transition-state spectroscopy employing femtosecond laser pulse trigger, as used by Iwakura *et al.* [215]. They used UV-femtosecond pulses to trigger the photochemical Claisen-Rearrangement, see Figure 36. The extension to vis-femtosecond pulses allowed the investigation of the CR of the electronic ground state, such as in the thermal Claisen-Rearrangement. Iwakura *et al.* were able to use excited Raman active molecular vibrational modes in the ground state to trigger the Claisen-Rearrangement by coherent molecular vibrational excitation, which follows the thermal reaction mechanism (Figure 36).

## Aliphatic Claisen Rearrangement



## Aromatic Claisen Rearrangement

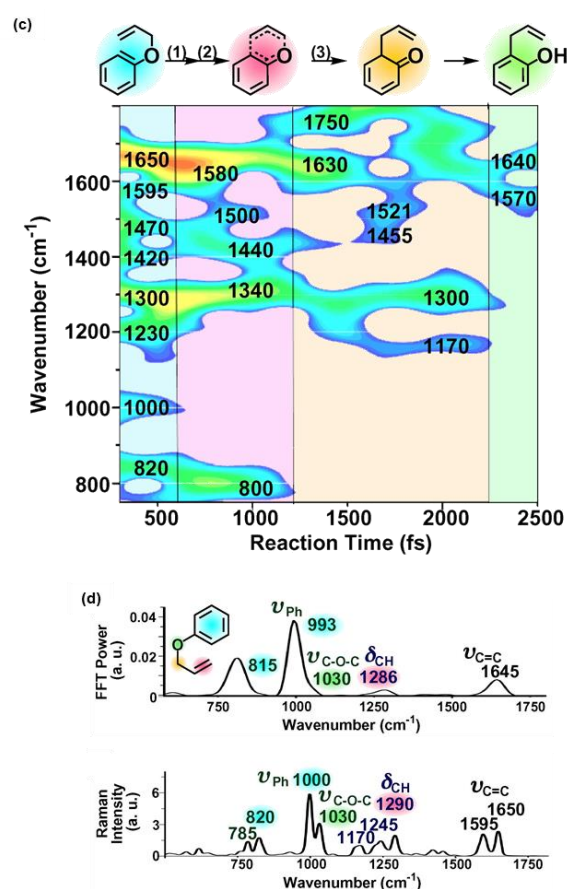


Figure 36. [left]: (a) Spectrogram of a Claisen Rearrangement (b) Raman spectrum of allyl vinyl ether and (c) Raman spectrum of allyl acetaldehyde induced by visible 5 fs pulses. Reprint with permission from MDPI. Reprint from Iwakura et al. [215]. [right]: (c) Spectrogram of an aromatic Claisen Rearrangement with assignment of reaction intermediates; (d) FFT power spectrum and Raman spectrum of the reactant (allyl phenyl ether). Reprint with permission from Elsevier B.V. Reprint from Iwakura et al. [216b].

By comparing the triggered reactions with UV- and vis-femtosecond laser triggered CR reactions of allyl-phenyl ether a different reaction path was seen, as demonstrated in Figure 37. While the photochemically excited reaction pathway occurred via radical transition state, the method of using coherent vibrational excitation, using vis-pulses, showed no radical formation. It rather showed the C-O weakening, followed by a dienone formation and loss of aromaticity as the aromatic geometry was broken. They could also see the enolization, leading to the final *ortho*-allyl phenol as the only product.



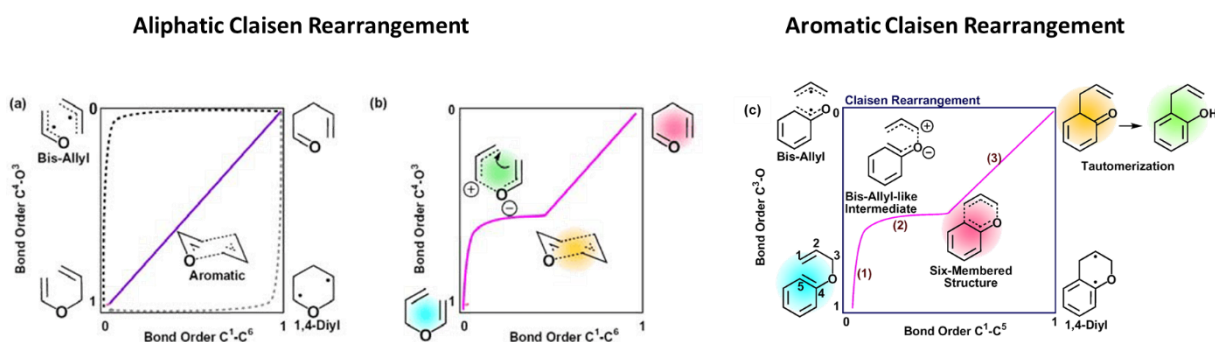


Figure 37. Transition-state profile of the aliphatic and aromatic Claisen Rearrangement. (a) Purple curve showing a profile of a concerted pathway via aromatic-type six-membered transition-state geometry, and black curve showing a bis-allyl type transition-state, and grey curve demonstrating a 1,4-diyli type radical transition-state. (b) Determined bond-orders from Iwakura *et al.* [215]. Reprint with permission from MDPI. Reprint from Iwakura *et al.* [215]. (c) Determined bond orders and proposed transition state profile for the aromatic Claisen Rearrangement by Iwakura *et al.* [216b]. Reprint with permission from Elsevier B.V. Reprint from Iwakura *et al.* [216b].

However, the mechanism of the thermal CR initiated by heating is still not clarified, since it is not a coherent process with randomly excited molecular vibrations according to the Boltzmann statistics. But the non-thermal coherent vis-TS spectroscopy was a first promising way in explaining the method a bit more accurate, as both have the same frontier-orbitals [215, 216].

In addition to the widely reported Claisen Rearrangement of allyl-phenyl ether, it is also described that propargyl-phenyl ether are able to undergo a Claisen Rearrangement analogous reaction. In that process the propargyl group forms an allene geometry of the propargyl group, while allyl-phenyl ether formed an allylic resonant group. The product is an *ortho*-butadiene cyclohexadienone intermediate which undergoes re-aromatization due to an enolization process to the *ortho*-allene phenol. However, since allenes are highly unstable compared to allyl groups, they undergo subsequent reactions, mostly described by a cyclization process to the 6-membered chromene ring, or via attack at the  $\beta$ -carbon atom of the allene-group, forming a furan ring [203]. Simulations by Shrinivasidan *et al.* [217] had shown, that fluorine containing components, especially cesium fluoride can promote the formation of the furan ring by Lewis-acid type catalysis.

**Alder-Ene reaction.** Another famous reaction and mechanistically similar to the Diels-Alder reaction, is the Alder-ene reaction, which was discovered by Kurt Alder in 1943 [194, 195, 198]. However, it is not a cycloaddition, but considered as a concerted pericyclic rearrangement

reaction. It is a C-C bond formation reaction employing an activated C- bond of an allylic compound (ene) and a multiple bond compound (the enophile). In the ene-reaction the enophile accepts a proton transfer, similar to an [1,5] sigmatropic hydrogen shift, and a C-C bond formation between a  $\pi$ -bond of the ene and the enophile, accompanied by a concomitant reorganization of the bonding. The simplest example is the reaction of propene (ene) and ethylene (enophile). As observed in the Diels-Alder reaction, a reverse reaction path is possible and described as retro-ene reaction. In comparison to the Diels-Alder cycloaddition, the ene reaction proceeds as well by a suprafacial orbital interaction, whereas both electrons of the allylic C-H  $\sigma$ -bond replace both  $\pi$ -electrons of diene compound in the DA cycloaddition. Because of a higher activation energy for the hydrogen shift compared to the C-C bond formation of the DA reaction, the ene-reaction requires higher energies for the reaction.

On the basis of the Diels-alder reaction the frontier orbital interaction according to Woodward and Hoffmann can be used to evaluate the mechanism and its affecting parameters of the used reagents. The reaction is considered to occur via the HOMO of the ene component and the LUMO of the enophile. As a consequence, the reaction is promoted by EWG substituents on the enophile and strain in the ene component. As the both reagents approach each other in a more boat-like transition state geometry, any substitution or environment favors the reaction when such a face-to-face alignment is supported. In order to undergo such a suprafacial arrangement, the C-H  $\sigma$ -bond of the ene has to be parallel with the p-orbital of the enophile. According to the WH rules, the components fulfill the  $(4n+2)$  condition and is thermally allowed.

Ene-components are  $\pi$ -bond components such as alkenes or alkynes with an activated hydrogen in the  $\alpha$ -position. Most widely studied examples are allylic and propargylic groups, but also arenes are of great interest. Studies of fused rings and strained enes have shown that lower activation energies are required and favor the alder-ene process [194]. Enophiles can be any alkene, but one reason for the synthetic importance of the reaction, is the fact that also heteroatom containing  $\pi$ -bonds can take part in an Alder-ene reaction. A widely used method is the carbonyl-ene reaction [194]. As one side of the enophile is attacked by the  $\pi$ -bond of the ene, while the other terminus accepts a proton, carbonyl groups are very good enophiles. Allenes can also undergo ene-reactions, but generally favor the formation of cyclobutanes. A famous example is the reaction of an allyl group with a maleimide or maleic anhydride.

Finally, there is one more aspect for the importance of that method. Apart from intermolecular ene-reactions, the intramolecular ene reaction plays a crucial role in the formation of larger cycles and cascade reactions. Three types depending on the connection of the enophile with the ene exist.

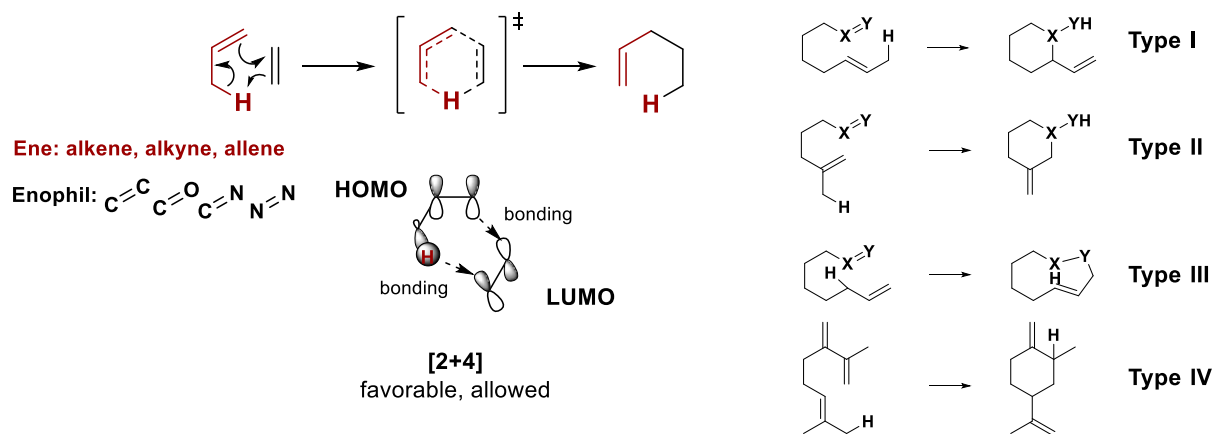


Figure 38. (a) Alder-ene reaction mechanism. (b) Types of ene-reactions.

Another variant of the Alder-ene reaction is the Conia-ene reaction, in which the allylic hydrogen containing group in the  $\alpha$ -position is replaced by an oxygen atom. Hence, vinyl alcohol as the ene and ethylene as the enophile might react that way [218]. More often it is described in enolizable keto group containing alkenes that undergo intramolecular Conia-ene cyclization, such as 1-yne-octa-7-one.

## [2+2] Cycloaddition

In 2+2 Cycloadditions two pi-bond containing compounds react via a four-membered transition state geometry to the cyclobutene product. Such components are for example alkenes, allenes or ketenes and isocyanates. However, according to WH rules, the suprafacial frontier orbital interaction is not allowed for thermal reactions, only via photoreactions. Nevertheless, the [2+2] cycloaddition is thermally allowed for a specific orientation. This is widely reported for the reaction of ketenes with allene, ketene or alkenes. The system does not follow the Hückel rule and does not have an aromatic-like transition state accordingly. The reaction is occurring asynchronous according to simulations and initiates by strong interactions of the ketenes sp carbon atom with both alkene carbon atoms [194, 195, 198].

## Cheletropic reactions

Another cycloaddition reaction, which is oftentimes overshadowed by the powerful use of the Diels-Alder cycloaddition, is the group of cheletropic addition, which are (n+1) cycloadditions, with n usually in the range from 1 to 3 atoms. According to IUPAC recommendations, the cheletropic reaction encompasses cycloadditions “across the terminal atoms of a fully conjugated  $\pi$ -system with formation of two new  $\sigma$ -bonds to a single atom of the reagent. There is formal loss of one  $\pi$ -bond in the substrate and an increase in coordination number of the relevant atom of the reagent.” [196, 197]. This reaction can also be reversed and is then called a cheletropic elimination and is driven by the entropic benefit of a gaseous molecule release. There exist a number of potential monocentric reagents, such as carbenes, carbon monoxide, nitrenes, dinitrogen, sulfoxide and nitrous oxide among many others. In general, any reagent with an unsaturated atomic center in which the valence shell lacks two electrons is a potential cheletropic monocentric reagent. For the substrate alkene, conjugated dienes, aromatic  $\pi$ -systems carbonyl compounds and any other hetero-1,3-diene can be used. The most studied example is the addition of sulfur dioxide to cis butadiene.

## Cascade reactions

In order to tailor molecular properties of materials in order to create specific materials properties, modifications are usually implemented by means of using modified monomers or post-polymerization modification. Either way, such a two-step approach requires time, leads to waste of resources, can face solubility issues, needs several purification steps with loss of yield. Furthermore, synthetic approaches oftentimes lead to degradation or incomplete conversion. When modifications are done prior to the polymerization, in monomers, strong protection-deprotection strategies and purifications to obtain high molecular weights have to be performed.

During recent years, the idea of consecutive reactions, which are initially started by an initiation reaction or external stimulus attained great interest. Such a sequence of consecutive reactions, whereas each step requires completion of the previous reaction is termed cascade-, tandem or domino reaction [219]. According to Tietze and Beifuss [219] a cascade reaction has three aspects:

- It is a process with two or more consecutive reactions involved and each step is the consequence of the previous step formed functional group
- The whole process has to take place under same conditions without adding any new reagent or catalyst
- The preliminary formation of a reactive intermediate is not counted, such as a reaction initiation by an ionic or radical initiator

Cascade reactions can occur between multi- or single components, intra- or intermolecular. It is not required for a multi-component system to involve multiple molecules [220]. A molecule which undergoes a cascade reaction based on various incorporated functional groups is counted as well. Cascade reactions can be based on radical chemistry [221, 222], nucleophilic reactions [222] or rearrangement [222, 223] and isomerization [222]. Especially the combination of subsequent pericyclic reactions is very powerful due to their atom efficiency. According to Trost [224] division of atom efficient reactions, additions, isomerization's, and rearrangements are the only reaction types with 100% atom efficiency. Another advantage is that the cascade of bond breaking and bond formation, once a cascade is initiated, proceeds without the requirement of isolating intermediates or changing reaction conditions. Cascade reactions can be initiated by reactive initiation, such as adding ionic or radical species or by thermo-, photo-mechano-stimulus.

Consecutive pericyclic reactions were used many times in the total synthesis [222]. They encompass the Claisen Rearrangement as initial step, followed by ene, oxa-Conia-ene, Diels-Alder or Cope Rearrangements [203, 225-228]. The tandem-reaction system of Claisen Rearrangement and Diels-Alder reactions can also be complemented by an ene-reaction, for instance via addition of maleimides. Such a combination was described by Wagner-Jauregg in 1931 [229]. It involves the CR followed by an addition reaction of a maleimide to the rearranged allyl group. The following styrene-type can undergo a [4+2] cycloaddition with additional maleimides. This reaction was combined with Claisen Rearrangement of *ortho*-allyl bisphenol A precursor for the preparation of resins [230].

Especially in the field of polymerization the concept of cascade reactions became very interesting in recent years. Hence, cascade reactions are nowadays used in radical cascade

reaction polymerization [231-233]. Here, a cascade is initiated and leads then to multiple steps during the propagation step prior addition of another monomer.

In 1997 the Tandem-Claisen-Rearrangement (TCR) has been introduced for *ortho*-allyloxy mono- and diamines in order to apply the Tandem-Claisen-Rearrangement in polymers [227]. Two aromatic *ortho*-hydroxy amines are linked by the introduction of dichloro isobutene in order to form an isobutenyl bis (aryl ether). The advantage of such a method lies in the versatility of potential molecules and polymers. Since many *ortho*-hydroxy amines are commercially available as well as other difunctional monomers, that are able to polymerize the used amines. In 1997 Hiattani *et al.* [226] published the imidization of such an isobutenyl bis (aryl ether) diamine. Further annealing led at higher temperatures as a consequence of the Thermal Rearrangement reaction to the corresponding polybenzoxazole [227]. In 2001 the use of isocyanates to form polyureas with isobutenyl bis (aryl ether) backbones were reported. The annealing forced the material to undergo a cyclization reaction to the benzoquinolinone by loss of aniline [234].

Another cascade reaction undergoing system is the use of benzoxazine groups, which are intensively studied by the groups of Takeichi [235] and Yagci [236]. Benzoxazines considered as phenolic resins, which are easily prepared from inexpensive reagents such as phenols, formaldehyde, and primary amines, were intensively studied due to the versatility as a consequence of the large number of phenols and amines [236]. Since various phenols and amines are commercially available as monomers, the possibility to tailor the materials properties is of great interest. Another advantage, such as reported for the Tandem Claisen Rearrangement process, is the fact that no catalyst is required. By incorporating vinyl, allyl, propargyl or epoxy groups, the materials can undergo further orthogonal reactions and structures can be controlled by the stimulus and stimulus protocol, used [235]. Zhang and Ishida [237] prepared a poly(benzoxazine amic acid) combining benzoxazine and imides, which were converted to polybenzoxazine upon heating at 180 to 200 °C followed by benzoxazole formation due to the TR process at 250 to 300 °C [238]. Both, the cascade reaction in amide and imide precursor was studied. Since benzoxazine ring opening and polymerizations are triggered by annealing, they can be combined with photo-labile/photoactive molecules. This potential offers the chance to rearrange precursor molecules by using consecutive stimulus processes. One example has been the use of photochemical

dimerization of coumarin containing benzoxazines above 300 nm by [2+2] cycloaddition as reported by Yagci *et al.* [236], followed by ring-opening polymerization of the benzoxazine groups upon subsequent heating.

The use of thermal and photochemically initiated reactions such as pericyclic and especially Click [239] reactions, mainly Diels-Alder- [240, 241] and Huisgen Cycloadditions [242], Thiolene [243, 244] and azide Click reactions [245, 246] and Claisen Rearrangement [234] are widely used in various high-performance materials, such as self-healing-[247], shape-memory materials [248], photo-switches [249], membrane materials[246], high performance resins [250] and stimuli-responsive materials [251, 252].





## PART III

# Scope of the Work



*Understanding a Question*

*is half an answer*

Socrates

The so-called Thermal Rearrangement of *ortho*-hydroxy polyimides and -amides, which is a thermally induced *ortho*-hydroxy polyimide to polybenzoxazole cyclization + decarboxylation reaction was initially described and presented in 1999 by Tullos *et al.* [124, 125] with the title “the unexpected conversion of *ortho*-hydroxy polyimides” [124]. Later in 2007 Ho-Bum Park considered that solid-state reaction as an innovative strategy to improve gas separation membranes [126]. However, these systems require high temperatures up to 400 °C and above [152]. Furthermore, the final TR product and mechanism is up to now not fully understood, which complicates the design of TR polymers with low-TR temperatures and state-of-the-art gas separation performance.

The main tasks of this PhD thesis, was therefore the goal to design TR polymers with low TR temperatures reaching full conversion below 400 °C, having onsets below 300 °C, while improving the gas separation performance, in relation to the Robeson Upper bond plot in competition to other gas separation materials (see Figure 39). In addition, the issue of physical aging of such highly porous materials has to be kept in mind.

Since the TR process is not fully understood and reasonable concerns about the currently hypothesized mechanism exists, experimental and theoretical support to refine the mechanism, and clarify the main structural effects on the TR process were desired.

A question, of the PhD thesis was, which effect does the type of backbone (amide, imide, amic acid), any possible modification of the amide, carboxylic and hydroxy group have. In addition, a reliable computational method to understand and describe TR polymer materials was established. That later part is nowadays very important, when it comes to the development of new innovative, next-generation materials. Computational support can save time, cost and provides a new access to structures, that are difficult to synthesize.

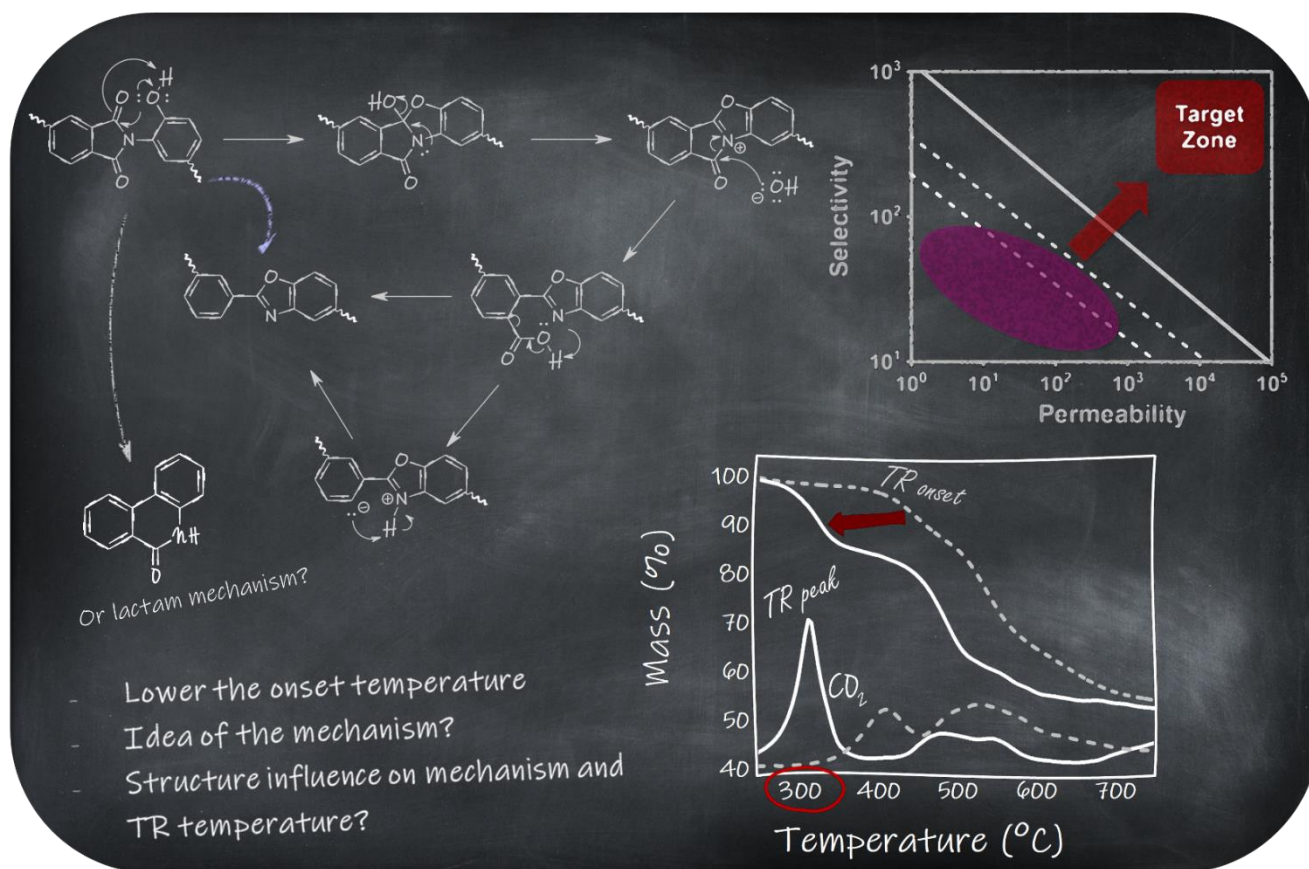
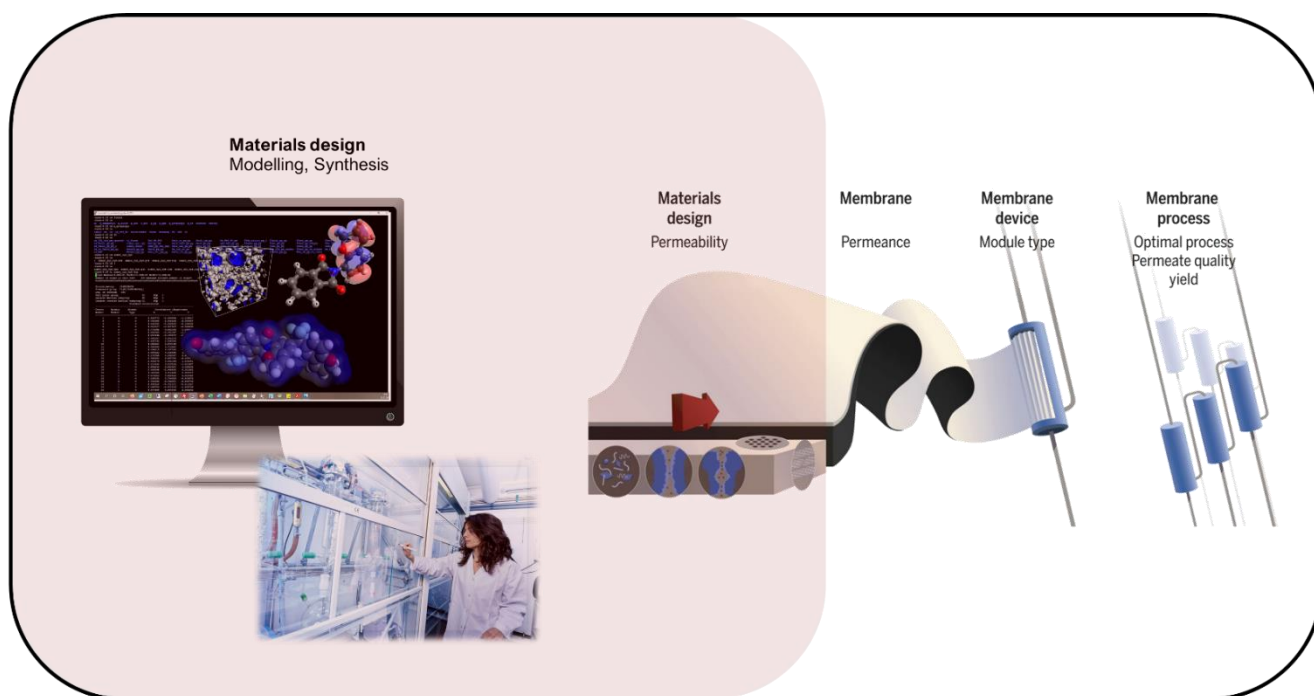


Figure 39. (Top) Scheme of area of research, highlighted in a whole membrane development process. The graphic was reprinted from Science, Park et al. [253] with permission from Rights & Permissions, Science family of journals; American Association for the Advancement of Science (AAAS). Materials design by simulation and modelling on the left side as well as the highlighting were added. (Bottom) Scheme of the tasks of this PhD work.

Freeman once described the materials design to development in membrane technology in his article "Maximizing the Right Stuff" [253] with the following figure, which is shown and adjusted.

## Critical Discussion of the Literature

During the last 21 years, several publications dealing with the TR process and TR materials have been published. Their potential to improve the use of polymeric membranes for gas separation is beyond all questions. However, the number of publications on the elucidation of the TR mechanism is still very low. The number of studies dealing with previously reported possibilities to trigger the TR process such as effects of the backbone, hydroxy modification and thermokinetics are still low. The main focus was put on investigations of intrinsically microporous backbones, gas separation performance investigations and the gas transport mechanism. However, the major obstacles regarding industrial applicability are the high annealing temperature, when it comes to commercialization. Only a few studies dealt with strategies to overcome these high temperatures [138, 139, 254-256].

The proposed mechanism considers a heterolytically elimination of a hydroxy group in solid state as a consequence of the nucleophilic intramolecular substitution reaction between the phenolic OH and the carbonyl imide group [125]. This is assumed to be unlikely, since hydroxy groups are no good leaving groups in substitution reactions, because C-OH bonds are usually very strong. Such ion containing intermediates require charges around to stabilize [257, 258]. Therefore, corresponding reactions that are accelerated, using polar solvents, occur often via ionic transition states in which bond breakage is more advanced than bond formation [259, 260]. In TR polymer films no stabilizing solvents are close nor is there a medium to promote a hydroxy group elimination and attack of the other carbonyl group. Furthermore, the attacking phenol group is a better leaving group. An equilibrium reaction with its equilibrium on the educt side is thus to be expected. So far no experimental and simulation investigation was performed to support this mechanism. Kostina *et al.* [128]. performed mechanistic studies, using DFT simulations to compare both mechanisms to form benzoxazoles and lactams. However, they did not discuss further mechanism for each product formation pathways.

In addition, there is still no clear determination, whether benzoxazole or lactam rings are formed.  $^{13}\text{C}$ -Solid-state NMR experiments, and FT-IR has been used in some studies [127-130, 133, 138, 140, 256]. Therefore, further investigations are necessary to strengthen the widely accepted idea of benzoxazole as the major or even only product.

Han *et al.* have shown that the type of imidization route affects the final film properties strongly [140]. Thermally imidized films lead to materials that surpass the upper bound plot for several gas pairs more distinctively than azeotropically imidized materials. The gas performance was explained by means of a more bimodal pore distribution with larger and smaller pores compared to azeotropically imidized materials. However, the main cause of this type of pore size distribution has not been discussed. Therefore, a detailed understanding of this phenomenon, in order to use it to tailor better performing TRPs. In that context, the reason for the higher permeability and selectivity of imide derived compared to amide derived thermally formed benzoxazoles was not targeted any further. No simulations of HPA precursor have been reported yet.

In order to understand the induced microporosity of TRPs, molecular modelling simulations might help. Unfortunately, the number of publications dealing with effects of the TR process is small. Two reports by Park *et al.* [190, 193] studied the geometrical effects at different temperatures to explain the TR process. Simulations of the pore size distributions were done to explain the high permselectivity by ellipsoidal pores. However, the final amorphous cells, which were investigated were constructed and equilibrated by using benzoxazole monomers. From experimental studies it is known that the microporosity comes from the rearrangement in solid-state and not only from the benzoxazole backbone itself. Polybenzoxazoles show significantly lower performances than TR formed PBOs [261]. Therefore, a molecular study involving the TR process in such a cell to understand the pore formation is highly necessary.

TRPs prepared by research groups around the world are very difficult to compare, as the final film properties depend strongly on the thermal protocol, type of oven, purge gas purity, solvent. A suggestion which parameters might be useful to compare materials among different studies have not been suggested so far but might be necessary to better understand the structural effects of new materials. This is fairly evident, when comparing the same material annealed at the same target temperature of different studies [127, 132, 138, 140, 141, 256]. It is

also critical, that there is no suggestion how the exact  $TR_{\text{onset}}$  and peak temperature should be determined for comparison reasons. As a consequence, different onset temperatures for widely used TRPs, such as 6FDA-HAB and 6FDA-APAF are presented [127, 132, 133, 138-141, 256]. The same problem occurs for the determination of the glass transition temperature of materials. 6FDA-HAB for instance is reported to have a  $T_g$  at 347 °C [139]. At the same time a strong correlation of the glass transition induced mobility and the TR process is supposed. This conclusion is difficult to confirm if various  $T_g$ - and TR temperatures for the same material exist [138, 139, 141, 256]. For instance, fast heating rates might have no strong effect on intramolecular decomposition reactions between stiff and flexible backbones. However, mobility dependent reactions, as the TR process, are likely to show a stronger gap between the reaction onset temperatures of a stiff and flexible materials [262]. Therefore, more thermokinetic analytics are necessary to understand the TR process.

In several studies the effect of OH group modifications were done [132, 140, 141, 263, 264]. Initially by the investigation of the imidization process by Han *et al.* the chemical imidization process was observed to lead to a highly permeable material [140]. This was referred to its higher total mass loss and the correspondingly formed voids after deacetylation and decarboxylation. Sanders *et al.* studied the effect of two other ester modifications [141]. Here, it was shown that larger groups tend to decompose at higher temperatures and affect the materials properties. In addition, Comesana *et al.* [132] described methoxy modifications. They proposed a radical decomposition pathway. Their proposed mechanism contained three radicals in their reaction intermediate, which is highly unlikely. In addition, their mechanism proposes a proton transfer to the HPI radical, which would lead to a positively charged intermediate rather than a neutral component as it still lacks one electron. Accordingly, the TR process of such a molecule might be unlikely as well. They also propose an equilibration between various protonated intermediates prior to the first step of the TR process. They suggest a protonation of the carbonyl group or the imide nitrogen atom as a first step, which isomerizes as an equilibration process. Such charged intermediates are very unlikely as earlier stated, due to the lack of stabilizing groups. The possibility of such a first step is based on the lower distance between the phenolic oxygen and the imide carbonyl group after the protonation of the nitrogen atom [132]. This is based on a semi-empirical calculation of such a structure. The tetrahedral geometry then leads to such a change of the distance. In that case

the negatively charged phenolate group has to rotate around the carbonyl bond, which is unlikely to occur for sterical reasons [127, 193, 265]. Additionally, the use of semi-empirical methods to elucidates reaction mechanism are not recommended, as these methods are do not calculate the energies sufficiently enough. Furthermore, this suggestion is based simply on geometrical reasons and electronic contributions are neglected.



## PART IV

# Results



*When you spring to an idea, and decide it  
is truth, without evidence, you blind  
yourself to other possibilities*

Robin Hobb

## **Thermally Rearranged Polymers (TRP)**

### *Molecular Modelling of the Reaction Mechanism*

The final mechanism of the Thermal Rearrangement mechanism is not completely clarified yet, and moreover, the present experimental data and simulation based results are not in common agreement with all research groups. In the theoretical background section, the theoretical considerations and different experimental approaches to confirm or disapprove a mechanism is given.

The first mechanism, based on the experimental findings and suggestions by Tullos *et al.* [124, 125], initiates by the reaction of the *ortho*-hydroxy group via protonation of the carbonyl group. Simultaneously a nucleophilic attack by the phenolic oxygen at the carbonyl C $\alpha$  occurs. The result is the first intermediate, which is a heterocyclic bicycle, containing nitrogen and oxygen atoms, as well as a hydroxy group (see Figure 40). Based on their original mechanism the hydroxy group cleaves heterolytically and forms a hydroxy ion. Afterwards or simultaneously, which has not been discussed yet in the literature, a hydroxy group attacks the opposite carbonyl group and forms an *ortho*-carboxyl benzoxazole structure, which is the second intermediate of the reaction process (Figure 40). The second intermediate undergoes decarboxylation to the corresponding polybenzoxazole. However, the heterolytical cleavage and formation of an ionic species in solid-state, without any charge stabilizing species, such as solvent molecules, is assumed to be very unlikely [257, 258]. Moreover, the hydroxy group is principally considered as a weak leaving group, compared to any alcohol, such as phenol. Alcohols can distribute the negative charge better than hydroxy groups. Accordingly, a

cleavage of the freshly formed bond by the phenol group is more likely to undergo a reverse reaction to the products. Therefore, this mechanism is considered to be doubted.

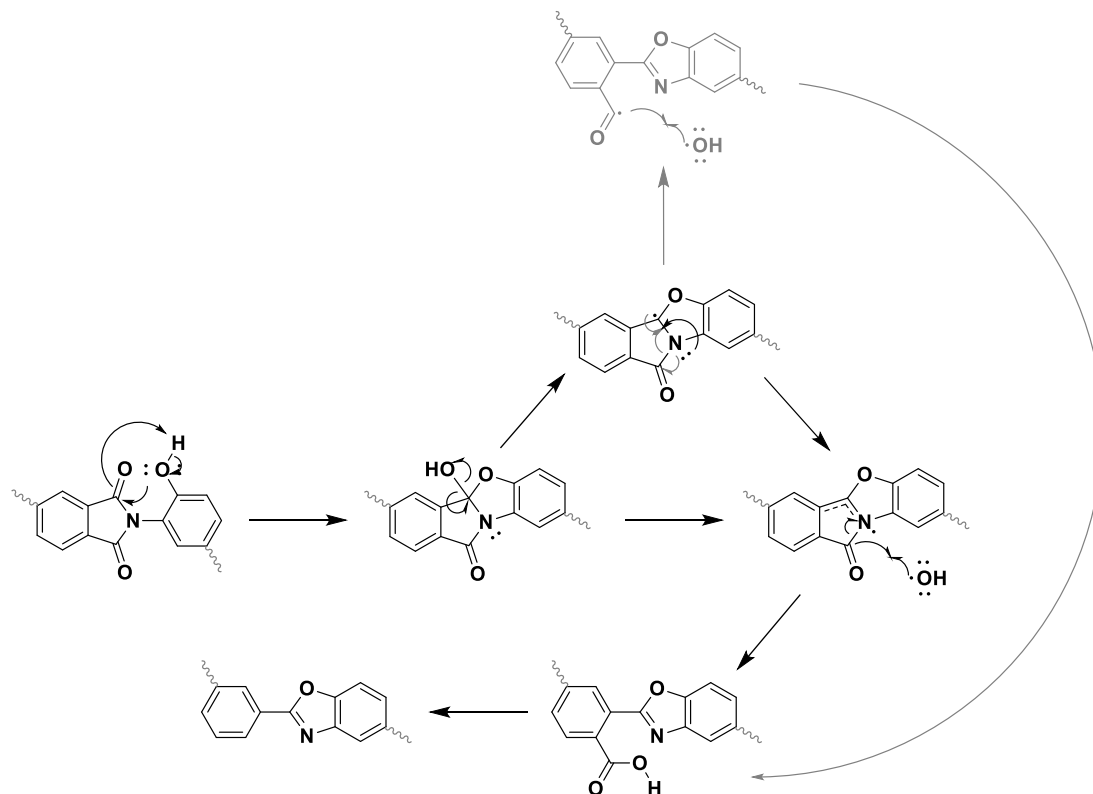


Figure 40. Reaction mechanism according to Tullos et al. [124, 125] is presented. In addition, the same mechanism via a radical route is shown in grey.

For further discussions, the literature reaction path, as shown in Figure 40, was simulated. The simulation was performed on the smallest model unit, which contained every required functionality for the TR reaction. The model is shown in Figure 41.

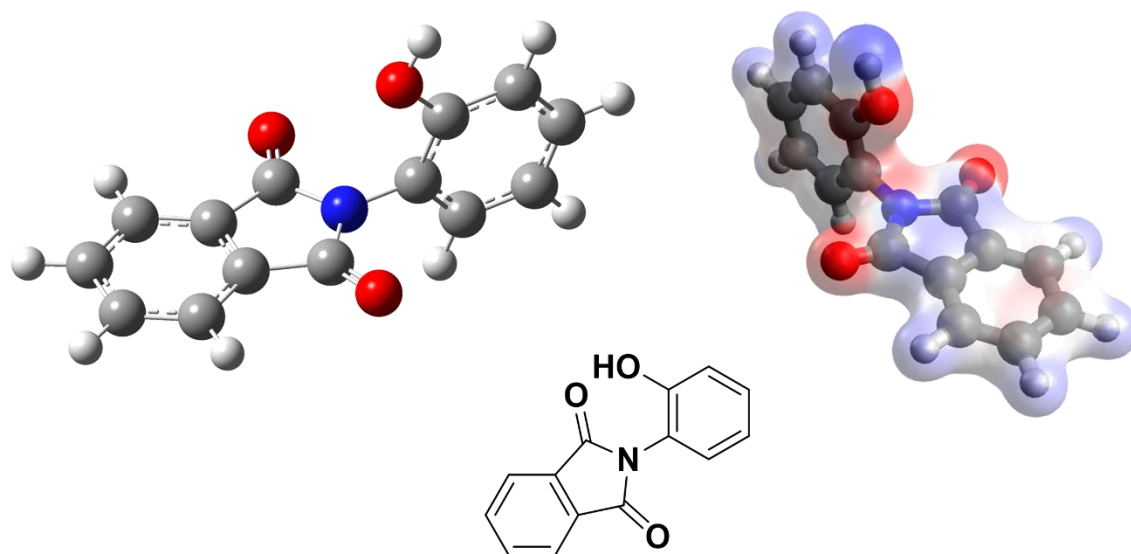


Figure 41. Model unit for the Thermal Rearrangement simulations. Model constructed in Gaussview 5.0 for the simulations on the left side and the determined electrostatic potential map of the model compound using full NBO simulation on the right side.

In Figure 42 some modeled geometries along the simulated intrinsic reaction coordinate (IRC), which describes the simulated reaction path, were chosen to demonstrate the reaction progress of the first step of the Thermal Rearrangement reaction. For the reaction to proceed, the carbonyl atom moves out of its planar structure towards phenol group, while the phenol unit turns around the dihedral angle of the imide bond. The rotational energy barrier for the rotation around this dihedral angle is shown in Figure 47. Accordingly, the highest energies were obtained for a narrowing of the phenol group with the carbonyl group. Therefore, as can be seen in Figure 42, in the transition state geometry the nitrogen atom proceeds into a pyramidal structure.

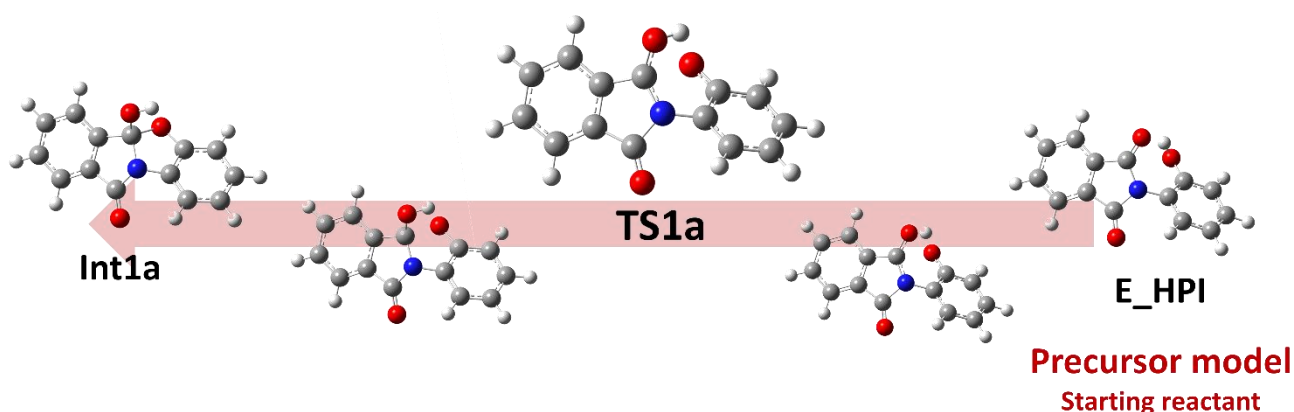


Figure 42. First step of the Thermal Rearrangement via nucleophilic attack of the ortho-hydroxy group at the imide carbonyl group via protonation.

For the second step, two considerations were made. First of all, the process occurs by heterolytically cleavage as proposed by Tullos *et al.* [124, 125] and corroborated by Park *et al.* in 2007. Another suggestion is a radical cleavage of the hydroxy group.

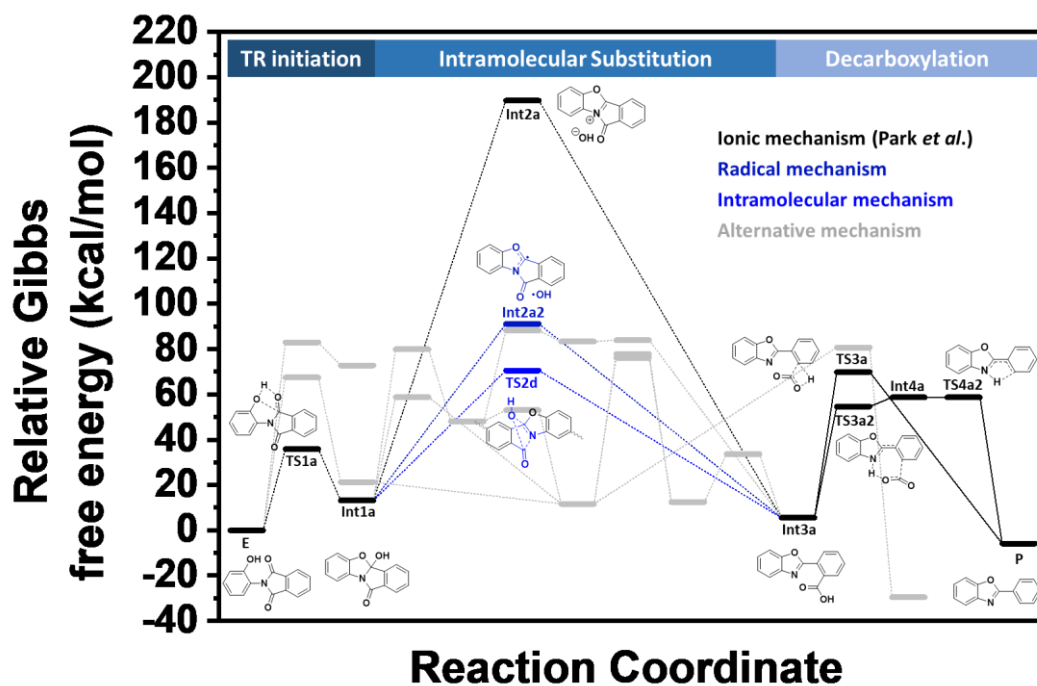


Figure 43. Reaction coordinate including all simulated mechanism for the Thermal Rearrangement. The mechanism proposed by Tullos *et al.* is highlighted in navy blue. The alternative radical reaction process proceeds via Int2a2. The first step (TS1a) is shown as well.

The reaction coordinate for both reactions (Figure 43) suggests that the ionic pathway according to Tullos *et al.* appears to occur very unlikely, due to the about twice as high transition state energy compared to the radical pathway. The ionic intermediate shows a very high single point energy and is higher than any simulated transition state. Interestingly, the radical mechanism requires only about half of the energy with 91.12 kcal mol<sup>-1</sup> compared to 189.72 kcal mol<sup>-1</sup>. However, from experiments, a radical reaction is also not considered to be the most reasonable path, since in that case other products, such as larger amounts of water would be expected, which are not found. Instead, despite the significant lower energy of this new mechanism a hydroxy group transfer mechanism is proposed.

This mechanism is based on the intramolecular reaction of the hydroxy group of int1a with the other carbonyl group by formation of the *ortho*-carboxyl benzoxazole. This process does not involve any reactive species such as ions or radicals and no other side products would be formed. Therefore, this mechanism is in agreement with data from TG-IR and TG-MS experiments, which only show CO<sub>2</sub> as the only released product [127, 132, 133]. In Figure 16 the transition state geometry and a few geometries from the intrinsic reaction coordinate of the proposed mechanism are shown.

The reaction occurs via cleavage of two  $\sigma$  bonds and formation of one  $\sigma$  and one  $\pi$ -bond. The bond between the carbonyl group and nitrogen atom weakens, which induces the required flexibility in order to bring the carbonyl group closer to the hydroxy group (highlighted in light blue in Figure 44). The bond lengths of the hydroxy group to either side is equivalent to 2.3 Å. Accordingly, the bond cleavage and formation occurs in a concerted reaction. According to Hückel's MO theory, the formation of  $\pi$ -bonds is energetically favored due to the delocalization of the electrons [266]. Therefore, the formation of a  $\pi$ - and  $\sigma$ -bond formation on the cost of two  $\sigma$ -bonds is energetically beneficial. In comparison to int1a, a gain of 7.6 kcal mol<sup>-1</sup> results from this reaction.

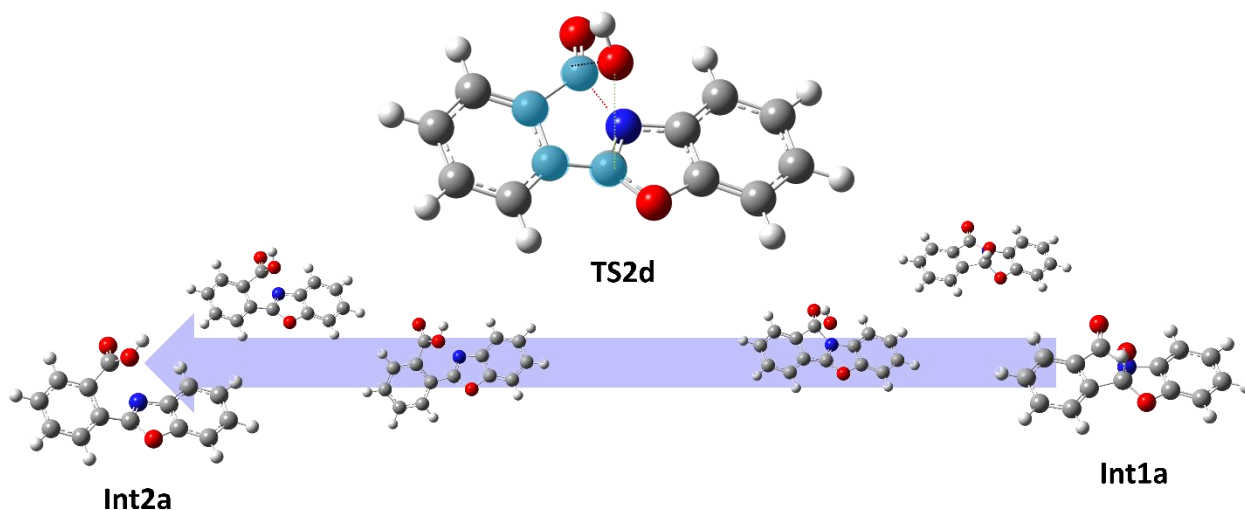


Figure 44. Second step of the Thermal Rearrangement reaction via hydroxy transfer mechanism.

However, since it requires about double of the energy compared to the first step, this step is the rate determining reaction step in such a small model reaction. The 3<sup>rd</sup> step is the decarboxylation and requires lower energies according to the simulated intrinsic reaction coordinate (see Figure 45).

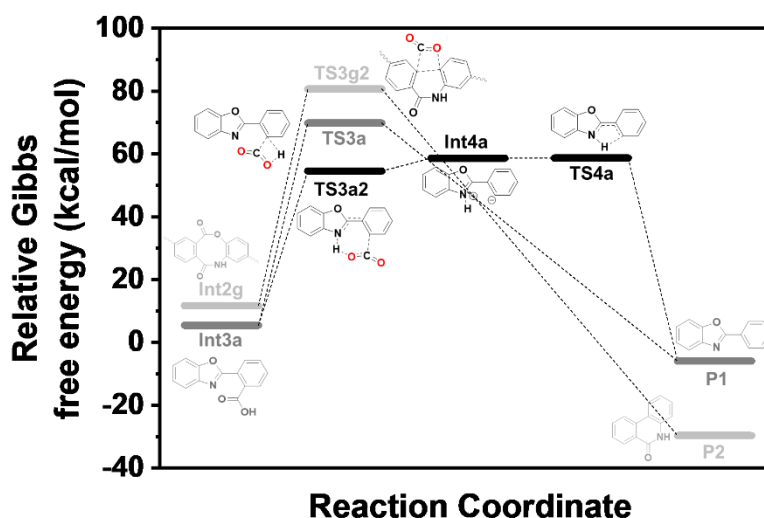


Figure 45. Decarboxylation reaction step of the Thermal Rearrangement.

The decarboxylation is assumed to occur via two pathways. One was shown in the work by Kostina *et al.* [128], which is the decarboxylation via hydrogen transfer from the carboxylic acid group to heteroaromatic ring. The other reaction path occurs via protonation of the benzoxazole nitrogen atom and subsequent decarboxylation. The result would be a negatively charged phenyl ion, which is then immediately protonated. Therefore, the same product is formed according to both mechanism. The mechanism via proton transfer from carboxyl to



aromatic ring is TS3a. The mechanism via benzoxazole protonation is termed TS3a2. The results are shown in Figure 45. The mechanism via TS3a2 appears to be 15 kcal mol<sup>-1</sup> lower compared to TS3a. Both transition state geometries are shown in Figure 46.

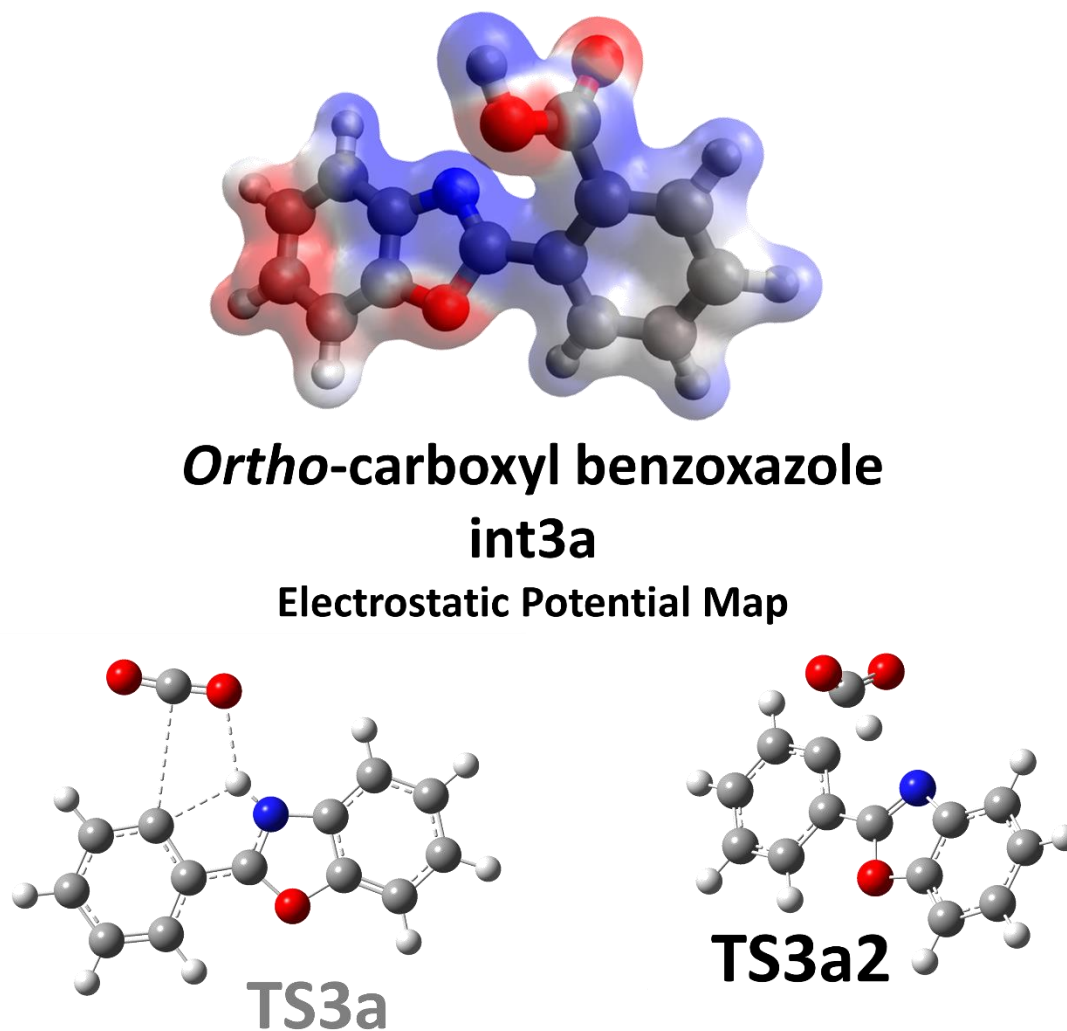


Figure 46. Intermediate *int3a* demonstrated as electrostatic potential map and both transition state geometries for the decarboxylation step.

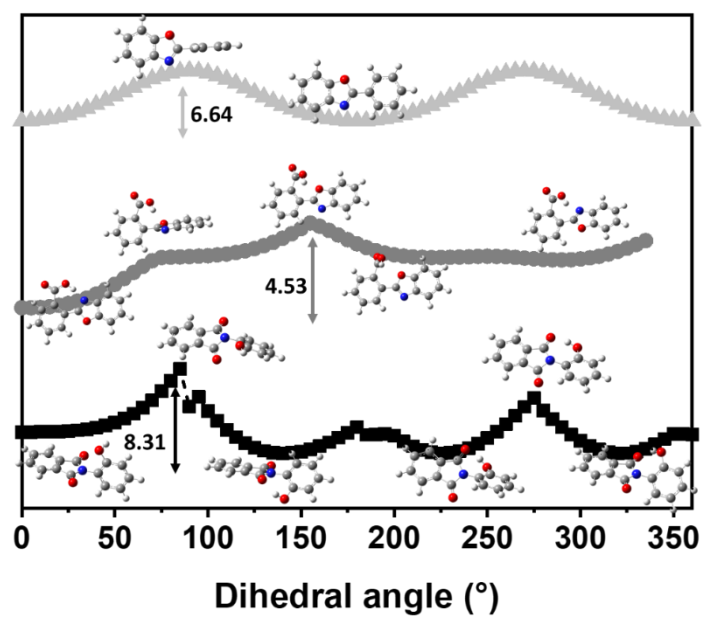


Figure 47. Simulation of a PES scan around the dihedral angle of the imide and benzoxazole bond.

# Thermally initiated Cascade Reaction Polymers (TCRP)

## *Polyimides with ortho-Allyloxy Groups*

### Effect of Allylation and the Degree of Allylation

TR polymer precursor based on either polyimide or polyamide backbones undergo a thermally initiated cyclization reaction due to a nucleophilic substitution of the phenol group and the neighboring imide carbonyl group. In the past different strategies were employed in order to tune the required temperature in terms of lowering the  $TR_{onset}$ . As stated in chapter *TR mechanism*, the TR process occurs between two monomeric units around the imide dihedral angle. The  $TR_{onset}$  temperatures are in the range from 290 to 450 °C[138, 254, 267]. In order to move both reactive centers close to each other, such a high energy input is required, due to the stiff imide bond and rotational barrier[127]. Therefore, using more flexible backbones are the most prominent and studied methods to lower the TR process, as restrictions of the rotations of each segment is reduced[254, 267]. However, these systems are still able to form strong hydrogen bonds, which lead to closer chain packing, as seen by high CTE in many polyimides and amides, and closer chain packing in turn reduced the free volume around the polymer chains and thus their degree of freedom. Other investigations used filler materials to disrupt these kinds of chain packing, however, such mixed matrix membranes contain additional compounds which increase the cost, complicate the film casting, and affect the gas diffusion pathways. Structural modifications were performed by using phenol modifications, such as ester and a methoxy modification was reported as well. In all these cases, the ether and ester group had to degrade prior undergoing a TR process, as a recovery of the phenolic group is required. Hence the ability to undergo TR depends on the stability of the modification group, which thoroughly requires 300 °C and above.

As described earlier, Tena *et al.*[256] published a mechanism, which proposes a lowered  $TR_{onset}$  temperature as a consequence of a formed phenolate intermediate, which is more nucleophilic compared to the neutral phenol group. Hence, they suggest the method of allylation of the phenol group. In that case, a full conversion of the *ortho*-hydroxy polyimide to the *ortho*-allyloxy modified precursor is important, since only allylated groups form phenolate groups as a consequence of the previous Claisen Rearrangement.

However, it is assumed that the enolization reaction to the phenol is much faster than the TR process initiation. In addition, the CR process occurs at temperatures, that are still lower compared to the reported TR onset temperature by Tena *et al.* Accordingly, in order to evaluate the relationship between the number of allyl modified *ortho*-hydroxy groups and the thermochemical tendency to undergo the cyclization reaction, as well as membrane specific properties such as density, free volume and gas separation performance, a set of allyloxy containing polyimides with different degrees of allylation in the range from 0 to 100% were prepared and analyzed. Moreover, the Claisen Rearrangement and its influence on subsequent reactions was investigated in detail.

### **Synthesis and characterization of modified precursor polyimides**

The requirement for the preparation and film property analysis of TR precursor films as well as the thermochemical behavior of different degrees of allylation is the preparation of an *ortho*-hydroxy polyimide with a molecular weight large enough to support a defect-free film formation. For that purpose, the reaction conditions have been optimized in order to reproduce the degree of allylation and also to reduce the number of possible side-reactions that might affect the thermochemical behavior.

For the investigation, the two most prominent TR polyimide backbones, 6FDA-HAB and 6FDA-APAF, were used. The synthesis and polyimide properties are described in detail in Chapter *Allylation*. The allylation has been done using sodium hydroxide, sodium hydride and potassium carbonate as catalysts in anhydrous DMF as a dipolar aprotic solvent, which dissolves the precursor polyimides very easily. As an allyl source allyl bromide and iodide was used. A Williamson-Ether synthesis approach was used to form allylated polyimides. While sodium hydroxide and sodium hydride led to tremendous poly (amic acid) formation and polymer degradation via hydrolysis, potassium carbonate appeared to be a promising candidate. Due to the easy purification, the possibility to scale-up and the use of cheap starting reagents, emphasis was put on the optimization of the K<sub>2</sub>CO<sub>3</sub> catalyzed Williamson-Ether synthesis approach.

The reaction was performed with 1 equivalent (eq) of K<sub>2</sub>CO<sub>3</sub> per repetition unit and 2.5 eq of allyl bromide at 40, 60 and 80 °C. While 40 °C did not yield any conversion after 6 h of reaction,

and polymer degradation was observed at 80 °C, the synthesis at 60 °C resulted in a 10% conversion of the phenol groups, without any poly (amic acid) or polymer backbone degradation within two hours. Therefore, the following optimization was conducted at 60 °C. In Figure 48 the variation of the  $K_2CO_3$  with 0.5, 1, 1.5 and 2.5 eq per repetition unit is shown. While reducing the amount of catalyst by half (0.5 eq  $K_2CO_3$ ), the overall conversion was lowered by about a half as well (5% conversion in 2 h). Nevertheless, an addition of 0.5 eq (to 1.5 eq  $K_2CO_3$ ) led to an increase of the conversion by a factor of 2.5, while doubling the amount of  $K_2CO_3$  (from 1 to 2 eq  $K_2CO_3$ ) increased the conversion by a factor of about 3. In addition, the conversion-time relationships in Figure 48 reveal that the reaction proceeds during the first 30 min, while no significant change was observed during the following 210 min.

The variation of the allyl bromide showed that 2.5 eq of allyl bromide at 1 eq  $K_2CO_3$  led to a hydroxy group conversion of 10%. Hence, the number of allyl bromide equivalents was increased to 5 and 10 eq, respectively. In Figure 48 it is demonstrated that no significant difference between 5 and 10 eq within two hours occurred. As a consequence, further reactions were performed using 2 eq of  $K_2CO_3$  and 5 eq of allyl bromide in DMF.

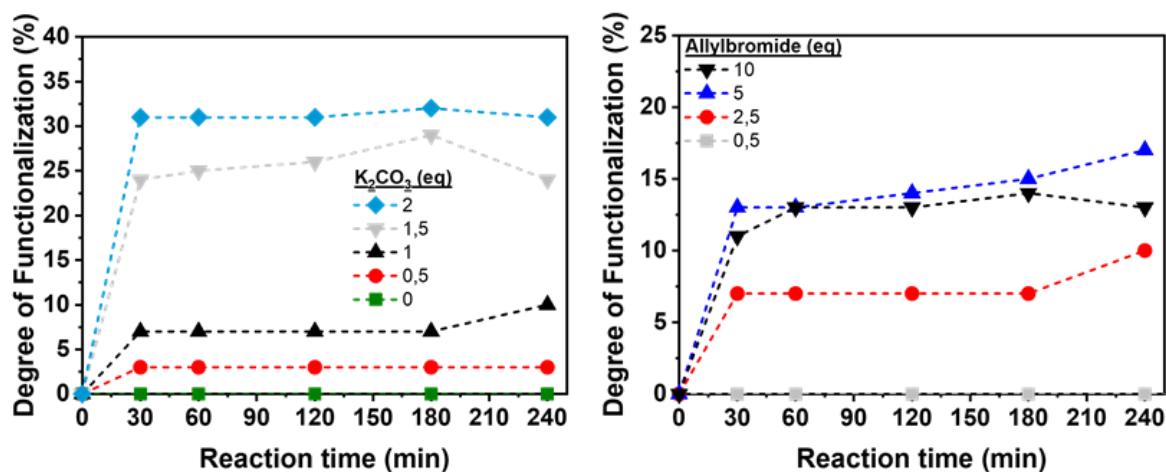


Figure 48. Plot of the degree of functionalization (allylation) versus reaction time with variation of (a)  $K_2CO_3$  and (b) allyl bromide[268].

Since every reaction revealed that no significant changes were observed after 30 min, a one-hour activation period with  $K_2CO_3$  followed by an one-hour reaction time after allyl bromide addition has been chosen. In order to increase the degree of allylation, the activation-conversion steps were repeated, until full conversion was achieved. With each addition, the degree of conversion increased until reaching 100% of conversion (see Figure 49). In total, five

cycles were required. The degree of allylation can be adjusted by the amount of catalyst, reagent, number of dosing cycles and reaction time of each cycle.

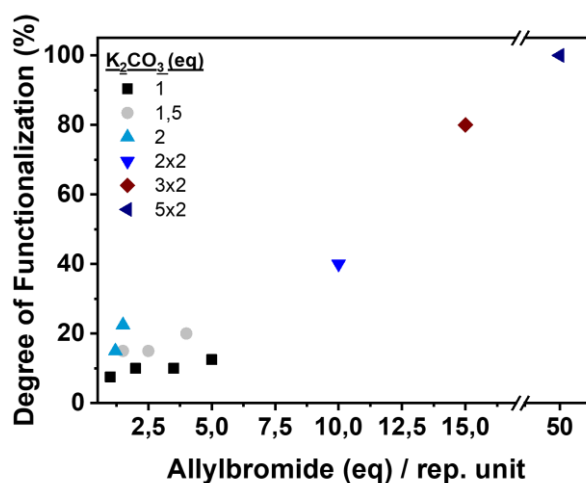


Figure 49. Plot of the degree of functionalization (allylation) versus total amount of allyl bromide equivalents per repetition unit added[268]

Figure 50 and Figure 51 show the  $^1H$ -NMR and FT-IR spectra of the pristine and fully converted polyimide. The conversion of the hydroxyl groups was confirmed by the disappearance of the OH peak (**k**), as well as the appearance of the allyloxy peaks (**i**, **g** and **h**, **h'**) that were assigned to the allylic position (**i**) at 4.78 ppm, and vinylic protons at 5.91 ppm (**g**) and 5.26 ppm (**h**, **h'**). Additionally, a downfield shift of the aromatic protons corresponding to the diamine (**d–f**), which are the ones proximate to the allyloxy group was observed. The degree of allylation (dA) was determined by the relation of the allylic proton (**i**) integral to the theoretical value of four protons in the case of a 100% allylated homopolymer. The peak assignment was supported by  $^1H$ , H-COSY, C, H-COSY and HSQC as well as  $^{13}C$ -NMR spectroscopy experiments (see Appendix, Figure 201)

The conversion was confirmed by means of FT-IR spectroscopy as well. The hydroxy group was absent ( $3000 - 3600\text{ cm}^{-1}$ ), while still very prominent in the *ortho*-hydroxy polyimide.

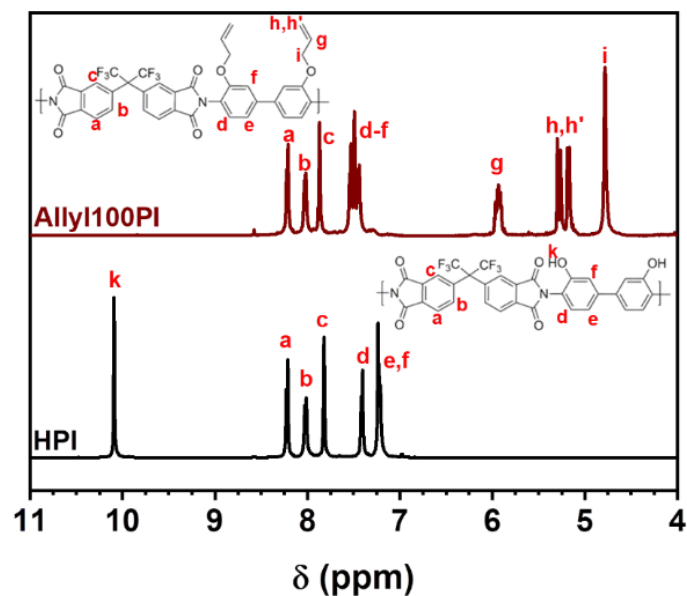


Figure 50. Stacked  $^1\text{H-NMR}$  spectrum of the allylated (Allyl100PI, maroon) and the pristine 6FDA-HAB polyimide (black) with signal assignments to their corresponding structure[268].

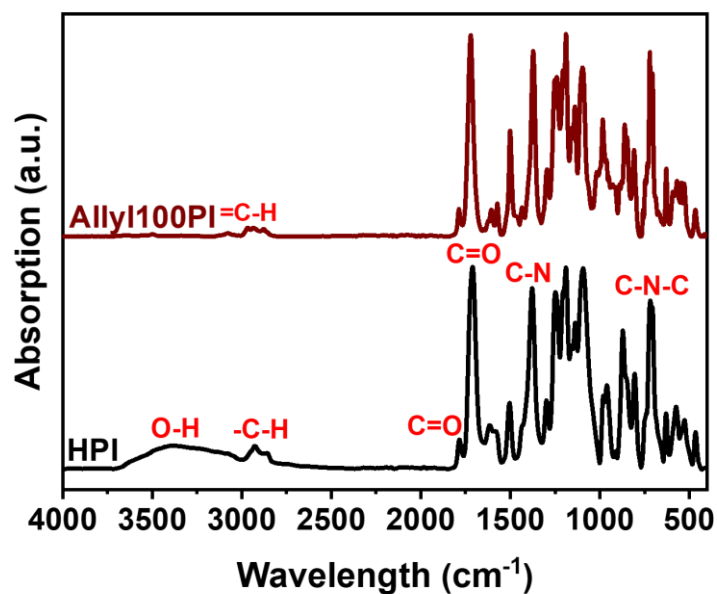


Figure 51. Stacked FT-IR spectrum of the allylated (Allyl100PI, maroon) and the pristine 6FDA-HAB polyimide (black) with vibration assignments to their corresponding functional group[268].

In Figure 52 the prepared 6FDA-HAB based *ortho*-Allyloxy polyimides with degrees of allylation in the range of 0 to 100% with 10, 15, 20, 40, 60, 80 and 100% of *ortho*-hydroxy to *ortho*-allyloxy conversion is depicted.

A gradual decrease of the hydroxy group peak at 10.4 ppm, and simultaneously an increase of the allylic peaks in the range from 4 to 6 ppm is shown. A strong change in the aromatic peak

pattern for the diamine corresponding peaks **d-f** can be seen, while the aromatic anhydride assigned peaks do not alter significantly.

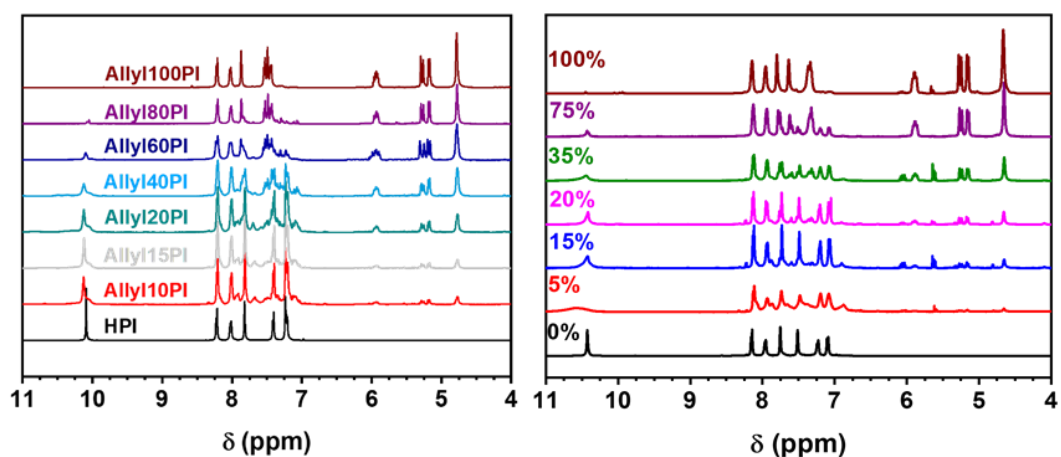


Figure 52. <sup>1</sup>H-NMR spectra of the allylated polyimides (a) 6FDA-HAB and (b) 6FDA-BisAPAF with different degrees of allylation[268].

For the investigation of the backbone dependence of the thermophysical properties of the material, the backbone 6FDA-BisAPAF was allylated as well, as stated earlier. The stacked spectra are shown in Figure 52. Figure 53 shows the expanded <sup>1</sup>H-NMR signals for each degree of allylation of 6FDA-HAB.



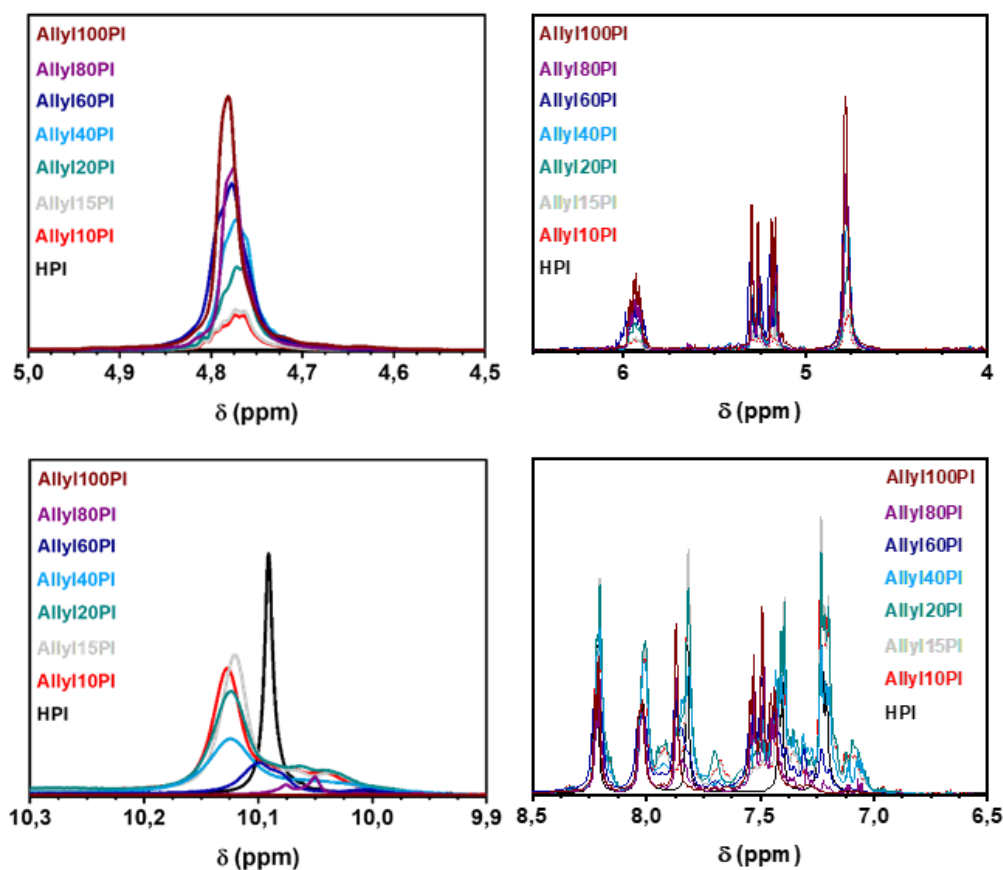


Figure 53. Expanded  $^1\text{H-NMR}$  spectrum of relevant peak evolution of each degree of allylation of the allylated polyimides based on 6FDA-HAB[268].

## Thermoanalysis

Differential scanning calorimetry (DSC) measurements were carried out in order to evaluate the thermal properties of the polymers. Crosslinking reactions or rearrangements, for instance in benzoxazines, which undergo benzoxazine ring opening and crosslinking, show exothermic peaks, that do not appear in a second cycle, as a consequence of their irreversibility[238, 269-272]. Therefore, DSC experiments were used to characterize the thermochemical behavior of allylated polyimides, as they have not been investigated in the literature. The heat flow curves, obtained by the first cycle of the DSC experiments, are shown in Figure 54, where three exothermic peaks were observed.

These peaks were attributed to irreversible chemical reactions since they did not occur in the second cycle of the DSC experiment (Figure 54). No other process took place during the cooling

and repeated heating scan. Additionally, these peaks did not appear in the unmodified polyimide either, which suggests that the process might be associated with the allyl units.

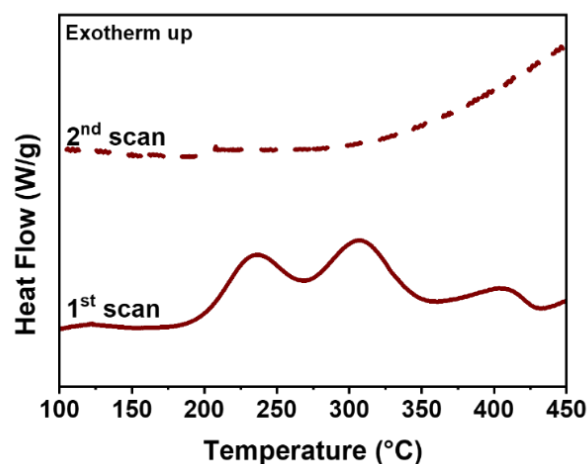


Figure 54. First and second heat flow scan by means of DSC of Allyl100PI[268].

In order to check if these reactions are accompanied by a weight loss, TG-IR experiments have been conducted. In Figure 59 the TG-IR with the corresponding DSC run is plotted. No significant mass loss prior 350 °C, in the range of the first two exothermic peaks, is detected. Hence, these reactions must be non-extrusion reactions. According to Trost *et al.*[224], full atom efficiency appears in isomerizations, rearrangements and addition reactions.

**Heat Flow Analysis (DSC) of Allyl100PI.** Fitting of the heat flow and analyzing the deconvoluted peaks, is suggesting, that there are two major reactions below 350 °C with overlapping on- and offsets between 250 and 300 °C appearing in the case of Allyl100PI-2 (Figure 55).

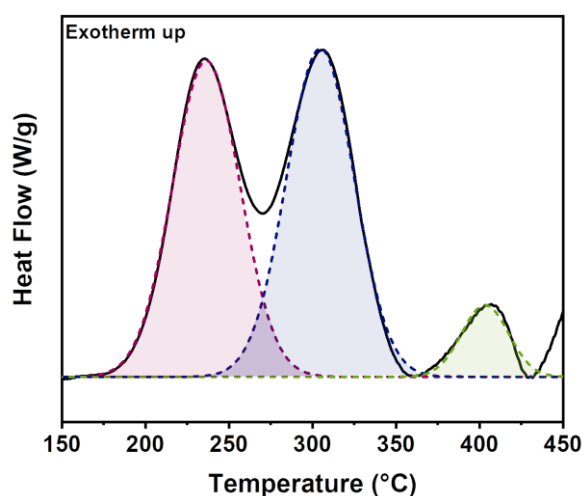


Figure 55. Heat flow curve of Allyl100PI, obtained by means of DSC experiments in the temperature range from 150 to 450 °C with a heating rate of 5 °C min<sup>-1</sup>. Deconvoluted peaks based on Gauss-Fitting are highlighted.

Studies of allyl-phenyl ether containing materials, such as allylated bisphenol-A as resins precursor, demonstrated Claisen Rearrangement processes in solid-state around 180 to 200 °C [273]. The first peak is therefore assumed to correspond to Claisen Rearrangement. A determination of the different processes was executed by various isothermal annealing (150, 175, 200, 225, 250 and 350 °C). The DSC runs after the isothermal annealing is shown in Figure 56 for each temperature. Afterwards, the structures were investigated by means of FT-IR (Figure 57) and <sup>1</sup>H-solution NMR spectroscopy (Figure 265 and Figure 279) as well as solid-state <sup>13</sup>C-solid-state NMR (Figure 58).

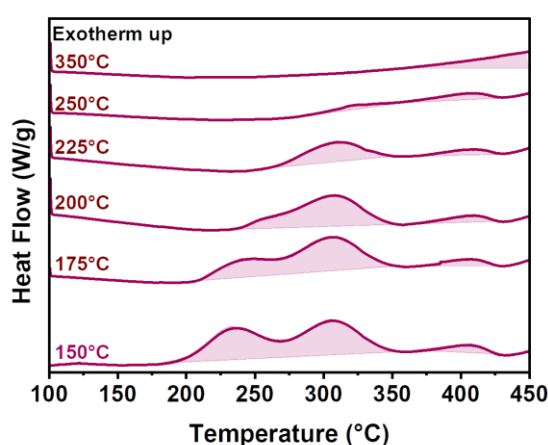


Figure 56. Heat flow curve of Allyl100PI, obtained by means of DSC experiments in the temperature range from 100 to 450 °C with a heating rate of 5 °C min<sup>-1</sup> after annealing at different temperatures (150, 175, 200, 225, 250 and 350 °C)[268].

The isothermal treatment at 200 °C for 10 h was identified as a suitable method to isolate the first thermal process. The NMR study evidenced the complete Claisen-Rearrangement since an increase of the hydroxy proton peak (**k**), as well as a decrease of the integral of the aromatic protons, was observed and quantified. However, Allyl100PI-2 was not completely soluble after that treatment. In fact, the materials with an allylation degree higher than 20% were not completely soluble after the annealing at 200 °C, suggesting that for allyl contents higher than 20%, the secondary chemical process must have been already initiated. Due to the insolubility of the fully allylated material (Allyl100PI) the structure was additionally characterized by means of <sup>13</sup>C-CP-MAS NMR-spectroscopy in the solid-state instead of liquid NMR.

The insolubility is a strong evidence, that crosslinking is occurring in these cases. Since no insolubility of the unmodified HPI-2 is observed below 300 °C, the phenomenon is attributed to the introduction of allyl groups. After the isothermal treatment at 250 °C, the second peak disappeared almost completely, indicating that the end of the second process was reached. A

gel-fraction of 99% and a high swelling ratio around 270% have shown, that each polymer chain appears to be crosslinked, but still more loosely, as the Allyl100PI film takes up nearly two times of the initial weight.

Other crosslinking sites are also possible, such as crosslinking between hexafluorinated dianhydride units after a thermal  $\text{CF}_3$  cleavage of the backbone. Anyhow, this radical elimination is assumed to be of less importance at 350 °C and no further evidence has been determined by means of TGA-FT-IR [118]. The possibility of an ene-reaction between the allyl group and an imide carbonyl group, cannot be ruled out, but has been neglected, since no significant change in the imide region after treatments at 250 °C was determined, as shown in the solid-state NMR spectra. In case of a thermal carbonyl-ene reaction, the carbonyl group is expected to rearrange to a hydroxy group. However, no hydroxy signal appeared after annealing at 350 and 400 °C. Hence, other crosslinking reactions have to be considered. The hydroxy peak in the IR spectra of HPI is absent in the thermally non-treated Allyl100PI, but recovers after treatments at 200 and 250 °C. The vinylic peak fades as the material is treated at 250 °C. This corroborates the assumption that the allyl units crosslink with their vinyl groups.

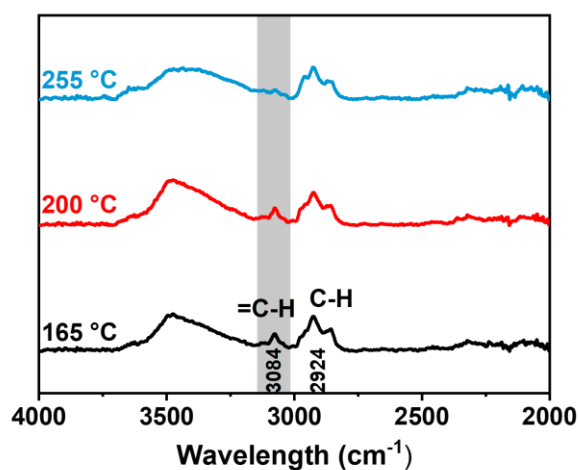


Figure 57. FT-IR spectrum of Allyl100PI after annealing at 165, 200 and 255 °C in the range from 2000 to 4000cm<sup>-1</sup>. [268]

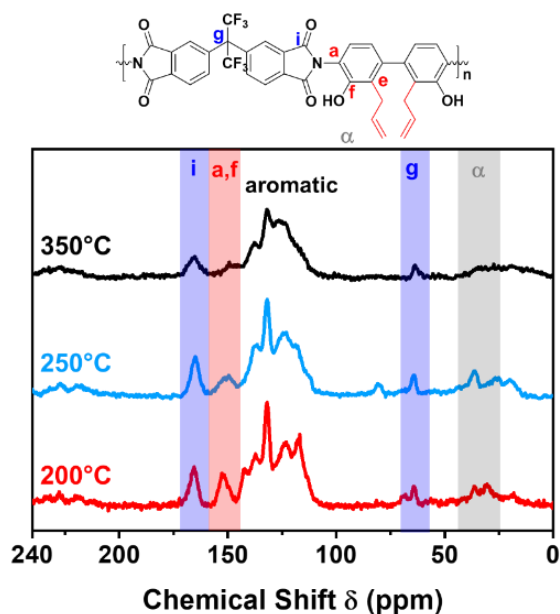


Figure 58.  $^{13}\text{C}$ -CP-MAS NMR spectrum of Allyl100PI after annealing at 200, 250 and 350 °C.

**TGA-FT-IR Analysis.** Upon heating the allyloxy polyimides at 350 °C was sufficient to eliminate the third process, which is related to a mass loss step, as both onset and peak temperatures of the exothermic peaks and the mass loss are the same. The TG-IR revealed that in the region from 350 to 450 °C only  $\text{CO}_2$  was formed, with a mass loss of 9.6%. This is the temperature region, typical for all reported Thermal Rearrangement polyimides. In case of a full conversion of the allyloxy polyimide to allylated polybenzoxazole, a mass loss of 10.2 % is expected. The third reaction, characterized by an exothermic heat flow in the DSC runs, is attributed to the Thermal Rearrangement or rather HPI-to-PBO cyclization

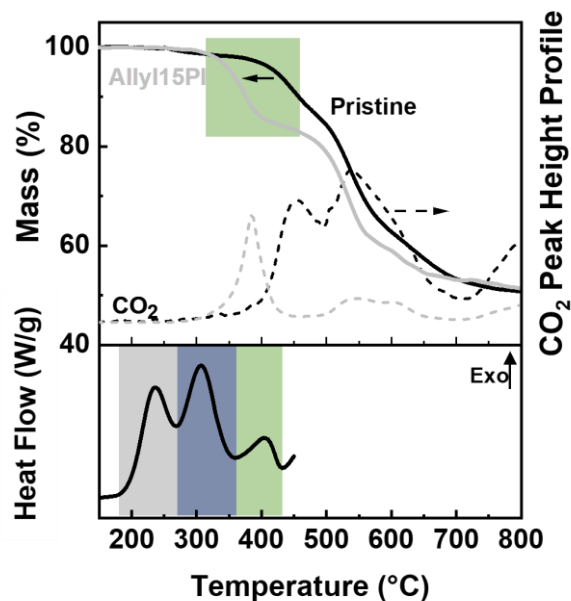
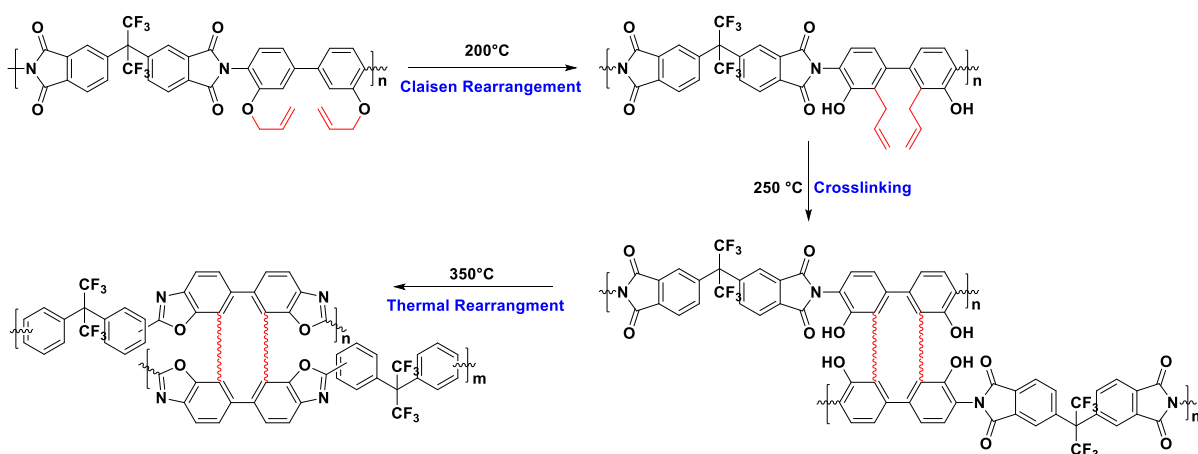


Figure 59. Mass loss curves obtained by means of TGA experiments of Allyl15PI and the pristine 6FDA-HAB in the range from 150 to 800 °C at a heating rate of 5 °C min<sup>-1</sup>. CO<sub>2</sub> gas evolution peak analysis (stacked lines) (top). Heat flow curve of Allyl-PI-2 obtained by means of a DSC experiment in the temperature range from 150 to 450 °C with a heating rate of 5 °C min<sup>-1</sup>.

FT-IR measurements of the isothermally treated films confirm these assumptions. As shown in Figure 57, the broad hydroxy band is observed above 3200 cm<sup>-1</sup> after 10 h at 250 °C, while the broad band is not present after 350°C for 2 h as a result of the cyclization reaction. In addition, the carbonyl peak disappeared. After these thermal treatments, a possible structure is proposed, shown in Scheme 1.



Scheme 1. Thermally induced consecutive reactions in Allyl-PI[268].

## Investigation of Degree of Functionalization.

**Heat-Flow.** In the previous section, it has been shown that allyl groups undergo a cascade of reactions including crosslinking and Thermal Rearrangement. Heat Flow measurements via DSC were performed in order to investigate the thermal initiated reactions of polyimides with different degrees of allylation. The exothermic peaks were seen for all materials, but the intensity of both peaks, below the  $T_{\text{onset}}$ , increased with respect to the number of allylated units in the polymer since more allyl groups are available to undergo any isomerization or reaction (Figure 60). Additionally, a decrease of the onset temperature for the first peak could be observed when the degree of allylation was rising.

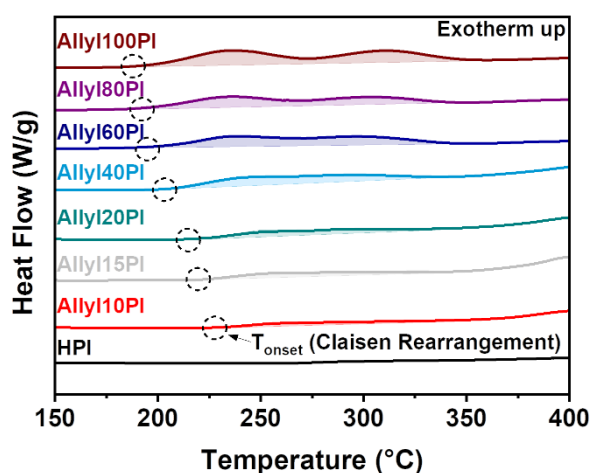


Figure 60. Heat flow curve of Allyl-PI-2, obtained by means of DSC experiments in the temperature range from 150 to 400 °C with a heating rate of 5 °C min<sup>-1</sup> for all allylated polyimides based on 6FDA-HAB[268].

**Gel-fraction and swelling experiments** were performed in order to evaluate the residual soluble part. The gel-fraction is linearly increasing from 96 to 100% for 10 to 100% of allylated polyimides (Figure 61). Simultaneously, the swelling ratio decreases gradually with the degree of allylation. As the number of present allyl groups increases, the number of crosslinks increases as well, and therefore the crosslinking density. As more allyl groups, capable to crosslink, are introduced, the more the probability to find crosslinks rises. As a consequence, the gel-fraction decreases, even though it is worth to mention that gel fraction at 10% allylation is already reasonably high. The increasing gel fraction is accompanied by decreasing swelling ratios. As the number of crosslinks increases, the network tightens, and the swelling is lower as restoring forces increase. The linear relationship between released heat, swelling and the degree of allylation suggests that the crosslinking process is linked to the allyl groups.

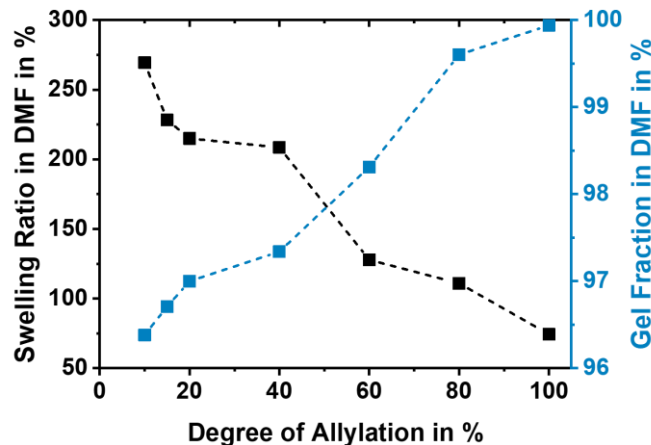


Figure 61. Swelling ratio (left, black) and gel fraction (blue, right) of all allylated polyimides as a function of the degree of allylation[268].

From these DSC experiments the released heat for the Thermal Rearrangement process is increasing at lower temperatures for materials with the lowest  $TR_{onset}$  temperature as well. (Figure 62).

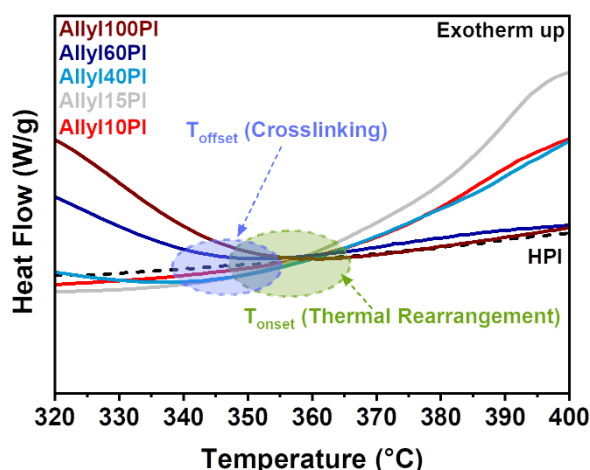


Figure 62. Heat flow curve in the range of the crosslinking offset ( $T_{offset}$ ) and TR onset ( $T_{onset}$ ) region between 320 and 400 °C for allylated polyimides with 10, 15, 40, 60 and 100% allylation.

**TGA-FT-IR Analysis.** While Allyl15PI, despite its significantly lower number of allyl groups compared to Allyl100PI, shows a higher heat release of  $149 \text{ kJ mol}^{-1}$  compared to  $43 \text{ kJ mol}^{-1}$ , its  $TR_{onset}$  temperature of the mass loss step is shifted downwards to  $285 \text{ °C}$ . This is a lowering by  $80 \text{ °C}$  compared to the pristine HPI. Additionally, the mass loss at  $400 \text{ °C}$  according to the TGA is 12% compared to 3.5% for Allyl100PI, respectively.

Hence, the degree of allylation also affects the  $TR_{onset}$  and peak mass loss curve obtained by means of TGA experiments of allylated polyimides with 0, 8, 15, 25, 50 and 100% allylation in



the range from 100 to 800 °C at a heating rate of 5 °C min<sup>-1</sup> (Figure 63). CO<sub>2</sub> gas evolution peak analysis by means of TGA-FT-IR analysis. The order of the onset temperature in terms of degree of allylation is 15 < 10 ~ 40 << 60 ~ 100 << 0. This order reveals that there is a non-linear relationship between the degree of allylation and the TR<sub>onset</sub>. This relationship is demonstrated for the on- and offset as well as the determined peak temperature from TG-IR measurements as a function of the degree of allylation (Figure 64, Figure 65).

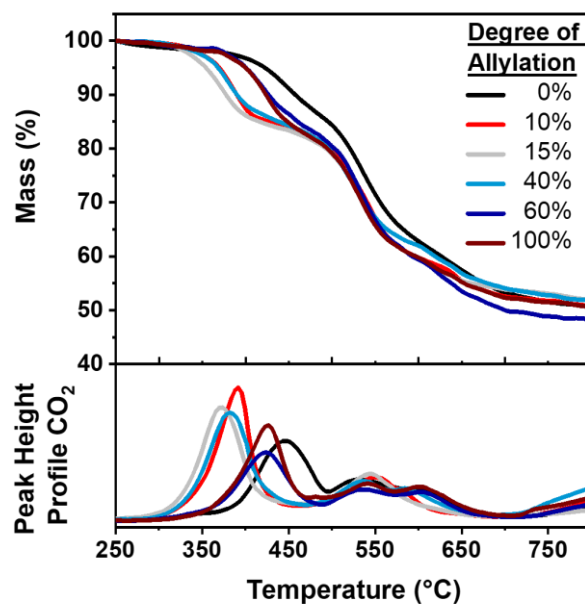


Figure 63. Mass loss curve obtained by means of TGA experiments of allylated polyimides with 0, 10, 15, 40, 60 and 100% propargylation in the range from 250 to 800 °C at a heating rate of 5 °C min<sup>-1</sup> (top). CO<sub>2</sub> gas evolution peak analysis by means of TGA-FT-IR analysis (bottom)[268].

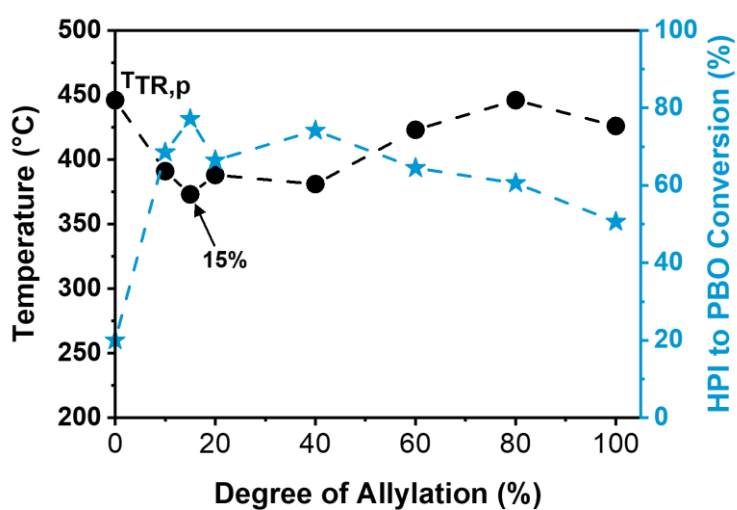


Figure 64. TR<sub>onset</sub> and -peak temperature (left axis, black) and HPI-to-PBO conversion (right axis, blue) as a function of the degree of allylation[268].

It was also noticed that the TR related weight loss step broadened for the materials with a degree of allylation (dA) above 40% and the pristine material, due to the lower onset rearrangement temperature. Therefore, the 1<sup>st</sup> weight loss step is clearly separated from the 2<sup>nd</sup> step, which is attributed to polymer degradation. The materials with 60, 80 and 100% of allyloxy groups in turn showed a narrower gap between the two processes. The pristine polyimide shows a strong overlap of the TR accompanied CO<sub>2</sub> mass loss and the degradation process. The allylated thermally rearranged materials in the following text are designated as TR-AllylXPBO.

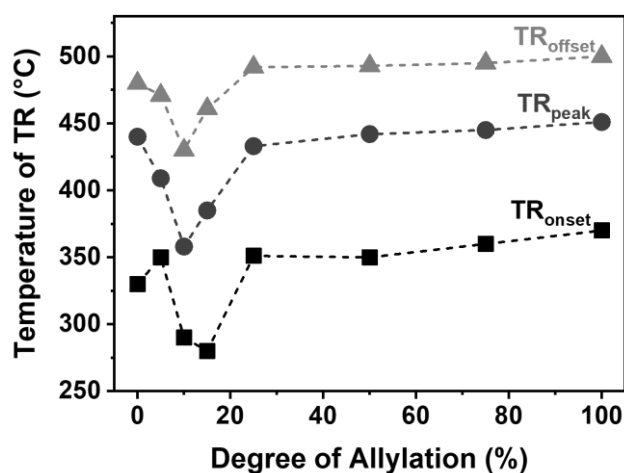


Figure 65. TR<sub>onset</sub>, -peak and -offset temperature as a function of the degree of allylation.

Studies by Calle and Guo *et al.* [138, 139] have shown that the mobility of polymer chains, correlated with the glass transition temperature, is a major factor when it comes to thermally initiated benzoxazole formation. However, glass transition temperatures could not be determined in this study by means of DSC measurements, since all exothermic peaks made it very difficult to observe an underlying endothermic glass transition step.

Moreover, even for the unmodified 6FDA-HAB polyimide, various glass transition temperatures were reported, proving the difficulty of the  $T_g$  determination of such a rigid material. Based on the finding that the material shows a clear non-linear relationship between the degree of allylation and the TR<sub>onset</sub> temperature and TR conversion, but a linear increasing tendency to crosslink seems to contradict the phenolate theory. The proposed mechanism in the literature, that a phenolate intermediate is formed due to the Claisen Rearrangement and responsible for the lowered TR process as a consequence of the increasing partial charge and nucleophilicity of the phenolate, has not been corroborated.

The highest conversion might have been expected in case of fully converted Allyl100PI. As the number of phenolate depends on the possibility to undergo Claisen-Rearrangement. In the case of the 15% allylated Allyl15PI, 85% of the *ortho*-functionality (OH-group) would undergo a conventional TR process, while only 15 % of the *ortho*-functionality (allyloxy groups) would form a faster reacting phenolate group. In addition, if the phenolate intermediate is responsible for a HPI-to-PBO formation, following immediately after the Claisen Rearrangement, TR conversions would have been detected in the temperature range of the CR process. The CR peaks at 240 °C, while no evidence of PBO or any TR related intermediate, nor a CO<sub>2</sub> loss, was found by means of spectroscopic, mass loss and calorimetric investigations. That study [256] also focused on the Claisen-Rearrangement rather than the crosslinking process, which is why the effect of crosslinking on the TR process is no part of the theory. Therefore, another relationship and reason for the lowered TR process temperatures for low degrees of allylation are suggested. It is assumed that the free allyl groups, as well as the crosslinked allyl groups, act as spacers and packing disruptors, which lead to inefficient polymer chain packing and reduced the number of formed hydrogen bonds.

*This disruption occurs already with a low degree of modification (10%) and intensifies with increasing degrees of allylation. At these low dA values, the packing disruption and thus the increased mobility still overcompensate the mobility restrictions due to the allyl crosslinking. Moreover, the probability of two allyl groups finding each other in order to crosslink is much lower at these low degrees of modification. As the number of allyl groups increases, the increasing number of formed crosslinks counterbalances the packing disruption by the allyl groups. After more than 50% of allylation, the number of crosslinks is so high, that the crosslinking induced mobility restrictions take over and cannot be compensated by the packing disruption [268].*

Calle *et al.*[144, 145] showed a similar effect of a diester as a crosslinker that led to packing disruption due to the presence of larger diester molecules, which compensate the effect of the mobility restrictions due to the crosslinking at a maximum of 20 mol% crosslinking units.

The material with the lowest TR<sub>onset</sub> temperature, Allyl15PI, was isothermally treated at 350 °C, 400 and 425 °C for 10 h to see how fast the full cyclization and decarboxylation is (Figure 66). At 350 °C the mass loss levels off after 5 h, but still shows only about 3% of weight loss. At 400 °C the mass loss at target temperature is already significantly higher, with 7%, whereas a

weight loss of 12.5% is expected, in case each repetition unit undergoes a TR process. A complete conversion takes 10 h at 400 °C, however about 50% of the repetition units reacted already after reaching the target temperature of 400 °C at a heating rate of 5 °C min<sup>-1</sup> the mass loss is even higher if 425 °C are used as target temperature. In that case, it takes about 2 h to achieve full conversion. However, upon further heating the mass loss continues slowly and appears to level off after 7 h, with a mass loss of 15% after 10 h. 10% mass loss occurred already after reaching 425 °C. In case only TR occurs at the beginning, this would mean a conversion of 80%.

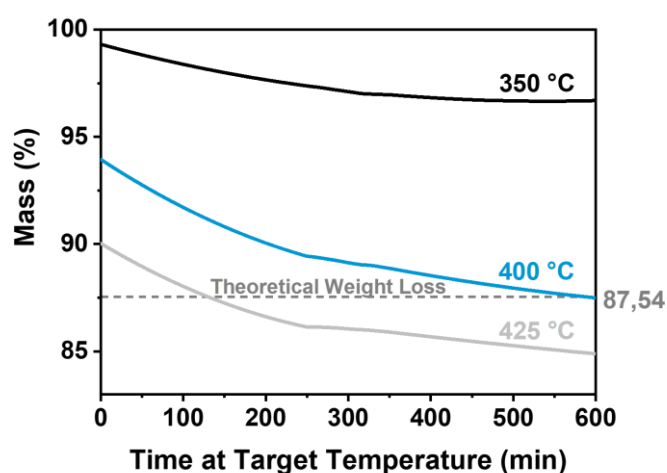


Figure 66. Mass loss curve obtained by means of isothermal TGA experiments of Allyl15PI at 350, 400 and 425 °C for 10 h[268].

### Broadband Dielectric Spectroscopy Measurements of the Thermal Relaxation Processes.

Further investigations of the effect of allyl modification to the cascade reaction process, in order to provide information about the polymer relaxation processes and the thermal imide-to-benzoxazole conversion, were done by means of broadband dielectric spectroscopy experiments. Polyimides usually exhibit two sub-glass relaxation processes, which are  $\gamma$ -relaxations at temperatures below 0 °C and  $\beta$ -relaxations at a temperature above 150 °C, both associated with localized motions of the polymer backbones side groups in the glassy state [274, 275]. BDS experiments with HPI2 and three allylated polyimides were accomplished by *in situ* measurement of the effect of the thermally induced reactions of the allyl groups. Figure 67 demonstrates the dielectric loss modulus  $\epsilon''$  of the four representative polyimides with 0, 15, 40 and 100% allylated units as a function of the temperature at a frequency of 10 Hz. Two sub-glass relaxation processes,  $\gamma$ - and  $\beta$ -relaxation, were observed between -100 and +100 °C ( $\gamma$ -relaxation) and above 200 °C ( $\beta$ -relaxation). The observed temperature ranges are in

agreement with those of other reported polyimides [274, 275]. The lower temperatures for  $\gamma$ -relaxation processes, owing to mainly non-cooperative and local motions in the polymer, are mainly attributed to phenylene ring-flips and rotations [77].

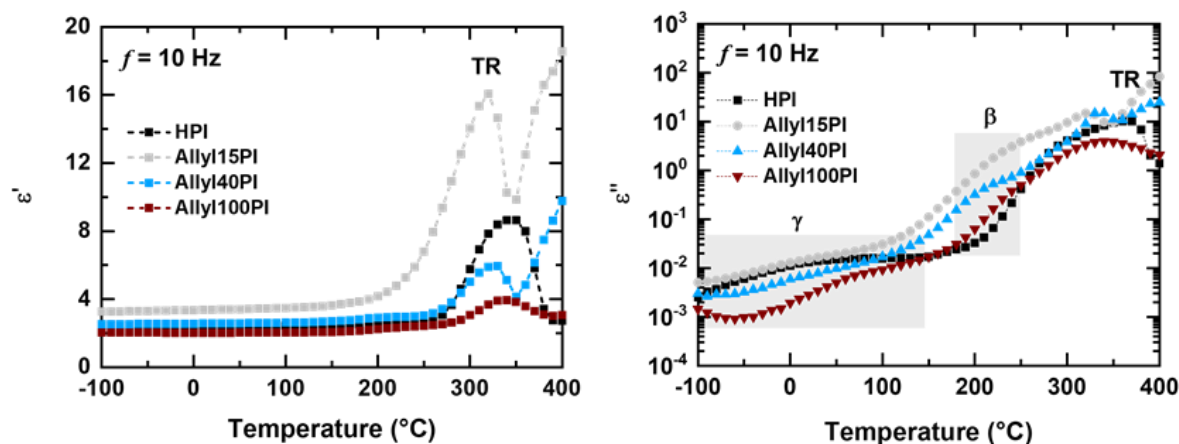


Figure 67. Dielectric permittivity (left) and dielectric loss (right) as a function of the temperature for the pristine and 15, 40 and 100% allylated polyimides[268].

The characteristic  $\gamma$ -relaxation process can be observed for all materials and shows a shift of the relaxation peak with respect to the degree of allylation. This observation could be correlated with the hindered rotational freedom of the diamine unit, due to the increasing number of allyl groups. The second peak of the dielectric loss modulus ( $\beta$ -relaxation process) shows a similar trend of the position and shape for the different materials. The onset and peak temperatures of  $\epsilon''$  shifts with increasing degree of allylation to higher temperatures for the  $\beta$ -relaxation process. These results indicate that the relaxation  $\beta$ -process affects the TR reaction. Allyl15PI has the lowest  $\text{TR}_{\text{onset}}$  temperature as well as the lowest  $\beta$ -relaxation onset temperature. The pristine material remains in the same temperature range similar to the 100% allylated polyimide, in the same manner as the TR onset and peak for both materials do (see TGA experiments, Figure 63 and Figure 65). The required temperature for the PBO conversion reaction depends on the mobility of the polymer chains as reported by Calle *et al.*[139], whereas HPI's with lower  $T_g$ 's usually have also lower TR temperatures as well. Moreover, Comer *et al.*[276, 277] showed that the  $\beta$ -relaxation temperature range decreases if the backbone is synthesized from more flexible diamines (BisAPAF vs. HAB). The allylated polyimides showed this relationship between increasing TR temperatures with increasing  $\beta$ -relaxation temperatures and relaxation times  $\tau_{\text{max}}$  in the same manner. Numerous mechanisms have been postulated for the  $\beta$ -relaxation of polyimides, yet. Commonly, the relaxation mechanisms were

described by a non-cooperative motion of the diamine[90], as well as a second process, caused by the anhydride, in a more cooperative motion[77, 276].

**Real part of the complex permittivity,  $\epsilon'$ .** The BDS experiments revealed, that  $\epsilon'$  increased rapidly after approaching temperatures above 200 °C, which is attributed to the TR process. The maximum of the  $\epsilon'$  peak shifts to higher temperatures with respect to the degree of allylation (Peak temperatures of 320 °C for Allyl15PI, and 340 °C for Allyl100PI) The relaxation times for the  $\beta$ -relaxation process of each polymer were calculated using the Havriliak–Negami equation [278]. The relaxation time  $\tau_{\max}$  versus the reciprocal temperature, allows to estimate the activation energy of the process (Figure 68). In all cases, the  $\beta$ -relaxation process of the polyimides follows a linear Arrhenius behavior. The activation energies  $\tau_{\infty}$  were calculated. Accordingly, 6FDA-HAB had an activation energy of 145 kJ/mol, while 115, 120 and 65 kJ/mol were determined for the 15%, 40%, and 100% allylated polyimides. These values are in accordance with reported data for the  $\beta$ -relaxation of aromatic polyimides (130-160 kJ/mol)[77].

The relaxation times of the  $\gamma$ -relaxation process could not be described by the Arrhenius equation, applying the used fitting process. Since Allyl15PI and Allyl40PI are copolymers, which contain randomly distributed allyl groups with up to three different types of diamine units.

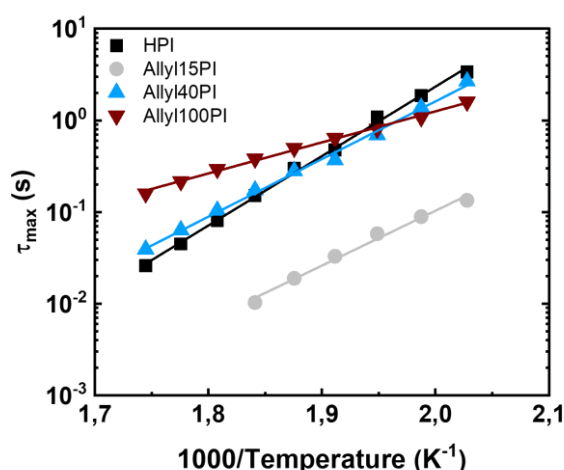


Figure 68. Relaxation times based on Havriliak-Negami fitting as a function of the reciprocal temperature[268].

**Backbone effect via TGA-FT-IR measurements.** In order to proof the effect of the degree of allylation, a set of allyloxy polyimides based on 6FDA-APAF with different degrees of allylation were prepared. The degree of allylation was determined by NMR spectroscopy and

especially the fully converted polyimide was confirmed via NMR spectroscopy and FT-IR spectroscopy. 6FDA-BisAPAF is next to 6FDA-HAB one of the most widely reported TR precursor backbones and shows a lower  $T_g$ - and TR temperature according to various studies. The degree of allylation varies slightly from the results of the 6FDA-HAB modification. 5, 15, 25, 35, 60, 75 and 100% of allylated 6FDA-BisAPAF (HPI-1) were prepared and thermophysically investigated by means of DSC and TG-IR experiments. In all cases the introduction of an allyl group leads to a decrease of the  $TR_{onset}$  and peak temperatures compared to the pristine material. The determination of the TR specific temperatures shows a similar pattern, as observed for 6FDA-HAB based precursor, which is a strong decrease of the  $TR_{onset}$  and peak temperature for low degrees of allylation and no significant differences above 20% of allylation. In the case of 6FDA-BisAPAF, the lowest onset temperature was determined for 5% and the lowest peak temperature for 20% of allylation. Since 6FDA-APAF is already more mobile compared to 6FDA-HAB, based on the introduction of a more flexible hexafluoroisopropylidene group, as quantified by the lower  $T_g$  and TR temperature (see Figure 69Figure 70).

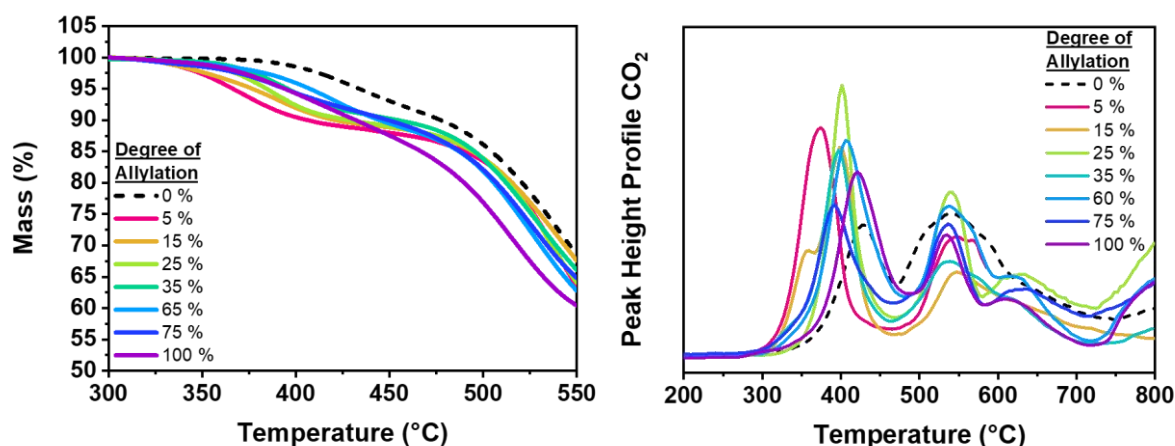


Figure 69. Mass loss curve obtained by means of TGA experiments of allylated polyimides with 0, 5, 15, 25, 35, 65, 75 and 100% allylation based on 6FDA-BisAPAF in the range from 300 to 550 °C at a heating rate of 5 °C min<sup>-1</sup>. (left). CO<sub>2</sub> gas evolution peak analysis by means of TGA-FT-IR analysis (right)[268].

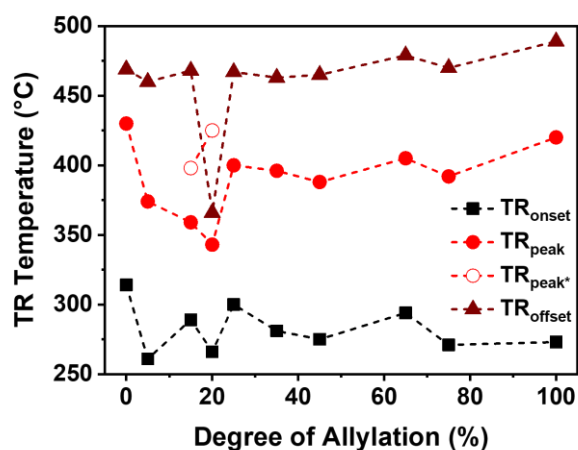


Figure 70. TR<sub>onset</sub>, peak and offset temperature as a function of the degree of allylation for allylated 6FDA-BisAPAF [268].

### Effect of Allyl Group Distribution along the Polymer.

The discussed results so far have shown a tremendous effect of the number of allyl groups in the polymers with respect to thermochemical properties. However, what has not been discussed yet is the influence of the distribution of the allyl groups. While fully modified Allyl100PI and Pristine PI are homopolymers, the materials with degrees of allylation between 5 and 80% have most likely randomly distributed allyl groups. Materials with a low degree of allylation, such as 5-20%, are very likely to have repetition units with a maximum of one allyl group per repetition unit, and also a large number of unmodified repetition units, so to say pristine repetition units. As the degree of allylation passes the 50% level, it is possible that every repetition unit carries one allyloxy group. However, the number of fully modified repetition units will increase, but still pristine repetition units and mono functionalized units will be present.

**Synthesis.** In order to check if the low TR<sub>onset</sub> temperature in case of 10 and 15% allylated PI is independent of the allyl group distribution, a fully allylated monomer based on HAB was synthesized and afterwards polymerized. Allyl100PI was synthesized in that way either as a reference, as it is expected that the polymerized and post-polymerization modified Allyl100PI should be of the same structure and hence show same thermochemical properties. For the discussion, the allylated polyimides based on modified HAB is designated as Co-AllylXYPI-Z, whereas XY refers to the degree of allylation 10, 15 and 100, and Z refers to the imidization method. *c* for chemical, *for* azeotropic and *t* for thermal imidization.



The 3,3'-dihydroxybenzidine (*p*HAB) was converted to the amic acid via reaction with phthalic anhydride in diethyl ether at room temperature for 24 h. The reaction is identical to the polyimide synthesis in which also an anhydride reacts with the diamine. However, here the anhydride is monofunctional as it is only used as a protective group. Due to the similar reactivity of the amine and hydroxy group, the imide-protection has been chosen as it is amine-selective and reported to be easily separated by hydrazinolysis [279]. In order to avoid any side reactions, like allylation of the amic acid N-H group, the amic acid was cyclodehydrated to the corresponding imide prior to the modification step. The third step was the allylation identical to the allylation of the polymer, using  $K_2CO_3$  as a base catalyst and allyl bromide as the allyl source in DMF. The full conversion was determined via NMR spectroscopy showing the hydroxy peak disappearing and the allyl peaks showing an integral corresponding to the expected number of protons, and similar to the peak pattern of the polymer. The NMR spectrum is shown in Figure 276.

In order to recover the amine group, the imide protection group was removed via hydrazinolysis as mentioned earlier. While most publications use high excess of hydrazine in alcohol at higher temperatures of 60 °C, in that case the hydrazine concentration was kept nearly stoichiometric and the reaction was performed at room temperature. The reason was, that hydrazine is known to form a diimide under oxidation [280-282], which is a brilliant reducing agent [283], and might reduce allyl groups to propyl groups. With the adapted synthesis route the allylated diamine HAB-allyl was synthesized and purified by means of extraction and re-crystallization.

In the last step of the allyloxy-polyimidization the conventional two-step imidization method via silylation of the allylated- and non-allylated diamine was used. Afterwards the poly (amic acid) was converted via chemical, thermal and azeotropic imidization. The full conversion of the amic acid to its corresponding imide form was confirmed via NMR-spectroscopy, and the high conversion of monomeric diamine by the absence of any amine peak in the NMR and also via GPC. In Figure 71 the mass loss of phthalic anhydride protected HAB based amic acid (Pho), imide (PHc), allylated imide (PHc-Allyl) and de-protected HAB-Allyl is shown, as well as their corresponding  $CO_2$  release profile.

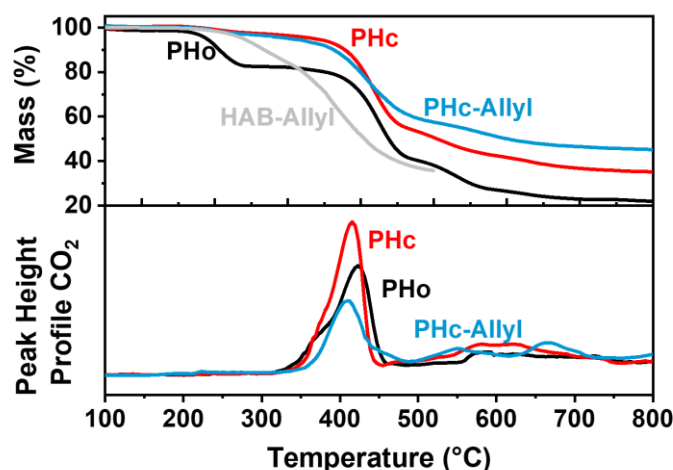


Figure 71. Mass loss curve obtained by means of TGA experiments of the amic acid (black), azeotropically imidized (red), allylated imidized (blue), deprotected and allylated monomer (grey) in the range from 100 to 800 °C at a heating rate of 5 °C min<sup>-1</sup> (top). CO<sub>2</sub> gas evolution peak analysis by means of TGA-FT-IR analysis (bottom)[268].

The DSC run of the azeotropically imidized homopolymerized Co-Allyl100PI is shown. It shows a nearly identical heat flow compared to Allyl100PI. Accordingly, showing that the Claisen Rearrangement and crosslinking occur independently of the molecular size (Figure 72).

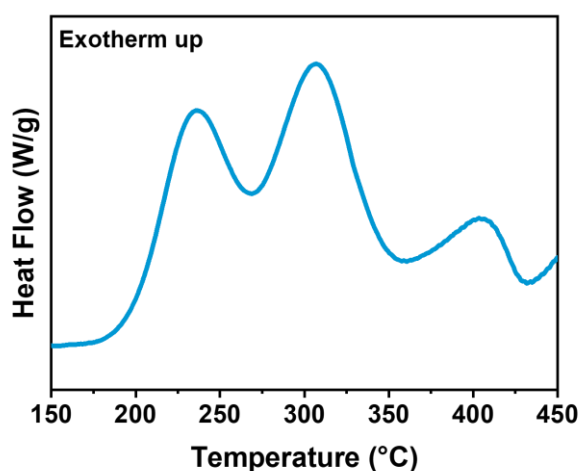


Figure 72. Heat flow curve of Allyl-PI-2 obtained by means of a DSC experiment in the temperature range from 100 to 400 °C with a heating rate of 5 °C min<sup>-1</sup> of the homopolymerized allylated-BisAPAF monomer to Co-Allyl100PI[268].

**TGA-Analysis.** In Figure 73 the mass loss curves of Co-Allyl10PI and Co-Allyl15PI for all three imidization methods are shown. The azeotropically imidized polymer shows two clear steps, with 360 °C TR<sub>onset</sub> and 390 and 400 °C TR<sub>peak</sub> temperature for the 10 and 15% allylated Co-Allyl-PI, respectively. The copolymerized poly (amic acid) shows, as expected, a previous weight loss step of 5%, beginning at 200 °C, corresponding to the cyclodehydration imidization process. The HPI-to-PBO conversion occurs as well but at higher temperatures

compared to the azeotropically imidized polymer. The chemically imidized material shows a weight loss onset at approximately 350°C with a broad weight loss.

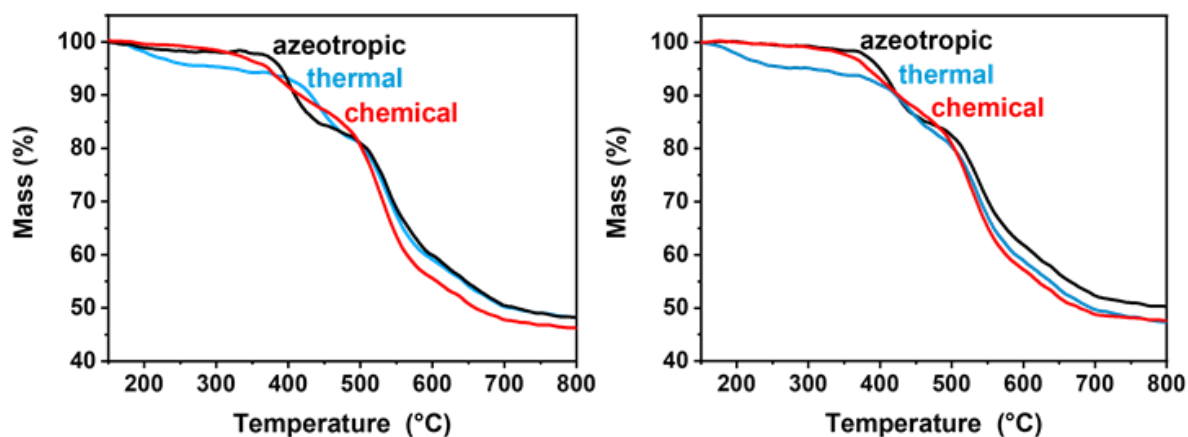


Figure 73. Mass loss curve obtained by means of TGA experiments of the copolymerized allylated polyimides with 10 (left) and 15% (right) of allylation, based on different imidization methods, such as azeotropic, chemical and thermal imidization in the range from 150 to 800 °C at a heating rate of 5 °C min<sup>-1</sup>[268].

Figure 74 shows the comparison the azeotropically imidized *post*-polymerization allylated polyimides and the HAB-allyl copolymerized and azeotropically imidized Co-Allyl-PI.

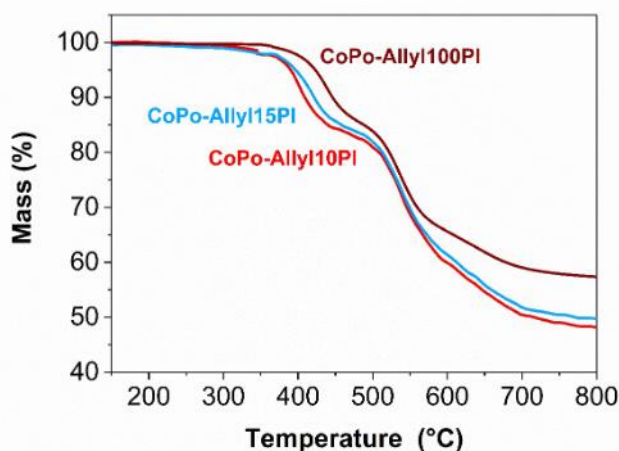


Figure 74. Mass loss curve obtained by means of TGA experiments of azeotropically imidized Co-polymers with 10, 15 and 100% allylation in the range from 100 to 800 °C at a heating rate of 5 °C min<sup>-1</sup>[268].

**In conclusion** the copolymerized allyloxy polyimides show a lower TR temperature for the 10 and 15% allyl containing polyimides compared to pristine 6FDA-HAB as well. The 100% allyl containing Co-Allyl100PI and Allyl100PI show nearly identical HPI-to-PBO cyclization reaction progress. However, the *post*-polymerization allylated polyimides show lower TR-onset temperatures for the PBO formation. The fact that the fully converted polymers (Allyl100PI and Co-Allyl100PI) show the same DSC and TGA profile, suggests that the route

has no significant effect on the thermochemical properties of homopolymers. Nevertheless, 10 and 15% allylated polyimides show strong differences, as they differ especially in the allyl group distribution. While co-polymers have only 2 or 0 allyl groups, whereas post-polymerization allylated polyimides can have also only one allyl group per repetition unit, and therefore in total more allyl group containing repetition units. If only one allyl group is present per repetition unit, the double amount of allyloxy group containing repetition units is present.

The result corroborates the idea, that the spacing effect and low degree of crosslinking in 10 and 15% allyloxy containing polyimides is responsible for the low  $TR_{\text{onset}}$  temperatures. In total the allyloxy spacer are more widely distributed supporting a better polymer chain packing disruption.

## **Film Properties**

**X-ray diffraction experiments** can be used to distinguish crystalline from amorphous materials based on the determined halo of the x-ray diffraction. From the peak position of the diffraction profile the average d-spacing can be calculated according to Bragg's equation. The d-spacing can be interpreted as the average distance between polymer chains and gives an idea of the chain packing. Highly chain disrupted polymer films have higher d-spacings. XRD measurements of the prepared polyimide films showed that the prepared polyimides are amorphous, and all materials show prior any thermal treatment a higher d-spacing with values above 0.6 nm compared to the unmodified 6FDA-HAB (0.55 nm), and are shown in Table 1. As a consequence of the allyl introduction, the spacing of polymer chains becomes evident, and with each introduced allyl group the number of hydrogen bonds decreases. The largest d-spacing is determined for Allyl60PI with 0.65 nm. Upon thermal treatment at 250 °C for 10 h, the d-spacing shows a linear relationship with respect to the degree of allylation. As the number of allyl groups and the crosslinking increases, the polymer chains cannot pack efficiently. Hence, the allyl-crosslinking causes a chain separation as proposed earlier as "chain-spacing effect".

Table 1. Overview of the TR conversion, density and *d*-spacing of the 350 °C (2 h) annealed allylated polyimides.

Allyl-PI	TR conversion (%)	Density (g cm <sup>3</sup> )	<i>d</i> -spacing (nm)
0	20.0	1.45	0.59
10	68.5	1.38	0.69
15	77.2	1.38	0.65
20	66.5	1.37	0.65
40	74.1	1.35	0.65
60	64.5	1.36	0.73
80	60.6	1.40	0.61
100	50.6	1.42	0.69

The allylated polymers showed, after annealing at 350 °C for 2 h, a broad halo. Among all materials, a narrow range of *d*-spacing values between 0.61 nm and 0.73 nm was determined. This means an increase with respect to the precursor materials and larger values and especially larger values compared to the pristine HPI. The pristine HPI showed an increase from 0.54 nm to 0.59 nm after 2 h at 350 °C. Moreover, a significant increase of 22% of the *d*-spacing occurred for the allylated material Allyl10PI (0.55 nm) compared to TR-Allyl10PBO (0.69 nm). The observed *d*-spacing *versus* degree of allylation trend correlates very well with the density evolution. The proposed crosslinking leads to a slight densification of the films after the curing step at 250 °C, as shown in Figure 75. Moreover, the increasing number of crosslinkers leads to a decrease of the density as the number of allyl units increases, which coincides with the increasing *d*-spacing values.

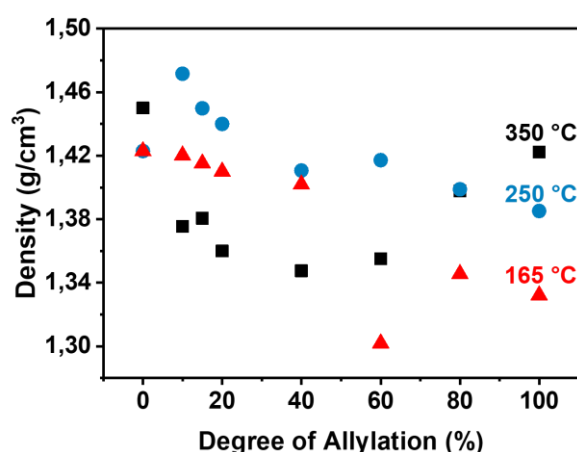


Figure 75. Density as a function of the degree of allylation for the films, annealed at 160 °C (red), 250 °C (blue), 350 °C (black)[268].

**Gas permeability.** Despite thermochemical advantages and achievements, the usability and improvement of the material towards gas separation tasks is a major application for

polyimides and especially thermally rearranged polymers. For that purpose, the herein presented materials were cast as thick films of average 50  $\mu\text{m}$ . The time-lag method to investigate the pure gas permeation properties is used in that case. The time-lag method uses a constant volume chamber before and after a membrane cell. The gas is released on the upstream side with a constant pressure and the downstream side pressure is determined. The time-lag between first contact of membrane and gas and the pressure increase on the downstream side can be used to calculate the diffusion coefficient of the investigated gas penetrant. Figure 76 shows the gas performance before any thermally induced reaction (165  $^{\circ}\text{C}$ , red) and after the described Claisen Rearrangement and Crosslinking (250  $^{\circ}\text{C}$ , blue). The permeability of  $\text{CO}_2$  shows no strong change for materials with less than 40% allyl groups. Nevertheless, the permeability increases linear with higher degrees of allylation. Interestingly, the treatment at 250  $^{\circ}\text{C}$  does not show a strong increase. Based on d-spacing and density experiments, an increase of the chain packing disruption with increasing number of allyl groups and crosslinks appears. Hence, space for the gas molecule to diffuse through the membrane increases as well, for which reason the diffusion and thus permeability increases. The materials composition does not change significantly, consequently a change of the solubility coefficient is not expected and not determined. On the other hand, the long isothermal treatment leads to proceeding relaxation of the polymer chains.

The same observation holds true for any other investigated gas. Especially the largest gas molecule,  $\text{CH}_4$ , does not show any strong differences in both cases.  $\text{H}_2$  in turn, shows a strong increase for the materials up to 20% of allylation and levels off until 80%. Treating the materials at 350  $^{\circ}\text{C}$  to induce the HPI-to-PBO conversion leads to a tremendous increase of the gas permeability for all gases. A strong linear increase until Allyl15PI can be observed and is attributed to the increasing PBO formation yield. Afterwards the permeability decreases for 20 and 40% of allylation and increases again, reaching the highest gas permeability of Allyl60PI among all tested materials. This is in agreement with the highest d-spacing (0.73 nm) and second lowest density next to Allyl40PI. Hence the large permeability is simply referred to the lowest chain packing among all materials, despite a 20% lower HPI-to-PBO conversion compared to Allyl15PI. An explanation for that observation could be the increased number of crosslinking allyl groups, but still lower crosslinking density compared to 80 and 100% of allylation.

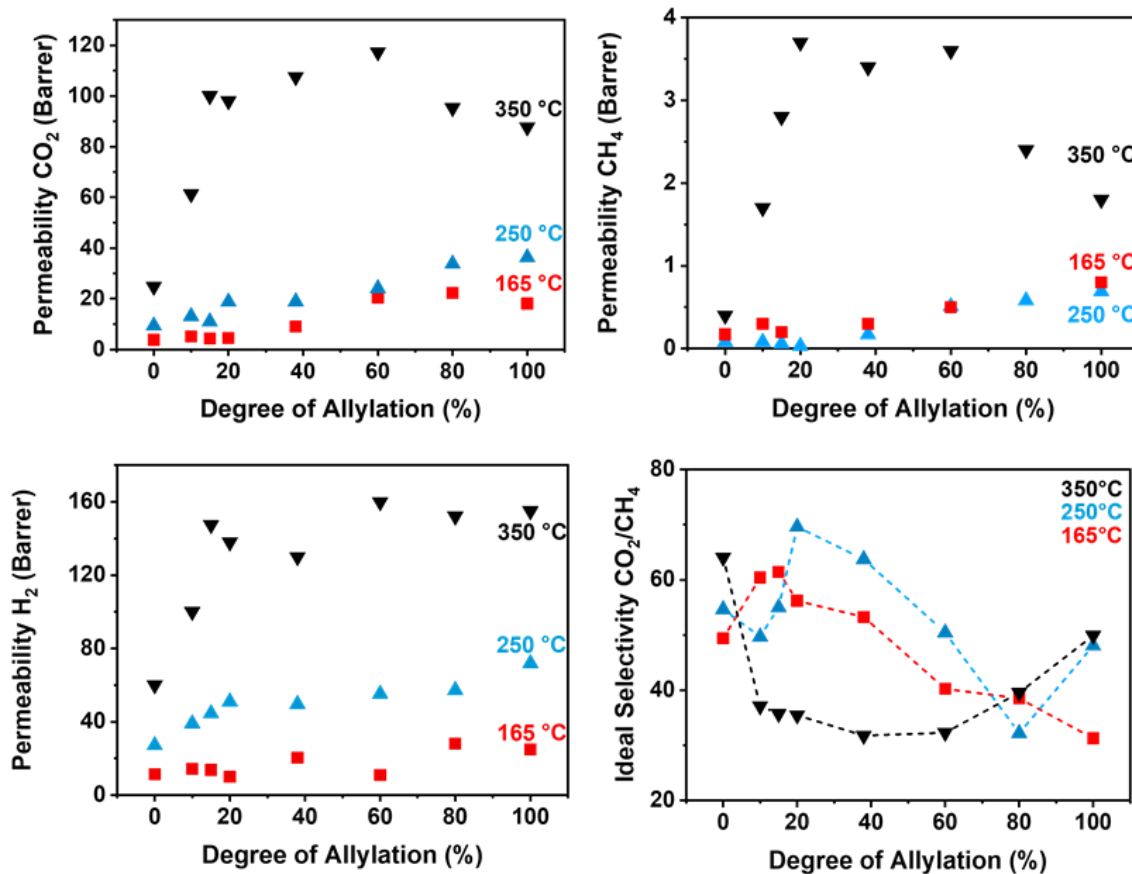


Figure 76. Permeability of CO<sub>2</sub> (top, left), CH<sub>4</sub> (top, right), H<sub>2</sub> (bottom, left) and ideal selectivity of CO<sub>2</sub> vs. CH<sub>4</sub> (bottom, right) as a function of the degree of allylation for materials annealed at 165 °C (red, ■), 250 °C (blue, ▲) and 350 °C (black, ▼)[268].

Another very important key factor when it comes to gas separation is its gas pair selectivity. One of the most important applications is the gas separation of CO<sub>2</sub> and CH<sub>4</sub>, such as in natural gas. Comparing the ideal selectivity for CO<sub>2</sub>/CH<sub>4</sub> among all 3 temperature treatments in Figure 77, show for 165 and 250 °C annealing an increase until 15 and 20%, respectively. Afterwards the selectivity decreases gradually. Based on the determined diffusion coefficients of both gases and the observation that H<sub>2</sub> permeate increases until 20% and levels off, suggests that below 20% smaller pores are formed, that are more permeable for H<sub>2</sub>, but also more for the smaller and more soluble CO<sub>2</sub> compared to CH<sub>4</sub>. An explanation is the formation of tighter areas in which the allyl density is low and more open areas in which the allyl groups are more prominent. As a consequence, small and rare pore channels are formed, which are therefore more permeable for gases with a smaller kinetic gas diameter.

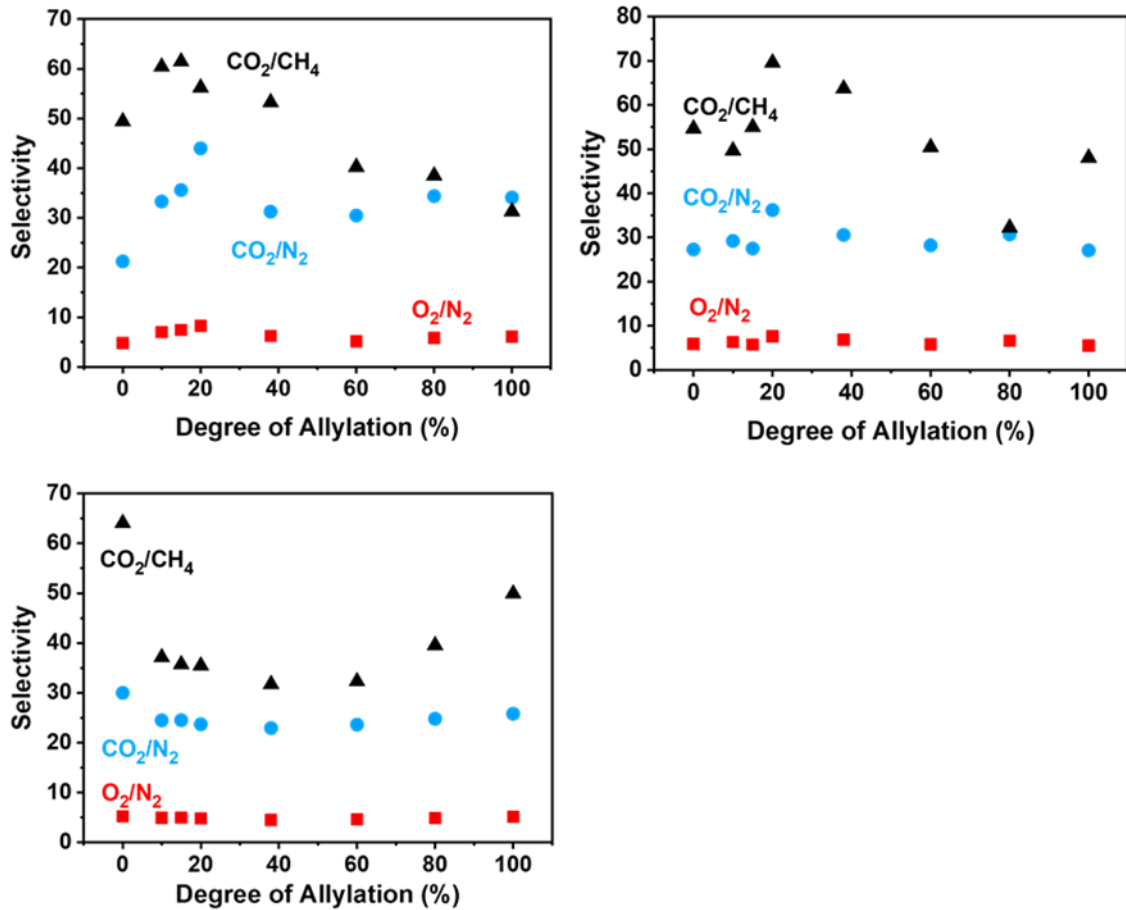


Figure 77. Ideal selectivity as a function of the degree of allylation for different gas pairs CO<sub>2</sub>/CH<sub>4</sub> (black, ▲), CO<sub>2</sub>/N<sub>2</sub> (blue, ●) and O<sub>2</sub>/N<sub>2</sub> (red, ■) after annealing at (a) 165 °C, (b) 250 °C and (c) 350 °C [268].

The prepared materials showed a strong increase of the gas performance properties as demonstrated by the presentation using a n upper bound plot (Figure 78). Most reported TR polymers are annealed at 400 and even 450 °C [139-142, 144, 145, 148, 152, 261, 263], causing polymer degradation and therefore very brittle materials. In this study materials such as Allyl100PI required only 350 °C for a close 2008 upper bound performance. With Allyl15PI a material was presented, which needs only 250 °C



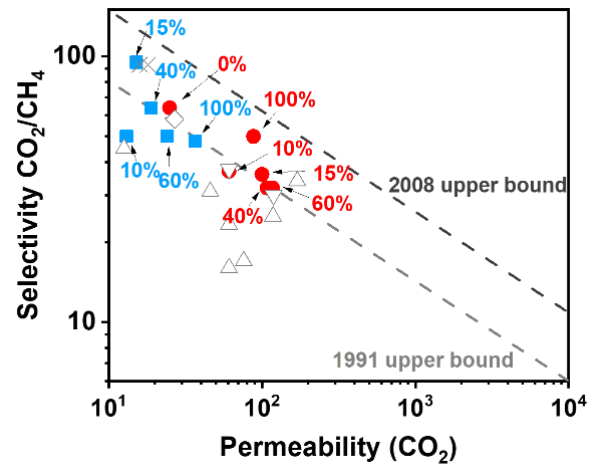


Figure 78. Upper bound plot for  $\text{CO}_2/\text{CH}_4$  with materials of this study after annealing at 250 °C (blue, ■) and 350 °C (red, ●)[268].

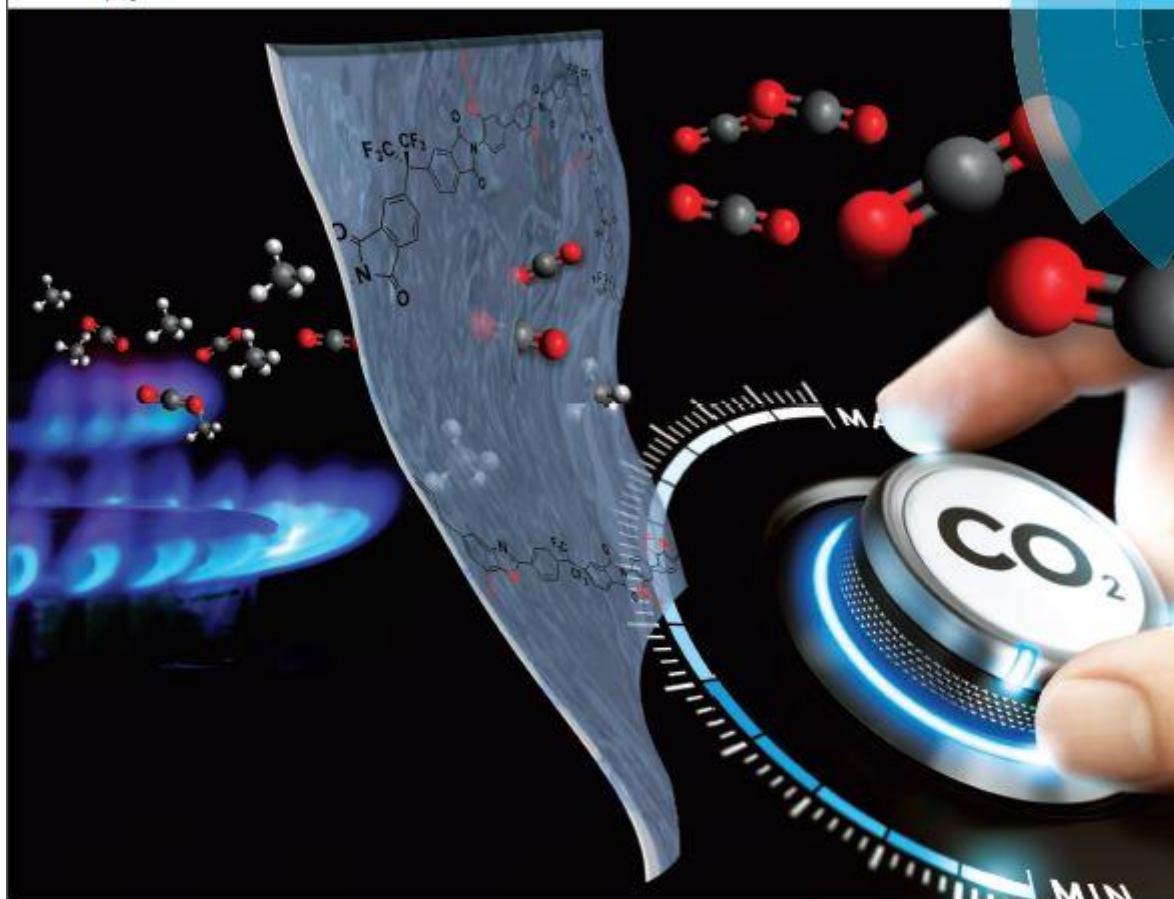
## Key Messages

- Summarizing the key facts of this chapter, a comprehensive thermochemical and film property characterizing study was performed by investigating a set of allylated polymers with different degrees of allylation of the phenolic group in pristine 6FDA-HAB.
- The theory that an intermediate phenolate formation after the allyl group migration during the Claisen Rearrangement process is responsible for the lowered TR temperature, as a consequence of the increased negative charge on the oxygen and therefore a higher nucleophilicity, was shown to be less likely as the fully converted material did not show the lowest TR onset and peak temperature. If the phenolate formation had been responsible, it would have been expected to see a linear decrease of the TR temperature with increasing degree of allylation.
- Beyond that, based on thermophysical experiments, such as DSC and TG-IR combined with solid-state spectroscopic characterizations, the presence of three thermally induced reactions in allylated *ortho*-hydroxy polyimides has been shown. Starting with the widely describe Claisen Rearrangement, the rearranged allyl groups crosslink forming crosslinks that inhibit the polymer chains to pack efficiently.
- At higher crosslinking degrees, as determined by means of swelling and gel-fraction experiments, the mobility of the polymer chains is too restricted to undergo the HPI-to-PBO formation easily which results in an increased TR temperature. As a consequence, the lowest TR temperature is determined with only 15% of allylation and a similar relationship is also shown for allylated 6FDA-BisAPAF as well.

- Studies of allylated monomer, which has been polymerized afterwards, have shown, that fully converted polymers show the same thermochemical behavior with similar  $TR_{\text{onset}}$  and  $TR_{\text{peak}}$  temperatures, showing that the synthesis route has nearly no effect on the thermochemical properties. However, in the case of 10 and 15% allylated polyimides the  $TR_{\text{onset}}$  is higher compared to the post-polymerization allylated Polymers with the same degree of allylation. Hence the distribution of allyl groups along the polymer chains is of utmost importance. While post-polymerization modified materials show randomly distributed allyl groups with repetition units carrying 0,1 or 2 allyl groups, in the copolymerized polyimides, repetition units carry 2 or no allyl group. Hence, the allyl groups are less widely distributed, leading to more concentrated allyl areas, which is why more pristine repetition units are present, that can undergo hydrogen bond formation more easily and therefore reduce the molecular mobility.
- Based on these findings, another relationship was formulated to be responsible for the observed TR temperatures. Allyl groups can act as spacer reducing the polymer chain packing efficiency, leading to more mobility which is reported to be mainly responsible for the TR initiation. As the number of allyl groups increases, the crosslinking density increases, and the material becomes more restricted. Hence low degrees of allylation lead to chain packing disruptors and increases the possibility to thermally rearrange. Therefore, chain spacer that do not significantly block pores, but disrupt chain packing and enable the regeneration of the TR required OH group is proposed as a very promising strategy to lower the TR temperature, while improving the gas performance at the same time in contrast to other methods such as using more flexible backbones.

# Polymer Chemistry

rsc.li/polymers



ISSN 1759-9962



PAPER  
Volkan Filiz, Volker Abietz *et al.*  
Thermal rearrangement of *ortho*-allyloxypolyimide membranes and the effect of the degree of functionalization

The results of the previous chapter were published in RSC Polymer Chemistry

(DOI: 10.1039/C8PY00530C (Paper) Polym. Chem., 2018, 9, 3987-3999). [268]

## Effect of Allyl Derivatives in Thermal Cascade Reactions

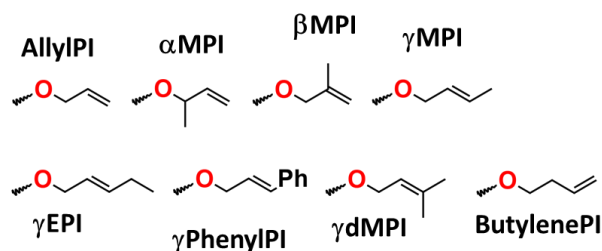
From previously discussed results in chapter *Polyimides with Ortho-Allyloxy Groups*, the main conclusion was to introduce spacer that are linked to the backbone, leading to more freedom to rotate due to inefficient chain packing, as it appears from this and recent studies by Calle *et al.* [139] and Guo *et al.*[138], that improved mobility of the backbone might lower the  $TR_{\text{onset}}$  temperature. Also crosslinking appears to be beneficial, especially for the separation of hydrogen, as long as the degree of crosslinking remains low. This led to the idea, that the substitution of one or more of the three carbon atoms along the allyl group, namely  $C\alpha$ - $C\gamma$ , could be a promising strategy to control the degree of crosslinking. Since a fully converted polyimide is more straight forward to reproduce and to scale-up, as we have seen that the degree of allylation can vary by using different backbones as their solubility, and reactivity is different as well. Introducing a modified allyl group can have a more pronounced impact on the mobility, as long as the degree of crosslinking is lower compared to plain allyl. Therefore, the increased degree of mobility due to the removal of any phenol bound hydrogen group and the increased spacing between polymer chains will not be overcompensated by crosslinking induced mobility restrictions. The study of the TR process of unmodified polyimides has shown that better stabilization of the intermediates and reactants might increase the relative Gibbs free energy with respect to the stabilized units. The idea is to introduce an allyl group with sterically hindered double bonds after the Claisen Rearrangement, inspired by the lower reactivity of methacrylate compared to acrylate[284] and lower reactivity of methylated dienophiles towards Diels-Alder reactions [194]. Moreover, in order to understand the underlying mechanism of each derivative and to get more information towards the lowered  $TR_{\text{onset}}$  temperature of allylated polyimides and to refine the mechanism and the effect of each mechanism, molecular dynamics and density-functional theory simulations were employed combined with a comprehensive thermokinetic analysis of the formed derivatives.

### Synthesis and characterization of modified precursor polyimides.

The following investigations were performed using 6FDA-BisAPAF as the pristine *ortho*-hydroxy polyimide precursor. 6FDA-APAF has a high glass transition temperature of 313 °C[139] compared to other backbones [139]. Beyond that, 6FDA-APAF is widely described as a promising TRP precursor in terms of gas separation membrane candidate [152]. However,

6FDA-HAB is often favored due to its higher molecular weight by means of the conventional two-step polycondensation method. Nevertheless, with the improved synthetic procedure for TRPs, the preparation of a high-molecular weight precursor was no limitation (see section *Synthesis*). A set of nine *ortho*-allyl derivative modified *ortho*-hydroxy polyimides were synthesized by means of a post-polymerization allylation using the Williamson-Ether synthesis approach (see Scheme 50 on page 389).

The conversion of the hydroxy groups to their ether modification, as shown in Scheme 50, was confirmed by <sup>1</sup>H-NMR and FT-IR spectroscopy (Figure 79 and Figure 80). In all cases the hydroxy peak at 10.4 ppm disappeared due to the complete conversion, whereas new vinylic, allylic and alkylic peaks appeared and were assigned to the corresponding allyl derivative structure (see single spectra Figure 264 - Figure 274 in *Appendix Allyl derivate*). The materials are designated as XY-PI, with X as  $\alpha$ ,  $\beta$ ,  $\gamma$  describing the position of the methyl group along the allyl (propene) chain and Y refers to M or E for a methyl or ethyl group, respectively (see Scheme 1).



Scheme 2. Synthesized allyl derivatives.

Using 3-Bromo-2-methylpropene for instance yields the  $\beta$ M-PI. The NMR spectrum of the fully converted  $\beta$ M-PI shows new peaks at 4.5 and 5 ppm, which were assigned to the vinylic protons and allylic protons. In addition, the FT-IR spectra show new peaks in the range between 2800 and 3100  $\text{cm}^{-1}$ , corresponding to the alkylic and vinylic bonds of the allyl derivative.

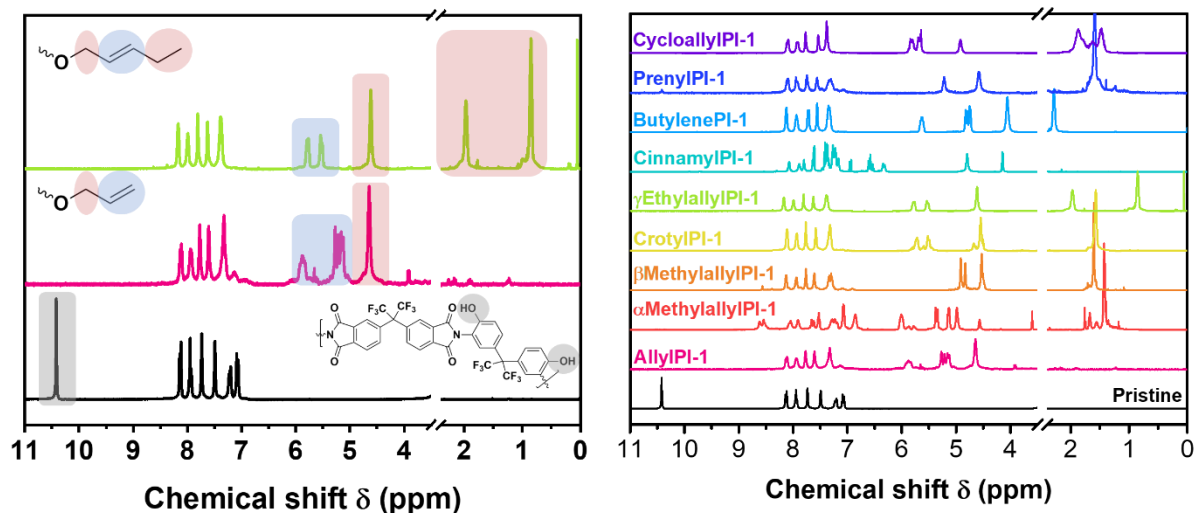


Figure 79. Stacked  $^1\text{H-NMR}$  spectra and allyloxy-group peak assignment for the pristine (black), allyl (pink) and  $\gamma$ Eallyloxy (green) polyimide (left).  $^1\text{H-NMR}$  Spectra of the synthesized polymers (right).

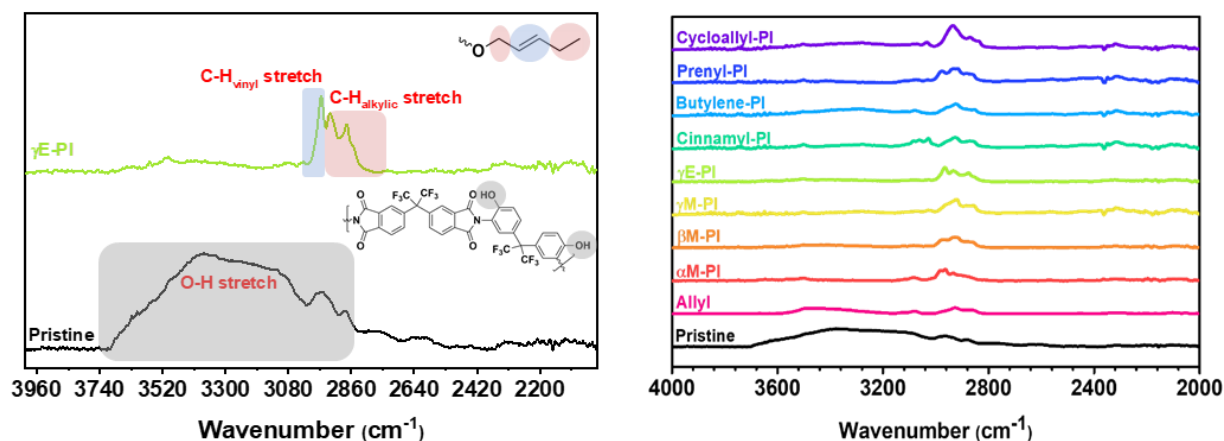
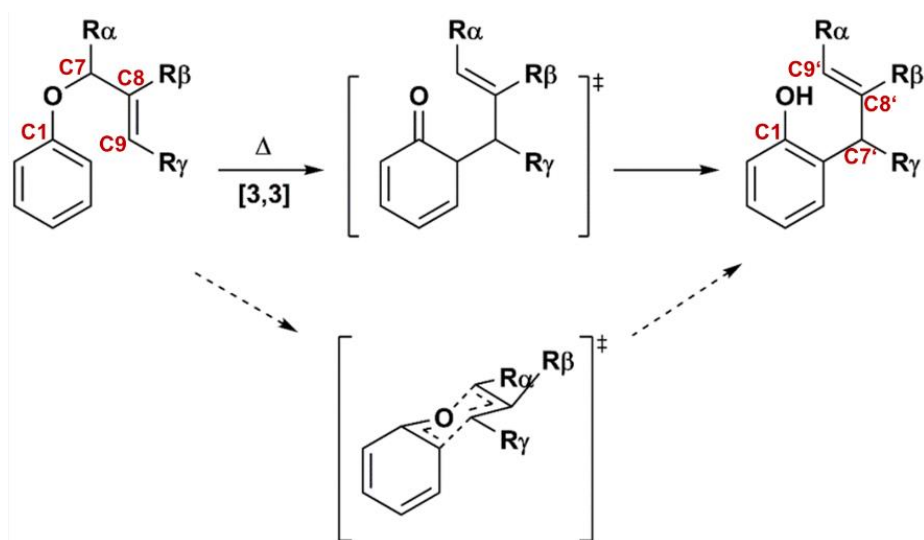


Figure 80. FT-IR Spectra of the synthesized polymers for the pristine (black) and  $\gamma$ Eallyloxy (green) polyimide (left). FT-IR Spectra of the synthesized polymers (right).

## Thermokinetic and -dynamic analysis.

The phenyl allyl ether group (PAG) is widely known to undergo an aromatic Claisen Rearrangement (CR) [203, 204]. However, apart from Claisen Rearrangement (CR) and crosslinking (Cx), a few studies have discussed a cyclization reaction (Cy), forming a tetrahydro benzofuran, and Cope Rearrangement (CoR) as well. The thermally induced reactions of the synthesized polyimide precursor, including the HPI-to-PBO cyclization (TR) were investigated employing thermokinetic and -dynamic analytics by means of DSC and TG-

IR. Aromatic phenyl allyloxy derivatives with a methyl group in  $\alpha$ ,  $\beta$ , and  $\gamma$ -position or an ethyl- or phenyl- group in  $\gamma$ -position were reported to undergo Claisen Rearrangement [285]. Nevertheless, both derivatives with a geminal methyl or an ethyl group in  $\gamma$ -position were reported to undergo a normal as well as a so-called abnormal aromatic Claisen Rearrangement [285]. The pericyclic Claisen Rearrangement mechanism and its corresponding substituent inversion is shown in Figure 39. It is noteworthy, that only in  $\beta$ -position (C8) substituted groups remain in the same position (C8') after the CR, while substituents change from C9 to C7', and C7 to C9', respectively.



Scheme 3. Claisen Rearrangement Mechanism, including its proposed six-membered transition state and the possible inversion of substituents in C7 and C9.

**DSC measurements** were used to investigate the heat flow between 50 and 450 °C of the allyl,  $\alpha$ - $\beta$ -,  $\gamma$ M-, as well as the  $\gamma$ E- and  $\gamma$ Phenyl-PI containing polyimides to investigate possible reactions and their extent (Figure 81). A very distinctive exothermic peak in the temperature range between 150 and 250 °C with a maximum around 240 °C can be seen for all derivatives, followed by a second exothermic maximum of variable intensity. In addition, no mass loss in the temperature range of both exothermic reactions can be observed (Figure 81), which corroborates the assumption, that these exothermic reactions might be assigned to an atom efficient rearrangement, isomerization or addition reaction [238, 268, 269, 286]. Just as observed for the allylated 6FDA-HAB in Figure 60 on page 109, the onset of subsequent peaks overlaps with the offset of precedent peaks, for which reason their process onsets cannot be



determined accurately. To distinguish the overlapping consecutive reactions for a better understanding of the reaction mechanism and the relationship of each reaction to each other, a peak deconvolution was performed after subtraction of the baseline and fitting by a gauss function.

*In all cases the deconvoluted peaks overlap, but not their onsets, which means that a full conversion of first peaks attributed reaction is not required for the consecutive reactions. Therefore, it is assumed that every formed product of the previous process is capable to initiate another reaction, hence proposing that the sequence of reactions for the materials are forming a reaction cascade.*

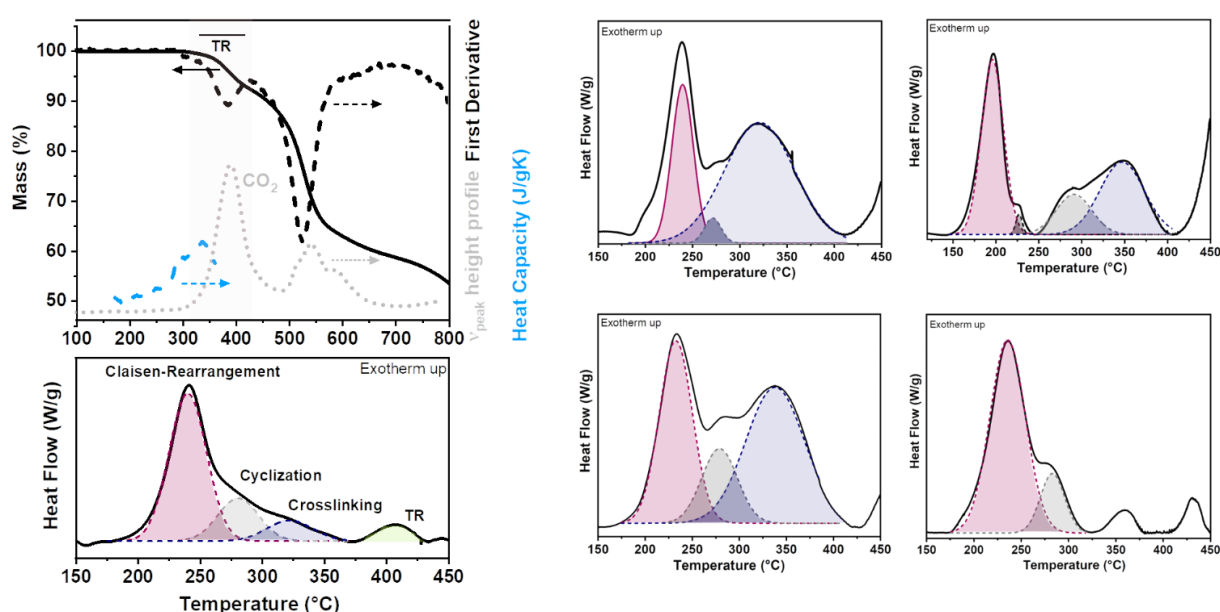


Figure 81. Heat flow curve obtained by means of DSC experiments in the temperature range from 150 to 450 °C with a heating rate of 5 °C min<sup>-1</sup> of the prepared polyimides with an allyl-,  $\alpha$ M-,  $\beta$ M-,  $\gamma$ M-,  $\gamma$ E- and  $\gamma$ Phenyl-modification (black) and their corresponding deconvoluted peaks with respect to the proposed processes Claisen Rearrangement (red), cyclization (grey), crosslinking (blue)

**The first process** is assigned to a Claisen Rearrangement CR as described before. This was proven by means of isothermal treatments at the onset temperature of the first exothermic peak and monitored by NMR measurements as shown in Figure 265.

The hydroxy peak at around 10.4 ppm is recovered, while a decrease of the number of aromatic protons of the diamine unit was determined, using aromatic anhydride protons as a reference. Despite that, no quantitative conversion to a soluble CR-product was observed. Applying shorter isotherms are not sufficient enough to promote a complete thermal Claisen

RearrangementCR, while longer isothermal treatments at the onset temperature already led to insoluble materials, mostly due to allyl crosslinking of formed C-allyl groups, but possibly also by not-rearranged O-allyl groups [268]. Cope Rearrangement is not possible due to a blocked *para*-position in 6FDA-BisAPAF based systems. However, partially cyclized units were detected by the executed isothermal treatments as well (Figure 279).

**The second and third process** (exothermic heat flow peaks) varies in their intensities and positions. For instance,  $\beta$ M-PI shows weak shoulders appearing as a broad run-off, while  $\gamma$ E shows a shoulder following the CR and following two isolated small exothermic peaks. Deconvoluted peaks revealed, that the second peak (grey) occurs between 250 and 300 °C and is more developed for  $\gamma$ M- and  $\beta$ M-PI compared to Allyl-PI. The grey peaks of  $\beta$ M- and  $\gamma$ E-PI show a more pronounced peak area compared to the third process peak (blue), whereas all other materials show a more distinct third peak area compared to the second peak area, in turn. In all cases, no mass loss occurs in the range of the first three exothermic peaks (Figure 81 and Figure 88). Therefore, it is assumed, that all reactions in the investigated allyl derivatives are atom efficient reactions, such as isomerization, rearrangement, or addition reactions.

Allyl,  $\gamma$ M and  $\alpha$ M in turn show a low area for the second peak (grey) compared to a significantly strong developed third peak (blue). The third exotherm can be easily seen without fitting. However, while the first and second peak show a narrow range from on to offset of about 100 °C, the third peak shows a fairly broad distribution of up to 150 °C in the range from 250 to 400 °C.  $\beta$ M and  $\gamma$ E in turn show significantly smaller ranges for the third process. In case of  $\beta$ M-PI only from 270 to 350 °C. These two processes are assigned to benzofuran formation and crosslinking, based on the observation of cyclized units in the NMR of soluble parts, while in all cases insoluble but swollen parts were detected corroborating crosslinking. To corroborate the suggested tendencies, solid state NMR experiments were conducted at annealing temperatures readily below the HPI-to-PBO formation onset.

The  $^{13}\text{C}$ -CP-MAS spectra shows the expected aromatic region in the range from 110 to 140 ppm and the carbon atoms **g** and **n**, which are assigned to the quaternary hexafluoroisopropylidene group. Peaks **g** and **n** do not change among different derivatives (Figure 82). In addition, a new peak ( $\beta$ ) arises between 80 to 90 ppm and is assigned to the  $\beta$ -carbon atom of the cyclized furan

product. Comparing all spectra reveal, that the peak evolution for the furan unit is significantly enhanced in case of  $\beta$ M-PI.  $\gamma$ M and  $\gamma$ E show small peaks, while  $\alpha$ M- and Allyl-PI shown no peak. The furan ring contains a  $\gamma$ -C atom which can be seen at 50 ppm and the methyl group at 110 ppm. Both peaks show the same trend as observed for the  $\beta$ -C peak. The solid-state carbon NMR spectrum just proved the findings of the liquid-NMR experiments (Figure 279) and heat flow measurement peak deconvolution. The NMR results were supported by FT-IR measurements of the same sample (Figure 83 and Figure 84).

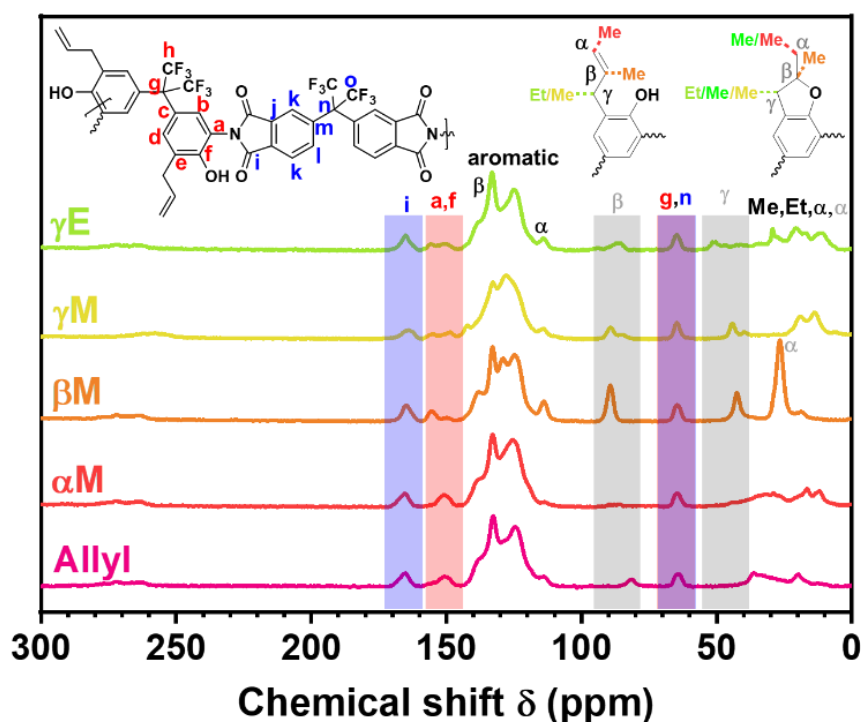


Figure 82.  $^{13}\text{C}$ -CP-MAS solid state NMR spectra of the prepared polyimides with an allyl-,  $\alpha$ M-,  $\beta$ M-,  $\gamma$ M-,  $\gamma$ E-modification after a thermal treatment at a temperature  $10^\circ\text{C}$  prior to the TRonset temperature for 10 min. Peaks are assigned to Cy- and CR-product.

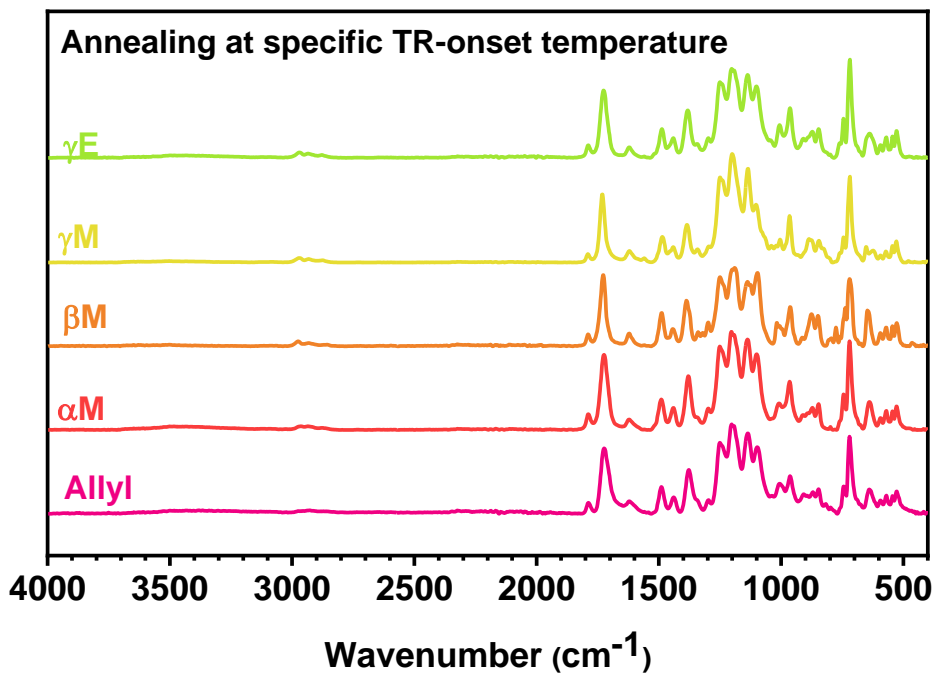


Figure 83. FT-IR spectra of the investigated Allyl-,  $\alpha$ M-,  $\beta$ M-,  $\gamma$ M-,  $\gamma$ E-PI after annealing at the TR onset temperature for 10 min.

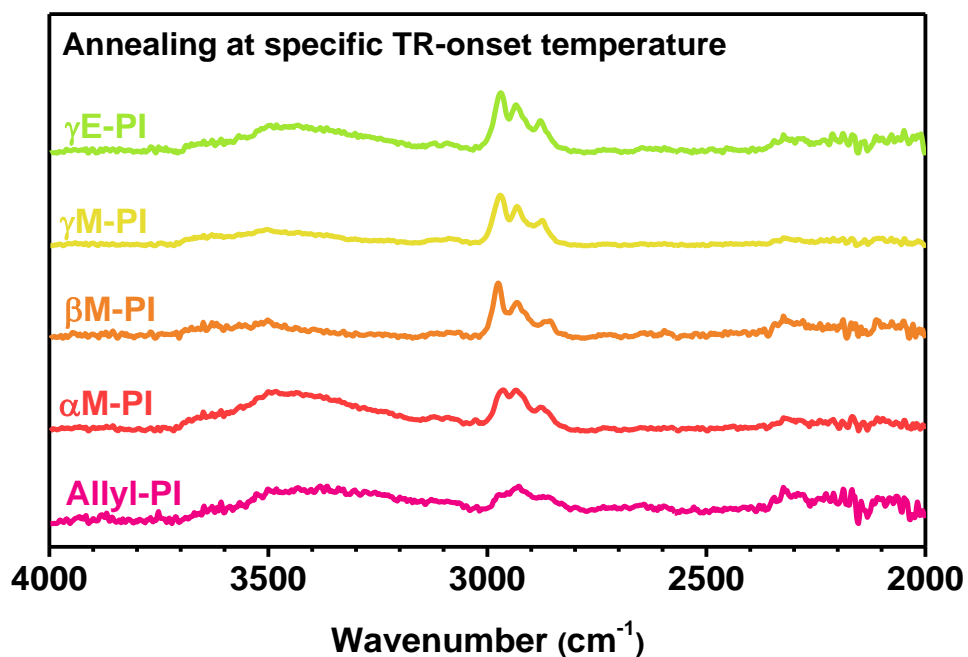


Figure 84. FT-IR spectra of the investigated Allyl-PI,  $\alpha$ M-PI,  $\beta$ M-PI,  $\gamma$ M-PI,  $\gamma$ E-PI after annealing at the TR onset temperature for 10 min.

Isothermal treatments show that the materials are highly insoluble and gel-fractions of more than 90% after annealing below 300 °C. The increasing gel-fraction with respect to the treatment temperature is shown in Figure 44. Gel-fraction measurements of Allyl- and  $\gamma$ M-PI

show higher gel-fractions after each annealing step compared to the  $\beta$ M- and  $\gamma$ E-substituted allyl modification, and both, Allyl- and  $\gamma$ M-PI surpassed 80% at 230 °C (Figure 85).

This observation coincides with the tendency of the evolution of the third peak. Allyl,  $\alpha$ M and  $\gamma$ M show the more pronounced third peak (corresponding to crosslinking).  $\beta$ M and  $\gamma$ E show a more distinctive second peak (cyclization) and small third peak and hence a lower gel fraction. The higher gel fraction ratio is explained by the lower amount of cyclized benzofuran units in allyl and  $\gamma$ M-PI. Cyclized units can not readily crosslink, as they lack a reactive group towards crosslinking. Moreover, they have sterically unhindered double bonds.

*Consequently, materials with free unsubstituted double bonds appear to crosslink more readily, compared substituted modifications, such as  $\alpha$ M and  $\beta$ M. Even though the normal Claisen product of  $\gamma$ E has free double bonds, the amount of crosslinking is decreased, since there is also a ratio of the abnormal Claisen product  $\gamma$ Ea, having a methyl group in  $\alpha$ - and  $\gamma$ -position.*

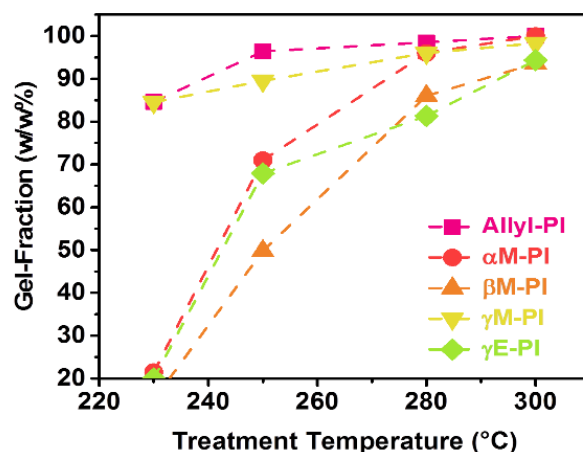


Figure 85. Gel-fraction of the thermally treated polyimide films of Allyl-,  $\alpha$ M-,  $\beta$ M-,  $\gamma$ M-,  $\gamma$ E-PI.

**In conclusion**, the *post*-CR reactions, such as cyclization and crosslinking, depend strongly on the allyl-modification. Any allyl modification, which lacks a substituent in  $\beta$ '- or  $\gamma$ '- position after the CR, show a distinctively separated exothermic peak pattern in the DSC of similar profile (two strong peaks, separated by a weak peak). In all of these cases, the cyclization of the *ortho*-allyl phenol unit to a benzofuran is much lower compared to  $\beta$ M-PI (supported by spectroscopic measurements). As a consequence, these materials show significant higher gel fractions.

**Non-CR Allyl Derivatives.** Among all prepared materials, three additionally prepared materials have not been discussed yet. Cycloallyl, which is a cyclohexenyl phenyl ether,  $\gamma$ dM-PI which is also known as prenyl and Butylene-PI, which has an additional methylene group. The first two are reported to undergo CR by catalysis [225]. Reports about butylene phenyl ether are not available. Cycloallyl- and  $\gamma$ dM-PI lose their modification around 250 °C by decomposition to the pristine HPI and cyclohexene or isoprene, respectively. This has been confirmed by mass loss evaluation of the released decomposition products (Figure 86). The weight loss step around 250 °C is in the range of the molecular weight of the modifications. Both, the IR-spectroscopy detected decomposition products analysis and the calculated mass loss suggest, that no other extrusion reaction occurs. Isothermal annealing at 250 °C for 30 min yielded soluble materials, identical to the pristine 6FDA-APAF. Butylene does not undergo a CR either, but also no other reactions were observed until its decomposition around 315 °C. Butylene-PI was still soluble after 30 min at 250 and 280 °C. Accordingly, the vinyl group does not undergo crosslinking at temperatures up to 280 °C.

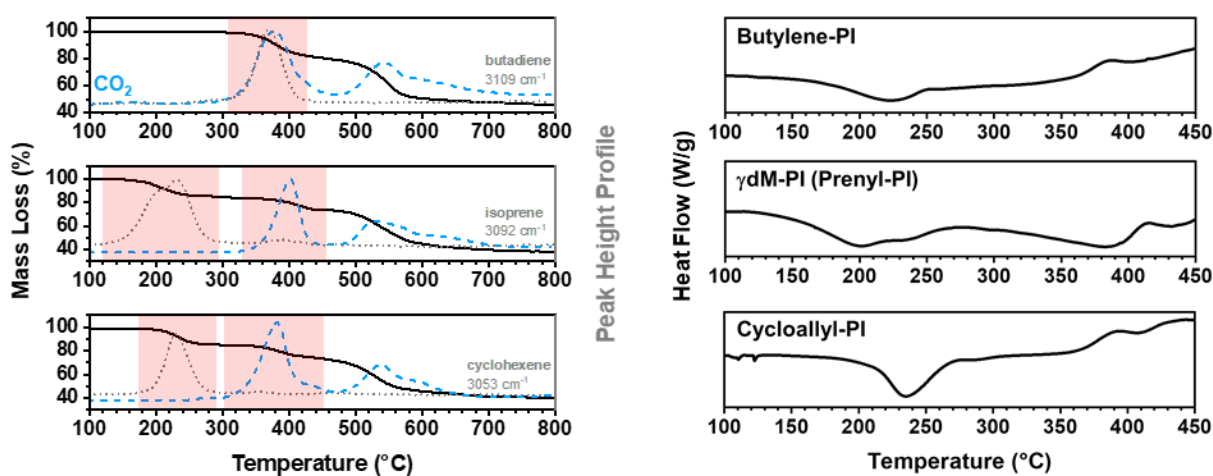


Figure 86. Mass loss curve obtained by means of TGA experiments of Butylene-PI, Prenyl-PI and Cycloallyl-PI in the range from 100 to 800 °C at a heating rate of 5 °C min<sup>-1</sup> including CO<sub>2</sub> gas evolution peak analysis (left). Corresponding Heat flow curves obtained by means of DSC experiments in the temperature range from 100 to 450 °C with a heating rate of 5 °C min<sup>-1</sup> (right).

## Thermokinetic investigation

Thermokinetic investigations based on non-isothermal model-free methods can be used to calculate the activation energy of heat rate sensitive reactions at different conversions. Despite that, the physical meaning of the calculated activation energy is widely discussed, its course can indicate changes of the reaction type, while its value can be used to categorize the type of

reaction better. In addition, the change of conversion rate helps to understand and visualize reaction rate changes. Therefore, such non-isothermal *isoconversional* methods were used to support the recently demonstrated results and the cascade reaction type. The applied methods are described in detail in chapter *Thermoanalytics* on page 401. Experimentally, DSC runs in the range of 180 to 375 °C were performed at different heating rates, 1, 2, 5, 10 and 20 °C min<sup>-1</sup>. The normalized and integrated heat flow curves were used to determine the overall conversion *versus* temperature ( $\alpha$ -T) (Figure 87). In all cases, the modifications show kind of a double sigmoidal curve profile. All five materials show nearly identical  $\alpha$ -T profiles within 0 and 40% of conversion. This observation can be explained, since all materials undergo initially a CR-process and show a very similar and symmetric peak. Such an indication is in common with the understanding of the reaction cascade initiation via recovery of the phenol group without losing the terminal double bond of the allyl group.

$\beta$ M-PI and  $\gamma$ E-PI have their maximum conversion rate at 45% of the global conversion, which is reached at the peak temperature of the first peak (240 °C).  $\gamma$ M reaches its maximum rate at a conversion of 25%, while  $\alpha$ M-PI follows at 29% and Allyl-PI at 38% conversion. Nevertheless,  $\alpha$ M-PI shows a CR peak temperature at a significantly lower temperature and its conversion rate increases fast at the beginning and nearly levels off at a conversion of 40%, whereas Allyl-,  $\beta$ M- and  $\gamma$ E-PI do not show such a conversion plateau.

$\gamma$ E-PI shows a post-CR abnormal CR reaction, but low tendency to cyclize and crosslink, while  $\beta$ M-PI shows a strong tendency to cyclize, but low crosslinking as well. Therefore, after the CR process of an allyloxy group is completed, the reaction cascade continues with consecutive reactions.  $\alpha$ M-PI shows a broad plateau compared to other materials. This is a consequence of the rapid increase of the CR conversion. Since subsequent reactions require higher temperatures than the CR process, the CR is completed before any consecutive reaction can even start, as clearly seen in the heat flow proceeding (DSC).

Arrhenius activation energy ( $E_A$ ) was determined for further discussion by means of *isoconversional* methods. All investigated materials show a slight decrease of the activation energy until 40% conversion. Allyl- and  $\gamma$ M-PI show an average activation energy of 120.5 and 118.6 kJ/mol, respectively.  $\beta$ M- and  $\gamma$ E-PI have activation energies of 156.0 and 176.9 kJ/mol. The higher activation energies are attributed to the overlapping processes, abnormal CR, and

cyclization, which contribute to the global activation energy within 10 to 40% conversion as well, while Allyl- and  $\gamma$ M-PI show mainly CR and crosslinking.

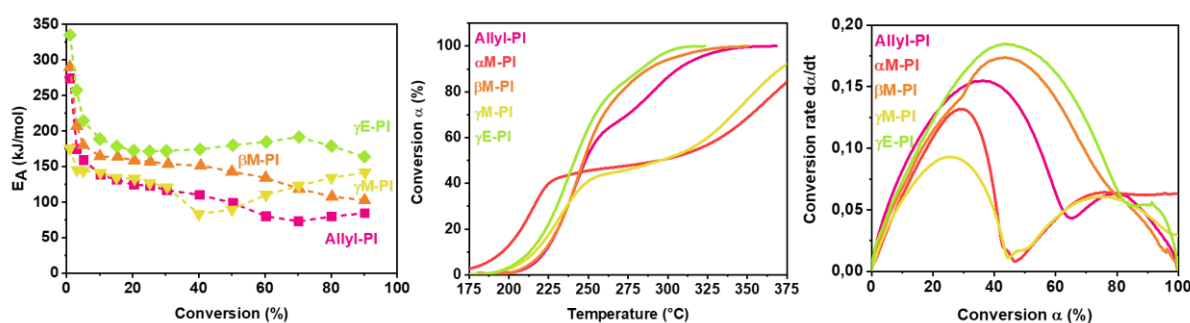


Figure 87. Conversion - temperature relationship with respect to the global process (left), conversion rate as a function of the conversion (middle) and course of the activation energy as a function of the global conversion based on the Kissinger method (right).

### Thermal Rearrangement (TR)

The required temperature to start the TR-process is reported to be lowered by using more flexible polyimide precursor with lower glass transition temperatures. However, the results of the investigation of the effect of the degree of allylation in chapter *Polyimides with Ortho-Allyloxy Groups* demonstrated that lower TR temperatures can be achieved by incorporating spacer at low degrees of crosslinking. The idea of adding a spacer was recently investigated by Japip *et al.* using ZIF-8 MOFs [255] as polymer chain spacer to lower the  $TR_{onset}$ .

Allyl groups are very likely to crosslink at higher temperatures [268]. The open task to answer is how the subsequent reactions, cyclization, and crosslinking, but also the type of crosslink and benzofuran cycle might have an impact on the TR temperature. Different allyl modifications not only have different tendencies to crosslink, but they also form crosslinks with substituents, that affect the flexibility of the crosslinked chain. Principally, if an hexene crosslink is formed, it is very flexible due to the methylene groups. However, if  $\gamma$ Ea-PI crosslinks the same way, there are four methyl groups along the hexene chain. Accordingly, such a substitution hinders free rotation of the methylene groups and reduce the flexibility of the whole phenolic unit.

**TGA-FT-IR Analysis.** The mass loss curves showed significant differences with respect to the  $TR_{onset}$ , -peak and -temperature range  $\Delta TR$  of all polyimides (see Table 2). Both  $\gamma$ -substituted materials  $\gamma$ M- and  $\gamma$ Phenyl-PI have the highest  $TR_{peak}$  of 413 and 423 °C, and  $TR_{onset}$  at 352 and 348 °C, respectively (see Figure 88, Figure 89). Despite that, both materials still have lower



$TR_{onset}$  and  $-peak$  temperatures compared to the pristine material 6FDA-BisAPAF.  $\gamma E$ -PI in turn is even up to 40 °C lower, having its  $TR$ -peak temperature at 359 °C, followed by  $\beta M$ -PI with 385 °C. Such a low  $TR_{onset}$  and  $TR_{peak}$  leads correspondingly to higher PBO conversions when isothermally heated (Table 2).

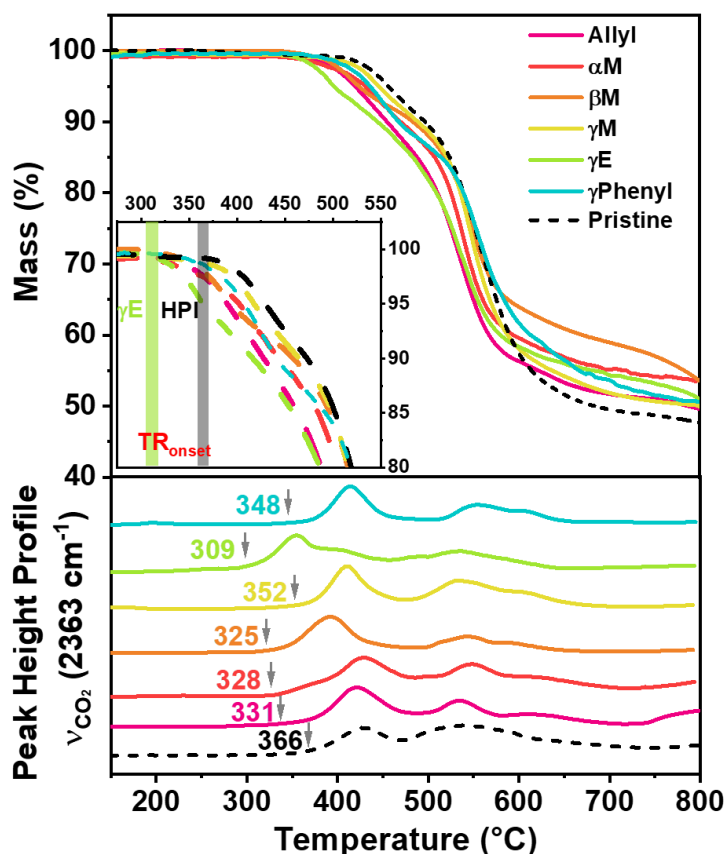


Figure 88. Mass loss curve obtained by means of TGA experiments of the prepared polyimides with an allyl-,  $\alpha M$ -,  $\beta M$ -,  $\gamma M$ -,  $\gamma E$ - and  $\gamma$ Phenyl-modification in the range from 100 to 800 °C at a heating rate of 5 °C  $min^{-1}$  (top).  $CO_2$  gas evolution peak analysis by means of TGA-FT-IR analysis runs (bottom).

$\alpha M$  shows a  $TR_{onset}$  at 328 °C, which is slightly higher than  $\beta M$ -PI with 325 °C and lower than Allyl-PI with 331 °C.  $\beta M$ -PI's high ratio of formed benzofuran units as described before, is assumed to disrupt the polymer chain packing. Additionally, as the number of benzofuran units increases, the availability of vinyl groups decreases, and hence the number of possible crosslinking groups. Therefore, the  $\beta M$ -PI provides the effect of spacing at low degrees of crosslinking compared to Allyl-PI. Questioning, if the large number of blocked phenolic-OH groups, due to the benzofuran units, does lower the overall  $TR$  conversion, results in lower number of  $TR$  undergoing units might be a consequence. Nevertheless, as a mass loss of 2 molecules of  $CO_2$  per repetition unit was observed by means of TGA and decomposition

product evolution analysis, no restriction of a full conversion is determined. Ring-opening reactions, followed by the TR reaction, such as in benzoxazine-phthalimide systems [238], are likely to occur in the case of benzofuran cycles.

With a  $TR_{onset}$  of 309 °C and a  $TR_{peak}$  temperature of 359 °C,  $\gamma$ E-PI shows the lowest TR temperatures ever reported, among all modified TR polymers and especially among hexafluoroisopropylidene group containing TRPs [132, 138, 139, 142, 148, 254, 256, 264].

So far, no TR precursor has been identified to rearrange at an annealing at 300 °C. The most promising TR precursor according to the  $TR_{onset}$  temperature are  $\beta$ M- and  $\gamma$ E-PI. Both materials were treated at 300 °C for 30 min, and a conversion of 14.6 % was determined for  $\beta$ M-PI, while  $\gamma$ E-PI converts to the corresponding PBO to an extent of 22% at 300 °C. No TR material with such a high TR conversion after a 300 °C treatment has been reported yet.

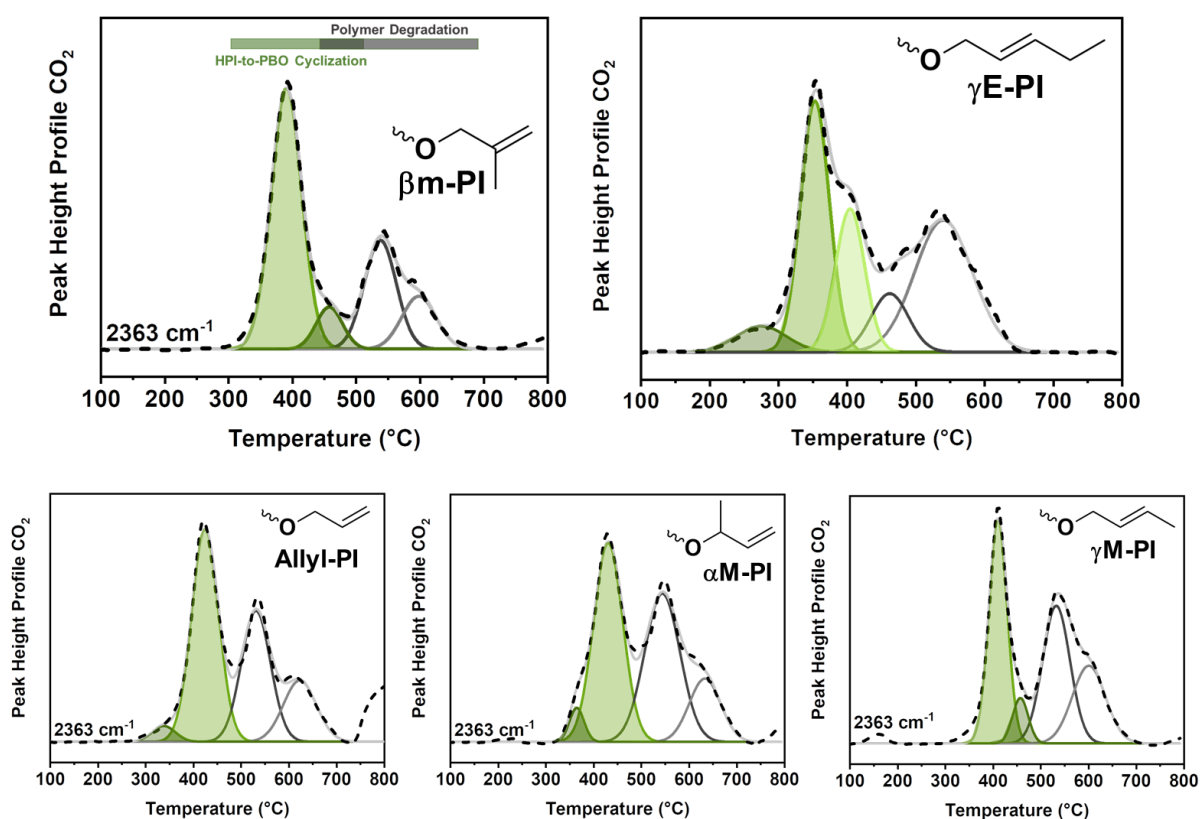


Figure 89.  $CO_2$  evolution peak height profile of  $2363\text{ cm}^{-1}$  (black dashed lines) and their deconvoluted peaks for the TR process (green) and degradation (grey) of allyl-,  $\alpha$ M-,  $\beta$ M-,  $\gamma$ M-,  $\gamma$ E-PI.

FT-IR spectra of each derivative after an annealing at 400°C for 60 min is shown in Figure 90. It corroborates the findings of the TGA experiments. The strongest decrease of the carbonyl peak at  $1750\text{ cm}^{-1}$  was observed for  $\beta$ M- and  $\gamma$ E-PI. The largest peak is shown for  $\gamma$ M-PI.

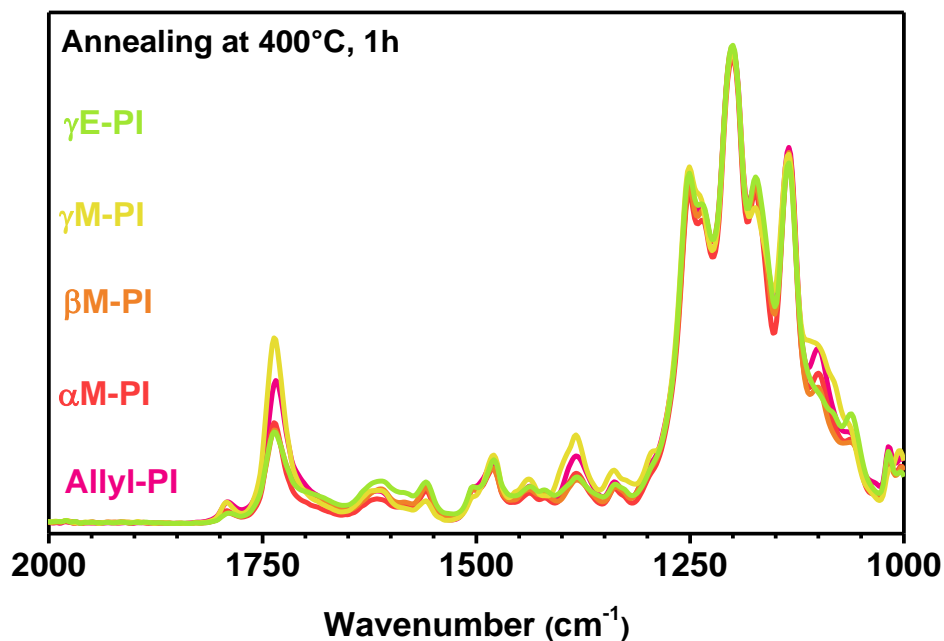


Figure 90. FT-IR spectra of the investigated allyl derivatives after an annealing step of 400 °C for 1 h in the range from 1000 to 2000  $\text{cm}^{-1}$ .

For the Allyl-PI as reference material and the two most promising TR precursor materials,  $\beta$ M- and  $\gamma$ E-PI, TGA curves after annealing at 150, 300, 350 and 400 °C are shown in Figure 91.

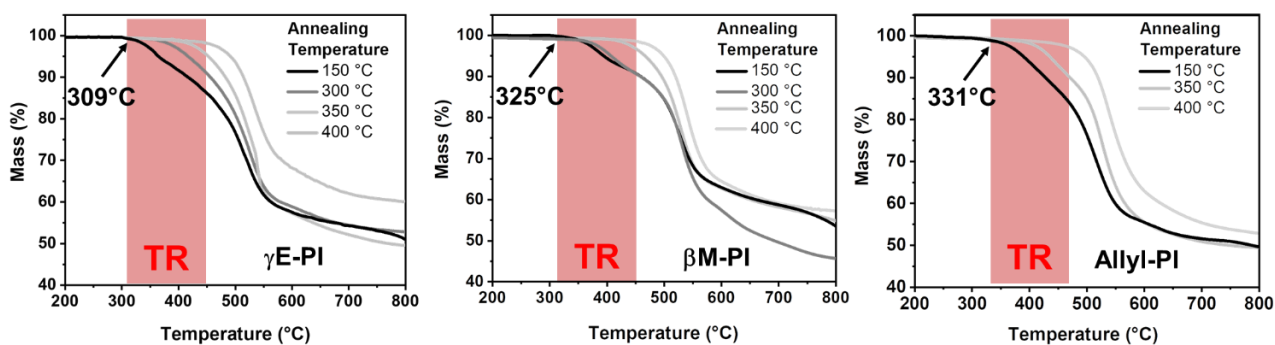
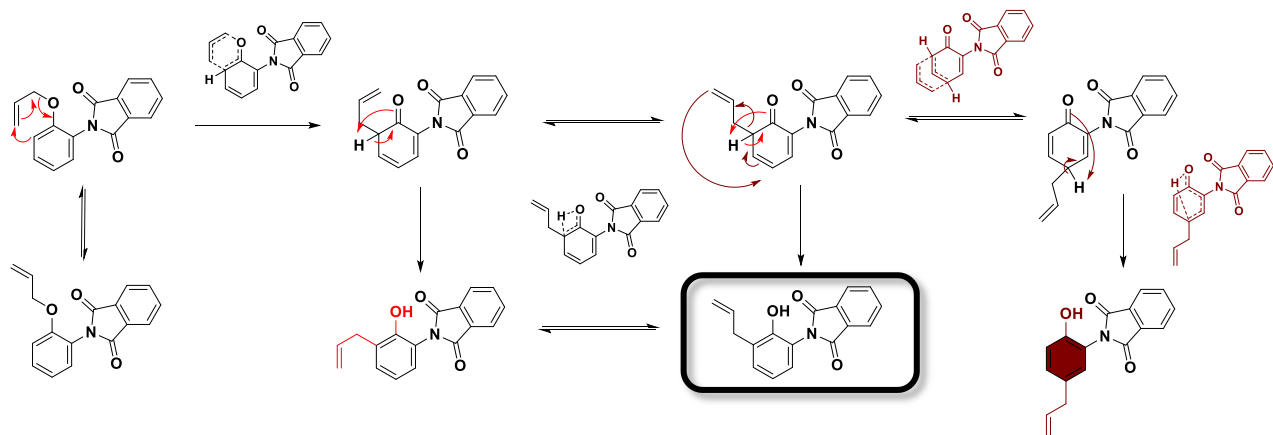


Figure 91. Mass loss curves by means of TGA measurements after thermal treatments at 150, 300, 350 and 400 °C for 24, 0.5, 2 h and 1 h, respectively, for the allyl-,  $\beta$ M-,  $\gamma$ E-modification.

Table 2. TR relevant determined temperatures  $TR_{onset}$ ,  $TR_{peak}$ ,  $TR_{offset}$  and the corresponding  $\Delta TR$ , as well as conversions at 300 (0.5 h) and 350 °C (2 h) for all investigated allyl-derivatives.

	<b>Tg</b>	<b>TR<sub>on</sub></b>	<b>TR<sub>p</sub></b>	<b>TR<sub>off</sub></b>	<b><math>\Delta TR</math></b>	<b>Mass loss</b>	<b>Conv.</b>	<b>Conv.</b>
<b>Modification</b>						<b>theo.</b>	<b>300</b>	<b>350</b>
<b>Pristine</b>	313	366	432	472	106	11.3	0	10
<b>Allyl-PI</b>		331	389	431	100	10.3	12.6	48.5
<b><math>\alpha</math>M-PI</b>	333	328	421	458	130	9.9	13.0	62.1
<b><math>\beta</math>M-PI</b>	302	325	385	429	104	9.9	14.6	84.0
<b><math>\gamma</math>M-PI</b>	289	352	413	448	96	9.9	13.6	52.1
<b><math>\gamma</math>E-PI</b>	296	309	359	420	111	9.7	22.5	99<

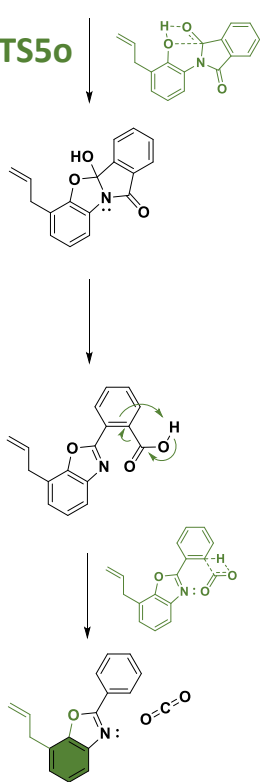


**Claisen-Rearrangement**

**Cope-Rearrangement**

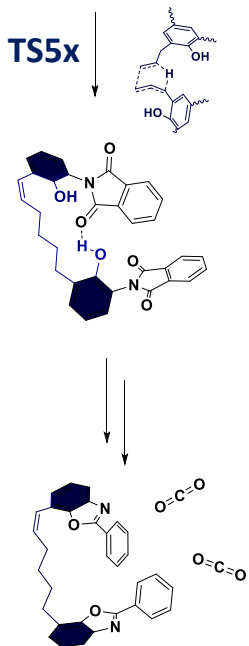


**TS5o**



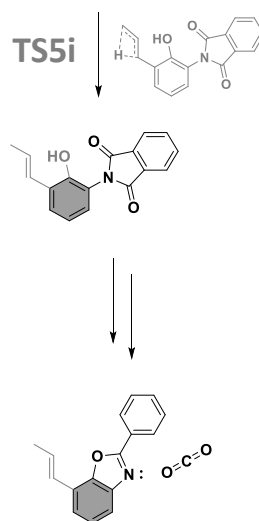
**Benzoxazole  
Formation**

**TS5x**



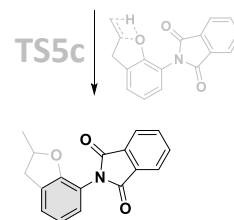
**Crosslinking**

**TS5i**



**Pi-bond  
isomerization**

**TS5c**



**Benzofuran  
Formation**

Scheme 4. Overview of possible thermally initiated reactions in aromatic allyl-phenyl ether. Claisen Rearrangement, benzoxazole formation (Thermal Rearrangement), crosslinking, double bond isomerization, Cope Rearrangement and benzofuran formation.

## Transfer to other backbones

The transfer of the promising effect by  $\beta$ Mallyoxy groups to other backbones was studied in order to propose it as a promising method for the preparation of high performance TRPs. The synthesis was executed with different backbones and was successful. Each phenol group of the investigated backbones was quantitatively converted to the corresponding *ortho*- $\beta$ Mallyoxy polyimide. The NMR spectra are shown in Figure 92. In each case, the hydroxy peak disappeared and the corresponding  $\beta$ Mallyl related peaks appeared at 4.0 ppm for the methylene group, and at 4.8 ppm for the terminal vinyl group protons. The methyl group evolves at 1.6 ppm.

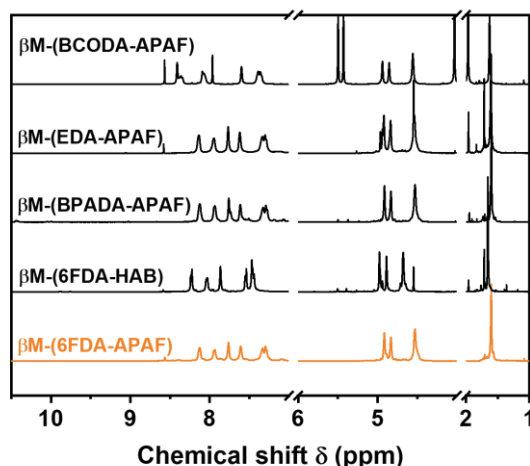


Figure 92.  $^1\text{H-NMR}$  spectra of the  $\beta$ Mallyoxy modified TR precursor.

The TR lowering effect was studied by executing TGA-FT-IR experiments (Figure 93) with an aliphatic backbone (BCODA-APAF) and a rather rigid backbone, namely 6FDA-HAB. In each case a lowering of the TR temperature was detected. However, the effect was more pronounced for the rigid densely packed 6FDA-HAB, since the addition of a chain disrupting modification, improves the polymer chain mobility most likely more, than in a polymer, which has already a large free volume around it. In the case of the aliphatic BCODA-APAF polymer, the onset for the TR temperature is significantly shifted to about 300 °C.

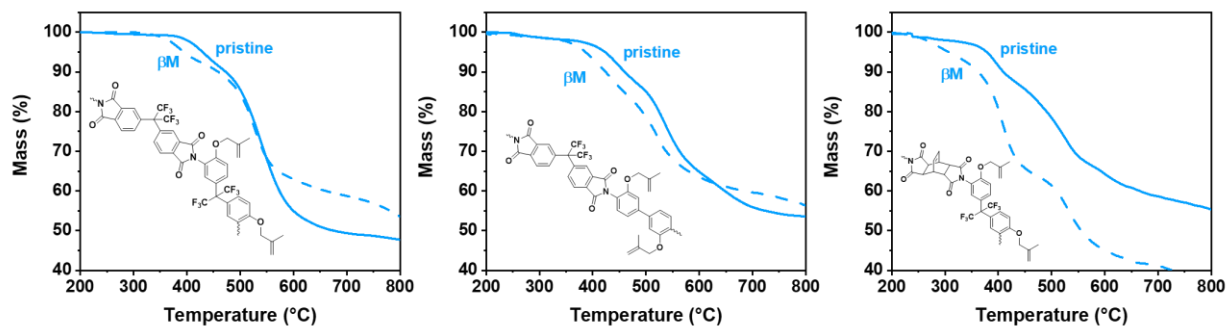
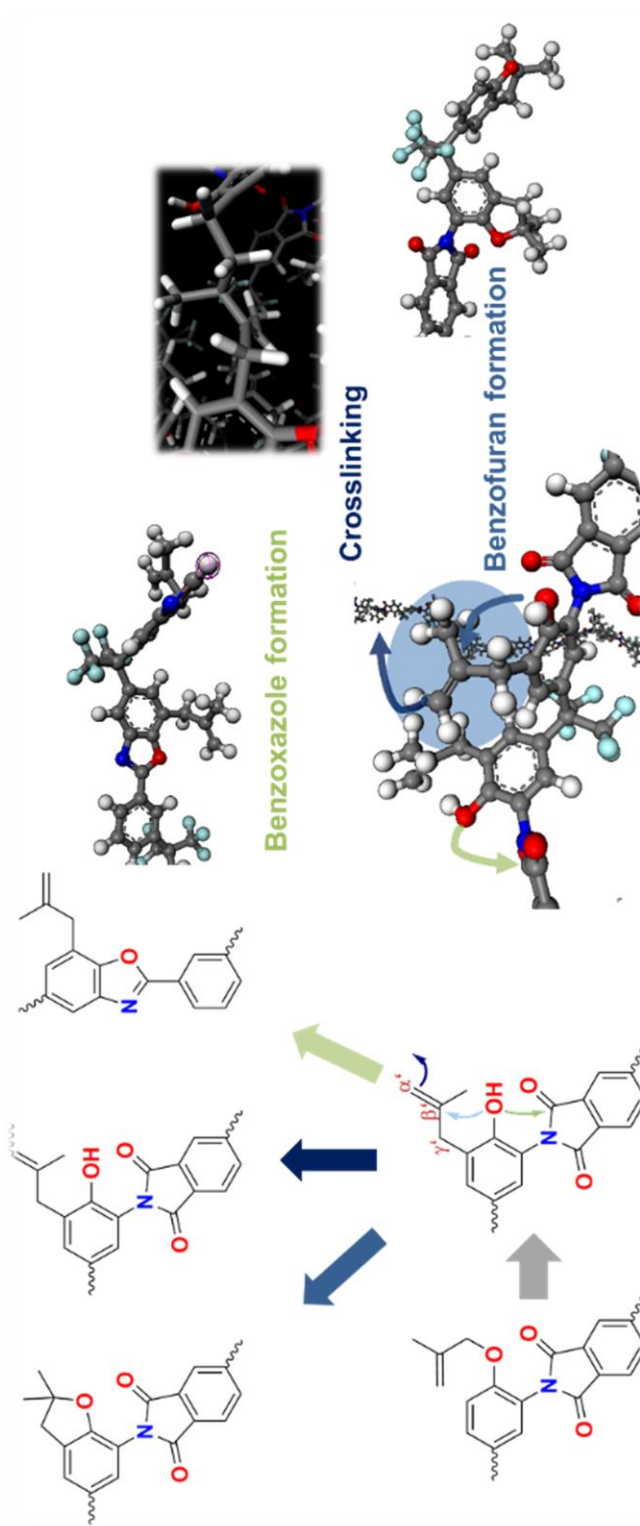


Figure 93. Mass loss curve for  $\beta$ Mallyl modified ortho-hydroxy polyimides as a function of the temperature in an inert argon atmosphere. From left to right, 6FDA-BisAPAF based-, 6FDA-HAB based- and BCODA-APAF based  $\beta$ M-PI.

## Key Messages

- Six materials with Allyl-,  $\alpha$ M-,  $\beta$ M-,  $\gamma$ M-,  $\gamma$ E- and  $\gamma$ Phenyl allyloxy units were prepared and demonstrated four thermally induced and consecutive reactions, demonstrated by calorimetrically determined heat flow curves, heat capacity, thermal mass loss coupled with gas evolution analysis.
- The extent of these reactions (Scheme 5) varies depending on the allyl modification, and none of them show simultaneous onset temperatures, they rather overlap or follow each other.
- The first three processes do not have a mass loss and are attributed to Claisen Rearrangement, allyl cyclization and allyl crosslinking.
- Allyl-,  $\gamma$ M- and  $\gamma$ Phenyl allyloxy groups show larger extents of crosslinking due to their free terminal vinyl groups.
- $\gamma$ Eallyloxy forms abnormal and normal Claisen products.
- $\beta$ Mallyloxy shows a high extent of cyclization to tetrahydro benzofuran.
- $\beta$ M- and  $\gamma$ Eallyloxy show low extents of crosslinking and the lowest onset temperature for the fourth process which was attributed to HPI-to-PBO formation, commonly described as Thermal Rearrangement.
- $\gamma$ E shows the lowest ever reported  $TR_{onset}$  temperature for a 6FDA-BisAPAF modified polyimide, and is only surpassed by highly flexible ether-containing polyimide backbones.
- Non-isothermal *isoconversional* methods were used to describe the thermokinetics of the thermally induced processes.
- Thermoanalytical findings were corroborated by  $^{13}C$ -CP-MAS NMR and FT-IR spectroscopy.





Scheme 5. Claisen-Rearranged  $\beta$ M-PI with possible thermally stimulated reactions, such as Thermal Rearrangement induced benzoxazole formation (TR), benzofuran formation (Cy) and crosslinking (Cx).

## Molecular Modelling Studies of *ortho*-Allyloxy Polyimides

To provide a theoretical foundation of the suggested processes, mechanism and cascade-reaction relationships quantum mechanical and molecular dynamics simulations were performed. The potential reactions of allyloxy-phenyl phthalimide units were simulated by transition state calculations (using TST Beryn optimization), followed by simulation of the corresponding intrinsic reaction coordinate.

**DFT-Simulations.** The simulations were performed using the smallest possible unit (PAG-Imide), shown in Figure 94. The calculations on crosslinking and TR reactions were performed under consideration of two such units. This is required for crosslinking and due to the fact that simulations in chapter *TR mechanism* have shown that stabilization of two close units can affect the transition state strongly. Furthermore, it was stated that the spacing effect lowers intermolecular stabilizations and physical complexations such as hydrogen bonds. Therefore, two neighboring units were used, simply called dimers, in the following discussion, to evaluate that effect.

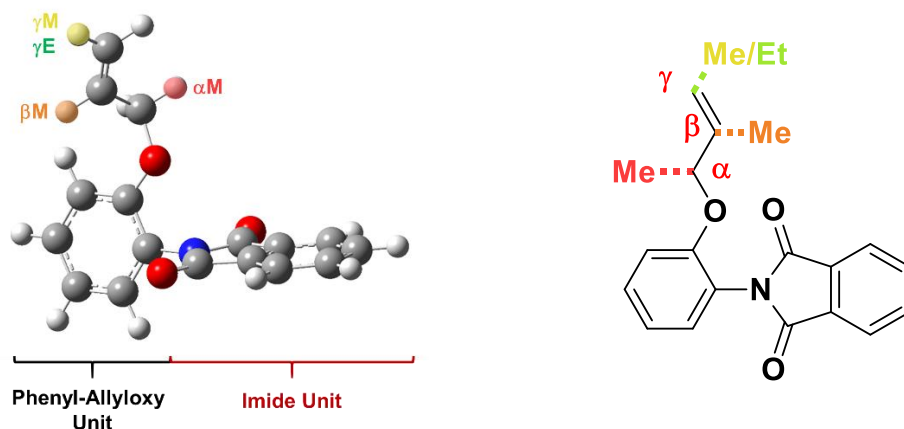
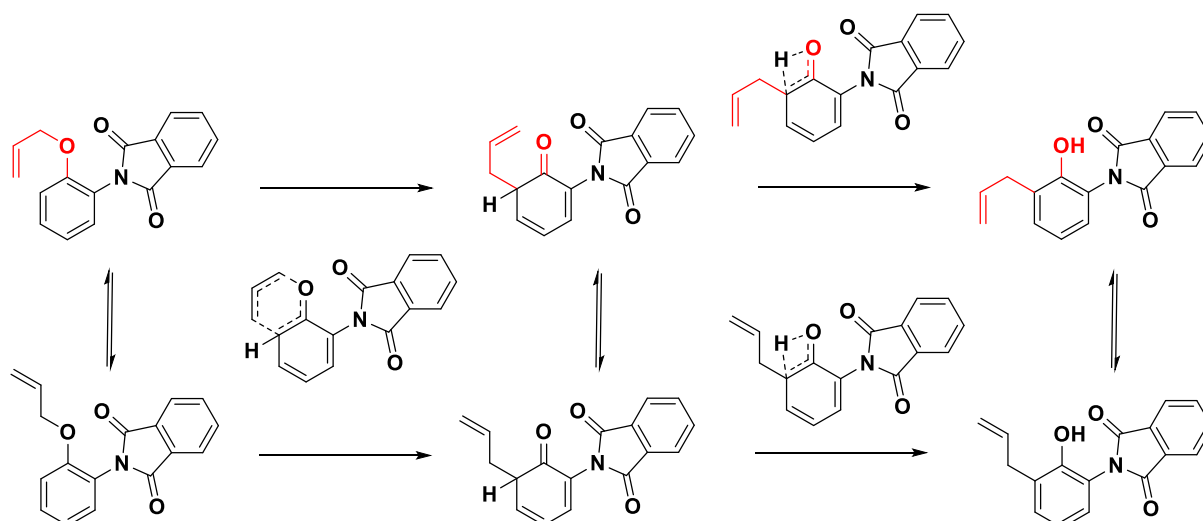


Figure 94. Simulation model for the phenyl allyloxy related reactions.

**The CR process** is in principle an aromatic *ipso* substitution type reaction. The first process is the Claisen Rearrangement reaction of the described allyloxy model. The CR process shows two steps, encompassing the intramolecular migration of the allyl group from *O*-Allyl to the *ortho*-allyl phenoxy group, *C*-Allyl, via TS2 (Scheme 6).



Scheme 6. Overview of the Claisen Rearrangement steps in their *cis*- and *trans*-form.

Experimentally the  $\alpha$ M-PI with its  $\alpha$ Mallyloxy group has shown to have the lowest onset temperature for the CR process. In comparison to the allyloxy group, the HOMO-LUMO gap is lowered by 0.21 eV (Allyl: 3,74 eV;  $\alpha$ M 3,53 eV). The distance of  $O_{\text{Phenol}}-C_{\alpha}$  of Allyloxy is shorter than  $C2-C_{\gamma}$  (2.21 Å/2.27 Å) compared to  $\alpha$ M (2.29 Å /2.31 Å). Accordingly, the transition state geometry of  $\alpha$ M appears to be more polar. The polarized bond breakage can be seen by means of the Mulliken charges between  $O_{\text{Phenol}}$  and  $C_{\alpha}$  (Allyl: -0.372/-0.208;  $\alpha$ M: -0.405/0.344)(Figure 95).

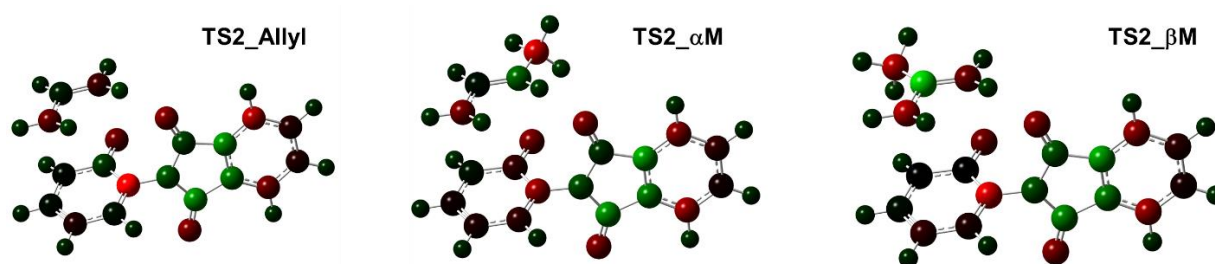
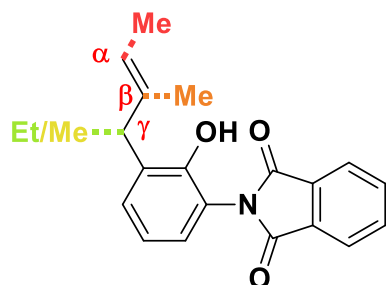


Figure 95. TS2 geometries for the Allyl-,  $\alpha$ M- and  $\beta$ M-PI model. The atoms are colored according to their calculated Mulliken charges.

The formed cyclic ketone is accompanied by a loss of aromaticity, and its relative energy varies strongly between 8 and 18 kcal/mol. With 8 kcal/mol,  $\alpha$ M is the derivative with the lowest intermediate energy, followed by allyl with 9 kcal/mol. The next derivative is  $\beta$ M with 13 kcal/mol. Obviously, the methyl group destabilizes the intermediate due to the interference with the hydrogen, since both are in *ipso* position. The first step is followed by the proton

migration step (TS4) to the final *ortho*-allyl phenol CR-product, P1 (Scheme 7). This second step shows an activation energy barrier about the double height compared to step 1.



Scheme 7. Structure of the simulated CR product P1 with highlights on positions of the substituents after the CR process.

The CR was simulated for the *trans*- and *cis* isomer of the model. The difference of the *cis* and *trans*-isomer with regard to its intermediates and products is very small, about 1-2 kcal/mol. While in the reactant the energy of the *cis* isomer is negligible lower, the *trans*-form of int4 and especially for P1 is lower.

In Addition, Int2 can undergo alternatively a Cope Rearrangement (CoR), which is lower than the 2<sup>nd</sup> CR step, with 36 kcal/mol, instead of 64 kcal/mol. Analogous to Int2, the intermediate structure Int4b is a cyclohexadienone with an allyl-substituent, but in *para*-position, which undergoes then a proton migration in a second step (TS5b). The second step requires 101 kcal/mol and is the largest energy barrier among all investigated reactions. The product is *para*-allyl phenol, *pC*-Allyl, P5. The simulated intrinsic reaction coordinate is shown in Figure 96.

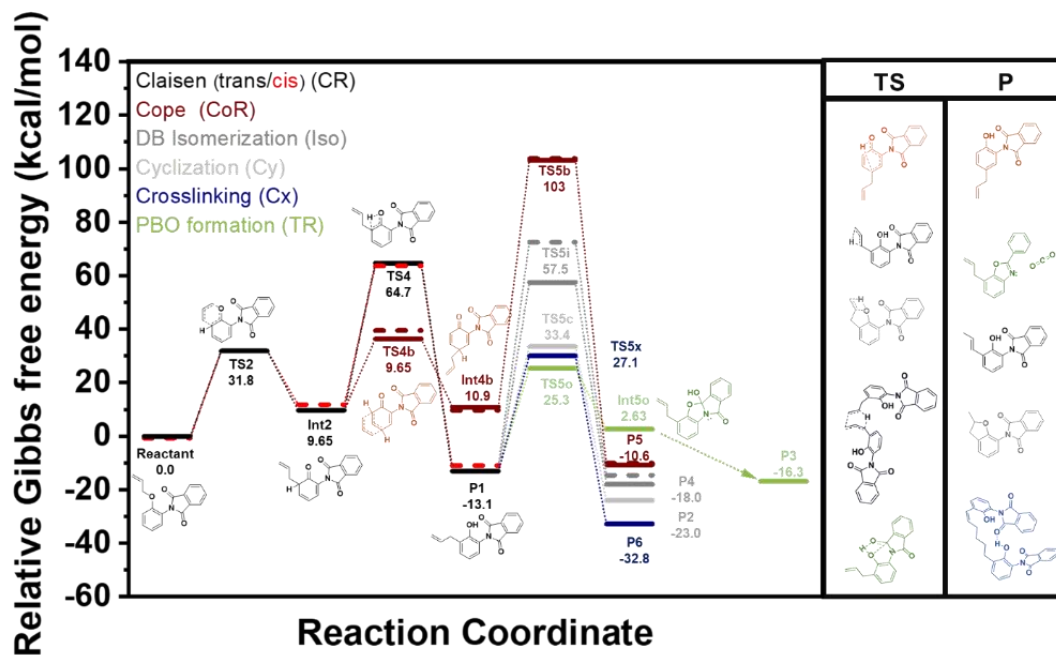


Figure 96. Simulated reaction coordinate of an allyl-phenyl ether-phthalimide model compound for the proposed reactions: Claisen- (black for trans, red for cis) and Cope Rearrangement (maroon), cyclization (light grey), double bond isomerization (dark grey), crosslinking (blue) and benzoxazole formation (green) based on DFT calculations.

The CR-product (P1) is possible to undergo different consecutive reactions, such as double bond isomerization (*Iso*), cyclization (*Cy*), crosslinking (*Cx*) and HPI-to-PBO formation (*TR*). It was observed by our experimental studies in polymers, that all materials undergo a thermally induced cascade of consecutive reactions, except *CoR* and *Iso*.

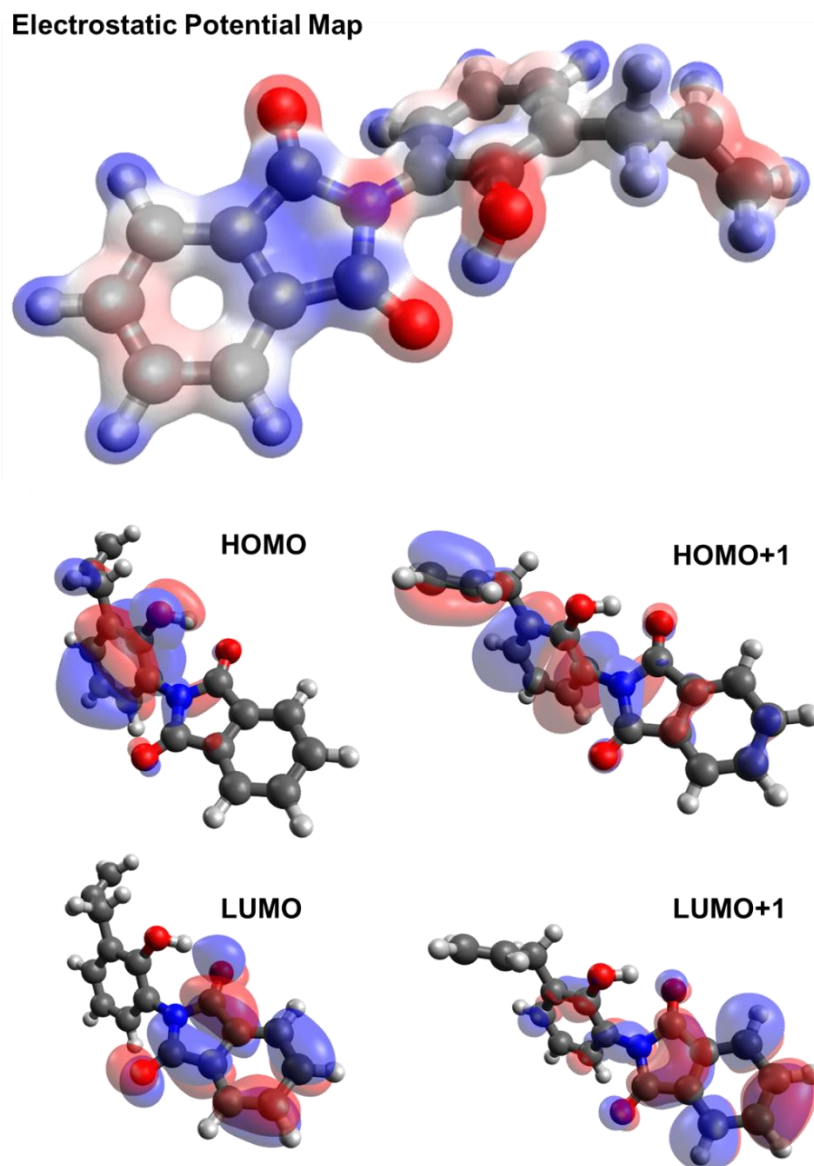


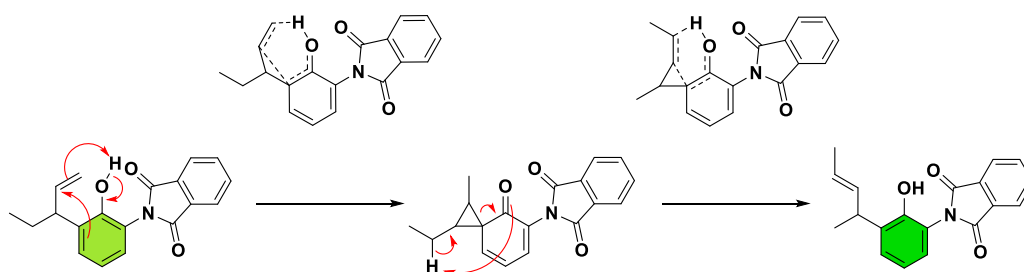
Figure 97. The electrostatic potential map shows the distributed electrostatic potential along the molecule, which is correlated to the electron density (top). The HOMO, HOMO+1, LUMO and LUMO+1 orbital of the P1 model are visualized as well (bottom).

Among the subsequent reactions, the highest transition state energy was calculated for the double bond *isomerization* (*iso*), while crosslinking (blue), cyclization (grey) and TR (green) are close to each other. In case of the crosslinking simulation the lowest energy alder-ene type crosslinking is shown. Various other crosslinking mechanism will be discussed later.

### **Abnormal Claisen-Rearrangement**

In the case of the  $\gamma$ Eallyloxy group an additional consecutive reaction is discussed in the literature, which follows a CR/Conia-oxa ene cascade reaction type (see Scheme 8). It involves two additional steps from the cyclohexadienone intermediate Int4. Protonation of the vinyl

group followed by an cyclopropene intermediate formation accompanied by a loss of aromaticity and the formation of cyclohexadienone, similar to Int4. A reprotonation of the keto-group, recovering the aromaticity and bond rearrangement,  $\alpha, \alpha', \gamma'$ -disubstituted *ortho*-allyl group is formed. The abnormal product is thermodynamically favored as it is 4 kcal/mol lower compared to the normal CR product ( $\gamma$ En). The second step has a larger activation energy barrier of 40.2 kcal/mol, first step is 25.5 kcal/mol, and still significantly lower compared to the largest step in CR with 68.9 kcal/mol (TS4). The transition-state geometries are shown in Figure 98, and the intrinsic reaction coordinate is shown in Figure 99.



Scheme 8. Overview of the normal (top) and abnormal (bottom) Claisen-Rearrangement Claisen Rearrangement steps in their *cis*- and *trans*-form.

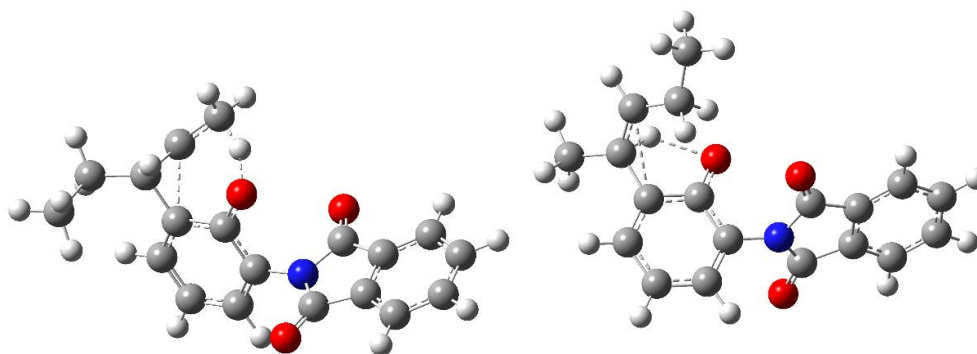


Figure 98. Transition State Geometry of TS5a and TS6a.

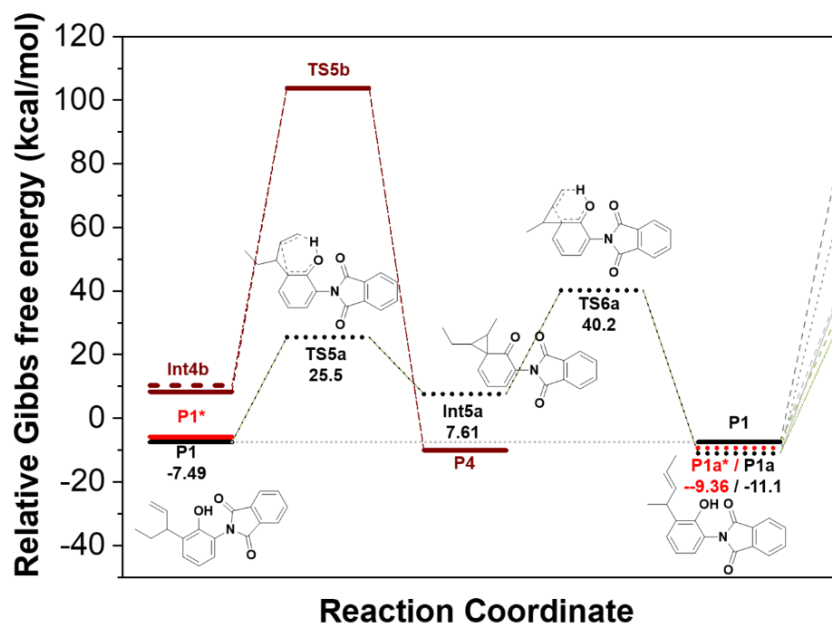


Figure 99. Simulated single-point energies of the geometry optimized reactants, products, intermediates, and transition-states of the abnormal Claisen Rearrangement reaction of the  $\gamma$ -allyl-imide model.

Other derivatives do not undergo the ab-CR, since no other  $\gamma'$ -CH<sub>2</sub> group is present for the re-protonation of the keto group in step 2. Any allyl derivative with a CH<sub>2</sub>R group in  $\gamma'$  is suitable to undergo such a *post*-CR reaction theoretically.

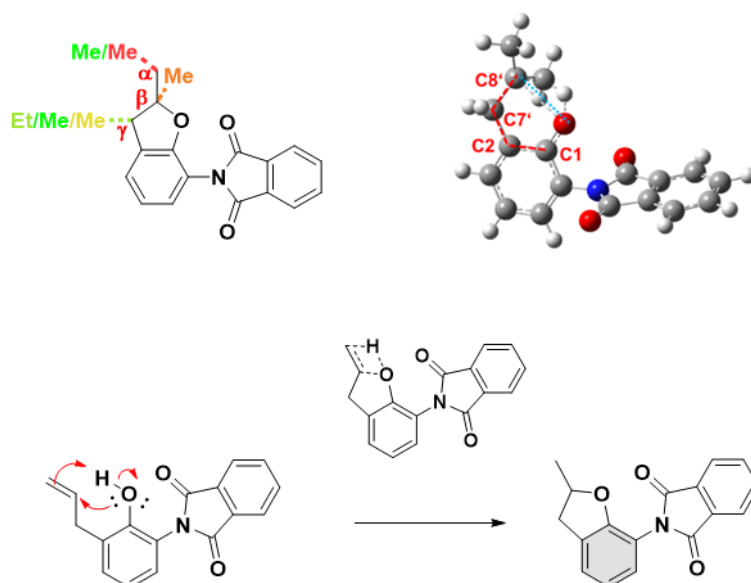


## Cyclization and Isomerization

The reaction coordinate for the benzofuran-cyclization of all allyl derivatives is demonstrated in Figure 100. It involves one step from the *ortho*-allyl phenol to the corresponding cyclized product, the tetrahydro benzofuran.

The cyclization occurs in *cis*-P1 via proton migration from phenol to the terminal allyl-C (C9'; C $\gamma$ ') and a nucleophilic attack of the phenol-O at the C8' atom. The reaction proceeds via a 4-membered transition state TS5c (Scheme 9, Figure 101).

While all calculated energies of TS5c are in the range of 33-36 kcal/mol, the  $\beta$ M modification shows a significantly lower TS energy for TS5c with 29 kcal/mol. Among all investigated materials, the highest tendency to favor cyclization was simulated for  $\beta$ M which is in agreement with the experimental results.  $\beta$ M-PI showed by far the strongest tendency to form benzofuran units (see DSC fitting and  $^{13}\text{C}$ -CP-MAS NMR on page 133), while the simulation resulted in significantly lower  $E_A$  for  $\beta$ M.



Scheme 9. Cyclized benzofuran-type product with highlights of the substituent positions after the cyclization reaction. Simulated Transition State Geometry for the cyclizing Allyl-PI model with highlights on the most important geometrical aspects of the reaction: Dihedral angle (red) and Phenol-O to C8' distance. Reaction scheme is shown as well (bottom).

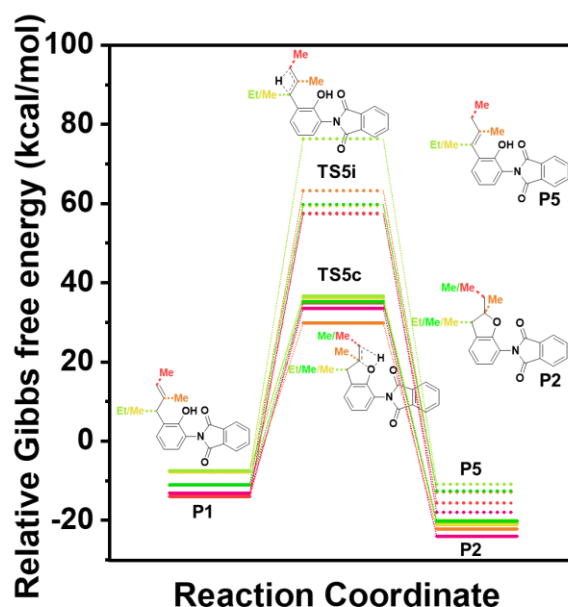


Figure 100. Simulated reaction coordinate of the cyclization and double bond isomerization process for the different allyl derivatives.

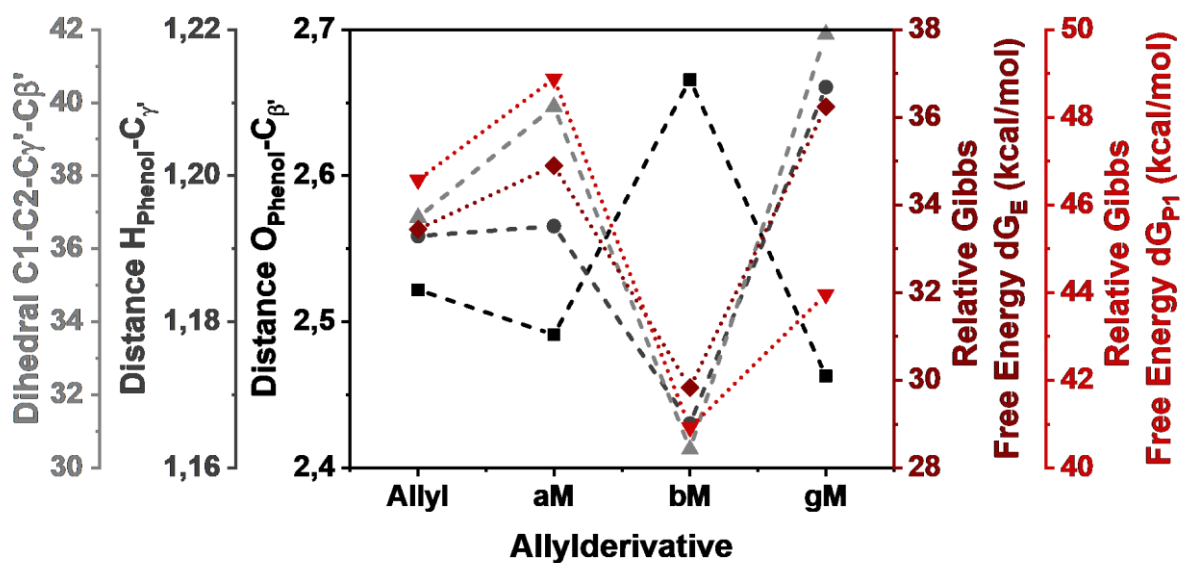


Figure 101. Geometrical and relative Gibbs Free Energies for each derivative.

## Crosslinking

The crosslinking of allyl groups is reported in different systems [268, 287], but the corresponding mechanism of aromatic and aliphatic allyl ether has not been investigated in detail, nor by quantum chemical methods. In principle, crosslinking requires two allyl groups, which have 3 possible crosslinking centers (C7', C8' and C9'). By means of DFT based

calculations, two model compounds might crosslink via 14 identified crosslinking reactions. Their energy barrier are shown in the reaction coordinate in Figure 102, as well as the six lowest energy pathway mechanism. For two CR product molecules (P1) to react, 5 different reaction centers and in total 8 reaction mechanisms were identified and simulated. The crosslinking mechanisms were named according to their reactive centers: “e” for C9’ ( $\gamma'$ , end), “m” for C8’ ( $\beta'$ , mid) and “a” for C7’ ( $\alpha'$ , allylic).

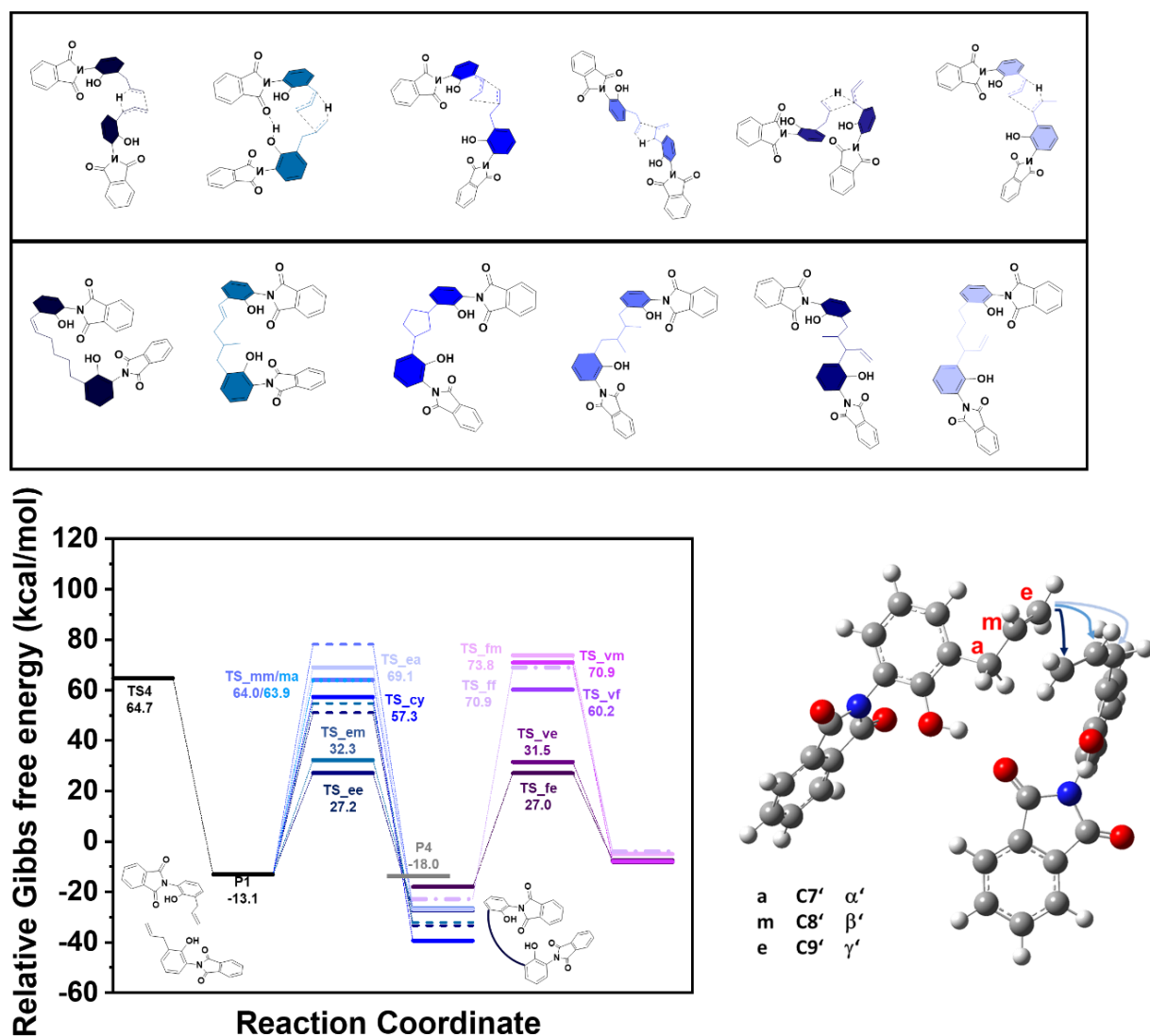


Figure 102. Scheme of the crosslinking mechanisms of the allylated unit comprising the allyl-phenol and phthalimide group and their corresponding product, respectively (top). Reaction coordinate of all crosslinking reactions including reactions between products P1 and P4 (bottom, left).

For instance, the ee-mechanism is a crosslinking reaction that occurs between C9’ (e) of one molecule with C9’ (e) of another molecule (Figure 103). The energy barrier among all simulated mechanisms varies in the range from 27 to 70 kcal/mol.

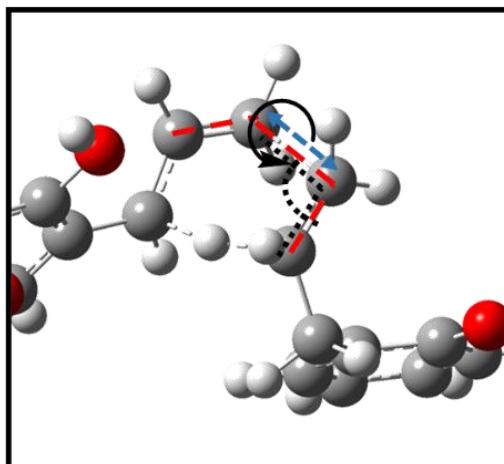


Figure 103. Reaction according to an Alder-ene mechanism between two allyl groups. Important geometrical parameter is highlighted: Dihedral angle (red), ene-ene distance (blue) and angle between enophil double bond (right group) and ene double bond (left group) (black).

**Alder-ene ee-mechanism.** The crosslinking reaction with the lowest energy barrier was found between two terminal vinylic C-atoms (C9') of the allyl group and occurs via a six-membered ring transition state (TS\_ee, 27 kcal/mol), as demonstrated in Figure 104. The proton of the allylic group (a, C7') migrates to C8' of the second allyl chain forming a hexamethyl-1-ene crosslink via a concerted addition reaction. This is an Alder-ene reaction between two alkenyl groups.

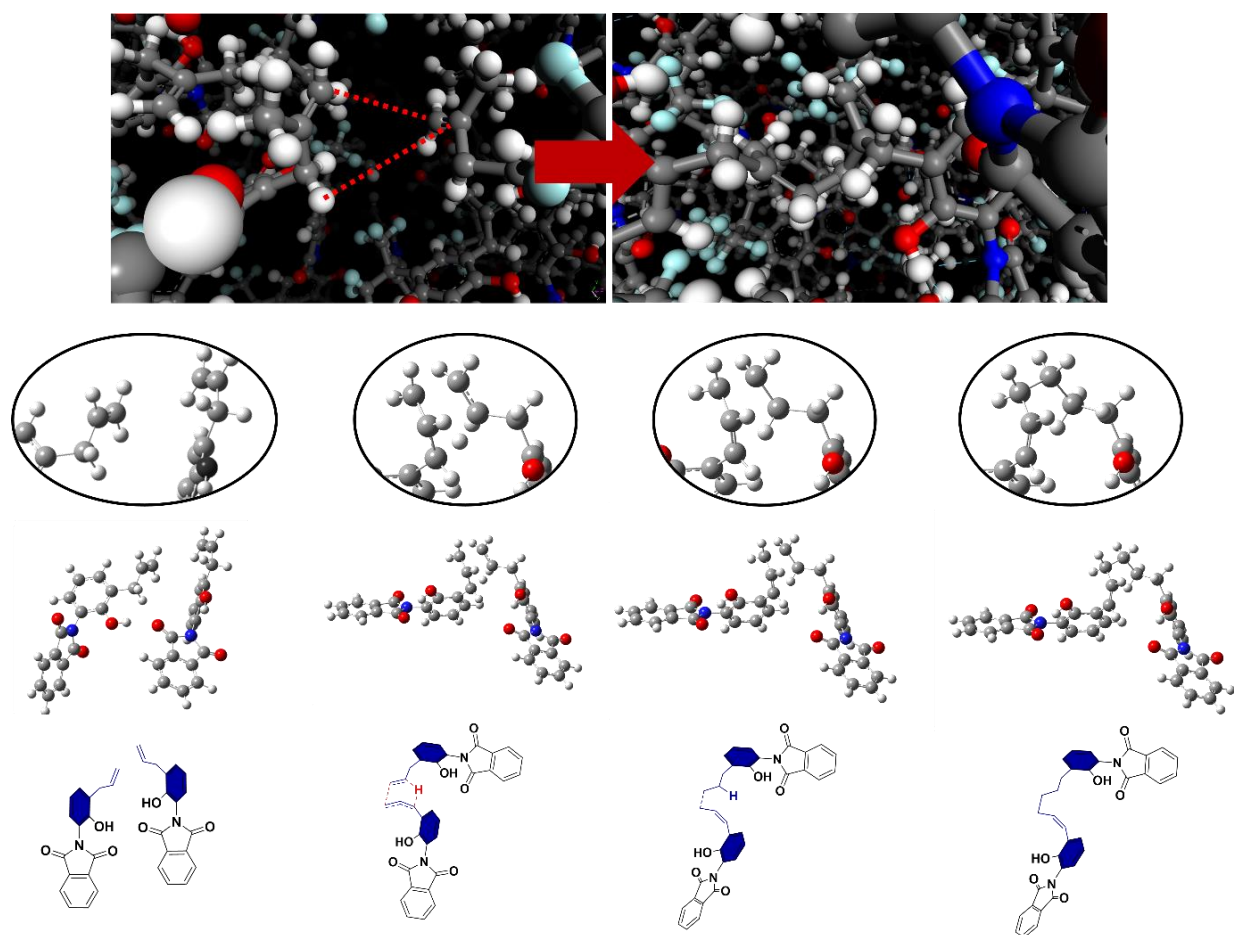


Figure 104. Course of the crosslinking process including structures from the simulated intrinsic reaction coordinate (IRC).

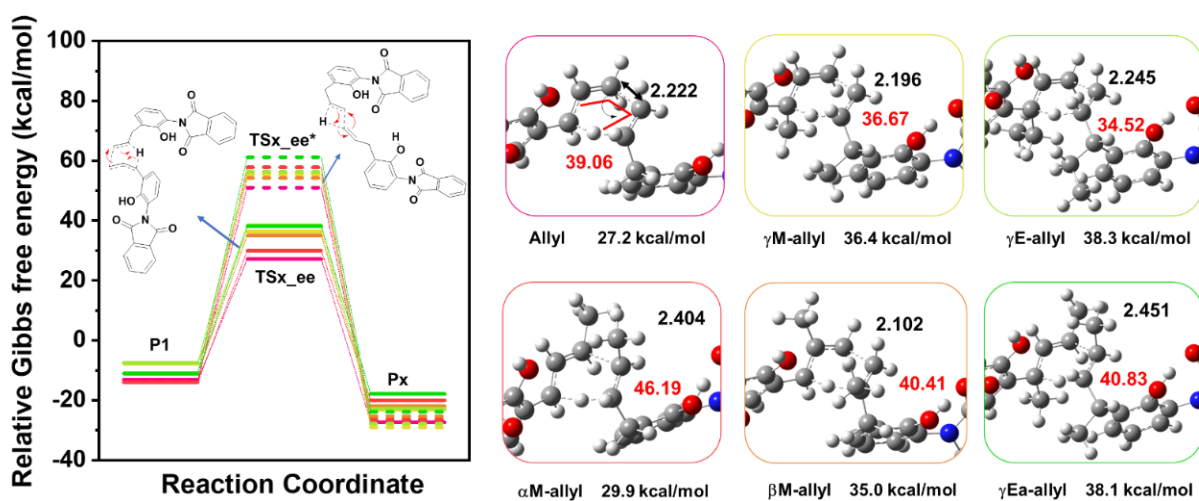


Figure 105. Simulated reaction coordinate for the crosslinking mechanism between terminal vinylic groups (ee mechanism) and zoom of the transition state with respect to the different modifications.

Another ee-crosslinking reaction between both terminal C9'-atoms proceeds via a four-membered ring transition state geometry. This time the proton migrates from the terminal C-atom C9' itself to the 2<sup>nd</sup> allyl group's C8'-atom, forming a crosslink with the other C9'.

**Alder-ene em-mechanism.** However, with 32 kcal/mol, the overall second lowest crosslinking energy of two crosslinking P1 molecules, takes place between a C8' and C9' atom via em-mechanism. Herein, an allylic proton migrates to C9' of the second allyl group. The em-mechanism yields a branched, 2-methyl-petamethyl-1-ene crosslink (Figure 106)

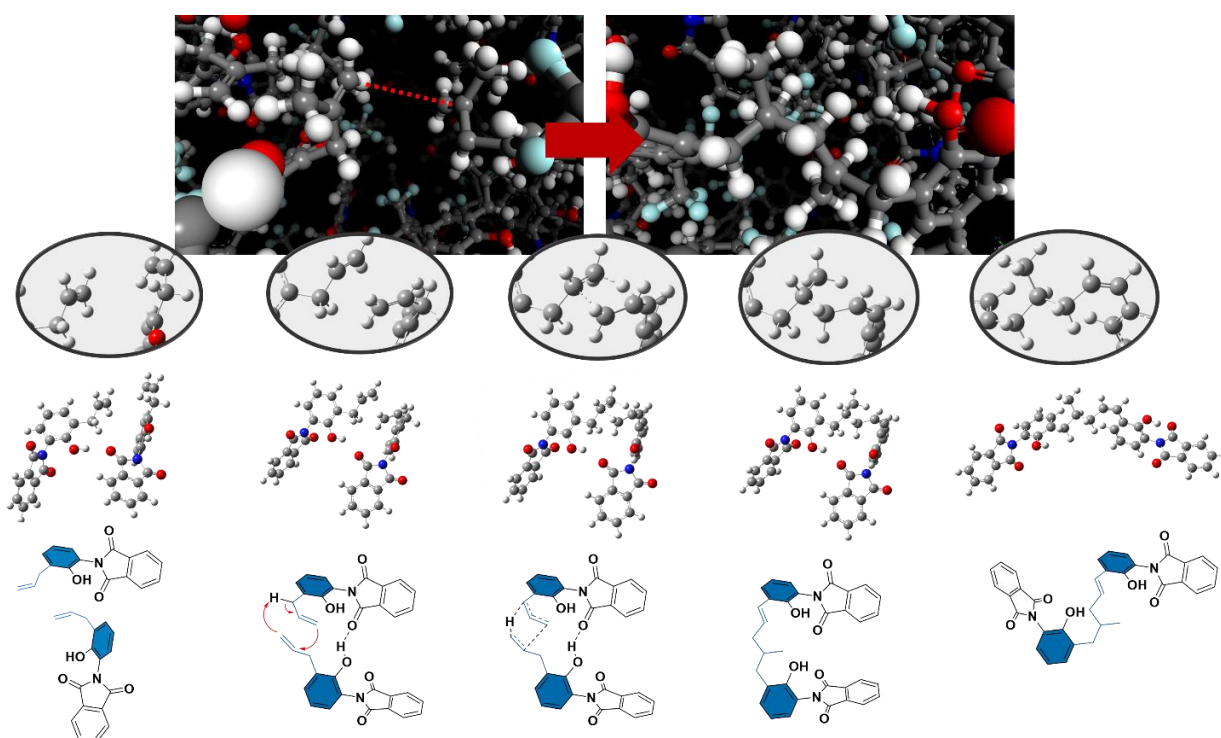


Figure 106. Course of the crosslinking process including structures from the simulated intrinsic reaction coordinate (IRC).

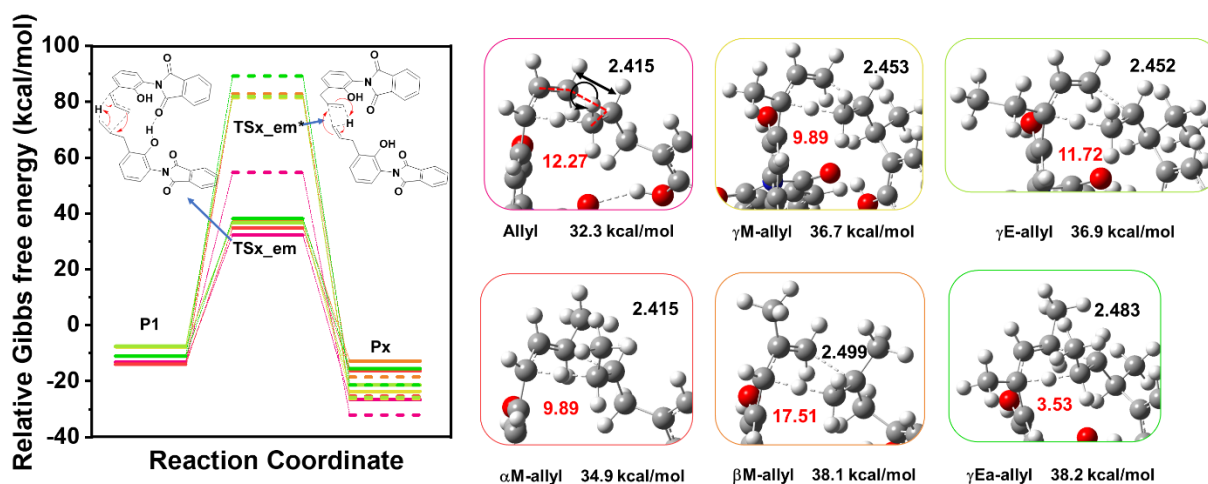


Figure 107. Simulated reaction coordinate for the crosslinking mechanism between terminal vinylic groups (*em* mechanism) and zoom of the transition state with respect to the different modifications

The *ee*- and *em*-crosslinking mechanism, both have 6-membered transition state geometries which require lower energies to form due to their larger stabilization compared to all other mechanism which involve 4- and 5-membered transition state geometries [288]. So far only the two most likely crosslinking mechanism were discussed, without taking into account, that the derivatives affect the electronic and steric conditions for the crosslinking reaction (Figure 105 and Figure 107). In case of the *ee*-mechanism, the largest activation barrier is found for  $\gamma$ - and  $\beta$ -substituted materials, with energies, relative to the starting material E, around 35 – 38 kcal/mol, while  $\alpha$ M and allyl have energies of only 29 and 27 kcal/mol, respectively. Nevertheless, if the transition state energy is calculated relative to its reacting molecule P1, a crosslinking tendency of  $\gamma$ Ea <  $\beta$ M <  $\gamma$ En <  $\gamma$ M <  $\alpha$ M < Allyl, is found, which is in accordance with the experimentally determined crosslinking tendencies by means of gel-fraction and DSC. In case of the *em*-mechanism the lowest energy barrier was simulated for the reaction of two allyl groups with 32 kcal/mol, followed by  $\alpha$ M with 34 and  $\gamma$ M with 36 kcal/mol. The largest energy of the TS was determined for  $\gamma$ Ea and  $\gamma$ En, with 38 and 38.5 kcal/mol, and  $\beta$ M with 38.1 kcal/mol, in relation to the reactant molecules E. In relation to P1 the order  $\gamma$ Ea <  $\beta$ M <  $\alpha$ M < Allyl <  $\gamma$ M <  $\gamma$ En was found.

**Additional crosslinking center and mechanism.** Crosslinking mechanism involving C7' and C8', such as TS<sub>ea</sub>, TS<sub>ma</sub>, TS<sub>mm</sub> require higher activation energies. All crosslinking reactions proceed by five-membered-ring transition state structure, except in the case of TS<sub>ma</sub>. Despite its higher energy barrier for the allyl-to-vinyl group isomerization, such *ortho*-



vinylidene-phenol products, such as P4, were reported before. Accordingly, these structures affect the crosslinking process as well. If P4 is formed, five potential crosslinking mechanism with the two vinylic carbon atoms C7' (v) and C8' (f) were simulated. The lowest energy barrier was found for reactions between the C9' atom of P1 and C8' (fe) or C7' (ve) of P4, with 27 and 31 kcal/mol, respectively.

**Molecular Dynamics Simulation on Crosslinking.** Quantum chemical calculations were employed to investigate the crosslinking and other reactions in small representative models of the reactive unit. These calculations are highly resource and time consuming and cannot be performed for larger systems, especially not if systems of several thousand atoms, like in polymer systems, are involved. In these cases, molecular dynamics simulations are used. These systems use system adapted forcefields, that calculate the electronic and structural properties.

Using small models in gas phase, means, that they have the freedom to diffuse and translate and rotate freely. In polymeric systems, where, in contrast to the simplified description in gas phase, where the mobility of the molecules are much higher, two or even more reactive groups, need to be within a reactive distance to each other. Polymers in solid-state are restricted regarding their freedom to translate and rotate due to their large mass, entanglements, larger number of physical interactions per molecule and co-operative nature to name a few reasons compared to small molecules, especially in gas or liquid phase. Approaching the rubbery state, polymer chains have sufficient energy to move around more freely, which increases the possibility of two reactive groups to come close enough to react with each other. However, in polymers these rotational and translational restrictions play a crucial role when it comes to inter-molecular reactions, such as crosslinking. Additionally, steric hindrance of the reactive groups might lower the feasibility of two reactive groups to come close enough to react.



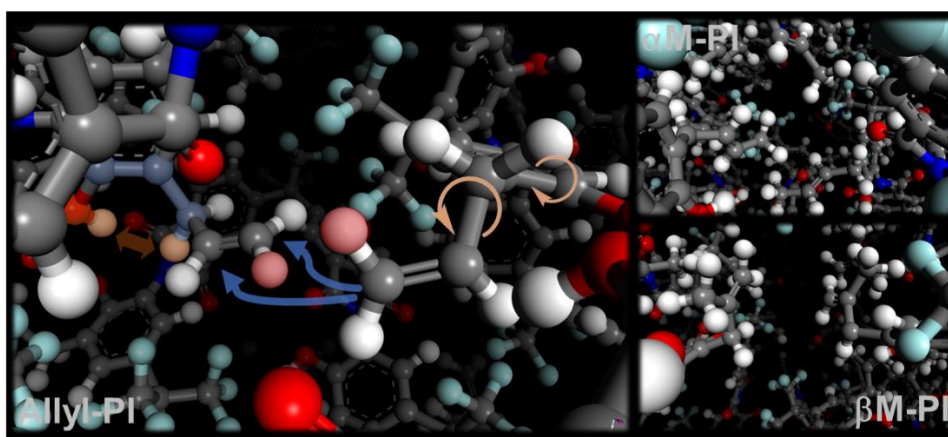


Figure 108. Image captures of typical allyl group orientations within a simulated amorphous cell of the allyl derivatives allyl-,  $\alpha$ M-,  $\beta$ M-,  $\gamma$ M-,  $\gamma$ E-PI.

Molecular dynamic simulations were performed for all Claisen-Rearranged derivatives. No difference was made between an ee- and em-crosslink during the whole crosslinking simulation. In Figure 108 an image capture of two close allyl groups is shown, as well as of the  $\alpha$ M- and  $\gamma$ M-derivative derivative. The molecular dynamic crosslinking simulation revealed that the unsubstituted plain allyl group appears to have the most crosslinks with 33 per 2 chains, followed by  $\gamma$ M-PI (29). The order with an increasing number of crosslinks is as follows  $\gamma$ Ea (21) <  $\gamma$ En (26) =  $\beta$ M (26) <  $\alpha$ M (27) <  $\gamma$ M (29) < Allyl (33). These findings are in accordance with DFT simulations for the ee-mechanism as well as the experimental gel-fraction results, in which Allyl- and  $\gamma$ M-PI show clearly the strongest tendency to crosslink, while  $\beta$ M and  $\gamma$ E showed the lowest degree of gel-fraction.

Careful observation of different frames of the simulation shows, that the allyl group migrates around its position more unhindered or restricted compared to methyl- and ethyl-substituted derivatives. Substituents interfere with each other by repulsive forces, separating the vinyl groups and avoid vinyl groups to come close enough.  $\gamma$ Mallyl has a restriction in C7', but it contains a free double bond which can easily crosslink via the Alder-ene ee-mechanism (as shown in Figure 109).  $\alpha$ -position substitutions make it difficult, especially for the ee- and em-crosslinking reactions (Figure 109). Therefore,  $\alpha$ M shows a lower number of crosslinks. The abnormal Claisen product  $\gamma$ Ea in turn shows same difficulties as  $\alpha$ M-PI, but additionally its rotation around the  $\gamma$ -C atom is restricted. In conclusion, the steric hindrance of the double bond reduces the possibility for two double bonds to come close enough to react, while a substitution at C7' lowers its freedom to rotate.

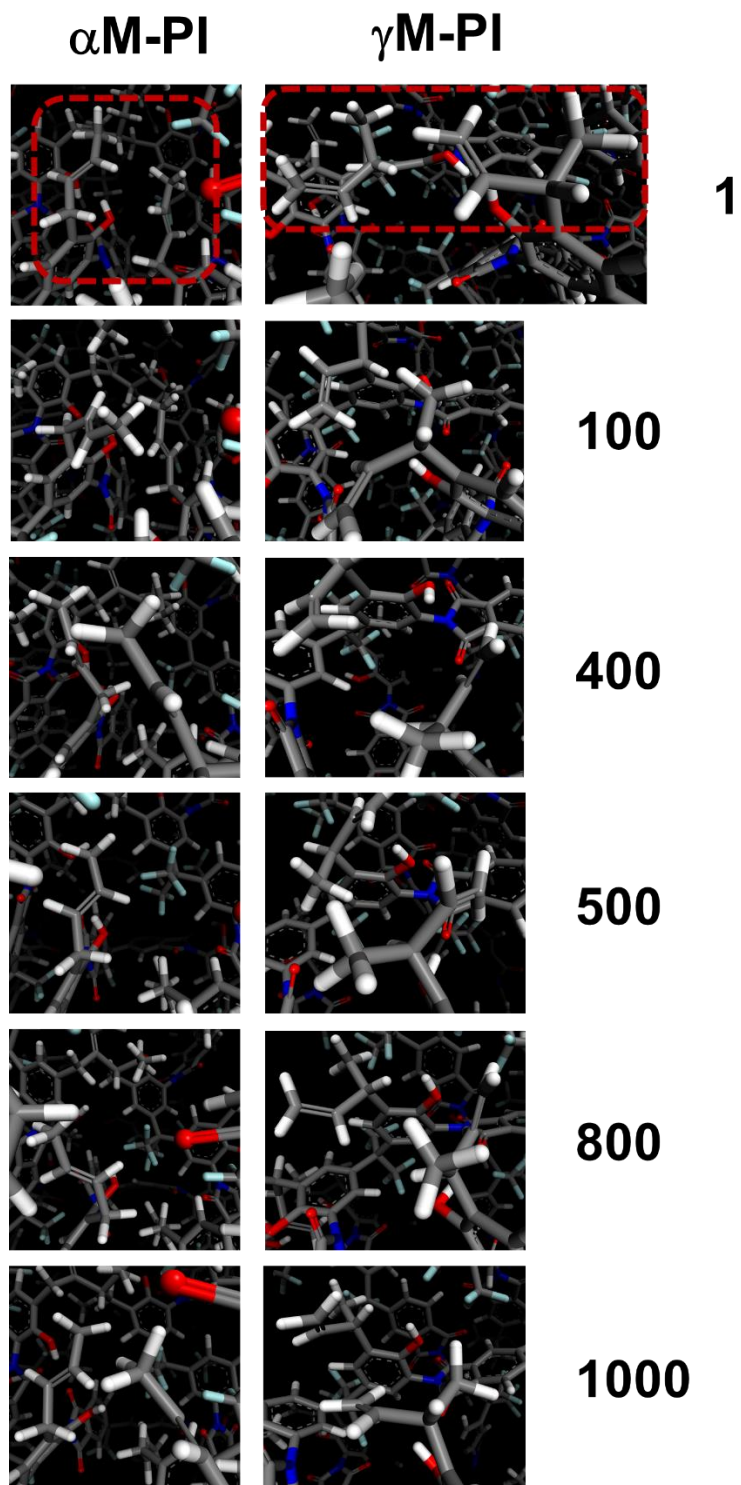
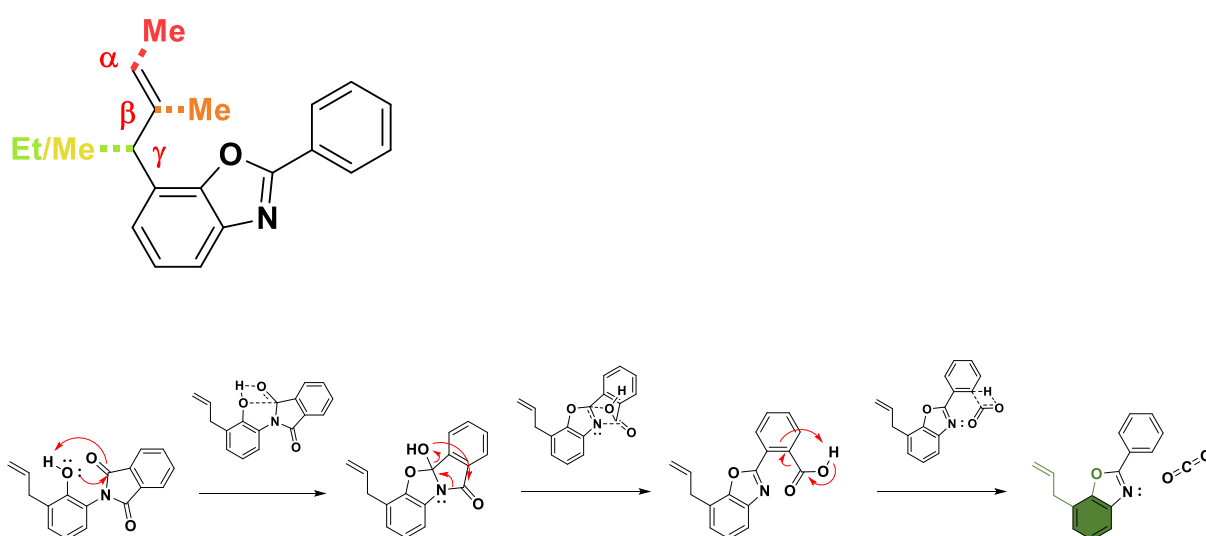


Figure 109. Snapshots of two allyl groups of the modifications  $\alpha$ M- and  $\gamma$ M-PI and their movement after 1, 100, 400, 500, 800 and 1000 ps of simulation time.

## Thermal Rearrangement

The Thermal Rearrangement mechanism is described in detail in section *Molecular Modelling of the Reaction Mechanism*. Further suggestions for a more likely reaction mechanism were proposed based on DFT- and molecular dynamic simulations. A mechanism comprising three steps, namely TR initiation, intramolecular transfer, and decarboxylation (Scheme 10). This reaction was calculated for a monomeric and dimer model. In these monomeric models, the effect of the substitution at the allyl group is expected not to have a strong influence, as it does not interfere with the reactive atoms and bonds.



Scheme 10. Thermally rearranged model of ortho-allyl benzoxazole (top) and HPI-to-PBO reaction mechanism (bottom).

These assumptions were corroborated by the calculated transition state energies (Figure 110). The activation energy barriers from P1 result in an activation barrier of 38.1 kcal/mol  $\pm$  0.31 kcal/mol. Here, no significant difference is determined. They rather differ if calculated relative to the pristine reactant E, as  $\gamma$ -substituted materials for instance have higher energies. Relative to E, the TS energies follow the order with increasing energies  $\alpha$ M (24) < Allyl (25) <  $\gamma$ Ea (26) <  $\beta$ M (27) <  $\gamma$ M (29) <  $\gamma$ En (30).

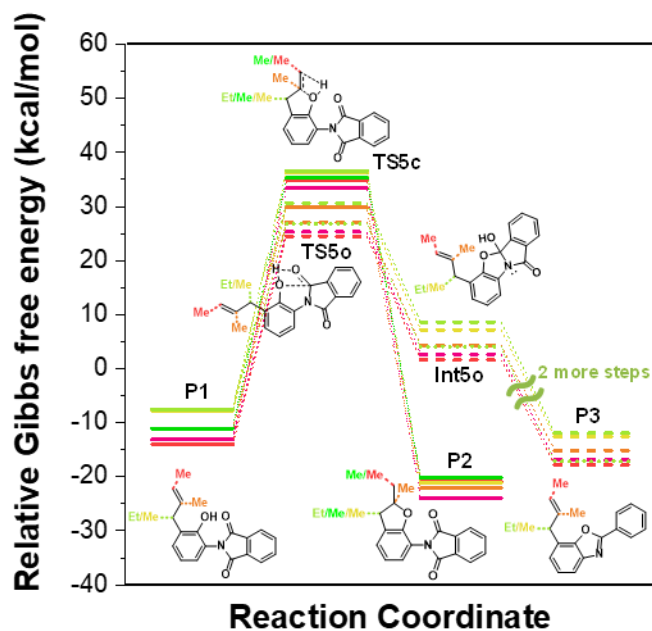


Figure 110. Simulated single-point energies of the geometry optimized reactants, products, and transition-states of the cyclization reaction of the HPI-to PBO formation (Thermal Rearrangement) of the allyl-imide models.

Since the allyl group induced disruption due to the efficient chain packing (spacing effect) is proposed to be responsible for the observed lower TR temperatures, a dimer model was used to calculate the TR process in a crosslinked and non-crosslinked system to determine the effect of the substituent on the reaction coordinate. A comparison of the dimer models, which involve the aspects of chain packing of these units better, than simulations in a single model, was performed. The calculation revealed the lowest activation energy barrier for  $\gamma$ Ea with 21 kcal/mol, followed by  $\alpha$ M, Allyl and  $\beta$ M with 23, 24 and 25 kcal/mol, respectively (see Figure 111). The  $\gamma$ -substituted modifications  $\gamma$ M and  $\gamma$ E show, each with 28 kcal/mol, a larger energy barrier to overcome. But in comparison to the pristine unmodified material, they show lower energies for the TR initiation step. This result also reflects our experimental studies in many ways. The lowest onset temperature for  $\gamma$ E, on one hand, but also a partial conversion, since there is a second TR step observed by DSC (significantly higher to the first TR-step and more similar to the TR temperatures of  $\gamma$ M). Accordingly, we found the lowest energy here for  $\gamma$ Ea but the highest for  $\gamma$ M and  $\gamma$ En, which are close to each other. In our experiments we observed a close onset temperature for allyl,  $\alpha$ M and  $\beta$ M, and we calculated a very narrow range of TS energies for the same modifications as well.

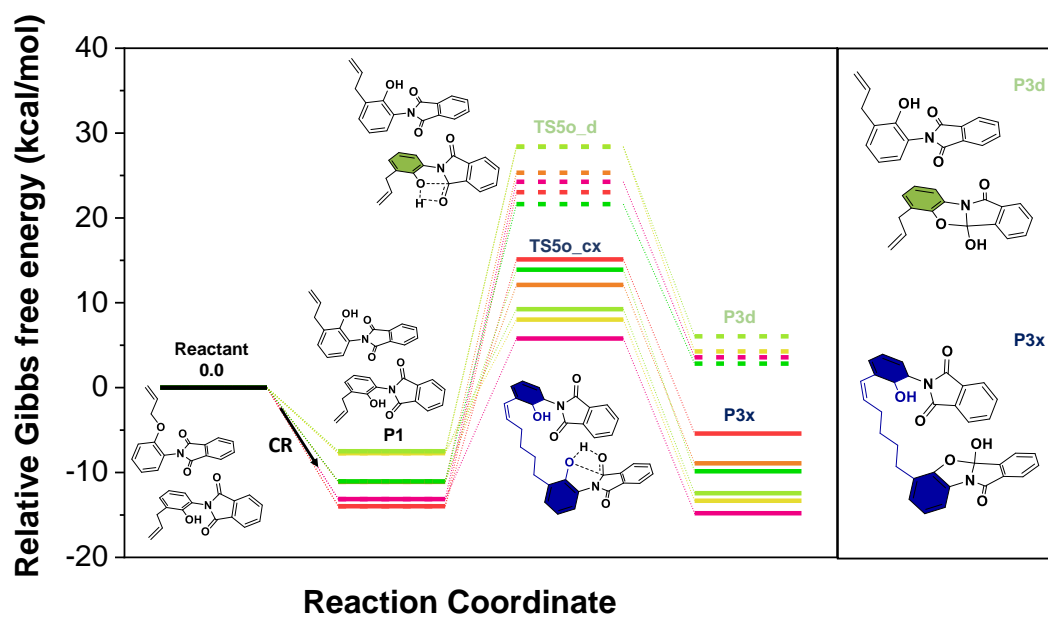


Figure 111. Simulated reaction coordinate for the first step of the HPI-to-PBO formation mechanism (according to Tullos et al. [124, 125]) with respect to the crosslinked (TS5o\_cx) and non-crosslinked (TS5o\_d) allyl derivatives.

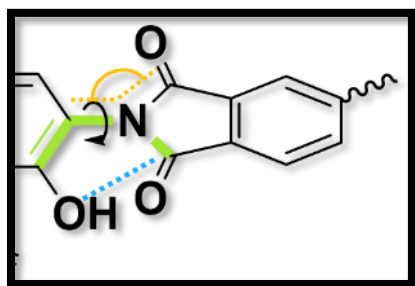


Table 3. Torsions (green) around the dihedral angle formed by the imide-bond and distance (blue) between the reactive nucleophilic phenolic-O atom and the electrophilic carbonyl C-atom for all crosslinked and uncrosslinked allyl-imide models.

	TS5od_		TS5ox_ee_		TS5ox_em6_	
	Torsion (°)	Distance O-C (Å)	Torsion (°)	Distance O-C (Å)	Torsion (°)	Distance O-C (Å)
Allyl	-27,784	2,135	-27,155	2,132	-27,831	2,144
αM	-27,756	2,135	-27,155	2,132	-27,165	2,131
βM	-27,688	2,133	-27,187	2,133	-28,025	2,143
γM	-28,255	2,142	-27,447	2,136	-27,356	2,139
γE	-28,981	2,152	-27,391	2,136	-27,477	2,140
γEa	-28,160	2,140	-27,480	2,137	-27,342	2,138

The TR reaction requires a certain degree of freedom with regard to the dihedral rotation of the imide group. In case of Allyl-PI, the molecules can come close to each other, which leads to restriction of their rotation. In case of  $\alpha$ M-PI the additional methyl group acts as a larger spacer than the simple Allyl group. Hence, the dihedral angle in  $\alpha$ M can be lowered compared to allyl, due to more freedom to rotate.  $\beta$ M shows the lowest dihedral angle and lowest activation energy, and the lowest distance between both reacting units (phenolic-O and Carbonyl-C).  $\gamma$ -substituted derivatives show the largest dihedral angle and larger distances of the reactive centers as well. By checking a geometric arrangement of three molecules, the possibility of  $\beta$ M to rotate more freely becomes clear, as the molecules are far apart from each other, as the  $\beta$ -Methyl group induces more space, due to its less flexible and branched group. The geometric parameters of the different TS<sub>50</sub> geometries are shown in Table 3.

Another effect of the substitution occurs within an *ortho*-ally phenol unit. Methylation in  $\gamma$ -position leads to close contact of the methyl and phenolic-OH group (Figure 112), once the  $\gamma$ M-allyl group rotates. Nevertheless, the TR process is also significantly affected by crosslinking. In case of crosslinked models, the highest energies are calculated for modifications with branched crosslinks, such as  $\alpha$ M,  $\beta$ M and  $\gamma$ Ea who have methyl groups in  $\gamma$ M- and  $\beta'$ - position (Figure 69).  $\gamma$ M and  $\gamma$ En are lower with 8 and 9 kcal/mol, respectively, whereas Allyl has only an activation energy of 6 kcal/mol in relation to the starting material, as a consequence of the higher flexibility and lower steric hindrance of the crosslink. The comparison of the overall activation energies for the crosslinked and non-crosslinked systems might confuse, as crosslinked systems seem to rearrange easier. A lower TR activation energy, despite the additional restrictions of the PAG-Imide unit. However, in such a two molecule system, they are more separated and independent from each other, which is true in a crosslinked dimer, but not realistic in a polymer for instance. Moreover, a strong contribution comes from the rotation of the imide unit, which is not restricted by crosslinking in such a model, but in a polymer with consecutive monomer units.



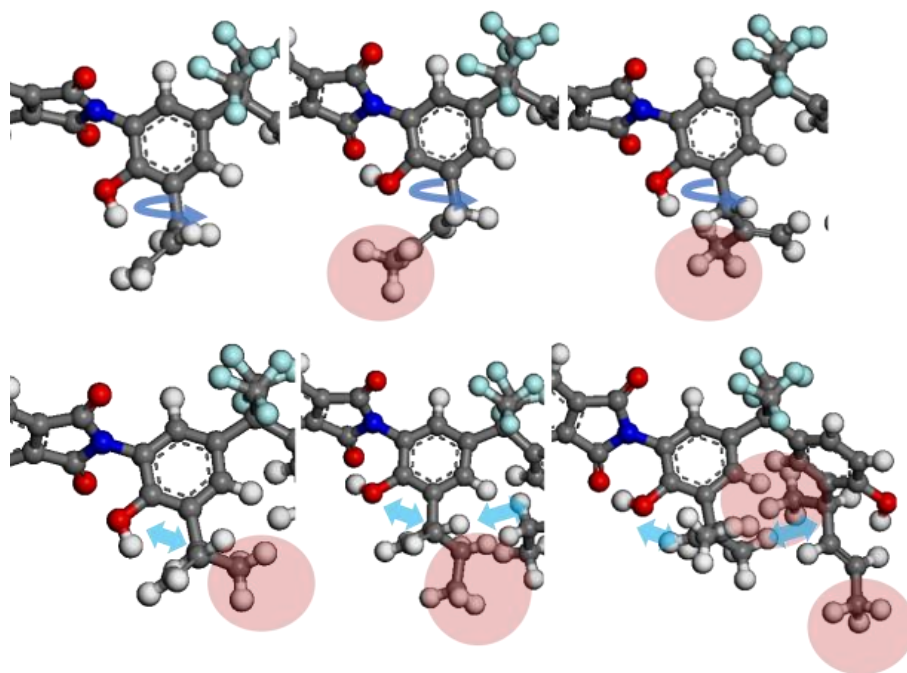


Figure 112. Image capture of the allyl-phenyl ether imide unit in a polymer. Modification areas are highlighted in red and blue arrows show the area of restricted motion as a consequence of the modification.

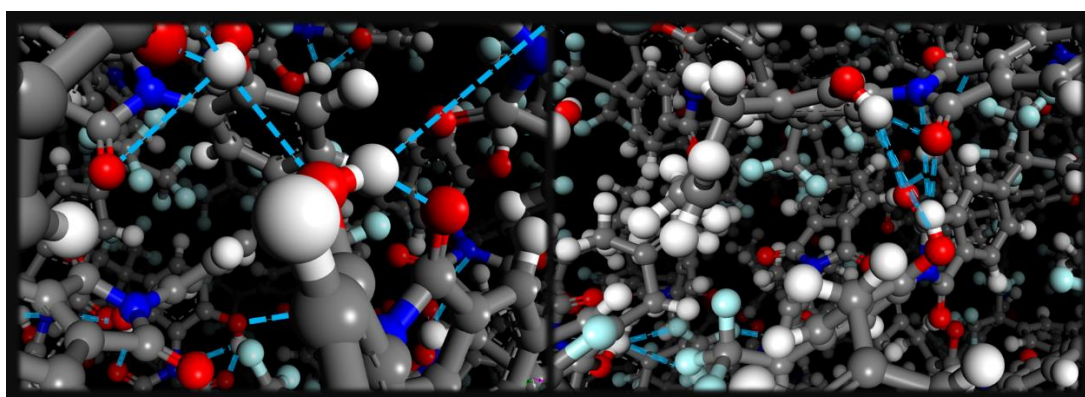


Figure 113. Hydrogen bond formation in pristine HPI (left) and  $\beta$ Mallyl modified HPI (right).

## Full Cascade Reaction Comparison with the Literature

The reaction mechanism proposed by Tena *et al.* [256] for allyloxy polyimides is based on the TR mechanism suggested by Park *et al.* [127]. However, for the allyloxy system they concluded the formation of a phenolate after the first CR step, the allyl group migration from O- to C-allyl. This process was succeeded by a proton migration from C2 to O<sub>Phenol</sub> in Claisen's theory. Tena *et al.* suggested a heterolytic cleavage of the aromatic hydrogen at C2, recovering the aromaticity and forming a phenolate rather than a phenoxy intermediate. The remaining electrons on O<sub>Phenolate</sub> cause an increased negative charge and consequently higher nucleophilicity. Therefore, the phenolate is more reactive towards the electrophilic imide carbonyl group. Heterolytic cleavages are widely known to require large energies and ionic intermediates are more likely to form, when solvent and additives are present to stabilize the ionic charge [289]. Aqueous electrolytes are compensated by a water cage for instance [290-292]. Simulations of ionic pathways for other reaction types have shown to require large energies [217] and ionic intermediates appear to exist only for very short times in solid-state [257].



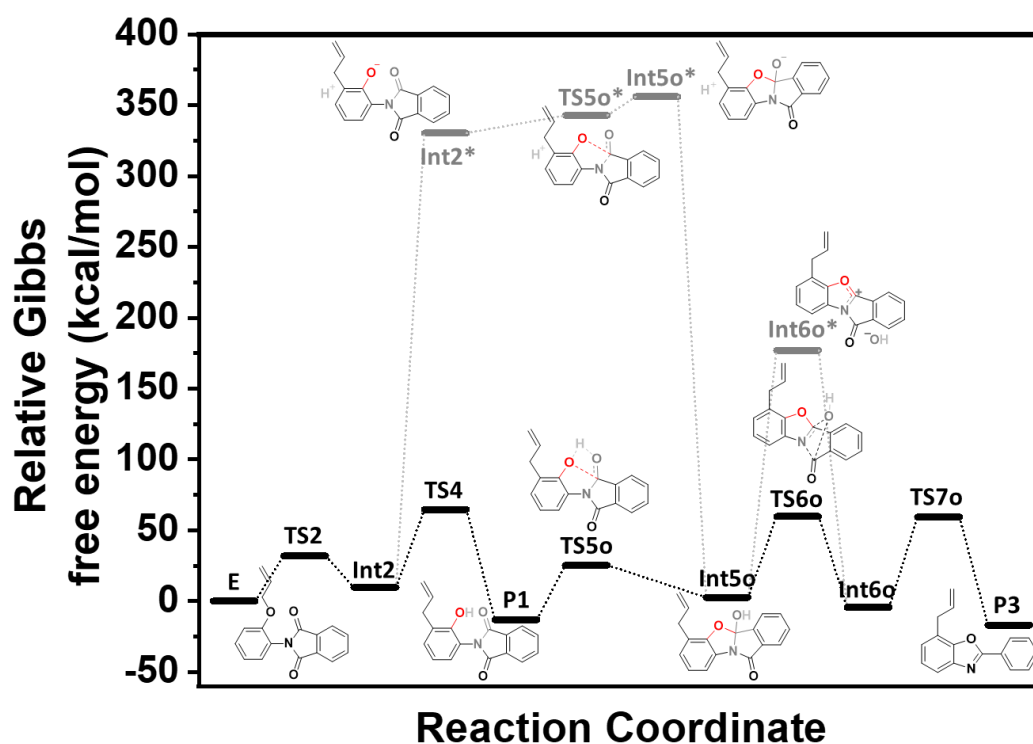


Figure 114. Reaction coordinate of the proposed Claisen Rearrangement promoted Thermal Rearrangement according to the literature (grey) and this study (black).

The CR process itself for instance as well as the Fries rearrangement are openly discussed to be polar but not ionic in total for example [225].

For comparison reasons the mechanism by Tena *et al.*[256] was simulated (Figure 114). As expected, after the first CR step, the formation of a phenolate and proton shows energies above 300 kcal/mol and five times higher than the phenoxy intermediate formation and the proton migration step from C2 to the phenoxy-O. This high energy barrier makes it highly unlikely to be overcome to proceed via an anionic intermediate. However, even in the case of an anionic intermediate, several factors come into account apart from the proposed nucleophilic character due to the negative charge. Electronic and steric reasons can facilitate or complicate a reaction mechanism. The negative charge is, based on the calculation of Mulliken charges (Figure 115), only 14% higher compared to the protonated phenol group. Phenolates tend to be more nucleophilic compared to phenol, and as a consequence of the mesomeric effect of the aromatic ring it is significantly more reactive to electrophiles compared to aliphatic alcohols and even more to ketones. Tena *et al.* assumed the formation of a phenolate, however DFT simulations

have shown that the C=O bond corresponds more to a carbonyl bond with 1.27 Å and is less polarized with a difference of 0.432. The electron density is high around the carbonyl group and the C2-C5 atom with its highest density and most negative Mulliken charge of -0.35 in *para* position (C4). These observations are more in accordance with the proposed cyclohexadienone intermediate with local conjugated double bonds in C2-C3 and C4-C5 and a CO carbonyl group. Despite the nucleophilicity, the electrophilicity of the counter part of the reaction is as important as the nucleophile. The Simulation reveals, that the formation of the allyl-phenol (P1) leads to a slightly larger imide carbonyl bond and a more positively charged carbonyl carbon atom. Apart from the electronic considerations, the proposed anionic intermediate shows a larger discrepancy of the dihedral angle between the imide and phenol unit, as well as a larger distance between both reacting centers, Phenol-O, and Imide-Carbonyl-C, compared to the *ortho*-allyl phenol.

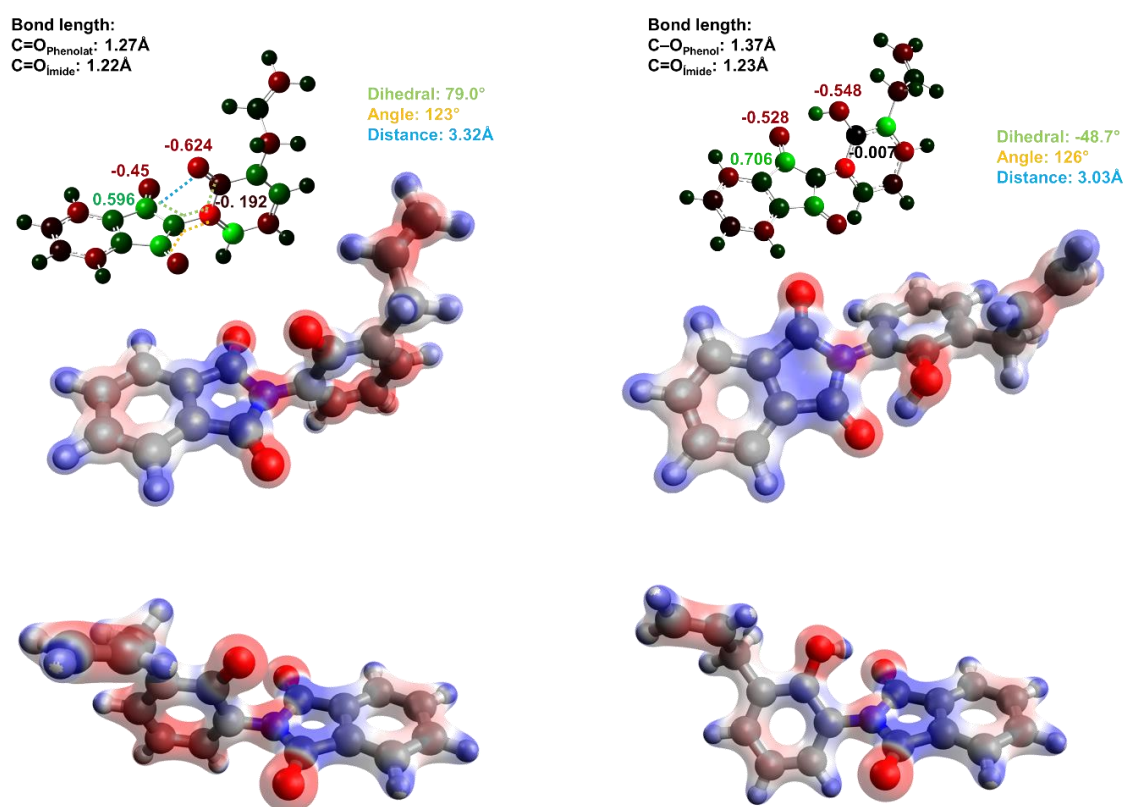


Figure 115. Visualization of the Mulliken charges, electrostatic potential map, and electron density (from the top down) of Int2\* (left) and P1 (right).

The proposed second step of the TR process was also ionic, based on the suggestion by Park *et al.* [127], calculated herein with TS energies of 150 kcal/mol, and nearly three times higher compared to the suggested transfer mechanism from chapter *TR mechanism*.

**Conclusion.** The lowest-energy path, proposed from chapter *TR mechanism*, was used as a fundament for the simulation of the TR mechanism in allyloxy-polyimide TR precursor in this study. A reaction cascade of CR and TR as well as CR and Cx+TR was calculated. All three pathways show significantly lower transition energies. The results in the allylated dimers and crosslinked dimers showed lower transition state geometry energies compared to the *ortho*-hydroxy imide in accordance with the experimentally determined thermokinetics of the TR process in allylated materials. Molecular modelling studies have shown the beneficial effect of low degrees of crosslinking and allyl as spacer compared to the pristine material, corroborating the spacing effect as being responsible for the lower TR<sub>onset</sub>, and making this mechanism from an electronic and molecular mechanic point of view more reasonable (Figure 116, Scheme 11).

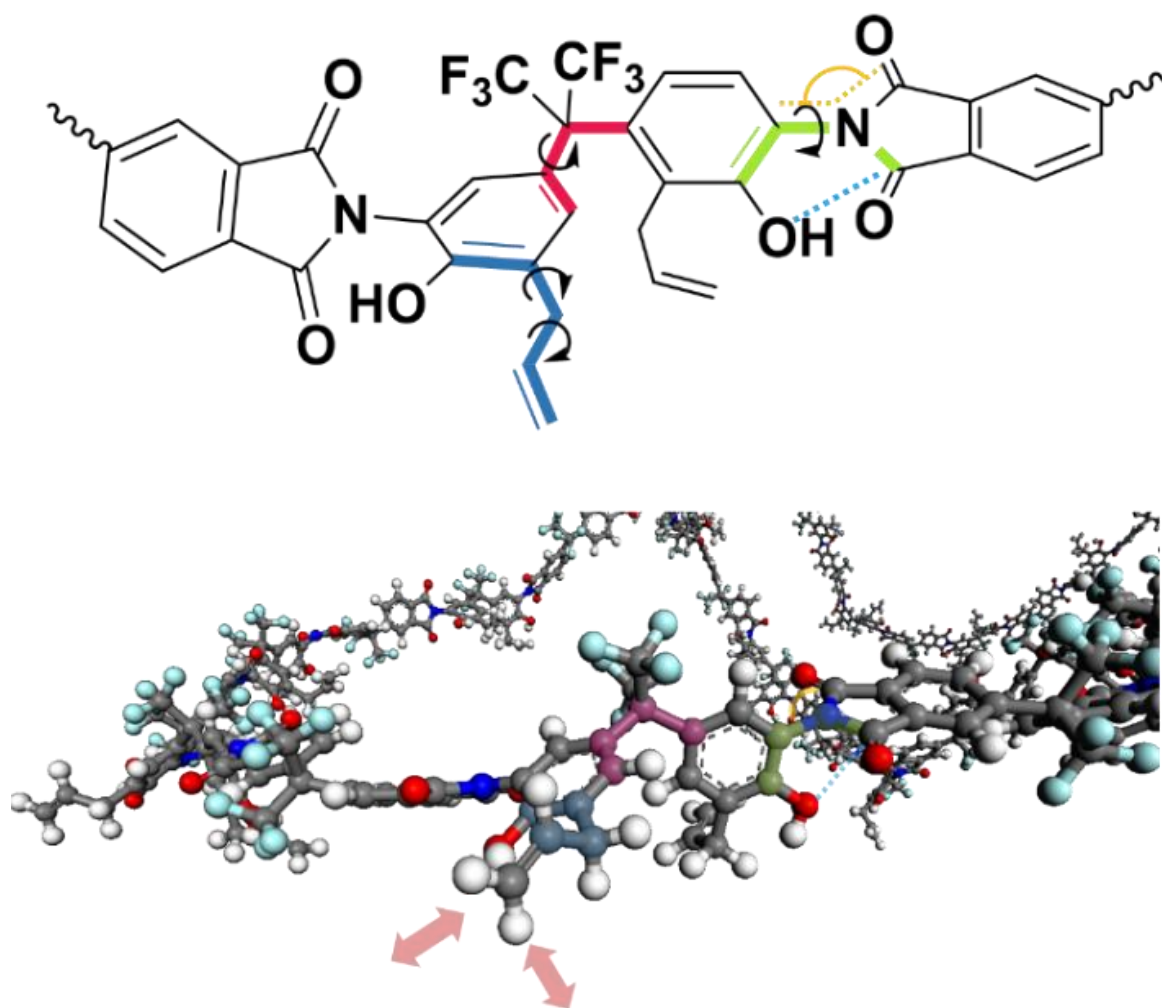
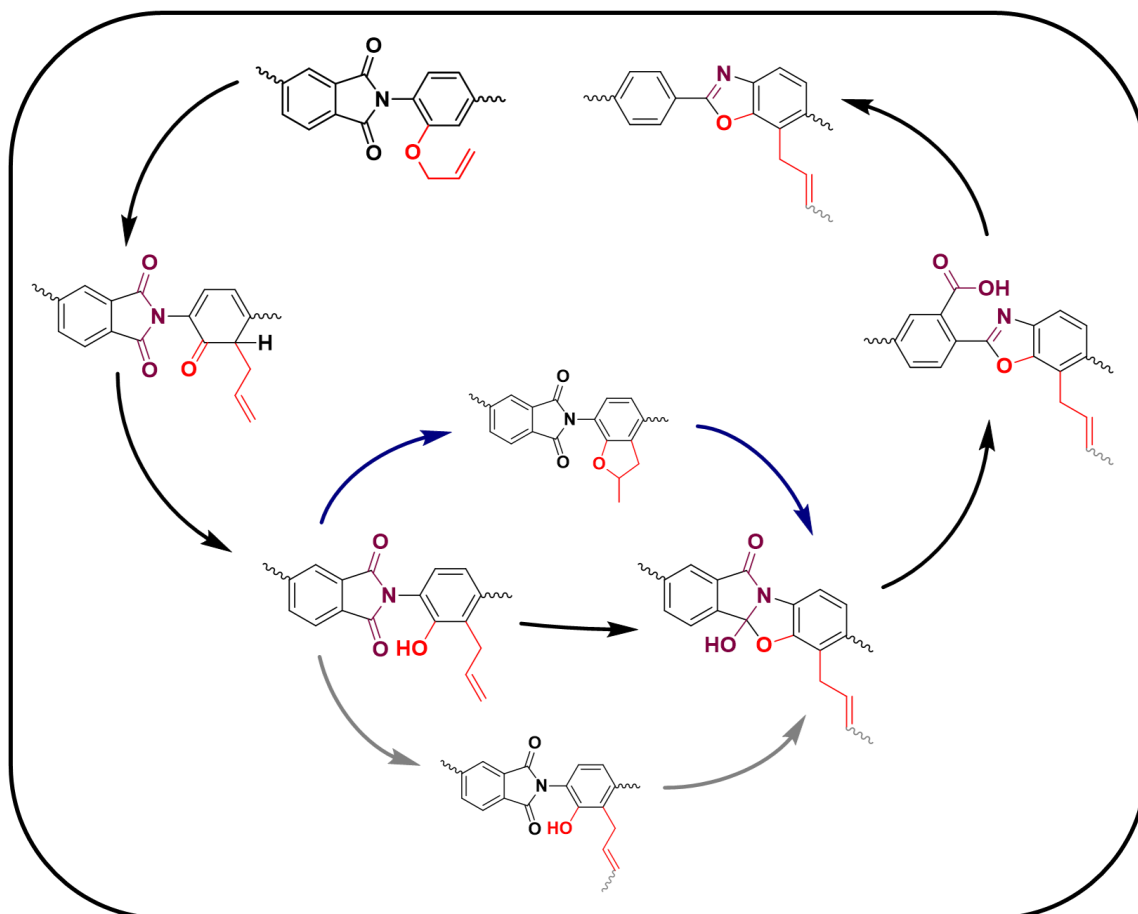


Figure 116. Scheme showing the mainly responsible dihedral angles, angle, and distance during the first step of the HPI-to-PBO formation reaction (top). Highlighted geometry parameters in a polymer model (middle) and example of allyl and  $\beta$ M-groups creating space between each polymer chain (bottom), highlighted by red arrows.



Scheme 11. Proposed thermally initiated cascade reaction of ortho-allyloxy polyimides.

## Key Messages

- Computational studies revealed, as key results, that the TR process depends strongly on the modification.
- Experimental results were confirmed by quantum chemical and molecular dynamics simulation to a high extend.
- Low Claisen Rearrangement temperature of  $\alpha$ MPI-1 was confirmed.
- Tendency to form furan cycles, with significant lower activation energies for the  $\beta$ MPI-1 model confirms the high number of furan rings according to the  $^{13}\text{C}$ -CP-MAS experiment.
- 14 Crosslinking mechanism were calculated. An Alder-ene crosslinking reaction mechanism was identified as the most reasonable one.
- Based on the identification of the crosslinking mechanism the experimental tendencies were corroborated.
- Molecular Modelling via MD simulations confirmed the crosslinking tendency and gave good insights into the effect of the crosslinks on the polymer properties.
- The TR mechanism was modeled.

## Film Properties

Previous results of the thermokinetic analysis and simulations revealed a strong variation of the formed structures. Claisen Rearrangement, Crosslinking, furan cyclization, benzoxazole cyclization (TR) were the simulated and experimentally observed reactions. Since all materials differ in their extent of crosslinking, substitution along the crosslinks and conversion to the polybenzoxazole for instance, significant changes of the film properties, especially gas separation performance, are expected. For that purpose, allyloxy-polyimide films of a thickness of 50  $\mu\text{m}$ , in average, were cast. These films were isothermally annealed at 300, 350 and 400  $^{\circ}\text{C}$ , respectively. The treatment occurred in a nitrogen flushed tube oven. Small pieces of the treated membrane were investigated by TGA to determine the residual mass loss in the TR temperature range in order to determine the HPI-to-PBO conversion.

$\beta\text{M}$ - and  $\gamma\text{E}$ -PI show high PBO conversions at 350  $^{\circ}\text{C}$  of 84 and 100%, respectively, as demonstrated in Figure 117, while at 400  $^{\circ}\text{C}$  both are fully converted. The conversion for  $\alpha\text{M}$  at 350  $^{\circ}\text{C}$  is slightly higher compared to  $\gamma\text{M}$  and Allyl. The conversion is inverse to the  $\text{TR}_{\text{onset}}$  temperature. As the required  $\text{TR}_{\text{onset}}$  temperature decreases, the conversion increases, respectively. Consequently, an effect to the density and fractional free volume of the annealed films is expected, as it is widely known that the HPI-to-PBO cyclization leads to lower densities and higher free volume as a result of the rigidification of the backbone, accompanied by the void formation due the  $\text{CO}_2$  release and additional thermally induced crosslinking [127].

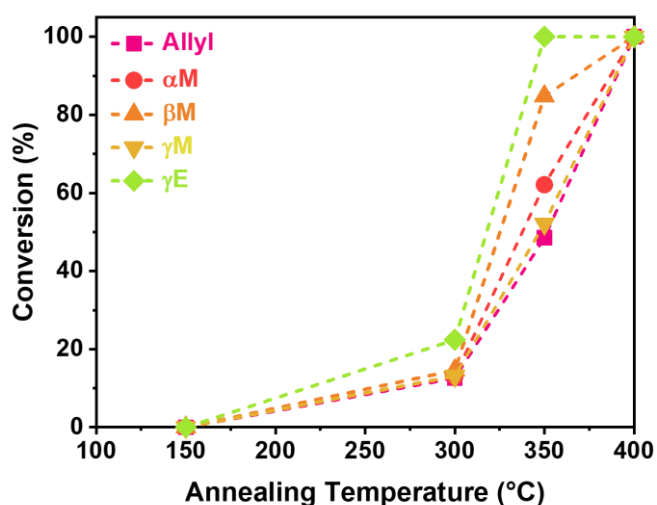


Figure 117. HPI-to-PBO conversion with increasing temperature treatments for the synthesized materials.

## Density and FFV

All precursor materials show a similar density around  $1.40 \text{ g/cm}^3$  (as shown in Table 5). The pristine material in turn has a density of  $1.49 \text{ g/cm}^3$ . The lowered density for the allyloxy polyimide precursor is explained by the lower number of hydrogen bonds, as no phenol groups to form hydrogen bonds are available and polymer chains are more separated to each other.

Nevertheless, the density dropped down to  $1.35 \text{ g cm}^{-1}$  after annealing at  $300 \text{ }^\circ\text{C}$  for 30 min for all materials. Above the glass transition temperature, polymers usually tend to densify as their degree of mobility increases [23, 55, 293]. Hence, they are able to overcome any non-equilibrium state and relax, which decreases the non-equilibrium free volume elements in a polymer film [23]. However, the allyloxy polyimides decrease their density. An explanation for that phenomenon can be found with regard to the crosslinking process. The formed crosslinks, combined with free allyl groups or benzofuran units, contribute to a polymer chain packing disruption [144, 145, 268]. Although large aliphatic crosslinks are formed, which usually are flexible chains, their methyl-groups along the crosslinking chain leads to restriction of free rotation. Accordingly, the density decreases (see Figure 118) and fractional free volume increases, results are summarized in Table 4.

It is noteworthy to mention, that the FFV calculation is based on density measurements with an experimental uncertainty, and no exact knowledge regarding the favored crosslinking mechanism and absolute number of crosslinks. Furthermore, the quantity of other formed structures is not exactly known. One example is the exact determination of the structural distribution of the normal and abnormal Claisen product in  $\gamma\text{E-PI}$ , as they cannot be distinguished easily by means of spectroscopic methods.



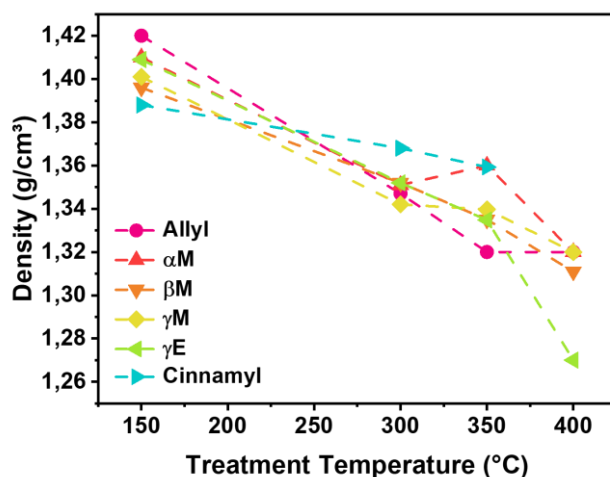


Figure 118. Density as a function of the annealing temperature in the range from 150 to 400 °C.

One of the most widely described thermal crosslinkers in polyimides is diaminobenzoic acid (DABA) [111, 121, 122, 294, 295]. While DABA does not crosslink until reaching temperatures above 300 °C [118], polymers of this study showed gel-fractions of 100% when approaching an annealing temperature of 300 °C. In addition, the use of DABA as diamine monomer replaces an *ortho*-hydroxy group containing diamine, such as BisAPAF or HAB. Therefore, the number of units, which can undergo a Thermal Rearrangement reaction, are lowered by the number of DABA monomers used during polymerization. *Ortho*-allyloxy polyimides contain monomers, which are capable to crosslink and undergo a Thermal Rearrangement reaction. Furthermore they crosslink at lower temperatures and convert to the PBO by TR at significant lower temperatures. In  $\gamma$ E-PI, a gel content of 100% and a TR conversion of 22% at 300 °C was determined.

### Molecular Modelling Studies

Based on the proposed mechanism and the experimental findings of the different *post*-CR reactions and PBO conversions, simulations to correlate the structural findings with gas separation related properties were performed to formulate a structure-property-performance relationship. The effect of crosslinking on the cell properties was investigated, but emphasis was put on the evaluation of an appropriate  $\beta$ M-PI model in order to understand the contributions of each structural influence as it appeared to be among the most promising materials for gas separation applications.

Fully Claisen-Rearranged polymer chains in an equilibrated amorphous cell via a 21-step method, as described in chapter *Characterization* was used. After generating a CR cell, the subsequent cascade reactions were modeled. At first by increasing the degree of crosslinking. This was done for two allylic groups, that are within a pre-defined radius of 5 Å, which has been determined as the distance between two geometry optimized  $\beta$ M-PI units at the starting point of their intrinsic reaction coordinate of a crosslinking reaction.

As the number of crosslinks increases, a decrease of the cell density, of all investigated amorphous cells occurs (Figure 122), while observing its largest impacts on  $\gamma$ E- and  $\gamma$ Ea-PI. Only Allyl-PI maintained its density throughout the crosslinking procedure. Materials, having substitutions in  $\gamma'$ -position showed the strongest density decrease, since their crosslinks are rigid, as a consequence of the vicinal methyl groups (both methyl groups are adjacent to each other, such as tail-tail bonds of methyl methacrylate). Consequentially, the allyl group cannot freely rotate due to the steric interaction of the  $\gamma'$ -methyl group and the phenolic -OH group. This is supported by means of a PES scan of the dihedral angle along the crosslink as demonstrated in Figure 119-Figure 121.

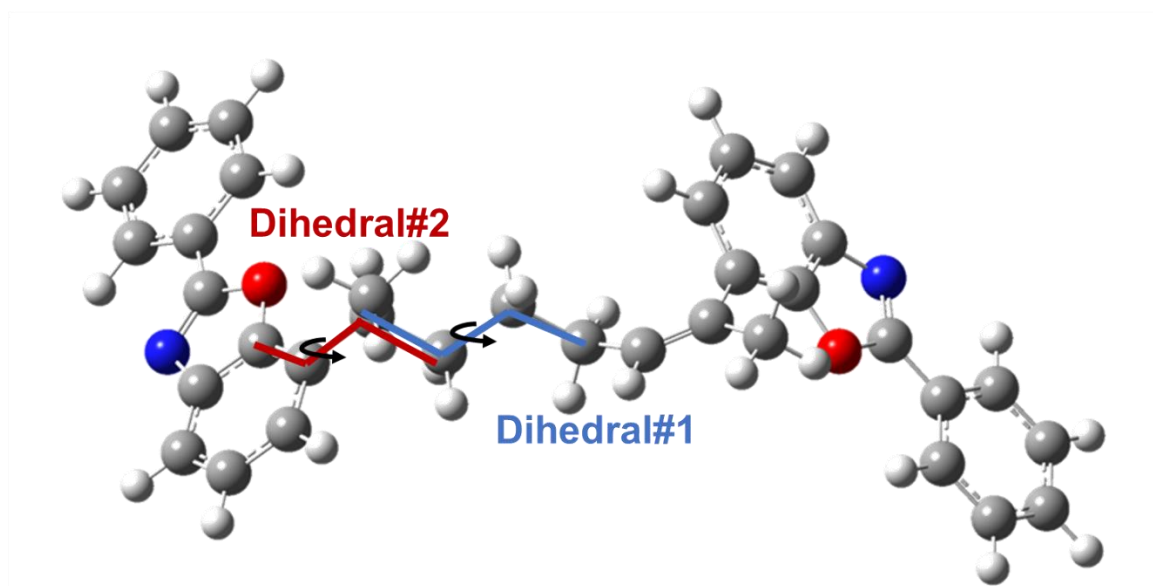


Figure 119. Visualization of the investigated dihedral angle of the studied allyl derivatives.

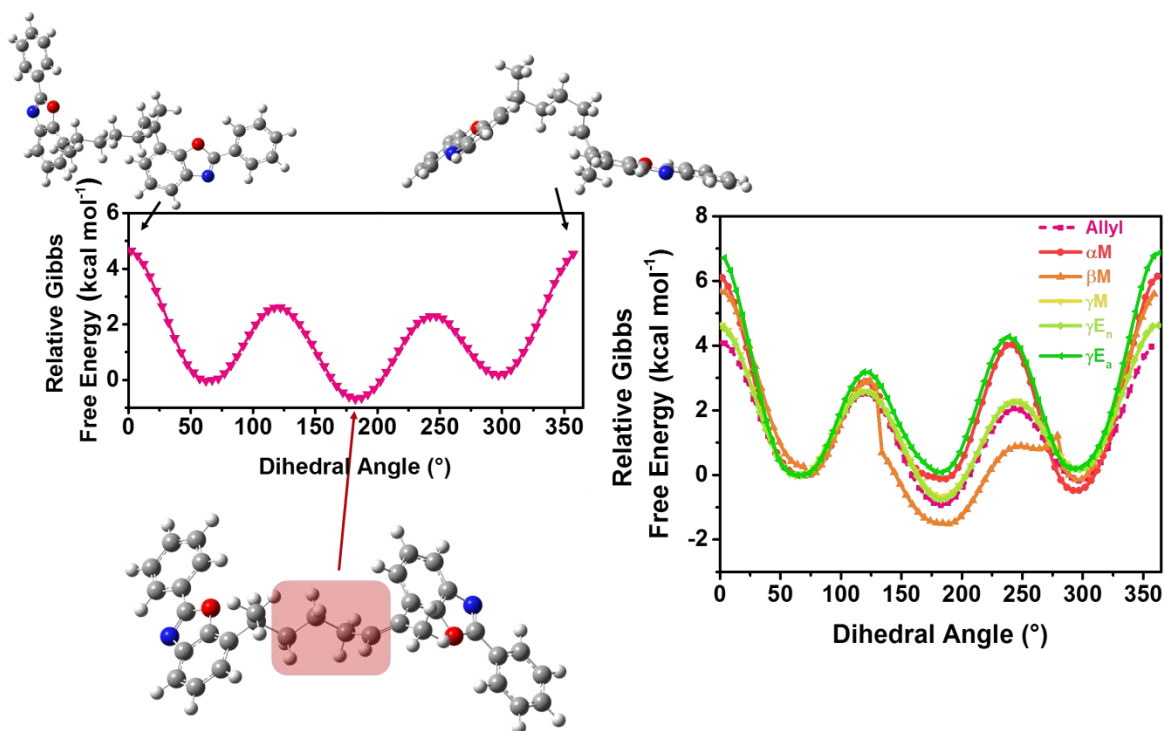


Figure 120. PES scan of the dihedral angle (red markup) of Allyl-PBO (left), PES scan of the dihedral angle of allyl derivatives  $\beta M$ -PBO,  $\gamma M$ -PBO,  $\gamma E_n$ -PBO and  $\gamma E_a$ -PBO.

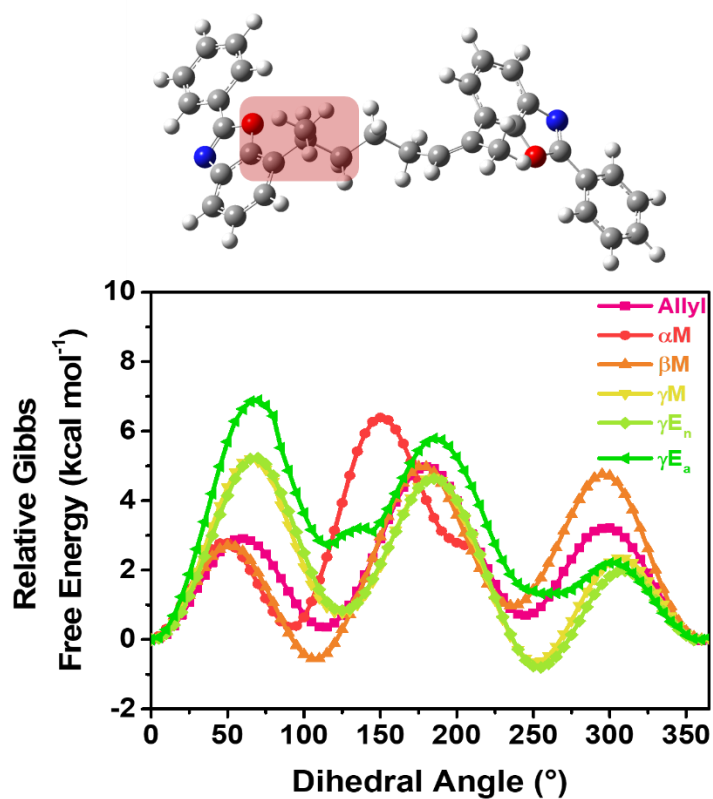


Figure 121. PES scan of the dihedral angle (red markup) of Allyl-PBO (left), PES scan of the dihedral angle of allyl derivatives  $\beta M$ -PBO,  $\gamma M$ -PBO,  $\gamma E_n$ -PBO and  $\gamma E_a$ -PBO.

As the number of crosslinks continues to increase, the density keeps increasing as well. The strongest density increase was observed for  $\gamma$ En-PI, most likely due to the large ethyl group that possibly densifies the created space between polymer chains, if the free volume elements are sufficiently small enough. The ee-crosslinks in the amorphous cells of each derivative are shown in Figure 123. For better visualization, the side groups are highlighted.

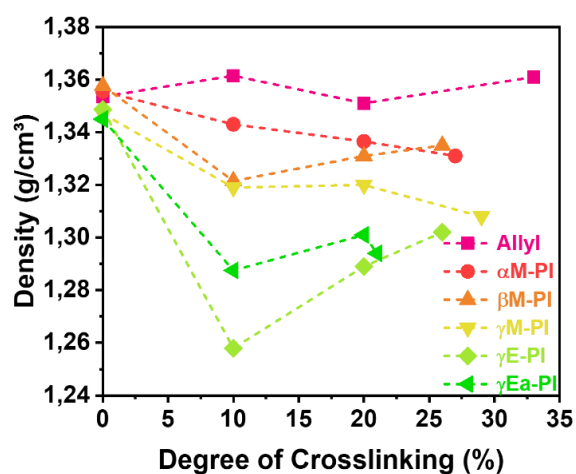


Figure 122. Density as a function of the degree of crosslinking of all allyl derivatives.

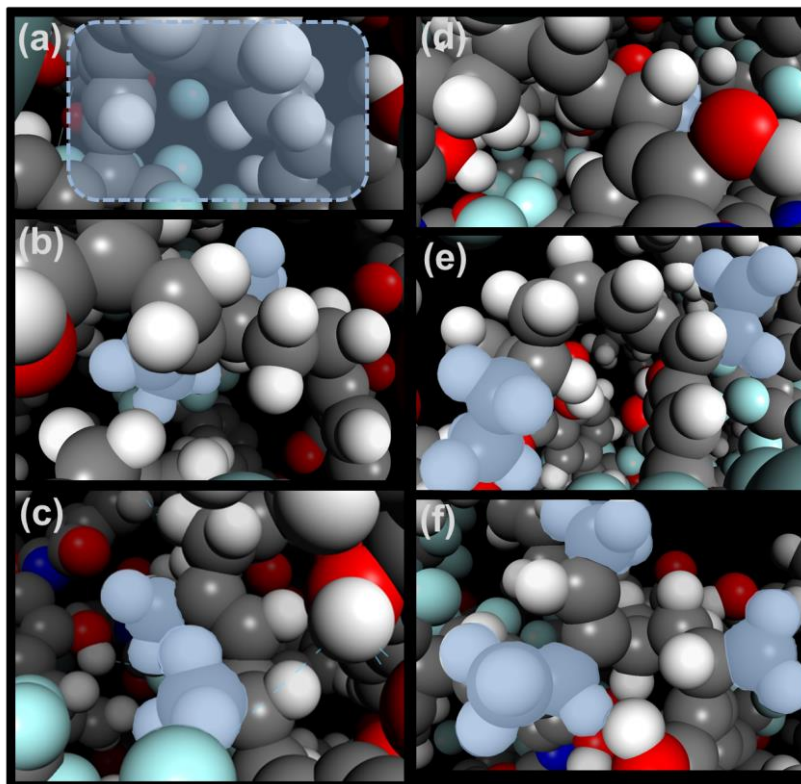


Figure 123. Micro voids in crosslinked amorphous cells of (a) Allyl-, (b)  $\alpha$ M-, (c)  $\beta$ M-, (d)  $\gamma$ M-, (e)  $\gamma$ En-(f)  $\gamma$ Ea-PI.

Aside from crosslinking, an additional effect becomes apparent, after carefully analyzing the free volume elements around the methyl groups (Figure 124). The steric interaction of methyl and trifluoromethyl groups leads to inefficient polymer chain packing and creates voids around them (clouds, grey side is the outside of the free volume elements surface). The number of those methyl-methyl or methyl-trifluoromethyl groups is more prominent for materials with methyl groups in  $\beta'$ - and  $\gamma'$ -position.

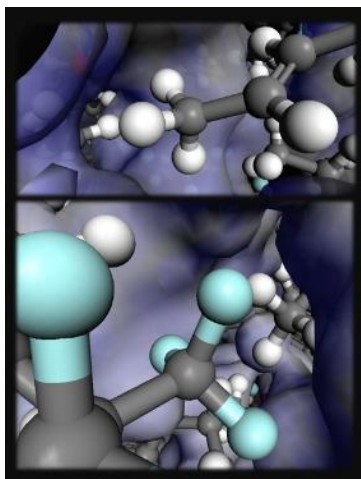


Figure 124. Methyl-methyl and methyl-trifluoromethyl group interactions and their free volume element formation (grey area).

Despite thermal crosslinking, cyclization reactions were observed by means of solid-state NMR experiments and supported by DFT simulations. Among all materials,  $\beta$ M-PI showed the largest amount of benzofuran cyclization, as well as a significant amount of benzoxazole units due to the low  $TR_{\text{onset}}$  temperature. In Figure 125, a representation of a  $\beta$ M-PI polymer chain, including its potential units (Cy, Cx, CR, TR) is shown to support further discussions, since  $\beta$ M-PI is discussed in more detail in the following section. The focus was put on  $\beta$ M-PI since it showed among the lowest TR related temperatures and highest tendency to form benzofuran groups, which are highly interesting for gas separation applications.

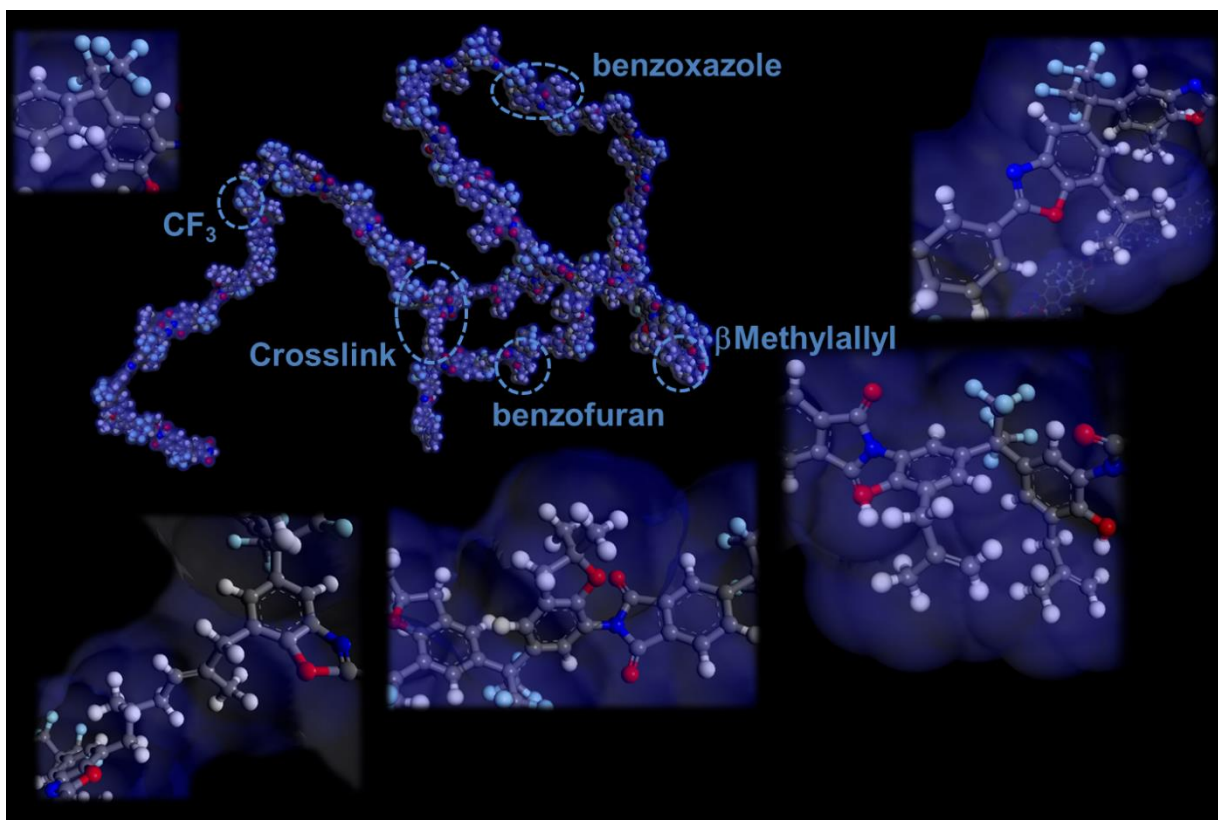


Figure 125.  $\beta$ M-PI polymer chain containing benzofuran, Claisen-Rearranged, crosslinked and thermally rearranged units.

For  $\beta$ M-PI, 50% of the non-crosslinked allyl groups were subjected to a benzofuran cyclization, according to the experimentally determined ratio by means of  $^1\text{H}$ -liquid and  $^{13}\text{C}$ -CP-MAS NMR studies. The corresponding model is called CyCx- $\beta$ M-PI.

In addition, in accordance with the experimentally determined reaction cascade, an HPI-to-PBO cyclization reaction (Thermal Rearrangement) was done. The residual 50% of phenol groups were then used to form PBO units. This model is described as (TCR) $\beta$ M-PI, with TCR for Thermal Cascade Reaction. As a reference, a  $\beta$ M-allyl containing PBO cell and a fully benzofuran containing polyimide, PBF- $\beta$ M-PI, was constructed (Figure 126).



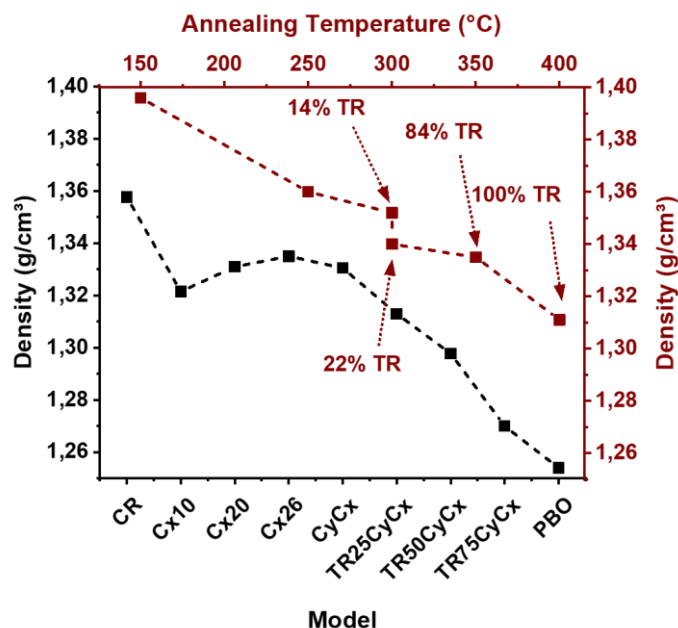


Figure 126. Experimental (maroon) and simulated density (black) depending on the structure and annealing temperature, respectively.

While the cell density might serve as a good indicator, whether a material might have a low or high free volume, the fractional free volume includes in its definition the Van der Waals volume of the polymer. Therefore, the free volume serves as a more suitable measure for the applicability as a gas separation film.

For the determination of the free volume of the modeled cells, a grid scan, implemented in the visualizer tool of Biovia Materials Studio® [296], was used. This grid scan determined the Connolly surface of the polymer and calculated the occupied and free volume. The free volume evolution for the different models is shown in Figure 127 and Figure 128. An increase of the free volume in correlation with a decrease of the density is observed as the degree of crosslinking increases.

It is noteworthy, that the reference PBF- $\beta$ M-PI showed a higher free volume compared to the crosslinked CxPBO- $\beta$ M. This observation suggests, that such methylated benzofuran rings disrupt efficient packing to a high extend.

The simulated free volume and surface areas can be used to evaluate the free volume element distribution. Park *et al.*[193] [190] reported the use of the accessible volume ( $V_{\text{accessible}}$ ) to the accessible solvent surface ( $S_{\text{accessible}}$ ) ratio as a measure of the goodness of a cell but also its pore

size. When the number of free volume elements increases by generating more small pores, the pore surface increases simultaneously. As a result, the volume to surface ratio decreases (Figure 127).

The crosslinking forces the polymer chains to separate from each other at low degrees of crosslinking (10%) by formation of larger pores. As a result, the free volume increases more than the surface area does. This in turn leads then to a higher free volume to surface ratio. Further crosslinking cycles increase the density and recompact the polymer matrix, which is in favor of the formation of small free volume elements. Thus, more free volume elements with higher surface to volume ratios are available and cause a V/S decrease, while the accessible free volume remains nearly constant.

Nevertheless, when crosslinked CxβM-PI undergoes a benzofuran formation of a small increase in free volume can be seen, as methylated furan units are likely to restrict efficient chain packing. These large pores lead to an increase of the V/S ratio, as the V/S ratio increases for larger pores.

The HPI-to-PBO cyclization with its inherent decarboxylation leads to free volume increases, since decarboxylation leads to formation of small pores, which are preserved due to rigid PBO and furan units as well as stiff and branched crosslinks. Such a free volume increase is in accordance with the experimental findings, in which the free volume increases from 18 to 20 to 22 % as the annealing temperature is raised.



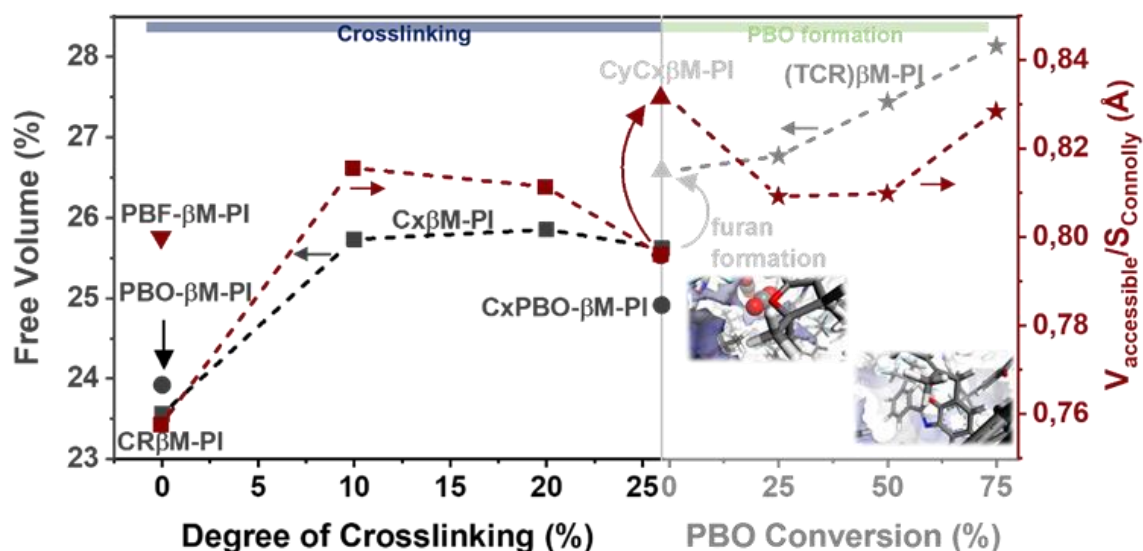


Figure 127. Free volume (grey) and accessible solvent surface to volume ratio (maroon) as a function of the degree of crosslinking from 0 to 26 (■). Reference materials PBF-βM-PI (▼) and PBO-βM-PI, CxPBO-βM-PI (●) are shown as well. From the final maximal crosslinked Cx26βM-PI the cyclized CyCxβM-PI (▲) and (TCR)βM-PI are shown (★).

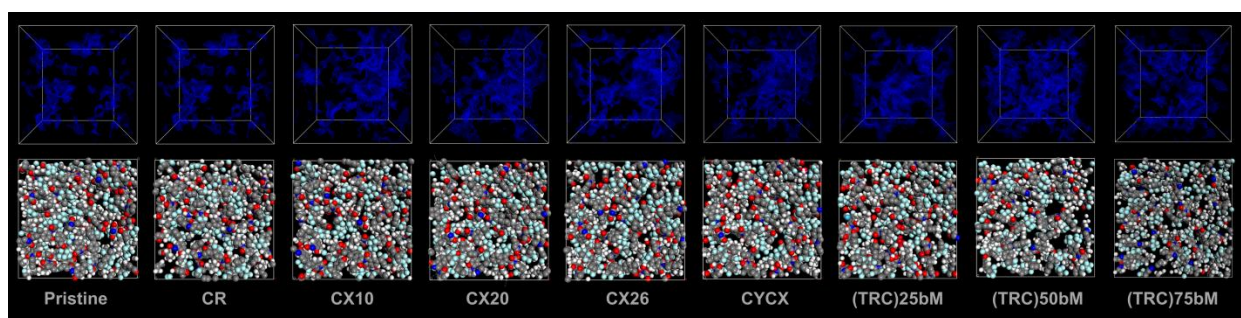


Figure 128. Evaluation of the free volume (top) and pore formation shown in corresponding amorphous cell slices (bottom) of pristine βM-PI, Claisen-Rearranged CRβM-PI, crosslinked structures CxβM-PI with increasing crosslink ratios 10, 20, 26, additionally cyclized CyCxβM-PI and partially HPI-to-PBO rearranged (TCR)βM-PI with conversion of 25, 50 and 75%.

The structural features of each reaction type of βM-PI, which contribute to the free volume characteristics are demonstrated in Figure 129. In Figure 129, the cell containing free volume elements (blue) and two representative slices of the CyCx- (left) and (TCR)βM-PI (right) model are presented. The corresponding images of the polymer chain of the highlighted spots in the free volume cells are shown in pictures (a) to (f).

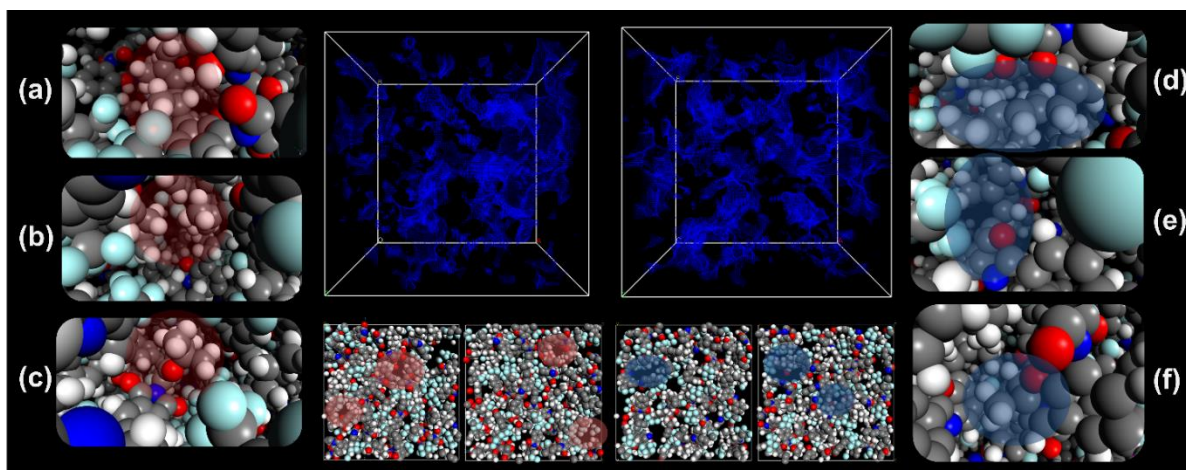


Figure 129. Visualization of the free volume (blue) inside of CyCx- $\beta$ M-PI (left) and partially (50%) HPI-to-PBO rearranged (TCR) $\beta$ M-PI (right). Outside images show (a) crosslinked (b) free  $\beta$ Mallyl groups (c) benzofuran unit of CyCx- $\beta$ M-PI, and (d) crosslinked (e) free  $\beta$ Mallyl groups (f) benzofuran unit of (TCR) $\beta$ M-PI.

In order to explain gas separation properties such as the selectivity of certain gas pairs, the same grid scan was used again to scan the accessible solvent surface as a function of an increasing probe radius for (TCR) $\beta$ M-PI model (Figure 130).

Figure 88 demonstrates the continuous drop of the free volume as a function of the probe radius. Since increasing probe radii are less able to penetrate the pores of a polymer cell. The accessible volume to accessible surface ratio increases slightly and drops after passing a radius of 1.5 Å. This drop indicates that many pores of a size are present, which does not allow penetrants with radii above 1.5 Å to access. Accordingly, pores are accessible by gases such as H<sub>2</sub> with a kinetic radius of around 1.45 Å. N<sub>2</sub> and CH<sub>4</sub>, however, have kinetic diameters which are too large for such elements. Another drop can be observed at 2.2-2.3 Å, which favors propylene rather than propane with Lennard-Jones radii of 2.3 and 2.5 Å, respectively. From these results a good H<sub>2</sub>/N<sub>2</sub> and H<sub>2</sub>/CH<sub>4</sub> as well as an elevated propylene/propane separation of  $\beta$ MPI is expected. The free volume visualization using probe radii of 1.4, 1.6 and 1.9 Å are shown in Figure 131 in order to demonstrate the free volume characterization.

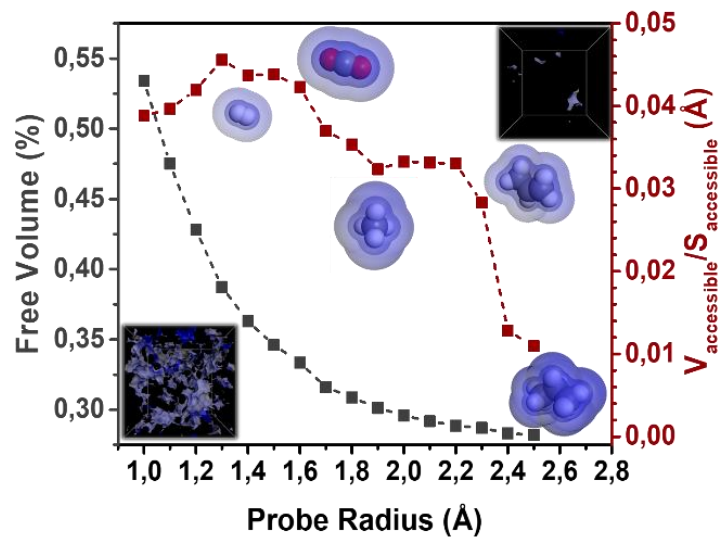


Figure 130. Free volume (grey) and accessible volume to surface ratio (maroon) as a function of an increasing probe radius (0.1 Å steps). Included is a visualization of a cell and its accessible solvent surface at a probe radius of 1.0 Å (left) and 2.5 Å (right) of (TCR) $\beta$ M-PI with 75% HPI-to-PBO conversion.

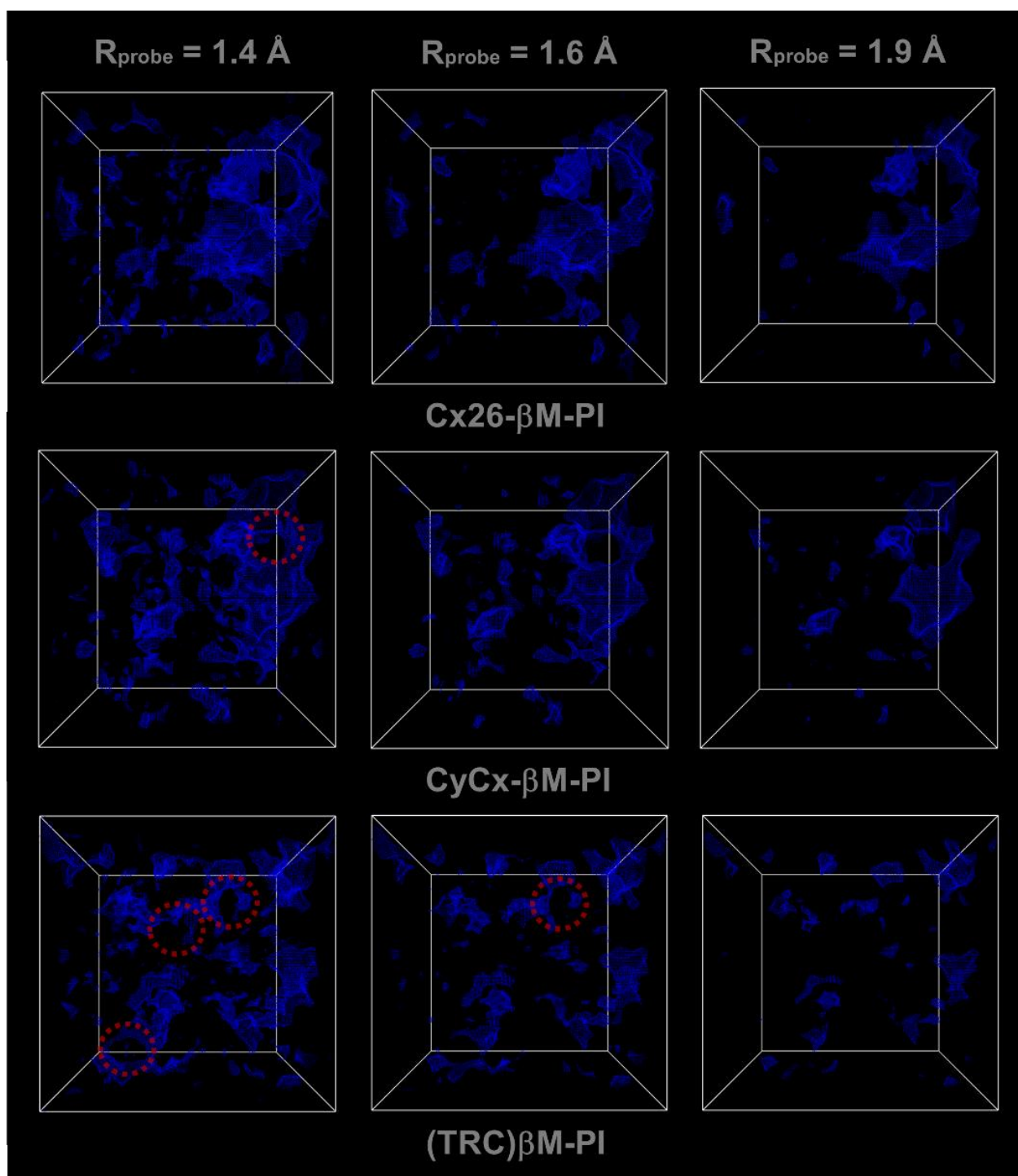


Figure 131. Accessible free volume at a probe radius of 1.4 Å (left), 1.6 Å (middle) and 1.9 Å (right) is shown for CyCx-βM-PI (top row) and (TRC)βM-PI (bottom row).

## Gas performance

The HPI-to-PBO cyclization is known to improve the gas performance by forming highly rigid and crosslinked polybenzoxazoles after a loss of 2 CO<sub>2</sub> molecules per repetition unit.

While crosslinking affects the gas separation performance, depending on the stiffness and number of crosslinks, the total number of crosslinked TRPs is very low. It is usually performed by copolymerization of diamines, that contain crosslinkable groups such as DABA [144, 145]. However, they are not capable to perform a TR process, as they do not have *ortho*-hydroxy groups. In order to achieve 20% of crosslinked repetition units, a decrease of the PBO content by 20% is the consequence for instance. Studies by Calle *et al.*[145] with DABA containing TRPs have shown an increase in the gas permeability until 15 mol% of DABA, and a decrease of the permeability as the number of DABA molecules and hence the degree of crosslinking increases any further.

The presented ally-containing polyimides have shown high PBO conversions in all cases, even at low annealing temperatures of 300 and 350 °C. This high degree of PBO conversion as well as the different structures make these materials highly interesting for gas separation performances.

The diffusion coefficient of each tested gas is expected to follow the trend of the calculated free volume, as the free volume serves as diffusion pathways for the penetrants. In Figure 132 the diffusion coefficient of all tested gases, obtained by pure gas separation measurements via the time-lag method is demonstrated. The plots show the trend for all allyl derivatives after annealing at 350 and 400 °C.

In both cases, the diffusion coefficients decrease with increasing penetrant size from helium to propane for all allyl derivatives. But CO<sub>2</sub> is not following this trend for increasing kinetic diameters. It is noteworthy, that molecular sieving materials are usually characterized by the kinetic diameter of a penetrant molecule. However, different definitions of molecular diameters exist, which vary mainly for more polar and condensable gases (CO<sub>2</sub> and larger hydrocarbons for instance). A comparison of the kinetic, collision, effective and Dal-Cin gas diameters for CO<sub>2</sub> reveals a strong variation, while diameters for unipolar gases are in a narrower range [1]. For instance, the collision diameter by Lennard-Jones (collision diameter),

neglects any shape-contributions, which results in a large CO<sub>2</sub> diameter [1]. A study by Robeson demonstrated, that the Dal-Cin diameter[18, 38] shows closer values to unity than the effective diameter by Chung. Accordingly, the use of the Dal-Cin diameter positions the CO<sub>2</sub> diffusion coefficient in a way, that it follows the diffusion coefficient – molecular diameter relationship.

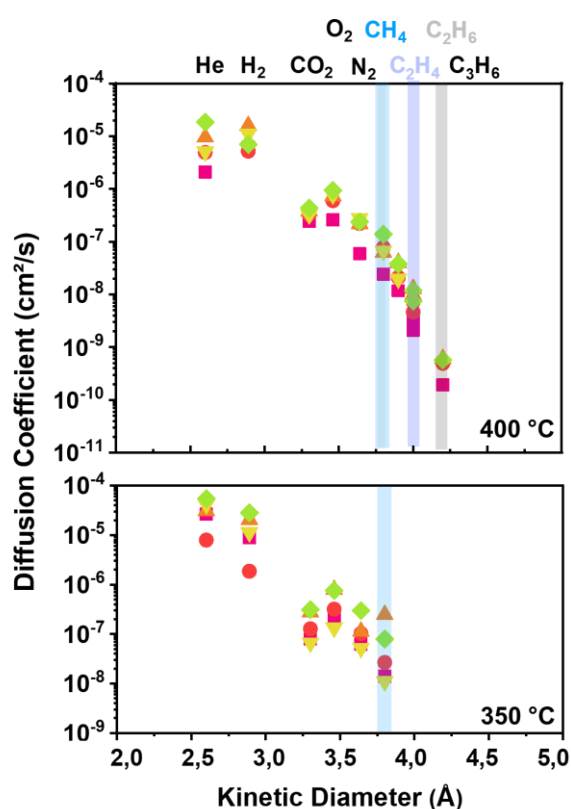


Figure 132. Diffusion coefficient of all tested gases as a function of the kinetic diameter for different allyl derivatives after annealing at 350 and 400 °C.

The diffusion coefficients of CO<sub>2</sub> are lower compared to O<sub>2</sub> and closer to N<sub>2</sub>. The results show no strong variation of the diffusion coefficient of CO<sub>2</sub> among all membranes, while the diffusion of CH<sub>4</sub> varies in a broader range. As a consequence, the strongest diffusion selectivity for CO<sub>2</sub>/CH<sub>4</sub> was observed in the case of Allyl-PI. Furthermore, Allyl-PI demonstrated the lowest diffusion coefficients. This observation is attributed to the high degree of crosslinking, while consisting of the most flexible crosslinks at the same time, which is corroborated by the PES scans of the dihedral angle of the crosslink in the corresponding crosslinked units.

Beyond that, a study by Zhang *et al.* [51] revealed a strong orientation effect of substituents with respect to the diffusion of penetrants. They studied spirochroman-based polyimides,

with CH<sub>3</sub>-groups in comparison to the same backbone with a simple H-group instead. Their study revealed that methyl group containing polyimides had lower CH<sub>4</sub> permeabilities, despite their higher fractional free volume in comparison to the corresponding H-containing polymers. This phenomenon was further explained with fluctuations of the methyl groups. These fluctuations caused diffusion pathway blocking for larger molecules, such as CH<sub>4</sub>. Thus, their conclusion was that bulkiness of the substituent affects free volume and gas diffusion as well as their orientation.

Figure 90 shows the change of the diffusion coefficient in relation to the untreated precursor as a result of the annealing temperature for the gases H<sub>2</sub>, CO<sub>2</sub> and CH<sub>4</sub> for five allyl derivatives. The highest diffusion coefficient change was measured for H<sub>2</sub>, followed by O<sub>2</sub> and CO<sub>2</sub>. For the penetrant H<sub>2</sub>, CO<sub>2</sub> and O<sub>2</sub> we represent their diffusion coefficient as a function of the annealing temperature, which correlates well with the HPI-to-PBO conversion.

In regard to the diameter of the penetrant gases, the H<sub>2</sub> diffusion coefficient is higher compared to CO<sub>2</sub> and CH<sub>4</sub>, whereas the difference between H<sub>2</sub> and CO<sub>2</sub> is larger, than between CO<sub>2</sub> and CH<sub>4</sub>. This can be explained by the size sieving effect, as H<sub>2</sub> is significantly smaller. Concerning the effect of the annealing temperatures, the strongest increase in gas diffusion of all penetrants was observed for the treatment at 350 °C, while the coefficient decreased only slightly after annealing at 400 °C in the case of H<sub>2</sub> (Figure 90). For instance, the Allyl-PI membrane has a H<sub>2</sub> diffusion coefficient of 5.09·10<sup>-6</sup> cm<sup>2</sup>/s (300 °C), followed by 8.84·10<sup>-6</sup> cm<sup>2</sup>/s (350 °C) and 6.20·10<sup>-6</sup> cm<sup>2</sup>/s (400 °C). The highest diffusion coefficient of H<sub>2</sub> was determined for γE-PI with 2.82·10<sup>-5</sup> cm<sup>2</sup>/s, followed by 2.05·10<sup>-5</sup> cm<sup>2</sup>/s (βM-PI), each after annealing for 2h at 350 °C. The order of diffusion coefficients of H<sub>2</sub> after 400 °C annealing is βM>γM>γE>Allyl>αM, and after 350 °C annealing it is γE>βM>γM>Allyl>αM. For CO<sub>2</sub>, highest values were measured for the 400°C treated materials again, with maximum diffusion coefficients for γE-PI and βM-PI with 4.38 and 3.79·10<sup>-7</sup> cm<sup>2</sup>/s, respectively.

The order of diffusion coefficients of CO<sub>2</sub> after 400 °C annealing is γE>βM>αM>γM>Allyl, and after 350 °C annealing it is γE>βM>αM>Allyl>γM. The order of diffusion coefficients at 350 °C reflects the order of PBO conversion. Even after a 400 °C treatment, where no residual CO<sub>2</sub> release was observed by TGA runs, suggesting a full conversion, the same order remains. As the conversion at 350 °C shows already 48% (Allyl-PI) and around 85 and 100% (βM- and γE-



PI), the degree of rearrangement in the membrane at 350 °C is already very large, while heating up to 400 °C brings no significant change in PBO conversion. Therefore, structural effects are stronger when comparing materials after 300 and 350 °C annealing compared to 350/400 °C.

At 400 °C a decrease of H<sub>2</sub> with a strong increase for the diffusion of CH<sub>4</sub> is observed. This indicates that small pores collapse upon fully PBO-conversion at high annealing temperatures. One important aspect, which is usually disregarded, when hexafluoroisopropylidene group containing polymers are annealed above 400 °C, is their decomposition with respect to the CF<sub>3</sub> groups. The decomposition leads to additional void formation and provides new crosslinking spots as well. This phenomenon in turn is very likely to manipulate the free volume characteristic and gas diffusion properties.

Taking the solubility difference of different gases in the membrane materials into account, the permeability (*P*) is obtained. The measured material specific permeability of each gas is plotted as a function of the annealing temperature for the gases H<sub>2</sub> and CO<sub>2</sub> in Figure 133.

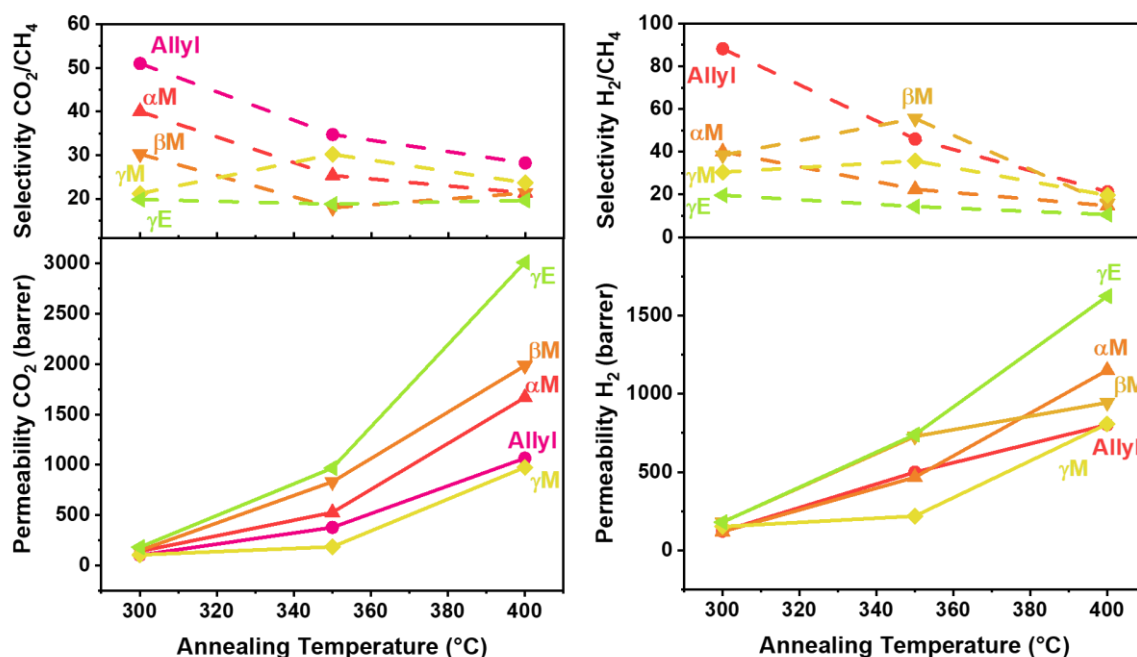


Figure 133. Permeability and selectivity of CO<sub>2</sub> and CO<sub>2</sub>/CH<sub>4</sub> (left) and H<sub>2</sub> and H<sub>2</sub>/CH<sub>4</sub> (right) for different allyl derivatives after annealing at 400 °C.

The CO<sub>2</sub> permeability increases as the increasing annealing temperature also leads to higher conversions of the HPI-to-PBO process, in accordance to the increase of the free volume and diffusion coefficient.



As  $\gamma$ E- and  $\beta$ M-PI have the highest PBO conversion, their permeability increase is expected to overcome all other materials. Figure 133 shows that the permeability reaches its largest values for  $\gamma$ E-PI, while  $\beta$ M-PI shows permeabilities even close to  $\gamma$ E-PI after annealing at 350 °C.

The order of the permeability of CO<sub>2</sub> follows for 350 and 400 °C treated materials the same trend, which is  $\gamma$ E> $\beta$ M>> $\alpha$ M>Allyl> $\gamma$ M. This is the inverse order compared to the TR<sub>onset</sub> with  $\gamma$ M>Allyl> $\alpha$ M> $\beta$ M>> $\gamma$ E.

The ratio of two penetrant permeabilities is the ideal selectivity  $\alpha$ . Literature screenings show, that most materials underlie the permselectivity trade-off relationship, in which permeabilities increase on the cost of their selectivity and *vice versa* [37-40, 297]. A careful comparison of P and  $\alpha$  of certain gas pairs shows that allylated materials show the same relationship (see Figure 91). However, the situation changes for the gas pairs CO<sub>2</sub>/CH<sub>4</sub> and H<sub>2</sub>/CH<sub>4</sub>.  $\beta$ M- and  $\gamma$ M-PI show an increase of both properties after annealing at 350 °C.  $\beta$ M-PI even shows the highest selectivity among all at 350 °C heated materials for the H<sub>2</sub>/CH<sub>4</sub> separation. Hence, the permeability order for H<sub>2</sub> is  $\gamma$ E~ $\beta$ M> $\alpha$ M~Allyl> $\gamma$ M and selectivity order is  $\beta$ M>Allyl> $\gamma$ M> $\alpha$ M> $\gamma$ E. Therefore more in-depth investigations were focused on  $\beta$ M-PI.

Figure 134 demonstrates the permeability and selectivity of certain gas pairs for annealed  $\beta$ M-PI membranes in relation to the thermally untreated material.

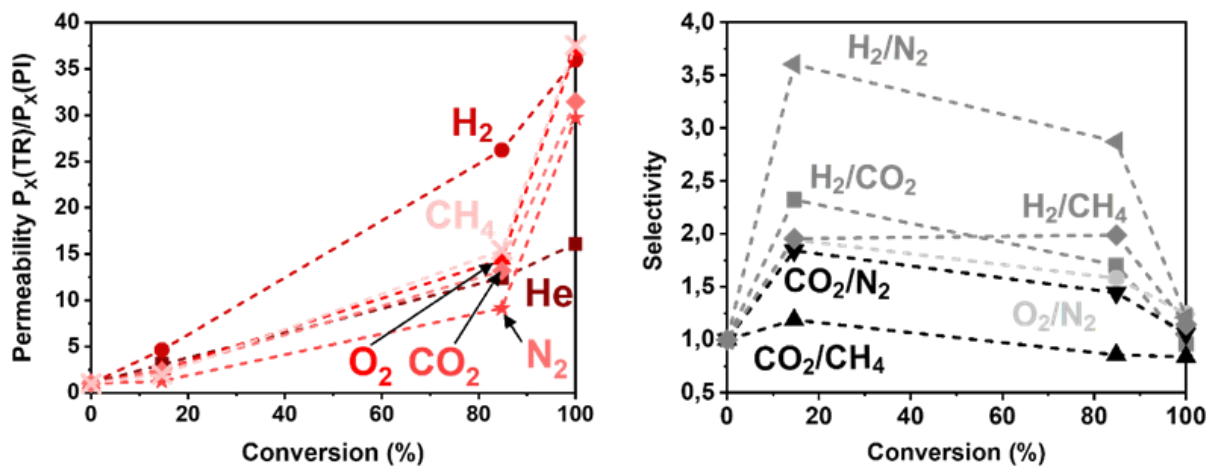


Figure 134. Permeability ratio of annealed (TR) to pristine material (PI) as a function of the achieved PBO conversion, for different gases He, H<sub>2</sub>, CO<sub>2</sub>, O<sub>2</sub>, N<sub>2</sub>, CH<sub>4</sub>.

As a consequence of the large permeability improvements of H<sub>2</sub> (25x) compared to N<sub>2</sub>, the H<sub>2</sub>/N<sub>2</sub> selectivity shows a selectivity increase factor of 3x after annealing at 350 °C.

Accordingly, the material demonstrates several benefits, such as a low (required) annealing temperature for large TR conversions and significantly improved H<sub>2</sub> permeability and H<sub>2</sub> selectivities for numerous industrially important gas pairs, mainly for the separation from N<sub>2</sub>.

It is assumed that crosslinked (CR+Cx) and non-crosslinked (CR) units undergo the TR process prior to benzofuran-containing (Cy) units, since they have to re-open and form a hydroxy group again. Hence, at 350 °C with 84% of HPI-to-PBO conversion, there are still benzofuran groups left.

The simulation of the free volume elements of the (TRC)βM-PI model, in Figure 85 and Figure 88, with 50% benzoxazole and 50% benzofuran groups, showed a distinctively fine distributed free volume characteristic, while stiff PBO groups preserved the formed pores. Small channels were visualized, which are accessible by probes with a radius of 1.0 to 1.5 Å, while larger molecules can only penetrate via large pores and don't show any accessible interconnected free volume elements (Figure 131).

In addition, as the simulation suggested, a good propylene/propane separation performance, based on the Connolly-Volume to -Surface ratio drop, once passing the kinetic radius of propylene, the separation of ethylene and propylene from ethane and propane was investigated. All hydrocarbon permeabilities increase in the order Allyl-PI < αM-PI < βM-PI < γE-PI, such as most penetrants did. In contrast, selectivities do not show an inverse trend, as largest selectivities for the propylene/propane separation were in fact determined for βM-PI and γE-PI, while also having the largest permeabilities (Figure 135). While all materials show a selectivity below 5 for ethylene to ethane, as commonly observed for most polymeric membranes [298, 299], the propylene/propane separation in the case of βM-PI is very competitive to state-of-the-art polymeric membrane materials [298, 299]. Despite the small diameter difference of only 0.38 Å of the penetrants, the selectivity of βM-PI for propylene/propane with 20 at a permeability of 123 Barrer is very high and in the range of many CMS membranes [298, 299]. However, the advantage of βM-PI compared to CMS materials is the significantly lower annealing temperatures and the polymer films were mechanically very stable and not brittle, making them more attractive for large-scale productions.

In Figure 135 a strong increase of the permeability for all hydrocarbons can be seen, except propane. Hence making it a very promising material for propylene purification applications, and others (Figure 136)

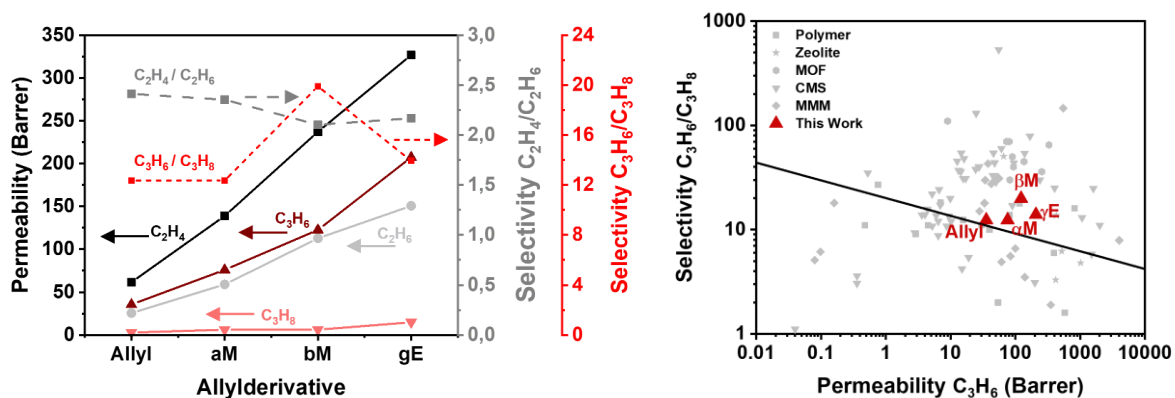


Figure 135. Permeability of tested hydrocarbons  $C_2H_4$  (■),  $C_2H_6$  (●),  $C_3H_6$  (▲),  $C_3H_8$  (▼) and selectivity  $C_2H_4/C_2H_6$  (grey, ■),  $C_3H_6/C_3H_8$  (red, ■) for allylderivatives exhibiting highest permselectivities upon tested polymer after annealing at 400 °C. Selectivity vs permeability of the propylene/propane separation. Upper bound line from ref. [300], plotted materials (grey) from ref. [299].

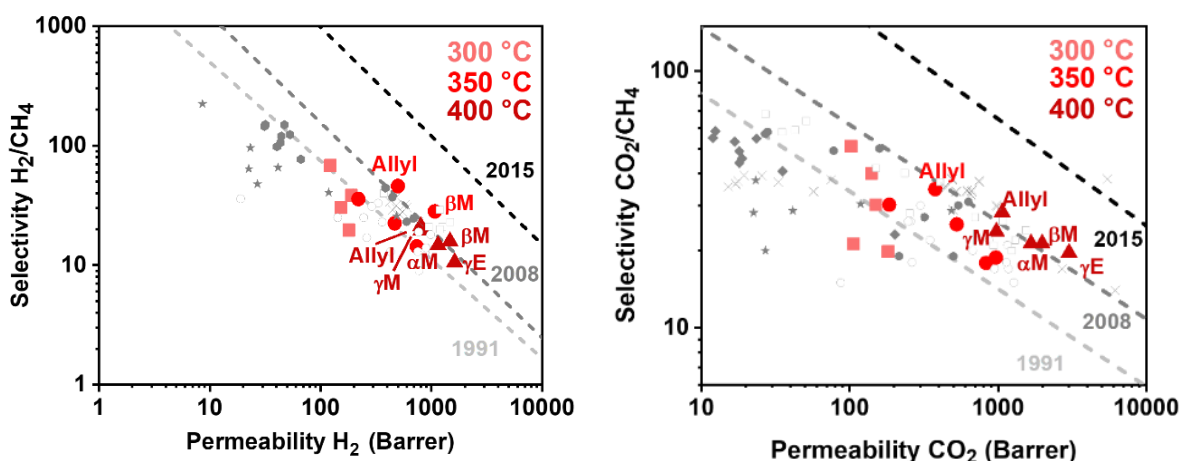


Figure 136. Gas pair selectivity vs gas permeability of tested gas pairs for different allylderivatives after annealing at 300 °C for 0.5 h (■), 350 °C for 2 h (●) and 400 °C for 1 h (▲), incorporated in the upper bound plot, including upper bounds of 1991, 2008 and 2015 [301]. Plotted gas/pairs are  $H_2/N_2$  vs.  $H_2$ ,  $CO_2/CH_4$  vs.  $CO_2$ ,  $H_2/CH_4$  vs.  $H_2$ . X Crosslinked and low  $TR_{onset}$  [117, 254, 255, 302] ● Hydroxy modifications [132, 141] ◆ Crosslinked [144, 145] ○ Spiro units [161, 162] □ Cardo units [159, 303] ★ Ether backbone [254, 267].

Table 4. Determined physical properties glass-transition temperature  $T_g$ , TR onset temperature  $TR_{on}$ , TR conversion TR%, density, fractional free volume FFV of Allyl-,  $\alpha$ M-,  $\beta$ M-,  $\gamma$ M- and  $\gamma$ E-PI.

Modification	$T_g$ (°C)	$TR_{on}$ (°C)	TR% (%)	Density (g/cm <sup>3</sup> )	FFV (%)
<b>Allyl-PI</b>	N.A.	331		1.42±0.017	17.3
<b>Allyl-PI 300 °C</b>			12.6	1.35±0.025	20.6
<b>Allyl-PI 350 °C</b>			48.5	1.33±0.016	20.9
<b>Allyl-PI 400 °C</b>			100	1.32±0.010	20.9
<b><math>\alpha</math>M-PI</b>	333	328		1.41±0.010	15.7
<b><math>\alpha</math>M-PI 300 °C</b>			13.0	1.36±0.001	16.6
<b><math>\alpha</math>M-PI 350 °C</b>			62.1	1.35±0.007	18.3
<b><math>\alpha</math>M-PI 400 °C</b>			100	1.32±0.007	20.8
<b><math>\beta</math>M-PI</b>	302	325		1.40±0.018	16.9
<b><math>\beta</math>M-PI 300 °C</b>			14.6	1.35±0.016	18.7
<b><math>\beta</math>M-PI 300 °C</b>			22.2	1.34±0.022	
<b><math>\beta</math>M-PI 350 °C</b>			84.8	1.31±0.013	20.6
<b><math>\beta</math>M-PI 400 °C</b>			100	1.31±0.013	22.3
<b><math>\gamma</math>M-PI</b>	289	352		1.40±0.007	15.9
<b><math>\gamma</math>M-PI 300 °C</b>			13.1	1.35±0.007	19.1
<b><math>\gamma</math>M-PI 350 °C</b>			52.1	1.34±0.01	18.1
<b><math>\gamma</math>M-PI 400 °C</b>			100	1.32±0.029	20.8
<b><math>\gamma</math>E-PI</b>	296	309		1.41±0.009	13.7
<b><math>\gamma</math>E-PI 300 °C</b>			22.4	1.35±0.013	16.7
<b><math>\gamma</math>E-PI 350 °C</b>			100	1.33±0.005	16.5
<b><math>\gamma</math>E-PI 400 °C</b>			100	1.27±0.038	20.4

## Key messages

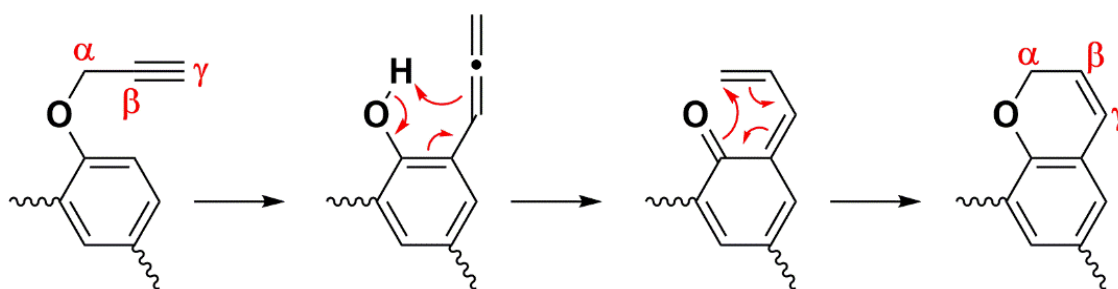
- The HPI-to-PBO conversion occurs already at 300 °C for  $\beta$ M- and  $\gamma$ E-PI, which has never been reported before for a TRP.
- Conversions after 2 h at 350 °C are higher than most TRPs after annealing at 450 °C.
- Density drops continuously.
- PES scans were used to predict the rigidity and restricted rotation of the formed crosslinks by the ee- and em-crosslinking mechanism.
- Effect of crosslinking was investigated towards molecular properties such as free volume and density, and a drop of the density, followed by increasing densities was shown.
- Supports the suggestion that low degrees of allylation are enough to disrupt the chain packing already.
- Further molecular dynamics studies, involving the *ortho*-allyl-to-benzofuran and HPI-to-PBO cyclization reaction, were conducted for  $\beta$ M-PI.
- Simulated properties, such as density were very close to the experimental findings, corroborating the developed method as useful tool to tailor and predict materials properties.
- Phenomenologic properties such as the free volume element types, such as interpore connections and Connolly volume-to-surface ratios, as pore size indicator, were in very good agreement with the experimental findings and supported the assumption, that benzofuran cycles form rigid small pores that separate hydrogen very efficiently, especially in addition to PBO formation.
- Simulations predicted high propylene/propane separation performance which was experimentally proven.

## Polyimides with *ortho*-Propargyloxy groups

### Propargylation

The investigation of allylated *ortho*-hydroxy polyimides has revealed that the degree of allylation, as well as the used allyl derivative affects the physicochemical properties in many cases. It affects the onset temperatures for the reaction, the degree of crosslinking, the tendency to undergo different consecutive reactions and therefore the thermal, mechanical, and electrical properties. Studies of  $\beta$ MAllyl-PI1 (previous chapter) demonstrated, that the formation of cyclic structures are beneficial for the TR process and the gas separation properties. Since all other allyl derivatives showed significantly lower ratios of cyclic ether formation, it was of main interest to find other ways to design another thermally stimulated cascade reaction polymer, which is capable of undergoing cyclization and as well as the HPI-to-PBO cyclization (TR) as well.

Propargyl phenyl ether are another class of potential thermal Claisen Rearrangement undergoing groups. The process proceeds similar to allyl phenyl ether, but forms a more reactive *ortho*-allene phenol product, which readily undergoes cyclization to the corresponding chromene type (Scheme 12).



Scheme 12. Claisen-Rearrangement Claisen Rearrangement of Propargyl phenyl ether.

Therefore, 6FDA-BisAPAF was converted from its HPI-form to the corresponding ether, according to the Williamson-Ether type synthesis, which was used for the synthesis of Allyl-PI as well. Full conversion of the hydroxy group to the propargyl ether was confirmed by means of  $^1\text{H-NMR}$  spectroscopy (Figure 137) by disappearance of the hydroxy peak at 10.4 ppm and the evolution of two new peaks. A singlett peak around 5.0 ppm corresponds

to both protons of the propargylic methylene group, while the terminal alkyne proton shows a peak at 3.5 ppm. In addition, FT-IR spectroscopy (Figure 138) showed the disappearance of the hydroxy group stretch vibration as well. Moreover, a new vibrational peak above 3200  $\text{cm}^{-1}$  and a weak band at 2100  $\text{cm}^{-1}$  appeared. Both bands correspond to stretch vibrations of the alkyne group, with the vibration of the terminal propargyl C-H-group above 3200  $\text{cm}^{-1}$  and the alkyne  $\text{C}\equiv\text{C}$ -group vibration around 2100  $\text{cm}^{-1}$ . The propargylated polyimide is named Propargyl-PI-1, but simply termed Propargyl-PI or PGPI-1 in the following sections.

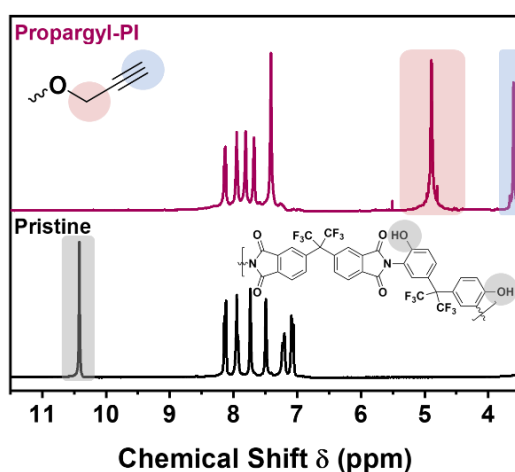


Figure 137.  $^1\text{H}$ -NMR spectrum of the pristine HPI and propargylated polyimide.

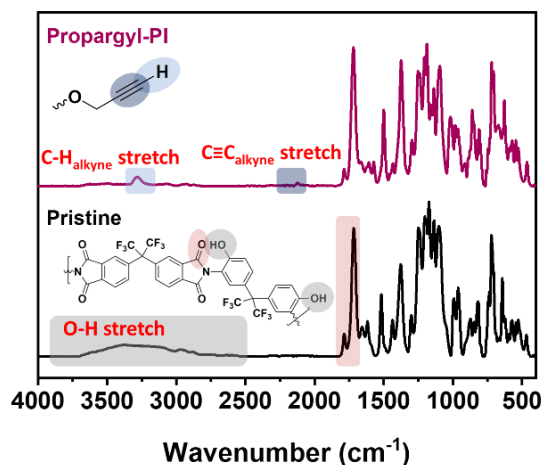


Figure 138. FT-IR spectrum of the pristine HPI and propargylated polyimide.

## Thermokinetic- and dynamic analysis

Thermoanalysis, using FT-IR coupled TGA and DSC experiments, were used to study the thermal reactions and potential cascade reactions. In Figure 139 the heat flow progress of PGPI-1 is shown. Two heating cycles were performed. The first heating shows a distinctive exothermic peak with a broad onset area, starting at 150 °C. The exotherm peaks at 250 °C. A subsequent small exothermic peak follows at an onset temperature of 350 °C with a peak at 360 °C, and another peak at 400 °C. No peak re-occurs in the second heating run, nor in the following cooling run, after the first cycle. The exothermic heat flow is therefore attributed to an irreversible reaction, such as the thermal reactions of the allylated polyimides.

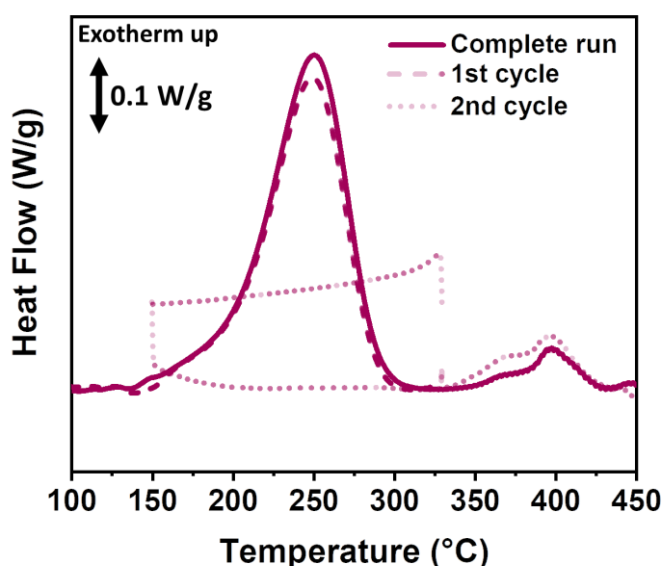


Figure 139. Heat Flow curve obtained by two heating cycles by means of DSC experiments at 5°C min<sup>-1</sup> of Propargyl-PI-1 (PGPI-1).

For further understanding of the underlying processes and the relationships of each process to each other, the PGPI-1 was investigated more in detail by different calorimetric techniques. First of all, the heat flow curve was fit, applying a Gauss fit followed by peak deconvolution (Figure 140). A very accurate fit was possible with an R<sup>2</sup> above 0.999. The deconvoluted peaks reveal three underlying processes. The broad onset area corresponds to the initial reactions, which corresponds to a broad peak, ranging from 150 to 300 °C. This initial peak shows a maximum at 225 °C. At 200 °C another reaction appears to start with high intensity and a narrow peak width. This second peak (grey area) peaks at 250 °C. At 250 °C a third process (blue) starts, with a peak at 360 °C and an offset temperature of 400 °C.



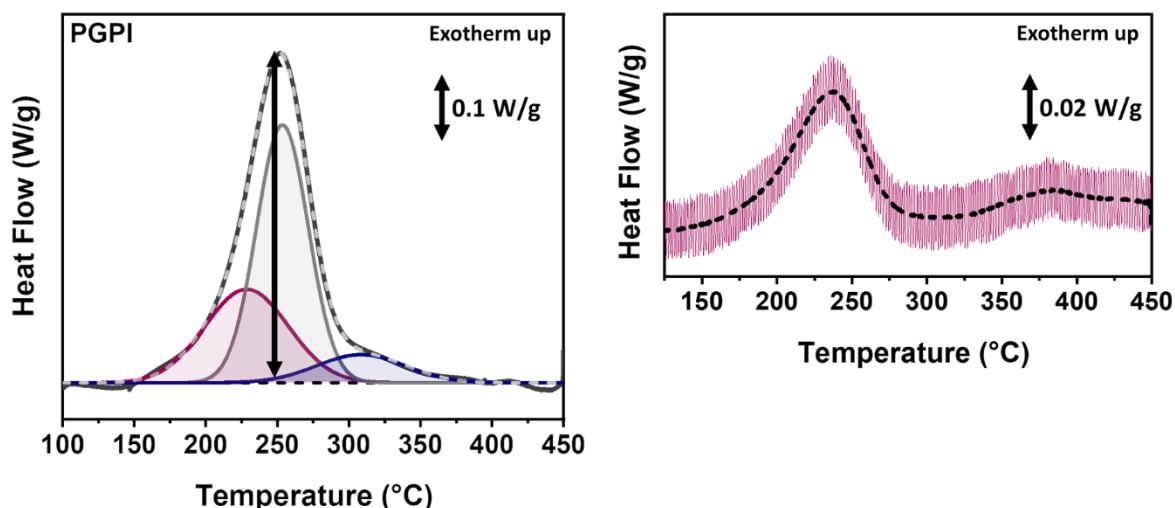


Figure 140. Heat Flow curve with deconvoluted peaks after fitting of the global DSC curve. Modulated DSC curves (right).

In order to separate the underlying peaks, various isothermal treatments of the polyimide were executed at different temperatures 80, 150, 175, 200, 225 and 250 °C for 2 and 5 h (Figure 141). The isothermal treatments reveal, that annealing below 200 °C leads to low conversions of the global process. After annealing at 175 °C for 2 h, the broad onset area disappeared. However, the strongest change in the heat flow curve can be seen after annealing at 200 °C. As a consequence, only about 50% of the initially released heat, were released after annealing at 200 °C for 2 h and re-measuring. Longer annealing times lead to even higher conversions. After annealing at 225 °C for 5 h or 250 °C for 2 h, no peak in the range from 150 to 275 °C occurs. The residual released heat upon re-measuring corresponds very well to the peak area of the third deconvoluted (blue) peak.

The full process also follows strong heat rate dependence. While very high heating rates, such as 20 °C per minute, show the full peak including a broad on- and offset area, low heating rates, such as 1 °C per minute, show a very weak heat flow and offsets about 100 °C lower compared to the highest heating rate. The heat rate dependence is used for non-isothermal isoconversional thermoanalysis in the later section of this study.

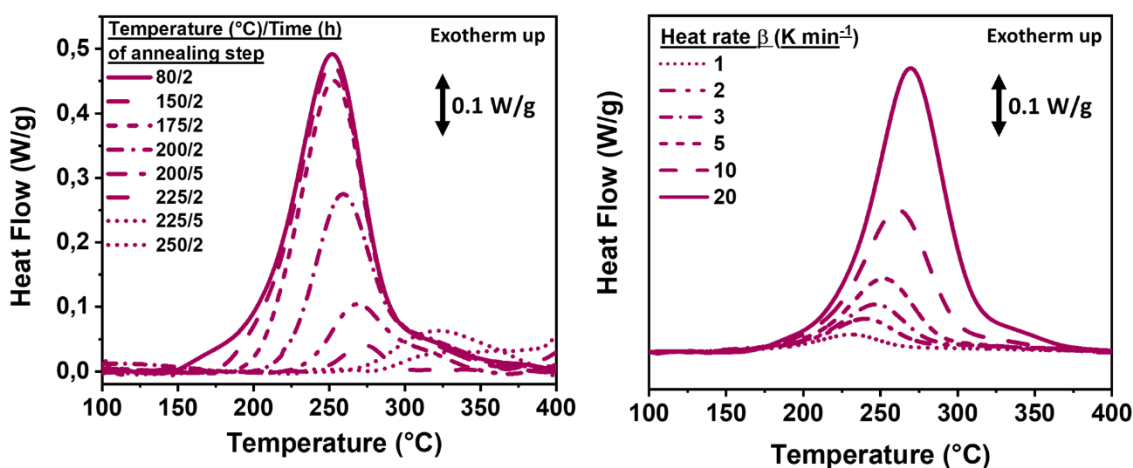


Figure 141. Heat flow curves after isothermal treatments at 80, 150, 175, 200, 225 and 250 °C for 2 and 5 h (left). DSC experiments at different heat rates 1, 2, 3, 5, 10 and 20 °C per minute.

In the previous section, exothermic reactions were attributed to rearrangement and crosslinking reactions without weight loss, except for the last step of the reaction cascade, the HPI-to-PBO formation, which was accompanied by a decarboxylation step. Materials that decomposed prior to the Claisen Rearrangement, showed endothermic peaks. In order to corroborate the type of reaction, mass loss curves by means of TGA were executed (Figure 146). The TGA reveals a thermal stability up to 350 °C, followed by a very weak and slow mass loss. 10% of the initial mass were lost at 480 °C. Nevertheless, in the temperature range of the observed exothermic heat flow, no mass loss occurs. Therefore, the reaction can also be attributed to addition, isomerization, or rearrangement reactions. The gas evolution analysis of the TGA experiments, as well as the initial weight loss area will be discussed more in detail at the end of this section. The focus of the following section emphasizes the irreversible reactions below 400 °C.

Non-isothermal isoconversional methods were used in order to describe the thermal reactions from a thermokinetic point of view. DSC experiments at six different heat rates 1, 2, 3, 5, 10 and 20 °C min<sup>-1</sup> were carried out for the determination of the kinetic parameters. For each heating rate, a conversion curve as a function of the temperature was plotted and is shown in Figure 142 (left). The conversion curve corroborates the previously observed increase of the reaction conversion after annealing at 200 °C. The isothermal treatments, shown in Figure 99, revealed only low conversions up to annealing temperatures above 200 °C. Annealing at 200 °C led to a decrease of the residual heat flow curve by about 50%. From Figure 142 the thermokinetic description shows, that the conversion increases strongly above 200 °C. The

conversion levels off after passing a temperature of 300 °C. The maximum conversion rate occurs at a conversion of 50%, which is the case at 250 °C at a heating rate of 5 °C min<sup>-1</sup>.

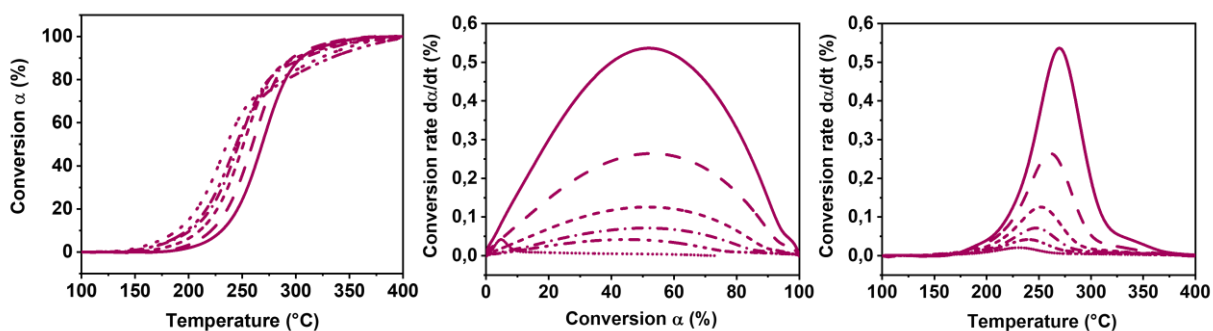


Figure 142. Conversion progress (left), conversion rate vs. conversion (middle) and conversion rate vs. temperature (right) at different heating rates of 1, 2, 3, 5, 10 and 20 °C min<sup>-1</sup> of PGPI-1.

From isoconversional methods, an activation energy can be obtained as a function of the global conversion of the process. A variation in the activation energy can be seen as a strong indicator of a new or additional process (Figure 143). Therefore, two models, the Friedman and KAS model were employed in order to calculate the activation energy. Figure 143 demonstrates small increase of the activation energy up to conversion of 10% and proceeds up to a conversion of 50% with a slight increase from 150 to about 200 kJ mol<sup>-1</sup>. The activation energy is in the range of Claisen Rearrangement reactions and in the range of the determined values for the allylated polyimides [304]. Both models follow the same trend and show similar activation energies, with slightly larger values for the Friedman model. After passing the global conversion of 50%, the activation energy increases strongly and nearly doubles at a conversion of 70%. 50% of conversion are reached with a heating rate of 5 °C min<sup>-1</sup> at 250 °C, while 70% conversion is reached at 275 °C. Taking the deconvoluted peaks from Figure 98 into account, reveals, that the third reaction (blue area) starts 250 °C and increases up to a temperature of 300 °C at a heating rate of 5 °C min<sup>-1</sup>.

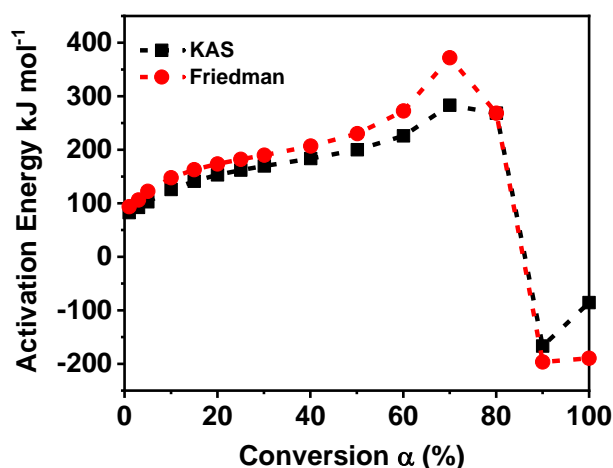


Figure 143. Activation energy as a function of the global conversion of the thermal reactions of PGPI. Friedman model (red) and KAS model (black) were employed to calculate the activation energy.

The thermokinetic analysis was able to corroborate the presence of three reactions, as modeled by the peak deconvolution of the global heat flow curve. Based on the findings of the allylated polyimides, the first step is likely to correspond to the Claisen Rearrangement reaction, followed by the consecutive cyclization to the chromene type.

The potential structure was investigated by means of NMR- and FT-IR spectroscopy (Figure 144) experiments, after annealing of the propargylated polyimide at different temperatures. Each material, even after annealing at 175 °C, leads to a gel (Figure 145). This corroborates, that PGPI-1 appears to crosslink at lower temperatures compared to Allyl-PI, which was able to dissolve after annealing below 200 °C. However, no recovery of the hydroxy peak was seen in the soluble part of the samples, which were annealed in the range from 150 to 225 °C. Moreover, FT-IR measurements did not show a change in the area of the hydroxy stretch vibration. This means, that the possible *ortho*-allene phenol product is not stable at these temperatures for sufficient amount of time. In addition, no allene vibration was observed, either. However, the alkyne vibration above 3200 cm<sup>-1</sup> disappears quickly after passing a temperature of 250 °C. Interestingly, annealing at 300 °C leads to a recovery of the phenolic group, as the hydroxy stretch vibration increases again. Accordingly, the formed cycles open above 300 °C. Therefore, the third process is likely to encompass crosslinking of the cyclized chromen units, and their re-opening as well. Therefore, the intermediate process, which was highlighted in grey in Figure 140, seems to cover the cyclization reaction. According to the literature, the formed rings, are thermodynamically favored and significantly more stable

compared to the initial propargyl ether. Therefore, such a large exothermic heat release of the second process can be explained.

In order to quantify the crosslinking process, gel-fraction and swelling measurements of PGPI-1 after annealing at 150, 175, 200, 225, 250 and 300 °C for 5 min were carried out (Figure 145). The samples were heated at a heating rate of 5 °C min<sup>-1</sup>, in analogy to the DSC experiments. In Figure 145 the swelling ratio and gel-fraction is shown. The gel-fraction increases slightly to 10% after annealing at 175 °C and increases to a gel content of 30% after annealing at 200 °C. Heating to 225 °C leads to a gel content of 90%. Simultaneously, the swelling ratio decreases from a maximum value of 1920% at 200 °C to a swelling ratio of 100% at 225 °C. As the number of crosslinks increases, the network tightens and accordingly less solvent can be absorbed, as the crosslinks do not allow the polymer chains to expand at high degrees of crosslinking. After annealing of 200 °C, only 30% of the polymer sample remained as a gel. Accordingly, the number of crosslinks is expected to be significantly lower. Therefore, the crosslinked polymer can easily swell.

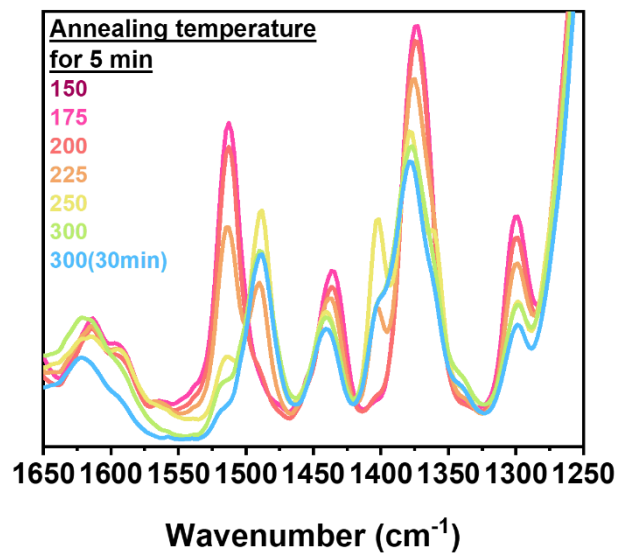
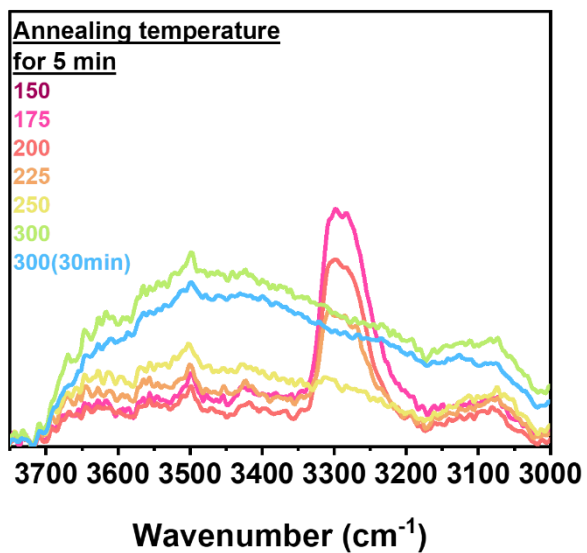
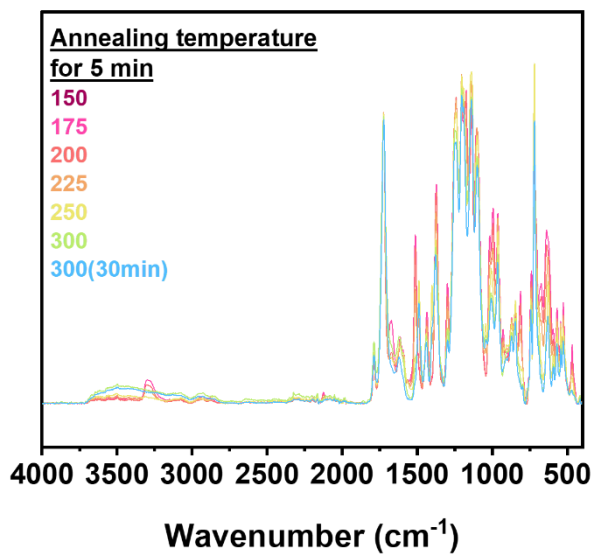


Figure 144. FT-IR Spectra of the annealed samples of PGPI-1 at 150, 175, 200, 225, 250, 300 °C for 5 min and 300 °C for 30 min.

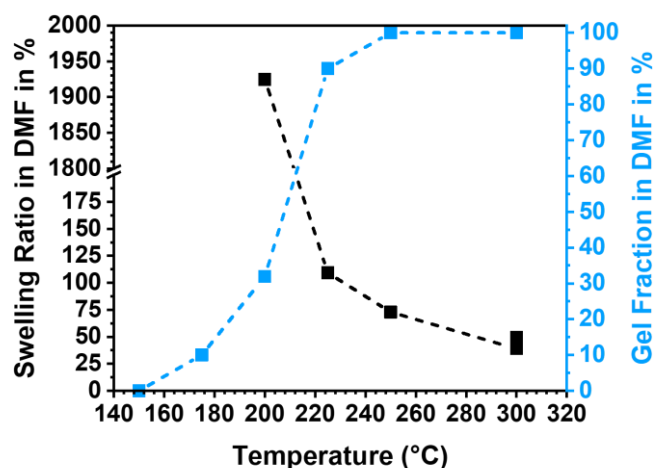


Figure 145. Gel-fraction (blue) and swelling ratio (black) of PGPI-1 as a function of the temperature. Experiments were done in DMF. The samples were heated at a heating rate of 5 °C per minute and each temperature was held for 5 min.

Previously, no mass loss accompanied reaction below 350 °C was observed. However, the TGA results show a slight mass loss above 350 °C (Figure 146). From decomposition gas evolution analysis by means of TGA-FT-IR experiments, the evolution of CO<sub>2</sub> was detected above 300 °C, with a distinct increase of the CO<sub>2</sub> release above 350 °C. The CO<sub>2</sub> release peaks at 425 °C and its offset overlaps with the onset of another CO<sub>2</sub>-releasing reaction, which is attributed to the polymer degradation (according to previous studies). The CO<sub>2</sub> evolution can be seen in the stacked FT-IR spectra in Figure 146 and Figure 147.

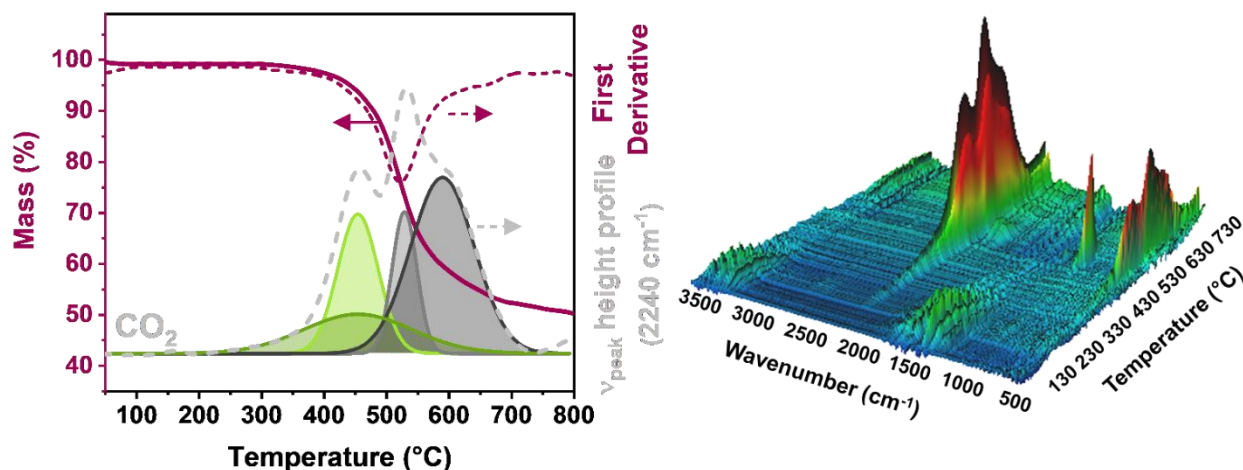


Figure 146. Mass loss curve of PGPI-1 in the temperature range from 50 to 800 °C at a heating rate of 5 °C per minute (left). Stacked FT-IR peaks from gas evolution analysis as a function of the temperature (right).

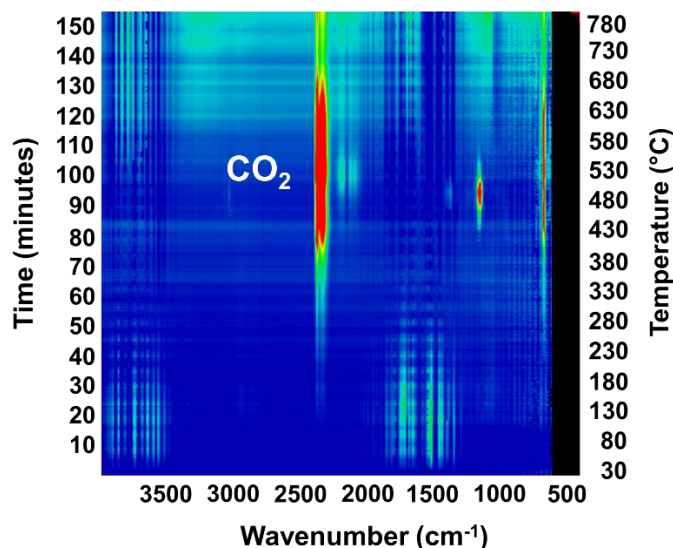


Figure 147. Stacked FT-IR peaks (2D) from gas evolution analysis as a function of the time. The corresponding temperatures are shown on the right side.

$\beta$ M-PI has shown, that despite the formation of furan cycles, a full HPI-to-PBO conversion was possible. Accordingly, the furan rings had to open at higher temperatures to recover the phenolic group, which then consecutively undergoes the so-called Thermal Rearrangement reaction. A similar process is required for the TR reaction of PGPI-1 which forms chromene and furan units. However, the FT-IR spectra of the samples, which were annealed at 300 °C, revealed already a recovery of the hydroxy groups. Therefore, the TR process might occur slowly at 300 °C but starts significantly above 350 °C. A full conversion of each hydroxy group, is obtained at 450 °C. Despite the relatively low onset temperature, the weight loss step is no clear step, rather a very broad and slow mass loss step. This means, that the TR conversion proceeds very slowly as well. This can be explained by the high degree of crosslinking and the very rigid crosslinks between furan or chromene rings. Therefore, the polymer chains are not very mobile and high temperatures are required, so that polymer chains are flexible enough in order to support the rotation around the imide bond, which is necessary for the TR reaction.



## Effect of the degree of propargylation

The degree of modification has been proven to be a good indicator to evaluate the effect of the modification on the polymer chain interactions and their mobility, but also shows strong influences towards film properties. In addition to the previous measurements of the degree of allylation, a set of four different degrees of propargylation with 8, 15, 25 and 50% were synthesized in addition to the unmodified and the full converted PGPI-1. The degree of propargylation was determined from  $^1\text{H-NMR}$  spectroscopy measurements via integration of the aromatic area as a reference for 12 protons and the propargyl specific strong singulett peak at 5 ppm, which corresponds to 4 protons in the case of 100% propargylation (Figure 148).

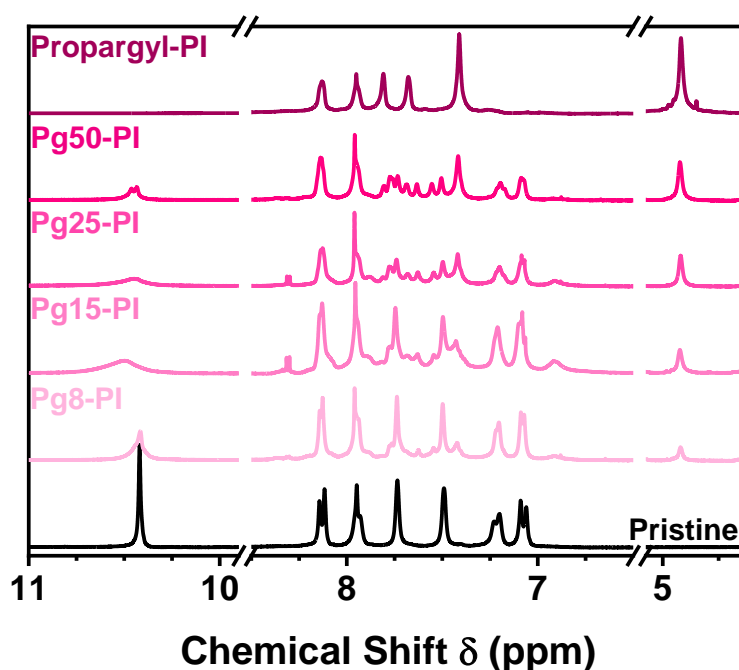


Figure 148. Stacked  $^1\text{H-NMR}$  spectra of the propargylated polyimide with a degree of propargylation of 0, 8, 15, 25, 50 and 100%.

In all cases the hydroxy peak at 10.4 ppm decreased as the degree of propargylation increased, while the peaks at 5 and 3.5 ppm increased. A change in the aromatic peak pattern was also detected. While the anhydride corresponding peaks above 7.5 ppm remained unchanged, the peaks between 7 and 7.5 ppm changed their positions and structure. Both aromatic peaks from the amine unit at 7 and 7.2 ppm decreased as the degree of propargylation increased. These are the aromatic proton peaks next to the hydroxy group and are therefore the most affected

peaks in terms of interaction and electronic changes due to the propargylation. The same observation was made for the allylation.

In addition, FT-IR spectra were recorded. While the fingerprint area below 1500  $\text{cm}^{-1}$  appeared to be, in principle, unchanged in all cases, the hydroxy stretch peak decreased from the pristine material to higher degrees of propargylation (Figure 149).

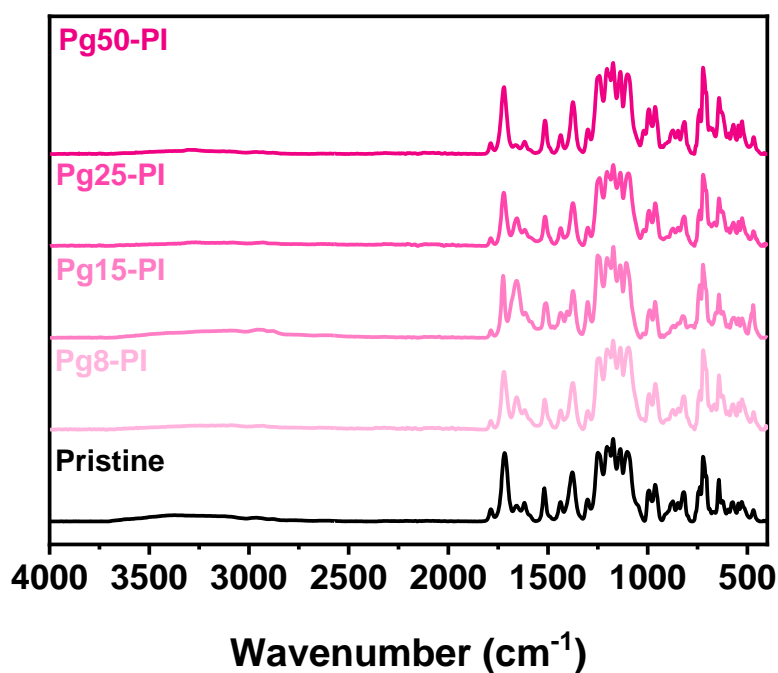


Figure 149. Stacked FT-IR spectra of the propargylated polyimide with a degree of propargylation of 8, 15, 25, 50%.

The integral of the heat flow curve, which is obtained by DSC measurements, corresponds to the released heat of the reaction, and increases as more groups are present, which undergo the specific reaction. Figure 150 shows the heat flow curves of each material. The overall amount of released heat decreases as the degree of propargylation decreases from 374  $\text{J g}^{-1}$  for PGPI-1 to 151  $\text{J g}^{-1}$  in the case of PG50PI and 34.0  $\text{J g}^{-1}$  for PG8PI. Apart from the quantity of exotherm heat release, the peak shifts to higher temperatures as the degree of propargylation decreases. Despite the assumption, that hydroxy groups, which are more present in less propargylated materials, act as catalysts [217], the inter molecular hydrogen bonds increase as the degree of propargylation decreases. However, in polymers, especially with these large and stiff propargyl modifications, the possibility for hydroxy groups to come close enough to the propargyl phenyl unit becomes very difficult. Moreover, apart from the peak temperature, the onset temperature appears to decrease with increasing degree of propargylation as well. The

broad onset area only appears in case of the 100% propargylated polyimide and as a weak shoulder in PG50PI as well. However, any other material with less than 50% converted hydroxy-to-propargyloxy groups tend not to show such a broad onset area, which was assigned to an additional reaction process. Since all materials undergo the Claisen Rearrangement and show a peak around 250 °C, but not every material shows a broad onset area, this confirms the suggestion, that the second deconvoluted peak (grey) can be assigned to the Claisen Rearrangement and cyclization.

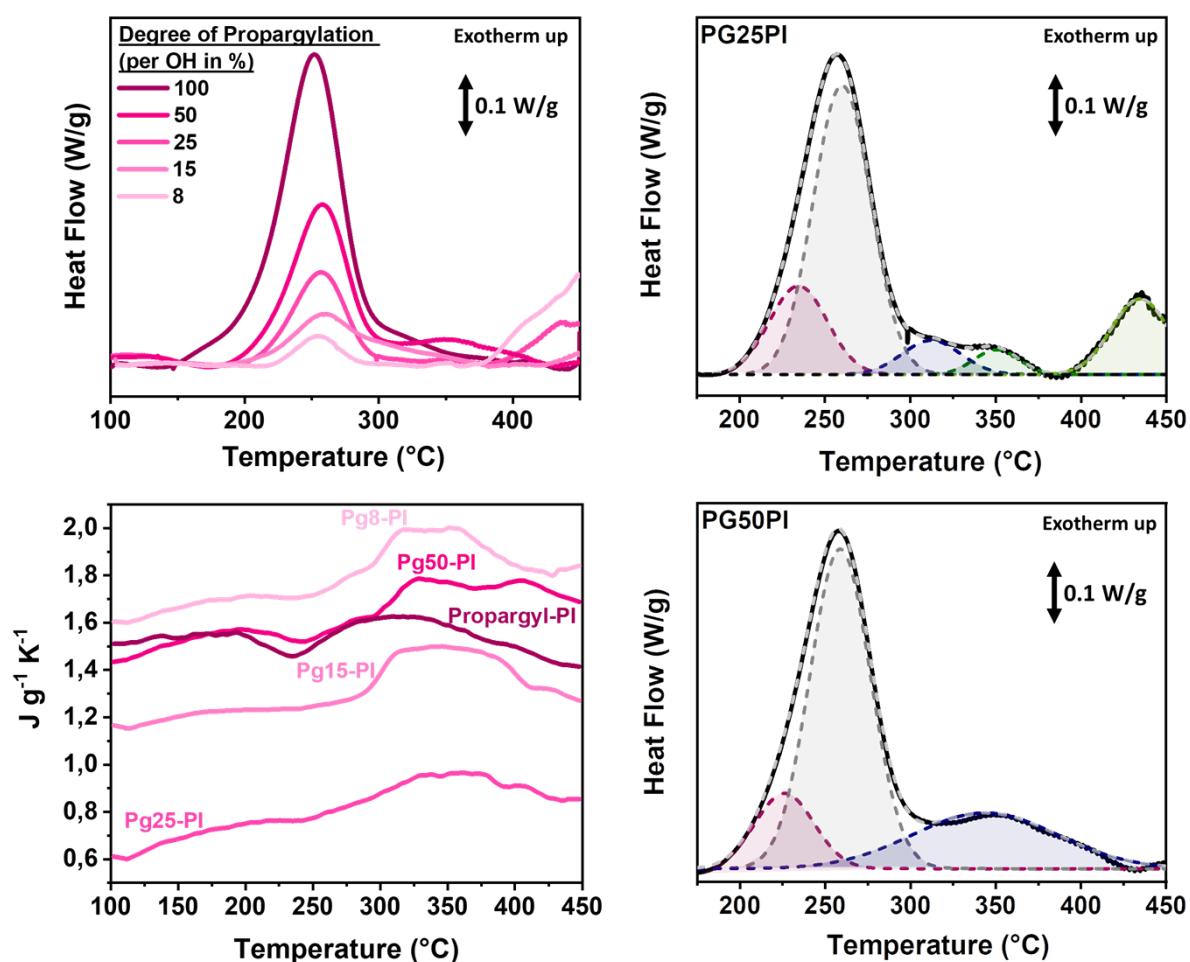


Figure 150. Heat flow curve (top left), heat capacity (bottom left) of the polyimides with different degrees of propargylation. Fitted heat flow curves of PG50PI (top right) and PG25PI (bottom right).

In addition to the heat flow curves, the heat capacity of each material was determined as well. A strong increase above 250 °C can be seen and is attributed to the crosslinking process. As crosslinked polymeric materials tend to show higher heat capacities. This is in accordance with our findings with allylated materials. Hence, this observation corroborates the assignment of the third deconvoluted peak to the crosslinking process.

Peak deconvolution was also performed for the propargylated polyimides with different degrees of propargylation. In Figure 108 the plots of PG50PI and PG25PI are shown. In both cases a small initial peak is present, followed by the large and intense grey peak, which is assigned to the Claisen Rearrangement and cyclization. Since both processes occur intramolecularly no strong variations were expected, except from the total heat release. However, the consecutive reactions vary slightly.

The possibility of extrusion reactions, that are connected to the exothermic reactions were investigated by means of TGA experiments (Figure 151). Moreover, the Thermal Rearrangement was investigated. In the temperature range from 200 to 300 °C as mass loss occurs as a matter of fact. From evolved gas analysis, it was shown that the released compound is DMF. Since DMF is used as the synthesis solvent, few amounts still remain after several washing steps. In that case, however, larger amounts were present and did not leave the polyimides, even after several re-precipitation steps. The amount of DMF in relation to the degree of propargylation was investigated by calculation of the molar amount of DMF in the polymer from the weight loss step. Calculations revealed, that one DMF molecule per three hydroxy groups is present. Therefore, a complexation between the carbonyl group, aldehyde-hydrogen, and amine group of DMF with three hydroxy groups appear to form three hydrogen bonds, which are strong in that case. The proposed hydrogen bonds are shown in Scheme 13.

However, apart from the solvent release at higher temperatures, a weight loss step at 350 °C can be observed. As the number of propargyl units decreases from 100 to 8% propargylation, the weight loss step becomes more distinct and shifts to lower temperatures. The materials with 8, 15 and 25% of propargylation show a well-defined step with onset temperatures of 317, 320 and 339 °C. The weight loss step for these materials correlates with the peak height profile of CO<sub>2</sub> from the evolved gas analysis. No other gas was determined to a large extent in the range of the weight loss step. FT-IR spectroscopy measurements show that the carbonyl peak decreases after annealing at 350 and 400 °C, which supports the suggestion, that the weight loss step is attributed to the HPI-to-PBO formation, the so-called Thermal Rearrangement reaction. It is noteworthy, that a strong dependence of the TR<sub>onset</sub> temperature to the degree of propargylation exists, as observed for Allyl-PI as well.

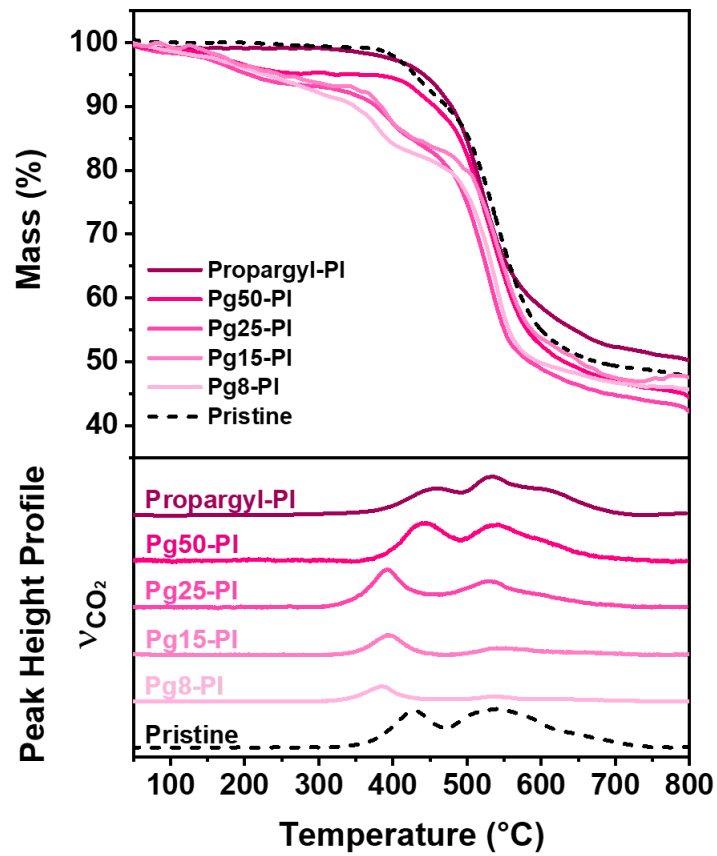
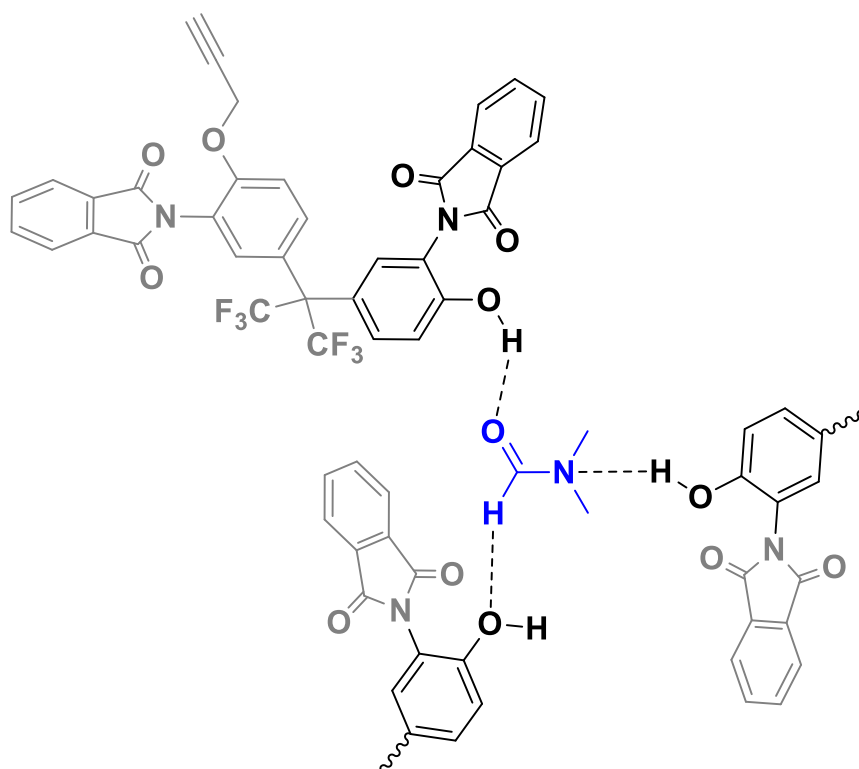


Figure 151. Mass loss curve obtained by means of TGA experiments of propargylated polyimides with 0, 8, 15, 25, 50 and 100% propargylation (top). CO<sub>2</sub> gas evolution peak analysis by means of TGA-FT-IR analysis.



*Scheme 13. Hydrogen bonding between three phenol groups and one DMF molecule.*

The CO<sub>2</sub> peak, which is attributed to the TR process, is in the range of the pristine polyimide, as seen in Figure 152. The TR<sub>onset</sub> shift for the propargylated materials in the range from 8 to 50% of propargylation can be clearly seen in the overlapping plot (Figure 152). In addition, the CO<sub>2</sub> profiles were fitted to visualize potential underlying CO<sub>2</sub> releasing processes. The range above 475 °C corresponds to the polymer degradation and is usually difficult to fit and to determine on- and offset temperatures, as various degradation processes occur simultaneously as the temperature increases even further. Anyhow, the TR step can be deconvoluted very easily using a Gauss fit and is visualized in green color. Comparing PG50PI and PG25PI shows the significantly lower TR<sub>onset</sub> temperature for PG25PI. Hence, PG25PI belongs to the 6FDA-BisAPAF modified polymers and TR precursor in general, with one of the lowest TR<sub>onset</sub> temperatures ever reported apart from βMallyl and γEallyl. However, as pointed out earlier for PGPI-1, the TR process proceeds slowly, as the degree of crosslinking increases strongly at higher temperatures and crosslinks between chromene, and furan units tend to be more rigid and restrict the degree of freedom of the polymer chain. Nevertheless, due to the very low onset temperature, the TR process shows a distinct separation from the polymer degradation process, while the pristine materials and PGPI-1 showed a strong overlap between both processes. The gap between each process is even more pronounced in case of PG15PI and

PG8PI, with low  $TR_{onsets}$  as well. As a consequence, all materials are very promising TR precursor materials.

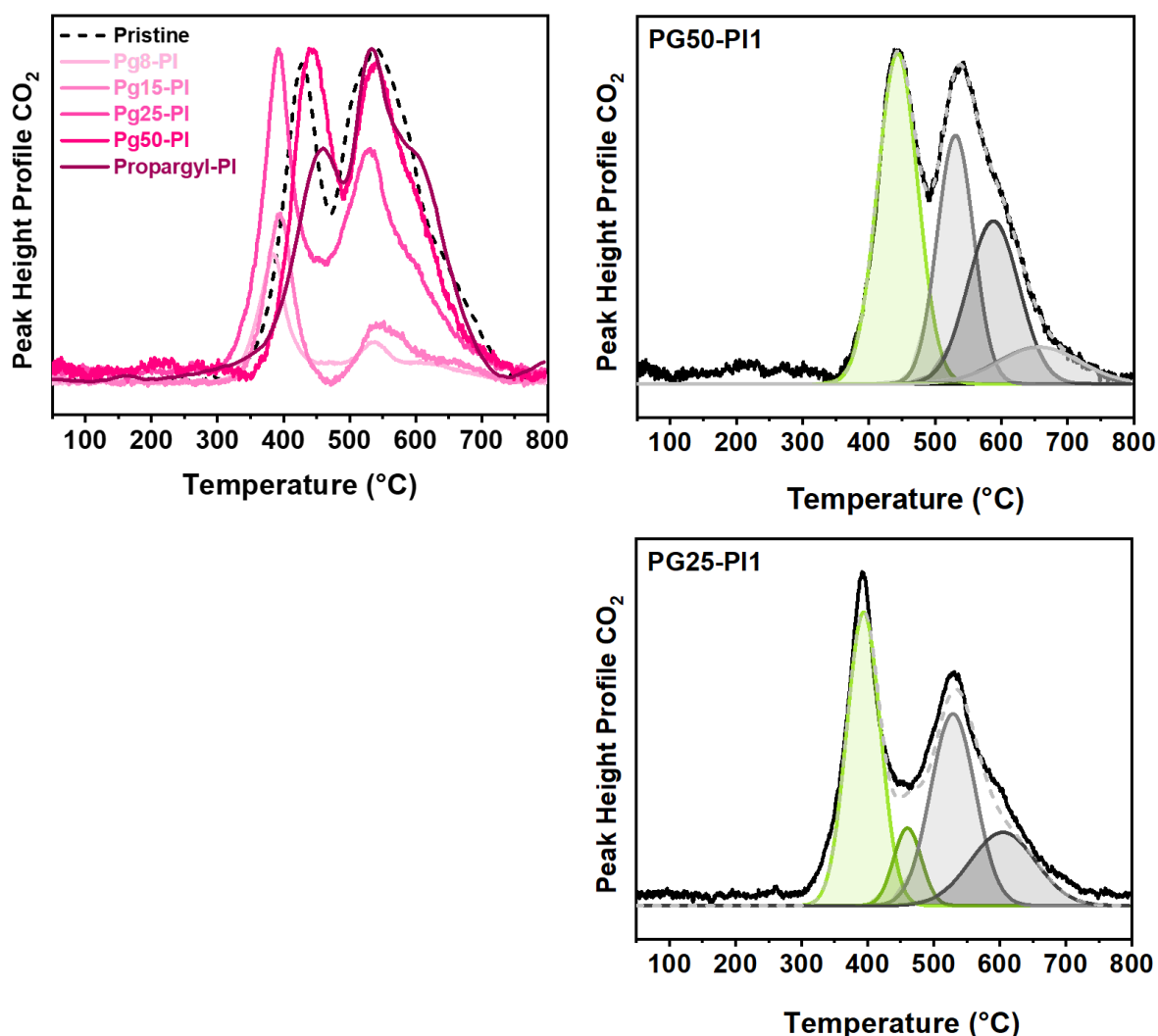


Figure 152.  $CO_2$  Peak height profile from evolved gas analysis of materials with degrees of propargylation in the range from 0 to 100% (top left).  $CO_2$  Peak height profile fitting of PG50PI (top right), PG25PI (bottom right) and PG8PI (bottom left).

### Effect of the Backbone

Polyimides offer a large variety of commercially available monomers. These monomers vary in terms of their rigidity, aromaticity, bulkiness, and even electronic properties. In previous studies a number of monomers have been proven to be highly interesting in order to evaluate modification properties and its thermal reactions based on different backbones. Therefore, BPADA as a highly flexible backbone (PGPI-4), EDA as a rigid anhydride (PGPI-3) and HAB as a rigid diamine compound in which, the propargyl units are very close to each other

compared to BisAPAF, were used (PGPI-2). In addition, a propargylated monomer was synthesized according to the procedure, which has been developed for the synthesis of the allylated diamine monomer and its polymerization, as described in the previous section and section *Monomer modification* on page 391. The reaction followed a phthalimide protection – hydroxy group propargylation and phthalimide deprotection sequence, followed by the polymerization. The goal was to synthesize a fully propargylated poly (amic acid). The poly (amic acid) is the precursor of each polyimide prior to its imidization, but chemically a carboxyl group containing polyamide. Therefore, PGPA (Propargyl-PAA) was synthesized to investigate the backbone effect in such a very polar environment and to study the thermal reactions which occur in the range of the thermal imidization process.

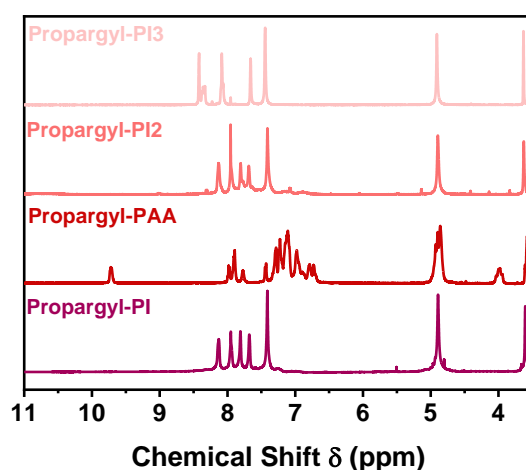


Figure 153. Stacked  $^1\text{H-NMR}$  spectra of the synthesized propargylated materials with various backbones based on 6FDA-BisAPAF, 6FDA-BisAPAF-Paa, 6FDA-HAB, EDA-APAF and BPADA-APAF.

The full conversion was confirmed in accordance with the NMR and FT-IR analysis of PGPI-1, as described earlier. In case of PGPA, the aromatic region varies due to the strongly different chemical environment, as polar amide and carboxyl groups are present. The amide N-H proton can be seen at 9.5 ppm. The NMR spectra are demonstrated in Figure 153.

The heat flow course shows in all five materials a similar pattern of a strong exothermic peak. However, at second glance a variation of the onset temperature and offset behavior can be seen. In all cases no weight loss step occurs during the exothermic reaction, as shown in Figure 154. The peak temperature of the global process does not follow any correlation with respect to the flexibility of the used diamine or dianhydride. The lowest peak temperature was



measured for the most rigid backbone PGPI-2, while the highest peak temperature was obtained for the most rigid anhydride PGPI-3.

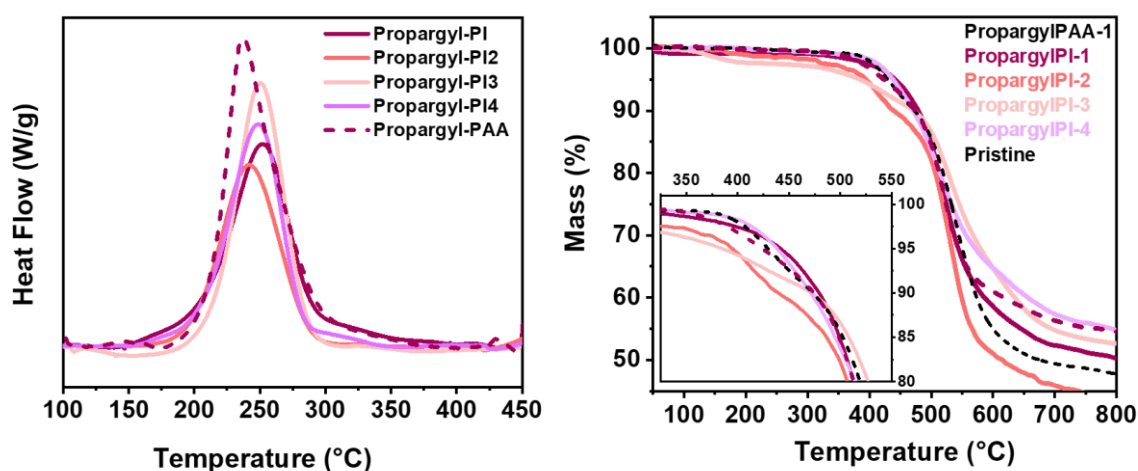


Figure 154. Heat flow curves (left) and mass loss curves (right) of the synthesized propargylated materials with various backbones based on 6FDA-BisAPAF, 6FDA-BisAPAF-Paa, 6FDA-HAB, EDA-APAF and BPADA-APAF.

Peak fitting supports the analysis of the on- and offset underlying reactions in order to find a relationship between the thermal initiated reactions and the backbone. Peak fitting reveals, that both rigid polyimides PGPI-2 and PGPI-3, based on 6FDA-HAB and EDA-APAF, show a narrow on- and offset temperature for the Claisen Rearrangement (see Figure 154). Both materials show a very symmetrical heat flow curve, and no other peak has been able to deconvolute from the fitted peak without uncertainty. This suggests that the cyclization of furan groups and the crosslinking are decreased compared to PGPI-1 and PGPI-4. PGPI-4, which is based on a highly flexible anhydride unit BPADA, shows a very similar peak shape compared to PGPI-1. Both materials have groups incorporated into the backbone, which allow a higher degree of mobility. 6FDA contains the hexafluoroisopropylidene unit, with larger fluorine atoms. BPADA contains an isopropylidene group and two ether bridges, which show high flexibility [139]. Accordingly, both polymer chains are expected to be more mobile, which is crucial, when it comes to crosslinking. Furthermore, PGPI-2 does not have any bridge between both chromene units. Therefore, both groups have to move away from each other by rotation along the biphenylene bond in order to not interfere with each other. On the other hand, the chromene group rotation is limited by the adjacent imide group. Therefore, PGPI-2 lacks the degree of flexibility compared to PGPI-1- and especially PGPI-4 strongly. As a consequence, the amount of crosslinking is expected to be significantly lower. However, since the broad offset area in PGPI-1 was attributed to crosslinking and ring opening, PGPI-2 does

not show these reactions to a high extent and lacks the corresponding peak (Figure 155). PGPI-4 shows the required flexibility, but the anhydride is quite large, since it contains four benzene rings (Figure 155). Hence, the chromene units, which tend to crosslink, have larger distances between each other. As a consequence, the crosslinking attributed third peak is lower compared to PGPI-1.

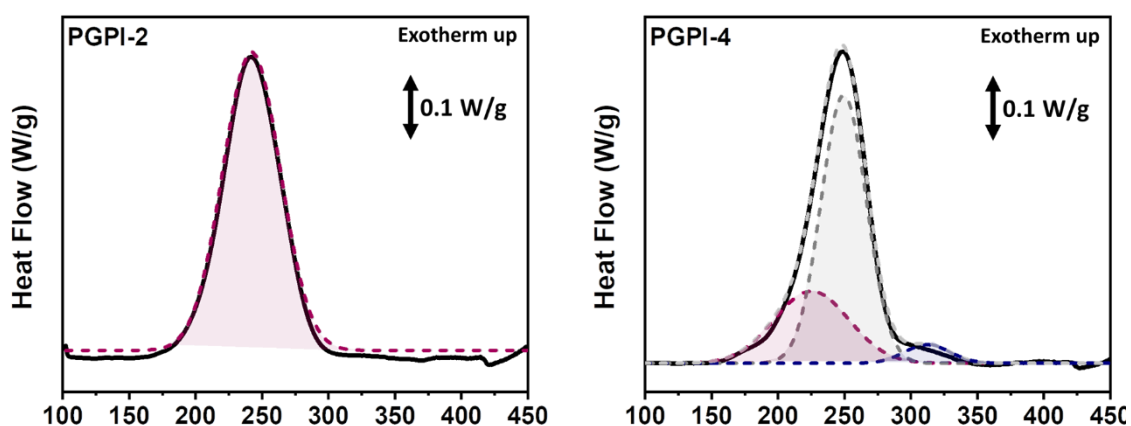


Figure 155. Heat flow of PGPI-2 and PGPI-4 obtained by means of DSC experiments in the temperature range from 100 to 450 °C with a heating rate of 5 °C min<sup>-1</sup>. Deconvoluted peaks based on Gauss-Fitting Fitting.

The Thermal Rearrangement was confirmed for PGPI-1 with respect to the CO<sub>2</sub> release, which was determined by means of the evolved gas analysis. However, the reaction proceeds very slowly due to the tight crosslinking. However, since crosslinking appeared to vary between more mobile propargylated polymers, such as PGPI-1 and PGPI-4, compared to more rigid PGPI-2 and PGPI-3, the TR<sub>onset</sub> and peak temperatures are expected to be influenced as well. Materials with lower degrees of propargylation and hence, lower degrees of crosslinking, have shown to have lower TR<sub>onset</sub> temperatures and a more distinct separation between TR process and polymer degradation. A comparison of rigid and more flexible propargylated polyimides by means of TGA-FT-IR measurements, Figure 154, show a similar observation. Furthermore, the weight loss step is more distinct, while the more flexible PGPI-4 shows a nearly identical mass loss curve as PGPI-1.

## Effect of the Derivative

Propargylated polyimides showed consecutive thermal cascade reactions in a similar manner to previously discussed Allyl-PI. However, propargylated materials have shown that the *ortho*-allene phenol product was not able to be isolated, and tends to a consecutive cyclization. Materials have shown to undergo a Claisen Rearrangement, cyclize into two different products, crosslink and open the corresponding rings again. This thermal cascade reaction sequence is more complex compared to Allyl-PI. However, substitutions in Allyl-PI, such as  $\beta$ Mallyl have shown a more complex sequence as well. Therefore, it was one of the most important questions, if the tendency for each thermal reaction can be promoted or suppressed by simply using propargyl derivatives instead of unmodified propargyloxy groups.

The propargyl group only contains two potential positions for substitution as a consequence of the triple bond. Hence, only in  $\gamma$ -position one substituent can be introduced, and in  $\alpha$ -position two hydrogen atoms can be substituted. For the study of the effect of the derivative the  $\alpha$ -substituted methyl derivative,  $\alpha$ MPGPI, was synthesized from 2-Bromo-butyne. In  $\gamma$ -position the substituents methyl, ethyl, trimethylsilyl and naphthyl were used. Each derivative was synthesized according to the Williamson-Ether synthesis procedure for PGPI-1, as described in the *Allylation and Propargylation* on page 388. In all cases orange-brown fibers were obtained. The solubility of each derivative was very high in common organic solvents, especially in dipolar aprotic solvents, such as DMF, DMAc, NMP, DMSO, acetone. High solubility was also determined for ethyl acetate, ethanol, chloroform and THF. For each derivative, a full conversion was achieved, as confirmed by means of  $^1\text{H-NMR}$  spectroscopy. The NMR spectra are shown in Figure 156. In all cases the hydroxy peak at 10.4 ppm disappeared completely, while a methylene peak of the propargylic protons appeared around 5 ppm. In each case, the number of protons fit to the expected four protons of the propargylic methylene group, except for  $\alpha$ MPGPI, which showed only an integral of 2 protons, since one hydrogen atom is substituted by a methyl group. In addition, the corresponding protons of the substituent were detected. Further NMR peak assignment can be seen in the appendix.

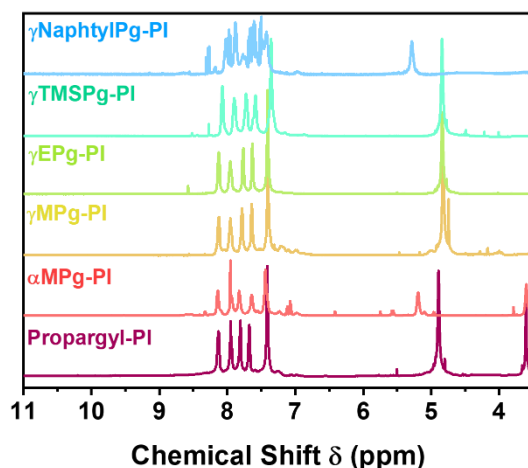


Figure 156. Stacked  $^1\text{H}$ -NMR spectra of the synthesized propargyl derivatives  $\alpha\text{MPGPI-1}$ ,  $\gamma\text{MPGPI-1}$ ,  $\gamma\text{EPGPI-1}$ ,  $\text{TMSPGPI-1}$ ,  $\text{NaphthylPGPI-1}$ .

The derivatives are separated into two categories for the purpose of the discussion. One category contains alkyl substituents, which are  $\alpha\text{MPGPI-1}$ ,  $\gamma\text{MPGPI-1}$  and  $\gamma\text{EPGPI-1}$ . The second category contains a heteroatom,  $\text{TMSPGPI}$ , which consists of a trimethylsilyl group and an aromatic substituent,  $\text{NaphthylPGPI-1}$ , which consists a naphthyl group.

The alkylic group shows a strong exothermic peak in the first heating cycle, like  $\text{PGPI-1}$  (Figure 157). However, a significant peak shift in both cases was observed.  $\alpha\text{MPGPI-1}$  shows a shift of the Claisen Rearrangement peak down to lower temperatures. The CR peak temperature of  $\alpha\text{MPGPI}$  is lower compared to  $\text{PGPI-1}$ . The peak deconvolution suggests in total two exothermic reactions, starting at  $150\text{ }^\circ\text{C}$ . The thermal reaction ends at an offset temperature of  $275\text{ }^\circ\text{C}$  and shows a gap until the next exothermic reaction starts at  $350\text{ }^\circ\text{C}$ . This second exothermic peak in above  $350\text{ }^\circ\text{C}$  was not detected to such an extent for  $\text{PGPI-1}$ . Any reaction above  $300\text{ }^\circ\text{C}$  will be discussed later.

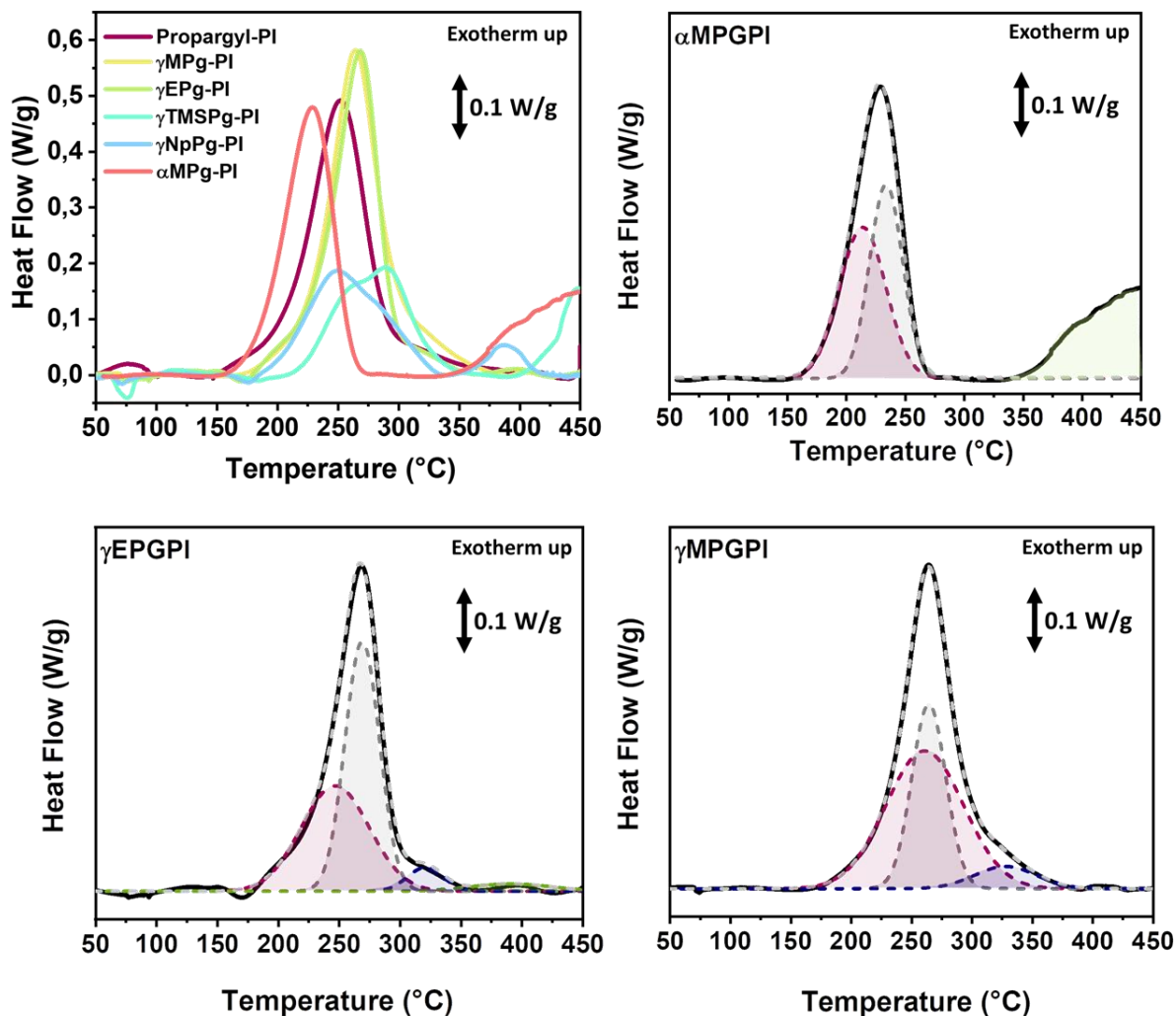


Figure 157. Superimposed heat flow curves of the synthesized propargyl derivatives (top left) and peak fitting and deconvolution analysis of the allylic derivatives  $\alpha$ MPGPI (top right),  $\gamma$ EPGPI-1 (bottom left) and  $\gamma$ MPGPI (bottom right).

Both  $\gamma$ -substituted derivatives,  $\gamma$ MPGPI-1 and  $\gamma$ EPGPI-1, show a similar heat flow profile to each other. Accordingly, no subsequent reaction of the ethyl group occurs. In both cases a shift of the peak to higher temperatures was observed. With 270 °C the peak is shifted by around 20 °C compared to PGPI-1, and about 50 °C higher compared to  $\alpha$ MPGPI-1. Other than  $\alpha$ MPGPI-1, a broad onset and offset temperature range was observed for both materials, similar to PGPI-1. The deconvoluted peaks show a similar peak pattern to PGPI-1 as well. The onset of the exothermic heat flow starts in both cases at 175 °C with a process, whose peak is similar to PGPI-1. However, the third process is significantly smaller compared to PGPI-1 in both cases. Even though,  $\gamma$ MPGPI-1, has a stronger shoulder than  $\gamma$ EPGPI-1. The third process was attributed to crosslinking. Hence, a lowered tendency to crosslink in case of  $\gamma$ MPGPI-1 is reasonable since it sterically hinders the double bonds to crosslink, after the chromene cyclization. In the case of  $\gamma$ EPGPI-1 the substituent at the  $\gamma'$ -position, lowers the chance of two

chromene units to come close enough to crosslink even more. Therefore, the crosslinking assigned peak is even lower in that case.

Both materials of the second derivative group, TMSPGPI-1, and NaphtylPGPI-1, show only a small exothermic peak, each with a very broad shoulder. While all alkylic derivatives have not shown a weight loss step prior 300 °C (Figure 158), both materials of the second group do show a significant weight loss step. In the case of TMSPGPI, the evolved gas analysis has shown that trimethylsilyl-propyne leaves the system. Hence, after the Claisen Rearrangement, the whole group seems to decompose. In the case of NaphtylPGPI-1, the naphthyl group is released, since naphthalene has been identified as a decomposition product.

From DSC investigation,  $\alpha$ MPGPI-1 does not show significant crosslinking, but another process above 350 °C appears to be more pronounced compared to any other propargyl derivative. The  $\gamma$ -substituted  $\gamma$ MPGPI-1 and  $\gamma$ EPGPI-1 do show a behavior similar to PGPI-1, but the amount of crosslinking is reduced.

Therefore, it is of high interest to investigate the effect of the substitution towards Thermal Rearrangement. Indeed,  $\gamma$ M- and  $\gamma$ EPGPI-1 show a mass loss curve with onset and peak temperatures of the mass loss step above 350 °C, which is nearly identical to PGPI-1 (Figure 158). Since DSC measurements suggested, that all three materials undergo similar reactions, their constitution is similar and affects the TR process in the same manner.  $\alpha$ MPGPI-1 on the opposite shows a strong variation of the reactions and an onset temperature around 300 °C for the TR related CO<sub>2</sub> release was determined (Figure 158 and Figure 159).  $\alpha$ MPGPI-1 shows a more distinct weight loss step with a CO<sub>2</sub> evolution peak temperature of 386 °C. With such a low onset temperature and moderately low TR peak temperature,  $\alpha$ MPGPI-1 adds to the propargyl-containing low TR-temperature materials, PG15PI-1 and PG25PI-1.

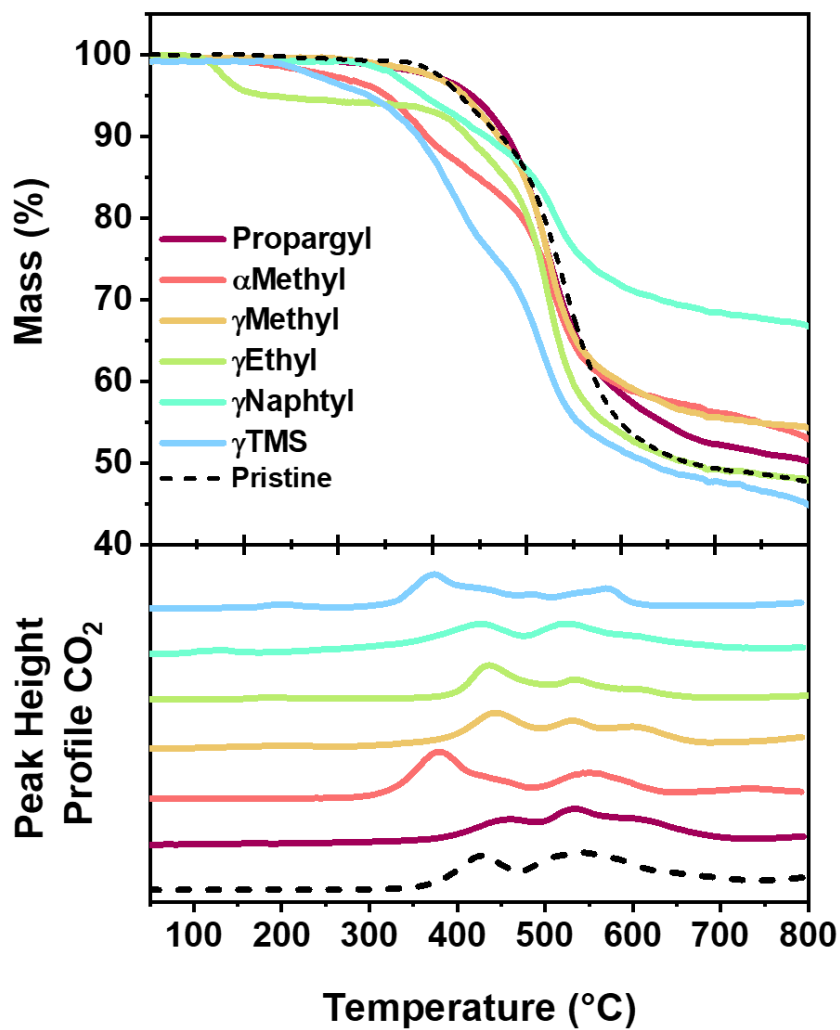


Figure 158. Mass loss curve obtained by means of TGA experiments of propargyl derivatives (top). CO<sub>2</sub> gas evolution peak analysis by means of TGA-FT-IR analysis.

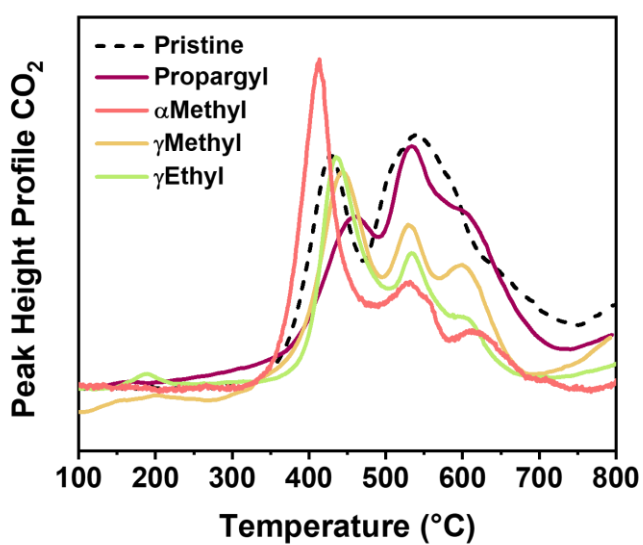


Figure 159. Peak height profile for the vibration at 2240 cm<sup>-1</sup>. The peak corresponds to CO<sub>2</sub>.

## Key Messages

- ➔ The propargylated *ortho*-hydroxy polyimide, PGPI-1, undergoes a set of consecutive thermal reactions (reaction cascade).
- ➔ Investigations by means of heat flow curves and thermo kinetic analysis reveal a thermal reaction cascade, which consists of
  - Claisen Rearrangement
  - Chromene and furan cyclization
  - Crosslinking
  - Ring opening
  - Thermal Rearrangement
- ➔ The assignment and identification of each reaction step was done by means of FT-IR, <sup>1</sup>H-NMR spectroscopy and gel-fraction measurements.
- ➔ The degree of propargylation affects the onset temperature and extent of the described reactions.
  - Lower degrees of propargylation show significantly lowered tendencies to crosslink.
  - A more distinct Thermal Rearrangement step was observed, as more readily available phenol groups are present and less crosslinking related mobility restrictions occur.
  - The TR<sub>onset</sub> temperature for materials with 8, 15 and 25% propargylation rank among the lowest ever reported TR materials.



- ➔ Backbones affect the thermal cascade strongly.
  - More flexible backbones show higher tendencies to crosslink and a slower TR process, while more rigid materials show lower crosslinking tendencies.
  
- ➔ Substitutions along the propargyl chains affect the process onset and peak temperatures and isothermal conversions strongly.
  - $\alpha$ -position methyl substituted  $\alpha$ MPGPI-1 shows the lowest onset and peak temperature for the Claisen Rearrangement process, of about 20°C lower compared to PGPI-1 and low crosslinking.
  
  - $\gamma$ -position methyl and ethyl substituted  $\gamma$ M- and  $\gamma$ EPGPI-1 show similar thermochemical behavior to each other and PGPI-1, but higher CR temperatures of 250 °C. Both materials show a lower tendency to crosslink.
  
  - $\alpha$ MPGPI-1 shows a low TR onset temperature around 300 °C and a distinct weight loss step, which is attributed to the TR process.
  
- ➔ The TR process can be visualized by means of DSC measurements above 350 °C for the low-TR-temperature materials.

## Molecular Modelling Studies

Many solid-state reactions are difficult to characterize, due to the lack of analysis methods to determine potentially formed structures. Especially in polymers, many reactions were only described by means of spectroscopic analysis and chemical intuition. Quantum mechanical simulations were used in the previous section, combined with molecular mechanic methods in order to support and consolidate the experimental findings. The identified reactions

- Claisen Rearrangement
- Furan cyclization
- Chromene cyclization
- Crosslinking
- Ring opening
- Thermal Rearrangement

have been simulated by means of DFT simulations based on a B3LYP/6-31g\*+ level of theory. The reactions were then manually performed in each amorphous cell using molecular mechanic methods, using the COMPASS force field. The simulation was employed in order to tackle the following questions

- What is the energetically favored cyclization reaction?
- Which type of crosslinking mechanism might occurs and how is it affected
- Which structures form during ring opening and
- Which reactions are likely to follow the ring opening?
- How might the full thermal cascade reaction look like

For the DFT simulations the smallest possible unit was constructed, which consists of all relevant functional units, which are the propargyl phenyl ether and the phthalimide unit. The model is shown in Figure 160.

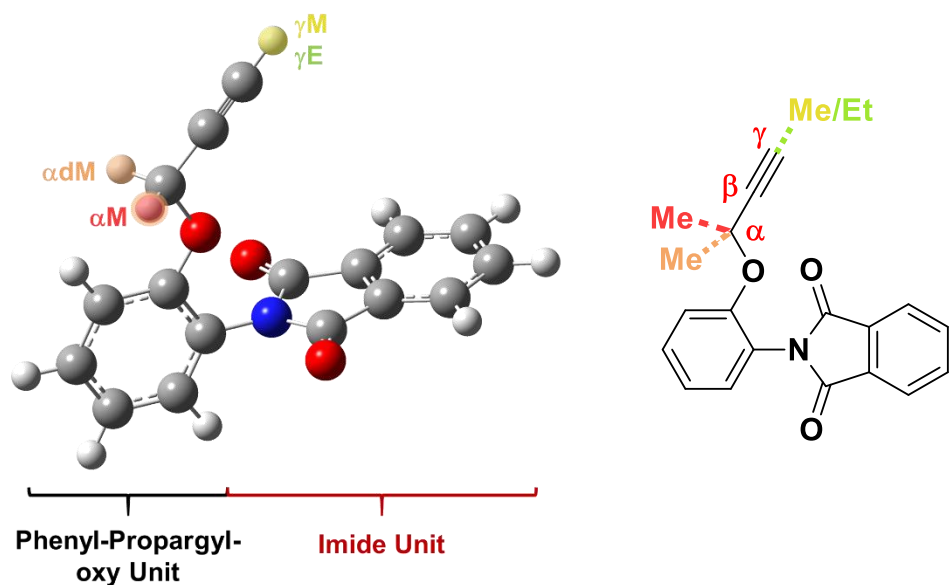
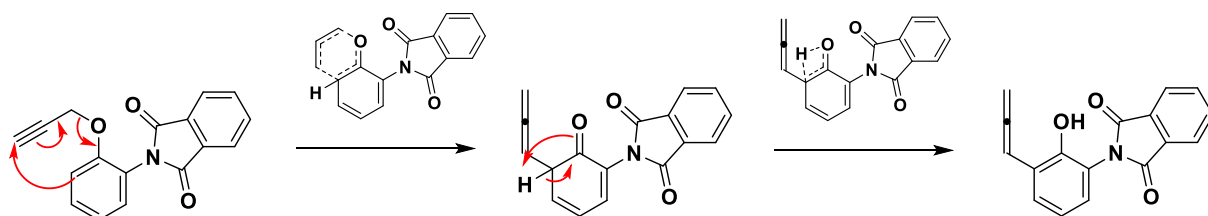


Figure 160. DFT simulation model consisting of a phenyl-propargyloxy unit and a phthalimide unit (left) and the corresponding projection formula.

## Claisen Rearrangement

The Claisen Rearrangement of phenyl propargyl ether proceeds analogously to the process in phenyl allyl ether. The major difference is that the initial group does not form the same group again, hence, propargyloxy does not form *ortho*-propargyl phenol. In the case of propargyl CR, a highly reactive *ortho*-allene phenol is formed. The general reaction scheme is shown in Scheme 14.



Scheme 14. Claisen Rearrangement reaction of phenyl propargyl ether.

In Figure 161 the simulated results of each single point energy of the transition state and intermediate structure of the Claisen Rearrangement and consecutive chromene and furan cyclization.

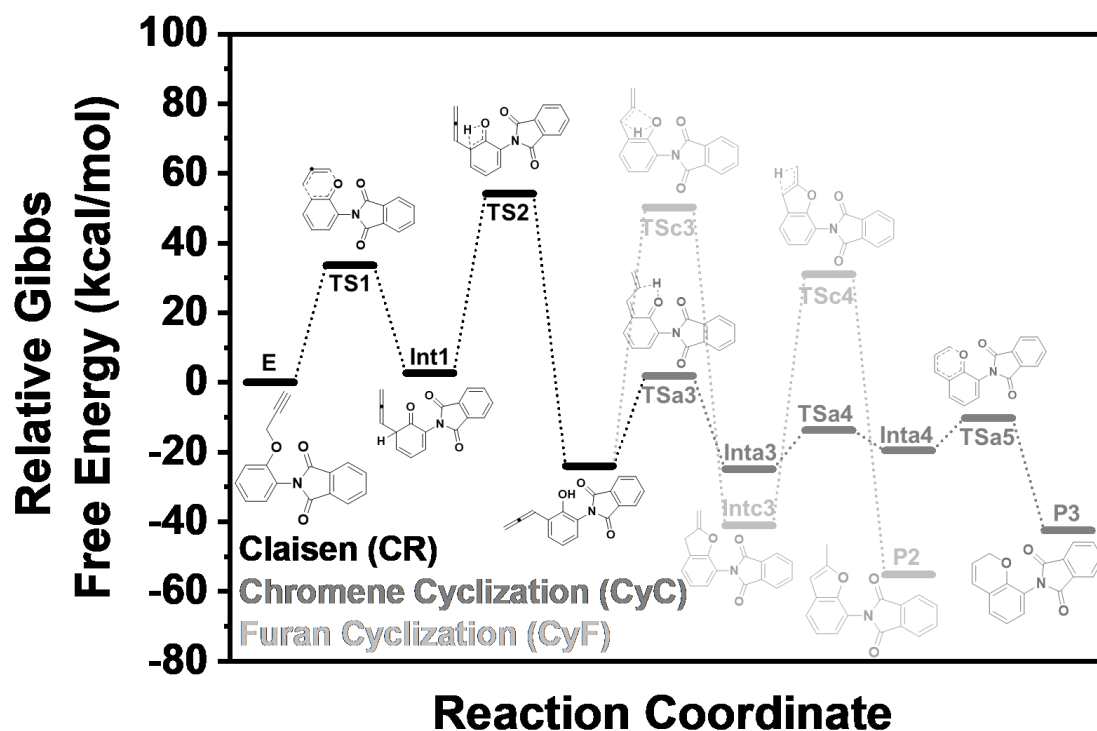
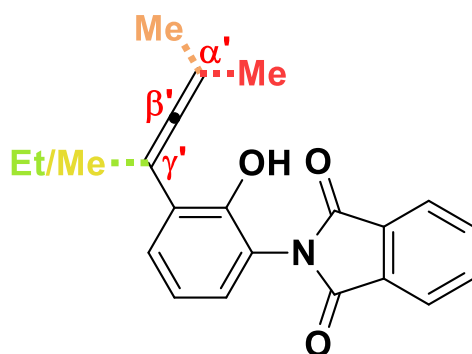


Figure 161. Reaction coordinate of the simulated reaction steps including transition states and intermediates for the Claisen Rearrangement (black), chromene cyclization (dark grey) and furan cyclization (light grey).

The first step is the bond breakage of the phenyl propargyl ether bond between  $O_{\text{Phenol}}$  and  $C_{\alpha}$ , and the simultaneous formation of a new C-C  $\sigma$  bond between  $C_2$  and  $C_{\gamma}$ . The energy of  $33.58 \text{ kcal mol}^{-1}$  is in the range of allylated models and to the literature. The first intermediate is Int1, and an *ortho*-allene cyclohexadienone phthalimide. The following step is a hydrogen migration to undergo the enol tautomerism forming the thermodynamically favored aromatic *ortho*-allene phenol (P1)(Scheme 15).



Scheme 15. Scheme of the Claisen-Rearranged product P1.

Afterwards P1 is able to undergo a protonation of the allene group, forming a cyclohexadienone intermediate again, which undergoes *cis-trans* isomerization followed by ring-closure between the terminal  $C\alpha'$  group and the phenolic oxygen atom. In contrast the *ortho*-allene phenol product P1 can undergo a nucleophilic attack of the phenol at the  $C\beta'$  atom of the allene group along with protonation of the  $C\gamma'$  atom via TSc3. The formed intermediate Intc3 isomerizes to the thermodynamically most favored product, the benzofuran product P2.

In Figure 162, the transition state geometries of the propargylated model and three derivatives is shown. The colors visualize the Mulliken charge, which was obtained by population analysis. The visualization of the charges shows, that the  $\alpha$ M derivative does not show a strong polarization of the migrating allene group, as the charge of both termini are about the same order. A similar observation can be made for  $\alpha$ dM, which is the double methylated propargyl group in  $C\alpha$  position. Interestingly, the allene group of the  $\gamma$ M derivative shows a positive charge at the C-C bond forming terminus and a negative charge at the bond breaking terminal C atom of the propargyl group.

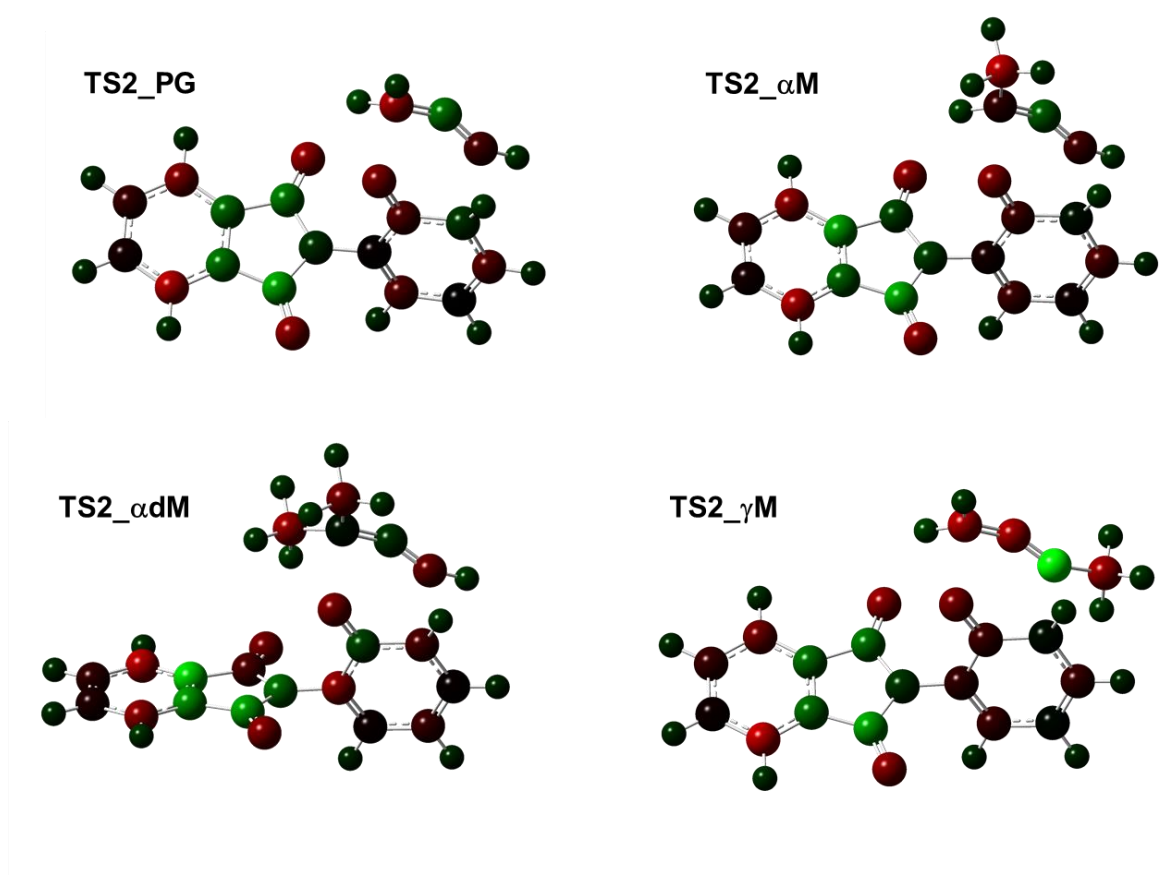


Figure 162. Transition state TS2 structure of the Claisen Rearrangement process for the propargyl model PG and three derivatives  $\alpha$ M,  $\alpha$ dM and  $\gamma$ MPG.

Table 5. Geometrical parameters, which are relevant for the Claisen Rearrangement and correspond to TS2.

	O-C=	C=C	C=C	=C-Car
PG	2.00567	1.36616	1.25594	2.11749
$\alpha$ M	2.07769	1.36866	1.25207	2.17553
$\alpha$ dM	2.15305	1.37298	1.24804	2.23062
$\gamma$ M	2.16028	1.35253	1.25730	2.18392
$\gamma$ E	2.15979	1.35264	1.25787	2.18451

The simulations reveal the lowest CR activation energy for the first step TS1 for the geminal methyl substituted  $\alpha$ dM derivative, followed by  $\alpha$ M. The propargyl model and the  $\gamma$ -substituted models  $\gamma$ M- and  $\gamma$ EPGPI show very similar activation energies above. The second step shows the same order, except, that  $\gamma$ -substituted derivatives show significant higher activation energies compared to PGPI (Figure 163). These simulation results are in full agreement with the experimental findings. The same order was experimentally determined, with  $\alpha$ M < PG <  $\gamma$ M ~  $\gamma$ E.

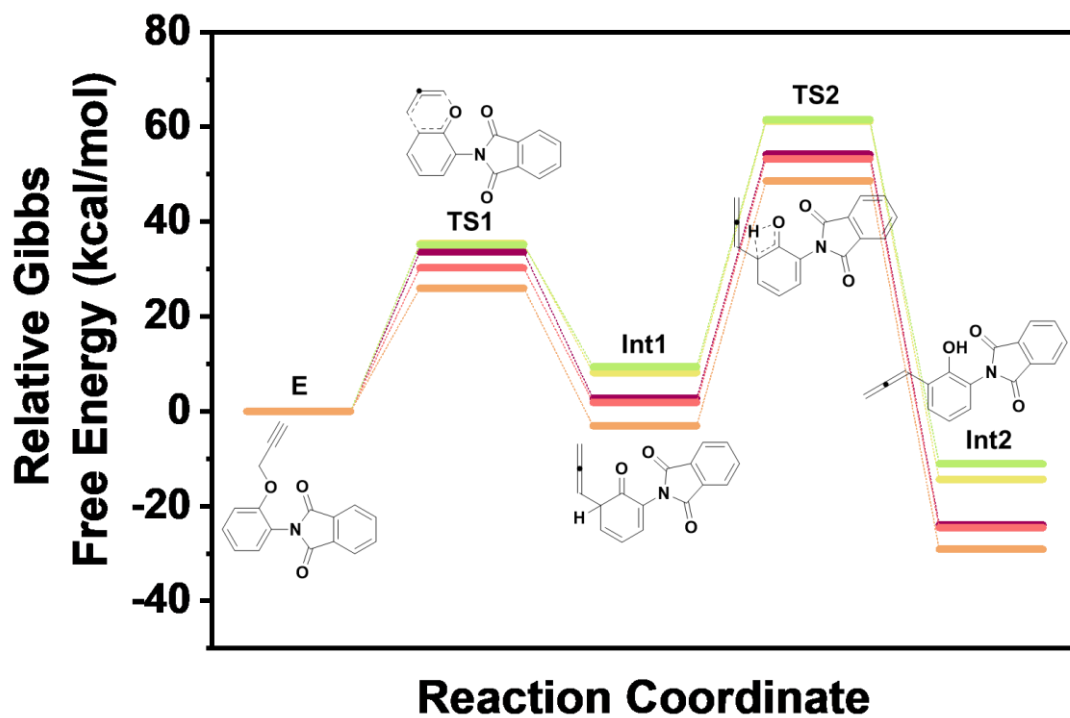
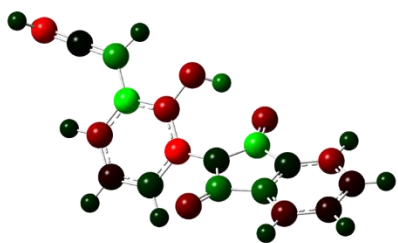
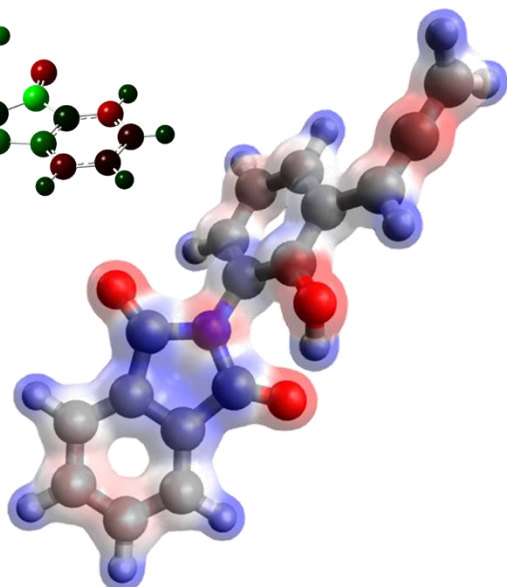


Figure 163. Reaction coordinate of the simulated reaction steps including transition states and intermediates for the Claisen Rearrangement of the propargyloxy derivative models.

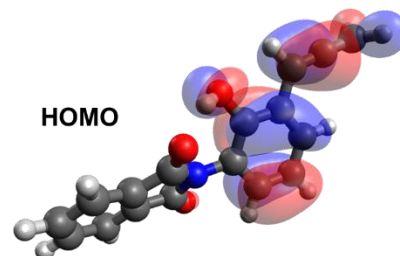
Mulliken type atomic charges



Electrostatic Potential Map



HOMO



LUMO

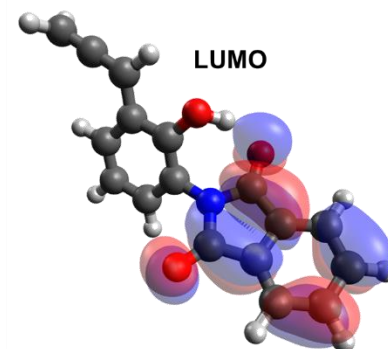
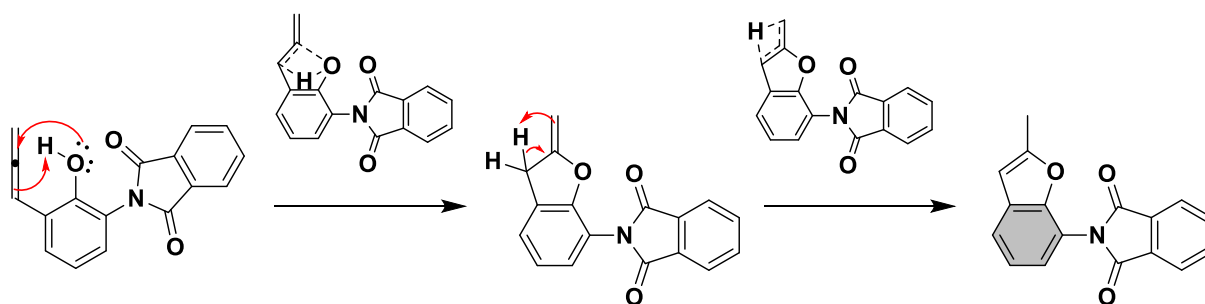


Figure 164. Model of P1 including visualization of the Mulliken type atomic charges, the electrostatic potential map, and the visualization of the HOMO and LUMO orbital of P1.

## Cyclization

The cyclization of P1 to the corresponding benzofuran occurs between the phenolic oxygen atom and C $\beta'$  (C8') via nucleophilic attack and simultaneous protonation of C $\gamma'$  (C7'). The reaction scheme is shown in Scheme 16.



*Scheme 16. Reaction scheme of the benzofuran cyclization.*

The second step is an isomerization forming a more substituted double bond, which is thermodynamically favored. The transition state geometry is shown in Figure 165.

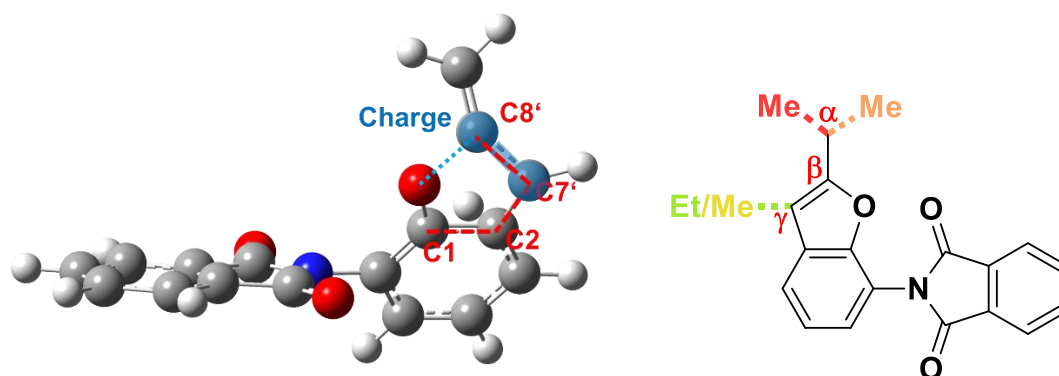


*Figure 165. Transition state geometry of TSc3 and the corresponding projection formula.*

The lowest energy barrier for the furan cyclization was simulated for  $\gamma$ EPGPI followed by  $\gamma$ MPGPI. The  $\alpha$ -substituted models and PGPI show a very similar activation energy for the first and second step. The reaction coordinate is shown in Figure 166.



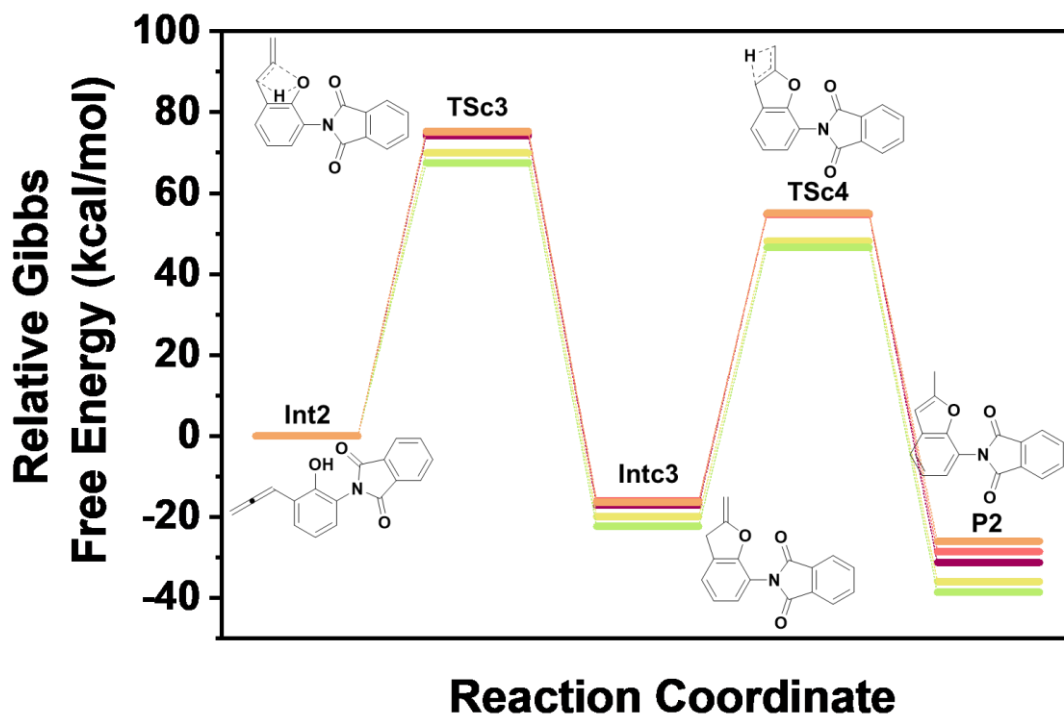
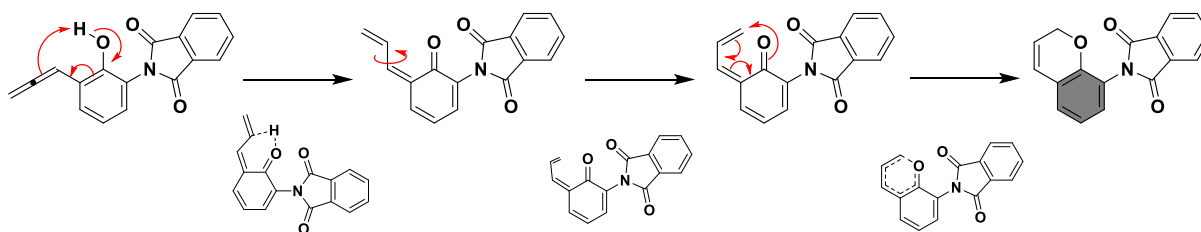


Figure 166. Reaction coordinate of the benzofuran cyclization for all simulated propargyl derivatives.

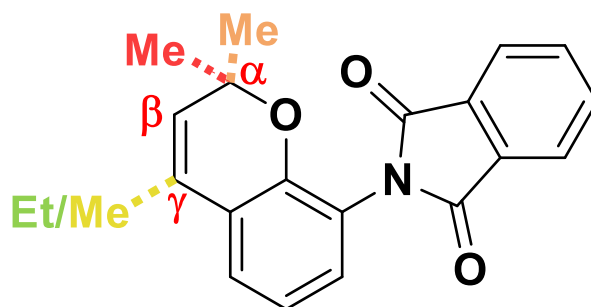
### Chromene cyclization

From Figure 161 we know that the reaction path of the chromene cyclization contains lower energy barrier steps, including the formation of an intermediate cyclohexadienone. The furan cyclization requires significantly more energy for both steps, however, the benzofuran product P2 has a lower single point energy compared to the chromene cycle. One reason of the stabilization might be a stronger electron delocalization and higher substitution of the double bond. The reaction mechanism for the chromene formation is shown in Scheme 17.



Scheme 17. Reaction mechanism for the chromene cyclization.

The final product is a cyclohexene ring with its double bond in  $\beta'$ - $\gamma'$  position. Depending which substitution is used, both, the  $\gamma$ M- and  $\gamma$ E-PGPI have a substitution in the final  $\gamma'$ -position, while  $\alpha$ M- and  $\alpha$ dMPGPI have their methyl groups at the methylene group, as shown in Scheme 18.



Scheme 18. Chromene product P3 with positions of the substituents.

The simulated reaction path is shown in Figure 167. The  $\gamma$ E derivative shows once more the lowest activation energy barrier for each step of the chromene cyclization. The second lowest activation energy, but reasonably higher is  $\gamma$ MPGPI. Both  $\alpha$ -substituted derivatives show higher energies, but lie in between  $\gamma$ E and the highest determined activation energy of PGPI. In all steps, PGPI shows the highest activation energy among all simulated materials for the chromene formation.

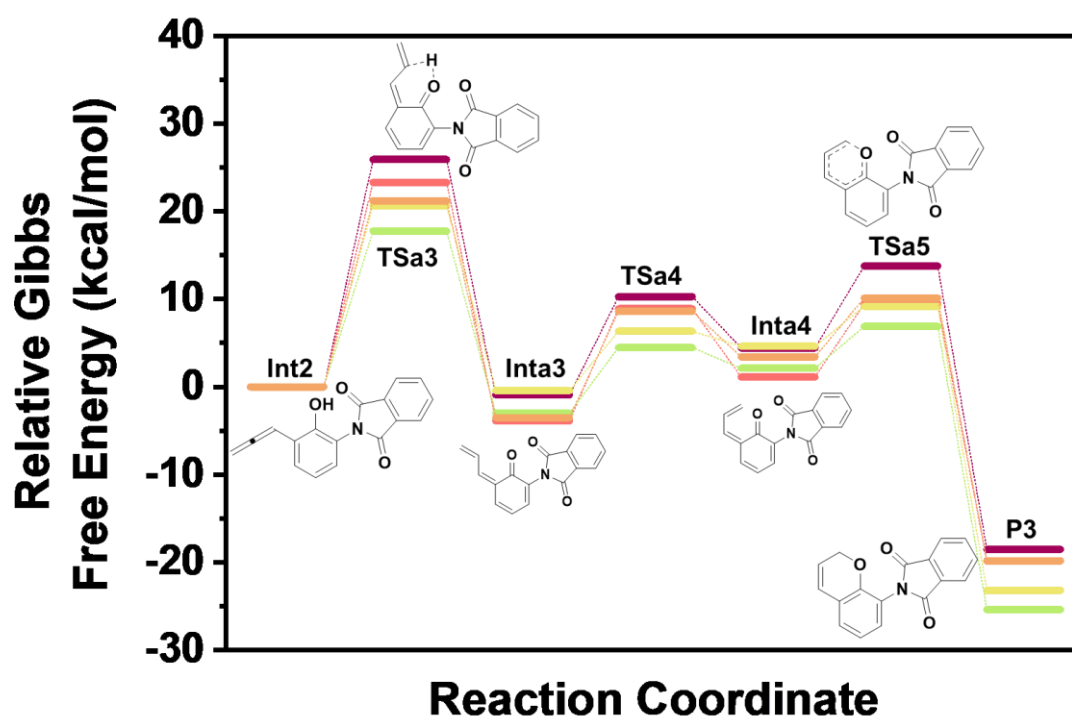


Figure 167. Reaction coordinate of the chromene formation of the simulated propargyl derivatives.

Interestingly, in both transition states (Figure 168), the dihedral angle, which describes the rotation of the allene group during the reaction, shows among the highest values in case of  $\gamma$ EPGPI, which showed the significant lowest activation energy on the other hand. While a larger dihedral angle C1-C2-C7'-C8' increases the distance for the proton migration from the phenol group to the allene  $\pi$ -bond, in TSa5 the higher dihedral angle increases the distance between the reacting phenone and C9' (see Table 6).

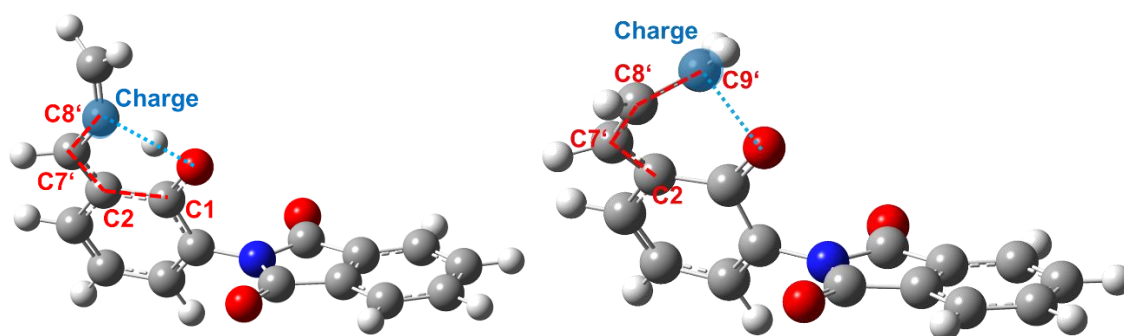


Figure 168. Transition state geometry TSa3 for the furan cyclization (left). Transition state geometry TSa5 for the chromene cyclization (right).

Table 6. Geometrical parameter which are considered to be relevant for the furan and chromene cyclization reaction.

Model	TSa3		TSa5				
	Dihedral (°)	M (C8')	Dihedral (°)	Distance	M (C7')	M (C8')	M (C9')
PG	7.690		27.207	2.14619			
$\alpha$ M	6.138		25.665	2.16403			
$\alpha$ dM	5.048		28.233	2.22687	-0.363	-0.263	0.437
$\gamma$ M	11.202		27.623	2.17302			
$\gamma$ E	11.851	-0.219	26.862	2.17779	0.169	-0.034	-0.285

The subsequent reactions of both products, P2 and P3, depend strongly on the steric accessibility and electronic properties. For that purpose, the Mulliken charges and electrostatic potential and electron density is discussed in more detail (Figure 127). The Mulliken charges show that the C7' of the furan product P2 has a positive atomic charge on the double bond involved carbon atom, while the corresponding atom of the chromene product P3 shows a negative atomic charge. The higher electron density of the double bond, leading to a more negative charge around the chromene double potential, can be seen by means of the electrostatic potential map as well (Figure 169). Here, the negative potential is localized around the oxygen atom and the double bond, while the furan ring contains a more localized negative potential only around the oxygen atom. The reason for the lower electron density around the

double bond in P2 is the stronger electron distribution in line with the methyl group. Therefore, the localization of the electron density on the double bond is reduced. From that electronic point of view, consecutive reactions of the double bond in chromene appear to be more susceptible towards nucleophilic reactions and reactions with electrophilic groups. Therefore, a higher crosslinking tendency is expected for the chromene product.

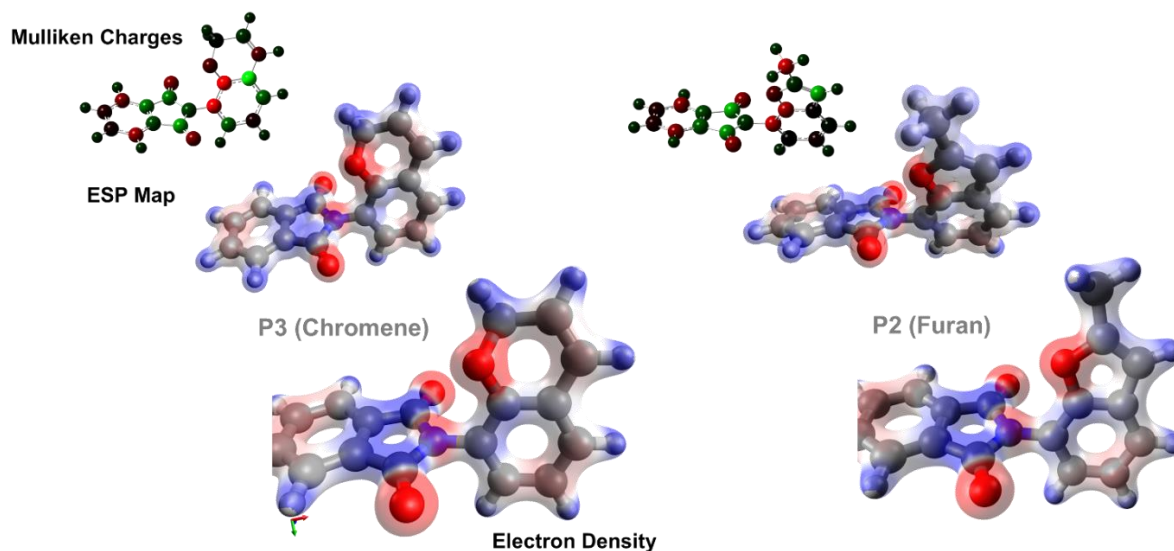
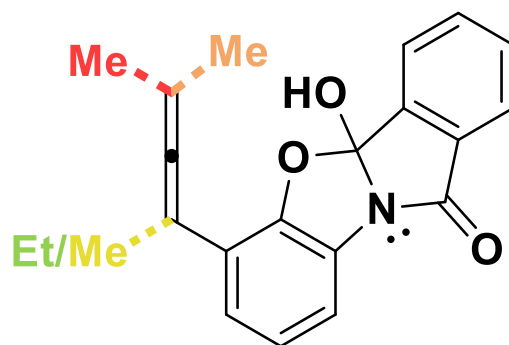


Figure 169. Visualization of the Mulliken charges, electrostatic potential map, and electron density of the chromene product P3 (left) and furan product P2 (right).

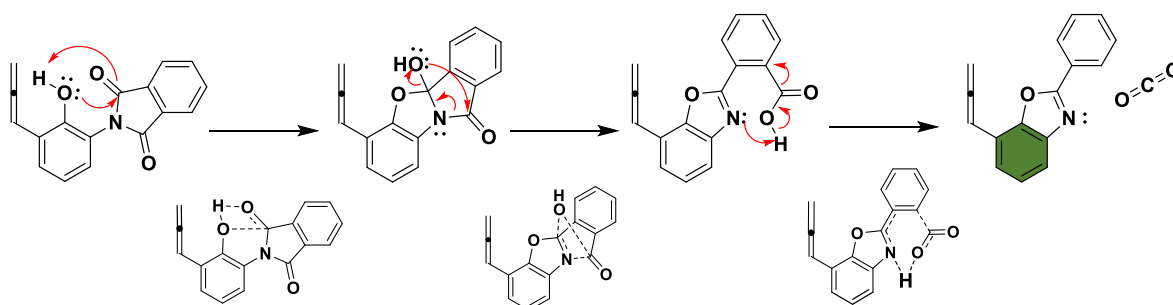
## Thermal Rearrangement

Another cyclization reaction of the *ortho*-allene phenol product P1 could be the cyclization-extrusion reaction, based on the nucleophilic reaction of the phenol group at the electrophilic imide carbonyl group, which leads to the formation of a bicyclic intermediate. This intermediate Into3 forms via an intramolecular hydroxy group transfer, according to suggested mechanism in Chapter *TR mechanism*, to the *ortho*-carboxyl benzoxazole product. After decarboxylation, which is the extrusion reaction, the final benzoxazole is formed. The first intermediate Into3 is shown in Scheme 19.



Scheme 19. Intermediate Into3 after intramolecular nucleophilic reaction of the phenol and imide group, which is the first step of the Thermal Rearrangement reaction.

The full reaction mechanism, including all three steps, is shown in Scheme 20.



Scheme 20. Reaction mechanism of the Thermal Rearrangement of P1 based on the simulated mechanism.

Other than the previous two cyclizations, the Thermal Rearrangement does not involve the allene group in the reaction and the cyclization occurs between both units and not only in the ether unit. However, differences in the activation energy barrier can be simulated for each derivative here as well. The simulation results for the first step of the TR process are shown in Figure 170. The significantly lowest energy barrier can be calculated for the  $\gamma$ E-derivative with 34 kcal mol<sup>-1</sup>.  $\gamma$ MPGPI is following with 37 kcal mol<sup>-1</sup>. The  $\alpha$ -group derivatives and PGPI show the highest energy barrier again with energies around 38 kcal mol<sup>-1</sup>.

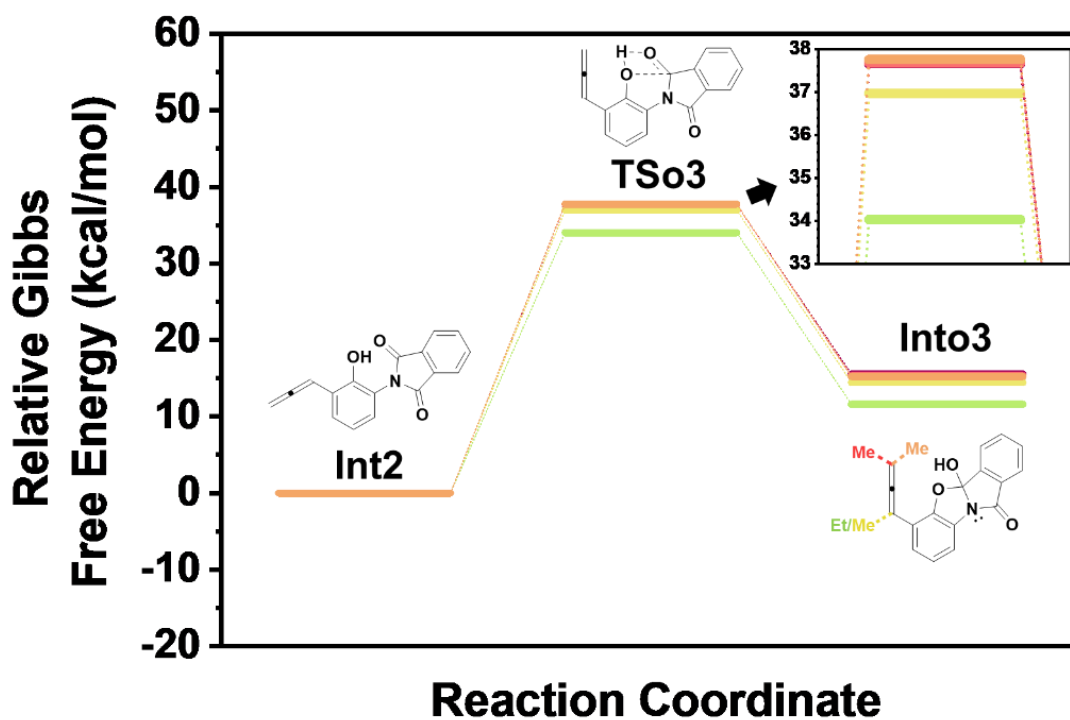
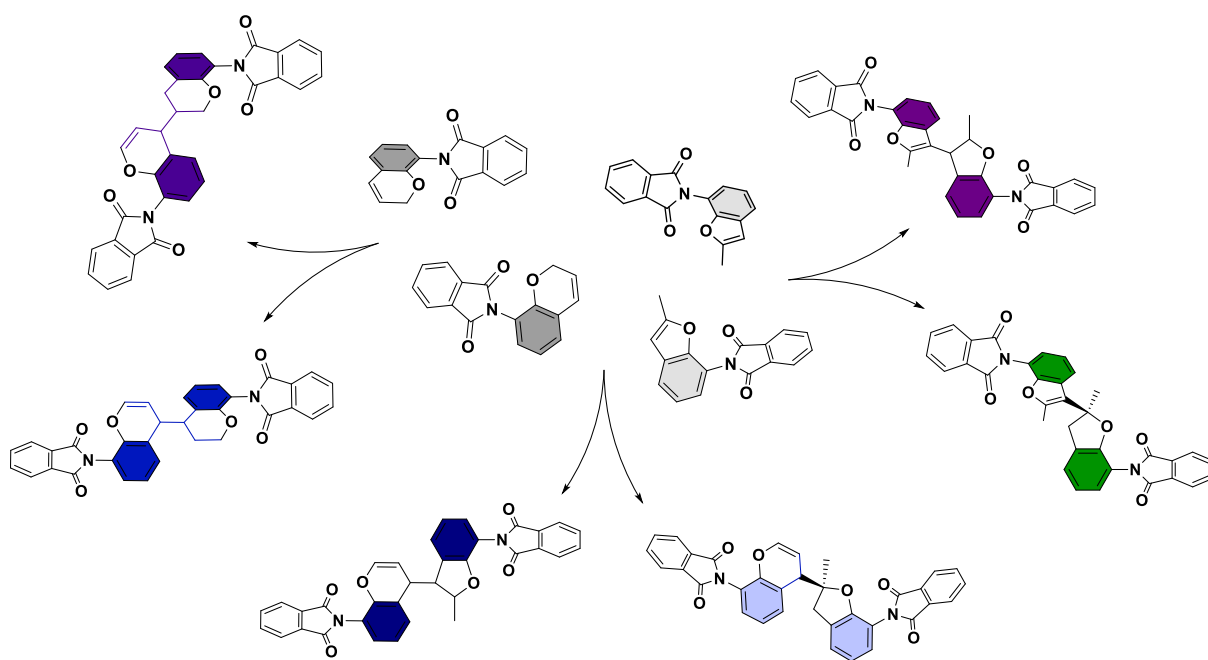


Figure 170. Reaction coordinate of the first step of the Thermal Rearrangement.

## Crosslinking

The experimental results revealed that the propargylated polyimides undergo crosslinking, which led to high gel contents and a significant exothermic heat flow was attributed to the crosslinking process. Simulations of the furan and chromene groups have shown, that especially the chromene product has a negative charge and higher electron density around the double bond, which might be the crosslinking center. Even though, the highly reactive allene group can principally undergo [2+2] cycloadditions, which are thermally allowed according to Woodward-Hoffmann rules, a specific perpendicular orientation, the steric hindrance and the limited mobility of the polymer chains make it very unlikely to get into such a position for the dimerization. Furthermore, dipolar cycloaddition could occur between allene and chromene groups. However, in all these cases, two units have to come close enough in a polymer to react, which is less likely, based on the limited mobility, compared to an intramolecular cyclization reaction. Therefore, it is expected, that the cyclization occurs in the majority and crosslinking reactions happen to occur between chromene and furan units. Potential crosslinks, which were in the following section simulated are shown in Scheme 21.



Scheme 21. Potential crosslinking products between chromene and furan units.

The chromene crosslinking was simulated via four pathways. Two mechanisms for each of the two vinyl carbon atoms (as the attacking side) were calculated. For each of the two reacting centers, a four-membered transition state geometry and a six-membered Alder-ene crosslinking mechanism was calculated. The schematic representation of each transition state and the corresponding product is shown in Figure 171. Moreover, two chromene models and their potential attacking sides are shown as well. The relative Gibbs free energies, the energy barrier, in relation to the starting material E is shown in Figure 172.

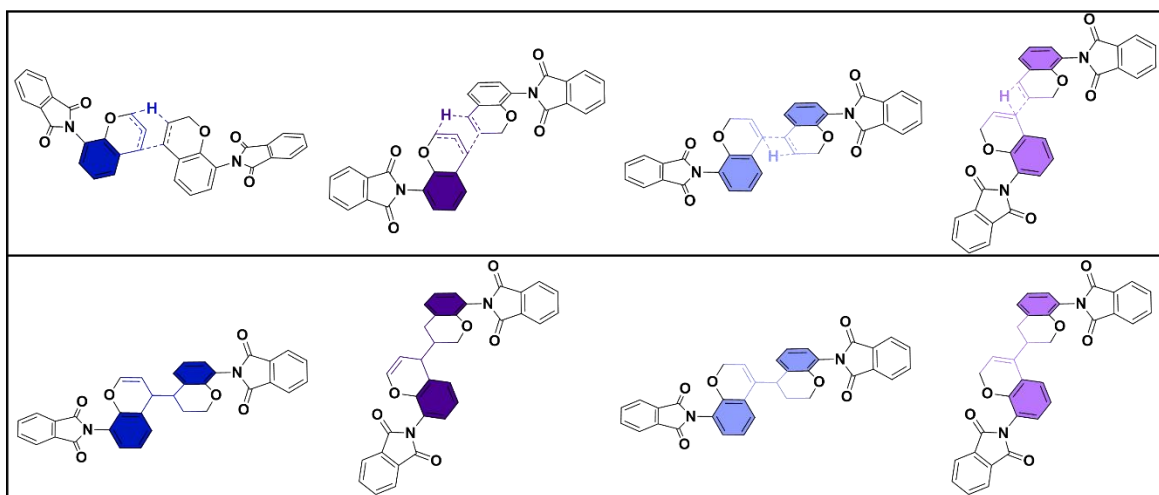


Figure 171. Transition state (TS) geometries visualized as projection formula for the four- (TSx4) a six-membered TS (TSx6) and the corresponding products for the propargyl model (top). Two constructed models of P3 and the reaction direction starting from  $\gamma'$  carbon atom from the left model.

The reaction between  $C_{\gamma'}$  (C7') and  $C_{\gamma'}$  (C7') is highlighted in blue and corresponds to the  $\gamma\gamma$ -mechanism, and reactions between  $C_{\gamma'}$  (C7') and  $C_{\beta'}$  (C8') correspond to the  $\gamma\beta$ -mechanism and are highlighted in purple. The crosslinking via four-membered transition state geometries is initiated by the proton transfer from  $C_{\gamma'}$  of the left (attacking) molecule to the  $C_{\beta'}$  atom of the right (attacked) molecule in case of the  $\gamma\gamma$ -mechanism. The TS is TSx4\_ $\gamma\gamma$ . Due to the proton transfer, the  $C_{\gamma'}$  atom becomes partially positive and an electrophilic attacking point. The binding electron pair from the proton migration remains at  $C_{\gamma'}$  of the left molecule, making it the nucleophilic center. The crosslinking reaction occurs between the double bond of the attacking molecule and the partially positive electrophilic  $C_{\gamma'}$  atom of the right (attacked) molecule.

In case of the  $\beta\gamma$ -mechanism, the proton migration occurs from  $C_{\gamma'}$  to  $C_{\gamma'}$  of the right molecule. As a consequence, the  $C_{\beta'}$  atom of the right molecule becomes the electrophilic center,



therefore the crosslinking occurs between  $C\gamma'$  of the left molecule (nucleophile) and  $C\beta'$  of the right molecule (electrophile). Accordingly, the mechanism is termed  $\gamma\beta$ -mechanism.

The reaction path following a six-membered transition state geometry is an Alder-ene reaction (Scheme 22, Figure 173). In case of the  $\gamma\gamma$ -mechanism, the proton from  $C\alpha'$  of the left molecule is migrating to the  $C\beta'$  position this time, making the  $C\gamma'$  of the right molecule again to the electrophilic center. Consequently, the proton in  $C\gamma'$  of the attacking molecule remains and the crosslinking occurs between the double bond of the left  $C\gamma'$  atom and the  $C\gamma'$  atom of the right molecule. The result of this mechanism is another position of the remaining double bond in the final product. The double bond is formed between  $C\alpha'$  and  $C\beta'$  of the attacking molecule. In the  $\gamma\beta$ -mechanism, the proton migration occurs from  $\alpha'$  to  $\gamma'$  and the crosslinking occurs therefore between  $\gamma'$  and  $\beta'$ .

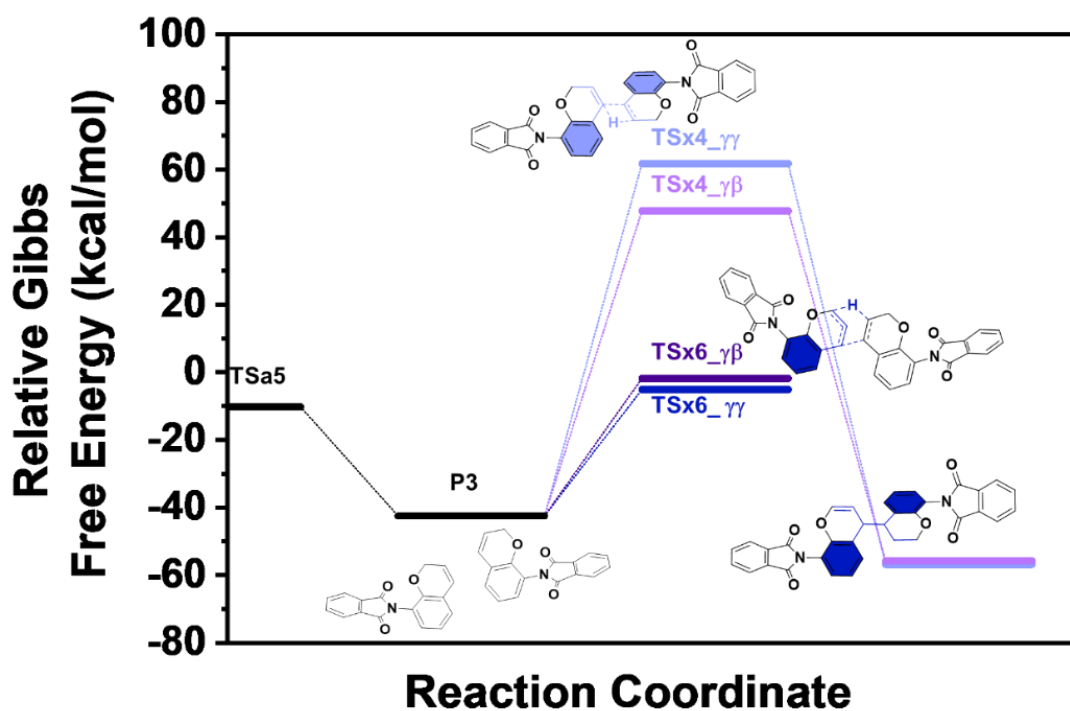
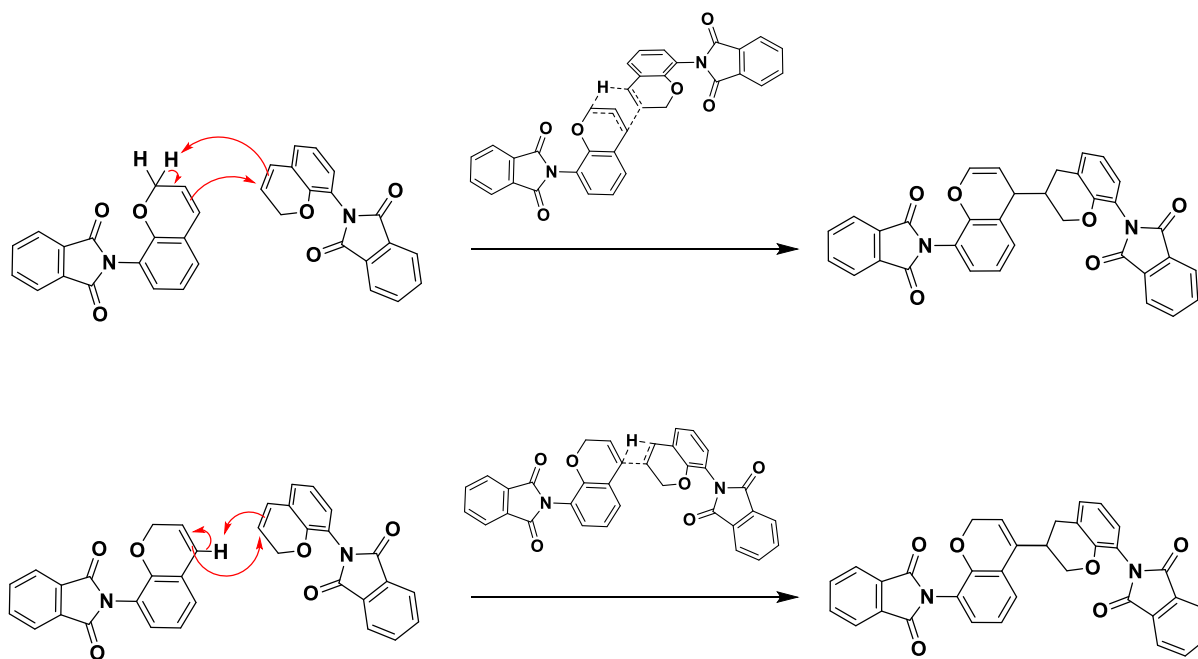


Figure 172. Reaction coordinate of the crosslinking reaction via four- (TSx4) and six-membered (TSx6) transition states. The reaction between  $C\gamma'$  ( $C7'$ ) and  $C\gamma'$  ( $C7'$ ) is highlighted in blue and corresponds to the  $\gamma\gamma$  mechanism and reactions between  $C\gamma'$  ( $C7'$ ) and  $C\beta'$  ( $C8'$ ) corresponding to the  $\gamma\beta$  mechanism is highlighted in purple.

The activation energy for the Alder-ene mechanism is significantly lower compared to the TSx4 pathway. This is due to the favored six-membered transition state geometry compared to the strained four-membered transition state geometry. The difference between the  $\gamma\gamma$ - and  $\gamma\beta$ -mechanism is very small. However, in the case of the TSx4 pathways, the  $\gamma\beta$ -mechanism

is favored, and 14 kcal mol<sup>-1</sup> lower compared to the  $\gamma\gamma$ -mechanism. The reaction mechanisms are shown in Scheme 22.



*Scheme 22. Reaction mechanism for the Alder-ene crosslinking reaction according to the  $\gamma\gamma$ - and  $\gamma\beta$ -mechanism.*

The geometries along the intrinsic reaction coordinate (IRC) are shown in Figure 173, including the transition state geometry TSx6\_ $\gamma\gamma$ . Following the geometries from two P3 models coming closer to each other and reacting to the corresponding crosslinked product Px6\_ $\gamma\gamma$  also shows the kinked geometry of the crosslinked product.

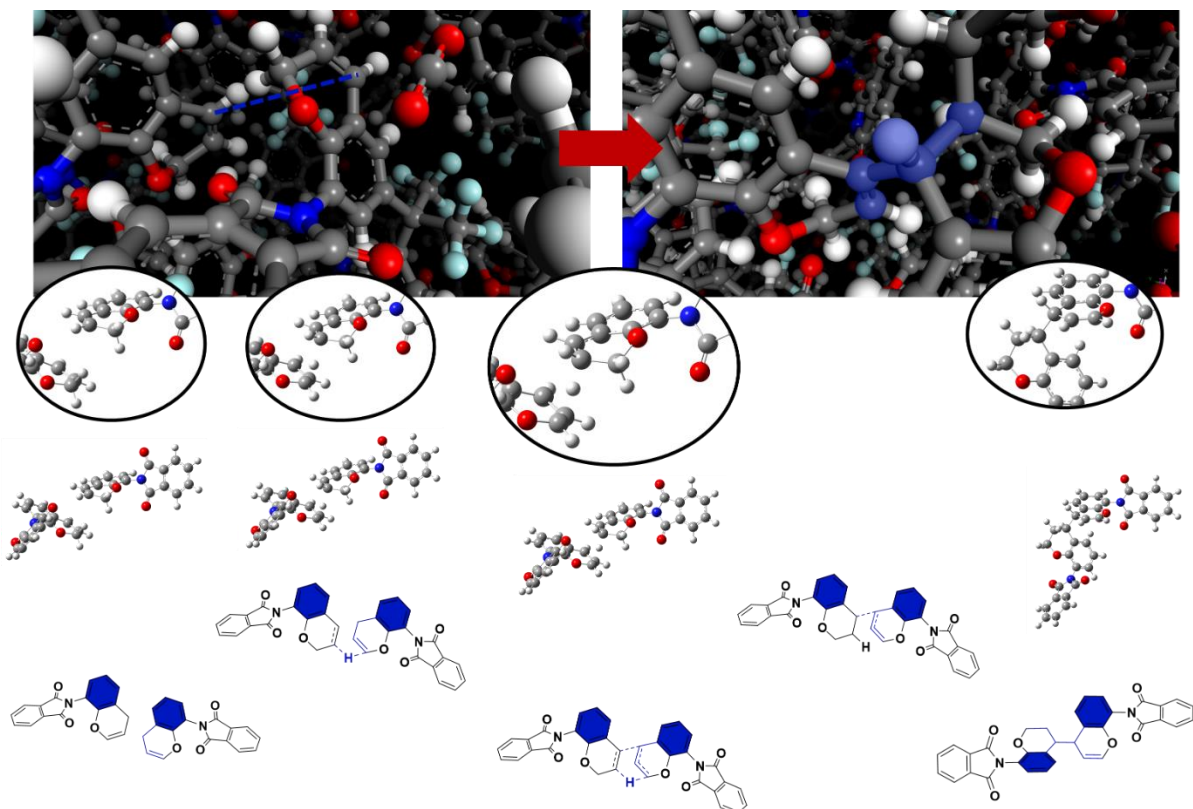


Figure 173. Alder-ene  $\gamma\gamma$ -crosslinking mechanism. Image capture before and after crosslinking in an amorphous cell (top), images of the structures along the IRC with the TSx6 in the middle (middle) and projection formula of the IRC corresponding structures as projection formula (bottom).

The crosslinking tendency was simulated for the derivatives as well (Figure 174). The TSx6 path is also significantly favored to the TSx4 pathway. Interestingly, the  $\gamma$ MPGPI-1 model shows the highest activation energy for the crosslinking reaction among the simulated materials. This is in accordance with the experimental findings. As anticipated, the methyl group in  $\gamma$ -position hinders both models to come close and get into a stabilized transition state geometry. Both methyl groups are oriented to the same side, for which reason both models have the largest distance of 3.411 Å to teach other compared to Propargyl with 2.814 Å. Furthermore, the TSx4 pathway is not possible for  $\gamma$ MPG, since no proton in  $C\gamma'$  for the proton migration is available. Moreover, the dihedral angle between all four vinyl carbon atoms  $C\beta'$ - $C\beta'$ - $C\gamma'$  is significantly larger with  $-18.356^\circ$  compared to  $-4.223^\circ$  of the PG model.

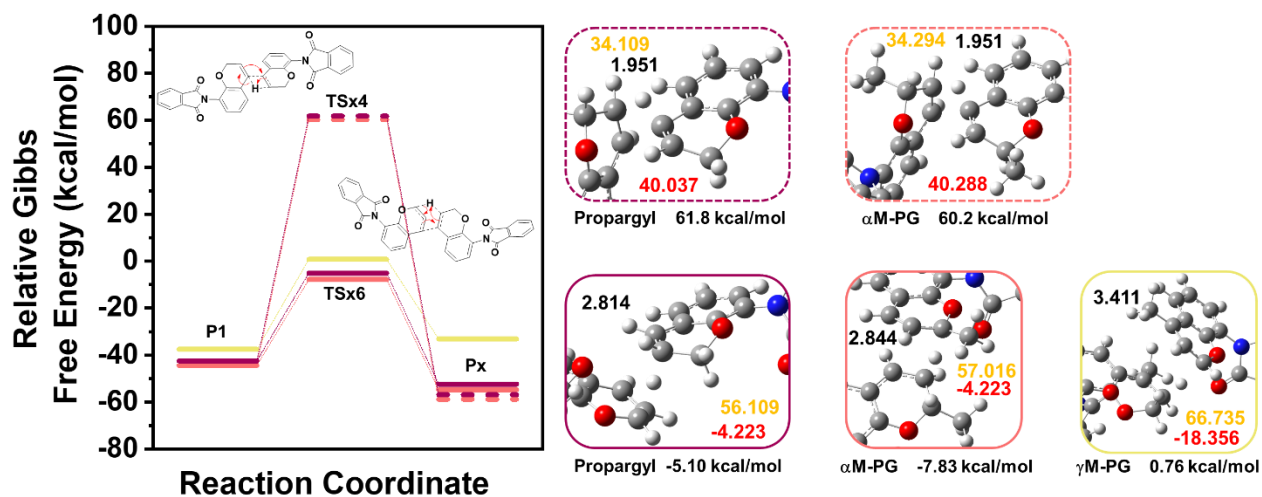


Figure 174. Reaction coordinate of the crosslinking pathways of each simulated propargyl derivative and images of the transition state geometry for each reaction and derivative.

The geometries along the IRC, including their projection formula visualization, are shown in Figure 175. The crosslinking reaction leads to rotation around  $90^\circ$  upwards due to the crosslinking between the  $\gamma'$  and  $\beta'$  carbon atom. This type of crosslinking therefore leads to a strong rearrangement effect of the polymer chains.

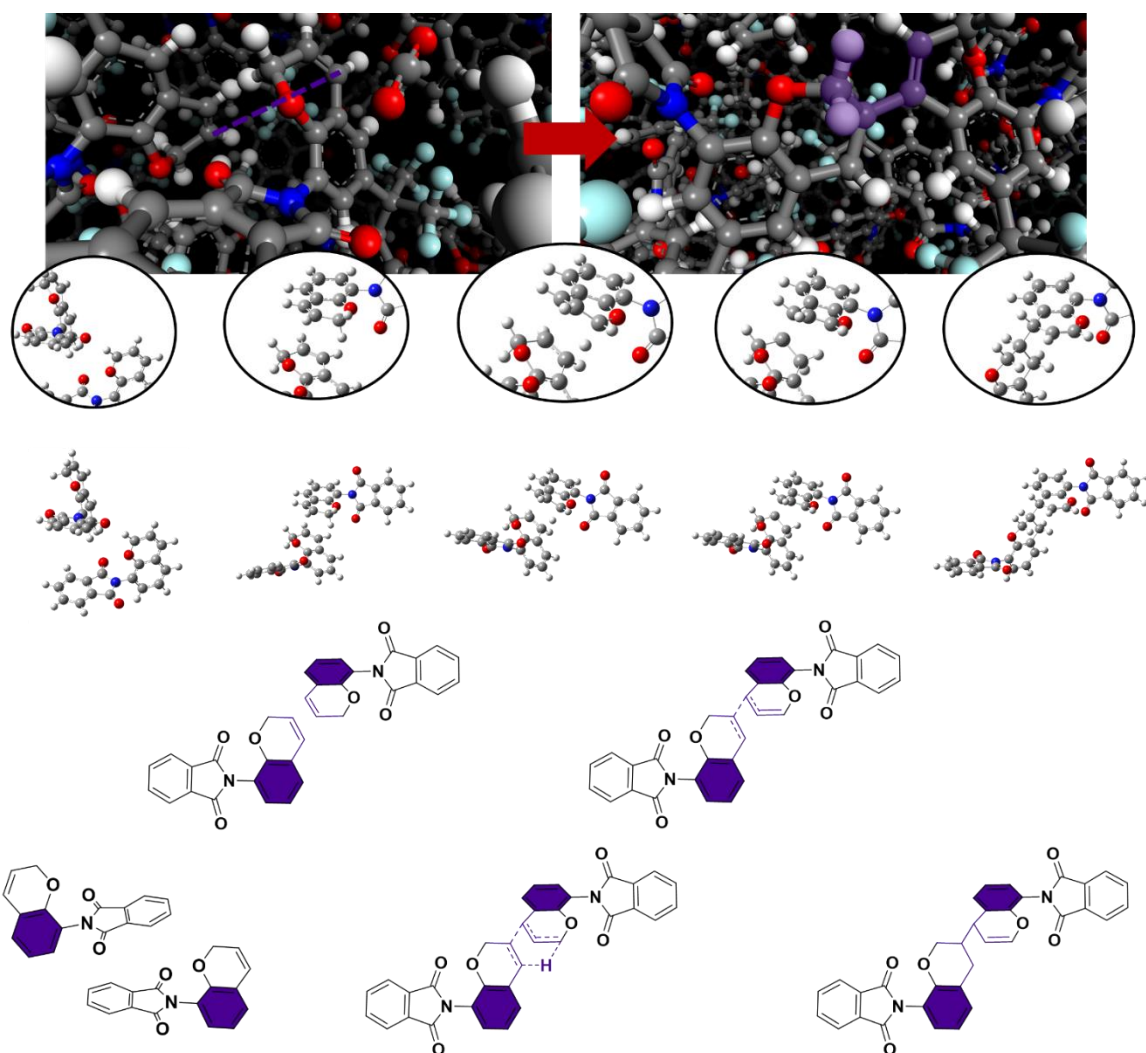


Figure 175. Alder-ene  $\gamma\beta$ -crosslinking mechanism. Image capture before and after crosslinking in an amorphous cell (top), images of the structures along the IRC with the TSx6 in the middle (middle) and projection formula of the IRC corresponding structures as projection formula (bottom).

The crosslinking reactions of the derivatives were simulated, and results are shown in Figure 176. The transition state geometry of the  $\gamma$ MPG model shows once more to have the highest single point energy among all simulated materials.  $\alpha$ MPG and Propargyl have about the same activation energies with a difference of only 1.53 kcal mol<sup>-1</sup>. Other than before, the  $\gamma\beta$ -mechanism proceeds in the case of the  $\gamma$ MPG model with both methyl groups pointing in opposite directions. Therefore, the distance between both models is significantly lower compared to the  $\gamma\gamma$ -mechanism. The distance between both models is 2.451 Å and therefore the difference to propargyl is only 0.235 Å, whereas the difference in the  $\gamma\gamma$ -mechanism was about the double.

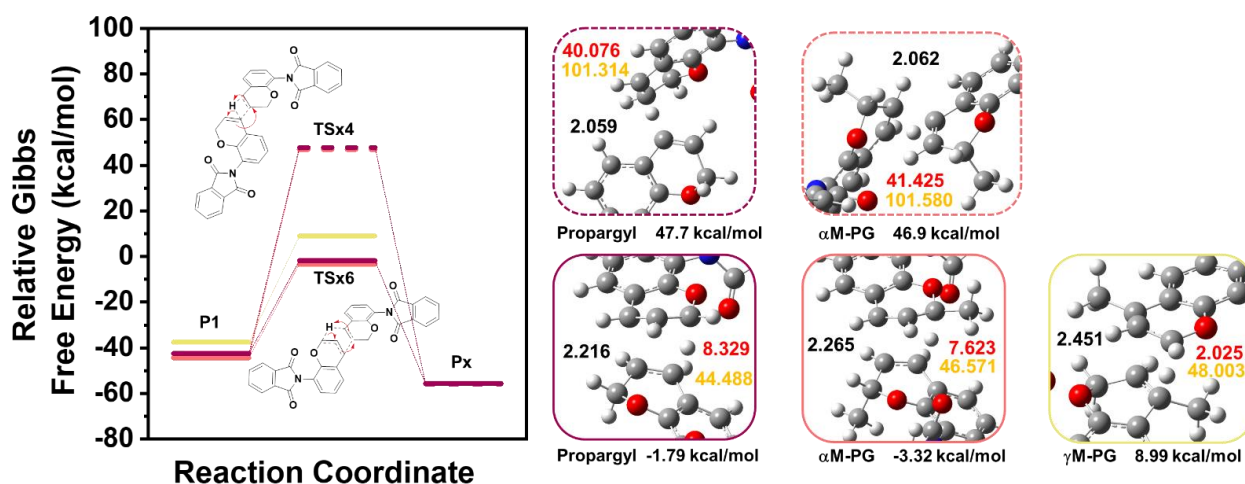
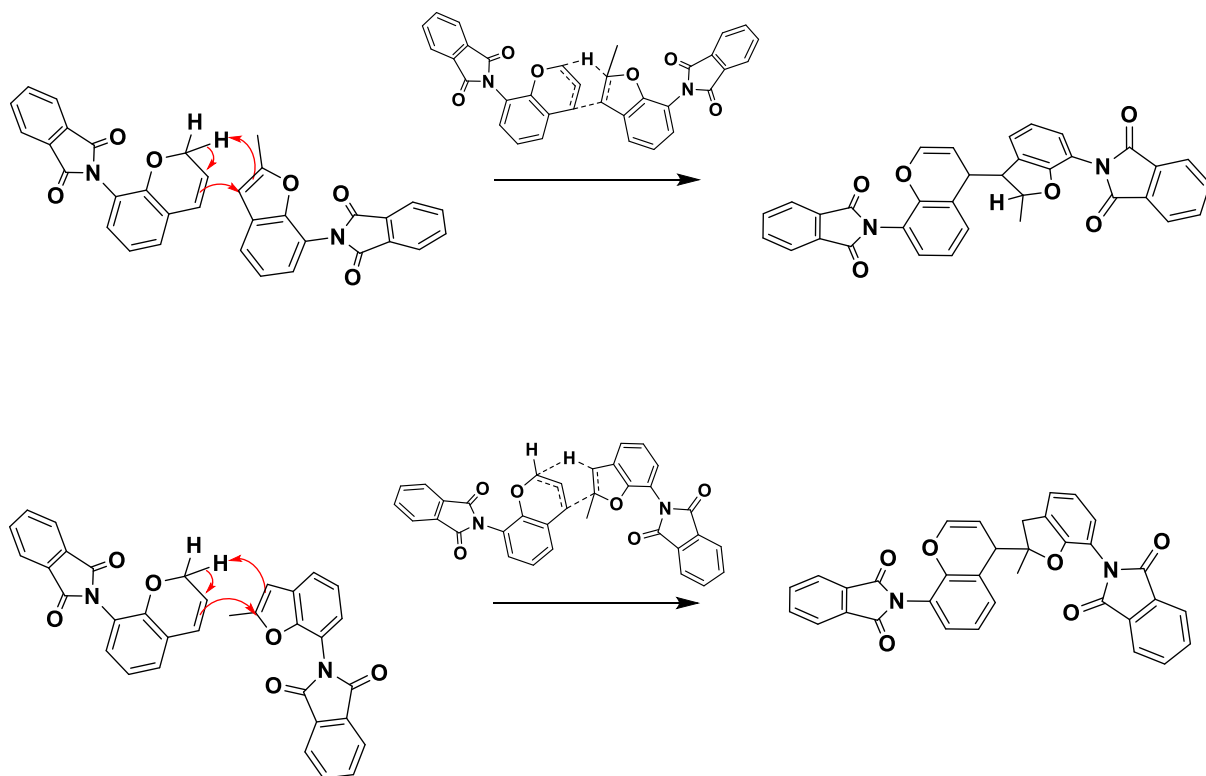


Figure 176. Reaction coordinate of the crosslinking pathways of each simulated propargyl derivative and images of the transition state geometry for each reaction and derivative.

## Furan-participating Crosslinking Reactions

In Scheme 21, the potential crosslinking reactions involved furan units (P2) as well. There are four possibilities to involve furan units. The simplest one is the crosslinking between a furan and a chromene group via six-membered transition state geometry, very similar to the chromene  $\gamma\gamma$ - and  $\gamma\beta$ -mechanism. In addition, two furan units can crosslink as well.

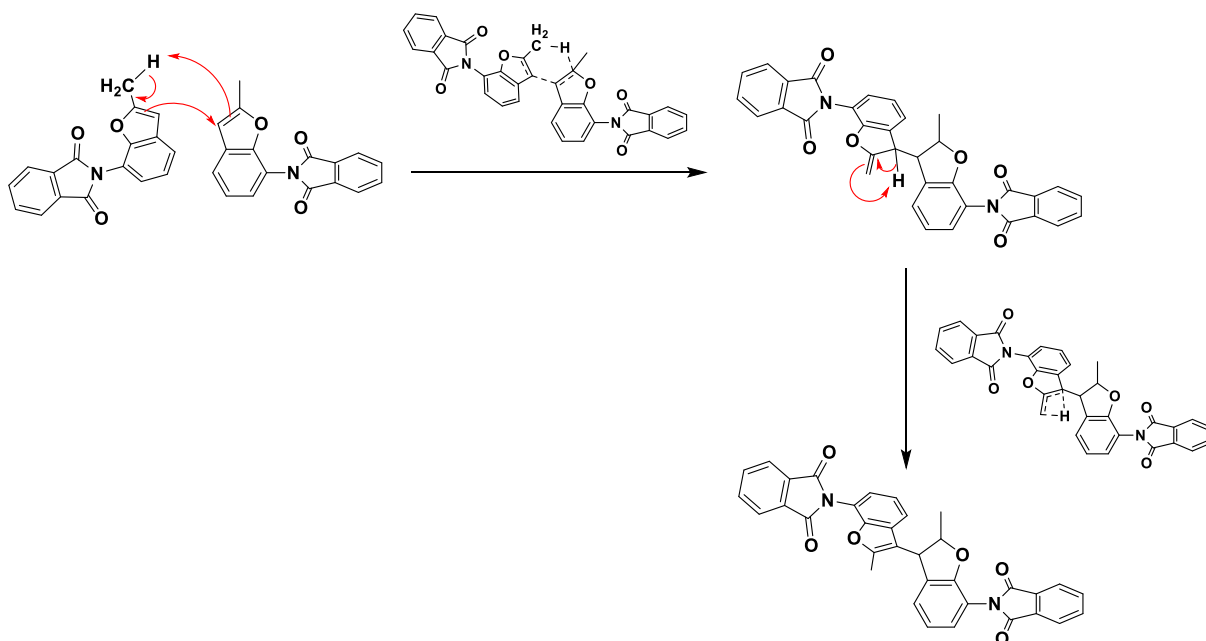
In Scheme 23 the reaction mechanism of the crosslinking between P2 and P3 is shown. Both mechanisms are very similar to the  $\gamma\gamma$ - and  $\gamma\beta$ -mechanism of two chromene units. The crosslinking between  $\gamma'$  carbon atoms proceed as well via two simultaneous steps. One proton of the methylene group of P3 migrates to the  $C\beta'$  atom of P2. The binding electron pair of the methylene group remains at P3 and forms a new  $\pi$ -bond between  $\alpha'$  and  $\beta'$ . The partially positive  $C\gamma'$  ( $C7'$ ) of P2 is then attacked in a second step via C-C bond formation from the P3  $\pi$ -bond. Via  $\gamma\beta$ -mechanism, the proton from  $\alpha'$  of P3 migrates herein to the  $C\gamma'$  atom of P2. The crosslink is then formed between  $\gamma'$  of P3 and  $\beta'$  of P2. The product of the  $\gamma\beta$ -mechanism is highly kinked due to the formed cardo structure.



Scheme 23. Crosslinking mechanism via six-membered transition state geometry between a chromene (P3) and a furan (P2) unit via  $\gamma\gamma$ - and  $\gamma\beta$ -mechanism.

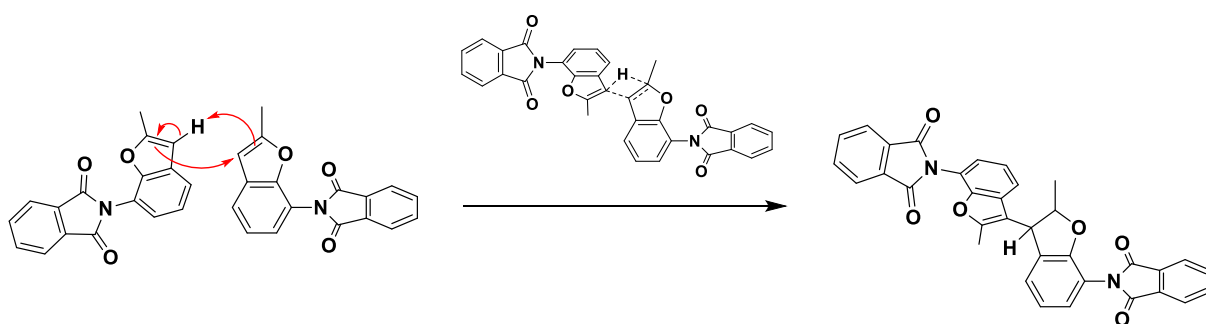
The crosslinking mechanism between two furan groups occurs also by proton migration from  $C\alpha'$  to  $C\beta'$  of the second furan model, while the final C-C bond formation proceeds via both  $C\gamma'$  atoms (Scheme 24). However, in that case the proton migration from  $C\alpha'$  does not originate from a methylene group, since furan groups do not contain a methylene group. In this mechanism, the proton comes from the methyl group, which is the  $C\alpha'$  atom. The mechanism involves an intermediate and two consecutive reaction steps. After proton migration and crosslinking in the first step, the intermediate Intx6c is formed. The intermediate contains a terminal double bond and isomerizes to form the higher substituted double bond.





Scheme 24. Crosslinking mechanism via six-membered transition state geometry (TSx6c) between two benzofuran groups (P2).

The crosslinking via four-membered transition state geometries is initiated by the proton transfer from C<sub>γ</sub>' of the left (attacking) molecule to the C<sub>β</sub>' atom of the right (attacked) molecule in case of the  $\gamma\gamma$ -mechanism (Scheme 25). The TS is TSx4c <sub>$\gamma\gamma$</sub> . Due to the proton transfer, the C<sub>γ</sub>' atom becomes partially positive and an electrophilic attacking point. The binding electron pair from the proton migration remains at C<sub>γ</sub>' of the left molecule, making it the nucleophilic center. The crosslinking reaction occurs then between the double bond of the attacking molecule and the partially positive electrophilic C<sub>γ</sub>' atom of the right (attacked) molecule.



Scheme 25. Crosslinking mechanism via four-membered transition state geometry (TSx4c) between two benzofuran groups (P2).

Figure 177 shows the results of the transition state geometry optimization and single point energy calculation for each transition state, product, and geometry of all Alder-ene crosslinking reactions between P2 or P3 models. The relative Gibbs free energies are referenced



to both starting materials P3+P3, P2+P3 or P2+P2, respectively, and not to the starting material E. Therefore, the absolute activation barrier was calculated, and influences of the higher stabilization energy of P2 models were compensated. The lowest Gibbs free energies were calculated for the crosslinking via an Alder-ene mechanism of two chromene groups. Slightly higher energies were obtained for the reaction between a chromene (P3) and a furan (P2) unit according to the Alder-ene reaction mechanism. However, the reaction between two furan units requires significantly larger energies. The calculated single-point energy for two P2 molecules to crosslink via a six-membered transition state geometry is 60 kcal mol<sup>-1</sup> higher compared to the lowest single point energy of all crosslinking mechanism (TSx6\_γγ). The second step of the furan crosslinking is, with 82 kcal mol<sup>-1</sup>, still significantly higher compared to 37.4 kcal mol<sup>-1</sup> of TSx6\_γγ (crosslinking of two P3 models). It is noteworthy, that in case of two furan models to crosslink, the process via a four-membered transition state is favored and about 9 kcal mol<sup>-1</sup> lower compared to the six-membered mechanism. The explanation is the proton migration from the methyl group in TSx6c. The CH acidity of a methyl group is significantly lower and the C-H bond of a sp<sup>3</sup> hybridized group more stabilized compared to the proton of a sp<sup>2</sup> hybridized π-bond. Therefore, significantly more energy is required to remove a proton from the methyl group to initiate the crosslinking reaction.

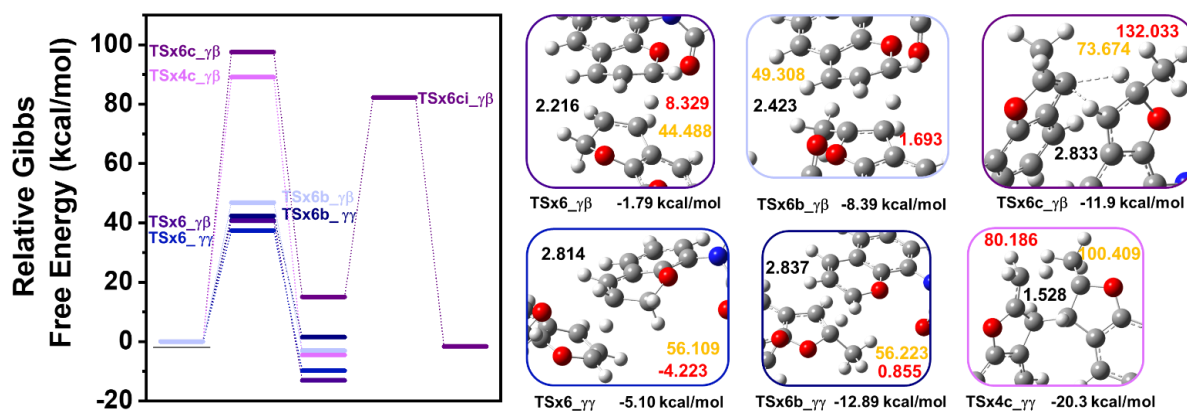
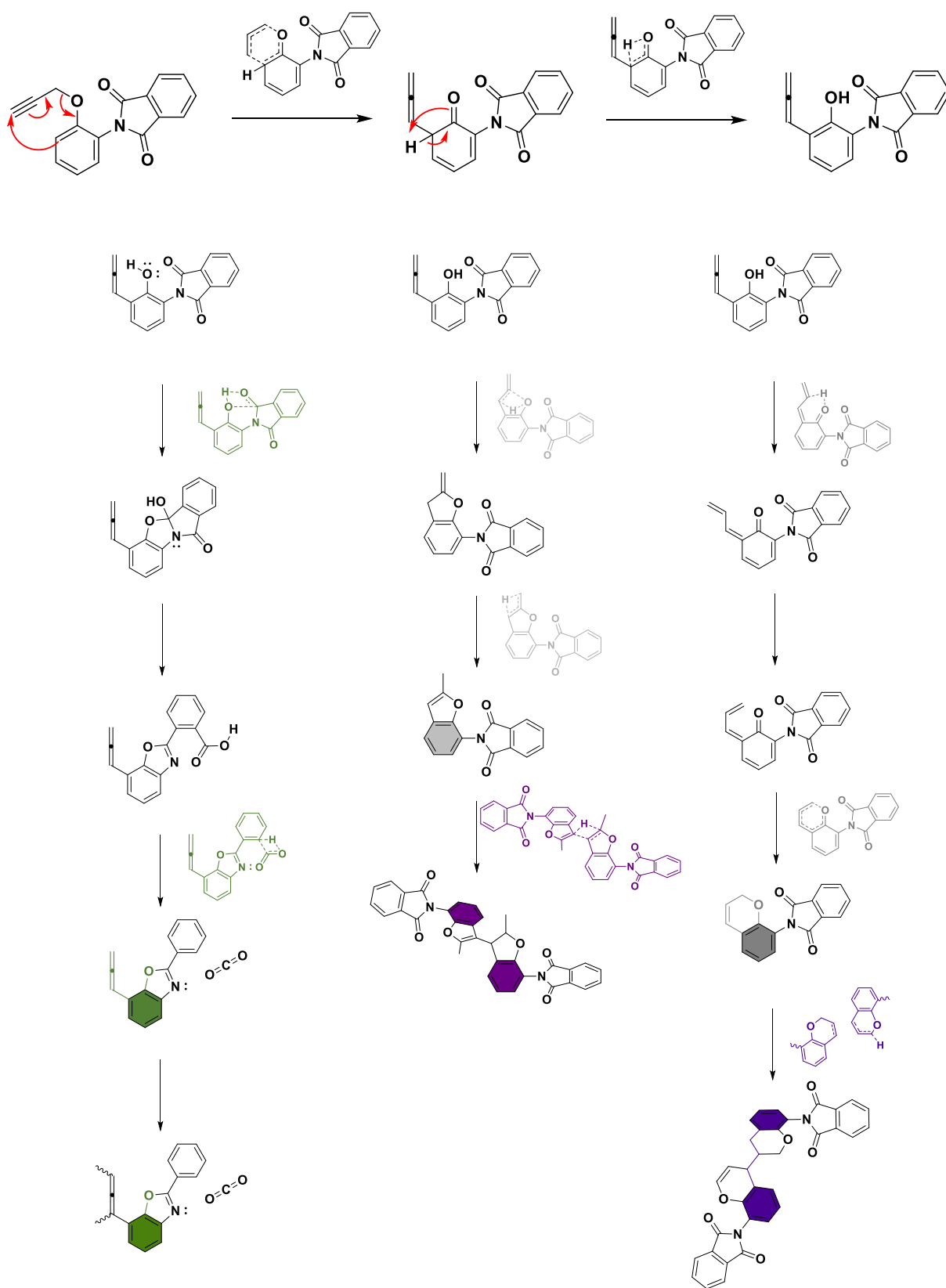


Figure 177. Reaction coordinate of all Alder-ene crosslinking mechanism between chromene and furan units. Additionally, the four-membered TS pathway of two furan units is demonstrated.

The reactions of phenyl-propargyl ether phthalimide units, which have been simulated and discussed so far, are summarized in Scheme 26.



Scheme 26. Overview of potential reactions of phenyl propargyl ether phthalimide units.

## Ring opening

The experimental results have shown, that at higher temperatures above 300 °C, the phenolic hydroxy group recovers, and that above 350 °C CO<sub>2</sub>, as the result of the TR reaction, is released. This means, that the formed chromene and furan rings have to re-open in order to recover the hydroxy group and undergo the PBO formation. In non-crosslinked structures this is the back reaction of the cyclization reaction, which is expected to occur less likely, as the products are thermodynamically favored and the activation barrier for the back reaction is high. Therefore, the ring-opening reaction of crosslinked models was performed. The possible reaction mechanism of both types of crosslinks ( $\gamma\gamma$  and  $\gamma\beta$ ) as well as both rings (chromene and chromane type). The overview also shows the simulated transition state of the ring opening and products (Figure 178).

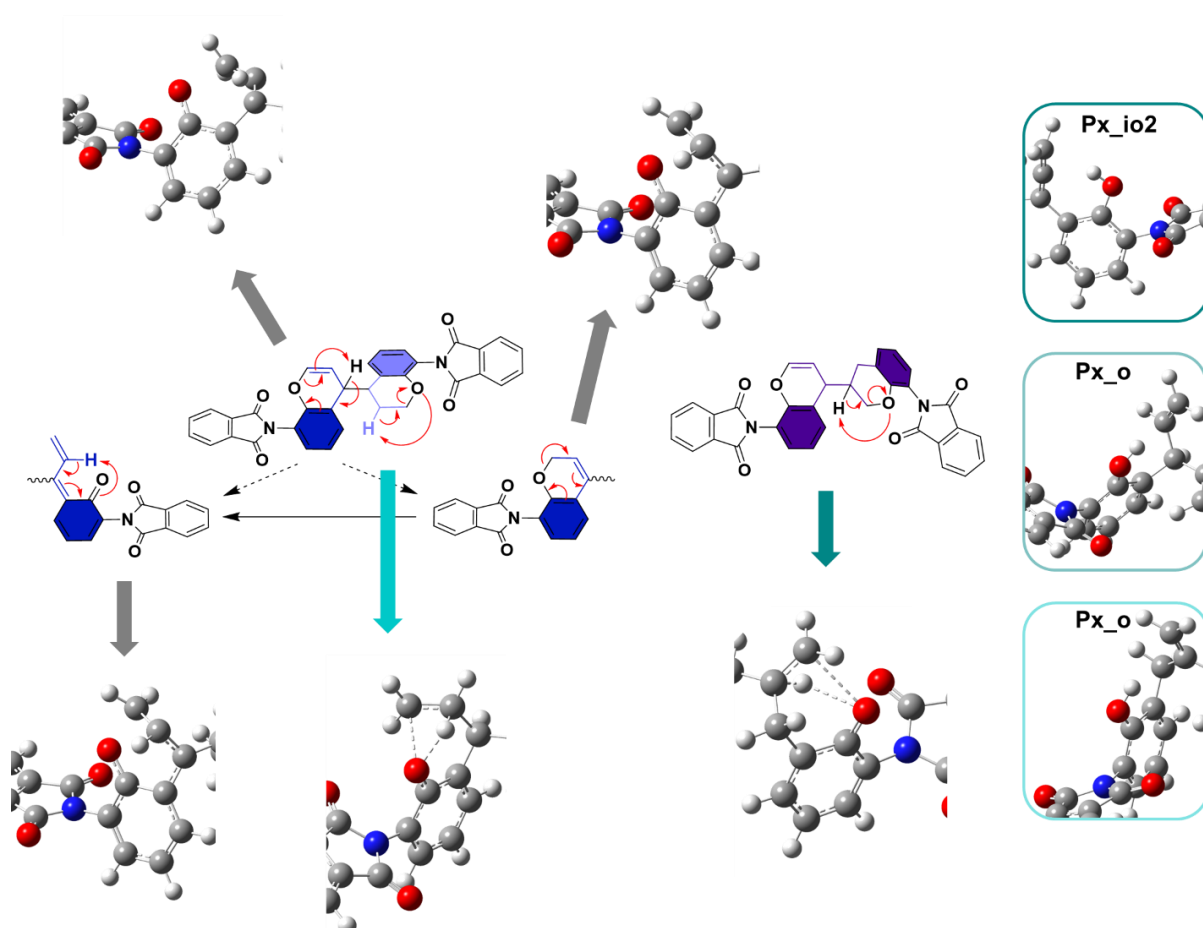


Figure 178. The possible reaction mechanism of both types of crosslinks ( $\gamma\gamma$  and  $\gamma\beta$ ) as well as both rings (chromene and chromane type). The overview also shows the simulated transition state of the ring opening and products.

According to Figure 178, the  $\gamma\gamma$ -crosslinked model contains two different types of ring structures, a chromene ring with a  $\pi$ -bond between C $\alpha'$  and C $\beta'$ , and a chromane ring, which

does not contain any  $\pi$ -bond. The chromene rings have two possibilities to re-open. One process is initiated by means of a proton migration from  $C\gamma'$  to  $C\alpha'$  with formation of a cyclohexadienone intermediate and the second process is initiated by the isomerization of the  $\pi$ -bond to  $C\beta'$ - $C\gamma'$  position followed by the back reaction of the chromene cyclization via a cyclohexadienone intermediate as well (grey pathway).

The chromane ring opens via protonation of the oxygen atom via four-membered transition state from the methylene group  $C\beta'$  (green pathway). The simulated single-point energies, leading to an intrinsic reaction coordinate for the described mechanism is shown in Figure 179 and Figure 180.

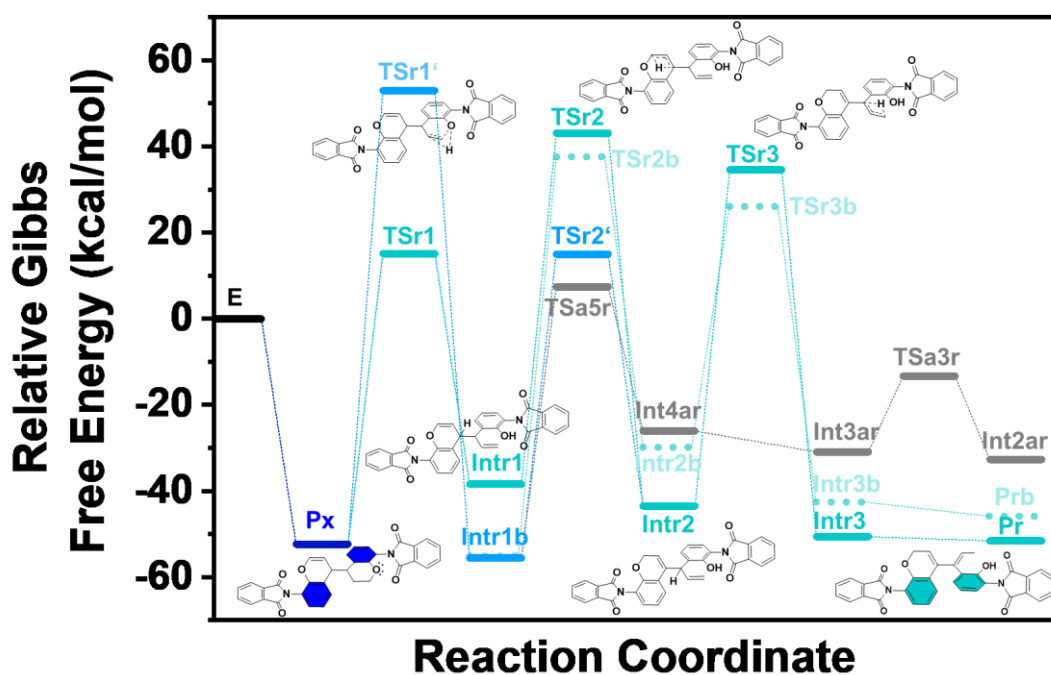


Figure 179. Reaction coordinate of each ring-opening reaction of  $\gamma$ -crosslinked chromene models Px.

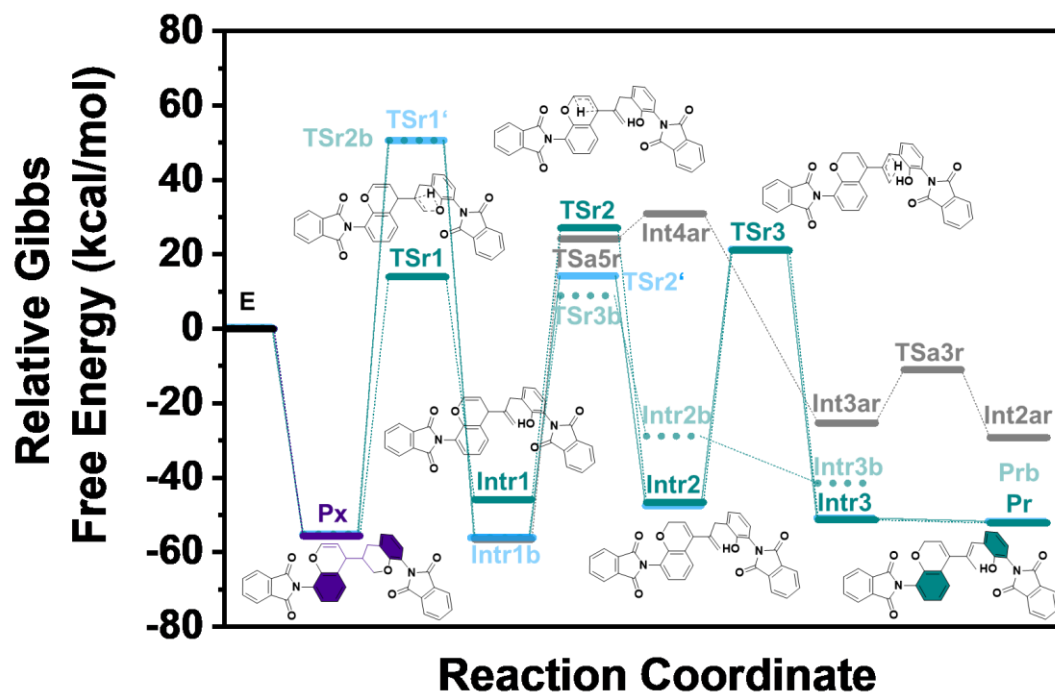


Figure 180. Reaction coordinate of each ring-opening reaction of  $\gamma\beta$ -crosslinked chromene models *Px*.

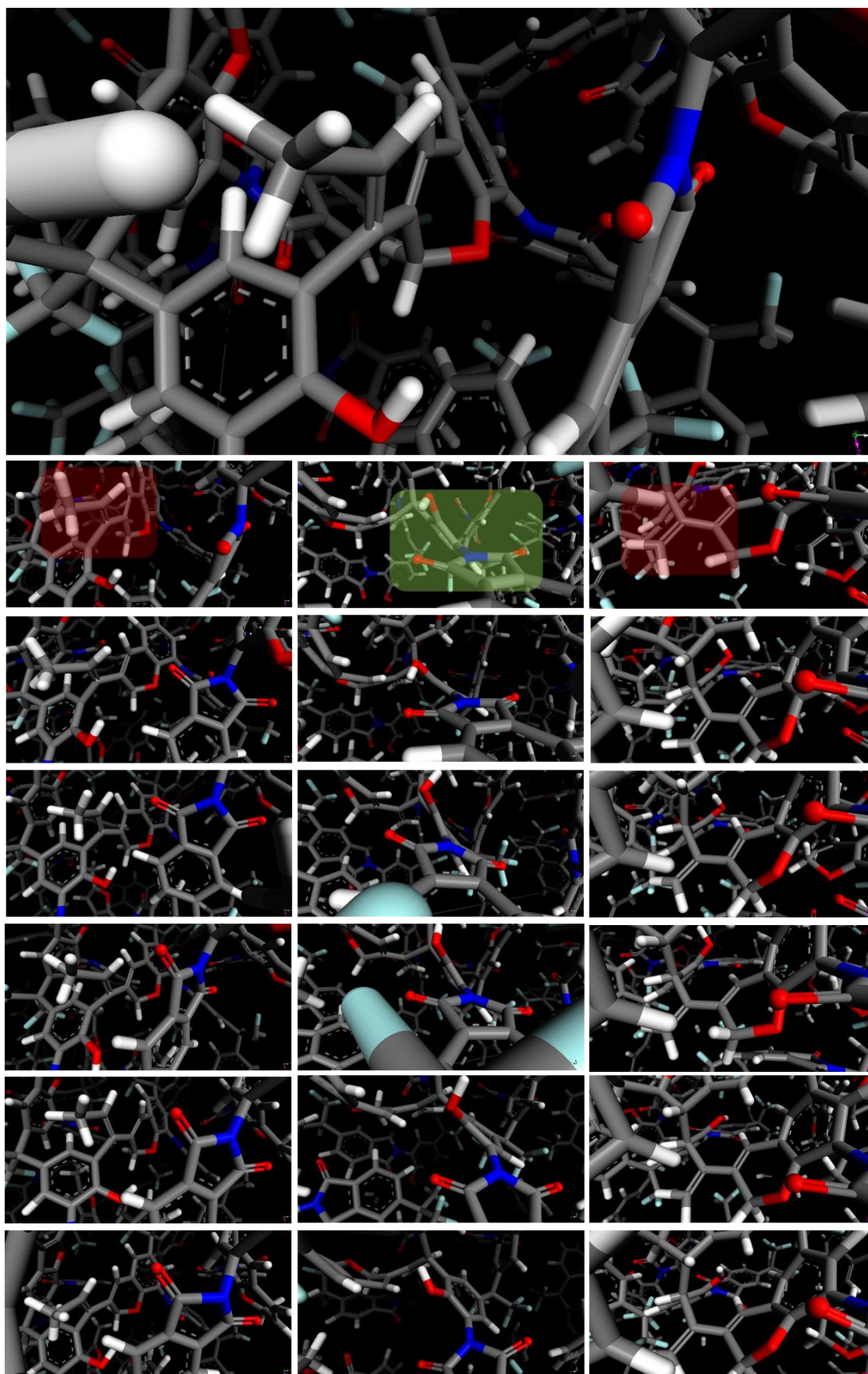


Figure 181. (top) Ring-opened crosslinked chromene units. (bottom, left row): Fluctuations of the ring opened double bond by time during; (bottom, middle row): TR relevant imide unit fluctuations and (bottom, right row): Fluctuations of a diene unit of two crosslinked an d ring-opened chromene units, by a MD simulation with a time of 500 ps during a NVT run.



After successful ring opening of the chromane ring, various consecutive reactions and functional groups are accessible as shown in Figure 182, Scheme 27 and Scheme 28. The ring opening of the chromane ring directly leads to an *ortho*-allyl phenol structure with a crosslink in  $C\gamma'$ . As known from experimental and simulation results of Allyl-PI, an *ortho*-allyl phenol group is capable to undergo a reaction cascade including further crosslinking of the terminal double bond, cyclization to the tetrahydrofuran structure, double bond isomerization and Thermal Rearrangement. However, if two isomerizations of each allyl double bond and the chromene double bond occur, then a conjugated diene system, in resonance with both aromatics, is possible. *Cis*-*trans* isomerization forms a *cis*-diene which could undergo a [4+2] Diels-Alder cycloaddition with another chromene group (red pathway) (see Figure 182). Alternatively, the recovered phenol group can undergo a Thermal Rearrangement to the corresponding PBO structure instead (green pathway). Since the Diels-Alder and Thermal Rearrangement reaction involve different functional groups of the formed diene, both reactions could occur simultaneously or consecutively. Since the Diels Alder reaction requires a third chromene unit and the mobility is highly restricted, due to the crosslinking, it is anticipated that the TR process is preferred as it occurs intramolecularly, despite the rotation restriction around the imide bond due to the crosslinking as well. In total up to five consecutive reactions can occur after the ring-opening (see Scheme 27, Scheme 28).

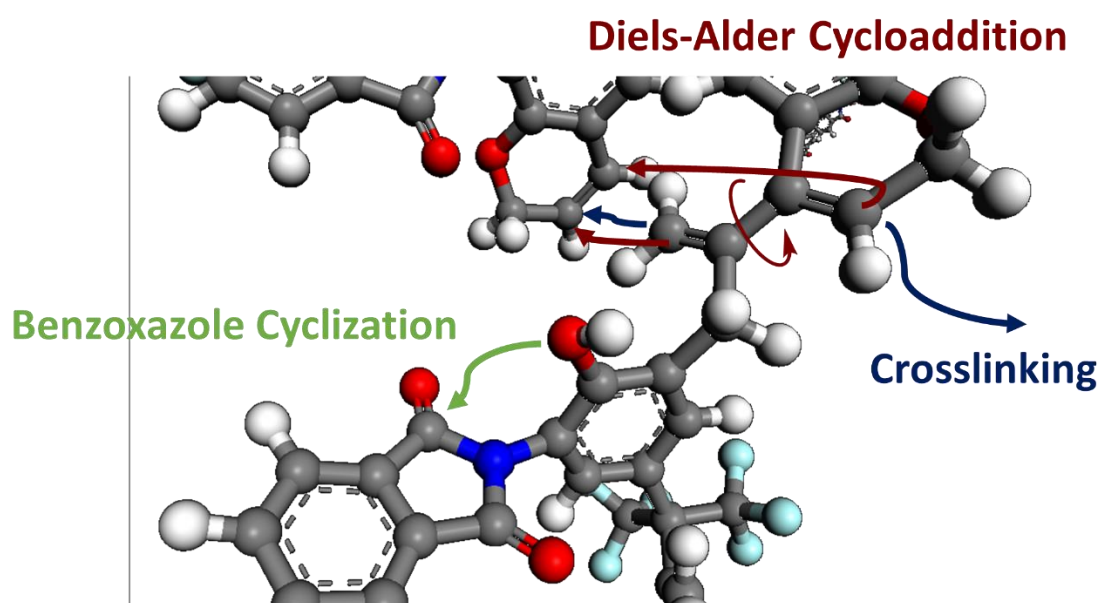
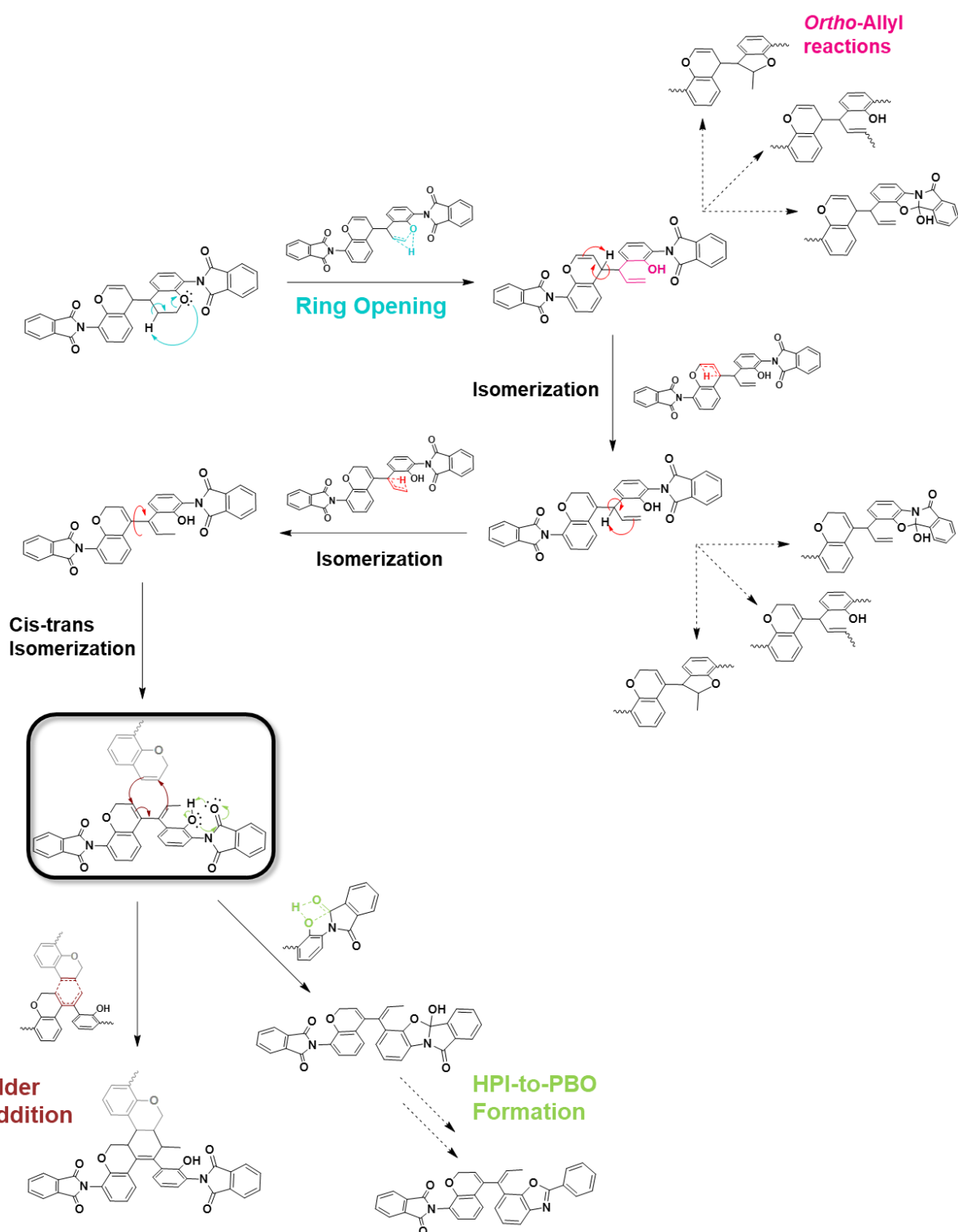


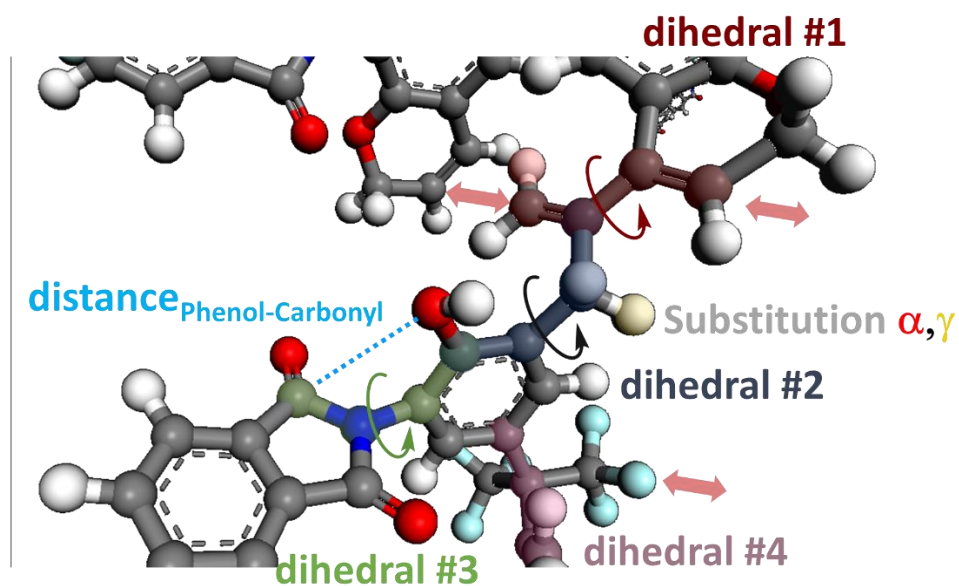
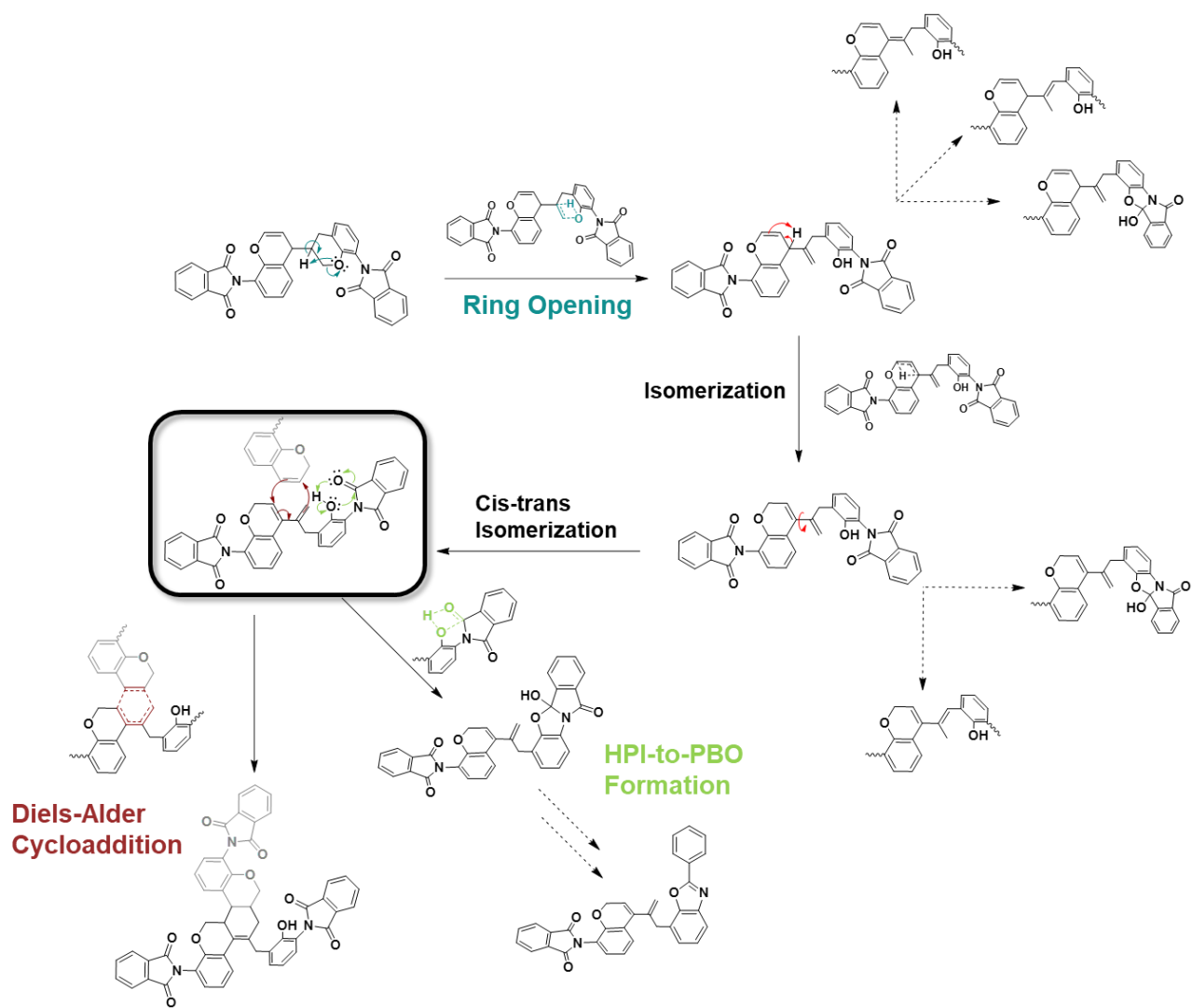
Figure 182. Overview of potential consecutive reactions after ring-opening of the chromane ring in  $\gamma\beta$ -crosslinked propargyl models.



Scheme 27. Overview of potential consecutive reactions after ring-opening of the chromane ring in  $\gamma$ -crosslinked propargyl models.

In the case of the  $\gamma\beta$ -crosslinked model, the cascade reaction to the Diels-Alder or TR product requires one double bond isomerization less, since the formed allyl group is crosslinked in C $\beta$ ' position. Therefore, the allyl double bond is already next to the chromene ring. Upon isomerization of the double bond in the chromene ring, the diene is formed.





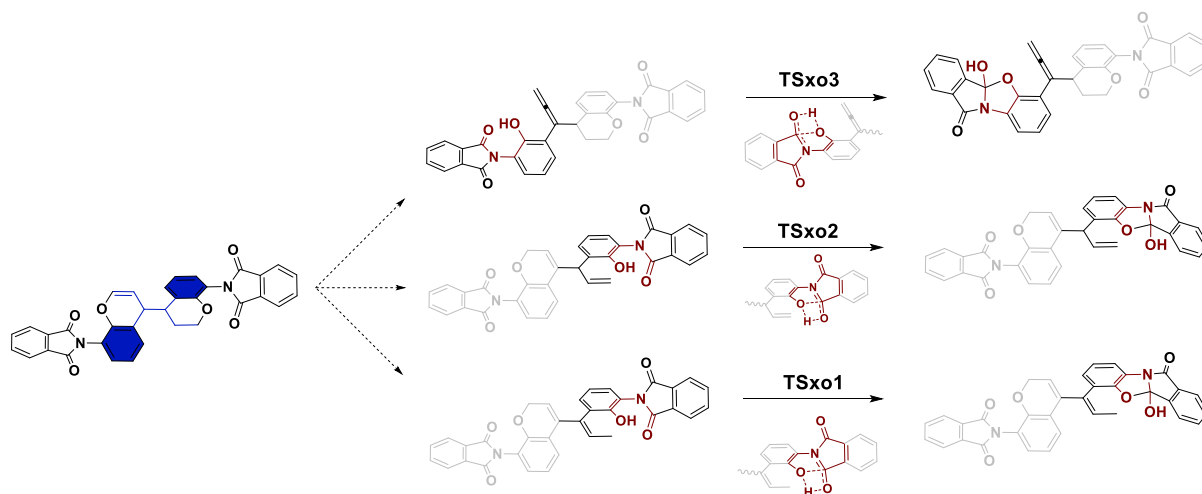
Scheme 28. Overview of potential consecutive reactions after ring-opening of the chromane ring in  $\beta\gamma$ -crosslinked propargyl models.

## Thermal Rearrangement

Thermal Rearrangement was simulated in discussed for a non-crosslinked model, starting from the *ortho*-allene phenol P1. Since the allene group is highly reactive, the consecutive cyclization to the chromene or furan structure is more likely. Moreover, the activation energy for the chromene cyclization is 12 kcal mol<sup>-1</sup> lower than the TR process. However, once the chromane rings are open, the phenol group is able to undergo the TR reaction, since the formed *ortho*-allyl group is less reactive. The ring-opened structure can even be isolated as shown in the FT-IR spectroscopy measurements of the annealed samples at 300 °C.

Nevertheless, the TR reaction depends strongly on the flexibility of the backbone, as results of Allyl-PI have shown. Further restrictions along the allyl or polymer chain have strong effects on the mobility and feasibility of the TR process as well.

In Scheme 29 the products of the ring-opening and their consecutive Thermal Rearrangement reaction are shown.



Scheme 29. Products of the ring-opening and their subsequent first step of the Thermal Rearrangement reaction.

The first step of the Thermal Rearrangement is a protonation of the imide carbonyl group, which leads to an increase of the electron deficiency of the carbonyl carbon atom in the way as it is done via acid-catalyzed esterification. The second reaction is then the nucleophilic attack of the phenolic oxygen atom at the carbonyl carbon atom. The result is a bicyclic intermediate Intxo. Nevertheless, the initial reaction of the TR process proceeds via a concerted mechanism, even though protonation and nucleophilic attack do not occur simultaneously. The rotation along the imide bond is hindered in the case of the crosslinked models, since they have to

rotate the whole attached unit as well, which is even more difficult in a polymer as cooperative motions of each segment, including the crosslinked polymer chains, needs to proceed. Therefore, the type of ring-opening also affects the feasibility of the TR reaction as well. In Figure 183 the transition state geometry TSxo1 and the TR affecting geometrical parameters are highlighted. As discussed for the unmodified and allylated polyimides, the dihedral angle and rotation along the imide bond is crucial for the TR process.

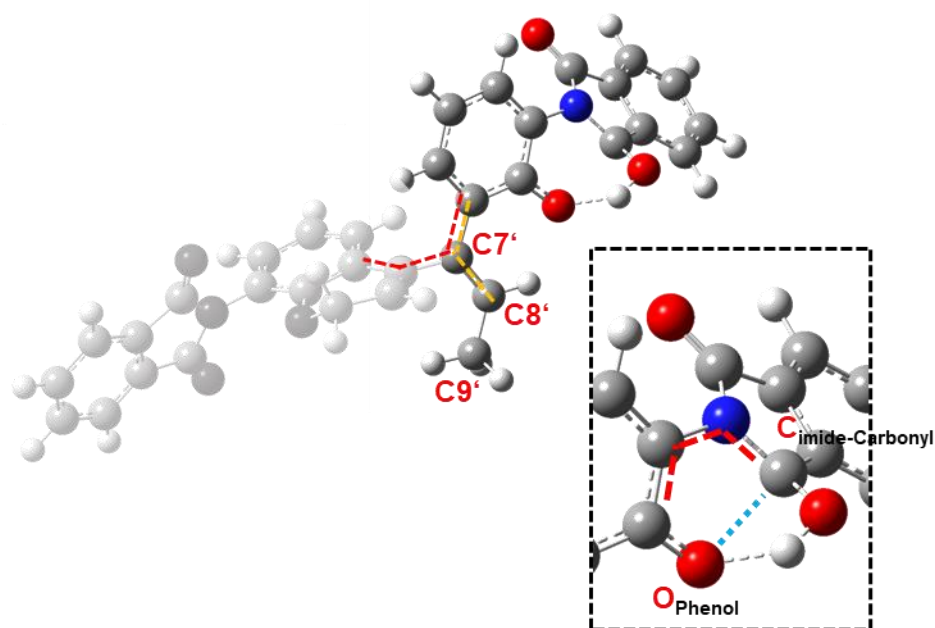


Figure 183. Transition state TSxo1. Dihedral angles (red), angle (yellow) and distance (blue) which affect the initial reaction of the Thermal Rearrangement are highlighted as dashed lines.

Three TR scenarios are possible. The results are shown in Scheme 29. The highest single point energy for the first TR step was determined for TSxo3. TSxo3 is the transition state structure based on the ring opening of the chromene ring. The formed *ortho*-allene group is highly reactive and very rigid. The energy of TSxo2 is 8 kcal mol<sup>-1</sup> lower compared to TSxo3 and corresponds to the *ortho*-allyl phenol product of the ring-opening. The lowest energy was determined for TSxo1 with 37 kcal mol<sup>-1</sup> (see Figure 184).

The results reveal the very strong influence of the precursor structure, again. From an electronic point of view, the vinyl group in conjugation with phenol is an electron donating group due to its +M effect, while the allyl group in TSxo2 is only weak electron donating due to its +I effect. The allene group on the other hand is -I [198] and from a steric point of view the most rigid group as it does not rotate or bend. As a consequence, steric and electronic effects

hinder the Thermal Rearrangement reaction, while electronic effect favor TSxo1. The comparison to the  $\gamma\beta$ -crosslinked models show, that the activation energies for each precursor are slightly higher compared to the  $\gamma\gamma$ -crosslinked and ring-opened units. In addition, the formed intermediate Intco1 is significantly more stabilized and shows a relative Gibbs free energy of 1.68 kcal mol<sup>-1</sup> with respect to the crosslinked model Px. In order to compare the activation energies of the TR reaction in ring-opened systems *versus* non-crosslinked systems of two models, which are close to each other, the TSxo1 energy is 11 kcal mol<sup>-1</sup> lower.

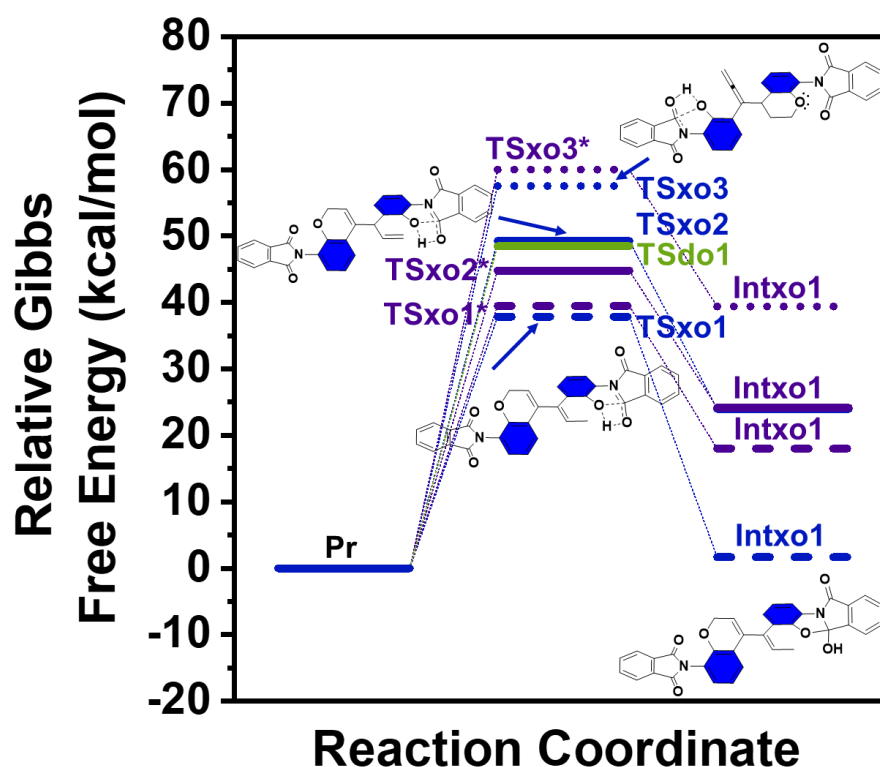


Figure 184. Reaction coordinate of the first step of the Thermal Rearrangement for each crosslinked ring-opened structure based on  $\gamma\gamma$ -crosslinked (blue) and  $\gamma\beta$ -crosslinked (purple) models.

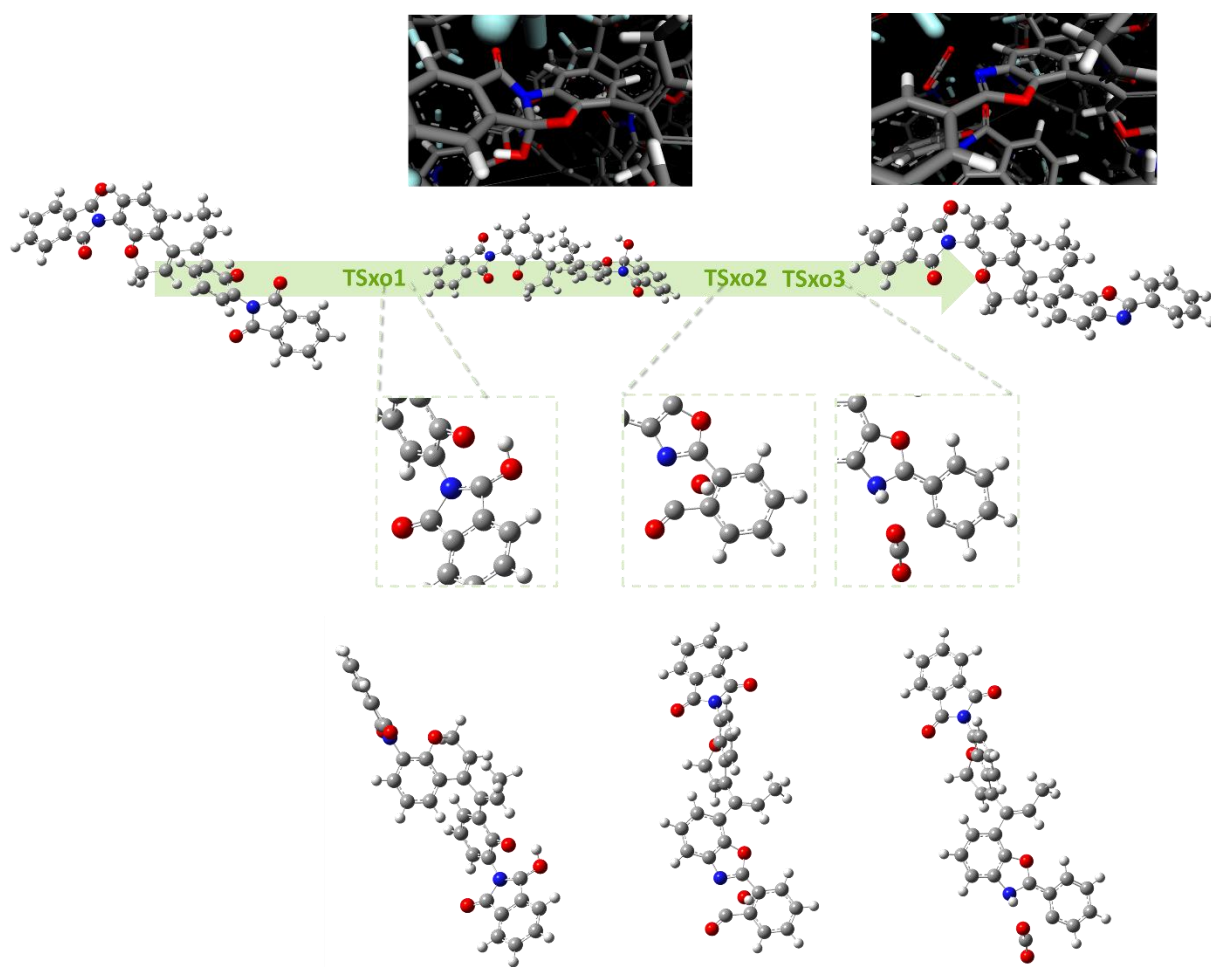
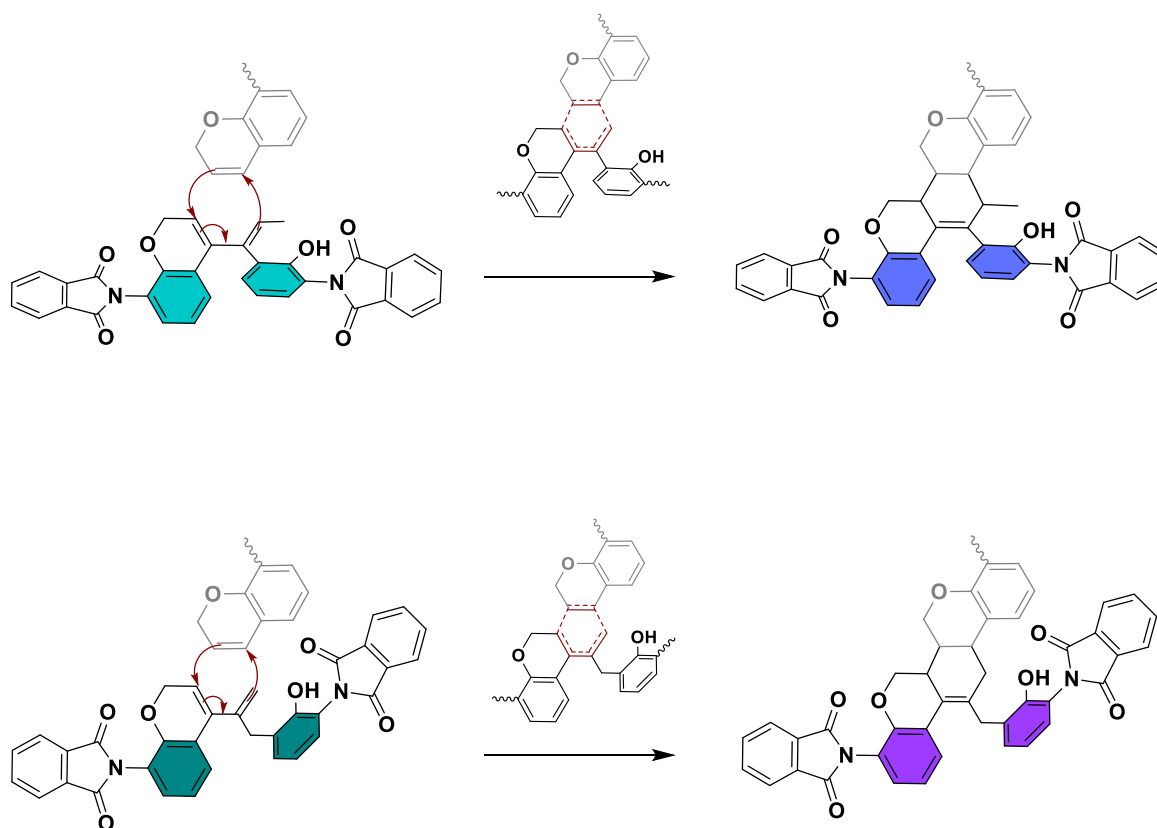


Figure 185. Overview of the Thermal Rearrangement reaction including all three transition states of all three steps of the TR reaction.

## Diels-Alder Cycloaddition

Both schemes, Scheme 27 and Scheme 28, have introduced the possibility of a [4+2] cycloaddition of the crosslinked models, after ring-opening and isomerization in order to form a *cis*-diene which can contribute as a diene in the Diels-Alder reaction, while a third chromene model reacts as dienophile. The consequence is a highly rigid and crosslinked network. The reaction mechanism for a  $\gamma\gamma$ - and  $\gamma\beta$ -crosslinked and ring-opened model as shown in Scheme 30.



Scheme 30. Reaction mechanism of the Diels Alder cycloaddition of the lowest ring-opened crosslinked structure based on the  $\gamma\gamma$ - (top) and  $\gamma\beta$ -crosslink (bottom) with a third chromene model.

Apart from the used diene, the chromene can have two different geometries, when entering the transition state. The chromene can react with the  $C_{\gamma'}$  atom at the vinyl group or chromene double bond. Therefore, four different reaction paths were simulated. Among all simulated pathways, the cycloaddition between the  $\gamma$ -model and the reaction via  $C_{\gamma'}$  of the chromene group from the dienophile with the vinyl group demonstrates the lowest activation energy. All other pathways show a very similar activation energy with a difference of maximum 2 kcal

mol<sup>-1</sup>. TSxc1 shows the lowest activation energy with 28 kcal mol<sup>-1</sup> with respect to the crosslinked model Pc, as reference system (Figure 186).

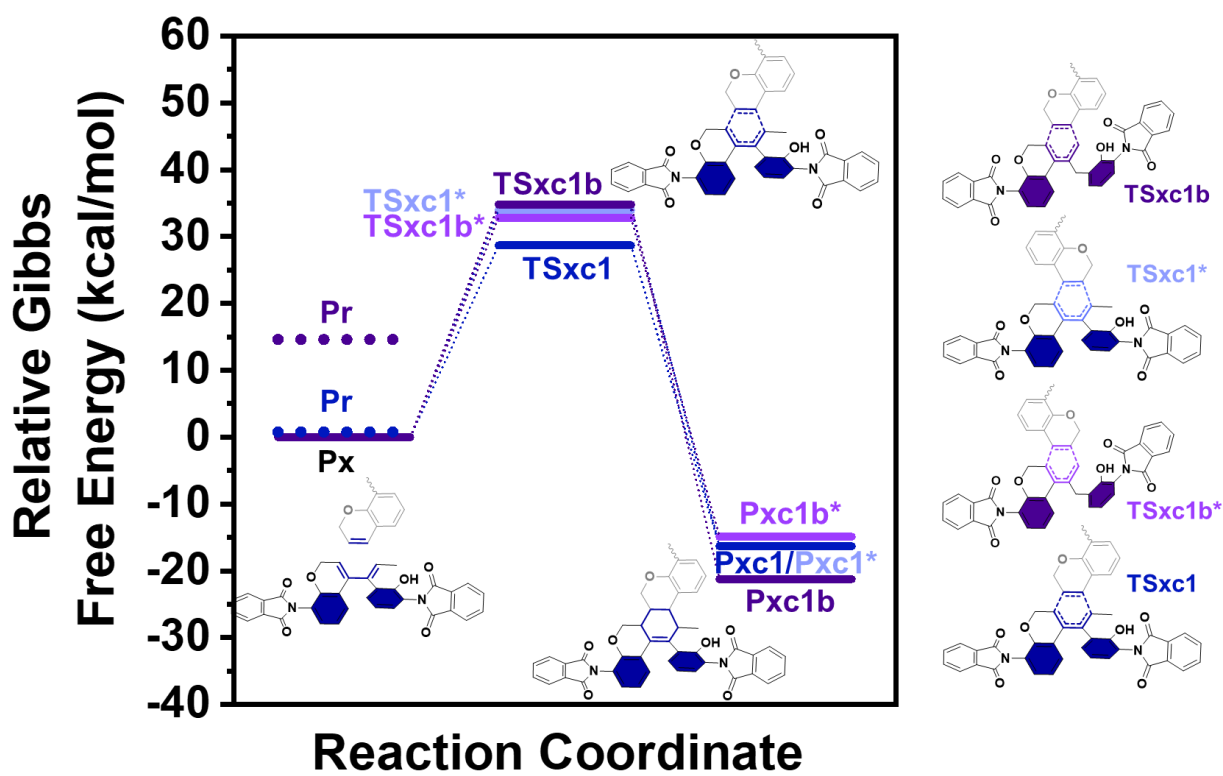


Figure 186. Reaction coordinate of the Diels-Alder cycloaddition for each crosslinked ring-opened structure based on  $\gamma\gamma$ -crosslinked (blue) and  $\gamma\beta$ -crosslinked (purple) models.

The geometries of the Diels-Alder cycloaddition reaction coordinate for TSxc1 and TSxc1b are shown in Figure 187. In addition, the image from a diene and chromene and the corresponding Diels-Alder product is shown Figure 187.

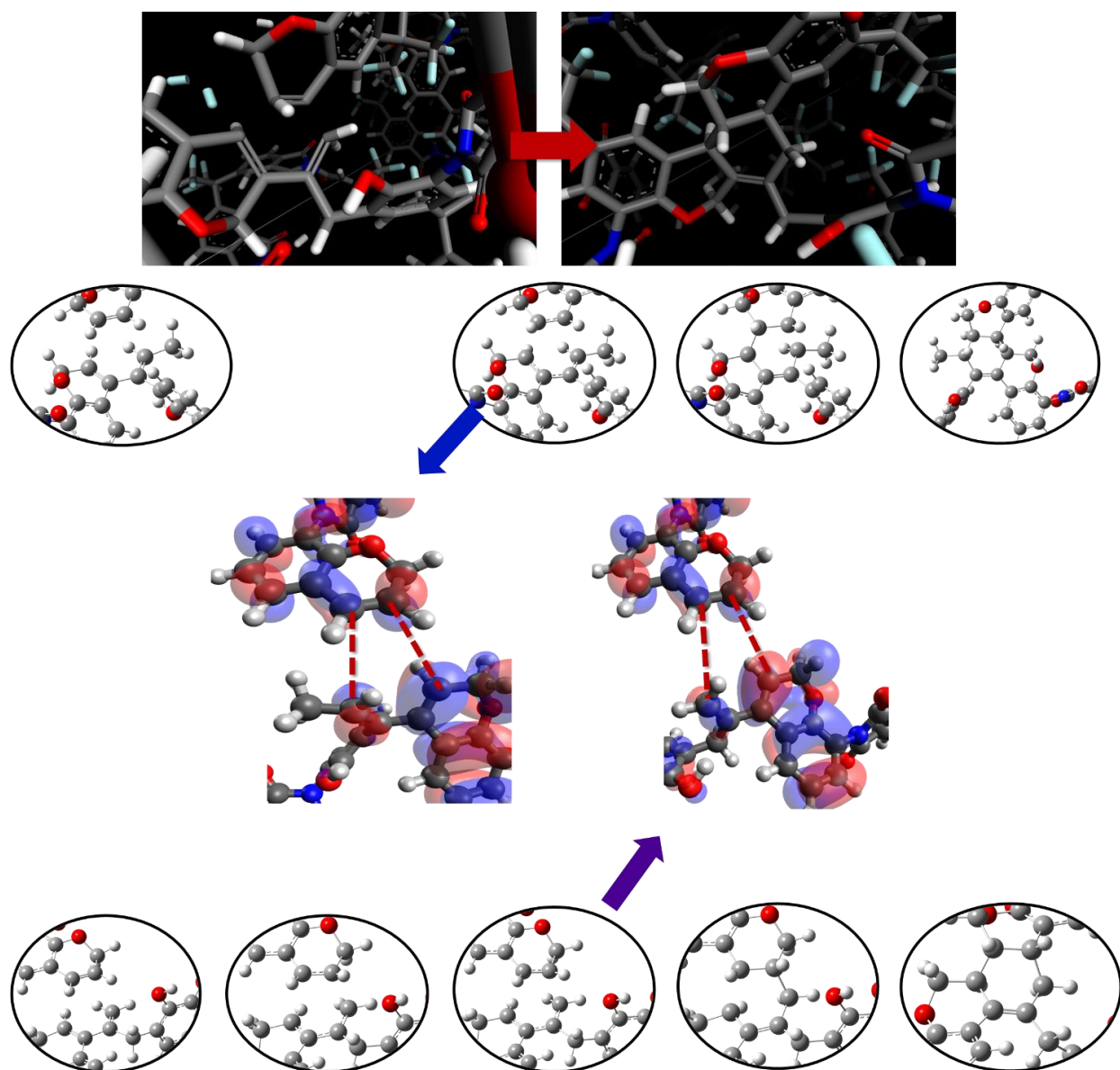
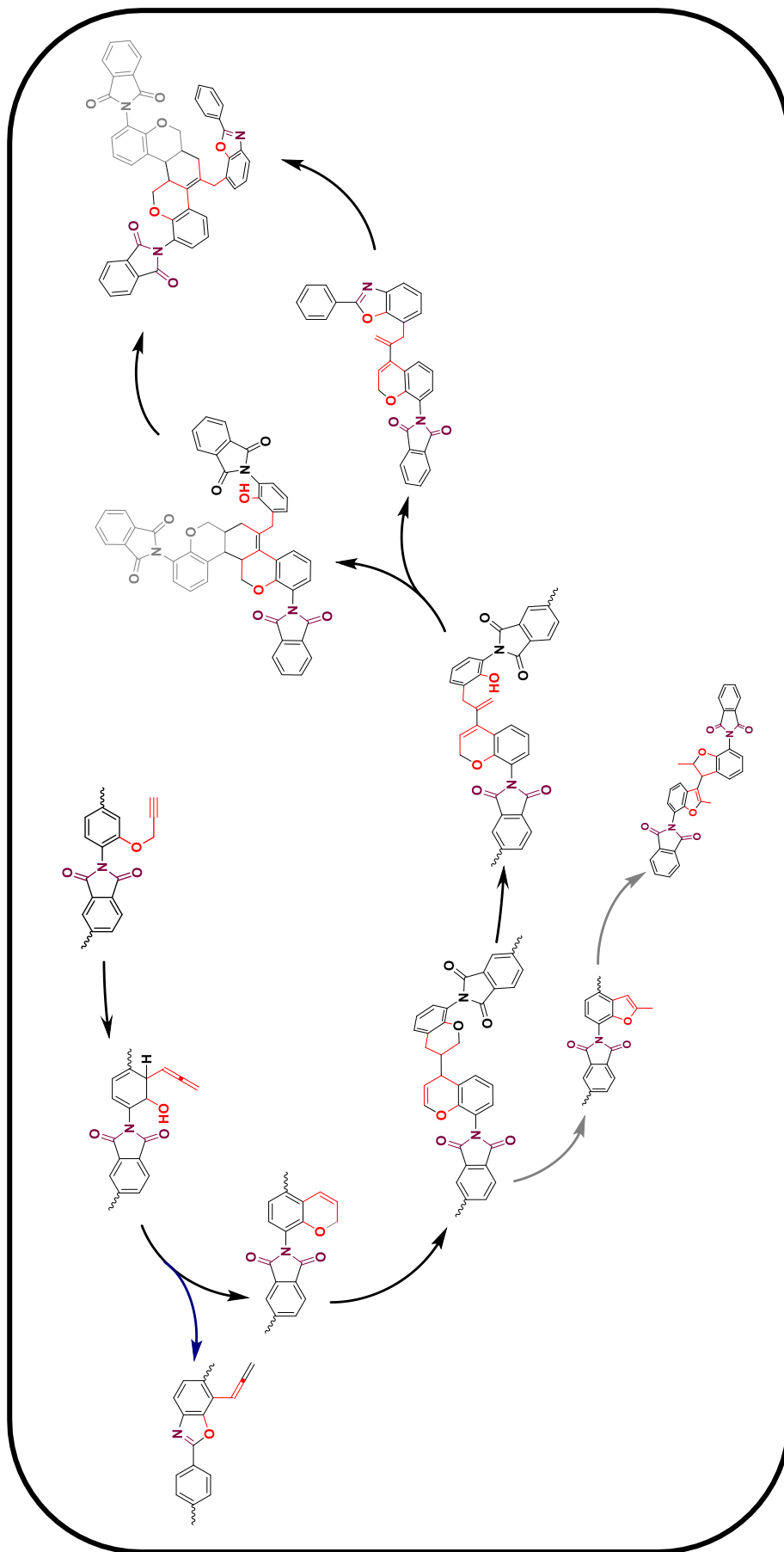


Figure 187. Image of a diene and dienophile in an amorphous cell and the resulting product (top), geometries of the IRC based on TScc1 and TSxc1b (bottom). The HOMO-orbital of the diene and LUMO-orbital of the dienophile are shown in the middle.



## Key Messages

- Propargyl phenyl ether – imide units undergo Claisen Rearrangement forming an *ortho*-allene group similar to the allyloxy Claisen-Rearrangement.
- The CR product is capable to undergo different subsequent steps, such as the PBO formation, crosslinking via cycloaddition, and even more often described two cyclization reactions forming either a five-membered furan ring or a six-membered chromene ring, which shows the lowest activation energy.
- Both cyclic structures contain a vinyl group in conjugation with the benzene ring and are likely to undergo crosslinking.
- The chromene rings appear to undergo crosslinking more readily compared to crosslinking of a furan and a chromene ring. However, the significant largest activation barrier was determined for the crosslinking of two furan groups.
- Crosslinking occurs between C7' and C7' or C8' of the second chromene unit forming  $\gamma\gamma$ - or  $\gamma\beta$ -crosslinks.
- The crosslinking might occur via a 4- or 5-membered transition state structure, whereas the six-membered transition state shown about half of the activation energy barrier and is more likely.
- Once it is crosslinked, a chromene and cyclohexyl ether ring exist. Both rings are able to open and initiate another cascade of reactions including isomerization and the possibility to undergo Diels-Alder cycloaddition with a third chromene unit or the hydroxy group undergoes a PBO formation reaction. The opened structure forms either an allyl or allene group, depending on the opened ring, and is capable to undergo further reactions such as cyclization to a five-membered ring or crosslinking.
- The most likely opening scenario is the ring opening of the cyclohexyl ether ring, forming an *ortho*-allyl group, which is crosslinked in  $\gamma'$ - or  $\beta'$ -position.
- A total cascade might contain 6 different structures, such as CR to *ortho*-allene, chromene cyclization, crosslinking, ring opening, Diels-Alder cycloaddition and HPI-to-PBO formation.



Scheme 31. Proposed thermally initiated reaction cascade of Propargyl-PI-1.

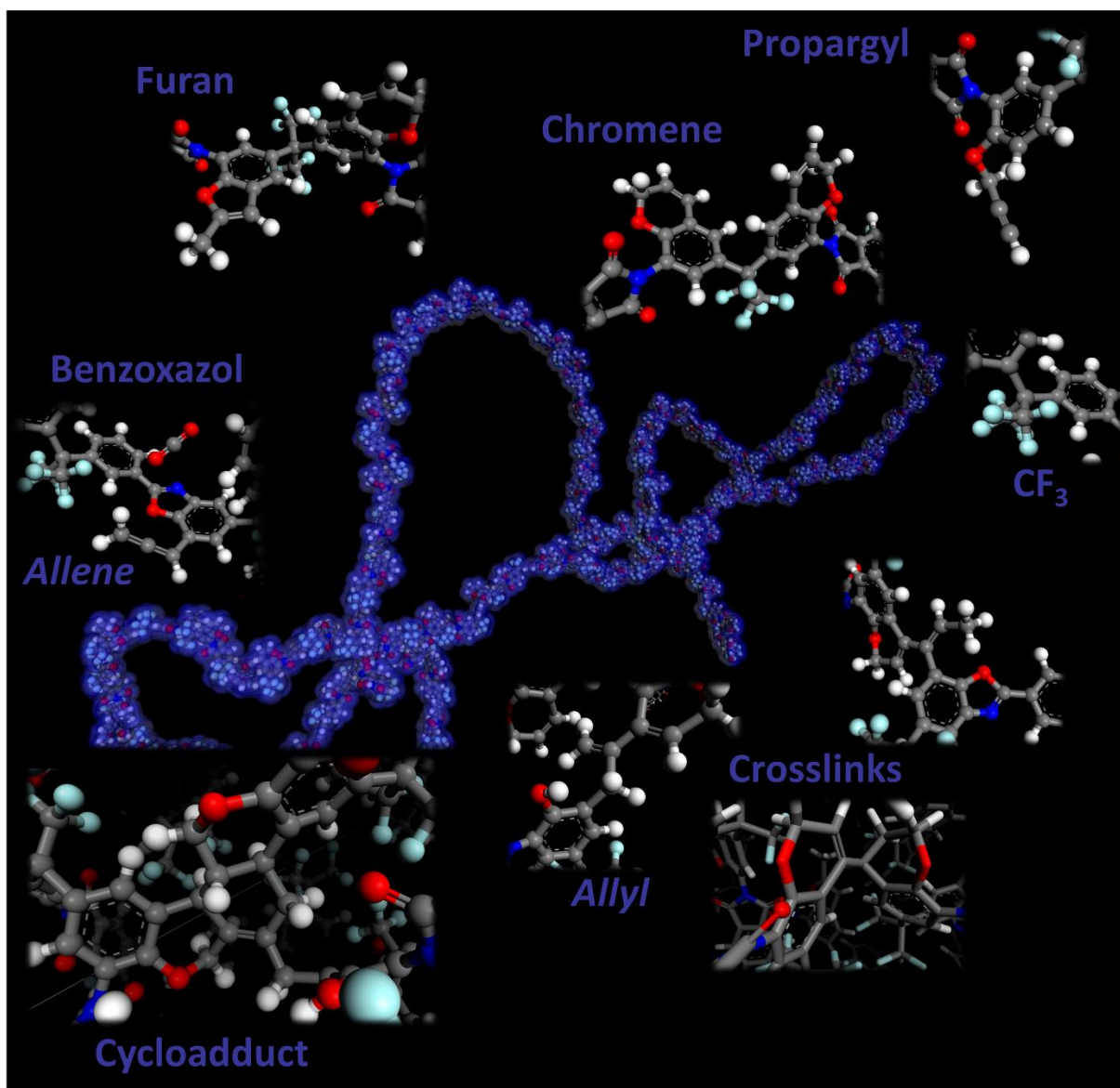


Figure 188. Simulated PGPI-1 chain with 33 repetition units and the accessible solvent surface. The specific units, that occur during an annealing procedure are expanded, based on the previously described simulations.

## Gas Separation

The DFT- and molecular dynamics simulations revealed the complex nature of possible consecutive reactions, which depend on the backbone, degree of propargylation and used derivative. Furthermore, the experimental results have shown, that the structure of the propargylated films changes consistently and is highly temperature sensitive. As a consequence, the film composition and structural parameter vary consistently as well. Therefore, it is tough to draw conclusions from the used annealing temperature back to the film properties. Nevertheless, in order to evaluate the materials with respect to their applicability as gas separation membranes, the gas separation performance was tested by using the constant volume-variable pressure method.

The change of the permeability of annealed PGPI-1 samples for various gases was measured and is shown in Figure 189. The increase of the permeability after annealing at 300 °C for 30 min was about a factor of 10 in case of CO<sub>2</sub>. The permeability increased from 23 Barrer to 258 Barrer. A stronger increase was determined for CH<sub>4</sub> with an increase from 0.31 Barrer to 18 Barrer, which is an increase of 58. Therefore, the CO<sub>2</sub>/CH<sub>4</sub> selectivity dropped from 76 to 14. The largest increase was determined for N<sub>2</sub> with a 67 times higher permeability.

However, annealing at 350 °C caused a more significant change in the permeability for each gas. The permeability of CO<sub>2</sub> increased by a factor of 4 compared to the 300 °C annealed sample. Moreover, the selectivity *versus* CH<sub>4</sub> increased up to 36. As a consequence, PGPI-1 surpasses the Robeson upper bound plot of 2008 for CO<sub>2</sub>/CH<sub>4</sub> by far and positions between the 2008 and 2015 upper bound (Figure 192). In comparison to the literature, PGPI-1 (350 °C) ranks among the highest permselective materials for CO<sub>2</sub>/CH<sub>4</sub> separation, making it a very promising material. It is noteworthy, that this performance is achieved after annealing at 350 °C, while most competitive materials were annealed at 450 °C [305-313]. In comparison to N<sub>2</sub>, the selectivity increased only by a factor of 2, leading to a H<sub>2</sub>/N<sub>2</sub> selectivity of 20.

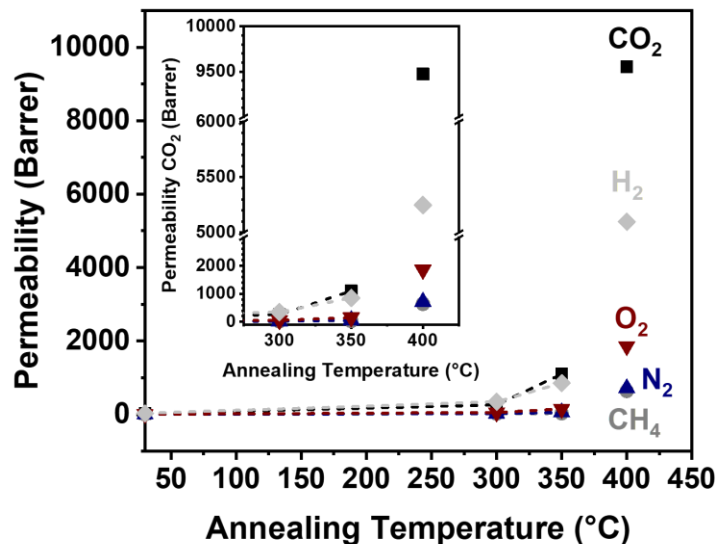


Figure 189. Permeability of CO<sub>2</sub> vs. annealing temperature of PGPI-1.

The H<sub>2</sub> permeability increased by a factor of about 2.5 and showed a permeability of 853 Barrer. Since CH<sub>4</sub> increased by a factor of less than 2, the selectivity of H<sub>2</sub> to CH<sub>4</sub> changed from 18 to 28.

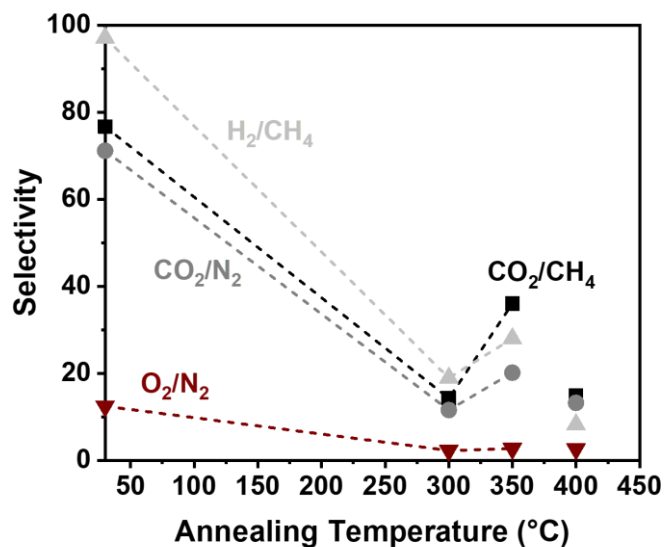


Figure 190. Selectivity of CO<sub>2</sub>/CH<sub>4</sub>, H<sub>2</sub>/CH<sub>4</sub>, CO<sub>2</sub>/N<sub>2</sub> and O<sub>2</sub>/N<sub>2</sub> vs. annealing temperature of PGPI-1.

Annealing at 400 °C for 1 h is a common method for TR polymers [152]. However, most studies use a heating rate of 5 °C min<sup>-1</sup> [12, 132, 133, 138, 139, 141, 144, 145, 148, 261, 267]. In such a case, the target temperature can be overheated, and thick films might have problems in order to follow the fast-heating ramp. Therefore, the materials in this study were slowly heated at 1 °C min<sup>-1</sup>. Furthermore, 400 °C annealing is very interesting, since the measured TR-related CO<sub>2</sub>

release peaks at 400 °C for PGPI-1. Therefore, a higher TR conversion is expected. As a result of the 400 °C treatment, the permeability increased significantly. For the gases CO<sub>2</sub> and H<sub>2</sub> the permeability increased to 9472 Barrer and 5249 Barrer, respectively. Nevertheless, the selectivity dropped for the gas pair CO<sub>2</sub>/CH<sub>4</sub> to 14 and in case of H<sub>2</sub>/CH<sub>4</sub> to 8. The selectivity of CO<sub>2</sub> *versus* N<sub>2</sub> dropped from 20 to 13. However, due to the very high permeability, the material positions above the 2008 upper bound as well (Figure 190).

Because of the strong increase of the permeability, a drop of the permeability as a consequence of physical aging, similar to other high permeable materials such as PIM-1, is expected. Therefore, the gas flux was measured for a period of 28 days. The permeability changes by time for the gases CO<sub>2</sub>, H<sub>2</sub>, CH<sub>4</sub>, O<sub>2</sub> and N<sub>2</sub> is shown in Figure 191. As expected, the permeability drops within the first week from 9472 Barrer to 5372 Barrer in the case of CO<sub>2</sub>. At the same time, the selectivity *versus* CH<sub>4</sub> increases from 14 to 17. After 28 days the permeability is 3243 Barrer, while the selectivity increased again to 22. The gas separation performance moves along the upper bound in the industrially attractive target zone. Therefore, it appears, that physical aging makes the polymer membrane of PGPI-1 after annealing at 400 °C an attractive material for natural gas separation. Moreover, when tracking the aging progress, the aging rate slowly levels off and slows down after the first week.

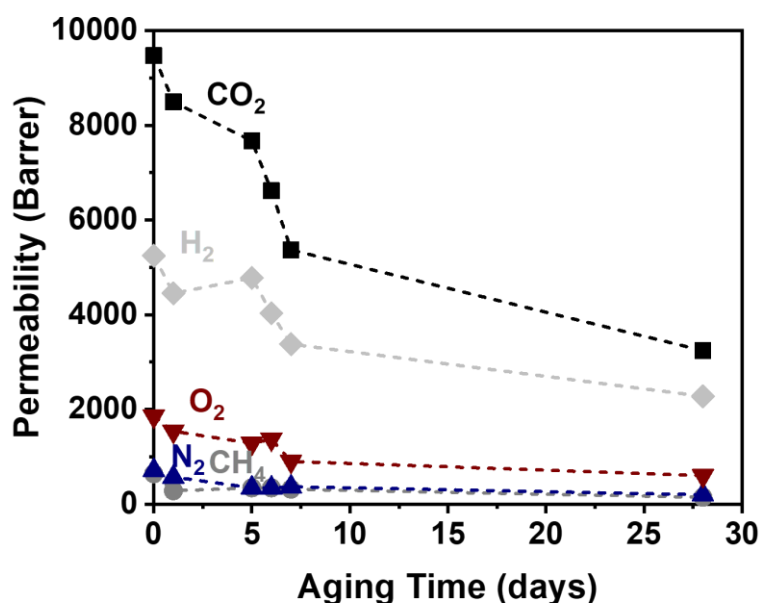


Figure 191. Permeability of CO<sub>2</sub>, H<sub>2</sub>, O<sub>2</sub>, N<sub>2</sub>, CH<sub>4</sub> as a function of the aging time.

So far, only PGPI-1 was discussed. However, a few other polymer materials were chosen for further gas separation based on a stable film formation and based on the thermochemical analytics. PG50PI and PG8PI-1 were investigated since stable thick films were obtained. Furthermore, PG8PI showed a very low  $TR_{\text{onset}}$  temperature. PGPI-2 and PGPI-3 were investigated since both gave excellent transparent defect-free films and showed a variation in the thermochemical behavior to PGPI-1, whereas both materials did not show a strong tendency to crosslink, as DSC experiments revealed.  $\gamma$ MPGPI-1 was chosen due to its lower tendency to crosslink as well and TMSPGPI was of high interest due to the large TMS group. Annealing at 350 °C causes PGPI-1 and PG50PI to be the most promising materials, while annealing at 400 °C added PGPI-2 as well. Despite its low permeability of 253 Barrer, the selectivity of 50 is very high for the  $\text{CO}_2/\text{CH}_4$  separation.

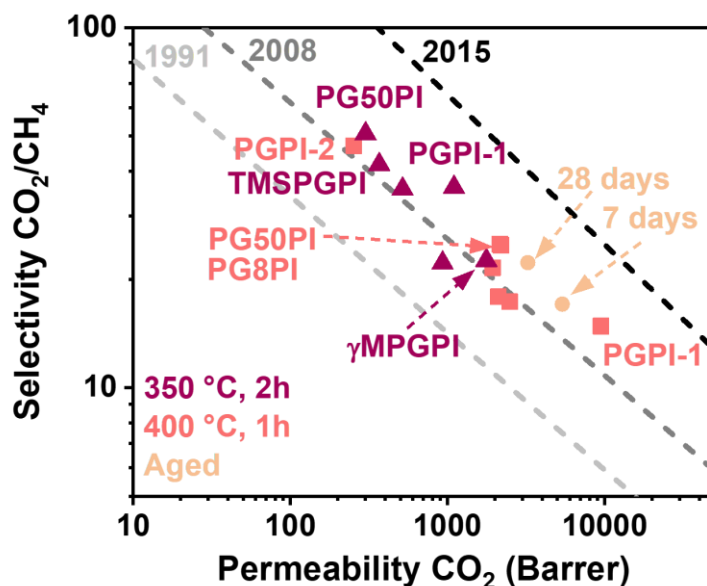


Figure 192. Robeson plot of  $\text{CO}_2/\text{CH}_4$  including propargylated polyimides after annealing at 350 and 400 °C.

Similar positions were found in the  $\text{H}_2/\text{CH}_4$  upper bound (Figure 193) as well, despite the very strong performance of TMSPGPI. With a permeability of 880 Barrer for  $\text{H}_2$ , TMSPGPI nearly surpasses even the 2015 Robeson upper bound material. Interestingly, TMSPGPI was also annealed at only 350 °C.

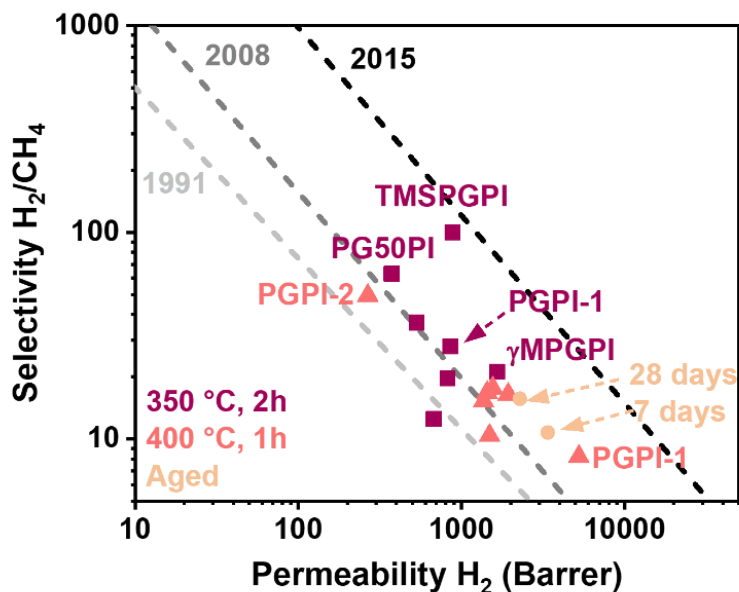


Figure 193. Robeson plot of H<sub>2</sub>/CH<sub>4</sub> including propargylated polyimides after annealing at 350 and 400 °C.

In addition to the mentioned gas pairs, the olefine and paraffine separation was investigated. While PGPI-3 did not show a strong gas separation performance when it comes to CO<sub>2</sub> purification, it shows an extraordinary gas separation performance for the ethylene/ethane separation. The determined selectivity for the 350 °C annealed material was 5.3 and even increased to 5.7 after annealing at 400 °C. This is a strong performance, since most materials, like the allylated materials have only selectivities between 2 and 3. Therefore, PGPI-1 after 350 °C shows an extraordinary ethylene separation performance with a selectivity of 4.9 as well (Figure 194).



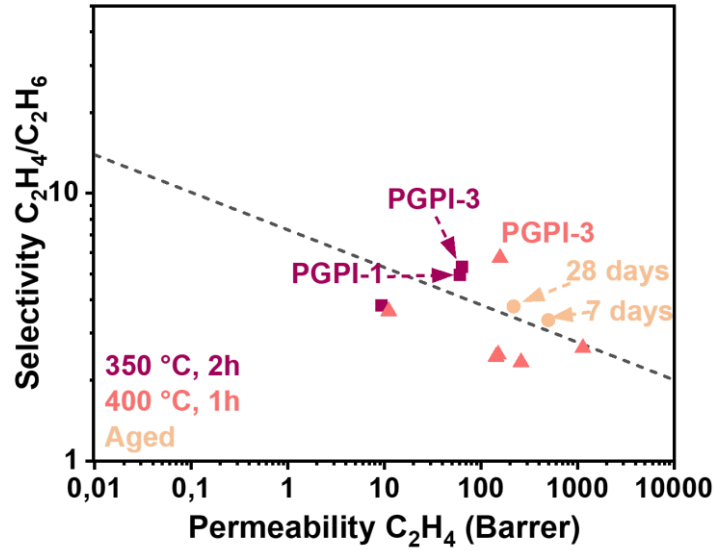


Figure 194. Robeson plot of  $C_2H_4/C_2H_6$  including propargylated polyimides after annealing at 350 and 400 °C.

In conclusion, the propargylated materials have shown a very strong dependence on the annealing temperature due to the large number of potential reactions in solid-state. Several materials have shown a 2008 upper bound surpassing performance for various gas pairs. Especially, after an annealing protocol with a target temperature of only 350 °C led to highly selective materials, which makes them competitive to the current state-of-the-art materials. Moreover, their performance reaches the industrially attractive target zone. TMSPGPI showed a very strong  $H_2$  separation performance and PGPI-3 is very promising for the ethylene purification.

# Thermally initiated Cascade Decomposition Polymers (TCDP)

## *Polyimides with ortho-Alkyloxy and Acyloxy Groups*

### Thermochemistry of *ortho*-alkyloxy and acyloxy polyimides

The previous sections described the way of modifying TR precursors by thermally active functional groups. Allyl and propargyloxy groups which undergo a thermally induced Claisen Rearrangement and consecutive cascade reactions

As a consequence of the cascade reactions, the phenol group recovers during the cascade and can undergo a TR reaction. The TR is lowered by polymer chain disruption and therefore increased degree of freedom with respect to its mobility. Nevertheless, another type of hydroxy group modification in TR precursors exists

A few allyl derivatives have shown that a loss of the modification also leads to recovery of the hydroxy group and that the TR process is lowered, since the polymer chains did not efficiently pack in the first place, giving the chains even after decomposition the space to rotate freely. Furthermore, the decomposition products might act as plasticizer, which enhances the polymer chain mobility as well. Sanders *et al.* [141] and Guo *et al.* [138] have shown that *ortho*-ester precursor result in very promising membrane materials due to the additional loss of the ester group. Sanders *et al.*[141] reported that the decomposition temperature depends strongly on the stability of the ester. Comesana *et al.*[132] investigated a methoxy and acetic modification in 6FDA-HAB. They claimed that the ester decomposes and PBO is most likely formed, while methoxy degrades via radical reaction mechanism, leading to highly crosslinked lactam. However, all of these studies do not investigate the effects in detail by means of thermo analytical methods and structural investigations apart from FT-IR spectroscopy. Furthermore, no backbones other than highly rigid 6FDA-HAB were used.

The butylene group decomposed at 300 °C with immediate TR formation, prenyl and cycloallyl degraded already at 250 °C. All of these ethers degraded significantly earlier than the methoxy group in 6FDA-HAB. However, prenyl and cycloallyl showed similar decomposition temperatures in 6FDA-HAB compared to 6FDA-BisAPAF. This suggests that

the intramolecular decomposition reaction is nearly independent of its environment in terms of polymer backbone.

Open questions are, if decomposition products have stronger effects on the chain mobility and therefore TR temperature in high- $T_g$  polyimides? How can the TR temperature and the film properties be tailored and tuned by the choice of the modification? Do other ether groups decrease the TR temperature as well? Is the TR process with methyl derivatives different to other ethers, as it probably does not decompose by elimination, which would lead to a highly reactive carbene. In case of a classical TR process, can an ethyl group be transferred in a way, as the hydrogen is transferred in unmodified TRPs?

Therefore 6FDA-BisAPAF based acetylated and methylated precursors were synthesized. The synthesis of the methylated polyimide MePI-1 was done by a Williamson ether synthesis via methyl iodide in DMF with potassium carbonate as a base catalyst. The acetylation was done by esterification using acetic anhydride as the acetate source and pyridine as a base catalyst for the reaction. The reaction was done in DMF as well. For further details with regard the synthetic procedure and the prepared materials and used reagents see chapter *Alkylation*. The alkylated materials MeOPI1, EOPI1, PrOPI1 and iPrOPI1, as well as the acyloxy derivatives MeCO<sub>2</sub>PI1, ECO<sub>2</sub>PI1, iBuCO<sub>2</sub>PI1, sBuCO<sub>2</sub>PI1 and tBuCO<sub>2</sub>PI1 were provided for further studies for this PhD thesis by U.Meis. Synthesis and characterization by means of <sup>1</sup>H-NMR, FT-IR, TGA-FT-IR, DSC were shown in the corresponding thesis, see [22].

The full conversion of the methyl ether was confirmed by means of <sup>1</sup>H-NMR spectroscopy (Figure 195), showing a full disappearance of the hydroxy peak at 10.4 ppm. In addition, a new peak at 4.0 ppm evolved with an integral of 6 in comparison to 12 protons in the case of the aromatic region. The acetylated spectrum showed a new peak at 2.0 ppm with an integral of 6 protons as well, corresponding to the 3 protons of the methyl group in the acetate modification. The FT-IR analysis showed that the O-H stretch vibration disappeared upon conversion to both groups (Figure 195). In case of the acetylated polyimide, the carbonyl peak at 1760 cm<sup>-1</sup> increased, due to the introduction of additional carbonyl groups.

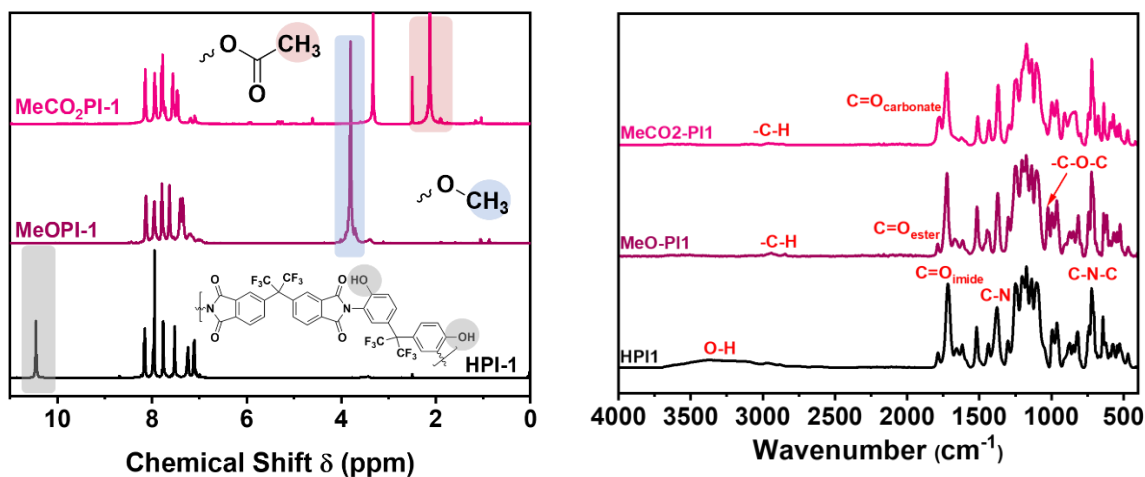


Figure 195.  $^1\text{H-NMR}$  (left) and FT-IR spectrum (right) of methylated (MeOPI-1, purple), acetylated (MeCO<sub>2</sub>PI-1, pink) and their corresponding pristine polyimide precursor 6FDA-BisAPAF (HPI-1, black)[22].

For the investigation of the effect of the polymer backbone in combination with the methoxy- and acetate functionalization, various TRP precursor backbones were modified. In the case of the methoxy modification APAF and HAB were polymerized separately with 6FDA, BPDA, BPADA and BCODA for comparison. In addition, APAF was polymerized with EDA. For the investigation of the acetate functionalization APAF was polymerized with 6FDA, BPDA, BPADA and EDA prior to its acetylation. In addition, 6FDA-HAB was acetylated as well. The  $^1\text{H-NMR}$  spectra revealed a full conversion in all cases (Figure 196), as confirmed by the disappearance of the phenol peak and the evolution of the methoxy and acetate CH<sub>3</sub> group, as described before.

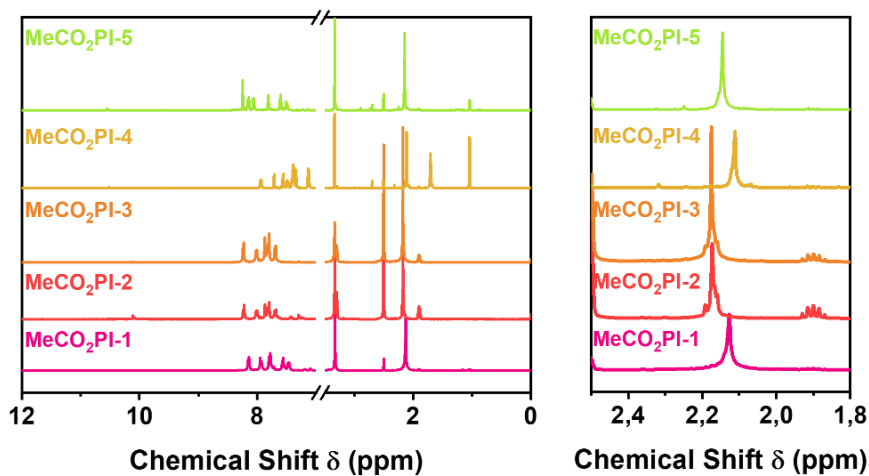


Figure 196.  $^1\text{H-NMR}$  spectrum of acetylated polyimides (left). Zoom into the chemical shift region of the acyloxy group (right)[22].

## Methylated *ortho*-Hydroxy Polyimides

### Thermoanalytics

Comesana *et al.* [132] studied the thermogravimetric analysis of 6FDA-HAB based methoxy and acetate containing polyimide precursor for the TR process. They concluded a decomposition of the acetate group leading to mainly benzoxazole structures, and a radical demethylation at very high temperatures for the methoxy functionalization. A radical reaction path to the corresponding highly crosslinked lactam product was assumed in the latter case. They drew their conclusion from TGA-MS measurements. Nevertheless, they did not discuss the fact, that 6FDA-HAB based polymers are among the stiffest TR precursors [139], which might have a strong influence on the TR process as unmodified 6FDA-HAB also revealed low TR conversion rates. Furthermore, their simulation was based on semi-empirical calculations of one transition-state structure suggestion and no experimental indications for the observation of two different products were given.

Therefore, the methoxy and acetate modifications were investigated in detail, as a TR reaction following the same path as observed for unmodified TR precursors is expected. However, in the case of methoxy-polyimides the transfer of a hydrogen from phenol to imide carbonyl group is replaced by a methyl cation transfer.

Figure 197 demonstrates the temperature-related mass loss curve, obtained by means of TGA-FT-IR analysis. In addition, the CO<sub>2</sub> and CH<sub>4</sub> peak height profiles are plotted as well as the first derivative of the mass loss curve. Furthermore, the differential scanning calorimetric measurement of the heat flow in the range from 150 to 450 °C is shown. The experiment reveals that no weight loss and no heat flow affecting process occurs up to a temperature of 300 °C. The onset of the determined CO<sub>2</sub> detection is at 301 °C, which correlates with the DTG and mass loss step onset temperature. With increasing temperatures, the CO<sub>2</sub> loss increases rapidly up to 345 °C. It then slows down and increases again rapidly after passing a temperature of 360 °C until a maximum CO<sub>2</sub> loss at 394 °C is reached. The mass loss curve decreases less pronounced afterwards until a minimum of the CO<sub>2</sub> release at 445 °C is reached and a second strong CO<sub>2</sub> producing process leads to an increased mass loss due to polymer degradation. Peak fitting reveals, that two different processes are expected in the range from 301 to 445 °C with peaks at 337 and 394 °C, respectively. The first process is rather small in its

intensity compared to the second process and the reason why a slow-down of the mass loss curve was observed at 345 °C. In addition, the formation of CH<sub>4</sub> with a very weak increase around 300 °C and a strong increase at 350 °C was determined. The CH<sub>4</sub> evolution peaks at 396 °C. Therefore, two processes or a change of the kinetics during the Thermal Rearrangement reaction is expected. Since chemical reactions induce a change of the heat flow in case of exo- and endothermic reactions, the process can be followed by calorimetric measurements. Hence, a DSC experiment with MeOPI-1 was performed in the range from 50 to 450 °C at a heating rate of 5 °C min<sup>-1</sup>. Interestingly, the heat flow increases at 321 °C and levels off at 345 °C but increases again very rapidly to a peak temperature of 425 °C. A comparison of the specific temperatures of the TGA and DSC measurement reveals that a decarboxylation already occurs at 301 °C, while a heat flow was not measured before 321 °C. However, both measurements show a decrease of the corresponding parameter (heat flow, CO<sub>2</sub> release) at the same temperature of 345 °C. Therefore, the first fit peak of the CO<sub>2</sub> peak height profile is attributed to the first fit peak of the heat flow curve. The second peaks in both measurements appear in a similar temperature range, but the heat flow is again slightly shifted to higher temperatures.

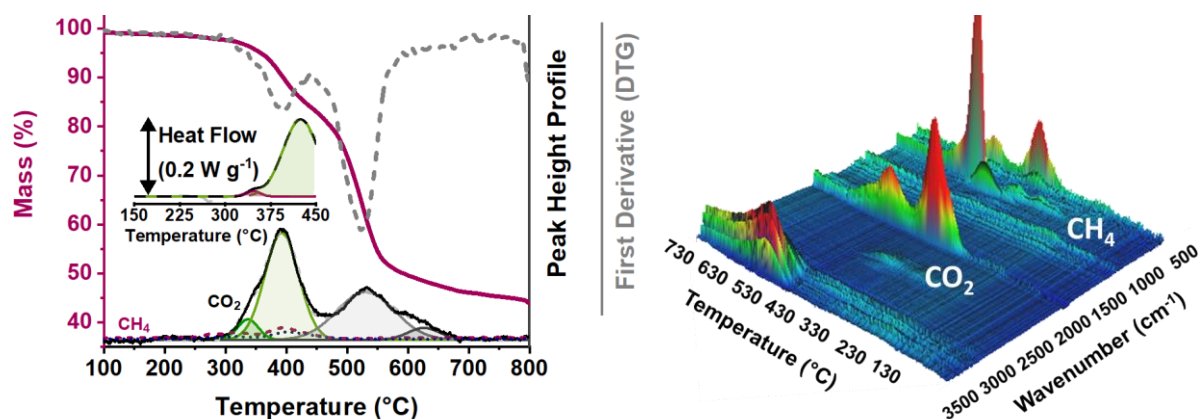


Figure 197. Temperature related mass loss curve for methylated 6FDA-BisAPAF (MeOPI-1) (purple). The CO<sub>2</sub> (black) and CH<sub>4</sub> (purple dashed) peak height profile from evolved gas analysis as well as the first derivative (grey dashed) of the mass loss curve is shown (left). The three-dimensional plot of all stacked FT-IR spectra (right)[22].

In Figure 198 the determination of the specific temperatures is shown, based on the tangent line method of the first derivative as well as the CO<sub>2</sub> peak height profile. The ascent or descent of the curve, respectively, is fitted by a tangent line. Their point of intersection is the corresponding temperature. If only CO<sub>2</sub> is responsible for the mass loss, then the Gram-Schmidt curve is identical to the CO<sub>2</sub> peak height profile and this is basically similar to the first

derivative. The Gram-Schmidt curve is the global curve of all added peak height profiles of each determined signal at a specific wavenumber. Therefore, the profile is identical to the peak height profile of only one wavenumber if only one signal is processed during mass loss. In the case of MeOPI-1 the mass loss is caused by release of  $\text{CH}_4$  and  $\text{CO}_2$  and varies therefore slightly from the  $\text{CO}_2$  peak height profile. However, since the mass loss is mainly caused by  $\text{CO}_2$  which is 2.75 times heavier than  $\text{CH}_4$  with  $44 \text{ g mol}^{-1}$  vs  $16 \text{ g mol}^{-1}$ , the first derivative appears very similar to the  $\text{CO}_2$  peak height profile, which is the reason why the determined temperatures are in agreement to each other. The mass loss curve and first derivative demonstrate the weight loss is starting at  $T_{d,\text{onset}}$  of 5% within  $44 \text{ }^\circ\text{C}$  (in the range from  $301$  to  $345 \text{ }^\circ\text{C}$ ), while it then starts to decrease more by 10% within  $100 \text{ }^\circ\text{C}$  from  $345$  to  $445 \text{ }^\circ\text{C}$ . The first deconvoluted  $\text{CO}_2$  peak of the TGA curve corresponds to a small heat flow increase, at which a low  $\text{CH}_4$  release was detected as well. However, the main process occurs within the second process, which is highlighted as the second deconvoluted peak in the TGA and DSC experiment. This second process involves the largest mass loss of about 10%, which consists of  $\text{CO}_2$  and  $\text{CH}_4$  simultaneously.

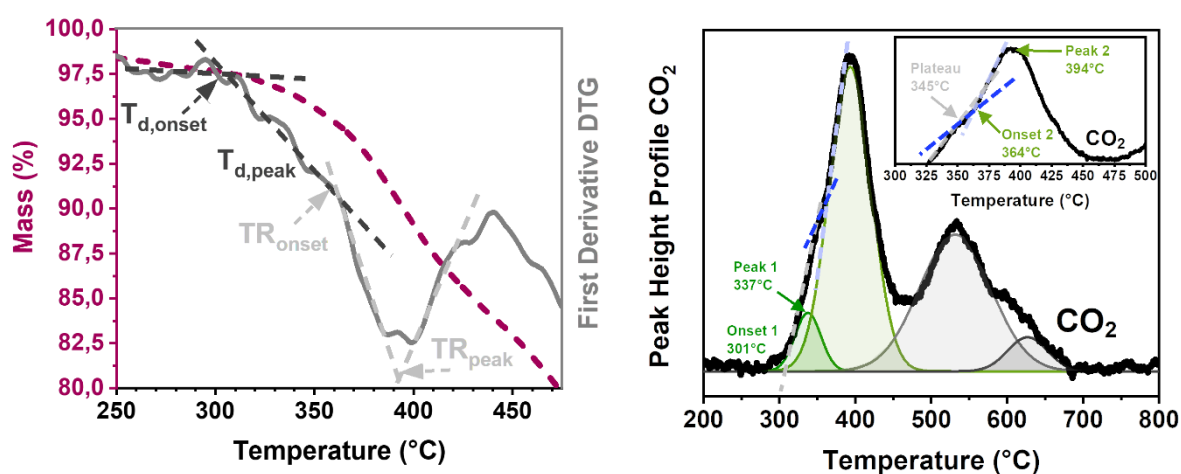


Figure 198. Mass loss curve and first derivative of MeOPI-1 including onset and peak temperature determination via tangent line evaluation (left). Peak height profile of  $\text{CO}_2$  including peak deconvolution and determination of the onset and peak temperatures via tangent line evaluation method (right) [22].

In order to understand the thermo analytical findings, FT-IR spectroscopy measurements were done of materials which were annealed at TR typical temperatures of  $350$ ,  $400$  and  $450 \text{ }^\circ\text{C}$  (Figure 199).

The comparison of the annealed polymers shows a strong variation of the non-aromatic vibrations. First of all, the carbonyl stretch vibration at  $1720 \text{ cm}^{-1}$  is significantly decreasing.

The carbonyl group corresponds to the imide unit. The decrease of the carbonyl group and simultaneous increase of the benzoxazole C=N stretch vibration at 1480 cm<sup>-1</sup> indicates the formation of benzoxazole groups, rather than lactams. The stretch vibration of the carbonyl group of  $\delta$ -lactams is usually strong and appears at 1650 cm<sup>-1</sup>, while amide N-H stretch vibrations are weak vibrations and can be found at 3500 cm<sup>-1</sup>. Neither of the lactam peaks was observed. Therefore, the suggested formation of lactams from *ortho*-methoxy polyimides by Comesana *et al.* [132] is not the case for methylated 6FDA-APAF (MeOPI-1). Furthermore, at 350 °C a strong decrease of the ether attributed peaks was observed, while no phenolic O-H vibration was detected. The ether attributed peaks are at 1100 and 1020 cm<sup>-1</sup> for the C-O-C ether vibration and at 2845 and 2940 cm<sup>-1</sup> for the C-H stretch vibration of the methyl group. This shows that the methoxy group undergoes a reaction, which involves the ether bond breakage and consecutive reaction of the phenolic oxygen atom. Such a process could be the reaction of the phenolic-O atom with the imide carbonyl group via methyl-group transfer to the imide carbonyl group according to the simulated TR mechanism in unmodified TR precursor polyimides. The subsequent reactions of the Thermal Rearrangement then led to the formation of a polybenzoxazole accompanied by the release of a molecule of CH<sub>4</sub> and CO<sub>2</sub>.

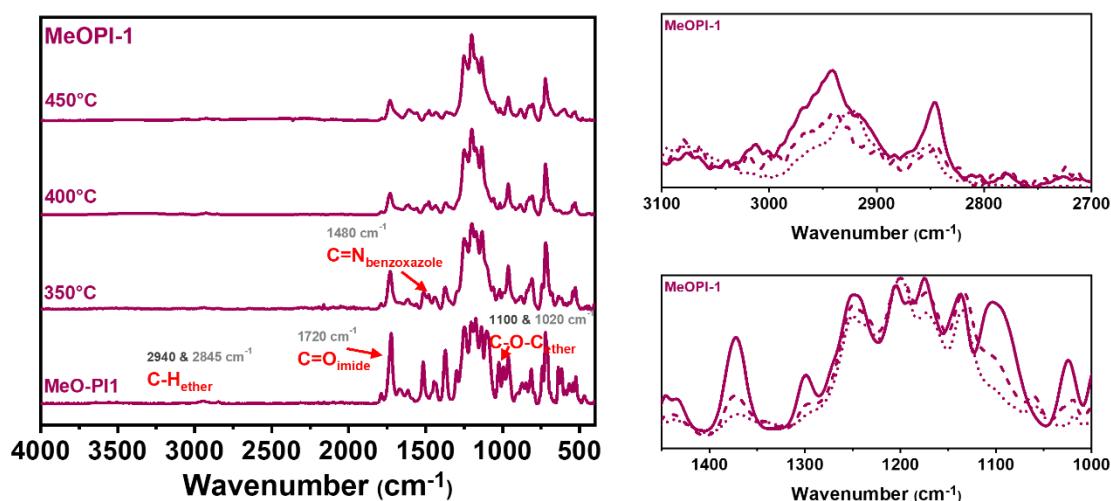


Figure 199. Stacked FT-IR spectra for MeOPI-1 after annealing at 80 °C (24 h), 350 °C (2 h), 400 °C (1 h) and 450 °C (0.5 h) (left). Zoom into the range from 2700 – 3100 cm<sup>-1</sup> (right, top) and 1000-1450 cm<sup>-1</sup> (right, bottom)[22].

DFT simulations were successfully implemented into the reaction mechanism evaluation of allylated and propargylated polyimides. Therefore, simulations of potential mechanism based on the experimental findings were executed. The simulated mechanisms were based on the reaction mechanism study of the unmodified polyimides. The reaction mechanism was



categorized into radical and non-radical chemistry-based reactions. In Figure 200 the non-radical reaction mechanisms are shown.

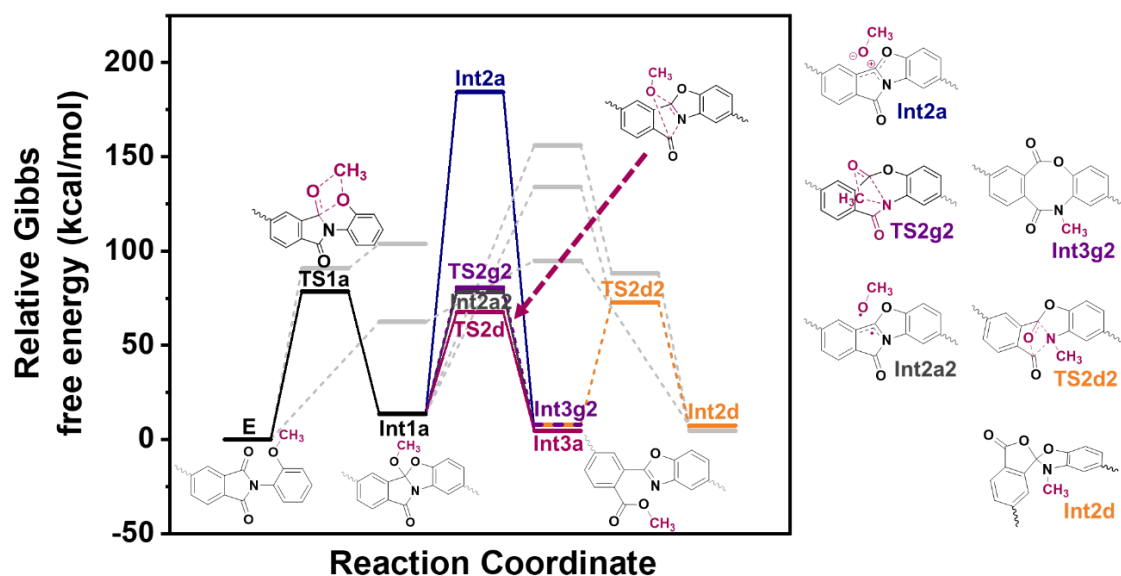


Figure 200. Reaction coordinate of the demethylation and Thermal Rearrangement reactions of methylated phenol-phthalimide models by means of DFT simulations. The RC shows the non-radical reactions. Transition state geometries and intermediates, starting material and products are shown.

The initial step of all reactions is the concerted methyl group transfer and nucleophilic phenol-imide cyclization reaction via TS1a. The TS1a reaction mechanism proceeds in the same manner such as the first step of the Thermal Rearrangement reaction of *ortho*-hydroxy polyimides. The difference is a methyl rather than a hydrogen shift in the case of methylated models. The second step varies now similar to HPI's. The conventional mechanism of HPI's includes the elimination of a hydroxy group from the first intermediate int1a. This was also calculated for the methylated model. Instead of a hydroxy group leaving the intermediate, it is a methoxy group, which is usually reported as a better leaving group. However, the conventional elimination mechanism is highly unlikely for methylated polyimides as well, as it exhibits a significantly higher activation energy compared to any other simulated mechanism. Since a radical elimination mechanism of the methoxy group of the intermediate int1a is supposed to be more likely in solid-state reactions without any solvent stabilization (required in order to stabilize an ionic transition state geometry and products), it was also calculated for the TR reaction in MeOPI. The activation energy for the radical mechanism compared to the ionic mechanism is still about half of the required energy. With  $78 \text{ kcal mol}^{-1}$  for the radical process and  $184 \text{ kcal mol}^{-1}$  for the ionic reaction. In contrast to HPI (unmodified

precursor) the activation energy decreases by about 3% for the formation of the ionic species and by 14% for the radical species. The result can be explained by the better stabilization of the radical due to the methyl group of the methoxy radical, while the methyl group is not capable to stabilize the negative charge in the same manner.

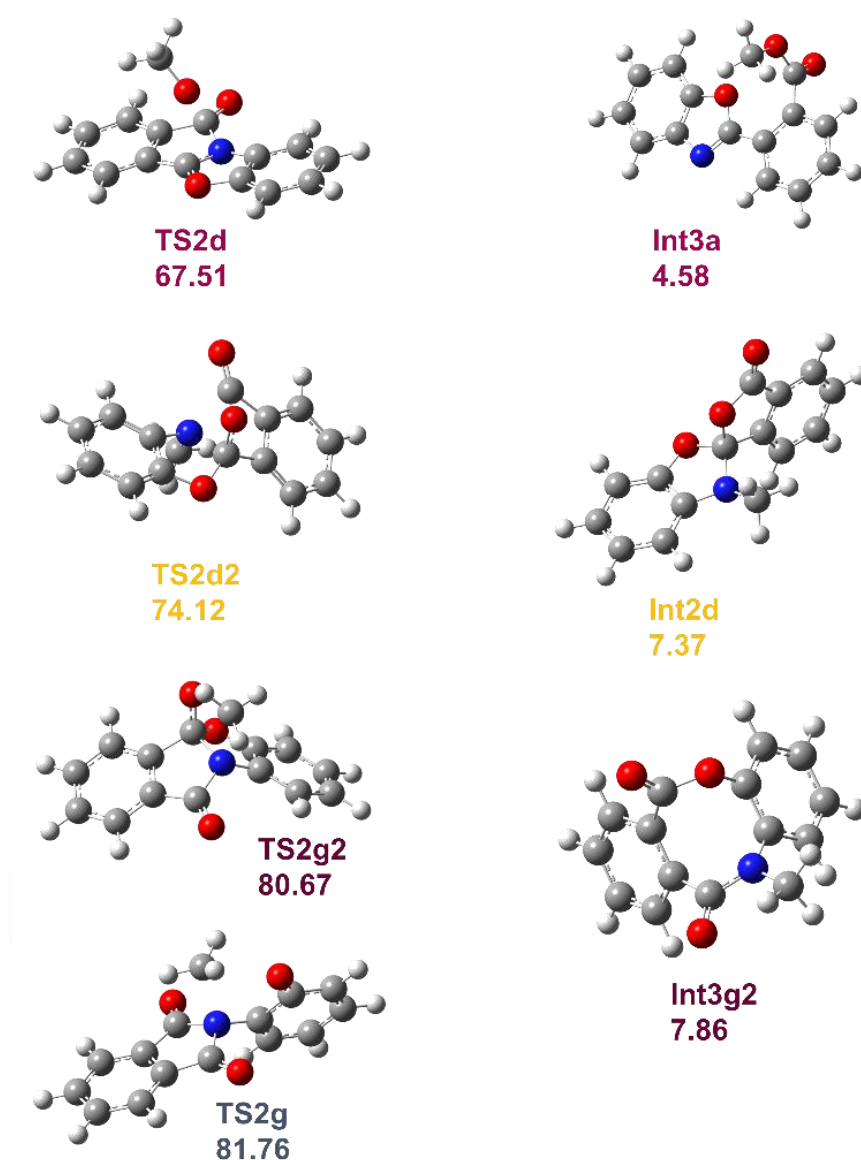
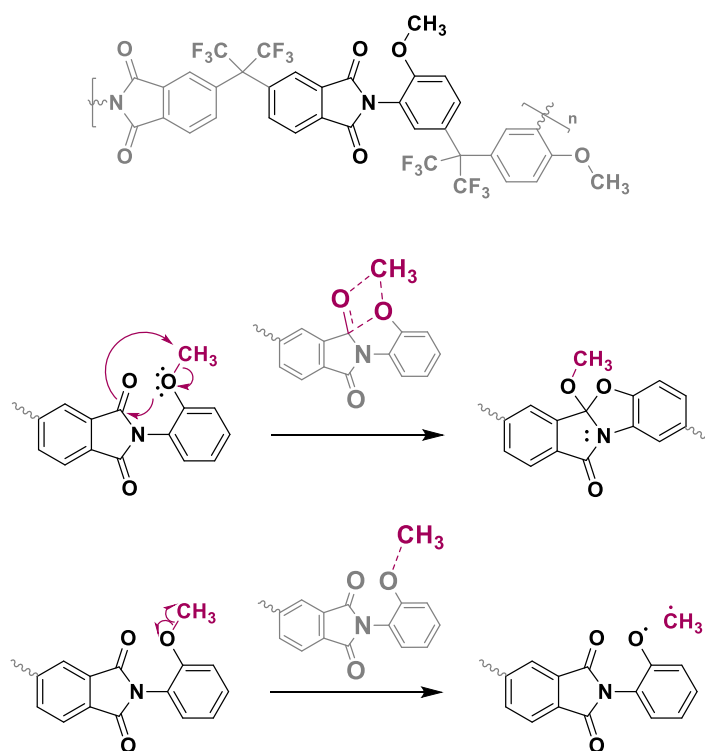


Figure 201. Transition state and intermediate geometries of the second step of the thermally initiated cascade decomposition reactions.

The lowest energy path was determined for the methoxy group transfer reaction within intermediate int1a. Principally it is an intramolecular nucleophilic reaction of the methoxy oxygen atom at the other carbonyl group. This process was confirmed by simulations as the most reasonable mechanism in unmodified *ortho*-hydroxy polyimides as well. The use of

methylated precursors, however, lowered the energy by 3 kcal mol<sup>-1</sup>. Interestingly, the decrease of the activation energy for the radical methoxy group elimination decreased by about 10% more compared to the transfer reaction. Therefore, both activation energies approach each other, and only a difference by 11 kcal mol<sup>-1</sup> is given. Another interesting mechanism is the intramolecular methyl group transfer in int1a from the present methoxy group to the amide nitrogen atom via TS2g2 to the *N*-methylated lactone-lactam intermediate int3g2. The *N*-methyl-analogous version of the imide-nitrogen atom methylation with subsequent lactone-lactam formation, as suggested by Comesana *et al.* [132], was not considered any further. The activation energy for the rotation of the formed phenolate along the imide dihedral angle is too large to overcome in comparison to the activation energy for any other simulated mechanism. This is the case, despite the fact, that the reaction of the *N*-methylated phenolate requires an activation energy of 80 kcal mol<sup>-1</sup> which is in the range of the most simulated mechanism. However, since the lactone-lactam intermediate formation by the *N*-methylation reaction via the suggested TS2g2 transition state does not involve any further high-energy rotations, it is hypothesized to be more reasonable to occur. The discussed reaction mechanisms are shown in Scheme 32 and Figure 202. The first and second step of the lowest energy path reaction via TS1a and TS2d is shown in Scheme 32 and Scheme 33.



Scheme 32. Mechanism of the first step of the thermally initiated cascade decomposition reactions. A nucleophilic attack and methyl transfer (TS1a) (top) and radical demethylation reaction (TS1r) (bottom).

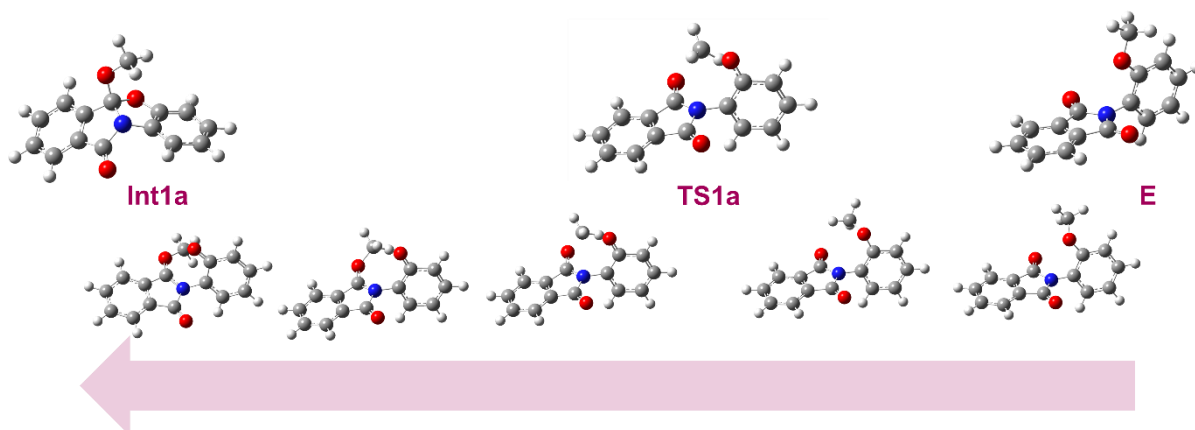
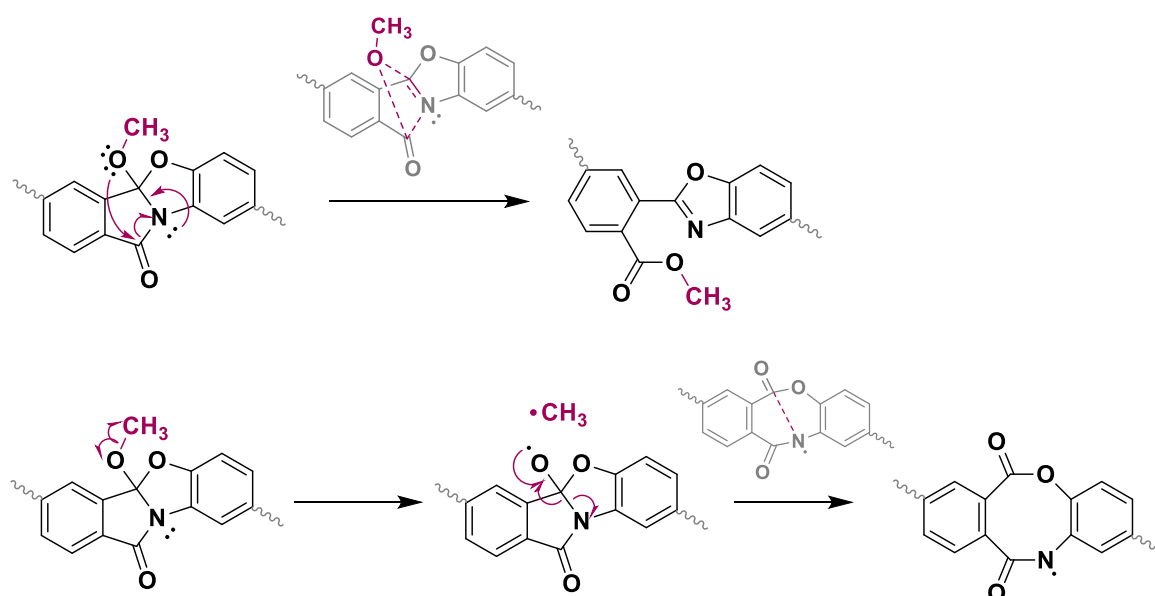


Figure 202. Chosen geometries along the intrinsic reaction coordinate for the first step of the reaction via TS1a of the methylated phenol-phthalimide model.



Scheme 33. Mechanism of the second step of the thermally initiated cascade decomposition reactions. An intramolecular nucleophilic attack via methoxy transfer, (TS2d) (top) and radical demethylation reaction of the intermediate int1a (TS2r) (bottom).

In Figure 203 the reaction coordinate for the simulated methyl radical species involving mechanisms is demonstrated. In addition, a decomposition of the methoxy group via intramolecular hydrogen transfer via three-membered transition state geometry was calculated as well. The reaction leads to the formation of a highly reactive carbene. Therefore, the transition state and following intermediate are thermodynamically and kinetically not favored and not discussed in more detail. A comparison of the activation energies of the radical reactions shows easily, that these reactions involve significantly larger energies for the highest energy step among each mechanism with respect to the non-radical reactions. The lowest energy reaction path was determined for the initial radical demethylation of the methoxy group in the starting model, leading to a methyl and phenol radical. Subsequent reactions do

not form the benzoxazole structure. The reaction of the phenol radical with the carbonyl group of the imide unit proceeds via formation of the int1a analogous radical int1e, which instantaneously rearranges via C-N bond breakage (TS2r). The result is the radical lactone-lactam intermediate int3r. Int3r forms the neutral int3g2 lactone-lactam intermediate via hydrogen abstraction from adjacent molecules via formation of CH<sub>4</sub>. The radical demethylation of int1a after the first step of the non-radical reaction pathway leads to int2r, which is the same intermediate as discussed for the previous reaction. The rearrangement occurs accordingly via TS2r to the lactone-lactam. Nevertheless, the radical oxygen atom in int2r might react as well with the carbonyl group, such as TS2d of the non-radical pathway, and forms a lactone intermediate int3r2. This process requires less energy than TS2r.

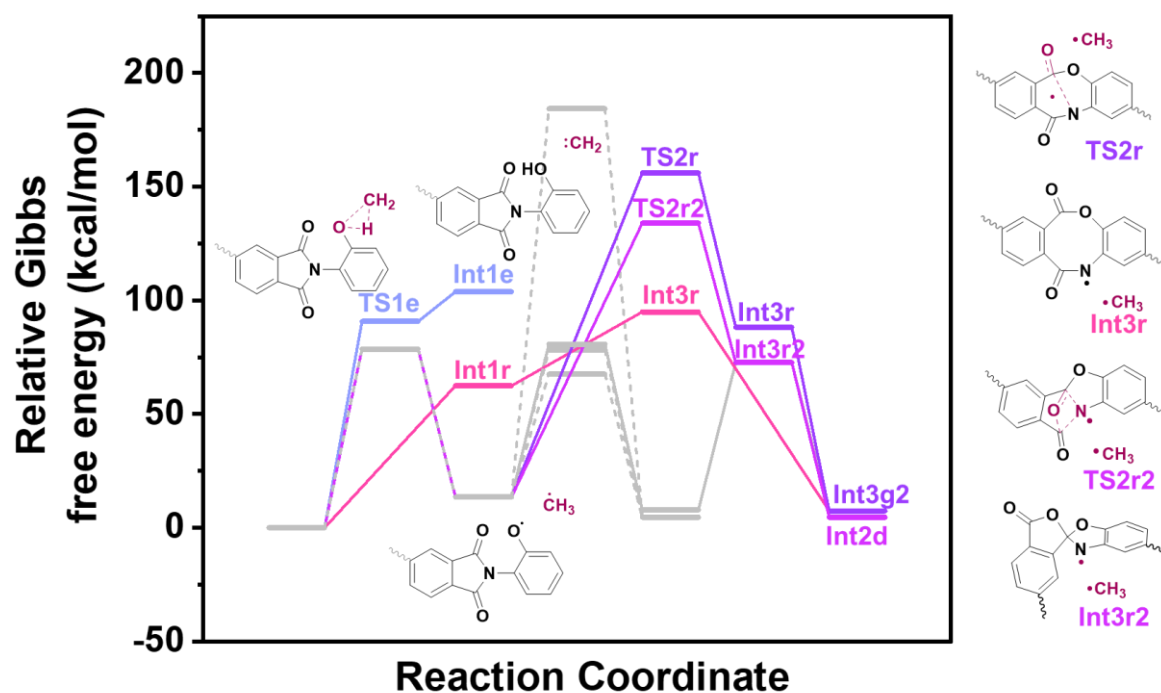
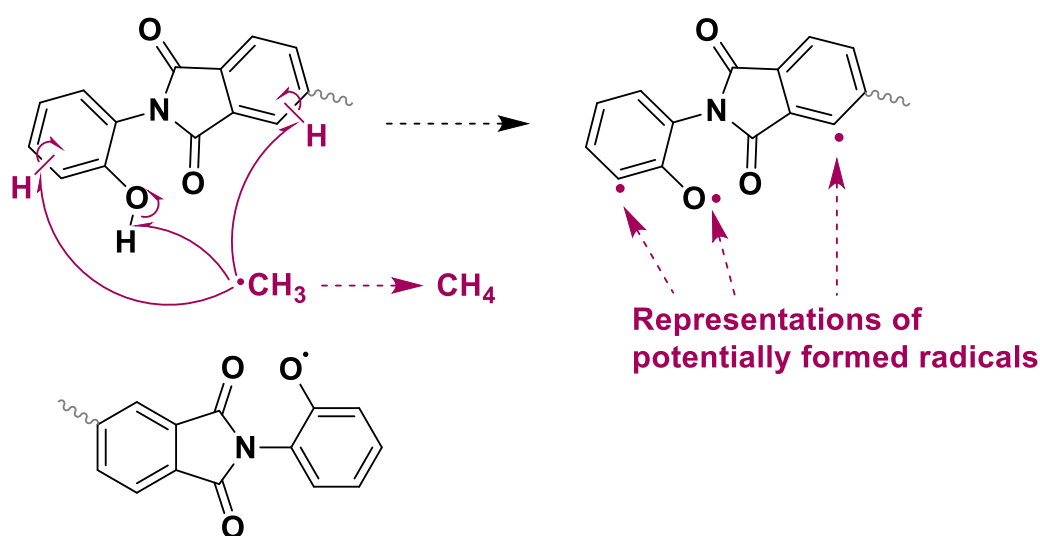


Figure 203. Reaction coordinate of the demethylation and Thermal Rearrangement reactions of methylated phenol-phthalimide models by means of DFT simulations. The RC shows the radical reactions. Transition state geometries and intermediates, starting material and products are shown.

TGA experiments have shown that CH<sub>4</sub> is formed during the reactions. From an experimental point of view, it is difficult to judge, whether CH<sub>4</sub> is formed from a methyl radical via hydrogen abstraction from any hydrogen containing group in other molecules of the polymer film, or from impurity trace gases in the glass fiber from the TGA oven to the FT-IR spectrometer. However, it is very reasonable that formed methyl radicals, which are very reactive, abstract hydrogens within the polymer matrix while diffusing through the polymer matrix. In most

aromatic polyimides the hydrogens are only present on the benzene rings. An abstraction of an aromatic hydrogen atom forms a phenyl radical which is highly unstable, hence very reactive. This would lead to crosslinking, analogously to the proposed benzoic acid crosslinking-decomposition-crosslinking mechanism, as reported for DABA containing polyimides by Koros *et al.* [118]. The formed biphenylene group is very tight and stiff and might change the film properties strongly. Therefore, the mechanism evaluation is very important when discussing the final materials properties. In any case, potential hydrogen abstractions from the model units are shown in Scheme 34.

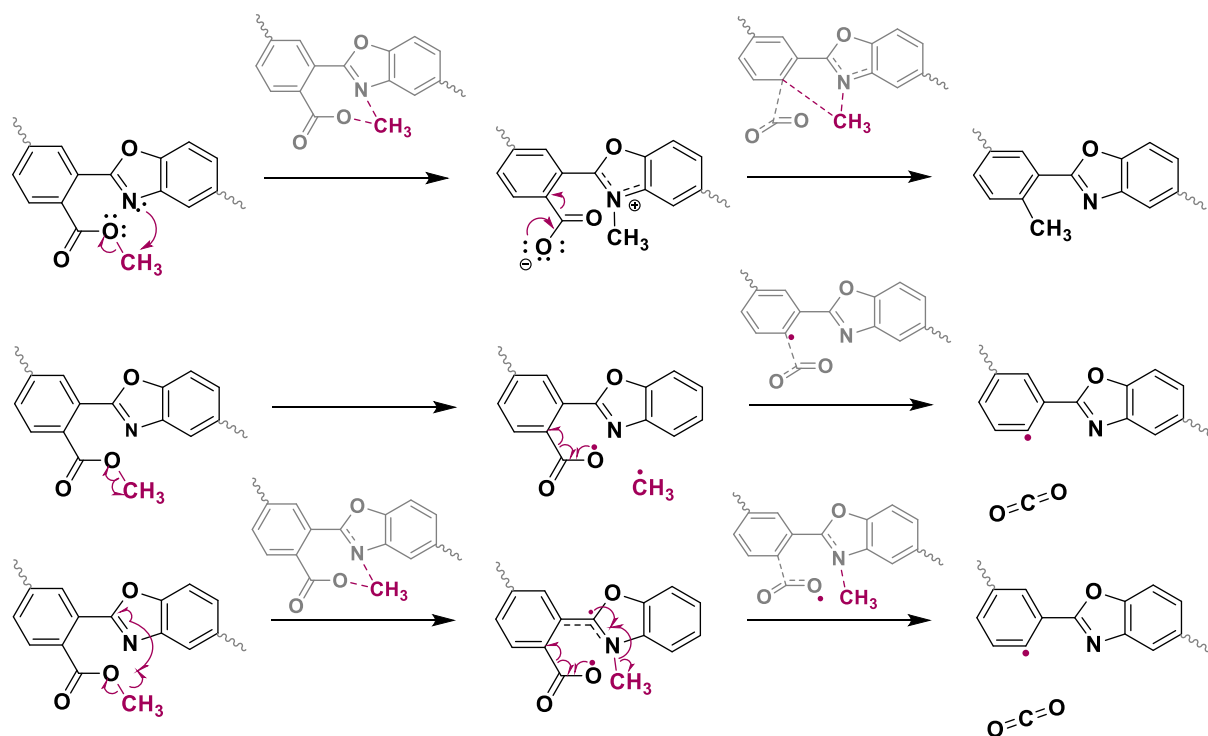


Scheme 34. Representations of potentially formed radicals upon radical demethylation of the starting molecule.

One very important open question from the performed DSC and TG-FT-IR experiments was, how the nearly simultaneous release of CO<sub>2</sub> and CH<sub>4</sub> can be explained in MeOPI-1. If the methyl group decomposes prior to the Thermal Rearrangement cascade via transition states TS1a, TS2d and TS3a2 (in HPI's), the detection of methane by means of coupled FT-IR spectroscopy should reveal an onset of the methane peak height profile before the CO<sub>2</sub> onset. However, the experiments have shown, that both gases are released at the same time. CO<sub>2</sub> starts even slightly earlier with respect to the temperature. Hence, a mechanism which does not release methane or a methane radical at an early stage is more reasonable. Among all discussed pathways, the reactions via TS2d (*ortho*-carboxylic methyl ester benzoxazole), TS2d2 (*N*-methyl lactone) and TS2g2 (*N*-methyl lactone-lactam) contain the methyl group until the last reaction step is approached. Since the lowest energy path via TS2d, transfer mechanism, is based on energetically aspects the most likely mechanism, and since no amide peaks were

detected via spectroscopic analysis, the formation of an *ortho*-carboxyl methyl ester benzoxazole structure is highly corroborated. Nevertheless, such a structure offers different possibilities to release CO<sub>2</sub> and CH<sub>4</sub>. Three reactions are demonstrated in Scheme 35.

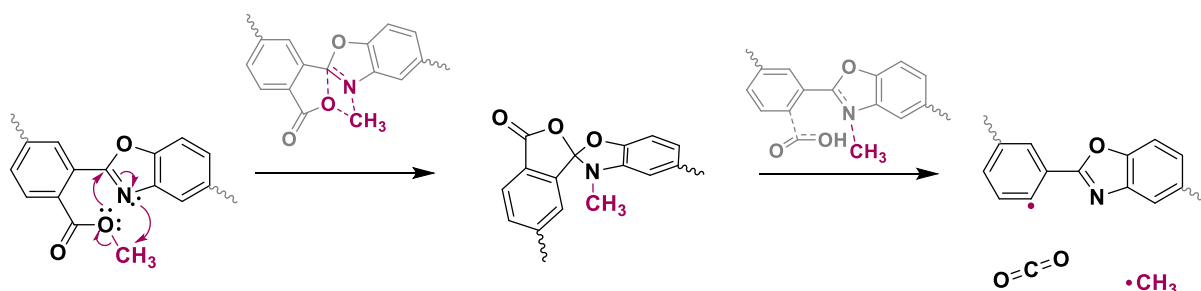
The first suggestion leads to the formation of an *ortho*-methyl group and no CH<sub>4</sub> release and is therefore unlikely. This process would be the analogous reaction to the third reaction of the TR reaction of HPI's (via TS3a2). The second mechanism is a radical decomposition, forming a CH<sub>3</sub> radical and decarboxylates subsequently. The formed phenyl radical would lead to biphenylene crosslinks afterwards. The third reaction involves the benzoxazole nitrogen atom as a catalyst, by transfer from the ester to the benzoxazole unit. Afterwards the carboxylic group decarboxylates and subsequently the *N*-methyl group decomposes. This would lead to a nearly simultaneous release of both gases.



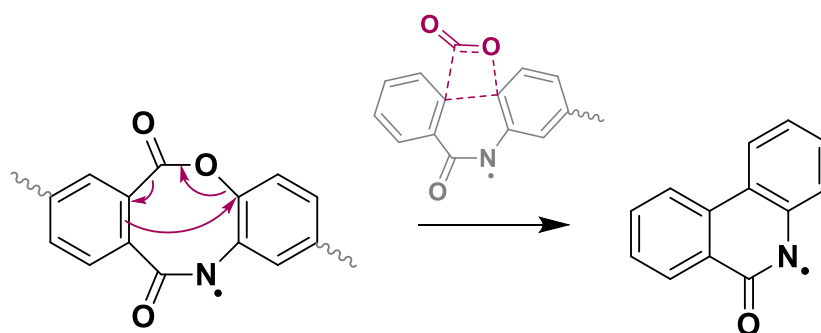
Scheme 35. Hypothesized mechanism for the decarboxylation reaction of the *ortho*-methyl ester benzoxazole.

However, the third process proceeds via a diradical, which is a highly reactive species. On the basis of these considerations a mechanism was evaluated, based on the third mechanism and the lactone pathway as demonstrated in Scheme 37. The first step involves the methyl cation transfer from the *ortho*-carboxylic ester to the sp<sup>2</sup>-hybridized benzoxazole nitrogen atom. In a concerted reaction the, now, negatively charged carboxyl group attacks the partially positive quaternary benzoxazole carbon atom. Consequently, a *N*-methylated oxazolidine-spiro-

lactone structure is formed. A second step is initiated by the radical homolysis reaction of the N-CH<sub>3</sub> bond. Subsequently the lactone ring opens via homolysis in order to re-form the benzoxazole structure. The formed carboxyl radical undergoes then a radical decarboxylation under formation of a phenyl radical structure (Scheme 36).



Scheme 36. Suggestion for the decarboxylation and demethylation mechanism of flexible methylated TR polyimide precursor in agreement with TG-FTIRFT-IR experiments.



Scheme 37. Decarboxylation mechanism for the formation of the lactam product.

## Acetylated *ortho*-Hydroxy polyimides

The modification of acetylated polyimides is no novelty and has been investigated by Sanders, Guo, Comesana, and Han *et al.* among other scientists [132, 140, 141]. These studies investigated mainly acetylated 6FDA-HAB, but acetylated 6FDA-APAF was investigated by Han *et al.* Each report focused on the decomposition and Thermal Rearrangement by means of TGA-MS experiments and the effect to the film properties, such as density, free volume, d-spacing and especially their gas separation performance. However, these studies did not investigate the thermochemical correlation between deacetylation and TR process in detail. None of the reported studies investigated the type of the reaction, whether intermolecular aspects affect the properties or only intramolecular mechanism. Furthermore, the backbone



effect was not part of a discussion and no simulations of the effect of the deacetylation on the thermophysical behavior was investigated. Therefore, despite the number of publications with regard to acetylated TRPs, there are still many open questions, which are important when it comes to the design of modified, in that case acetylated, TR precursor materials.

Hence, a TGA-FT-IR experiment was conducted and correlated with calorimetric measurements by means of DSC experiments. The results are shown in Figure 204. No weight loss until 250 °C was observed for MeCO<sub>2</sub>PI-1 (AcPI-1). With an onset temperature around 250 °C a weight loss is observed via thermogravimetric analysis. The weight loss proceeds until 294 °C and reaches a short plateau at 310 °C. At this point the materials lost a mass of 1.4%. According to the evolved decomposition gas analysis via on-line FT-IR spectroscopy, the released molecule is acetic acid. The DSC does not show a strong effect. The formation of acetic acid occurs as a consequence of the deacetylation reaction of the acetylated phenol units, and acetic acid is formed by residual moisture in the film and especially purge gas flux. The reason for the plateau might be the stabilization of the residual acetyloxy groups by the formed phenol groups, via hydrogen bonding. But the conversion of residual water content, might decrease the deacetylation rate. Nevertheless, at 320 °C the weight loss rate increases continuously until a maximum rate at 386 °C is reached, and another plateau is reached at 427 °C. At the maximum rate, a weight loss of 5.5% was recorded, while in total a weight loss of 10% was determined. The strong weight loss rate increase after passing 320 °C is mainly attributed to the Thermal Rearrangement reaction, since the evolved decomposition gas analysis revealed the detection of CO<sub>2</sub>. The CO<sub>2</sub> release is attributed to the TR related decarboxylation reaction.

The calorimetric shows an endothermic heat flow at 310 °C until a maximum is reached at 364 °C. At 410 °C the endothermic peaks change into a slightly exothermic heat flow, in case no base line shift occurs (Figure 204 and Figure 206).

From these observations, the drawn conclusion is that initially some acetylated groups start to deacetylate, probably catalyzed by residual water. However, after that initial deacetylation, the temperature is not sufficient enough to proceed without any catalyst. It is hypothesized, that the formed phenol groups stabilize the residual acetyl groups. After passing 320 °C the formed phenol groups undergo a benzoxazole formation accompanied by decarboxylation,

the Thermal Rearrangement reaction. The increasing temperature and loss of stabilizing phenol groups leads to an increase of the deacetylation rate. This correlates with the onset of the endothermic heat flow. The maximum heat flow is reached at 364 °C, which does not correlate with the maximum peak height profile of the acetic acid group. However, as the CO<sub>2</sub> peak height profile increases continuously and therefore the TR rate, which is correlated with an exothermic reaction, at 364 °C the TR exothermal heat flow appears to overcome the deacetylation induced endothermal heat flow. Since the deacetylation maximum is reached at 389 °C, the deacetylation rate decreases afterwards. At 410 °C the CO<sub>2</sub> release rate is surpassing the acetic acid release. At that point, the TR process becomes the primary process in the polymer film.

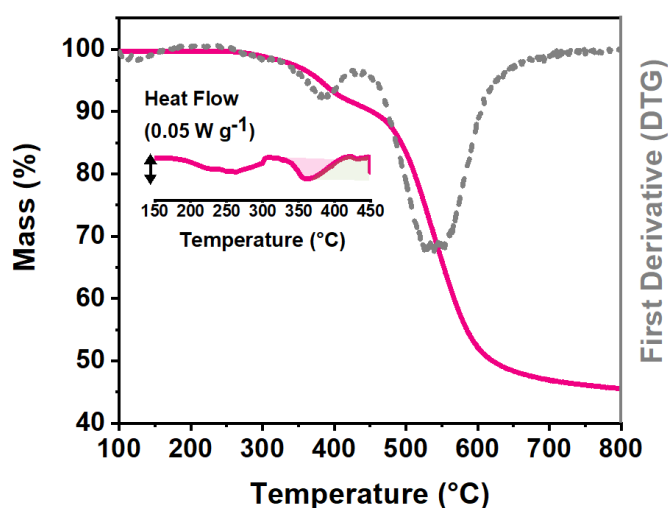


Figure 204. Mass loss curve obtained by means of TGA experiments of methylated 6FDA-BisAPAF (MeCO<sub>2</sub>PI-1) (pink). The first derivative (grey dashed) of the mass loss curve is shown[22].

Finally, another important aspect is that a weight loss of 10% at the following plateau at 427 °C does not correspond to a full conversion, which would be a weight loss of 18.3% (see Figure 205). Accordingly, either some acetyloxy groups remain at that temperature and therefore no TR process occurs, or the polymer becomes too rigid to proceed to full completion of the polybenzoxazole formation.

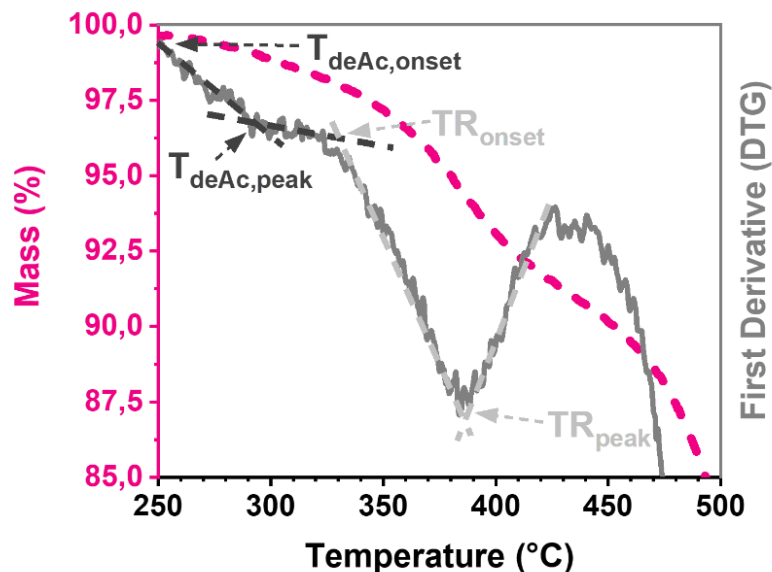


Figure 205. Mass loss curve and first derivative of MeCO<sub>2</sub>PI-1 including onset and peak temperature determination via tangent line evaluation (left)[22].

In order to answer the questions regarding to the possible products and conversion, the acetylated polyimide films were annealed at TR specific temperatures and treatment times, such as the methylated polymer films as well. The results are demonstrated in Figure 207.

At 350 °C after an annealing of 2 h, the phenolic O-H stretch vibration can be observed, other than in the methylated material. Furthermore, the intensity of the imide carbonyl peak at 1720 cm<sup>-1</sup> did not alter significantly. However, the carbonyl peak at 1780 cm<sup>-1</sup> which is attributed to the acetyloxy group, decreased strongly. Both results are in agreement, and suggest, that deacetylation of the acetyloxy groups occurred, while no subsequent TR reaction is necessarily initiated. Otherwise, no O-H vibration had been present, such as in the case of MeOPI-1. After annealing at 400 °C however, the imide carbonyl peak decreased significantly, and the acetyloxy carbonyl peak as well as the ester bond vibration at 980 cm<sup>-1</sup> disappeared completely. An increase of the weak benzoxazole related C=N stretch vibration at 1480 cm<sup>-1</sup> can be seen as well. These results suggest that a nearly quantitative deacetylation occurred at 400 °C and a high PBO formation conversion as well. Nevertheless, from results at 350 °C it is seen, that the deacetylation and TR process do not proceed to completion even after 2 h annealing time and that the formation of phenol groups does not lead to a consecutive TR reaction after each deacetylation step.

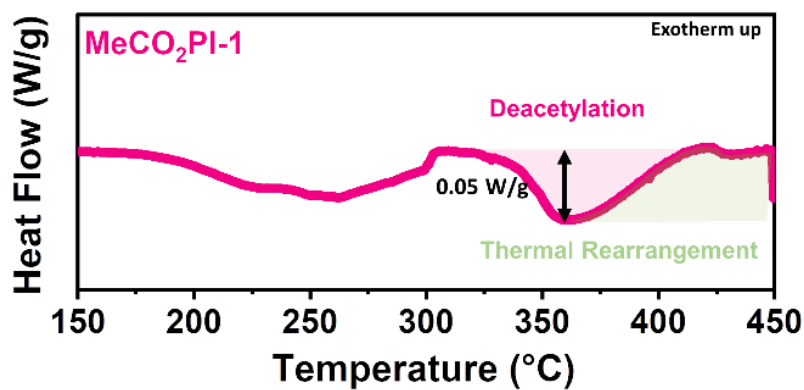


Figure 206. MeCO<sub>2</sub>PI-1 obtained by means of DSC experiments in the temperature range from 150 to 450 °C with a heating rate of 5 °C min<sup>-1</sup>. Deconvoluted peaks based on Gauss-Fitting are highlighted[22].

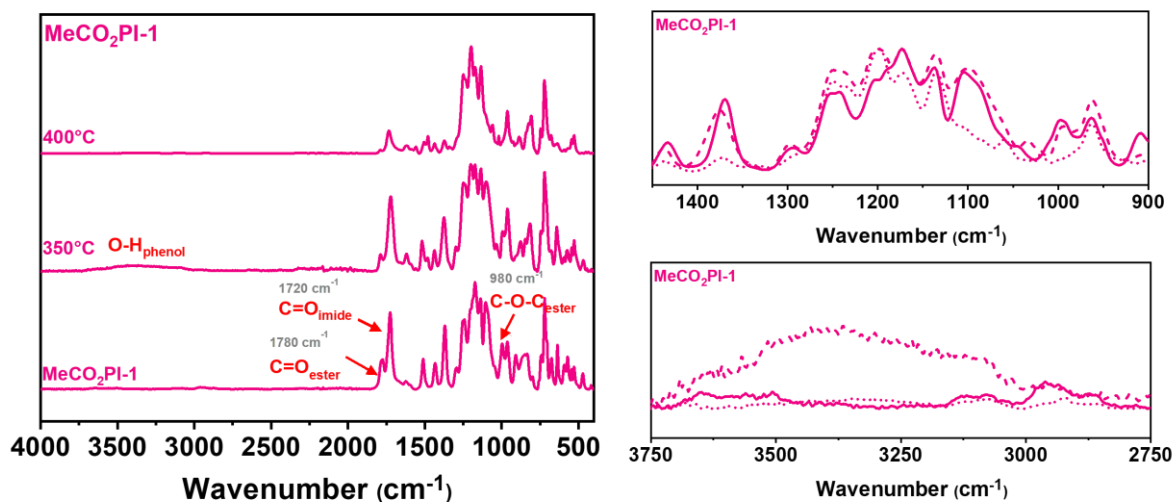
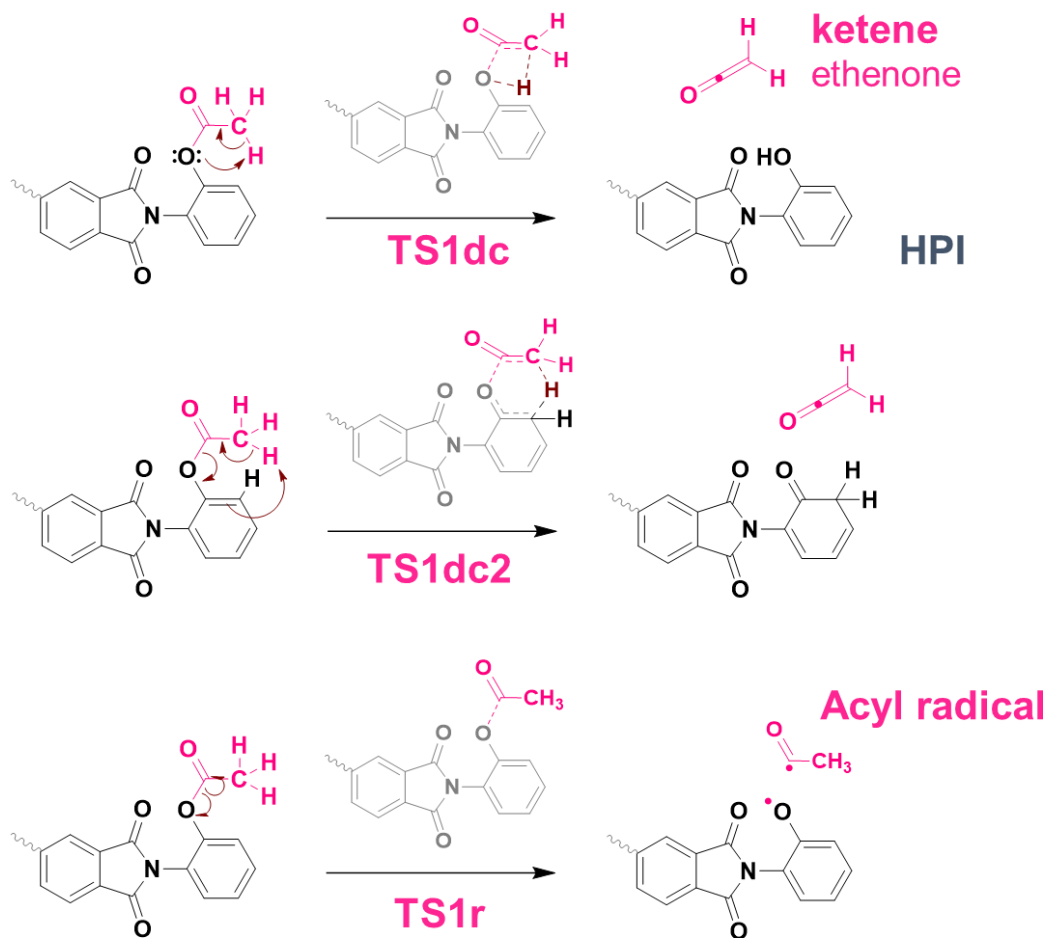


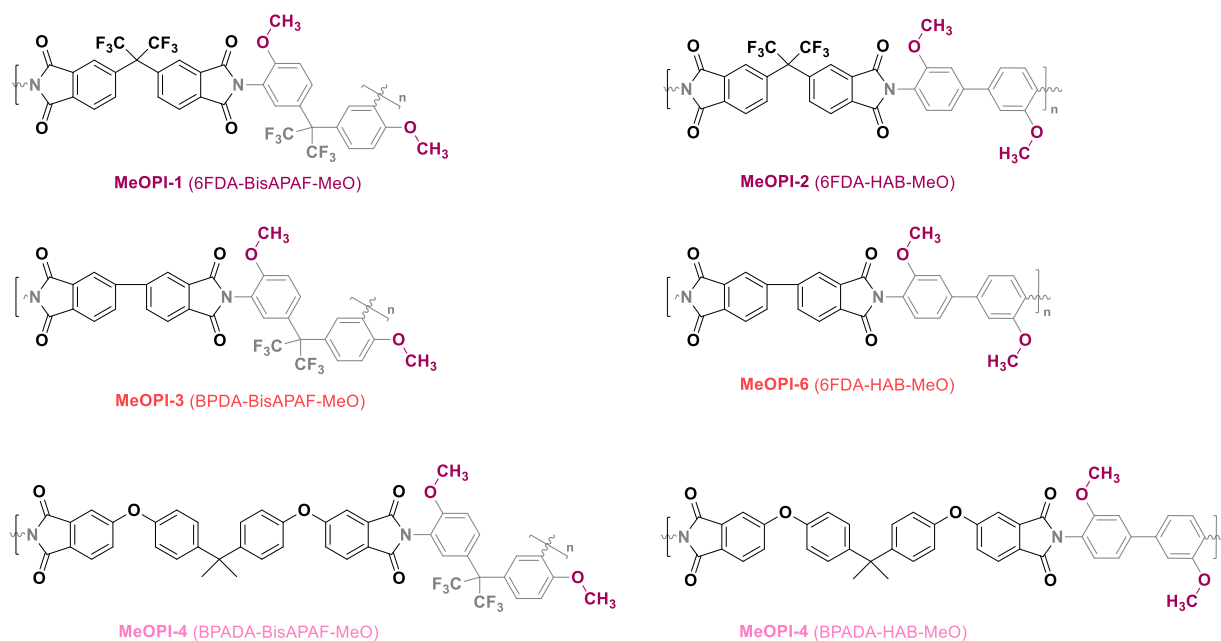
Figure 207. Stacked FT-IR spectra for MeCO<sub>2</sub>PI-1 after annealing at 80 °C (24 h), 350 °C (2 h), and 400 °C (1 h)(left). Zoom into the range from 2750 – 3750 cm<sup>-1</sup> (right, bottom) and 9000-1450 cm<sup>-1</sup> (right, top)[22].



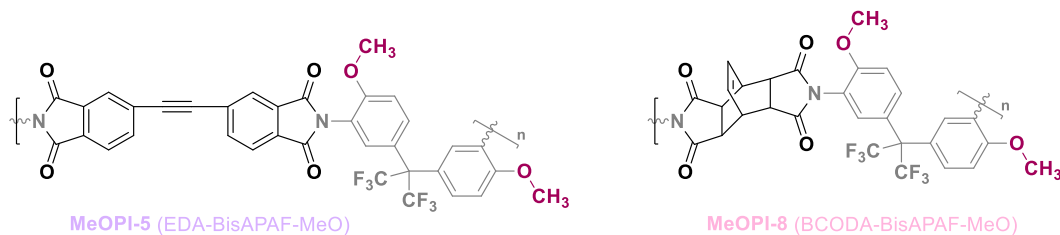
Scheme 38. Reaction mechanism of the deacetylation reaction via hydrogen transfer reactions TS1dc (top), TS1dc2 (middle) and radical decomposition via TS1r (bottom).

## Backbone effect

The results of the thermochemical reactions and conversion are not in agreement with the results for methylated 6FDA-HAB as reported by Comesana *et al.* [132]. Nevertheless, the DFT simulations and hypothesized TR mechanism of flexible *ortho*-methoxy containing polyimides were in agreement with the thermoanalytical experiments. The conclusion was, that the methyl group can be transferred to the imide carbonyl group according to the TR mechanism for unmodified TR precursor polyimides. Nevertheless, the mechanism can vary if the backbone is too rigid to undergo a TR process via methyl shift. As a consequence of methoxy group introduction, the free rotation of the phenol and imide group is hindered. Therefore, highly rigid backbones might not be able to provide the degree of flexibility to allow both units to enter a geometry which is appropriate for the initiation of the Thermal Rearrangement reaction.



Scheme 39. Synthesized methylated TR polyimide precursor for the effect of the diamine and dianhydride flexibility.



Scheme 40. Synthesized methylated TR polyimide precursor for the investigation of the effect of conjugated and aliphatic anhydrides.

In order to investigate the effect of the backbone in *ortho*-methoxy polyimides and the hypothesis of the presence of two mechanism for these systems, a set of methylated *ortho*-hydroxy polyimides was synthesized and thermoanalysis via TGA-FT-IR and DSC measurements was done. For that purpose, backbones with high and low glass transition temperatures were chosen (Scheme 39 and Scheme 40). Backbones with the more flexible diamine, BisAPAF, were MeOPI-1, -3, -4, -5 and -8. All other materials were based on the more rigid diamine, HAB. The lowest glass transition temperature backbone was based on BPADA (MeOPI-4 and -7), while the most rigid anhydride was BPDA (MeOPI-3 and -6). MeOPI-1 and -2 were based on 6FDA as anhydride. MeOPI-2 was synthesized according to the procedure, described by Comesana *et al.* [132], in order to obtain the same chemical composition for comparison reasons.

The experimentally determined heat flow curves were investigated by means of DSC experiments. The results are shown in Figure 208. The heat flow curves for the BisAPAF

containing polymers show an exothermic increase with onsets in the range from 310 °C (MeOPI-5) to 321 °C (MeOPI-1). These materials show an exothermic peak, while all HAB-based polymers did not show such a peak, while an exothermic increase appears to start at the end of the measurement at about 420 °C. This observation indicates that the more flexible *ortho*-methoxy polyimides undergo an exothermic chemical reaction at temperatures below 400 °C, while the more rigid HAB-based polyimides were not able to undergo such a reaction below 400 °C. However, it is worth to notice that the BisAPAF based polyimides MeOPI-1, -3 and -4 do not show a strong variation of the onset and peak temperature of the exothermic heat flow peak despite their strong variations of the glass transition temperature.

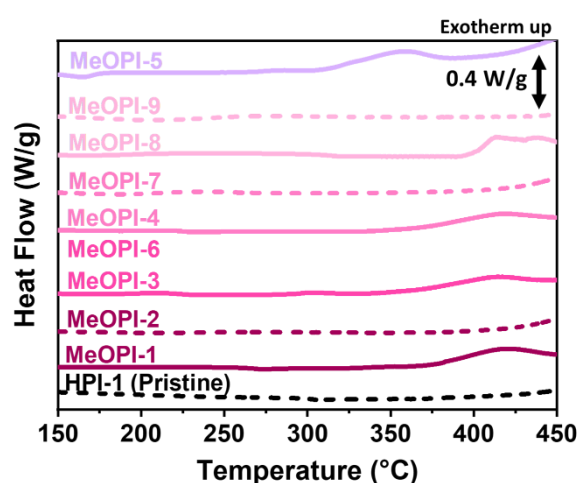


Figure 208. Measured heat flow by means of DSC experiments for all methylated polyimides. Straight lines are BisAPAF based polymers and dashed lines are based on HAB containing polyimides. The heat flow curve of the pristine unmodified polyimide 6FDA-BisAPAF is shown as dashed black line.

Thermogravimetical measurements were executed in order to confirm the correlation of the exothermic reaction with methane and CO<sub>2</sub> mass loss, as described for MeOPI-1, while no weight loss occurs for the more rigid polyimides below 400 °C. The results are shown in Figure 209. Among the tested materials, all BisAPAF containing materials, including the pristine polyimide, show a mass loss step. Furthermore, the trend of the mass loss step of the polymers MeOPI-1, -3, -4 and -5 shows the same relationship to each other as determined by means of DSC experiments. This means, that MeOPI-5, which showed the lowest onset temperature of the exothermic reaction in the DSC, did also show the lowest mass loss onset temperature. While MeOPI-1, -3 and -4 did not show any strong variation of the onset and peak temperature for the reaction, the TGA curves were very identical for all materials. MeOPI-8, which was the

only aliphatic anhydride containing polyimide, showed a broad exothermic heat flow curve above 400 °C in the DSC, which correlates well with a strong mass loss at 400 °C.

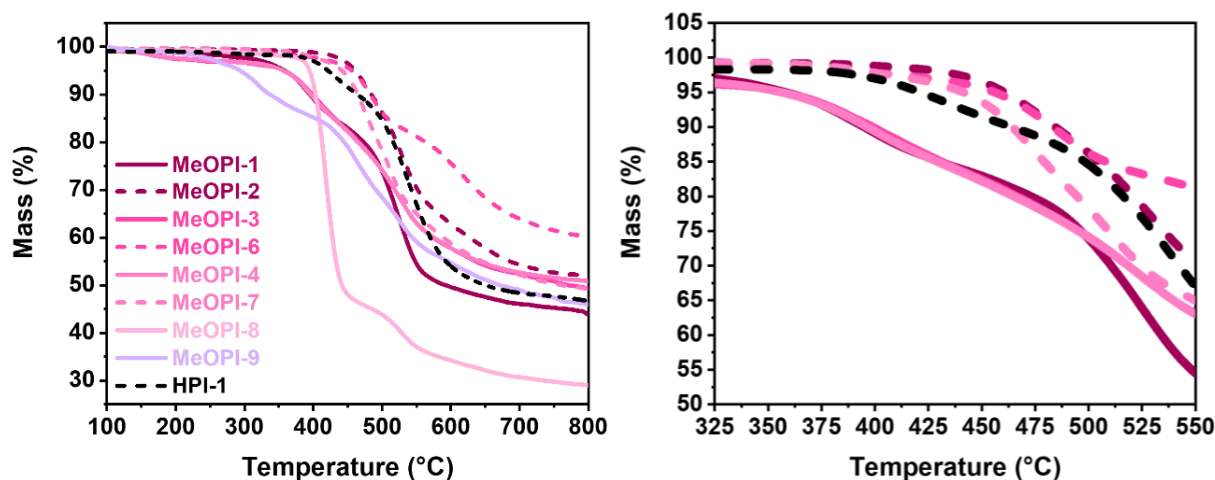


Figure 209. Measured mass loss by means of TGA experiments for all methylated polyimides. Straight lines are BisAPAF based polymers and dashed lines are based on HAB containing polyimides. The mass loss curve of the pristine unmodified polyimide 6FDA-BisAPAF is shown as dashed black line (left). Zoom into the range from 325 to 550 °C for MeOPI-1, -2, -3, -4, -6, and -7 (right).

Moreover, the results in Figure 209 reveal as well, that all HAB-based *ortho*-methoxy polyimides show significantly higher onset temperatures for the mass loss, which is in agreement with the significantly higher onset of the exothermal heat flow in the DSC experiments. These materials showed similar onset temperatures for the exothermic heat flow, which is also in agreement with the mass loss related reaction according to the TGA for all materials.

Finally, it is worth to mention, that the methylation of BisAPAF based precursors reveals two strong advantages with regard to the major task in the field of Thermally Rearranged polyimide membranes to lower the  $TR_{\text{onset}}$  temperature. The methylation caused a decrease of the  $TR_{\text{onset}}$  temperature by 60 °C in the case of 6FDA-APAF (HPI-1) and MeOPI-1.

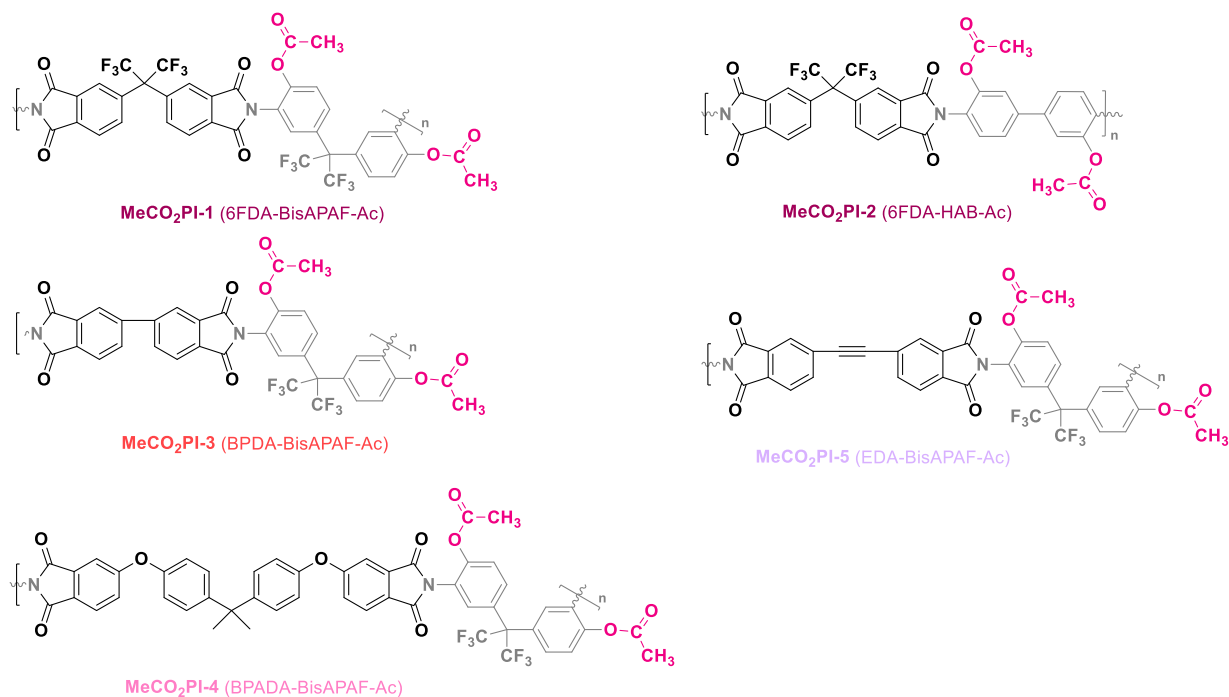
Methylated polyimides show in both cases, that the amine's flexibility enables initiation of the TR reaction, and therefore the reason, whether a methylated precursor undergoes the methyl shift TR reaction or radical demethylation TR reaction. Moreover, the initiation of the TR reaction depends mainly on the rotation around the dihedral angle between the phenol and imide unit, which leads to an increase of the  $TR_{\text{onset}}$  temperature of low- $T_g$  precursors and lowers the  $TR_{\text{onset}}$  temperature for high- $T_g$  polyimides. While most high- $T_g$  precursors show



rigid backbones with a lack of the degree of mobility, they also are usually more efficiently packed. The methylation leads to a chain packing disruption and induces a higher degree of freedom for translation. Flexible precursors, however, lose their advantage, as the steric hindrance of the introduced methyl groups decrease the flexibility around the imide bond. Therefore,  $T_{R_{onset}}$  temperatures come closer to each other. In the case of the HAB-based polyimides, the methoxy group needs to decompose radically as initiation for the consecutive TR reaction. This intramolecular process is affected by the electronic properties of the aromatic backbone, but only slightly. Therefore, the initiation of the TR reaction depends on the homolytic break of the ether bond, which has about the same magnitude for each backbone. Since the homolytic cleavage requires more energy than the methyl shift, the required temperatures for the TR initiation are significantly higher.

The Thermal Rearrangement of acetylated polyimides has shown to occur after deacetylation of the acetyloxy groups to ketenes or carboxylic acid prior benzoxazole cyclization reaction. Therefore, other than methoxy group containing precursors, the change of the flexibility of the backbone is expected to have no significant effect, since the deacetylation occurs intramolecularly within the phenol unit. No Thermal Rearrangement proceeds via acetyl group transfer. However, from the investigation of acetylated 6FDA-BisAPAF, MeCO<sub>2</sub>PI, the conclusion was drawn, that formed phenol groups might stabilize the acetyl groups prior 320 °C.

The heat flow curves for acetylated backbones are shown in Figure 210. Four BisAPAF based acetylated polyimides and one HAB-based acetylated polyimide, MeOPI-2, were investigated. In all cases an endothermic heat flow above 300 °C was determined. The comparison of the BisAPAF based polymer precursors demonstrates, that the lowest onset temperature was determined for the most rigid backbone MeOPI-3, while the highest onset temperature was determined for the most flexible backbone MeOPI-4. MeOPI-5 shows a lower onset temperature than the more flexible MeOPI-1. This means, that the deacetylation onset temperature increases with increasing flexibility of the anhydride, since glass transition temperature and deacetylation temperature are inverse to each other.



Scheme 41. Synthesized acetylated TR polyimide precursors for the effect of the diamine and dianhydride flexibility.

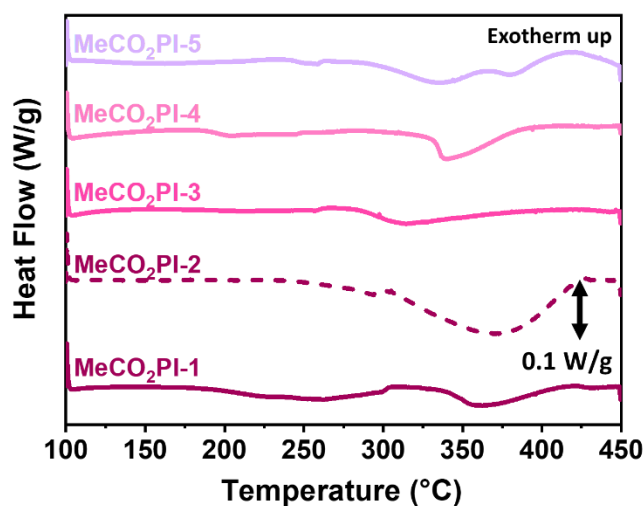


Figure 210. Measured heat flow by means of DSC experiments for all acetylated polyimides. Straight lines are BisAPAF based polymers and dashed lines are based on HAB containing polyimides.

The HAB based MeOPI-2 shows a low deacetylation onset at about 270 °C as well, but a very broad peak for the deacetylation up to 410 °C. This observation is more likely to explain because the observed heat flow shows the additive heat flow from the endothermic deacetylation and exothermic Thermal Rearrangement which overlap at a certain point. At the beginning only deacetylation occurs, but once the deacetylated groups are present, they are capable to undergo the TR process. With increasing temperatures and proceedings of both reactions, the exothermic heat flow overcomes the endothermic heat flow. In all BisAPAF

based acetylated polymers, the HPI-1 precursor is recovered after deacetylation, which has a significantly lower  $TR_{\text{onset}}$  temperature compared to the recovered 6FDA-HAB from MeOPI-2. Accordingly, the TR reaction occurs at higher temperatures, therefore no TR caused exothermic heat flow occurs and only the endothermic heat flow can be detected, as the TR process initiates at higher temperatures. This might also explain, why the intensity of the endothermic peak of MeOPI-2 is significantly stronger compared to each other material.

The TGA experiments are shown in Figure 211. The mass loss curves reveal that the lowest onset for the mass loss was observed for MeCO<sub>2</sub>PI-5, followed by MeOPI-1 and -2 which are close to each other. The highest onset was determined for MeCO<sub>2</sub>PI-1. There exists no correlation between backbone flexibility and TR reaction onset.

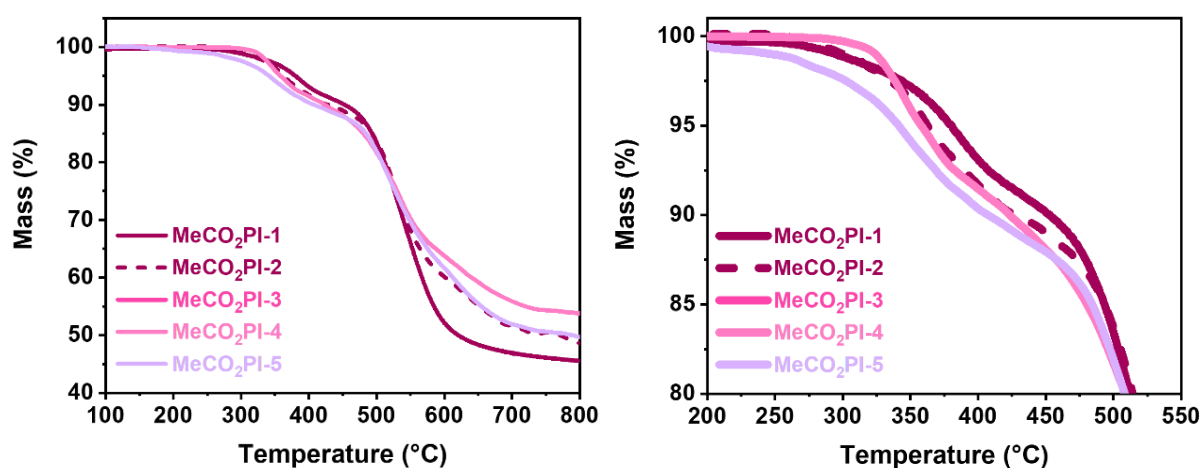


Figure 211. Measured mass loss by means of TGA experiments for all acetylated polyimides. Straight lines are BisAPAF based polymers and dashed lines are based on HAB containing polyimides (left). Zoom into the range from 200 to 550 °C for MeCO<sub>2</sub>PI-1, -2, -3, -4 and -5 (right).

The investigations have shown, that a very strong discrepancy between the modification group decomposition and Thermal Rearrangement mechanism between both types of modifications, but also a very different correlation between modification and backbone effect has been seen. While methoxy groups are not able to undergo an elimination reaction by abstraction of a proton from a C $\beta$  atom, the comparison is in terms of the decomposition mechanism rather difficult. The hydrogen transfer from CH<sub>3</sub> to the phenolic oxygen atom would lead to decomposition by formation of a highly reactive carbene, which is very unlikely according to the DFT simulation.

## Ethylated *ortho*-Hydroxy Polyimides

In order to compare ether and ester modifications, based on similarly large modification groups with the same possibility to undergo an elimination reaction, an ethoxy modification was investigated. The difference between the acetyloxy and ethoxy group is the presence of a carbonyl group on C $\alpha$  in case of MeCO<sub>2</sub>PI-1.

An overview of the mass loss-temperature relationship and its first derivative, as well as the peak height profile for ethylene and CO<sub>2</sub> attributed signals from evolved gas analysis are plotted for EOPI-1. In addition, the heat flow curve from DSC measurements is shown in Figure 212 and Figure 213.

No mass loss below 300 °C was detected. The onset of the mass loss starts at 327 °C according to evaluations from the mass loss curve but first derivative as well (Figure 213). The onset of the mass loss is attributed to the loss of CO<sub>2</sub> according to the CO<sub>2</sub> peak height profile. Fitting of the CO<sub>2</sub> peak height profile has shown that only one peak can be fit, so no further peak deconvolution was modeled. Accordingly, only one process is assumed to be responsible for the decarboxylation reaction. However, the onset of the ethylene release was determined at slightly higher temperatures of 345 °C. The peak temperature for the CO<sub>2</sub> and ethylene release was observed at 396 and 407 °C, respectively. After the onset temperature was passed, the CO<sub>2</sub> peak height profile increased continuously. It is interesting to notice, that the unsaturated alkyl group is released, whereas methylated polyimides have shown, that the saturated alkyl group, namely CH<sub>4</sub>, was formed.

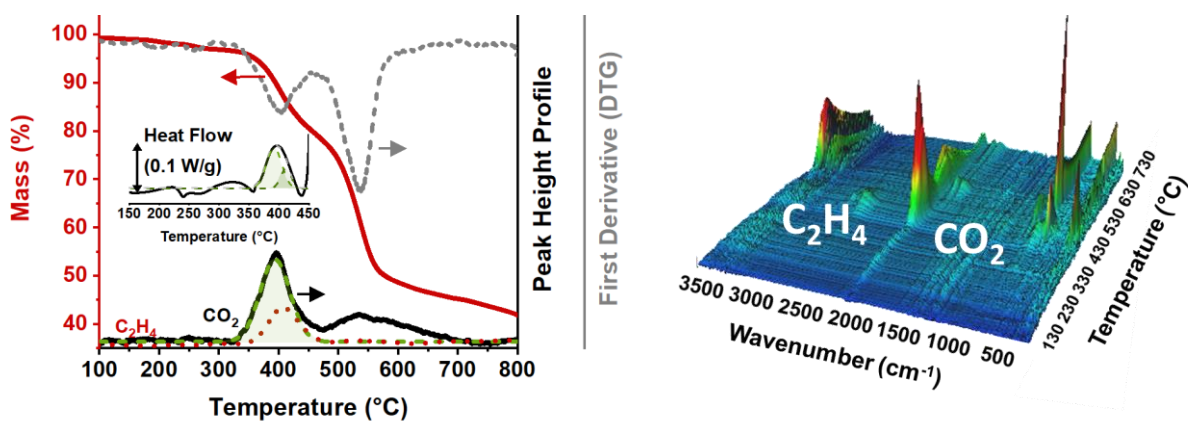


Figure 212. Temperature related mass loss curve for EOPI-1 (red). The CO<sub>2</sub> (black) and C<sub>2</sub>H<sub>4</sub> (red dashed) peak height profile from evolved gas analysis as well as the first derivative (grey dashed) of the mass loss curve is shown (left). The three-dimensional plot of all stacked FT-IR spectra (right)[22].

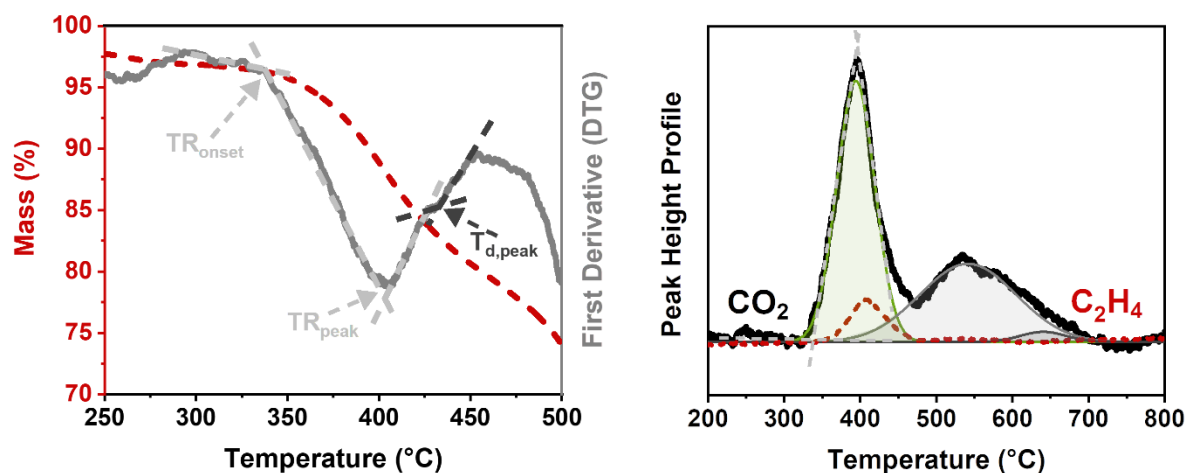


Figure 213. Mass loss curve and first derivative of EOPI-1 including onset and peak temperature determination via tangent line evaluation (left). Peak height profile of CO<sub>2</sub> including peak deconvolution and determination of the onset and peak temperatures via tangent line evaluation method (right) [22].

Therefore, an elimination reaction is assumed similar to the elimination process of acetyl groups to the corresponding ketene. Accordingly, an elimination and phenol recovery in agreement with the acetyloxy mechanism is expected, followed by a conventional Thermal Rearrangement process of the then formed *ortho*-hydroxy polyimide HPI-1.

The heat flow curve in Figure 214 shows a strong exothermic peak starting at 326 °C, and a peak temperature at 420 °C. Peak deconvolution revealed two peaks, attributed to two exothermic processes accordingly. Deconvoluted peaks start at 326 °C, respectively. Their peak temperatures are at 345 and 424 °C.

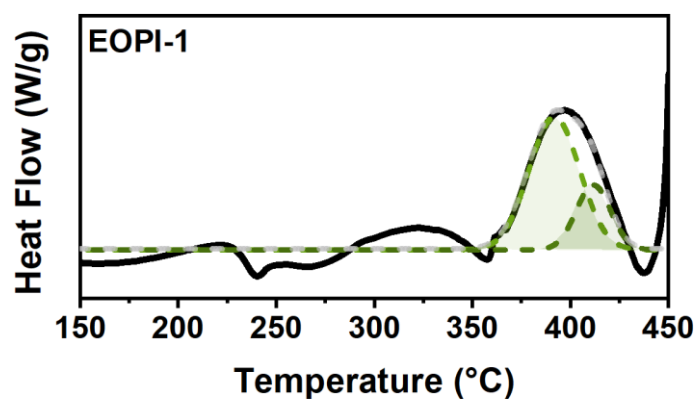


Figure 214. Heat Flow curve of EOPI-1 measured by means of a DSC experiment at a heating rate of  $5\text{ }^{\circ}\text{C min}^{-1}$ . [22]

In Figure 215 the mass loss curves, and their first derivatives are shown for EOPI-1 after annealing the corresponding film at  $350\text{ }^{\circ}\text{C}$  and  $400\text{ }^{\circ}\text{C}$ , as described for MeOPI-1 and MeCO<sub>2</sub>PI-1 as well. After annealing at  $350\text{ }^{\circ}\text{C}$  for 2 h a very strong shift of the decomposition onset temperature to  $420\text{ }^{\circ}\text{C}$  was determined and no pronounced step was observed. The conversion of all ethoxy groups was determined to 72%. Annealing at  $400\text{ }^{\circ}\text{C}$  shifted the decomposition onset temperature of the film even more to  $461\text{ }^{\circ}\text{C}$ . The conversion for a TR process was calculated to be 93.3%. EtOPI-1, EthoxyPI, shows a strongly decreased TR<sub>onset</sub> temperature compared to the pristine polymer. The TR<sub>onset</sub> was determined to be  $59\text{ }^{\circ}\text{C}$  lower. Hence, the introduction of ethyl groups appears to be a promising method to lower the TR<sub>onset</sub> temperature as well.

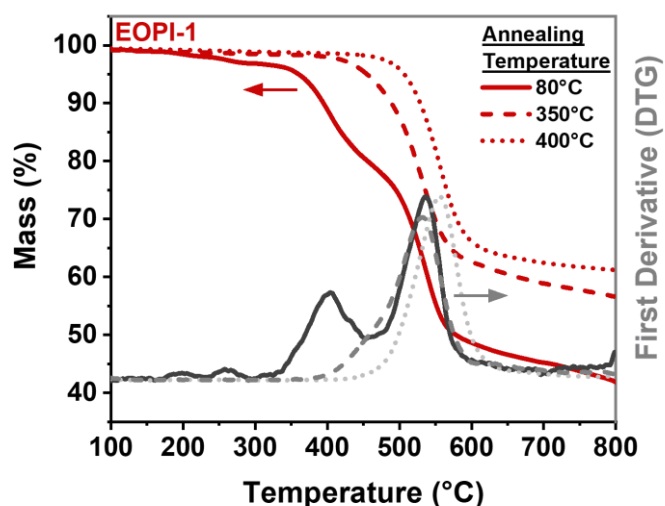


Figure 215. Temperature related mass loss curve for EOPI-1 (red) as well as the first derivative (grey) of the mass loss curve is shown after annealing at  $80\text{ }^{\circ}\text{C}$  for 24 h,  $350\text{ }^{\circ}\text{C}$  for 2 h and  $400\text{ }^{\circ}\text{C}$  for 1h [22].

The thermochemical behavior of EOPI-1, in comparison to the methylated and acetylated polymers, performed similar to the methylated version. From simulation and mechanism evaluations in combination with thermoanalytical and spectroscopical investigations, the methylated model reactions were significantly different from the acetyloxy models. Since methyl groups do not have a C $\alpha$  atom, such as acetyl groups, the elimination mechanism via formation of an unsaturated releasing group is not possible. From that point of view, the ethyl modification is able to undergo an acetyloxy group analogous decomposition reaction, since it differs only in the absence of the carbonyl oxygen atoms and contains a C $\alpha$  atom as well. Therefore, a competition between a methyl-transfer and acetyl elimination -analogous reaction is reasonable. For that reason, FT-IR spectroscopy experiments were executed after treatments at TR polymer typical annealing procedures (see Figure 216). The clearly detected ether stretch vibrations from the phenyl ethyl ether bonds are shown by stretch vibrations for the ether bond at 1100 cm<sup>-1</sup> and the C-H stretch vibration of the ethyl group at 2940 cm<sup>-1</sup> can be monitored. After annealing at 350 °C both vibrations nearly completely disappeared. Furthermore, the carbonyl group at 1720 cm<sup>-1</sup> decreased significantly, while a weak C=N stretch vibration from the formed benzoxazole ring was observed. It is noteworthy, that the phenol O-H vibration did not evolve as a consequence of the annealing. This is in contrast to the observations of the acetylated polyimide, which did show an O-H vibration. This means that an ether bond breaking reaction occurs, without regenerating a phenol group. Further heating decreases the carbonyl group even more, but no hydroxy vibration from re-formed phenol units was observed. This observation is in agreement with the results for MeOPI-1. MeOPI-1 is expected to undergo a concerted methyl transfer and nucleophile cyclization reaction of the phenolate-imide unit. Therefore, the methyl ether bond broke, while no phenol was formed. Acetylated polymers demonstrated that the acetyl group decompose at the beginning and forms phenol groups, which were recorded via FT-IR spectroscopy. These findings are in agreement with the similar heat flow pattern of MeOPI and EOPI. This suggested a similar reaction with similar reaction enthalpies. Nevertheless TG-FT-IR experiments revealed the formation of ethylene, which would be an elimination product.

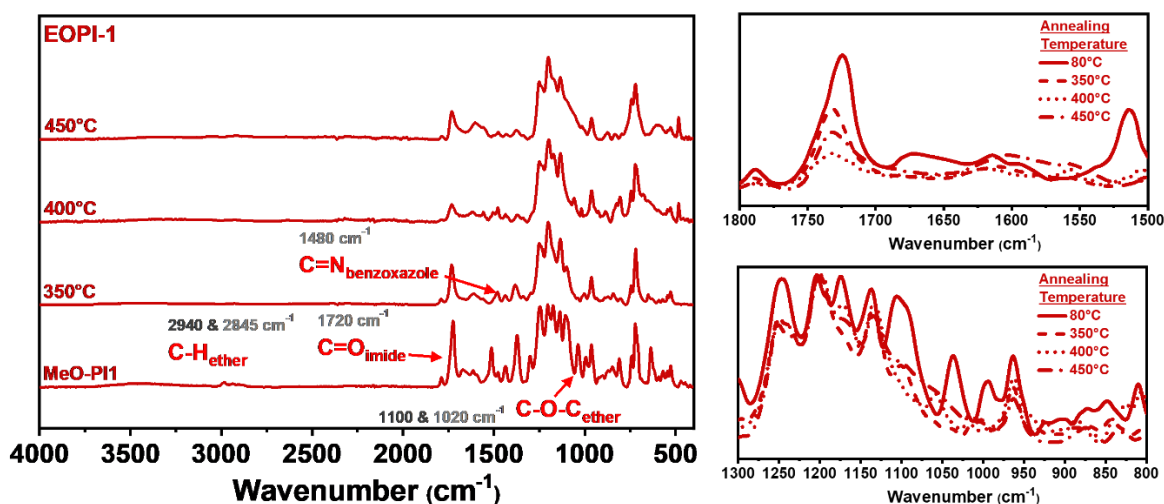


Figure 216. Stacked FT-IR spectra for EOPI-1 after annealing at 80 °C (24 h), 350 °C (2 h), 400 °C (1 h) and 450 °C (0.5 h) (left). Zoom into the range from 1500 –18 00  $\text{cm}^{-1}$  (right, top) and 800-1300  $\text{cm}^{-1}$  (right, bottom)[22].

Therefore, DFT simulations were used to support the experimental finds and answer the question, why heat flow, mass loss and spectroscopic data point to a mechanism, which is identical to MeOPI. The formation of ethylene, however, suggest, an elimination reaction of the ethyl group at the end of the reaction, for which reason, ethylene and  $\text{CO}_2$  are detected around the same time. In Figure 217 the simulated reaction coordinate is shown. Three reactions, which lead to a direct loss of the ethene group were simulated. These are the decomposition mechanisms via TS1b and TS1b2, which are elimination reactions via hydrogen shift from the ethyl  $\text{C}_\beta$  atom to the phenol oxygen atom in case of TS1b. This mechanism proceeds analogously to the elimination of the acyl group of  $\text{MeCO}_2\text{PI}$  to the corresponding ketene. In addition, a second elimination pathway was simulated, but proceeded via a two-step mechanism and had in total a higher energy due to an activation energy of  $86 \text{ kcal mol}^{-1}$  for the highest energy step of that pathway (TS2b2). The first step is a hydrogen shift from  $\text{C}_\beta$  of the ethyl group to the aromatic C atom *ortho* to the ethoxy group and formation of a cyclohexadienone. The second step is the hydrogen transfer to the phenone carbonyl group under re-aromatization. This process is principally a Keto-enol tautomerization. The third process is a radical decomposition, which is energetically slightly higher compared to the first elimination reaction. The transition state geometries and intermediates of these three mechanisms are shown in Figure 218, the reaction mechanism is shown in Scheme 42 and Scheme 43.



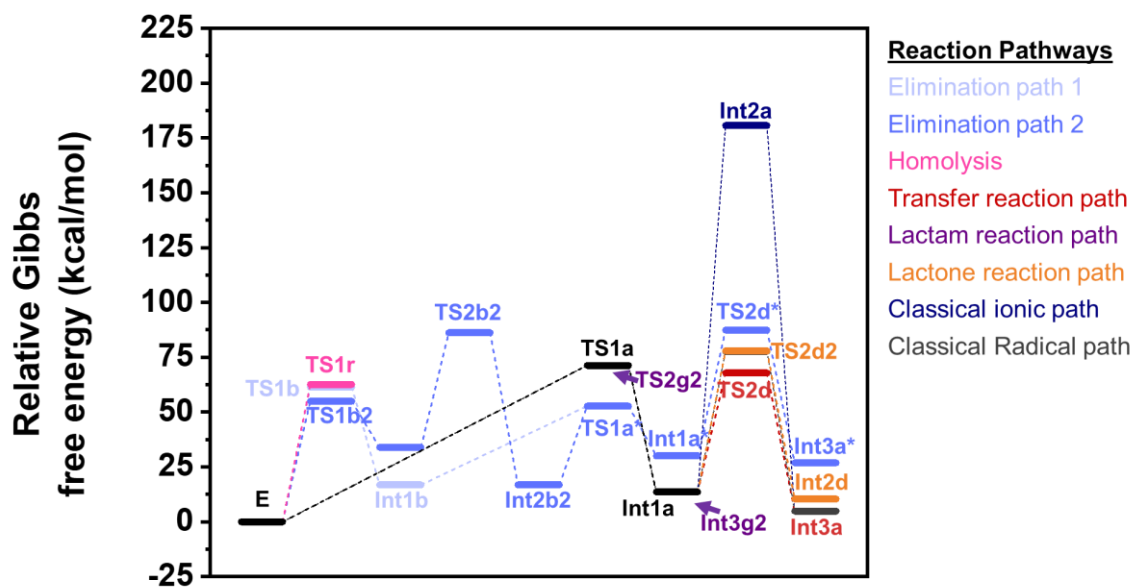


Figure 217. Reaction coordinate of the ethoxy decomposition and Thermal Rearrangement reactions of ethylated phenol-phthalimide models by means of DFT simulations.

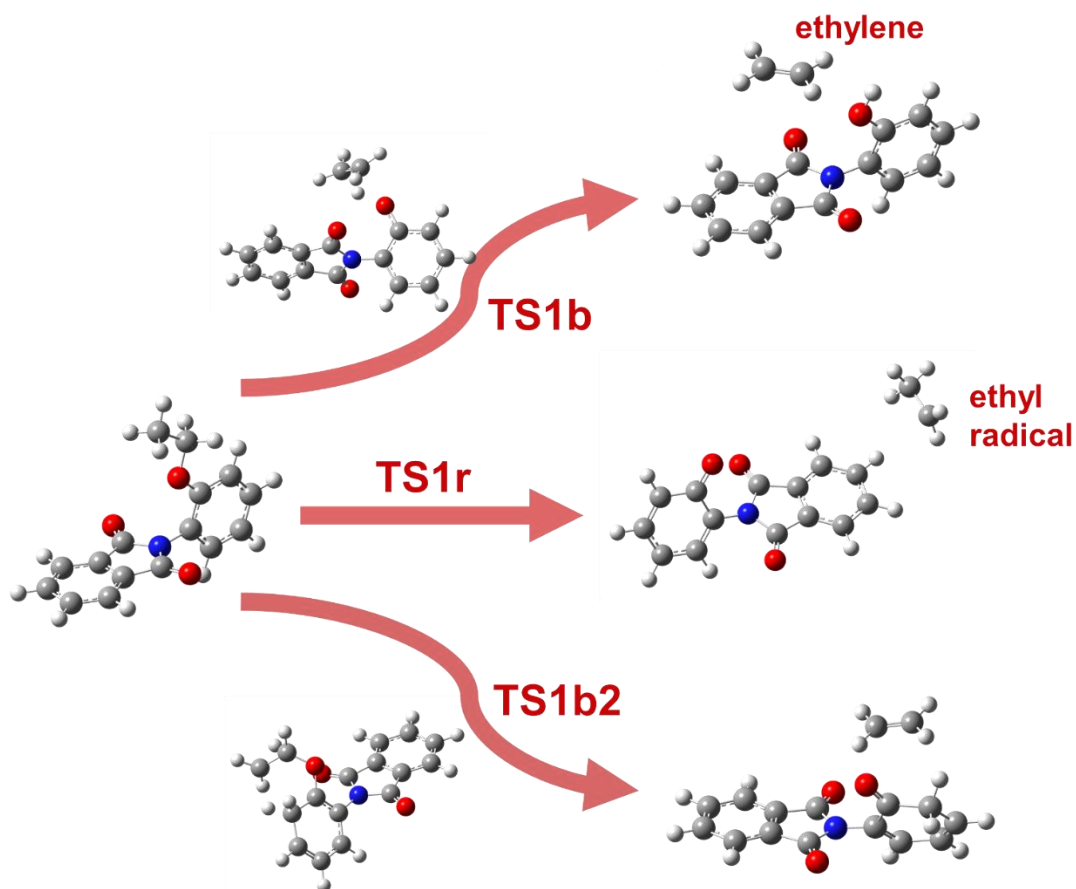
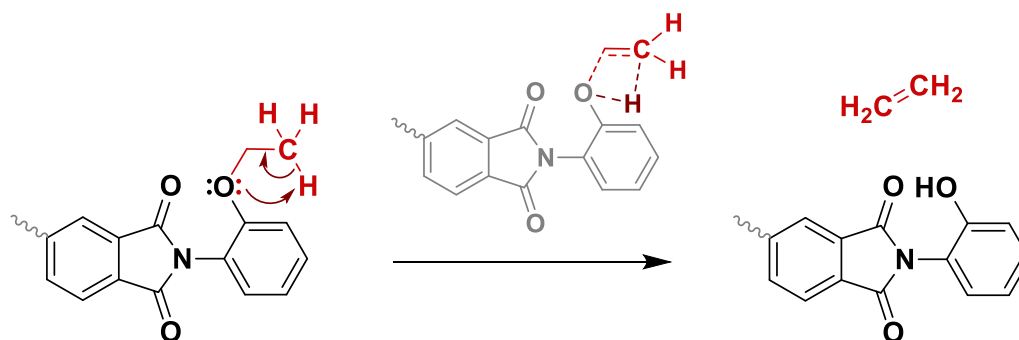
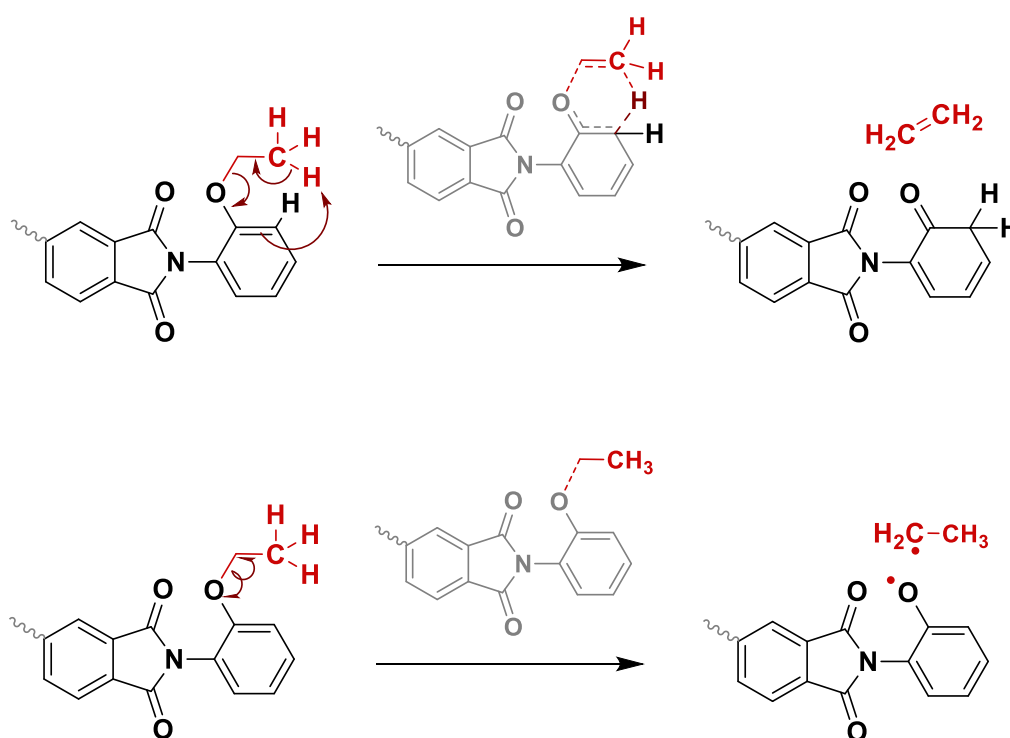


Figure 218. Starting ethoxy containing phenol-phthalimide model and the three ethoxy decomposition reactions via elimination reactions, TS1b and TS1b2, and the radical decomposition TS1r.



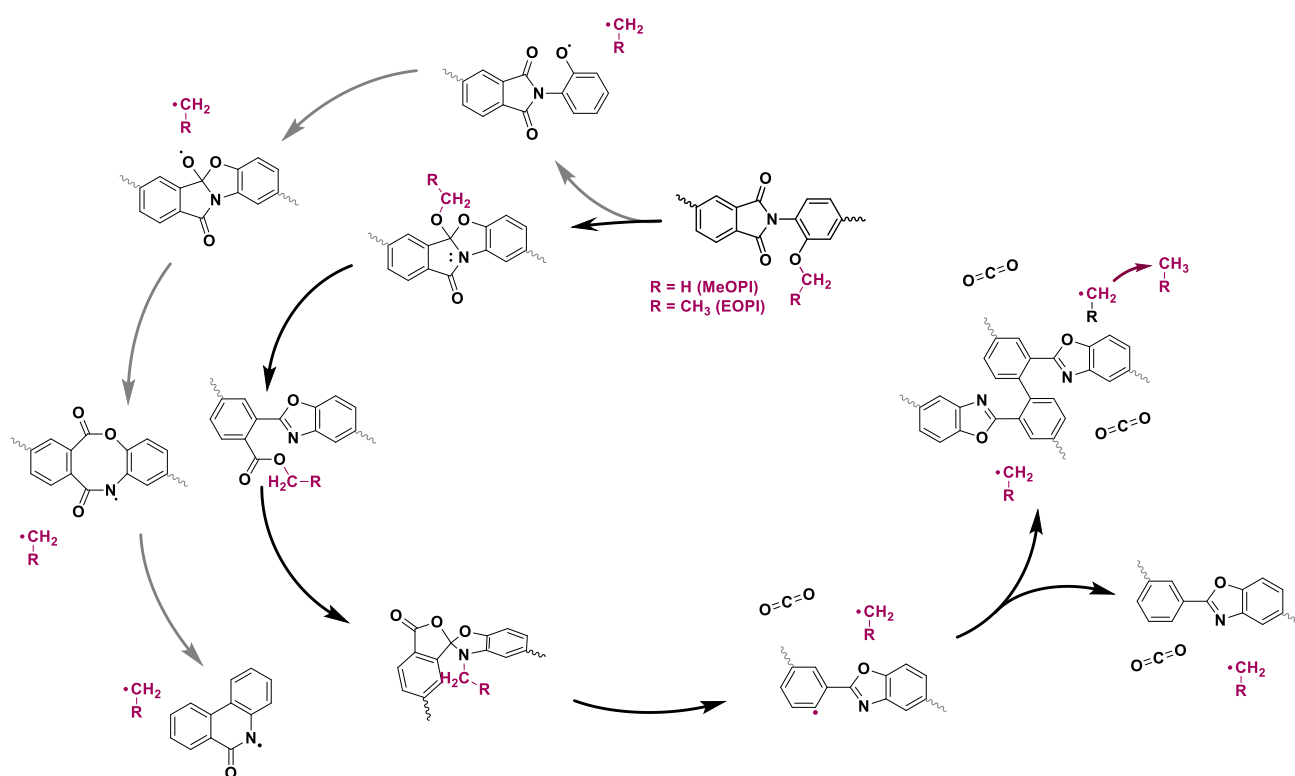
Scheme 42. Elimination of the ethoxy group via intramolecular hydrogen shift and recovery of the ortho-hydroxy imide in one step (TS1b).



Scheme 43. First step of the elimination of the ethoxy group via intramolecular hydrogen shift and recovery of the ortho-hydroxy imide via two-step reaction mechanism ((TS12b)) (top). Radical decomposition of the ethoxy group via TS1r (bottom).

The products of the decomposition reactions are ethylene and the *ortho*-hydroxy polyimide, which can then undergo a Thermal Rearrangement reaction according to the transfer mechanism. In contrast, an ethyl-group transfer mechanism based on the transfer mechanism for unmodified TRP and identical to the methyl transfer reaction of MeOPI via TS2a showed the transition state and intermediate geometries as well following the lowest energy reaction coordinate. The first step of this transfer reaction is with 78 kcal mol<sup>-1</sup> higher compared to the elimination reaction 1 with 61 kcal mol<sup>-1</sup> (TS1b) and radical decomposition with 62 kcal mol<sup>-1</sup>

(int1r). Nevertheless, following the consecutive reaction coordinates for each pathway, the ethyl transfer mechanism is the lowest energy path, since the second step, the nucleophilic reaction of the ethoxy group within int1a, is about 20 kcal mol<sup>-1</sup> lower. The conventional ionic reaction and its radical pendant have higher energies as well. The energy for the lactone formation of the lactone path via TS2d2 is about 3 kcal mol<sup>-1</sup> higher compared to MeOPI. Therefore, in total, the ethyl transfer mechanism similar to MeOPI is energetically preferred, but due to the small differences in energies, and the irreversibility of the decomposition, and therefore non-reversibility of the reaction, both processes are in competition to each other. However, since spectroscopic measurements did not show any phenol groups, and the evolved gas analysis of the TGA-FT-IR experiment did not show that ethylene left the system prior to CO<sub>2</sub>, the simulation findings and experimental results support the transfer mechanism for EOPI models (Scheme 44).



Scheme 44. Proposed thermally initiated decomposition cascade reaction of ortho-methoxy and ortho-ethoxy containing polyimides.

## Alkyloxy modifications

The thermochemical reactions of methoxy and ethoxy groups *ortho* to the imide units were investigated in detail. However, a better understanding of reaction mechanism and which structural aspects affect the thermochemical and thermophysical behavior in a certain way are best described by analyzing the effects of variations of the chemical composition of those groups. In addition to methoxy and ethoxy, another linear group, propyloxy, and two branched alkyloxy functionalities, *isopropyloxy* and *isobutyloxy*, were synthesized and investigated. The synthesis of these groups was carried out by means of a Williamson-Ether synthesis with the corresponding alkyl iodide according to the synthesis route that has been used for the methylation. The successful synthesis was confirmed by the absence of the phenol peak in the NMR and absence of the phenolic O-H vibration in the FT-IR spectrum. Furthermore, aliphatic peaks of the protons of alkyloxy groups were assigned, and integration and peak pattern corresponded to the expected peak splitting. Therefore, the full conversion of each derivative was confirmed (Figure 219).

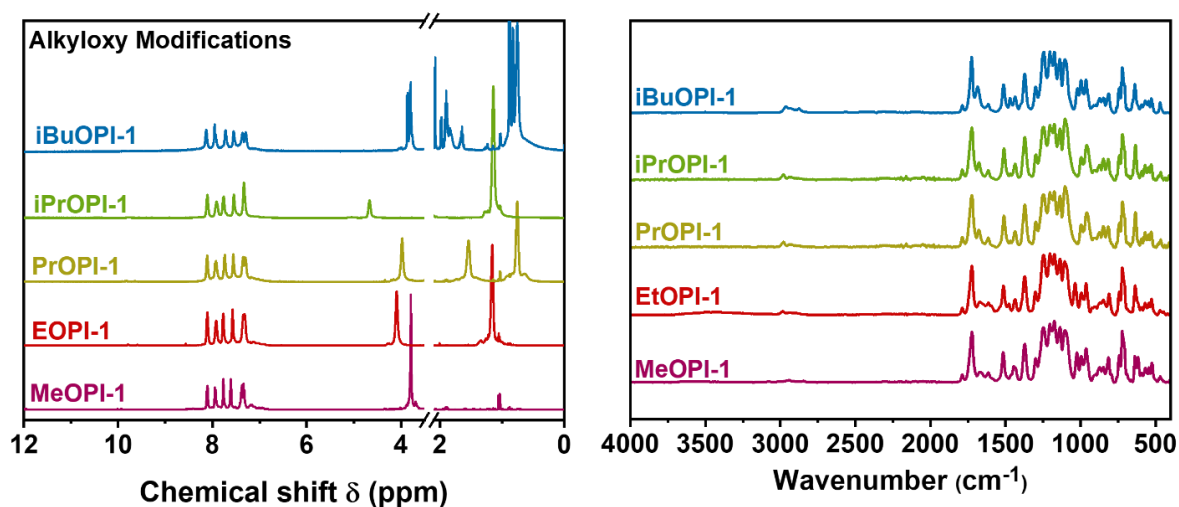


Figure 219. <sup>1</sup>H-NMR spectra (left) and FT-IR spectra (right) of the alkylated *ortho*-hydroxy polyimides, partially from [22].

The thermochemical behavior was investigated by thermoanalytical methods, including the calorimetric measurement of the heat flow in order to monitor phase changes and chemical reactions. In Figure 220, the heat flow *versus* temperature is shown. The exothermic peak corresponding to the thermal rearrangement and elimination reaction, in case of EOPI1, was previously discussed. The heat flow of the propyloxy modified material PrOPI1 shows a clear

glass transition temperature at 211 °C, which is lower compared to MeO- and EOPI1, follows the typical glass transition temperature relationship of increasing chain length of modifications, as widely described for polyacrylates with increasing number of CH<sub>2</sub> units [314]. In addition, the exothermic heat flow for the Thermal Rearrangement can clearly be seen, but its intensity is significantly lower compared to MeO- and EOPI1. The branched modification *i*PrOPI1, which is an *isopropoxy* group in turn shows a higher T<sub>g</sub>, due to its branched structure. Nevertheless, the decomposition of the *isopropoxy* group is endothermic and therefore an endothermic heat flow with a peak at 410 °C and an onset temperature of 350 °C was determined. Two C $\alpha$  atoms with three hydrogen atoms exist in *i*PrOPI1. The degree of freedom with respect to rotations is significantly lower compared to EOPI1, due to their bulky size. Since the elimination reaction is endothermic, while the Thermal Rearrangement is exothermic, in the case of *i*PrOPI1, only the endothermic elimination can be monitored by means of DSC measurements, since it occurs at lower temperatures and the TR process shifts to higher temperatures. The assumption is that the methoxy, ethoxy and propoxy modifications require higher temperatures to eliminate or undergo an alkyl-transfer initiated TR process. At these temperatures, the transferred heat is already sufficient enough to initiate the Thermal Rearrangement. The increased degree of freedom with respect to mobility of the polymer chains due to the elimination's product around the phenol-imide unit facilitates the TR process as well. This has also been observed for ButylenePI1 in section *Thermokinetic and -dynamic analysis*.. The butylene group decomposed to butadiene and an overlap of the butadiene and CO<sub>2</sub> formation (due to the TR process) were determined by evolved gas analysis. In the case of *i*PrOPI1 the *isopropyl* group decomposes to propene earlier than propene is eliminated from PrOPI1. Therefore, the endothermic heat flow is more pronounced compared to the other derivatives.

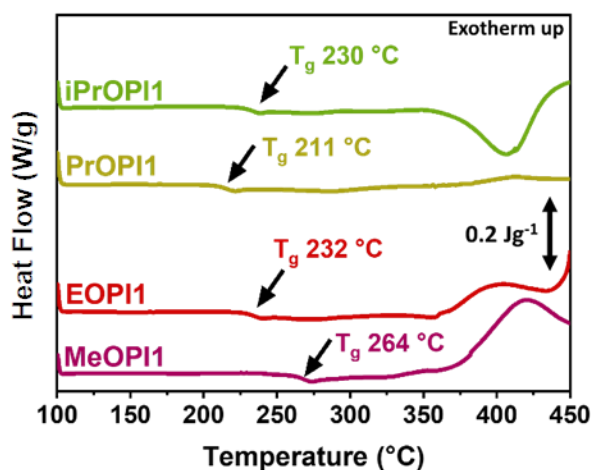


Figure 220. Heat flow curves obtained by means of DSC measurements of the *ortho*-alkyloxy polyimides[22].

The heat flow curve is a good indicator for a chemical reaction. Unfortunately, it only shows a global heat flow, which means that compensating heat flows can result in a misleading netto curve. If the chemical reactions are related to decomposition and release of a small molecule, the thermogravimetric analysis in combination with on-line FT-IR measurements is an excellent tool to investigate those reactions (Figure 221 and Figure 222). In the case of the herein described *ortho*-alkyloxy polyimides, an elimination of the alkyl group followed by the Thermal Rearrangement with a CO<sub>2</sub> release can be monitored.

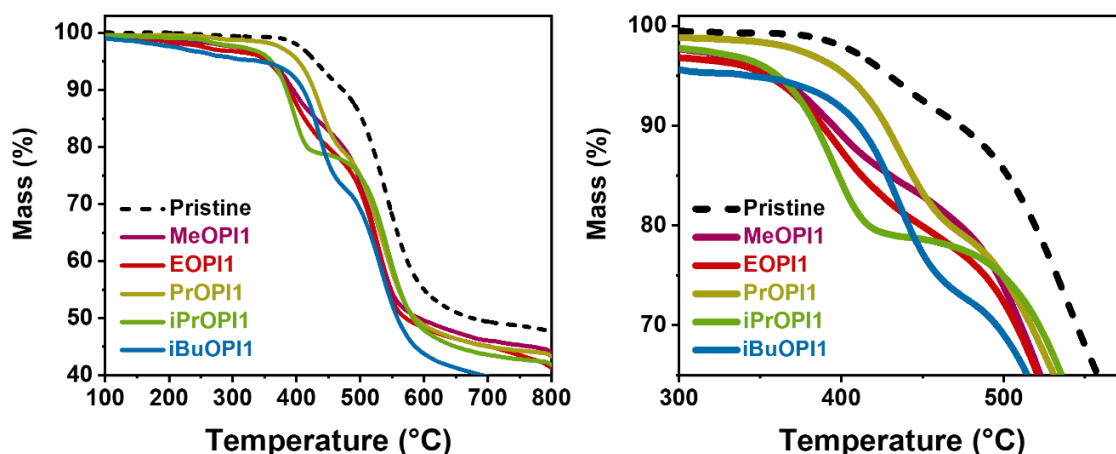


Figure 221. Mass loss curve of the *ortho*-alkyloxy polyimides (left) and zoom into the decomposition region (right)[22].

The mass loss onset temperatures of MeOPI1 and EOPI1 were previously described as close to each other. The course of the decomposition gas detection changes with an increasing temperature, whereas MeOPI1 appears to slow down compared to EOPI1. The next larger

modification, PrOPI1, in turn shows a significantly larger onset temperature for the mass loss. The mass loss corresponds to the elimination of propene, which starts at 345 °C and CO<sub>2</sub> due to the Thermal Rearrangement at 338 °C. The onset of both gas evolutions is in the same temperature range. The peak temperatures for the elimination and TR process are 438 and 435 °C, respectively. Hence, the assumption that the elimination reaction is immediately followed by the TR process can be confirmed by the evolved gas analysis. The *isopropyl* modification on the other hand leads to the same decomposition product, namely propene, but the onset and peak temperature is significantly shifted to lower temperatures with 314 and 411 °C, respectively. The onset and peak temperature correspond very well to the heat flow onset and peak. However, other than expected from the heat flow curve, the TR process does not follow the elimination, it occurs simultaneously as observed for any other alkyloxy modification as well. Otherwise, two steps would have been expected in the TGA curve (mass loss curve) and a shift of the CO<sub>2</sub> detection to temperatures higher than the onset and peak temperature for the propene release.

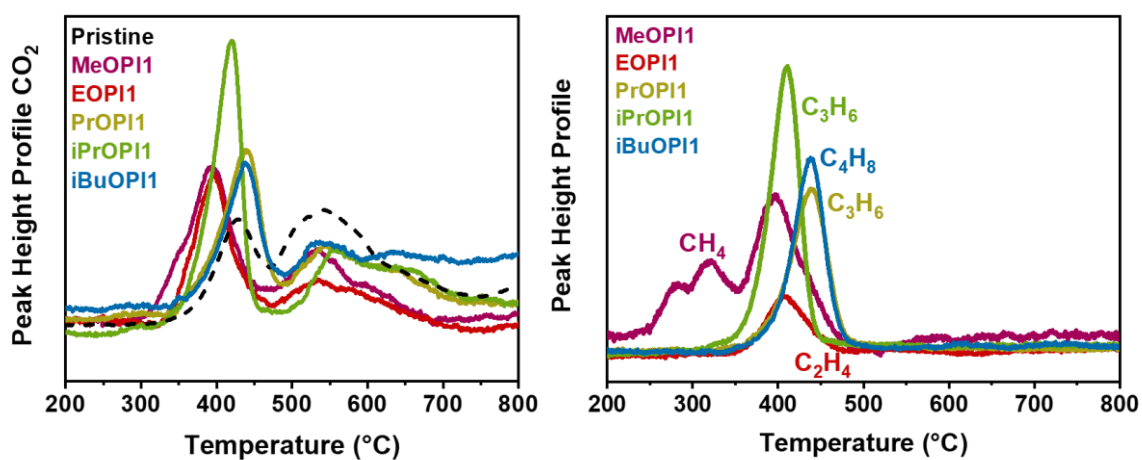


Figure 222. Peak height profile of CO<sub>2</sub> (left) and the decomposed alkylene group (right) obtained from evolved gas analysis[22].

The *isobutyloxy* modification as the largest synthesized ether group, showed a nearly identical behavior compared to PrOPI1. Chemically it is very similar to PrOPI1. The difference is an additional methyl group at C $\beta$ . Accordingly, the decomposition mechanism is expected to be very similar and therefore the onset and peak temperatures as well as the course of the reaction are also expected to be close to each other (Figure 223). An overview of the glass transition temperature, decomposition onset and peak temperature, as well as the TR<sub>onset</sub> and peak temperature are shown in Figure 180.

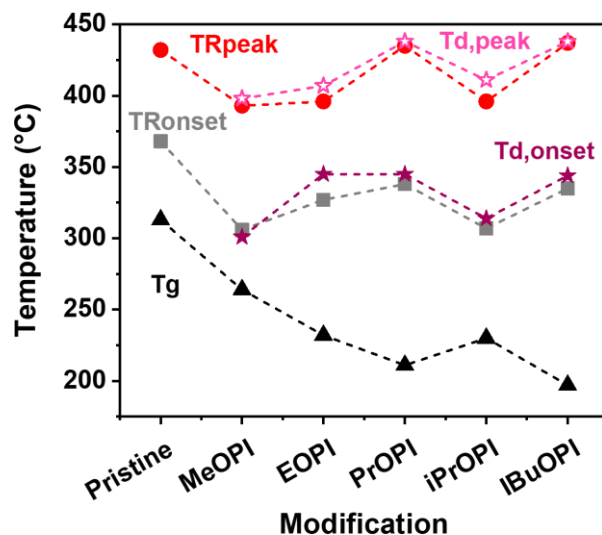


Figure 223. Overview of the glass transition temperature, decomposition onset and peak temperature, TR onset and peak temperature for each alkyloxy modification.

The structural changes were investigated after each annealing step by means of FT-IR spectroscopy as shown in Figure 224. While only slight changes of the composition were found after annealing at 350 °C in comparison to the spectra in Figure 219, the composition changes tremendously after annealing at 400 °C. The imide carbonyl groups disappeared almost completely at 1720  $\text{cm}^{-1}$ , as well as the C-O-C ether related stretch vibration at 1100  $\text{cm}^{-1}$ . The latter observation was supported by the loss of the ether related aliphatic C-H stretch vibration of the alkyloxy C-H groups (2940  $\text{cm}^{-1}$ ).

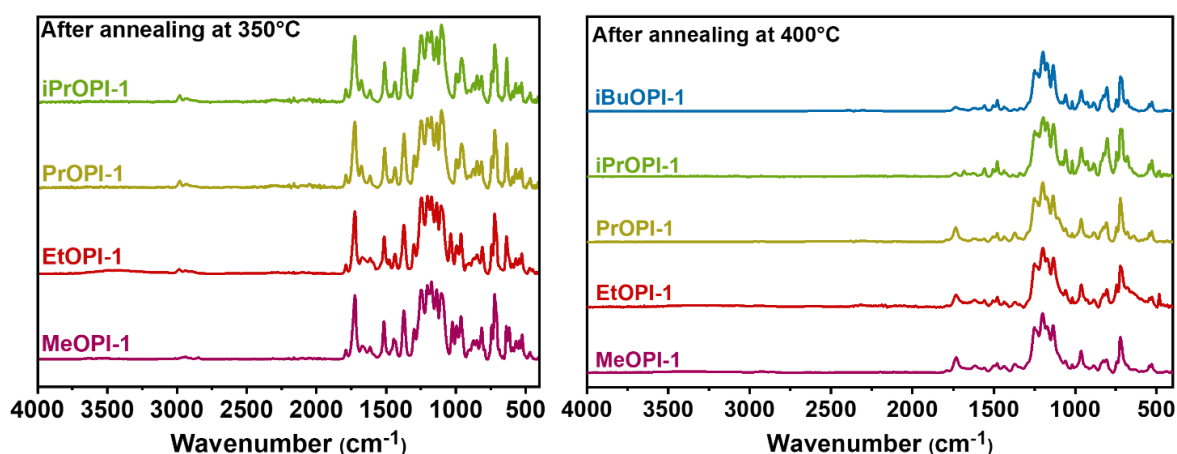


Figure 224. FT-IR spectra of the ortho-alkyloxy polyimides after annealing at 350 and 400 °C, for 2 and 1 h, respectively[22].



The experimental findings were supported by DFT simulations of a model compound. The left plot of Figure 225 shows the activation energies of two elimination reactions, elimination 1 and 2, and a radical homolysis of the phenol-O to alkyl bond. In addition, the alkyl-imide-N transfer reaction mechanism based on the suggestion by Comesana *et al.* [132] for the pristine material was simulated. Finally, the transfer mechanism as described in section *Molecular Modelling of the Reaction Mechanism* was calculated for an alkyl transfer initiation step as well. The comparison shows, that for the pristine material the transfer mechanism is the most likely reaction mechanism, as the required energy is significantly lower compared to other mechanism. When an *ortho*-methoxy group rather than a simple phenol group is used, then the homolysis and N-transfer mechanism show lower activation energies. The situation changes again for EOPI and PrOPI, since they exhibit a C $\beta$  atom, which can be deprotonated under elimination according to an E2 elimination reaction mechanism. For these materials, the elimination 1 mechanism, which is the E2 elimination, shows the lowest activation energies. This reaction is not considered for MeOPI as it does not have a C $\beta$  atom. The elimination from the methyl group would form a highly reactive carbene group and is unlikely. However, the determined reaction path is not necessarily the one with the lowest initial activation energy, but rather the one with the lowest activation energy barriers. For that purpose, the second step was analyzed of each mechanism as well and is shown in the right plot. For MeOPI the subsequent reaction step of a homolysis reaction requires large energies. The same is true for the N-methylation reaction. The N-methylation reaction also requires a nitrogen atom flip in order to bring the phenol group close enough to the imide carbonyl group to react. The overall lowest activation energy was determined for the second step of the transfer mechanism for all materials. Accordingly, the methoxy transfer mechanism is assumed to be the most reasonable mechanism for MeOPI,

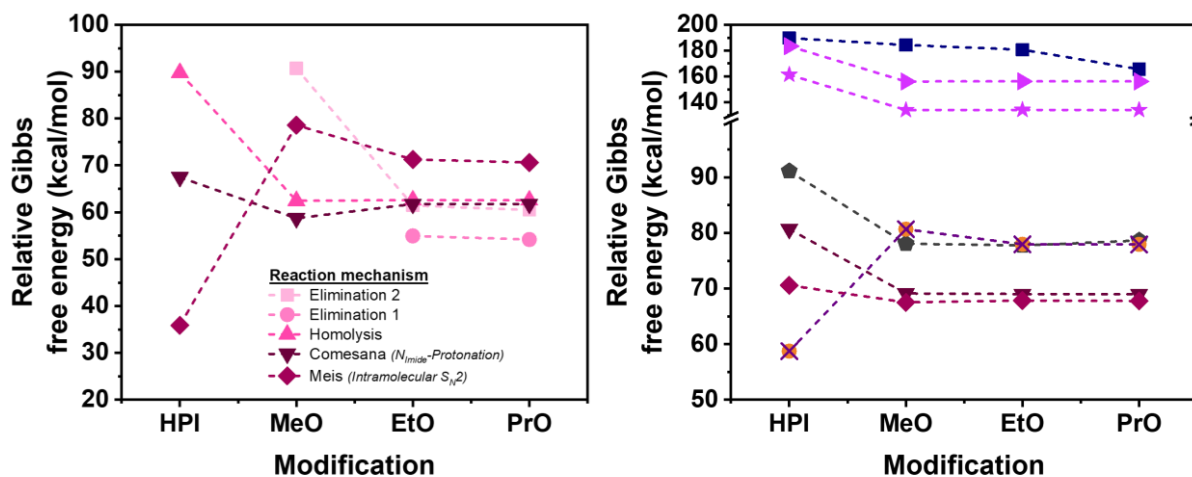


Figure 225. Gibbs free energies relative to the starting *ortho*-alkyloxy phenyl phthalimide model structure for the different reaction mechanism of the first step (left plot) and second step (right plot) of the different simulated decomposition-TR reaction mechanism

## Acyloxy modifications

Another group of the modification of the *ortho*-hydroxy group is the introduction of an acyloxy group. The simplest acyloxy group, the acetyloxy group, was discussed in the previous section. The acetylated polymer is the final structure if the poly (amic acid) is chemically imidized. The reaction is typically executed in NMP and base catalyzed using pyridine and *N,N*-dimethyl amino pyridine as catalyst. Therefore, a set of six acyloxy modified polyimides was synthesized. Each was obtained by the acetylation method, except for the *sec*butyl ester, which has been synthesized via addition of the corresponding acyl chloride. The successful and quantitative conversion was determined by means of  $^1\text{H-NMR}$  and FT-IR spectroscopy (see Figure 226). The synthesized derivatives are shown in section *Esterification*.

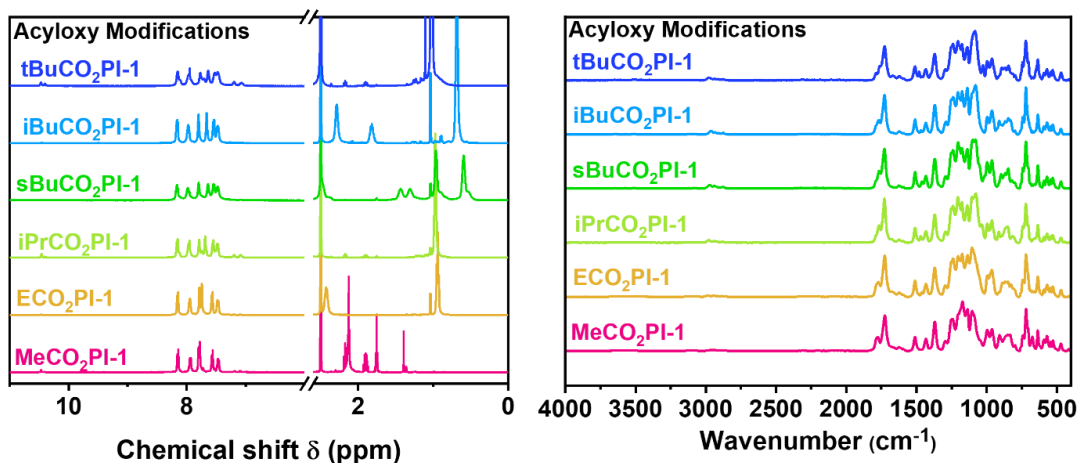


Figure 226.  $^1\text{H-NMR}$  spectra (left) and FT-IR spectra (right) of the acylated ortho-hydroxy polyimides[22].

The thermoanalysis was done for all acylated polymers according to the measurement parameters, which were used for the analysis of the alkyloxy polyimides. The heat flow curves are shown in Figure 227. When comparing all materials, two important events occur. The first process is the glass transition at the glass transition temperature region, whose midpoint was determined and included in Figure 185. The lowest  $T_g$  was observed for *sec*ButyrylPI ( $s\text{BuCO}_2\text{PI}$ ) with  $205\text{ }^\circ\text{C}$  and *isobutyryl*PI ( $i\text{PrCO}_2\text{PI}$ ) with  $213\text{ }^\circ\text{C}$ . The highest  $T_g$  was measured for AcetylPI ( $\text{MeCO}_2\text{PI}$ ) with  $264\text{ }^\circ\text{C}$ . The glass transition temperature continuously decreased as the number of methylene units increases as observed for alkylated TRPs as well. The second event is correlated with an endothermic heat flow, which occurs only in the first heating cycle. This endothermic heat flow ranges from nearly  $300$  to  $450\text{ }^\circ\text{C}$ . The pivalic group ( $t\text{BuCO}_2\text{PI}$ ) does not show such an endothermic heat flow. In  $\text{MeCO}_2\text{PI}$  this type of reaction was identified by correlation with the TGA curve and decomposition gas analysis. For  $\text{MeCO}_2\text{PI}$  the process is the deacetylation reaction under formation of the corresponding carboxylic acid and ketene as well as the pristine material. The ketene is more pronounced during the initial period of the deacetylation reaction, while at higher temperatures the detection of acetic acid was dominating.

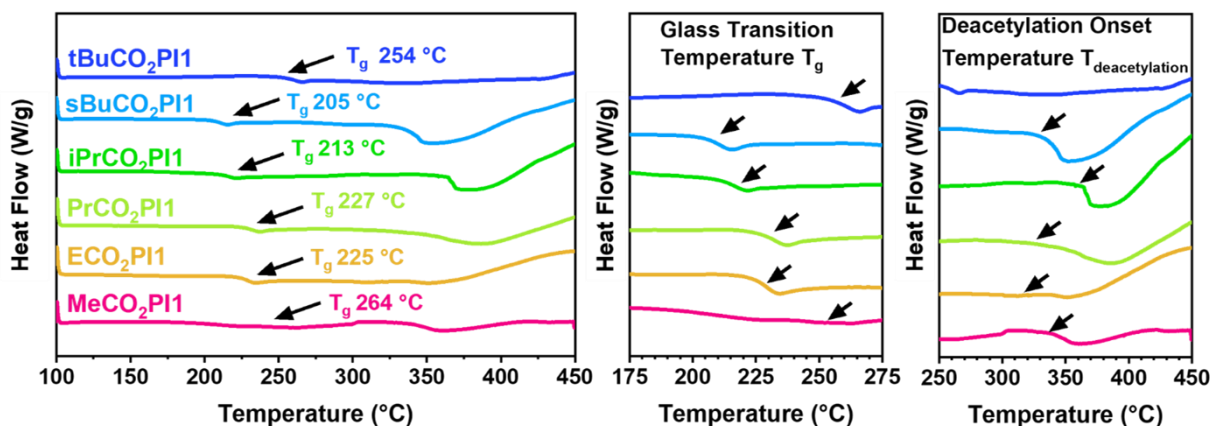


Figure 227. Heat flow curves obtained by means of DSC measurements of the ortho-acyloxy polyimides[22].

The mass loss curves in Figure 228 reveal a mass loss step between 300 and 450 °C which correlates well with the calorimetric measurement. Except for *t*BuCO<sub>2</sub>PI1, all polymers show an onset below 400 °C, and are close to each other with the lowest onset at 300 °C for MeCO<sub>2</sub>PI1 and lowest peak temperature with 340 °C for *i*BuCO<sub>2</sub>PI1. The onset temperatures were the same for all materials and determined to 320 °C, apart from MeCO<sub>2</sub>PI1 (300 °C) and *s*BuCO<sub>2</sub>PI1 (310 °C). The peak temperatures varied for all investigated polymers. Apart from *t*BuCO<sub>2</sub>PI1, it is *i*PrCO<sub>2</sub>PI1 with the highest peak temperature at 415 °C. The corresponding peak height profiles of the detected decomposition gases are shown in Figure 229.

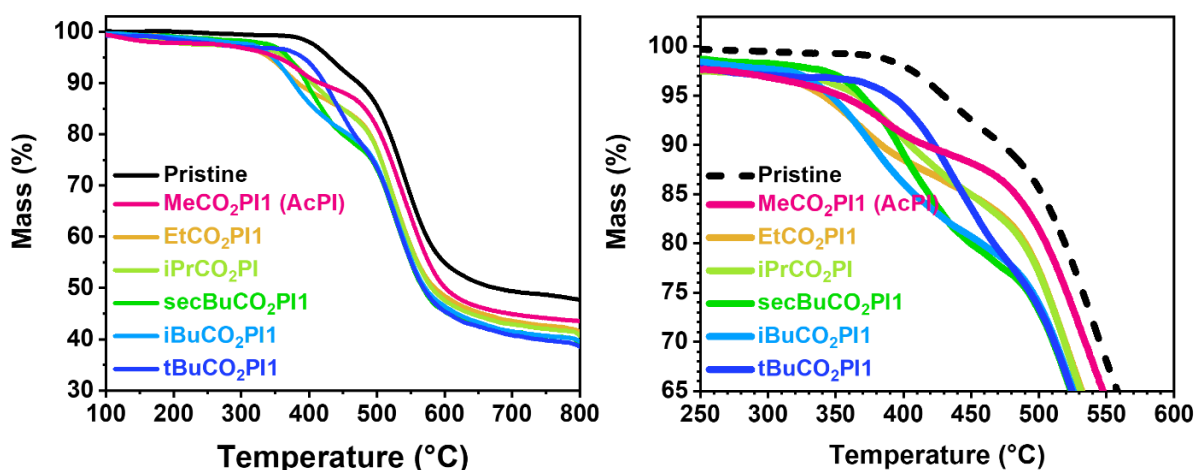


Figure 228. Mass loss curves for the acyloxy modifications (left) and zoom into the first mass loss step region (right).[22]

The peak height profiles of the most prominent signals were extracted from the Gram-Schmidt curve of the DCE. In all cases the most significant profile was obtained for CO<sub>2</sub> which is released due to the Thermal Rearrangement as well as degradation processes. Therefore, the commonly observed peak height profile is a two-peak profile for each process, whereas the

degradation peak is usually rather broad as it starts around 480 °C for the most TR precursor and continues until 700 to 800 °C. Moreover, other gases than CO<sub>2</sub> were detected as well. In each case characteristic carboxylic acid C-H stretch vibration at around 2900 cm<sup>-1</sup> was found in addition to the carboxylic acid carbonyl and O-H stretch vibrations. The spectra of each carboxylic acid compound was identified as the carboxylic acid, which corresponded to the acetyloxy group, respectively. In addition, for all components, except *t*BuCO<sub>2</sub>PI1, a ketene related peak was identified, which can be found around 2120 cm<sup>-1</sup>. Two modifications have shown that carbon monoxide was formed at higher temperatures above 450 °C. These two were *i*PrCO<sub>2</sub>PI1 and *t*BuCO<sub>2</sub>PI1.

The decomposition of each acyloxy group to the ketene and carboxylic acid group was discussed for MeCO<sub>2</sub>PI1 from a mechanistic point of view in section *Acetylated ortho-Hydroxy polyimides* on page 294. This occurs via an E2 elimination reaction in the same way, as observed for the alkyloxy modifications. In that sense the acetyloxy and ethoxy group reacted according to the same mechanism. Differences arose especially from electronic and steric aspects. As a consequence of the carbonyl group on C $\alpha$  in acyloxy groups, the electron density at C $\beta$  is reduced and the rotation of the trigonal planar carbonyl group is significantly lower compared to the tetrahedral methylene group in alkoxy modifications. Another important mechanistic aspect is that unsubstituted C $\beta$  atoms have lower activation barriers for the rotation around the O-C $\alpha$ -C $\beta$ -H dihedral. Therefore, the best conformation for the transition state geometry can be obtained if the C $\beta$  atom can rotate more freely and is not sterically hindered. A comparison to the alkyloxy modifications has shown, that the decomposition temperature was significantly affected by these parameters, since the *isopropoxyloxy* group at a lower electron density at C $\alpha$  and was sterically hindered due to the interfering methyl groups. These considerations are the basis for the discussion of the decomposition mechanism of each material.

Among all materials, a decomposition of the acyloxy group occurred prior to the CO<sub>2</sub> release due to the Thermal Rearrangement accompanied decarboxylation step. However, the ketene and carboxylic acid formation initiated at the same onset temperature, but the intensity of the ketene detection increased more rapidly, while the carboxylic acid detection increased slowly. Therefore, the same reaction sequence, as described for MeCO<sub>2</sub>PI1, is assumed for the investigated acyloxy derivatives as well. The initial decomposition occurs via E2 elimination

to the corresponding ketene, which undergoes fast dimerization on the way throughout of the membrane and in the gas phase before it approaches the on-line FT-IR spectrometer. Furthermore, the ketenes react with low amount of moisture in the gas phase by forming the carboxylic acid, since ketenes are highly reactive towards nucleophiles. Since no water formation was detected by side reactions or degradation, it was either immediately consumed or is not present. Therefore, a decomposition pathway by reaction of water with the acyloxy group is highly unlikely. Another potential mechanism in order to obtain a carboxylic acid as decomposition product is the cleavage of the phenol bond between the aromatic carbon C1 and the phenol oxygen atom. Such a process would proceed via a radical homolysis reaction and require more energy and lower the overall Thermal Rearrangement conversion, since in that case, no reactive phenol group is present for the TR reaction. Therefore, this mechanism was ruled out, since TGA experiments revealed that nearly every formed phenol group undergoes the TR reaction.

The Thermal Rearrangement occurred then in consecutive order to the deacylation as monitored by the CO<sub>2</sub> release. The TR<sub>onset</sub> temperatures were determined in the range from 346 (MeCO<sub>2</sub>PI1) to 397 °C (*t*BuCO<sub>2</sub>PI1). Upon deacylation, the phenol group is recovered and undergoes the TR process by reaction with the imide carbonyl group.

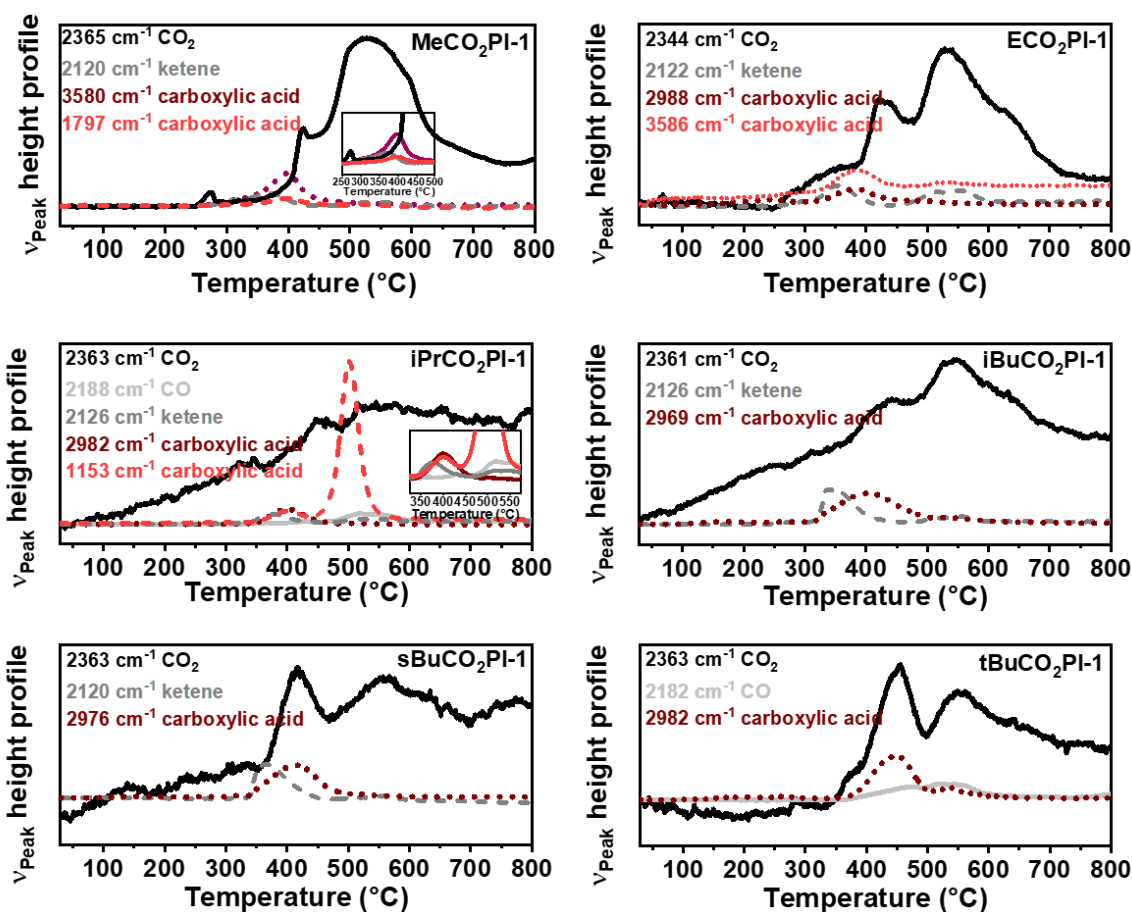


Figure 229. Peak height profiles for each acyloxy modification.  $CO_2$  was detected in all cases (black curve), as well as the modification corresponding carboxylic acid group and ketene[22].

A comparison of the ketene and carboxylic acid formation, Thermal Rearrangement reaction and glass transition with respect to their specific onset and peak temperatures are shown in Figure 230.

Calle *et al.* and Guo *et al.* claimed that there is a strong correlation between the glass transition temperature and the Thermal Rearrangement onset [138, 139]. This was justified by the higher mobility of the polymer chains as soon as it transfers to the rubbery state. The comparison of the  $T_g$  and TR reaction in the case of the acetylated materials did not correlate as observed for the *ortho*-alkyloxy polyimides as well (see Figure 230). This is attributed to the fact that the initial step here is the decomposition. While the glass transition occurs at lower temperatures than the deacylation, it does not affect the TR reaction, since the glass transition of the material changes once the decomposition occurred. This means, that the glass transition temperatures are expected to change continuously during the decomposition process as highlighted by the study of Guo *et al.* in 2013 [138]. A better correlation can be found by the deacylation and Thermal Rearrangement specific temperatures. The course of the peak temperature of the

ketene formation agrees very well with the  $TR_{\text{onset}}$  temperature and the peak of the carboxylic acid formation corresponds very well with the  $TR_{\text{peak}}$  temperature (see Figure 230). This is reasonable according to the proposed mechanism, that the TR temperature depends on the recovery of the phenol group and is therefore strongly correlated to the deacylation reaction. The initial ketene formation as the major deacylation path is therefore the starting point of the initiation of the TR reaction. The TR peak is obtained, once the majority of the acyloxy groups are decomposed. Accordingly, the peak temperatures of the carboxylic acid formation and TR reaction show the same course of the reaction.

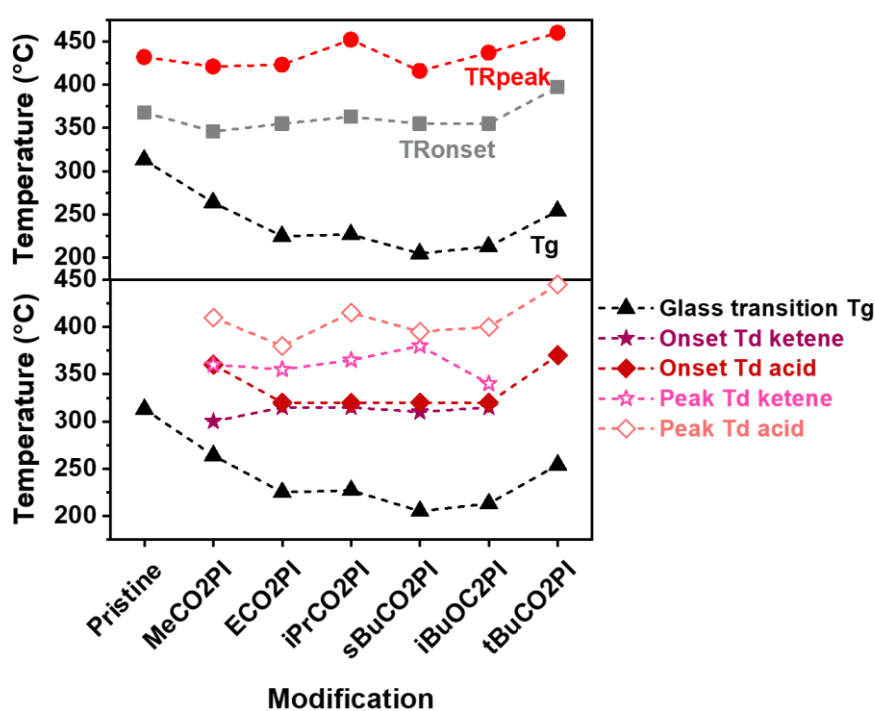


Figure 230. Characteristic temperatures of the acyloxy modifications including the onset temperature for the detection of the corresponding ketene and carboxylic acid as well as the peak temperature, glass transition temperature, and Thermal Rearrangement onset and peak temperature.

The acylated films were annealed in order to monitor their TR reaction process and in order to obtain the film properties at a later stage. Annealing at a typically low TR annealing protocol at 350 °C for 2 h and a more commonly used annealing temperature of 400 °C for 1 h was used. The composition was analyzed by means of FT-IR measurements (see Figure 231 and Figure 232). Interestingly, the carbonyl stretch vibration at 1720  $\text{cm}^{-1}$  did not alter significantly after annealing at 350 °C, but the carbonyl stretch vibration at 1780  $\text{cm}^{-1}$  decreased. An increase of the phenolic O-H stretch vibration was found as well. However, annealing at 400 °C led to a strong decrease of the peak intensity of the carbonyl at 1720  $\text{cm}^{-1}$  as well. These observations



were in agreement with the findings for MeCO<sub>2</sub>PI1, that at 350 °C the decomposition temperature of the acyloxy group, in that case the acetyloxy group, was surpassed therefore it decomposed and recovered the phenol group. Since the deacylation temperature was determined to be around 310 to 320 °C, it is reasonable that the deacylation proceeds in each case. Nevertheless, annealing at 400 °C was then sufficient enough to promote the TR reaction and cause a decrease of the imide carbonyl group at 1720 cm<sup>-1</sup>. The spectrum reveals as well that the lowest conversion was observed for the *t*BuCO<sub>2</sub> group, which was the only material without ketene formation. Hence, another decomposition-TR sequence is expected. The lowest TR<sub>onset</sub> temperature was determined for MeCO<sub>2</sub>PI1 and ECO<sub>2</sub>PI1, which is in agreement with the reaction process according to the IR measurements. The lowest carbonyl signal was detected for MeCO<sub>2</sub>PI1 and followed by ECO<sub>2</sub>PI1.

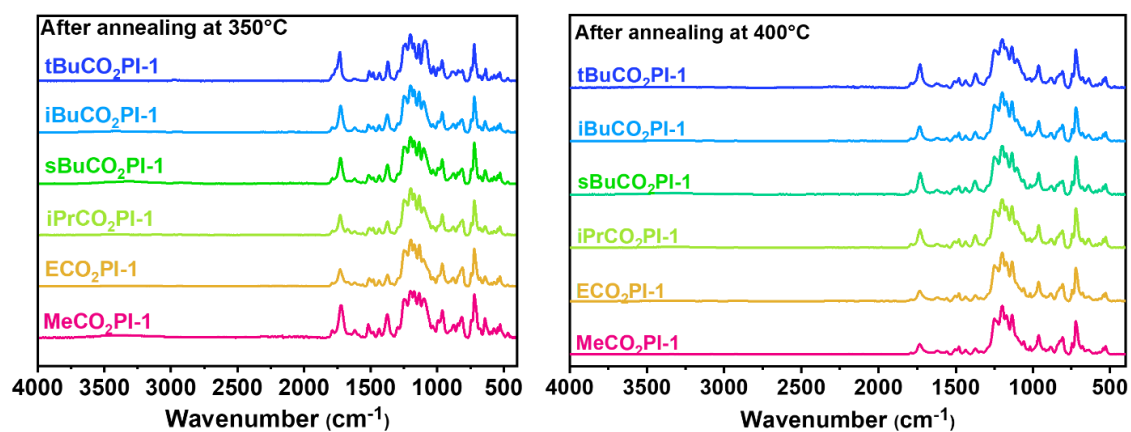


Figure 231. FT-IR spectra of the ortho-acyloxy polyimides after annealing at 350 and 400 °C, for 2 and 1 h, respectively[22].

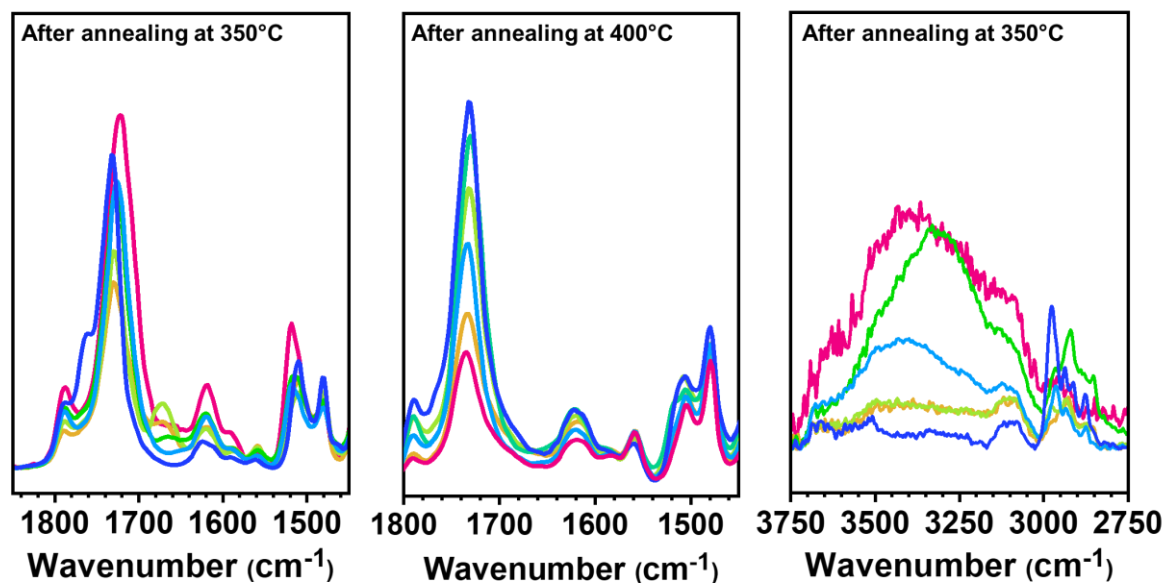


Figure 232. FT-IR spectra of the region of the imide carbonyl ( $1720\text{ cm}^{-1}$ ) and benzoxazole ( $1480\text{ cm}^{-1}$ ) stretch vibration of the ortho-acyloxy polyimides after annealing at 350 and 400 °C, for 2 and 1 h, respectively[22].

In addition, two other derivatives were synthesized. Based on the derivatives MeCO<sub>2</sub>PI1 and ECO<sub>2</sub>PI1, the fluorinated versions with respect to the terminal methyl group were prepared. The thermoanalysis in Figure 233 revealed a significantly lower decomposition temperature. An endothermic heat flow was determined in both cases and corresponded to a significant mass loss. The mass loss of the trifluoroacetic component was determined to be 28% and initiated at 100 °C until 325 °C. The synthesis caused a formation of the trifluoroacetic acid which is a very strong acid and caused a partial polymer chain degradation. According to the extracted peak height profiles from the Gram-Schmidt curve of the TGA-FT-IR experiments, the formation of carbon monoxide and especially fluoroform at two stages (Figure 234) was determined. In addition, two peaks for the CO<sub>2</sub> release were found. The initial fluoroform and CO<sub>2</sub> release was assigned to the degradation of the trifluoroacyloxy group. Since no C $\alpha$ -connected proton is available to undergo an E2 elimination reaction, this reaction path is blocked as shown in Scheme 43. Therefore, a reaction mechanism similar to *t*BuCO<sub>2</sub>PI1 is expected in which the methyl groups are substituted by the fluorine atoms in CF<sub>3</sub>CO<sub>2</sub>PI1. A radical decomposition leads therefore to the formation of carbon monoxide and a CF<sub>3</sub> radical which abstracts a hydrogen throughout the penetration through the polymer film. The CO<sub>2</sub> formation is explained similar to *t*BuCO<sub>2</sub>PI1 by the radical homolysis reaction of the phenol C-O bond to the aromatic ring. The significantly lower onset and peak temperature compared to *t*BuCO<sub>2</sub>PI was rationalized by means of the strong electron withdrawing effect of the

fluorine atoms because of the strong negative inductive effect due to the high electronegativity of fluorine. A second CO<sub>2</sub> release correlating with a mass loss step was attributed to the Thermal Rearrangement reaction. The onset of the TR reaction was 320 °C and the peak temperature was 440 °C. This is highly interesting, because despite the significantly lower loss of the protective group, the TR reaction did not start at significant lower temperatures, even though the phenol group was already partially recovered prior 300 °C. While all other materials started the TR process during the decomposition of the acyloxy group, here a full decomposition occurred prior to the TR reaction.

The CF<sub>3</sub> version of the propionic derivative was obtained by conversion of the phenol groups with equivalents of the acidic chloride. The purification of this modification was straight forward and gave a high-molecular weight pure material in high yield. The decomposition of the fluorinated propanoic group started at 234 °C and peaked at 332 and 397 °C with respect to the trifluoropropanoic acid formation (Figure 234). The peak of the ketene of the trifluoropropanoic group was determined at 420 °C at an onset temperature of 372 °C. The CO<sub>2</sub> evolution significantly started at 352 °C and peaked at 414 °C. The onset temperature for the deacylation by carboxylic acid formation was lower with 234 °C compared to 315 °C in case of the non-fluorinated derivative. The second peak, which occurs simultaneously to the ketene formation in the range from 332 to 372 °C, was higher compared to ECO<sub>2</sub>PI1. The TR temperature onset and peak temperature was nearly identical. The ketene formation might occur at low temperatures of 234 °C due to the electron withdrawing effect of the trifluoromethyl group. The E2 elimination reaction is possible due to the presence of a C $\beta$  hydrogen atom. Nevertheless, no ketene was detected initially. It is hypothesized that the higher reactivity due to the higher electrophilicity, as a consequence of the EWG effect, makes the ketene more susceptible towards reactions with moisture in the purge gas stream and residual water in the membrane and on the membrane surface. The formed ketene was unsymmetric, and according to the literature symmetric ketenes are significantly more stable compared to unsymmetric ketenes [315, 316]. After decomposition, the Thermal Rearrangement reaction proceeds in the same way as described for ECO<sub>2</sub>PI1.

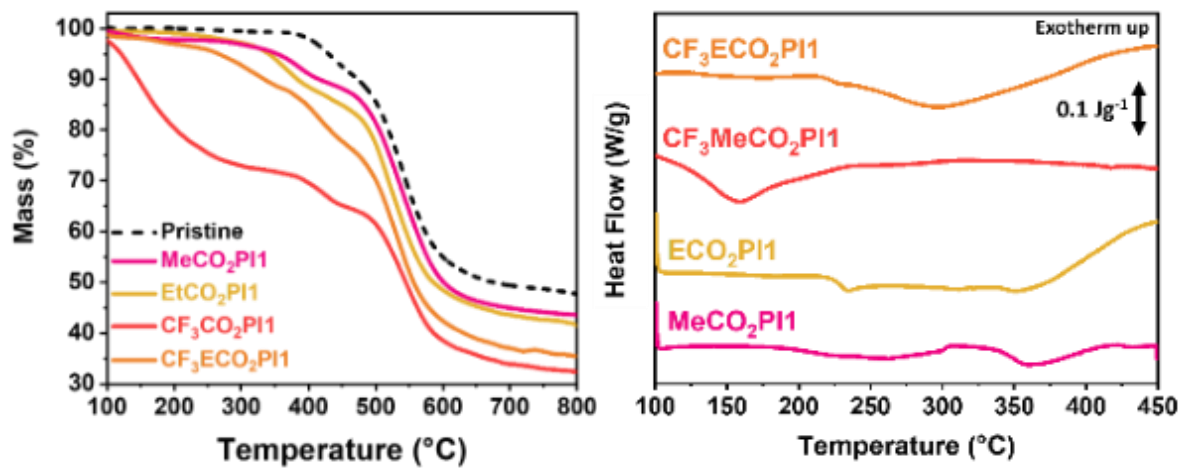


Figure 233. Mass loss curve (left) and heat flow curve (right) of fluorinated modifications CF<sub>3</sub>CO<sub>2</sub>PI1 and CF<sub>3</sub>ECO<sub>2</sub>PI1 and their corresponding non-fluorinated version.

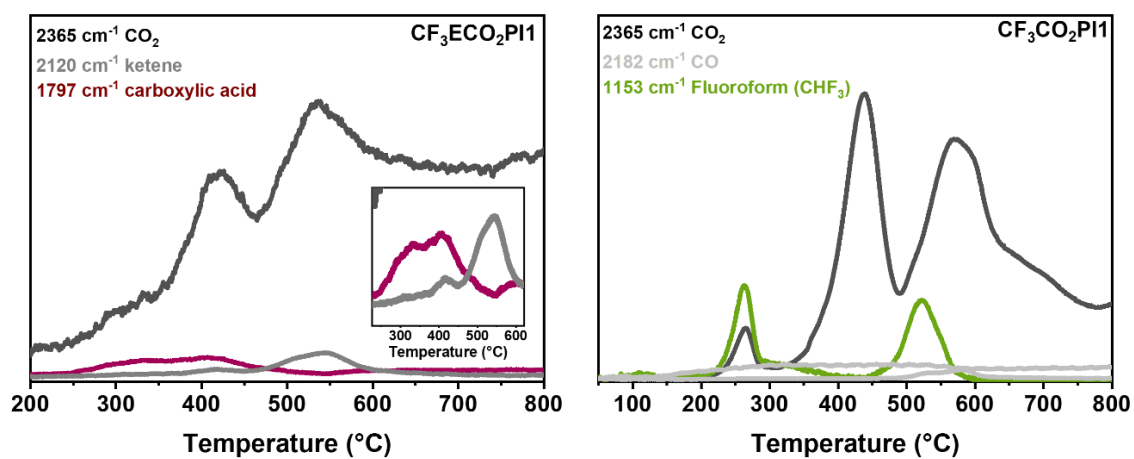


Figure 234. Peak height profile of the fluorinated acyl modifications of CF<sub>3</sub>ECO<sub>2</sub>PI1 (left) and CF<sub>3</sub>CO<sub>2</sub>PI1 (right).

## *Thermoreactive decomposition cascade reactions of ortho-carbonate Polyimides*

In the previous section a category of TR precursors was presented, which had a common characteristic, namely a protective group of the phenol group in the diamine unit. This group had to be thermally deprotected in order to initiate a Thermal Rearrangement reaction. This two-step sequence is a cascade-type reaction in a broader sense, but not categorized as one within this study. The elimination reactions of the alkyloxy and acyloxy polymers were very similar, as they both proceeded via an E2 elimination reaction. The structural difference between both groups were the oxidation state of C $\alpha$ , which consisted of a carbonyl group rather than a methylene group. If the oxidation state of C $\alpha$  is increased by inserting another oxygen atom between the C $\alpha$  and C $\beta$  atom, organic carbonates are formed.

The synthesis can be done via esterification with the corresponding pyro carbonate or chloroformate. The synthesis procedure was adapted from the acetylation with acidic chlorides and acetone was used as a solvent instead. A set of eight derivatives and in total three different backbones for the simplest representant, the methyl carbonate, were synthesized.

The successful synthesis was confirmed by means of <sup>1</sup>H-NMR and FT-IR spectroscopy (see Figure 235). Full conversion was evidenced by the absence of the hydroxy peak and the O-H stretch band in the FT-IR spectrum. Furthermore, the methyl group of the carbonate was observed in the NMR spectrum below 4 ppm. Ether stretch vibrations corresponding to the C-H of the methyl group appeared at 2940 cm<sup>-1</sup> and C-O-C vibrations occurred at 1100 and 1020 cm<sup>-1</sup> in addition to the pristine spectrum. Important is the carbonyl vibration at 1780 cm<sup>-1</sup> in addition to the imide carbonyl vibration at 1720 cm<sup>-1</sup>.

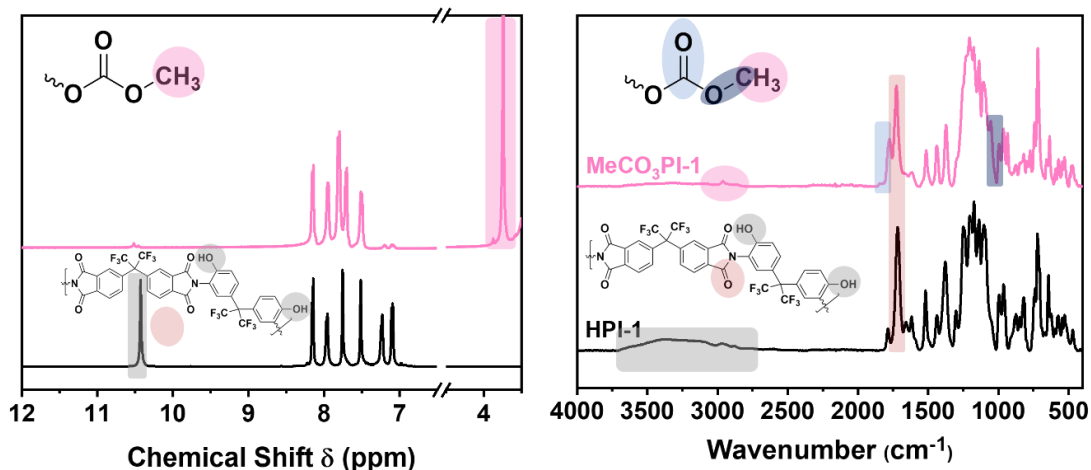


Figure 235. <sup>1</sup>H-NMR (left) and FT-IR spectrum (right) of MeCO<sub>3</sub>PI-1 and the unmodified HPI-1 (6FDA-BisAPAF).

Carbonate esters are highly oxidized and used in chemical synthesis for protection of nucleophilic groups [279]. The Tsuji-Trost coupling reaction uses palladium catalysts to prepare ether from carbonates accompanied by decarboxylation of the ether and formation of an electrophilic alkylic cation species [317, 318]. This species reacts with nucleophiles under etherification. Based on these considerations, carbonate ester was synthesized in order to investigate the thermal behavior in dependence of the modification. Based on the observations for alkyloxy and acyloxy modifications a decomposition is expected, which is assumed to occur at lower temperatures due to the CO<sub>2</sub> release as entropic driving force. The etherification is then of interest for further comparison with the corresponding alkyloxy modified polyimide.

Accordingly, a TG-FT-IR experiment was performed, and the decomposition gas evolution was analyzed. The mass loss curve and the stacked peak height profile are shown in Figure 236. The CO<sub>2</sub> peak height profile was extracted from the Gram-Schmidt curve and plotted in the TGA plot in Figure 236 (left).

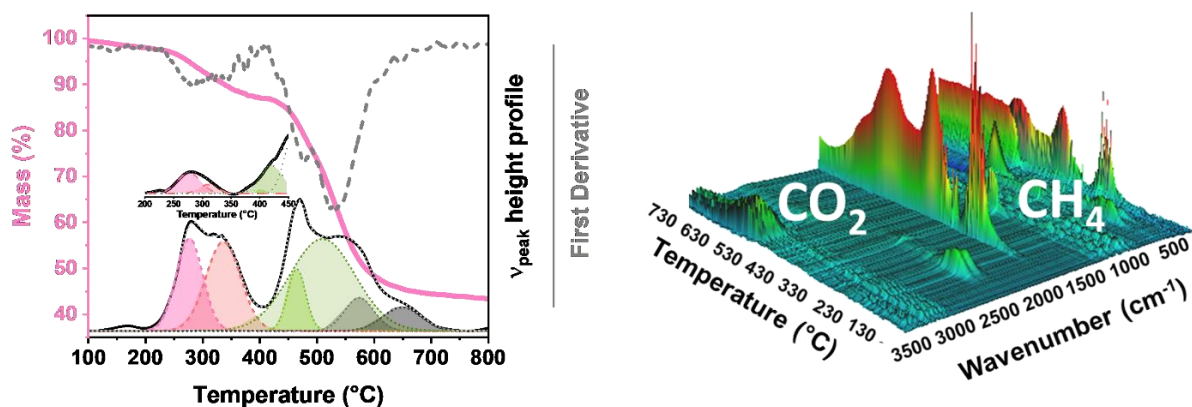


Figure 236. Temperature related mass loss curve for MeCO<sub>3</sub>PI-1 (rose). The CO<sub>2</sub> (black) peak height profile from evolved gas analysis as well as the first derivative (grey dashed) of the mass loss curve is shown (left). The three-dimensional plot of all stacked FT-IR spectra (right).

A broad weight loss step starting at 228 °C until 411 °C was observed. The weight loss of 10.9% was slightly higher than a theoretical weight loss of simply 2 CO<sub>2</sub> molecules would suggest, which would be 9.9%. However, the offset of the weight loss step was overlapping with the onset of another weight loss initiation. The weight loss initiation of the second step was determined as 411 °C. Nevertheless, a clear offset and onset determination by the first derivative and global CO<sub>2</sub> peak height profile was not possible. A peak deconvolution based on a Gauss fit, however, suggested that the second weight loss corresponding reaction starts already at 350 °C. Therefore, the higher weight loss might be explained by the initiation of the second reaction before the first finishes. Since no other gas evolved in this temperature range, as seen in the 2D-plot of the stacked Gram-Schmidt curve in Figure 236, a decarboxylation reaction of the carbonate ester is assumed.

The heat flow curve, obtained by DSC measurements (Figure 237), revealed an exothermic reaction in the range of the first weight loss step. In the case of the formation of an ether by decarboxylation of the methyl carbonate ester, an exothermic reaction due to the entropic contribution by the CO<sub>2</sub> release and new bond formation of the ether is expected. It is noteworthy that the CO<sub>2</sub> peak height profile as well as the heat flow curve have two deconvoluted peaks with similar onset and peak temperatures. While the onset for the CO<sub>2</sub> loss and heat flow onset for the first peak are 228 and 224 °C, respectively, their peak temperatures are determined as 279 °C for the CO<sub>2</sub> loss and 278 °C for the heat flow peak. For the second deconvoluted peak, an onset temperature for the CO<sub>2</sub> loss and heat flow were determined at 252 °C and 273 °C, respectively. The peak temperatures for the second deconvoluted peak were 335 °C and 312 °C.

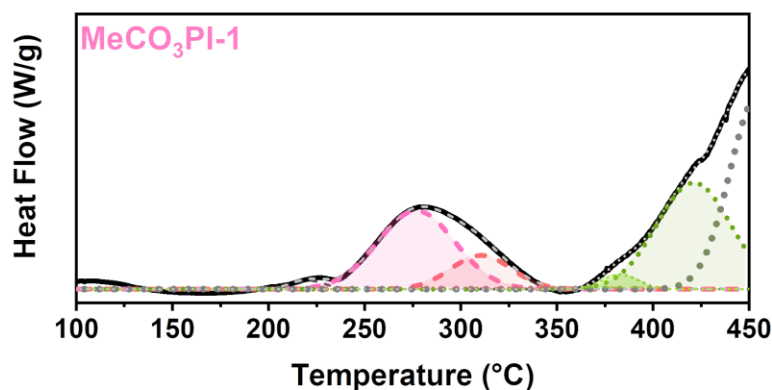


Figure 237. Heat flow curve, obtained by DSC experiments, for MeCO<sub>3</sub>PI-1.

In order to understand the process better, the MeCO<sub>3</sub>PI-1 polymer was heated up to 300 °C in the DSC with a heating rate of 5 °C min<sup>-1</sup> and then cooled down immediately with 10 °C min<sup>-1</sup>. From these samples <sup>1</sup>H-NMR were made. Some parts were insoluble, but the majority was still soluble. The NMR was plotted against the initial precursor and the NMR spectra of MeOPI-1, which is the methoxy polyimide. The results are shown in Figure 238. The spectrum shows that a strong decrease of the peak intensity of the methyl group in MeCO<sub>3</sub>PI-1 occurred, but a new peak by a slightly lower chemical shift evolved, which was on the same position as the methyl group in the MeOPI-1. This was taken as proof of the methyl transfer reaction from the methyl carbonate ester to the phenol group, forming the corresponding methyl ether, which is accompanied by a decarboxylation as evidenced by TGA-FT-IR.

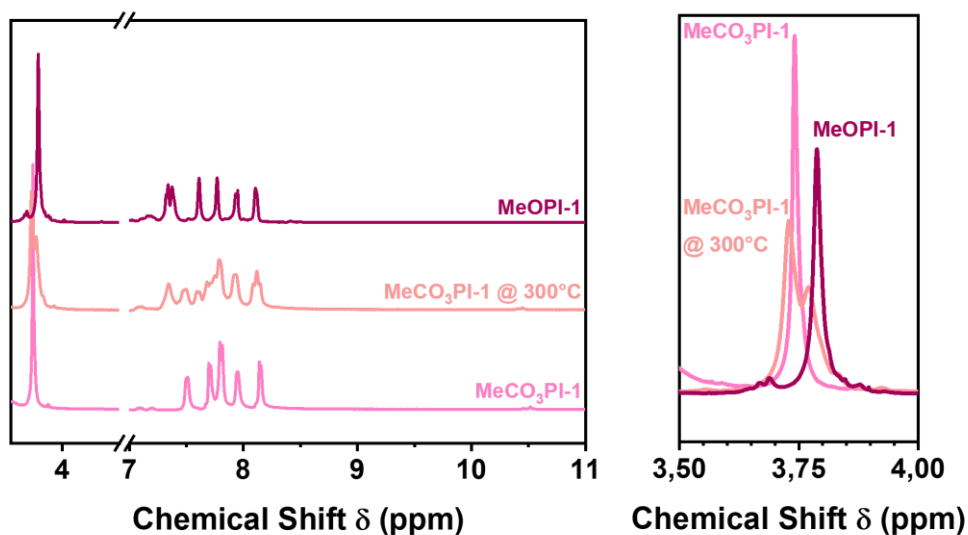


Figure 238. <sup>1</sup>H-NMR spectrum after annealing MeCO<sub>3</sub>PI-1 to 300 °C with a heating rate of 5 °C min<sup>-1</sup> in the DSC under nitrogen and immediate cool-down by a cooling rate of 10 °C min<sup>-1</sup>. In addition, the thermally untreated carbonate ester and methoxy polyimide MeOPI-1 are shown.



Annealing at 300 °C for 30 min of the corresponding films also showed a change in the FT-IR spectra (Figure 239 and Figure 240). While a decrease of the carbonate ester corresponding carbonyl stretch vibration at 1774 cm<sup>-1</sup> occurred, new peaks at 1100 and 1020 cm<sup>-1</sup>, typically corresponding to ether bonds, arose. Furthermore, a comparison with the FT-IR spectrum of MeOPI-1 has shown, that the same stretch vibrations can be found. Accordingly, this is taken as another corroboration of the methyl transfer reaction.

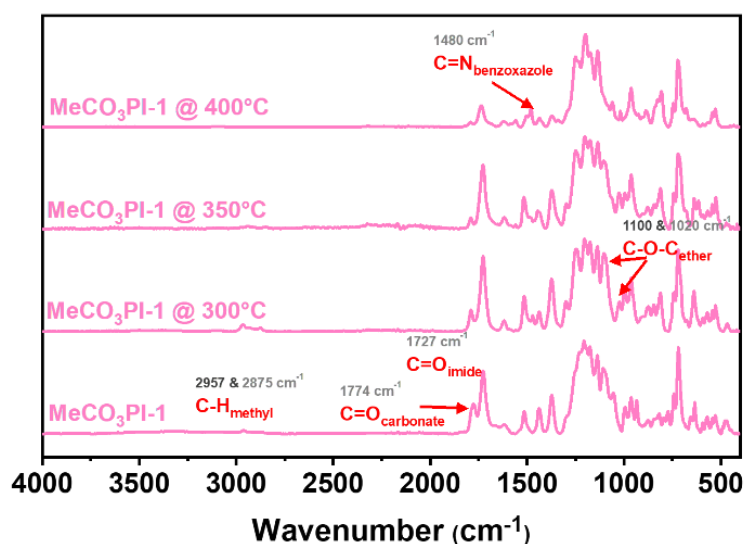


Figure 239. Stacked FT-IR spectra of the methyl carbonate ester modified MeCO<sub>3</sub>PI-1 after annealing at 300, 350 and 400 °C for 0.5, 2 and 1 h, respectively.

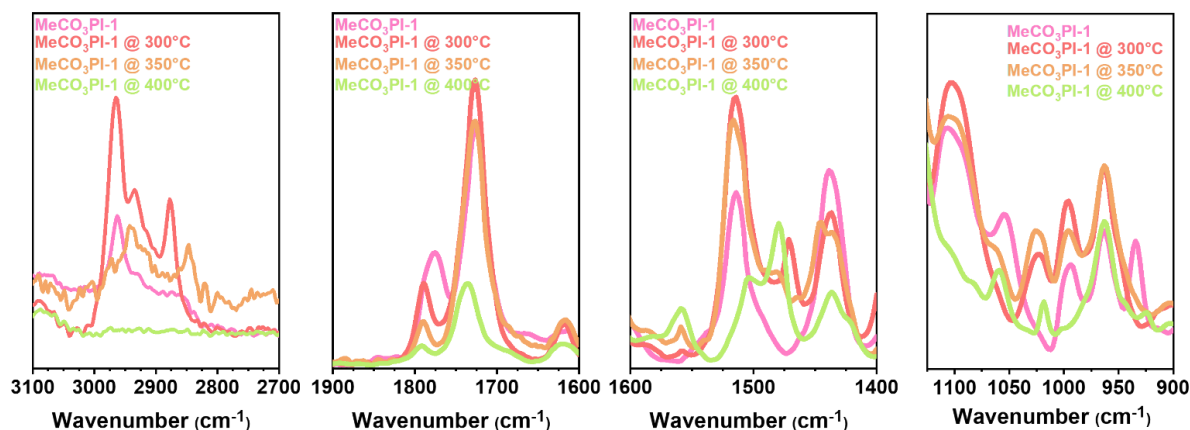


Figure 240. Zoom into the stacked FT-IR spectra of the methyl carbonate ester modified MeCO<sub>3</sub>PI-1 after annealing at 300, 350 and 400 °C for 0.5, 2 and 1 h, respectively.

The polymer films of MeCO<sub>3</sub>PI-1 were treated at 300 °C for 30 min in order to evaluate the performance after decarboxylation of the carbonate ester and at 350 and 400 °C for 2 h and 2 h, respectively, in order to compare the performance to other TR materials of this study. The TGA curves after annealing are shown in Figure 241. The annealing showed, that 24.2% of the

overall methyl-transfer and Thermal Rearrangement reaction proceeded. The corresponding TGA mass loss curve shows similar characteristic onset and peak temperatures to the *ortho*-methoxy polyimide. A more pronounced shift of the weight loss step was measured after annealing at 350 °C for 2 h. According to the conversion determination, 55.0% of the global process were done, while annealing to 400 °C converted the polymer to an extent of 82.2%. Accordingly, 350 °C are sufficient to promote the conversion of the methyl-transfer and decarboxylation reaction to completion. However, even after annealing at 400 °C no full completion of the TR process was achieved. This result is in contrast to the observation with MeOPI-1. The conversion of MeOPI-1 after annealing at 400 °C was 96.7%. This is explained by the fact, that some of the methyl carbonate groups decompose, especially after passing the peak temperature of the reaction, to the pristine 6FDA-BisAPAF by decomposition to carbon monoxide and methanol. The conversion of the *ortho*-methoxy polyimide, however, was determined to be higher at 350 and 400 °C annealing procedures compared to 6FDA-BisAPAF. As a consequence, the methylated units undergo the TR process preferably, while the unmodified groups do not readily react. Therefore, the conversion of MeOPI-1 is higher compared to MeCO<sub>3</sub>PI-1.

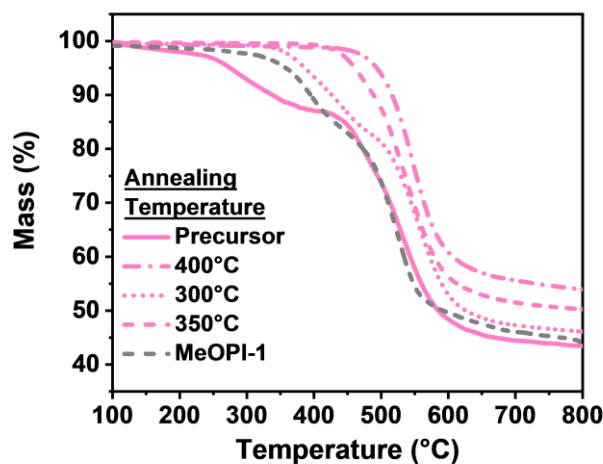


Figure 241. Mass loss curves after annealing of MeCO<sub>3</sub>PI-1 films at 300, 350 and 400 °C for 0.5, 2 and 1 h, respectively. The precursor TGA curve and the TGA curve of MeOPI-1 were added as well.

A comparison of the solid-state NMR spectrum, which was obtained by <sup>13</sup>C-CP-MAS experiments of MeOPI-1 and MeCO<sub>3</sub>PI-1 in Figure 242 have shown that very similar structures were observed for both materials after annealing at 400 °C for 1 h. The peaks at 142, 156, and 163 ppm were slightly larger for the annealed MeCO<sub>3</sub>PI-1. These peaks were assigned to the benzoxazole structure as a result of the Thermal Rearrangement. Accordingly, the lower

conversion, as evidenced by TGA measurements, was confirmed by the solid-state NMR experiment as well.

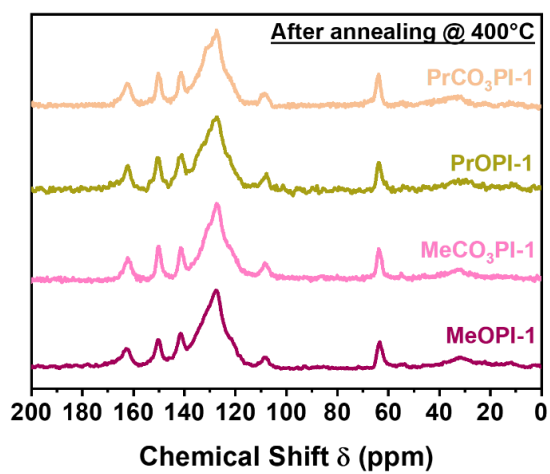


Figure 242.  $^{13}\text{C}$  CP-MAS NMR spectra of  $\text{MeOPi-1}$ ,  $\text{MeCO}_3\text{PI-1}$ ,  $\text{PrOPI-1}$ , and  $\text{PrCO}_3\text{PI-1}$  after annealing these polymers at 400 °C for 1 h.



## PART V

# Discussion



*A person who never made a mistake  
never tried anything new*

Albert Einstein

## Thermal Cascade Reaction Polymers

Thermally Rearranged Polymers are principally known for 22 years now, since their first intense study by Tullos *et al.* in 1999, when they reported an “unexpected thermal conversion of *ortho*-hydroxy-containing polyimides to polybenzoxazoles” [124]. They presented a mechanism, which involved a nucleophilic attack of the phenol group at the imide carbonyl group via formation of an aromatic heteroatom-bicyclic intermediate. Subsequently, a heterolytical cleavage of the formed hydroxy group was suggested and a simultaneous second nucleophilic attack of a hydroxy species at the other carbonyl group, leading to an *ortho*-carboxyl group containing polybenzoxazole, was proposed. This intermediate appears to be more stable, however, at the high temperatures required for such a solid-state cyclization reaction, the carboxyl group decarboxylates immediately. As a result, all research groups so far have been using TGA combined with a mass spectrometer or FT-IR spectrometer in order to execute an evolved decomposition gas analysis to monitor the reaction.

The number of investigations of such a reaction, especially when performed in polymers, increased rapidly after the 2007 publication by Park and Moo-Lee *et al.* [126], which used the solid-state reaction for the first time in polyimide films for the use as microporous gas separation membranes. Due to the rigidification, crosslinking and small pore formation, as a consequence of the decarboxylation reaction and CO<sub>2</sub> release, these materials improved with respect to their permeability and selectivity, while most polymeric membranes either improve one or the other, since they suffer from a permeability-selectivity tradeoff relationship.

Nevertheless, the major challenge remains to reduce the high temperature for the reaction. Widely used polymers such as 6FDA-BisAPAF and 6FDA-*p*HAB start their TR reaction, followed by TGA-IR, above 360 °C, according to measurements during this PhD study. The results are in agreement with the majority of the publications of these two TR polymers. These high temperatures already lead to partial degradation, uncontrolled crosslinking, for instance

due to the degradation of  $\text{CF}_3$  groups [118], and no commercially available support has been successfully established for an easy scale-up method which withstands these high temperatures for the best of my knowledge. Therefore, many scientists tried to lower the TR temperature for the last 14 years [138, 139, 254, 255, 267].

The most materials so far, were treated at 450 °C for 30 to 60 min to achieve conversions over 80% [152]. Only a rare number of reports were able to use annealing protocols at 350 °C and 400 °C in order to achieve reasonable conversions, for instance Guo and Calle *et al.* [138, 267]. The most materials, which were able to show high conversions were based on an aromatic polyether backbones. For instance, BPADA and ODPA based polyimide precursor were synthesized. In addition, Calle *et al.* prepared an aromatic ether-based diamine in order to lower the TR temperature [139, 267]. The TRP's with the lowest TR temperatures are also discussed in Section *Effect of the backbone* on page 43.

TBAHPB based TR precursor showed  $T_g$ 's of 245 and 304 °C, and a  $\text{TR}_{\text{onset}}$  of 316 and 321 °C. Interestingly, they still have high TR peak- and estimated offset temperatures of 396 and 424 °C ( $\text{TR}_{\text{peak}}$ ) for 6FDA-TBAHPB and BPADA-TBAHPB [139], respectively. However, the lowest  $\text{TR}_{\text{onset}}$  temperatures of this study were based on a flexible, hexafluoroisopropylidene (Bisphenol AF-type) based diamine 6FBAHPP, which had  $T_g$ 's of 234 and 280 °C (BPADA and 6FDA) and a  $\text{TR}_{\text{onset}}$  of 290 and 300 °C [139]. Lu *et al.* published the synthesis of aromatic fluorene containing polyether cardo backbones with "Low thermal rearrangement temperatures" [254] according to their title, with onset temperatures around 325 °C and peak temperatures of 371 °C for their 6FDA-based polyimide. However, the improved flexibility leads to efficient chain packing and therefore a lower number of non-equilibrium excess free volume, which favors high permeabilities. Accordingly, most materials showed performances around or below the Robeson Upper bound since the TR temperature and gas permeability behave in a kind of trade-off relationship as well if the design of the materials is based on lower  $\text{TR}_{\text{onset}}$  temperatures by preparing low- $T_g$  polymers.

For the design of novel low TR temperature-based polymers, it was crucial to understand the TR affecting parameters in order to make the right changes. Therefore, various backbones were synthesized and investigated by means of DSC and TGIR experiments and discussed in contrast to various reported TRPs based on non-commercially available monomers. The



experiments in section *Thermokinetic and -dynamic analysis*. revealed a very strong  $T_g$  relationship as reported by Calle and Guo *et al.* as well [138, 139], for the non-modified materials. However, these reports only correlated the  $T_g$  and TR temperature, but no structural correlation between amine and anhydride rigidity with respect to the TR temperature and relaxation processes were made in detail. Comer *et al.* already reported the strong TR temperature increase of the more rigid HAB containing TRP by means of broadband dielectric spectroscopy and dynamical-mechanical analysis[274, 277].

Accordingly, the first very important outcome of the investigations for the elucidation of the reaction mechanism is the observation that the TR process depends on the flexibility of the backbone and is therefore correlated to the glass transition temperature as an approximated indirect measure of the flexibility of polymer chains. However, it is not necessarily the  $T_g$ -lowering caused structural parameters themselves, but the segmental mobility, which is best described by the dihedral angle of the imide bond and the mobility of the amine unit. Improvements by modifying TR polymers should therefore target the mobility of these two units.

In addition, since no complete agreement on the mechanism and final product of the TR process exists, among TR polymer scientists worldwide, further investigations of the formed product were targeted. Due to the insoluble and low-swelling character of converted TRPs, the number of analysis methods is significantly decreased. Therefore, Raman and CP-MAS experiments were executed. While Raman methods were not successful due to the fluorescence of the aromatic backbone, CP-MAS was successfully executed. It is noteworthy that Park and also Smith *et al.* investigated the final structure of converted 6FDA-HAB and 6FDA-BisAPAF, respectively [133, 140]. They used  $^{13}\text{C}$ -CP-MAS experiments and suggested the formation of benzoxazole as the final product of the TR process. However, the signals of their CP-MAS experiments were still broad and a clear indication of the formation of benzoxazole rather than the second suggested structure, a lactam [128], were missing.

Further DFT simulations for potential mechanism were performed. According to the mechanism by Park, based on the suggestion by Tullos *et al.* a heterolytical cleavage of a hydroxy group in solid-state is proposed. This is expected to be very unlikely from a theoretical organic chemistry point of view with respect to the stability of the formed ions.

Generally, the formed intermediate can reverse to the starting HPI, as long as no degradation or consecutive irreversible reaction occurs. Therefore, the nucleophilic attack can be reversed. The addition of any nucleophile to a carbonyl group leads to a tetrahedral intermediate, which commonly rearranges to the carbonyl group by elimination of the better leaving group. In the case of the TR reaction, this means, that either the phenol or the bicyclic hydroxy intermediate formed. Since phenolic residues are better leaving groups, because they can accommodate the negative charge better due to the delocalized nature of the aromatic ring, whereas hydroxy groups are known to be very weak leaving groups [198]. Therefore, esterification reactions for instance are performed under acidic or base catalysis [198]. The formed hydroxy group is also not stabilized by surrounding solvent or any charged species. Accordingly, an improvement was made by suggesting a radical mechanism based on simulation within this PhD study. This lowered the reaction barrier already by 50%. A homolytic cleavage of the hydroxy group is more likely to occur in solid state. However, such a process would also lead to an increased number of water molecules formed during the reaction by radical abstraction of hydrogens from the polymeric surrounding, which is experimentally not the case. It was therefore suggested that another intramolecular nucleophilic reaction occurs. The process is depicted in Figure 44 and a reaction of the hydroxy group of the first intermediate with the other carbonyl group via a tricyclic transition-state geometry is expected. Since it is a kind of a hydroxy group transfer, this reaction was called transfer mechanism in order to distinguish it from the hetero- and homolytic elimination-addition reaction mechanism. Other mechanisms were simulated, among which two reaction mechanisms are also very reasonable, but showed higher energy barriers. The lactam mechanism involves a proton transfer from the intermediates hydroxy group to the tertiary amide nitrogen atom under simultaneous bond cleavage and formation of an amide-ester ring system which decarboxylates under formation of a  $\delta$ -lactam structure. However, the lactam formation was previously ruled out due to the absence of any experimental evidence. The second process is called the lactone-mechanism or spiro mechanism, since this emphasizes the special character of the formed intermediate.

The first two steps are identical to the steps of the lactam formation, except for the decarboxylation reaction. This intermediate is then expected to undergo an intramolecular nucleophilic attack of the carbonyl oxygen atom of the amide carbonyl group at the ester carbonyl-C atom under formation of a lactone intermediate with a spirocenter. The activation

energy is not reasonably higher than the proposed transfer mechanism, and lower compared to the homo- and heterolytically process. It also leads to a tremendous structure geometry rearrangement, causing the TR related rearrangement and rigidification. Subsequent lactone ring opening and decarboxylation in analogy to thermally treated phthalide containing polymer membranes as reported by Zhang *et al* [51, 117, 287].

The simulation of the spiro- and transfer mechanism are very important for the design of future TR polymers, as they reveal that disrupted chain packing might also be beneficial for the second step as it prevents the intermediates to be stabilized by means of hydrogen bond as shown by the stabilization energy of the various dimer arrangements. Since carboxylic dimers are among the strongest hydrogen bonds, an efficient chain packing led to strong hydrogen bonding between two *ortho*-carboxyl groups of two segments.

Accordingly, the experimental and simulation results, suggested a reasonable reaction mechanism in agreement with the experimental results. The formation of benzoxazole was experimentally corroborated, the units that were affecting the TR the most were identified and suggestions for the TR polymer design were made (Figure 243).

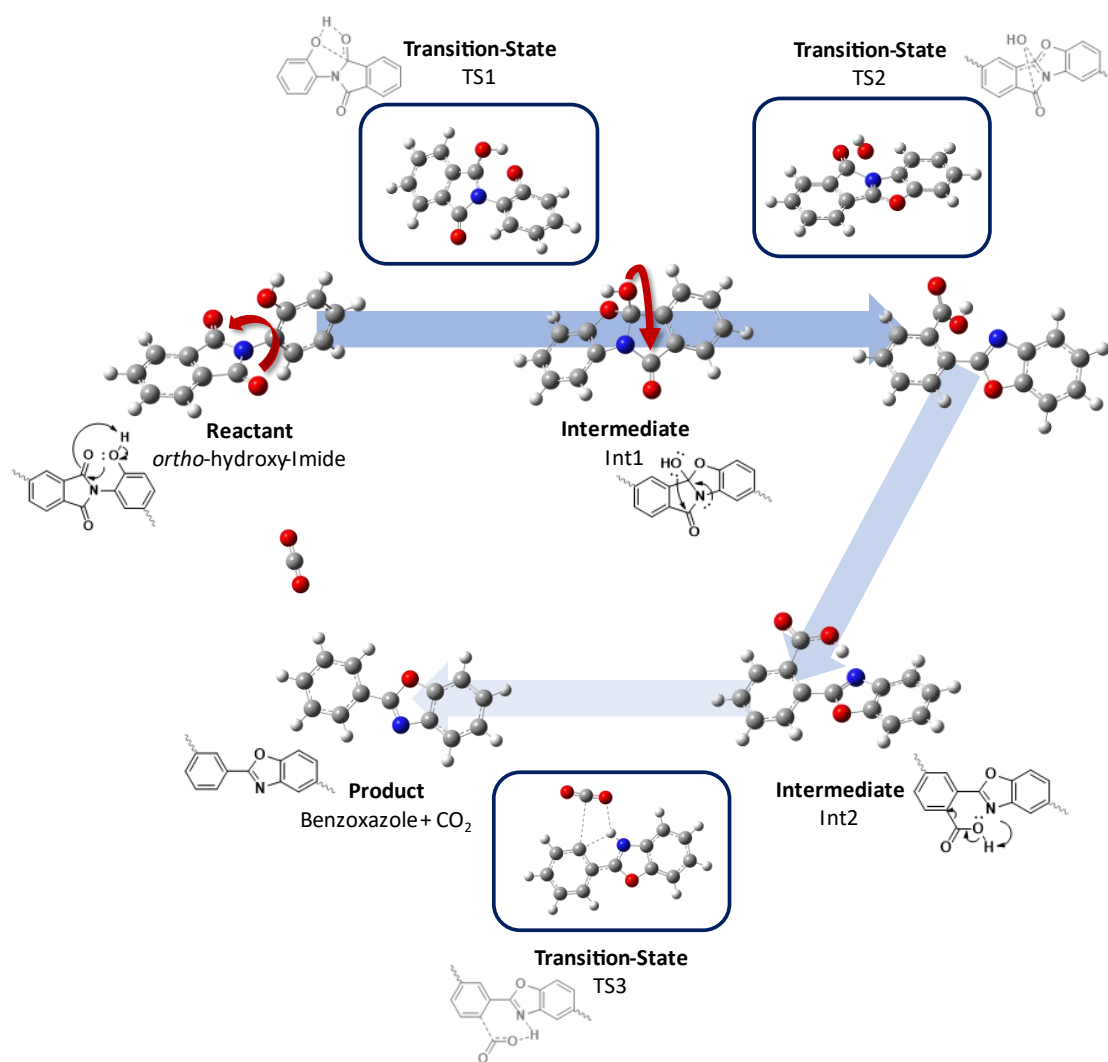


Figure 243. Simulated reaction mechanism by means of DFT (B3LYP/6-31G+\*). Reactant, intermediates, transition-state geometries and product is shown. The underlying mechanism is the described transfer mechanism.

Accordingly, in this study a different approach was chosen to lower the TR temperature compared to the simple use of low  $T_g$  components. The approach basically encompasses the introduction of new functionalities, which improve the segmental mobility of the amine unit by polymer chain packing disruption (Figure 244). In addition, the modifications were chosen to not only lower the TR temperatures, but significantly improve the membrane performance by increasing the initial processability, chemical resistance, aging rate, and perm selectivity of various gas pairs at the same time.

For that purpose, two strategies were designed and executed. The basic idea of both strategies is the protection of the phenol group, which eliminates the availability of hydrogen bonds and disrupts the chain packing. Upon heating, the phenol group needs to be recovered for the TR process, which is fulfilled by either decomposition of the modification or by means of another

Thermal Rearrangement. According to Tena *et al.*, the introduction of an allyl group can undergo a Claisen Rearrangement reaction in order to recover the phenolic group [256]. They claimed, that a phenolate is formed, which shows a higher nucleophilicity towards the partially positive and therefore electrophilic imide carbonyl group. Therefore, three types of structurally very similar modifications are discussed, which undergo either rearrangement or elimination according to the literature. The compared materials are based on the introduction of either a propyl, allyl or propargyl group.

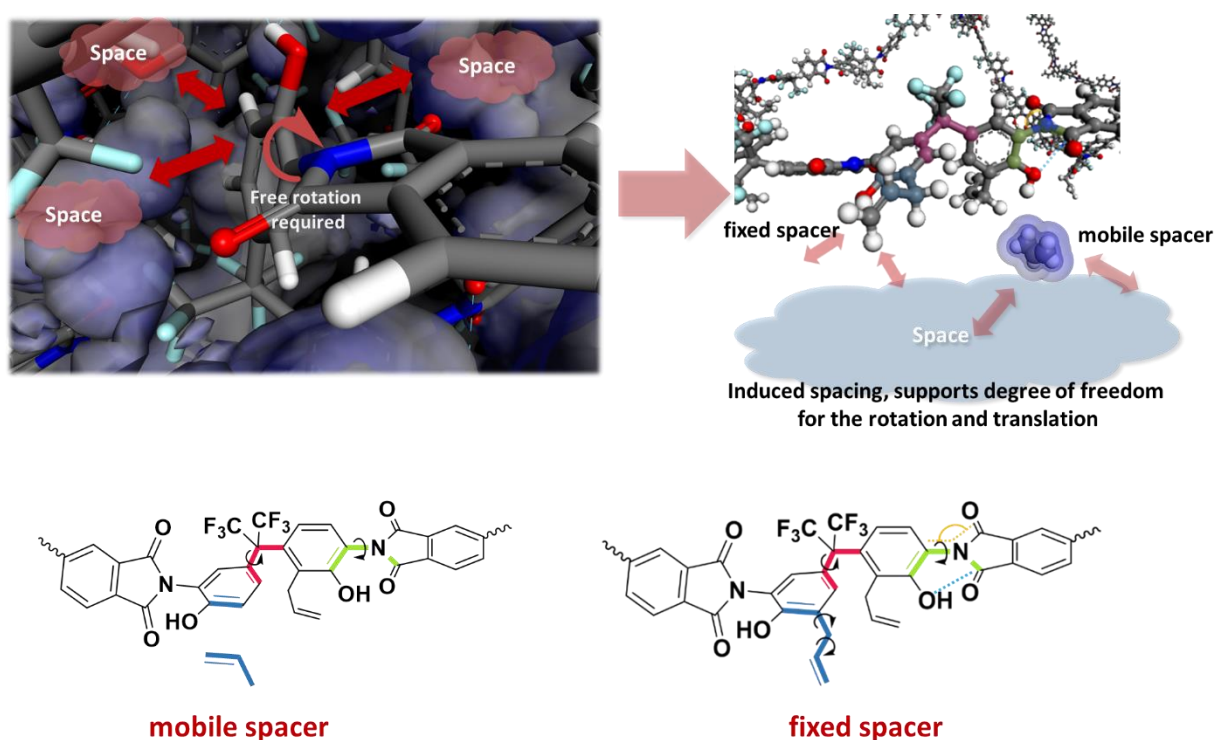


Figure 244. Conceptual design of the material modification towards lowered TR-specific temperatures by means of introduction of fixed and free spacer to separate polymer chains.

From a structural point of view, the difference between PrOPI1, Allyl-PI1 and Propargyl-PI1 is very small, as they all differ only in the type of the terminal bond of the corresponding *ortho*-hydroxy modification.

While PrOPI1 is imply a saturated propyloxy group, which consists only of sigma bonds, the allyl group has two  $sp^2$  hybridized carbon atoms  $C\beta$  and  $C\gamma$ , whereas Propargyl contains a triple bond and is therefore  $sp$ -hybridized.

However, in terms of flexibility this small change means a huge difference. While the propyl chain is capable to move freely, with respect to rotation around their dihedral angle, due to the two methylene groups, Allyl shows a stiff terminal bond and contains only one flexible

methylene group. However, angles of  $120^\circ$  are possible and a flip at the  $C_\beta$  atom is possible. On the other hand, propargyl contains a short (about 120 ppm) terminal triple bond, without any hydrogen at  $C_\beta$  and not flexibility at all, only the same methylene group is available. Therefore, when properties of propyloxy, allyloxy or propargyloxy polymers are investigated, which are related to relaxation and chain interaction properties, one has to keep in mind that these changes of the flexibility of the sidechains affects these properties strongly [198].

These three materials were synthesized and investigated by means of thermoanalysis, structure determination and simulation and part of three projects within this PhD study. In Figure 245 a comparison of the thermoanalytical results with respect to mass loss, heat flow, decomposition gas analysis and their structure determination is shown. All three materials are stable until  $300^\circ\text{C}$  but show a completely different thermochemical and thermophysical behavior up to a temperature of  $300^\circ\text{C}$ . The simplest representant of these C3-modifications, PrOPI1, does not show any chemical reaction or physical change, apart from its glass transition at  $210^\circ\text{C}$ . In the same study other alkyloxy modifications, such as methyl- and ethyl ether were studied. A nearly linear glass transition temperature decrease from methyl to propyl was demonstrated. Accordingly, the increase of the modification by addition of methylene groups increases the chain disruption and causes an increased degree of freedom, which was also confirmed by molecular modelling of the mean-square displacement as an indicator for the mobility of a polymer chain. Such an additional excess non-equilibrium free volume causes a higher relaxation rate of these groups, which is also known for many other polymers with aliphatic side chains [314]. For instance, the  $T_g$  decreases in the order from methyl acrylate to butyl acrylate [314]. Therefore, the combination of the glass transition temperature and MSD changes, indicates a chain spacing effect and a high degree of freedom to rotate. Nevertheless, if the terminal bond of the propyloxy group is changed to a double bond, leading to allyloxy, a very different behavior is demonstrated between  $100$  and  $300^\circ\text{C}$ . No decomposition occurs here as well, but heat flow measurements revealed a sequence of exothermic reactions. Thermokinetic analysis by means of non-*isothermal isoconversional* methods according to the Friedman and KAS method were performed. In addition, the exothermic peaks were deconvoluted by Gauss fitting in order to estimate the number of underlying processes. In combination with structure determination by means of FT-IR and  $^{13}\text{C}$ -CP-MAS NMR experiments, a thermally initiated cascade sequence of a Claisen Rearrangement, crosslinking

and benzofuran cyclization was found. Interestingly, the tendency to undergo the aforementioned reaction cascade, varies strongly in dependence of the type of allyl modification, which is discussed later. A glass transition temperature determination of Allyl-PI is very difficult, since the continuous change of the materials composition affects the thermal properties and therefore the glass transition temperature as well. For instance, the determined increasing degree of crosslinking, leading to a gel content of 100% at 300 °C, changes the film density, free volume, and flexibility, which affects the  $T_g$ . Calorimetric analysis of samples annealed at 200 and 220 °C showed  $T_g$ 's of 236 and 256 °C, respectively, demonstrating the continuous  $T_g$  increase. Molecular simulations have even shown, that at low degrees of crosslinking an increase of the mobility, as indicated by a higher mean square displacement, was obtained. This was justified by the increased chain separation of these few crosslinks and additional distortion of the system. When the degree of crosslinking increased, the polymer chain became a tighter network, which decreased the overall mobility and caused a decrease of the mean-square displacement. Therefore, a glass transition temperature determination was executed by completing the thermal reaction cascade, followed by a cool-down and re-heating cycle. The obtained glass transition temperature of 286 °C was significantly larger compared to PrOPI. However, the glass-transition temperature, prior to the Claisen Rearrangement, initiated cascade reactions might have been closer to PrOPI. It is noteworthy, that the experimentally observed single cascade reactions were simulated and have corroborated the observed mechanism, including the competitive nature of the cyclization and crosslinking reaction as both have similar activation barrier energies, and the strong thermodynamically stabilization due to the crosslinking, and accordingly a high negative reaction enthalpy, which agrees very well with the large released heat (exothermic heat flow), especially for the crosslinking deconvoluted peak.

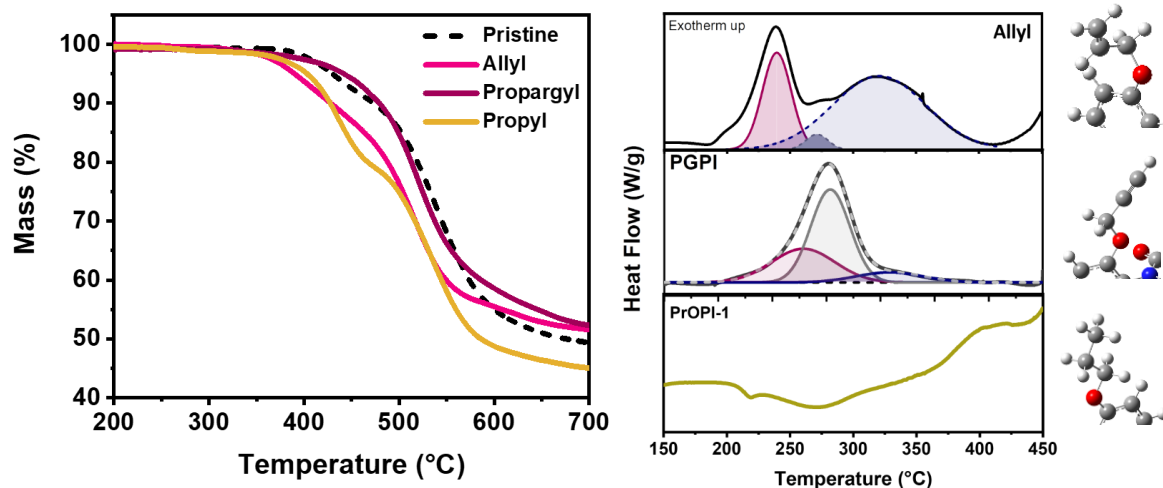


Figure 245. (left) Mass loss curves for the allylated, propargylated, propylated and unmodified polyimide. (right) Corresponding heat flow curves and simulated structures of the allylated, propargylated and propylated model.

When propargyloxy is used instead of allyl- and propyloxy groups, the thermal behavior changes again, strongly. For the propargylated material a thermokinetic analysis supported by modelling was executed as well. No decomposition prior 300 °C was observed as well. The calorimetric experiments by means of DSC have shown, that a similar heat flow pattern to Allyl-PI occurred. However, only one strong peak was determined at a similar temperature of 250 °C, while the Claisen-Rearrangement peaked at 240 °C. The higher temperature for the CR process in the case of Propargyl-PI might be reasonable, since the propargyl group is rather stiff, and shows higher activation barriers for the rotation, compared to the allyl modification. The Claisen-Rearrangement occurs between the aromatic C2 position and the terminal C $\gamma$  of the propargyl group, as bending of the propargyl chains towards the aromatic ring is required. The simulation has shown that a similar transition state geometry can be determined. In the case of allyl, the allyl group becomes resonant along the whole C3 group, with partial double bonds between C $\alpha$ -C $\beta$  and C $\beta$  to C $\gamma$ . Propargyl however could form an allene anyway, which would still cause a 180° angle at C $\beta$ . Other than that, the overall reaction path of both starting materials is quite similar, but in case of Propargyl an *ortho*-allene phenol group is formed, whereas Allyl forms an *ortho*-allyl phenol unit. Since allenes are significantly more reactive, for instance via dimerization similar to ketenes [194], the formed product is thermodynamically less stabilized. Immediate consecutive reactions are therefore more reasonable for the propargylated material. This product is therefore more an intermediate type and was not recovered by means of thermal analysis and structure determination, whereas the CR product of Allyl-PI was obtained in high yield. Furthermore, FT-IR studies have shown,



that the O-H stretching vibration was detectable in annealed Allyl-PI samples, however, no O-H vibration was determined before approaching 300 °C. Accordingly, no heat flow offset or plateau after the CR process was determined for Propargyl-PI in comparison to Allyl-PI. The overall normalized heat, obtained by integration of the heat flow curve was 2.5 times larger with about 330 kJ mol<sup>-1</sup> compared to 134 kJ mol<sup>-1</sup> for Allyl-PI, respectively. The potential underlying reactions were investigated in an analogous way to Allyl-PI. Peak deconvolution has shown that three underlying peaks can be distinguished by deconvolution. A strong peak, which was attributed to the CR process was determined as well, even though the structure determination was more hindered this time, since the gel content was higher for the propargylated material, and liquid-NMR was therefore very difficult to perform. However, propargylated polyimides yielded a smaller peak starting even before the CR starts. The First peak was difficult to assign to a specific process based on the FT-IR results. The thermokinetic analysis revealed an increase of the activation energy for the first 20% of conversion before it remained nearly constant (only a slight increase was determined) until 50% conversion. Allyl-PI showed a decrease and then a nearly constant activation energy with respect to the temperature as well. Both nearly constant areas proceed in the temperature range of the CR process, which shows that during that range, nearly no other reaction starts. However, the small increase and the overlap of the deconvoluted peaks, suggests that in both cases, Allyl and Propargyl, another reaction already initiates. Accordingly, no complete conversion of the CR process is required for the follow-up reactions. Every Claisen-Rearranged unit is then capable to undergo consecutive reactions as soon as the required temperatures are sufficient enough, for example to crosslink or cyclize (Figure 246). The simulations have demonstrated that both reactions have activation barriers which are not higher than the previous steps. Accordingly, with increasing temperature, the energy input is sufficient to initiate both reactions immediately after the CR reaction of a single unit is done. However, it is worth to notice, that the Alder-ene type crosslinking reaction requires two allyl or propargyl units to occur, while the cyclization is an intramolecular process within the same unit. Since the calorimetric experiments were done for polymers in solid-state rather than small model compounds in gas phase, the additional aspect of polymer chain mobility in order to bring two or more allyl/propargyl units together to react becomes crucial. This fact favors the intramolecular cyclization reaction, which has been seen to occur at an earlier stage for Allyl-PI.

Above 300 °C reactions were determined for all three materials, PrOPI, Allyl-PI and Propargyl-PI. Among these materials, PrOPI loses its propyloxy group completely by decomposition to propene and CO<sub>2</sub> as evidenced by decomposition gas evaluation. Thermogravimetric analysis with a coupled FT-IR spectrometer was used for that purpose. It was suggested, based on these thermoanalytical findings and DFT simulations, that the propyl group decomposes by an elimination reaction, forming propene, under recovery of the *ortho*-hydroxy polyimide at about 350 °C. Interestingly, the simulations have shown that the decomposition temperature and subsequent Thermal Rearrangement require nearly the same activation energies, while experimental results have shown that the energy input must be nearly the same as well, as both materials exhibit onset temperatures for the decomposition and Thermal Rearrangement in the same range as well. The TR<sub>onset</sub> is despite the fact that a propyl group has to be removed before starting the TR reaction, still lower by 16 °C compared to the pristine material. That is also interesting, since the product of the decomposition is the same material. However, the lowering of the TR temperature was observed for other alkyloxy modifications as well and also the compounds ButylenePI, PrenylPI and CycloAllyl-PI from the Allyl study in section *Polyimides with ortho-Allyloxy Groups*, which decomposed rather than rearrange by CR, showed the same TR lowering. This was attributed to the increased free volume around the polymer chain and higher degree of freedom to rotate. This of course corroborates the assumption that increased mobility around the amine unit is crucial to lower the TR. Since the decomposition occurs at the amine unit, the spot of the highest decomposition product location is next to the amine and accordingly next to the imide group in the polyimide. Hence, the decomposition produces a kind of swelling, and chain spacing leads to lowering of the TR<sub>onset</sub> temperature. This led to the formulation of a Thermal decomposition cascade reaction mechanism for modified TR polymers, which decompose to the pristine material followed by TR.

The second approach was based on the non-decomposition reaction induced recovery of the phenol-imide group by rearrangement reactions. Allyl-PI and Propargyl-PI are two representatives of this new group of TR polymers. Both materials recover the required phenol group by means of a Claisen Rearrangement reaction. However, partial cyclization can block the phenol group again. Nevertheless, according to the observed mass loss which corresponds ideally to two molecules of CO<sub>2</sub> per repetition unit and CO<sub>2</sub> as the only decomposition product, show that these open at higher temperatures and full TR conversion is still possible. Even

though crosslinking occurs to a high extent and these cycles are formed as well, the  $TR_{\text{onset}}$  and peak temperatures as well as the conversion after annealing at 350 and 400 °C exceed the most reported TR polymers by far. Only a few numbers of polyether based aromatic TR polyimides have shown competitive TR temperatures. However, their gas performance was around or below the 2008 and 1991 Robeson Upper bound for several gas pairs [254, 267], while best performances were demonstrated for fluorinated TR polymers, such as 6FDA-BisAPAF, acetylated 6FDA-BisAPAF or BisAPAF based bismaleimide precursor [140, 148, 264]. Above 300 °C, both materials, Allyl-PI and PropargylPI underwent further chemical reactions. Allyl-PI basically only undergoes a polyimide to polybenzoxazole cyclization reaction. The density of Allyl-PI therefore decreases to 1.33 and to 1.32 g cm<sup>-3</sup> upon annealing at 350 and 400 °C, respectively. The pore formation due to the TR reaction is partially compensated by the densification, due to additional crosslinking reactions of the allyl groups. Accordingly, no big changes of the film density were measured at 400 °C, even though the TR conversion increased from 48 to 100%. Propargyl-PI-1 appears to be more complicated above 300 °C. Another reaction cascade is initiated by opening of the formed chromene rings. The opened rings form *ortho*-allyl or *ortho*-allene units. However, the ring opening with the *ortho*-allyl product is thermodynamically favored according to the performed simulations. The opening was confirmed by FT-IR analysis after annealing at 300 °C. The allyl group can undergo the reactions, which were discussed for Allyl-PI already. It is therefore principally an Propargyl to Allyl reaction cascade, and since the polyimide backbone undergoes an *ortho*-hydroxy polyimide to polybenzoxazole rearrangement, the complete cascade reaction can be viewed as an Propargyl-PI to CxAllylPBO rearrangement. However, the allyl groups can be isomerized to a vinyl group, which forms a diene unit within its crosslinked unit. This diene is then principally able to undergo a Diels-Alder cycloaddition with a non-crosslinked chromene group. According to the DFT simulations, such a reaction requires activation energies, which are not significantly larger than any other reaction in such a model. However, here two crosslinked chromene groups and a free chromene group, which makes in total three molecules, are required for such a reaction. In polymers under solid-state conditions this is highly restricted, especially at high degrees of crosslinking. As a consequence of the additional crosslinking, the density increases and competes with the density decreasing TR process. A spectroscopic determination was rather difficult. The Thermal Rearrangement was confirmed by means of FT-IR measurements and is based on theoretical considerations and molecular

dynamic simulations, more likely to occur. This reaction is also hindered, as the diamine unit cannot rotate around the TR reaction responsible dihedral angle that easily. However, the reaction occurs inter-segmental, and with segmental between two monomeric units are meant, but not intermolecularly and is therefore an intramolecular reaction. Therefore, the overall TR conversion at 350 and 400 °C is significantly lower compared to Allyl-PI.

### Consecutive determined reaction products

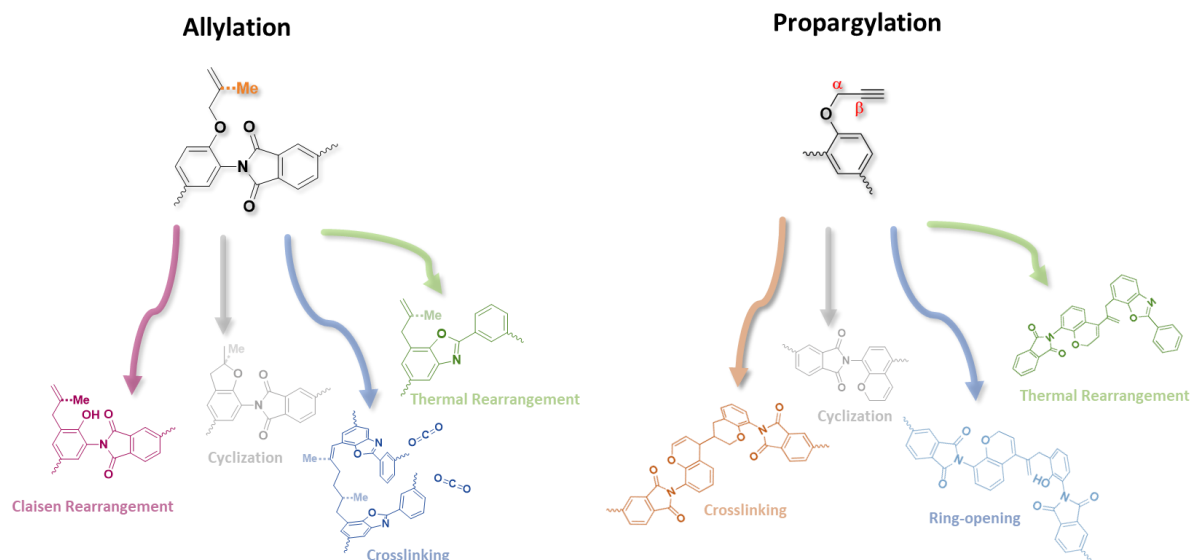


Figure 246. Determined consecutive reaction products of the allylated and propargylated materials.

The gas separation performance of all three materials was surpassing the 2008 upper bound for CO<sub>2</sub>/CH<sub>4</sub>, H<sub>2</sub>/CH<sub>4</sub>, ethylene/ethane and propylene/propane separation as well as O<sub>2</sub>/N<sub>2</sub> after annealing at 350 and 400 °C. Annealing at 350 °C, which is a lower TR treatment temperature than most materials have to be treated at, in order to achieve high PBO conversions around 50% and more, showed a conversion of 48% and a selectivity of 40 at a permeability of 4000 Barrer for CO<sub>2</sub>. A selectivity of 40 is important since the industry requires materials with selectivities above 31 [7]. Furthermore, due to the crosslinking and low thermal treatment, the chemical, mechanical, thermal properties are improved, and the plasticization and aging effect is expected to be reduced as well. In addition, the separation performance of olefines and paraffines proved to be highly competitive to other reported materials. Therefore, Allyl-PI is a very promising material for future gas separation and pervaporation tasks. In comparison, Propargyl-PI showed an even significantly more pronounced improvement of the gas separation performance. The untreated precursor showed comparable gas separation

performances to other TR precursors and Allyl-PI prior to any annealing step. The CO<sub>2</sub> gas separation was about 23 Barrer and the selectivity of CO<sub>2</sub>/CH<sub>4</sub> was very high with 76. Annealing at 300 °C for 30 min caused an increase to 100 Barrer for Allyl-PI as a consequence of the crosslinking, which formed a tight and stiffened network. Therefore, the selectivity remained reasonably high with 56 for CO<sub>2</sub>/CH<sub>4</sub> and 68 for H<sub>2</sub>/CH<sub>4</sub>. In case of Propargyl-PI the permeability increased to 258 Barrer. However, the selectivities for all gas pairs were very low. For instance, the separation of CO<sub>2</sub> from CH<sub>4</sub> was 15. The crosslinks in Propargyl are, other than those in Allyl, very stiff and tight. Accordingly, the density decreases in Allyl-PI from 1.42 to 1.35 g cm<sup>-3</sup> upon annealing at 300 °C. Nevertheless, the density Propargyl-PI increased from 1.32 to 1.45 g cm<sup>-3</sup>.

Hence, a very tight network has formed. Furthermore, structural investigations have shown, that the formed chromene cycles partially open and form C<sub>γ</sub>- and C<sub>β</sub>-crosslinked *ortho*-allyl groups and recovered the phenol group. This can result in further pore blocking by the more flexible allyl group, despite its crosslink, and the phenol group can undergo hydrogen bonding. The situation changes when the films were annealed at 350 °C and higher temperatures. While Allyl demonstrated an increase by 300 Barrer as mentioned before, the permeability for CO<sub>2</sub> in Propargyl-PI increased by a factor of nearly 5 to about 1200 Barrer. In addition, the selectivity increased as well. A selectivity of 34 was determined in the case of CO<sub>2</sub>/CH<sub>4</sub>. Accordingly, this material surpasses the selectivity limit of 31, shows a high permeability of 1200 Barrer and surpasses the 2008 Robeson Plot by far and approaches the 2015 upper bound. Therefore, Propargyl-PI1-350°C ranks as one of the best polymeric gas separation materials based on pure gas measurements. The crosslinking makes these materials mechanically, chemically, and thermally stable and plasticization effects are expected to be lowered. Moreover, while most TR polymers are commonly annealed at 450 °C in order to achieve these high permselectivities, this material was treated at only 350 °C. As a consequence, side reactions, such as degradation do not occur. The gas separation of other gas pairs was also extraordinarily large. However, most reported microporous polymeric membranes are not tested for their olefine/paraffine separation. Annealing at 400 °C resulted in another very strong increase. The initial permeability was about 9000 Barrer, with a selectivity of 15 for CO<sub>2</sub>/CH<sub>4</sub>. In addition, the ethylene/ethane separation was upper bound with 1138 Barrer and still a 2.6 selectivity.

In total, both materials start with a very similar composition, but the small differences of the terminal double or triple bond in Allyl- or Propargyl-PI, respectively, make a big difference with respect to their thermally initiated reactions and therefore the materials properties, especially the film properties are very different from each other. The difference becomes even more pronounced when a propyloxy group is used instead, as this one only decomposes above 300 °C. As a consequence, a PBO is formed analogously to the pristine material. However, the loss of propylene, which diffuses through the membrane, affects the film density, free volume and in total the polymer chain packing as well. Therefore, the measured gas performance varied to polymer films based on unmodified 6FDA-BisAPAF. PrOPI1, after annealing at 400 °C, had a permeability of 1631 Barrer for CO<sub>2</sub> and a CO<sub>2</sub>/CH<sub>4</sub> selectivity of 22. This means, that selectivities are comparable to Allyl-PI, but permeabilities are about 600 Barrer higher. In contrast to Propargyl-PI the selectivity is higher by about 50%, when fresh as-annealed films are compared. However, the permeability is about six times lower. The physical aging over six months in turn led to a comparable selectivity of Propargyl and fresh PropylPI1, but the CO<sub>2</sub> permeability was still about twice as high.

One great advantage, despite the many improvements, due to the incorporation of any of these three groups has not been discussed yet. It is the possibility to tailor a specific TR polymer precursor or polyimide for a very specific task by choosing among many parameters. Any chemist is able to target specific properties by choosing from

- Polyimide, poly (amic acid) or polyamide
- Backbone structure
- Alkyloxy, Allyloxy or Propargyloxy modification
- The degree of modification
- A derivative of any of the three modifications
- Annealing target temperature and annealing time
- Purge gas

The studies included the investigation of the backbone, degree of modification and the variation of the allyloxy and propargyloxy group by using different commercially available

allyl- or propargyl-based halogenides as reactants. The advantage of the modification reaction is that, except for  $\alpha$ Mallyl and cycloAllyl-PI, every synthesis was done according to the same synthetic route, which also led to full conversion, easy purification, easy scale-up and no side-reaction or degradation. The result was in nearly any case a good film forming still high-molecular weight polymer.

The variation of the backbone has shown, that basically the same reactions occur, independently of the backbone, since every reaction, except the crosslinking and cycloaddition occurs intramolecular. However, the required temperatures and conversions varied strongly. More flexible backbones showed still lower  $TR_{\text{onset}}$  temperatures, but the difference to the unmodified material becomes more pronounced for more rigid backbones. This observation is reasonable, as rigid backbones, such as 6FDA-HAB pack more efficiently and have a low degree of freedom with respect to their mobility. Therefore, a polymer chain packing disrupting modification such as a flexible allyl group can induce the mobility more in relation compared to a backbone, which is already very flexible and is even hindered by the additional groups.

The degree of modification in both materials, Allyl- and Propargyl-PI, can be seen as a great opportunity to vary the polymer properties. A strong correlation of the number of allyl and propargyl groups with respect to solubility and after annealing to crosslinking was demonstrated. The incorporation of more groups enhances the solubility and therefore their processability. The degree of crosslinking increases with the number of modifications, since more crosslinkers are present. At degrees of crosslinking below 40% the density decreases continuously for all materials. At low annealing temperatures, due to low degrees of crosslinking, which leads to chain separation and at high temperatures, due to the Thermal Rearrangement conversion, which has been demonstrated to be lower for low degrees of modification. The reason for that is that low modification levels disrupt the chain packing, but crosslinking is still low. At a certain point, the number of allyl and propargyl groups becomes so large, that the crosslinking tightens the network and restricts the mobility of the polymer chains. Accordingly, the spacing effect is overcompensated and the  $TR_{\text{onset}}$  temperature increases. High degrees of crosslinking and lower degrees of Thermal Rearrangement cause an increase of the density and inter-chain spacing, as demonstrated by XRD measurements. In case of Propargyl-PI, the presence of a low degree of propargylation with respect to the

Thermal Rearrangement is interesting for another reason. While Allyl-PI benefits from low modification levels as a consequence of the induced chain disruption and increase of the mobility, which is important for such an inter-segmental reaction, the propargylated materials undergo a chromene cyclization after the CR process and have tight crosslinks. Therefore, they need to re-open first before undergoing any TR reaction. At low crosslinking levels, the majority of the phenol groups are not modified and can readily undergo the TR process. At that point, the low degree of crosslinking acts as well as chain spacer and additionally lowers the TR temperature. Therefore, it is noteworthy that despite the high restrictions and low conversions for Propargyl-PI, both propargylated materials with 8 and 15% propargylation have shown to have the lowest  $TR_{onset}$  temperatures of any modified TR precursor and next to polyether based TRPs also among the lowest  $TR_{onset}$  temperatures at all. Allyl15 and Allyl40PI-1 showed competitive  $TR_{onset}$  temperatures. However, the gas performance for these materials was around the Robeson Plot of 2008 for many gas pairs, but not as competitive as Propargyl-PI-1 with full propargylation.

Finally, the aspect of using derivatives of allyl and propargyloxy groups is worth to discuss. Materials with methyl groups at different positions along the C3 chain were used, since these are commercially available. The number of derivatives for propargyl is reduced as substitutions can only occur at  $C_c$  and  $C_\gamma$ . Most propargyl derivatives are  $\gamma$ -substituted as the  $C_\gamma$  atom is C-H acidic and can easily be converted, for instance to  $\gamma$ -trimethylsilyl propargyloxy.

Both classes of TCRPs, allyl and propargyl, showed strong variations with respect to the thermal behavior and accordingly their chemical and physical properties depending on the type of derivative. Allyl modifications with free allyl groups after the Claisen Rearrangement, which are all  $\gamma$ -substituted allyl modifications, such as  $\gamma$ Mallyl,  $\gamma$ Eallyl,  $\gamma$ Phenyl and also Allyl-PI show higher tendencies to crosslink. This was confirmed by DFT simulations of 14 different crosslinking mechanism. The most plausible mechanism occurred between the terminal  $C_\gamma$  and another  $C_\gamma$  or  $C_\beta$  atom of another allyl group according to an Alder-ene crosslinking reaction. Careful investigations of the mechanisms, following their intrinsic reaction coordinate, showed that the free accessibility of the reactive centers causes a lower-energy transition state geometry as no steric constraints occur. Studies of the fluctuations of these allyl groups via molecular dynamics simulations have proven these observation to be even more



important in polymers, as their possibility to arrange adequately depends strongly on the mobility of the polymer chain. However, the higher tendency to crosslink and the produced tightening and restricted mobility caused a less pronounced decrease of the  $TR_{\text{onset}}$  temperature compared to the pristine material. However, despite the crosslinking, the onset temperature was about 20 °C lower for  $\gamma$ MAllyl-PI. In contrast the  $\gamma$ -substituted materials of propargyloxy groups tend to lower the degree of crosslinking. The reason for that is, that the substitution location along the C3 chain does not change in propargyl groups, while it does in allyl groups. Accordingly, the  $\gamma$ -substitutes remain at the double bond and therefore the spot for the crosslinking. Furthermore, the formed chromene rings are less flexible compared to allyl groups, therefore the additional methyl groups decrease the crosslinking a lot. When comparing transition state geometries, two chromene units have to arrange with their methyl groups opposite to each other. In combination with the fact that such an arrangement of the groups is difficult in polymers, this effect is very plausible. It becomes more complicated if the  $\gamma$ -substituent even increases to ethyl, naphthyl or trimethylsilyl. The gas separation performance of  $\gamma$ MPropargyl was significantly higher than that of  $\gamma$ Mallyl. While  $\gamma$ Mallyl showed a CO<sub>2</sub> permeability of 185 Barrer at 350 °C, and a selectivity of 30, the  $\gamma$ MPropargyl modification had a CO<sub>2</sub> permeability of 1765 Barrer at a selectivity of 22.6.  $\gamma$ E-modifications are very interesting to discuss here as well. When an ethyl group is introduced at the  $\gamma$ C atom of an allyl unit, it undergoes another consecutive reaction after the CR process, the so-called abnormal CR. This is a type of Conia-oxa ene rearrangement from the normal product, a  $\gamma'$ -ethyl substituted allyl group to a  $\alpha'\gamma'$  methyl substituted allyl group. Accordingly, both groups are present in the polymer and therefore a free double bond which can undergo crosslinking more easily and a highly substituted modification with a methylated double bond, which cannot easily approach each other for crosslinking. MD simulations have shown that the normal product undergoes crosslinking similar to  $\gamma$ Mallyl and led to nearly the same degree of crosslinking. DFT simulations revealed a lower activation energy barrier than the abnormal product, which showed among the highest barriers. MD simulations of the abnormal product have shown that the degree of crosslinking was significantly lower. This was in agreement with the gel-fraction experiments.  $\gamma$ Eallyl showed the lowest gel-content among all allyl derivatives. The high substitution made these allyl groups excellent chain disruptors and combined with a low degree of crosslinking, which was proven to be beneficial for the TR reaction, caused a strong decrease of the  $TR_{\text{onset}}$  temperature. The  $TR_{\text{onset}}$  for  $\gamma$ EAllyl-PI was

309 °C and next to 8 and 15% Propargyl containing 6FDA-BisAPAF it was the material with the lowest  $TR_{\text{onset}}$  temperature among all non-ether TRPs ever reported (see Figure 247). In propargyl chains, the  $\gamma$ -ethyl substitution did not undergo an abnormal-CR reaction. If the substitution is located at the methylene group, which means at the  $C\alpha$  atom, then in both cases, the Claisen-Rearrangement occurs at lower temperatures. The explanation is the same in both cases. The  $C\alpha$  is more stabilized by the inductive effect of the methyl groups, and as a consequence the charge of the  $C\alpha$  and  $C\gamma$  atom become very close to each other. The breaking and forming bonds in the transition state geometries are compared to other derivatives in the same range. Accordingly, the CR mechanism proceeds more by a polar or even ionic manner. The HOMO-LUMO gap is lowered in both cases compared to other derivatives. In the case of Allyl-PI and  $\alpha$ MAllyl-PI the difference is 0.21 eV. The tendency to crosslink in  $\alpha$ MAllyl-PI is lower at temperatures below 280 °C and increases to yield about a gel content of nearly 100% at 300 °C. In the case of  $\alpha$ MPGPI1 the crosslinking also tends to be lowered. Even though the chromene double bond is principally freely accessible, the transition state geometry of the Alder-ene crosslinking via a six-membered transition state geometry has to proceed with the methyl group of both crosslinking partners on the same side. This lowers the chances of successful crosslinking in polymers since their mobility is too low to enter such a specific position in a large number. As a consequence, the deconvoluted exothermic heat flow peak for the crosslinking appears to be very low. One substitution pattern is only possible in the case of Allyl-PI, which is the methylation at the  $C\beta$  atom. The  $\beta$ MAllyl-PI showed the highest tendency to undergo the benzofuran cyclization reaction, which was evidenced by  $^{13}\text{C}$ -CP-MAS experiments. In addition, gel-fraction measurements have shown, that  $\beta$ MAllyl-PI had the lowest crosslinking tendency next to  $\gamma$ EAllyl-PI. This is attributed to the methyl group at the double bond, which decreased the tendency for  $\alpha$ MAllyl-PI and is responsible for the low degree of crosslinking of  $\gamma$ Eallyl and  $\gamma$ MPGPI as well. Hence, the sterically hindered double bond does not readily crosslink. The lower tendency was also confirmed by means of quantum mechanical calculations via DFT simulation. However, the high number of benzofuran groups, which was estimated to be in the range of 50%, with its two methyl groups, leads to very inefficient chain packing. This strong polymer chain packing disruption and the low tendency to crosslink as well as the low number of crosslinkers present in the material, leads to good conditions for the TR reaction. Therefore, the  $TR_{\text{onset}}$  is reasonably low with 325 °C and more importantly the conversion at 350 °C was already 84% and 100% after annealing at 400 °C. In

contrast the  $\gamma$ EAllyl-PI had a conversion of 100%, already after annealing at 350 °C, which has not been reported yet. Moreover, the CO<sub>2</sub> release and a mass loss were determined based on a decomposition gas analysis of membranes, which were annealed at 300 °C for 2 h. Allyl-PI These are the highest conversions at an annealing at only 300 °C. To the best of my knowledge, no material has been reported yet to undergo an HPI-to-PBO reaction during 300 °C annealing.

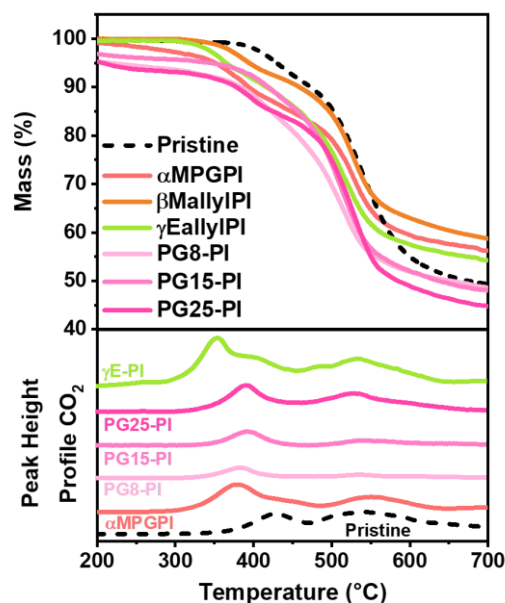


Figure 247. Mass loss curves and carbon dioxide peak height profile from decomposition gas evolution analysis of the TCRP materials with the lowest TRonset and -peak temperatures.

As a consequence,  $\beta$ MAllyl-PI and  $\gamma$ EAllyl-PI showed permeabilities of 80 and 900 Barrer for CO<sub>2</sub> after annealing at 350 °C and 1984 Barrer and 3011 Barrer for CO<sub>2</sub> after annealing at 400 °C. Only acetylated TR precursor showed higher permeabilities among all modified TRPs [132, 141, 163]. But they required an *isothermal* treatment at 450 °C. No propargylated material demonstrated such a high permeability for CO<sub>2</sub>, except for the unmodified Propargyl-PI1. However, in comparison to the 3011 Barrer, the unmodified Propargyl-PI-1 had a CO<sub>2</sub> permeability of 3440 Barrer at only 375 °C for 90 min annealing underlining the extraordinary performance of Propargyl-PI1. The high performance of Propargyl-PI is expected to be caused by the numerous randomly distributed structural features of the rigid chromene crosslinked network, with few highly rigid cycloaddition products and benzoxazole units, which lead to stiff structures that preserve the formed voids, which are connected by slightly more flexible pores. These flexible pores are areas with higher hexafluoroisopropylidene groups and non-

crosslinked segments. As a consequence, high diffusion pathways are formed, leading to high gas diffusion and permeabilities, while these interconnectivities favor high selectivities for gas pairs with large differences in their kinetic diameters such as H<sub>2</sub> and CO<sub>2</sub> *versus* methane. Such a pore structure is also the reason for the increased permeability and selectivity for the thermally rearranged pristine polyimide. In allylated polymers the crosslinked structures are not that rigid as the allyl crosslinking forms five to six-membered aliphatic crosslinks which are flexible. The flexibility decreases as the number of substituents increases. In  $\gamma$ Eallyl four methyl groups are distributed by means of an end-to-end Alder-ene crosslinking mechanism (ee\_mechanism). Accordingly, the gas separation of  $\gamma$ Eallyl-PI is very high. However, the large size of the crosslinker leads to larger pathways. Therefore, the selectivity of Propargyl-PI-1 is higher.

In conclusion, the investigation of allylated, alkylated and propargylated *ortho*-hydroxy polyimides revealed, that both strategies of having decomposition based and rearrangement-based cascade reaction undergoing offer the possibility to lower the Thermal Rearrangement onset temperature and tailor the polymer properties by variations of different parameters such as backbones, derivatives, annealing temperatures etc., the type of formed structures can partially being controlled in dependence of these chosen parameters. This offers any material scientist a large toolbox to tailor specific materials for gas separation membranes but potentially for pervaporation, nanofiltration and fuel cell membrane applications as well. The prepared materials compete on the highest level with other TR polymers and the lowest TR temperatures and highest gas separation performances were determined (Figure 248).

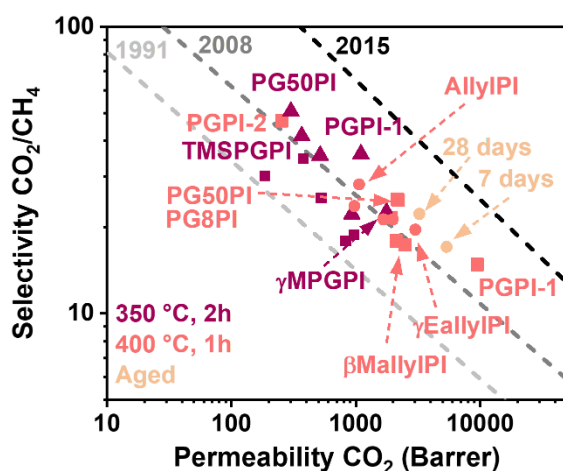


Figure 248. Robeson Upper bound plot for CO<sub>2</sub>/CH<sub>4</sub> for the best propargylated and allylated annealed materials.

## Thermal Cascade Decomposition Polymers

At this stage, thermoreactive films from cascade reaction undergoing allylated and propargylated polyimides were presented. In addition, another category of thermal decomposition reaction polyimide as Thermal Rearrangement membrane precursor were presented, whereas they also undergo kind of a simpler cascade reaction compared to the allylated and propargylated materials, since the decomposition is required for the consecutive TR reaction.

Three categories of *ortho*-hydroxy modifications were investigated in detail. These were alkyloxy, acyloxy and carbonate ester modifications. The difference between these three classes is basically the state of oxidation of the C $\alpha$  atom. The acyloxy modifications contain in contrast to the alkoxy modifications a carbonyl at C $\alpha$ , while the carbonate esters are connected to an additional oxygen atom, making it in total an organic carbonate. The comparison of the three smallest modifications, namely MeOPI-1, MeCO<sub>2</sub>PI-1, and MeCO<sub>3</sub>PI-1, were investigated in detail by using thermal analysis and structure determination methods, such as FT-IR and <sup>1</sup>H-NMR, <sup>13</sup>C-CP-MAS NMR. A comparison of their mass loss curves, and corresponding decomposition gas analysis revealed that very different processes take place. However, in all three polymers, the conversion to a polybenzoxazole structure via Thermal Rearrangement occurs, but to different extents.

The methyl ether as the overall smallest modification of this study, demonstrated a high potential as a TR precursor polymer. The onset temperature for the Thermal Rearrangement was determined by means of evaluation of the first derivative, mass loss curve and CO<sub>2</sub> peak height profile. The determined temperature was 306 °C, which means it ranks among the lowest TR temperatures, that have been reported for a TR precursor so far. Interestingly, it is even lower than the very low TR<sub>onset</sub> temperature of  $\gamma$ EAllyl-PI-1, which started the reaction at 309 °C. However, the peak temperature was higher with 393 °C. The conversion of 96.7% after annealing at 400 °C was reasonably high. This result was surprising, especially since Comesana *et al.* reported that the methoxy functionality does not undergo a TR process unless it is decomposed [132], which was suggested to occur via a radical mechanism above 400 °C. Conversions of only 14% after annealing at 400 °C and 61% after annealing at 450 °C were

obtained. The suggestion within these studies made in this thesis, was that the type of thermal reactions, especially the TR mechanism depends strongly on the backbone flexibility. According to Guo and Calle *et al.* [139], it is known that the backbone flexibility increases the TR rate enormously. This is attributed to the higher segment polymer chain mobility at lower temperatures compared to rigid backbones. As a consequence, these polymers with low glass transition temperatures can rotate around the dihedral angle of the imide bond more easily and undergo a TR reaction. 6FDA-BisAPAF in contrast to 6FDA-HAB has a lower  $T_g$  and a lower TR temperature. The fluorine group in the diamine unit act as chain packing disruptors and cause a local free volume element around the diamine as well. Therefore, despite the higher glass transition temperature compared to BTDA-APAF or PMDA-APAF for instance, the TR conversions were larger according to Calle *et al.*'s data [139]. The suggested TR reaction mechanism is an initial proton transfer from the phenol group to the imide carbonyl oxygen atom. This protonation increases the electrophilicity of the carbonyl group, as it induces a partial positive charge location at the carbonyl C atom. The phenolic oxygen atom then attacks the carbonyl group via a nucleophilic attack simultaneously. This process is not possible if the phenol group is protected, and the protective groups do not decompose at lower temperatures or rearrange. For instance, in chapter *Thermal Cascade Reaction Polymers* a strategy was proposed to introduce a chain packing disruption element while having a phenol group present for the TR reaction, which is accessible by post-polymerization modification. The principal type of modification was a propargyloxy or allyloxy modification, accordingly an ether as well. In these studies, derivatives were investigated which did not rearrange to the phenol, but decompose, namely prenyl-, cycloallyl- and ButylenePI. These materials, however, decomposed at temperatures which were below 300 °C. Therefore, the pristine materials were recovered and underwent a TR process. The elimination occurred via E2 mechanism by transfer of a proton from the C $\beta$  atom to the phenol oxygen. The elimination product was an unsaturated decomposition product. In the case of the butylene ether, butadiene was formed. Prenyl decomposed to *isoprene* and cycloallyl, which is basically a cyclohexene ring decomposed to cyclohexadiene. Methyl groups do not have a C $\beta$  atom. Accordingly, a decomposition by means of elimination mechanism E2 is not possible. Comesana proposed a radical cleavage of the ether bond, based on TGA-MS investigations [132]. However, in 6FDA-BisAPAF based methoxy modification CH<sub>4</sub> as decomposition product was detected at the same time as TR related CO<sub>2</sub> release. If a homolytic cleavage of the methyl group would be the

case, a CH<sub>4</sub> evolution onset before that of CO<sub>2</sub> would be expected. Furthermore, a temperature of 306 °C is considered to be too low for such a homolysis reaction. Therefore, an analogous reaction path to the mechanism of the pristine 6FDA-BisAPAF polymer is suggested. This would take place by means of a methyl group transfer from phenol oxygen to the carbonyl group. This leads to the formation of an intermediate with methyl ether functionality, by the concerted reaction of the phenolic oxygen atom at the carbonyl C atom in an analogous way to the proposed mechanism for the TR mechanism in pristine TRPs. This process is possible, since the methyl group is the smallest possible group, and a steric hindrance with the imide units is rather low. The simulation reveals an increase of the activation energy compared to the pristine material, while a radical cleavage becomes energetically more reasonable for the methylated polymers, compared to the pristine material. However, the subsequent reactions of the radical or homolytic pathway have significantly higher activation energies and involve very high energy intermediates due to the radical nature. The subsequent reactions of the methyl-transfer mechanism, however, are lower and the complete reaction path and therefore mechanism becomes more reasonable. Furthermore, the experimental results corroborate the mechanism. Solid-state NMR and FT-IR spectroscopy support the formation of polybenzoxazole. In the case of a radical pathway, it is likely to observe the formation of a lactam product.

How can the lowered TR temperature be explained, if the activation barrier appears to be significantly higher (78.6 kcal mol<sup>-1</sup> versus 35.9 kcal mol<sup>-1</sup>)? The simulations of model compounds do not take into account that the rotations around bond angles and torsional dihedral angles are additionally restricted in polymers. The first TR reaction step depends on the free rotation around the dihedral angle. Therefore, materials with lower glass transition temperatures preferably undergo the TR process at lower temperatures. Therefore, the contribution of the mobility to the final outcome is significant. One method to improve the mobility and lower the TR temperature was demonstrated in chapter *Thermal Cascade Reaction Polymers* by introducing a spacer. The approach chosen here is to separate the polymer chains by polymer chain packing disruption via protection of the phenol group. This effect was also observed by Sanders *et al.* and Smith *et al.* who have shown that the T<sub>g</sub> is lower when the material is acetylated [141]. No hydrogen bonds can be formed by the phenol group and the formation of charge-transfer complexes is restricted as well. In that case the modification

group neither decomposes nor rearranges within the diamine unit but takes part by the TR reaction itself. Therefore, it is less of a thermal decomposition cascade reaction polymer. However, the study of different backbones has shown, that an anhydride was polymerized with BisAPAF and methylated *versus* an anhydride was polymerized with HAB and methylated (or dianisidine was used as diamine), a shift of the TR temperature occurred. The investigation of the heat flow of each material has shown that exotherms below 400 °C were observed, with rigid and flexible dianhydrides. However, once HAB is used instead, the exothermic heat flow started at the end of the measurements, significantly above 400 °C. This was consistent with the TG-IR experiments. Mass loss steps occurred at significantly lower temperatures in correlation to the heat flow measurements compared to the HAB -based polyimides.

Larger alkyloxy groups were able to undergo an elimination reaction according to an E2 mechanism. As a consequence, the TR temperatures increased as the pristine 6FDA-BisAPAF was formed, predominantly. However, the ethyl group appears to be of intermediate size, which is why both reactions might be plausible. Ethylene was observed as decomposition component; however, this alone does not explain the final mechanism. If the ethyl group is transferred to the carbonyl group in the same way, then it could be eliminated from the first intermediate or the second intermediate of the reaction mechanism, which is an *ortho*-carboxyl benzoxazole, in that case an *ortho*-carboxyl ethyl ester benzoxazole. Since the ethylene evolution did not occur prior to the CO<sub>2</sub> release, it is assumed that the mechanism for MeOPI is also possible for EOPI. In both cases high conversions above 90% at 400 °C were measured.

In contrast the use of acetyl groups for the modification of the pristine material appears to behave completely different. Even though it is basically the smallest derivative of the acyloxy category, it is a C<sub>2</sub> group, such as ethoxy. In contrast to the methoxy derivative, the acetyloxy group contains a C $\beta$  atom, which can be deprotonated. Hence, an elimination reaction according to an E2 mechanism is possible as well. This mechanism is also confirmed by TGA-IR experiments which revealed the formation of a ketene, which would be the direct elimination product. In addition, carboxylic acids were found, when acyloxy derivatives were investigated. This might be due to the reaction of the highly reactive ketene with moisture in the purge gas or membrane. These findings are in agreement with studies by other groups [132]. The loss of the acetyl group prior to the TR process suggests, that a decomposition



occurs, leading to the pristine TRP which undergoes a TR process once the thermal energy is sufficient enough, which means at higher temperatures. This observation, that the acetyl group decomposes prior to the TR process supports the idea, that the Ethoxy polyimide EOPI undergoes a different process including an elimination reaction, since no decomposition occurs to a high extent before the TR process occurs. The Ether modification Butylene-PI did decompose above 300 °C. Immediately after decomposing to the pristine polyimide, it underwent a TR reaction. This can be clearly seen by a slight shift of the butadiene formation onset and peak temperature to lower temperatures compared to the TR related CO<sub>2</sub> release. Therefore, even if high temperatures for the elimination of the ethyl group would be required, the evolution of ethylene should appear before detecting CO<sub>2</sub>. In acyloxy modifications, such as the acetylated polyimide MeCO<sub>2</sub>PI-1, the negative inductive effect of the carbonyl group might decrease the bond strength between the phenol oxygen and carbonyl carbon atom.

In addition, other derivatives were investigated. In contrast to the alkyloxy groups, the ester modifications, larger than acetyl, appeared to decompose nearly at the same temperature onset. Accordingly, the elimination reaction was not strongly affected by the size and structure of the acyloxy group. The impact on the stability of the ester bond appears not to be affected strongly. However, this situation changes when fluorinated ester groups were investigated. A propionic group was introduced with fluorination of the terminal carbon atom. Therefore, an elimination reaction was still possible, since the C $\beta$  atom was still available for deprotonation in order to initiate the E2 mechanism. Nevertheless, the strong electron withdrawing effect of the fluorine atoms lowers the C-H bond strength and makes it even more C-H acidic, such as methylene groups in diketones. Therefore, a significantly lower decomposition temperature was determined. Using a modification with fluorinated C $\beta$  atoms, such as the trifluoroacetyloxy group caused a complete change of the mechanism. No ketene was formed since fluorine was not transferred to the phenol oxygen atom. Therefore, no elimination occurs according to E2. The observation of fluoroform and carbon monoxide rather suggested that the modification decomposed radically. The same observation was made for the pivalic group. The pivalic group is a *tert*butyl acyloxy modification. No hydrogen atom is present at C $\beta$  as well. Hence, no elimination reaction occurs that way. The decomposition products were *isobutene* and carbon monoxide as well as CO<sub>2</sub> and the corresponding carboxylic acid, but no ketene.

Accordingly, the radical decomposition to carbon monoxide and *isobutene* appears to be the predominant decomposition mechanism.

In contrast to these two categories, a third class was introduced, namely carbonates. The decomposition of carbonate esters proceeds via transfer of the alkyl group to the phenol oxygen atom under decarboxylation. This mechanism was confirmed by TGA-FT-IR and  $^{13}\text{C}$ -CP-MAS as well as FT-IR experiments. After annealing at 300 °C, the smallest representant, the  $\text{MeCO}_3\text{PI-1}$ , lost about 10%, which corresponds to two molecules of  $\text{CO}_2$  per repetition unit. Furthermore, FT-IR and  $^1\text{H}$ -NMR experiments have shown that the methyl carbonate group decomposed, while signals for the methyl ether formation evolved. Furthermore, the TGA curve, FT-IR and NMR spectrum appear to look nearly identical to the data of  $\text{MeOPI-1}$ . This mechanism was also confirmed for the ethyl, propyl, *isobutyl*, and butyl carbonate ester. However, as the alkyl groups increased, the overall stability decreased. Therefore, the *isobutyl* carbonate decomposed to the *isobutyl* ether, but decomposed immediately afterwards by elimination to *isobutene* and the pristine polymer. The branched carbonates with *isopropyl* and *tertbutyl* groups decomposed at lower temperatures completely. The steric hindrance of these groups makes a transfer to the phenol group rather difficult.

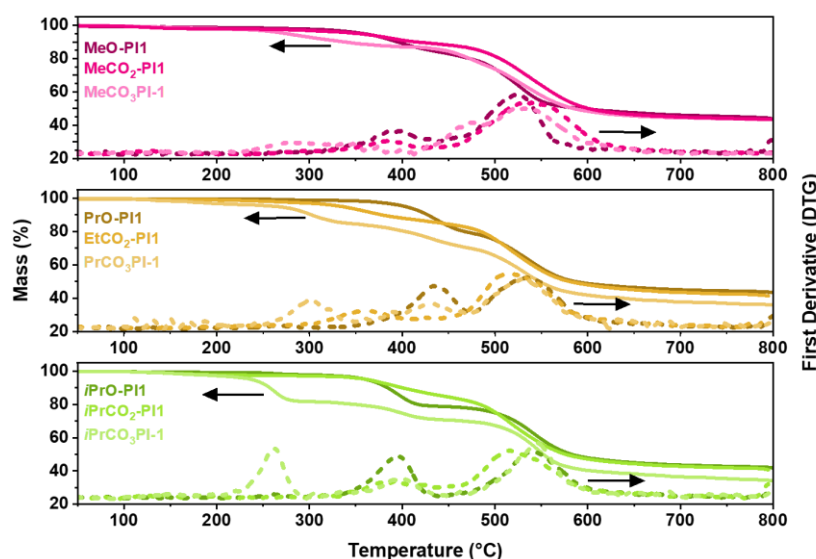


Figure 249. Comparison of the mass loss curve and its first derivative of representative alkoxy, acyloxy and carbonate ester modifications.

Finally, two interesting materials have to be discussed shortly.  $\text{AllylCO}_3$ - and  $\text{PropargylCO}_3\text{PI-1}$ . These consist of an allyl or propargyl group. Both materials have shown to form the

corresponding ether as well. Accordingly, they underwent similar reactions to the ones, that were discussed in the previous section for Allyl- and Propargyl-PI-1. After decarboxylation, the formed allyloxy and propargyloxy groups are above their onset temperatures which were determined for the Claisen Rearrangement of the Allyl-PI-1 and Propargyl-PI-1 in chapter *Effect of Allyl Derivatives in Thermal Cascade Reactions* on page 173 and in chapter *Polyimides with ortho-Propargyloxy groups* on page 245. Hence, these two materials combine both aspects of decomposition cascade reaction polymers and cascade reaction polymers. Principally, their thermally initiated cascade reaction sequence is extended by the intramolecular transfer and decarboxylation reaction prior to the Claisen Rearrangement induced reactions.

With respect to the gas separation performance, the methylated and ethylated alkyloxy polyimides MeOPI-1 and EOPI-1 have demonstrated a very competitive performance for the gas separation of CO<sub>2</sub>/CH<sub>4</sub>. Both materials surpassed the upper bound of 2008 after annealing at 400 °C. The methylated material was additionally treated at 450 °C and surpassed even the 2015 Robeson upper bound. In addition, EOPI-1 has shown a very high gas separation performance for the gas pair CO<sub>2</sub>/CH<sub>4</sub>, when only annealed at 350 °C. A permeability for CO<sub>2</sub> of 1228 Barrer at a selectivity of 32 enters even the suggested target area for industrial applications, which requires selectivities above 30 [7]. Furthermore, the lower TR annealing temperature prevents the material to undergo side reactions or degradation and requires less energy, while most competitive materials were treated at 450 °C. The esters showed all upper bound performances as well, however the trifluoro propionic CF<sub>3</sub>CO<sub>2</sub>PI-1 has demonstrated a strong performance for the separation of CO<sub>2</sub>/CH<sub>4</sub> as well after annealing at 400 °C with about 14000 Barrer. This makes it the most permeable TR polymer that has been published yet, to the best of my knowledge. However, it is remarkable, that despite the high permeability, a selectivity of 25 was still very high. After 6 months, the permeability was still 6600 Barrer at a selectivity of 22.5 for CO<sub>2</sub>/CH<sub>4</sub>. In total, a large set of new materials with diverse functionalities was prepared and investigated in detail. Their mechanism was explained based on intense thermoanalytical investigations combined with structure determining methods such as <sup>1</sup>H-NMR, <sup>13</sup>C-CP-MAS NMR and FT-IR, supported by DFT and molecular dynamic simulations. Many materials revealed a lower TR temperature within this study, proofing the strategy of a protection group decomposition cascade reaction to form polybenzoxazoles as a reliable method. Materials with very low TR temperatures and high PBO conversions were presented,

especially after low annealing temperatures of 350 °C. In total, this class of polymers presents the 6FDA-APAF based modification with the lowest ever reported  $TR_{onset}$  temperature and the highest permeable TR polymer. Furthermore, the 2008 upper bound for various gas pairs was succeeded by the most materials even after 350 °C annealing procedures. EOPI-1 demonstrated a material which located in the industrial target zone (Figure 250).

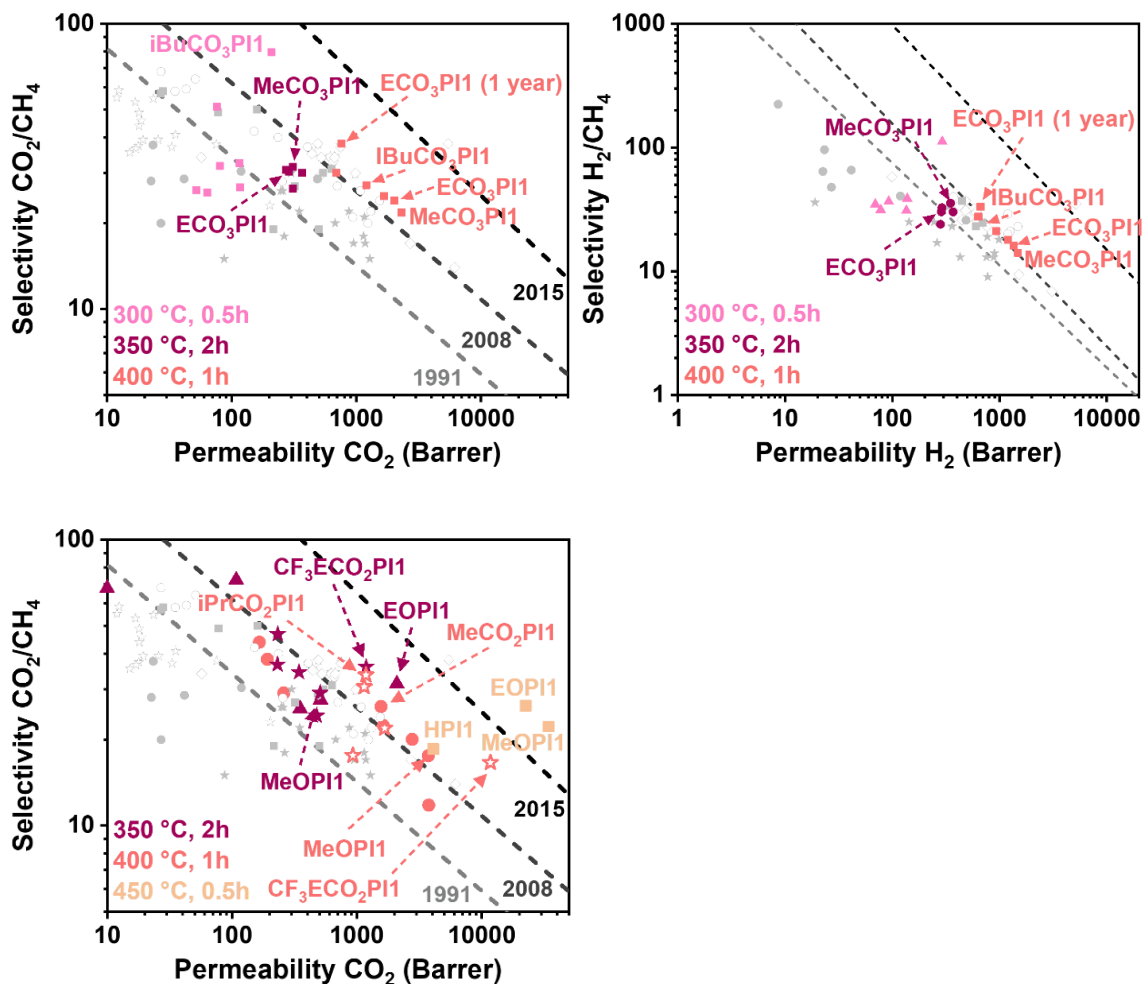


Figure 250. Robeson Plot for the best Alkyloxy-, Acyloxy and Carbonateester modifications.

PART VI  
Outlook



*Your input determines your outlook. Your outlook determines your output, and your output determines your future*

Zig Ziglar

### General

The executed studies in this thesis have been performed to understand the TR mechanism and the effect of any structural influence. Among these influencing structural groups, numerous phenol modifications, such as ether, ester, carbonate, allyl-and propargyl ether were investigated as well as the effect and modification of poly (amic acid)s. These new insights give any organic chemist a powerful tool to tailor specific *ortho*-hydroxy polyimide precursor based on the gained knowledge. The idea was, that different structural combinations based on different backbones, modifications, and the type of polymer: Polyimide, polyamide, poly (amic acid) can be synthesized for further improvement and to extend the number of reported Thermally Rearranged Polymers.

Based on the physical and film properties, such as gas separation, any membrane engineer and application scientist can decide, which polymeric TR system is suitable for his application and process based on a large library of TR polymers and their thermochemical behavior.

In addition, large deviations of the cost of the polymers, any industry related application-oriented person is capable to choose the right material depending on the task and available investment pool. There are still many possibilities to tailor the membrane performance. The following section is covering different ideas from different points of view. New ideas and extension of the present work is discussed as well as suggestions with respect to the use of the materials from this study is given in detail.

## For synthetic chemists

**Combination of presented modifications.** The large number of modifications have revealed that different groups vary strongly in their thermochemical but also physical properties, even though structural changes are sometimes very little, for instance ethoxy vs. *isopropoxy*-modifications. Some modifications have been proven to be beneficial on gas separation (propargyl, methyl, ethyl,  $\beta$ Mallyl), more specifically the variations whether a material shows high selectivity or permeability are large. At 350 °C for instance, ethoxy showed a larger permeability and selectivity compared to methoxy, which changed when heated to 400 °C. Allyl showed higher selectivities, while  $\beta$ Mallyl showed higher permeabilities, whereas  $\beta$ Mallyl for instance has shown higher permeability and selectivity for H<sub>2</sub> separation tasks. Some materials are more improving the TR temperature (allyl) compared to other materials (propargyl). Therefore, the investigation of different combinations of *ortho*-hydroxy modified polymers to provide a large variety of materials is highly recommended and to see how different modifications interact with each other in terms of TR<sub>onset</sub>. Interesting combinations for a lower TR temperature might be the combination of low degrees of allylation with residual hydroxy groups being converted to ethoxy or methoxy units. The combinations can and should be done as blends in comparison to copolymers, such as block- and random copolymers.

**Backbone and phenol group modification.** The modification of the phenolic hydroxy group is a convenient way to affect the Thermal Rearrangement reaction. Methoxy and allyloxy modifications have been shown to be suitable to lower the TR temperature. Both systems improve the TR process by improving the degree of freedom for each repetition unit. In order to further lower the TR process, it is important to promote electronic properties. Hence, an investigation of the effect of *meta*-substituents on the phenol-amine unit is highly interesting. The question is if any electron-donating group might improve the nucleophilicity of the phenol group. On the other hand, modifications *ortho* to the anhydride group are interesting in order to see if the reaction can be manipulated by increasing the electrophilicity of the imide carbonyl group by using electron-withdrawing groups. A scheme covering the main aspects is shown below (Figure 251).



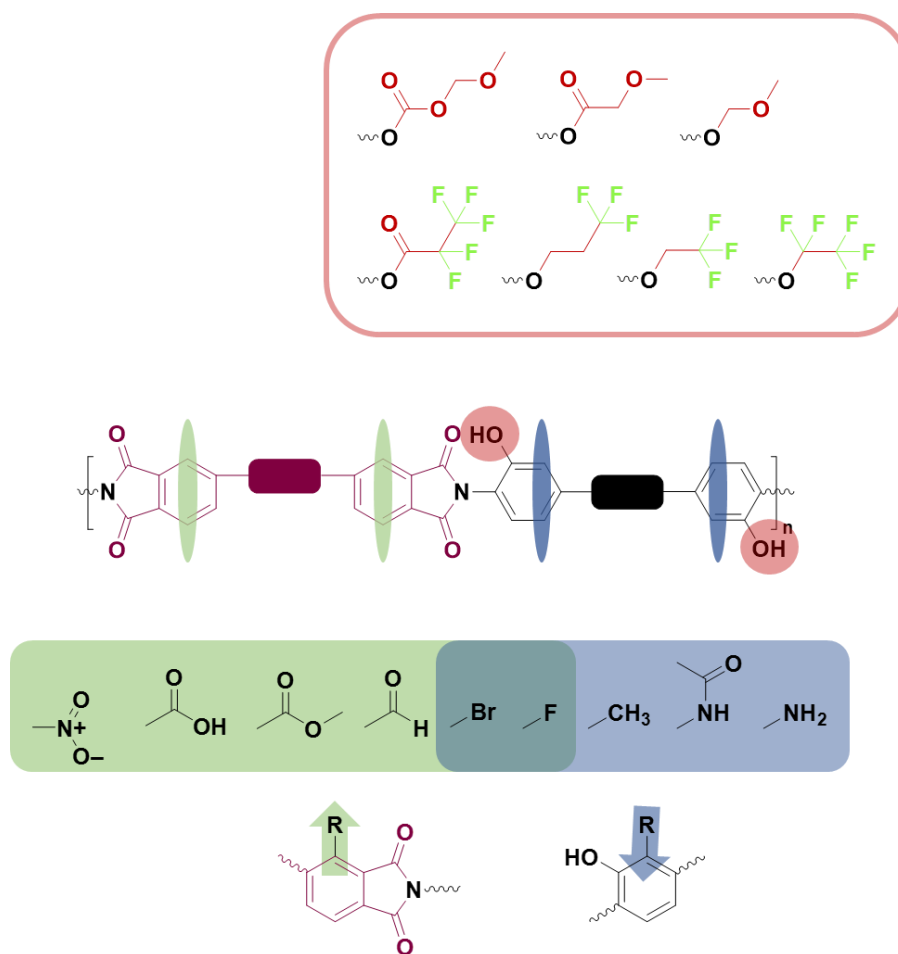
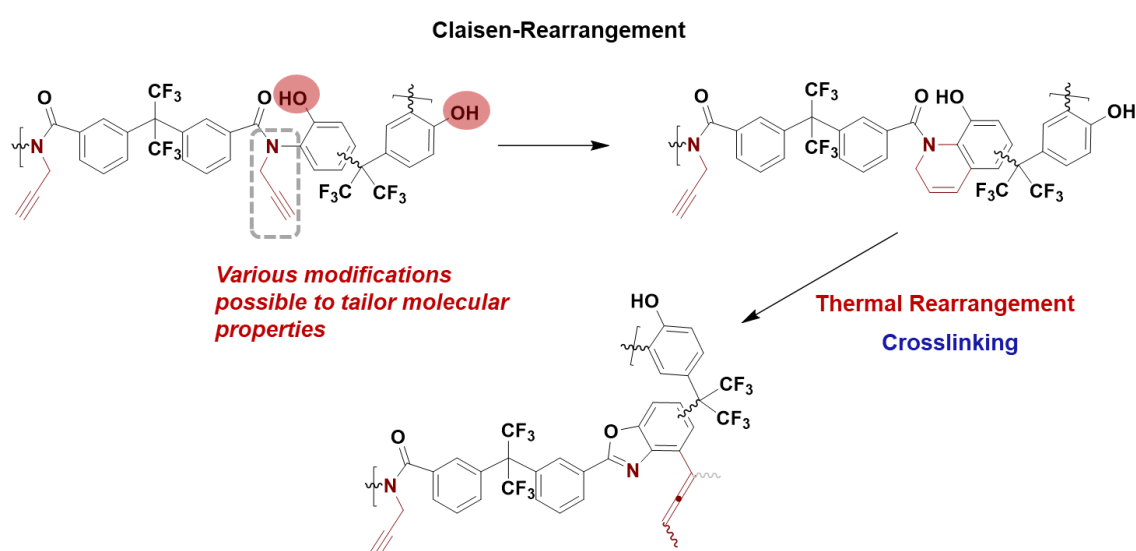


Figure 251. Overview of potential target spots for modifications. A group of interesting, fluorinated ester and ether modifications.

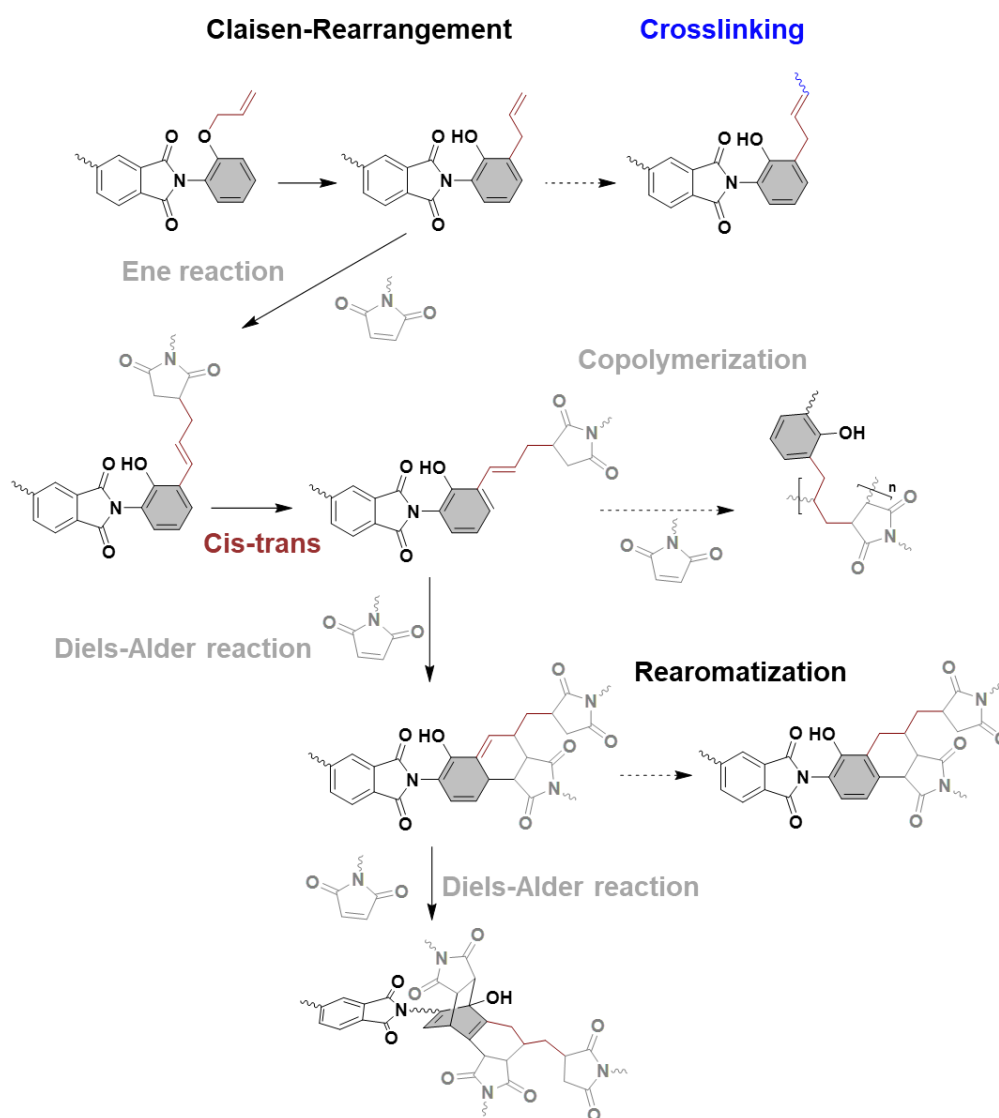
The number of modifications can be extended by adding more electron donating and withdrawing groups along the allyl- and propargyl group. Studies with methoxy substituted allyl-phenyl ether have shown a strong Claisen Rearrangement accelerating effect. Such groups can be considered to be interesting to promote any of the *post*-Claisen-Rearrangement reactions, such as the cyclization or isomerization reaction. As furan formations have been identified to be promising for gas separation applications, a synthetic approach to improve its formation can be done that way. The same holds true for propargyl derivatives, but also other modifications can be improved that way. For instance, the investigation of *ortho*-hydroxy modification with methoxy ethylene glycol and the corresponding ester and carbonate, namely methoxy acetate and methoxy ethyl carbonate (see Figure 201). Also, the investigation of further fluorinated substituents is interesting, as trifluoro propanoyl modified HPI has been shown to be very promising.

**Introduction of cascade reaction undergoing modifications at the amide-N atom.** Only a few reports, mainly investigated by works of NASA research centers [319-321], have shown that mono-alkyl modified diamines can also be used to polymerize polyamides from them. The consequence is that the number of hydrogen-bonds is strongly decreased as the amide group does not form a hydrogen bond at all. Furthermore, if long alkyl chains are used, they disrupt efficient chain packing. This is believed to increase the solubility and processability of polyamides, it opens up a large number of possible modifications. Several cascade-reaction undergoing groups can be introduced, such as allyl- and propargyl modifications, such a cascade is shown in Scheme 45. As *ortho*-hydroxy polyamides form polybenzoxazoles at significantly lower TR temperatures, these systems are promising for the use of thin film composite membranes. The improved mobility might even lower the TR temperature and further reactions, such as Claisen Rearrangement, Cyclization and Crosslinking might improve their separation performance, as demonstrated in polyimides in this study. The synthetic approach might be to use polyamides and post-modify them by adjusting the used alkyl reagent. Another approach might be to protect the hydroxy group and modify only the amine group, which is then used for further polymerization. The hydroxy group protection can be removed or kept, in case that the protective group decomposes prior 200 °C in order to recover the phenol group for the polybenzoxazole conversion.



Scheme 45. Overview of a proposed *N*-propargylation based Claisen-Rearrangement and Thermal Rearrangement reaction cascade in polyamides.

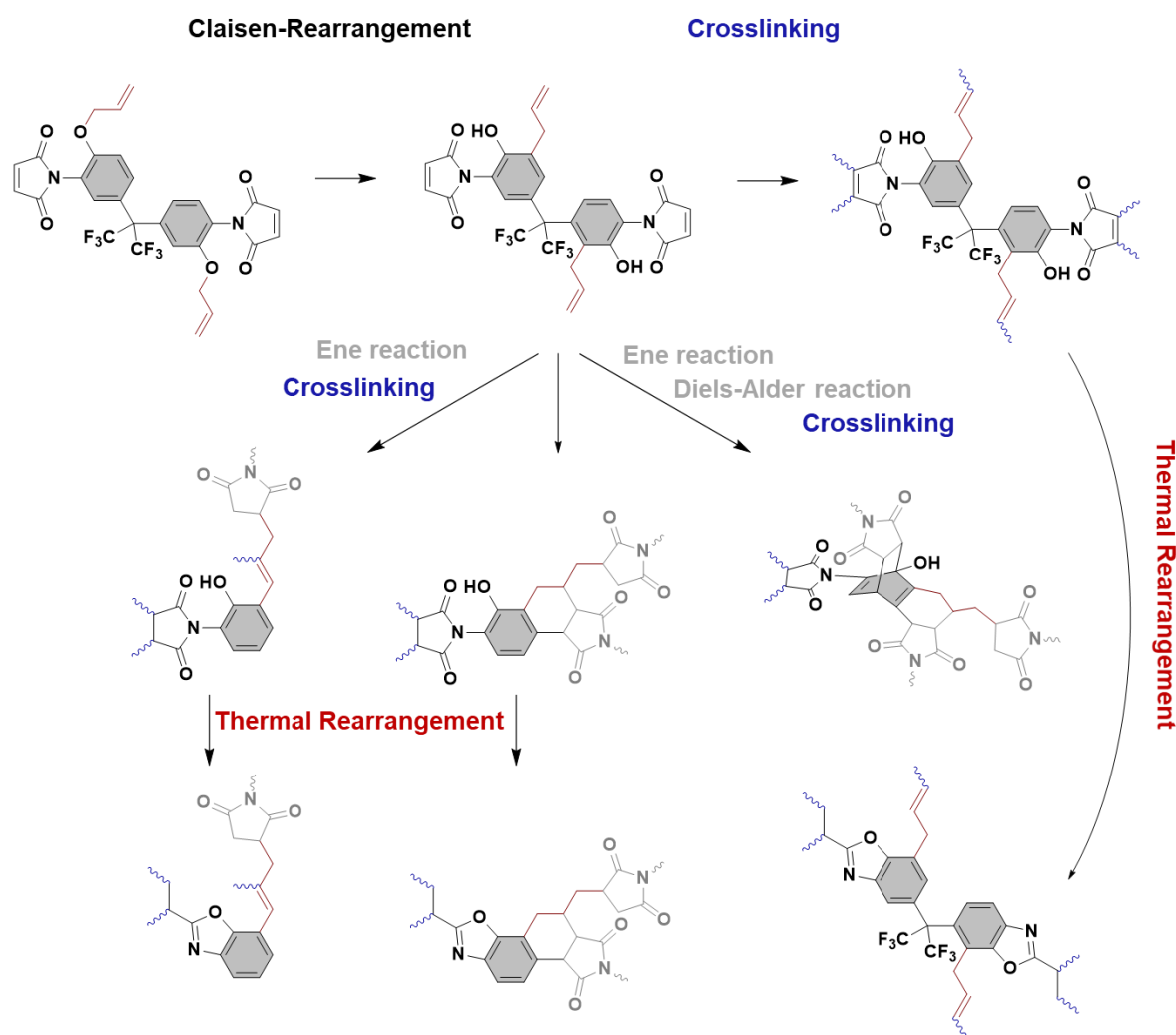
**Allyl-Bismaleimide Cascade Reaction Polymers.** There has not been much reported about the use of bismaleimides as TR membrane materials, especially in combination with hydroxy modifications. One publication of bismaleimide TR precursor by Do and Lee *et al.* was published with extraordinary gas separation performance in blends and pure bismaleimide networks [148]. Since allylated bisphenol A is widely known to undergo Wagner-Jauregg reactions, which are a cascade of post-Claisen rearrangement cycloaddition reactions, the combination of that concept with TR in bismaleimide precursors might be an innovative and new field of high-performance materials (Scheme 46).



Scheme 46. Reaction cascade scheme of potential reactions of allylated polyimides and bismaleimides.

In Addition, the use of propargylated polyimides with bismaleimide, as well as the pure casting and annealing of propargylated and allylated bismaleimides is an interesting way to extend the idea of using bismaleimides as membrane precursor efficiently. This can be

extended by using allylated oligomers instead of polymers in order to change the network structure (Scheme 47).



Scheme 47. Reaction cascade scheme of potential reactions of allylated bismaleimides.

**Photo-stimulated Rearrangement in Polymers in solid-state.** All studies in this PhD thesis focused on the use of heat as a trigger for the chemical solid-state reactions. However, numerous reactions are reported to undergo via irradiation with UV light. Such treatments might be gentler and can be controlled more easily as reactions, based on the involved bonds, can be more specifically induced by choosing specific monochromatic light source. Reports on photo-initiated Claisen- and Fries Rearrangement are available and azo-group containing polyimides in the backbone or as side groups offer new possibilities. In addition, the use of microwaves and electronic stimulation is of high interest.

**Intensification of research studies on the circularity of polyimides, -amides and polybenzoxazoles.** In addition, the world is experiencing strong effects of climate changes and

observing numerous contaminations with plastics. Many materials are for one-use only and their recycle plans are often not available. While polyimides are famous for their chemical and thermal resistance, polybenzoxazoles as a product of the TR process, are even more chemically and thermally stable, especially due to the inherent crosslinking. This makes any process of restoring, recycling, or remanufacturing very difficult. Therefore, further studies towards recycling are new and important, not only for TRPs itself, but for polyimides and polybenzoxazoles as expensive and important high-end materials in general.

## **For Membrane-Engineers**

While most investigations in the synthetic lab are very close related to the applications scientist or membrane engineer, such as the investigation of crosslinking for instance, the membrane engineer is very interested when it comes to scale-up, film casting, mechanical robustness, and easy and convenient ways to tailor the membrane properties with a set of available materials.

Therefore, the use of blends is widely used, as well as the crosslinking via additional crosslinking agents. Based on the insights gained in this PhD thesis, a number of materials that are capable to crosslink without additional crosslinkers in order to suppress aging and plasticization are available (allyl, propargyl, poly (amic acids)). In addition, modifications to use lower annealing temperatures to reach sufficient conversions to thermally initiated units, such as chromene, furan or benzoxazole, favoring the stability of the membrane are shown. Finally, highly selective ( $\beta$ Mallyl, propargyl, allyl) and permeable materials (propargyl,  $\beta$ Mallyl,  $\gamma$ Eallyl, CF<sub>3</sub>propanoyl, methoxy) were provided. In order to tailor the separation properties, the combination of these groups can be used to adapt the membranes properties via blending to the specific membrane task. For instance, the combination of propargyl and ethoxy at annealing of only 350 °C might lead to a highly crosslinked and therefore aging and plasticization resistant material, with high permeability while maintaining selectivity for more polar and small gases.

The use of UV light to improve the membrane performance of allyloxy-, propargyloxy- and ester-modified TR precursor might be interesting in combination with low temperature annealing. One suggestion might be the use of photo-active groups and low TR temperature

containing materials, such as  $\gamma$ E- and  $\beta$ Mallyl-PI. As this might lead to the possibility to cast thin film composite membranes, whose support layer does not degrade under the present conditions.

Finally, the investigation of further applications, such as pervaporation and desalination with propargyl- and allyloxy containing materials is promising due to their controllable degree of crosslinking, depending on the degree of modification and the use of the derivative. Therefore, very dense materials can be used by using allyl- and crotyl modified *ortho*-hydroxy polyimides, while larger fluxes can be reached using Propargyloxy or  $\beta$ Mallyloxy modified polyimides, even at annealing at 300 °C and below.

## **For Application-Scientists and Industry**

Finally, all studies and improvements should keep in mind, that the investigation of the chemistry of these systems is done to improve materials properties to have them in use as high-performance new state-of-the-art materials. While any publication on polymeric membranes in the field of gas separation starts with the remark on the motivation to provide materials to lower the carbon footprint by making the synthesis and application more efficient, the number of materials in use in the field of gas separation is still very low. Reasons for that is the lack of scale-up and price. Therefore, the exchange of backbone materials to cheaper resources, especially sustainable materials is important. One of these materials might be the 4,4'-(Ethyne-1,2-diyl) diphthalic anhydride containing polyimide, such as EDA-APAF and its modified systems (Figure 252). The EDA containing anhydride is cheaper compared to fluorinated monomers and in terms of recycling non-fluorinated decomposition products are formed and plants require lower safety regulations as no HF is formed. EDA is an excellent monomer for large molecular weights and easy and safe to handle. The gas separation performance was one of the best materials in terms of a reasonable permeability – selectivity trade-off among all investigated and also reported polyimide backbones.

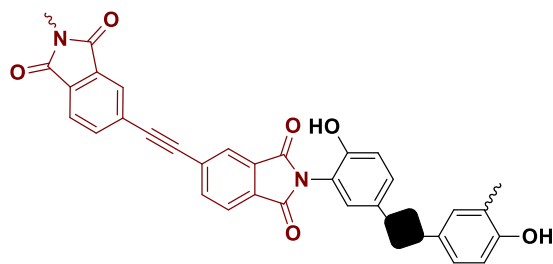


Figure 252. Ethynyl diphtalicanhydride (EDA) containing polyimide.

Therefore, further implementation of EDA containing polyimides and TRPs in blends might be a suitable way. Furthermore, a known method as described earlier is the end-group functionalization with 4-Phenylethynylphthalic anhydride [322], which might be capable to react with EDA-polyimide by crosslinking. Hence, the combination of ethynyl containing units in the backbone as well as end group offers a variety of tools to tailor cheap, safe polymeric systems.





PART VII

Experimental Section



## EXPERIMENTAL

---

*There is no such thing as a failed experiment,  
only experiments with unexpected outcomes*

Richard Buckminster Fuller

### Synthesis

#### Chemicals

Aromatic dianhydride 2,2'-bis(3,4-dicarboxy-phenyl) hexafluoropropane dianhydride (6FDA), Biphenyl-3,3',4,4'-tetracarboxylic dianhydride (BPDA), 4,4'-(4,4'-Isopropylidenediphenoxy)bis(phthalic anhydride) (BPADA), Benzene-1,2,3,5-tetracarboxylic dianhydride (PMDA), Bicyclo[2.2.2]oct-7-ene-2,3,5,6-tetracarboxylic dianhydride (BCODA) and the diamine 2,2-Bis-(3-amino-4-hydroxyphenyl)-hexafluoropropane (BisAPAF) were purchased from Sigma-Aldrich; The dianhydride 4,4'-(Ethyne-1,2-diyl)diphthalic dianhydride (EDA), 2,2-Bis(4-carboxyphenyl)hexafluoropropane dicarboxylic acid (6FDC) and the diamine 3,3'-dihydroxy-4,4'-diamino-biphenyl (HAB) were purchased from TCI Chemicals Germany and dried at 150 °C in vacuum for 12 h prior to use. Anhydrous *N*-methyl pyrrolidone (NMP, ≥98%), trimethylsilyl chloride (CTMS, ≥98%), pyridine (Py), *N,N*-dimethyl amino pyridine (DMAP), *p*-xylene and anhydrous *N,N*-dimethyl formamide (DMF), *N,N*-dimethyl acetamide (DMAc), ethanol, methanol, and diethyl ether (Et<sub>2</sub>O) were purchased from Sigma-Aldrich and used as received.

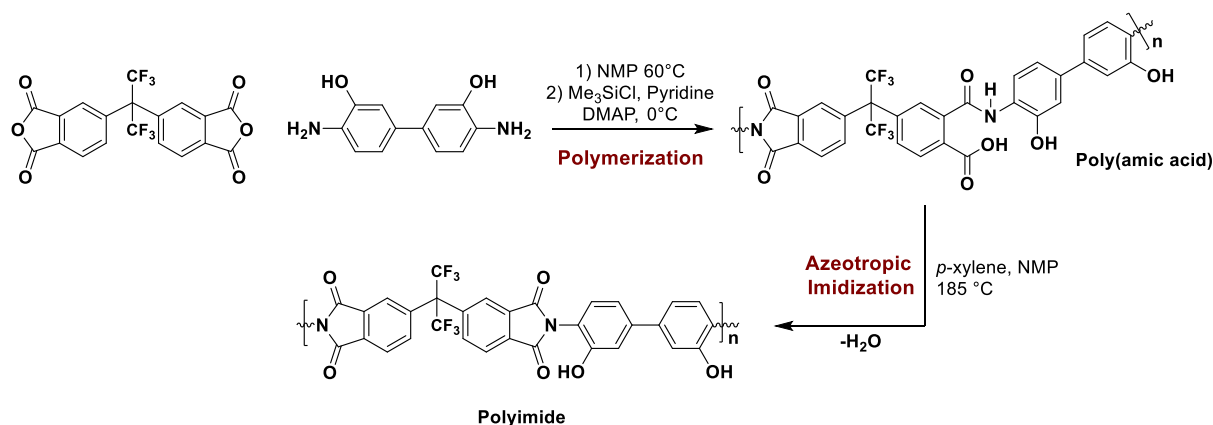
#### Polyimide synthesis

The *ortho*-hydroxy polyimide precursor were synthesized by a one-pot two step polycondensation method via *in-situ* silylation activation and azeotropic imidization step. The synthesis of all polyimides was carried out according to the same synthetic procedure. The synthesis is exemplified using 6FDA-HAB as the final polyimide (Scheme 48).

HAB (4.30 g; 20 mmol) was introduced into a three-necked round-bottom flask, equipped with a mechanical stirrer and a gas inlet and outlet. 6 mL NMP was added, as the solvent, and the amine suspension was stirred at 60 °C under argon until completely dissolved. The solution

was cooled down to 0 °C in an ice bath for 15 Min. CTMS (5.30 mL; 42 mmol) and pyridine (3.39 mL; 42 mmol) were added simultaneously, followed by the addition of DMAP (0.51 g; 4.20 mmol). After 5 Min the ice bath was removed and the formed suspension stirred for a minimum of two hours to ensure the complete silylation of the amino groups, while the temperature raised to room temperature. 6FDA (8.80 g; 20 mmol) and an additional 15 mL of NMP were then added and the resulting mixture was cooled to 0 °C and stirred overnight, whereas the temperature of the ice bath increased to room temperature. In order to keep the temperature as long as possible as low as possible, a Dewar vessel was used for the ice bath.

The next day, after a minimum reaction time of 16 h, the viscous mixture was heated with a heat gun at 60 °C until the turbid suspension became shining schlieren. Afterwards the mixture was stirred for further 2 h. Subsequently, the azeotropic imidization route was used to convert the poly (amic acid) to the corresponding polyimide. Therefore, *p*-xylene (8 mL) was added to the vigorously stirred viscous solution. The temperature was raised to 185 °C and maintained for 6 h to promote complete imidization. The formed water was removed as a *p*-xylene/water azeotropic mixture from the solution and residuals of the *p*-xylene were removed under reduced pressure. The polymer was precipitated in deionized water and washed several times with deionized water. The polymer was then dried under vacuum at 100 °C, re-dissolved in NMP and reprecipitated in water and washed with *isopropanol*, followed by drying over night at 100 °C. Finally, the product was dissolved in acetone and re-precipitated in water and washed in *isopropanol* at 50 °C. The cleaned product was then dried for two days at 120 °C under reduced pressure in a vacuum oven.



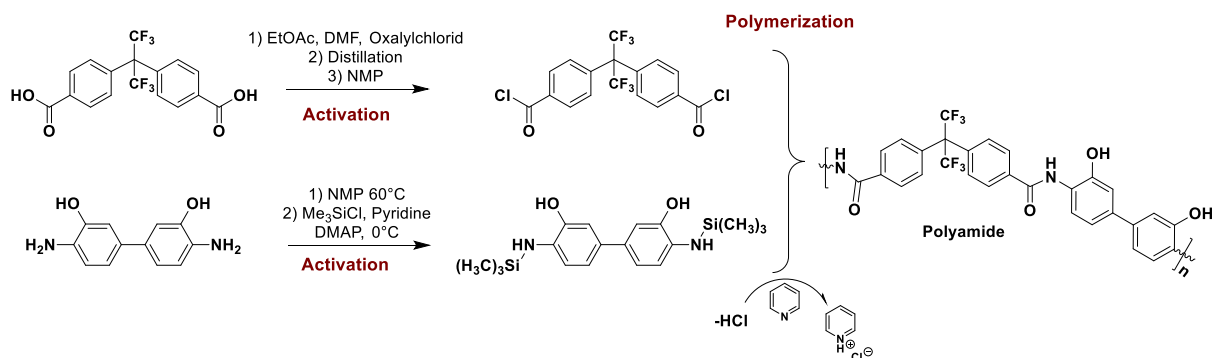
Scheme 48. Synthesis route of the polymerization of ortho-hydroxy polyimides according to the two-step polycondensation via in-situ silylation activation step.

## Polyamide synthesis

The *ortho*-hydroxy polyamide precursors were synthesized by a one-pot two step polycondensation method via *in-situ* acid chloride and silylation activation and condensation step (Scheme 49). The synthesis of all polyamides was carried out according to the same synthetic procedure. The synthesis is exemplified using 6FCI-HAB as the final polyamide.

HAB (4.30 g; 20 mmol) was introduced into a three-necked round-bottom flask, equipped with a mechanical stirrer and a gas inlet and outlet. 6 mL NMP was added, as the solvent, and the amine suspension was stirred at 60 °C under argon until completely dissolved. The solution was cooled down to 0 °C in an ice bath for 15 Min. CTMS (5.30 mL; 42 mmol) and pyridine (3.39 mL; 42 mmol) were added simultaneously, followed by the addition of DMAP (0.51 g; 4.20 mmol). After 5 Min the ice bath was removed and the formed suspension stirred for minimum of 2 h to ensure the complete silylation of the amino groups, while the temperature raised to room temperature. In a separate flask, the dicarboxylic acid 6FDC was dissolved in ethylacetate until completely dissolved (5 mL). Five droplets of anhydrous DMF were added to the solution and the solution was cooled down in an ice bath. After 30 mMin, oxalylchloride (4.0 mL, 1.2 eq/COOH) was added with a Luer-Lock syringe. The solution was stirred overnight for a minimum of 16 h to ensure the complete chlorination of the carbonyl groups to the corresponding acid chloride, while the temperature raised to room temperature. In order to keep the temperature as long as possible as low as possible, a Dewar vessel was used for the ice bath.

The next day, the solvent and residual oxalyl chloride was removed via distillation under reduced pressure at room temperature, re-dissolved in NMP and evacuated under stirring for further 2 h. The dicarboxylic acid chloride solution was then added dropwise to the amine suspension. Afterwards the mixture was stirred for 24 h. The polymer was precipitated in deionized water and washed several times with deionized water. The polymer was then dried under vacuum at 100 °C, re-dissolved in NMP and reprecipitated in water and washed with *isopropanol*, followed by drying over night at 100 °C. Finally, the product was dissolved in acetone and re-precipitated in water and washed in *isopropanol* at 50 °C. The cleaned product was then dried for two days at 120 °C under reduced pressure in a vacuum oven.



Scheme 49. Synthesis route of the polymerization of ortho-hydroxy polyamides via in-situ chlorination and silylation activation step.

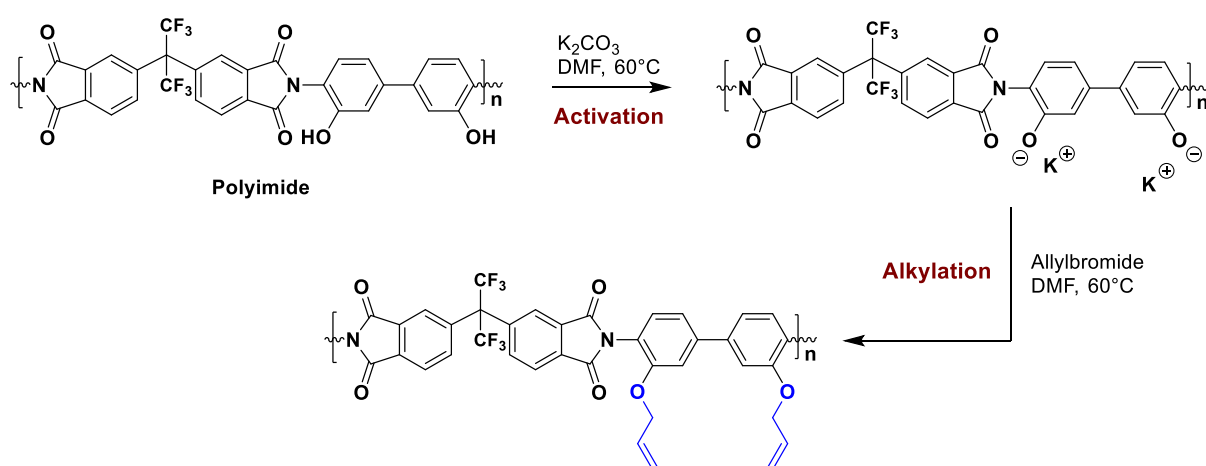
## Allylation and Propargylation

The allylation agent allyl bromide (AllylBr), propargylation agent propargyl bromide (PropargylBr) and the base potassium carbonate ( $K_2CO_3$ ) was purchased from Sigma-Aldrich. The carbonate was dried at 130 °C in vacuum for 12 h and ground before use. The used allyl- and propargyl derivatives are shown in Table 7.

Table 7. Used allylation- and propargylation agents.

IUPAC name	Trivial name	Modification code
<b>3-bromo propene</b>	Allyl bromide	Allyl
<b>3-chloro-butene</b>	$\alpha$ Methyl allyl chloride	$\alpha$ M
<b>2-methyl-3-bromo propene</b>	$\beta$ Methyl allyl bromide	$\beta$ M
<b>3-methyl-3-bromo propene</b>	$\gamma$ Methyl allyl bromide	$\gamma$ M
<b>3-ethyl-3-bromo propene</b>	$\gamma$ Ethyl allyl bromide	$\gamma$ E
<b>3-phenyl-3-bromo propene</b>	$\gamma$ Phenyl allyl bromide	$\gamma$ Phenyl
<b>3,3'-dimethyl-3-bromo propene</b>	$\gamma,\gamma'$ -diMethyl allyl bromide	$\gamma,\gamma'$ -dM
<b>3-bromo cyclohexene</b>	Cycloallyl bromide	Cycloallyl
<b>4-bromo butene</b>	Butylene bromide	Butylene
<b>3-bromo propyne</b>	Propargyl bromide	PG
<b>3-chloro-butyne</b>	$\alpha$ Methyl propargyl bromide	$\alpha$ MPG
<b>3-methyl-3-bromo propyne</b>	$\gamma$ Methyl propargyl bromide	$\gamma$ MPG
<b>3-ethyl-3-bromo propyne</b>	$\gamma$ Ethyl propargyl bromide	$\gamma$ EPG
<b>3-trimethylsilyl-3-bromo propyne</b>	$\gamma$ TMS propargyl bromide	$\gamma$ TMSPG
<b>3-naphtyl-3-bromo propyne</b>	$\gamma$ Naphtyl propargyl bromide	$\gamma$ NpPG

The allylated and propargylated materials were synthesized via a Williamson-Ether Synthesis type of reaction (Scheme 50) using potassium carbonate as a mild base in DMF as an apolar protic solvent and the corresponding allyl- or propargyl derivative bromide as alkyl halogenide source. The synthesis is described in the following procedure for Allyl-PI as a representative. The synthesis of allylated and propargylated polyimides with different backbones were synthesized according to the same procedure. The modified HPIs are listed in Table 8.



Scheme 50. Alkylation synthesis route for the synthesis of ortho-Allyloxy polyimides.

The 6FDA-HAB *ortho*-hydroxy polyimide (7,7 g; 10 mmol) was dissolved in anhydrous DMF (75 mL) in a three-necked round bottom flask under argon atmosphere at  $60^\circ C$ . The activation of the phenolic hydroxyl groups was carried out by adding dried potassium carbonate (2,8 g; 40 mmol; 4 eq) to the vigorously stirred mixture. After 2h of activation, the allyl bromide (4,3 mL; 40 mmol; 4 eq) was added to the suspension. The mixture went turbid and was stirred under these conditions for 2 h, whereas 2 equivalents of potassium carbonate was added after 4 h in total and allyl bromide was added as well after 8 h in total. The addition of carbonate was repeated after 20 h and another addition of allyl bromide was done after 22 h in total. After 24 h the mixture was cooled down to room temperature and precipitated in deionized water. The polymer was repeatedly washed with water and methanol, and dried in a vacuum oven at  $80^\circ C$  for 48 h, re-dissolved in NMP and reprecipitated in water and washed with isopropanol, followed by drying over night at  $100^\circ C$ . Finally, the product was dissolved in acetone and re-precipitated in water and washed in isopropanol at  $50^\circ C$ . The cleaned product was then dried for two days at  $120^\circ C$  under reduced pressure in a vacuum oven.

Table 8. Synthesized allylated and propargylated polyimides.

Backbone	Modification	Materials code
6FDA-APAF	Allyl	Allyl-PI-1
6FDA-HAB	Allyl	Allyl-PI-2
6FDA-APAF	$\alpha$ M	$\alpha$ MPI-1
6FDA-APAF	$\beta$ M	$\beta$ MPI-1
6FDA-HAB	$\beta$ M	$\beta$ MPI-2
BPADA-APAF	$\beta$ M	$\beta$ MPI-3
6FDA-APAF	$\gamma$ M	$\gamma$ MPI-1
6FDA-APAF	$\gamma$ E	$\gamma$ EPI-1
6FDA-APAF	$\gamma$ Phenyl	$\gamma$ PhenylPI-1
6FDA-APAF	$\gamma,\gamma$ -dM	PrenylPI-1
6FDA-APAF	Cycloallyl	CycloAllyl-PI-1
6FDA-APAF	Butylene	ButylenePI-1
6FDA-APAF	PG	PGPI-1
6FDA-HAB	PG	PGPI-2
EDA-APAF	PG	PGPI-3
BPADA-APAF	PG	PGPI-4
6FDA-APAF	$\alpha$ MPG	$\alpha$ MPGPI-1
6FDA-APAF	$\gamma$ MPG	$\gamma$ MPGPI-1
6FDA-APAF	$\gamma$ EPG	$\gamma$ EPGPI-1
6FDA-APAF	$\gamma$ TMSPG	$\gamma$ TMSPGPI-1
6FDA-APAF	$\gamma$ NpPG	$\gamma$ NpPGPI-1

The  $\alpha$ M-PI synthesis was varied since the allyl source used was a chloride. The synthesis started by first dissolving the *ortho*-hydroxy polyimide (2,6 g; 3.3 mmol) in anhydrous DMF (25 mL) in a three-necked round bottom flask under argon atmosphere at 60 °C. The activation of the phenolic hydroxyl groups was carried out by adding dried potassium carbonate (2,3 g; 16.5 mmol; 5 eq) to the mixture and stirred. After 2 h the 3-Chloro-1-butene (1,74 mL; 16.5 mmol; 5 eq) was added to the solution. The mixture was stirred under these conditions for one day, whereas 2 equivalents of potassium carbonate and halogen alkane were added

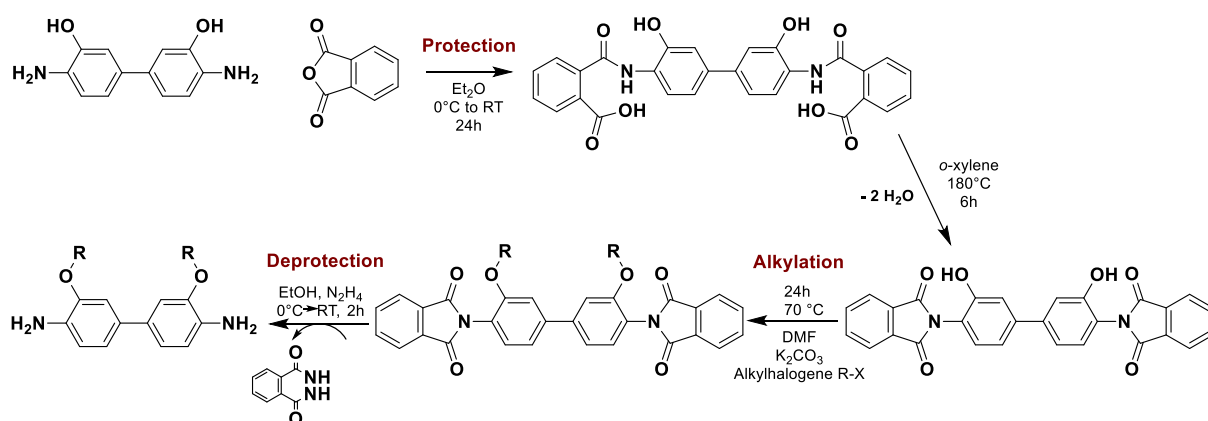


after 4 and 12 h. After 24 h the mixture was cooled down to room temperature and precipitated in deionized water. The polymer was repeatedly washed with water and methanol, and dried in a vacuum oven at 80 °C for 72 h.

The synthesis of cycloallyl-PI was done by dissolving the HPI in anhydrous DMF. Afterwards 6 eq of potassium carbonate were added, and after 30 min, 2 eq of cyclohexyl bromide per hydroxy group was added in one portion. After 6 h the procedure was repeated and stirred overnight. The next day, the polymer was precipitated and washed as described for the Allyl-PI.

### Monomer modification

The synthetic route for the monomer modification is shown in Scheme 51. In order to investigate the influence of the total number of allyl groups by comparing randomly distributed allyloxy units *versus* only fully and non-fully converted repetition units. Furthermore, modified poly (amic acid)s were targeted as the post-polymerization modification might lead to hydrolysis and alkylation of the amide-N. A synthesis route was established via an amine-specific protection-deprotection method, since amine groups would convert to the *N*-dialkyl and non-polymerizable afterwards. The first step was a protection of the amine group with phthalic acid anhydride giving an imide, which was then converted to the corresponding *ortho*-alkoxy monomer. Afterwards, the imide protection group was removed via hydrazinolysis. The obtained and purified monomer was then used for polymerization.



Scheme 51. Synthesis route of the *ortho*-hydroxy diamine modification.

### Monomer protection

HAB (4.3 g; 20 mmol) and phthalic acid anhydride (7.4 g; 50 mmol) were suspended in diethyl ether (40 mL) in a Schlenk flask and stirred in an ice bath under argon for 48 h, whereas the temperature of the ice bath increased to room temperature. The suspension solidified and the solid was filtered off, washed several times with diethyl ether and water, and was dried under vacuum at 80 °C. The azeotropic imidization route was used to convert the phthalic acid anhydride protected diamine (Paa-HAB) from its amic acid form to the corresponding imide. Therefore, Paa-HAB (8.545 g; 20 mmol) was dissolved in 10 mL NMP and *o*-xylene (8.0 mL) was added to the vigorously stirred solution. The temperature was raised to 180 °C and kept for 6 h to promote complete imidization. The formed water was removed from the solution via azeotropic distillation and residual *o*-xylene was removed under reduced pressure at the end of the reaction. The phthalimide-protected diamine (PI-HAB) was precipitated in deionized water and washed several times with distilled water and methanol. The PI-HAB was dried under vacuum at 100 °C for 24 h.

### Alkylation of the protected monomer

The *ortho*-hydroxy groups of the protected diamine were converted to the corresponding alkyloxy group, herein as allylic ether group by a Williamson-ether type synthesis (see Scheme 51). PI-HAB (5.3 g; 1. mmol) was dissolved in anhydrous DMF (8.0 mL) in a three-necked round bottom flask under argon atmosphere at 70 °C. The activation of the hydroxy groups was carried out by adding dried potassium carbonate (2.3 g; 2. mmol) to the mixture under vigorous stirring. After 4 h the allyl bromide (4.5 mL; 5 mmol) was added to the solution. The mixture was stirred under these conditions for two hours, whereas the same amount of potassium carbonate and allyl bromide were added after 4 h again. After 48 h the mixture was cooled down to room temperature and precipitated in deionized water. The allylated-protected diamine (PI-HAB Allyl) was repeatedly washed with water and methanol and dried in a vacuum oven at 120 °C for 72 h.

### Monomer deprotection

The phthalimide protected allylated diamine (PI-HAB Allyl) was deprotected by means of hydrazine addition under cleavage of phthalhydrazide. PI-HAB Allyl (5.9 g; 1 mmol) was suspended in ethanol (10 mL) under argon and cooled in an ice bath. An aqueous solution of hydrazine (35 wt.%) (0.21 mL; 2.4 mmol) was added dropwise. During the synthesis, the suspension turned into a clear solution due to the addition of hydrazine and became turbid again very quickly because of the phthalhydrazide formation, as demonstrated in Figure 253. The solid was filtered off after 2 h and washed with ethanol several times. The ethanol was evaporated under reduced pressure at room temperature. The residuals were suspended in methanol and the solid was filtered off. The methanol was evaporated under reduced pressure followed by several washing steps in water, followed by recrystallization from ethyl acetate.

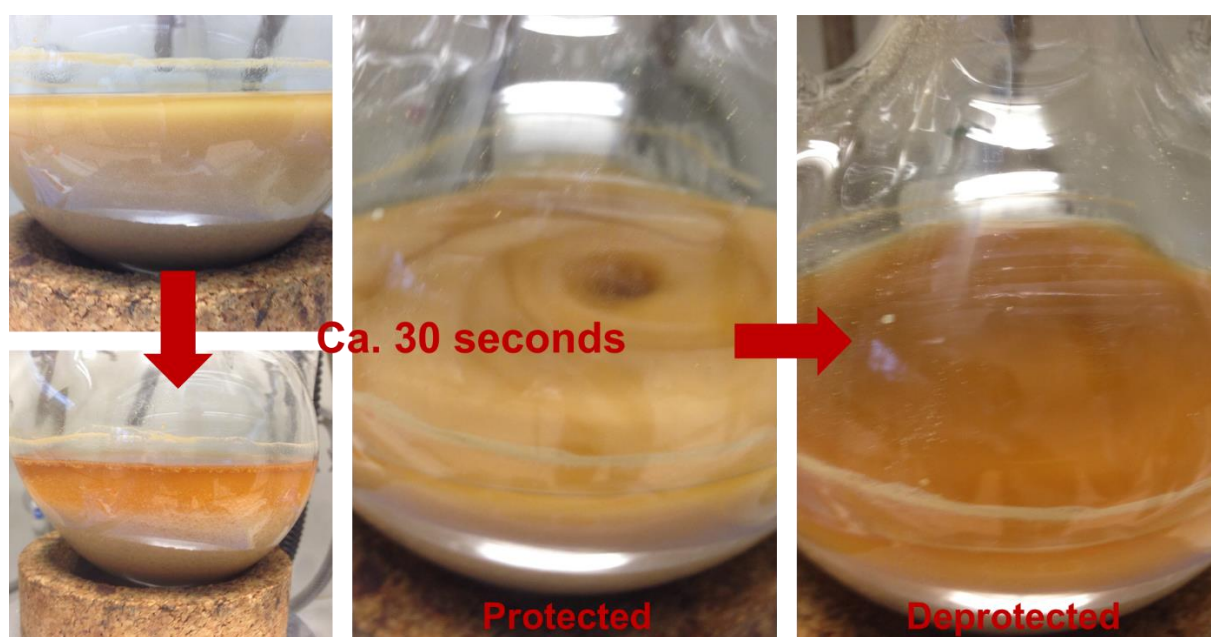
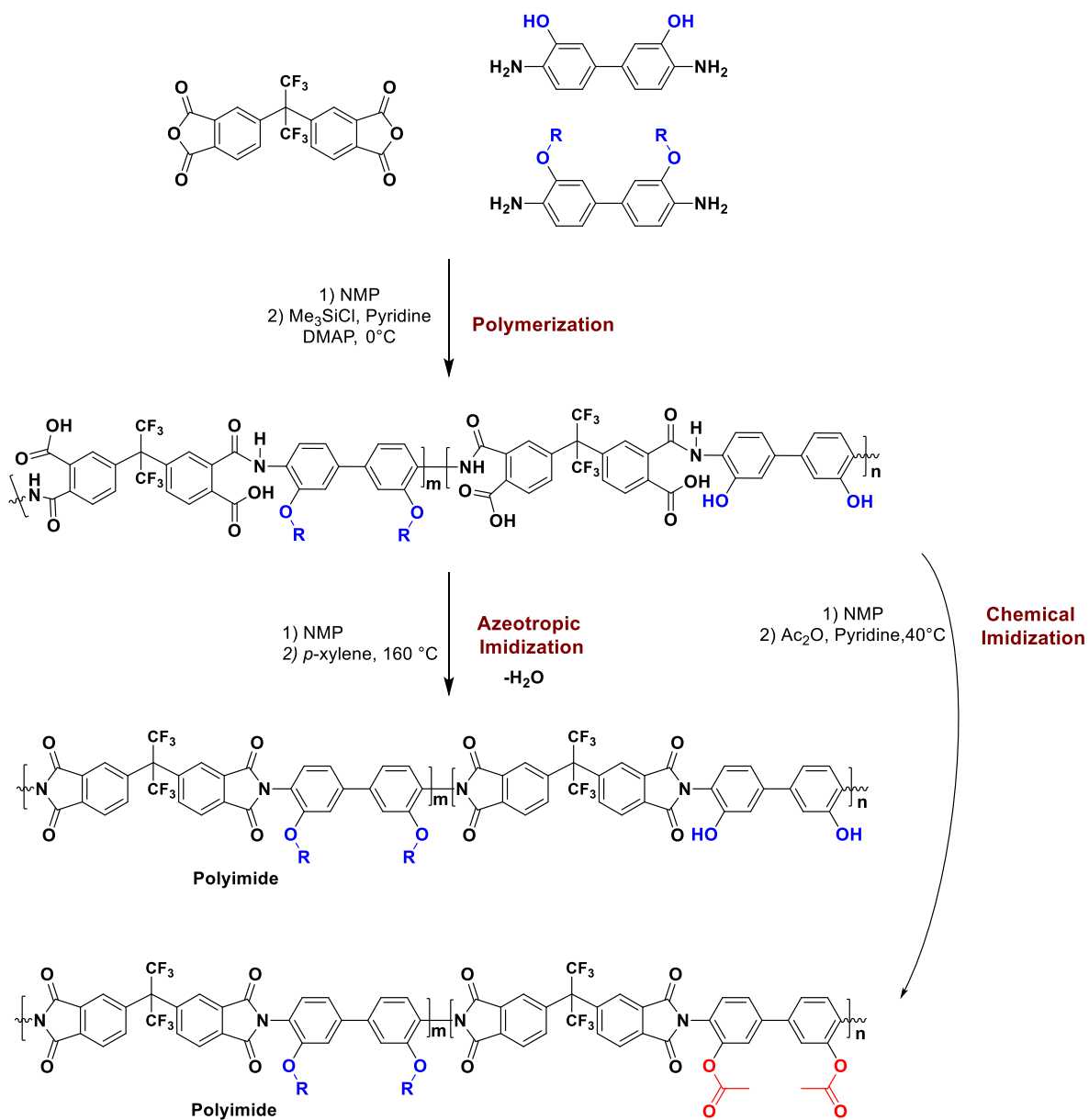


Figure 253. Photographs of the deprotection synthesis via hydrazinolysis.

### Synthesis of 6FDA-HAB precursor polymer

The *ortho*-Allyloxy polyimide precursor based on HAB, HAB-Allyl and 6FDA was synthesized by a two-step polycondensation reaction (Scheme 52). The procedure for CoPo-Allyl10PI is described as follows. HAB (4.3 g; 18 mmol) and HAB-Allyl (0.59 g; 2 mmol) was charged to a three-necked flask, equipped with a mechanical stirrer and a gas inlet, and stirred in 15 mL of NMP at room temperature under argon until completely dissolved. 6FDA (8.8 g; 20 mmol) and

additional 15 mL of NMP were then added and the resulting mixture was cooled to 0 °C and stirred overnight, whereas the temperature of the ice bath increased to room temperature. The azeotropic imidization route was used to convert the poly (amic acid) to polyimide. Therefore, *p*-xylene (8 mL) was added to the vigorously stirred viscous solution. The temperature was raised to 160 °C and kept for 8 h to promote complete imidization. The formed water was removed as a *p*-xylene/water azeotropic mixture from the solution and residuals of the *p*-xylene were removed under reduced pressure. The polymer was precipitated in deionized water and washed several times with distilled water and methanol. The polymer was then dried under vacuum at 100 °C.

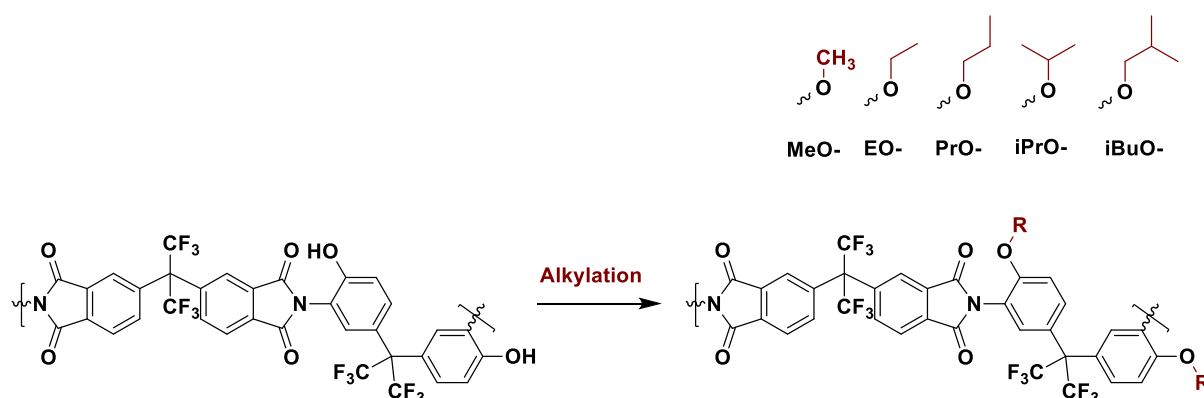


Scheme 52. Synthesis route for the co-polymerization of modified and unmodified diamines via two-step polycondensation reaction via different imidization methods.

## Alkylation

The *ortho*-hydroxy groups of the precursor polyimide were etherified with the corresponding alkyl halide. The synthesis is exemplified by methylation of the *ortho*-hydroxy group, leading to MeOPI-1, which is based on 6FDA-BisAPAF. MeOPI-1 was modified by first dissolving the *ortho*-hydroxy polyimide (1,5 g; 2 mmol) in anhydrous DMF (15 mL) in a three-necked round bottom flask under argon atmosphere at room temperature. The activation of the hydroxyl groups was carried out by adding dried potassium carbonate (0,56 g; 4 mmol) to the mixture and stirred. After 0.5 h the alkyl halide (0,99 mL; 16 mmol) was added to the solution. The mixture was stirred under these conditions for 24 h. After 24 h the mixture was precipitated in deionized water. The polymer was repeatedly washed with water and cyclohexane, reprecipitated from tetrahydrofuran and dried in a vacuum oven at 60 °C for 72 h.

The polymers are designated as RO-PI-X, whereas R refers to the alkyl group and X labels the used backbone according to Table 9, and are shown in Scheme 53. In the case of Methoxy (MeOPI), different backbones were used.



Scheme 53 Overview of all synthesized *ortho*-alkoxy polyimides.

Table 9. Alkylated polyimides. Materials with a \* were provided by U.Meis [22].

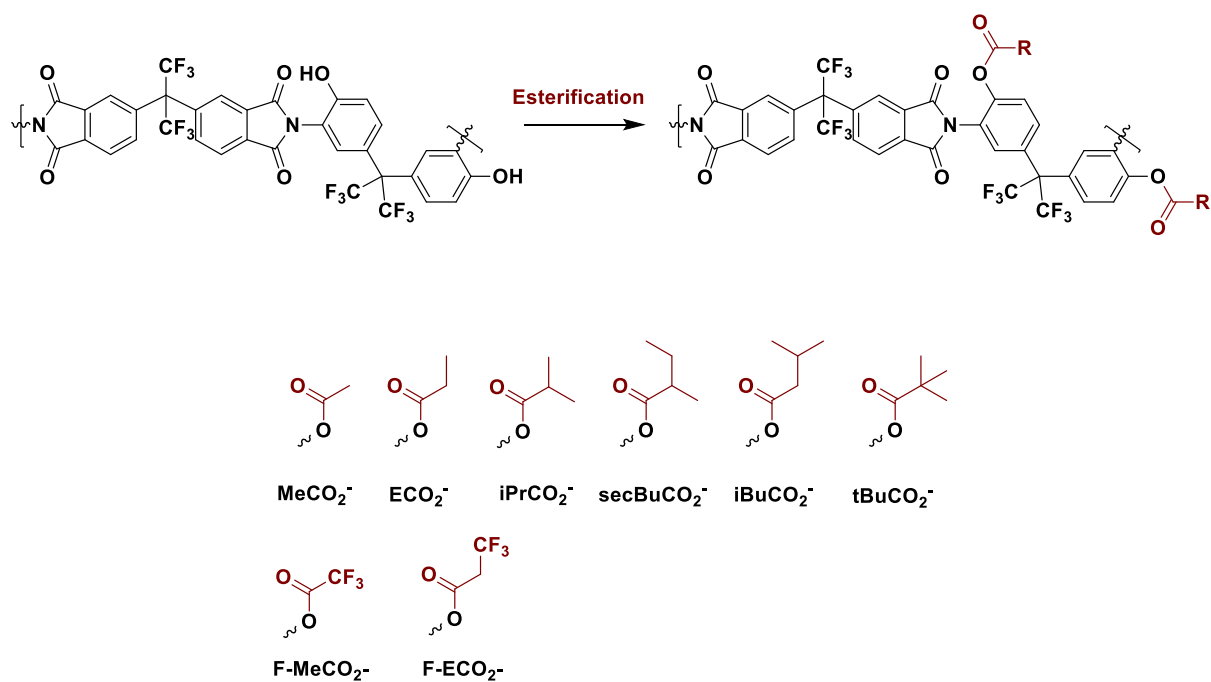
Backbone	Alkylation type	Material Code
6FDA-BisAPAF	Methylation (MeO)	MeOPI-1*
6FDA-BisAPAF	Ethylation (EO)	EOPI-1*
6FDA-BisAPAF	Propylation (PrO)	PrOPI-1*
6FDA-BisAPAF	Isopropylation ( <i>i</i> PrO)	<i>i</i> PrOPI-1*
6FDA-BisAPAF	Isobutylation ( <i>i</i> BuO)	<i>i</i> BuOPI-1
6FDA-HAB	Methylation (MeO)	MeOPI-2
BPADA-APAF	Methylation (MeO)	MeOPI-4

<b>BPADA-HAB</b>	Methylation (MeO)	MeOPI-7
<b>BPDA-APAF</b>	Methylation (MeO)	MeOPI-3
<b>BPDA-HAB</b>	Methylation (MeO)	MeOPI-6
<b>BCODA-APAF</b>	Methylation (MeO)	MeOPI-8
<b>BCODA-HAB</b>	Methylation (MeO)	MeOPI-9
<b>EDA-APAF</b>	Methylation (MeO)	MeOPI-5
<b>PMDA-APAF</b>	Methylation (MeO)	MeOPI-10

### Esterification

The *ortho*-hydroxy groups of the precursor polyimide were esterified with the corresponding anhydride. MeCO<sub>2</sub>PI-1 (Acetyl) was modified by first dissolving the *ortho*-hydroxy polyimide (1,5 g; 2 mmol) in NMP (15 mL) in a three-necked round bottom flask under argon atmosphere at 60 °C. Pyridine was added (0,32 mL; 4 mmol) and acetic anhydride (0,56 mL; 6 mmol) was added to the solution. The mixture was stirred under these conditions for 24 h. After 24 h the mixture was precipitated in deionized water. The polymer was repeatedly washed with water and cyclohexane, reprecipitated from tetrahydrofuran and dried in a vacuum oven at 60 °C for 72 h.

The polymers are designated as RCO<sub>2</sub>PI-*X*, whereas R refers to the acyl group and *X* labels the used backbone according to Table 10, and are shown in Scheme 54. In the case of the acetylated HPI (MeCO<sub>2</sub>PI) different backbones were used. The additional materials are listed in Table 10. The procedure was described in [22].



Scheme 54. Overview of all synthesized ortho-acyloxy polyimides.

Table 10. Acylated polyimides. Materials with a \* were provided by U.Meis [22].

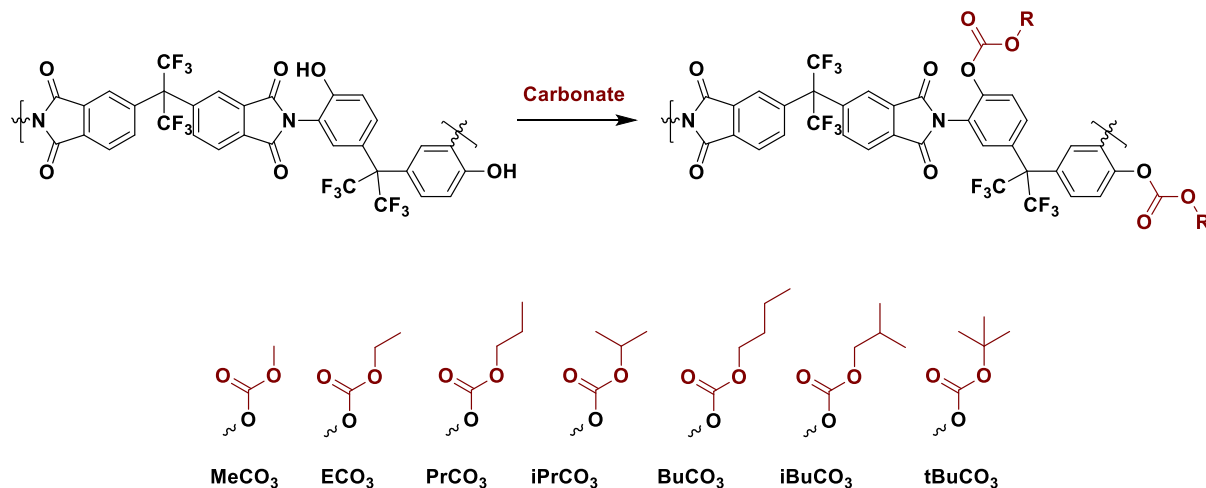
Backbone	Acylation group	Material Code
6FDA-BisAPAF	Acetyl ( $\text{MeCO}_2$ )	$\text{MeCO}_2\text{PI-1}^*$
6FDA-BisAPAF	Propanoyl ( $\text{ECO}_2$ )	$\text{ECO}_2\text{PI-1}^*$
6FDA-BisAPAF	isobutyryl ( $\text{iPrCO}_2$ )	$\text{iPrCO}_2\text{PI-1}^*$
6FDA-BisAPAF	secbutyl ( $\text{sBuCO}_2$ )	$\text{sBuCO}_2\text{PI-1}^*$
6FDA-BisAPAF	tertbutyl ( $\text{tBuCO}_2$ )	$\text{tBuCO}_2\text{PI-1}^*$
6FDA-BisAPAF	isovaleric ( $\text{iBuCO}_2$ )	$\text{iBuCO}_2\text{PI-1}^*$
6FDA-BisAPAF	Trifluoroacetyl ( $\text{CF}_3\text{MeCO}_2$ )	$\text{CF}_3\text{MeCO}_2\text{PI-1}$
6FDA-BisAPAF	Trifluoropropanoyl ( $\text{CF}_3\text{ECO}_2$ )	$\text{CF}_3\text{ECO}_2\text{PI-1}$
6FDA-HAB	Acetyl ( $\text{MeCO}_2$ )	$\text{MeCO}_2\text{PI-2}$
BPADA-APAF	Acetyl ( $\text{MeCO}_2$ )	$\text{MeCO}_2\text{PI-4}$
BPDA-APAF	Acetyl ( $\text{MeCO}_2$ )	$\text{MeCO}_2\text{PI-3}$
EDA-APAF	Acetyl ( $\text{MeCO}_2$ )	$\text{MeCO}_2\text{PI-5}$



## Carbonate synthesis

The *ortho*-hydroxy groups of the precursor polyimide were esterified with the corresponding chloroformate or pyro carbonate. MeCO<sub>3</sub>PI-1 was modified by first dissolving the *ortho*-hydroxy polyimide (1,5 g; 2 mmol) in anhydrous acetone (20 mL) in a three-necked round bottom flask under argon atmosphere at room temperature. The activation of the hydroxyl groups was carried out by adding dried potassium carbonate (0,56 g; 4 mmol) to the mixture and stirred. After 0.5 h the methyl chloroformate (1,24 mL; 16 mmol) was added to the solution. The mixture was stirred under these conditions for 24 h. After 24 h the mixture was precipitated in deionized water. The polymer was repeatedly washed with water and cyclohexane, reprecipitated from tetrahydrofuran and dried in a vacuum oven at 60 °C for 72 h.

The polymers are designated as RO-PI-X, whereas R refers to the alkyl group and X labels the used backbone according to Table 11, and are shown in Scheme 55. In the case of the methyl carbonate ester (MeCO<sub>3</sub>PI) different backbones were used. The additional materials are listed in Table 11.



Scheme 55. Overview of all synthesized ortho-carbonate ester polyimides.

Table 11. Carbonate ester polyimides, which were synthesized and used.

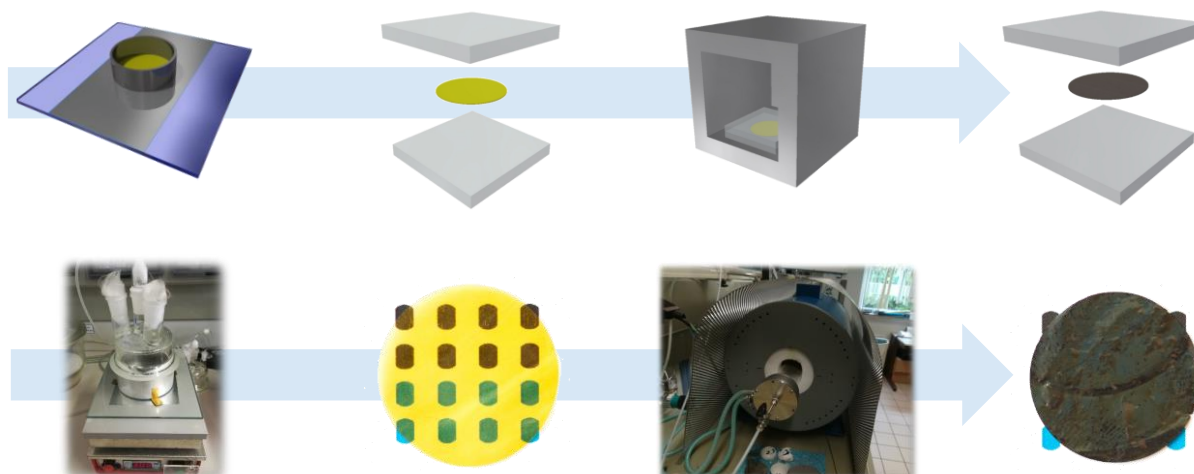
Backbone	Carbonate derivative	Material Code
6FDA-BisAPAF	Methyl (MeCO <sub>3</sub> )	MeCO <sub>2</sub> PI-1
6FDA-BisAPAF	Ethyl (ECO <sub>3</sub> )	ECO <sub>2</sub> PI-1
6FDA-BisAPAF	Propyl (PrCO <sub>3</sub> )	<i>i</i> PrCO <sub>2</sub> PI-1
6FDA-BisAPAF	<i>is</i> opropyl ( <i>i</i> PrCO <sub>3</sub> )	sBuCO <sub>2</sub> PI-1

6FDA-BisAPAF	<i>isobutyl</i> ( <i>i</i> BuCO <sub>3</sub> )	<i>t</i> BuCO <sub>2</sub> PI-1
6FDA-BisAPAF	<i>tertbutyl</i> ( <i>t</i> BuCO <sub>3</sub> )	<i>i</i> BuCO <sub>2</sub> PI-1
6FDA-BisAPAF	<i>nbutyl</i> ( <i>n</i> BuCO <sub>3</sub> )	CF <sub>3</sub> MeCO <sub>2</sub> PI-1

## Film Preparation

Polymer films, with thicknesses between 50 and 70  $\mu\text{m}$ , were solution cast from a 10 wt% solution in THF. The dissolved polymers were filtered using a 0.31  $\mu\text{m}$  syringe filter and cast onto a dry glass plate at room temperature in an argon atmosphere. Cast films were then dried in a vacuum oven overnight at 100  $^{\circ}\text{C}$  to evaporate the residual solvent.

The defect-free polymer was sandwiched between two glass plates to avoid curling and placed in a tube furnace. The thermal treatment was performed under nitrogen flow (150 mL/min), see Scheme 56.



Scheme 56. Film preparation and annealing method.

## Thermal annealing

The temperature protocol for the polymer films for analysis of the film properties, which was used for the documented experiments in this work is shown in Figure 254.

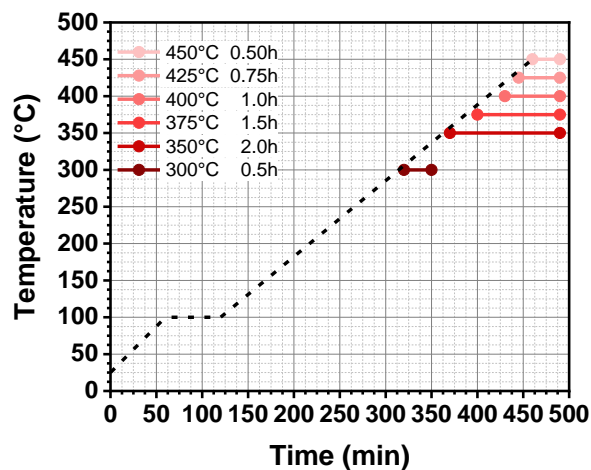


Figure 254. Annealing procedure for the polymer films with isothermal periods depending on the target temperatures from 300 to 450 °C.

## Characterization

The polymers were characterized by  $^1\text{H}$ - and  $^{13}\text{C}$ -NMR spectroscopy employing a Bruker AVIIIHD spectrometer at 500 MHz, with deuterated dimethyl sulfoxide ( $\text{DMSO-d}_6$ ) as the solvent.  $^{13}\text{C}$ -CP-MAS experiments were done on a Bruker Avance II 400. In addition,  $^{13}\text{C}$ -CP-MAS experiments were executed on a Bruker Avance I 700 MHz at the NMR spectroscopy facility of the department of chemistry at the University of Hamburg.  $^{15}\text{N}$ -,  $^{13}\text{C}$ -CP-MAS and  $^1\text{H}$ -HR-MAS spectroscopy was performed using a Bruker AVANCE III Ultrashield Plus 800 MHz (18.8T) narrow bore (54 mm) spectrometer at the spectroscopy facility of the Materials Research Laboratory, University of California Santa Barbara.

The molecular weight of the functionalized polyimides was determined by gel permeation chromatography (GPC) based on standard polystyrene calibration in DMAc with the addition of lithium chloride. A Waters 717plus instrument equipped with PSS GRAM columns [GRAM pre-column (dimension 8 – 50 mm) and two GRAM columns of different porosity (3000 Å and 1000 Å, respectively) with dimension of 8 · 300 mm and particle size of 10 µm. The flow rate was 1,0 mL min<sup>-1</sup> using a VWR-Hitachi 2130 pump, and a Shodex RI-101 refractive index detector was used.

Attenuated total internal reflectance - Fourier transform infrared spectroscopy (ATR-FT-IR) measurements were performed using a Bruker alpha ATR in a spectral range of 400-4000  $\text{cm}^{-1}$  with an average of 32 scans and a resolution of 4  $\text{cm}^{-1}$ .

Differential scanning calorimetry (DSC) was performed with a differential scanning calorimeter DSC1 (Mettler-Toledo) in a temperature range between 30 and 450  $^{\circ}\text{C}$  under nitrogen (60  $\text{mL m}^{-1}$ ) and at a heating rate of 5  $\text{K min}^{-1}$  to study the thermally induced transitions of the synthesized polyimides. Approximately 8 mg of the polymer sample were transferred into a 40  $\mu\text{L}$  sealed aluminum pan with a pierced lid. For thermokinetic investigations the DSC runs were performed with a total mass of about 3 mg at heating rates of 2, 3, 5, 6, 8, and 9  $^{\circ}\text{C min}^{-1}$ . For the glass transition determination, the materials were heated up to 320  $^{\circ}\text{C}$  and cooled down afterwards at a heating rate of 5 and cooling rate of 10  $^{\circ}\text{C min}^{-1}$ . The glass transition was determined during the second cycle.

Thermogravimetric analysis (TGA) was performed using a TGA-DSC2 Thermogravimetric Analyzer (Mettler-Toledo) over the range of 25 to 800  $^{\circ}\text{C}$  with a heating rate of 5  $^{\circ}\text{C min}^{-1}$  in an argon (20  $\text{mL min}^{-1}$ ) or synthetic air atmosphere. In order to determine the  $\text{CO}_2$  as well as other volatile products evolution during TR-process, the thermogravimetric analyzer was coupled with a FT-IR spectrometer Nicolet iS50 (Thermo Scientific), which recorded in the spectral range of 400-4000  $\text{cm}^{-1}$  with a resolution of 4  $\text{cm}^{-1}$  and a total number of 64 scans per spectrum. The conversion of the Thermal Rearrangement process for each material after different isothermal treatments was determined using the following equation:

$$\text{conversion (\%)} = \frac{\text{mass loss}_{\text{experimental}}}{\text{mass loss}_{\text{theoretical}}} \times 100 \quad (13)$$

Evolved gas analysis was performed with a mass spectroscopy accessory in addition to the TG-IR experiments for some samples. The used device was a TA Discovery Thermo-Gravimetric Analyzer (TGA) and Mass Spectrometer (MS). The experiments were carried out in the range from 25  $^{\circ}\text{C}$  to 600  $^{\circ}\text{C}$  with a heat rate of 5  $^{\circ}\text{C min}^{-1}$  under argon atmosphere. The experiments were done at the TEMPO laboratory of the Materials Research Laboratory, University of California Santa Barbara.

Dielectric spectroscopy experiments were accomplished using an Alpha-AN high-resolution dielectric analyzer (Novocontrol Technologies GmbH, Montabaur, Germany), as described

elsewhere. Polymer films, with thicknesses in the range of 100–200  $\mu\text{m}$ , were cast from a polymer solution in DMAc under nitrogen flow. After that, the films were washed overnight with methanol and then dried under vacuum at 150  $^{\circ}\text{C}$  for 24 h. The films were directly placed on a gold-coated cylindrical brass electrode. A second gold-coated brass electrode was placed on top of the sample. Afterwards, the two brass plates containing the sample were inserted into the thermally controlled chamber of the spectrometer. The diameter of the electrodes was 40 mm for the lower electrode and 20 mm for the upper; therefore, the examined area was 400  $\text{mm}^2$ . The sample was heated up to 150  $^{\circ}\text{C}$  for 1 h in order to favor the adhesion between the sample and the brass plates. The temperature of 150  $^{\circ}\text{C}$  was chosen in order to prevent Thermal Rearrangement of the polymer film. The temperature was varied in the range of  $-100$  to  $+420$   $^{\circ}\text{C}$ , in increments of 10  $^{\circ}\text{C}$ , with a stabilization time of 60 s, derivation 0.1  $^{\circ}\text{C min}^{-1}$  and an error of 0.1  $^{\circ}\text{C}$ . The frequency was in the interval of  $10^{-3}$  up to  $10^6$  Hz starting from high to low frequencies.

The solubility of the polymers before thermal treatment was determined by mixing of approximately 5 mg of each sample in 2 mL of the corresponding solvent at room temperature for 120 h at 50  $^{\circ}\text{C}$ .

The gel-fraction of the membranes were determined by soaking the membranes in DMF as an appropriate solvent for the materials. The films were soaked in the solvent for 120 h and weighed before ( $w_1$ ) and after drying ( $w_3$ ) them in vacuum at 150  $^{\circ}\text{C}$  for 72 h. The gel-fraction and swelling ratio were calculated by the following equations (14) and (15)

$$\text{gel - fraction (\%)} = \frac{w_3}{w_1} \times 100 \quad (14)$$

$$\text{swelling - ratio (\%)} = \frac{w_2}{w_1} \times 100 \quad (15)$$

The density of the membranes was determined by using a Mettler Toledo XP105 balance equipped with a density determination kit. The samples were weighed in air and *isooctane* according to the buoyancy method. Isooctane has been chosen as a liquid with known density since it is wetting the membrane perfectly and is not absorbing into the membrane. The density was calculated using the following equation (16)

$$\rho_{membrane} = \frac{w_{air}}{w_{air} - w_{liq}} \rho_{liq} \quad (16)$$

with  $\rho_{membrane}$  as the membrane density ( $\text{g cm}^{-3}$ ),  $w_{air}$  and  $w_{liq}$  as the weight of the membrane in air and *isooctane* (g), and  $\rho_{liq}$  is the density of *isooctane* ( $\text{g cm}^{-3}$ ).

Based on the density data, the fractional free volume (FFV) of the membranes before the thermal treatments was estimated according to the following equation (17) and (18)

$$V_{sp} = \frac{m}{\rho_{membrane}} \quad (17)$$

$$FFV = \frac{V_{sp} - 1.3xV_w}{V_{sp}} \quad (18)$$

Where  $V_{sp}$  is the specific molar volume of the polymer membrane and  $V_w$  is the van der Waals molar volume according to Bondi's group contribution theory [94, 323].

Mechanical properties were studied using uniaxial tension tests using a universal testing machine, the Zwick Z020 apparatus, with a 100 N load cell at room temperature. The samples had dimensions of 40 mm length and 4.7 mm width and were clamped at both ends. The initial gap was 15 mm, and the elongation rate was  $5 \text{ mm min}^{-1}$ . The average values were determined from five measurements for each material.

X-ray diffraction measurements of the membranes were done using a Siemens D5000 diffractometer with  $\text{Cu K}\alpha$  radiation with a wavelength of 0.154 nm at a step size of  $0.1^\circ \text{ min}^{-1}$  and a step time of 4 s in the  $2\theta$  range of  $2\text{--}45^\circ$ . The average d-spacing value was calculated via Bragg's equation (19)

$$n\lambda = 2d \sin\theta \quad (19)$$

with the diffractometer wavelength  $\lambda$ , interchain distance  $d$  and Bragg angle  $\vartheta$ . The gas permeation properties were determined using a constant volume variable pressure method (time-lag method) realized in an in-house designed and built experimental facility [324]

The single gas permeability  $P$  of H<sub>2</sub>, He, N<sub>2</sub>, O<sub>2</sub>, CH<sub>4</sub>, CO<sub>2</sub>, C<sub>2</sub>H<sub>4</sub>, C<sub>2</sub>H<sub>6</sub>, C<sub>3</sub>H<sub>6</sub>, C<sub>3</sub>H<sub>8</sub> was measured at 30 °C and a feed pressure of 1000 mbar. From the linear increase of the downstream pressure rise as a function of the time ( $dp/dt$ ) the permeability of each gas could be calculated via (20)

$$P = \frac{273.15Vl}{76T\Delta pA} \frac{dp}{dt} \quad (20)$$

with permeability  $P$  (Barrer), membrane thickness  $l$  (cm), downstream chamber volume  $V$  (cm<sup>3</sup>) temperature  $T$  (K), pressure difference  $\Delta p$  ( $=p_{\text{upstream}}-p_{\text{downstream}}$ ) (cm Hg) and effective membrane area  $A$  (cm<sup>2</sup>). Based on the calculated permeability of each gas, the ideal selectivity  $\alpha_{x/y}$  of each gas pair could be calculated, as shown in equation (21)

$$\alpha_{x/y} = \frac{P_x}{P_y} \quad (21)$$

The used facilities and setups are shown in Figure 255.



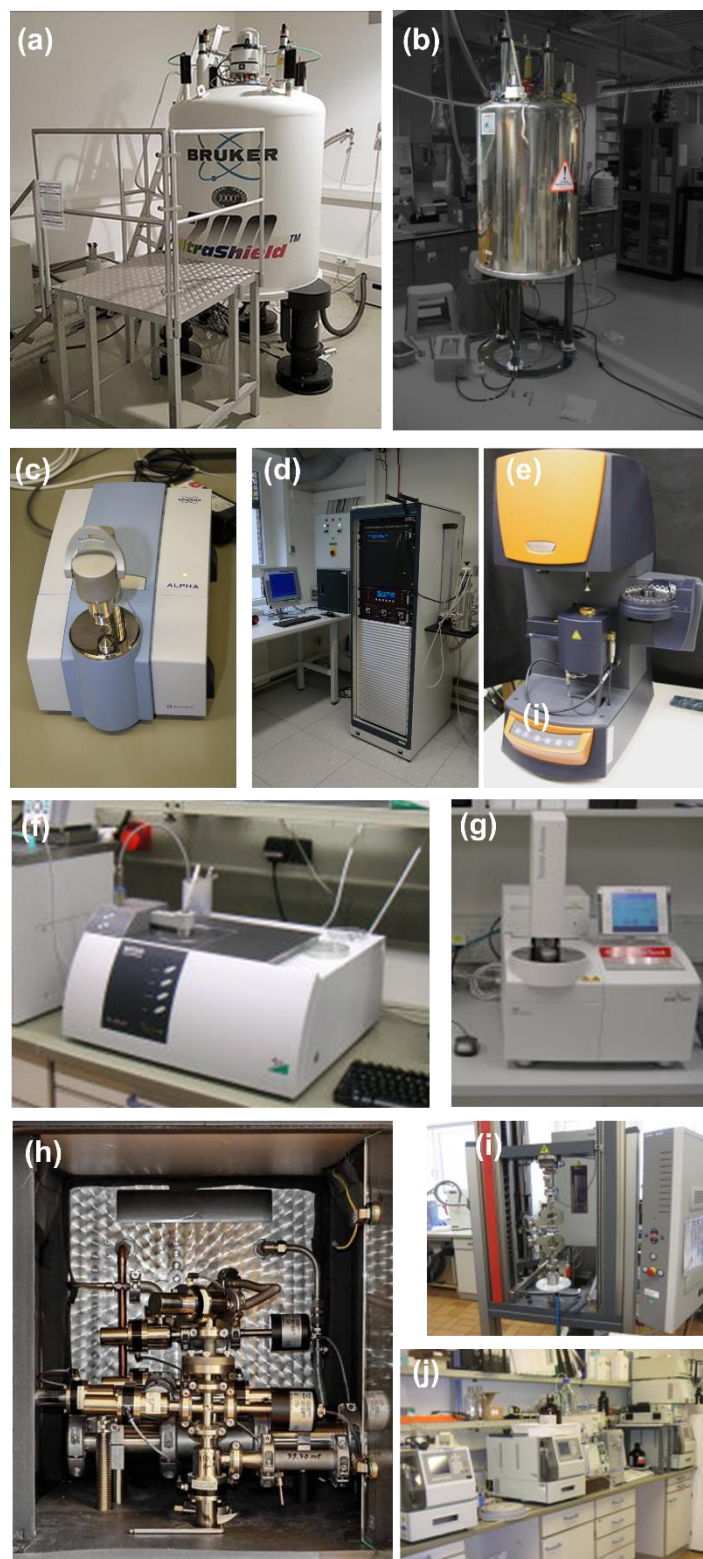


Figure 255. Overview of the used analytical devices: (a) NMR for  $^{13}\text{C}$ -CP-MAS experiments by Dr. Joo-Lee; (b)  $^{13}\text{C}$ ,  $^{15}\text{N}$  and  $^1\text{H}$  CP-MAS NMR by Jaya Nolt and Dr. Jerry Hu (UCSB); (c) Benchtop FT-IR spectrometer; (d) BDS dielectric spectrometer; (e) TGA-MS (UCSB); (f) TGA-FT-IR; (g) DSC; (h) Time-lag method; (i) tensile testing; (j) GPC.



## Computational methodology

### Molecular Dynamics

The molecular dynamic simulations were done using Materials Studio 8.0 (Biovia, San Diego) software. All calculations were done using the COMPASS force field. The Ewald-method for the long-range Coulomb interactions and atom-based summation method for the Van-der-Waals interactions were used. In the case of PBO rings, two adjustments were done. First of all, the nitrogen atoms forcefield parameter in PBO rings were changed from n2a (N, sp<sup>2</sup>, aromatic) to n3a (N, sp<sup>2</sup>, aromatic), and additionally the oxygen atoms in the PBO rings were adjusted from o2a (O, sp<sup>2</sup>, aromatic) to o (O, generic) to fulfill the rigid and coplanar structure and properties of PBO rings.

For the investigation of the polymer properties, polymer models were built, and amorphous cells were constructed. In a first step the monomers were constructed, and geometry optimized with a total cycle of 50000. From these monomers, the corresponding polymers or copolymers were constructed and optimized by an energy minimization step. A general scheme is shown in Scheme 57

From these optimized polymer models several amorphous cells were constructing, following the Theodorou/Suter method [168, 169, 171], which is implemented in the Amorphous Cell module of Materials Studio. Every cell was constructed from two polymer chains, each containing 40 repetition units at an initial density of 0.1 g cm<sup>-3</sup> at 303 K under periodic boundary conditions. The final packing of the cell at the final density was obtained after a compression-decompression procedure (Table 12). A long final *NpT*-MD run of 300 ps and *NVT* run of 500 ps was carried out to equilibrate the model. with a time-step of 1 femtosecond. The temperature control was performed by using a Nosé thermostat. A validity check was done by varifying a stable energy and density after long MD runs. In order to check the quality of the boxes the ratio of the accessible volume (AV) to accessible solvent surface (ASA) and its gradient by varying the probe radius from 1.0 to 2.0 Å with steps of 0.1 Å was done. The final cell size of the packing models was about (40 Å)<sup>3</sup>.

Table 12. Overview of the compression-decompression-relaxations procedure to generate amorphous cells.

<b>Step#</b>	<b>Temperature (K)</b>	<b>Pressure (GPa)</b>	<b>Time (ps)</b>	<b>Ensemble</b>
1	600		50	<i>NVT</i>
2	303		50	<i>NVT</i>
3	303	0.003	50	<i>NPT</i>
4	600		50	<i>NVT</i>
5	303		100	<i>NVT</i>
6	303	0.05	50	<i>NPT</i>
7	600		50	<i>NVT</i>
8	303		100	<i>NVT</i>
9	303	0.3	50	<i>NPT</i>
10	600		50	<i>NVT</i>
11	303		100	<i>NVT</i>
12	303	0.15	5	<i>NPT</i>
13	600		5	<i>NVT</i>
14	303		10	<i>NVT</i>
15	303	0.06	5	<i>NPT</i>
16	600		5	<i>NVT</i>
17	303		10	<i>NVT</i>
18	303	0.0001	5	<i>NPT</i>
19	600		5	<i>NVT</i>
20	303		10	<i>NVT</i>
21	303	0.0001	300	<i>NPT</i>
<b>Final</b>	303		500	<i>NVT</i>

The thermally induced reactions were simulated by manual bond formation and breakage of the corresponding process. The procedure for crosslinking, was done in allylated and propargylated cells, the Thermal Rearrangement reaction, decomposition (MeO-, EO- and MeCO<sub>2</sub>PI cells).

Crosslinking of allyl and propargyl groups was performed for corresponding cells, if the crosslinking groups were close to each other within a pre-specified cut-off distance of 5 Å. The cut-off distance was the distance of the corresponding groups to each other at the beginning of an IRC calculation from quantum mechanical DFT simulations. The crosslinking was performed by manual bond formation and double bond rearrangement according to the simulated lowest-energy crosslinking procedure by means of DFT simulations. After each crosslinking cycle, a geometry optimization of the cell, followed by a 50 ps *NpT* and 50 ps *NVT* run according to the above defined parameters. Each crosslinking cycle involved the formation of 10 crosslinks until less than 10 crosslinks were possible (Table 13).

Table 13. Procedure for each crosslinking step.

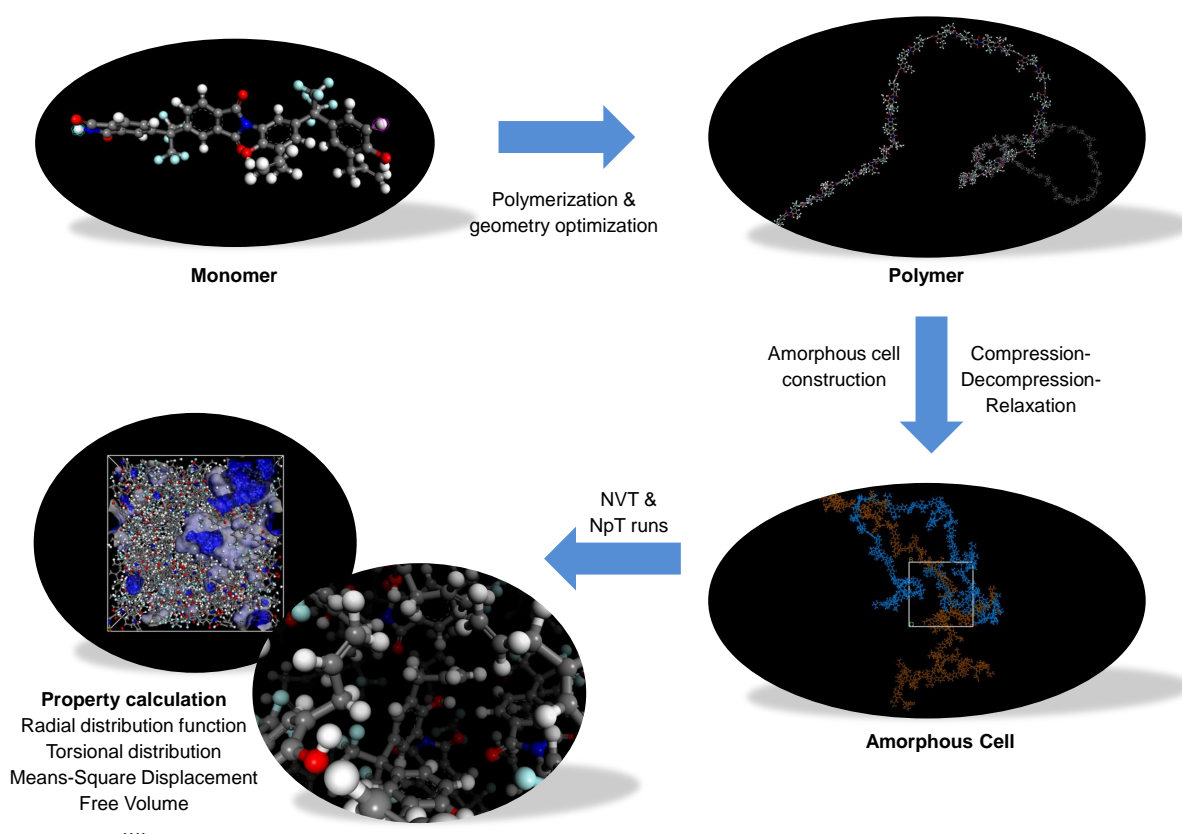
Task	Job type	Temperature (K)	Pressure (GPa)	Time (ps)
Energy	Geometry	573	0.0001	
	Optimization			
Dynamics	<i>NpT</i>	573	0.0001	50
Dynamics	<i>NVT</i>	573	0.0001	50

The Thermal Rearrangement was done by (1) bond formation between O1 and C1\*, followed by (2) bond formation of O1\* and C2\* of Int1 and bond breakage between O1\* and C1\*, as well as C2\* and N. The obtained structure was iPBO and was relaxed by a geometry optimization, 50 ps *NpT* and 50 ps *NVT* run. After that the carboxylic acid group was decarboxylated by breakage of the bond between C4\* and C2\*, followed by a geometry optimization, 200 ps *NpT* and 500 ps *NVT* run. Finally the CO<sub>2</sub> molecules were removed and a 300 ps *NpT* and 500 ps *NVT* run at 303 K was done. Each TR cycle involved the rearrangement of 20 imide groups.

Decomposition of methyl and ethyl groups in MeO and EOPI, as well as ketene from MeCO<sub>2</sub>PI (AcPI) was done by breaking the connecting ether or ester bond and re-bond the hydrogen atoms by means of the hydrogen adjustment feature. After each decomposition cycle, a

geometry optimization of the cell, followed by a 50 ps  $NpT$  and 50 ps  $NVT$  run according to the above defined parameters. Each decomposition cycle involved the bond breakage of 30 ether or ester, respectively.

The analysis of the structure properties, such as the torsional distribution, length distribution of certain subunits, as well as the radial distribution function (RDF) and the means-square displacement (MSD) was done by means of long 0.5 ns runs with a  $NVT$ -ensemble at a specific temperature. The final free volume and MSD characteristics were done from the final  $NVT$  run at 303 K with a time-step of 1 femtosecond. The temperature control was performed by using a Nosé thermostat.



Scheme 57. Overview of the workflow from (1) monomer design and geometry optimization, (2) polymer building, (3) amorphous cell construction, followed by a 21-step equilibration procedure including compression-decompression-relaxation and equilibration runs, (4) analytics via long  $NVT$  or  $NpT$ -runs.

**The free volume analysis** was performed using the visualizer tool of materials studio. The free accessible volume (FAV), defined by the cell volume  $V$  and the probe accessible volume  $V_{\text{probe}}$ , was determined by the ratio as show in equation (22)

$$FAV (\%) = \frac{V - V_{Probe}}{V} \times 100 \quad (22)$$

### **DFT simulations**

Quantum mechanical calculations have been performed with the Gaussian09 software package [325] on a density functional theory of B3LYP level. All reactant-, product- and intermediate-geometries were optimized at the B3LYP/6-31+G\* level. Transition states were modeled in the GaussView 5.0 package and optimized by Berny transition state optimizations on a B3LYP/6-31+G\* level of theory. The transition states were verified by having only one imaginary frequency. Intrinsic reaction coordinate (IRC) calculations were carried out to confirm the transition state structure and to simulate the reaction coordinate. Final structures were the geometry optimized to connect the transition state to the associated reactant, intermediate and product, respectively. The structures of the reactants, intermediates and products are shown in the support information.



PART VIII

**Bibliography**





*The only thing  
that you absolutely have to know,  
is the location of the library*  
Albert Einstein

## BIBLIOGRAPHY

1. Freeman, B., Yampolskii, Y., and Pinnau, I., *Materials Science of Membranes for Gas and Vapor Separation*. 2006: Wiley.
2. Strathmann, H., *Introduction to Membrane Science and Technology*. 2011: Wiley.
3. Matteucci, S., Yampolskii, Y., Freeman, B.D., and Pinnau, I., *Transport of Gases and Vapors in Glassy and Rubbery Polymers*, in *Materials Science of Membranes for Gas and Vapor Separation*. 2006. p. 1-47.
4. Poloni, L., Polegato Moretti M., *Waterproof and vapor-permeable sole for shoes U.S.*, Editor. 2020, Geox SpA: United States. p. 11.
5. S.p.a., G. *Our Technology*. 2021 [cited 2021 14.03.2021]; Available from: <https://www.geox.com/int/technologygeox>.
6. Kita, H., *Zeolite Membranes for Pervaporation and Vapor Permeation*, in *Materials Science of Membranes for Gas and Vapor Separation*. 2006. p. 373-389.
7. Baker, R.W. and Low, B.T., *Gas Separation Membrane Materials: A Perspective*. *Macromolecules*, 2014. **47**(20): p. 6999-7013.
8. Kayvani Fard, A., McKay, G., Buekenhoudt, A., Al Sulaiti, H., Motmans, F., Khraishah, M., and Atieh, M., *Inorganic Membranes: Preparation and Application for Water Treatment and Desalination*. *Materials*, 2018. **11**(1): p. 74.
9. Tul Muntha, S., Kausar, A., and Siddiq, M., *Progress in Applications of Polymer-Based Membranes in Gas Separation Technology*. *Polymer-Plastics Technology and Engineering*, 2016. **55**(12): p. 1282-1298.
10. Yampolskii, Y., *Polymeric Gas Separation Membranes*. *Macromolecules*, 2012. **45**(8): p. 3298-3311.
11. Bernardo, P. and Drioli, E., *Membrane gas separation progresses for process intensification strategy in the petrochemical industry*. *Petroleum Chemistry*, 2010. **50**(4): p. 271-282.
12. Sanders, D.F., Smith, Z.P., Guo, R., Robeson, L.M., McGrath, J.E., Paul, D.R., and Freeman, B.D., *Energy-efficient polymeric gas separation membranes for a sustainable future: A review*. *Polymer*, 2013. **54**(18): p. 4729-4761.
13. *Membrane technology's 25 year evolution*. *Filtration & Separation*, 2007. **44**(9): p. 32-34.
14. Graham, T., XVIII. *On the absorption and dialytic separation of gases by colloid septa*. *Philosophical Transactions of the Royal Society of London*, 1866. **156**: p. 399-439.
15. Loeb, S., *The Loeb-Sourirajan Membrane: How It Came About*, in *Synthetic Membranes*.. 1981, American Chemical Society. p. 1-9.
16. Kentish, S.E., *110th Anniversary: Process Developments in Carbon Dioxide Capture Using Membrane Technology*. *Industrial & Engineering Chemistry Research*, 2019. **58**(28): p. 12868-12875.

17. Cussler, E.L., *Diffusion: Mass Transfer in Fluid Systems*. 3 ed. Cambridge Series in Chemical Engineering. 2009, Cambridge: Cambridge University Press.
18. Wijmans, J.G. and Baker, R.W., *The Solution–Diffusion Model: A Unified Approach to Membrane Permeation*, in *Materials Science of Membranes for Gas and Vapor Separation*. 2006. p. 159-189.
19. Crank, J. and Park, G.S., *Diffusion in Polymers*. 1968: Academic Press.
20. *Membrane Transport Theory*, in *Membrane Technology and Applications*. 2012. p. 15-96.
21. Fick, A., *Ueber Diffusion*. *Annalen der Physik*, 1855. **170**(1): p. 59-86.
22. Meis, U., *Synthesis and characterization of functionalized ortho-hydroxy polyimides*, *Master thesis, University of Hamburg*, in *University Hamburg*. 2018.
23. Low, Z.-X., Budd, P.M., McKeown, N.B., and Patterson, D.A., *Gas Permeation Properties, Physical Aging, and Its Mitigation in High Free Volume Glassy Polymers*. *Chemical Reviews*, 2018. **118**(12): p. 5871-5911.
24. Menczel, J.D., Judovits, L., Prime, R.B., Bair, H.E., Reading, M., and Swier, S., *Differential Scanning Calorimetry (DSC)*, in *Thermal Analysis of Polymers*. 2009. p. 7-239.
25. Jansen, J.C., *Glass Transition Temperature (T<sub>g</sub>)*, in *Encyclopedia of Membranes*, E. Drioli and L. Giorno, Editors. 2016, Springer Berlin Heidelberg: Berlin, Heidelberg. p. 1-3.
26. Cangialosi, D., Boucher, V.M., Alegría, A., and Colmenero, J., *Physical aging in polymers and polymer nanocomposites: recent results and open questions*. *Soft Matter*, 2013. **9**(36): p. 8619-8630.
27. Doghieri, F., Quinzi, M., Rethwisch, D.G., and Sarti, G.C., *Predicting Gas Solubility in Membranes through Non-Equilibrium Thermodynamics for Glassy Polymers*, in *Materials Science of Membranes for Gas and Vapor Separation*. 2006. p. 137-158.
28. Thornton, A.W., Nairn, K.M., Hill, A.J., and Hill, J.M., *New relation between diffusion and free volume: I. Predicting gas diffusion*. *Journal of Membrane Science*, 2009. **338**(1): p. 29-37.
29. Mercea, P., *Models for Diffusion in Polymers*, in *Plastic Packaging*. 2008. p. 123-162.
30. Brandt, W.W. and Anysas, G.A., *Diffusion of gases in fluorocarbon polymers*. *Journal of Applied Polymer Science*, 1963. **7**(5): p. 1919-1931.
31. DiBenedetto, A.T., *Molecular properties of amorphous high polymers. II. An interpretation of gaseous diffusion through polymers*. *Journal of Polymer Science Part A: General Papers*, 1963. **1**(11): p. 3477-3487.
32. Paul, D.R., Garcin, M., and Garmon, W.E., *Solute diffusion through swollen polymer membranes*. *Journal of Applied Polymer Science*, 1976. **20**(3): p. 609-625.
33. Paul, D.R. and McSpadden, S.K., *Diffusional release of a solute from a polymer matrix*. *Journal of Membrane Science*, 1976. **1**: p. 33-48.
34. Seiffert, S., *Physical Chemistry of Polymers*. 2020: De Gruyter.
35. Meis, D., *Studies of crosslinked polybutadiene based fixed carrier membranes for natural gas separation*, in *Department of Chemistry*. 2015, University of Hamburg: Hamburg.
36. Vieth, W.R., Howell, J.M., and Hsieh, J.H., *Dual sorption theory*. *Journal of Membrane Science*, 1976. **1**: p. 177-220.
37. Robeson, L.M., *Correlation of separation factor versus permeability for polymeric membranes*. *Journal of Membrane Science*, 1991. **62**(2): p. 165-185.
38. Dal-Cin, M.M., Kumar, A., and Layton, L., *Revisiting the experimental and theoretical upper bounds of light pure gas selectivity–permeability for polymeric membranes*. *Journal of Membrane Science*, 2008. **323**(2): p. 299-308.

39. Robeson, L.M., *The upper bound revisited*. Journal of Membrane Science, 2008. **320**(1): p. 390-400.
40. Comesaña-Gándara, B., Chen, J., Bezzu, C.G., Carta, M., Rose, I., Ferrari, M.-C., Esposito, E., Fuoco, A., Jansen, J.C., and McKeown, N.B., *Redefining the Robeson upper bounds for CO<sub>2</sub>/CH<sub>4</sub> and CO<sub>2</sub>/N<sub>2</sub> separations using a series of ultrapermeable benzotriptycene-based polymers of intrinsic microporosity*. Energy & Environmental Science, 2019. **12**(9): p. 2733-2740.
41. Freeman, B.D., *Basis of Permeability/Selectivity Tradeoff Relations in Polymeric Gas Separation Membranes*. Macromolecules, 1999. **32**(2): p. 375-380.
42. Bogert, M.T. and Renshaw, R.R., *4-Amino-0-Phthalic acid and some of its Derivatives 1*. Journal of the American Chemical Society, 1908. **30**(7): p. 1135-1144.
43. Bryant, R.G., *Polyimides*, in *Ullmann's Encyclopedia of Industrial Chemistry*. p. 1-27.
44. Wilson, D., Stenzenberger, H.D., and Hergenrother, P.M., *Polyimides*. 2013: Springer Netherlands.
45. Ni, H.-j., Liu, J.-g., Wang, Z.-h., and Yang, S.-y., *A review on colorless and optically transparent polyimide films: Chemistry, process and engineering applications*. Journal of Industrial and Engineering Chemistry, 2015. **28**: p. 16-27.
46. Ma, P., Dai, C., Wang, H., Li, Z., Liu, H., Li, W., and Yang, C., *A review on high temperature resistant polyimide films: Heterocyclic structures and nanocomposites*. Composites Communications, 2019. **16**: p. 84-93.
47. Sezer Hicyilmaz, A. and Celik Bedeloglu, A., *Applications of polyimide coatings: a review*. SN Applied Sciences, 2021. **3**(3): p. 363.
48. Morikawa, A., *Synthesis and Characterization of Novel Polyimides*, in *High Performance Polymers and Engineering*, 2011, p. 205-242.
49. Liaw, D.-J., Wang, K.-L., Huang, Y.-C., Lee, K.-R., Lai, J.-Y., and Ha, C.-S., *Advanced polyimide materials: Syntheses, physical properties and applications*. Progress in Polymer Science, 2012. **37**(7): p. 907-974.
50. Yang, Y., Jung, Y., Cho, M.D., Lee, S.G., and Kwon, S., *Transient color changes in oxidative-stable fluorinated polyimide film for flexible display substrates*. RSC Advances, 2015. **5**(71): p. 57339-57345.
51. Zhang, C., Cao, B., and Li, P., *Thermal Oxidative Crosslinking of Phenolphthalein-based Cardo Polyimides with Enhanced Gas Permeability and Selectivity*. Journal of Membrane Science, 2017. **546**.
52. Zhang, Q., Tsai, C.-Y., Li, L.-J., and Liaw, D.-J., *Colorless-to-colorful switching electrochromic polyimides with very high contrast ratio*. Nature Communications, 2019. **10**(1): p. 1239.
53. Dinan, F.J., Schwartz, W.T., Wolfe, R.A., Hojnicky, D.S., Clair, T.S., and Pratt, J.R., *Solid-State <sup>13</sup>C-NMR spectral evidence for charge transfer complex formation in aromatic diimides and dianhydrides*. Journal of Polymer Science Part A: Polymer Chemistry, 1992. **30**(1): p. 111-118.
54. Kawakami, H., Mikawa, M., and Nagaoka, S., *Gas permeability and selectivity through asymmetric polyimide membranes*. Journal of Applied Polymer Science, 1996. **62**(7): p. 965-971.
55. Duthie, X., Kentish, S., Pas, S.J., Hill, A.J., Powell, C., Nagai, K., Stevens, G., and Qiao, G., *Thermal treatment of dense polyimide membranes*. Journal of Polymer Science Part B: Polymer Physics, 2008. **46**(18): p. 1879-1890.

56. Ando, S., Matsuura, T., and Sasaki, S., *Coloration of Aromatic Polyimides and Electronic Properties of Their Source Materials*. Polymer Journal, 1997. **29**(1): p. 69-76.
57. Sroog, C.E., *Polyimides*. Journal of Polymer Science: Macromolecular Reviews, 1976. **11**(1): p. 161-208.
58. Zhou, Y., Chen, G., Wang, W., Wei, L., Zhang, Q., Song, L., and Fang, X., *Synthesis and characterization of transparent polyimides derived from ester-containing dianhydrides with different electron affinities*. RSC Advances, 2015. **5**(96): p. 79207-79215.
59. Kolegov, V.I., *The effect of side reactions on the molecular weight characteristics of polyamidoacids*. Polymer Science U.S.S.R., 1976. **18**(8): p. 1929-1938.
60. Kolegov, V.I. and Frenkel, S.Y., *Theoretical investigation of the formation of condensation polymers-polyamidoacids*. Polymer Science U.S.S.R., 1976. **18**(8): p. 1919-1929.
61. Chen, W., Chen, W., Zhang, B., Yang, S., and Liu, C.-Y., *Thermal imidization process of polyimide film: Interplay between solvent evaporation and imidization*. Polymer, 2017. **109**: p. 205-215.
62. Koton, M.M., Meleshko, T.K., Kudryavtsev, V.V., Nechayev, P.P., Kamzolkina, Y.V., and Bogorad, N.N., *Investigation of the kinetics of chemical imidization*. Polymer Science U.S.S.R., 1982. **24**(4): p. 791-800.
63. Kreuz, J.A., Endrey, A.L., Gay, F.P., and Sroog, C.E., *Studies of thermal cyclizations of polyamic acids and tertiary amine salts*. Journal of Polymer Science Part A-1: Polymer Chemistry, 1966. **4**(10): p. 2607-2616.
64. Laius, L.A., Bessonov, M.I., Kallistova, Y.V., Adrova, N.A., and Florinskii, F.S., *Infrared spectral absorption study of the formation kinetics of polypyromellitimide (PPMI)*. Polymer Science U.S.S.R., 1967. **9**(10): p. 2470-2478.
65. Pryde, C.A., *IR studies of polyimides. I. Effects of chemical and physical changes during cure*. Journal of Polymer Science Part A: Polymer Chemistry, 1989. **27**(2): p. 711-724.
66. Young, P.R. and Chang, A.C., *FTIR characterization of advanced materials*. SAMPE Quarterly, 1986. **17**: p. 32.
67. Morawetz, H., *Structure-solubility relationships in polymers*, Frank W. Harris and Raymond B. Seymour, Eds., Academic Press, New York, 1977, 271 pp. \$13.00. Journal of Polymer Science: Polymer Letters Edition, 1977. **15**: p. 634-634.
68. Liaw, D.-J., Liaw, B.-Y., Hsu, P.-N., and Hwang, C.-Y., *Synthesis and Characterization of New Highly Organosoluble Poly(ether imide)s Bearing a Noncoplanar 2,2'-Dimethyl-4,4'-biphenyl Unit and Kink Diphenylmethylene Linkage*. Chemistry of Materials, 2001. **13**(5): p. 1811-1816.
69. Sahadeva Reddy, D., Chou, C.-H., Shu, C.-F., and Lee, G.-H., *Synthesis and characterization of soluble poly(ether imide)s based on 2,2'-bis(4-aminophenoxy)-9,9'-spirobifluorene*. Polymer, 2003. **44**(3): p. 557-563.
70. Kim, Y.-H., Kim, H.-S., and Kwon, S.-K., *Synthesis and Characterization of Highly Soluble and Oxygen Permeable New Polyimides Based on Twisted Biphenyl Dianhydride and Spirobifluorene Diamine*. Macromolecules, 2005. **38**(19): p. 7950-7956.
71. Hsiao, S.-H., Yang, C.-P., and Yang, C.-Y., *Synthesis and properties of polyimides, polyamides and poly(amide-imide)s from ether diamine having the spirobichroman structure*. Journal of Polymer Science Part A: Polymer Chemistry, 1997. **35**(8): p. 1487-1497.
72. Hsiao, S.-H. and Yang, C.-Y., *Synthesis and evaluation of novel polyimides derived from spirobichroman diether anhydride*. Journal of Polymer Science Part A: Polymer Chemistry, 1997. **35**(13): p. 2801-2809.

73. Han, F., Ding, M., and Gao, L., *Polyimides from 3,3'-dioxo-[1,1']-spirodiphtalan-5,5',6,6'-tetracarboxylic dianhydride* This project was supported by the National Natural Science Foundation of China. *Polymer*, 1999. **40**(13): p. 3809-3813.
74. Liaw, D.-J., Chang, F.-C., Leung, M.-k., Chou, M.-Y., and Muellen, K., *High Thermal Stability and Rigid Rod of Novel Organosoluble Polyimides and Polyamides Based on Bulky and Noncoplanar Naphthalene-Biphenyldiamine*. *Macromolecules*, 2005. **38**(9): p. 4024-4029.
75. Hergenrother, P.M., Watson, K.A., Smith, J.G., Connell, J.W., and Yokota, R., *Polyimides from 2,3,3',4'-biphenyltetracarboxylic dianhydride and aromatic diamines*. *Polymer*, 2002. **43**(19): p. 5077-5093.
76. Lan, Z., Li, C., Yu, Y., and Wei, J., *Colorless Semi-Alicyclic Copolyimides with High Thermal Stability and Solubility*. *Polymers (Basel)*, 2019. **11**(8).
77. Calle, M., García, C., Lozano, A.E., de la Campa, J.G., de Abajo, J., and Álvarez, C., *Local chain mobility dependence on molecular structure in polyimides with bulky side groups: Correlation with gas separation properties*. *Journal of Membrane Science*, 2013. **434**: p. 121-129.
78. Baker, R.W., *Membrane Technology and Application*, 2011, Wiley.
79. Strathmann, H., *Asymmetric polyimide membranes for filtration of non-aqueous solutions*. *Desalination*, 1978. **26**(1): p. 85-92.
80. Favvas, E.P., Katsaros, F.K., Papageorgiou, S.K., Sapalidis, A.A., and Mitropoulos, A.C., *A review of the latest development of polyimide based membranes for CO<sub>2</sub> separations*. *Reactive and Functional Polymers*, 2017. **120**: p. 104-130.
81. Bos, A., Pünt, I.G.M., Wessling, M., and Strathmann, H., *CO<sub>2</sub>-induced plasticization phenomena in glassy polymers*. *Journal of Membrane Science*, 1999. **155**(1): p. 67-78.
82. Krol, J.J., Boerrigter, M., and Koops, G.H., *Polyimide hollow fiber gas separation membranes: preparation and the suppression of plasticization in propane/propylene environments*. *Journal of Membrane Science*, 2001. **184**(2): p. 275-286.
83. Lee, J.S., Madden, W., and Koros, W.J., *Anti-plasticization and plasticization of Matrimid® asymmetric hollow fiber membranes – Part A. Experimental*. *Journal of Membrane Science*, 2010. **350**(1-2): p. 232-241.
84. Zhou, C., *The accelerated CO<sub>2</sub> plasticization of ultra-thin polyimide films and the effect of surface chemical cross-linking on plasticization and physical aging*. *Journal of Membrane Science*, 2003. **225**(1-2): p. 125-134.
85. Budd, P., Msayib, K., Tattershall, C., Ghanem, B., Reynolds, K., McKeown, N., and Fritsch, D., *Gas separation membranes from polymers of intrinsic microporosity*. *Journal of Membrane Science*, 2005. **251**(1-2): p. 263-269.
86. Budd, P.M., Elabas, E.S., Ghanem, B.S., Makhseed, S., McKeown, N.B., Msayib, K.J., Tattershall, C.E., and Wang, D., *Solution-Processed, Organophilic Membrane Derived from a Polymer of Intrinsic Microporosity*. *Advanced Materials*, 2004. **16**(5): p. 456-459.
87. Budd, P.M., McKeown, N.B., and Fritsch, D., *Free volume and intrinsic microporosity in polymers*. *Journal of Materials Chemistry*, 2005. **15**(20).
88. Santiago-García, J.L., Álvarez, C., Sánchez, F., and de la Campa, J.G., *Gas transport properties of new aromatic polyimides based on 3,8-diphenylpyrene-1,2,6,7-tetracarboxylic dianhydride*. *Journal of Membrane Science*, 2015. **476**: p. 442-448.
89. Sanaeepur, H., Ebadi Amooghin, A., Bandehali, S., Moghadassi, A., Matsuura, T., and Van der Bruggen, B., *Polyimides in membrane gas separation: Monomer's molecular design and structural engineering*. *Progress in Polymer Science*, 2019. **91**: p. 80-125.

90. Kochi, M., Chen, C., Yokota, R., Hasegawa, M., and Hergenrother, P., *Isomeric Biphenyl Polyimides. (II) Glass Transitions and Secondary Relaxation Processes*. High Performance Polymers, 2005. **17**(3): p. 335-347.
91. Ding, M., *Isomeric polyimides*. Progress in Polymer Science, 2007. **32**(6): p. 623-668.
92. Tanaka, K., Okano, M., Kita, H., Okamoto, K.-i., and Nishi, S., *Effects of Trifluoromethyl Side Groups on Gas Permeability and Permselectivity in Polyimides*. Polymer Journal, 1994. **26**(10): p. 1186-1189.
93. Bera, D., Chatterjee, R., and Banerjee, S., *Aromatic polyamide nonporous membranes for gas separation application*. e-Polymers, 2021. **21**(1): p. 108-130.
94. Bondi, A.A., Wiley, J., and Sons, *Physical Properties of Molecular Crystals, Liquids, and Glasses*. 1968: Wiley.
95. Beckman, E.J., Hoefling, T.A., Van Opstal, L., Koningsveld, R., and Porter, R.S., *Mean field lattice equations of state: VI. Prediction of volume and surface parameters via Bondi's group contribution theory*. Fluid Phase Equilibria, 1994. **99**: p. 121-133.
96. Fried, J.R. and Hu, N., *The molecular basis of CO<sub>2</sub> interaction with polymers containing fluorinated groups: computational chemistry of model compounds and molecular simulation of poly[bis(2,2,2-trifluoroethoxy)phosphazene]*. Polymer, 2003. **44**(15): p. 4363-4372.
97. Song, N., Ma, T., Wang, T., Shi, K., Tian, Y., Yao, H., Zhang, Y., and Guan, S., *Crosslinked microporous polyimides with polar substituent group for efficient CO<sub>2</sub> capture*. Microporous and Mesoporous Materials, 2020. **293**: p. 109809.
98. Basu, S., Khan, A.L., Cano-Odena, A., Liu, C., and Vankelecom, I.F.J., *Membrane-based technologies for biogas separations*. Chemical Society Reviews, 2010. **39**(2): p. 750-768.
99. Wang, H., Wang, M., Liang, X., Yuan, J., Yang, H., Wang, S., Ren, Y., Wu, H., Pan, F., and Jiang, Z., *Organic molecular sieve membranes for chemical separations*. Chemical Society Reviews, 2021. **50**(9): p. 5468-5516.
100. Weiber, E.A., Meis, D., and Jannasch, P., *Anion conducting multiblock poly(arylene ether sulfone)s containing hydrophilic segments densely functionalized with quaternary ammonium groups*. Polymer Chemistry, 2015. **6**(11): p. 1986-1996.
101. An, H., Lee, A.S., Kammakakam, I., Sang Hwang, S., Kim, J.-H., Lee, J.-H., and Suk Lee, J., *Bromination/debromination-induced thermal crosslinking of 6FDA-Durene for aggressive gas separations*. Journal of Membrane Science, 2018. **545**: p. 358-366.
102. Maier, G., Yang, D., and Nuyken, O., *Poly(ether-ketone)s with indan structure elements*. Die Makromolekulare Chemie, 1993. **194**(7): p. 1901-1914.
103. Guzmán-Lucero, D., Palomeque-Santiago, J.F., Camacho-Zúñiga, C., Ruiz-Treviño, F.A., Guzmán, J., Galicia-Aguilar, A., and Aguilar-Lugo, C., *Gas Permeation Properties of Soluble Aromatic Polyimides Based on 4-Fluoro-4,4'-Diaminotriphenylmethane*. Materials (Basel, Switzerland), 2015. **8**(4): p. 1951-1965.
104. Wang, S., Tong, X., Wang, C., Han, X., Jin, S., Wang, D., Yao, J., and Chen, C., *The spirochroman-based polyimides with different side groups: from structure–property relationships to chain packing and gas transport performance*. RSC Advances, 2021. **11**(9): p. 5086-5095.
105. Luo, S., Liu, Q., Zhang, B., Wiegand, J.R., Freeman, B.D., and Guo, R., *Pentiptycene-based polyimides with hierarchically controlled molecular cavity architecture for efficient membrane gas separation*. Journal of Membrane Science, 2015. **480**: p. 20-30.
106. Favvas, E.P., Katsaros, F.K., Papageorgiou, S.K., Sapolidis, A.A., and Mitropoulos, A.C., *A review of the latest development of polyimide based membranes for CO<sub>2</sub> separations*. Reactive and Functional Polymers, 2017. **120**: p. 104-130.

107. Wang, Z., Isfahani, A.P., Wakimoto, K., Shrestha, B.B., Yamaguchi, D., Ghalei, B., and Sivaniah, E., *Tuning the Gas Selectivity of Tröger's Base Polyimide Membranes by Using Carboxylic Acid and Tertiary Base Interactions*. *ChemSusChem*, 2018. **11**(16): p. 2744-2751.
108. Ma, X., Abdulhamid, M.A., and Pinnau, I., *Design and Synthesis of Polyimides Based on Carbocyclic Pseudo-Tröger's Base-Derived Dianhydrides for Membrane Gas Separation Applications*. *Macromolecules*, 2017. **50**(15): p. 5850-5857.
109. Abdulhamid, M.A., Ma, X., Miao, X., and Pinnau, I., *Synthesis and characterization of a microporous 6FDA-polyimide made from a novel carbocyclic pseudo Tröger's base diamine: Effect of bicyclic bridge on gas transport properties*. *Polymer*, 2017. **130**: p. 182-190.
110. Vanherck, K., Koeckelberghs, G., and Vankelecom, I.F.J., *Crosslinking polyimides for membrane applications: A review*. *Progress in Polymer Science*, 2013. **38**(6): p. 874-896.
111. Balçık, M., Velioğlu, S., Tantekin-Ersolmaz, S.B., and Ahunbay, M.G., *Can crosslinking improve both CO<sub>2</sub> permeability and plasticization resistance in 6FDA-pBAPS/DABA copolyimides?* *Polymer*, 2020. **205**: p. 122789.
112. Wind, J.D., Staudt-Bickel, C., Paul, D.R., and Koros, W.J., *The Effects of Crosslinking Chemistry on CO<sub>2</sub> Plasticization of Polyimide Gas Separation Membranes*. *Industrial & Engineering Chemistry Research*, 2002. **41**(24): p. 6139-6148.
113. Bléger, D. and Hecht, S., *Visible-Light-Activated Molecular Switches*. *Angewandte Chemie International Edition*, 2015. **54**(39): p. 11338-11349.
114. Okamoto, S., Sudo, A., and Endo, T., *Molecular design and synthesis of crosslinked polyimides using radical isomerization of vinylcyclopropane with thiols*. *Journal of Applied Polymer Science*, 2021. **138**(22): p. 50529.
115. Zhang, M., Deng, L., Xiang, D., Cao, B., Hosseini, S.S., and Li, P., *Approaches to Suppress CO<sub>2</sub>-Induced Plasticization of Polyimide Membranes in Gas Separation Applications*. *Processes*, 2019. **7**(1): p. 51.
116. Jin, P., Cao, F., and Luo, Q., *Multi-responsive diarylethene-phenolphthalein hybrids by multiple stimuli*. *Tetrahedron*, 2016. **72**(35): p. 5488-5494.
117. Zhang, C., Cao, B., and Li, P., *Thermal oxidative crosslinking of phenolphthalein-based cardo polyimides with enhanced gas permeability and selectivity*. *Journal of Membrane Science*, 2018. **546**: p. 90-99.
118. Qiu, W., Chen, C.-C., Xu, L., Cui, L., Paul, D.R., and Koros, W.J., *Sub-Tg Cross-Linking of a Polyimide Membrane for Enhanced CO<sub>2</sub> Plasticization Resistance for Natural Gas Separation*. *Macromolecules*, 2011. **44**(15): p. 6046-6056.
119. Wind, J.D., Paul, D.R., and Koros, W.J., *Natural gas permeation in polyimide membranes*. *Journal of Membrane Science*, 2004. **228**(2): p. 227-236.
120. Rezac, M.E., Todd Sorensen, E., and Beckham, H.W., *Transport properties of crosslinkable polyimide blends*. *Journal of Membrane Science*, 1997. **136**(1): p. 249-259.
121. Eguchi, H., Kim, D.J., and Koros, W.J., *Chemically cross-linkable polyimide membranes for improved transport plasticization resistance for natural gas separation*. *Polymer*, 2015. **58**: p. 121-129.
122. Staudt-Bickel, C. and J. Koros, W., *Improvement of CO<sub>2</sub>/CH<sub>4</sub> separation characteristics of polyimides by chemical crosslinking*. *Journal of Membrane Science*, 1999. **155**(1): p. 145-154.
123. Shao, L., Liu, L., Cheng, S.-X., Huang, Y.-D., and Ma, J., *Comparison of diamino cross-linking in different polyimide solutions and membranes by precipitation observation and gas transport*. *Journal of Membrane Science*, 2008. **312**(1): p. 174-185.

124. Tullos, G. and Mathias, L., *Unexpected thermal conversion of hydroxy-containing polyimides to polybenzoxazoles*. *Polymer*, 1999. **40**(12): p. 3463-3468.
125. Tullos, G.L., Powers, J.M., Jeskey, S.J., and Mathias, L.J., *Thermal Conversion of Hydroxy-Containing Imides to Benzoxazoles: Polymer and Model Compound Study*. *Macromolecules*, 1999. **32**(11): p. 3598-3612.
126. Park, H.B., Jung, C.H., Lee, Y.M., Hill, A.J., Pas, S.J., Mudie, S.T., Van Wagner, E., Freeman, B.D., and Cookson, D.J., *Polymers with Cavities Tuned for Fast Selective Transport of Small Molecules and Ions*. *Science*, 2007. **318**(5848): p. 254-258.
127. Park, H.B., Han, S.H., Jung, C.H., Lee, Y.M., and Hill, A.J., *Thermally rearranged (TR) polymer membranes for CO<sub>2</sub> separation*. *Journal of Membrane Science*, 2010. **359**(1): p. 11-24.
128. Kostina, J., Rusakova, O., Bondarenko, G., Alentiev, A., Meleshko, T., Kukarkina, N., Yakimanskii, A., and Yampolskii, Y., *Thermal Rearrangement of Functionalized Polyimides: IR-Spectral, Quantum Chemical Studies, and Gas Permeability of TR Polymers*. *Industrial & Engineering Chemistry Research*, 2013. **52**(31): p. 10476-10483.
129. Hodgkin, J.H., Liu, M.S., Dao, B.N., Mardel, J., and Hill, A.J., *Reaction mechanism and products of the thermal conversion of hydroxy-containing polyimides*. *European Polymer Journal*, 2011. **47**(3): p. 394-400.
130. Hodgkin, J.H. and Dao, B.N., *Thermal conversion of hydroxy-containing polyimides to polybenzoxazoles. Does this reaction really occur?* *European Polymer Journal*, 2009. **45**(11): p. 3081-3092.
131. Schab-Balcerzak, E., Jikei, M., and Kakimoto, M.-a., *Thermal Rearrangement of Poly(o-hydroxyimide)s Synthesized from 4,6-Diaminoresorcinol Dihydrochloride*. *Polymer Journal*, 2003. **35**(2): p. 208-212.
132. Comesaña-Gándara, B., de la Campa, J.G., Hernández, A., Jo, H.J., Lee, Y.M., de Abajo, J., and Lozano, A.E., *Gas separation membranes made through thermal rearrangement of ortho-methoxypolyimides*. *RSC Advances*, 2015. **5**(124): p. 102261-102276.
133. Smith, Z.P., Czenkusch, K., Wi, S., Gleason, K.L., Hernández, G., Doherty, C.M., Konstas, K., Bastow, T.J., Álvarez, C., Hill, A.J., Lozano, A.E., Paul, D.R., and Freeman, B.D., *Investigation of the chemical and morphological structure of thermally rearranged polymers*. *Polymer*, 2014. **55**(26): p. 6649-6657.
134. Ba, C. and Economy, J., *Preparation of PMDA/ODA polyimide membrane for use as substrate in a thermally stable composite reverse osmosis membrane*. *Journal of Membrane Science*, 2010. **363**(1): p. 140-148.
135. Liu, F., Wang, L., Li, D., Liu, Q., and Deng, B., *A review: the effect of the microporous support during interfacial polymerization on the morphology and performances of a thin film composite membrane for liquid purification*. *RSC Advances*, 2019. **9**(61): p. 35417-35428.
136. Weigelt, F., Escorihuela, S., Descalzo, A., Tena, A., Escolástico, S., Shishatskiy, S., Serra, J.M., and Brinkmann, T., *Novel Polymeric Thin-Film Composite Membranes for High-Temperature Gas Separations*. *Membranes*, 2019. **9**(4): p. 51.
137. Karami, P., Khorshidi, B., McGregor, M., Peichel, J.T., Soares, J.B.P., and Sadrzadeh, M., *Thermally stable thin film composite polymeric membranes for water treatment: A review*. *Journal of Cleaner Production*, 2020. **250**: p. 119447.
138. Guo, R., Sanders, D.F., Smith, Z.P., Freeman, B.D., Paul, D.R., and McGrath, J.E., *Synthesis and characterization of thermally rearranged (TR) polymers: effect of glass*



- transition temperature of aromatic poly(hydroxyimide) precursors on TR process and gas permeation properties.* Journal of Materials Chemistry A, 2013. **1**(19): p. 6063-6072.
139. Calle, M., Chan, Y., Jo, H.J., and Lee, Y.M., *The relationship between the chemical structure and thermal conversion temperatures of thermally rearranged (TR) polymers.* Polymer, 2012. **53**(13): p. 2783-2791.
  140. Han, S.H., Misdan, N., Kim, S., Doherty, C.M., Hill, A.J., and Lee, Y.M., *Thermally Rearranged (TR) Polybenzoxazole: Effects of Diverse Imidization Routes on Physical Properties and Gas Transport Behaviors.* Macromolecules, 2010. **43**(18): p. 7657-7667.
  141. Sanders, D.F., Guo, R., Smith, Z.P., Stevens, K.A., Liu, Q., McGrath, J.E., Paul, D.R., and Freeman, B.D., *Influence of polyimide precursor synthesis route and ortho-position functional group on thermally rearranged (TR) polymer properties: Pure gas permeability and selectivity.* Journal of Membrane Science, 2014. **463**: p. 73-81.
  142. Comesaña-Gándara, B., Hernández, A., de la Campa, J.G., de Abajo, J., Lozano, A.E., and Lee, Y.M., *Thermally rearranged polybenzoxazoles and poly(benzoxazole-co-imide)s from ortho-hydroxyamine monomers for high performance gas separation membranes.* Journal of Membrane Science, 2015. **493**: p. 329-339.
  143. Deng, L., Xue, Y., Yan, J., Lau, C.H., Cao, B., and Li, P., *Oxidative crosslinking of copolyimides at sub-T<sub>g</sub> temperatures to enhance resistance against CO<sub>2</sub>-induced plasticization.* Journal of Membrane Science, 2019. **583**: p. 40-48.
  144. Calle, M., Doherty, C.M., Hill, A.J., and Lee, Y.M., *Cross-Linked Thermally Rearranged Poly(benzoxazole-co-imide) Membranes for Gas Separation.* Macromolecules, 2013. **46**(20): p. 8179-8189.
  145. Calle, M., Jo, H.J., Doherty, C.M., Hill, A.J., and Lee, Y.M., *Cross-Linked Thermally Rearranged Poly(benzoxazole-co-imide) Membranes Prepared from ortho-Hydroxycopolyimides Containing Pendant Carboxyl Groups and Gas Separation Properties.* Macromolecules, 2015. **48**(8): p. 2603-2613.
  146. Ma, C. and Koros, W.J., *High-performance ester-crosslinked hollow fiber membranes for natural gas separations.* Journal of Membrane Science, 2013. **428**: p. 251-259.
  147. Lambert, J.B. and Marsmann, H., *Spektroskopie: Strukturaufklärung in der Organischen Chemie.* 2012: Pearson, Higher Education.
  148. Do, Y.S., Lee, W.H., Seong, J.G., Kim, J.S., Wang, H.H., Doherty, C.M., Hill, A.J., and Lee, Y.M., *Thermally rearranged (TR) bismaleimide-based network polymers for gas separation membranes.* Chemical Communications, 2016. **52**(93): p. 13556-13559.
  149. Wang, M., Zhao, J., Wang, X., Liu, A., and Gleason, K.K., *Recent progress on submicron gas-selective polymeric membranes.* Journal of Materials Chemistry A, 2017. **5**(19): p. 8860-8886.
  150. Wang, Y., Ma, X., Ghanem, B.S., Alghunaimi, F., Pinnau, I., and Han, Y., *Polymers of intrinsic microporosity for energy-intensive membrane-based gas separations.* Materials Today Nano, 2018. **3**: p. 69-95.
  151. Corrado, T. and Guo, R., *Macromolecular design strategies toward tailoring free volume in glassy polymers for high performance gas separation membranes.* Molecular Systems Design & Engineering, 2020. **5**(1): p. 22-48.
  152. Lee, W.H., Seong, J.G., Hu, X., and Lee, Y.M., *Recent progress in microporous polymers from thermally rearranged polymers and polymers of intrinsic microporosity for membrane gas separation: Pushing performance limits and revisiting trade-off lines.* Journal of Polymer Science, 2020. **58**(18): p. 2450-2466.

153. Luo, S., Wiegand, J.R., Kazanowska, B., Doherty, C.M., Konstas, K., Hill, A.J., and Guo, R., *Finely Tuning the Free Volume Architecture in Iptycene-Containing Polyimides for Highly Selective and Fast Hydrogen Transport*. *Macromolecules*, 2016. **49**(9): p. 3395-3405.
154. Luo, S., Zhang, Q., Bear, T.K., Curtis, T.E., Roeder, R.K., Doherty, C.M., Hill, A.J., and Guo, R., *Triptycene-containing poly(benzoxazole-co-imide) membranes with enhanced mechanical strength for high-performance gas separation*. *Journal of Membrane Science*, 2018. **551**: p. 305-314.
155. Alghunaimi, F., Ghanem, B., Wang, Y., Salinas, O., Alaslai, N., and Pinnau, I., *Synthesis and gas permeation properties of a novel thermally-rearranged polybenzoxazole made from an intrinsically microporous hydroxyl-functionalized triptycene-based polyimide precursor*. *Polymer*, 2017. **121**: p. 9-16.
156. Luo, S., Liu, J., Lin, H., Kazanowska, B.A., Hunckler, M.D., Roeder, R.K., and Guo, R., *Preparation and gas transport properties of triptycene-containing polybenzoxazole (PBO)-based polymers derived from thermal rearrangement (TR) and thermal cyclodehydration (TC) processes*. *Journal of Materials Chemistry A*, 2016. **4**(43): p. 17050-17062.
157. Luo, S., Zhang, Q., Zhu, L., Lin, H., Kazanowska, B.A., Doherty, C.M., Hill, A.J., Gao, P., and Guo, R., *Highly Selective and Permeable Microporous Polymer Membranes for Hydrogen Purification and CO<sub>2</sub> Removal from Natural Gas*. *Chemistry of Materials*, 2018. **30**(15): p. 5322-5332.
158. Yerzhankyzy, A., Ghanem, B.S., Wang, Y., Alaslai, N., and Pinnau, I., *Gas separation performance and mechanical properties of thermally-rearranged polybenzoxazoles derived from an intrinsically microporous dihydroxyl-functionalized triptycene diamine-based polyimide*. *Journal of Membrane Science*, 2020. **595**: p. 117512.
159. Yeong, Y.F., Wang, H., Pallathadka Pramoda, K., and Chung, T.-S., *Thermal induced structural rearrangement of cardo-copolybenzoxazole membranes for enhanced gas transport properties*. *Journal of Membrane Science*, 2012. **397-398**: p. 51-65.
160. Budd, P.M. and McKeown, N.B., *Highly permeable polymers for gas separation membranes*. *Polymer Chemistry*, 2010. **1**(1).
161. Shamsipur, H., Dawood, B.A., Budd, P.M., Bernardo, P., Clarizia, G., and Jansen, J.C., *Thermally Rearrangeable PIM-Polyimides for Gas Separation Membranes*. *Macromolecules*, 2014. **47**(16): p. 5595-5606.
162. Li, S., Jo, H.J., Han, S.H., Park, C.H., Kim, S., Budd, P.M., and Lee, Y.M., *Mechanically robust thermally rearranged (TR) polymer membranes with spirobisindane for gas separation*. *Journal of Membrane Science*, 2013. **434**: p. 137-147.
163. Meckler, S.M., Bachman, J.E., Robertson, B.P., Zhu, C., Long, J.R., and Helms, B.A., *Thermally Rearranged Polymer Membranes Containing Tröger's Base Units Have Exceptional Performance for Air Separations*. *Angewandte Chemie International Edition*, 2018. **57**(18): p. 4912-4916.
164. Han, S.H., Lee, J.E., Lee, K.-J., Park, H.B., and Lee, Y.M., *Highly gas permeable and microporous polybenzimidazole membrane by thermal rearrangement*. *Journal of Membrane Science*, 2010. **357**(1): p. 143-151.
165. Gelb, L.D., *Modeling Amorphous Porous Materials and Confined Fluids*. *MRS Bulletin*, 2009. **34**(8): p. 592-601.
166. Thomson, K.T. and Gubbins, K.E., *Modeling Structural Morphology of Microporous Carbons by Reverse Monte Carlo*. *Langmuir*, 2000. **16**(13): p. 5761-5773.

167. McGreevy, R.L., *Reverse Monte Carlo modelling*. Journal of Physics: Condensed Matter, 2001. **13**(46): p. R877-R913.
168. Theodorou, D.N. and Suter, U.W., *Atomistic modeling of mechanical properties of polymeric glasses*. Macromolecules, 1986. **19**(1): p. 139-154.
169. Theodorou, D.N. and Suter, U.W., *Detailed molecular structure of a vinyl polymer glass*. Macromolecules, 1985. **18**(7): p. 1467-1478.
170. Flory, P.J., *Foundations of Rotational Isomeric State Theory and General Methods for Generating Configurational Averages*. Macromolecules, 1974. **7**(3): p. 381-392.
171. Theodorou, D.N., *Principles of Molecular Simulation of Gas Transport in Polymers*, in *Materials Science of Membranes for Gas and Vapor Separation*. 2006. p. 49-94.
172. Fried, J.R., *Molecular Simulation of Gas and Vapor Transport in Highly Permeable Polymers*, in *Materials Science of Membranes for Gas and Vapor Separation*. 2006. p. 95-136.
173. Theodorou, D.N., *Hierarchical modelling of polymeric materials*. Chemical Engineering Science, 2007. **62**(21): p. 5697-5714.
174. Fortunato, M.E. and Colina, C.M., *pysimm: A python package for simulation of molecular systems*. SoftwareX, 2017. **6**: p. 7-12.
175. Consta, S., Wilding, N.B., Frenkel, D., and Alexandrowicz, Z., *Recoil growth: An efficient simulation method for multi-polymer systems*. The Journal of Chemical Physics, 1999. **110**(6): p. 3220-3228.
176. Sadanobu, J. and III, W.A.G., *The continuous configurational Boltzmann biased direct Monte Carlo method for free energy properties of polymer chains*. The Journal of Chemical Physics, 1997. **106**(16): p. 6722-6729.
177. Hofmann, D., Fritz, L., Ulbrich, J., Schepers, C., and Böhning, M., *Detailed-atomistic molecular modeling of small molecule diffusion and solution processes in polymeric membrane materials*. Macromolecular Theory and Simulations, 2000. **9**(6): p. 293-327.
178. Hofmann, D., Heuchel, M., Yampolskii, Y., Khotimskii, V., and Shantarovich, V., *Free Volume Distributions in Ultrahigh and Lower Free Volume Polymers: Comparison between Molecular Modeling and Positron Lifetime Studies*. Macromolecules, 2002. **35**(6): p. 2129-2140.
179. Heuchel, M., Hofmann, D., and Pullumbi, P., *Molecular Modeling of Small-Molecule Permeation in Polyimides and Its Correlation to Free-Volume Distributions*. Macromolecules, 2004. **37**(1): p. 201-214.
180. Heuchel, M., Böhning, M., Hölck, O., Siegert, M.R., and Hofmann, D., *Atomistic packing models for experimentally investigated swelling states induced by CO<sub>2</sub> in glassy polysulfone and poly(ether sulfone)*. Journal of Polymer Science Part B: Polymer Physics, 2006. **44**(13): p. 1874-1897.
181. Radue, M.S., Varshney, V., Baur, J.W., Roy, A.K., and Odegard, G.M., *Molecular Modeling of Cross-Linked Polymers with Complex Cure Pathways: A Case Study of Bismaleimide Resins*. Macromolecules, 2018. **51**(5): p. 1830-1840.
182. Larsen, G.S., Lin, P., Hart, K.E., and Colina, C.M., *Molecular Simulations of PIM-1-like Polymers of Intrinsic Microporosity*. Macromolecules, 2011. **44**(17): p. 6944-6951.
183. Hart, K.E., Abbott, L.J., and Colina, C.M., *Analysis of force fields and BET theory for polymers of intrinsic microporosity*. Molecular Simulation, 2013. **39**(5): p. 397-404.
184. Larsen, G.S., Hart, K.E., and Colina, C.M., *Predictive simulations of the structural and adsorptive properties for PIM-1 variations*. Molecular Simulation, 2014. **40**(7-9): p. 599-609.

185. Hart, K.E., Abbott, L.J., McKeown, N.B., and Colina, C.M., *Toward Effective CO<sub>2</sub>/CH<sub>4</sub> Separations by Sulfur-Containing PIMs via Predictive Molecular Simulations*. *Macromolecules*, 2013. **46**(13): p. 5371-5380.
186. Abbott, L.J. and Colina, C.M., *Porosity and Ring Formation in Conjugated Microporous Polymers*. *Journal of Chemical & Engineering Data*, 2014. **59**(10): p. 3177-3182.
187. Kupgan, G., Abbott, L.J., Hart, K.E., and Colina, C.M., *Modeling Amorphous Microporous Polymers for CO<sub>2</sub> Capture and Separations*. *Chem Rev*, 2018. **118**(11): p. 5488-5538.
188. Karayiannis, N.C., Mavrantzas, V.G., and Theodorou, D.N., *Detailed Atomistic Simulation of the Segmental Dynamics and Barrier Properties of Amorphous Poly(ethylene terephthalate) and Poly(ethylene isophthalate)*. *Macromolecules*, 2004. **37**(8): p. 2978-2995.
189. Heuchel, M., Fritsch, D., Budd, P.M., McKeown, N.B., and Hofmann, D., *Atomistic packing model and free volume distribution of a polymer with intrinsic microporosity (PIM-1)*. *Journal of Membrane Science*, 2008. **318**(1): p. 84-99.
190. Park, C.H., Tocci, E., Kim, S., Kumar, A., Lee, Y.M., and Drioli, E., *A Simulation Study on OH-Containing Polyimide (HPI) and Thermally Rearranged Polybenzoxazoles (TR-PBO): Relationship between Gas Transport Properties and Free Volume Morphology*. *The Journal of Physical Chemistry B*, 2014. **118**(10): p. 2746-2757.
191. Fang, W., Zhang, L., and Jiang, J., *Gas Permeation and Separation in Functionalized Polymers of Intrinsic Microporosity: A Combination of Molecular Simulations and Ab Initio Calculations*. *The Journal of Physical Chemistry C*, 2011. **115**(29): p. 14123-14130.
192. Carta, M., Malpass-Evans, R., Croad, M., Rogan, Y., Jansen, J.C., Bernardo, P., Bazzarelli, F., and McKeown, N.B., *An efficient polymer molecular sieve for membrane gas separations*. *Science*, 2013. **339**(6117): p. 303-7.
193. Park, C.H., Tocci, E., Lee, Y.M., and Drioli, E., *Thermal Treatment Effect on the Structure and Property Change between Hydroxy-Containing Polyimides (HPIs) and Thermally Rearranged Polybenzoxazole (TR-PBO)*. *The Journal of Physical Chemistry B*, 2012. **116**(42): p. 12864-12877.
194. Vogel, P. and Houk, K.N., *Organic Chemistry: Theory, Reactivity and Mechanisms in Modern Synthesis*. 2019: Wiley.
195. Clayden, J., Greeves, N., and Warren, S., *Organic Chemistry*. 2012: OUP Oxford.
196. IUPAC, *Compendium of Chemical Terminology, 2nd ed. (the "Gold Book")*. Compiled by A. D. McNaught and A. Wilkinson. . Blackwell Scientific Publications, Oxford (1997). Online version (2019-) created by S. J. Chalk. ISBN 0-9678550-9-8. <https://doi.org/10.1351/goldbook>.
197. Muller, P., *Glossary of terms used in physical organic chemistry (IUPAC Recommendations 1994)*. *Pure and Applied Chemistry*, 1994. **66**(5): p. 1077-1184.
198. Carey, F.A. and Sundberg, R.J., *Advanced Organic Chemistry: Part A: Structure and Mechanisms*. 2007: Springer US.
199. Woodward, R.B. and Hoffmann, R., *Stereochemistry of Electrocyclic Reactions*. *Journal of the American Chemical Society*, 1965. **87**(2): p. 395-397.
200. Woodward, R.B. and Hoffmann, R., *The Conservation of Orbital Symmetry*. *Angewandte Chemie International Edition in English*, 1969. **8**(11): p. 781-853.
201. Hiersemann, M., and Nubbemeyer, U., *The Claisen Rearrangement: Methods and Applications*, 2007, Wiley.

202. Nicolaou, K.C., Snyder, S.A., Montagnon, T., and Vassilikogiannakis, G., *The Diels–Alder Reaction in Total Synthesis*. Angewandte Chemie International Edition, 2002. **41**(10): p. 1668-1698.
203. Martín Castro, A.M., *Claisen Rearrangement over the Past Nine Decades*. Chemical Reviews, 2004. **104**(6): p. 2939-3002.
204. Claisen, L., *Über Umlagerung von Phenol-allyläthern in C-Allyl-phenole*. Berichte der deutschen chemischen Gesellschaft, 1912. **45**(3): p. 3157-3166.
205. Takahashi, K., Mikami, K., and Nakai, T., *Sequential claisen-ene approach to carbocyclization: A new entry to a steroid c/d ring synthon*. Tetrahedron Letters, 1988. **29**(41): p. 5277-5280.
206. Schobert, R. and Gordon, G.J., *Bioactive Heterocycles from Domino Wittig-Pericyclic Reactions*. Current Organic Chemistry, 2002. **6**(13): p. 1181-1196.
207. Lauer, W.M., Doldouras, G.A., Hileman, R.E., and Liepins, R., *The Abnormal Claisen Rearrangement of Crotyl p-Carboethoxyphenyl Ether*. The Journal of Organic Chemistry, 1961. **26**(12): p. 4785-4790.
208. White, W.N., and Norcross, B.E., *The ortho-Claisen Rearrangement. III. The Rearrangement of  $\beta$ -Alkylallyl Aryl Ethers*, Journal of the American Chemical Society, 1961, **83**(15): p. 3265-3269.
209. White, W.N., and Norcross, B.E., *The ortho-Claisen Rearrangement. II. The Rearrangement of cis- and trans- $\gamma$ -Substituted Allyl Aryl Ethers*, Journal of the American Chemical Society, 1961, **83**(8): p. 1968-1974.
210. White, W.N., Gwynn, D., Schlitt, R., Girard, C., and Fife, W., *The ortho-Claisen Rearrangement. I. The Rearrangement of Substituents on the Rearrangement of Allyl p-X-Phenyl Ethers*, Journal of the American Chemical Society, 1958, **83**(13): p. 3271-3277.
211. Jefferson, A. and Scheinmann, F., *Molecular rearrangements related to the Claisen rearrangement*. Quarterly Reviews, Chemical Society, 1968. **22**(3): p. 391-421.
212. Meyer, M.P., DelMonte, A.J., and Singleton, D.A., *Reinvestigation of the Isotope Effects for the Claisen and Aromatic Claisen Rearrangements: The Nature of the Claisen Transition States*. Journal of the American Chemical Society, 1999. **121**(47): p. 10865-10874.
213. Burrows, C.J. and Carpenter, B.K., *Substituent effects on the aliphatic Claisen rearrangement. 1. Synthesis and rearrangement of cyano-substituted allyl vinyl ethers*. Journal of the American Chemical Society, 1981. **103**(23): p. 6983-6984.
214. Goering, H.L., and Jacobson, R.R., *A Kinetic Study of the ortho-Claisen Rearrangement*, Journal of the American Chemical Society, 1958, **80**(13): p. 3277-3285.
215. Iwakura, I., Kaneko, Y., Hayashi, S., Yabushita, A., and Kobayashi, T., *The reaction mechanism of Claisen rearrangement obtained by transition state spectroscopy and single direct-dynamics trajectory*. Molecules, 2013. **18**(2): p. 1995-2004.
216. (a) Iwakura, I., Yabushita, A., Liu, J., Okamura, K., Kezuka, S., and Kobayashi, T., *A new reaction mechanism of Claisen rearrangement induced by few-optical-cycle pulses: Demonstration of nonthermal chemistry by femtosecond vibrational spectroscopy*. Pure and Applied Chemistry, 2013. **85**(10): p. 1991-2004. (b) Iwakura, I., Yabushita, A., and Kobayashi, T., *Non-thermal reaction triggered by a stimulated Raman process using 5-fs laser pulses in the electronic ground state: Claisen rearrangement of allyl phenyl ether*. Chemical Physics Letters, 2011. **4-6**: p. 567-571.
217. Srinivasadesikan, V., Dai, J.K., and Lee, S.L., *Quantum mechanistic insights on aryl propargyl ether Claisen rearrangement*. Org Biomol Chem, 2014. **12**(24): p. 4163-71.

218. Conia, J.M., *Syntheses of Cyclopropylcarbonyl Compounds*. Angewandte Chemie International Edition in English, 1968. **7**(8): p. 570-577.
219. Tietze, L.F. and Beifuss, U., *Sequential Transformations in Organic Chemistry: A Synthetic Strategy with a Future*. Angewandte Chemie International Edition in English, 1993. **32**(2): p. 131-163.
220. Pellissier, H., *Asymmetric domino reactions. Part A: Reactions based on the use of chiral auxiliaries*. Tetrahedron, 2006. **62**(8): p. 1619-1665.
221. Curran, D.P. and Chen, M.-H., *Radical-initiated polyolefinic cyclizations in condensed cyclopentanoid synthesis. Total synthesis of (±)-Δ<sup>9</sup>(12)-capnellene*. Tetrahedron Letters, 1985. **26**(41): p. 4991-4994.
222. Nicolaou, K.C., Edmonds, D.J., and Bulger, P.G., *Cascade Reactions in Total Synthesis*. Angewandte Chemie International Edition, 2006. **45**(43): p. 7134-7186.
223. Nicolaou, K.C., Petasis, N.A., Uenishi, J., and Zipkin, R.E., *The endiandric acid cascade. Electrocyclizations in organic synthesis. 2. Stepwise, stereocontrolled total synthesis of endiandric acids C-G*. Journal of the American Chemical Society, 1982. **104**(20): p. 5557-5558.
224. Trost, B., *The atom economy—a search for synthetic efficiency*. Science, 1991. **254**(5037): p. 1471-1477.
225. Jefferson, A., and Scheinmann, F., *Molecular rearrangement related to the Claisen rearrangement*, Q. Rev. Chem. Soc., 1968, **22**: p. 391-421.
226. Hiratani, K. and Albrecht, M., *The tandem Claisen rearrangement in the construction of building blocks for supramolecular chemistry*. Chemical Society Reviews, 2008. **37**(11): p. 2413-2421.
227. Hiratani, K., Kasuga, K., Goto, M., and Uzawa, H., *Tandem Claisen Rearrangement: A Novel, One-Step Synthesis of Calixarene Analogues from Macrocyclic Polyethers*. Journal of the American Chemical Society, 1997. **119**(51): p. 12677-12678.
228. Song, L., Huang, F., Guo, L., Ouyang, M.A., and Tong, R., *A cascade Claisen rearrangement/o-quinone methide formation/electrocyclization approach to 2H-chromenes*. Chem Commun (Camb), 2017. **53**(44): p. 6021-6024.
229. Wagner-Jauregg, T., *Über addierende Hetero-polymerisation*. Berichte der deutschen chemischen Gesellschaft (A and B Series), 1930. **63**(11): p. 3213-3224.
230. Emmerling, W.N. and Hallensleben, M.L., *Synthese von polyimiden durch thermische Addition von 1,1-Diphenyläthylen mit Bismaleimiden*. European Polymer Journal, 1977. **13**(3): p. 179-184.
231. Huang, H., Wang, W., Zhou, Z., Sun, B., An, M., Haeffner, F., and Niu, J., *Radical Ring-Closing/Ring-Opening Cascade Polymerization*. Journal of the American Chemical Society, 2019. **141**(32): p. 12493-12497.
232. Peterson, G.I. and Choi, T.-L., *Cascade polymerizations: recent developments in the formation of polymer repeat units by cascade reactions*. Chemical Science, 2020. **11**(19): p. 4843-4854.
233. Zhu, N., Chiou, M.-F., Xiong, H., Su, M., Su, M., Li, Y., Wan, W.-M., and Bao, H., *The Introduction of the Radical Cascade Reaction into Polymer Chemistry: A One-Step Strategy for Synchronized Polymerization and Modification*. iScience, 2020. **23**(3): p. 100902.
234. Yang, G., Tokuhisa, H., Koyama, E., Matsuzono, S.-I., and Hiratani, K., *Novel polyureas having isobutenyl bis(aryl ether) moieties in the polymer main chain: Synthesis, tandem Claisen rearrangement, and thermal patterning on polymer film surface using microthermal analyzer*. Journal of Applied Polymer Science, 2002. **84**(12): p. 2287-2293.

235. Agag, T. and Takeichi, T., *Novel Benzoxazine Monomers Containing p-Phenyl Propargyl Ether: Polymerization of Monomers and Properties of Polybenzoxazines*. *Macromolecules*, 2001. **34**(21): p. 7257-7263.
236. Yagci, Y., Kiskan, B., and Ghosh, N.N., *Recent advancement on polybenzoxazine – A newly developed high performance thermoset*. *Journal of Polymer Science Part A: Polymer Chemistry*, 2009. **47**(21): p. 5565-5576.
237. Wang, Y., You, S., Hu, J., and Zhang, K., *Synthesis and Properties of Benzoxazine Monomers Bearing Both 3-Methyltetrahydrophthalimide and Nitrile Groups: Para-Para vs. Ortho-Ortho*. *Macromolecular Research*, 2020. **28**(1): p. 74-81.
238. Zhang, K., Liu, J., and Ishida, H., *An Ultrahigh Performance Cross-Linked Polybenzoxazole via Thermal Conversion from Poly(benzoxazine amic acid) Based on Smart o-Benzoxazine Chemistry*. *Macromolecules*, 2014. **47**(24): p. 8674-8681.
239. Kolb, H.C., Finn, M.G., and Sharpless, K.B., *Click Chemistry: Diverse Chemical Function from a Few Good Reactions*. *Angewandte Chemie International Edition*, 2001. **40**(11): p. 2004-2021.
240. Diels, O. and Alder, K., *Synthesen in der hydroaromatischen Reihe*. *Justus Liebigs Annalen der Chemie*, 1928. **460**(1): p. 98-122.
241. Blackman, M.L., Royzen, M., and Fox, J.M., *Tetrazine Ligation: Fast Bioconjugation Based on Inverse-Electron-Demand Diels–Alder Reactivity*. *Journal of the American Chemical Society*, 2008. **130**(41): p. 13518-13519.
242. *Proceedings of the Chemical Society. October 1961*. *Proceedings of the Chemical Society*, 1961(October): p. 357-396.
243. Lowe, A.B., *Thiol-ene “click” reactions and recent applications in polymer and materials synthesis*. *Polymer Chemistry*, 2010. **1**(1): p. 17-36.
244. Posner, T., *Beiträge zur Kenntniss der ungesättigten Verbindungen. II. Ueber die Addition von Mercaptanen an ungesättigte Kohlenwasserstoffe*. *Berichte der deutschen chemischen Gesellschaft*, 1905. **38**(1): p. 646-657.
245. Slater, M., Snauko, M., Svec, F., and Fréchet, J.M.J., *“Click Chemistry” in the Preparation of Porous Polymer-Based Particulate Stationary Phases for  $\mu$ -HPLC Separation of Peptides and Proteins*. *Analytical Chemistry*, 2006. **78**(14): p. 4969-4975.
246. Neumann, S., Bengtson, G., Meis, D., and Filiz, V., *Thermal Cross Linking of Novel Azide Modified Polymers of Intrinsic Microporosity – Effect of Distribution and the Gas Separation Performance*. *Polymers*, 2019. **11**(8): p. 1241.
247. Liu, Y.-L. and Chuo, T.-W., *Self-healing polymers based on thermally reversible Diels–Alder chemistry*. *Polymer Chemistry*, 2013. **4**(7): p. 2194-2205.
248. Liu, Z.-C., Zuo, B., Lu, H.-F., Wang, M., Huang, S., Chen, X.-M., Lin, B.-P., and Yang, H., *A copper(i)-catalyzed azide–alkyne click chemistry approach towards multifunctional two-way shape-memory actuators*. *Polymer Chemistry*, 2020. **11**(22): p. 3747-3755.
249. Becht, S., Sen, R., Bullmann, S.M., Dreuw, A., and Jaeschke, A., *“Click-Switch” – one-step conversion of organic azides into photochromic diarylethenes for the generation of light-controlled systems*. *Chemical Science*, 2021.
250. Dai, X., Li, P., Sui, Y., and Zhang, C., *Synthesis and performance of flexible epoxy resin with long alkyl side chains via click reaction*. *Journal of Polymer Science*, 2021. **59**(7): p. 627-637.
251. Guaresti, O., García–Astrain, C., Aguirresarobe, R.H., Eceiza, A., and Gabilondo, N., *Synthesis of stimuli–responsive chitosan–based hydrogels by Diels–Alder cross–linking ‘click’*

- reaction as potential carriers for drug administration. *Carbohydrate Polymers*, 2018. **183**: p. 278-286.
252. Sun, H., Kabb, C.P., Sims, M.B., and Sumerlin, B.S., *Architecture-transformable polymers: Reshaping the future of stimuli-responsive polymers*. *Progress in Polymer Science*, 2019. **89**: p. 61-75.
253. Park, H.B., Kamcev, J., Robeson, L.M., Elimelech, M., and Freeman, B.D., *Maximizing the right stuff: The trade-off between membrane permeability and selectivity*. *Science*, 2017. **356**(6343).
254. Lu, Y., Zhang, J., Xiao, G., Li, L., Hou, M., Hu, J., and Wang, T., *Synthesis and gas permeation properties of thermally rearranged poly(ether-benzoxazole)s with low rearrangement temperatures*. *RSC Advances*, 2020. **10**(30): p. 17461-17472.
255. Japip, S., Erifin, S., and Chung, T.-S., *Reduced thermal rearrangement temperature via formation of zeolitic imidazolate framework (ZIF)-8-based nanocomposites for hydrogen purification*. *Separation and Purification Technology*, 2019. **212**: p. 965-973.
256. Tena, A., Rangou, S., Shishatskiy, S., Filiz, V., and Abetz, V., *Claisen thermally rearranged (CTR) polymers*. *Science Advances*, 2016. **2**(7): p. e1501859.
257. Deshlahra, P., Carr, R.T., and Iglesia, E., *Ionic and Covalent Stabilization of Intermediates and Transition States in Catalysis by Solid Acids*. *Journal of the American Chemical Society*, 2014. **136**(43): p. 15229-15247.
258. Gounder, R. and Iglesia, E., *The Roles of Entropy and Enthalpy in Stabilizing Ion-Pairs at Transition States in Zeolite Acid Catalysis*. *Accounts of Chemical Research*, 2012. **45**(2): p. 229-238.
259. Keaveney, S.T., Haines, R.S., and Harper, J.B., *Ionic liquid solvents: the importance of microscopic interactions in predicting organic reaction outcomes*. *Pure and Applied Chemistry*, 2017. **89**(6): p. 745-757.
260. Morita, T., Ladanyi, B.M., and Hynes, J.T., *Polar solvent contributions to activation parameters for model ionic reactions*. *The Journal of Physical Chemistry*, 1989. **93**(4): p. 1386-1392.
261. Calle, M., Lozano, A.E., and Lee, Y.M., *Formation of thermally rearranged (TR) polybenzoxazoles: Effect of synthesis routes and polymer form*. *European Polymer Journal*, 2012. **48**(7): p. 1313-1322.
262. Menczel, J.D. and Prime, R.B., *Thermal Analysis of Polymers: Fundamentals and Applications*. 2014: Wiley.
263. Liu, W. and Xie, W., *Acetate-Functional Thermally Rearranged Polyimides Based on 2,2-Bis(3-amino-4-hydroxyphenyl)hexafluoropropane and Various Dianhydrides for Gas Separations*. *Industrial & Engineering Chemistry Research*, 2014. **53**(2): p. 871-879.
264. Meckler, S.M., Bachman, J.E., Robertson, B.P., Zhu, C., Long, J.R., and Helms, B.A., *Thermally Rearranged Polymer Membranes Containing Troger's Base Units Have Exceptional Performance for Air Separations*. *Angew Chem Int Ed Engl*, 2018. **57**(18): p. 4912-4916.
265. Lei, H., Qi, S., and Wu, D., *Hierarchical multiscale analysis of polyimide films by molecular dynamics simulation: Investigation of thermo-mechanical properties*. *Polymer*, 2019. **179**: p. 121645.
266. Fleming, I., *Molecular Orbitals and Organic Chemical Reactions*. 2011: Wiley.
267. Calle, M. and Lee, Y.M., *Thermally Rearranged (TR) Poly(ether-benzoxazole) Membranes for Gas Separation*. *Macromolecules*, 2011. **44**(5): p. 1156-1165.



268. Meis, D., Tena, A., Neumann, S., Georgopoulos, P., Emmeler, T., Shishatskiy, S., Rangou, S., Filiz, V., and Abetz, V., *Thermal rearrangement of ortho-allyloxypolyimide membranes and the effect of the degree of functionalization*. *Polymer Chemistry*, 2018. **9**(29): p. 3987-3999.
269. Zhang, K., Liu, J., and Ishida, H., *High performance crosslinked polyimide based on main-chain type polybenzoxazine*. *RSC Adv.*, 2014. **4**(107): p. 62550-62556.
270. Zhang, K. and Ishida, H., *Thermally stable polybenzoxazines via ortho-norbornene functional benzoxazine monomers: Unique advantages in monomer synthesis, processing and polymer properties*. *Polymer*, 2015. **66**: p. 240-248.
271. Zhang, K. and Ishida, H., *Smart Synthesis of High-Performance Thermosets Based on ortho-Amide-Imide Functional Benzoxazines*. *Frontiers in Materials*, 2015. **2**.
272. Zhang, K. and Ishida, H., *An anomalous trade-off effect on the properties of smart ortho-functional benzoxazines*. *Polymer Chemistry*, 2015. **6**(13): p. 2541-2550.
273. Reghunadhan Nair, C.P., Krishnan, K., and Ninan, K.N., *Differential scanning calorimetric study on the Claisen rearrangement and thermal polymerisation of diallyl ether of bisphenols*. *Thermochimica Acta*, 2000. **359**(1): p. 61-67.
274. Comer, A.C., *Dynamic Relaxation Properties of aromatic Polyimides and Polymer Nanocomposites*, in *Chemical and Materials Engineering*. 2011, University of Kentucky.
275. Khazaka, R., Locatelli, M.L., Diaham, S., Bidan, P., Dupuy, L., and Grosset, G., *Broadband dielectric spectroscopy of BPDA/ODA polyimide films*. *Journal of Physics D: Applied Physics*, 2013. **46**(6): p. 065501.
276. Comer, A.C., Kalika, D.S., Rowe, B.W., Freeman, B.D., and Paul, D.R., *Dynamic relaxation characteristics of Matrimid® polyimide*. *Polymer*, 2009. **50**(3): p. 891-897.
277. Comer, A.C., Ribeiro, C.P., Freeman, B.D., Kalakkunnath, S., and Kalika, D.S., *Dynamic relaxation characteristics of thermally rearranged aromatic polyimides*. *Polymer*, 2013. **54**(2): p. 891-900.
278. Havriliak, S. and Negami, S., *A complex plane representation of dielectric and mechanical relaxation processes in some polymers*. *Polymer*, 1967. **8**: p. 161-210.
279. Wuts, P.G.M., *Greene's Protective Groups in Organic Synthesis*. 2014: Wiley.
280. Masaji, O., Masaru, O., and Seiichi, T., *The Reactions of cis, trans, trans-1, 5, 9-Cyclododecatriene. IV. Selective Reactions with cis-Addition Reagents*. *Bulletin of the Chemical Society of Japan*, 1966. **39**(2): p. 316-320.
281. Nozaki, H. and Noyori, R., *Preparation of cis-Cyclododecene, Cyclododecyne, and Cyclododecanone*. *The Journal of Organic Chemistry*, 1965. **30**(5): p. 1652-1654.
282. Ohno, M. and Okamoto, M., *Reactions of cis, trans, trans-1,5,9-cyclododecatriene II. A simple preparation of cis-cyclododecene by selective reduction with diimide*. *Tetrahedron Letters*, 1964. **5**(35): p. 2423-2426.
283. Wilke, G., Bogdanovič, B., Borner, P., Breil, H., Hardt, P., Heimbach, P., Herrmann, G., Kaminsky, H.-J., Keim, W., Kröner, M., Müller, H., Müller, E.W., Oberkirch, W., Schneider, J., Stedefeder, J., Tanaka, K., Weyer, K., and Wilke, G., *Cyclooligomerization of Butadiene and Transition Metal  $\pi$ -Complexes*. *Angewandte Chemie International Edition in English*, 1963. **2**(3): p. 105-115.
284. Dolinski, N.D., Page, Z.A., Discekici, E.H., Meis, D., Lee, I.-H., Jones, G.R., Whitfield, R., Pan, X., McCarthy, B.G., Shanmugam, S., Kottisch, V., Fors, B.P., Boyer, C., Miyake, G.M., Matyjaszewski, K., Haddleton, D.M., de Alaniz, J.R., Anastasaki, A., and Hawker, C.J., *What happens in the dark? Assessing the temporal control of photo-*

- mediated controlled radical polymerizations*. Journal of Polymer Science Part A: Polymer Chemistry, 2019. **57**(3): p. 268-273.
285. Ichikawa, H. and Maruoka, K., *Aliphatic and Aromatic Claisen Rearrangement*, in *The Claisen Rearrangement*. 2007. p. 45-116.
286. Li, F.Y., Xiao, Y., Chung, T.-S., and Kawi, S., *High-Performance Thermally Self-Cross-Linked Polymer of Intrinsic Microporosity (PIM-1) Membranes for Energy Development*. Macromolecules, 2012. **45**(3): p. 1427-1437.
287. Zhang, C., Li, P., and Cao, B., *Decarboxylation crosslinking of polyimides with high CO<sub>2</sub>/CH<sub>4</sub> separation performance and plasticization resistance*. Journal of Membrane Science, 2017. **528**: p. 206-216.
288. *IV. Maximizing Transition-State Stability During Ring Formation*. 2021.
289. Hou, G. and Cui, Q., *Stabilization of Different Types of Transition States in a Single Enzyme Active Site: QM/MM Analysis of Enzymes in the Alkaline Phosphatase Superfamily*. Journal of the American Chemical Society, 2013. **135**(28): p. 10457-10469.
290. Acevedo, O. and Armacost, K., *Claisen Rearrangements: Insight into Solvent Effects and "on Water" Reactivity from QM/MM Simulations*. Journal of the American Chemical Society, 2010. **132**(6): p. 1966-1975.
291. Debnath, S. and Mondal, S., *A computational (DFT) study on aza-Claisen rearrangement: Effect of temperature, solvent and substitution on activation barrier*. Computational and Theoretical Chemistry, 2014. **1046**: p. 42-48.
292. Yang, L., Zhao, J., Yang, X., Chen, M., and Xue, Y., *Effects of solvents on the DACBO-catalyzed vinylogous Henry reaction of isatin with 3,5-dimethyl-4-nitroisoxazole "on-water" and in solution from QM/MM MC simulations*. RSC Advances, 2019. **9**(9): p. 4932-4941.
293. Ma, X., Ghanem, B., Salines, O., Litwiller, E., and Pinnau, I., *Synthesis and Effect of Physical Aging on Gas Transport Properties of a Microporous Polyimide Derived from a Novel Spirobifluorene-Based Dianhydride*. ACS Macro Letters, 2015. **4**(2): p. 231-235.
294. Askari, M., Xiao, Y., Li, P., and Chung, T.-S., *Natural gas purification and olefin/paraffin separation using cross-linkable 6FDA-Durene/DABA co-polyimides grafted with  $\alpha$ ,  $\beta$ , and  $\gamma$ -cyclodextrin*. Journal of Membrane Science, 2012. **390-391**: p. 141-151.
295. Thür, R., Lemmens, V., Van Havere, D., van Essen, M., Nijmeijer, K., and Vankelecom, I.F.J., *Tuning 6FDA-DABA membrane performance for CO<sub>2</sub> removal by physical densification and decarboxylation cross-linking during simple thermal treatment*. Journal of Membrane Science, 2020. **610**.
296. BIOVIA, D.S., BIOVIA Materials Studio, 8.0, San Diego: Dassault Systèmes, 2021.
297. Robeson, L.M., Smith, Z.P., Freeman, B.D., and Paul, D.R., *Contributions of diffusion and solubility selectivity to the upper bound analysis for glassy gas separation membranes*. Journal of Membrane Science, 2014. **453**: p. 71-83.
298. Hou, J., Liu, P., Jiang, M., Yu, L., Li, L., and Tang, Z., *Olefin/paraffin separation through membranes: from mechanisms to critical materials*. Journal of Materials Chemistry A, 2019. **7**(41): p. 23489-23511.
299. Miranda, D.M.V., Dutra, L.D.S., Way, D., Amaral, N., Wegenast, F., Scaldaferrri, M.C., Jesus, N., and Pinto, J.C., *A Bibliometric Survey of Paraffin/Olefin Separation Using Membranes*. Membranes (Basel), 2019. **9**(12).
300. Burns, R.L., and Koros, W.J., *Structure-Property Relationships for Poly(pyrrolone-imide) Gas Separation Membranes*, Macromolecules, 2003, **36**(7): p. 2374-2381.

301. Swaidan, R., Ghanem, B., and Pinnau, I., *Fine-Tuned Intrinsically Ultramicroporous Polymers Redefine the Permeability/Selectivity Upper Bounds of Membrane-Based Air and Hydrogen Separations*. ACS Macro Letters, 2015. **4**(9): p. 947-951.
302. Dose, M.E., Chwatko, M., Hubacek, I., Lynd, N.A., Paul, D.R., and Freeman, B.D., *Thermally cross-linked diaminophenylindane (DAPI) containing polyimides for membrane based gas separations*. Polymer, 2019. **161**: p. 16-26.
303. Aguilar-Lugo, C., Álvarez, C., Lee, Y.M., de la Campa, J.G., and Lozano, Á.E., *Thermally Rearranged Polybenzoxazoles Containing Bulky Adamantyl Groups from Ortho-Substituted Precursor Copolyimides*. Macromolecules, 2018. **51**(5): p. 1605-1619.
304. de la Viuda, M.R., Tena, A., Neumann, S., Willruth, S., Filiz, V., and Abetz, V., *Novel functionalized polyamides prone to undergo thermal Claisen rearrangement in the solid state*. Polymer Chemistry, 2018. **9**(29): p. 4007-4016.
305. Fu, S., Sanders, E.S., Kulkarni, S.S., and Koros, W.J., *Carbon molecular sieve membrane structure–property relationships for four novel 6FDA based polyimide precursors*. Journal of Membrane Science, 2015. **487**: p. 60-73.
306. Hazazi, K., Ma, X., Wang, Y., Ogieglo, W., Alhazmi, A., Han, Y., and Pinnau, I., *Ultra-selective carbon molecular sieve membranes for natural gas separations based on a carbon-rich intrinsically microporous polyimide precursor*. Journal of Membrane Science, 2019. **585**: p. 1-9.
307. Karunaweera, C., Musselman, I.H., Balkus, K.J., and Ferraris, J.P., *Fabrication and characterization of aging resistant carbon molecular sieve membranes for C3 separation using high molecular weight crosslinkable polyimide, 6FDA-DABA*. Journal of Membrane Science, 2019. **581**: p. 430-438.
308. Kim, Y.K., Lee, J.M., Park, H.B., and Lee, Y.M., *The gas separation properties of carbon molecular sieve membranes derived from polyimides having carboxylic acid groups*. Journal of Membrane Science, 2004. **235**(1-2): p. 139-146.
309. Kiyono, M., Williams, P.J., and Koros, W.J., *Effect of pyrolysis atmosphere on separation performance of carbon molecular sieve membranes*. Journal of Membrane Science, 2010. **359**(1-2): p. 2-10.
310. Ma, X., Swaidan, R., Teng, B., Tan, H., Salinas, O., Litwiller, E., Han, Y., and Pinnau, I., *Carbon molecular sieve gas separation membranes based on an intrinsically microporous polyimide precursor*. Carbon, 2013. **62**: p. 88-96.
311. Salinas, O., Ma, X., Litwiller, E., and Pinnau, I., *Ethylene/ethane permeation, diffusion and gas sorption properties of carbon molecular sieve membranes derived from the prototype ladder polymer of intrinsic microporosity (PIM-1)*. Journal of Membrane Science, 2016. **504**: p. 133-140.
312. Salinas, O., Ma, X., Litwiller, E., and Pinnau, I., *High-performance carbon molecular sieve membranes for ethylene/ethane separation derived from an intrinsically microporous polyimide*. Journal of Membrane Science, 2016. **500**: p. 115-123.
313. Swaidan, R., Ma, X., Litwiller, E., and Pinnau, I., *High pressure pure- and mixed-gas separation of CO<sub>2</sub>/CH<sub>4</sub> by thermally-rearranged and carbon molecular sieve membranes derived from a polyimide of intrinsic microporosity*. Journal of Membrane Science, 2013. **447**: p. 387-394.
314. Simon, P.F.W. and Fahmi, A., *Polymere - Chemie und Strukturen: Herstellung, Charakterisierung und Werkstoffe*. 2019: Wiley-VCH GmbH.

315. Gong, L., McAllister, M.A., and Tidwell, T.T., *Substituent effects on ketene structure and stability: an ab initio study*. Journal of the American Chemical Society, 1991. **113**(16): p. 6021-6028.
316. Tidwell, T.T., *The First Century of Ketenes (1905–2005): The Birth of a Versatile Family of Reactive Intermediates*. Angewandte Chemie International Edition, 2005. **44**(36): p. 5778-5785.
317. Trost, B.M. and Fullerton, T.J., *New synthetic reactions. Allylic alkylation*. Journal of the American Chemical Society, 1973. **95**(1): p. 292-294.
318. Tsuji, J., Takahashi, H., and Morikawa, M., *Organic syntheses by means of noble metal compounds XVII. Reaction of  $\pi$ -allylpalladium chloride with nucleophiles*. Tetrahedron Letters, 1965. **6**(49): p. 4387-4388.
319. Clair, A.K.S. and Johnston, N.J., *Ether polyphenylquinoxalines. II. Polymer synthesis and properties*. Journal of Polymer Science: Polymer Chemistry Edition, 1977. **15**(12): p. 3009-3021.
320. Greenwood, T.D., Kahley, R.A., Wolfe, J.F., Clair, A.S., and Johnston, N.J., *N-methyl-substituted aromatic polyamides*. Journal of Polymer Science: Polymer Chemistry Edition, 1980. **18**(3): p. 1047-1059.
321. Greenwood, T.D., Armistead, D.M., Wolfe, J.F., Clair, A.K.S., Clair, T.L.S., and Barrick, J.D., *N-Propargyl-substituted aromatic polyamides: preparation and thermal crosslinking*. Polymer, 1982. **23**(4): p. 621-625.
322. Alam, S. and Varma, I.K., *Thermal behaviour of ethynyl and ethenyl terminated imide resins*. Journal of Thermal Analysis and Calorimetry, 1998. **51**(1): p. 275.
323. Park, J.Y. and Paul, D.R., *Correlation and prediction of gas permeability in glassy polymer membrane materials via a modified free volume based group contribution method*. Journal of Membrane Science, 1997. **125**(1): p. 23-39.
324. Shishatskii, A.M., Yampolskii, Y.P., and Peinemann, K.-V., *Effect of film thickness on density and gas permeation parameters of glassy polymers*, Journal of Membrane Science, 1996. **112**: p. 275-285.
325. Gaussian 09, R.A., M. J. Frisch, G. W. Trucks, H. B. Schlegel, G. E. Scuseria, M. A. Robb, J. R. Cheeseman, G. Scalmani, V. Barone, G. A. Petersson, H. Nakatsuji, X. Li, M. Caricato, A. Marenich, J. Bloino, B. G. Janesko, R. Gomperts, B. Mennucci, H. P. Hratchian, J. V. Ortiz, A. F. Izmaylov, J. L. Sonnenberg, D. Williams-Young, F. Ding, F. Lipparini, F. Egidi, J. Goings, B. Peng, A. Petrone, T. Henderson, D. Ranasinghe, V. G. Zakrzewski, J. Gao, N. Rega, G. Zheng, W. Liang, M. Hada, M. Ehara, K. Toyota, R. Fukuda, J. Hasegawa, M. Ishida, T. Nakajima, Y. Honda, O. Kitao, H. Nakai, T. Vreven, K. Throssell, J. A. Montgomery, Jr., J. E. Peralta, F. Ogliaro, M. Bearpark, J. J. Heyd, E. Brothers, K. N. Kudin, V. N. Staroverov, T. Keith, R. Kobayashi, J. Normand, K. Raghavachari, A. Rendell, J. C. Burant, S. S. Iyengar, J. Tomasi, M. Cossi, J. M. Millam, M. Klene, C. Adamo, R. Cammi, J. W. Ochterski, R. L. Martin, K. Morokuma, O. Farkas, J. B. Foresman, and D. J. Fox, Gaussian, Inc., Wallingford CT, 2016.
326. *Nobel Prize for Physics, 1952*. Nature, 1952. **170**(4335): p. 911-912.
327. Moore, J.C., *Gel permeation chromatography. I. A new method for molecular weight distribution of high polymers*. Journal of Polymer Science Part A: General Papers, 1964. **2**(2): p. 835-843.
328. Czichos, H., Saito, T., and Smith, L.E., *Springer Handbook of Materials Measurement Methods*. 2007: Springer Berlin Heidelberg.

329. ASTM E473-21, *Standard Terminology Relating to Thermal Analysis and Rheology*, ASTM International, West Conshohocken, PA, 2021, [cited 2021 14.03.2021]; Available from: [www.astm.org](http://www.astm.org).
330. Wunderlich, B., *Thermal analysis of polymers*. Journal of thermal analysis, 1973. **5**(1): p. 117-136.
331. Watson E.S., O.N.M.J., *Differential microcalorimeter* 1962, Applied Biosystems Inc: United States. p. 10.
332. Toledo, M. *Flash DSC 2+ – Flash Dynamisches Differenzkalorimeter*. 2021; [cited 2021 14.03.2021]; Available from: [https://www.mt.com/de/de/home/products/Laboratory\\_Analytics\\_Browse/TA\\_Family\\_Browse/Flash\\_DSC/FlashDSC2.html#overviewpm](https://www.mt.com/de/de/home/products/Laboratory_Analytics_Browse/TA_Family_Browse/Flash_DSC/FlashDSC2.html#overviewpm).
333. Schawe, J.E.K. and Hütter, T., *TOPEM® - the latest innovation in temperature modulated DSC*. 2004.
334. Jaeger, G., *The Ehrenfest Classification of Phase Transitions: Introduction and Evolution*. Archive for History of Exact Sciences, 1998. **53**(1): p. 51-81.
335. Horie, K., Barón, M., Fox, R.B., He, J., Hess, M., Kahovec, J., Kitayama, T., Kubisa, P., Maréchal, E., Mormann, W., Stepto, R.F.T., Tabak, D., Vohlídal, J., Wilks, E.S., and Work, W.J., *Definitions of terms relating to reactions of polymers and to functional polymeric materials (IUPAC Recommendations 2003)*. Pure and Applied Chemistry, 2004. **76**(4): p. 889-906.
336. Vyazovkin, S. and Sbirrazzuoli, N., *Isoconversional Kinetic Analysis of Thermally Stimulated Processes in Polymers*. Macromolecular Rapid Communications, 2006. **27**(18): p. 1515-1532.
337. Vyazovkin, S., Burnham, A.K., Favergeon, L., Koga, N., Moukhina, E., Pérez-Maqueda, L.A., and Sbirrazzuoli, N., *ICTAC Kinetics Committee recommendations for analysis of multi-step kinetics*. Thermochimica Acta, 2020. **689**: p. 178597.
338. Vyazovkin, S., *Isoconversional Kinetics of Thermally Stimulated Processes*. 2015: Springer International Publishing.
339. Vyazovkin, S., *Kissinger Method in Kinetics of Materials: Things to Beware and Be Aware of*. Molecules, 2020. **25**(12): p. 2813.
340. Toledo, M. *Measuring Density with Laboratory Balance*. 2021 [cited 2021 03.03.2021]; Available from: [https://www.mt.com/de/en/home/applications/Laboratory\\_weighing/density-measurement.html#publications](https://www.mt.com/de/en/home/applications/Laboratory_weighing/density-measurement.html#publications).
341. Britannica, The Editors of Encyclopaedia, *Archimedes' principle*, Encyclopedia Britannica, 29 May. 2020, [cited 2021 03.03.2021]; Available from: <https://www.britannica.com/science/Archimedes-principle>.
342. Daynes, H.A. and Smith, S.W.J., *The process of diffusion through a rubber membrane*. Proceedings of the Royal Society of London. Series A, Containing Papers of a Mathematical and Physical Character, 1920. **97**(685): p. 286-307.
343. Barrer, R.M. and Rideal, E.K., *Permeation, diffusion and solution of gases in organic polymers*. Transactions of the Faraday Society, 1939. **35**(0): p. 628-643.
344. Frisch, H.L., *The Time Lag in Diffusion*. The Journal of Physical Chemistry, 1957. **61**(1): p. 93-95.
345. Mano, E.B. and Durao, L.A., *Review of laboratory methods for the preparation of polymer films*. Journal of Chemical Education, 1973. **50**(3): p. 228.

346. Pye, D.G., Hoehn, H.H., and Panar, M., *Measurement of gas permeability of polymers. I. Permeabilities in constant volume/variable pressure apparatus*. Journal of Applied Polymer Science, 1976. **20**(7): p. 1921-1931.
347. Rutherford, S.W. and Do, D.D., *Review of time lag permeation technique as a method for characterisation of porous media and membranes*. Adsorption, 1997. **3**(4): p. 283-312.
348. *ASTM D1434-82(2015)e1, Standard Test Method for Determining Gas Permeability Characteristics of Plastic Film and Sheeting*, ASTM International, West Conshohocken, PA, 2015, [cited 2021 14.03.2021]; Available from: [www.astm.org](http://www.astm.org).
349. Kremer, F. and Schönhal, A., *Broadband Dielectric Spectroscopy*. 2012: Springer Berlin Heidelberg.
350. Goldbeck, G., and Court, C., *The Economic Impact of Materials Modelling*. 2016, [cited 2021 11.03.2021]; Available from: <https://doi.org/10.5281/zenodo.44780>.
351. Covestro Deutschland AG, *How Quantum Computing can benefit chemistry*. 2020 [cited 15/03/2021]; Available from: <https://www.covestro.com/press/how-quantum-computing-can-benefit-chemistry/>.
352. Deglmann, P., Schäfer, A., and Lennartz, C., *Application of quantum calculations in the chemical industry – An overview*. International Journal of Quantum Chemistry, 2015. **115**(3): p. 107-136.
353. Gartner, T.E. and Jayaraman, A., *Modeling and Simulations of Polymers: A Roadmap*. Macromolecules, 2019. **52**(3): p. 755-786.
354. BASF SE, *Digitalization in research and development*. [cited 2021 14.03.2021]; Available from: [https://www.BASF.com/global/en/who-we-are/innovation/how-we-i/our-RnD/Digitalization\\_in\\_R-D.html](https://www.BASF.com/global/en/who-we-are/innovation/how-we-i/our-RnD/Digitalization_in_R-D.html)
355. Jensen, F., *Introduction to Computational Chemistry*. 2017: Wiley.
356. Lewars, E.G., *Computational Chemistry: Introduction to the Theory and Applications of Molecular and Quantum Mechanics*. 2016: Springer International Publishing.
357. Pariser, R. and Parr, R.G., *A Semi - Empirical Theory of the Electronic Spectra and Electronic Structure of Complex Unsaturated Molecules. I*. The Journal of Chemical Physics, 1953. **21**(3): p. 466-471.
358. Pariser, R. and Parr, R.G., *A Semi - Empirical Theory of the Electronic Spectra and Electronic Structure of Complex Unsaturated Molecules. II*. The Journal of Chemical Physics, 1953. **21**(5): p. 767-776.
359. Senftle, T.P., Hong, S., Islam, M.M., Kylasa, S.B., Zheng, Y., Shin, Y.K., Junkermeier, C., Engel-Herbert, R., Janik, M.J., Aktulga, H.M., Verstraelen, T., Grama, A., and van Duin, A.C.T., *The ReaxFF reactive force-field: development, applications and future directions*. npj Computational Materials, 2016. **2**(1): p. 15011.
360. Warshel, A., *Multiscale Modeling of Biological Functions: From Enzymes to Molecular Machines (Nobel Lecture)*. Angewandte Chemie International Edition, 2014. **53**(38): p. 10020-10031.
361. Hinchliffe, A., *Molecular Modelling for Beginners*. 2011: Wiley.
362. Harvey, J., *Computational Chemistry*. 2018: Oxford University Press.
363. Hohenberg, P. and Kohn, W., *Inhomogeneous Electron Gas*. Physical Review, 1964. **136**(3B): p. B864-B871.
364. Kohn, W. and Sham, L.J., *Self-Consistent Equations Including Exchange and Correlation Effects*. Physical Review, 1965. **140**(4A): p. A1133-A1138.
365. Becke, A.D., *Density-functional exchange-energy approximation with correct asymptotic behavior*. Physical Review A, 1988. **38**(6): p. 3098-3100.

366. Becke, A.D., *Density - functional thermochemistry. III. The role of exact exchange*. The Journal of Chemical Physics, 1993. **98**(7): p. 5648-5652.
367. Lee, C., Yang, W., and Parr, R.G., *Development of the Colle-Salvetti correlation-energy formula into a functional of the electron density*. Physical Review B, 1988. **37**(2): p. 785-789.
368. Perdew, J.P., Burke, K., and Wang, Y., *Generalized gradient approximation for the exchange-correlation hole of a many-electron system*. Physical Review B, 1996. **54**(23): p. 16533-16539.
369. Mayo, S.L., Olafson, B.D., and Goddard, W.A., *DREIDING: a generic force field for molecular simulations*. The Journal of Physical Chemistry, 1990. **94**(26): p. 8897-8909.
370. Weiner, S.J., Kollman, P.A., Case, D.A., Singh, U.C., Ghio, C., Alagona, G., Profeta, S., and Weiner, P., *A new force field for molecular mechanical simulation of nucleic acids and proteins*. Journal of the American Chemical Society, 1984. **106**(3): p. 765-784.
371. Rappe, A.K., Casewit, C.J., Colwell, K.S., Goddard, W.A., and Skiff, W.M., *UFF, a full periodic table force field for molecular mechanics and molecular dynamics simulations*. Journal of the American Chemical Society, 1992. **114**(25): p. 10024-10035.
372. Dauber-Osguthorpe, P., Roberts, V.A., Osguthorpe, D.J., Wolff, J., Genest, M., and Hagler, A.T., *Structure and energetics of ligand binding to proteins: Escherichia coli dihydrofolate reductase-trimethoprim, a drug-receptor system*. Proteins: Structure, Function, and Bioinformatics, 1988. **4**(1): p. 31-47.
373. Sun, H., *COMPASS: An ab Initio Force-Field Optimized for Condensed-Phase Applications Overview with Details on Alkane and Benzene Compounds*. The Journal of Physical Chemistry B, 1998. **102**(38): p. 7338-7364.
374. Sun, H., Ren, P., and Fried, J.R., *The COMPASS force field: parameterization and validation for phosphazenes*. Computational and Theoretical Polymer Science, 1998. **8**(1): p. 229-246.





PART IX

Appendix



*Success depends on how many*

*Experiments you can fit into 24 hours.*

Thomas A. Edison

## Chemicals

Table 14. Used chemicals for the execution of synthetic and analytical experiments of this PhD studies.

Chemical	CAS#	H-Statements	P-Statements	GHS Symbol
1-Iodo-3-methyl butane	541-28-6	226- 302	210- 301+312+330	02, 07
1-Iodopropane*	107-08-4	226- 315- 319- 332- 335- 341- 351- 410	210- 273- 303+361+353- 304+340+312- 305+351+338- 308+313	02, 07, 08, 09
1-Propanol	71-23-8	225- 318- 336	210- 280- 305+351+338- 310	02, 05, 07
2-Iodopropane	107-08-4	226- 315- 319- 332- 335- 341- 351- 410	210- 273- 303+361+353- 304+340+312- 305+351+338- 308+313	02, 07, 08, 09
2-Methyl-3-bromopropene	1458-98-6	225- 302+332- 314- 411	210- 273- 280- 305+351+338	02, 05, 07, 09
2-Propanol	67-63-0	225- 319- 336	210- 233- 240- 241- 242- 305+351+338	02, 07
3,3'-Dihydroxybenzidine*	2373-98-0	315- 319- 373- 351	201- 260- 264- 280- 308+313- 337+313	07, 08
3-Brom-1-propene*	106-95-6	225- 301+331- 314- 340- 350- 400	201- 210- 280- 301+310+330- 303+361+353- 305+351+338+310	02, 05, 06, 08, 09
3-Bromo cyclohexene	1521-51-3	226- 315- 319- 335	210- 302+352- 305+351+338	02, 07
3-Bromo propyne*	106-96-7	225- 301- 304- 314- 335- 336- 361d- 373	201- 210- 280- 301+330+331- 303+361+353- 305+351+338+310	02, 05, 06, 08
3-Iodo-propene	556-56-9	225- 314	210- 280- 301+330+331- 303+361+353- 305+351+338	02, 05
4-Bromo-butene	5162-44-7	225- 317- 319- 334- 335	210- 280- 302+352- 305+351- 338	02, 07, 08
4-Chloro-1-butyne	51908-64-6	301	301+310	06
Acetic acid	64-19-7	226- 314	210- 280- 303+361+353- 305+351+338+310	02, 05

Acetic anhydride	108-24-7	226- 302- 314- 330	210- 280- 301+312+330- 303+361+353- 304+340+310- 305+351+338+310	02, 05, 06
Acetone	67-64-1	225- 319- 336	210- 233- 240- 241- 242- 305+351+338	02, 07
Allyl alcohol	107-18-6	225- 301+311+331- 315- 319- 335- 400	210- 273- 280- 301+310+330- 302+352+312- 304+340+311	02, 05, 09
Allyl methyl carbonate	35466-83-2	226- 315- 319- 335	210- 302+352- 305+351+338	02, 07
Allyl chloroformate	2937-50-0	226- 301- 314- 330	210- 233- 280- 303+361+353- 304+340+310- 305+351+338	02, 05, 06
Argon	7440-37-1	280	410+403	04
Bis(2-methyl-2-propanyl) dicarbonate**	24424-99-5	226- 330- 315- 317- 318- 335	210- 260- 280- 304+340+310- 305+351+338+310- 370+378	02, 05, 06
Butyl chloroformate	592-34-7	226- 314- 331	210- 280- 301+330+331- 303+361+353- 304+340+311- 305+351+338	02, 05, 06
Carbon dioxide	124-38-9	280	410+403	04
Diethyl ether	60-29-7	224- 302- 336- EUH019- EUH066	210- 301+312+330- 403+233	02, 07
Dimethylsulfoxide-d <sub>6</sub>	2206-27-1	Kein gefährlicher Stoff oder gefährliches Gemisch gemäß der Verordnung (EG) Nr. 1272/2008.		
Ethane	74-84-0	220- 280	210- 377- 381- 403	02, 04
Ethanol	64-17-5	225- 319	210- 305+351+338	02, 07
Ethyl chloroformate	541-41-3	225- 301- 314- 330	210- 280- 301+310+330	02, 05, 06
Ethylene	74-85-1	220- 280- 336	210- 410+403	02, 04, 07
Helium	7440-59-7	280	403	04
Hydrazine monohydrate	7803-57-8	226- 301+311- 314- 317- 330- 350- 410	210- 273- 280- 303+361+353- 304+340+310- 305+351+338	02, 05, 06, 08, 09
Hydrogen	1333-74-0	220- 280	210- 377- 381- 410+403	02, 04
Iodoethane*	75-03-6	226- 302- 315- 317- 319- 334- 335- 341	210- 280- 301+312- 303+361+353- 304+340+312- 308+313	02, 07, 08
Iodomethane*	74-88-4	226- 301+331- 312- 315- 319- 335- 351- 410	201- 210- 273- 280- 301+310+330- 302+352+312	02, 06, 08, 09
Isobutanol	78-83-1	226- 315- 318- 335- 336	210- 280- 304+340+312- 305+351+338+310- 403+235	02, 05, 07
Isobutanoyl chloroformate	543-27-1	226- 302- 314- 331	210- 280- 301+330+331- 303+361+353- 304+340+311- 305+351+338	02, 05, 06

Isobutyrylchloride	79-30-1	225- 314	210- 280- 305+351+338- 310	02, 05
Isopropyl chloroformate*	108-23-6	225- 304- 314- 317- 330- 336- 361d- 373- 412	210- 280- 301+310+331- 301+330+331- 303+361+353- 304+340+310- 305+351+338+310	02, 05, 06, 08
Isovaleric anhydride	2082-59-9	314	260- 280- 303+361+353- 305+340+310- 305+351+338	04
Maleic anhydride	108-31-6	302- 314- 317- 334- 372- EUH071	260- 280- 384- 303+361+353- 304+340+310- 305+351+338	04, 06, 07
Methane	74-82-8	220- 280	210- 377- 381- 410+403	02, 04
Methanol	67-56-1	225- 301+311+331- 370	210- 233- 280- 301+310- 303+361+353- 304+340+311	02, 06, 08
Methyl chloroformate	79-22-1	225- 302+312- 314- 330	210- 260- 280- 284- 305+351+338- 310	02, 05, 06
<i>N, N</i> -Dimethylacetamide	127-19-5	312+332- 319- 360D	201- 280- 302+352+312- 304+340+312- 305+351+338- 308+313	07, 08
<i>N, N</i> -Dimethyl aminopyridine	1122-58-3	301- 310- 315- 319- 335	280- 301+310+330- 302+352+310- 304+340+312- 305+351+338- 337+313	06
Nitrogen	7727-37-9	280	410+403	04
<i>N</i> -Methyl-pyrrolidinone	872-50-4	315- 319- 335- 360FD	201- 202- 261- 302+352- 305+351+338- 308+313	07, 08
<i>NN</i> -Dimethylformamide	68-12-2	226- 312- 332- 319- 360D	210- 280- 303+361+353- 304+340+312- 305+351+338- 308+313	02, 06, 07
Oxalyl chloride	79-37-8	225- 260- 314- 331- 335	210- 231+232- 280- 303+361+353- 304+340+310- 305+351+338	02, 05, 06
Oxygen	7782-44-7	270- 280	220- 244- 370+376- 403	03, 04
Palladium dichloride	7647-10-1	290- 302- 317- 318- 410	234- 273- 280- 301+312- 302+352- 305+351+338	05, 07, 09
Phthalic anhydride	85-44-9	302- 315- 317- 318- 334- 335	280- 301+312+330- 302+352- 305+351+338+310	05, 07, 08
Potassium carbonate	548-08-7	315- 319- 335	261- 264- 271- 280- 302+352- 305+351+338	07
Potassium <i>tert</i> -butoxide	865-47-4	225- 319- 332- 335	210- 261- 305+351+338	02, 07
Propane	74-98-6	220- 280	210- 377- 403- 410	02, 04
Propanoyl chloride	79-03-8	225- 302- 314- 331- EUH014	210- 280- 303+361+353- 304+340+310- 305+351+338- 403+233	02, 05, 06
Propargyl chloroformate	35718-08-2	226- 302- 311+331- 314	210- 280- 301+330+331- 303+361+353- 304+340+311- 305+351+338	02, 05, 06

Propyl chloroformate	109-61-5	225- 302- 314- 331	210- 280- 301+330+331- 303+361+353- 304+340+311- 305+351+338	02, 05, 06
Propylene	115-07-1	220- 280	210- 377- 381- 410+403	02, 04
Pyridine	110-86-1	225- 302+312+332- 315- 319	210- 280- 301+312- 303+361+353- 304+340+312- 305+351+338	02, 07
Pyromellitic anhydride	89-32-7	317- 318- 334	261- 280- 280- 284- 304+340- 305+351+338+310	05, 08
Sodium hydride	7646-69-7	228- 260- 290- 314	210- 231+232- 260- 280- 303+361+353- 305+351+338+310	02, 05
Sodium hydroxide	1310-73-2	290- 314	260- 280- 301+330+331- 303+361+353- 305+351+338	05
Tetrabrommethane	558-13-4	302- 315- 318- 335	280- 301+312+330- 302+352- 305+351+338+310	05, 07
Tetra butyl ammonium bromide	1643-19-2	302- 319- 412	273- 301+312+330- 305+351+338	07
Tetra butyl ammonium hydroxide	2052-49-5	225- 301+311+311- 314- 370	210- 280- 301+310+330- 301+330+331- 303+361+353- 305+351+338+310	02, 05, 06, 08
Tetrachlorophthalic anhydride	117-08-8	317- 318- 334- 350- 373- 410	201- 261- 273- 280- 305+351+338- 308+313	05, 08, 09
Tetraethyl ammonium hydroxide		314	280- 301+330+331- 303+361+353- 305+351+338+310	05
Tetramethyl ammonium hydroxide	75-59-2	301- 310- 314- 371- 373- 412	273- 280- 301+310+330- 301+330+331- 303+361+353- 305+351+338+310	05, 06, 08
Thionyl chloride	7719-09-7	302- 314- 331	260- 280- 303+361+353- 304+340+310- 305+351+338- 403+233	05, 06
Trifluoroacetic anhydride	407-25-0	314- 332- 412	273- 280- 301+330+331- 303+361+353- 304+340+312- 305+351+338+310	05, 07
Trifluoroacetic acid	76-05-1	314- 332- 412	261- 273- 280- 303+361+353- 304+340+310- 305+351+338	05, 07
Trifluoropropanoyl chloride	2516-99-6	314	280- 305+351+338- 310	05
Triphenylphosphine	603-35-0	302- 317- 318- 372	280- 301+312+330- 302+352- 305+351+338+310+314	05, 07, 08









\* Asterisk highlighted chemicals are categorized as CMR. See Table 9.

\*\* Boc anhydride//Di-*tert*-butyl pyrocarbonate

Table 15. Used CMR categorized chemicals for the execution of synthetic and analytical experiments of this PhD studies.

Chemical	Trivial name/ Short name	CAS#	CMR category
1-Iod-propane	Propyliodid	107-08-4	2
2-Methylpyrolidinone	NMP	872-50-4	1B
3,3'-Dihydroxybenzidine	HAB	2373-98-0	2
3-Bromo propene	Allyl bromide	106-95-6	1B
3-Bromo propyne	Propargyl bromide	106-96-7	2
Hydrazine monohydrate		7803-57-8	1B
Iodoethane	Ethyl iodide	75-03-6	2
Iodomethane	Methyl iodide	74-88-4	2
Isopropyl chloroformate		108-23-6	2
N, N-Dimethylacetamide	DMAc	127-19-5	1B
N, N-Dimethylformamide	DMF	68-12-2	1B

Table 16. GHS pictograms according to the Globally Harmonized System of Classification and Labelling of Chemicals.

	<b>GHS 09</b> <b>Environmental Hazard</b>		<b>GHS 05</b> <b>Corrosives</b>
	GHS 02 Flammables		GHS 06 Acute Toxicity
	GHS 03 Oxidizers		GHS 07 Harmful – Irritants, Sensitizers
	GHS 04 Gases under pressure		GHS 08 Specific Toxicity Hazards

Classification and labelling of hazardous chemicals by the “Globally Harmonized System of Classification and Labelling of Chemicals (GHS)” according to the “Regulation (EC) No 1272/2008 on classification, labelling and packaging of substances and mixtures (the 'CLP Regulation')”



Appendix: Results from

## Thermally Rearranged Polymers (TRP)

*Molecular Modelling of the Reaction Mechanism*

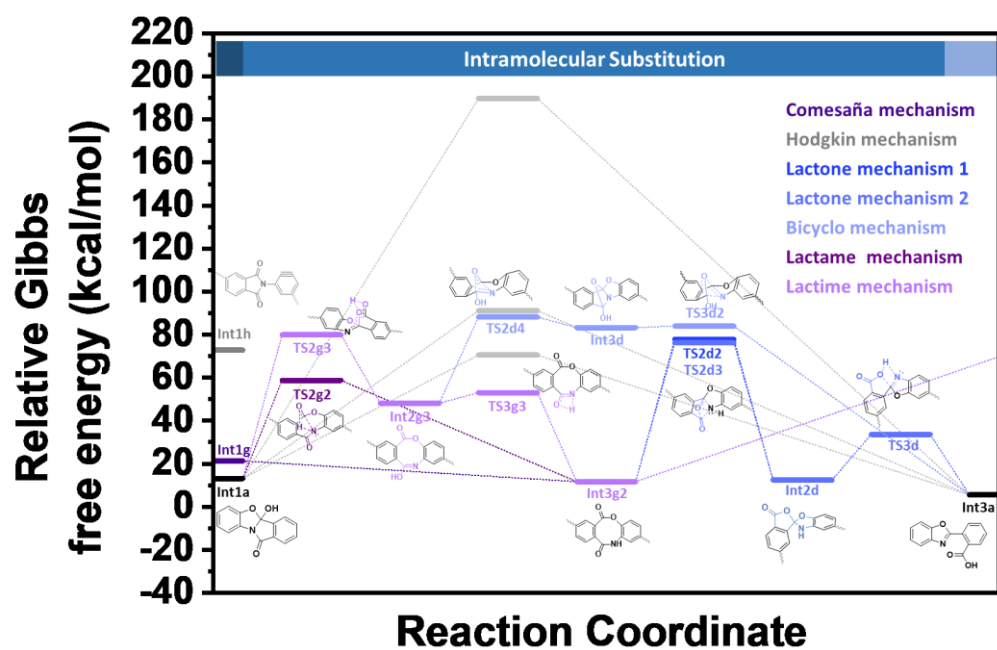


Figure 256. Additional reaction mechanism reaction coordinates, which are not considered for further discussion.

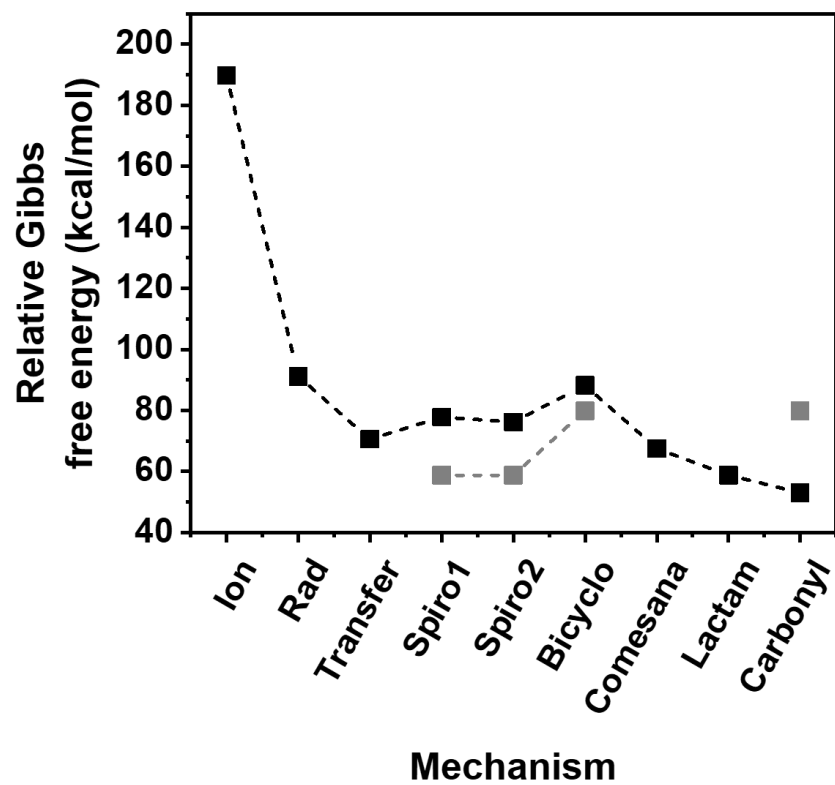


Figure 257. Comparison of the simulated first step of each reaction mechanism.

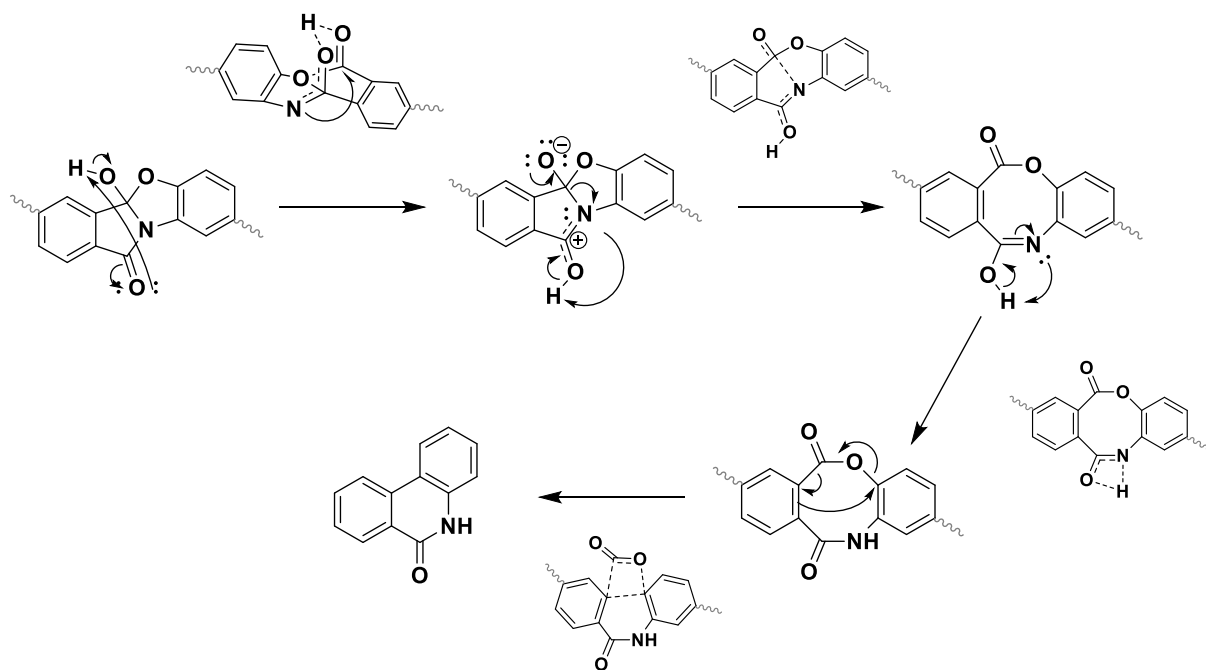


Figure 258. Lactam formation mechanism.

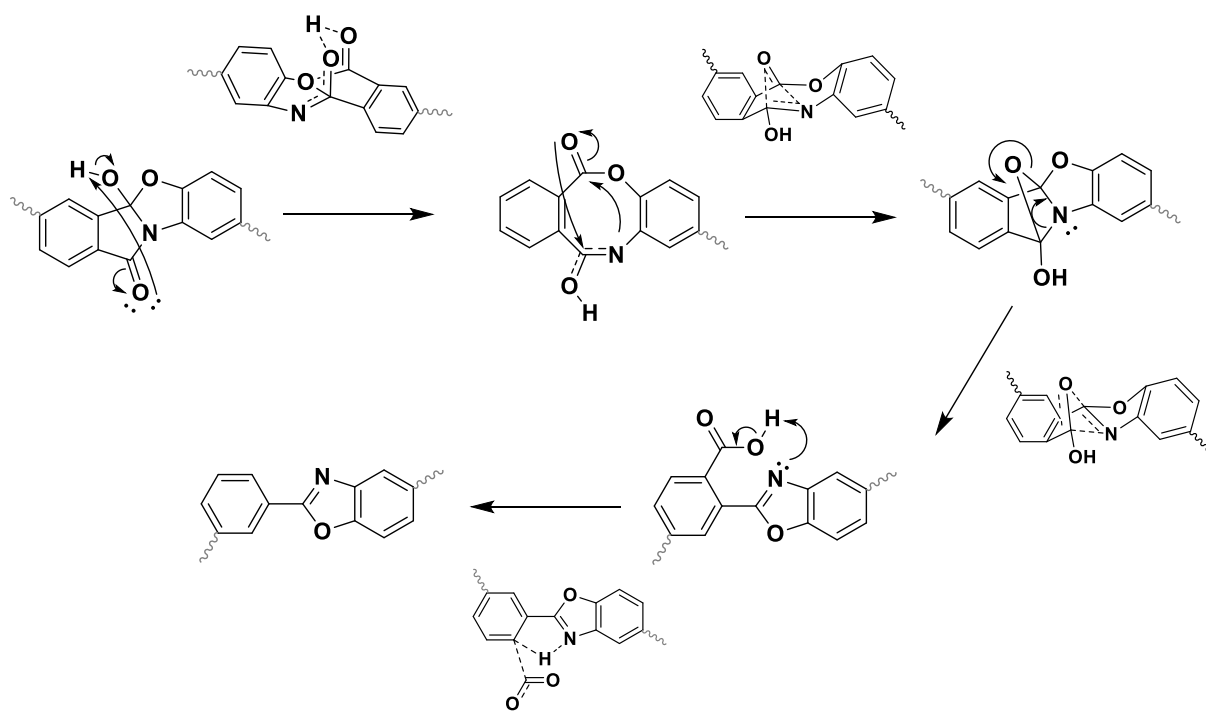


Figure 259. Alternative lactam formation mechanism.

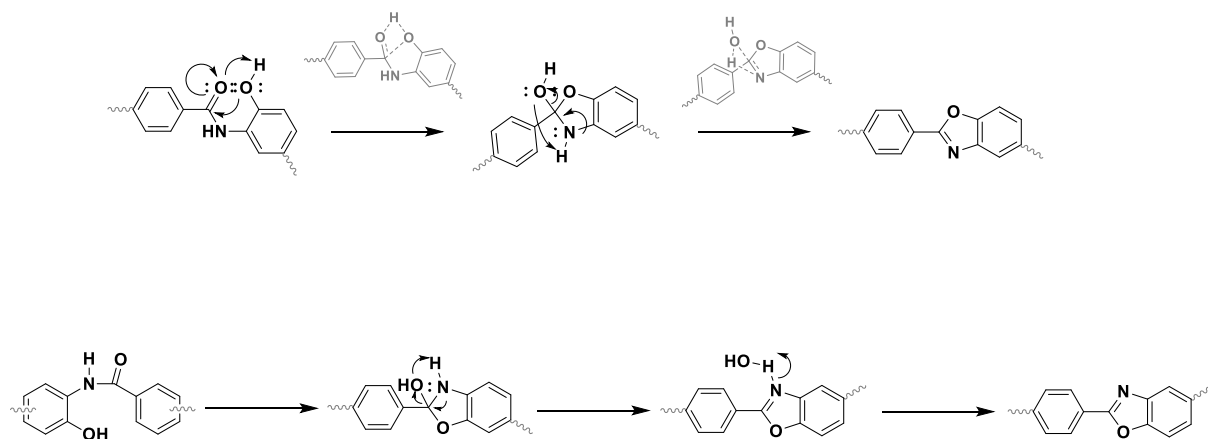


Figure 260. Thermal Rearrangement in ortho-hydroxy polyamides.

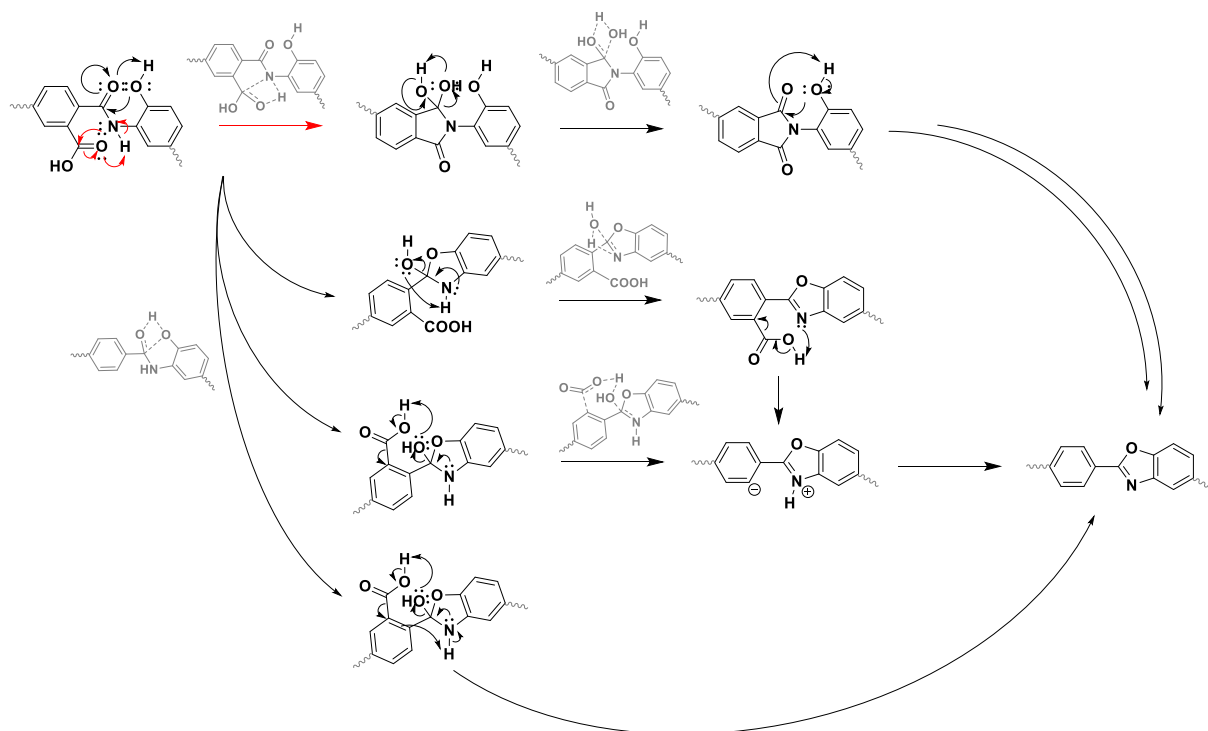


Figure 261. Thermal imidization and rearrangement in ortho-hydroxy poly(amic acids).

# Thermally initiated Cascade Reaction Polymers (TCRP)

## *Polyimides with Ortho-Allyloxy Groups*

### Effect of Allylation and effect of the degree of allylation

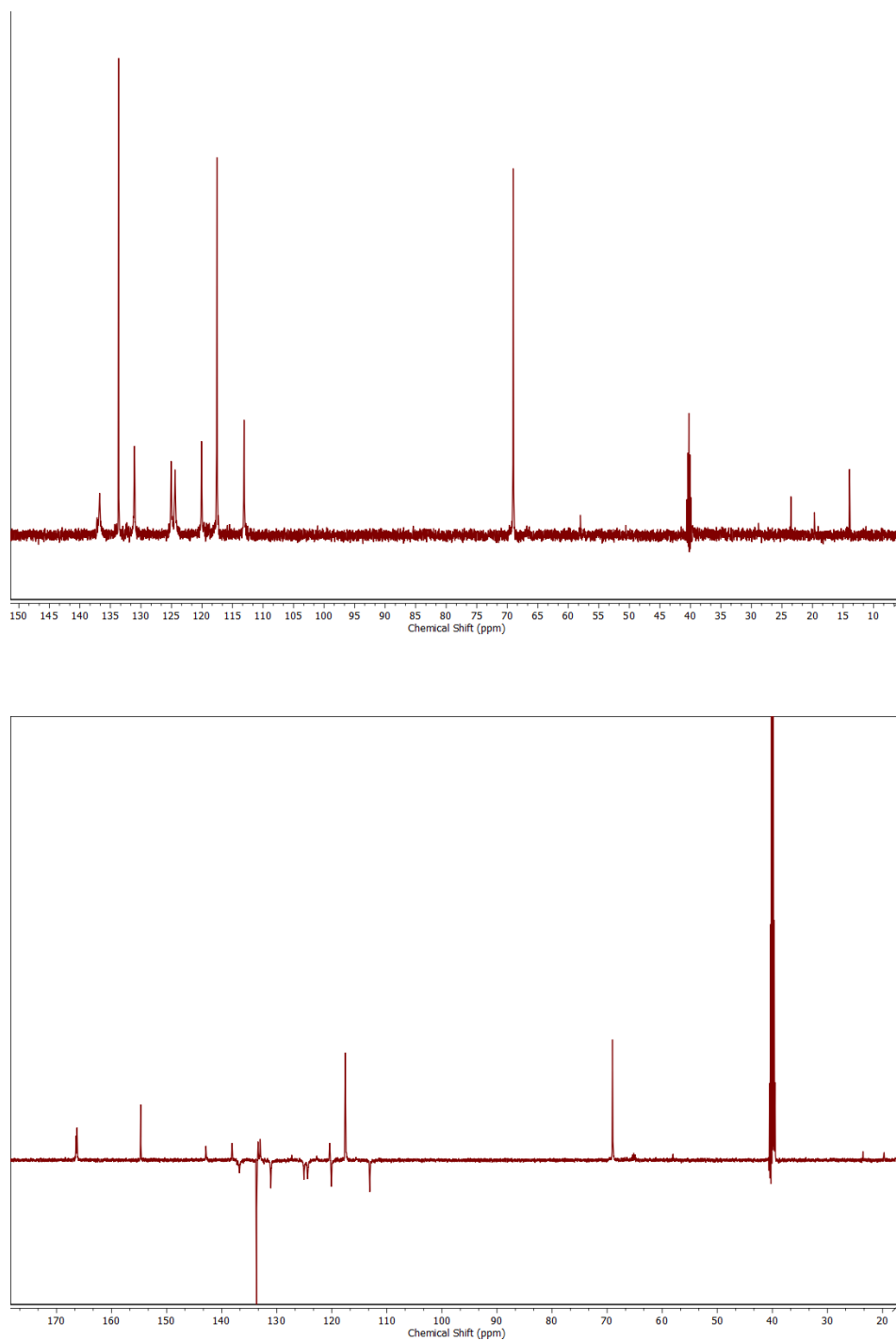


Figure 262.  $^{13}\text{C}$ -NMR spectra of Allyl100PI-2 (6FDA-HAB Allyl) with dept45 (top) and deptq135 (bottom) method.

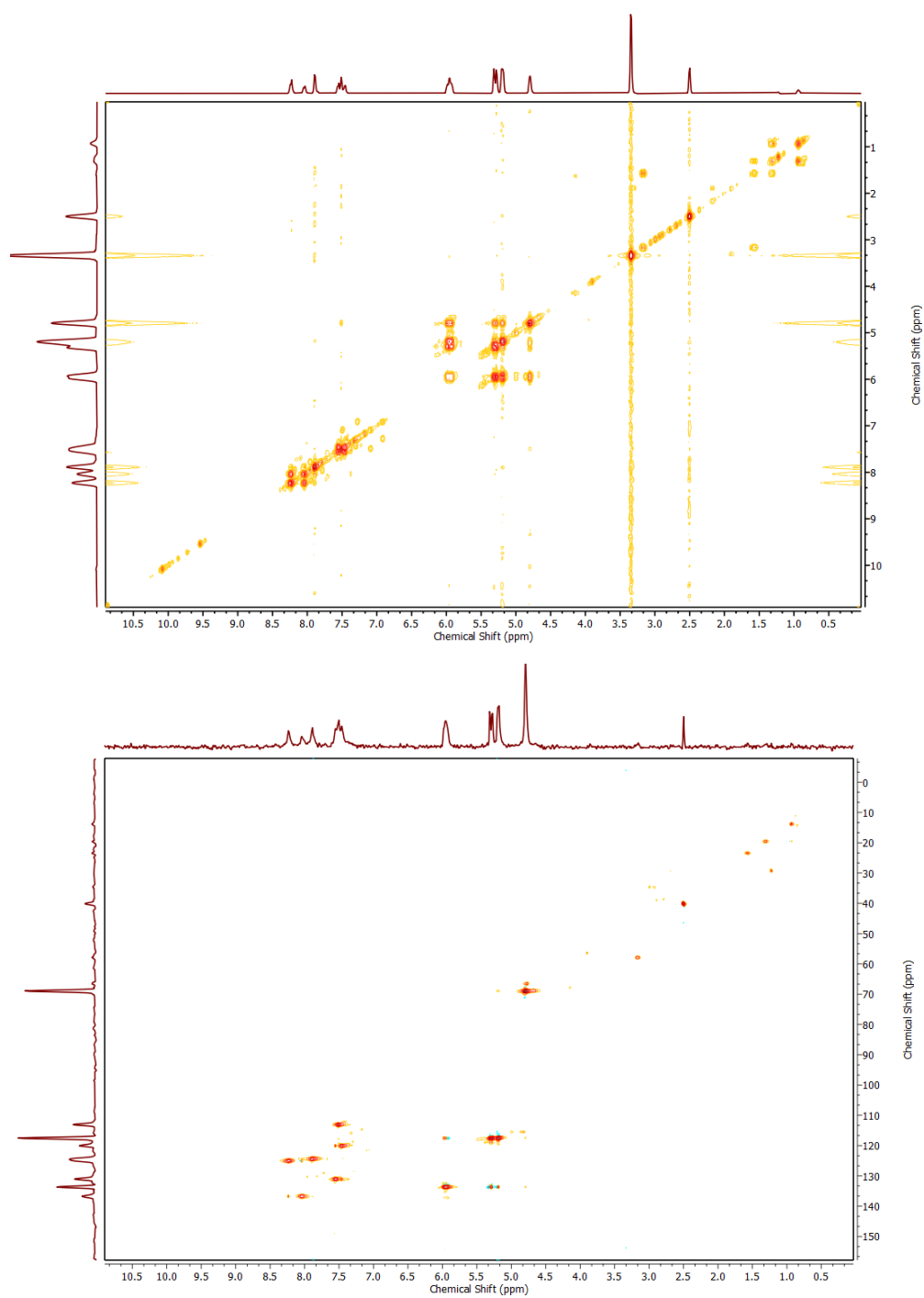


Figure 263. 2D NMR spectra of Allyl100PI-2 (6FDA-HAB Allyl) with H, H-COSY (top) and HSQC (bottom) method.

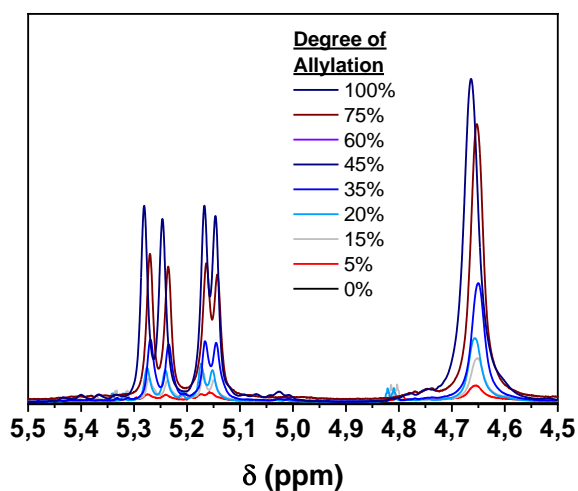


Figure 264.  $^1\text{H}$ -NMR spectra of Allyl-PI-1 (6FDA-BisAPAF Allyl) samples with different degrees of functionalization. Methylene group at 4.65 ppm and terminal vinyl  $\text{CH}_2$  group at 5.2 ppm.

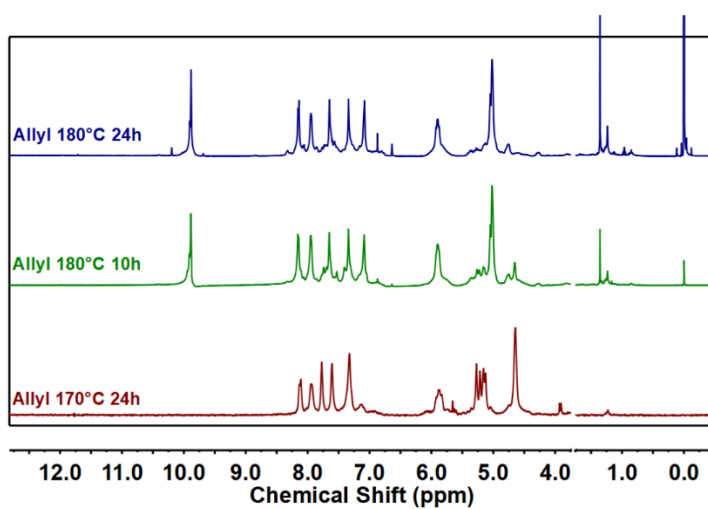


Figure 265.  $^1\text{H}$ -NMR spectra of thermally treated Allyl-PI at its first exothermic reaction onset showing that there is a complete Claisen Rearrangement conversion after 10h.



## Effect of Allyl Derivatives in Thermal Cascade Reactions

### Allyl-PI

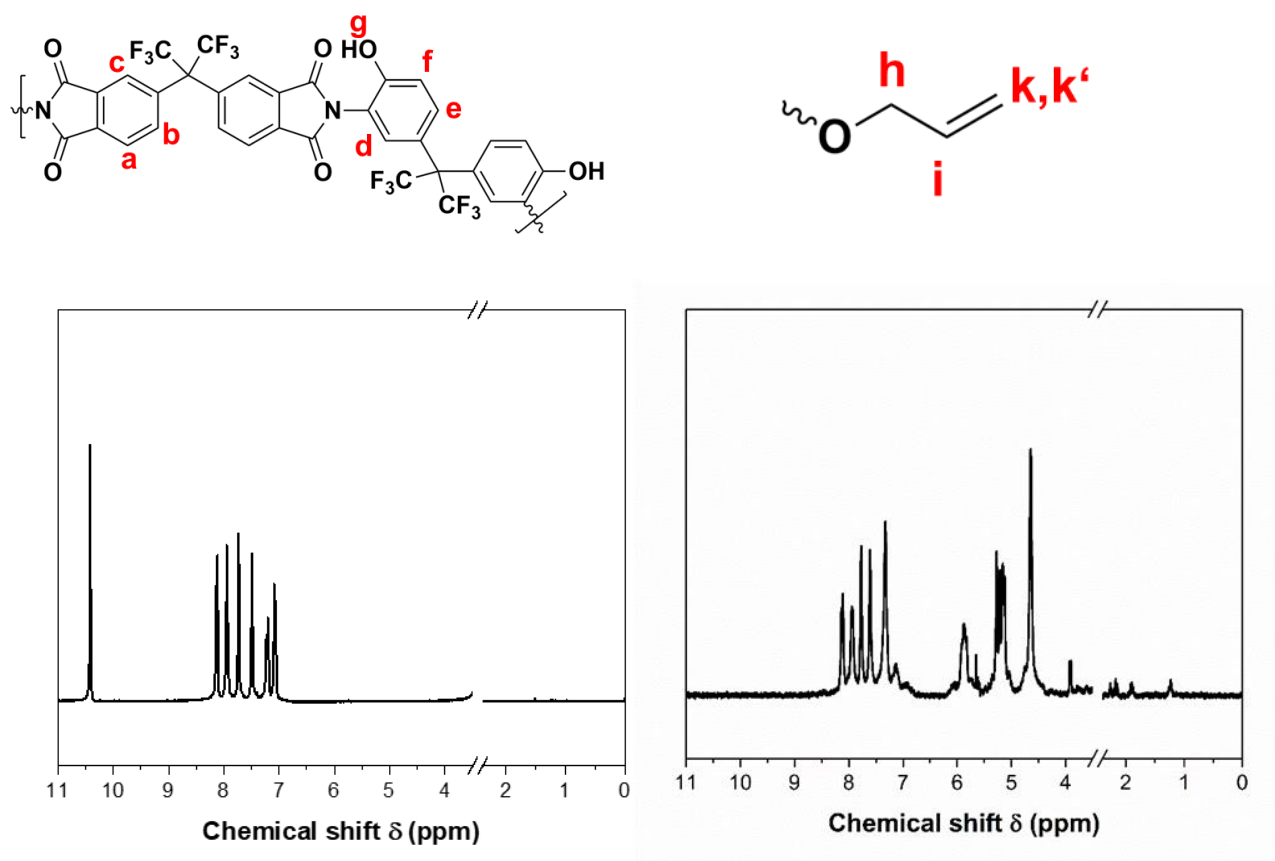
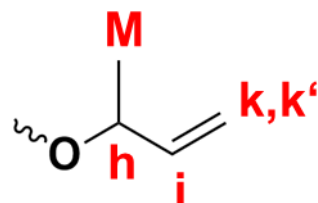
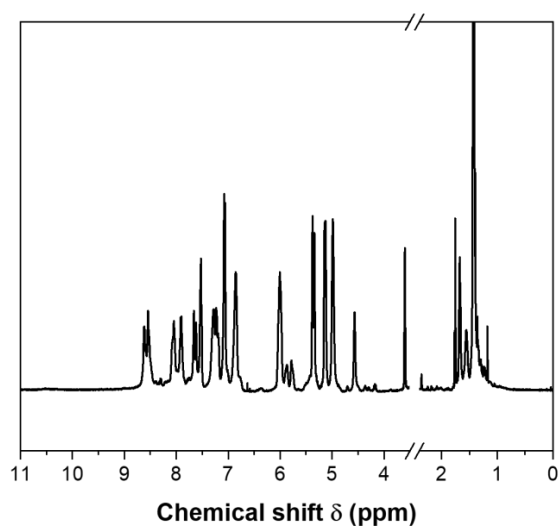


Figure 266. <sup>1</sup>H-NMR spectrum 6FDA-BisAPAF (HPI-1) and Allyl-PI.

Molecular weight:  $M_n$  (g/mol), =  $2.09 \cdot 10^4$ ,  $M_w$  (g/mol), =  $6.69 \cdot 10^4$ ,  $D = 3.2$ . IR: 3084 (w, C-H str., alkene); 2923, 2872 (w, C-H str., alkane); 1789 (s, C=O str, imide); 1725 (w, C=O str, imide); 1615 (w, C=C str., alkene); 1273, 1205 (s, C-O-C str., ether). <sup>1</sup>H NMR (DMSO-d<sub>6</sub>, ppm); 7.3-8.2 (m, 12 H, aromatic, a-f); 5.8-5.9 (m, 4 H, vinyl, k, k'); 5.1-5.3 (m, 2 H, vinyl, i); 4.6 (s, 4 H, allylic, h).

### $\alpha$ MPI-1



Molecular weight:  $M_n$  (g/mol), =  $8.53 \cdot 10^3$ ,  $M_w$  (g/mol), =  $1.87 \cdot 10^4$ ,  $\bar{D} = 2.2$ . IR: 3082 (w, C-H str., alkene); 2979, 2962 (w, C-H str., alkane); 1789 (s, C=O str, imide); 1725 (w, C=O str, imide); 1615 (w, C=C str., alkene); 1273, 1205 (s, C-O-C str., ether).  $^1\text{H}$  NMR (DMSO- $d_6$ , ppm); 7.3-8.2 (m, 12 H, aromatic, **a-f**); 5.5 (d, 4 H, vinyl, **k, k'**); 5.4-5.3 (m, 2 H, vinyl, **i**); 4.6 (s, 2 H, allylic, **h**); 1.4 (s, 6 H, allylic, **M**).

## $\beta$ MPI-1

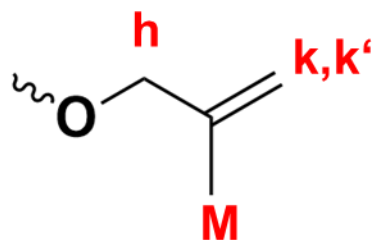
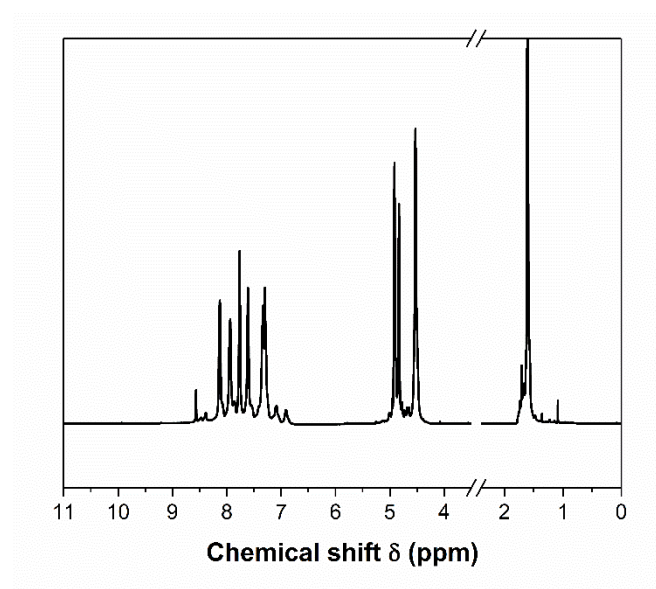


Figure 268.  $^1\text{H}$ -NMR spectrum  $\beta$ M-PI.

Molecular weight:  $M_n$  (g/mol), =  $2.47 \cdot 10^4$ ,  $M_w$  (g/mol), =  $9.91 \cdot 10^4$ ,  $D = 4.0$ . IR: 3082 (w, C-H str., alkene); 2979, 2962 (w, C-H str., alkane); 1789 (s, C=O str, imide); 1725 (w, C=O str, imide); 1615 (w, C=C str., alkene); 1273, 1205 (s, C-O-C str., ether).  $^1\text{H}$  NMR (DMSO- $d_6$ , ppm); 7.3-8.2 (m, 12 H, aromatic, **a-f**); 4.8-4.9 (m, 4 H, vinyl, **k, k'**); 4.5 (s, 4 H, allylic, **h**); 1.6 (s, 6 H, allylic, **M**).

$\gamma$ M-PI (Crotyl-PI)

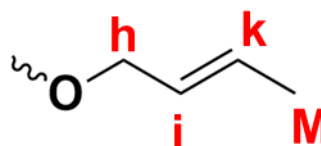
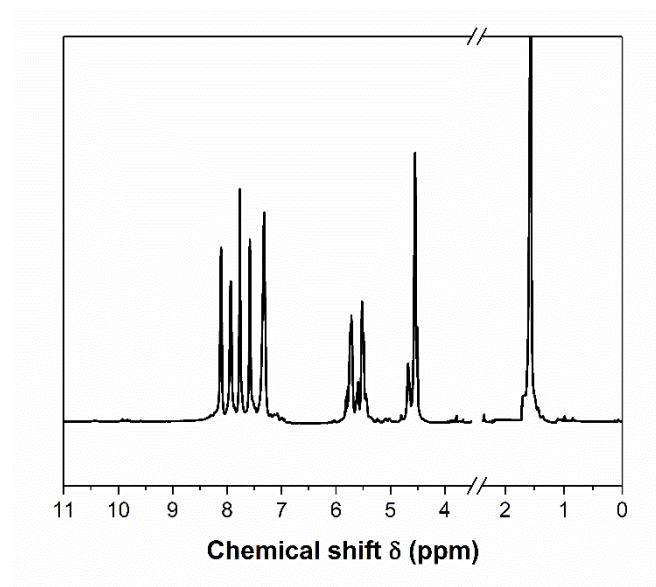


Figure 269.  $^1\text{H}$ -NMR spectrum  $\gamma$ M-PI.

Molecular weight:  $M_n$  (g/mol), =  $2.06 \cdot 10^4$ ,  $M_w$  (g/mol), =  $7.11 \cdot 10^4$ ,  $D = 3.4$ . IR: 3082 (w, C-H str., alkene); 2979, 2962 (w, C-H str., alkane); 1789 (s, C=O str, imide); 1725 (w, C=O str, imide); 1615 (w, C=C str., alkene); 1273, 1205 (s, C-O-C str., ether).  $^1\text{H}$  NMR (DMSO- $d_6$ , ppm); 7.3-8.2 (m, 12 H, aromatic, **a-f**); 4.45-4.81 (m, 2 H, vinyl, **k**); 5.45-5.81 (m, 2 H, vinyl, **i**); 4.5 (s, 4 H, allylic, **h**); 1.6 (s, 6 H, allylic, **M**).

$\gamma$ E-PI

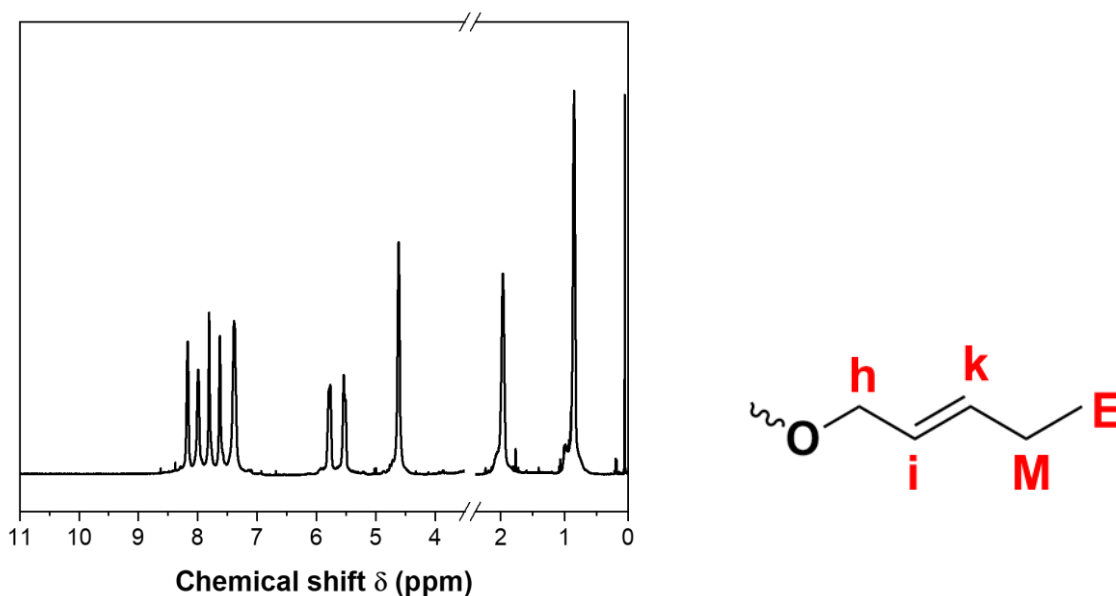


Figure 270. <sup>1</sup>H-NMR spectrum  $\gamma$ E-PI.

Molecular weight:  $M_n$  (g/mol), =  $5.36 \cdot 10^4$ ,  $M_w$  (g/mol), =  $7.88 \cdot 10^4$ ,  $D = 1.5$ . IR: 3082 (w, C-H str., alkene); 2979, 2962 (w, C-H str., alkane); 1789 (s, C=O str, imide); 1725 (w, C=O str, imide); 1615 (w, C=C str., alkene); 1273, 1205 (s, C-O-C str., ether). <sup>1</sup>H NMR (DMSO-d<sub>6</sub>, ppm); 7.3-8.2 (m, 12 H, aromatic, **a-f**); 4.45-4.81 (m, 2 H, vinyl, **k**); 5.45-6.00 (m, 2 H, vinyl, **i**); 4.5 (s, 4 H, allylic, **h**); 2.0 (s, 4 H, allylic, **M**), 0.9 (s, 6 H, methyl, **E**).

### $\gamma$ Phenyl-PI (Cinnamyl-PI)

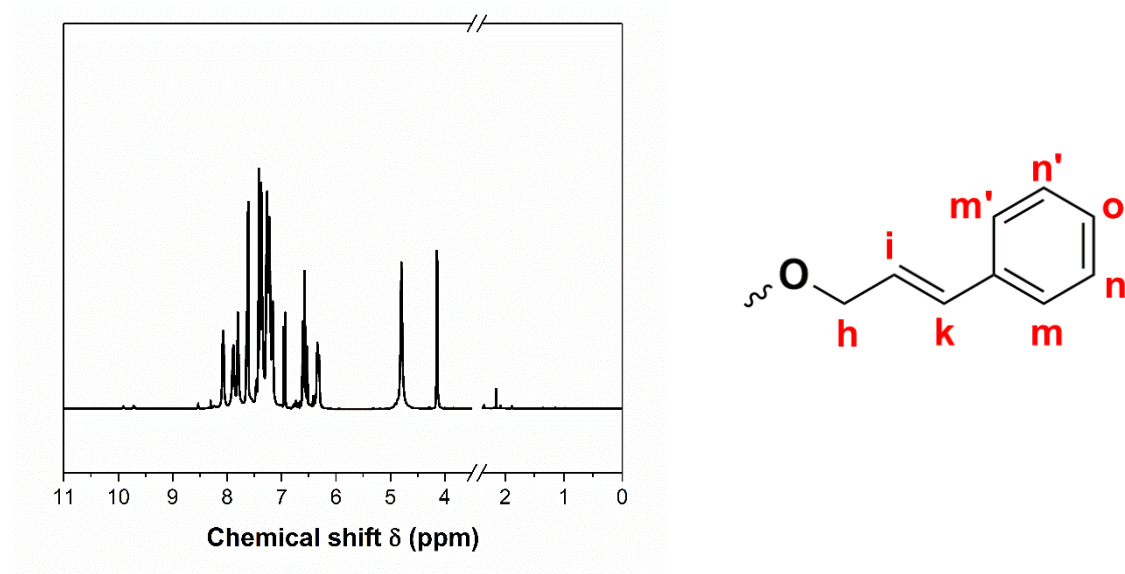


Figure 271. <sup>1</sup>H-NMR spectrum Cinnamyl-PI ( $\gamma$ Phenyl-PI).

Molecular weight:  $M_n$  (g/mol), =  $3.38 \cdot 10^4$ ,  $M_w$  (g/mol), =  $1.22 \cdot 10^5$ ,  $D = 3.6$ . IR: 3082 (w, C-H str., alkene); 3030 (w, C-H str., aromatic); 2979, 2962 (w, C-H str., alkane); 1789 (s, C=O str, imide); 1725 (w, C=O str, imide); 1615 (w, C=C str., alkene); 1273, 1205 (s, C-O-C str., ether). <sup>1</sup>H NMR (DMSO-d<sub>6</sub>, ppm); For specific assignments see Figure S7: 7.2-8.3 (m, 12 H, aromatic, **a-f**); 7.1-7.6 (m, 10 H, aromatic cinnamyl, **m-o**); 6.2-6.8 (m, 4 H, vinyl, **i, k**); 4.9 (s, 4 H, allylic, **h**).

$\gamma$ dM-PI (Prenyl-PI)

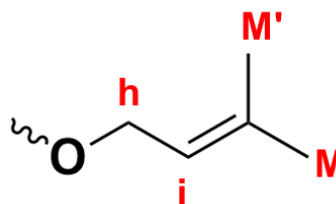
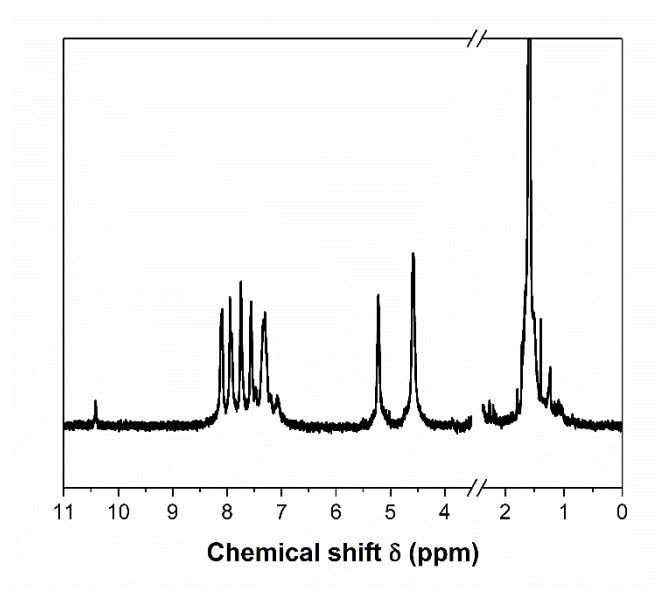


Figure 272.  $^1\text{H}$ -NMR spectrum Prenyl-PI ( $\gamma$ dM-PI).

Molecular weight:  $M_n$  (g/mol), =  $6.92 \cdot 10^4$ ,  $M_w$  (g/mol), =  $1.04 \cdot 10^5$ ,  $D = 1.5$ . IR: 3082 (w, C-H str., alkene); 2979, 2962 (w, C-H str., alkane); 1789 (s, C=O str, imide); 1725 (w, C=O str, imide); 1615 (w, C=C str., alkene); 1273, 1205 (s, C-O-C str., ether).  $^1\text{H}$  NMR (DMSO- $d_6$ , ppm); 7.3-8.2 (m, 12 H, aromatic, **a-f**); 5.25 (s, 2 H, vinyl, **i**); 4.6 (s, 4 H, allylic, **h**); 1.8 (s, 12 H, allylic, **M, M'**).

## Butylene-PI

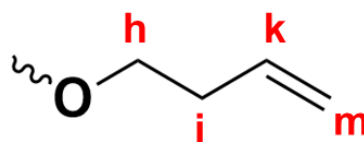
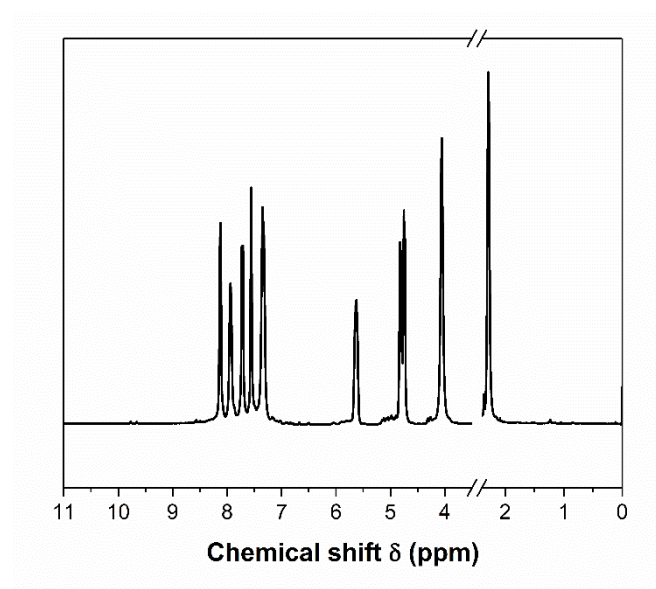


Figure 273.  $^1\text{H}$ -NMR spectrum Butylene-PI.

Molecular weight:  $M_n$  (g/mol), =  $2.24 \cdot 10^4$ ,  $M_w$  (g/mol), =  $8.43 \cdot 10^4$ ,  $D = 3.8$ . IR: 3082 (w, C-H str., alkene); 2979, 2962 (w, C-H str., alkane); 1789 (s, C=O str, imide); 1725 (w, C=O str, imide); 1615 (w, C=C str., alkene); 1273, 1205 (s, C-O-C str., ether).  $^1\text{H}$  NMR (DMSO- $d_6$ , ppm); 7.3-8.2 (m, 12 H, aromatic, **a-f**); 5.5-5.7 (m, 4 H, vinyl, **m**); 4.6-4.9 (m, 4 H, vinyl, **k**); 4.0 (s, 4 H, allylic, **i**); 2.1 (s, 4 H, methylene, **h**).



## Cycloallyl-PI

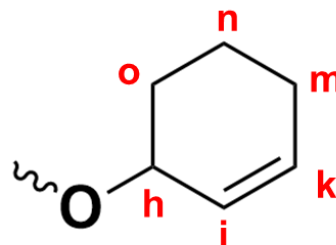
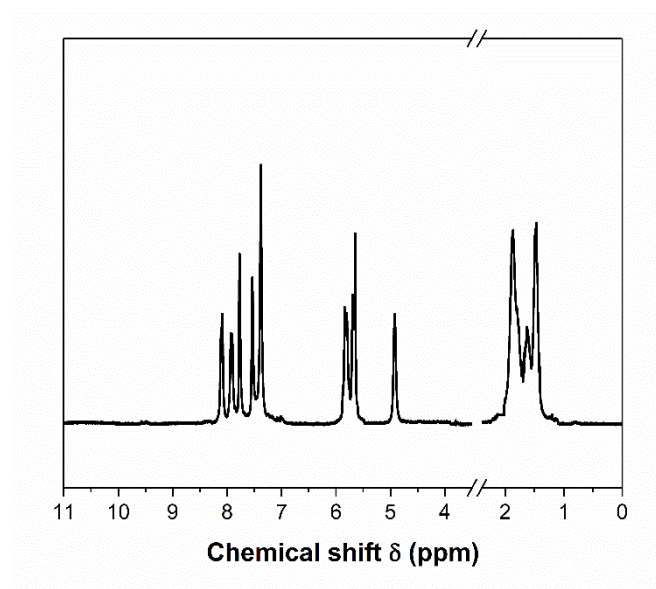


Figure 274.  $^1\text{H}$ -NMR spectrum Cycloallyl-PI.

Molecular weight:  $M_n$  (g/mol), =  $2.56 \cdot 10^4$ ,  $M_w$  (g/mol), =  $8.77 \cdot 10^4$ ,  $D = 3.4$ . IR: 3082 (w, C-H str., alkene); 2979, 2962 (w, C-H str., alkane); 1789 (s, C=O str, imide); 1725 (w, C=O str, imide); 1615 (w, C=C str., alkene); 1273, 1205 (s, C-O-C str., ether).  $^1\text{H}$  NMR (DMSO- $d_6$ , ppm); 7.3-8.2 (m, 12 H, aromatic, **a-f**); 5.6-6.0 (m, 4 H, vinyl, **i, k**); 5.0 (s, 2 H, allylic, **h**); 1.2-2.1 (s, 12 H, allylic, **m-o**).

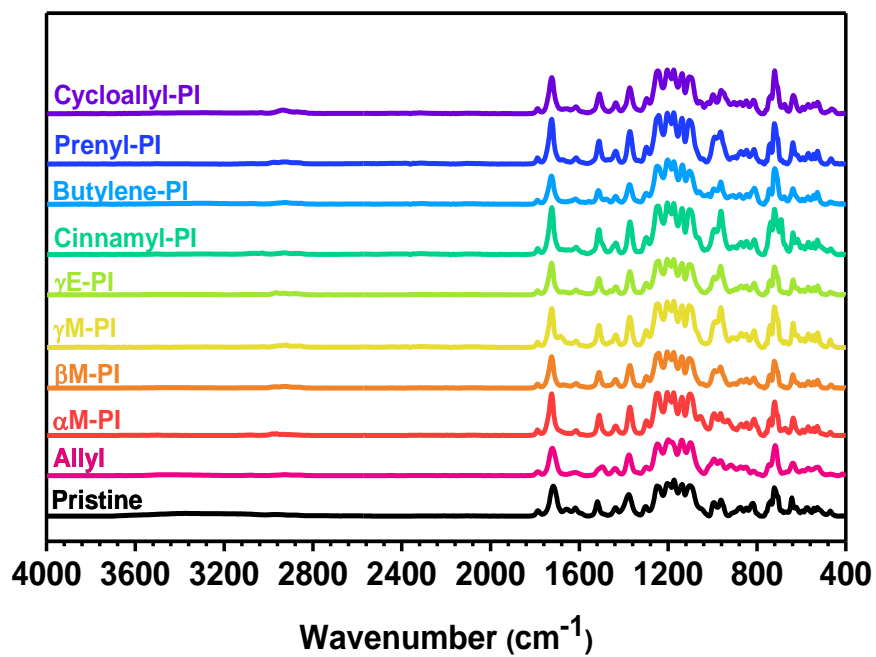


Figure 275. FT-IR spectrum of the synthesized allyl derivatives precursor.

## Monomer modification (from [268])

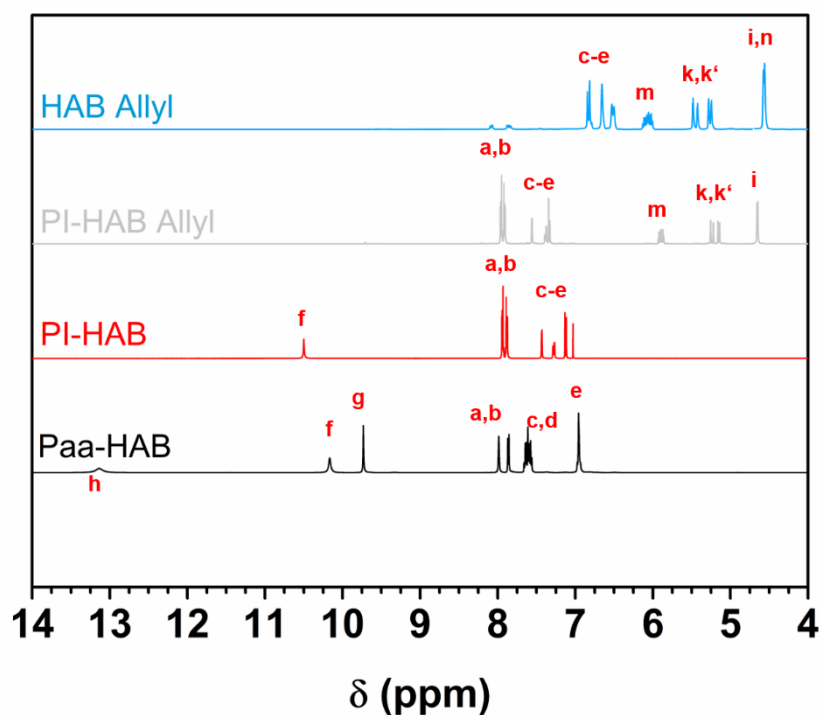
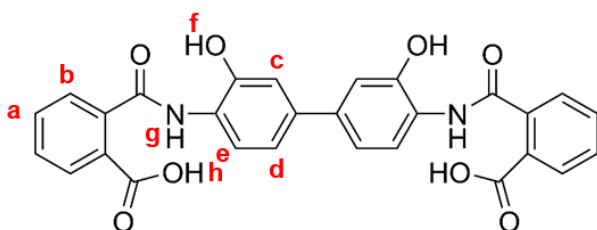
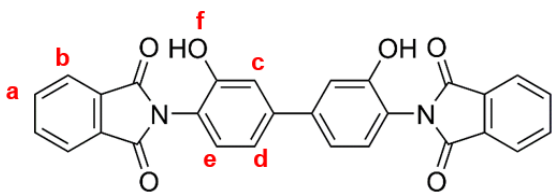


Figure 276. Stacked <sup>1</sup>H-solution-state NMR (DMSO-d<sub>6</sub>, 500 MHz) spectra of the phtalic acid anhydride protected HAB diamine in its amic acid form (black), imidized form (red) and after the allylation (grey) as well as after deprotection (blue) [268].

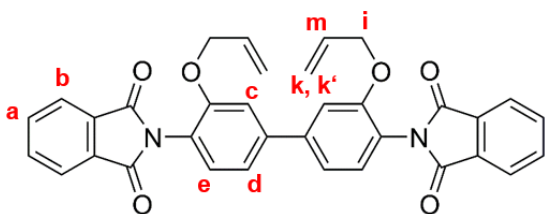
## Overview of the new monomers (chemical structure and <sup>1</sup>H-NMR characterization)



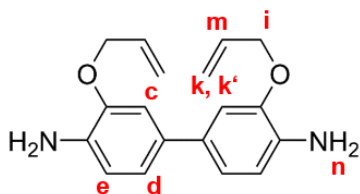
Paa-HAB: <sup>1</sup>H NMR (DMSO-d<sub>6</sub>, ppm); For specific assignments see Figure S8: 13.2 (br s, 2 H, carboxyl, **h**); 10.2 (s, 2 H, hydroxyl, **f**); 9.5 (s, 2 H, amide, **g**); 7.7-7.9 (m, 8 H, aromatic, **a, b**); 7.5-7.7 (m, 4 H, aromatic, **c, d**); 6.9 (s, 2 H, aromatic, **e**).



PI-HAB:  $^1\text{H}$  NMR (DMSO- $d_6$ , ppm); For specific assignments see Figure S8: 10.4 (s, 2 H, hydroxyl, **f**); 7.7-7.9 (m, 8 H, aromatic, **a**, **b**); 7.0-7.5 (m, 6 H, aromatic, **c-e**).



PI-HAB Allyl:  $^1\text{H}$  NMR (DMSO- $d_6$ , ppm); For specific assignments see Figure S8: 7.7-7.9 (m, 8 H, aromatic, **a**, **b**); 7.0-7.3 (m, 6 H, aromatic, **c-e**); 5.8-6.0 (m, 2 H, vinyl, **m**); 5.3-5.5 (dd, 4 H, vinyl, **k,k'**); 4.5 (s, 4 H, allylic, **i**).



HAB Allyl:  $^1\text{H}$  NMR (DMSO- $d_6$ , ppm); For specific assignments see Figure S8: 7.4-7.9 (m, 6 H, aromatic, **c-e**); 5.8-6.0 (m, 2 H, vinyl, **m**); 5.3-5.6 (dd, 4 H, vinyl, **k,k'**); 4.5 (s, 4 H, allylic, **i**); 4.5 (s, 4 H, amine, **n**).

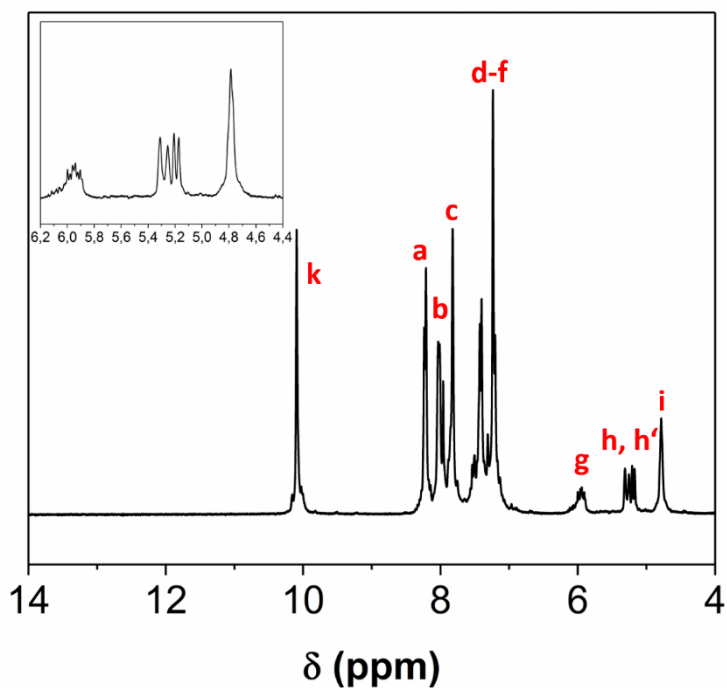
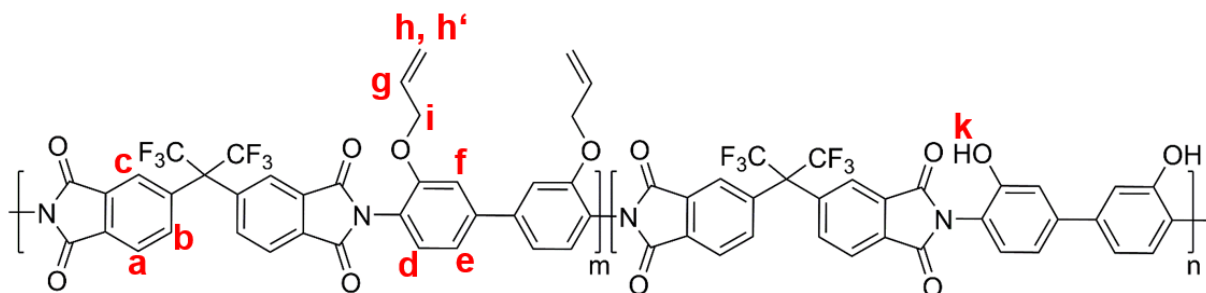


Figure 277.  $^1\text{H}$ -solution-state NMR ( $\text{DMSO-}d_6$ , 500 MHz) spectra of the copolymerized CoPo-Allyl15PI [268].



CoPo-Allyl15PI ( $m = 15$ ;  $n = 85$ ):  $^1\text{H}$  NMR ( $\text{DMSO-}d_6$ , ppm); For specific assignments see Figure S9: 10.1 (s, 1.7 H, hydroxyl, **k**); 7.2-8.3 (m, 12 H, aromatic, **a-f**); 5.8-6.2 (m, 0.3 H, vinyl, **g**); 5.6-5.8 (m, 0.6 H, vinyl, **h,h'**); 4.4 (s, 0.6 H, allylic, **i**).

# Thermoanalytics of Allylderivatives

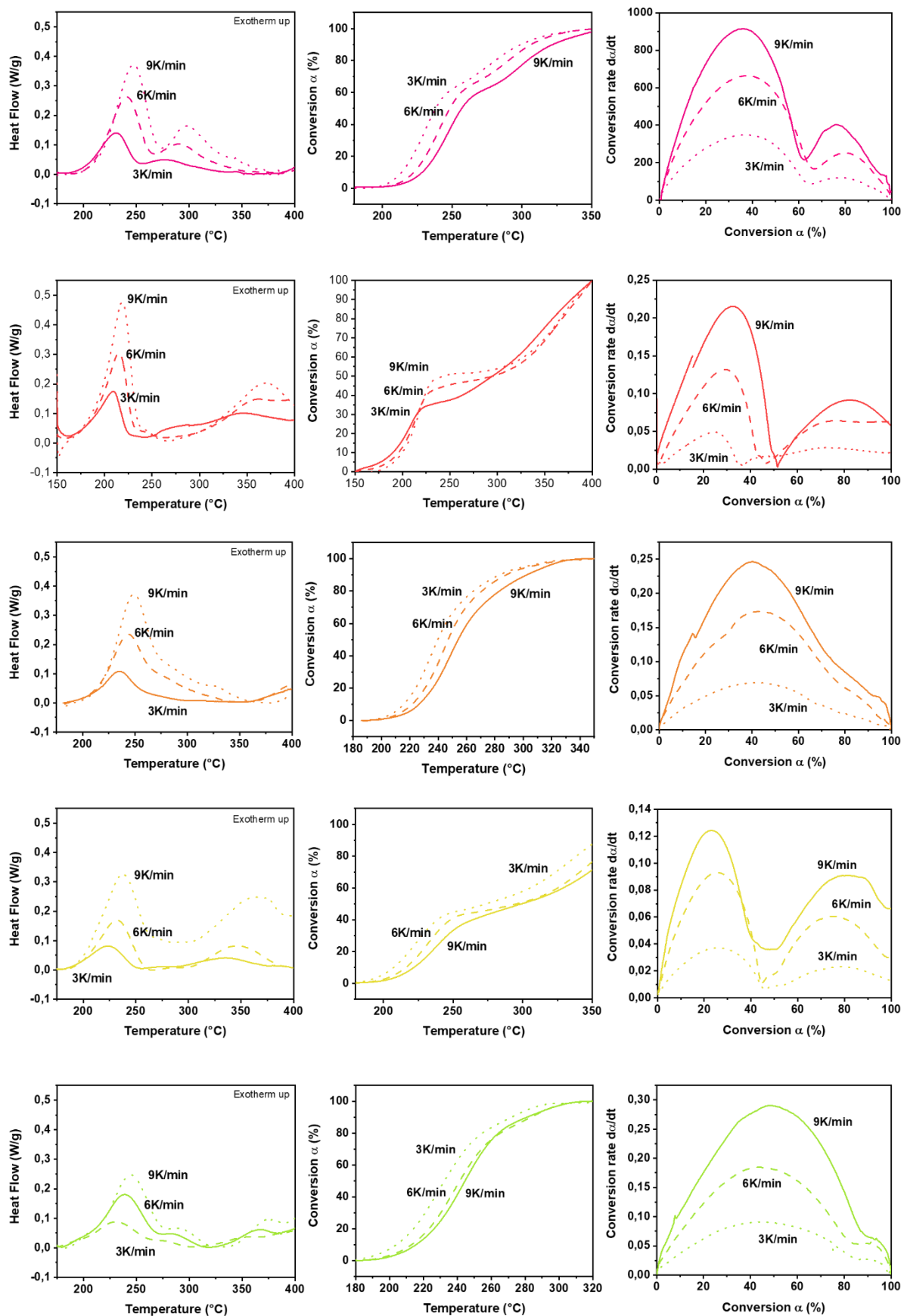


Figure 278. Thermokinetic analysis by means of DSC experiments for the allyl derivatives  $\alpha$ M-,  $\beta$ M-,  $\gamma$ M- and  $\gamma$ EPI-1 as well as Allyl-PI-1. The analysis was done by non-isothermal isoconversional methods. The plots show from left to right the heat flow curves at heating rates of 3, 6 and 9 K min<sup>-1</sup>. The temperature dependent conversion in the middle and conversion rate vs. conversion.

Table 17. Results of the thermokinetic evaluation of Allyl-PI using the KAS- and Friedman method.

KAS method			Friedman method		
Conversion $\alpha$ (%)	E <sub>A</sub> [kJ/mol]	SD	Conversion $\alpha$ (%)	E <sub>A</sub> [kJ/mol]	SD
1,0	273,8	95,9	1,1	124,0	58,3
3,1	174,9	0,8	3,1	117,8	14,0
5,2	159,4	3,0	5,2	107,3	11,4
10,4	138,6	3,1	10,4	110,1	12,3
15,3	131,5	4,2	15,3	106,7	16,3
20,4	124,3	7,1	20,4	103,1	18,6
25,3	123,2	9,2	25,3	100,9	21,4
30,4	116,9	8,4	30,4	95,8	21,6
40,3	110,2	13,6	40,3	87,9	25,7
50,3	98,9	19,9	50,3	65,3	35,0
60,3	80,1	21,7	60,5	8,4	
70,1	73,1	23,0	70,1	98,0	43,5
80,2	79,8	36,5	80,2	128,2	1,3
90,2	84,5	43,6	90,2	100,2	66,8

Table 18. Results of the thermokinetic evaluation of  $\alpha$ M-PI using the KAS- and Friedman method.

KAS method			Friedman method		
Conversion $\alpha$ (%)	E <sub>A</sub> [kJ/mol]	SD	Conversion $\alpha$ (%)	E <sub>A</sub> [kJ/mol]	SD

<b>1,0</b>	53,7	8,8	1,0	81,2	13,7
<b>3,0</b>	88,3	0,4	3,0	145,5	19,8
<b>5,0</b>	116,7	10,2	5,0	177,7	19,3
<b>10,0</b>	180,3	12,0	10,0	256,2	1,4
<b>15,0</b>	266,1	15,8	15,0	374,6	54,9
<b>20,0</b>	410,1	107,1	20,0	-568,3	1381,0
<b>25,1</b>	875,9	593,6	25,1	635,3	66,9
<b>30,0</b>	78,6	1148,8	30,0	1679,8	400,9
<b>40,0</b>	-60,7	1,5	40,0	-124,1	0,9
<b>50,0</b>	-38,2	7,3	50,0	-3,0	12,4
<b>60,0</b>	55,8	155,5	60,0	145,6	10,2
<b>70,0</b>	221,1	0,3	70,0	269,4	49,5
<b>80,0</b>	312,9	39,5	80,0	433,0	126,9
<b>90,0</b>	108,9	394,0	90,0	282,3	367,9

Table 19. Results of the thermokinetic evaluation of  $\beta$ M-PI using the KAS- and Friedman method.

KAS method			Friedman method		
Conversion $\alpha$ (%)	$E_A$ [kJ/mol]	SD	Conversion $\alpha$ (%)	$E_A$ [kJ/mol]	SD
<b>1,0</b>	290,1	117,2	1,0	284,1	213,5
<b>3,1</b>	207,1	79,4	3,1	204,8	73,1
<b>5,0</b>	180,1	51,5	5,0	195,8	45,7
<b>10,1</b>	164,5	42,3	10,1	205,5	42,5
<b>15,5</b>	163,5	37,9	15,5	199,9	23,3
<b>20,5</b>	158,8	28,0	20,5	194,6	19,2
<b>25,4</b>	157,0	23,9	25,4	192,0	20,5
<b>30,7</b>	153,7	22,9	30,7	188,1	24,1
<b>40,6</b>	151,6	22,4	40,6	182,8	31,8
<b>50,0</b>	143,0	22,4	50,0	163,3	35,0
<b>60,2</b>	134,3	24,7	60,2	143,2	44,6



<b>70,3</b>	118,8	29,9	70,3	123,1	50,3
<b>80,3</b>	107,8	31,2	80,3	128,0	37,9
<b>90,1</b>	102,8	28,8	90,1	137,4	38,0

Table 20. Results of the thermokinetic evaluation of  $\gamma$ M-PI using the KAS- and Friedman method.

KAS method			Friedman method		
Conversion $\alpha$ (%)	$E_A$ [kJ/mol]	SD	Conversion $\alpha$ (%)	$E_A$ [kJ/mol]	SD
<b>1,0</b>	184,3	323,8	1,1	137,1	237,59
<b>3,8</b>	75,8	173,2	3,1	56,2	221,38
<b>5,1</b>	16,1	259,6	5,0	-5,2	344,55
<b>10,3</b>	-266,2	731,9	10,3	-420,5	1064,94
<b>15,3</b>	283,6	226,4	15,4	419,6	394,91
<b>20,2</b>	164,7	31,44	20,0	252,5	116,22
<b>25,3</b>	132,8	29,83	25,5	184,3	32,22
<b>30,2</b>	122,3	39,85	30,1	157,9	45,99
<b>40,2</b>	85,1	10,17	40,5	51,6	19,81
<b>50,1</b>	93,3	37,47	50,2	71,4	45,28
<b>60,1</b>	118,0	97,28	60,0	126,2	57,25
<b>70,2</b>	144,3	114,3	70,1	181,7	59,23
<b>80,1</b>	170,0	103,4	80,1	204,4	53,16
<b>90,2</b>	206,0	130,4	90,2	209,9	35,07

Table 21. Results of the thermokinetic evaluation of  $\gamma$ E-PI using the KAS- and Friedman method.

KAS method			Friedman method		
Conversion $\alpha$ (%)	$E_A$ [kJ/mol]	SD	Conversion $\alpha$ (%)	$E_A$ [kJ/mol]	SD
1,0	335,0	266,0	1,0	285,4	268,2
3,1	257,6	164,8	3,1	209,6	104,0
5,1	214,6	93,5	5,1	177,7	52,1
10,1	188,8	56,9	10,1	170,0	33,1
15,3	178,5	39,6	15,3	166,2	24,4
20,3	172,5	31,2	20,3	168,7	21,3
25,1	171,6	28,9	25,1	170,1	21,3
30,2	172,3	25,9	30,2	174,7	20,2
40,4	174,4	25,3	40,4	183,3	23,7
50,3	180,1	24,4	50,3	193,7	26,6
60,4	184,9	29,9	60,4	197,1	35,9
70,3	191,6	36,9	70,3	208,3	55,8
80,1	178,9	44,4	80,1	198,1	104,4
90,1	163,9	32,1	90,1	187,3	48,8

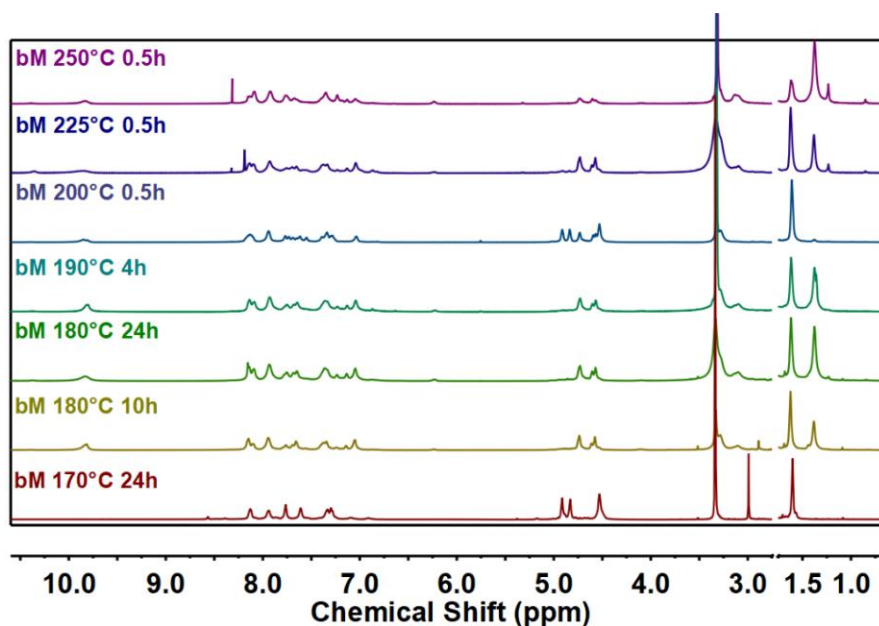


Figure 279.  $^1\text{H-NMR}$  spectra of thermally treated  $\beta\text{M-PI}$  at its first exothermic reaction onset showing that there is a complete Claisen Rearrangement conversion after 10 h, with a subsequent cyclization reaction of the allyl-unit. The cyclization occurs faster at higher temperatures as shown.

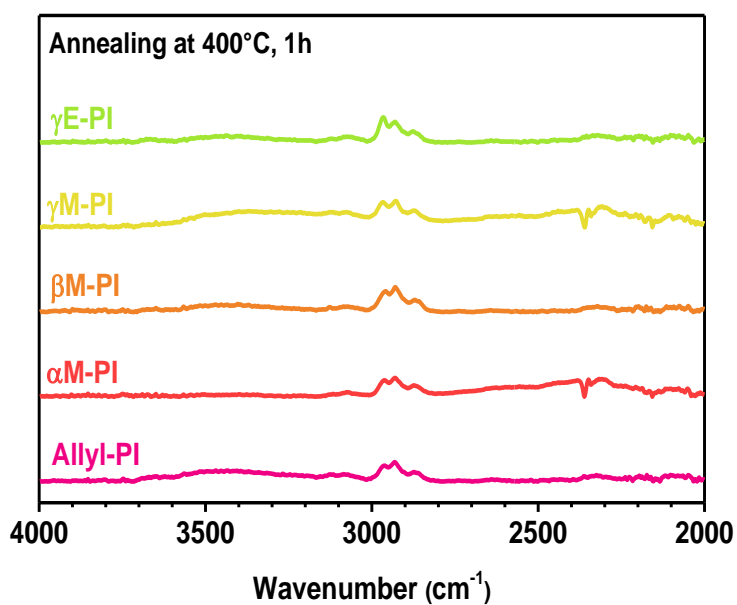


Figure 280. FT-IR spectra of  $\alpha\text{M-}$ ,  $\beta\text{M-}$ ,  $\gamma\text{M-}$  and  $\gamma\text{EPI-1}$  as well as  $\text{Allyl-PI-1}$  after annealing at  $400\text{ }^\circ\text{C}$  for 1 h.

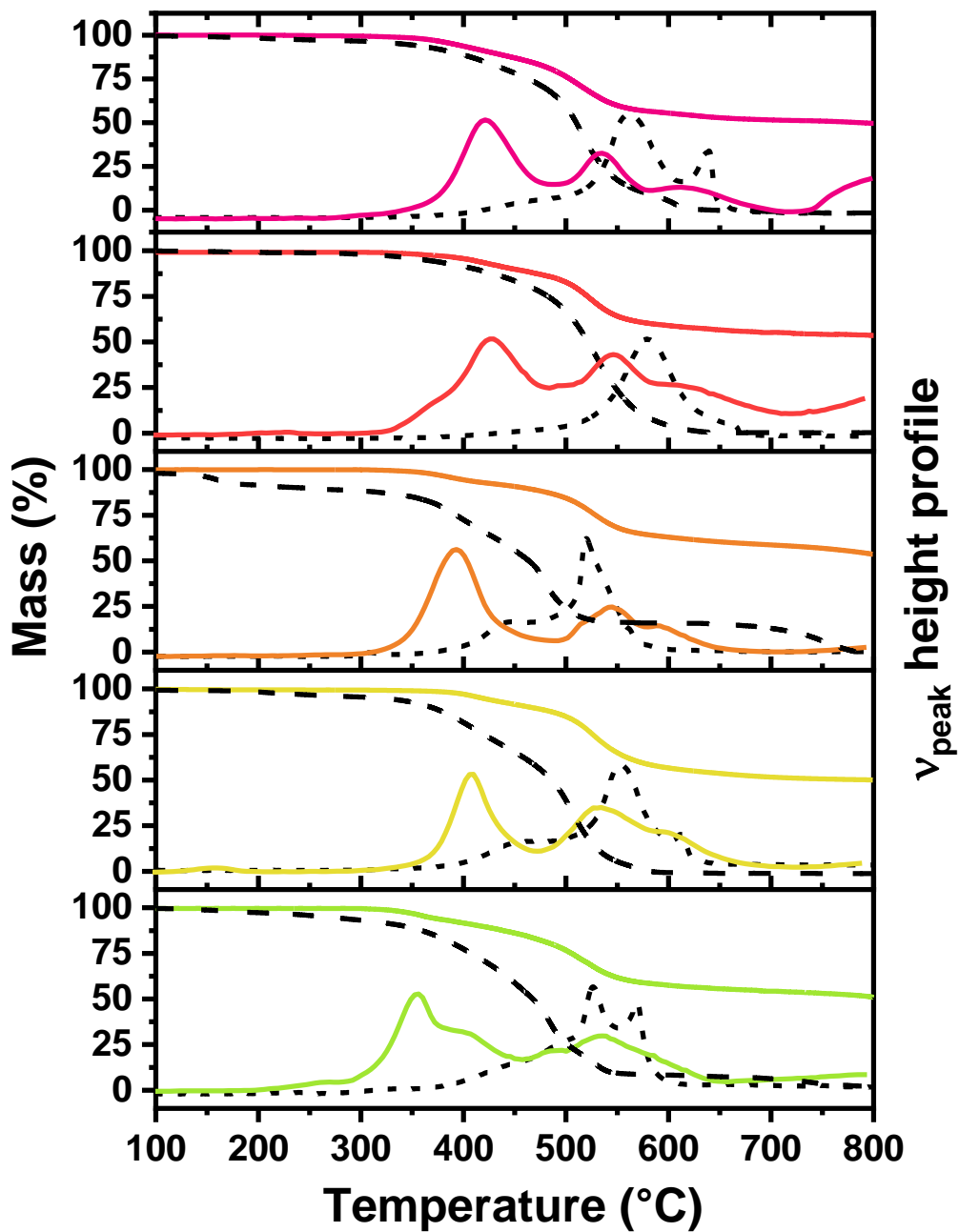
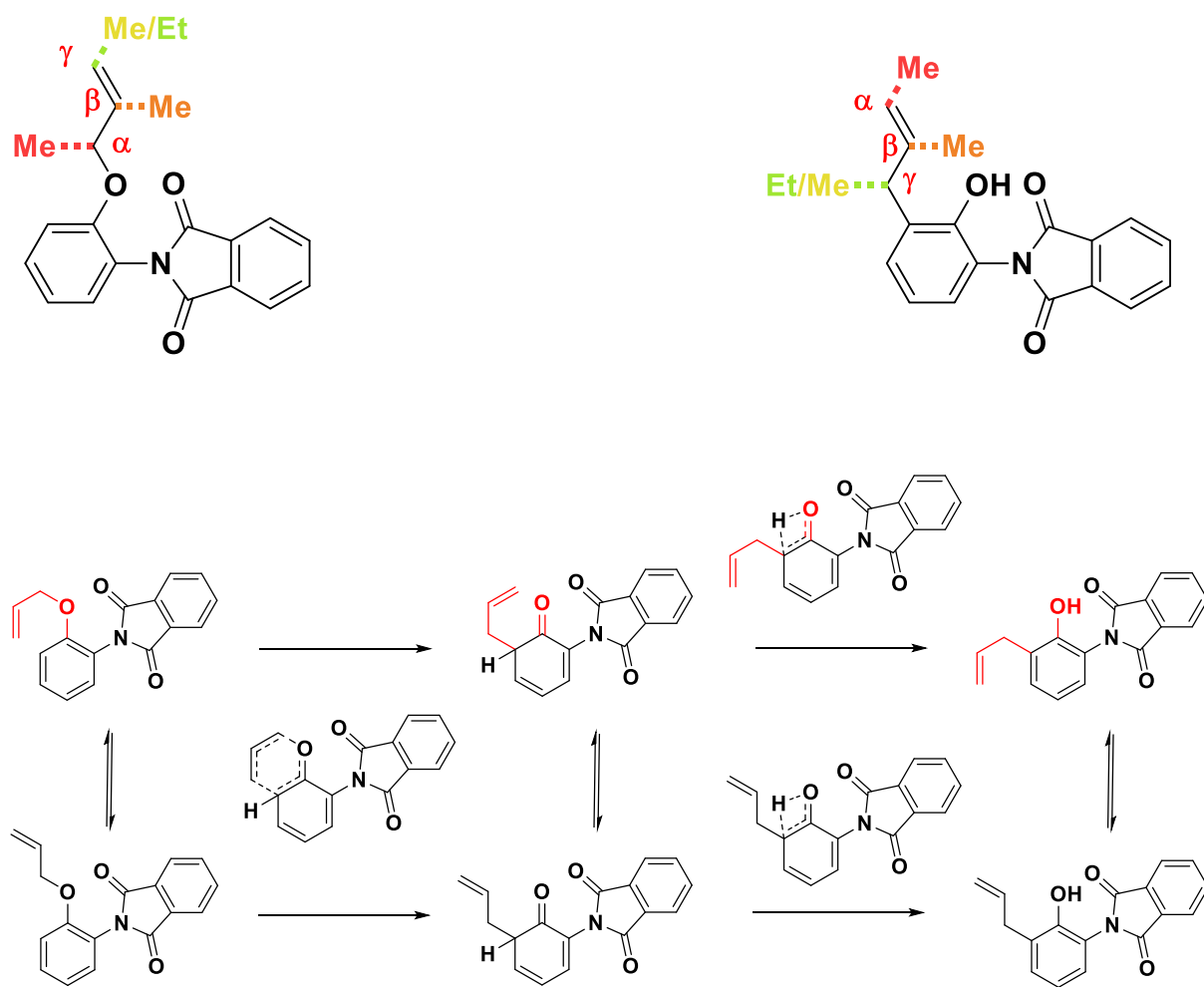


Figure 281. Mass loss curve of  $\alpha$ M-,  $\beta$ M-,  $\gamma$ M- and  $\gamma$ EPI-1 as well as Allyl-PI-1 as a function of the temperature in an inert argon atmosphere (straight line) and synthetic air atmosphere (dashed line). In addition, the corresponding CO<sub>2</sub> peak height profiles obtained by TG-IR runs as well are shown for the experiments in argon and synthetic air, respectively.

# Computational Methods

## Quantum Mechanical DFT Simulation

### Claisen-Rearrangement



Scheme 58. Overview of the Claisen Rearrangement steps in their cis- and trans-form.

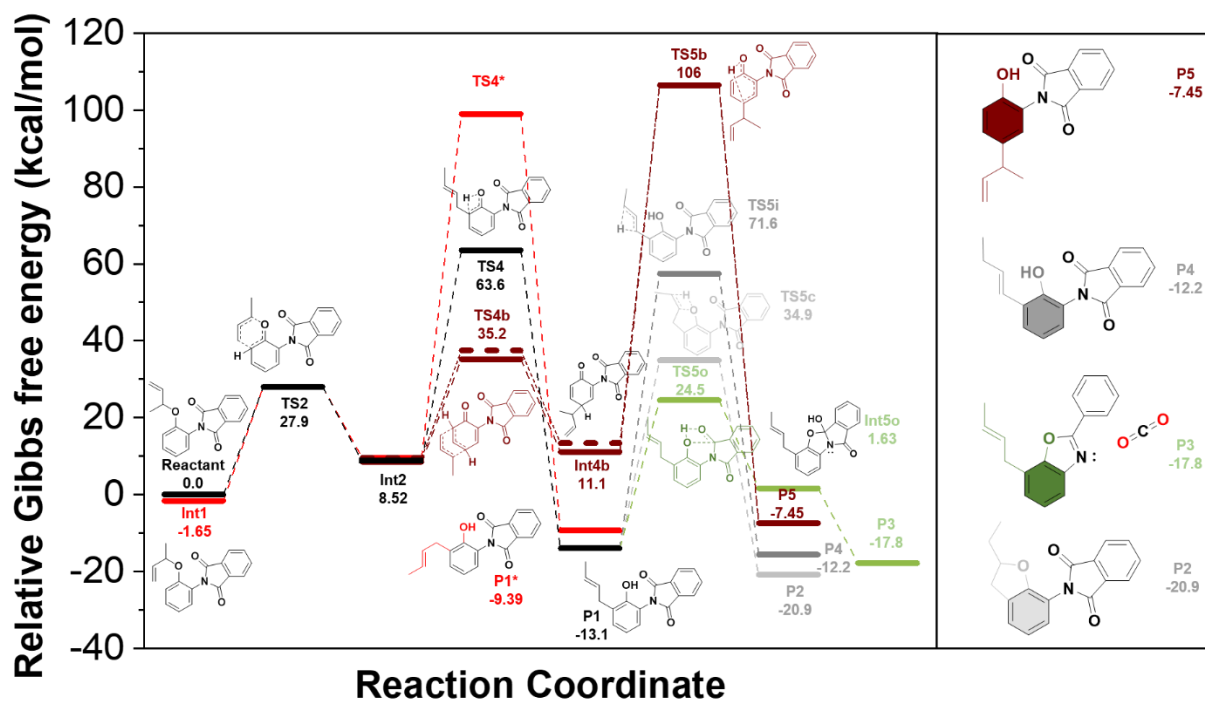


Figure 282. Simulated single-point energies of the geometry optimized reactants, products, intermediates, and transition-states of the cascade-type reactions of the  $\alpha$ Mallyl-Imide model.

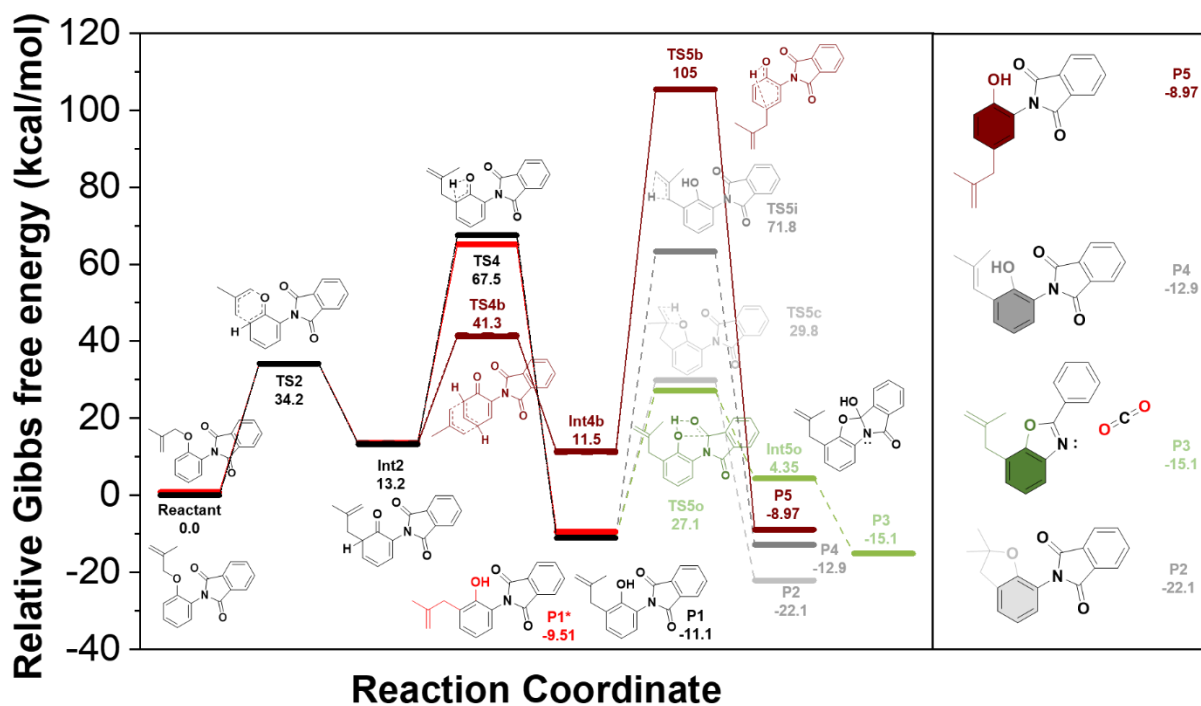


Figure 283. Simulated single-point energies of the geometry optimized reactants, products, intermediates, and transition-states of the cascade-type reactions of the  $\beta$ Mallyl-Imide model.

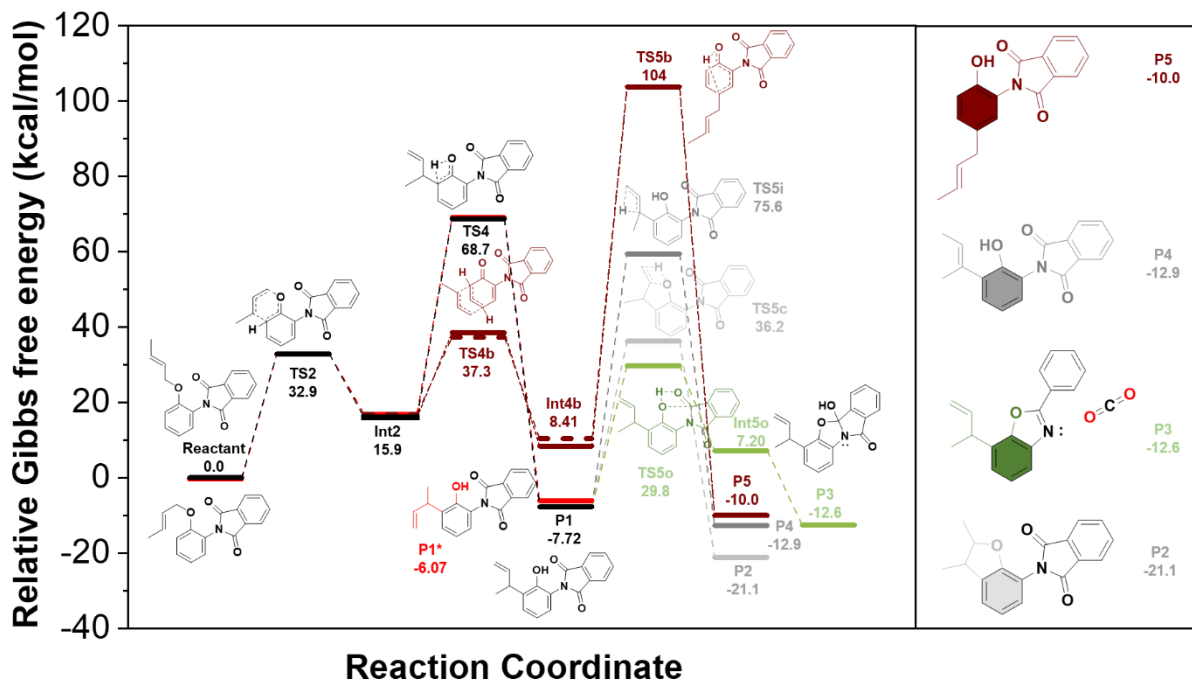


Figure 284. Simulated single-point energies of the geometry optimized reactants, products, intermediates, and transition-states of the cascade-type reactions of the  $\gamma$ Mallyl-Imide model.

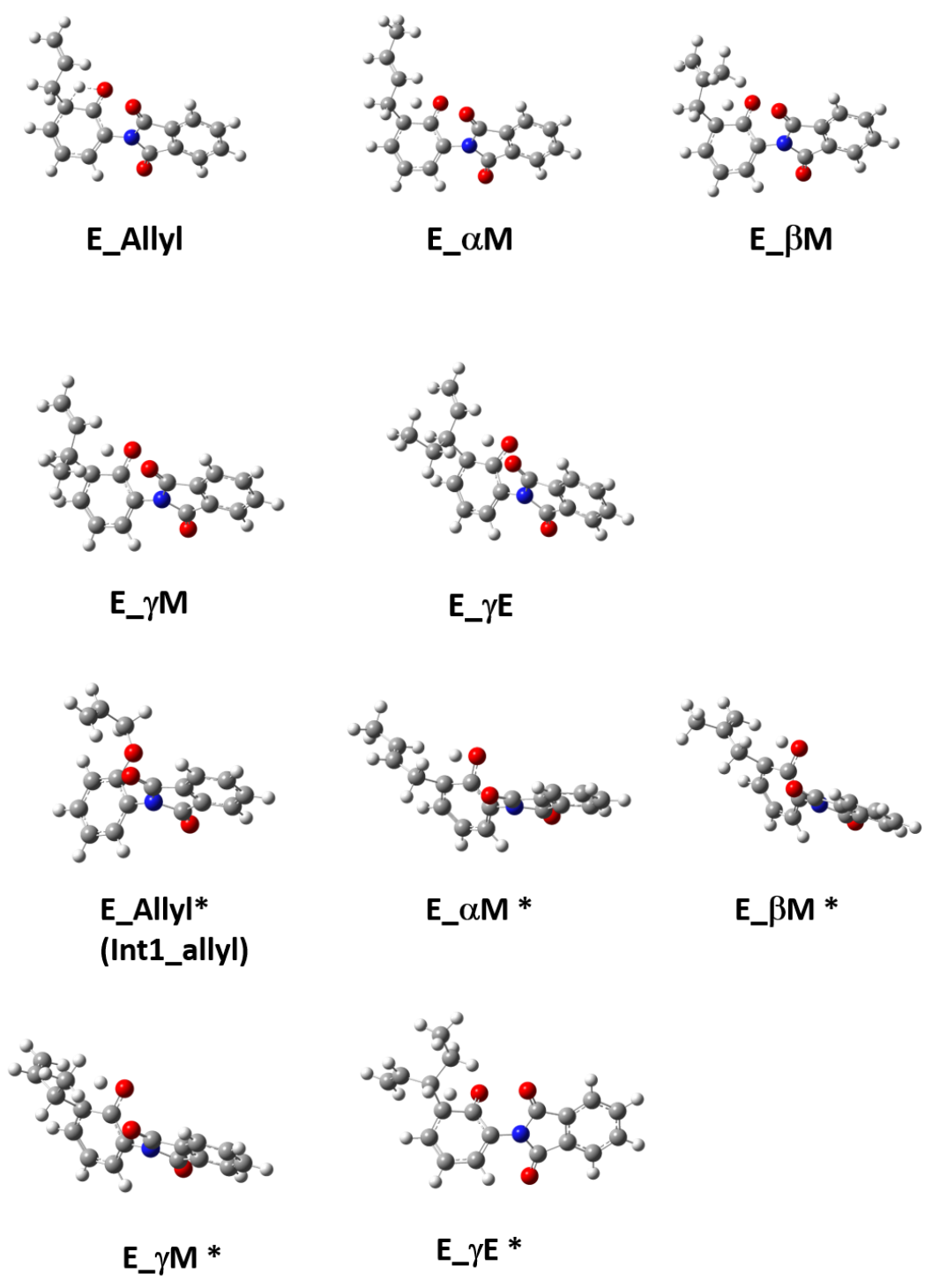


Figure 285. Geometry optimized structures of the educt of all simulated allyl derivatives. Structures with an asterisk are the corresponding cis isomer int1.



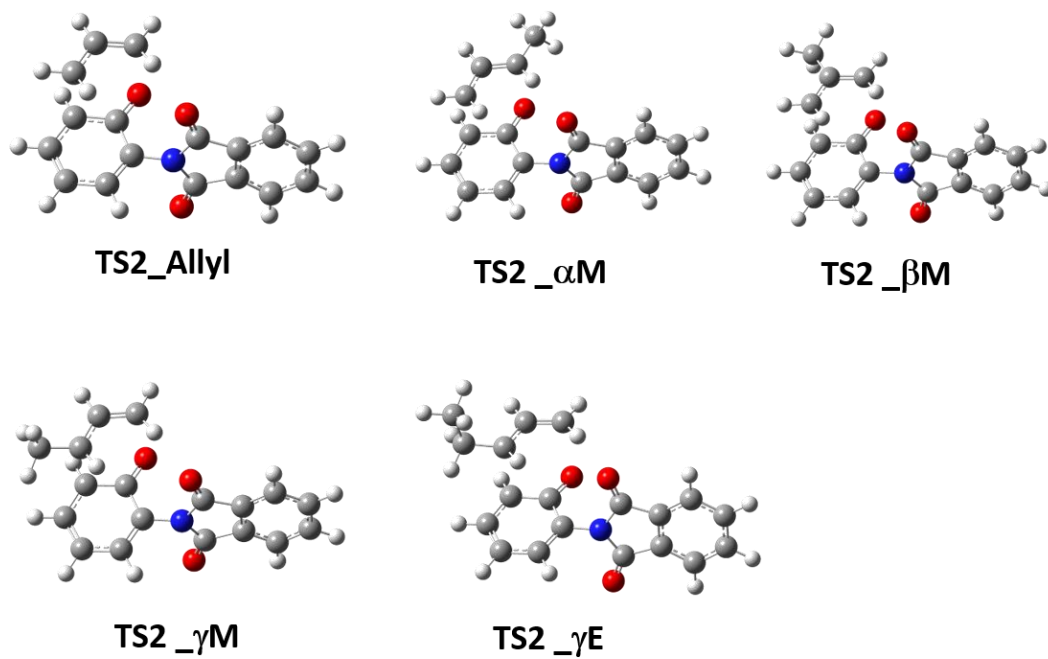


Figure 286. Geometry optimized transition-state structures TS2 of the CR process of all simulated allyl derivatives.

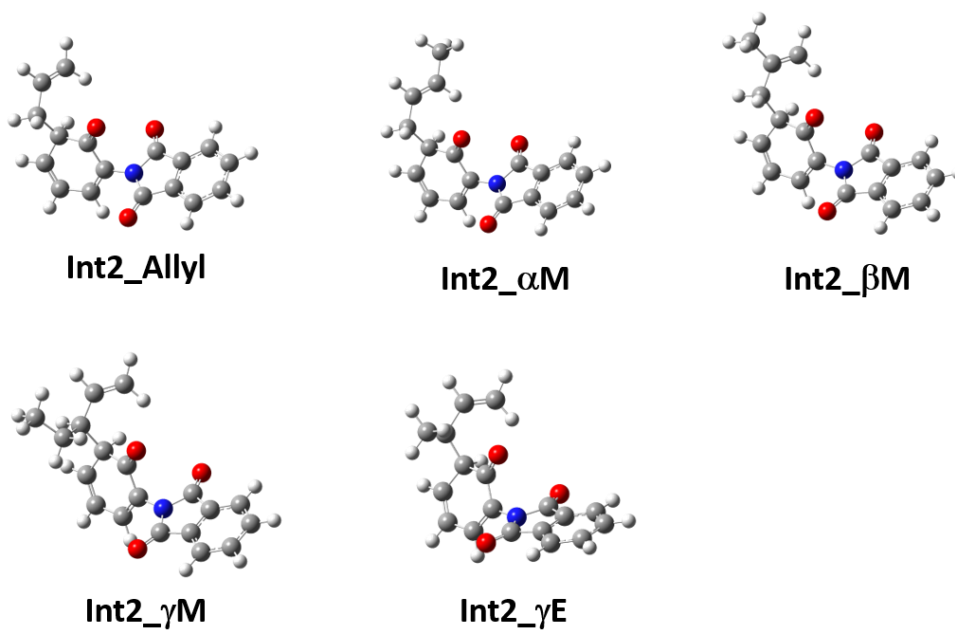


Figure 287. Geometry optimized intermediate structures Int2 of the CR process of all simulated allyl derivatives.

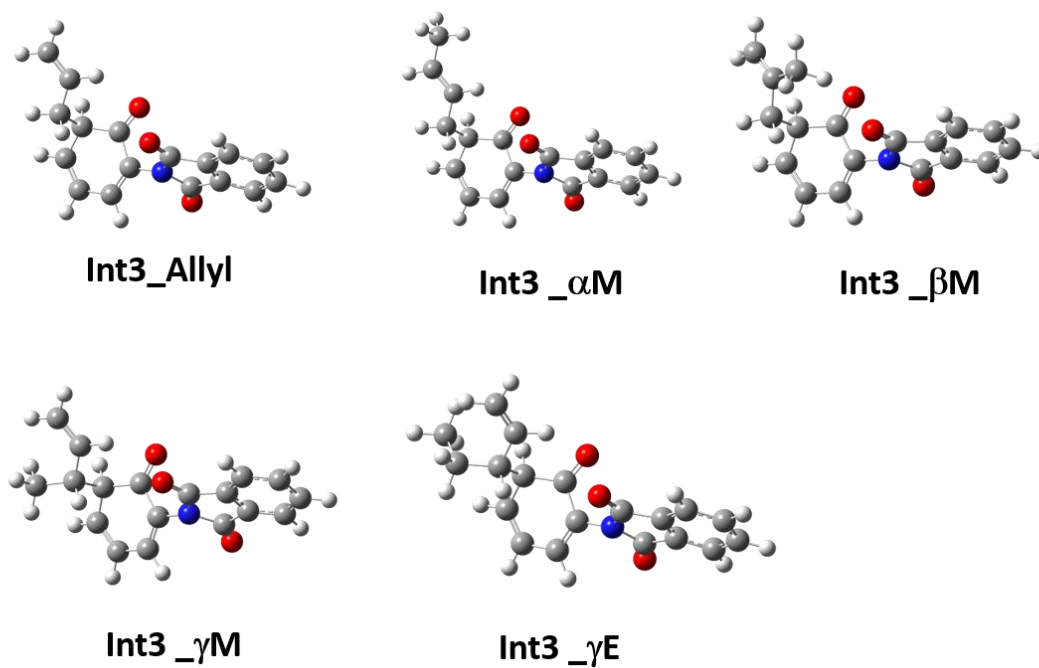


Figure 288. Geometry optimized intermediate structures Int2 of the CR process of all simulated allyl derivatives.

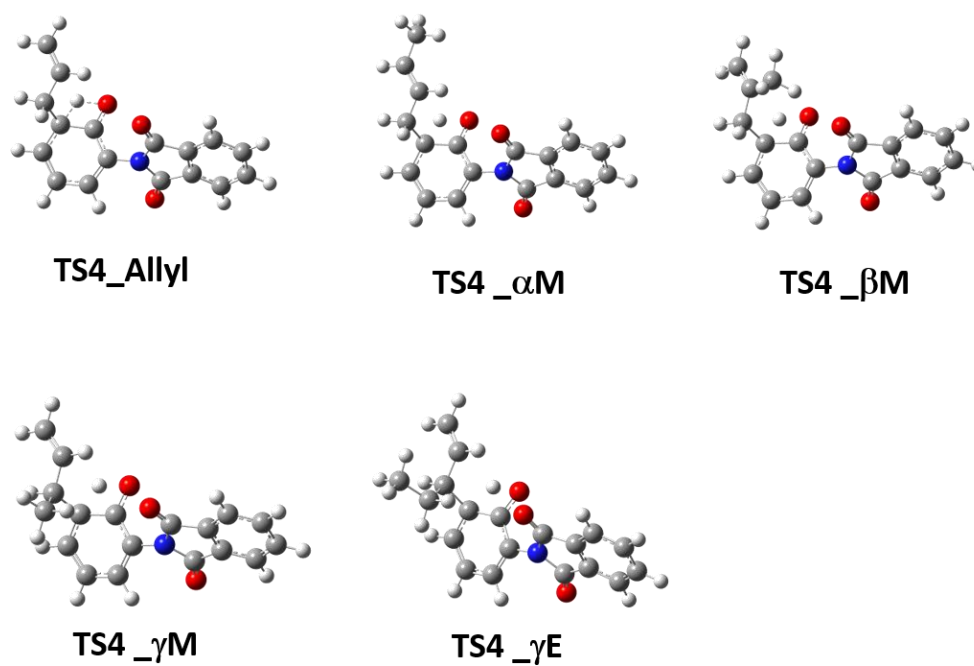


Figure 289. Geometry optimized transition-state structures TS4 of the CR process of all simulated allyl derivatives.

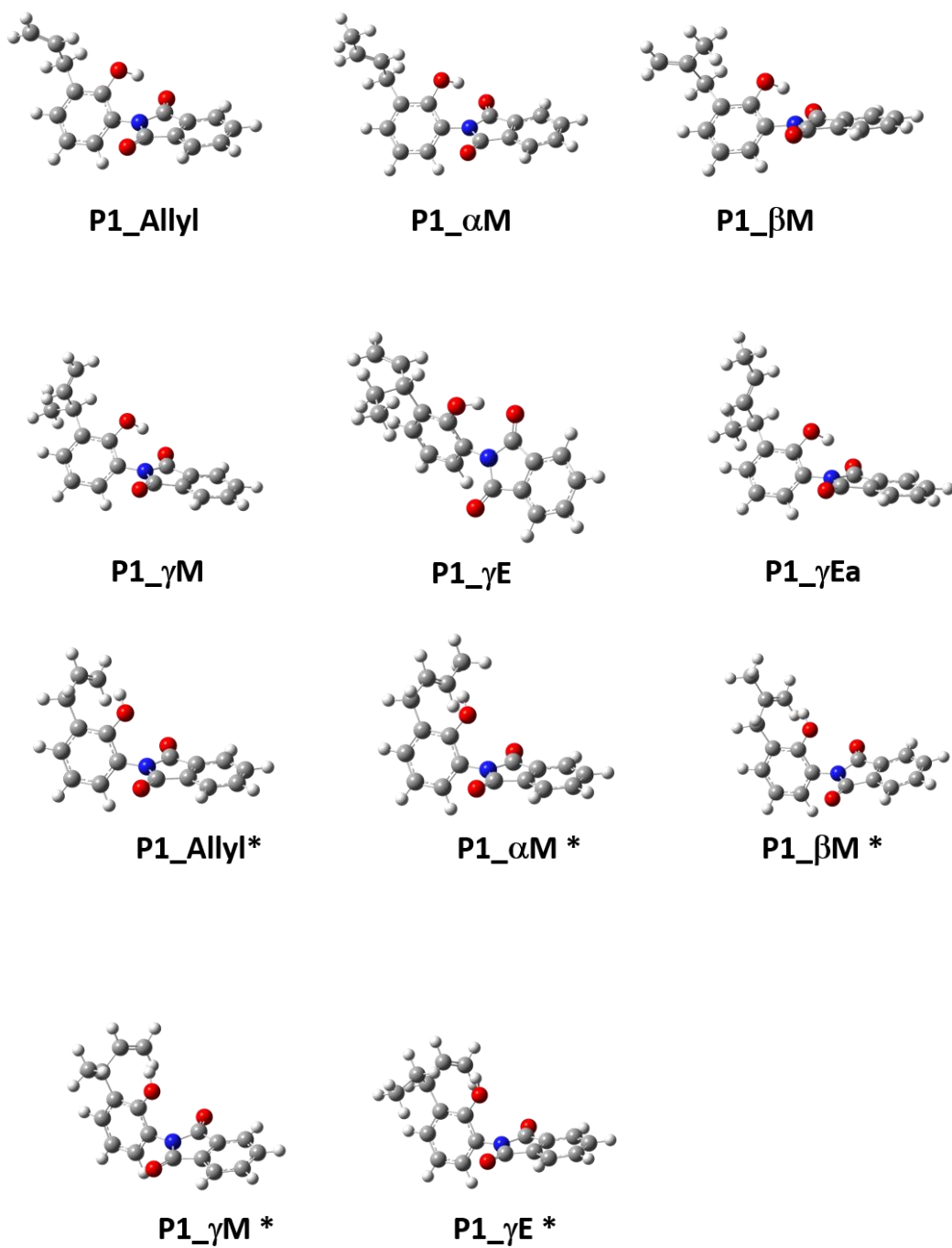


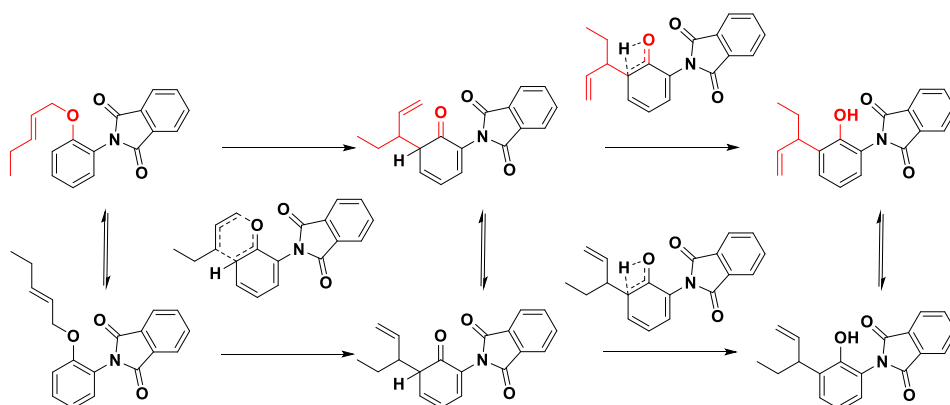
Figure 290. Geometry optimized product structures P1 of the CR process of all simulated allyl derivatives. Structures with an asterisk are the corresponding cis isomer.

Table 22. Single-Point energies, dipole momentum, imaginary frequency, and the simulated energy in relation to the starting structure E\_Model.

<b>E_</b>				
<i>Model</i>	Energy	Dipole momentum	IF [cm <sup>-1</sup> ]	dG <sub>rel</sub> (kcal/mol)
<b>Allyl</b>	-936,11	2,09		0
<b>aM</b>	-975,43	2,25		0
<b>bM</b>	-975,43	2,11		0
<b>gM</b>	-975,43	2,60		0
<b>gE</b>	-1014,75	2,59		0
<b>TS2_</b>				
<b>Allyl</b>	-936,06	1,93	-330,33	31,82
<b>aM</b>	-975,39	2,45	-253,9	27,97
<b>bM</b>	-975,38	2,00	-337,88	34,18
<b>gM</b>	-975,38	2,48	-298,75	32,86
<b>gE</b>	-1014,70	2,59	-283,87	32,92
<b>Int3_</b>				
<b>Allyl</b>	-936,09	2,24		9,65
<b>aM</b>	-975,42	1,82		8,52
<b>bM</b>	-975,41	2,48		13,25
<b>gM</b>	-975,41	2,34		15,91
<b>gE</b>	-975,41	2,28		18,22
<b>TS4_</b>				
<b>Allyl</b>	-936,01	2,39	-2177,12	64,73
<b>aM</b>	-975,33	2,00	-2175,44	63,57
<b>bM</b>	-975,33	2,63	-2184,80	67,52
<b>gM</b>	-975,32	2,37	-2185,63	68,71
<b>gE</b>	-1014,64	2,40	-2186,65	68,91
<b>P1_</b>				
<b>Allyl</b>	-936,13	4,52		-13,13
<b>aM</b>	-975,45	4,08		-13,98
<b>bM</b>	-975,45	4,72		-11,09

gM	-975,45	4,24	-7,72
gE	-1014,76	4,24	-7,49

### Abnormal Claisen-Rearrangement



Scheme 59. Normal and abnormal Claisen Rearrangement of  $\gamma$ E-PI.

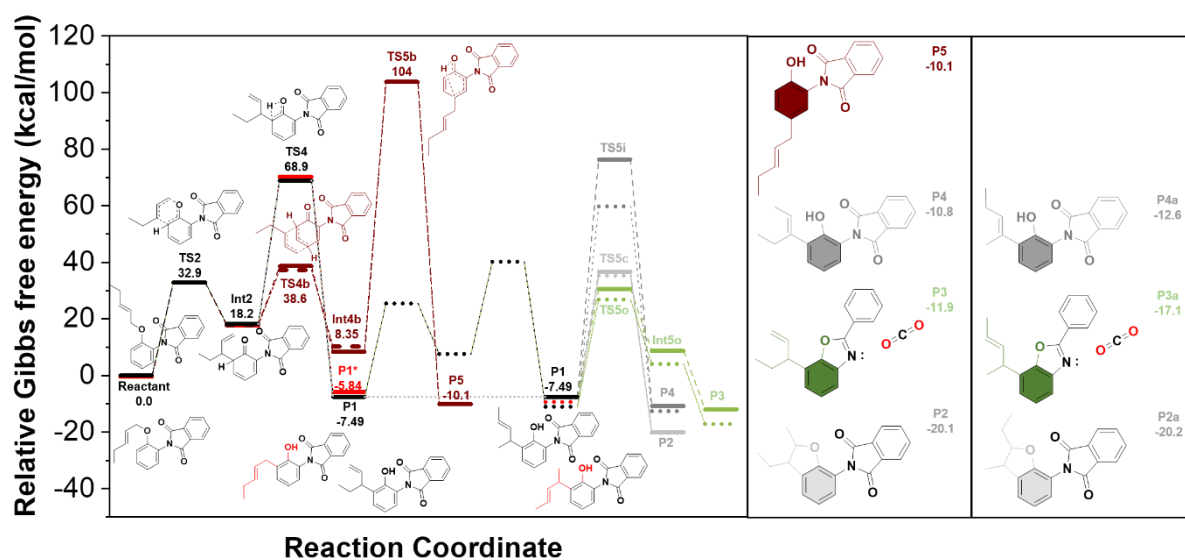


Figure 291. Simulated single-point energies of the geometry optimized reactants, products, intermediates, and transition-states of the cascade-type reactions of the  $\gamma$ Eallyl-Imide model.

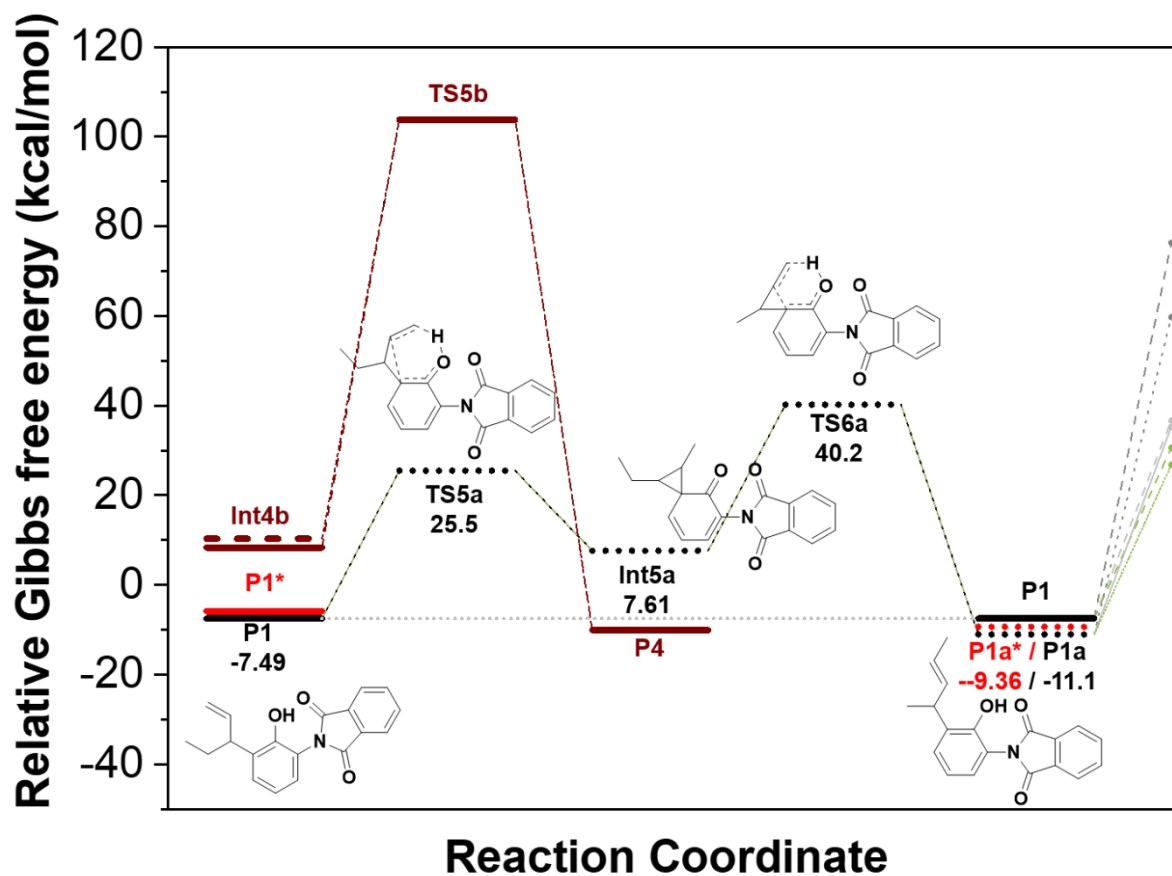


Figure 292. Simulated single-point energies of the geometry optimized reactants, products, intermediates, and transition-states of the abnormal Claisen Rearrangement reaction of the  $\gamma$ -allyl-imide model.

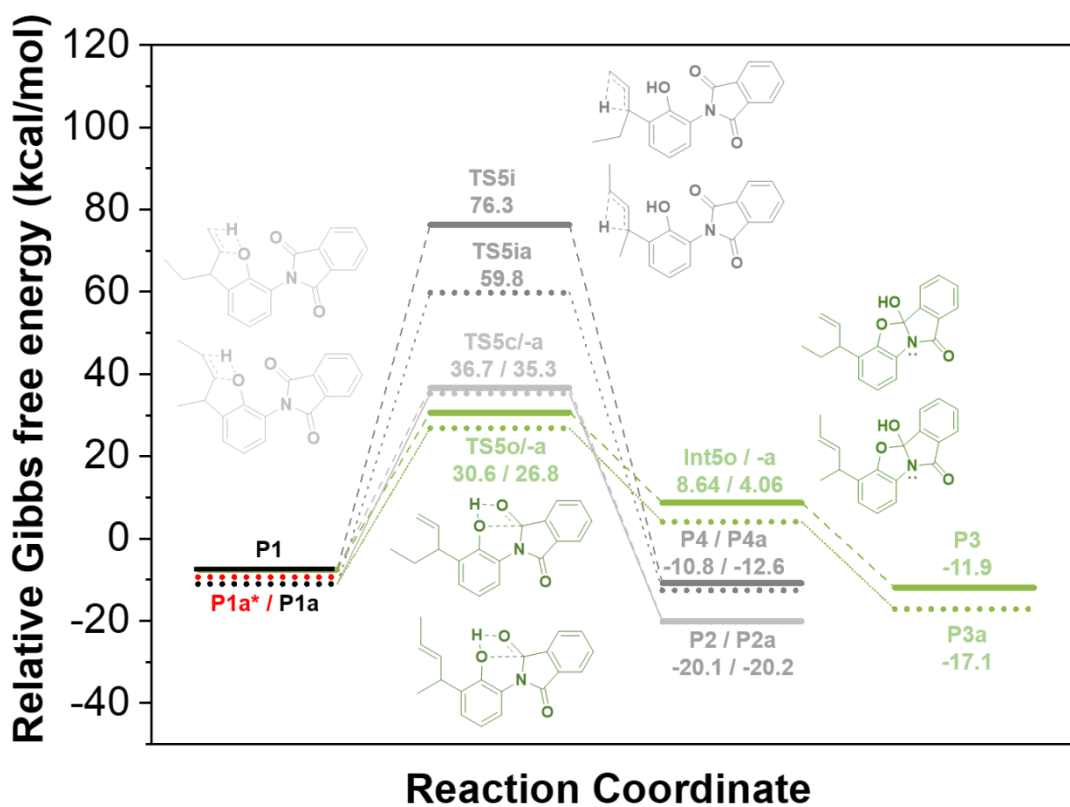


Figure 293. Simulated single-point energies of the geometry optimized reactants, products, intermediates, and transition-states of the Thermal Rearrangement (HPI-to-PBO) reaction of the  $\gamma$ Eallyl-Imide model.

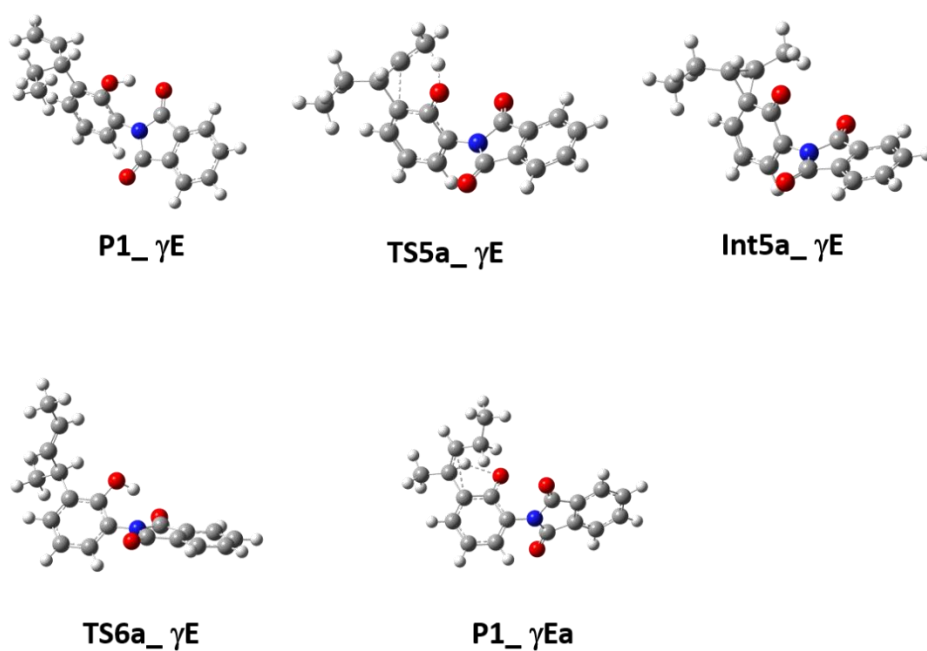


Figure 294. Geometry optimized structures of the abnormal CR process of the  $\gamma$ Eallyl-Imide model.

Table 23. Single-Point energies, dipole momentum, imaginary frequency, and the simulated energy of the abnormal CR in relation to the starting structure.

<b>Model</b>	<b>Energy</b>	<b>Dipole momentum</b>	<b>IF [cm<sup>-1</sup>]</b>	<b>dG<sub>rel</sub> (kcal/mol)</b>
<b>P1_gE</b>	-1014,76	4,24		-7,49
<b>TS5a_gE</b>	-1014,71	2,12	-943,06	25,51
<b>Int5a_gE</b>	-1014,74	1,66		7,61
<b>TS6a_gE</b>	-1014,69	4,69	-342,42	40,21
<b>P1_gEa</b>	-1014,77	4,05		-11,05



## Cis-Trans Isomerization

Between E and Int1

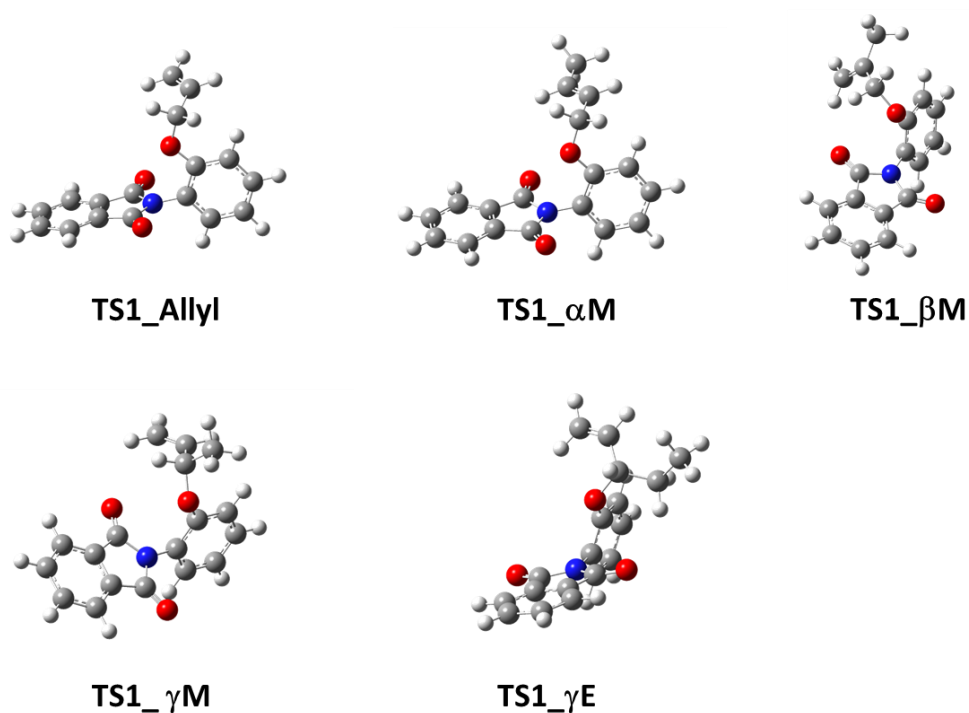


Figure 295. Geometry optimized transition-state structures of the cis-trans isomerization process of the starting material E.

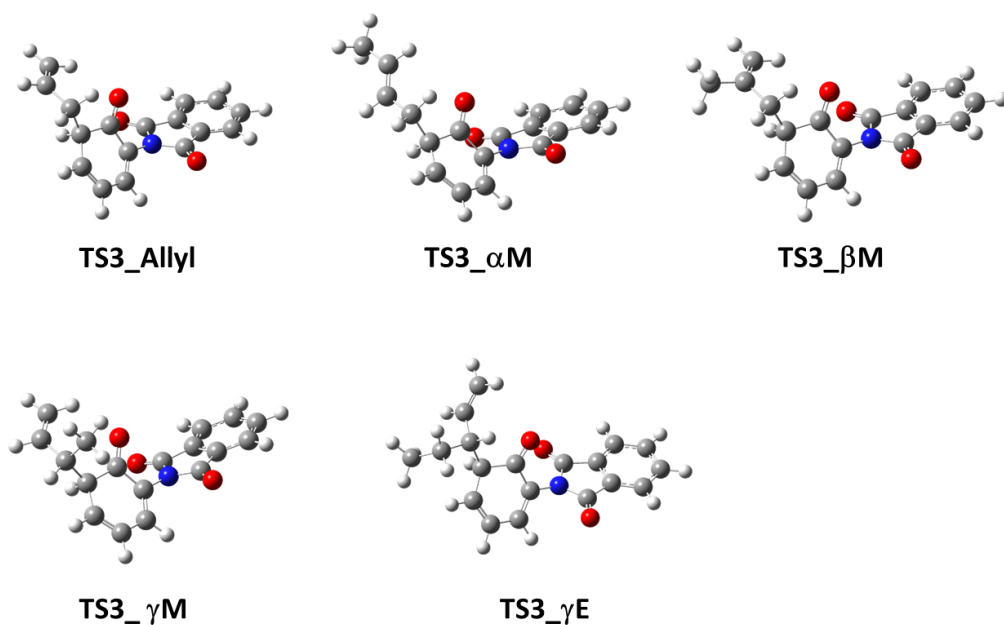


Figure 296. Geometry optimized transition-state structures of the cis-trans isomerization process of the product of the first step of the Claisen Rearrangement.

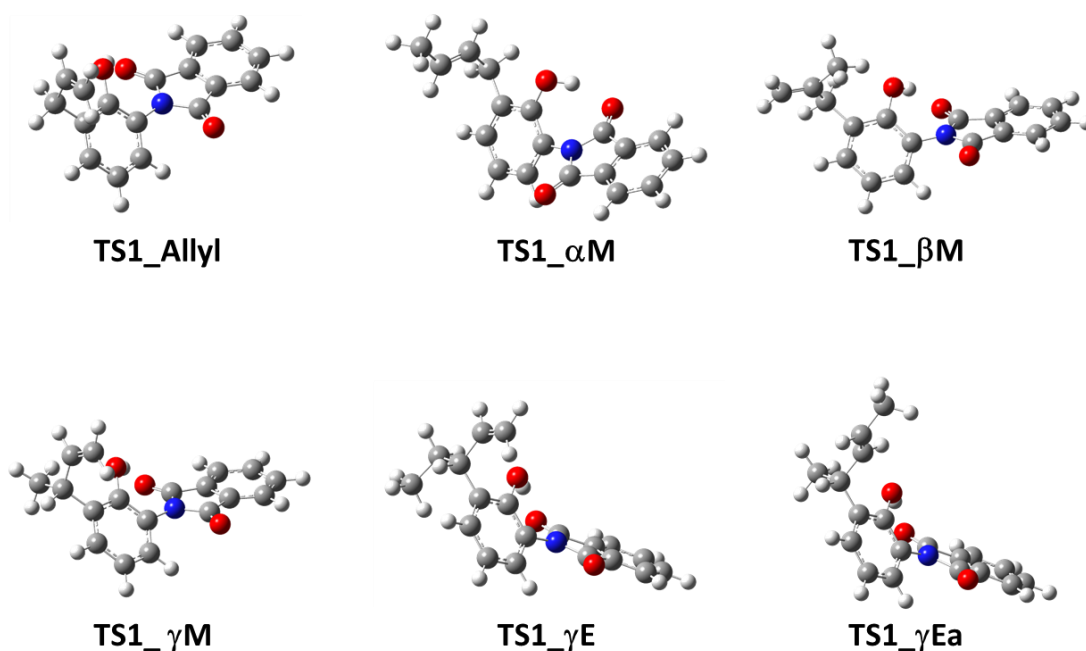


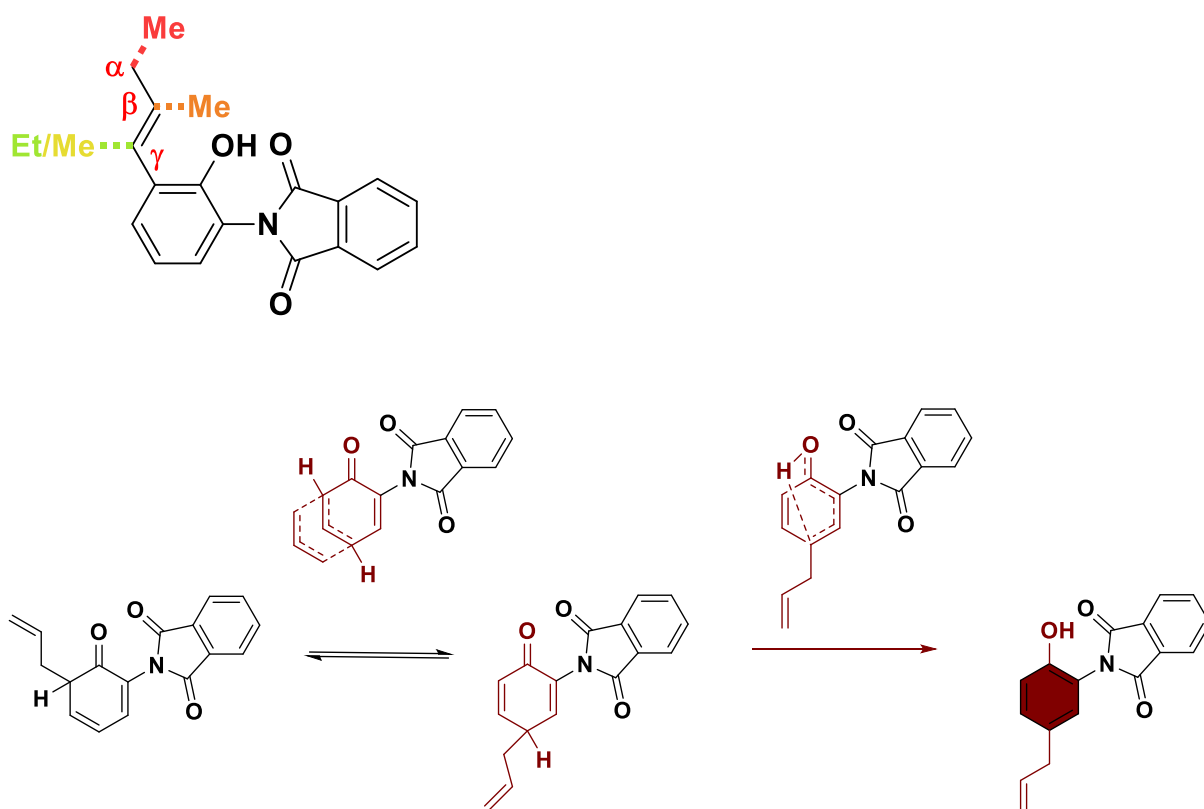
Figure 297. Geometry optimized transition-state structures of the cis-trans isomerization process of the final product of the Claisen Rearrangement.

Table 24. Single-Point energies, dipole momentum, imaginary frequency, and the simulated energy in relation to the starting structure, of the cis-trans isomerization of each step of the Claisen Rearrangement.

<b>TS1_</b>				
<b>Model</b>	<b>Energy</b>	<b>Dipole momentum</b>	<b>IF [cm<sup>-1</sup>]</b>	<b>dG<sub>rel</sub> (kcal/mol)</b>
<b>Allyl</b>	-936,11	2,12	-91,54	1,88
<b>aM</b>	-975,43	2,46	-73,49	-0,04
<b>bM</b>	-975,42	2,30	-152,16	8,59
<b>gM</b>	-975,42	2,38	-51,19	5,89
<b>gE</b>	-1014,74	2,39	-221,72	7,08
<b>E* (Int1_)</b>				
<b>Allyl</b>	-936,11	2,06		-0,71
<b>aM</b>	-975,43	2,25		-1,65
<b>bM</b>	-975,43	2,18		0,79
<b>gM</b>	-975,43	2,13	,	-0,34
<b>gE</b>	-1014,75	2,13		-0,37
<b>TS3_</b>				
<b>Allyl</b>	-936,09	2,16	-87,91	0,80
<b>aM</b>	-975,41	1,72	-207,08	2,61
<b>bM</b>	-975,41	2,03	-42,89	1,01
<b>gM</b>	-975,40	2,00	-83,12	1,79
<b>gE</b>	-1014,72	1,77	-196,86	4,12
<b>Int2_</b>				
<b>Allyl</b>	-936,09	1,94		11,83
<b>aM</b>	-975,42	1,44		9,54
<b>bM</b>	-975,41	1,69		13,54

<b>gM</b>	-975,41	1,8		16,86
<b>gE</b>	-1014,72	1,86		17,69
<b>TS6_</b>				
<b>Allyl</b>	-936,13	4,31	-11,91	0,40
<b>aM</b>	-975,45	4,08	-95,6	-2,13
<b>bM</b>	-975,45	4,69	-185,12	0,38
<b>gM</b>	-974,44			0,81
<b>gE</b>	-1014,76	4,35	-82,42	0,87
<b>gEa</b>	-1014,76	4,19	-199,44	-5,43
<b>P1*_</b>				
<b>Allyl</b>	-936,13	1,55		-10,98
<b>aM</b>	-975,45	1,87		-9,39
<b>bM</b>	-975,45	1,70		-9,51
<b>gM</b>	-975,44	1,52		-6,07
<b>gE</b>	-1014,76	1,48		-5,84
<b>gEa</b>	-1014,77	1,98		-9,36

## Cope Rearrangement



Scheme 60. Overview of the Cope-RearrangementCope Rearrangement (CoR) steps.

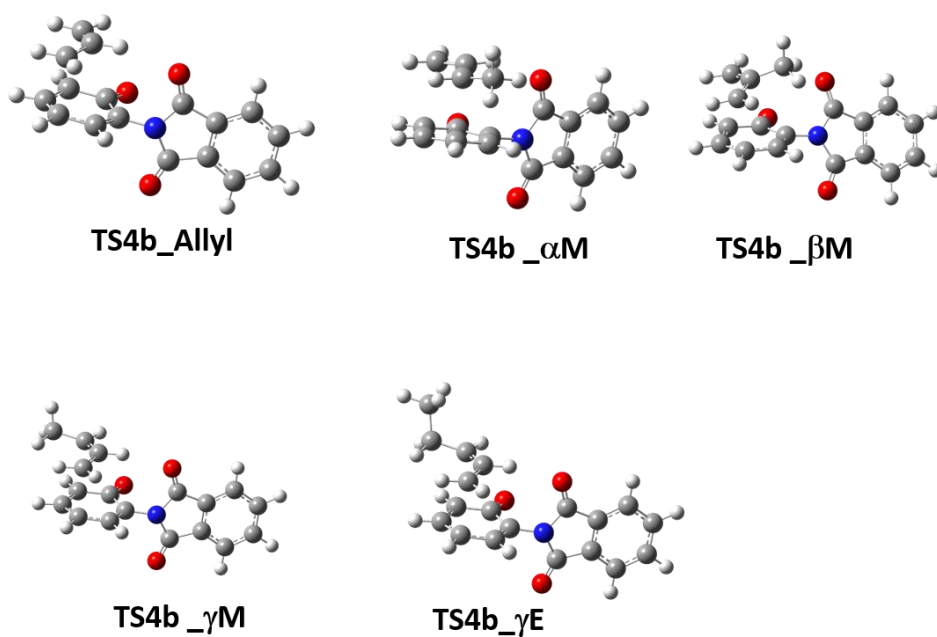


Figure 298. Geometry optimized transition-state structures of the first step of the CoR process of the Allyl-Imide models.

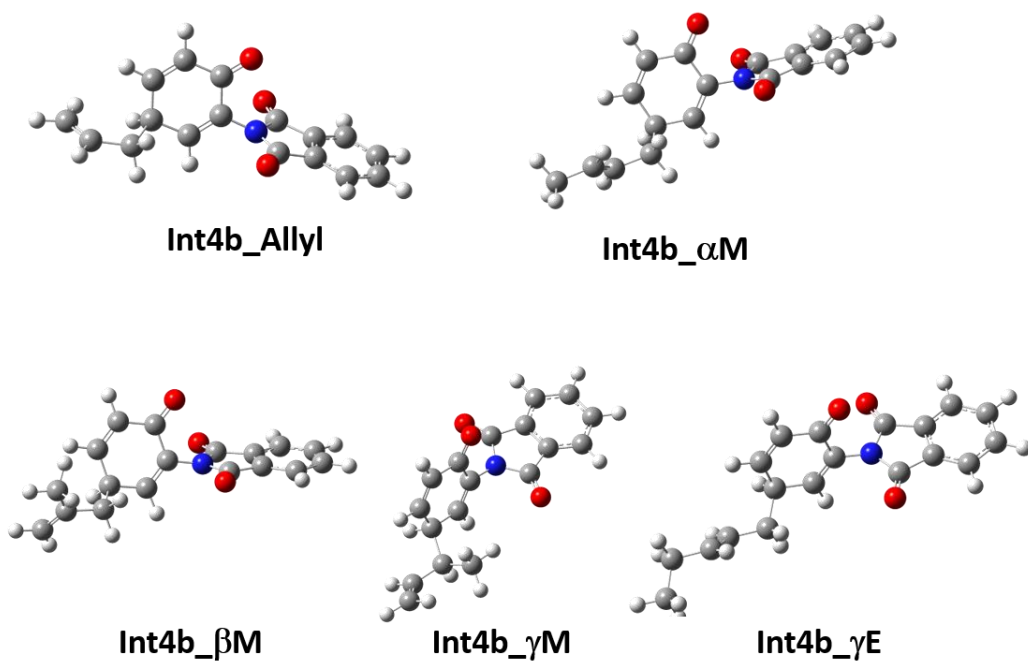


Figure 299. Geometry optimized intermediate structures of the first step of the CoR process of the Allyl-Imide models.

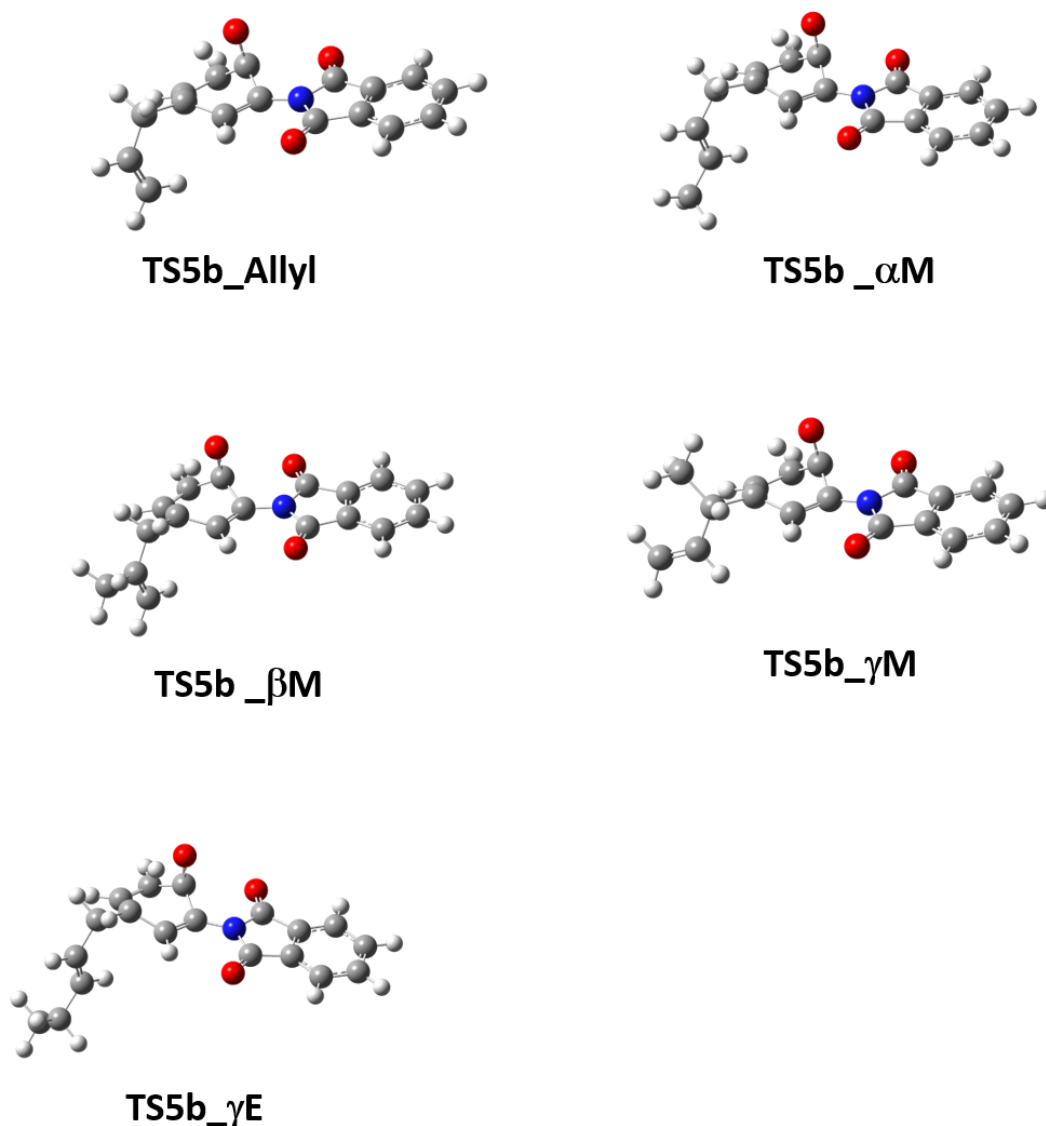


Figure 300. Geometry optimized transition-state structures of the second step of the CoR process of the Allyl-Imide models.

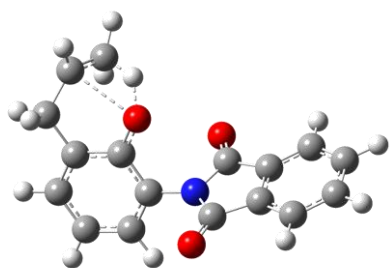
Table 25. Single-Point energies, dipole momentum, imaginary frequency, and the simulated energy in relation to the starting structure, of the CoR.

<b>Int3_</b>				
<b>Model</b>	<b>Energy</b>	<b>Dipole momentum</b>	<b>IF [cm<sup>-1</sup>]</b>	<b>dG<sub>rel</sub> (kcal/mol)</b>
<b>Allyl</b>	-936,09	2,24		9,65
<b>aM</b>	-975,42	1,82		8,52
<b>bM</b>	-975,41	2,48		13,25
<b>gM</b>	-975,41	2,34		15,91
<b>gE</b>	-975,41	2,28		18,22

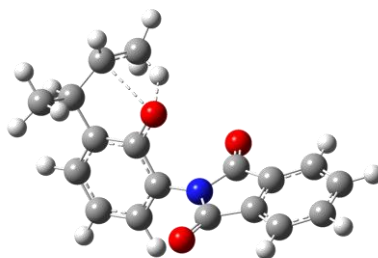
<b>TS4b_</b>				
<b>Allyl</b>	-936,05	4,09	-154,46	36,34
<b>aM</b>	-975,37	4,80	-204,82	35,18
<b>bM</b>	-975,37	3,52	-238,92	41,27
<b>gM</b>	-975,37	3,96	-209,00	38,58
<b>gE</b>	-1014,69	4,03	-201,11	38,64
<b>Int4b_</b>				
<b>Allyl</b>	-936,09	3,95		10,89
<b>aM</b>	-975,41	4,33		11,10
<b>bM</b>	-975,42	3,26		11,45
<b>gM</b>	-975,42	3,64		8,41
<b>gE</b>	-1014,74	3,68		8,35
<b>TS5b_</b>				
<b>Allyl</b>	-935,95	3,39	-1778,46	103,20
<b>aM</b>	-975,26	3,35	-1771,72	106,49
<b>bM</b>	-975,27	3,69	-1778,05	105,35
<b>gM</b>	-975,27	3,09	-1779,61	103,84
<b>gE</b>	-1014,58	3,14	-1778,23	103,76
<b>P5_</b>				
<b>Allyl</b>	-936,13	3,95		-10,65
<b>aM</b>	-975,45	3,91		-7,46
<b>bM</b>	-975,45	4,17		-8,97
<b>gM</b>	-975,45	3,53		-10,02
<b>gE</b>	-1014,77	3,55		-10,08

## Cyclization and isomerization

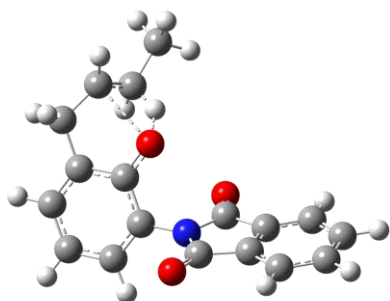
### Cyclization



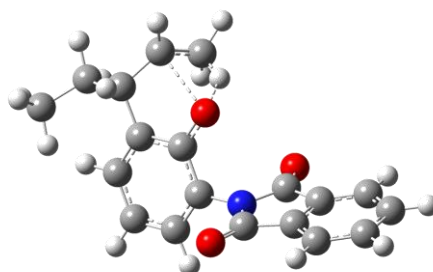
**TS5c\_allyl**  
**33.4 kcal/mol**



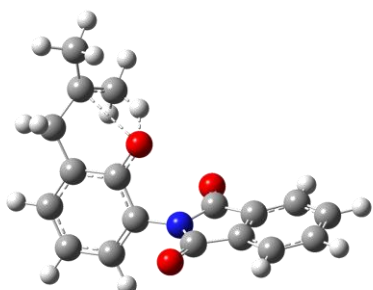
**TS5c\_γM**  
**36.2 kcal/mol**



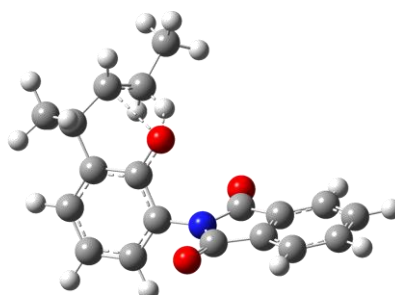
**TS5c\_αM**  
**34.9 kcal/mol**



**TS5c\_γE**  
**36.7 kcal/mol**



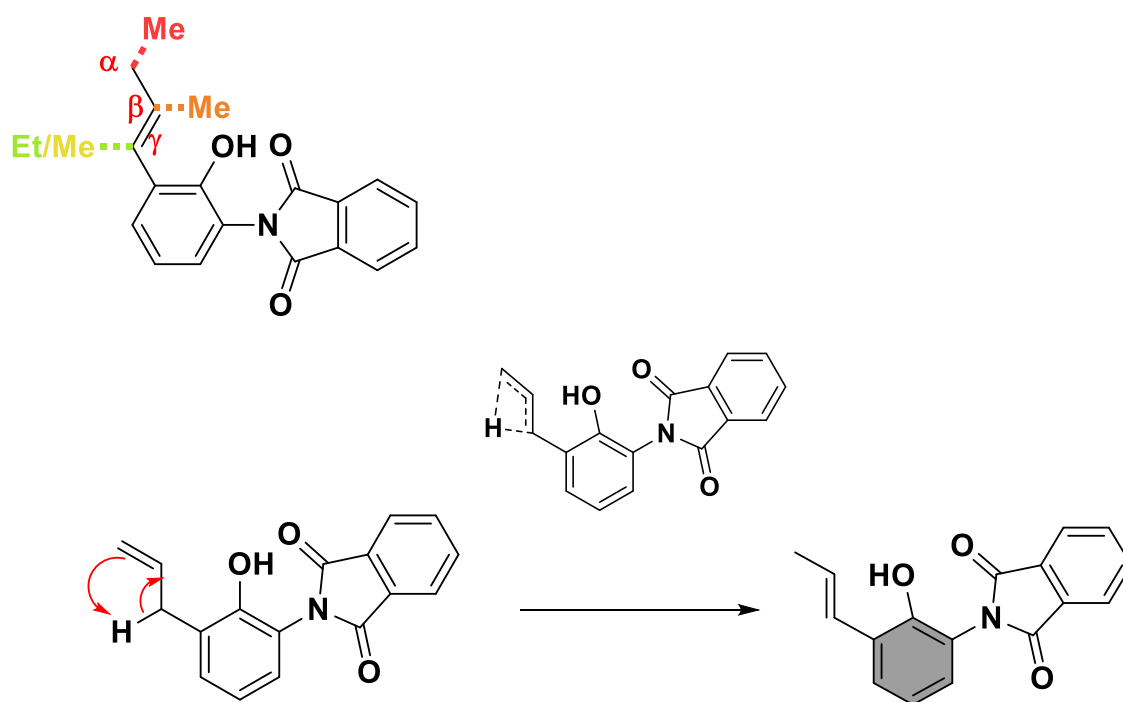
**TS5c\_βM**  
**29.8 kcal/mol**



**TS5c\_γEa**  
**35.3 kcal/mol**

*Figure 301. Geometry optimized transition-state structures of the benzofuran cyclization process of the Allyl-Imide models.*

## Isomerization



Scheme 61. Overview of the double bond isomerization of the allyl group.

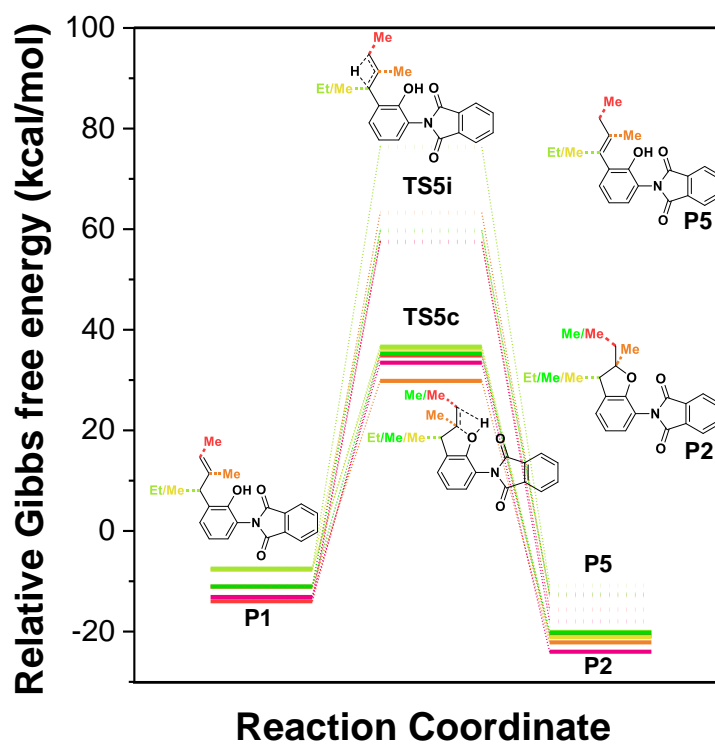


Figure 302. Simulated single-point energies of the geometry optimized reactants, products, and transition-states of the cyclization reaction of the ortho-allyl-phenol to benzofuran of the Allyl-imide models.



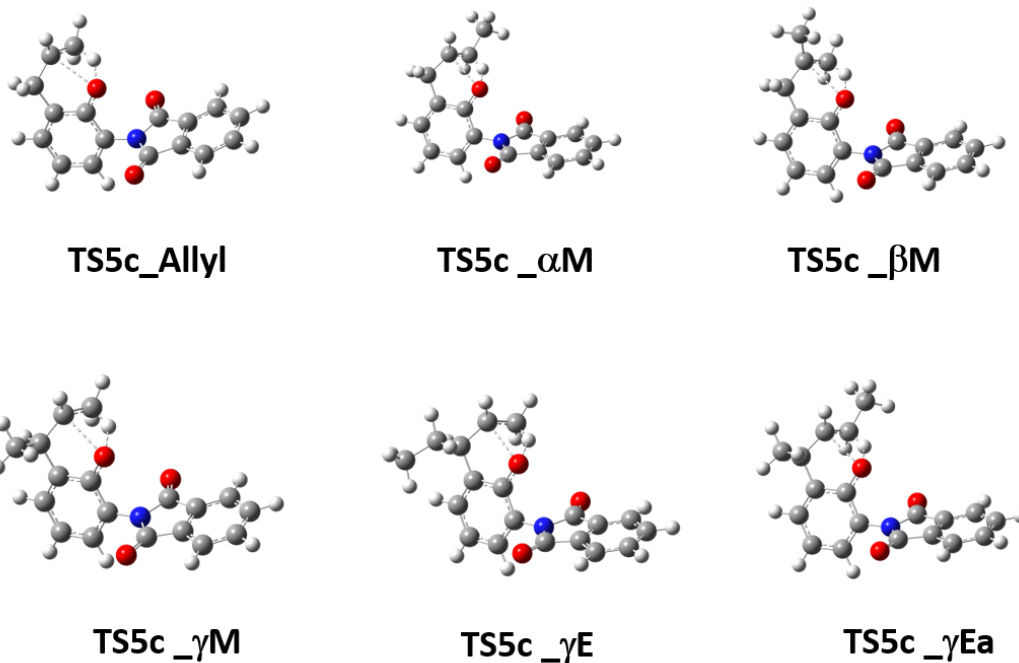


Figure 303. Geometry optimized transition-state structures of the ortho-allyl-phenol to benzofuran reaction of the Allyl-imide models.

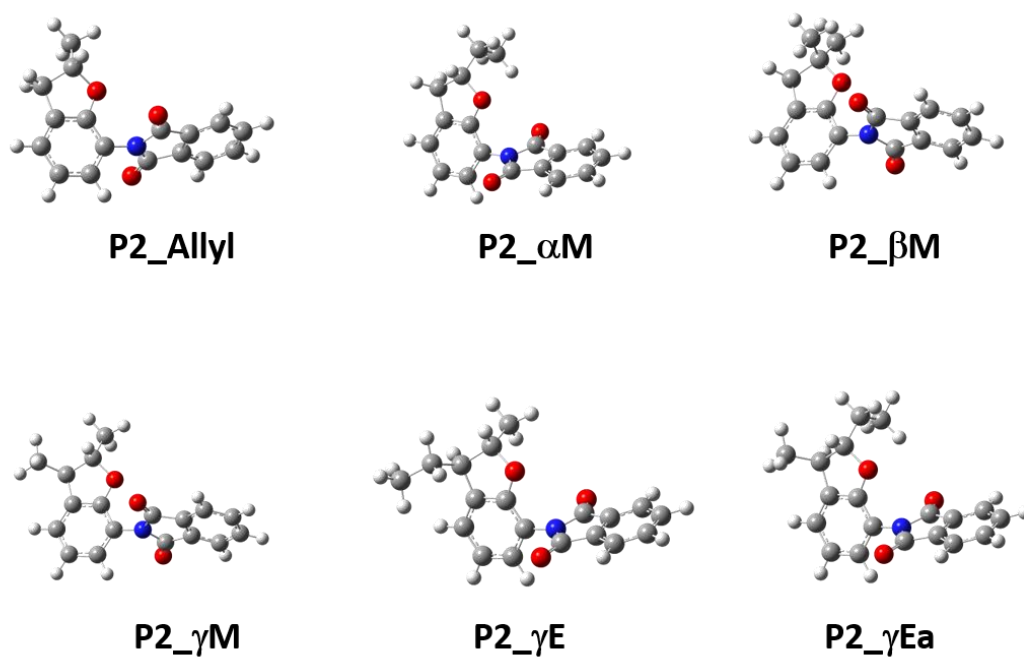


Figure 304. Geometry optimized product structures of the ortho-allyl-phenol to benzofuran reaction of the Allyl-imide models.

Table 26. Single-Point energies, dipole momentum, imaginary frequency, and the simulated energy in relation to the starting structure, of the ortho-allyl-phenol to benzofuran reaction.

<b>TS5c_</b>				
<b>Model</b>	<b>Energy</b>	<b>Dipole momentum</b>	<b>IF [cm<sup>-1</sup>]</b>	<b>dG<sub>rel</sub> (kcal/mol)</b>
<b>Allyl</b>	-936,056	3,792	-853,410	33,444
<b>aM</b>	-975,375	4,196	-787,910	34,899
<b>bM</b>	-975,387	5,363	-518,630	29,834
<b>gM</b>	-975,375	3,554	-1040,770	36,241
<b>gE</b>	-1014,692	3,532	-996,080	36,652
<b>gEa</b>	-1014,694	3,998	-907,070	35,290
<b>P2_</b>				
<b>Allyl</b>	-936,148	1,834		-23,999
<b>aM</b>	-975,464	1,878		-20,878
<b>bM</b>	-975,470	1,947		-22,137
<b>gM</b>	-975,467	1,785		-21,119
<b>gE</b>	-1014,782	1,705		-20,070
<b>gEa</b>	-1014,782	1,825		-20,226

## Isomerization

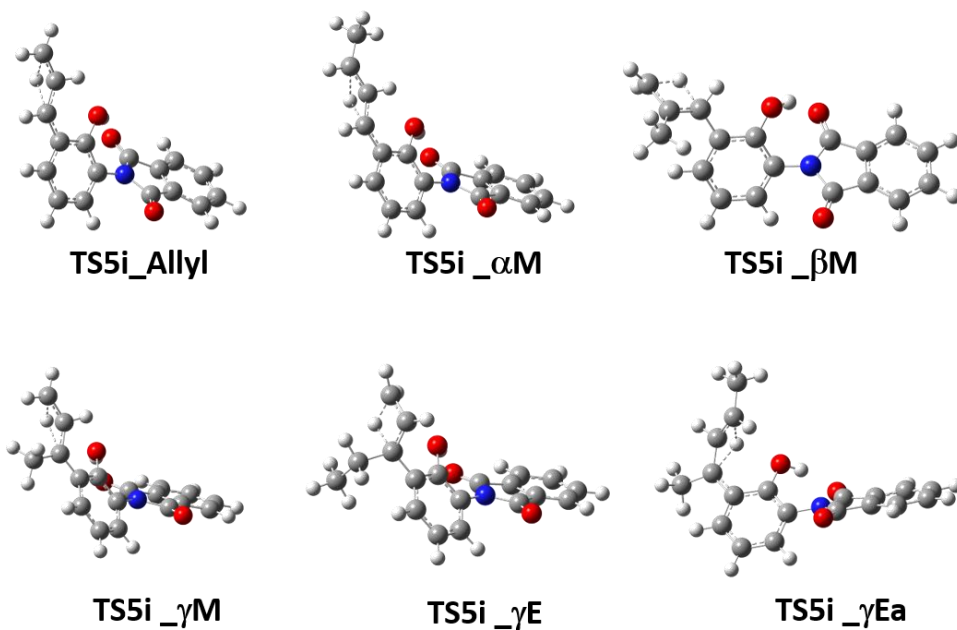


Figure 305. Geometry optimized transition-state structures of the double bond isomerization of the Allyl-imide models.

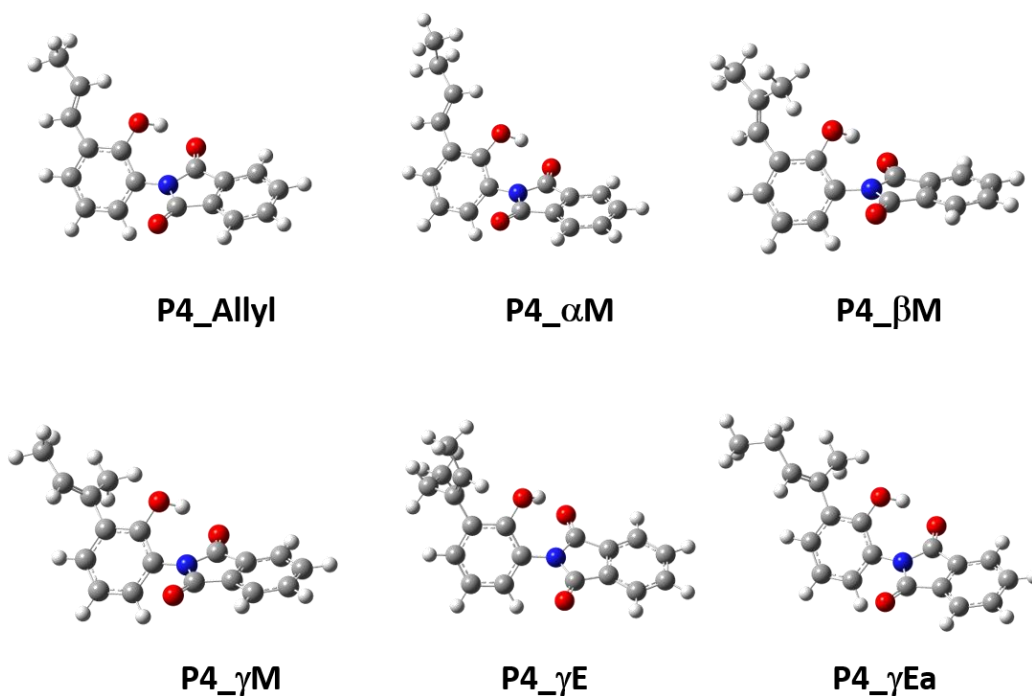


Figure 306. Geometry optimized product structures of the double bond isomerization of the Allyl-imide models.

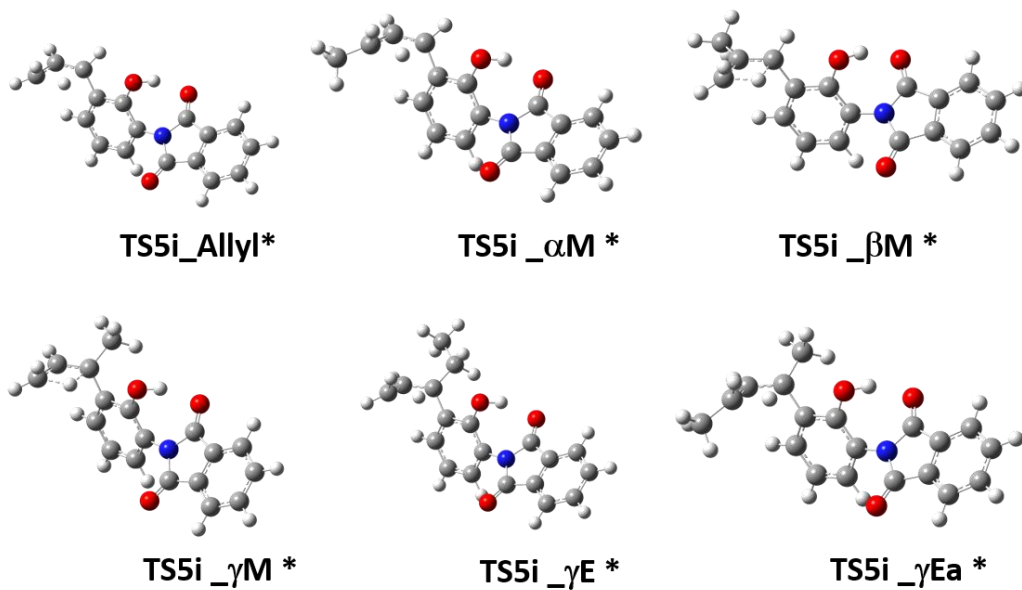


Figure 307. Geometry optimized transition-state structures of the double bond isomerization of the cis-Allyl-imide models.

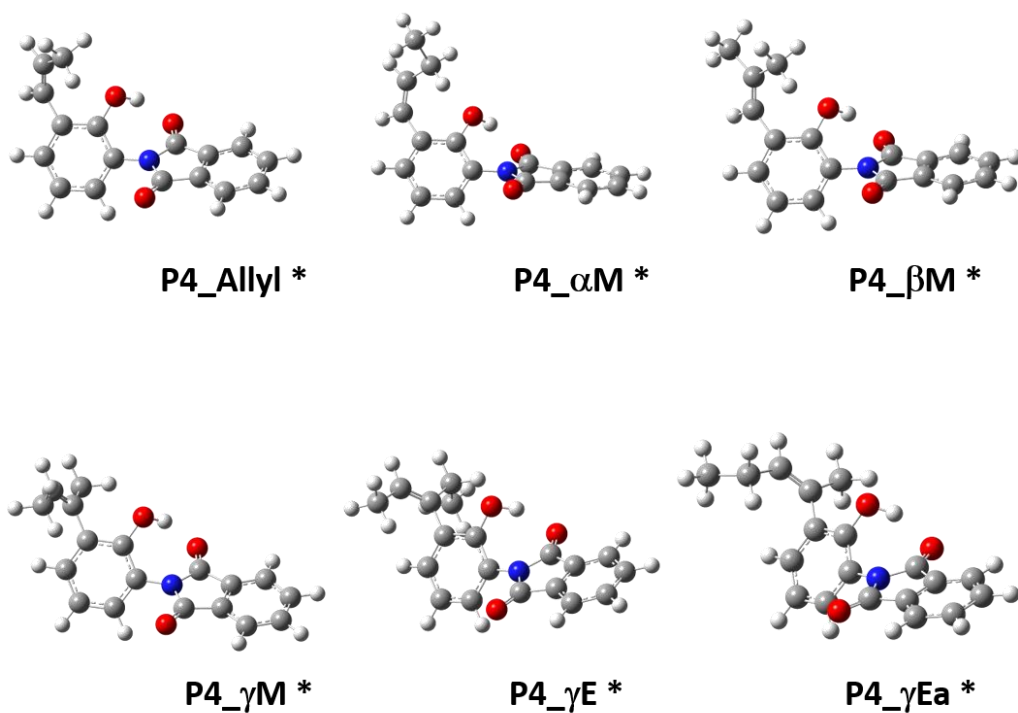


Figure 308. Geometry optimized product structures of the double bond isomerization of the cis-Allyl-imide models.

Table 27. Single-Point energies, dipole momentum, imaginary frequency, and the simulated energy in relation to the starting structure, of the double bond isomerization.

<b>TS5i_</b>				
<b>Model</b>	<b>Energy</b>	<b>Dipole momentum</b>	<b>IF [cm<sup>-1</sup>]</b>	<b>dG<sub>rel</sub> (kcal/mol)</b>
<b>Allyl</b>	-936,018	4,461	-605,000	57,533
<b>aM</b>	-975,339	3,737	-514,700	57,437
<b>bM</b>	-975,334	4,101	-1830,050	63,277
<b>gM</b>	-975,338	4,325	-602,350	59,446
<b>gE</b>	-1014,629	4,514	-1853,280	76,338
<b>gEa</b>	-1014,655	3,974	-554,620	59,764
<b>P4_</b>				
<b>Allyl</b>	-936,138	4,166		-17,984
<b>aM</b>	-975,456	4,184		-15,643
<b>bM</b>	-975,455	3,960		-12,880
<b>gM</b>	-975,453	3,991		-12,677
<b>gE</b>	-1014,768	3,848		-10,841
<b>gEa</b>	-1014,770	4,025		-12,582

## Thermal Rearrangement

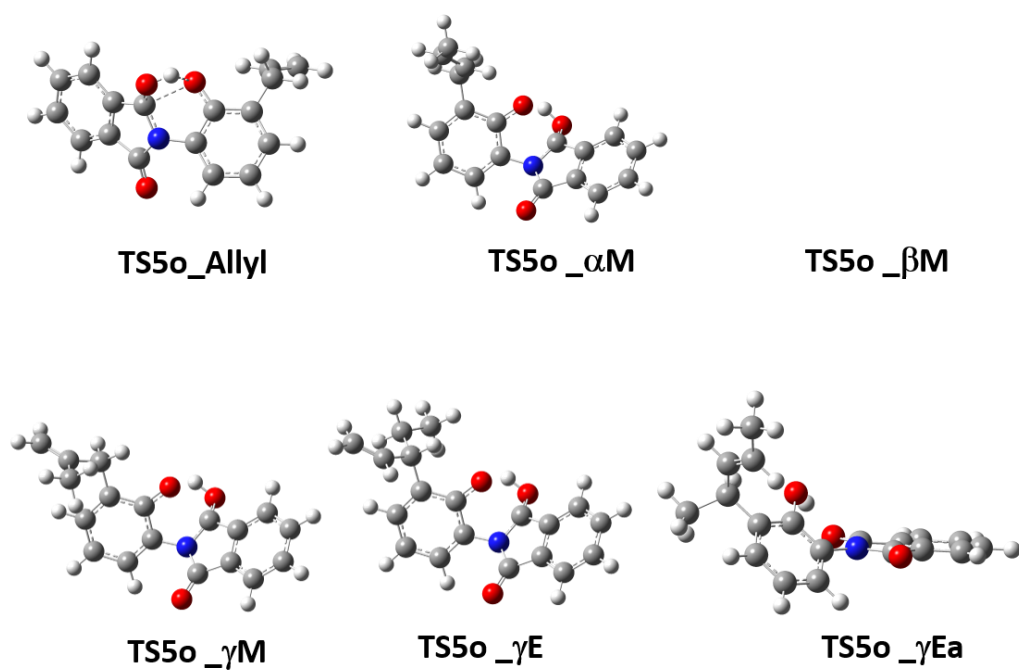


Figure 309. Geometry optimized transition-state structures of the HPI-to-PBO formation (Thermal Rearrangement) of the allyl-imide models.

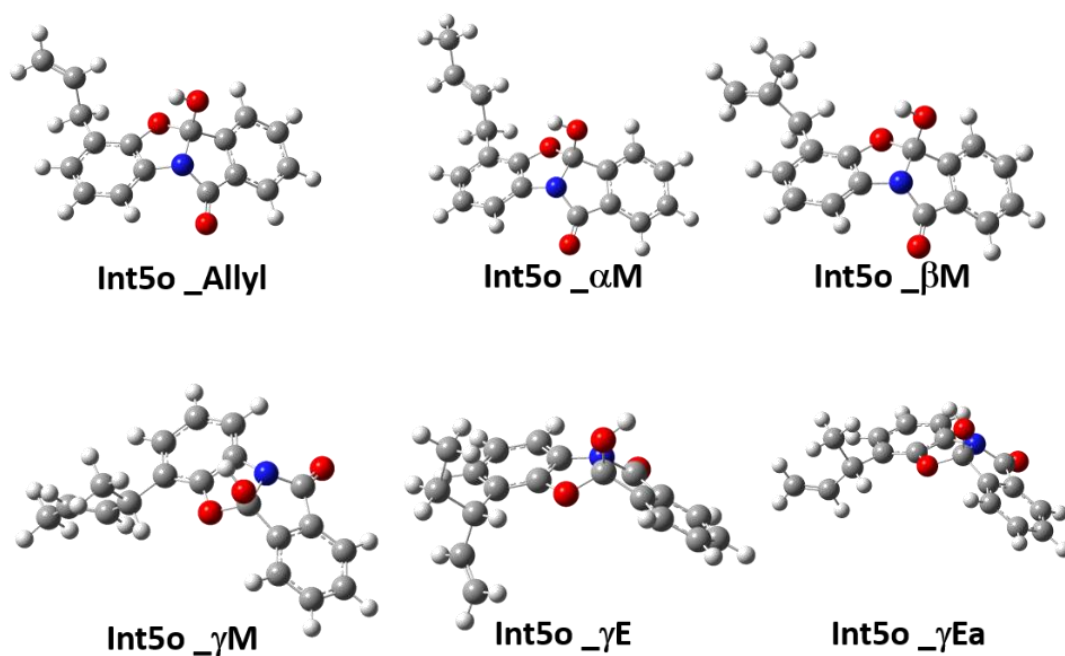


Figure 310. Geometry optimized intermediate structures of the HPI-to-PBO formation (Thermal Rearrangement) of the allyl-imide models.

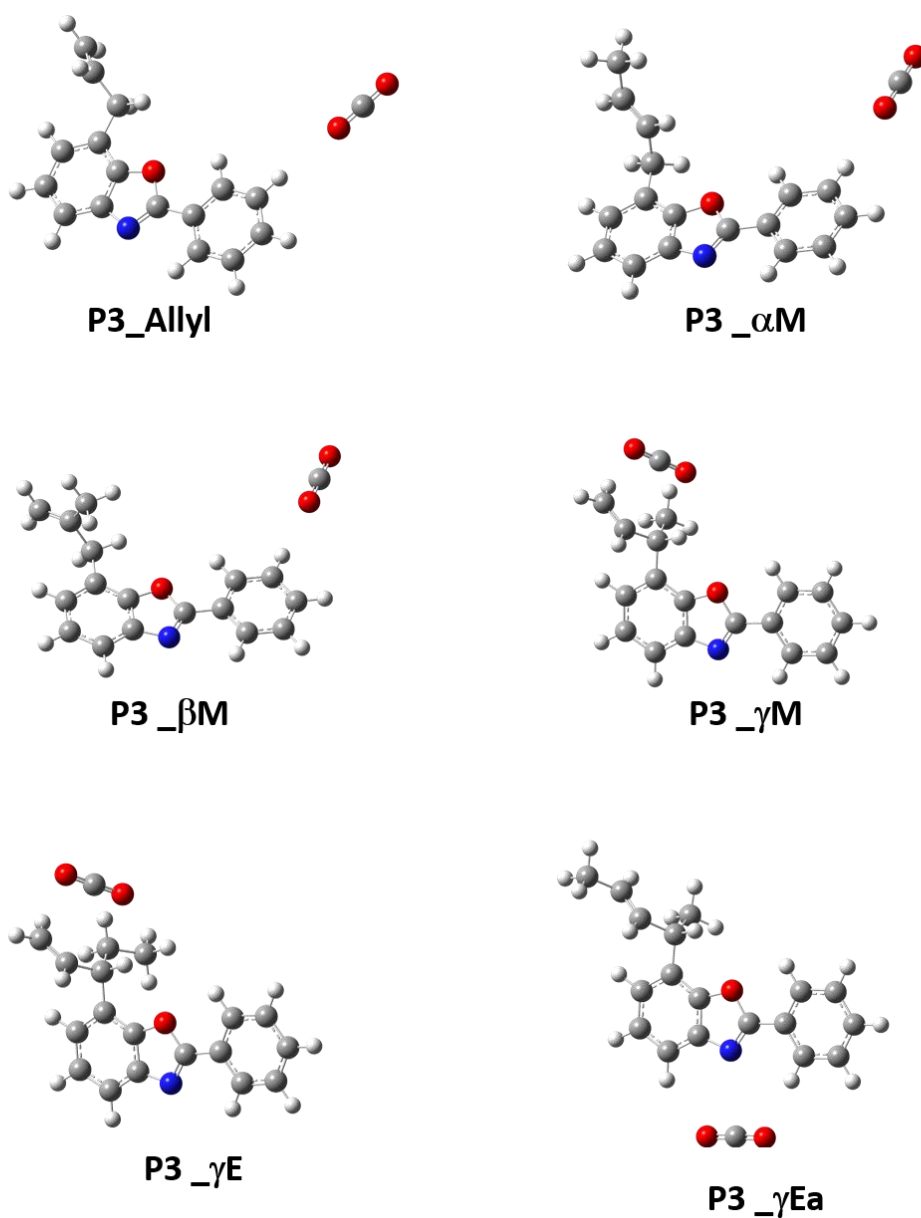


Figure 311. Geometry optimized product structures of the HPI-to-PBO formation (Thermal Rearrangement) of the allyl-imide models.

Table 28. Single-Point energy (SPE), dipole momentum, imaginary frequency (IF) and the simulated energy in relation to the starting structure  $\Delta G_{rel}$ , of the HPI-toPBO formation (Thermal Rearrangement).

<b>TS5o_</b>				
<b>Model</b>	<b>SPE</b>	<b>Dipole momentum</b>	<b>IF [cm<sup>-1</sup>]</b>	<b><math>\Delta G_{rel}</math> (kcal/mol)</b>
<b>Allyl</b>	-936,07	4,35	-294,51	25,33
<b>aM</b>	-975,39	4,12	-296,08	24,52
<b>bM</b>	-975,39	4,52	-288,78	27,08
<b>gM</b>	-975,39	4,45	-287,91	29,80
<b>gE</b>	-1014,70	4,41	-290,11	30,65
<b>gEa</b>	-1014,71	4.01	-288,76	26,83
<b>Int5o_</b>				
<b>Allyl</b>	-936,11	2,41		2,63
<b>aM</b>	-975,43	2,75		1,63
<b>bM</b>	-975,43	2,52		4,35
<b>gM</b>	-975,42	2,57		7,20
<b>gE</b>	-1014,74	2,82		8,65
<b>gEa</b>	-1014,74	2,80		4,06
<b>P3_</b>				
<b>Allyl</b>	-747,55	1,32		-16,87
<b>aM</b>	-786,87	1,64		-17,82
<b>bM</b>	-786,87	1,39		-15,13
<b>gM</b>	-786,86	1,45		-12,57
<b>gE</b>	-826,18	1,43		-11,95
<b>gEa</b>	-826,18	1,71		-17,14

## Crosslinking

Table 29. Single-Point energy (SPE) and the simulated energy in relation to the starting structure  $\Delta G_{rel}$ , of two allyl-imide models in relation to the starting material and CR product



P1. P1 is the CR product, P4 is the product of the double bond isomerization. P1\_P1 is a dimer consisting of two P1 structures, and P1\_P4 consists of a P1 and P4 model.

Dimer	SPE (Hartree)	$\Delta G_{rel}$ (Rel. to E) (kcal/mol)	$\Delta G_{rel}$ (Rel. to P1) (kcal/mol)	SPE (Hartree)	$\Delta G_{rel}$ (Rel. to E) (kcal/mol)	$\Delta G_{rel}$ (Rel. to P1) (kcal/mol)
	P1_P1			P1_P4		
<b>Allyl</b>	-1872,269	-17,824	-13,127	-1872,278	-23,566	-17,984
<b>aM</b>	-1950,914	-18,930	-13,979	-1950,918	-21,615	-15,643
<b>bM</b>	-1950,912	-15,820	-11,088	-1950,918	-19,677	-12,879
<b>gM</b>	-1950,899	-12,731	-7,72	-1950,907	-18,090	-12,676
<b>gE</b>	-2029,532	-12,470	-7,492	-2029,536	-14,792	-10,84
<b>gEa</b>	-2029,544	-16,102	-11,052	-2029,546	-17,716	-12,582

Table 30. Single-Point energy (SPE) of the crosslinked models. SPE of all models for various crosslinking mechanism between both allyl groups.

Px_	SPE (Hartree)					
	Allyl	aM	bM	gM	gE	gEa
<b>ee_</b>	-1872,284	-1950,915	-1950,922	-1950,915	-2029,549	-2029,547
<b>ee_b</b>	-1872,293	-1950,925	-1950,927	-1950,925	-2029,557	-2029,556
<b>em_6</b>	-1872,283	-1950,909	-1950,907	-1950,916	-2029,546	-2029,543
<b>mm_b/c</b>	-1872,283	-1950,918		-1950,910	-2029,531	-2029,547
<b>ea</b>	-1872,283	-1950,920	-1950,914	-1950,909	-2029,536	-2029,531
<b>ma</b>	-1872,279	-1950,916	-1950,887	-1950,891	-2029,521	-2029,523
<b>fe</b>	-1872,290	-1950,911	-1950,917	-1950,922	-2029,554	-2029,544
<b>ve</b>	-1872,291	-1950,911	-1950,918	-1950,909	-2029,531	-2029,532
<b>fm</b>	-1872,286	-1950,920		-1950,916	-2029,548	-2029,537
<b>vm</b>	-1872,291	-1950,922	-1950,903			
<b>fa</b>	-1872,276	-1950,911	-1950,882	-1950,884	-2029,514	-2029,517

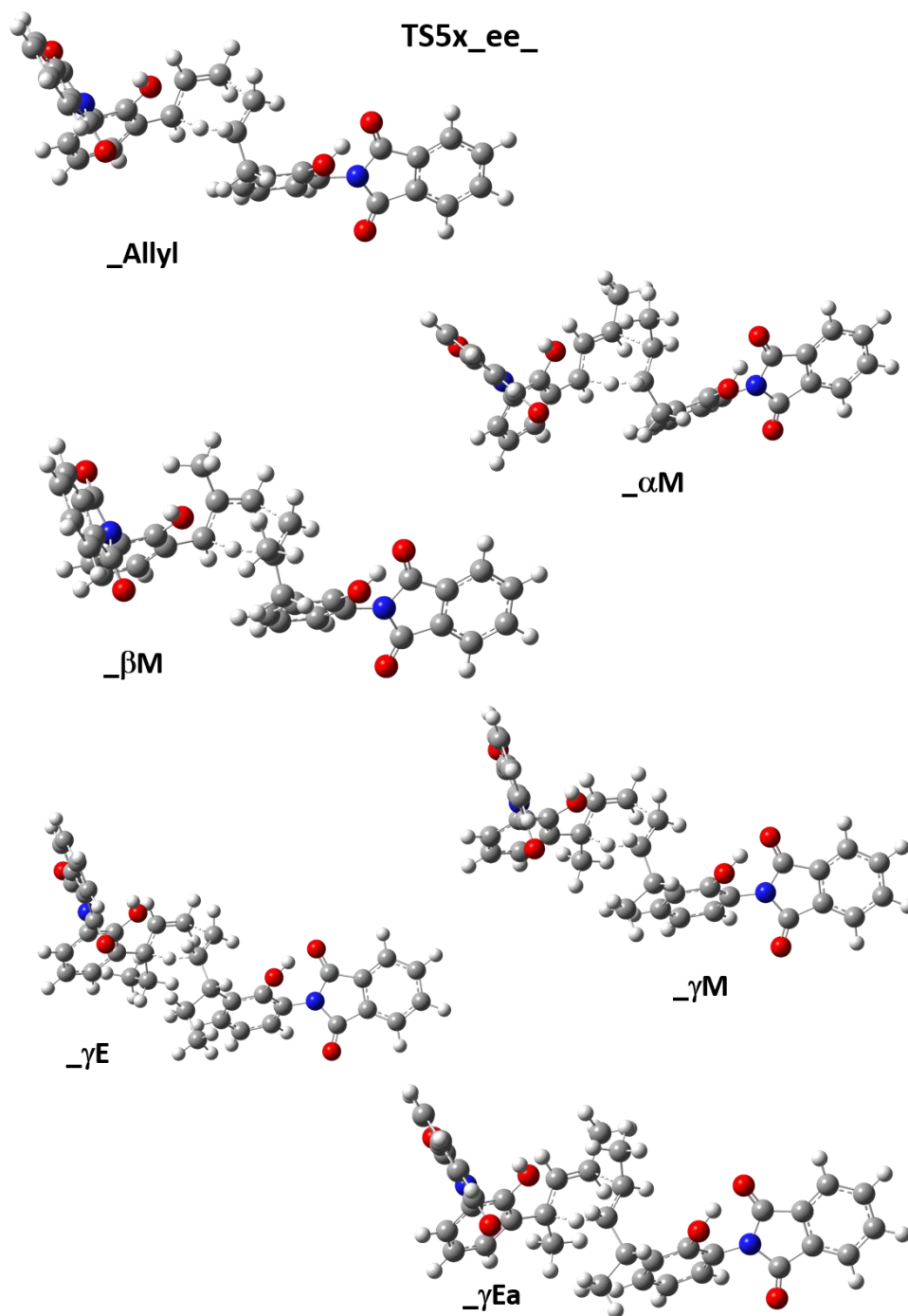


Figure 312. Geometry optimized transition-state structures of the allyl-crosslinking via C3-C3 atoms allyl group of the allyl-imide models (ee-mechanism).

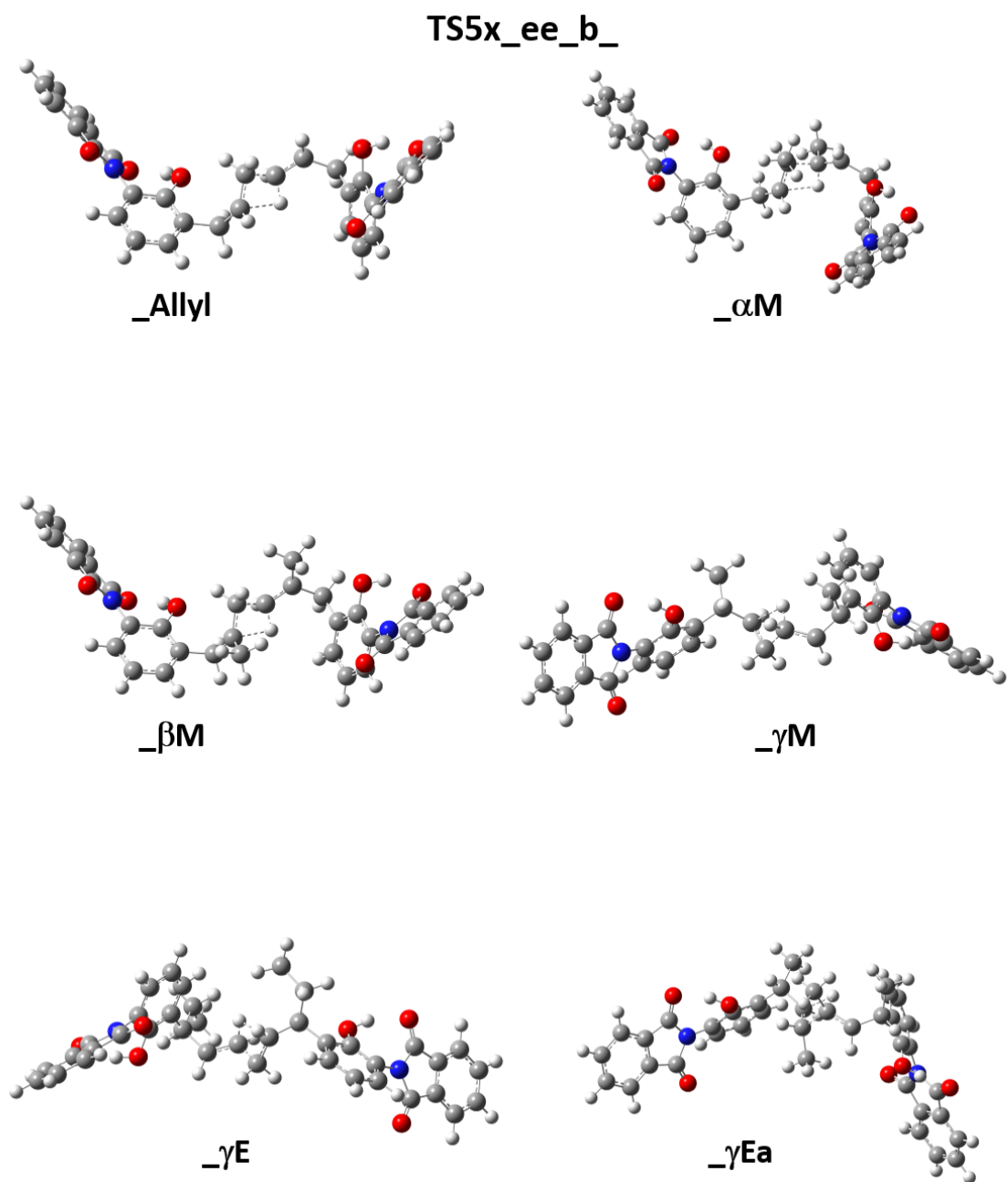


Figure 313. Geometry optimized transition-state structures of the allyl-crosslinking via C3-C3 atoms allyl group of the allyl-imide models (ee\_b-mechanism).

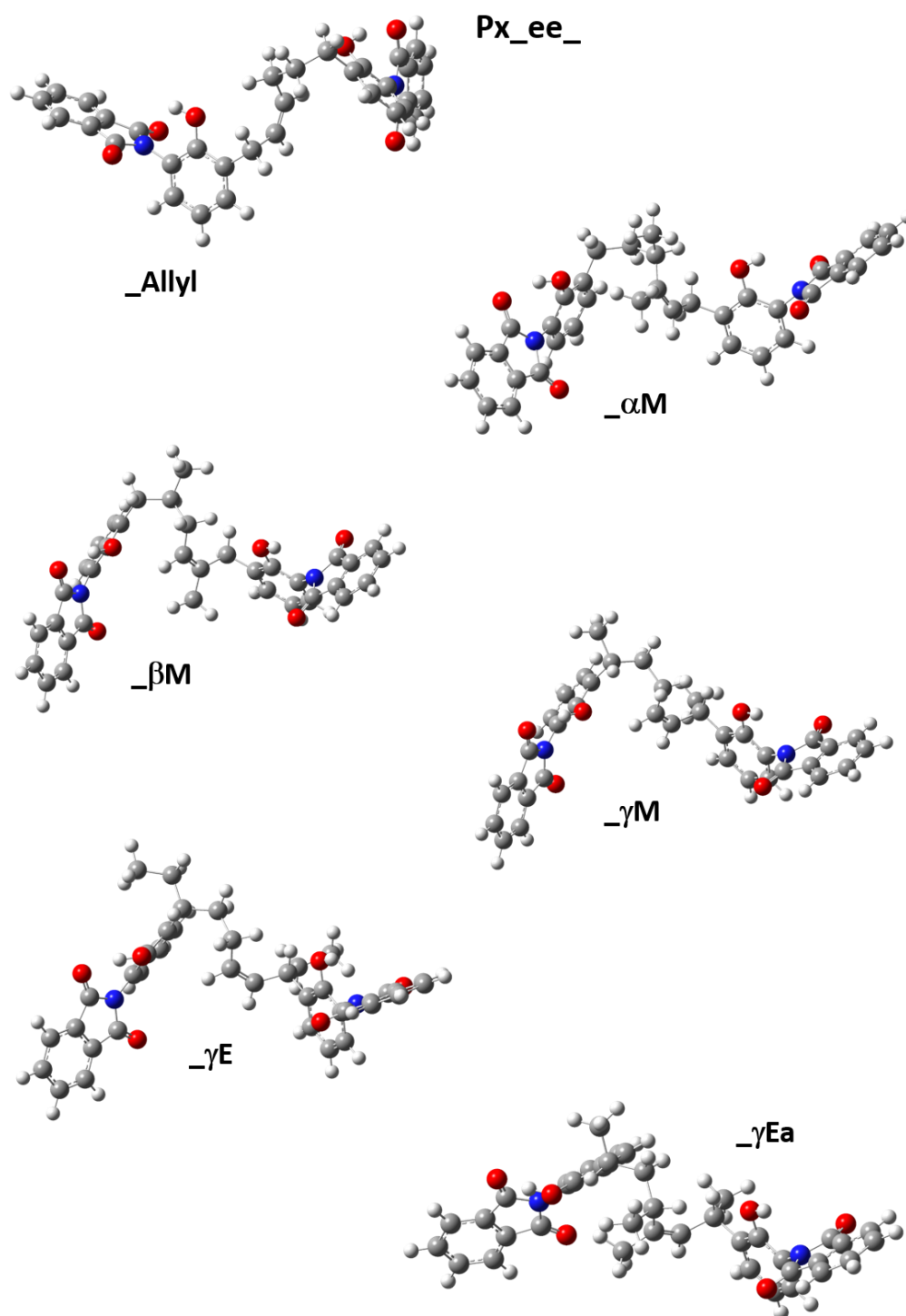


Figure 314. Geometry optimized product structures of the crosslinked allyl-imide models (ee-mechanism).

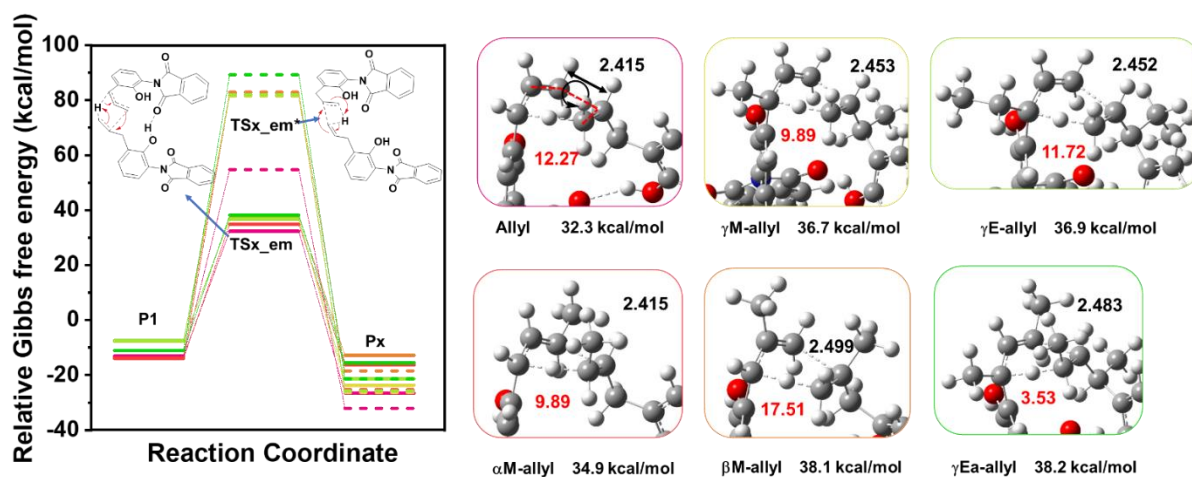


Figure 315. Simulated reaction coordinate for the crosslinking mechanism between terminal-internal vinylic groups (em) (left) and zoom of the reactive part of the transition state with respect to the different modifications.

Table 31. Simulated energy in relation to the starting structure  $\Delta G_{rel}$  and imaginary frequency (IF) of the uncrosslinked ( $Ex_{-}$ ), transitions-state structure ( $TS5x_{-}$ ) of the crosslinking and product structure ( $Px_{-}$ ) of the allyl crosslinking of the allyl-imide model.

ee <sub>-</sub>	$\Delta G_{rel}$ (Rel. to E) (kcal/mol)		IF (cm <sup>-1</sup> )	
	Ex <sub>-</sub>	TS5x <sub>-</sub>	Px <sub>-</sub>	TS5x <sub>-</sub>
<b>Model</b>				
<b>Allyl</b>	-13,127	27,169	-27,388	-1250,13
<b>aM</b>	-13,979	29,935	-19,984	-1142,16
<b>bM</b>	-11,088	35,005	-21,971	-1226
<b>gM</b>	-7,720	36,354	-23,170	-1310,83
<b>gE</b>	-7,492	38,366	-22,797	-1309,83
<b>gEa</b>	-11,052	38,054	-17,866	-1211,18
<b>ee<sup>*</sup></b>				
<b>Allyl</b>	-13,127	29,209	-32,837	-384,890
<b>aM</b>	-13,979	31,292	-24,869	-1188,660
<b>bM</b>	-11,088	36,677	-26,737	-1208,550
<b>gM</b>	-7,720	32,544	-30,898	-1243,200
<b>gE</b>	-7,492	35,313	-30,089	-1253,030
<b>gEa</b>	-11,052	33,576	-25,420	-1306,030

<b>ee_b_</b>				
<b>Allyl</b>	-13,127	50,984	-33,334	-515,51
<b>aM</b>	-13,979	57,763	-26,352	-336,06
<b>bM</b>	-11,088	54,229	-25,328	-415,68
<b>gM</b>	-7,720	55,443	-29,085	-520,41
<b>gE</b>	-7,492	56,255	-27,819	-533,5
<b>gEa</b>	-11,052	61,168	-23,891	-460,24
<b>dG<sub>rel</sub> (kcal/mol)</b>				
<b>IF (cm<sup>-1</sup>)</b>				
<b>em6_</b>	<b>Ex_</b>	<b>TS5x_</b>	<b>Px_</b>	<b>TS5x_</b>
<b>Allyl</b>	-13,127	32,303	-26,545	-1227,66
<b>aM</b>	-13,979	34,886	-16,335	-1151,11
<b>bM</b>	-11,088	38,124	-12,808	-1158,13
<b>gM</b>	-7,720	36,716	-23,660	-1205,91
<b>gE</b>	-7,492	36,861	-21,379	-1199,75
<b>gEa</b>	-11,052	38,208	-15,525	-1084,38

<b>dG<sub>rel</sub> (kcal/mol)</b>				
<b>IF (cm<sup>-1</sup>)</b>				
<b>mm_</b>	<b>Ex_</b>	<b>TS5x_</b>	<b>Px_</b>	<b>TS5x_</b>
<b>Allyl</b>	-13,127	64,001	-26,634	-520,79
<b>aM</b>	-13,979	60,830	-21,379	-649,51
<b>bM</b>				
<b>gM</b>	-7,720	74,550	-19,778	-513,92
<b>gE</b>	-7,492	75,089	-11,412	-494,92
<b>gEa</b>	-11,052	68,292	-18,291	-822,53
<b>mm*</b>	<b>Ex_</b>	<b>TS5x_</b>	<b>Px_</b>	<b>TS5x_</b>
<b>Allyl</b>	-13,127	78,151	-26,634	-1650,38
<b>aM</b>	-13,979	86,059	-21,379	-1608,15
<b>bM</b>				
<b>gM</b>	-7,720	85,054	-19,778	-1696,15
<b>gE</b>	-7,492	85,685	-11,412	-1692,02
<b>gEa</b>	-11,052	92,829	-18,291	-1707,15

ea_				
<b>Allyl</b>	-13,127	69,092	-26,868	-1376,76
<b>aM</b>	-13,979	69,826	-22,692	-1419,45
<b>bM</b>	-11,088	73,776	-16,818	-1318,76
<b>gM</b>	-7,720	67,167	-19,162	-1237,74
<b>gE</b>	-7,492	68,296	-14,570	-1206,82
<b>gEa</b>	-11,052	67,296	-8,297	1307,65

ma_	dG <sub>rel</sub> (kcal/mol)			IF (cm <sup>-1</sup> )	
	Ex_	TS5x_	Px_	TS5x_	
<b>Allyl</b>	-13,127	63,904	-23,946	-1337,86	
<b>aM</b>	-13,979	65,139	-20,443	-1354,95	
<b>bM</b>	-11,088	68,318	-0,262	-1336,76	
<b>gM</b>	-7,720	68,010	-7,781	-1318,6	
<b>gE</b>	-7,492	68,396	-5,307	-1309,36	
<b>gEa</b>	-11,052	67,669	-3,254	-1351,52	
<b>mm_b_</b>					

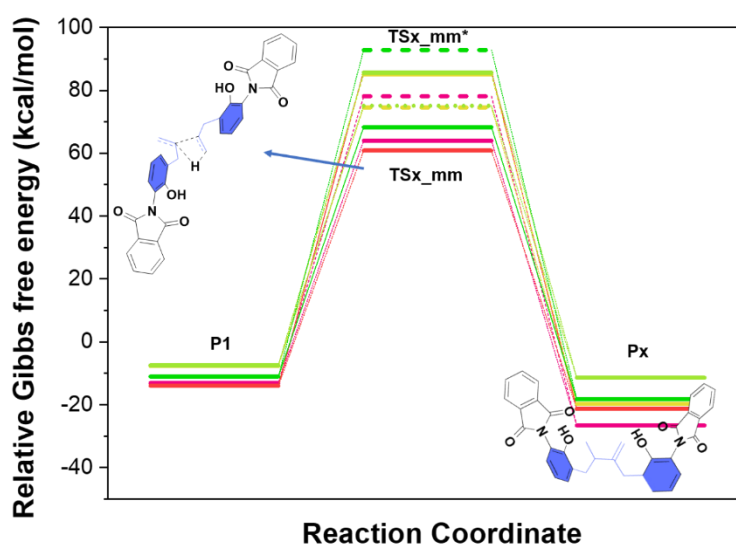


Figure 316. Simulated single-point energies of the geometry optimized reactants, products, and transition-states of the crosslinking reaction between C2 (m) groups, via mm- and mm\*-mechanism.

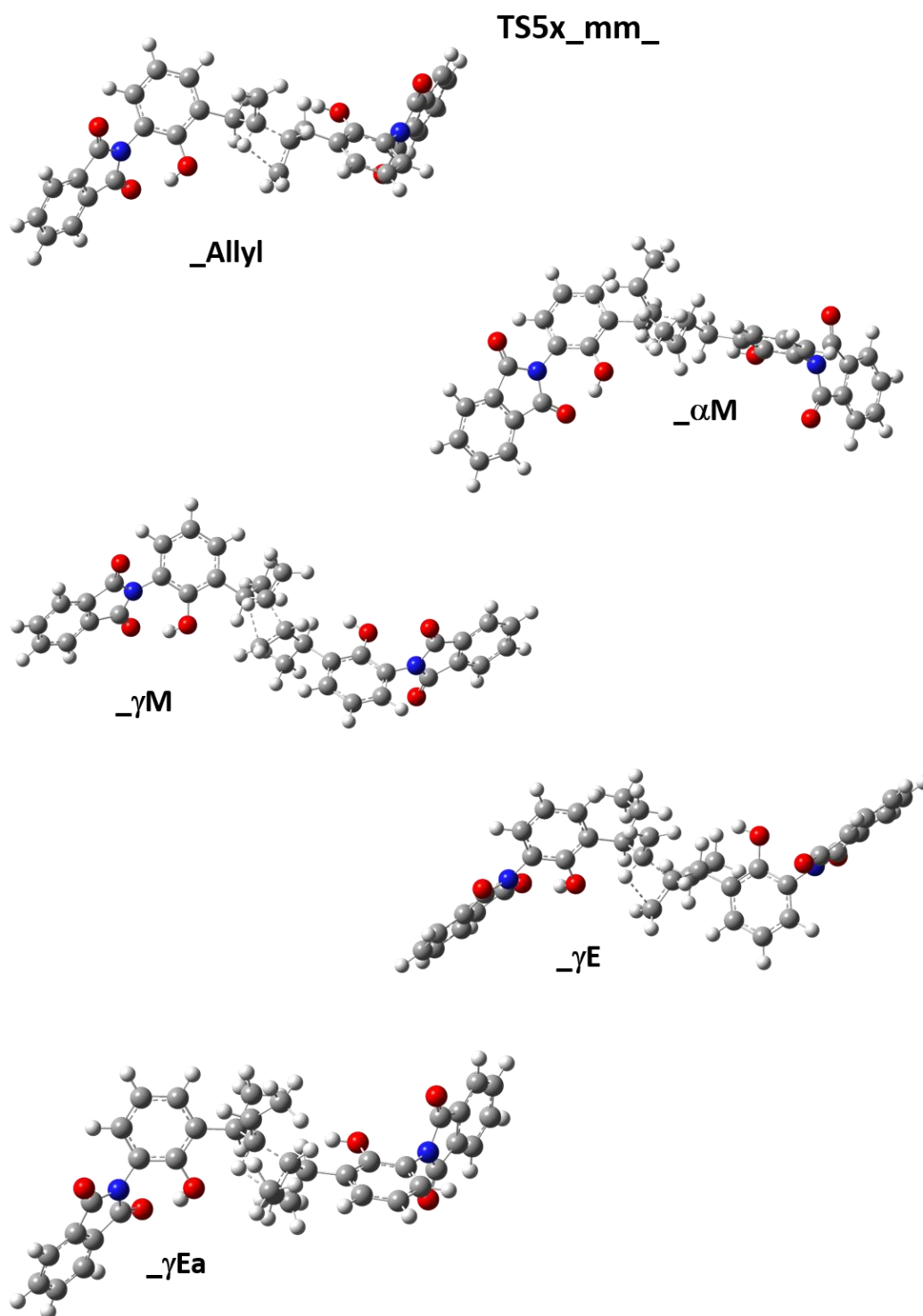


Figure 317. Simulated single-point energies of the geometry optimized transition-state structures of the crosslinking reaction between C2 (m) groups, via mm-mechanism.



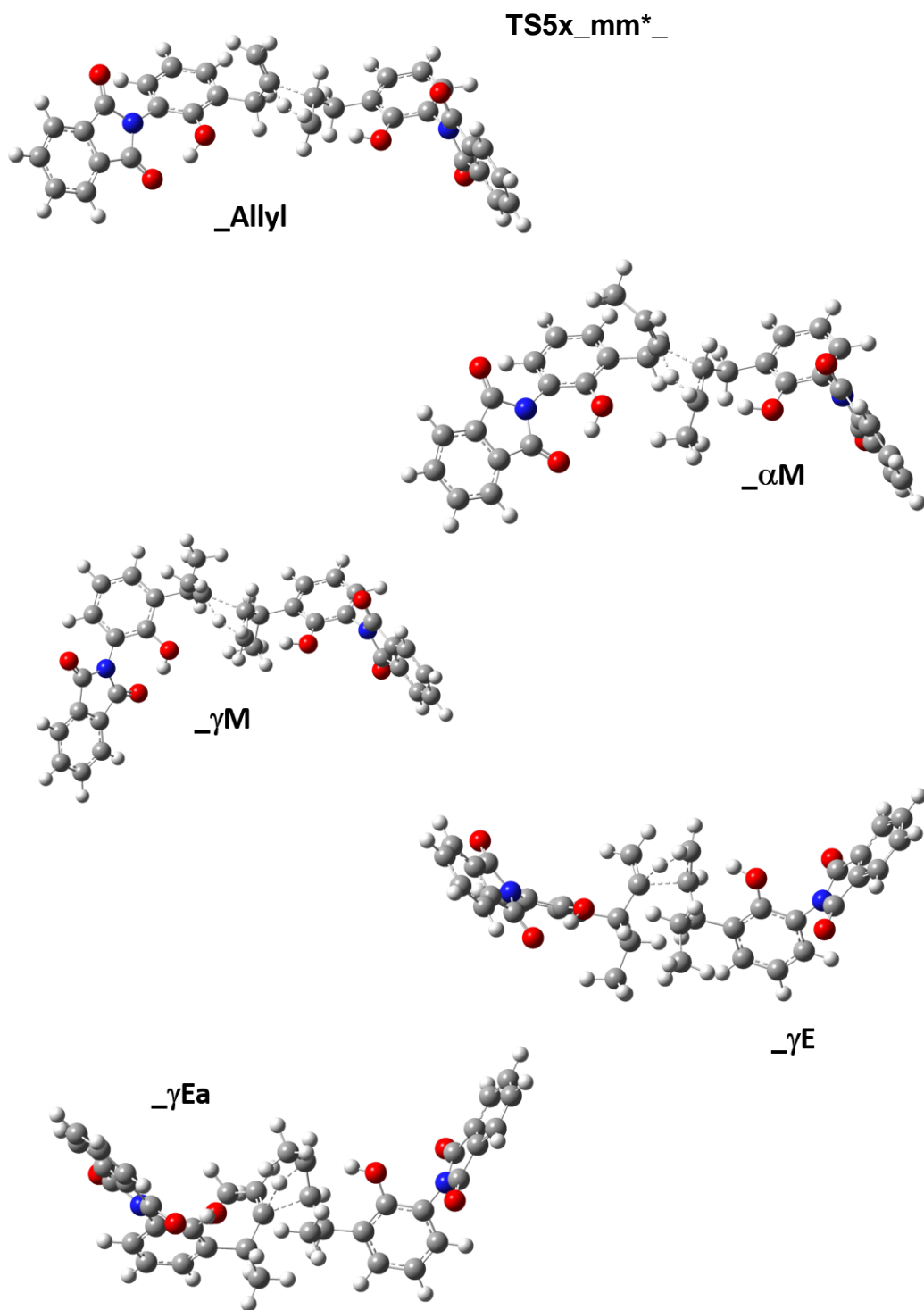


Figure 318. Simulated single-point energies of the geometry optimized transition-state structures of the crosslinking reaction between C2 (m) groups, via mm\*-mechanism.

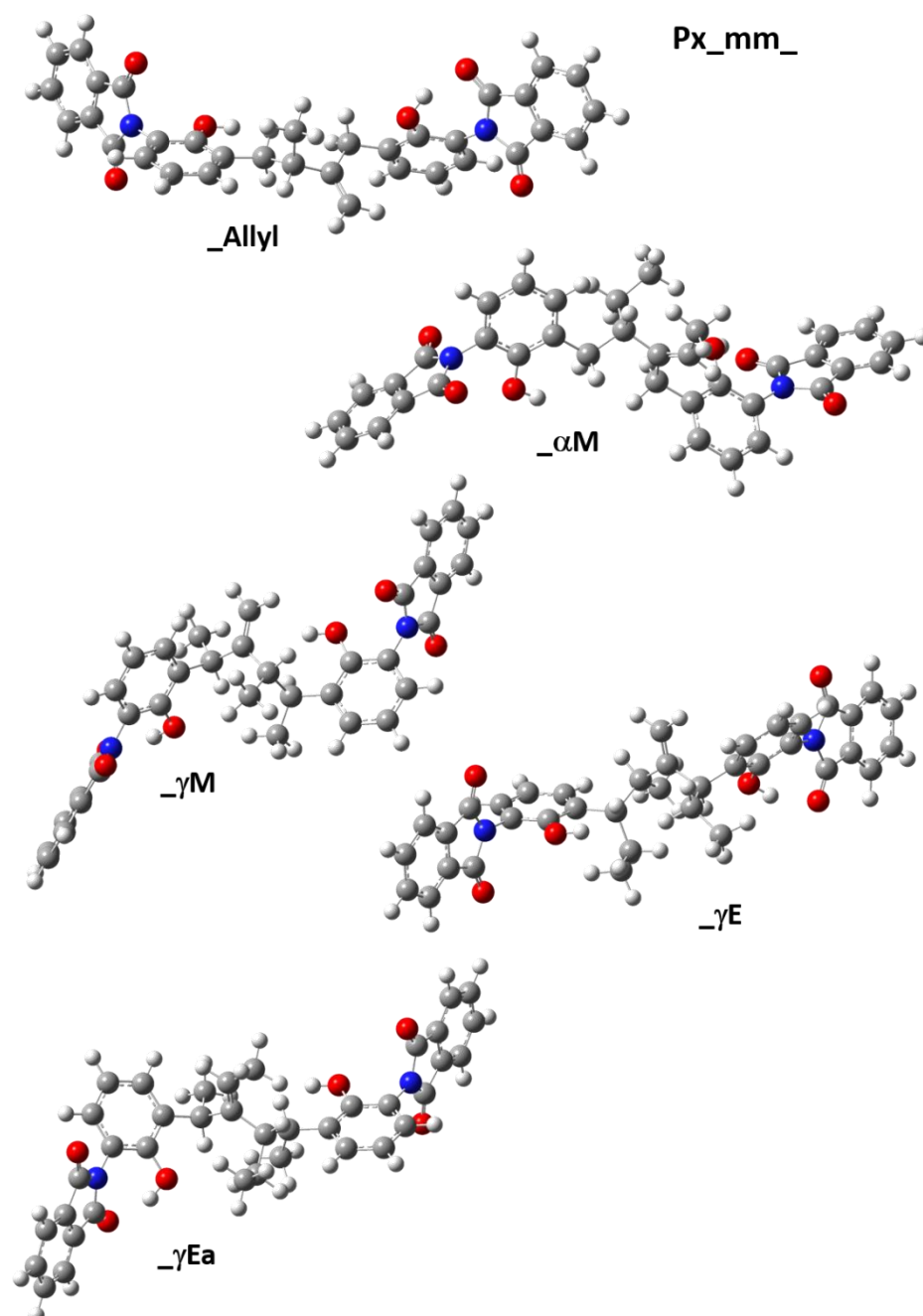


Figure 319. Simulated single-point energies of the geometry optimized product structures of the crosslinking reaction between C2 (m) groups, via mm-mechanism.

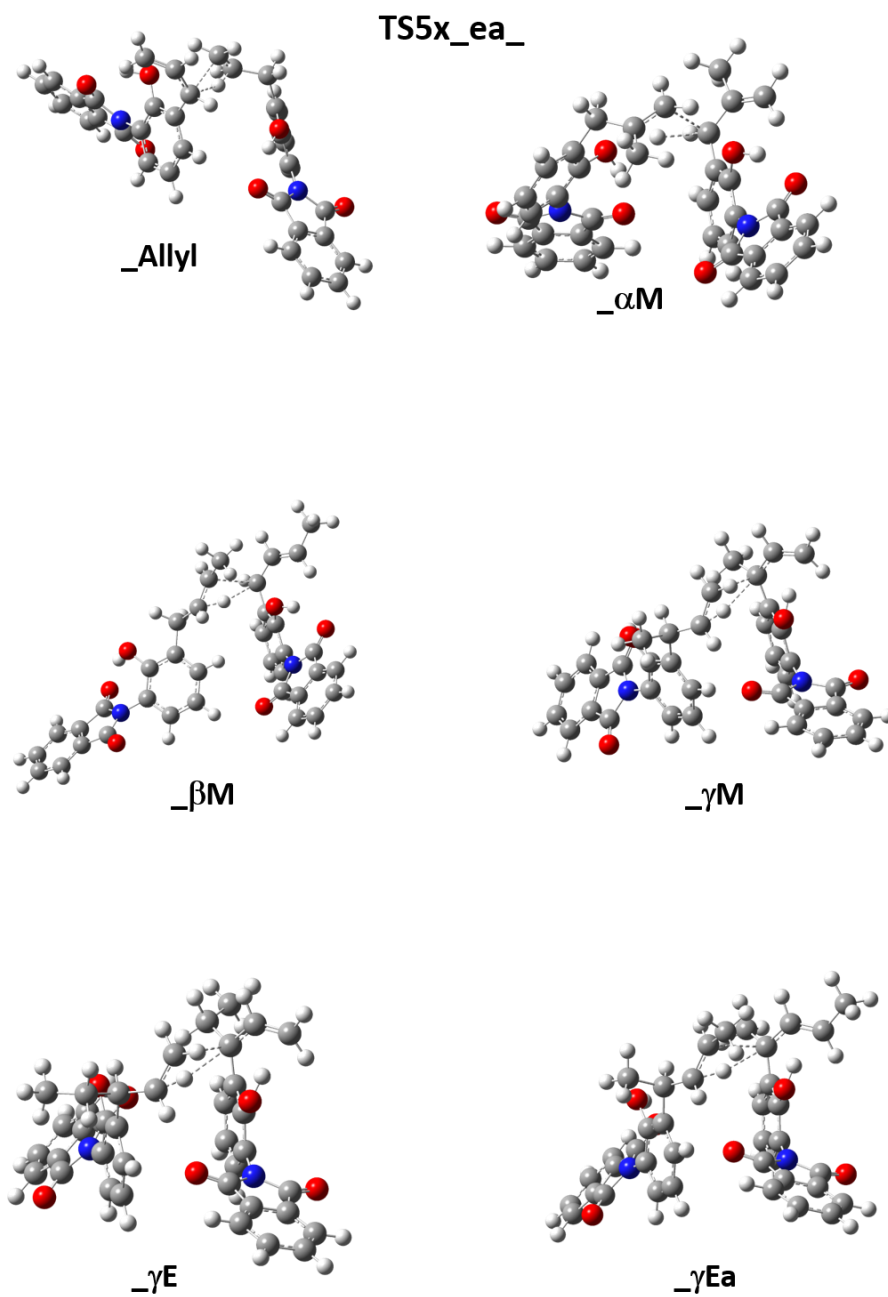


Figure 320. Simulated single-point energies of the geometry optimized transition-state structures of the crosslinking reaction via ea-mechanism.

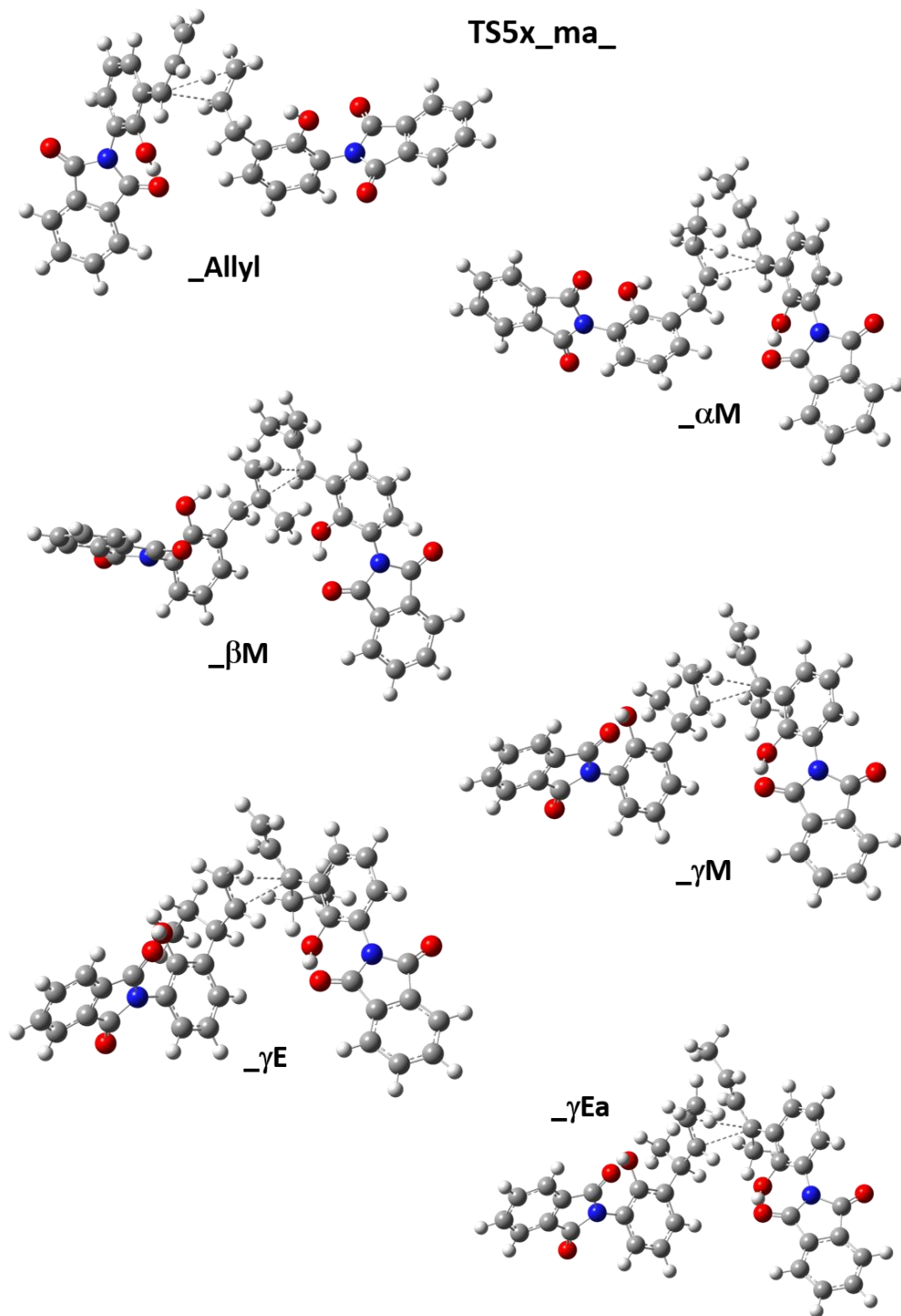


Figure 321. Simulated single-point energies of the geometry optimized transition-state structures of the crosslinking reaction via ma-mechanism.

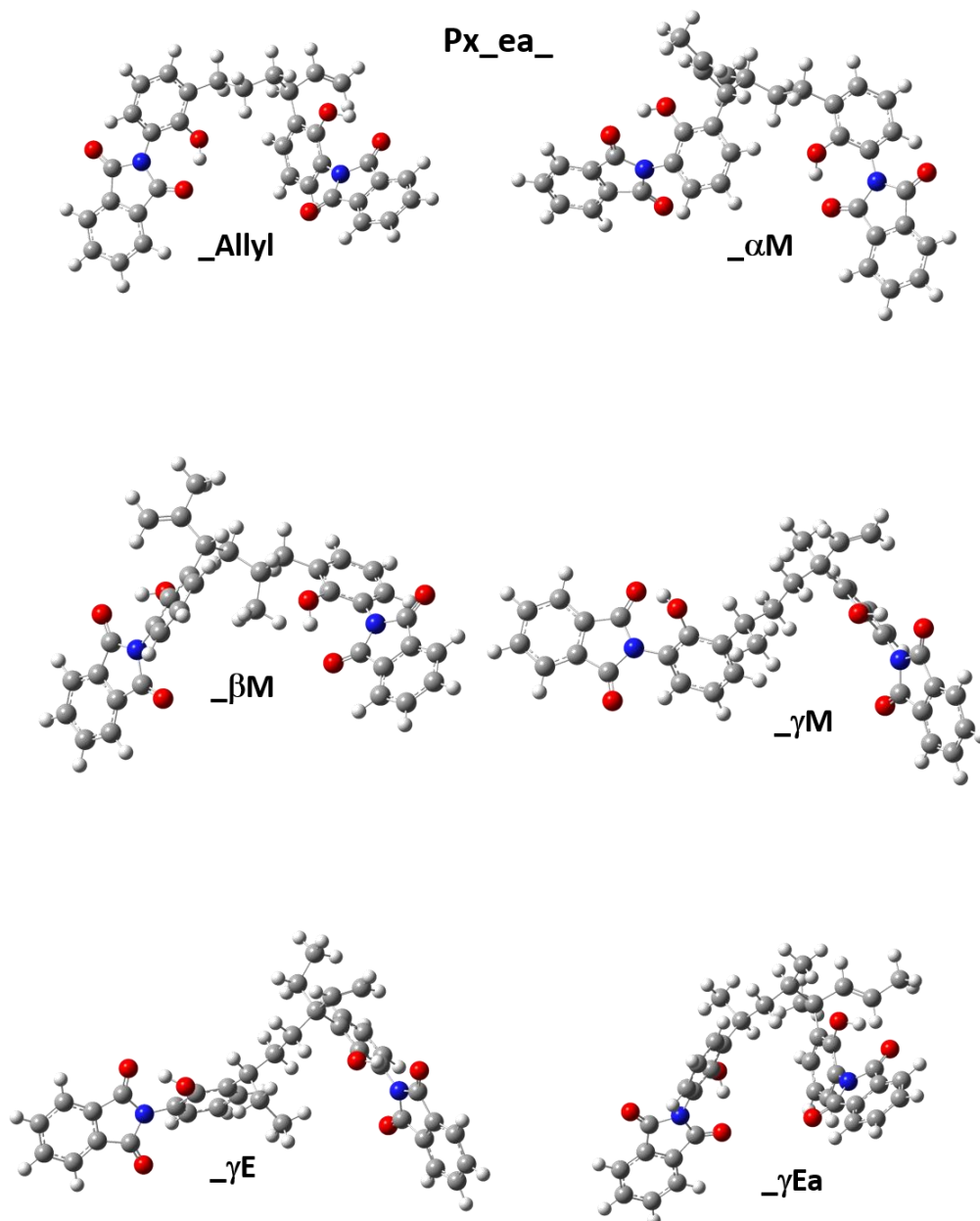


Figure 322. Simulated single-point energies of the geometry optimized product structures of the crosslinking reaction via ea-mechanism.

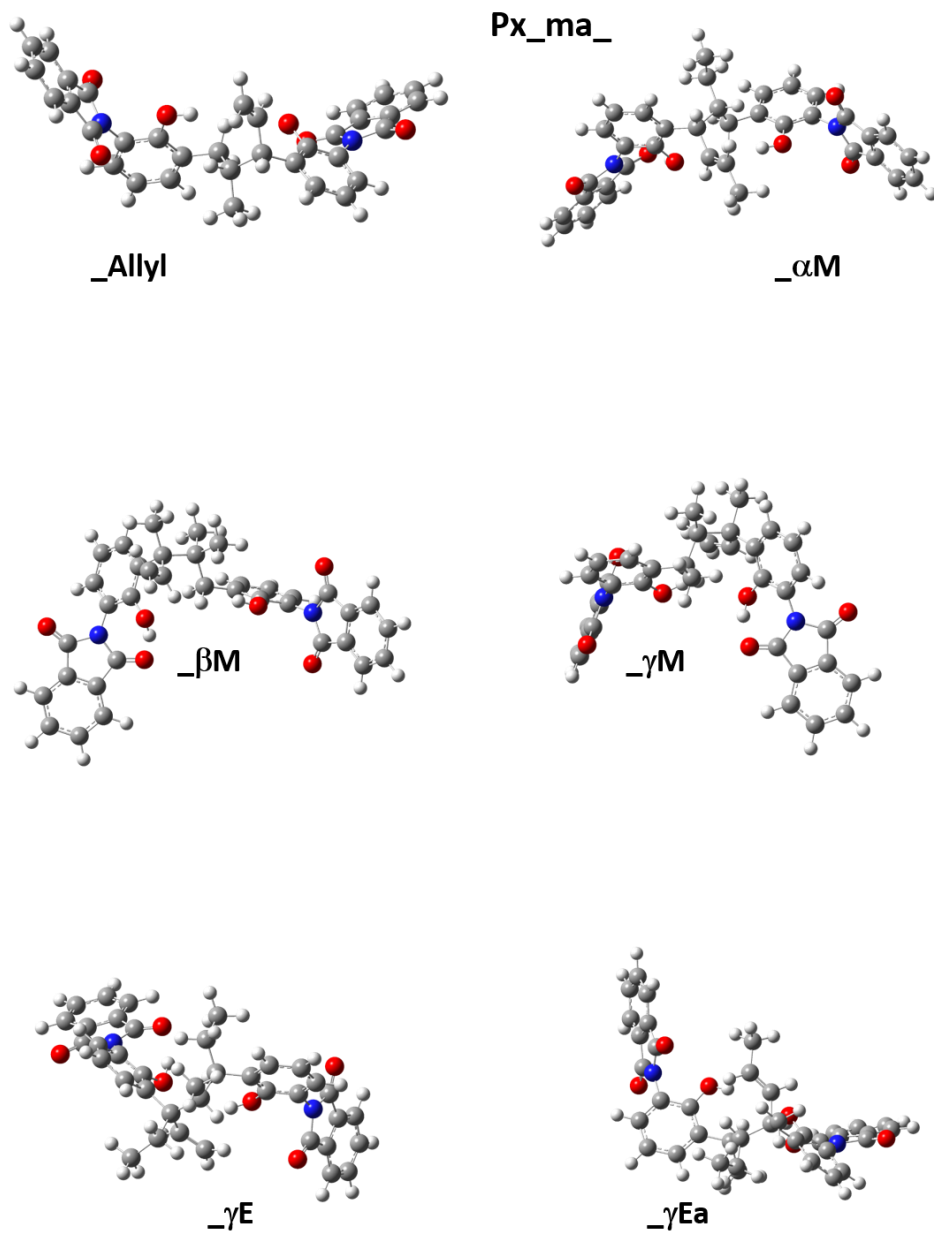


Figure 323. Simulated single-point energies of the geometry optimized product structures of the crosslinking reaction via ma-mechanism.

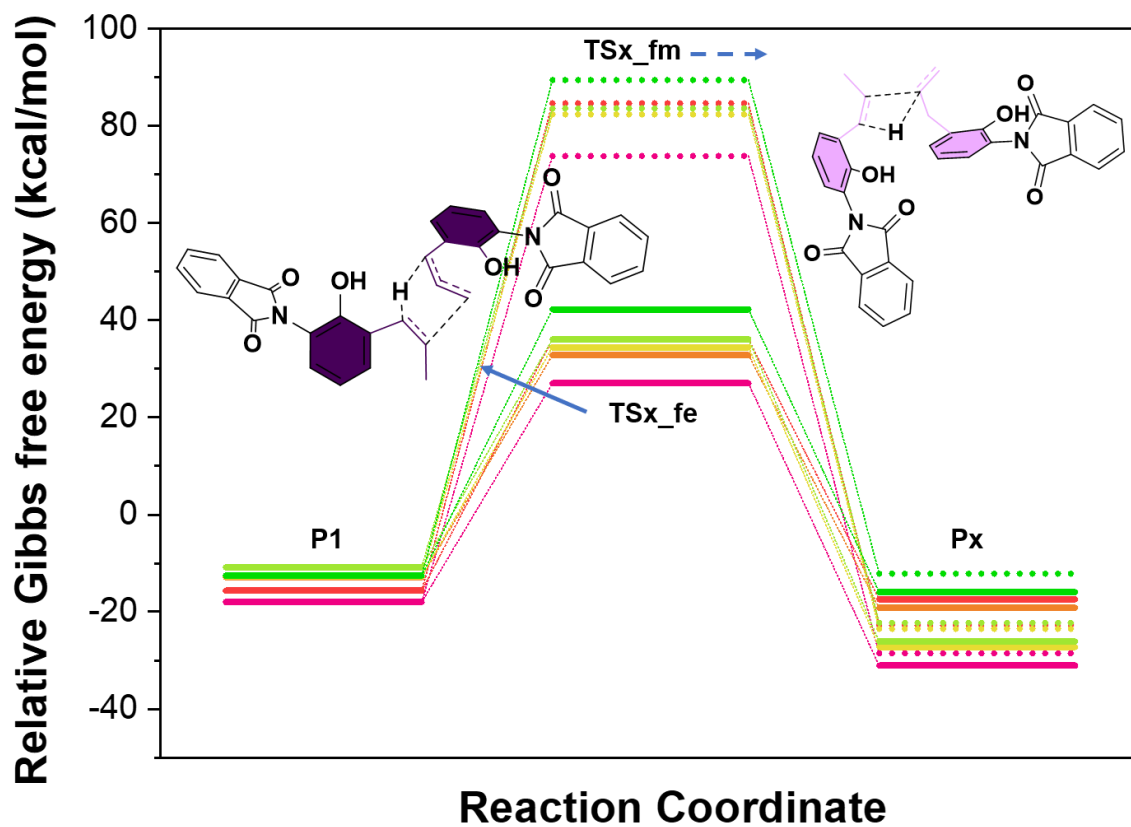


Figure 324. Simulated single-point energies of the geometry optimized reactants, products, and transition-states of the crosslinking reaction between C2 (of P1) and C2 (of P4) groups via fm- and C3 (of P1) and C2 (of P4) groups via fe-mechanism.

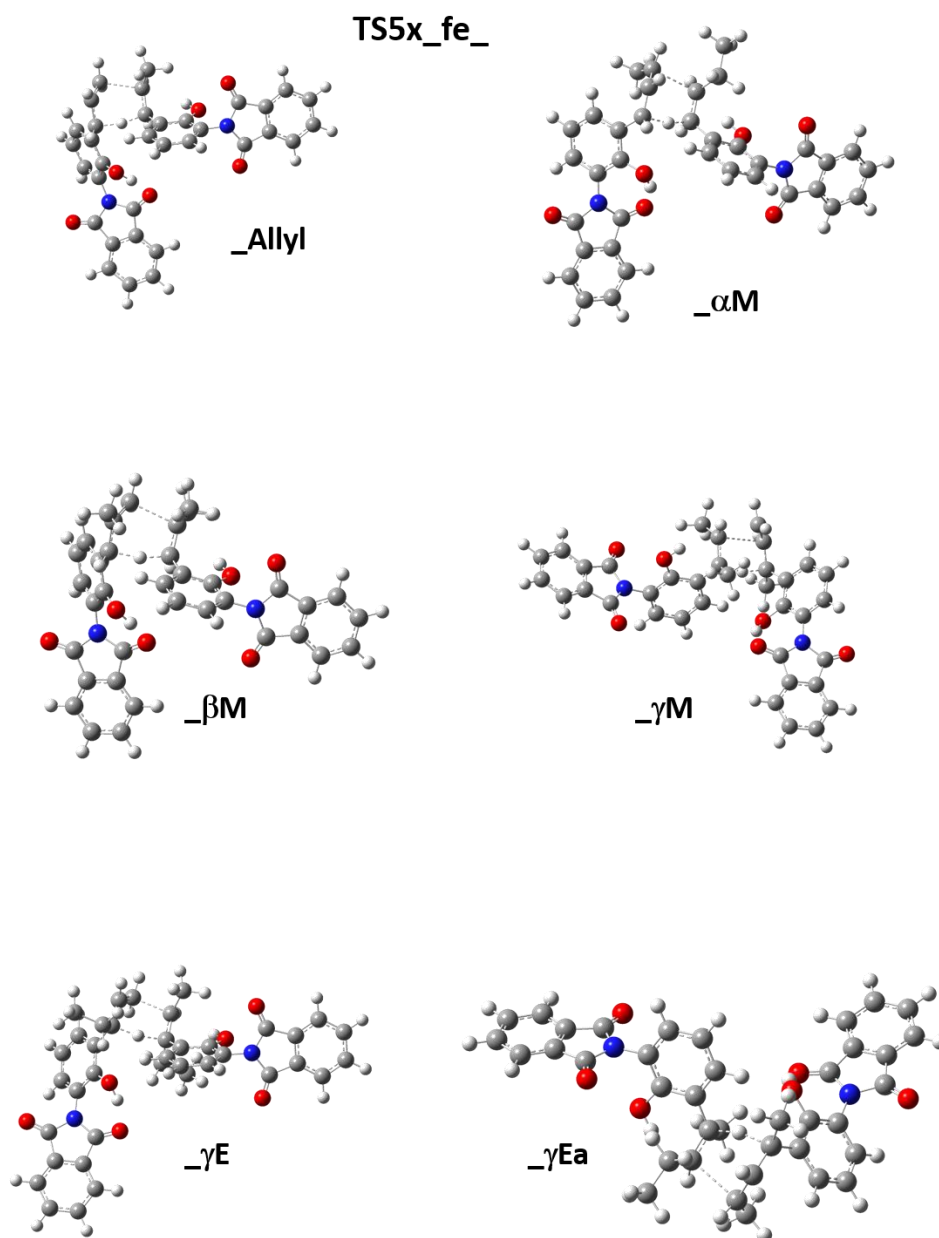


Figure 325. Simulated single-point energies of the geometry optimized transition-state structures of the crosslinking reaction via fe-mechanism.



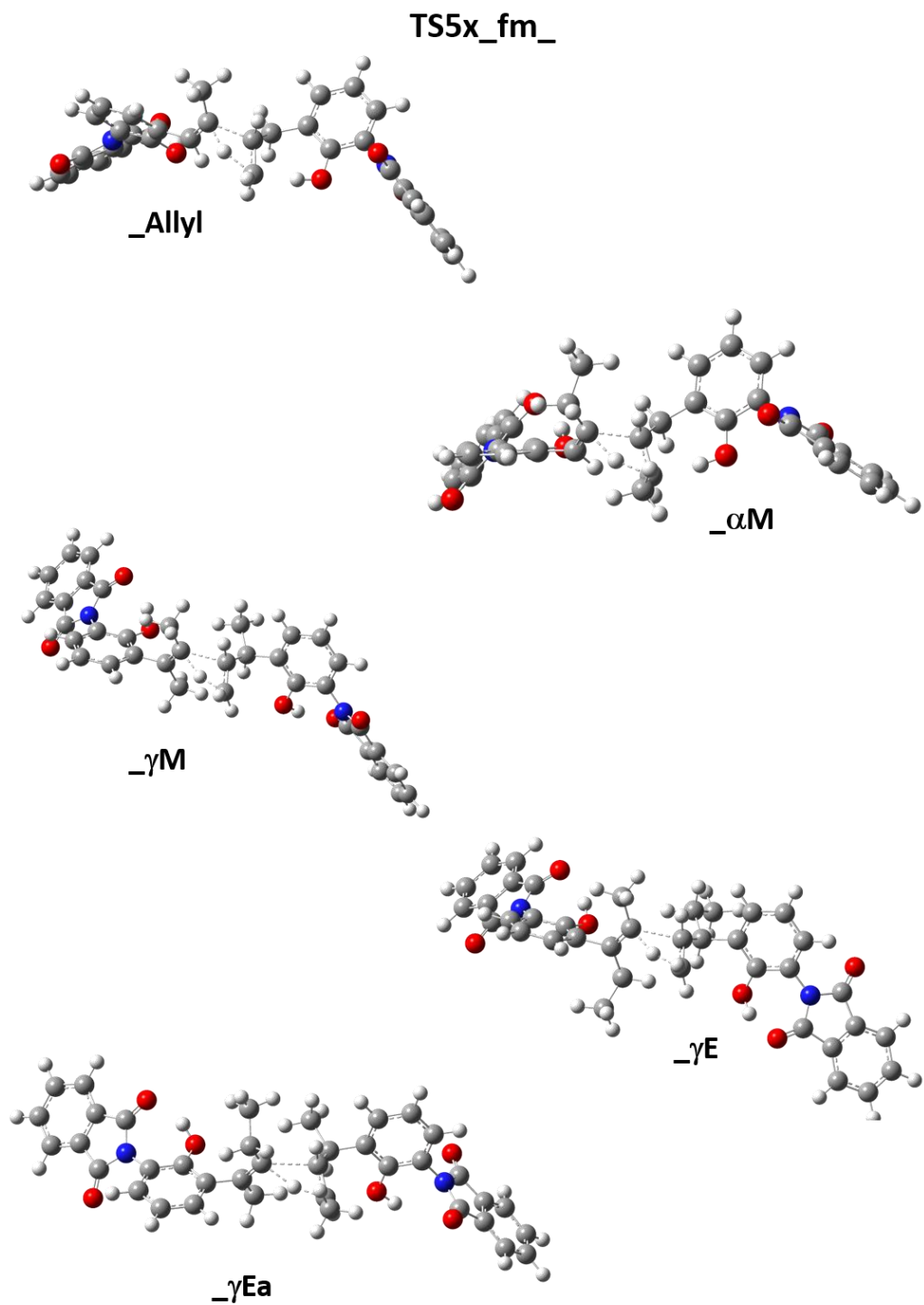


Figure 326. Simulated single-point energies of the geometry optimized transition-state structures of the crosslinking reaction via fm-mechanism.

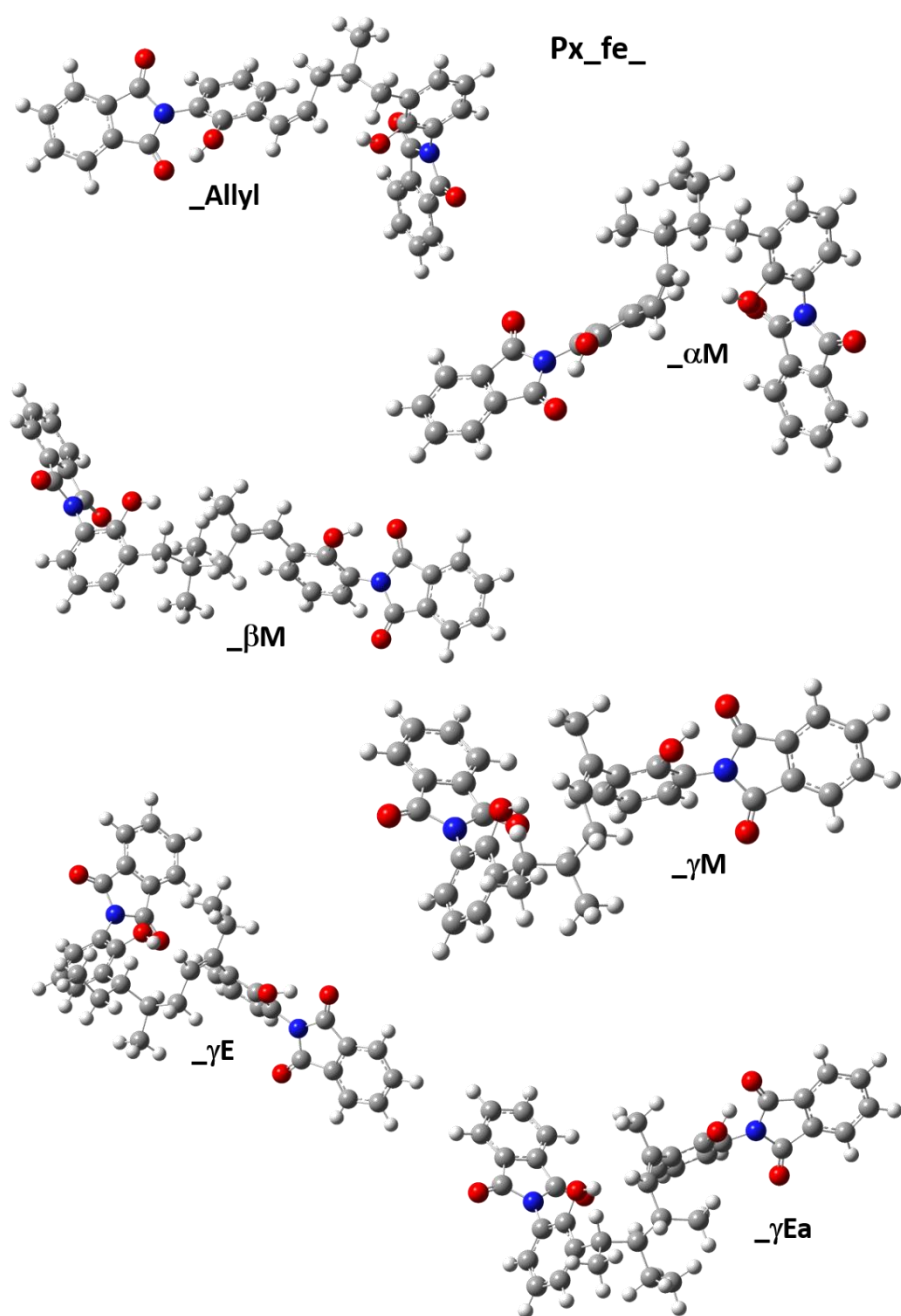


Figure 327. Simulated single-point energies of the geometry optimized product structures of the crosslinking reaction via fe-mechanism.

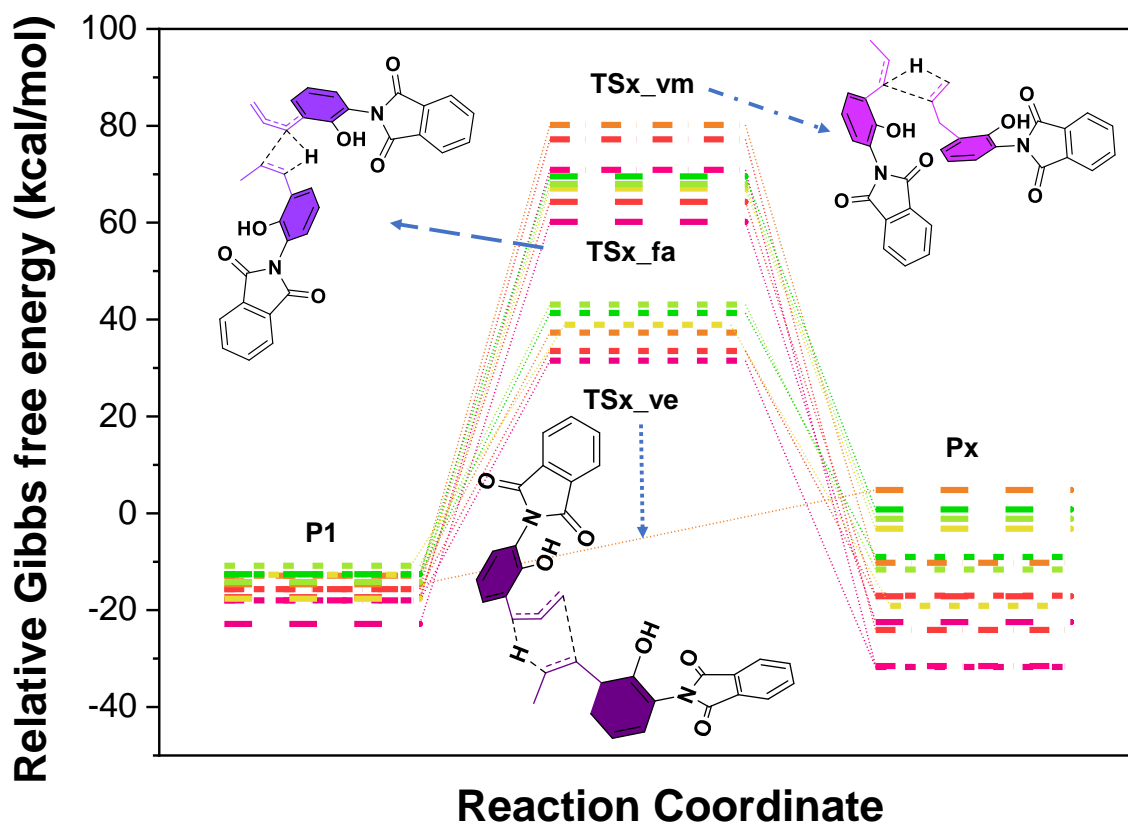


Figure 328. Simulated single-point energies of the geometry optimized reactants, products and transition-states of the crosslinking reaction between C2 (of P1) and C1 (of P4) groups via vm- and C1 (of P1) and C2 (of P4) groups via fa, as well as C3 (of P1) and C1 (of P4) groups via fa -mechanism.

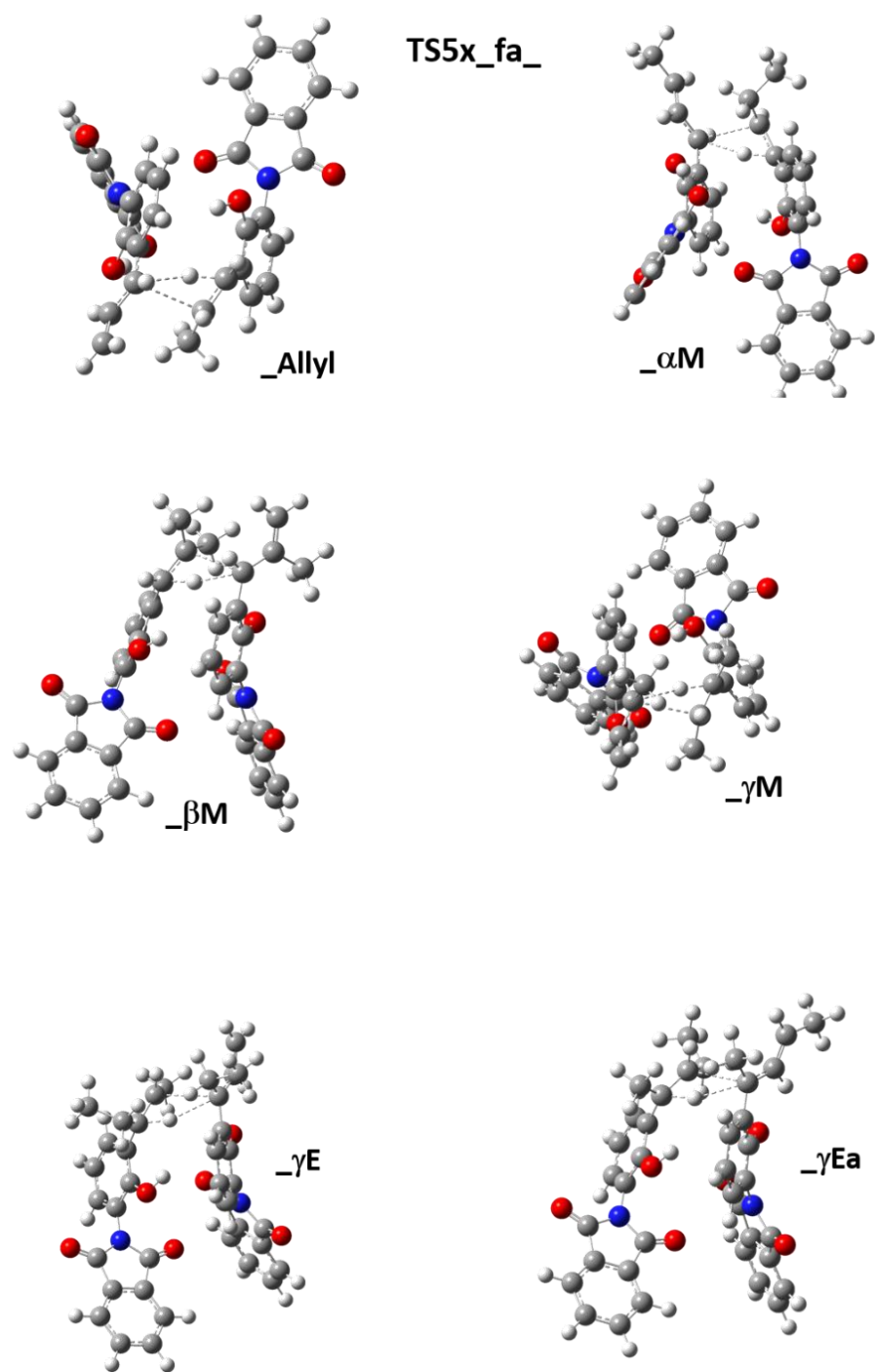


Figure 329. Simulated single-point energies of the geometry optimized transition-state structures of the crosslinking reaction via fa-mechanism.

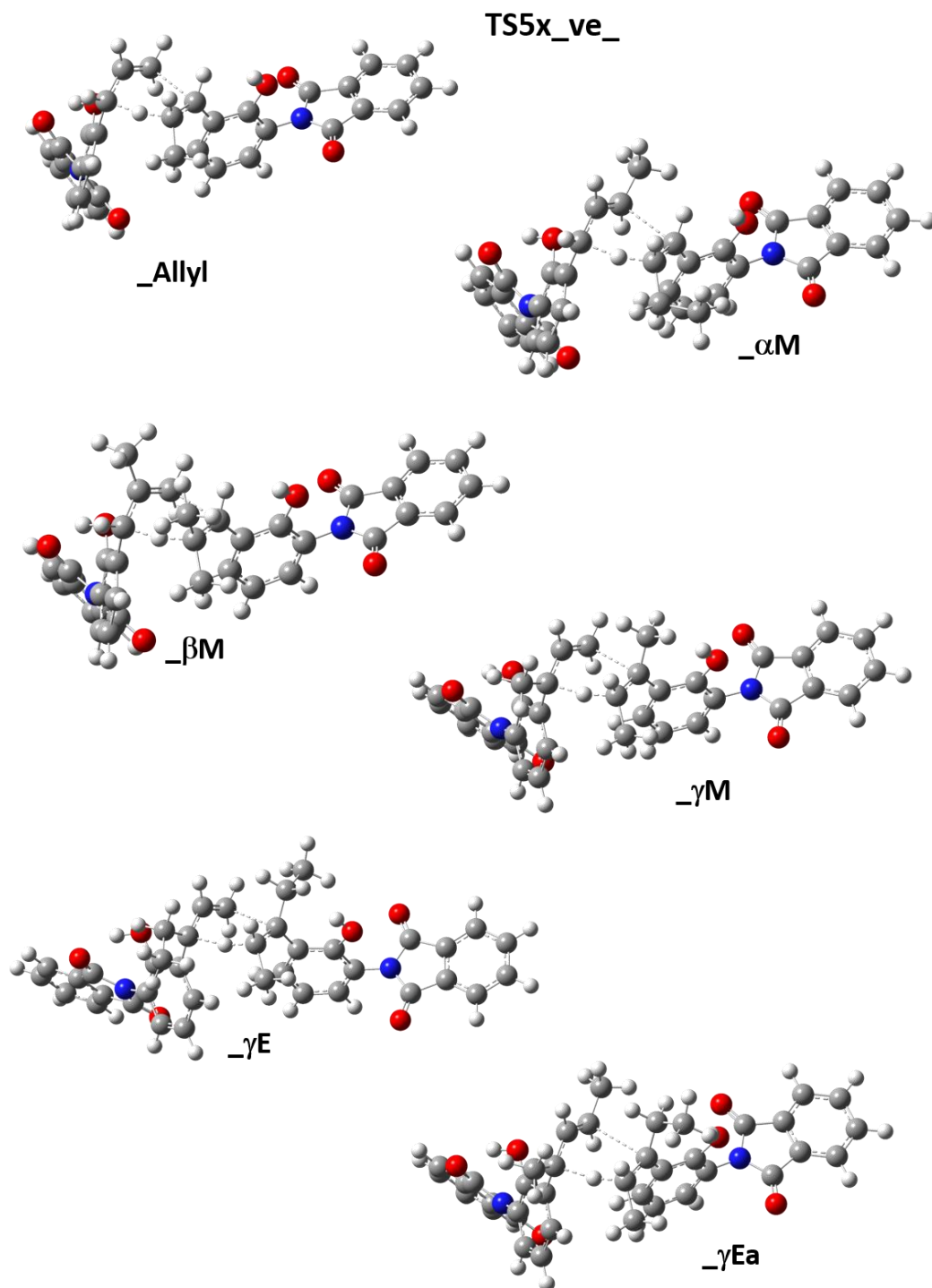


Figure 330. Simulated single-point energies of the geometry optimized transition-state structures of the crosslinking reaction via ve-mechanism.

TS5x\_vm\_

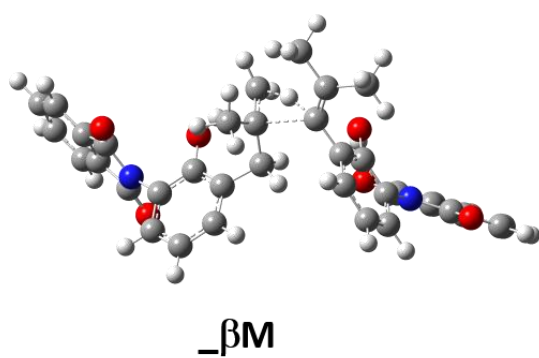
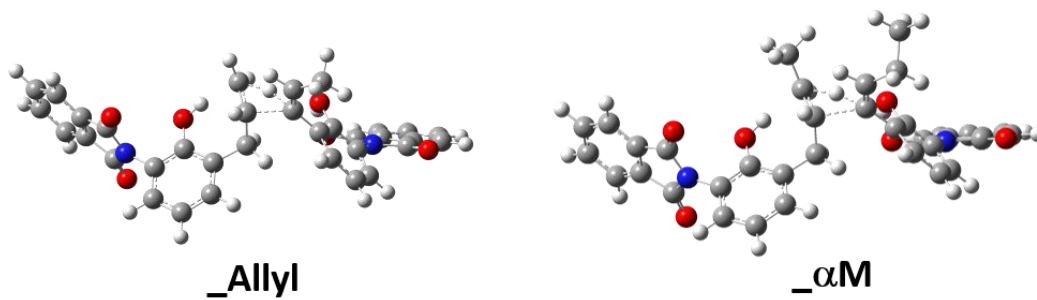


Figure 331. Simulated single-point energies of the geometry optimized transition-state structures of the crosslinking reaction via vm-mechanism.

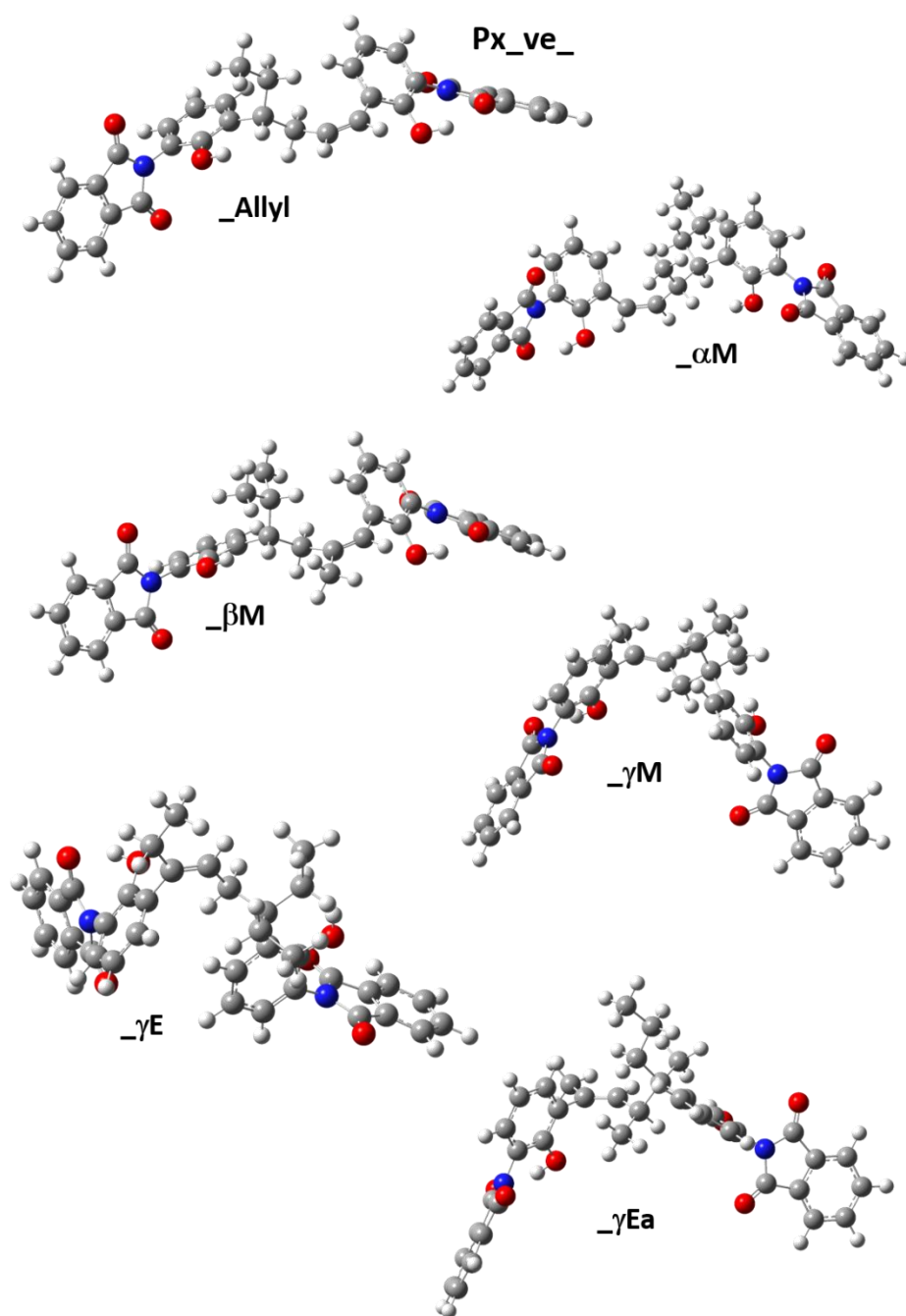


Figure 332. Simulated single-point energies of the geometry optimized product structures of the crosslinking reaction via ve-mechanism.

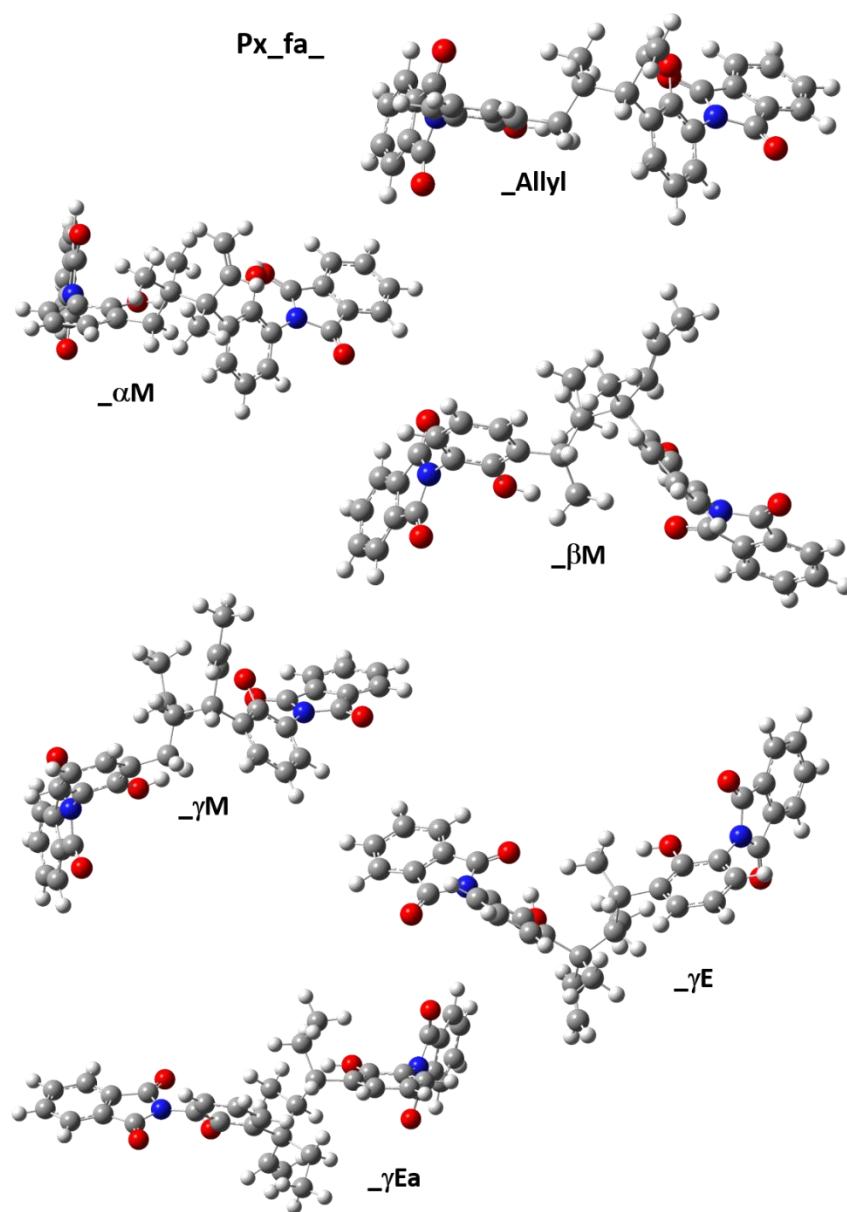


Figure 333. Simulated single-point energies of the geometry optimized product structures of the crosslinking reaction via fa-mechanism.



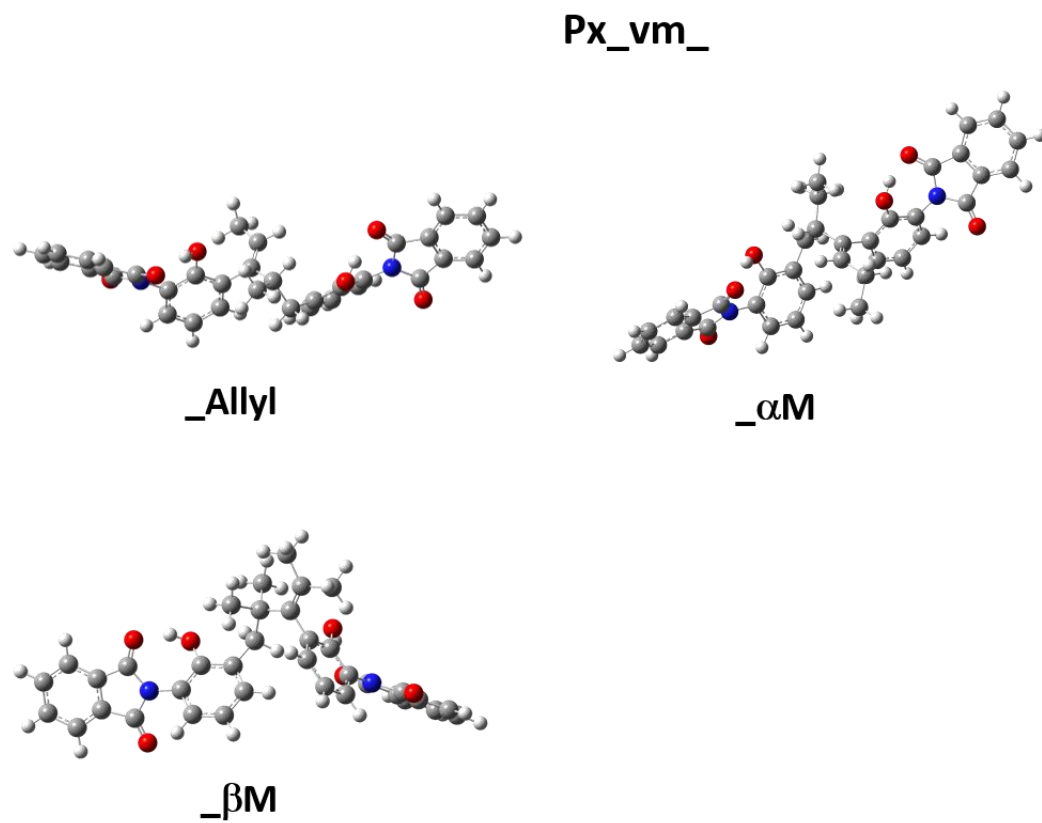


Figure 334. Simulated single-point energies of the geometry optimized product structures of the crosslinking reaction via vm-mechanism.

Table 32. Simulated energy in relation to the starting structure  $\Delta G_{rel}$  and imaginary frequency (IF) of the uncrosslinked ( $Ex_{-}$ ), transitions-state structure ( $TS5x_{-}$ ) of the crosslinking and product structure ( $Px_{-}$ ) of the allyl crosslinking of the allyl-imide model

fe_	dG <sub>rel</sub> (kcal/mol)			IF (cm <sup>-1</sup> )
	Ex_	TS5x_	Px_	TS5x_
<b>Model</b>				
<b>Allyl</b>	-17,984	27,013	-31,075	-1244,450
<b>aM</b>	-15,643	36,069	-17,387	-1156,660
<b>bM</b>	-12,879	32,809	-19,172	-1229,130
<b>gM</b>	-12,676	34,436	-27,227	-1386,230
<b>gE</b>	-10,840	36,060	-26,131	-1403,290
<b>gEa</b>	-12,582	42,239	-15,980	-1254,360
<b>fm_</b>				
<b>Allyl</b>	-17,984	73,782	-28,530	-1658,140
<b>aM</b>	-15,643	84,630	-22,723	-1767,360
<b>bM</b>				
<b>gM</b>	-12,676	82,357	-23,512	-2044,670
<b>gE</b>	-10,840	83,575	-22,254	-2052,010
<b>gEa</b>	-12,582	89,415	-12,139	-1933,160
<b>ve_</b>				
<b>Allyl</b>	-17,984	31,496	-31,721	-1056,550
<b>aM</b>	-15,643	36,069	-17,387	-977,980
<b>bM</b>	-12,879	37,295	-19,773	-1116,420
<b>gM</b>	-12,676	38,921	-19,090	-992,920
<b>gE</b>	-10,840	43,112	-11,604	-777,990
<b>gEa</b>	-12,582	41,363	-9,031	-612,580
<b>vm_</b>				
vm_	dG <sub>rel</sub> (kcal/mol)			IF (cm <sup>-1</sup> )
	Ex_	TS5x_	Px_	TS5x_
<b>Allyl</b>	-17,984	70,913	-31,528	-1722,580
<b>aM</b>	-15,643	77,196	-24,096	-1614,430

<b>bM</b>	-12,879	80,186	-10,200	-1935,240
<b>gM</b>				
<b>gE</b>				
<b>gEa</b>				
<b>fa_</b>				
<b>Allyl</b>	-22,841	60,170	-22,475	-1381,920
<b>aM</b>	-17,306	64,305	-17,145	-1398,220
<b>bM</b>	-14,671	69,037	4,8165	-1398,900
<b>gM</b>	-17,633	67,045	-3,171	-1365,840
<b>gE</b>	-14,189	67,963	-1,147	-1338,290
<b>gEa</b>	-12,582	69,547	0,797	-1389,810

## Thermal Rearrangement of Crosslinked Models

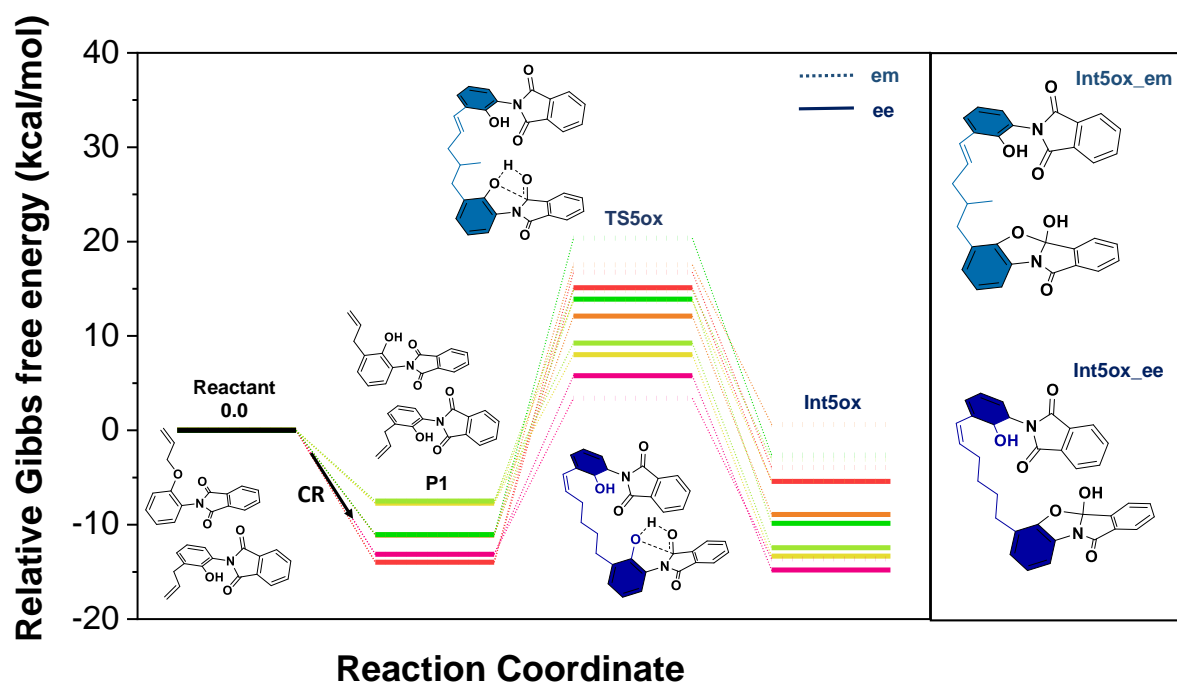


Figure 335. Simulated single-point energies of the geometry optimized reactants, products, and transition-states of the HPI-to-PBO reaction of crosslinked allyl-imide models following the ee- and em6-mechanism.

TS5ox\_ee\_

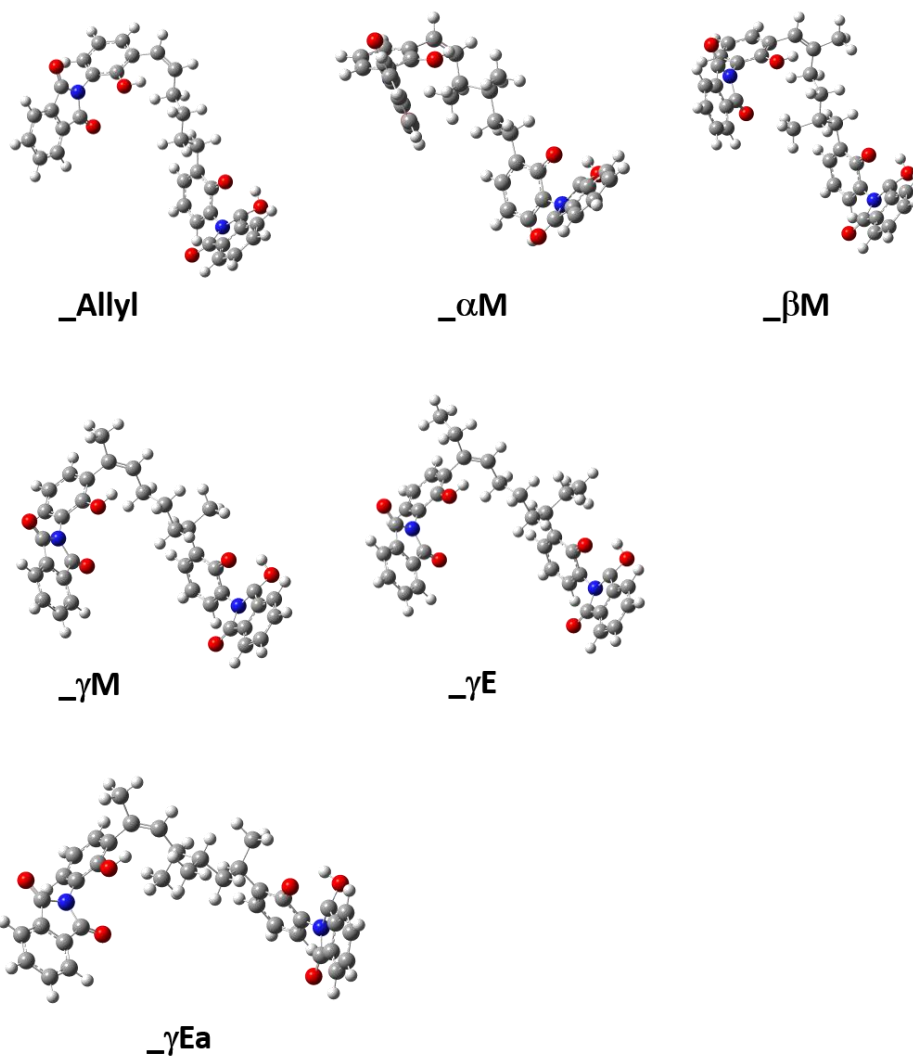


Figure 336. Simulated single-point energies of the geometry optimized transition-state structures of the HPI-to-PBO reaction of ee-crosslinked allyl-imide models.

# Int5ox\_ee\_

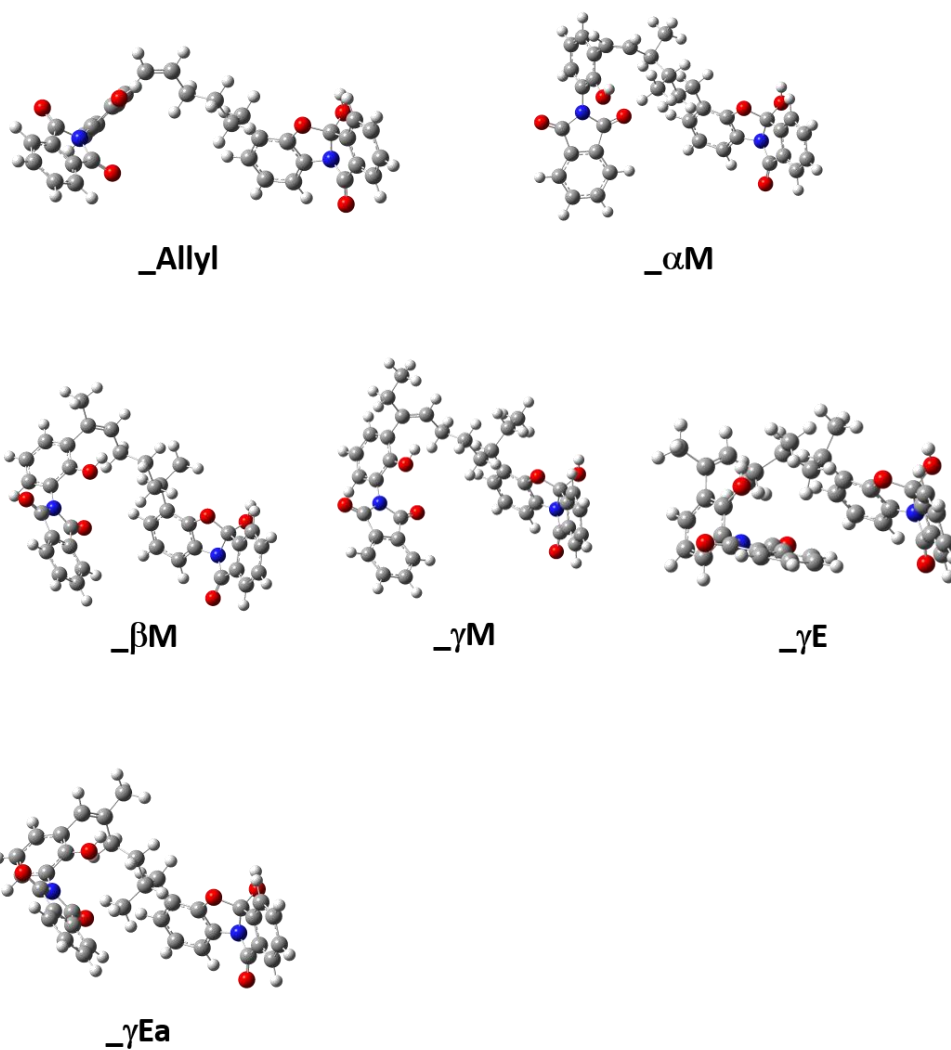


Figure 337. Simulated single-point energies of the geometry optimized intermediate structures of the HPI-to-PBO reaction of ee-crosslinked allyl-imide models.

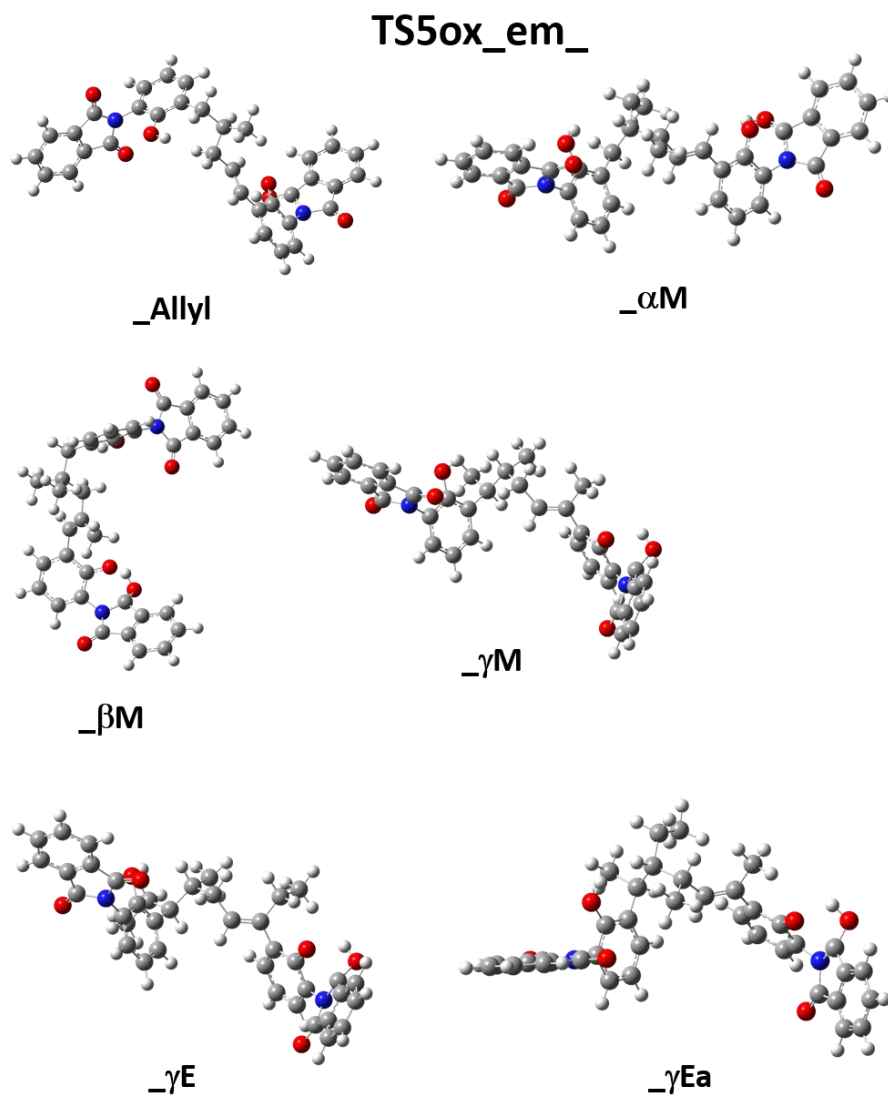
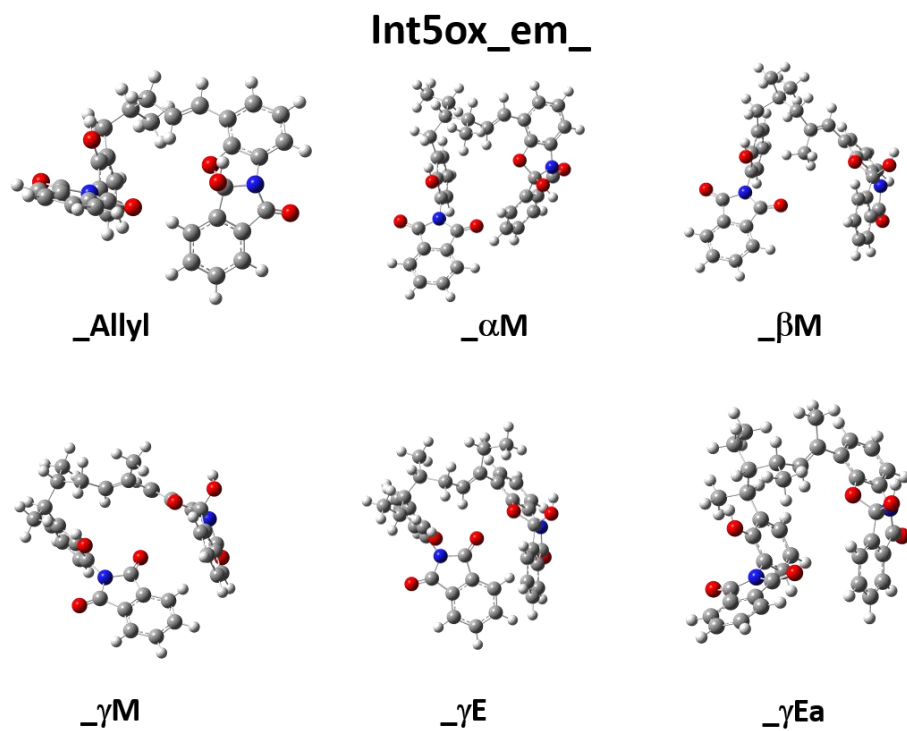


Figure 338. Simulated single-point energies of the geometry optimized transition-state structures of the HPI-to-PBO reaction of em6-crosslinked allyl-imide models.



**Figure 339.** Simulated single-point energies of the geometry optimized intermediate structures of the HPI-to-PBO reaction of em6-crosslinked allyl-imide models.



Table 33. Single-Point energy (SPE) of the transitions-state structure (TS5ox\_) and intermediate structure (Int5ox\_) of the crosslinked and HPI-to-PBO rearranged models.

SPE (Hartree)				
ee_		TS5ox_	Int5ox_	P5ox_*
<b>Model</b>				
<b>Allyl</b>	-1872,284	-1872,231	-1872,264	-1495,125
<b>aM</b>	-1950,915	-1950,859	-1950,892	-1573,756
<b>bM</b>	-1950,922	-1950,868	-1950,901	-1573,759
<b>gM</b>	-1950,915	-1950,866	-1950,900	-1573,760
<b>gE</b>	-2029,549	-2029,498	-2029,532	
<b>gEa</b>	-2029,547	-2029,490	-2029,528	-1652,390
<b>em_</b>				
<b>Allyl</b>	-1872,283	-1872,235	-1872,262	-1495,126
<b>aM</b>	-1950,909	-1950,857	-1950,890	-1573,741
<b>bM</b>	-1950,907	-1950,859	-1950,886	-1573,754
<b>gM</b>	-1950,916	-1950,857	-1950,887	-1573,757
<b>gE</b>	-2029,546	-2029,489	-2029,517	-1652,378
<b>gEa</b>	-2029,543	-2029,480	-2029,517	-1652,373

\*after CO<sub>2</sub> loss (377,181 Hartree of both CO<sub>2</sub> molecules)

Table 34. Simulated energy in relation to the starting structure  $\Delta G_{rel}$  of the transitions-state structure (TS5ox\_) and intermediate structure (Int5ox\_) of the crosslinked and HPI-to-PBO rearranged models.

ee_ Model	$\Delta G_{rel}$ (Rel. to E) (kcal/mol)	
	TS5ox_	Int5ox_
<b>Allyl</b>	5,789	-14,801
<b>aM</b>	15,113	-5,411
<b>bM</b>	12,112	-8,920
<b>gM</b>	8,026	-13,329
<b>gE</b>	9,248	-12,432
<b>gEa</b>	13,910	-9,855
em_ <b>Allyl</b>	3,402	-13,617
<b>aM</b>	16,756	-3,931
<b>bM</b>	17,543	0,611
<b>gM</b>	13,698	-5,335
<b>gE</b>	14,825	-3,062
<b>gEa</b>	20,367	-2,619

## Thermal Rearrangement of two models

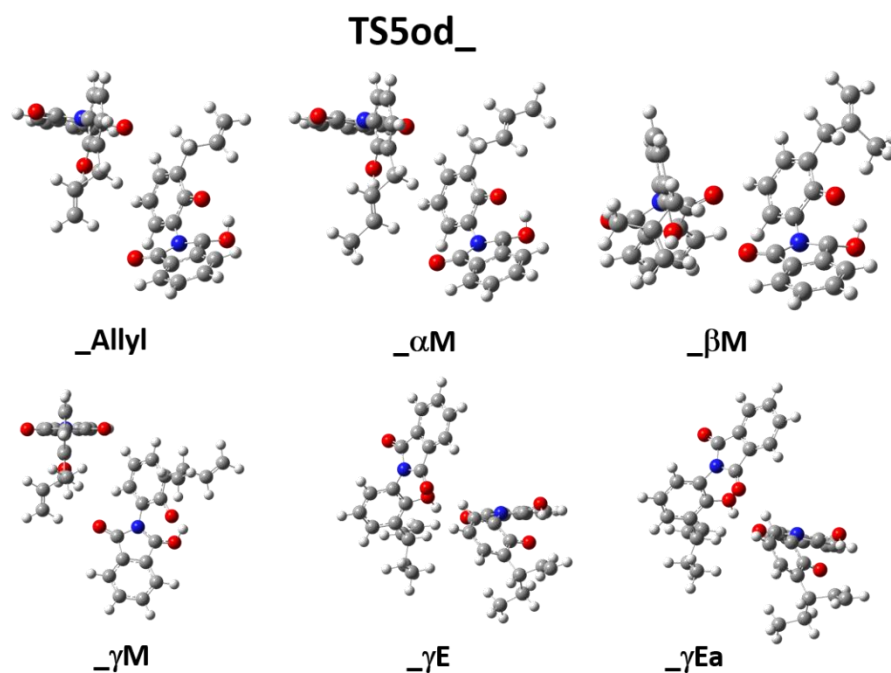


Figure 340. Simulated single-point energies of the geometry optimized transition-state structures of the HPI-to-PBO reaction allyl-imide models in a dimer arrangement.

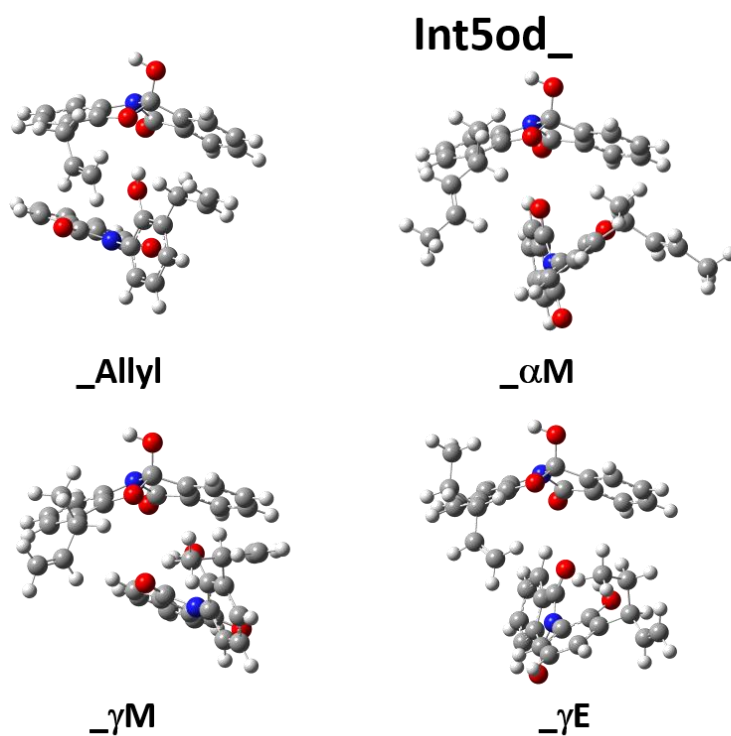


Figure 341. Simulated single-point energies of the geometry optimized intermediate structures of the HPI-to-PBO reaction allyl-imide models in a dimer arrangement.

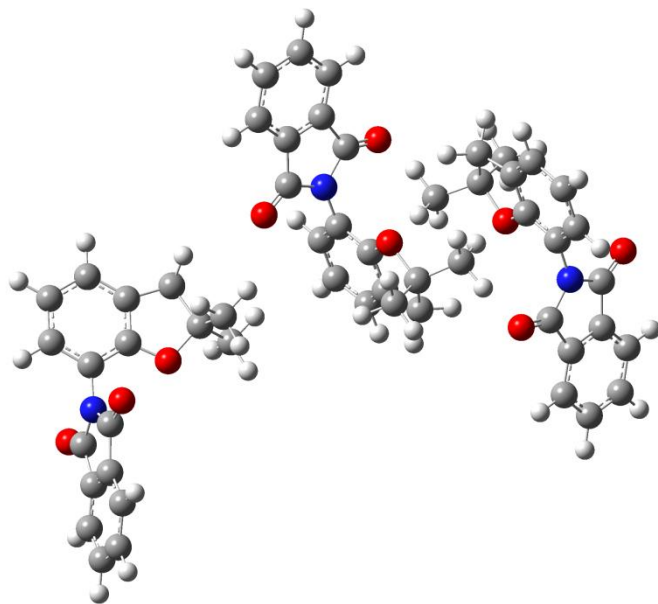
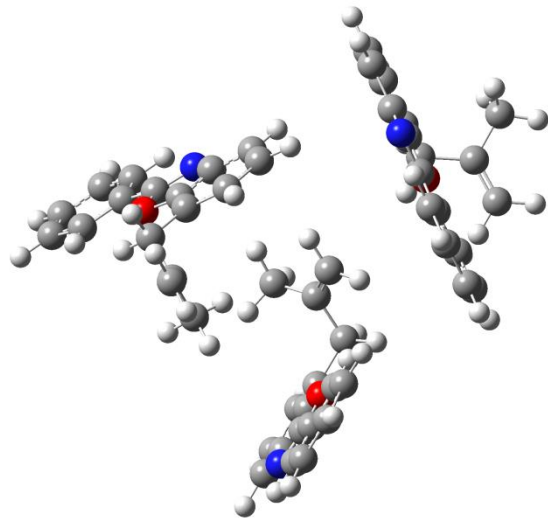
Table 35. Simulated energy in relation to the starting structure  $\Delta G_{rel}$  of the transitions-state structure (TS5od\_) and intermediate structure (Int5od\_) of the HPI-to-PBO rearranged models in a dimer arrangement.

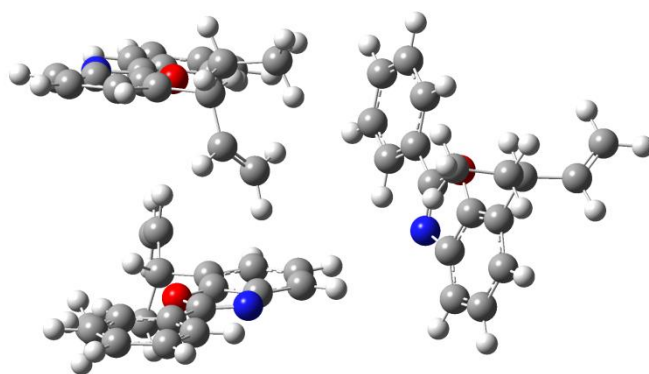
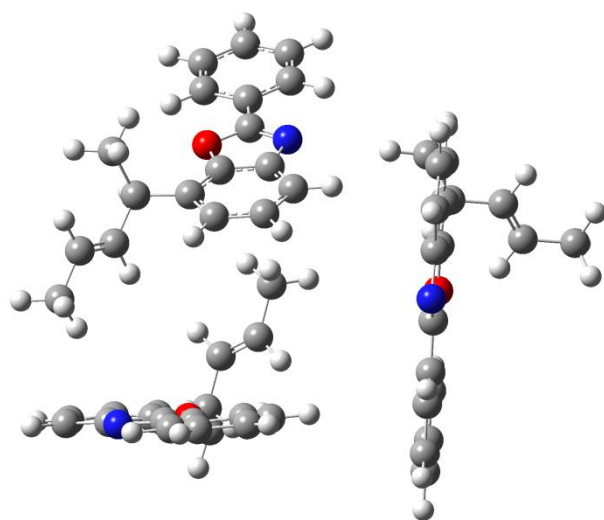
Model	$\Delta G_{rel}$ (Rel. to E) (kcal/mol)		
	Dimer	TS5od_	Int5od_
<b>Allyl</b>	-30,951	24,266	3,585
<b>aM</b>	-32,910	23,035	
<b>bM</b>	-26,909	25,327	
<b>gM</b>	-20,451	28,413	4,274
<b>gE</b>	-19,962	28,382	6,045
<b>gEa</b>	-27,154	21,633	2,834

Table 36. Single-Point energy (SPE) of the transitions-state structure (TS5od\_) and intermediate structure (Int5od\_) of the HPI-to-PBO rearranged models.

Model	SPE (Hartree)			
		TS5od_	Int5od_	P5od_*
<b>HPI</b>	-1638,816	-1638,765	-1638,807	
<b>Allyl</b>	-1872,261	-1872,202	-1872,235	-1495,093
<b>aM</b>	-1950,906	-1950,847		
<b>bM</b>	-1950,905	-1950,847		
<b>gM</b>	-1950,891	-1950,833	-1950,872	
<b>gE</b>	-2029,524	-2029,467	-2029,503	
<b>gEa</b>	-2029,536	-2029,478	-2029,508	

### Orientation of three model structures





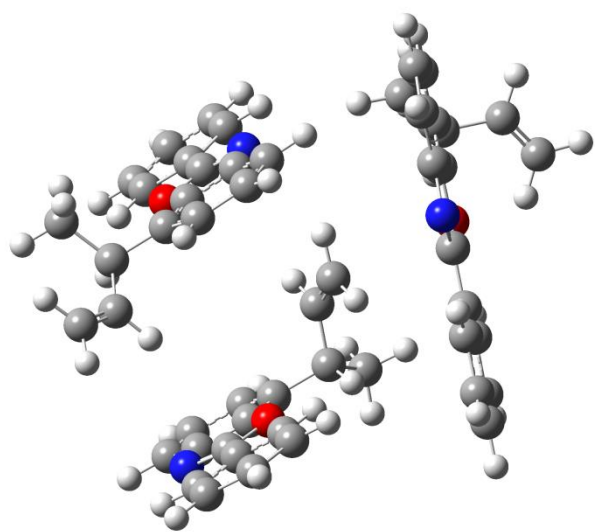


Figure 342. Geometry optimized structures of three models of each allyl derivative.

Simulations of the proposed structures of the comparison literature mechanism by Tena *et al.*

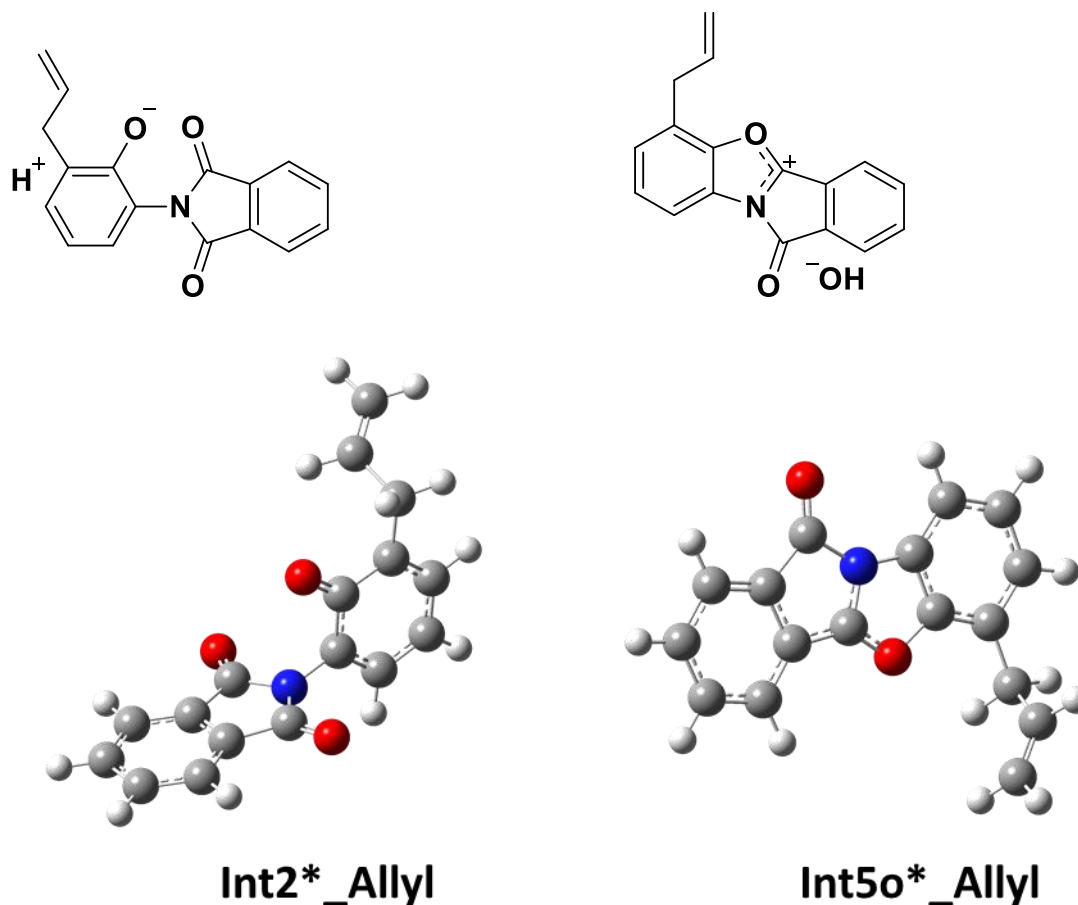


Figure 343. Geometry optimized product structures of the HPI-to-PBO formation (Thermal Rearrangement) of the allyl-imide models of the comparison literature mechanism by Tena *et al.* [256].

Table 37. Single-Point energy (SPE), dipole momentum, imaginary frequency (IF) and the simulated energy in relation to the starting structure  $\Delta G_{rel}$ , of the HPI-to-PBO formation (Thermal Rearrangement).

Structure	SPE	Dipole momentum	IF [cm <sup>-1</sup> ]	$\Delta G_{rel}$ (kcal/mol)
<b>Int2*</b>	-935,58	7,55		330,24
<b>TS5o*</b>	-935,56			342,78
<b>Int5o*</b>	-935,54	7,55		356,01



## Molecular Dynamics Simulation

Table 38. Details of the simulated models.

<b>Modification</b>	<b>#atoms</b>	<b>#chains</b>	<b>#repetition units</b>	<b>Density</b>
Allyl-PI	4624	2	33	1,354 ± 0,005
αM-PI	5020	2	33	1,356 ± 0,007
βM-PI	5020	2	33	1,358 ± 0,004
γM-PI	5020	2	33	1,347 ± 0,001
γE-PI	5416	2	33	1,349 ± 0,004
γEa-PI	5416	2	33	1,345 ± 0,008
cbm	5020	2	33	1,349 ± 0,003

Table 39. Properties of the final simulated crosslinked models.

<b>Modification</b>	<b>#Crosslinks</b>	<b>Density (@573K)</b>	<b>Density (@303K)</b>
Allyl-PI	33±2	1,282 ± 0,006	1,361 ± 0,014
αM-PI	27±3	1,270 ± 0,000	1,331 ± 0,001
βM-PI	26±1	1,263 ± 0,005	1,335 ± 0,014
CyCx-βM-PI	26±1	1,219 ± 0,005	1,343 ± 0,005
(TCM)βM-PI	26±1	1,147 ± 0,005	1,305 ± 0,005
γM-PI	29±1	1,232 ± 0,002	1,308 ± 0,000
γE-PI	26±1	1,224 ± 0,013	1,302 ± 0,011
γEa-PI	21±1	1,242 ± 0,03	1,252 ± 0,04

Table 40. Overview of determined parameter and properties obtained by molecular modelling simulations.

Code	Atom#	Crosslinks	Density
Allyl	4624	0	1.354±0.005
Allyl10cx	4624	10	1.362±0.012
Allyl20cx	4624	20	1.351±0.009
Allyl33cx	4624	33	1.361±0.014
αM-PI	5020	0	1.356±0.007
αM-PI10cx	5020	10	1.343±0.001
αM-PI20cx	5020	20	1.337±0.009
αM-PI27cx	5020	27	1.331±0.001
βM-PI	5020	0	1.358±0.005
βM-PI10cx	5020	10	1.322±0.024
βM-PI20cx	5020	20	1.331±0.012
βM-PI26cx	5020	26	1.335±0.014
PBF- βM-PI	5020	0	1.349±0.003
γM-PI	5020	0	1.347±0.001
γM-PI10cx	5020	10	1.319±0.000
γM-PI20cx	5020	20	1.320±0.001
γM-PI29cx	5020	29	1.308±0.000
γE-PI	5416	0	1.349±0.004
γE-PI10cx	5416	10	1.258±0.041
γE-PI20cx	5416	20	1.289±0.019
γE-PI26cx	5416	26	1.302±0.013
γEa-PI	5416	0	1.345±0.008
γEa-PI10cx	5416	10	1.288±0.012
γEa-PI20cx	5416	20	1.301±0.005
γEa-PI21cx	5416	21	1.252±0.050

Table 41. Overview of free volume analysis of βM-PI.

Code	Crosslinks	Density	Free Volume (%)	Free Volume/ Connolly Surface (Å)
βM-PI	0	1.358±0.005	23.58±0.36	0.76±0.019
βM-PI10cx	10	1.322±0.024	25.73±1.82	0.88±0.006
βM-PI20cx	20	1.331±0.012	25.85±2.38	0.87±0.031
βM-PI26cx	26±1	1.335±0.014	25.62±1.83	0.84±0.0006
CyCx-βM-PI	26±1	1.331 ± 0.011	26.58±0.006	0.83±0.014
(TCM)βM-PI	26±1	1.313±0.016	26.77±0.010	0.81±0.04
(TCM)βM-PI	26±1	1.298 ± 0.013	27.44±0.009	0.81±0.027
(TCM)βM-PI	26±1	1.270±0.007	28.14±0.006	0.83±0.023
PBF- βM-PI	0	1.349±0.003	25.63±0.295	0.79±0.021

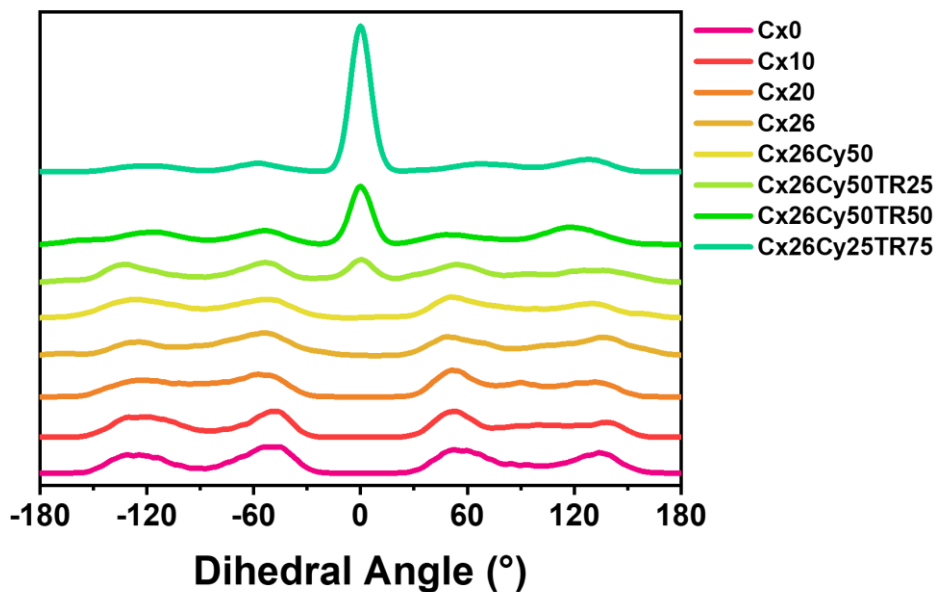


Figure 344. Torsion distribution for the imide-phenol dihedral torsion with increasing degree of crosslinking (0-26) and CyCx-βM-PI, (TCR)βM-PI with 25, 50 and 75% HPI-to-PBO conversion.

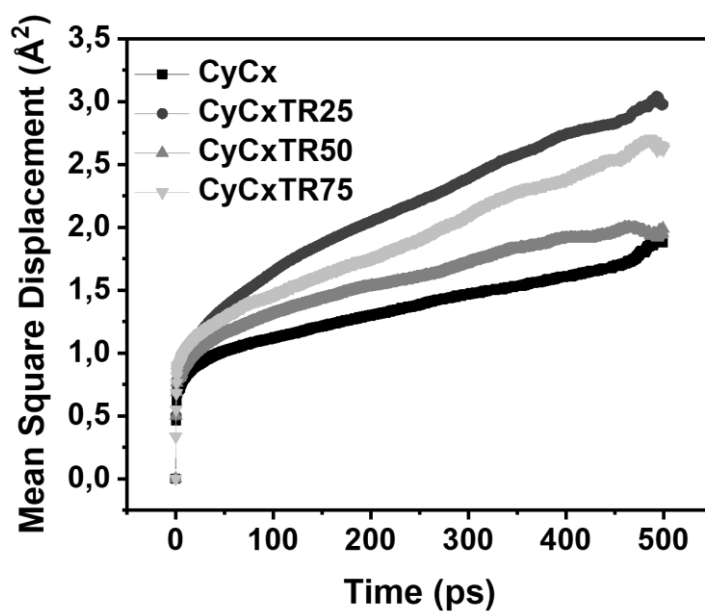


Figure 345. Mean-Square Displacement for CyCx-βM-PI, (TCR)βM-PI with 25, 50 and 75% of HPI-to-PBO conversion.

## Gas-Separation Performance Allylderivatives

Table 42. Overview of determined gas diffusion coefficients of He, H<sub>2</sub>, CO<sub>2</sub>, O<sub>2</sub>, N<sub>2</sub> and CH<sub>4</sub>.

Material	Annealing	Diffusion coefficient [ $10^{-8}$ cm <sup>2</sup> /s]					
		He	H <sub>2</sub>	CO <sub>2</sub>	O <sub>2</sub>	N <sub>2</sub>	CH <sub>4</sub>
<b>Allyl-PI</b>	<b>300</b>	200	509	2.99	9.42	2.44	0.47
<b>bM-PI</b>		680	702	5.51	16.8	3.89	0.83
<b>gM-PI</b>		554	285	3.62	8.63	1.37	0.62
<b>gE-PI</b>		593	1147	7.68	26.8	7.96	2.17
<b>Cinnamyl-PI</b>		139	85.2	1.14	5.71	2.33	0.04
<b>Prenyl-PI</b>		631	458	3.03	10.5	1.01	0.35
<b>Butylene-PI</b>		196	108	4.89	10.9	4.07	1.25
<hr/>							
<b>Allyl-PI</b>	<b>350</b>	2638	883	7.92	22.6	6.27	1.39
		792	185	12.8	31.7	10.2	2.66
<b>bM-PI</b>		3070	2050	27.5	78.5	11.2	6.30
<b>gM-PI</b>		4130	1126	6.69	13.4	5.20	1.10
<b>gE-PI</b>		5431	2825	31.2	75.8	29.9	7.92
<b>Cinnamyl-PI</b>		1217	120	8.49	14.6	6.37	2.49
<b>Prenyl-PI</b>			1110	9.74	27.9	9.31	0.45
<b>Butylene-PI</b>		1736	1471	8.19	24.1	6.65	1.18
<hr/>							
<b>Allyl-PI</b>	<b>400</b>	210	621	24.2	25.9	5.95	2.41
<b>αM-PI</b>		491	518	32.9	59.9	22.2	7.78
<b>βM-PI</b>		952	1580	37.9	72.8	21.9	6.21
<b>γM-PI</b>		507	1110	32.4	77.5	27.5	6.71
<b>γE-PI</b>		1850	696	43.8	94.4	23.8	13.9
<hr/>							
<b>bM-PI</b>	<b>150</b>	41.8	188	3.35	14.3	3.32	0.52
	<b>300 1'</b>		1400	4.12	7.22	2.55	0.72
	<b>300 30'</b>	680	702	5.51	16.8	3.89	0.83
	<b>300 120'</b>	228	1293	8.21	16.3	2.43	1.76
	<b>350</b>	3070	2050	27.5	78.5	11.2	6.30
	<b>400</b>	952	1580	37.9	72.8	21.9	6.21

Table 43. Overview of determined gas permeability of He, H<sub>2</sub>, CO<sub>2</sub>, O<sub>2</sub>, N<sub>2</sub> and CH<sub>4</sub>.

Material	Annealing	Permeability [Barrer]					
		He	H <sub>2</sub>	CO <sub>2</sub>	O <sub>2</sub>	N <sub>2</sub>	CH <sub>4</sub>
<b>Allyl-PI</b>	<b>300</b>	247	122	102	17.9	3.91	1.39
<b>βM-PI</b>		180	189	149	29.3	5.38	4.94
<b>γM-PI</b>		151	152	106	23.1	5.33	4.99
<b>γE-PI</b>		167	180	181	36.5	10.6	9.16
<b>Cinnamyl-PI</b>		95.8	99.8	50.6	10.3	3.81	3.59
<b>Prenyl-PI</b>		155	141	84.5	18.5	4.13	3.63
<b>Butylene-PI</b>		142	140	120	25.8	9.08	6.41
<hr/>							
<b>Allyl-PI</b>	<b>350</b>	423	499	377	58.3	14.9	10.9
<b>αM-PI</b>		727	467	527	101	25.4	20.8
<b>βM-PI</b>		728	1075	831	169	38.3	38.2

$\gamma$ M-PI		204	219	185	22.8	8.15	6.14
$\gamma$ E-PI		531	739	968	162	51.9	51.6
Cinnamyl-PI		226	269	249	55.1	22.8	19.2
Prenyl-PI		271	295	236	50.9	13.1	11.7
Butylene-PI		287	289	225	48.5	11.6	7.19
<b>Allyl-PI</b>	<b>400</b>	613	803	1066	221	52.6	37.8
$\alpha$ M-PI		752	1151	1669	291	88.3	78.2
$\beta$ M-PI		944	1475	1984	434	125	93.1
$\gamma$ M-PI		575	808	975	171	52.5	41.2
$\gamma$ E-PI		913	1624	3011	526	189	153
$\beta$ M-PI	<b>150</b>	58.7	40.9	63.1	11.8	4.19	2.48
	<b>300</b>		122	110	18.6	4.86	3.23
	<b>300</b>	180	189	149	29.3	5.38	4.94
	<b>350</b>	728	1075	831	169	38.3	38.2
	<b>400</b>	944	1475	1984	434	125	93.1

Table 44. Overview of determined gas selectivity certain gas pairs.

<b>Selectivity</b>							
<b>Material</b>	<b>Annealing</b>	<b>H<sub>2</sub>/CO<sub>2</sub></b>	<b>H<sub>2</sub>/N<sub>2</sub></b>	<b>H<sub>2</sub>/CH<sub>4</sub></b>	<b>O<sub>2</sub>/N<sub>2</sub></b>	<b>CO<sub>2</sub>/CH<sub>4</sub></b>	<b>CO<sub>2</sub>/N<sub>2</sub></b>
<b>Allyl-PI</b>	<b>300</b>	1.20	31.3	88.2	4.6	51	26.1
$\beta$ M-PI		1.27	35.2	38.4	5.4	30.2	27.7
$\gamma$ M-PI		1.44	28.5	30.5	4.3	21.2	19.9
$\gamma$ E-PI		0.99	16.9	19.7	3.4	19.8	17.1
<b>Cinnamyl-PI</b>		1.97	26.2	27.8	2.7	14.1	13.3
<b>Prenyl-PI</b>		1.68	34.2	38.9	4.5	23.3	20.5
<b>Butylene-PI</b>		1.17	15.4	21.8	2.8	18.6	13.2
<b>Allyl-PI</b>	<b>350</b>	1.32	33.4	45.9	3.9	34.7	25.3
$\alpha$ M-PI		0.89	18.4	22.4	4.0	25.3	20.8
$\beta$ M-PI		1.29	28.1	28.2	4.4	21.8	21.7
$\gamma$ M-PI		1.18	26.9	35.7	2.8	30.2	22.7
$\gamma$ E-PI		0.76	14.2	14.3	3.1	18.8	18.7
<b>Cinnamyl-PI</b>		1.08	11.8	13.8	2.4	12.8	10.9
<b>Prenyl-PI</b>		1.25	22.6	25.3	3.9	20.2	18.1
<b>Butylene-PI</b>		1.29	24.9	40.2	4.2	31.3	19.4
<b>Allyl-PI</b>	<b>400</b>	0.75	15.3	21.2	4.2	28.2	20.3
$\alpha$ M-PI		0.69	13.0	14.7	3.3	21.3	18.9
$\beta$ M-PI		0.74	11.8	15.8	3.5	21.3	15.9
$\gamma$ M-PI		0.83	15.4	19.6	3.2	23.7	18.6
$\gamma$ E-PI		0.54	8.6	10.6	2.8	19.6	15.9
$\beta$ M-PI	<b>150</b>	0.65	9.8	16.5	2.8	25.5	15.0
	<b>300</b>	1.10	25.0	37.7	3.8	34.0	22.7
	<b>300</b>	1.27	35.2	38.4	5.4	30.2	27.7
	<b>350</b>	1.29	28.1	28.2	4.4	21.8	21.7
	<b>400</b>	0.74	11.8	15.8	3.5	21.3	15.9

Table 45. Overview of determined gas diffusion coefficients of ethylene, ethane, propylene, and propane.

<b>Diffusion coefficient [<math>10^{-8}</math> cm<sup>2</sup>/s]</b>					
<b>Material</b>	<b>Annealing</b>	<b>C<sub>2</sub>H<sub>4</sub></b>	<b>C<sub>2</sub>H<sub>6</sub></b>	<b>C<sub>3</sub>H<sub>6</sub></b>	<b>C<sub>3</sub>H<sub>8</sub></b>
<b>Allyl-PI</b>	<b>400</b>	1.18	0.35	0.21	0.019
<b>αM-PI</b>		2.11	0.72	0.46	0.049
<b>βM-PI</b>		4.00	1.28	0.98	0.06
<b>γE-PI</b>		3.8	1.19	0.74	0.057

Table 46. Overview of determined gas permeability of ethylene, ethane, propylene, and propane.

<b>Permeability [Barrer]</b>					
<b>Material</b>	<b>Annealing</b>	<b>C<sub>2</sub>H<sub>4</sub></b>	<b>C<sub>2</sub>H<sub>6</sub></b>	<b>C<sub>3</sub>H<sub>6</sub></b>	<b>C<sub>3</sub>H<sub>8</sub></b>
<b>Allyl-PI</b>	<b>400</b>	61.5	25.5	35.5	2.88
<b>αM-PI</b>		139	59.0	76.0	6.15
<b>βM-PI</b>		237	113	123	6.16
<b>γE-PI</b>		327	151	207	14.9

Table 47. Overview of determined gas selectivity certain gas pairs.

<b>Selectivity</b>				
<b>Material</b>	<b>Annealing</b>	<b>C<sub>2</sub>H<sub>4</sub>/ C<sub>2</sub>H<sub>6</sub></b>	<b>C<sub>3</sub>H<sub>6</sub>/ C<sub>3</sub>H<sub>8</sub></b>	
<b>Allyl-PI</b>	<b>400</b>	2.4	12.3	
<b>αM-PI</b>		2.4	12.4	
<b>βM-PI</b>		2.1	19.9	
<b>γE-PI</b>		2.2	13.9	

## Effect of Propargyl Derivatives in Thermal Cascade Reactions

Structure determination

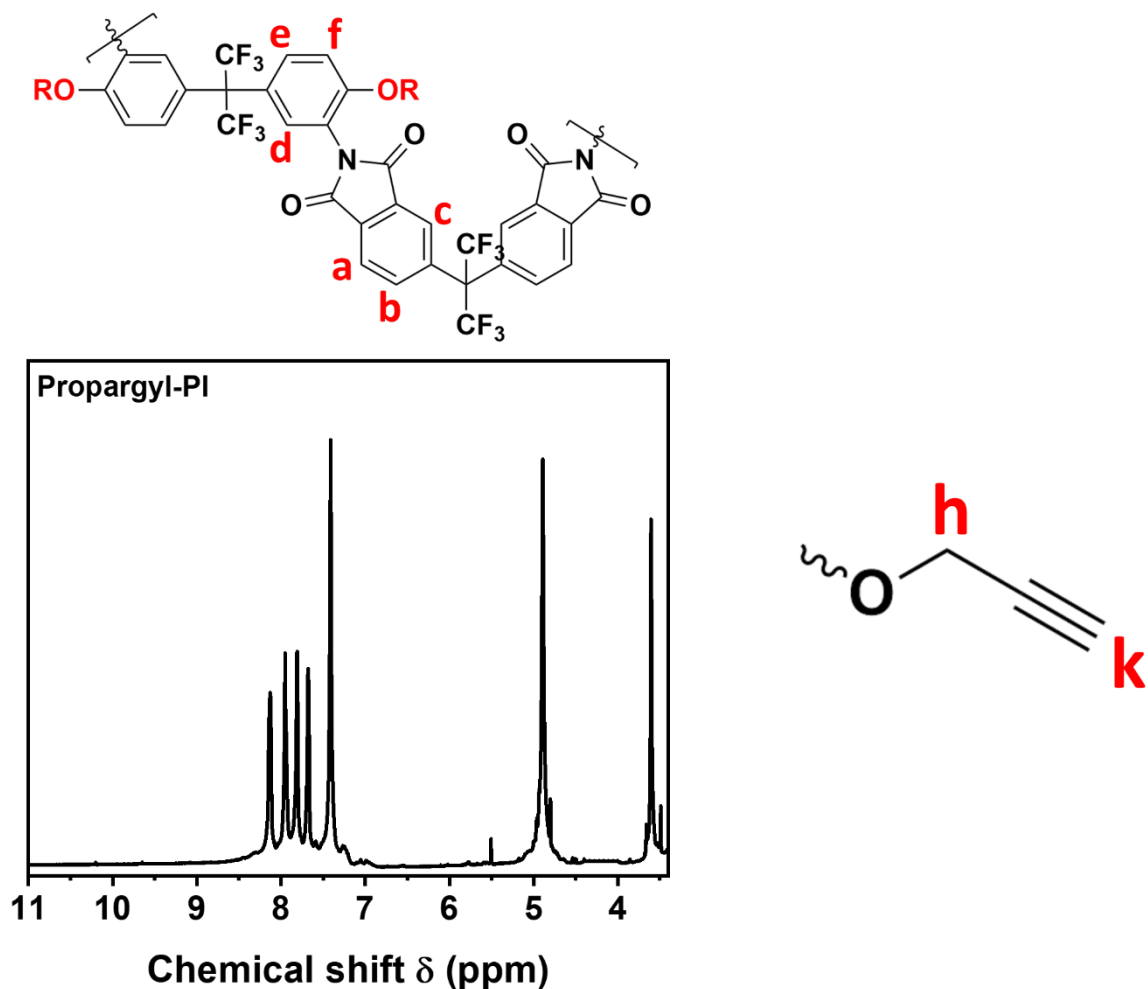


Figure 346. <sup>1</sup>H-NMR spectrum and assigned peaks to the corresponding protons of the repetition unit of Propargyl-PI1.

IR: 3288 (w, C-H str., alkyne); 2122 (w, C-H str., alkane); 1791 (s, C=O str, imide); 1720 (w, C=O str, imide); 1017 (s, C-O-C str., ether). <sup>1</sup>H NMR (DMSO-d<sub>6</sub>, ppm); 7.3-8.2 (m, 12 H, aromatic, a-f); 3.6 (s, 2 H, vinyl, k); 4.9 (s, 4 H, methylene, h).

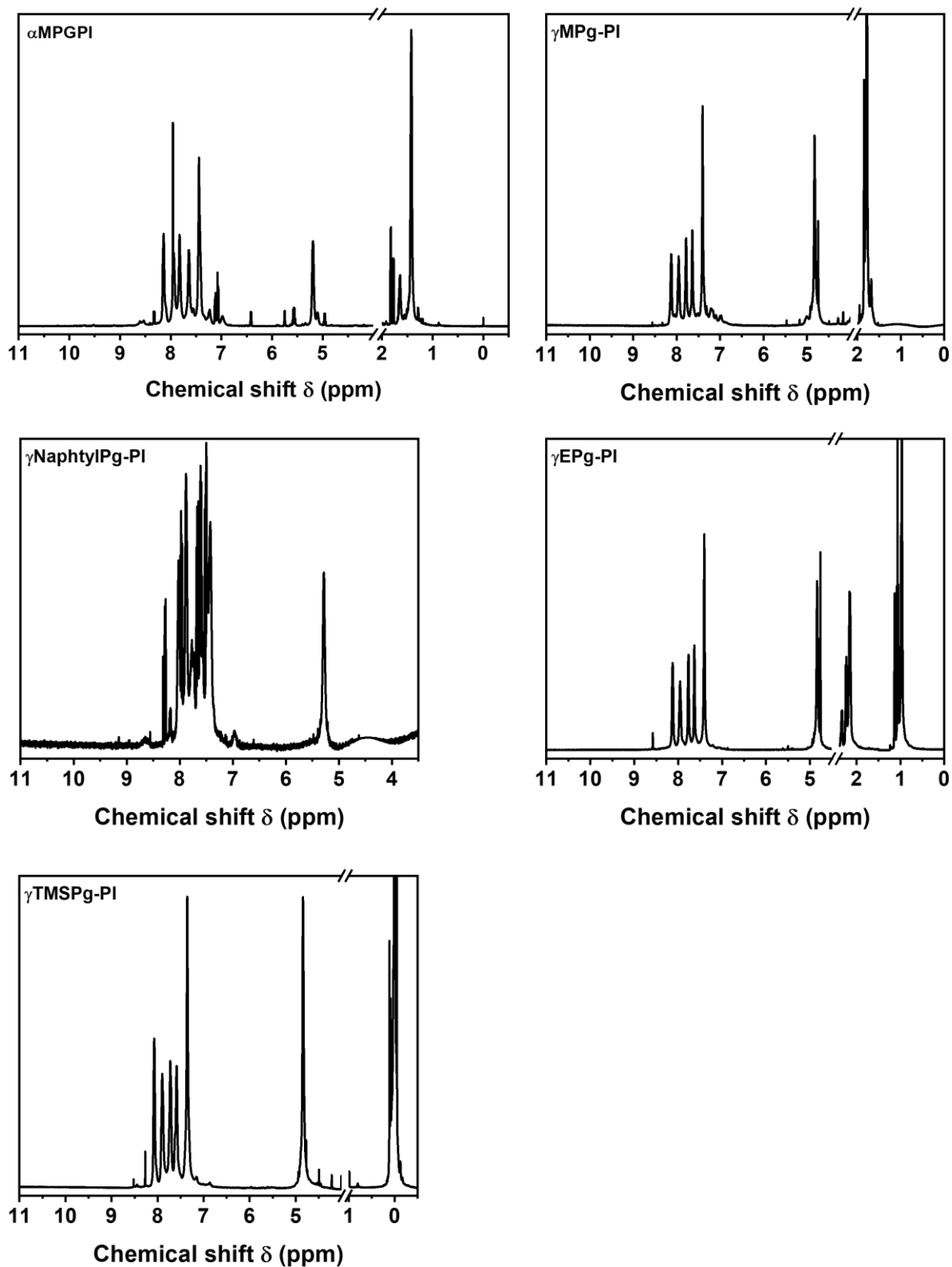
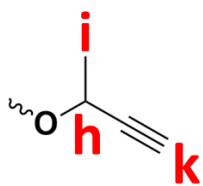


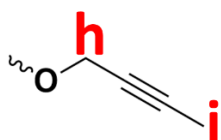
Figure 347.  $^1\text{H-NMR}$  spectra of the Propargyloxy derivatives  $\alpha\text{M-}$ ,  $\gamma\text{M-}$ ,  $\gamma\text{E-}$ ,  $\gamma\text{TMS-}$  and  $\gamma\text{NpPGPI-1}$ .





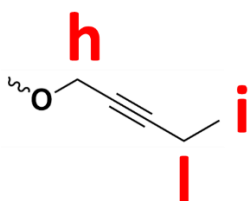
#### $\alpha$ MPGPI-1

IR: 3288 (w, C-H str., alkyne); 2122 (w, C-H str., alkane); 1790 (s, C=O str, imide); 1721 (w, C=O str, imide); 1017 (s, C-O-C str., ether).  $^1\text{H}$  NMR (DMSO- $d_6$ , ppm); 7.3-8.2 (m, 12 H, aromatic, a-f); 3.6 (s, 2 H, vinyl, k); 5.2 (s, 2 H, methylene, h), 1.4 (s, 6 H, methyl, i).



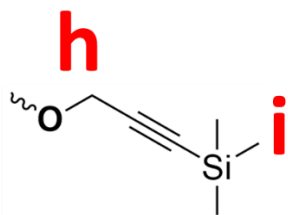
#### $\gamma$ MPGPI-1

IR: 3290 (w, C-H str., alkyne); 2122 (w, C-H str., alkane); 1791 (s, C=O str, imide); 1720 (w, C=O str, imide); 1017 (s, C-O-C str., ether).  $^1\text{H}$  NMR (DMSO- $d_6$ , ppm); 7.3-8.2 (m, 12 H, aromatic, a-f); 4.9 (s, 4 H, methylene, h), 1.8 (s, 6 H, methyl, i).



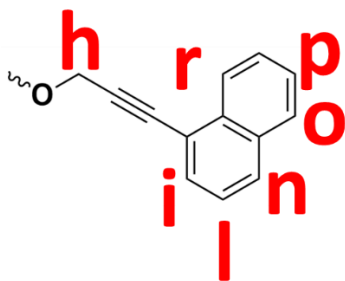
#### $\gamma$ EPGPI-1

IR: 3288 (w, C-H str., alkyne); 2122 (w, C-H str., alkane); 1791 (s, C=O str, imide); 1720 (w, C=O str, imide); 1017 (s, C-O-C str., ether).  $^1\text{H}$  NMR (DMSO- $d_6$ , ppm); 7.3-8.2 (m, 12 H, aromatic, a-f); 4.9 (s, 4 H, methylene, h), 2.0 (s, 4 H, methyl, l), 1.0 (s, 6 H, methyl, i).



**$\gamma$ TMSPGPI-1**

IR: 3288 (w, C-H str., alkyne); 2122 (w, C-H str., alkane); 1791 (s, C=O str, imide); 1720 (w, C=O str, imide); 1017 (s, C-O-C str., ether).  $^1\text{H}$  NMR (DMSO- $d_6$ , ppm); 7.3-8.2 (m, 12 H, aromatic, **a-f**); 4.9 (s, 4 H, methylene, **h**), 0 (s, 18 H, Si-methyl, **i**).



**$\gamma$ N $\pi$ PGPI-1**

IR: 3288 (w, C-H str., alkyne); 2122 (w, C-H str., alkane); 1791 (s, C=O str, imide); 1720 (w, C=O str, imide); 1017 (s, C-O-C str., ether).  $^1\text{H}$  NMR (DMSO- $d_6$ , ppm); 7.3-8.2 (m, 26 H, aromatic, **a-f**); 5.3 (s, 4 H, methylene, **h**).

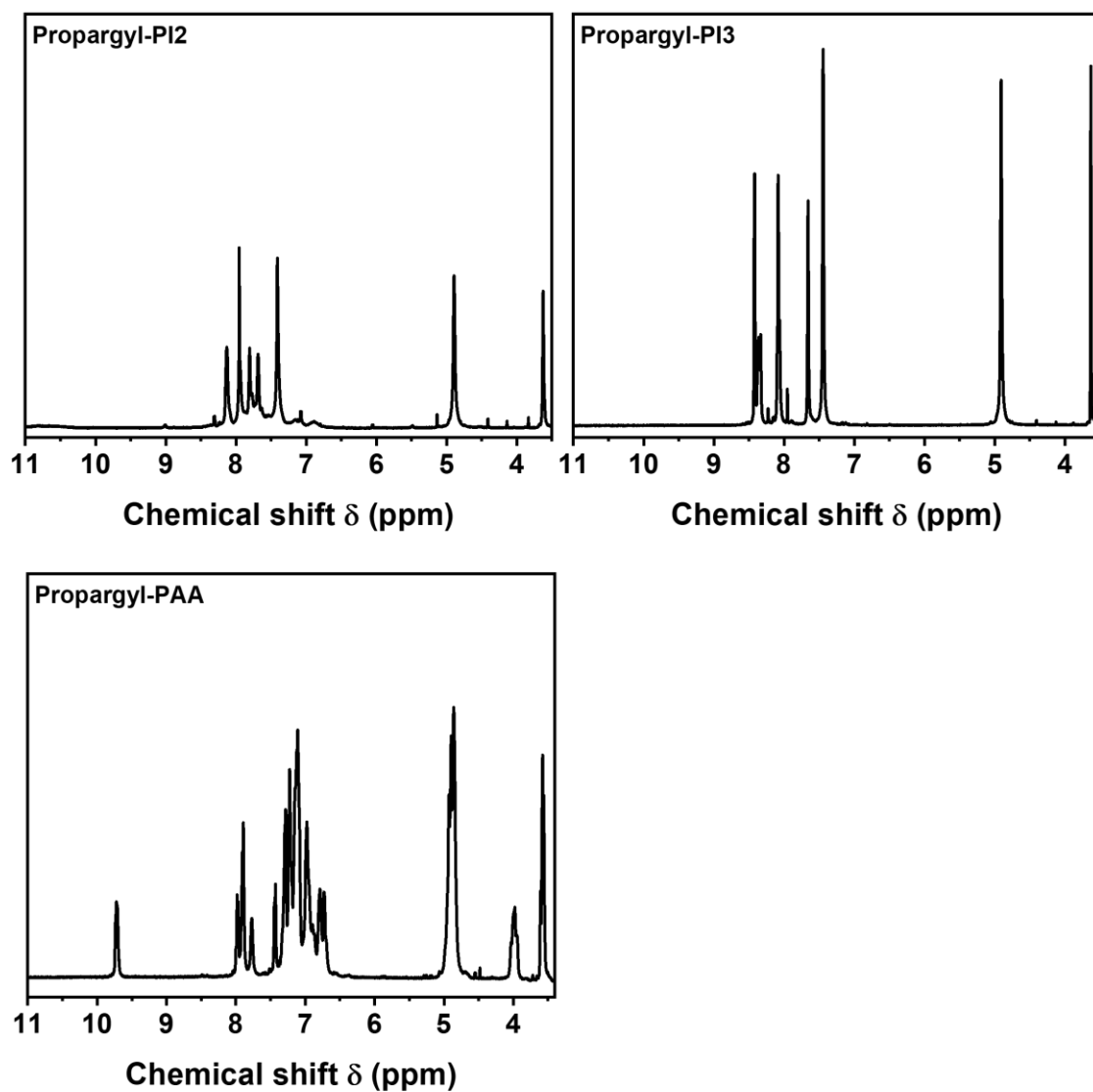


Figure 348. <sup>1</sup>H-NMR spectra of the Propargyloxy modified backbones Propargyl-2, Propargyl-3 and the propargyloxy modified poly (amic acid) Propargyl-PAA.

### PGPI-2

IR: 3288 (w, C-H str., alkyne); 2122 (w, C-H str., alkane); 1791 (s, C=O str, imide); 1720 (w, C=O str, imide); 1017 (s, C-O-C str., ether). <sup>1</sup>H NMR (DMSO-d<sub>6</sub>, ppm); 7.2-8.2 (m, 12 H, aromatic, a-f); 3.6 (s, 2 H, vinyl, k); 4.9 (s, 4 H, methylene, h).

### PGPI-3

IR: 3288 (w, C-H str., alkyne); 2122 (w, C-H str., alkane); 1791 (s, C=O str, imide); 1720 (w, C=O str, imide); 1017 (s, C-O-C str., ether). <sup>1</sup>H NMR (DMSO-d<sub>6</sub>, ppm); 7.3-8.5 (m, 12 H, aromatic, **a-f**); 3.6 (s, 2 H, vinyl, **k**); 4.9 (s, 4 H, methylene, **h**).

### PGPAA

IR: 3288 (w, C-H str., alkyne); 2122 (w, C-H str., alkane); 1791 (s, C=O str, imide); 1720 (w, C=O str, imide); 1017 (s, C-O-C str., ether). <sup>1</sup>H NMR (DMSO-d<sub>6</sub>, ppm); 9.8 (s, 2 H, amide N-H, **h**); 6.5-8.3 (m, 12 H, aromatic, **a-f**); 3.6 (s, 2 H, vinyl, **k**); 4.9 (s, 4 H, methylene, **h**).

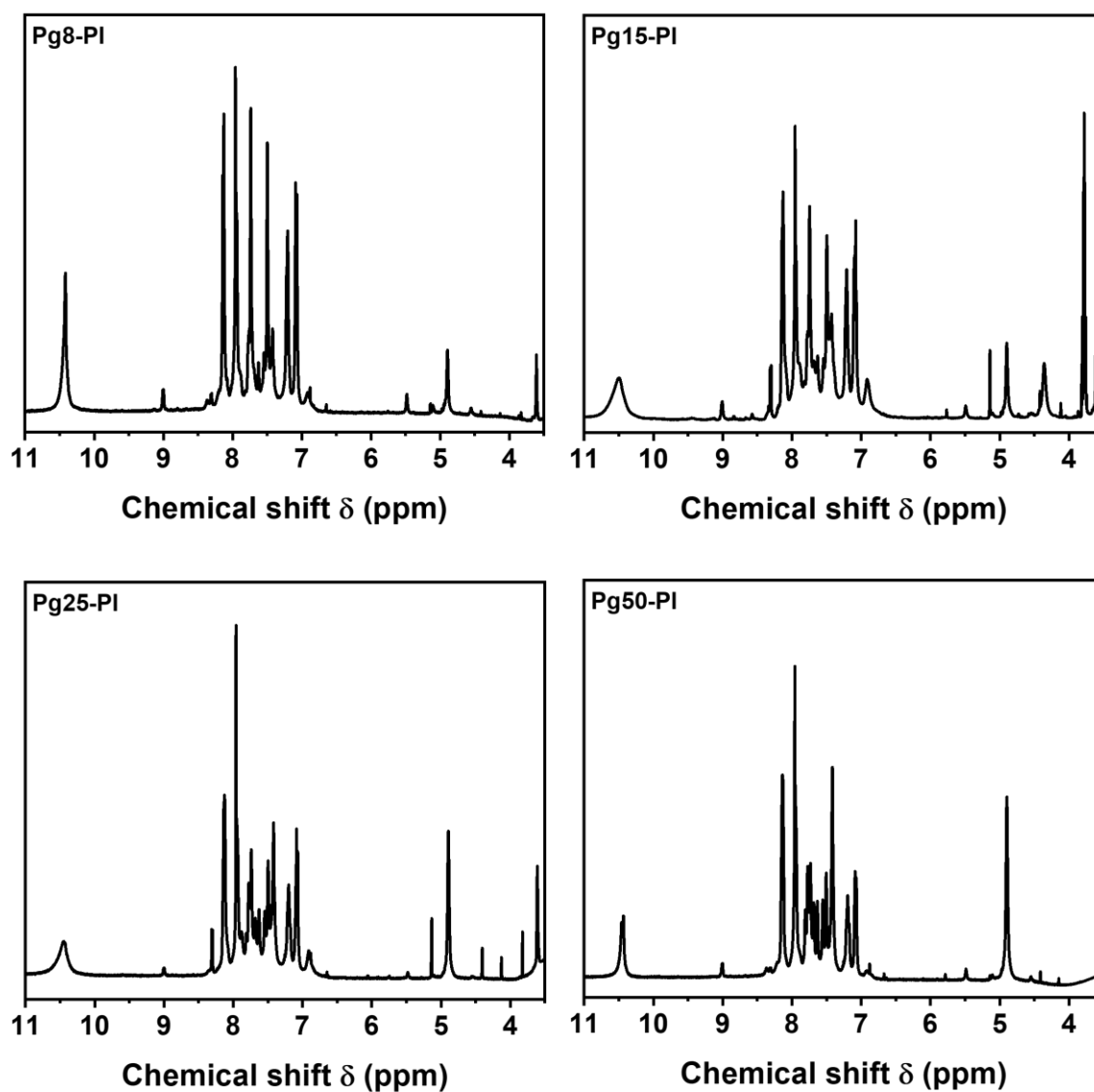


Figure 349. <sup>1</sup>H-NMR spectra of the synthesized propargylated 6FDA-BisAPAF polyimides with degrees of propargylation of 8, 15, 25 and 50%.

### PG8-PI-1

IR: 3288 (w, C-H str., alkyne); 2122 (w, C-H str., alkane); 1791 (s, C=O str, imide); 1720 (w, C=O str, imide); 1017 (s, C-O-C str., ether). <sup>1</sup>H NMR (DMSO-d<sub>6</sub>, ppm); 10.5 (s, 0.15 H, O-H); 7.3-8.2 (m, 12 H, aromatic, **a-f**); 3.6 (s, 0.15 H, vinyl, **k**); 4.9 (s, 0.3 H, methylene, **h**).

### PG15-PI-1

IR: 3288 (w, C-H str., alkyne); 2122 (w, C-H str., alkane); 1791 (s, C=O str, imide); 1720 (w, C=O str, imide); 1017 (s, C-O-C str., ether). <sup>1</sup>H NMR (DMSO-d<sub>6</sub>, ppm); 10.5 (s, 0.3 H, O-H); 7.3-8.2 (m, 12 H, aromatic, **a-f**); 3.6 (s, 0.3 H, vinyl, **k**); 4.9 (s, 0.5 H, methylene, **h**).

### PG25-PI-1

IR: 3288 (w, C-H str., alkyne); 2122 (w, C-H str., alkane); 1791 (s, C=O str, imide); 1720 (w, C=O str, imide); 1017 (s, C-O-C str., ether). <sup>1</sup>H NMR (DMSO-d<sub>6</sub>, ppm); 10.5 (s, 0.5 H, O-H); 7.3-8.2 (m, 12 H, aromatic, **a-f**); 3.6 (s, 0.5 H, vinyl, **k**); 4.9 (s, 1 H, methylene, **h**).

### PG50-PI-1

IR: 3288 (w, C-H str., alkyne); 2122 (w, C-H str., alkane); 1791 (s, C=O str, imide); 1720 (w, C=O str, imide); 1017 (s, C-O-C str., ether). <sup>1</sup>H NMR (DMSO-d<sub>6</sub>, ppm); 10.5 (s, 1 H, O-H); 7.3-8.2 (m, 12 H, aromatic, **a-f**); 3.6 (s, 1 H, vinyl, **k**); 4.9 (s, 2 H, methylene, **h**).

## Thermokinetics

Table 48. Results of the thermokinetic evaluation of Propargyl-PI using the KAS- and Friedman method.

KAS method		Friedman method	
Conversion $\alpha$ (%)	$E_A$ [kJ/mol]	Conversion $\alpha$ (%)	$E_A$ [kJ/mol]
1,0	82.6	1,0	93.7
3,1	92.3	3,1	106.1
5,2	102.9	5,2	122.3
10,4	125.8	10,4	147.8
15,3	141.2	15,3	162.8
20,4	153.0	20,4	173.5
25,3	161.9	25,3	182.2
30,1	169.7	30,1	190.0
40,1	183.6	40,1	207.0
50,1	200.0	50,1	230.1
60,1	226.0	60,1	272.6
70,1	283.3	70,1	372.0
80,1	268.5	80,1	268.5
90,0	.166.8	90,0	-196.6
100	85.7	100	-189.7

Table 49. Claisen-rRearrangement specific temperatures and released heat.

	Polymer	T <sub>cr,on</sub> °C	T <sub>cr,p</sub> °C	T <sub>cr,off</sub> °C	$\Delta H$ J g <sup>-1</sup>
Degree	8	226.0	256.8	276.7	34.0
Propargylation	15	213.4	261.5	290.2	80.9
	25	214.7	257.1	299.9	91.59
	50	214.3	258.1	294.6	151.7
	100	203.2	252.0	291.7	374.7
Backbone	-2	200.9	242.5	291.1	338.3
PGPI-	-3	180.0	250.8	356.0	351.4
	-4	160.0	249.4	286.5	397.4
Derivative	$\alpha$ M	150.1	229.3	275.1	314.2
	$\gamma$ M	224.7	264.1	370.0	371.8
	$\gamma$ E	224.1	269.0	356.0	

Table 50. Claisen-Rrearrangement specific temperatures and released heat.

Polymer	TRonset	TRpeak	Conversion (theoretical)	Conversion (experimental)
	°C	°C	%	%
PG8	317	384	11.3	8.4
PG15	320	393	11.2	10.1
PG25	339	391	11.1	8.9
PG50	370	438	10.9	6.3
PGPI	375	459	10.3	11.2
PAA	362	405	14.1	5.6
PGPI-2	380	410	12.6	8.9
PGPI-3	-	-	12.2	-
PGPI-4	359	440	9.5	8.9
$\alpha$ M	320	375	10.1	11.7
$\gamma$ M	378	443	10.1	11.7
$\gamma$ E	392	434	10.0	7.3
$\gamma$ TMS	329	426	9.9	21.0
$\gamma$ Np	321	374	9.5	24.9

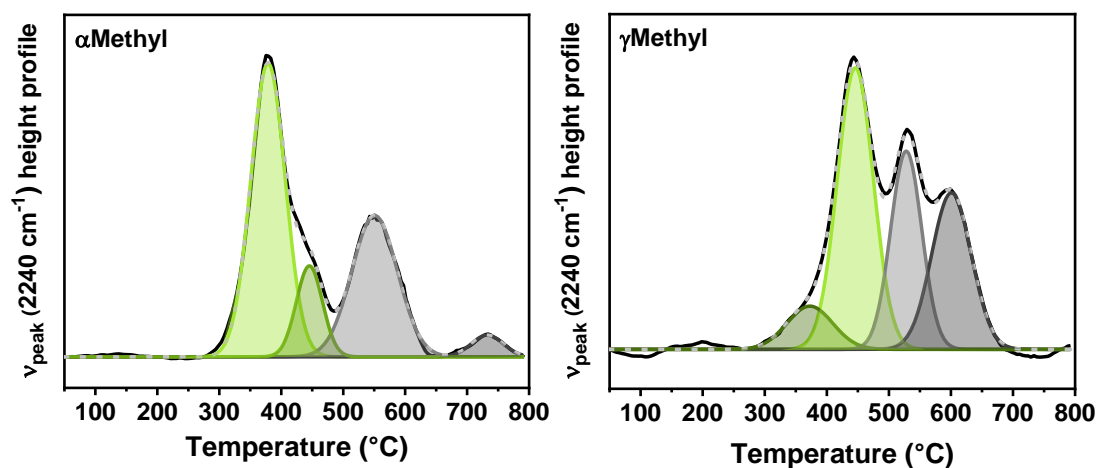


Figure 350. Peak height profile at 2240 cm<sup>-1</sup>, corresponding to CO<sub>2</sub>, for the Propargyloxy derivatives  $\alpha$ MPGPI-1 and  $\gamma$ MPGPI-1.

## Gas-Separation Performance ortho-Propargyloxy Polyimides

Table 51. Overview of determined gas permeability of He, H<sub>2</sub>, CO<sub>2</sub>, O<sub>2</sub>, N<sub>2</sub> and CH<sub>4</sub>.

		<b>Permeability [Barrer]</b>					
<b>Material</b>	<b>Annealing</b>	<b>He</b>	<b>H<sub>2</sub></b>	<b>CO<sub>2</sub></b>	<b>O<sub>2</sub></b>	<b>N<sub>2</sub></b>	<b>CH<sub>4</sub></b>
<b>Propargyl</b>	<b>30°C</b>	23	29.9	23.3	4.0	0.9	0.6
	<b>300°C</b>	273	343	258	53	23	18
	<b>350°C</b>	629	854	1098	147	56	30.5
	<b>400°C</b>	2486	5249	9472	1855	716	638
<b>50</b>	<b>350°C</b>	341	373	301	56	14	6
<b>25</b>		-	677	539	134	68	54
<b>8</b>		523	531	517	90	25	15
<b>gM</b>		1151	1651	1765	306	117	78
<b>TMS</b>		644	881	367	102	15	8.8
<b>50</b>	<b>400°C</b>	1068	1439	2151	372	107	86
		849	1489	2485	431	145	143
		197	267	253	42	12	5
		-	1078	1566	246	68	44



## Analytical methods

### Nuclear Magnetic Resonance Spectroscopy (NMR)

The NMR spectroscopy is one of the most powerful methods for the identification of organic molecules. The NMR spectroscopy dates to Edward Mills Purcell and Felix Bloch who shared the 1952 Nobel prize in physics for the development of the NMR spectroscopy [326]. Since then, various methods were developed to investigate samples in each condition and to investigate other molecular properties such as diffusion or porosity, and even inorganic molecules. The improvement of the spectrometer allowed to get highly resolved spectra from solid samples, whereas most analysis techniques fail the analysis of non-liquid samples [147].

The basic principle of the NMR technique is based on the magnetic interaction of an atomic nucleus and an external field, which yields information of the electronic environment around an atom. The key feature of any atomic nucleus is its angular momentum, which is a quantum mechanical property. In a classical sense, one can imagine the nucleus to rotate. The easiest example is hydrogen, in which one electron and one positive nuclide is available. Due to the rotation of the charged nucleus, a magnetic momentum is initiated. The angular momentum can only have specific values due to its quantization via its spin quantum number  $I$ . Therefore, only values of  $I=0, \frac{1}{2}, 1, \frac{3}{2} \dots$  are possible. Only nuclides with valid  $I$ -values apart from  $I=0$  have a spin and can be detected by NMR measurements, since only these nuclides have a magnetic momentum, which is the basic feature. This is the case of nuclides with atomic numbers and/or mass numbers that are odd-numbered. Examples are  $^1\text{H}$ ,  $^{13}\text{C}$ ,  $^{19}\text{F}$ ,  $^{15}\text{N}$  or  $^{31}\text{P}$ . In a magnetic field,  $B_0$ , the magnetic energy levels of an atomic nucleus are split into  $2I+1$  energy levels, which is called the Zeeman-effect. In the case of  $^1\text{H}$  with  $I=1/2$ , there exist two energy levels. One level with its magnetic moment vector in the direction of  $B_0$  (+z direction) and one in the opposite direction. The number of nuclides in both energy levels is determined by the Boltzmann-statistic with more nuclei in the energetically lower level (+z direction precession). The frequency of the magnetic momentum around the external field  $B_0$  is called the Larmor-frequency  $\omega_0$ . This frequency is proportional to the magnetogyric constant  $\gamma$ .

$$\Delta E = h\nu_0 = h\omega_0 = \gamma h B_0 \quad (22)$$

In modern Fourier-Transformation based spectrometer the experiment is based on a pulse procedure. The radio frequent pulse, which induces a changing field  $B_1$ , does not only contain one frequency. It is a monochromatic continuous band of frequencies. Other frequencies decrease symmetrically from  $\nu_1$  according to the chosen pulse length and period. If the broadcast frequency and the pulse length are chosen appropriately, then all resonance frequencies of each, to investigate, nuclei are excited at the same time. The excitation leads to a change of the spin distribution of both energy levels. Consequently, the macroscopic magnetic momentum along z changes. Due to an induced perpendicular force, due to  $B_1$ , the preceding spins are forced into the x,y-plane, inducing a magnetic moment  $M_x$  and  $M_y$ , other than 0. After stopping the pulse, the nuclides relax back to their equilibrium state. The relaxation of the  $M_z$  change occurs mainly due to transfer of the additional excitation energy to adjacent atoms, or solvent molecules. This process is called the spin-lattice relaxation  $T_1$ . The interaction of opposite spins causes a change of both spin directions. This occurs randomly and restores the  $M_x M_y$  magnetization back to zero and is called the spin-spin relaxation  $T_2$ . During the acquisition time  $t_{acq}$  (of 50 ms to a few seconds), a transient signal, the free induction decay (FID) is recorded. By means of Fourier-Transformation the NMR spectrum is obtained. In order to increase the signal-to-noise ratio, as NMR signal principally tend to be weak, a larger number of experiments is repeated, and their FIDs are time averaged.

Electrons around a nucleus are negatively charged and move around, which also leads to a magnetic momentum. This magnetic momentum affects  $B_0$  at the nucleus and changes therefore the effective local magnetic field  $B_{loc}$  at the nucleus. The variation of  $B_0$  by the electrons is called shielding and described by the shielding constant. The shift of the original resonance frequency is called the chemical shift. By subtraction of the resonance frequency from a reference resonance frequency, usually from TMS, divided by the reference resonance frequency yields the chemical shift which is usually plotted in a NMR spectrum. If electron withdrawing groups are attached to an atom of interest, then the local electron density around that atom is reduced and the local magnetic field is close to  $B_0$ . In that case, higher RF pulses are necessary to induce a change of the energy level population to induce a signal. Accordingly, the signal of a proton next to an electron withdrawing group or atom is shifted to high frequencies, which is also called downfield. Accordingly, groups such as carbonyl compounds are shifted to high frequencies, while alkylic protons are more shifted high field.

Another important parameter which occurs directly by the interaction of neighboring nuclei, is the indirect spin-spin-coupling. Two neighboring protons A and X in a molecule can be either + or -1/2. The micromagnetic field around them depends on the spin state and affects the environment of the neighboring proton as well. Therefore, the proton A has a neighbor proton X with + or -1/2. Therefore, the magnetic field of A is affected in two ways. This changes the local magnetic field and therefore the required frequency to induce a magnetization and FID. Accordingly, proton A shows two signals, in equal intensity, a so-called doublet. If more protons are around proton A, then the spin-spin coupling becomes more complicated and multiplets occur. The strength of the coupling effect is quantified by the coupling constant, which is the frequency difference between two neighboring peaks of a multiplet. The mechanism is based on the direct binding electron interactions. If a second magnetic field  $B_2$  is applied which corresponds to the frequency of the coupling atom, the coupling interaction can be avoided and only single-peak spectra occur. This is the case in broadband decoupled  $^{13}\text{C}$ -NMR spectra in order to visualize only carbon atoms due to the decoupling of the C-H interaction. In order to detect the number of protons that are attached to each carbon atom, a so-called DEPT (distortion less enhancement by polarization transfer) pulse sequence is used. The results are spectra in which  $\text{CH}_3$ ,  $\text{CH}_2$ , CH and quaternary C- atoms can be distinguished.

If samples in solid-state are measured, the experiments are significantly more challenging, as relaxation times are slower, since solids cannot move and do not interact with solvent molecules and each other. Therefore, the lattice-spin relaxation is decreased. In addition, coupling can occur via direct coupling of the individual magnetic fields of each nucleus. Due to the fast movement in solution, this effect is compensated, but not in solid states. Furthermore, in solution the fast movement of the molecules lead to broad distributed orientations of the molecules and their nuclei, which is in total averaged along all orientations. In solids, that is not the case, therefore a so-called anisotropy of the shielding occurs, therefore no average chemical shift and individual resonance frequency per nuclei occurs, but numerous, which broadens each peak significantly. For all these issues, modern techniques were developed to overcome these problems. Decoupling of the dipole coupling occurs by applying a strong second magnetic field  $B_2$  which eliminates the D-coupling. The use of a magic angle of  $55^\circ 44'$  of the probe position eliminates the anisotropy as it averages all coordinates of the molecule. In addition, very high rotation frequencies of 10000 Hz and more

are used to eliminate the anisotropy effect. Finally, in order to overcome the slow relaxation issue, a polarization transfer from protons to carbon atoms is executed by applying a second magnetic field in order to transfer the fast relaxation of protons to carbons.

### Fourier-Transform Infrared Spectroscopy (FT IR)

FT-IR Spectroscopy is a fast and simple analytical method to get structural information of the organic compound. The results are demonstrated as transmission and absorption plot *versus* wavenumber. The wavenumber is a reciprocal to the wavelength and proportional to the vibration frequency.

Molecules have vibrational modes, which are oscillating atom movements along their equilibrium position, these normal modes, can be described by a ball-spring model. Every non-linear molecule has  $3N-6$  normal modes. Since the molecular vibrations are quantized, which means only specific amounts of energy can be absorbed, only IR beams with specific frequencies and thus energy, can be absorbed. The energy which is absorbed corresponds to the energy between two states, for instance the ground state and first excited state. Wavenumbers are easier to handle and while frequencies have values of  $3 \times 10^{10} \text{ cm}^{-1}$ , wavenumbers have values around  $10^3 \text{ cm}^{-1}$  which are easier to handle [147].

The absorption corresponds to the residual light intensity, detected at the detector, divided by the initial light intensity and follows Lambert-Bouguer-Beer

$$A = \log_{10} \frac{I}{I_0} = \log_{10} \frac{I}{T} = \log_{10} \frac{100}{\%T} \quad (23)$$

with absorption  $A$ , intensity  $I$ , initial intensity  $I_0$  and transmission  $T$ .

In organic chemistry, absorptions of most interest are in the range from  $400$  to  $4000 \text{ cm}^{-1}$ , as these are the energies required for vibrational bands of the most functional groups. Two categories of vibrations exist, the stretching and deformation vibrations. Stretching vibrations can be symmetrical or asymmetrical, for instance  $\text{CH}_2$  groups. Deformation or bending vibrations can be of scissoring, rocking, wagging, or twisting type. Only in case of a molecular oscillating dipole moment, as a consequence of the vibrational motions, interact with the

electric field of the IR beam are able to occur, and give characteristic signals in corresponding spectra. This leads to a change in the dipole moment of the molecule and a vibration band is observed. The peak intensity depends on the dipole moment. As the dipole moment change becomes larger, the intensity increases. On a molecular basis speaking, once the molecule absorbs energy, it goes into the excited state. Once the molecule returns to the ground state, it releases energy by means of rotational, collision and translational processes. If bending and stretching vibrations are compared, it is obviously that stretching vibrations occur at higher wavenumbers and correspond to higher energy absorptions. Stretching requires more energy. From an analogous point of view, it is easier to bend a spring, than to stretch it (C-H stretching:  $2960\text{ cm}^{-1}$  vs C-H bending:  $1470\text{ cm}^{-1}$ ) [147].

IR spectra can be affected in many ways. This means, that any stabilizing and fixation of the bond, for instance by ionic interactions or hydrogen bonding influences the observed absorption pattern. Therefore, the same compound looks different when it is investigated in solid, liquid or gas phase. Coupled vibrations are vibrations that are interfered by each other due to a connection, usually with a more polar atom and often times if resonant structures exist, such as in anhydrides. Hydrogen bonding lowers the stretching vibration frequencies and also affects the band's shape and intensity. As a consequence, they broaden and become more intense. As the hydrogen bond strength increases, the O-H frequency decreases. The effect of strong hydrogen bonds is pronounced in carboxylic acids who form dimers with very polar O-H groups. Non-hydrogen bond peaks of O-H occur only in vapor phase, high dilution with non-polar solvents or by prevention of hydrogen bonding, as a consequence of steric hindrance. In amines the effect is lower, as amines are less electronegative. The region of an IR spectrum below  $1500\text{ cm}^{-1}$  is called the fingerprint region. As every molecule is different in the fingerprint region, every absorption pattern is unique. It contains mainly bending vibrations but also some low frequency vibrations such as in C-C, C-O or C-N bonds.

IR spectroscopy can be used to identify compounds, estimate their purity, detect functional groups, study hydrogen bonds, as well as to calculate force constants and reaction progress.

**Experimental setup.** The main aspect of Fourier-Transformation IR is the Michelson-Interferometer. Such a spectrometer consists of two mirrors  $m_1$  and  $m_2$  perpendicular to each other. Mirror  $m_1$  is fixed, while mirror  $m_2$  can be moved along a distance of few mm very

exactly. In addition, there is a beam splitter, which is a half mirror between both mirrors. 50% pass the half mirror to mirror m2 and 50% are split to m1. From each mirror the radiation is reflected again and so 50% go back to the light source and 50 % are reflected towards the detector. In case of a monochromatic beam the radiation is only coherent in case, that both mirrors have the same distance from the half mirror. As m2 moves, the radiation is not coherent and goes down to zero at  $x=l/2$ . Within the FT-IR spectrometer, the light source emits continuous light of all wavelengths. As a consequence, a complicated interferogram results with intensities based on the optical path difference of each mirror position. A FT transforms from time to frequency domain for the final spectrum.

In attenuated total reflection (ATR) IR spectroscopy, the light passes through a crystal and interacts with the sample. As a consequence of the refractive index of the crystal. The total reflection then forms an evanescent wave and interacts with the sample. In areas where the sample is in contact with the evanescent wave, specific parts of the IR beam are absorbed based on the sample composition. The totally reflected IR light lacks the absorbed parts and thus is attenuated, hence the name “attenuated total reflectance” (ATR).

## **Gel Permeation Chromatography (GPC)**

GPC or often described as size exclusion chromatography (SEC) and gel filtration chromatography, is in principle a separation method based on the variable retention of molecules of different sizes. The chromatographic system uses a column, packed with a stationary phase and a mobile phase, such as a solvent (Figure 351).

The separation of molecules, subsequently described for polymers, is strictly based on the size of the polymers in solution. After the polymer sample is dissolved in an appropriate solvent, polymers form coils, which size and shape are dependent on the used solvent and its interactions with it [314]. Once the polymer sample is injected into a set of columns, it permeates through the packing material, the beads. These beads are usually porous crosslinked polymer gels with pores of different sizes [327]. As a consequence, small molecules fit in the most pores more readily while larger polymers and molecule in general do not fit into numerous or even no pore and permeate through the column with low retention.

Therefore, large molecules come out first, with nearly no retention, followed by molecules of decreasing size until the smallest particle leave the column at the latest, accordingly, with larger retention times. This separation process can be described as partitioning. Usually, a set of columns is used in order to separate the injection mixture efficiently and partition it into every single component. A representation is shown in Figure 351. As molecules elute from the column successively from larger polymer coils to smaller ones, they are detected by various methods, such as an ultraviolet (UV)-, refractive index (RI), viscosity and multi-angle laser light scattering (MALLS) detector [314]. While RI-detectors are less sensitive than a UV-vis detector, the UV-vis detector cannot detect UV-vis inactive components [328]. MALLS offers the great potential of measuring an absolute value for  $M_w$  and the radius of gyration ( $R_g$ ); However, it is an expensive and dust-sensitive detector method [328]. The physical property which is obtained, is the elution volume, which, assuming a constant flow rate, can be transferred to retention time for ease of measurement. The determined data is then taken and compared to a calibration curve that has been determined prior to the measurement of the mixture of interest. Such a calibration is simply spoken a SEC measurement of a molecule mixture of known composition and weight distribution. As a consequence, based on the assignment of a specific molecular weight to the corresponding measured elution volume/retention time, a correlation can be drawn, and the weight distribution of the unknown mixture can be calculated. Such calibration materials are usually polymer standards, often polystyrene in a broad range of molecular weights up to  $1\,000\,000\text{ g mol}^{-1}$ . Therefore, the SEC based determination is not the absolute molecular weight as obtained by light scattering methods [314], since the molecular weight is calculated based on a polymer standard which might vary to the investigated polymer mixture in terms of interactions with the mobile phase and coil behavior.

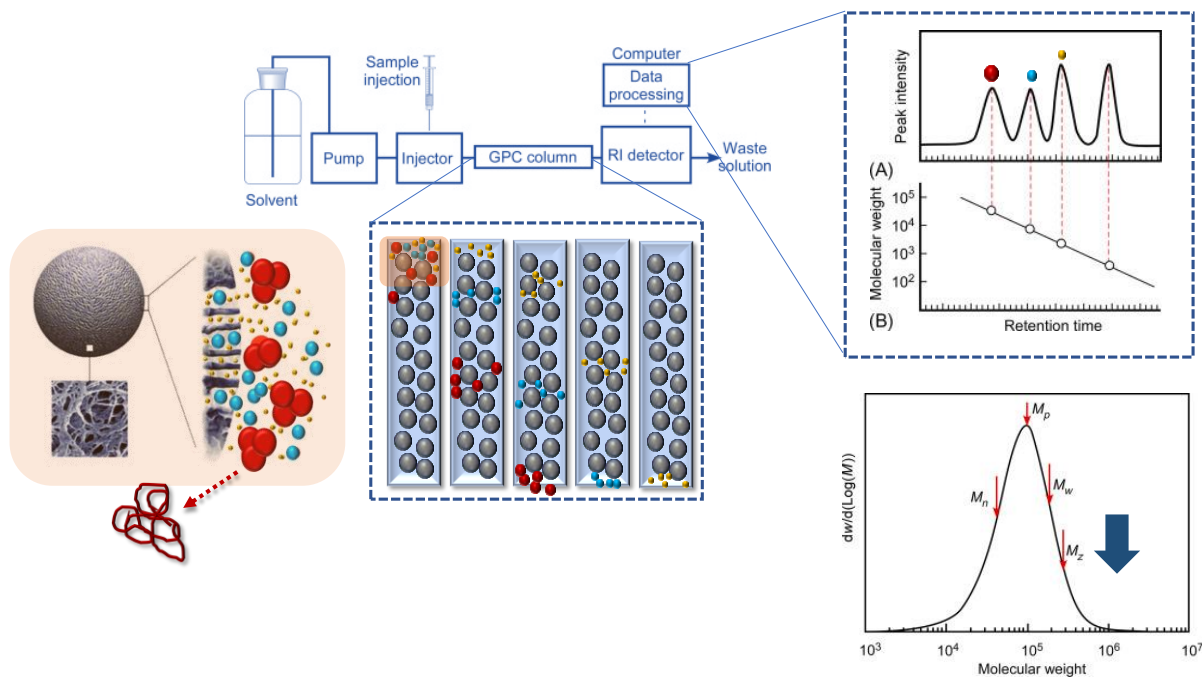


Figure 351. Basic experimental setup including the basic principle of size-exclusion within the porous substrate. On the right-hand side, the evaluation of a SEC measurement yielding specific molecular weight values [based and adapted from GE-Healthcare. 2010b. Gel filtration: Principles and Methods. Sweden: GE Healthcare Biosciences].

By means of SEC, it is possible to determine the number- ( $M_n$ ), weight- ( $M_w$ ), z-average-molecular weight ( $M_z$ ) simultaneously. From ratios, such as  $M_w/M_n$  the molecular weight distribution can be evaluated and is known as the polydispersity index PDI.  $M_n$  and  $M_w$  are defined as follows

$$M_n = \frac{\sum M_i N_i}{\sum N_i} \quad (24)$$

$$M_w = \frac{\sum M_i^2 N_i}{\sum M_i N_i} \quad (25)$$

with  $N_i$  as number of polymer molecules  $I$  of the molecular weight  $M_i$ .

## Differential Scanning Calorimetry (DSC)

The DSC method is a microcalorimetric technique, which records the heat flux rate of a sample and a reference, while subjecting both to a temperature program, which involves heating or cooling (ASTM standard E473 [329]). The heat flux contains important information, like phase changes and heat of reaction (Figure 352), which allows to evaluate further physical properties such as porosity, purity, level of crystallinity, blend composition and direct thermophysical properties such as the crystallization and melting temperature, the glass transition



temperature, the heat capacity, and the heat of reaction and decomposition temperature [24, 262, 330]. Since the first DSC was put on the market by Perkin-Elmer in 1963 [331], the improvement of the techniques and methods involved and increased the applicability to various materials and their properties and extended the use of DSC experiments. Basically, two types of DSC instruments exist, which are the power compensation DSC and heat flux DSC.

The heat flux DSC technique involves a measurement cell, which contains two identical sample holders, one for the sample pan and one for the reference pan (Figure 352). Sample holder are elevations of a thermoelectric disc of medium thermal conductivity. Both sample holders are separated by a heat leakage bridge in order to ensure that no heat is transferred between both pans. Each temperature sensor is located at the base of the sample holder platform. The cell is surrounded by a heating block. The cell is associated with a furnace to provide the linear heating ramp. The whole cell is purged by an inert gas such as nitrogen or argon under normal conditions. However, other gases such as synthetic air or carbon dioxide can be used as well. The physical description of the heat flux DSC can be written as

$$\frac{\Delta Q}{\Delta t} = \frac{\Delta T}{R} \quad (26)$$

with heat  $Q$ , time  $t$ , temperature difference between sample and reference sensor  $\Delta T$  and the thermal resistance of the thermoelectric disc  $R$ .

The experiment occurs via heating by means of the furnace, which leads to a heat flow via the disc to the samples. Therefore, an identical position of the sample and reference pan is crucial in order to ensure that the same amount of heat is transferred to each pan equally. In that case  $\Delta T$  is zero. At that point, the system is in steady-state equilibrium. If this is perturbed by a phase transition or chemical reaction for instance, then a differential signal is produced. The signal is proportional to the difference of the heat flow rates to reference and sample according to

$$Q_S - Q_R \propto \Delta T \quad (27)$$

$$\Delta T = T_S - T_R \quad (28)$$

The measured heat flow  $Q_m$  is then calculated by the temperature difference and a proportionally factor  $k'$ , which is determined by calibration

$$Q_m = -k' \cdot \Delta T \quad (29)$$

**The heating rate** defines the rate at which a sample is heated per time interval. The most common heating rate is  $10 \text{ }^\circ\text{C min}^{-1}$ . Modern instruments allow heating rates in the range from  $0.1 \text{ }^\circ\text{C min}^{-1}$  to  $100 \text{ }^\circ\text{C min}^{-1}$ . Special techniques, such as the flash-DSC allows heating rates of  $3000000 \text{ }^\circ\text{C min}^{-1}$  (MT Flash DSC 2+) [332]. High heating rates, however, can lead to a strong decrease of the temperature resolution, as large temperature gradients in the sample occur. This leads to a high thermal lag within the sample, as it cannot follow the heating rate fast enough [262]. This is also the case if large sample mass is used. For better resolution on the cost of sensitivity, low heating rates and low sample mass is used. Usually, sample mass is in the range from 3 to 10 mg, while larger amounts are used for heat capacity measurements and lower amounts are used for the determination of the purity [24]. This is also the case for the cooling rate. When cooling rate and heating rate are changed, then the shape and position of the DSC curve and its specific temperatures changes. Therefore, trends and processes have to be investigated under reproducible conditions. The cooling rate for instance plays a crucial role when it comes to the preparation of the samples with the same thermal history for a second experimental cycle.

**Temperature-modulated DSC.** On heating rate method, which has not been mentioned yet is the variable heating rate or modulated temperature. While normal heating rate modes are

$$T(t) = T_0 + \beta_0 \cdot t \quad (30)$$

A periodic modulation term is added to the linear heating rate function,

$$T(t) = T_0 + \beta_0 \cdot t + T_A \cdot \sin(\omega t) \quad (31)$$

with the angular modulation frequency  $\omega$  and the amplitude  $T_A$ .  $\beta_0$  is the linear underlying heating rate. Depending on the magnitude of the amplitude, the periodic function can be larger than the underlying heating rate and therefore heating and cooling change periodically ( $T_A \omega > \beta_0$ ). The heating rate fluctuates between  $\beta_0 \pm T_A \omega$ . As the amplitude decreases to  $T_A \omega = \beta_0$  the

heating rate varies between heating and isothermal mode. If the amplitude becomes even smaller and the product  $T_A \omega < \beta_0$  then only heating occurs.

Modulated DSC experiments allow the separation between a reversible and irreversible heat flux which forms the globally determined heat flux by traditional measurements. This allows the separation of reversible transitions such as glass transitions, which are overlapped by another irreversible process such as solvent evaporation or a chemical reaction.

**A specific TMDSC method**, developed by Mettler-Toledo, is the TOPEM® technique [333]. The TOPEM® method [333] provides a separation of temperature- and time-dependent processes. While most TMDSC method as described, use a sinusoidal temperature modulation, this method applies a time series of random temperature pulses of various time ranges. As a consequence, the broadband of frequencies allows the determination of time- and temperature dependent processes at various frequencies simultaneously. Hence, frequency dependent processes can be distinguished from processes that are independent of the frequency of the modulation. This allows the  $c_p$  determination within one experiment.

**Sample preparation.** Sample pans are based on high-purity metals, such as aluminum, platinum, silver, or copper. The sample mass is commonly weighed on a highly sensitive balance and the pan is closed with a flat lid using a “crimper”, which seals the lids. The lids are punched out at the center of the lid in order to allow the inert gas to have contact with the sample and to ensure a constant pressure during the whole measurement.

Important thermodynamic elements are explained shortly. The base of DSC methods is the physical property heat, which is defined as a transfer of energy caused by a temperature difference of two systems. Under constant pressure, as it is the case in most processes and DSC experiments, the heat equals the enthalpy  $H$  of the system. Therefore, DSC experiments allow to calculate the enthalpy differences, if the heat capacity is known. The most important quantity, however, is temperature since it is the only determined physical quantity and it principally describes the average kinetic energy of atoms or molecules. If heat changes are proportional to the change of the temperature, the intensity of the DSC curve is proportional to the heat capacity in absence of any phase transition or reaction. The heat capacity at constant pressure is defined as

$$C_p = \left( \frac{\delta Q}{\delta T} \right)_p = \left( \frac{\partial H}{\partial T} \right)_p \quad (32)$$

Commonly determined thermodynamic processes and quantities are phase transitions and their onset and peak temperatures. According to Ehrenfest two phase transitions can be distinguished [334], namely transitions of first- and second order. First order transitions are present, when the first derivative of the free energy as a function of the temperature shows discontinuity. This includes entropy and enthalpy for instance and accordingly, melting, evaporation, crystallization and condensation are first order phase transitions. If the first derivative is continuous but the second is not, then such a phase transition is called second order. Such as process is occurring when the heat capacity – temperature relationship is discontinuous. In DSC experiments this is the case when the heat capacity jumps, such as in sub- $T_g$  transitions. The process of melting occurs when a crystalline sample becomes an isotropic liquid under uptake of heat to induce a phase change, which is called the heat of fusion. If an isotropic liquid changes to a crystalline solid, it is called crystallization and the temperature of the start of such a process under cooling is the crystallization temperature. In amorphous polymers the glass transition temperature plays a crucial role, as it marks the change from the glassy state to the rubbery state. Amorphous polymers in the glassy state exist in non-equilibrium condition, which means they are not in a fully relaxed state. At this point the polymers segmental translational motion is frozen and only vibrational motion is active. After passing the glass transition range, the supplied energy is sufficient enough to induce translational motions and the polymer is able to undergo further relaxations. Principally, the glass transition is a jump of the heat capacity and accordingly a second-order phase transition. However, as the process does not occur at a specific temperature, but more in a temperature range, the glass transition is a kinetic transition. While sub- $T_g$  relaxation processes are termed  $\beta$ ,  $\gamma$  or  $\delta$ , the glass transition is referred to a relaxation. The glass transition temperature is a very important measure, as it can mark the highest application temperature of a polymer or the lowest processing temperature. The glass transition does not show any heat of transition, as this is only the case in first-order phase transitions. An empirical rule says that specific heat capacity increases at the glass transition are  $11 \text{ J K}^{-1}\text{mol}^{-1}$  for a mobile unit in a polymer backbone [330]. Larger units such as phenylene rings can result in increases by two or three times [330]. The range of the glass transition can be about  $5 \text{ }^\circ\text{C}$  but easily become  $50\text{-}60 \text{ }^\circ\text{C}$

broad. Sometimes glass transitions do not show a nearly perfect jump. They rather show a hysteresis or a very broad or overlapped by other processes or simply measurement artifacts. Since the glass transition is highly heating rate dependent (lower  $T_g$ 's at lower heating rates), a real glass transition follows such a heating rate dependence, hence a set of four experiments at different heating rates, such as 1, 2, 10 and 20 °C min<sup>-1</sup> can support the identification of a glass transition.

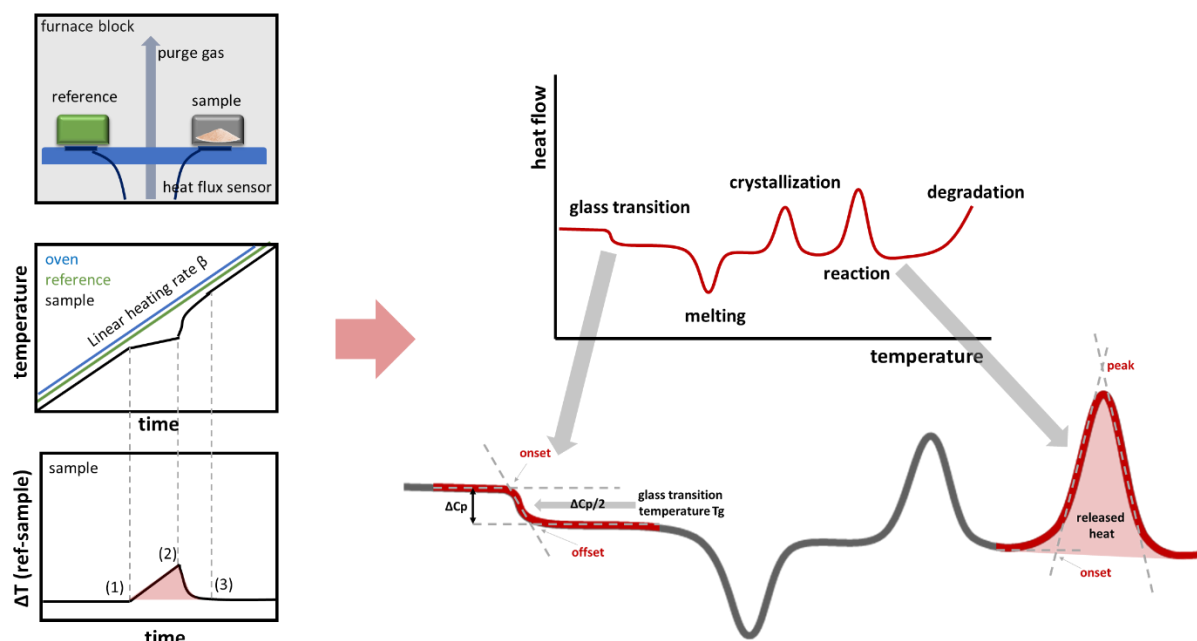


Figure 352. [left]: Basic setup of a DSC oven and resulting temperature-time curves. [right]: Heat flow curve, obtained by a DSC measurement, with exemplified processes that might occur in a heated material, as well as a possible way of analysis of the characteristic parameters.

## Thermogravimetric Analysis (TGA)

Thermogravimetric analyzers (TGA) generally track and record the mass and temperature changes of the sample as well as the environment temperature and time [262, 330]. Modern TGAs can use programs with variable heating or cooling ramps, isothermal holds and if required, a combination of all of them. Accordingly, the use of TGA allows to investigate decomposition and degradation processes [335], and if extrusion reactions are of main interest, they can be monitored by dynamic and isothermal programs. In addition, depending on the purge gas it is possible to study oxidation reactions by means of mass increase or mass loss in case of oxidative pyrolysis.

A thermogravimetric analyzer consists of a highly precise micro balance which is in connection with a sample pan. Sample pans are usually made from aluminum. The balance and pan are positioned inside of a furnace, which can be controlled by the temperature program. After determination of the initial mass of the sample under equilibrium state with respect to purge flux, pressure, temperature and stabilization of the micro balance, the temperature program starts, and the mass change is continuously determined and recorded (Figure 353).

Commercially available TGA setups can be distinguished by three different instrumental designs. They differ in the construction of the micro balance design. The balance can be either loaded from the top, bottom, or side.

Two features are very important. One is the protective tube around the sample pan in order to separate it from the thermoelements for heating or cooling and to provide a homogenous non-tubular gas flux. Second feature is a thermocouple which measures the temperature of the sample in order to record the mass loss as a function of the sample temperature and not necessarily of the environment temperature. The bottom loading is based on a hook connected to the balance, which requires the sample pan to be hang onto it. The purge gas then enters sideways perpendicular to the sample and leaves the system in the same direction. Side loadings consist of a micro balance which is connected to the sample horizontally and the purge gas enters from the balance side and flows over the sample pan and leaves the system in the same direction as well. Purge gas fluxes are usually in the range of 20 to 200 mL min<sup>-1</sup> and the most widely used gases are nitrogen and argon as inert gases or synthetic air or oxygen for oxidative conditions. However specific gases such as CO<sub>2</sub> can be used as well. Modern symmetrically built TGAs have highly sensitive symmetrical electromagnetic-optical balances with a counter pan as counterweight to reduce the required electromagnetic force, which enhances the micro balance sensitivity.

To investigate the decomposition products in order to specify, for example, the order of decomposition products and to get more information, for instance on the stability of certain groups or even to support thermochemical mechanism developments, TGAs can be coupled to gas chromatographs, FT infrared spectrometer or mass spectrometer on-line to the furnace and pan. The decomposed products are analyzed by these techniques or combinations of the

and is called an evolved gas analysis (TGA-EGA) [262]. Coupling of TGA and FT-IR, is therefore often called TGA-FT-IR experiments. From these datasets, the absorption bands of each recorded spectrum are simultaneously integrated over the spectral regions of interest or even the entire spectral range. The determined intensity *versus* time plot is the Gram-Schmidt curve. From such a Gram-Schmidt curve the specific peak height profile at a specified wavelength, such as  $2240\text{ cm}^{-1}$  in case of free  $\text{CO}_2$  for instance, can be extracted (see Figure 353). The mass loss can then be correlated with the peak height profile. If one mass loss step is only referred to one decomposition product, then the first derivative (DTG curve) is often identical to the Gram-Schmidt (GS) curve which is identical to the peak height profile of the pure decomposition gas. Otherwise, the GS curve is an overlap of all decomposition products peak height profiles. In addition, the TGA itself can also be coupled with the instrumentation technique of a DSC or DTA in order to extend the amount of data within one measurement.

One important question is the margin of error and the uncertainty of the experiment as well as the limitations. Common crucibles allow the use of 5-50 mg samples. Average experiments with aluminum pans are done in the range from room temperature to  $1000\text{ }^\circ\text{C}$  at moderate heating rates of  $5\text{ to }20\text{ }^\circ\text{C min}^{-1}$ . Commercial micro balances have measurement ranges of 1 to 5 g, with resolution of 0.1 to  $1.0\text{ }\mu\text{g}$ . Heating rates from  $0.02\text{ to }250\text{ K min}^{-1}$ . However, it always depends on the preparation of the sample as well. Potential errors are impure crucible, which contain thermolabile impurities. The sample out of a big sample, can be a bad representative if the sample batch is not homogenous. The samples can contain impurities, such as solvents, catalysts etc. and the type of sample is important. Large particles do pack less efficient than small particles, and therefore more free volume between the samples containing gases are present. Furthermore, the contact to the crucible is different. Additional errors could be an impure purge gas, which includes oxidizing gases or moisture. Gas composition and flow rate of the purge gas also affects the temperature measurement of the thermocouple near the sample pan and therefore leads to misleading sample temperatures. Above  $500\text{ }^\circ\text{C}$  radiation becomes the dominant heat-transfer mechanism and affects the true temperature of a sample. Changes of the gas density at high temperatures can lead to buoyancy phenomena, which can be eliminated by using an empty reference pan. For the best performance, regular calibrations of the temperature detection and micro balance are required. The temperature calibration usually occurs via utilizing reference materials with a known Curie point, at which the

material does not longer have magnetic properties, which is located at the offset of the weight loss.

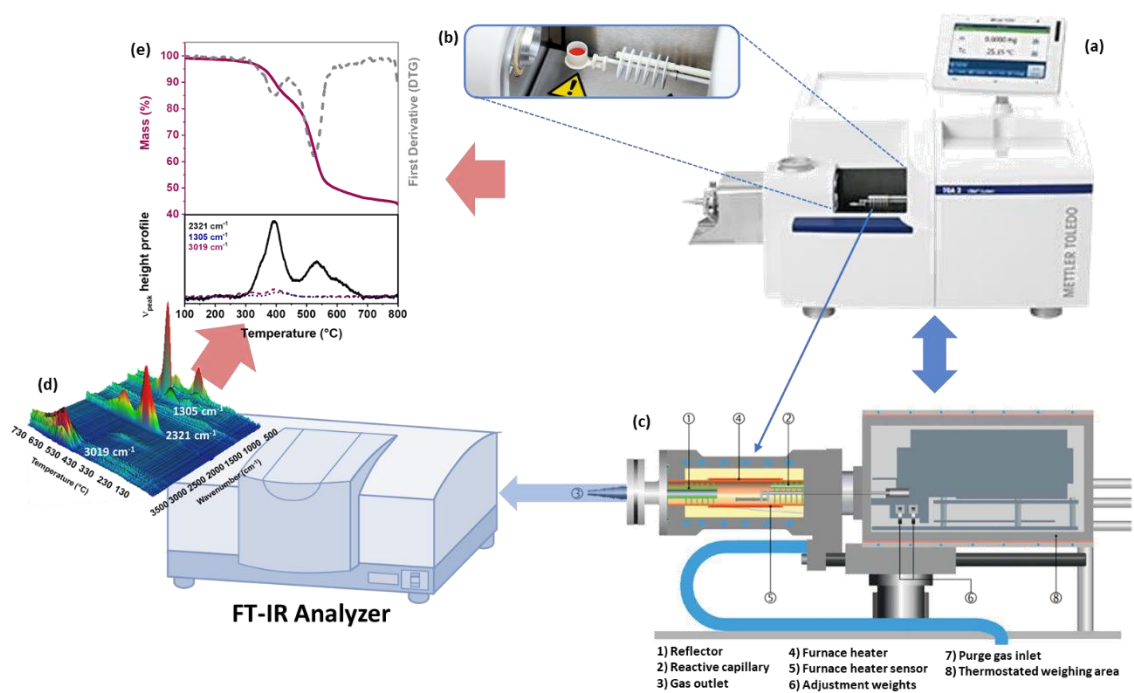


Figure 353. Representation of (a) a thermogravimetric analyzer, (b) the oven and sample holder and (c) scheme of the setup (reprinted with permission from Mettler Toledo). (d) Schematic coupling to a FT-IR spectrometer and its output of stacked FT-IR spectra which give (e) a thermogravimetric mass loss curve and Gram-Schmidt curve, and extracted peak height profile of specific wavenumbers, that are of major interest.

### Non-isothermal Isoconversional methods[336, 337]

Process kinetics deal with the experimental measurement and parameterization of the process rates. Meanwhile, thermal analysis deals with thermally stimulated reactions and processes, i.e., a process or reaction, which is initiated by a temperature change. Such processes or reactions can be kinetically described by means of their conversion rate,

$$\frac{d\alpha}{dt} = k(T)f(\alpha) \quad (33)$$

Where  $da/dt$  is the conversion rate,  $k(T)$  is the temperature dependent rate constant and  $f(\alpha)$  the conversion dependent reaction model.

The conversion of a process is experimentally measured as a fraction of the total change in a process-specific physical property, such as. mass loss or heat release. The most often used



method is DSC. It measures the heat flow per time or temperature, which gives by temperature integration the reaction enthalpy per temperature. The conversion is defined as

$$\alpha = \frac{H(t)}{H_{tot}} \quad (34)$$

and the conversion rate,

$$\frac{d\alpha}{dt} = \frac{dH}{dt} \cdot \frac{1}{H_{tot}} \quad (35)$$

with the enthalpy  $H$ .

However, the conversion can only represent the global or apparent change and not that of a specific process in case of a multi-step process. Therefore, determined kinetic parameters are global or apparent and not intrinsic kinetic parameters corresponding to each individual step, since the parameters are affected by other kinetic parameters and diffusion. It is noteworthy that the activation energy, for instance, is more of a global value of all single step activation energies. The activation energy  $E_a$  here cannot be understood in a traditional way, like an activation barrier for chemical reactions [24, 262, 336]. Thus,  $E_a$  is not assumed as a constant, it can vary with  $T$  and  $\alpha$ .

Applying the Arrhenius equation, and introducing the heating rate  $\beta$ , since non-isothermal experiments were conducted, we easily obtain,

$$\beta \frac{d\alpha}{dt} = A \exp\left(\frac{-E_\alpha}{RT}\right) f(\alpha) \quad (36)$$

which leads to its integral form

$$g(\alpha) = \frac{A}{\beta} \int_0^T \exp\left(\frac{-E_\alpha}{RT}\right) dT \quad (37)$$

with  $A$  as pre-exponential factor,  $\beta$  as heating rate,  $E_a$  as conversion specific activation energy,  $R$  as ideal gas constant and  $T$  the absolute temperature.

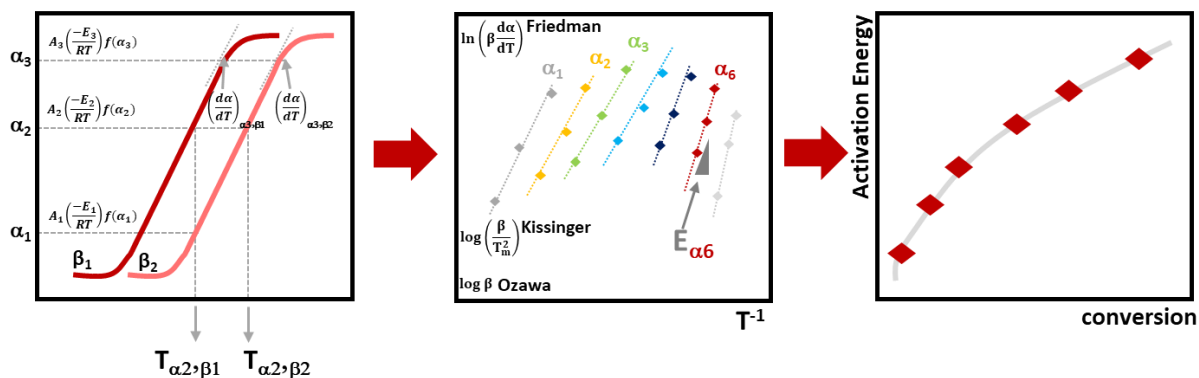


Figure 354. Process of determination of the conversion-dependent activation energy from (left) determination of temperatures at specific conversions for different heating rates; (middle) plot of the method versus reciprocal temperature to determine the activation energy of each specific conversion and (right) the activation energy versus conversion plot.

In systems, where many reactions may occur at a time and follow different multi-step mechanism, more complex if they act autocatalytically, *isoconversional* methods have been proven to be one of the methods of choice [338].

*Isoconversional* methods use the *isoconversional* principle, which states that the reaction rate at constant extent of the conversion is only a function of the temperature [337]. Hence, the logarithmic equation, when  $\alpha = \text{const.}$ , gives

$$\left[ \frac{\partial \ln(d\alpha / dt)}{\partial T^{-1}} \right]_{\alpha} = -\frac{E_{\alpha}}{R} \quad (38)$$

Strictly speaking, the *isoconversional* principle holds true for single steps, but works as a good approximation, since it treats the process by applying multi single-step kinetic equations, whereas each individual step is associated with a certain extent of the total conversion.

Among *isoconversional* methods, the most common differential *isoconversional* method is the Friedman-method for non-isothermal experiments,

$$\ln \left[ \beta \left( \frac{d\alpha}{dt} \right)_{\alpha} \right] = \ln [f(\alpha) A_{\alpha}] - \frac{E_{\alpha}}{RT_{\alpha}} \quad (39)$$

At each conversion  $\alpha$ ,  $E_{\alpha}$  is determined from the slope of  $\ln [\beta (da/dt)_{\alpha}]$  against  $1/T_{\alpha}$ .

Using the integral form with the *isoconversional* principle by using a non-isothermal program we get,

$$\ln\left(\frac{\beta}{T_\alpha^B}\right) = \text{const} - C\left(\frac{E_\alpha}{RT_\alpha}\right) \quad (40)$$

Where  $B$  and  $C$  are parameters which depend on the applied type of the temperature integral approximation. If the Doyle approximation is used, we get the Ozawa-Flynn-Wall integral method, and with the Murray-White approximation [338] with  $B=2$  and  $C=1$  we get,

$$\ln\left(\frac{\beta}{T_\alpha^2}\right) = \text{const} - \frac{E_\alpha}{RT_\alpha} \quad (41)$$

which is the Kissinger-Akahira-Sunose (KAS) method [24, 262, 330, 339].

### **X-Ray Diffraction (XRD) Spectroscopy[23, 328]**

Scattering methods, i.e., the small- and wide-angle X-ray scattering (SAXS and WAXS), are commonly used methods to analyze porous and phase-separated materials to obtain information of their morphologies and empty space. However, their interpretation of potential free volume elements and free volume characteristics in total is rather difficult in amorphous polymers. The methods of X-ray scattering were mainly applied for the investigation of more structured materials. Nevertheless, these techniques have been proven to be helpful to estimate the pore size based on the determined d-spacing. The d-spacing defines the intersegmental distance and is hence a good measure of the pore sizes of amorphous polymer films.

An advantage of the method is, that it is non-destructive and XRD devices are usually widely used and available. Furthermore, the interchain or intersegmental distances are highly sensitive to time, temperature and hence to the thermal history and therefore interesting in terms of physical aging measurements.

The measurement principle is based on scanning a solid polymer film in a wide-angle (2-45 °θ) goniometer. In such a gonio- or diffractometer a monochromatic beam of high energy (x-ray) is produced. The entering beams are now reflected at the surface or enter the solid. The entering waves either pass through the sample or once they hit an atom, they are reflected with the same angle of their entering. In case of highly ordered atoms with a specific distance

d, the reflected waves interfere coherently with each other and produce a diffraction maximum according to Braggs Law

$$n\lambda = 2d \sin \theta \quad (42)$$

with  $n$  as a positive integer,  $\lambda$  for the x-ray wavelength (nm),  $d$  the interatomic distance (nm) and  $\theta$  glancing angle ( $^\circ$ ). Any reflection at divergent positions from  $d$  leads to destructive interference. Positive interferences can be seen by a halo, whereas broad and usually not more than two halos are obtained for amorphous polymers. Since amorphous polymers show no high order of their polymer chains, the number of available interchain distances is fairly large, therefore only broad peaks are obtained. However, the maximum peak was successfully used in the past to correlate interchain distances and pore size distributions from other methods.

### Density[328]

Depending on the state of aggregation of the sample, various methods can be used for determining the density from ultrasonic probes, via densitometer to gravimetric methods such as pycnometer, displacement technique and the buoyancy method. While some are more useful for solutions, the gravimetric methods are used for solids usually [328, 340]. Among these methods, the buoyancy technique is the most widely used method, which utilizes the Archimedes' principle [341]:

“Any object totally or partially immersed in a fluid is buoyed up by a force equal to the weight of the fluid displaced by the object.” — Archimedes of Syracuse, 250 BC

As a consequence, by accurate determination of the weight of a solid sample in air and in a liquid of known density, the density can be calculated by acquiring the weight of the displaced liquid (*isooctane* in that case). The weight of the displaced liquid depends on the upward force reducing the weight of the samples. As the density increases, the displaced liquid weight becomes more as the upward buoyant force is reduced. The principle is shown in Figure 237, the calculation is shown in equation (43) and (44),

$$\rho = \frac{m_a}{m_a - m_l}(\rho_l - \rho_a) + \rho_a \quad (43)$$

$$V = \alpha \frac{m_a - m_l}{\rho_l - \rho_a} \quad (44)$$

with  $\rho$  as the sample density,  $\rho_l$  density of the auxiliary liquid (*isooctane*),  $\rho_a$  density of air (0.0012 g/cm<sup>3</sup>),  $m_a$  weight of the sample in air,  $m_l$  weight of the sample in the liquid,  $\alpha$  the balance correction factor of 0.99985.



Figure 355. Balance and density kit with sketch of the density kit including description of each part. Reprint with permission from Mettler-Toledo.

Since the density determination is carried out with an auxiliary liquid, the temperature change must be taken into account for the calculations. While solids are mostly insensitive to small temperature changes, the density of the liquid is affected strongly. As a consequence, the temperature has a greater effect with liquids and causes therefore density changes of 0.1 to 1‰ per 1 °C [340].

Air bubbles can have strong effects as well as grease traces from solvent-resistant solids should be removed. A bubble with a 1 mm diameter can cause a buoyancy of up to 0.5 mg for instance [340]. For the density determination many standards and norms exist. The most commonly used are the ISO 1183-1, OIML G 14, and the ASTM-D-792: Standard Test Methods for Density and Specific Gravity Standard.

A simple film density determination was done following the procedure as described. First the density kit was mounted properly. The setup is shown in Figure 355. Afterwards, the temperature was noticed, the balance was tared. Subsequently, the weight at air was determined after placing the sample and waiting for stabilization. The values were written

down each 30 seconds. Afterwards the sample was put into the basket in *isooctane*. The values were written down each 30 seconds for 5 min until no significant changes were observed.

### Constant Volume/Variable Pressure Method („Time-Lag “Experiments)

The gas flux through polymeric membranes is commonly measured by one out of three possible setups, which have the 1) constant-pressure variable-volume 2) constant-volume variable-pressure and 3) mixed-gas permeation measurement [328]. Experiments (1) and (2) are used for pure gas separation task, which are more readily available and easier to handle and a good method of choice in order to screen potential membrane materials. As discussed more in detail in chapter *Gas Separation Membranes*, from one experiment all three relevant properties, which are permeability, diffusivity and solubility can be obtained [1, 342-347]. Under assumption of a constant diffusion coefficient (neglecting the effects of concentration dependence) according to Crank and Park[19], the gas flux across a membrane into a constant volume at time  $t$ , gives under steady-state conditions

$$N_t = \frac{DC_{feed}}{l} \left( t - \frac{l^2}{6D} \right) \quad (45)$$

with diffusion coefficient  $D$ , gas concentration on the feed side  $C_{feed}$ , membrane thickness  $l$ , and time  $t$ . A typical gas flux *versus* time curve is shown in Figure 357 for various gases. The intercept of the steady-state region of  $N_t$  with the time-axis defines the so-called time-lag  $\theta$  [19, 343, 344], from which the diffusion coefficient can be obtained according to

$$D = \frac{l^2}{6\theta} \quad (46)$$

The theoretical foundation for the setup was derived by Daynes in 1920 [342] and used to develop a system to measure the time-lag and steady-state flow in polymeric membranes by Barrer and coworkers in 1930 [328, 343].

The setup for a constant-volume variable pressure (CVVP) method is illustrated in Figure 356. Using the CVVP method, the measured permeate flux is monitored by measuring the pressure

increase on the permeate (downstream) side of the membrane in a constant volume  $V_1$  (and  $V_2$  if required). The feed mode is a dead-end separation and uses a permeate cell as shown in Figure 239. In order to perform a CVVP experiment, the film is inserted into the permeate cell onto a non-woven filter paper or sheet for stabilization of the thick film and then put onto a sintered-metal disc. Both materials have a negligible effect onto the gas transport as their gas permeability is significantly higher and therefore no resistance for the gas flux. After the film is placed in the cell, an O-ring is inserted into the system in order to make sure, that no leaks for the gas at the outside of the films exists. As a consequence of the reduced gas accessible area of the membrane, it is important to measure and notice the active area. This can be done by pressing the ring under vacuum into a soft material such as a support sheet. The O-ring leaves then an imprint, which can be measured. In some cases, membranes are covered by an additional aluminum ring or tape. This is required if the ring to membrane contact might lead to fracture of the film. After the film is clamped into the cell and closed, the whole system is evacuated on both, the upstream and downstream side in order to degas the films and measuring system for a specific time. A reservoir is then filled by the gas of interest up to a specified pressure and the reservoir is closed. Prior to the start of the measurement, a leak test is performed. This leak test is done by closing the valves, which are connected to the pump and the pressure increase on the downstream side is monitored. For accurate experiments, this rise should be at least one order of magnitude lower to the measured steady-state flux [328]. After the leak test, the experiment is started by opening the valves, which connect the gas reservoir with the permeate cell and permeate volume on the downstream side. The pressure is measured by commercially available pressure gauges or transducers.

The recommended testing procedure according to the ASTM for the standard test method for determining gas permeability characteristics of plastic film and sheeting is described in ASTM D1434-82(2015)e1 [348].

For a successful measurement it is very important to have a uniform defect-free film, since pin holes and cracks open up to and better accessible pathways for the feed gas and consequently to significantly higher permeabilities, since the predominant Knudsen-diffusion in such holes is several orders of magnitude higher compared to the gas transport in dense membranes [1, 328]. Furthermore, uniformity is important, since the permeability is calculated as the thickness-nominated gas flux and depends therefore on the determined thickness, which is

usually measured by a digital micrometer. Furthermore, it is important to have a homogeneous heat circulation and constant temperature in the whole measurement chamber throughout the complete experiment, supported by accurate temperature determination, as the gas flux is strongly temperature dependent. Moreover, the purity of the used gas especially in terms of moisture, is very important as more permeable impurities might give wrong impressions on the gas diffusion of the gas of interest.

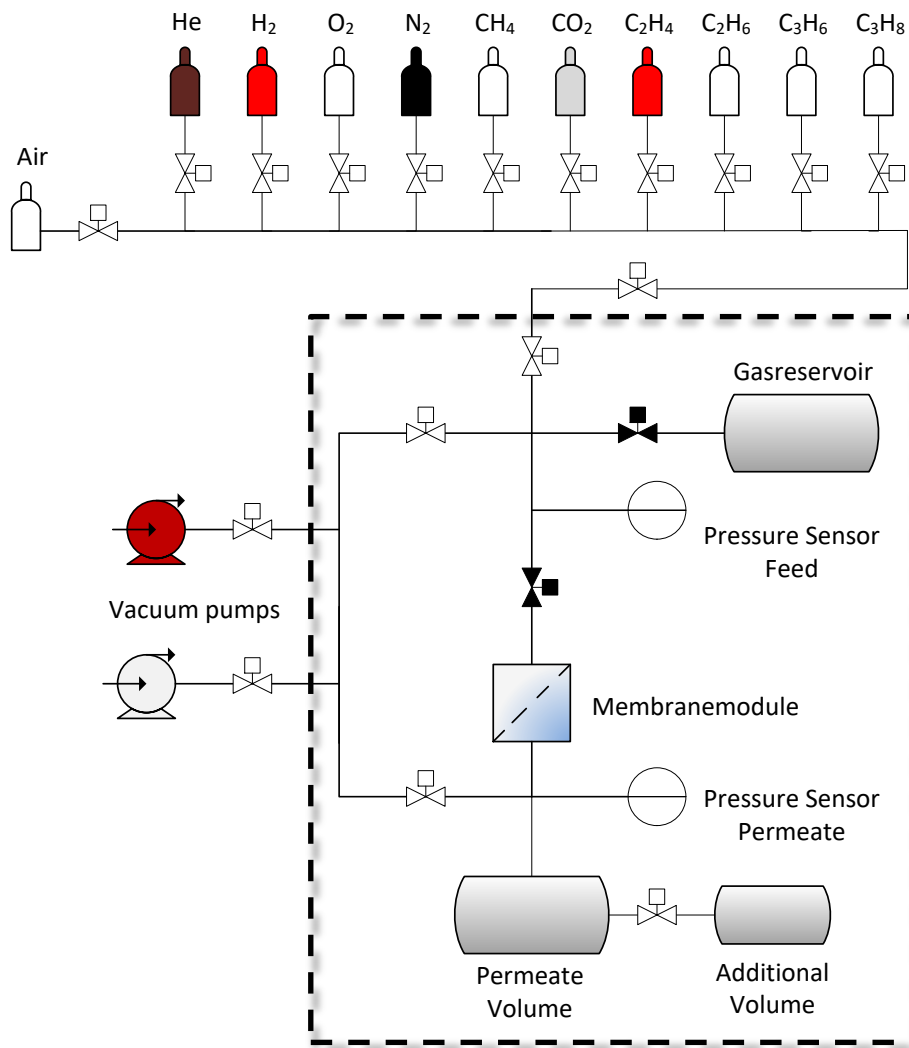


Figure 356. Experimental setup of the constant-volume variable pressure ("time-lag") method.



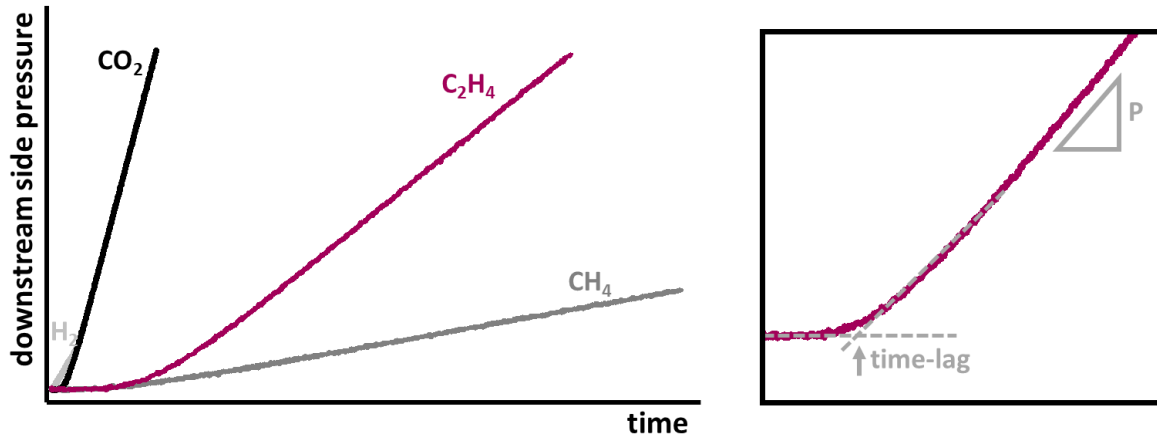


Figure 357. [left]: Time-lag curve of various gases, which is the plot of the pressure versus time. [right]: Determination of permeability and time-lag from a time-lag curve.

## Tensile Testing

The mechanical properties of a material, such as a polymer film, can be of high importance when it comes to application testing, as the materials challenges become very harsh sometimes. In order to check if a material can withstand these conditions, its elastic and strength properties are of interest. By using stress-strain tests a materials property such as the tensile modulus or elongation at break can be obtained. This can be obtained by uniaxial tensile testing. For this test specific test specimen are prepared with broader endings, which are fixed on each side of the tensile testing machine [328]. The test is performed by gradually increasing the load until it fractures. The elongation of the polymeric film between both fixed ends is recorded. From the relation of the elonged sample to the initial sample length, the engineering strain  $\epsilon$  can be obtained.

$$\epsilon = \frac{\Delta L}{L_0} = \frac{L - L_0}{L_0} \quad (47)$$

With  $L_0$  as the initial length (mm),  $L$  the final elonged length (mm) and  $\Delta L$  the change of the length (mm). The engineering stress  $\sigma$  (Pa) can be calculated by the measured tensile force  $F_n$  and the cross-section of the specimen  $A$ .

$$\sigma = \frac{F_n}{A} \quad (48)$$

From these results, the Young's modulus  $E$  which is the modulus of elasticity in tension can be determined. The Young's modulus describes the tensile stiffness of the material and is the ratio of the stress and strain in the linear elastic region of a stress-strain curve (Figure 358).

$$E = \frac{\sigma}{\epsilon} \quad (49)$$

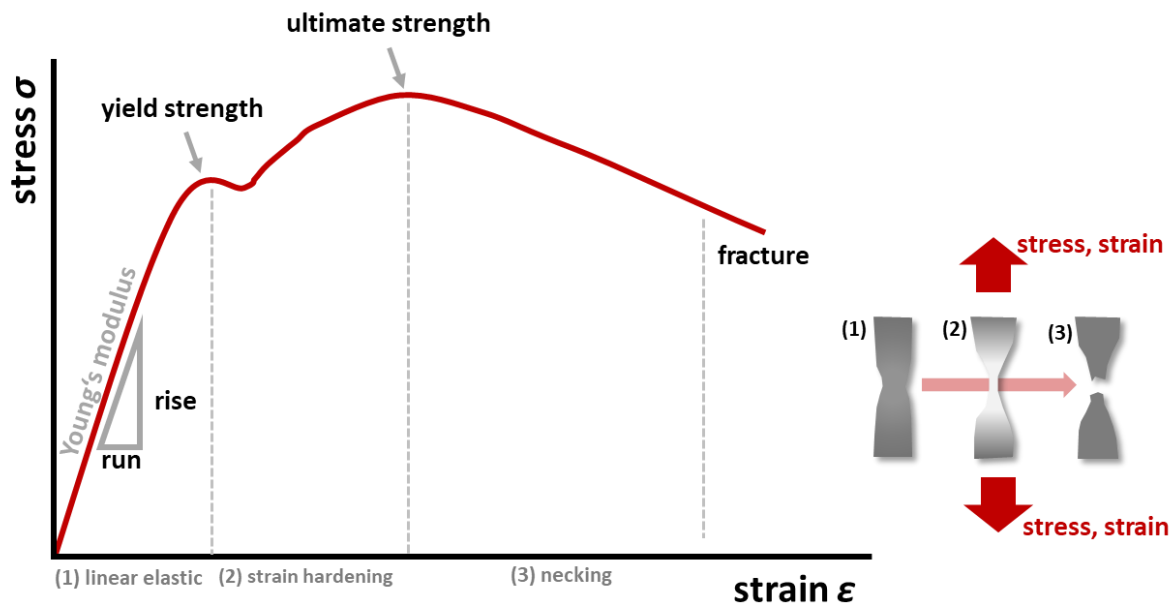


Figure 358. Stress-strain curve of a polymeric material including a visualization of the necking process of a testing specimen.

## Broadband Dielectric Spectroscopy (BDS)

Dielectric spectroscopy or electrochemical impedance spectroscopy is a widely used method to study the response of a material, such as a polymer film, under exposure of an applied electric field. As a consequence of the electric field stimulus, the induced polarization causes a charge equilibrium shift of the material, which means that induced charges align in different directions, with positive charges aligning in the direction of the electric field and negative charges opposite to it [349]. The way on how a specific material reacts to an external electrical field varies in a number of potential mechanisms. Types of polarization are (1) induced dipole polarization, (2) orientation polarization, (3) interfacial polarization and (4) charge migration polarization. Each polarization mechanism occurs at a specific frequency reciprocal to the characteristic time of the occurring process. Among the above-mentioned mechanisms, the induced dipolar polarization is a resonant process and can be divided into electronic and

atomic polarization. While electronic polarization is a consequence of the displacement of electrons from their equilibrium position and accordingly a shift of the electron density, atomic polarization is the result from an equilibrium displacement of atoms. In comparison the atomic polarization is small compared to electronic polarization processes. In addition, the mechanism of orientation polarization relies on the presence of permanent and induced dipoles. In contrast to the induced dipole polarization, the orientation polarization depends strongly on the constitution and conformation of dielectric materials and is therefore the process to investigate, when motional transitions are studied. Furthermore, the interfacial polarization is a process which takes place in heterogeneous materials such as composites. In such materials an interphase between two or more components is present and charges are accumulated at these transition zones. Finally, charge migration polarization, which occurs when charges migrate through the material and contribute to conduction, such as in fuel cell membranes. The latter process can come from ionic species such as impurities or ion transport, such as in ion-exchange membranes.

In dielectric spectroscopy the response of a material is determined as a function of the frequency. Physical quantitative properties that are obtained by BDS are the dielectric permittivity and DC electrical conductivity as well as the dielectric constant  $\epsilon'$  and loss  $\tan \delta$ . In a dynamic measurement mode, the applied electric field is alternating, the field strength  $E(t)$  electric displacement  $D(t)$  are described according to

$$E(t) = E_0 \exp(i\omega t) \quad (50)$$

$$D(t) = D_0 \exp i(\omega t - \delta) \quad (51)$$

with  $E_0$  and  $D_0$  as system constants, angular frequency of the applied field  $\omega$  (Hz) and time  $t$  (s). The dielectric constant  $\epsilon^*$  is obtained by the relationship of  $E(t)$  to  $D(t)$ , leading to

$$\epsilon^* = \frac{D(t)}{E(t)} = \frac{D_0}{E_0} \exp(-i\delta) = \epsilon_0 (\cos \delta - i \sin \delta) = (\epsilon_0 \cos \delta) - i(\epsilon_0 \sin \delta) = \epsilon' - i\epsilon'' \quad (52)$$

$$\tan \delta = \frac{\epsilon''}{\epsilon'} \quad (53)$$

To calculate physical properties, such as the relaxation time from which molecular transitions can be estimated and molecular process being described, the dielectric response has to be modeled. In most polymeric materials, the relaxation processes are based on orientation polarization and non-Debye type. The individual relaxations of the system can be determined according to the Havriliak-Negami (HN) modification [349]

$$\varepsilon' - i\varepsilon'' = \varepsilon_U + \frac{\varepsilon_R - \varepsilon_U}{[1 + (i\omega\tau_{HN})^a]^b} \quad (54)$$

With  $\varepsilon_R$  and  $\varepsilon_U$  for the relaxed and unrelaxed dielectric constant of each relaxation and  $\tau_{HN}$  for the characteristic relaxation time. Parameters  $a$  and  $b$  account for non-Debye relaxation behavior. In total, especially broadband dielectric spectroscopy offered a technique to describe molecular dynamics on different time scales in order to understand electric but also molecular motional properties and processes.

## Computational Chemistry

Computational chemistry as a general term involves all methods of computational supported calculations of molecular properties. With the improvement of computer-based technologies and equipment and the improvement of software developments, as well as their bug fixes, the computational based studies increased rapidly. Several software developers marketed their tools and programs and techniques. Within these programs, the tools were continuously studied and re-designed by applicants as well. The value of computational chemistry-based studies came also into focus of large industrial chemistry companies and these methods are nowadays widely used to tailor material properties prior taking these ideas to the lab [350-354]. In many cases hybrid studies were performed, in which experimentally determined properties were simulated in order to support the theories and to explain the results on more consolidated findings.

Computational chemistry can help by investigations of molecular geometries. This includes the calculations of molecular shapes, bond-length, dihedrals, and angles. Apart from structural properties, the energies of molecules and their transition state geometries can be obtained and

used for kinetic investigations. Determinations of electron density and electrostatic potential maps help to understand reactivities, such as nucleophilic and electrophilic character. Based on these primary molecular properties, easily accessible experimental data can be simulated such as NMR, IR, Raman, and UV-Vis's spectra. Properties of macromolecules, such as their melting and glass transition temperature or XRD spectra are possible to simulate. These results help to support any chemist to formulate reaction mechanism and design new molecules and materials with tailored properties [353].

A great support of computational visualization and the trajectory of molecules is given when chemists develop reaction mechanism. While structures via projected formulas are easy to catch, they do not give an idea of the constraints and distances of groups to each other, which is crucial to the possibility of certain reactions. An own example is shown. Nevertheless, the use of computational methods, even for simple visualization purposes, requires a fundamental knowledge of the user in order to provide reasonable information and to avoid misleading postulations.

There exists a broad toolbox of methods for the computational chemist to target specific questions. Depending on the used machines, required resources and scale of the simulated system, a suitable method has to be chosen. The trade-off herein is always size of the molecular system and simulation time, as well as accuracy *versus* time. Among these methods, it can be distinguished between molecular mechanics, which are based on ball-spring descriptions for the atom-bond models. In that case variations of the energy by changing geometrical properties until the lowest energy is found can be done and large molecules can be processed in that way [355]. In addition, first-principal methods, commonly known as *ab initio* calculations can be used to describe a quantum mechanical system. *Ab initio* methods are based on solving the fundamental Schrödinger equation. However, *ab initio* simulations are significantly slower compared to molecular mechanics. Since the Schrödinger equations can only be calculated exactly for the hydrogen atom, every larger molecule simulation is based on approximations [356]. An intermediate level is the use of semiempirical methods. Semiempirical calculations are based on the Schrödinger equation as well, but more approximations are used. Instead of calculating each integral, semiempirical methods use parametrizations, based on experimental data, which makes this method a semiempirical method. It is slower compared to molecular mechanics but much faster than *ab initio*

calculations. The newer DFT method which dates back to the 1980s [356], while semiempirical methods were already discussed in the 1950s [357, 358], the DFT method is based on the Schrödinger equation as well, but it calculates the electron distribution of a molecule directly, rather than solving the wavefunction. Finally, molecular dynamic methods are used to investigate the law of motions of molecules, such as gas and solvent trajectories, as well as polymeric or protein systems. Their calculations are not based on electronic considerations, but forcefields to characterize atoms in molecules. Therefore, chemical reactions can be calculated in that way, unless molecular dynamic methods are combined with so called reactive forcefields [359] based on DFT or semiempirical methods for instance or QM/MM hybrid simulations [360].

The following theoretical background is based on various detailed computational chemistry books [353, 355, 356, 361, 362].

### **The potential energy surfaces**

The potential energy surface is a crucial concept with respect to the simulation of electronic properties and performing geometry optimizations. Considering a diatomic molecule, such as H-F, as two balls connected by a spring, as it is used in molecular mechanics. When the bond length is changed by stretching or compressing away from its equilibrium position  $q_e$ , then the energy of the system is changed as well. At each position, which is on hold (frozen), the molecule is motionless and contains a potential energy. If the energy is plotted *versus* its position or bond length, a line is obtained, which describes the potential energy variation. In addition to the described model, real molecules vibrate and rotate continuously and therefore its kinetic energy is always non-zero. As molecules are quantized, they can have only specific amounts of potential energy. The different quantized energy levels are decreasing in their distance in real molecules with increasing quantization numbers. The occupation can be calculated by Boltzmann statistics. At lower energy levels, and closer to the equilibrium position the vibration levels can be simplified by a harmonic oscillator description (quadratic potential energy relation to the position  $q-q_e$ ). When bond lengths increase significantly, then the potential energies deviate from this simplification, as real molecules are better represented by an anharmonicity, which is important when it comes to bond breakages. At high distances from the equilibrium position, the potential energy term does not follow a quadratic approximation anymore (i.e. Morse-Potential).

Commonly molecules of interest have more complex geometries. The smallest change is the addition of another atom, making it a three-atomic molecule. A simple molecule would be H<sub>2</sub>O. In addition to the geometric parameter of the two O-H bond lengths, there exists the angle between H-O-H. Assuming a symmetry with both O-H lengths to be identical, there is a two-parameter system described by the bond length  $q_1$  and angle  $q_2$ . The energy *versus*  $q_1$ ,  $q_2$  plot is accordingly a three-dimensional graph of a two-dimensional potential energy surface [356]. Replacing one H atom by F (making it HFO), or allowing symmetries with two different bond lengths of O-H, then the potential energy is a function of three geometrical different parameters. Accordingly, a three-dimensional potential energy surface has to be drawn as four-dimensional graph, a hypersurface [356]. The minimum of such a hypersurface is described by the first derivative of the potential energy with each parameter to be zero,  $dE/dq_1 = dE/dq_2 = dE/dq_3 = 0$ . Helpful representations of complex hypersurfaces can be made when various parameters are held constant and only the variation of one parameter is investigated. This can be visualized by slices made out of the potential energy surface as shown in Figure 359.

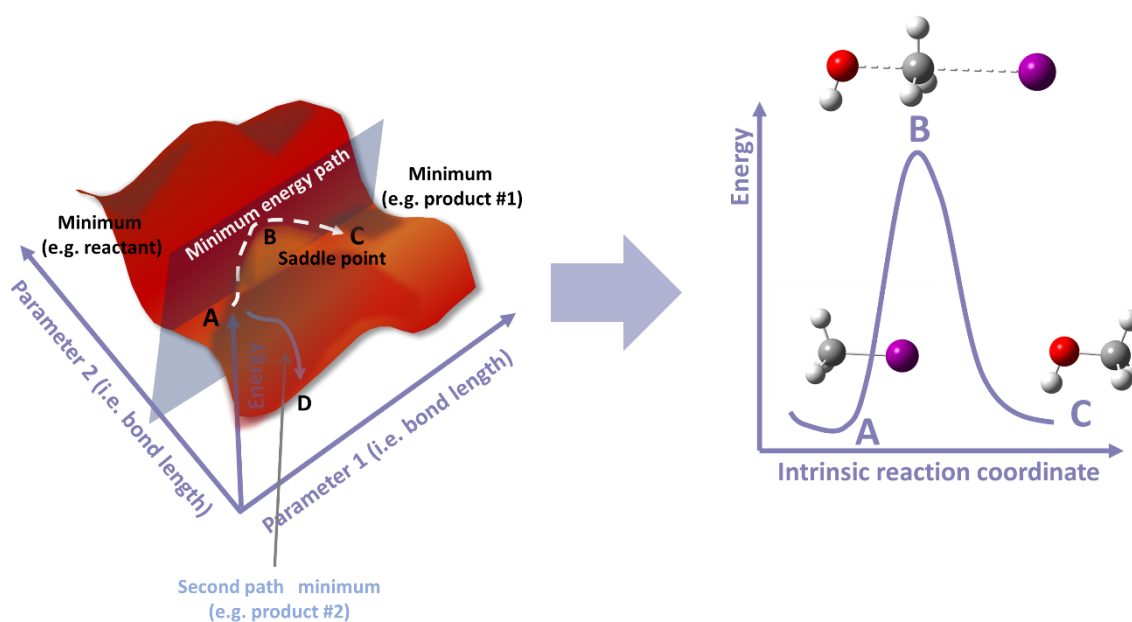


Figure 359. Potential energy surface and a slice along the minimum energy path, which represents b) a one-dimensional reaction coordinate, from which the energy barrier can be obtained based on reactant, product and transition-state geometry optimization and calculation of the ir single-point energy [based on (14/03/2021)  
[https://commons.wikimedia.org/wiki/File:Potential\\_Energy\\_Surface\\_and\\_Corresponding\\_Reaction\\_Coordinate\\_Diagram.png#file](https://commons.wikimedia.org/wiki/File:Potential_Energy_Surface_and_Corresponding_Reaction_Coordinate_Diagram.png#file)].

A potential energy surface contains important points when it comes to the description of chemical reactions. These are the minima, maxima and saddle points which are the stationary

points. These points shall be explained by the example of the cyclization of linear ozone to its isomer *isoozone*, which is a three-membered ring. The bond length of each O-O bond can be assumed to be identical, so that the system is described by the parameters bond length and angle O-O-O. Cutting out a slice along the lowest energy path from geometry A to C, shows how both minima are connected via transition state geometry B and the 2D graph is called the reaction coordinate which is actually a composite of both parameters, as it follows a reaction path and not necessarily one parameter. These stationary points are mathematically described by the first derivative of the potential energy with respect to each geometric parameter to be zero. At this point, the energy surface is flat. The transition state structure is a maximum along the intrinsic reaction coordinate (IRC). However, this is only true along the IRC. In any other direction it is a minimum. Therefore, it is described as a saddle point of the PES. Mathematically the difference, is that a minimum has a second derivative larger than zero with respect to each geometrical parameter. A saddle point, however, has a second derivative larger than zero for all parameters, except one, which is the reaction coordinate. At that point it is a maximum and therefore the second derivative is smaller than zero. It is important to differ between transition state and transition structure. While transition state is the definition within a thermodynamic concept, following Eyring's transit-state theory, the transition structure is the geometry with the potential energy located on the maximum of the reaction coordinate. Once molecules become larger, their description depends on more parameters and becomes more complicated. Such systems can have saddle points of higher order, which means the PES contains stationary points at which two rather than only one second derivative is lower than zero. If in such a complex system, two parameters are varied, but all others had been optimized, the PES is called a relaxed PES.

### **Geometry Optimization**

The location or finding of a location of a stationary point on a PES by systematical variation of a geometry via specific algorithm until a stationary point is found is a geometry optimization (see Figure 360). It involves the calculation of the corresponding geometry and its energy. The calculation of minima is usually called an energy minimization, which differs from finding transition structures via transition state optimizations.



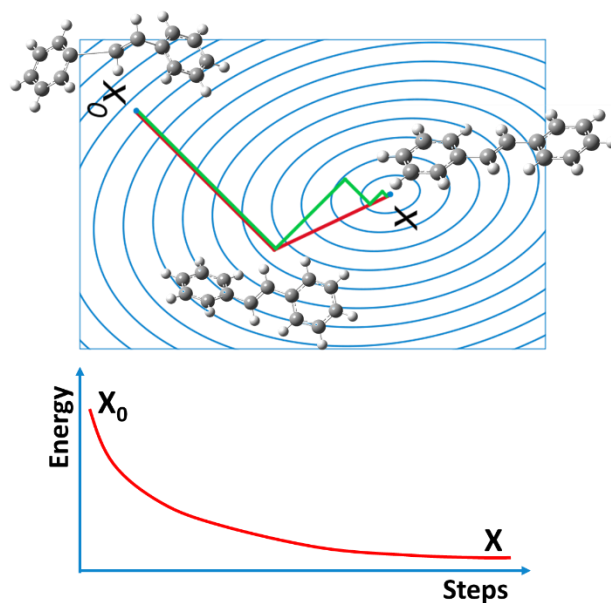


Figure 360. Principle of a geometry optimization calculation to a minimum as exemplified by an iterative energy minimization from an initial input structure [based on [https://commons.wikimedia.org/wiki/File:Conjugate\\_gradient\\_illustration.svg](https://commons.wikimedia.org/wiki/File:Conjugate_gradient_illustration.svg)].

Geometry optimizations do not guarantee to end up in the global minimum. Furthermore, the minimum is not found within one optimization step. The number of necessary steps depends of course on the algorithm, but also on the input structure. The nearest minimum is nowadays usually found within ten steps, but the minimum depends on the input structure as illustrated in Figure 244.

Most algorithms use the first and second derivative of the energy with respect to each parameter to find the minimum.

Optimization methods are usually done using cartesian coordinates, which means in case of a three atomic molecule to involve nine coordinates as each atom is described by  $x$ ,  $y$ ,  $z$ , which are  $q_1$ ,  $q_2$  ...  $q_9$ . The first and second derivatives of these parameters were calculated and treated as matrices, which are a convenient way of handling linear equations in general. The matrix of the first and second derivatives are called gradient and Hessian or force constant matrix, respectively.

Hence, the optimization method requires an input geometry, gradient matrix and Hessian. The input is a good guess, the gradients are derived from orbital coefficients and integrals, and the initial Hessian can be derived from molecular mechanics. The calculated geometry is not the final structure, since the real potential is not quadratic and does not exactly follow the used equation, which was used as a harmonic approximation. The new geometry  $q_1$  can be used

with its new gradient and Hessian matrices to calculate another optimized geometry  $q_2$  and so on, until a preliminarily defined stop criterium is fulfilled. Hessian matrices, however, are not calculated at each point, they are rather incrementally updated as a change of the gradient by the change of the geometry between the current and previous geometry.

The herein outlined method is the Newton-Raphson method.

In order to verify a stationary point, the vibrational frequencies of the corresponding geometry are calculated. For that purpose, the normal-mode frequencies are determined.

The calculation can be done by using the Hessian matrix, which contains the second derivatives, and describes accordingly the force constants, with  $E$  as the vibrational energy. Diagonalization of the Hessian gives a direction matrix, the eigenvector, and a  $k$ -matrix, eigenvalue, which contains the force constants. Mass weighing of these force constants by its reduced mass  $\mu$  allows to calculate the corresponding normal mode of each bond. At a minimum, all force constants have positive eigenvalues. Since the second derivative describes the derivative of the gradient (first derivative), the calculated eigenvalue is negative for a maximum. Accordingly, the frequency of a negative force constant, is an imaginary number (square root of a negative number). Therefore, a TS, maximum along the IRC, is described by one imaginary frequency.

### **Other optimization methods**

Various methods to minimize the energy are reported, which can be reduced to a few methods, which are explained in the following section.

**Steepest descent (SD) method.** A series of function evaluation is performed in the opposite direction of the gradient vector  $g$ , which points to the direction at which the function increases. Minimization requires the function to decrease. Accordingly, this is repeated until a function increase is determined. Once a point is reached at which the function increases, the minimum is approximated by interpolation of the calculated points. From this new point, a new gradient is calculated and the calculations in  $-g$  direction is repeated, another line search. One drawback is the fact, that each line search is perpendicular to each other. Therefore, the new direction does not necessarily start from the best new starting point along the previous line search. As the minimum is approached, it rather oscillates around it and its convergence rate decreases

drastically. This method is very simple and often used to determine a good starting point, since it guarantees to lower the function.

**Conjugated gradient (CG) method.** This method is closely related to the steepest descent method. Other than the steepest descent method, the conjugated gradient method performs each line search along a line, that is conjugated to the previous search directions and not in the direction of the gradient. Each new line search is accordingly done in the direction based on the gradient and previous line search directions. CG methods are also very resource-efficient and have better convergence characteristics than the SD method. However, only minima can be detected by this method, and when deviations from a quadratic surface occurs, the simulation oftentimes needs to be restarted.

Apart from these widely described methods, there exist others such as augmented Hessian methods, Hessian update methods or truncated Hessian methods.

For finding transition structures, by identifying saddle points, other approaches are used, as saddle points are mathematically more complicated than minima. Two categories exist. The interpolation methods and methods using local information. Interpolation methods require that initial structure and product be known, and the TS geometry accordingly is located somewhere between both points. Local methods use the information of the function and its derivatives to find a saddle point. However, these methods require good initial geometries. The linear synchronous transit (LST) method is a so-called coordinate driving method, and all coordinates are linearly varied between starting geometry and product geometry. When all variables are changed at the same rate, an interpolation of the highest energy structures leads to the direction of the highest energy, which is then the transition structure. However, in most cases these methods only approximate the TS. The quadratic synchronous transit (QST) uses the LST maximum and from there the energy is minimized in perpendicular directions and the QST path is searched for a maximum energy. Further methods are the synchronous transit-guided quasi-Newton (STQN), sphere optimization. Two-structure interpolation methods use two structures to be optimized to approximate the TS from both sides. For these methods, several algorithms such as the saddle, Line-Then-Plane or Step-and-Slide algorithm exist. Next to it, multistructure interpolation methods.

## QM Theory

In the previous section the quantized nature of molecules was shortly described, by the mathematical description of quantized energy levels of the vibration of a diatomic molecule. The molecule was described as a ball and spring model which has potential energy depending on the stretch-length of the bond, in that case the spring. Apart from vibration quantization, atoms and therefore molecules, are quantized with respect to their translation, vibration, rotation, spin. These quantum numbers are used for the calculation of quantum chemical properties such as the energy, for instance of a vibration and its frequency, but also rotational energies, dipole moments and furthermore properties such as the electron affinity or ionization potential can be obtained by the calculation of molecular orbital energies, based on their different energy levels and population of these levels, which follows statistical thermodynamics.

$$i\hbar \frac{\partial \Phi(R, t)}{\partial t} = \hat{H}\Phi(R, t) \quad (55)$$

The application of computational chemistry methods is based on quantum mechanics, as these describe the molecular system completely. The state of a molecule is described by its time-dependent Schrödinger equation (equation 55). With that mathematical description, the time-related evolution of the system of interest can be calculated. Each molecular system is basically described by means of the wavefunction, whose square of the function describes the probability of each of  $N$  particles in that system, namely the nuclei and electrons, to be determined. When investigating the Schrödinger equation, the left-hand side describes the time-dependent variation of the wavefunction, while the right-hand side would determine the change of the wavefunction by applying the Hamilton operator, who contains terms for the kinetic and potential energy. When larger systems are investigated, the number of nuclei and electrons can increase rapidly and therefore additional parametrizations for each particle have to be applied. This leads to a significant increase of the system describing number of wavefunctions and makes the calculation not only time-consuming, but rather impossible. Therefore, some approximations were used to make the calculation of larger systems possible. As a matter of fact, only the hydrogen atom with one proton and one electron, can be calculated by means of the Schrödinger equation exactly. First of all, the time variable is removed, as time-invariant wavefunctions are accurate enough for most problems. Second of all, the

number of parameters is reduced and focused on the electrons via separation of the wavefunction in two parts. One describing the electrons and one describing the nuclei. Phenomenological it is justified by the fact that electrons move much faster due to their lower mass and affect chemical reactions more the nuclei do (Born-Oppenheimer approximation). Therefore, the distribution of electrons is calculated for a fixed set of nuclei coordinates  $R_N$ , which are described by the nuclei wavefunction  $\Theta(R_N)$ . This approximation is called the Born-Oppenheimer approximation. The complete wavefunction  $\Phi(r, R_N)$  is the product of  $\Theta(R_N)$  and the electronic description  $\Psi(r)$ . The electronic Schrödinger equation is then

$$\hat{H}_{\text{electronic}}\Psi(r) = E\Psi(r) \quad (56)$$

It is now the job of the computational chemistry method based of theoretical methods to solve or approximate the electronic Schrödinger equation. Various methods are at the end linked to one method, the Hartree-Fock (HF) method.

### Hartree-Fock theory

The Hartree-Fock (HF) theory is based on the assumption, that electrons move very fast within molecules, that their motions are independent from each other. As electrons can interact strongly, as described via Coulomb's law, the approximation is still possible. For that purpose, the overall electronic wavefunction can be split in  $n$  simple wavefunctions for each of the  $n$  electrons, which are also described as molecular orbitals.

$$\Psi(r_1, r_2, \dots, r_n) = \psi_1(r_1) \times \psi_2(r_2) \dots \times \psi_n(r_n) \quad (57)$$

Since electrons spin according to their spin quantized energy levels, their wavefunctions have to be described by incorporating the spin term. Therefore, wavefunctions are better described by their spatial part  $\psi(r)$  and their spin part  $\sigma(\omega)$ . The product is then called a molecular spin orbital  $\chi(r, \omega)$ . The spin coordinate  $\omega$  can be either up or down, and more simply described as  $\alpha(\omega)$  or  $\beta(\omega)$  spin part for the up and down spin, respectively. Furthermore, another important addition, is the fact that electrons are treated as being identical rather than individual descriptions. This is accommodated by expressing the overall wavefunction as a product of each molecular spin orbital, resulting in a combination of products of all orbitals with

permutation of the electrons between each product. The combination of these products can be expressed by a determinant of the resulting matrix which is called the Slater-determinant. Each combination is chosen to fulfil the antisymmetry criterion, that each permutation of an electron pair leads to a negative wavefunction. This is based on the Pauli principle, stating that no more than two electrons are allowed to be described by the same spatial part of the molecular spin orbital  $\psi$ . The molecular spin orbitals then have to differ in their spin orbital, so two electrons cannot be described by the same molecular spin orbital.

$$E_{approx} = \int \Psi_{approx}(r) E \Psi_{approx}(r) dr = \int \Psi_{approx}(r) \hat{H}_{electronic} \Psi_{approx}(r) dr \quad (58)$$

with  $\hat{H}$  as the Hamiltonian, consisting of five terms, which are the kinetic energies of the both electrons, and the potential energy of the attraction of nucleus and each electron separately, as well as a potential energy term for the electron repulsion. Based on equation (58) under the premise that the wavefunction is normalized (square of the wavefunction over all coordinates  $r$  is 1, which means the electron has to be somewhere in a finite space), the approximated energy  $E_{approx}$  can be calculated

$$E = \sum_{i=1}^n h_{ii} + \sum_{i=1}^n \sum_{j=i+1}^n (J_{ij} - K_{ij}) \quad (59)$$

With  $h_{ii}$ ,  $J_{ij}$  and  $K_{ij}$  referring to various integrals over different molecular orbitals (MO).  $h_{ii}$  are one-electron terms, describing the shape of the MO.  $J_{ij}$  refers to the measure of the Coulomb repulsion energy and includes two different MO's.

### The Hartree-Fock self-consistent field (SCF) method

Various computational methods exist to approximate an energy, which is close to the exact energy, if the Schrödinger Equation would be possible to solve exactly. Among various methods, the so-called *ab initio* methods, which are first-principal methods, because they use only physical constants for the calculations and no empirical parameters, were studied in detail. The HF-SCF method uses the so-called Fock equations.

The Fock-equations were obtained by inserting the Slater-determinant into the electronic Schrödinger equation (equation 58) and rearranging it. The formed one-electron Fock operator

calculates an energy  $\epsilon$  for the molecular orbitals  $\psi$ . From the one-electron Fock operator a many-electron wavefunction is calculated anyway, since the operator contains terms to describe the electron-electron interactions. The molecular orbitals  $\psi(r)$  are linear combinations of simpler and easier to calculate functions  $\varphi(r)$ .

These functions are typically chosen to represent each of the occupied atomic orbitals the best way. The full set is called the basis set. These functions are not changed during a calculation, only the coefficients  $c_{ij}$  are varied and are the unknown parameters that have to be solved. These coefficients are not varied to lower stepwise the energy of the system. The whole process, however, has to be solved iteratively, since the electron-electron interactions and therefore the Fock operator depend on the shape of the orbitals and accordingly on the coefficients, which are unknown. For that purpose, the whole calculation is started by guessing the values of the coefficients. From these, a Fock operator is formed, and the orbitals are calculated, which are then the basis for a new cycle. This is repeated until certain convergence criteria are fulfilled, which means when specific quantities do not significantly change, specifically their gradient does not pass a certain threshold. The most important outcome of these calculations is the total energy, which is reasonably good, but differs about 1% from the real energy, which can make up thousands of  $\text{kJ mol}^{-1}$  as the calculated energies are really high [356]. Furthermore, orbital energies, and occupation, which helps to identify the HOMO (Highest occupied molecular orbital) and LUMO (Lowest unoccupied molecular orbitals) orbitals for further analysis, such as the ionization potential, can be determined. The HOMO and LUMO orbitals are usually of greatest interest, as these orbitals are usually the places, where the reactions occur in a molecule or between molecules.

### **Basis sets**

Basis sets are as mentioned before, the sets of functions from which via linear combinations the wavefunctions are calculated in order to solve the Schrödinger equation computationally. Various basis sets exist, from which a user has to choose. For the right decision it is important to understand, that large basis sets are necessary in order to have enough functions  $\varphi$  to describe the true molecular orbitals as close as possible. However, higher accuracy always comes in with higher computational efforts to calculate the system.

For the design of basis sets, it was found that atomic orbital-like functions are very good functions for the calculation of molecular orbitals by *ab initio* methods. The atomic orbitals of hydrogen atoms can be exactly determined and are calculated to have the form

$$\phi_{nlm}(r, \theta, \varphi) = NY_{lm}(\theta, \varphi)P(r)e^{-\xi r} \quad (60)$$

With the principal, angular and magnetic quantum numbers  $n$ ,  $l$  and  $m$ , the spherical polar coordinates to describe a position relative to the nucleus  $(r, \theta, \varphi)$ .  $N$  (normalization constant),  $Y_{lm}$  (spherical harmonic function),  $P(r)$  (polynomial function), and  $\xi$  as an exponent affecting the decline of the function. Functions based on this form are called Slater functions, and usually not used due to the high time consumption when they are used for calculations. Commonly Gaussian functions are used, which correspond to an analytical closed form

$$\phi_{nlm}(r, \theta, \varphi) = NY_{lm}(\theta, \varphi)P(r)e^{-\xi r^2} \quad (61)$$

The main difference of Gaussian functions in comparison to Slater functions appears at large value of  $r$  and very small nucleus centered values of  $r$ . It is important to notice, that Gaussian functions themselves are combinations of elementary, so-called primitive, Gaussian function  $G_i$  with different  $\xi$  in each function. Such combinations are then called contracted Gaussian basis functions with  $n$  primitive Gaussian functions in a contracted function.

$$\phi = \sum_i^{n_{contr}} d_i G_i(\xi_i) \quad (62)$$

Each primitive Gaussian enters with a different weight, which is given by the coefficients  $d_i$ . The simplest basis set one can choose is a minimal basis set, which is the smallest basis set which could be used to obtain reasonable results for MO's. They consist of one contracted basis function for each occupied AO in the atoms. A common basis set of such a type is STO-3G, which means it is a Slater-type orbital with contractions of three primitive Gaussian functions.

However, these basis sets tend to fail, when electron distribution changes occur, for instance via bond breakage or changes of the electron distribution along a chemical bond. This can lead to an expansion or contraction of an atomic orbital. If two basic functions are used to describe an occupied atomic orbital, it is called double-zeta (DZ, double- $\xi$ ). They can cover the problem



of atomic orbital polarization or orbital breathing more accurately. For the sake of save computational time, the use of DZ-basis sets is often restricted to valence atomic orbitals, which are the one that change more significantly due to changes in the chemical environment. Therefore, core and valence atomic orbitals can be split, which leads to split-valence basis sets. Therefore, apart from the minimal basis set of STO-3G, there exist numerous basis sets with specified functions for each element of the periodic table and designed for different systems and molecule sizes. The 3-21G basis set is a split-valence double-zeta basis set. The number 3-21 means, that the core orbitals are calculated by means of one basis function of three Gaussians, while the valence orbitals are split into an inner and outer shell, in which the inner shell is represented by two Gaussians and the outer shell by one Gaussian. This allows the basis to set more flexibility in order to adapt to changes in the electron distribution by adjusting the basic functions to the MO's. Polarization functions \* can be added to heavier atoms to accommodate for larger electron systems. If polarization functions are required for H and He as well, the use of \*\* polarization functions is employed.

The 6-31G\* basis set is a split-valence basis set with 6 Gaussians used within one basis function for the core orbitals, and a split of the valence shell into an outer and inner shell, with three Gaussians describing the basis function for the inner valence shell and one Gaussian for the calculation of the outer valence shell. It gives better results for the geometries and energies compared to the former basis set, but it is about five times slower as well. If electrons are present in a system which are more loosely bond, such as lone-pair electrons, they are usually at higher distances with respect to the nucleus to be found. Such expanded electron clouds, especially in heteroatoms and anions, are therefore better described by adding diffuse functions. They lead to a slower fall off of the functions as the distance  $r$  increases. Commonly, a basis set with diffuse functions uses one diffuse function based on one Gaussian for each atomic orbital of the valence shell. A calculation of a methylene carbene via 6-31G would use in total 19 functions, while 6-31++G\* uses already 25 basis functions and 6-31++G\*\* uses 31 basis functions.

In addition, larger basis sets, such as 6-311G\*\* are mostly used in subsequent calculations or simple single-point energy calculations.

One important basis set related error is the basis set superposition error. If interaction energies between two fragments A and B are calculated and the system AB. If the region of the basic functions of A overlaps with the location of the wavefunction B, the basis set can partially be increased by the functions from A and leads to a variation of the determined energy of B in comparison to the isolated fragment of B.

## Density Functional Theory

The *ab initio* and semiempirical methods are approaches to analyze molecules by solving the Schrödinger equation by constructing many-electron wavefunctions. However, in the 1980s a different approach came up, which put the electron density distribution function  $\rho(x, y, z)$ , rather than the wavefunction, in the center of the calculation algorithm. One advantage, when it comes to accuracy *versus* time consumption is the fact, that wavefunction calculations require  $4n$  variables (three spatial variables and the spin variable), while the electron density function only uses three variables in total. It is furthermore a more intuitively comprehensible property, and especially an accessible observable. However, it is noteworthy, that the exact mathematical form of the DFT functional is not known.

Current DFT methods are based on the Kohn-Sham approach. Which were developed based on two theorems by Hohenberg and Kohn in 1964 [363]. The first of these fundamental theorem's states, that all properties of a molecule in its electronic ground state are determined by ground state electron density function  $\rho_0(x, y, z)$ . Accordingly, any ground state property can be obtained by calculations of the electron density.

$$\rho_0(x, y, z) \rightarrow E_0 \quad (63)$$

Therefore, the ground state energy is a functional of the ground state electron density. Moreover, this theorem basically states that a functional exists, from which the properties can be calculated. However, the functional is still unknown.

The second Hohenberg-Kohn theorem states that any trial electron density function will lead to an energy, which his higher or equal to the true ground state energy.

$$E_v[\rho_t] \geq E_0[\rho_0] \quad (64)$$

With the trial electronic density  $\rho_t$  and  $E_0[\rho_0]$  is referred to the true ground state energy at the true ground state electronic density  $\rho_0$ . For that purpose, the trial density has to satisfy a criterion, similar to the wavefunction normalization, which is

$$\int \rho_t(r) dr = n \quad (65)$$

Basically, Kohn and Sham developed the Kohn-Sham (KS) approach for calculating Kohn-Sham energies in a very similar manner to the variational approach of the Hartree-Fock method [364]. Thus, the KS-approach means that the molecular energy is calculated via a sum of terms, from which one small term involves the unknown functional. In addition, the KS orbitals and their energies are calculated by starting with an initial guess of the electron density. The calculation of the molecular properties follows then an iterative process similar to the HF SCF method.

The approach is based on separating in two parts. One of them is a noninteracting reference system, a system in which no electron interaction occurs and can therefore be calculated accurately. The real deviations of the electron correlations are put into another term which requires the functional.

The general ground state electronic energy  $E_0$  of a real molecule is calculated by the sum of kinetic energies  $T$ , electron-nucleus attraction potentials  $V_{Ne}$  and the electron-electron repulsion potentials  $V_{ee}$  as a function of the ground state electron density  $\rho_0$

$$E_0 = \langle T[\rho_0] \rangle + \langle V_{Ne}[\rho_0] \rangle + \langle V_{ee}[\rho_0] \rangle \quad (66)$$

The nucleus-electron attraction term in the middle can be written as a classical electrostatic attraction potential energy expression, so that the kinetic and potential energy terms are left. The KS approach is based on separation of the interacting from the noninteracting system. Accordingly, the kinetic term  $\langle T[\rho_0] \rangle$  is separated into the kinetic term for the real electronic kinetic energy  $\langle T[\rho_0]_{real} \rangle$  and the reference system  $\langle T[\rho_0]_{ref} \rangle$ , which gives the deviation of the real system, expressed as

$$\Delta \langle T[\rho_0] \rangle \equiv \langle T[\rho_0]_{real} \rangle - \langle T[\rho_0]_{ref} \rangle \quad (67)$$

Similarly, a deviation of the electronic potential energy  $\Delta\langle V_{ee} \rangle$  is defined by a real term and the reference term which is described as a classical charge-cloud coulomb repulsion energy, which covers the sum of all repulsion energies for infinitesimal volume elements separated by the distance  $r_{12}$ .

$$\Delta\langle V_{ee}[\rho_0] \rangle = \langle V_{ee}[\rho_0] \rangle_{real} - \iint \frac{\rho_0(r_1)\rho_0(r_2)}{r_{12}} dr_1 dr_2 \quad (68)$$

Both reference terms can be summarized as the deviation from the classical system and are described as the exchange-correlation energy  $E_{xc}$ . Using a Slater-determinant to express occupied spin molecular orbitals, the Kohn-Sham spin orbitals of the reference system can be calculated. Each orbital consists of a spatial orbital  $\psi_i^{KS}$  and a spin function  $\alpha$  or  $\beta$ . Accordingly, the ground state energy term is rewritten as

$$E_0 = - \sum_{nuclei A} Z_A \int \frac{\rho_0(r_1)}{r_{1A}} dr_1 - \frac{1}{2} \sum_{i=1}^{2n} \langle \psi_i^{KS}(1) | \nabla_1^2 | \psi_i^{KS}(1) \rangle + \frac{1}{2} \iint \frac{\rho_0(r_1)\rho_0(r_2)}{r_{12}} dr_1 dr_2 + E_{xc}[\rho_0] \quad (69)$$

Differentiation of  $E_0$  with respect to the spatial Kohn-Sham molecular orbitals under orthonormal conditions leads to the Kohn-Sham equations. The Kohn-Sham operator includes the terms of the above terms and the exchange correlation potential, which is a functional derivative of the exchange-correlation energy, respectively. The obtained eigenvalues are the Kohn-Sham energy levels. In contrast to the HF method, which gives an exact solution of an approximation of the real energy, the KS-DFT method is an approximate solution to an exact energy description.

In order to solve the Kohn-Sham orbitals and energy levels

1. Geometry specification
2. Basis set and functional specification
3. Initial guess of the electron density
4. Calculate from there an initial guess of the exchange-correlation potential from  $\delta E_{xc}/\delta \rho$
5. Calculation of the KS operator
6. Calculation of KS matrix elements

7. Orthogonalization of the KS matrix and energy level matrix
8. Calculate improved electron density from first-iteration values of the KS MO's
9. Repeat from step 4
10. Calculate energy after convergence

Among the numerous functionals, that exist a few categories of functionals are used in KS-DFT. These are the local density approximation, the local spin density approximation, the gradient-corrected functionals, *meta*-generalized gradient approximation functionals and hybrid general gradient approximation functionals. The latter are functionals which incorporate HF exchange, which is the correction energy to the classical Coulomb repulsion. The used percentage of the HF exchange energy term varies. The most widely used and described hybrid functional is B3LYP [365-367] which is based on B3PW91 [368].

## **Molecular Mechanics**

So far, the described methods were based on quantum mechanical descriptions of atoms and molecules with the major challenge of approximating the real situation of a molecule and to calculate an energy which is higher than the true energy. These calculations involve very complex integrals and determinants and use an iterative process to approach a low energy. With higher levels of theory, the computational costs and resource demand increases rapidly. Therefore, for large systems this becomes a nearly impossible job. When large molecules such as enzymes and polymers are investigated, several thousands of atoms and electrons are part of it. For these large systems, another type of methodology is used, the molecular mechanics or also known as force field method.

In molecular mechanics, the molecules are basically described as ball and springs. The atoms have different sizes and a variational level of hardness and the bonds have, like springs, different stiffness and length. The energy is accordingly expressed as a parametric function of the nuclear coordinates of the atoms. Each term involves parameters which are fit to experimental or higher-level computational data. In that manner, the electrons as particles and their quantum mechanical aspects are neglected.

The idea and foundation of molecular mechanics goes back to the experimental observation that a kind of transferability between different molecules composed of similar or identical structural units, functional groups, exists. Specific bond length, for instance C-H, bond lengths

are about the same in different molecules. Vibrational frequencies, determined by means of FT-IR spectroscopy, are usually in the same range for the same structural units in different molecules. The heat of formation for instance increases linearly within the homologous series of linear alkanes with each additional methylene group. Therefore, the parametrization of specific units can be used to describe molecules and use the same set of descriptions for analogous units in other molecules (Figure 361). This means that no individual solution for any new molecule has to be made in order to simulate physical properties of a set of different molecules.

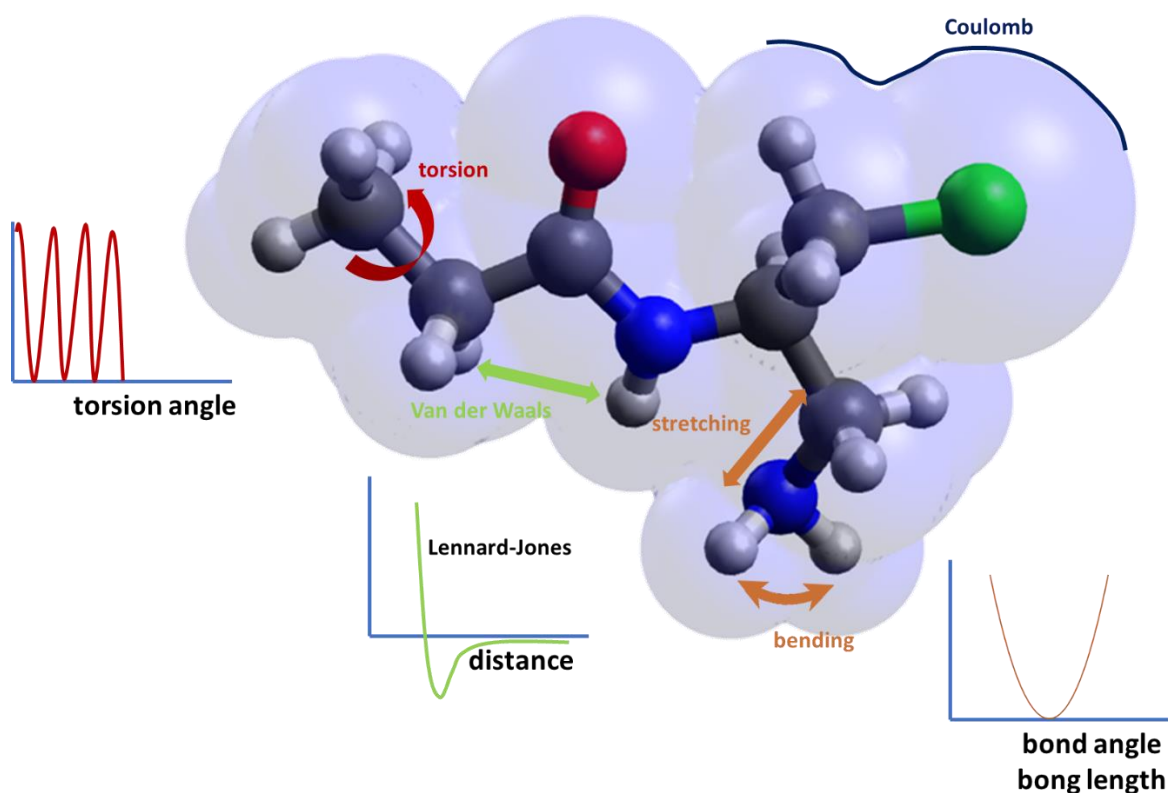


Figure 361. Geometric and molecular interactions within a modelled molecule, symbolized by means of exemplified bending, torsion, stretching, its Van der Waals interaction and the molecular surface which is correlated with the coulombic interactions. In addition exemplified energy profiles of these parameters are shown.

## Force fields

The energy of a molecular system is calculated by means of the force field energy, the energy that is based on the force field description of the molecular system (Figure 361). The terms involved are

$$E_{FF} = E_{str} + E_{bend} + E_{tors} + E_{vdw} + E_{el} + E_{cross} \quad (70)$$

with the stretching energy ( $E_{str}$ ), bending energy ( $E_{bend}$ ), torsional energy ( $E_{tors}$ ), the non-bonded atom-atom interactions ( $E_{vdw}$  and  $E_{el}$ ) and coupling of the first three described terms via  $E_{cross}$ .

Special atom types have to be defined for specific bonds. For instance, the carbon atom in cyclopropane is  $sp^3$  hybridized just as in its linear form of *n*-propane. However, geometrical differences, such as the angle and dihedrals, affect the final geometry significantly and are not comparable. Accordingly, for the carbon atom in a three-, four-, five-membered ring and higher different parametrizations occur, which are included for each term for a specific atom type. Therefore, the angle of  $60^\circ$  in cyclopropane is used rather than the  $110^\circ$  in the linear acyclic propane. Another example is a C-N bond, which differs if it is a single, double, or triple bond and it differs if it is part of a cyclic or acyclic system. Therefore, specific atom types were developed to describe an -C=N bond in benzoxazole other than in oxazolidine or carbodiimide for instance.

**Stretch Energy.** This is the energy term describing the energy of stretching a bond between two Atoms A and B, which is commonly evaluated as a Taylor expansion around the bond length  $R_0$ .  $R_0$  is the equilibrium or natural bond length. However, in large molecules  $R_0$  will not be the equilibrium bond length but rather shifted to higher values due to the influence of bond stretching and torsion around it. In its simplest form it is

$$E_{str}(\Delta R^{AB}) = k^{AB}(\Delta R^{AB})^2 \quad (71)$$

With  $\Delta R^{AB} = (R^{AB} - R_0^{AB})$ , and  $k^{AB}$  as the second derivative of the energy with respect to the natural bond length, which is according to Hooke's law the force constant and the form (71) is described as the harmonic oscillator. In more complex systems, when the system cannot be described accurately by the harmonic oscillator, other terms are added via polynomial expansion or the Morse potential is used.

**Bending energy.** The bending around a bending angle between three atoms A-B-C the energy can be expressed as harmonic approximation

$$E_{str}(\theta^{ABC} - \theta_0^{ABC}) = k^{ABC}(\theta^{ABC} - \theta_0^{ABC})^2 \quad (72)$$

Such a second order expansion is usually accurate enough, when the chemical region below a value of approximately 40 kJ mol<sup>-1</sup> above the curve bottom of the energy curve is investigated. Otherwise, additional terms or the exact form from electronic structure calculations must be used. The calculation loses accuracy if the central atom B is sp<sup>2</sup> hybridized. The large energy cost to make the preferred planar form to a pyramidal structure would only be achieved with large force constants, which make the system unrealistically stiff. Therefore, an additional term  $E_{oop}$  with the out-of-plane angle  $\chi$  is used, for such an out-of-plane bending. The additional term would be

$$E_{oop}(\chi) = k^B \chi^2 \quad (73)$$

**Torsional energy.** A torsional energy is associated with the energy change of a rotation of a A-B and C-D bond to each other around the bond B-C in a A-B-C-D four-atom sequence. Accordingly, the formed angle  $\omega$  is described in the range from 0 to 360 or -180 to +180°. Such a torsional energy term deviates from the previously energy terms, since the torsion is periodic, so a rotation of 360° should give the same energy. The non-bonded terms contribute as well and the deviation from the minimum energy structure is likely to occur because of the low energy cost of a distortion via torsional variation. The term for  $E_{tors}$  in its simplest form is written as a Fourier series

$$E_{tors}(\omega) = \sum_{n=1} V_n \cos(n\omega) \quad (74)$$

A more general form, which also shifts the zero point of the potential by an addition of one per term and a phase factor  $\tau$  is

$$E_{tors}(\omega^{ABCD}) = \frac{1}{2} V_1^{ABCD} [1 + \cos(\omega^{ABCD} - \tau_1)] + \frac{1}{2} V_2^{ABCD} [1 - \cos(2\omega^{ABCD} - \tau_2)] + \frac{1}{2} V_3^{ABCD} [1 + \cos(3\omega^{ABCD} - \tau_3)] \quad (75)$$



**Van der Waals energy.** The van der Waals energy is one of both non-bonded energy terms. It describes the attraction or repulsion between atoms that are non-bonded. An example are interactions of CH<sub>4</sub> molecules or methyl groups with each other. Interactions that are non-polar in their interaction. The  $E_{vdw}$  becomes very large at short distances due to repulsive interactions due to the interaction of electron clouds of both atoms. This leads to Exchange and Coulomb interactions between the electrons of both clouds. At high distances, the interactions become zero, while at intermediate distances both clouds can interact by attraction due to dipole-dipole interactions, which are physically better described as being caused by electron correlation. Temporary shifts of the electron cloud due to their motions, induce a dipole moment, which in turn induces a charge polarization in the adjacent molecules, which leads to attraction between both. The force of such a potential is called dispersion or London force. A very general form is

$$E_{vdw}(R^{AB}) = E_{repulsion}(R^{AB}) - \frac{C^{AB}}{(R^{AB})^6} \quad (76)$$

One of the most widely known and used potentials, that fulfil the requirements of having very positive values at small distances, a negative value at the van der Waals distance and approaching zero at large distances, is the Lennard-Jones (LJ) potential

$$E_{LJ}(R) = \frac{C_1}{R^{12}} - \frac{C_2}{R^6} \quad (77)$$

Other potentials, such as the buffered 14-7, or Hill type potential.

**Electrostatic energy.** Electrostatic interactions due to the molecularly internal distribution of the electrons between two centers creates a positive and negative part of a molecule. For example, highly electronegative groups, such as oxygen atoms in carbonyl groups cause a partially negative charge at the oxygen atom and a partially positive charge at the carbonyl carbon atom. The interaction of charged functional groups for instance can be expressed by the Coulomb potential, which is defined for the interaction between point charges with atomic charges  $Q$ , dielectric constant  $\epsilon$  and the distance between both point charges  $R^{AB}$

$$E_{el}(R^{AB}) = \frac{Q^A Q^B}{\epsilon R^{AB}} \quad (78)$$

The atomic charges can be assigned via empirical rules, but it is more accurate to fit electrostatic potential from electronic structure calculation methods.

**Cross terms.** All discussed terms so far are general energy expressions, which are part of each force field. Effects on one term can affect other terms as well in real molecules. For instance, if the equilibrium angle of water ( $105^\circ$ ) is reduced to  $90^\circ$  by compression, then the natural bond length  $R_0$  increases from 0.958 to 0.968 Å. This is reasonable, as the hydrogen atoms come closer and experience increased repulsion. Hence, the O-H bond length increases. Nevertheless, such a correlation would not follow by simply calculating all five energy expressions. Hence, a sixth term includes a set of terms which couple the bonded terms in different manners and can couple two or more terms. The most important coupling term is the stretch-bend correlation

$$E_{str/bend} = k^{ABC} (\theta^{ABC} - \theta_0^{ABC}) [(R^{AB} - R_0^{AB}) - (R^{BC} - R_0^{BC})] \quad (79)$$

Other corrections could be the parameter correction by atoms that are not directly involved. 1-Fluoroethane for example would show a strong effect on the C-C bond by the influence of the electronegative fluorine atom. A consequence would be a shortening of the C-C bond. This issue can be improved by adding a correction to the natural bond length  $R_0^{CC}$  of the ethyl group (CC),

$$R_0^{CC-F} = R_0^{CC} + \Delta R_0^F \quad (80)$$

## Force fields

Various force fields exist, and the user must choose appropriately, which force field is suitable to the task, which is not always a straightforward question to answer. To tackle many different aspects of bonding and non-bonding interactions. The main aspects to answer prior use of a force field is

- 1) What is the functional form of each energy term in the force field equation?
- 2) How many cross terms to couple the first three terms are included?
- 3) How are the parameters fitted, what information were used?

Three classes exist in general. Class I are force fields used for large molecules, such as polymers and biopolymers, which use simple terms, for instance only the harmonic functions and no cross terms. For the van der Waals term the LJ potential is used. Medium sized molecules, are commonly calculated with class II force fields, which include cross terms and even quartic expansions of the stretch and bend term. They target to simulate vibration frequencies for instance. Class II force fields are of the highest accuracy and include electronic polarization and neighboring atom effects, such as hyperconjugation.

**Dreiding.** The Dreiding forcefield is a general forcefield, which allows reasonable predictions for many structures, but not as accurate as specialized forcefields do. Due to its low limitation to various structures, it is interesting to use for molecules, which lack experimental data. Parameters were obtained by a rule-based approach on simple hybridization rules. It is based on harmonic valence terms and a cosine-Fourier expansion term. It uses the LJ potential to express the van der Waals energy. It goes back to Mayo *et al.* in 1990 [369].

**AMBER.** AMBER, which is short for assisted model building and energy refinement by Weiner *et al.* from 1984 [370], was developed for the simulation of biopolymers, such as proteins and nucleic acids. The parameterization was done via calibration against experimental data from neutron diffraction and microwave experiments in connection with quantum chemical studies.

**Universal Forcefield.** This is a harmonic forcefield, in which bond stretching is described via a harmonic term, while angle bending is expressed via a three-term Fourier cosine expansion. The Van der Waals potentials are described by the LJ potential. It covers the full periodic table and is moderately accurate for calculating conformational energy differences and geometries of organic molecules. The parameterization is done via a parameter generator by combining atomic parameters, using a set of rules. The forcefield was developed by Rappé *et al* in 1992 [371]. The forcefield is a general purpose forcefield.

**CVFF.** The consistent valence force field with cross term enhancements and a few anharmonic terms. It is a general forcefield and presented by Dauber-Osguthorpe *et al.* in 1988 [372]. It can generate parameters if no specific parameter is available. IT was designed for peptides and amino acids and extended as augmented CVFF for materials science applications. The bond-stretching term is extended by a Morse potential.

**PCFF forcefield.** The polymer consistent forcefield is based on the CFF91 forcefield and designed for organic and polymeric materials. Polymers such as polycarbonates are intensively studied using PCFF. It is validated for a large list of functional groups such as carbonates, carbamates, urethanes, silanes and ureas as well as zeolites.

**COMPASS.** COMPASS (Condensed-phase optimized molecular potentials for atomistic simulation studies) is the first *ab initio* forcefield which gives accurate results of gas-phase and condensed phase properties, such as the cohesive energy density for molecules and polymers [373, 374]. It is a consistent forcefield, like PCFF, and differs especially in the parameterization of the functional groups. The form is

$$\begin{aligned}
E_{pot} = & \sum_b [K_2(b - b_0)^2 + K_3(b - b_0)^3 + K_4(b - b_0)^4] \\
& + \sum_\theta [H_2(\theta - \theta_0)^2 + H_3(\theta - \theta_0)^3 + H_4(\theta - \theta_0)^4] \\
& + \sum_\phi [V_1[1 - \cos(\phi)] + [V_2[1 - \cos(2\phi)] + [V_3[1 - \cos(3\phi)]] \\
& + \sum_x K_x x^2 + \sum_b \sum_{b'} F_{bb'}(b - b_0)(b' - b'_0) + \sum_\theta \sum_{\theta'} F_{\theta\theta'}(\theta - \theta_0)(\theta' - \theta'_0) \\
& + \sum_b \sum_\theta F_{b\theta}(b - b_0)(\theta - \theta_0) \\
& + \sum_b \sum_\phi (b - b_0)(V_1 \cos(\phi) + V_2 \cos(2\phi) + V_3 \cos(3\phi)) \\
& + \sum_{b'} \sum_\phi (b' - b'_0)(V_1 \cos(\phi) + V_2 \cos(2\phi) + V_3 \cos(3\phi)) \\
& + \sum_\theta \sum_\phi (\theta - \theta_0)(V_1 \cos(\phi) + V_2 \cos(2\phi) + V_3 \cos(3\phi)) \\
& + \sum_\phi \sum_\theta \sum_{\theta'} K_{\phi\theta\theta'} \cos(\phi)(\theta - \theta_0)(\theta' - \theta'_0) + \sum_{i>j} \frac{q_i q_j}{\epsilon r_{ij}} + \sum_{i>j} \left[ \frac{A_{ij}}{r_{ij}^9} - \frac{B_{ij}}{r_{ij}^6} \right] \\
& + \sum_{i>j} \left\{ D_0 \left[ \exp\left(-\left(\frac{y}{2}\right)\left(\frac{r_{ij}}{R_0} - 1\right)\right)^2 - 2 \exp\left(-\left(\frac{y}{2}\right)\left(\frac{r_{ij}}{R_0} - 1\right)\right) \right] f_s - (1 - f_s) \frac{C_6}{r_{ij}^6} \right\}
\end{aligned} \tag{80}$$

In the form of the COMPASS forcefield quadratic polynomials for the first term, bond stretching, and the second term, angle bending, is used. The torsional term is expressed as a

three-term Fourier expansion. Terms 5 to 11 are cross terms. The van der Waals term is expressed as the inverse 9<sup>th</sup>-power term for the repulsive description.

The parameterization is based on a previous forcefield CFF. Most of the parameterized data is derived from *ab initio* calculations. First atomic partial charges were obtained by calculation of *ab initio* electrostatic potentials (ESP) via a constrained ESP approach to solidify the transferability. Valence parameters were calculated by CFF *ab initio* parameterization techniques using total energies and their first and second derivatives with respect to the cartesian coordinates of the atom. In addition, the forcefield was optimized with focus on experimental data. The van der Waals parameters were optimized.

The COMPASS forcefield was strongly validated by liquid, polymer and crystal simulations using molecular dynamics simulations.

The forcefield was developed for most inorganic, organic molecules and especially for polymers in condensed-phase and isolation. Properties, such as the cohesive energy density, dipole moments, vibrational frequencies, conformational energies, and molecular structures are accurately simulated. It is further strongly validated for solid-state properties.

## **Molecular Dynamics**

Many materials science questions are related to the question on how a system behaves by time at specific finite temperatures and how do other components interact in a classically physical way, such as swelling, penetration or adsorbing. One possibility is to simulate a system by letting it evolve using the dynamical equation of Newton's second law, if nuclei are assumed to be heavy enough to behave as classical particles.

$$F = ma = m \frac{d^2r}{dt^2} \tag{81}$$

with the force  $F$ , mass of the nuclei  $m$ , acceleration  $a$ , position  $r$ . The position after a specific time  $\Delta t$  can be estimated by using a Taylor expansion.

$$q(t + \Delta t) = q(t) + \frac{dq(t)}{dt} \Delta t + \frac{d^2q(t)}{dt^2} \frac{\Delta t^2}{2} + \dots \quad (81)$$

For MD simulations, first, a model system has to be chosen by taking into account that the number of atoms increases the computational costs. With higher level force fields, the number of parameters increases rapidly otherwise. Afterwards it is necessary to generate the initial structure, which is usually done using visualization tools or text input. In addition, the method must be chosen. These can be *ab initio*, DFT or molecular mechanics and in some cases hybrid quantum mechanical- and molecular mechanics methods must be used. However, in most cases, especially when large molecules, such as polymers are investigated, the choice is to use molecular mechanics. If the system of interest is close to previously studied and reported systems, an appropriate forcefield can be chosen. Otherwise, adaptations must be made. The fourth step of a molecular dynamics simulation involves the assignment of initial velocities for each atom. According to eq (82) a system at a given finite temperature will have a kinetic energy of

$$E_{kin} = \sum_{i=1}^N \frac{m_i |v_i|^2}{2} = \frac{3}{2} N k_B T \quad (82)$$

To match the above equation for the kinetic energies, one can choose to assign random velocities for each atom, followed by scaling each velocity by a constant.

The fifth step of a MD simulation is the propagation of the trajectory for a specified and required number of time steps  $n_{step}$ . One very crucial part of this step is the integration of the trajectory and the chosen time step  $\Delta t$ , which must be shorter than the time range of the fastest motion in the system. The chosen time step must be long enough to determine a total trajectory which is long enough, with a number of steps that is small enough to achieve an accurate integration. The total trajectory time is described by  $\Delta t \times n_{step}$ . A fast H-X vibration, for instance, with vibrations around 3000 – 4000  $\text{cm}^{-1}$  has vibrational periods of about 10 fs. Therefore, typically time steps are chosen between 0.1 and 1 fs. Before setting up a simulation, it is also

required to choose an ensemble, which is basically a statistical mechanical description. To implement the equations of Newton's second law, via Verlet's equations, which were derived from them, is done under periodic boundary conditions by which the total energy  $E$ , number of atoms  $N$  and volume  $V$  at each time step remains constant. Such a system is called the  $NVE$  ensemble. Nevertheless, since most experiments are done under isothermal or isobaric conditions, another ensemble, such as  $NVT$  or  $NpT$  are chosen.  $NVT$  means, that the number of particles  $N$ , volume  $V$  and temperature is constant throughout the simulation. Simulations under  $NVT$  conditions require modifications of the equations of motion by using thermostats. The Nosé-Hoover thermostat for example uses the introduction of fictitious particles in an extended system. Apart from the Nosé-Hoover thermostat, there exist the Berendsen thermostat, Andersen thermostat and Langevin dynamics. Applying  $NpT$  conditions requires accordingly the use of a barostat.

## ACKNOWLEDGEMENT

This is actually the part, which makes the most fun to write (apart from the results section of course). The work of a Ph.D thesis is sometimes a long and sometimes an even longer process. While I followed this path from a Master Student all across the experimental work part of my PhD thesis up to starting to work at a chemical company, I dealt with people that supported me and helped me. A Ph.D work in cooperation with colleagues is a great thing and more and better ideas evolve that way. Therefore, I would like to start by thanking everyone for his support and part of this journey. First of all, I would like to thank Prof. Abetz for giving me the opportunity to work with such a great team on a very interesting topic. I was able to organize my research very independently, which gave me the space and opportunity to work on many aspects and to work as the researcher, the way I appreciate it to work. I am thankful for the discussions and of course for the support, that I was allowed to spend eight months at the MRL, UCSB in Santa Barbara as a visting researcher. Thank you for allowing me to work with the molecular modelling tools at the end of my thesis in order to learn these new techniques as well.

I very appreciate and am truly thankful for working with you, Volkan. You supported me during my thesis, and I have to admit, it wasn't always easy with me. I always had my ideas and thoughts and wanted to do new things, even at the very end of my experimental time in Geesthacht. Thank you for letting me work independently and for supporting me. It was always great to talk to you about chemistry but also about everything else. Thank you!

About my colleagues Silvio, Petra, Ivonne and Silke--what can I say. You are amazing. You did and you do a great job in what you do. The way you help and support and the incredibly professional way, how you do the works. You sometimes helped me, before I even asked. Silvio's knowledge about thermoanalysis and microporous polymers extends that of most students and scientists on that topic. With your experience and kind way to help, this whole story was possible. Apart from that, you have the curiosity and motivation to find out new things, independently if it is your research or from others day by day. I was always thankful



for that and I appreciated you as a colleague and even more as a friend (still). Ivonne and Petra and Silke were always the good spirits. You organized everything, even if we, students, asked for the 10<sup>th</sup> time, you still helped us. Everyone of you helped and supported me a lot and even after my time in Geesthacht, you were there to help. Thank you all so much!

I thank everyone else at the Institute of course. Sergey for all the fruitful discussions regarding membranes and polymers. You really “live” in that membrane world and you love it, and to see your passion about membranes was always inspiring. Thank you for that.

I also have to thank Anke, Christian, Maria, Karabi, Thomas, Judith, Sarah and Elvin, Florian. It was always a pleasure to work with you and to have lunch with you. Anke and Christian, you always had the right words and suggestions, when I needed them. I always knew and I know, that I can always count on you, as you helped during the last five years, whenever I asked you for it. I appreciate you a lot and I'm happy to see you the next time.

Thanks to everyone in the institute who helped and supported me. Thorsten for helping with the Server, Thomas for NMR support and discussions and Maren for help with GPC experiments. Prokopios and Sofia for scientific discussions, help with dielectric measurements and for all non-chemistry topics as well, it was always great to talk to you.

I also want to thank Alberto, for getting me into the topic of TR polymers.

I also want to take the opportunity to thank everyone at the “Studienbüro and Promotionsbüro” at the university for your help and advices during the last ten years, thank you a lot.

I also wanted to thank all my colleagues at Covestro, who, especially during the last weeks, did everything possible to give me the time and freedom to organize myself. Thank you for taking away any pressure in order to manage both sides. This helped me a lot. Thanks for your support and I want to thank my colleague Johannes for all the important discussions about quantum mechanical simulations, which was always very helpful and made it much easier and faster for me to execute the simulations.

I also want to thank the team in Santa Barbara, who by now either have their own research groups or work in the chemical industry. I appreciated, that I was able to take part in some of your projects and that I could learn so many new techniques. I'm happy that we weren't only colleagues, but became friends and I enjoyed my time a lot. Thanks to Craig, who also gave me the chance to be there and to work on these projects.

I also want to thank Patric and Anika, who were my supervising professor and supervisor in the lab during my 5 months stay in Lund, Sweden. I went there and it was the first time, that I worked with membranes. I learned a lot from you both. I was able to take part in a project and I got my first publication, which was truly inspiring for me and that is how I came into the membrane community and decided to work on membranes for my PhD studies. I always appreciated your open-minded discussions, even after my stay. I hope to hear from you in the future and see you the next time I visit Lund.

Finally, I want to thank my family and friends. During the last two years, I was very busy and did not take the time, that I should have to. I thank you so much for understanding and supporting me. I thank my parents and parents-in-law and my sister Cyrielle and my brother René for everything, especially during the last five years. I also want to thank Jakob and Kim, who spend the time with me, since our first day at the university. I shared the first fumehood with you, and let's see if it is also the last one, since we are again colleagues, just 400km south of Hamburg. I don't know, how the years at the university would have been without you two. I appreciate you as great friends. This was a tough time, but I couldn't have done it without my family and friends in the same way and I think you know how thankful I am, cause the open space in this text is not enough to describe it and this goes especially to my wife Ulli and my little wild and crazy daughter Emily. For the last two years, there were so many evenings, weekends that I had to spend on analyzing and writing. Especially within the first 4 months of Emily, this was very tough. Thank you so much for supporting me, having my back and being there for me. You are the greatest and I'm very happy to have much more time with you.

## Eidesstattliche Erklärung

Hiermit versichere ich an Eid statt, die vorliegende Dissertation selbst verfasst und keine anderen als die angegebenen Hilfsmittel benutzt zu haben. Die eingereichte schriftliche Fassung entspricht der auf dem elektronischen Speichermedium. Ich versichere, dass diese Dissertation nicht in einem früheren Promotionsverfahren eingereicht wurde.

16.03.2021,   
Datum, Unterschrift

## Statement in Lieu of an Oath

I hereby declare in lieu of an oath that I have written this thesis on my own and that I have not used any other resources or aids than the ones referred to in this thesis. This thesis has never been submitted in any form for any other examination. No other doctorate was attempted or pursued at a different location.

16.03.2021   
Date, signature